



***Chapter 1***  
**Communication Engineering, Systems, and  
Networks**



المؤتمر العربي الليبي الدولي الخامس للهندسة الكهربائية والإلكترونية 23-26/10/2010 طرابلس ليبيا





# Impact of Introducing a Hot spot micrcell On Capacity-Coverage Stability in a WCDMA mobile network

Mohamed Elalem; melalem@ryerson.ca. EC Dept,  
Dr.A.S.Akki EE Dept Al-Fateh University,  
and Dr. L. Zhao Ryerson University, ON, Canada

## Abstract

Since the natural user distribution is not uniform over any geographical region and the real traffic load changes inside the cell; many times, there exist hotspots; or small regions of high-traffic density inside macrocells. The presence of these hotspots will cause coverage reduction. If the base station serves a large number of users from the high-traffic regions (hotspots), then it must block access to users located elsewhere in the (larger) intended coverage area. Therefore, the actual coverage area of the macrocell base station shrinks in order to support the hotspot users. So if this hotspot users are served individually by an own microcell, their disturbances on the macrocell base station will be reduced and the coverage area will not be affected by their jam. This may be done by installation of hotspot microcells BS inside the existing macrocell BS. A cellular system that contains both macrocells and microcells is referred to as a two-tier system[1]. Hotspots have not been studied extensively in the past. Most of studies focus on algorithms and techniques to improve the capacity and performance of the network in the presence of hotspots. There has been a lack of researches that specifically studies properties of hotspots in detail[2][3][4].

## I. Introduction

In Wideband Code Division Multiple Access (WCDMA), the Coverage and capacity are dependent ; it is interference-limited system, meaning that if the traffic increases, the serving cell radius decreases, hence the phenomena of cell breathing occurs. One of them is inversely proportional to the other. A great deal of work has been done over the last

decade to study optimal CDMA cell design in order to minimize the number of cell sites required while maintaining the grade of services Earlier studies have examined the uplink performance of two-tier CDMA systems, most of them deal with the user capacity calculation and the impact of various parameters on this calculations with support of simulations. [5], show how to compute the uplink user capacity (two-cell) system using exact and



approximate methods While in [6] it is examined the effect of transmit power constraints on the uplink performance of the same system model, they developed a reliable analytical method for computing the capacity as a function of maximum transmit power constraint the study was supported by simulations and highly accurate results were obtained.

The same authors of the previous ref. study in [7] the effect of soft handoff on capacity of a CDMA two tier system by using simulation, they conclude that there is some enhancement in capacity compared to hard handoff and this improvement will become more modest as the system be more wideband. This paper differs slightly from previous work where the coverage stability is our objective by maintain the same or better capacity, since the presence of hotspot regions will cause coverage reduction and block access to users located else where in the (larger) intended coverage area. Therefore, the actual coverage area of the macrocell base station shrinks in order to support the hotspot users. So if this hotspot users are served individually by an own microcell, their disturbances on the macrocell base station will be reduced and the coverage area will not be affected by their jam.

Installing low-power microcell in an existing macrocell may enhance the capacity and attempt to keep the stability of the coverage area supported by the existing high-power macrocell BS . In this paper we study the gains in capacity and coverage and design some system parameters as power ratio and the location of the microcell from the macrocell.

The main two types of microcell hotspot and the benefits of this approach are given below. The types of microcells can be studied in one of two pictures: 1.

Overlay microcells which are small cells arranged almost all of the coverage area of the larger (umbrella) macrocells and effectively serve as an alternate "system" which users can access. There may be several factors used by the cellular system in deciding how users are assigned to different tiers. For example, users may be assigned to tiers according to their mobility; fast moving users are given access to macrocells and slow-moving or pedestrian users are given access to microcells. As another example, users may be assigned to tiers according to their data rates; high-data-rate users are given access to microcells and low-bit-rate voice users are given access to macrocells. This type of architecture was studied in several papers and the result of most of them leads to high cross-tier interference (and so poor capacity performance) because of:

- I. the large number of microcells, and
- II. the lack of handoff between tiers.

Hotspots have been studied extensively in the past, there has been some work that considers hotspots to balance the traffic and reduce congestions. Most of them focus on algorithms and techniques to improve the capacity and performance of the network in the presence of hotspots. There has been a lack of research that specifically studies properties of hotspots in detail.

This motivated the authors in [4] to conclude that different carriers must be assigned to different tiers to avoid excessive cross-tier interference. The overall performance of these dual-carrier systems can be determined by considering them as two independent, non-interacting CDMA systems. But this approach needs higher spectrum efficiency (measured in user capacity per carrier) and so more cost. This motivates us to use the second type which



is Hotspot microcell using the same carrier in both tiers.

2. Hotspot microcells are placed in small regions inside macrocells where there is high user density and installed in an existing cellular system to provide coverage only in smaller regions within macrocells. All base stations transmit a pilot signal, a new user in the system decides to communicate with the base station whose pilot signal it receives with the highest power. In other words, users can initially communicate with either macrocells or microcells. As users move around in this system, they may be handed-off from one base station to another. In determining the performance of hotspot microcells operating in a single-carrier CDMA system, it is important to quantify the effect of cross-tier interference. Increasing demands for capacity require the use of microcells. Overlaying a microcell on an existing macrocell provides the capacity for hot spot areas, shadowed regions, and downtown, etc. Sharing the same frequency by CDMA in overlay-underlay cell is a desirable approach:

The following benefits may be gained when using Hotspot microcells 1- Macrocell BS has antenna tower with height of 30 m or more, microcell BS are smaller, low cost units mounted on sites of building or on lamp posts with antenna heights of at most 10 m.

2- Macrocells have cell radius of 1 Km to 10 Km, while microcells have cell radius less than 1 Km, this reflects the reduction of low power level needed to be transmitted.

3- One other way to measure the benefits of microcells is to compare the total number of user capacity supported in a two-tier system as opposed to the single-tier system under the same hotspot condi-

tions. A larger user capacity means that the system supports a larger number of users per unit bandwidth, which in turn implies higher revenues (customer calls) per unit cost (spectrum).

4- Another benefit of deploying hotspot microcells lies in the resulting coverage area of the system. This benefit can be measured as the size of the geographical region over which users are given access. The gains in user capacity and coverage area depend greatly on the amount of cross-tier interference in the system; the performance gains are reduced as this interference increases. An other measure of gain is using The Capacity-Coverage Product (CCP) concept that is introduced in [8] (the idea is borrowed from an analogy of Bandwidth-Distance Product used in fiber optic system). This CCP is a criteria to provide maximum capacity with maximum coverage at certain system parameters and it may be used in the planning phase to optimize UMTS networks.

After this introduction the rest of the paper will be organized as follow: Section II draws the model of the system, while section III gives a numerical method to compute the cross-interference which is divided into two subsections. Section IV gives a direct way to find the Macrocell-to-Microcell Power Ratio. This section is followed by two sections which are illustrating the improvement of the system by this approach with help of a practical example. The conclusion is listed in section VII.

## II. The system Model and Assumptions

A hotspot microcell is embedded within a macrocell and operates over the same bandwidth as the larger cell. We are also

given that a macro cell BS of antenna height  $h_m$  and that of microcell is  $h_\mu$ . The Macrocell BS is placed at the origin and the microcell BS is a distance  $D$  from it as shown in Fig.(1). We assume that the coordinate axes are chosen such that the microcell lies at point  $(D,0)$ .

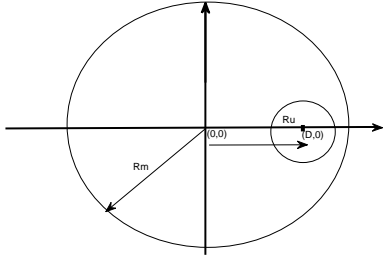


Figure 1: Geometric Configuration for the system model

The region of interest at the beginning phase is working properly with  $N_{old}$  active users which satisfy required performance  $E_b/N_o$  and cell loading factor  $\mu$ . Now number of users are increased such that the required number of active users is  $N$ , this will reduce the coverage. So a microcell is introduced within the macrocell such that  $N_m$  users in the macrocell and  $N_\mu$  users in the microcell, all transmitting at rate  $R$  on the Uplink. The number of users  $N$  in the system is thus  $N = (N_m + N_\mu)$ . The macrocell has a radius of  $R_m$  and that of microcell is  $R_\mu$ . Also perfect power control is assumed. All users's transmit powers are received equally at their BS. The required received power at the BS is  $S_m$  for the macrocell and  $S_\mu$  for microcell.

Avoiding complexity we will not consider the thermal noise power because of its finite value compared with the interference

value. The received  $E_b/N_o$  of macrocell is

$$\left(\frac{E_b}{I_o}\right)_m = \frac{G_p S_m}{\alpha(N_m - 1)S_m(1 + f_{mm}) + \alpha N_\mu S_\mu f_{\mu m}} \quad (1)$$

$G_p = W/R$  (Processing Gain)

The first term of the denominator is the sum of interferences from the macrocell users. Here  $f_{mm}$  denotes the macrocell-to-macrocell interference factor.

The second term of denominator is the interference from the microcell where  $f_{\mu m}$  is the micro-to-macro/cell interference factor.

Similarly, the received  $E_b/I_o$  of microcell is

$$\left(\frac{E_b}{I_o}\right)_\mu = \frac{G_p S_\mu}{\alpha(N_\mu - 1)S_\mu + \alpha N_m S_m f_{m\mu}} \quad (2)$$

where the first term of denominator is the interference from microcell and the second term is the interference from macrocell,  $f_{m\mu}$  denotes the macro-to-micro/cell interference factor. The interference from other microcells is ignored here, assuming that there is only the objective microcell. Before calculating the macrocell capacity with the interference from the microcell, let us think about the macrocell capacity,  $N_{m-pole}$ , for the case where there is no microcell. By eliminating the interference from the microcell in equation(1), we get

$$\left(\frac{E_b}{I_o}\right)_m = \frac{G_p}{\alpha(N_{m-pole} - 1)(1 + f_{mm})} \quad (3)$$

which gives:

$$N_{m-pole} = \frac{G_p}{\left(\frac{E_b}{I_o}\right)_m \alpha (1 + f_{mm})} + 1 \quad (4)$$

If the same work is done for microcell we get:

$$N_{\mu-pole} = \frac{G_p}{\left(\frac{E_b}{I_o}\right)_\mu \alpha} + 1 \quad (5)$$



Assuming that there is no other microcells in the region of interest.

Through some manipulations of the equations (2),( 3),( 4), and (5), we can obtain the capacity of the macrocell and microcell with mutual interferences

$$N_{\mu} = N_{\mu-pole} - N_m f_{m\mu} \psi \quad (6)$$

$$N_m = N_{m-pole} - \frac{N_{\mu} f_{\mu m}}{\psi(1 + f_{mm})} \quad (7)$$

where  $\psi$  is the ratio of the required received power of the macrocell to that of the microcell.

$$\psi = \frac{S_m}{S_{\mu}} \quad (8)$$

Combining (6) and (7), by eliminating  $\psi$ , gives the following relation for the capacity of the macrocell in terms of that of the microcell:

$$N_m = \frac{N_{m-pole}}{1 + \frac{N_{\mu} f_{m\mu} f_{\mu m}}{(N_{\mu-pole} - N_{\mu})(1 + f_{mm})}} \quad (9)$$

$N_m$  depends on the product of  $f_{m\mu}$  and  $f_{\mu m}$ . As the  $f_{m\mu} \cdot f_{\mu m}$  product increases, the capacity of the macrocell decreases.

### III. CROSS-TIER INTERFERENCE

In macro/microcellular CDMA systems, there exist four kinds of other cell interferences., the macrocell-to-macrocell interference. The microcell-to-microcell interference, the macrocell-to-microcell interference, and the microcell-to-macrocell interference. The last two are known as cross-tier interferences. Here we describe the method to calculate the cross-tier interference factors. A geometric approximation is adopted for the calculation of the microcell-to-macrocell interference factor. The area of the macrocell is divided into three regions for the

integration during the calculation of the macrocell-to-microcell interference.

#### A. Microcell-to-Macrocell Interference

The up-link total power of microcell users  $S_T$  (the sum of all users' transmit power) is obtained.[9]:

$$S_T = \int_0^{R_{\mu}} \int_0^{2\pi} S_{\mu} x^{\gamma} \rho x dx d\theta = \frac{2N_{\mu} S_{\mu} R_{\mu}^{\gamma}}{\gamma + 2} \quad (10)$$

where  $\gamma$  is the path loss exponent,  $\mathbf{x}$  is the location of the user, and  $\rho$  is density of microcell users ( $\rho = N_{\mu}/\pi R_{\mu}^2$ ), and  $S_1$  is the power transmitted by user 1, and is given as

$$S_1 = \frac{2S_{\mu} R_{\mu}^{\gamma}}{\gamma + 2} \quad (11)$$

If the users are assumed to lie uniformly on the circumference of a circle of radius  $R_{\mu-eq}$ , it can be shown that  $R_{\mu-eq}$  is related to  $R_{\mu}$  by :

$$R_{\mu-eq} = \left(\frac{2}{\gamma + 2}\right)^{\frac{1}{\gamma}} R_{\mu} \quad (12)$$

The interference from the microcell to the macrocell separated by distance  $D$  is given by [10]:

$$f_{\mu m} = \frac{1}{2\pi S_{\mu}} \int_0^{2\pi} \frac{S_1 d\theta}{(D^2 + R_{\mu-eq}^2 - 2DR_{\mu-eq} \cos(\theta))^{\gamma/2}} \quad (13)$$

Here the interference is normalized by the required received power  $S_{\mu}$ . The above integration may be solved analytically if  $\gamma$  is even. If it is four, the integration solution may be expressed as hyper-geometric function as follows:

$$f_{\mu m} = \frac{R_{\mu}^4 (D^2 + R_{\mu-eq}^2)}{3|D^2 - R_{\mu-eq}^2|} \quad (14)$$

This is obtained by using equation(11)

$$\frac{S_1}{S_\mu} = \frac{2R_\mu^\gamma}{\gamma + 2}$$

For different values of  $\gamma$  the integration (13) should be solved numerically. Table (1) shows the values of  $f_{\mu m}$  at different distances from the macrocell BS for the case of  $\gamma = 3.5$ . Clearly, this factor decreases as the microcell BS is being far from the macrocell BS.

Table 1: The values of  $f_{\mu m}$  at different distances

D	2r	3r	4r	5r	6r	10r
$f_{\mu m}$	0.446	0.379	0.358	0.349	0.344	0.337

### B. Macrocell-to-Microcell Interference

The macrocell-to-microcell interference factor is defined as the ratio of the out-interference caused by the users of macrocell received at the microcell BS to the in-cell interference caused by the users of macrocell which is given by [9]:

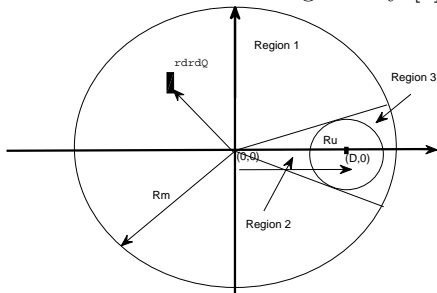


Figure 2: Geometric Configuration for the three regions

$$f_{\mu m} = \frac{1}{2\pi R_m} \int \int \left( \frac{r^2}{(r^2 + D^2 - 2rD \cos(\theta))} \right)^{\gamma/2} r dr d\theta \quad (15)$$

To solve this integration, we divide the cell area into three regions as shown in Fig

(2). The three regions have the following limits[9]:

$$\mathfrak{R}_1 \in \left\{ \begin{array}{l} 0 < r < R_m \\ \theta_1 < \theta < 2\pi - \theta_1 \end{array} \right\}.$$

$$\mathfrak{R}_2 \in \left\{ 0 < r < \min(R_m, D \cos \theta - D_o) \right\}.$$

$$\mathfrak{R}_3 \in \left\{ 0 < r < \min(R_m, D \cos \theta + D_o) \right\}.$$

Where  $\theta_1 = \sin^{-1}\left(\frac{R_\mu}{D}\right)$ ,  $D_o = \sqrt{R_\mu^2 - D^2 \sin^2 \theta}$ , and  $0 < \theta < \theta_1$

If the microcell lies outside of the macrocell, the region 3 becomes  $r = R_m$  resulting the integration of this region to be zero, and integration of region 2 becomes  $0 < r < R_m$ . We should double the integration resulting of regions 2 and 3, because the regions of the same size exist in the upside area.

### IV. Macrocell-to-Microcell Power Ratio

In the previous section, we defined the ratio of the required receive power of the macrocell to that of the microcell. From equations (6) and (7), the effects of the power ratio on the capacity can be seen. These equations have the form of subtracting some amounts from its maximum capacity, where the amounts are composed of the power ratio and the interference factors.

To maximize the system capacity, the power ratio should be set to attenuate the effect of interference on capacity. However, making the power ratio small to achieve the high microcell capacity in (6) will decrease the macrocell capacity as can be shown in (7). If the power ratio is set to be large, the microcell capacity will decrease. The power ratio to balance the number of users of macrocell and microcell is shown below.

By replacing  $N_m$  of equation (6) by the (7), the power ratio can be obtained as a

function of  $N_\mu$  and  $N_m$

$$\psi = \frac{(N_{\mu-pole} - N_\mu)}{f_{m\mu} N_{\mu-pole}} + \frac{N_\mu f_{\mu m}}{N_m (1 + f_{mm})}$$

$f_{mm}$  has a typical value equal (0.55)[10]. Hence, the three interference factors ( $f_{mm}$ ,  $f_{m\mu}$  and  $f_{\mu m}$ ) are known the power ratio can be found using (16) as a function of number of users in the microcell. Also the number of active users in the macrocell can be found as a function of the microcell active users using eq.(7).

## V. Design Parameters

First let us suggest a new criteria which is a product of capacity and coverage (CCP) as a measure of system performance, borrowing this from an analogy of **Bandwidth-Distance Product** used in **fiber optic** systems.

A given cell area of radius  $R_m$  (as shown in Fig.3 served by a macrocell base station, designed to serve  $N_{old}$  active users with loading factor  $\mu$  and  $E_b/I_o$  and for a certain GoS . So  $CCP_m$  is  $N_{old}R_m$

Now Suppose that the number of users is increased by  $C\%$  to become  $N = N_{old}(1 + C)$

This means that the subscribers at the old coverage area will not all be served because  $r < R_m$ . Even if they are served, their GoS and performances will be below the requirement, and the loading factor will be above the design requirements or  $N$  may reach or exceed macrocell pole capacity.

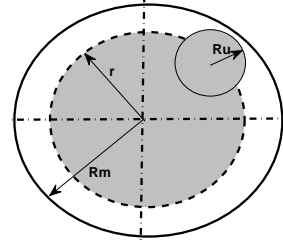


Figure 3: Two tier CDMA System

To guarantee continuity of services within the original design coverage area for all users, a microcell of radius  $R_\mu$  is to be introduced in the macrocell to take part of the load from the macrocell base station.

The objective is to increase the resulting coverage radius  $r$  to the old coverage radius  $R_m$  or more.

That is to make  $CCP_{new} \geq CCP$

This can be written as

$$CCP_{new} = CCP_{mac} + CCP_{mic} = N_m R_m + N_\mu R_\mu \quad (17)$$

Then  $N_m R_m + N_\mu \times R_\mu \geq N_{old} \times R_m$

**The following questions have to be considered:**

- 1- What is in general  $CCP_m$  formula for this two tier system?
- 2- What is the load sharing between the micro and macro cells? i.e.  $N_m$  and  $N_\mu$  as a function of the percentage increase of the active users?.
- 3- What is the appropriate microcell coverage radius  $R_\mu$  compared to  $R_m$ ?
- 4- What is the appropriate power ratio of macro to micro cell BS as a function of percentage load increase?

To answer these questions we will assume that both cells will work with same cell loading, so:  $\mu_\mu = \mu_m$

$$\frac{N_{\mu}}{N_{\mu-pole}} = \frac{N_m}{N_{m-pole}} \quad (18)$$

And hence

$$N_m + N_{\mu} = N_{old}(1+C) \Rightarrow N_{\mu} = N_{old}(1+C) - N_m$$

Solving equation (18) for  $N_{\mu}$  we get

$$N_{\mu} = \frac{(1+C)N_{old}}{\left[\frac{N_{m-pole}}{N_{\mu-pole}} + 1\right]} \quad (19)$$

Now we may obtain  $N_m$

$$N_m = \frac{N_{m-pole}(1+C)N_{old}}{N_{m-pole} + N_{\mu-pole}} \quad (20)$$

To maintain  $CCP$  and the same coverage radius  $R_m$ , the new  $CCP$  must be  $CCP_{new} = CCP_{mac} + CCP_{mic} = N_m \times R_m + N_{\mu} \times R_{\mu} \geq CCP$

$$R_{\mu} \geq \frac{R_m(N_{old} - N_m)}{N_{\mu}} \quad (21)$$

Using Equations (18), (19) and (20) we get:

$$\frac{R_{\mu}}{R_m} \geq \frac{N_{\mu-pole} - C \times N_{m-pole}}{(1+C) \times N_{\mu-pole}} \quad (22)$$

$$CCP_{new} = R_m N_m + R_{\mu} \times N_{\mu} = R_m \left( N_m + \frac{R_{\mu}}{R_m} N_{\mu} \right).$$

$$\text{Let } \omega = \frac{R_{\mu}}{R_m}$$

$$CCP_{new} = R_m(N_m + \omega N_{\mu}) \quad (23)$$

Using equations (18), (19) and (20), Eq.(23) becomes:

$$CCP_{new} = R_m \frac{(1+C)N_{old}[N_{m-pole} + \omega N_{\mu-pole}]}{N_{\mu-pole} + N_{\mu-pole}} \quad (24)$$

where  $\omega$  must satisfy the condition in equation (21). Fig.6 shows a relation between the power ratio of the macro to micro/cell base station versus the relative location of the microcell at different

percentage of user increase, the power ratio can be calculated from equation (16).

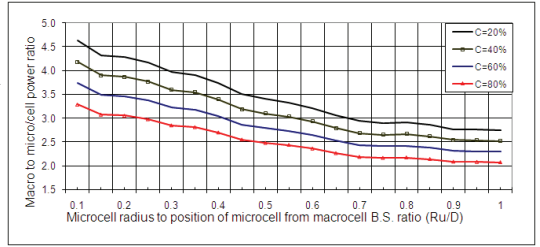


Figure 4: Power ratio of macro to micro/cell vs  $R_{\mu}/D$  at different percent of user increase

## VI. Numerical Results

Using the MatLab Function:  $dblquad('function', xmin, xmax, ymin, ymax)$ , the integration of Eq.15 is solved at certain values of D and R and the results are listed in Table (2) (the radius of the macrocell is normalized to unity; ( $R_m = 1Km$ ))

$R_{\mu}/D$	$f_{m\mu}$	$R_{\mu}/D$	$f_{m\mu}$
0.10	0.320	0.15	0.345
0.20	0.348	0.25	0.358
0.30	0.377	0.35	0.383
0.40	0.402	0.45	0.431
0.50	0.446	0.55	0.456
0.60	0.481	0.65	0.502
0.70	0.526	0.75	0.534
0.80	0.531	0.85	0.542
0.90	0.563	0.95	0.565
1.00	0.568		

Table 2: The values of mutual interference at different distance ratios

Eq.16 is plotted in Fig.5 which illustrates the relation between macro VS



micro cell users at different distances.

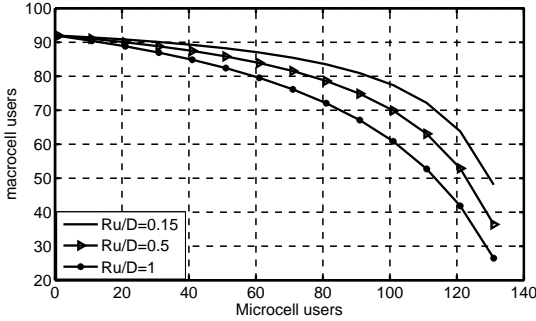


Figure 5: Macrocell users vs Microcell users

The Macrocell to Microcell Power Ratio  $\psi$  as a function of microcell active user is drawn in Fig.6. It is clear that the effect of the distance ratio  $D/R_\mu$  is very small. Once the number of microcell active users is assigned, the ratio of powers  $\psi = \frac{S_m}{S_\mu}$  is known.

One can note that as  $R_\mu/D$ , increases, the over all capacity decreases, this is because when the microcell BS gets near from the macrocell BS, the mutual interference will increase and hence the capacity decreases.

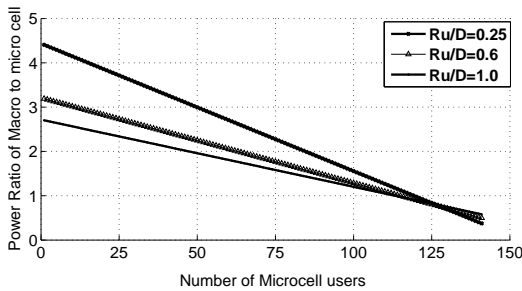


Figure 6: Power Ratio VS Microcell active users

As an example, we will suppose the operating point is at cell loading of 70%

for the bit rate of 14.4Kbps,  $E_b/I_o = 5dB$  and only one class of service with voice activity factor of 3/8 is assumed. If we assume an increase in the traffic by 40%. The objective is to design the two tier system parameters to keep the same system performance or better.

From ref.[11],[12], the radius of the cell at the given cell loading is 1.22 km

$$N_{old} = 146 \times 0.7 = 102$$

$$\text{Eq.4 gives } N_{m-pole} = 146$$

$$\text{Eq.5 gives } N_{\mu-pole} = 225$$

$$CCP(old) = R_m \times N_{old} = 124.44 \text{ user.Km}$$

$$N_{new} = (1 + 0.4) \times 65 \approx 143$$

$$\text{Eq. 18 leads to } N_\mu = \frac{143}{146/225+1} \approx 87$$

$$N_m = 143 - 87 = 56 \text{ (From Eq.19)}$$

$$\text{If we choose } \omega = 0.6 \Rightarrow R_\mu = 0.50 \times 1.22 = 732 \text{ m.}$$

$$CCP_{new} = CCP_{mac} + CCP_{mic} = N_m \times R_m + N_\mu \times R_\mu:$$

$$= 56 \times 1.22 + 87 \times 0.610 = 150 \text{ user.km}$$

This is greater than the old value, meaning that the performance still satisfies.

The power ratio can be calculated from Eq.20, assuming that the microcell base station is installed at a distance such that  $R_\mu/D = 1 (f_{\mu m} = 0.568 \text{ from Table (1) and } f_{m\mu} \text{ is read from Table(2)})$

Substituting in Eq.16 leads to  $\psi = 2.6$ , this value of power ratio  $\psi$  can also be read from the Fig.4

So the required received power at the microcell base station is approximately equal to 2.234 times the required received power at the macrocell base station, i.e if the minimum required received power at the Macrocell BS is  $-100dBm$ , then the minimum required received power at the Microcell BS should be  $(-100dBm + 10\log(2.234)) = -96.5dBm$



## VII. Conclusion

To improve the performance, a two tier system consisting of macrocell/microcell BSs is studied. The microcell is installed where users are estimated to be high. This Hotspot cell will provide services to those extra users effecting coverage and performance for the rest of the users. this approach makes a more stable coverage and prevents the cell from extensive breathing. With this insertion of microcell BS, a cross-tier interferences come into sight. A method to approximate this interference for specific assumptions is given. The overall CCP improvement is noticed. Closed form formulas to calculate several design system parameters as the diameter of microcell and the power ratio between the tiers are driven. It is pointed in the last example that although the capacity is increased but the system performance is still maintained at the same link quality.

## REFERENCES

- [1] Shaline Kishore, *Capacity and Coverage in Two Tier Cellular CDMA Networks*, Ph.D. thesis, Princeton University in Canada, Jan. 2003.
- [2] Robin Coombs and Raymond Steele, "Introducing microcells into macrocellular networks : A case study," *IEEE Transaction on Comm.*, vol. 47, no. 4, April 1999.
- [3] F. Adelantado, O. Sallent, J. Perez-Romero, and R. Agustí, "Impact of traffic hotspots in 3g wcdma networks," .
- [4] Chih lin I, Larry J, Greenstein, and Richard D. Gitlin, "A microcell/ macrocell cellular architecture for low and high-mobility wireless users," *IEEE Transactions On Vehicular Technology*, 1990.
- [5] et. al S. Kishore, "Uplink capacity in a cdma macrocell with a hotspot microcell: Exact and approximate analyses," *IEEE Transactions on Wireless Communications*, vol. 2, no. 2, pp. 364–374, Mar. 2003.
- [6] Stuart C. Schwartz H. Vincent Poor Shaline Kishore, Larry J. Greenstein, "User capacity in a cdma macrocell with a hotspot microcell: Effects of transmit power constraints and finite dispersion," *IEEE Transactions on Wireless Communications*, 2003.
- [7] H. Vincent Poor Stuart C. Schwartz Shaline Kishore, Larry J. Greenstein, "Soft handoff and uplink capacity in a two-tier cdma system," *IEEE Transactions on Wireless Communications*, vol. 1, no. 1, Mar. 2005.
- [8] Mohamed A. Elalem and Dr. Akki, "Uplink capacity- coverage product in a cdma mobile network," in *Wireless and Optical Communication*, A.Vukovic, Ed., 2008, vol. 1, pp. 53–57.
- [9] Ho Joon Kim Dong Hee Kim, Dong Do Lee and IEEE Keum Chan Whang, Members, "Capacity analysis of macro/microcellular cdma with power ratio control and tilted antenna," *IEEE Transactions On Vehicular Technology*, vol. 49, no. 1, Jan. 2000.
- [10] Harri Holma and Antti Toskala, *WCDMA for UMTS*.
- [11] Kiseon Kim and Insoo Koo, *CDMA Systems Capacity Engineering*, Artech House USA, 2005.
- [12] Mohamed A. Elalem, "Uplink capacity- coverage product in a cdma mobile network," M.S. thesis, Al-Fateh Univeristy, 2007.



# Interference Mitigation Using Power Control in Cognitive Radio Networks

Mohamed Elalem , Dr.Lian Zhao, Zaiyi Liao  
Electrical and Computer Engineering Department  
Ryerson University, ON, Canada, M5B 2K3

## Abstract

One of the challenging problems of Cognitive Radio (*CR*) is the interference which occurs when a cognitive radio accesses a licensed band but fails to notice the presence of the licensed user. To allow the cognitive radio to access the same spectrum band where the primary user is operating creates a problem, the cognitive radio may interfere with the primary system, and hence degrading the quality of service for the primary receiver.

In this paper we propose an adaptive power control scheme for Cognitive Radio. The proposed scheme estimates the distance between the primary user and the Cognitive Radio, using the SNR as proxy for distance. On the basis of this information the Cognitive Radio adaptively changes its transmit power to prevent the primary user from harmful interference.

By this scheme, CR can perform intelligently to determine the maximum level of the transmission power which does not cause any harmful interference to the primer users quality of service.

## I. Introduction

With the increasing demand and explosion growth in wireless services over the past several years, the spectrum becomes more congested especially in the bands below 3GHz. On the other hand, extensive measurements taken reveal a typical utilization of 0.5% in the 3-4 GHz band which drops more in higher bands[1]. Recent survey has proved that most of the radio frequency spectrum is vastly *under-utilization*.

The FCC reported vast temporal and

geographic variations in the use of allocated spectrum with utilization ranging from 15% to 85%. In order to utilize this spectrum (white spaces), the FCC announced *Cognitive Radio* technology as a candidate to implement negotiated or opportunistic spectrum sharing [2]. Cognitive Radio is an intelligent wireless communication that is aware of its surrounding environment and uses the methodology of understanding-by-building to learn from the environment and adapts its internal states to make corresponding changes in certain operating parameters

[3].

In Cognitive Radio, unlicensed users (secondary users) are allowed to share the licensed spectrum where primary users are absent in specific time and/or allocation. By detecting particular spectrum holes and jumping into them rapidly, Cognitive Radio improves the utilization of the spectrum significantly.

Traditionally, a large amount of spectrum bands have already been assigned to different users who often referred to as Primary Users (PUs). They have the exclusive right to use these bands. This inflexible policy has already been a huge waste of spectrum resources. While Cognitive Radio allows the unauthorized users called as Secondary Users (SUs) to use the licensed bands when such bands are vacant by PUs. Therefore Cognitive Radio can economically enhance the spectrum efficiency.

The fundamental requirements for SUs is to avoid interference to the potential PUs in their vicinity. To guarantee a high spectrum efficiency while avoiding any kind of harmful interference to the licensed users (PUs), some important functionalities should be provided by Cognitive Radio which includes: spectrum sensing, dynamic frequency selection and transmit power control[4]. These main functions can be summarized as following:

- Spectrum Sensing : Detection unused spectrum and sharing the spectrum without harmful interference with other users.
- Spectrum Management: capturing the best available spectrum to meet users requirements (QoS, bit rate, ...).
- Spectrum mobility: maintaining seamless communication requirements during the transition to better spectrum.
- Spectrum sharing: providing the fair

spectrum scheduling method among the co-existing (SUs).

Among different spectrum sensing schemes [5] for reliably identifying the spectrum holes, *Energy Detection* incurs a very low implementation cost and is hence widely used. It has a good resistance against a fast time varying radio environment where none a priori knowledge about the PUs is available (non-coherent detector). In order to identify the presence of PUs with unknown frequency locations, energy detector serves as the optimal sensing scheme since they only need to measure the power of the received signal. Fig. 1 is a block diagram of an energy detector, the band-pass filter is used to limit the bandwidth of the input signal. It is followed by a squaring device used to measure the received energy and the integrator determining the observation interval  $T$ . After the integrator is a threshold device, comparing the output of the integrator  $Y$  with predetermined threshold to decide whether the signal is present or not.

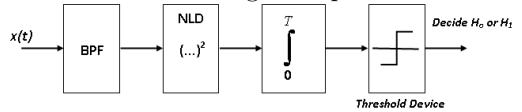


Figure 1: Block diagram of a simple energy detector

One of the most problems of CR is the interference which occurs when a SU accesses a licensed band but fails to detect the presence of the licensed user. To address this problem, the CR should be designed to co-exist with the licensed user without creating harmful interference.

Power control which has been employed for improving the link performance in cellular networks can also be applied



to CR networks. However, power control of CR networks is more complicated, in that it should not only consider the quality of service (QoS) requirements of the SUs, but also protect the PU communication link. Since the PU communication has priority over the SU communication, it is impossible for the SUs to share the PU channel deteriorating the link quality of the PU communication. Thus, SUs should always check the estimated interference at the primary receiver after determining their transmission powers.

Several interference mitigation techniques have been presented for CR systems [6, 7, 8]. In [8], an orthogonal frequency division multiplexing (OFDM) was considered as a candidate for cognitive radio to avoid the interference by leaving a set of sub-channels unused, which can provide a flexible spectral shape that fills the spectral gaps without interfering with the PUs. There are two categories in the power control for CR networks: centralized and distributed power control. For the centralized power control, a central manager controls the transmission power of all users within its coverage.

A transmission power control system using Fuzzy Logic System was proposed in [9]. With the built-in fuzzy power controller, the SU is able to dynamically adjust its transmission power in response to the changes of the interference level caused by the SU to the PU. In [10], considering the interference temperature constraints, the optimal power control problem was modeled as a concave minimization problem. In [9, 10], no SU is allowed to transmit before receiving authorization from the manager. Furthermore, all information required for managing the network should be known to the central

entity, and very heavy signaling is inevitable.

For the distributed power control, on the other hand, each user controls its transmission power by itself using only local information. However, since the interference temperature at the primary receiver cannot be identified by the local information, it is difficult that the QoS requirement for the PU is guaranteed in the distributed power control. Thus, an additional process is needed to let the SUs recognize the interference temperature at the primary receiver. In [7], a Joint Coordination and Power Control (JCPC) algorithm was proposed based on the game theory. The transmission power of each SU in the set is distributively allocated in the power control phase.

In [8] an example of a power control rule which allows the secondary user to adapt its transmit power while guaranteeing an acceptable level at the primary receivers is presented. A coherent detection is assumed as a signal detection, where a pilot signal is used to allow users to measure the local SNR of the primary signal which can then be used as a proxy for distance from the primary transmitter. Armed with this information, secondary user can approximate their distance from the primary transmitter and adjust their transmit power accordingly.

To avoid the interference to the licensed users, the transmit power of the cognitive radio should be limited based on the locations of the licensed users. However, it is difficult to locate the licensed users for the cognitive radio in practice because the channels between the cognitive radio and the licensed users are usually unknown. Furthermore, the environment where the system is in operation may have large delay spread and

hence the channel model is complicated by fading, shadowing and path loss effects. Unlike in [8], in this paper, we present a power control approach in CR systems based on spectrum sensing information in order to approximate the distance from the primary transmitter and then estimate the required power which can be transmitted by Cognitive Radio while guaranteeing the protection of the primary user from harmful interference. the interference to the PU due to the presence of cognitive radios. This approach consists of two steps:

- The shortest distance between a licensed receiver and a CR is derived from the spectrum sensing side information.
- Then, the transmit power of the cognitive radio is determined based on this shortest distance to guarantee quality of service for the licensed user.

Because the worst case is considered in this approach where the CR is the closest to the licensed user, the proposed power control approach can be applied to the licensed user in any location.

The remaining of the paper is organized as follows: Section II illustrates the system model. Section III defines the problem formulation which is divided into two subsections; the first one adapts the energy sensing as a base to estimate the probabilities of false alarm, detection and missing, while the second gives the power control algorithm. Section IV supports the work with a numerical example followed by the conclusion in Section V.

## II. System Model

Our model is illustrated in Fig.2.

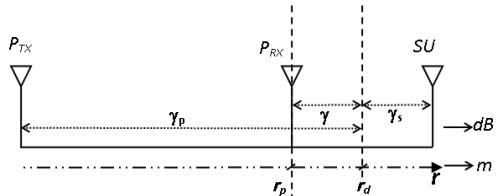


Figure 2: The system model

The licensed user formed by a Transmitter-Receiver pair, co-exists in the same area with a secondary user. The primary transmitter  $P_{TX}$  communicates with the primary receiver  $P_{RX}$  with the transmit power  $S_p$ . Some system parameters are declared as follows: The distance  $r_d$  is the radius of a circle around the primary transmitter which represents the *decodable* region within which the signal-to-noise ratio (SNR) of decodability occurs in the absence of interference to the primary receiver.  $r_p$  is the radius of a circle around the primary transmitter which denotes the *protection* region within which the primary receiver must be guaranteed successful reception even in the presence of the cognitive radio.  $\gamma_p(dB)$  is the signal attenuation due to the distance  $r_d$ .  $\gamma$  is the margin of protection in dB which is a measure of how much interference above the noise floor the primary system can tolerate. For the secondary system  $SU$ , before accessing the channel, the cognitive radio acts as a listener to detect from the received signal whether the PU is in operation. Let  $r(m)$  denotes the distance between the  $P_{TX}$  and  $SU$ . In practice, it is difficult to obtain the value of  $r$  because the signals from the  $P_{TX}$  and the channel are both unknown to the cognitive radio. Thus, computing  $r$  will be a



challenging problem. Another challenging issue is to allow the cognitive radio to access the same spectrum band where the PU is operating. In such case, the cognitive radio may interfere with the primary system, thereby, degrading the quality of service for the PU. To reduce the interference, the transmit power  $S_s$  of the cognitive radio should be limited based on the tolerable interference to the primary receiver which depends on the distance between the cognitive radio and the primary receiver. However, it is difficult for the cognitive radio to locate the primary receiver which can be at any location inside the protection region.

To address this problem, the worst case scenario is investigated in this paper where the the primary receiver  $P_{RX}$  is located at the crossing point between the boundary of the protection region and the line from the  $P_{TX}$  to the cognitive radio as shown in Fig. 2. By maintaining the transmit power of the cognitive radio  $S_c$  for the above worst case, the quality of service for the primary receiver can be guaranteed at any location inside the protection region. It can be seen from Fig. 2 that the transmit power of the cognitive radio  $S_s$  which is allowed to inflict tolerable interference on the  $P_{RX}$  depends on the SNR loss ( $\gamma + \gamma_s$ ) in  $dB$ . Note the SNR loss due to the distance ( $r$ ) is given by  $\xi = \gamma_s + \gamma_p(dB)$ . Then, the transmit power control problem is essentially converted to the problem of evaluating the SNR loss  $\xi$  due to  $r$  for a given  $\gamma$  and  $\gamma_p$ . We assume here that the channel between any two terminals in our model experiences flat Rayleigh fading and path loss. The propagation power attenuation is characterized by  $\alpha(r) = r^{-\nu}$ , where  $\nu$  denotes the power loss exponent which depends on the channel type between ter-

minals, which is in the range of 2 (LOS free space attenuation) up to more than 6 (crowded obstacles area). An average value of  $\nu = 3.5$  will be chosen throughout this paper which corresponds to the urban environment attenuation.

### III. Problem Formulation

We present a power control algorithm based on spectrum sensing side information to efficiently utilize the spectrum by allowing the cognitive radio to co-exist with the primary system.

We firstly propose an idea of determining the distance  $r$  between the  $P_{TX}$  and the  $SU$  from spectrum sensing. Then, we show that the transmit power of the cognitive radio  $S_s$  can be controlled based on this distance in order to guarantee  $QoS$  to the  $P_{RX}$ .

#### A. Energy Based Spectrum Sensing

Spectrum sensing is to decide between the following two hypotheses:

$$H_0 : x(t) = n(t), \quad 0 < t \leq T$$

$$H_1 : x(t) = hs(t) + n(t), \quad 0 < t \leq T \quad (1)$$

where  $x(t)$  is the received signal at the  $SU$ ,  $s(t)$  is the transmitted signal from the  $P_{TX}$ ,  $n(t)$  is the Additive White Gaussian Noise (AWGN) modeled as  $\mathfrak{N}(0, \sigma^2)$ ,  $T$  denotes the observation time, and  $h$  is the overall channel gain coefficient including the Rayleigh fading and propagation losses. Let us define the instantaneous SNR as  $\eta = |hs(t)|^2/\sigma^2$ . If the signal amplitude follows a Rayleigh distribution, then the SNR follows an exponential distribution.

A great challenge of spectrum sensing for the cognitive radio is to detect the



presence of the  $P_{TX}$  with limited information about the channel  $h$  and the transmitted signal  $s(t)$ . In such a scenario, the energy detector has been shown as the optimal detector for a zero-mean constellation of  $s(t)$  [11].

Specifically, the energy of the received signal, denoted by  $Y$  in Fig. 1, is collected in a fixed bandwidth  $W$  and a time slot duration  $T$  and then compared with a pre-designed threshold  $\delta$ , if  $Y \geq \delta$  then the cognitive radio assumes that the primary system is in operation, i.e.,  $H_1$ . Otherwise, it assumes  $H_0$ .

The average probability of detection, false alarm, and missing of energy detection (The miss detection occurs when the  $P_{RX}$  is in operation but the cognitive radio fails to sense it) over Rayleigh fading channels can be given by, respectively, [5, 12, 13]:

$$\begin{aligned}
 P_d &= \mathbf{E} \left[ P_r \{ H_1 / H_1 \} \right]_{\eta} \\
 &= e^{-\frac{\delta}{2}} \sum_{n=0}^{\gamma-2} \frac{1}{n!} \left( \frac{\delta}{2} \right)^n + \left( \frac{1+\bar{\eta}}{\bar{\eta}} \right)^{\gamma-1} \\
 &\quad \times \left( e^{-\frac{\delta}{2(1+\bar{\eta})}} - e^{-\frac{\delta}{2}} \sum_{n=0}^{\gamma-2} \frac{1}{n!} \left( \frac{\delta \bar{\eta}}{2(1+\bar{\eta})} \right)^n \right)
 \end{aligned} \quad (2)$$

$$P_f = \mathbf{E} \left[ P_r \{ H_1 / H_0 \} \right]_{\eta} = \frac{\Gamma(m, \delta/2)}{\Gamma(m)} \quad (3)$$

$$P_m = \mathbf{E} \left[ P_r \{ H_0 / H_1 \} \right]_{\eta} = 1 - P_d \quad (4)$$

where  $\bar{\eta}$  denotes the average SNR at the cognitive radio.  $\mathbf{E}[\cdot]_{\eta}$  represents the expectation over the random variable  $\eta$  which is exponential distributed.  $P_r\{\cdot\}$  is the probability.  $\Gamma(\cdot, \cdot)$  is the *incomplete gamma function* and  $\Gamma(\cdot)$  is the

*gamma function*. Finally,  $m$  is *Time Bandwidth product*  $TW$  with  $m = 5$  is chosen throughout this paper.

The path loss due to the distance  $r$  can be given by

$$\xi = -10 \log(r^{-\nu}) = 10 \log\left(\frac{S_p}{\sigma^2}\right) - 10 \log(\bar{\eta}) \quad (5)$$

From (5), we can obtain

$$\bar{\eta} = \frac{S_p}{\sigma^2} r^{-\nu} = \frac{S_p/\sigma^2}{10^{\xi/10}} \quad (6)$$

Using equations (2),(4), and (6), a relationship between  $P_m$  and distance  $r$  (or  $\xi$ ) can be obtained for specific values of  $S_p/\sigma^2$  and path loss exponent factor  $\nu$ . i.e

$$P_m = f(r) \quad (7)$$

It is obvious that the distance  $r$  (or  $\xi$ ) can be decided by  $P_m$  by certain mathematical manipulations. Fig. 3 shows  $P_m$  versus the distance  $r$  for different transmit SNR ( $S_p/\sigma^2$ ) (SNR is chosen to be 60, 80 and 100)dB from the top to the bottom respectively, and  $\nu = 3.5$  and  $P_f = 0.01$ .

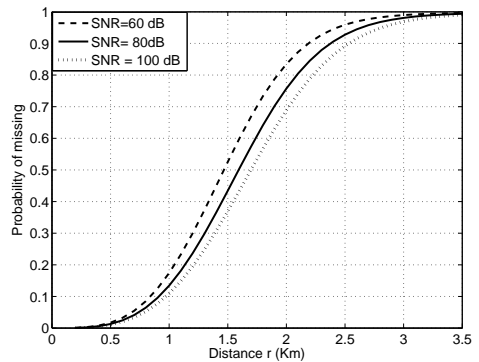


Figure 3: Probability of missing versus distance (false alarm probability =0.01)

Numerical results demonstrate that when the cognitive radio is far from the





primary transmitter, a high probability of missing is obtained. For a fixed distance  $r$ , a higher transmit SNR can get a better sensing performance, i.e., a lower  $P_m$ .

The detector may estimate the probability of missing  $P_m$  as follows. Define  $K$  as:

$$K(Y_i) = \begin{cases} 1 & \text{if } Y_i > \delta \\ 0 & \text{otherwise} \end{cases} \quad (8)$$

for  $i = 1, \dots, N$  (number of time slots), where  $Y_i$  denotes the energy collected by the cognitive radio in time slot  $i$ . So,  $P_m$  (estimated value) can be obtained as:

$$\tilde{P}_m = 1 - \frac{1}{N} \sum_{i=1}^N K(Y_i) \quad (9)$$

Hence  $P_m$  is calculated,  $r$  can be obtained from (7).

### B. Power Control Algorithm

Sometimes, during the spectrum sensing the presence of the primary user could not be properly detected. As a result the overall system performance will be degraded significantly due to the interference from the cognitive radio. In this section, we propose a transmit power control method to address this problem by mitigating the interference due to the presence of the cognitive radio.  $P_{RX}$  can successfully decode the received signal from  $P_{TX}$  in the presence of the  $SU$  if the signal-to-interference-plus-noise ratio (SINR) of the  $P_{RX}$  is above a certain threshold, say  $\gamma_d$ , i.e.,  $\text{SINR} \geq \gamma_d$ .

The  $QoS$  requirement of the primary receiver requires:

$$\frac{\dot{S}_p}{\dot{S}_s + \sigma^2} \geq 10^{\gamma_d/10}$$

$$\dot{S}_s \leq \dot{S}_p 10^{-\gamma_d/10} - \sigma^2 \quad (10)$$

where  $\dot{S}_p$  and  $\dot{S}_s$  denote the received signal power at the primary receiver from the  $P_{TX}$  and the  $SU$ , respectively.

Now we may express  $\dot{S}_p$  on the protected border in terms of SNR as

$$10 \log\left(\frac{\dot{S}_p}{\sigma^2}\right) = \gamma_d + \gamma$$

$$\dot{S}_p = \sigma^2 10^{(\frac{\gamma_d + \gamma}{10})} \quad (11)$$

From (10) and (11) we can solve for  $\dot{S}_s$ :

$$\dot{S}_s \leq \sigma^2 (10^{\frac{\gamma}{10}} - 1) \quad (12)$$

The power constrains must consider a primary receiver and secondary transmitter as close as possible, with the primary on the edge of the protected area and the secondary on the the edge of the no-talk zone [8], (12) leads to:

$$S_s \alpha_{21}(r - r_p) \leq (10^{\frac{\gamma}{10}} - 1) \sigma^2$$

$$S_s \leq (10^{\frac{\gamma}{10}} - 1) \sigma^2 (\alpha_{21}(r - r_p))^{-1} \quad (13)$$

where  $\alpha_{21}(\cdot)$  is the propagation path loss between the primary transmitter and secondary receiver. We may write  $r_p$  in terms of SNR as:

$$10 \log\left(\frac{S_p}{\sigma^2}\right) - 10 \log\left(\frac{S_p \alpha_{11}(r_p)}{\sigma^2}\right) = \gamma_p - \gamma$$

$$\alpha_{11}(r_p) = 10^{\frac{-\gamma_p + \gamma}{10}}$$

$$r_p = \alpha_{11}^{-1}\left(10^{\frac{-\gamma_p + \gamma}{10}}\right)$$

where  $\alpha_{11}(\cdot)$  is the propagation path loss between the primary transmitter and primary receiver and  $\alpha_{11}^{-1}(\cdot)$  is its inverse function.

Next, we solve for distance  $r$  in terms of SNR

$$10 \log\left(\frac{S_p}{\sigma^2}\right) - 10 \log\left(\frac{S_p \alpha_{12}(r)}{\sigma^2}\right) = \gamma_p + \gamma_s$$



$$\alpha_{12}(r) = 10^{\frac{-\gamma_p - \gamma_s}{10}}$$

and then

$$r = \alpha_{12}^{-1} \left( 10^{\frac{-\gamma_p - \gamma_s}{10}} \right)$$

For simplicity we assume that  $\alpha_{ij}(\cdot), \forall i, j$  is characterized by  $\alpha(\cdot) = (\cdot)^{-\nu}$  as mentioned above.

Using the above results and equation (13), we may obtain:

$$10 \log \left( \frac{S_s}{\sigma^2} \right) \leq \gamma_p + 10 \log(10^{\gamma/10} - 1) +$$

$$10\nu \log \left( (10^{\gamma_s/10})^{1/\nu} - (10^{-\gamma/10})^{1/\nu} \right) = g \quad (14)$$

Equation (14) is only function of  $(\gamma_s)$  for fixed values of  $\gamma$  and  $\nu$ . It can be seen that a value of the allowable  $S_s$  depends on the SNR loss  $\gamma_s$ . Since the location of the  $P_{RX}$  is usually unknown for the cognitive radio, it is difficult to get the value of  $\gamma_s$ . In this work, we consider the worst case that the  $P_{RX}$  is located at the closet point to the cognitive radio. In this case, from Fig. 2, we have

$$\gamma_s = \xi - \gamma_p \quad (15)$$

By substituting (15) into (14), we can see that  $S_s$  can be decided by  $\xi$ , we can get:

$$\begin{aligned} S_s^{max} &= g(\xi - \gamma_p) + 10 \log(\sigma^2) \\ &= g(-10 \log(r^{-\nu}) - \gamma_p) + 10 \log(\sigma^2) \end{aligned} \quad (16)$$

$S_s^{max}$  determines the maximum value of  $S_s$  in dB and  $r$  has been obtained from the spectrum sensing side information in Section III-A. As a result, the transmit power of the cognitive radio which is allowed to guarantee a good quality of service for the  $P_{RX}$  can be derived by the following algorithm:

- ▷ Find missing probability from Eq. 9.
- ▷ Derive a relation for distance form Eq. 7.
- ▷ Find the max secondary transmitted power from Eq. 16.

Fig. 4 shows the maximum allowed transmitted power by the Cognitive radio versus  $SNR\xi(dB)$  for the same parameters used in Fig. 3. It gives a comparison between our approach given by (16)(represented by a line) and that given by equation (9) (represented by a dashed line)for reference [8]. The two approaches seem to be closed.

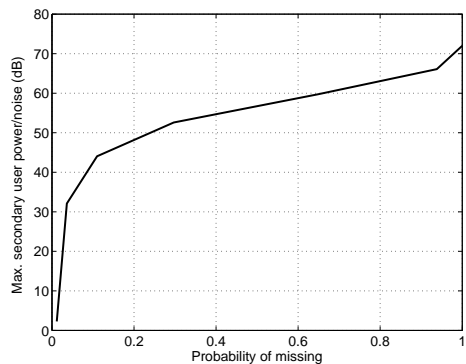


Figure 4: Probability of missing versus distance (false alarm probability = 0.01)

#### IV. Numerical Example

A numerical example is presented below to demonstrate the potential of the proposed power control method in cognitive radio systems. we assume that the system parameters have the following values:  $\gamma_p = 50dB$ ,  $\gamma = 2dB$ ,  $P_f = 0.05$ , and  $SNR_p = S_p/\sigma^2 = 80dB$

The channel environment is assumed to have flat Rayleigh fading and path loss. In order to allow the cognitive radio to share the spectrum with the primary sys-



tem while guaranteeing a good quality of service to the  $P_{RX}$  characterized by the inequality (10), the transmit power of the cognitive radio ( $S_s^{max}$ ) should be designed judiciously.

Because it is difficult to locate the primary receiver for the cognitive radio, we consider the worst case scenario where the primary receiver is the nearest to the cognitive radio, as shown in Fig. 2. From (7) we can obtain  $P_m$  vs.  $\xi$  as shown in Fig. 5. This shows the relationship between  $P_m$  and the SNR loss due to the distance  $r$ .

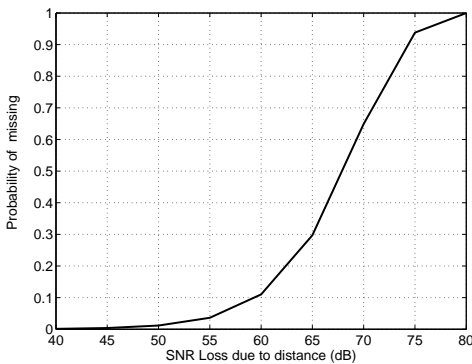


Figure 5: Probability of missing versus  $\xi$ (dB)

We can establish the relationship between  $S_s^{max}/\sigma^2$  and  $P_m$  as illustrated in Fig. 6. By calculating  $P_m$  from (9), the maximum transmit power  $S_s^{max}$  can be determined to guarantee the quality of service for the licensed user in the presence of the cognitive radio.

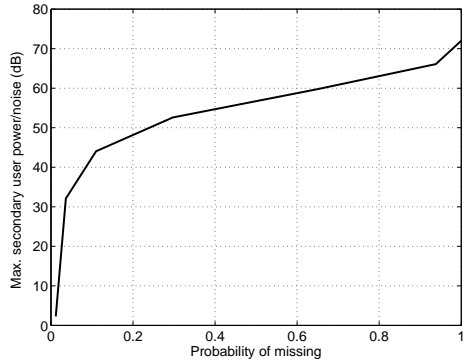


Figure 6:  $S_s^{max}/\sigma^2$  versus the prob. of missing

Since the maximum power of  $S_s$  is evaluated according to the worst case where the primary receiver is the nearest to the cognitive radio, we expect that this power control algorithm may be applied to a primary receiver in any other location.

## V. Conclusion

The aim of this paper is to investigate the coexistence of the primary and the cognitive networks while guaranteeing the protection of the primary user from harmful interference. A case of a primary user and a cognitive radio sharing spectrum simultaneously is considered. To limit the interference to the primary user, we developed a power control approach which intelligently adjusts the transmit power of the cognitive radio while maintaining quality of service for the primary user. The transmit power is controlled by the spectrum sensing side information based on energy detector. The probability of missing which actually includes the implicit location information of the primary user. Numerical results were presented to show that the proposed approach may provide a reliable quality of service for the primary user in any location while enhancing the spectrum utilization.



## REFERENCES

- [1] M. Zou, C. Zhao, B. Shen, and K. Kwak, "Decode-and-forward protocol based cooperative spectrum sensing," *Third 2008 International Conference on Convergence and Hybrid Information Technology*, 2008.
- [2] D. Cabric, S. Mishra, and R. Brodersen, "Implementation issues in spectrum sensing for cognitive radios," in *Asilomar Conference on Signals, Systems, and Computers*, 2004.
- [3] S. Haykin, "Cognitive radio: brain-empowered wireless communications," *IEEE J. Sel. Areas in Commun.*, vol. 23, pp. 201–220, Feb 2004.
- [4] I. Akyildiz, W. Lee, M. Vuran, and S. Mohanty, "Next generation/dynamic spectrum access/cognitive radio wireless networks: A survey," *Broadband and Wireless Networking Laboratory, School of Electrical and Computer Engineering, Georgia Institute of Technology, Atlanta*, May 2006.
- [5] F. Digham, M. Alouini, and Marvin K. Simon, "On the energy detection of unknown signals over fading channels," *IEEE TR. on Comm.*, vol. 55, Jan 2007.
- [6] T. Hillenbrand, A. Krohn, and F. Jondral, "Mutual interference in OFDM-based spectrum pooling systems," in *Proc. IEEE VTC*, vol. 44, pp. 1873–1877, May 2004.
- [7] V. Chakravarthy, A. Shaw, M. Temple, and J. Stephens, "Cognitive radio an adaptive waveform with spectral sharing capability," in *Proc. WCNC, New Orleans, USA*, vol. 2, pp. 724–729, Mar 2005.
- [8] N. Hoven and A. Sahai, "Power scaling for cognitive radio," *WCNC, Maui, Hawaii, USA*, vol. 1, pp. 250–255, June 2005.
- [9] T. Le and Q. Liang, "An efficient power control scheme for cognitive radios," *WCNC, Hong Kong, Asia's World City*, pp. 2559–2563, 2007.
- [10] W. Wang and T. Peng and W. Wang, "Optimal power control under interference temperature constraint in cognitive radio network," *WCNC, Hong Kong, Asia's World City*, pp. 116–120, 2007.
- [11] A. Sahai, N. Hoven, and R. Tandra, "Some fundamental limits on cognitive radio," in *Proc. of Allerton Conference., Monticello*, Oct 2004.
- [12] F. Digham, M. Alouini, and M. Simon, "On the energy detection of unknown signals over fading channels," *Department of Electrical and Computer Engineering University of Minnesota Minneapolis, MN USA.*, 2003, Technical report.
- [13] A. Ghasemi and E. Sousa, "Collaborative spectrum sensing for opportunistic access in fading environments," *Electrical and Computer Engineering Department University of Toronto Toronto, Ontario, Canada*, 2005, Technical report.



## Making the Case for WDM-PON-Based FTTH in Libyan Market

Ibrahim Khorwatt<sup>1</sup>, Osama Sasi<sup>2</sup>, Nabil Naas<sup>3</sup>

(1) Aljeel Aljadeed for Technology, Tripoli, Libya, i.khorwatt@aljeel.ly

(2) Horizon communication and Technology, Tripoli, Libya osama@horizon.ly

(3) Electrical and Electronic Engineering Department, Alfateh University, Tripoli, Libya nabil.naas@ee.edu.ly

**Abstract-** Optical access networks are considered to be definite solutions to the problem of upgrading current congested access networks to ones capable of delivering future broadband integrated services. However, the high deployment and maintenance cost of traditional point-to-point architectures is a major economic barrier. Current TDM-PON architectures are economically feasible, but bandwidth-limited. In this paper, we focus on the WDM PON technology and investigate many related issues among them are: (1) the network scalability in terms of transmission length, split ratio, and transmission speed; (2) the feasibility of the bidirectional transmission on different wavelengths on the same fiber across the access network; (3) the value of the ONU modulation of upstream data on continuous waves provided by the OLT, which eliminates the need for tunable components at ONUs. The significance of the last issue stems from the fact that the tunable components are much more sophisticated compared to conventional EPON and GPON systems and requires an additional network control unit.

### I. Introduction

Fiber-To-The-Home (FTTH) solutions today vary from high-bandwidth, symmetrical and dedicated FTTH to traditional Time Division Multiplexing Passive Optical Network (TDM PON) such as Gigabit PON (GPON) solutions that are asymmetrical, share bandwidth among users and are not neither flexible nor scalable to address various residential requirements and enterprises in one infrastructure [1].

FTTH solutions provide more bandwidth than traditional copper-based access networks. Nowadays, many vendors and service providers are gravitating toward Wavelength Division Multiplexing (WDM) PON-based FTTH systems which increase bandwidth by dividing a single fiber into multiple wavelengths, as shown in Figure 1.

Each wavelength is capable of carrying the same bandwidth that previously carried in the entire fiber [2].

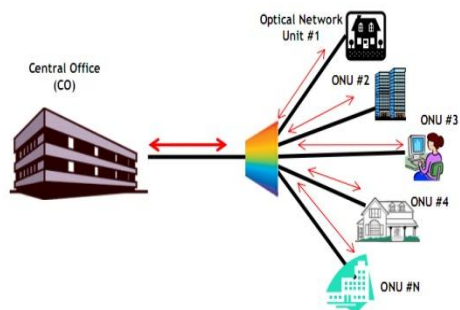


Figure 1: WDM-PON based FTTH [3]

The WDM-PON technology is the newest generation of fiber-based solutions available [4]. It is a technology which multiplexes multiple wavelengths (colors) on a single optical fiber to carry different



signals. A single type of an Optical Network Unit (ONU) can be used for each subscriber to perform wavelength modulation and demodulation functions; this type of ONUs is called a colorless ONU [4]. In order to make an ONU a colorless device, an alternative WDM PON network based on a reflective architecture is used. Much work about the colorless ONU has been proposed. Wavelength-locked Fabry-Perot Laser Diode (F-P LD) is one of them, since it is believed that the F-P LD is the most economical optical source.

In this paper, we first review the need for WDM PON in Libya. Then, the design of WDM PON is introduced in a case study. Finally, our concluding remarks are presented.

## II. The need for WDM-PON Technology

Libya nowadays has become a bandwidth-hungry country. Many types of services that require high bandwidth become desirable. As the telecommunication technology offers new types of applications, it is very important to satisfy the bandwidth requirement of these applications. The problem is that the user bandwidth is growing more symmetrical with the popularity of user-generated content and peer-to-peer networking involving high-resolution video and other latency-sensitive applications. Many network access solutions such as dial up Connection, Asymmetric Digital Subscriber Line (ADSL), and Worldwide Interoperability for Microwave Access (WiMAX) are currently used in Libya. FTTH is rapidly becoming the preferred wire line solution for access networks, and the newest employed architecture in Libya is GPON that provides about 68 Mbps for

downstream and about 40Mbps for upstream to each home using 1:32 splitting ratio. It seems enough for now, but unfortunately, it would not be enough for tomorrow's applications such as 3D-computer games, Super HDTV (SHDTV), and virtual reality, which is considered as the most advanced and challenged technology in the 3D vision applications.

Only WDM PON can cope with this expected huge bandwidth demands, as shown in Figure 2, and all other TDM PONs will not be able to handle the future demands in Libya. As a matter of fact, traditional PONs faces many obstacles in upgrading, since all of them use the TDM technique. As a result, as traffic demands increase, the TDM PON becomes overloaded and accordingly users will need to get dedicated bandwidths that prevent them from using Ethernet solutions.

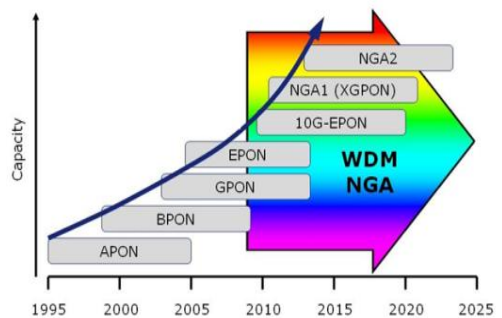


Figure 2: Bandwidth demand versus years [5]

WDM PON provides virtual point-to-point connectivity through a dedicated wavelength. This feature brings many inherent advantages: unlimited bandwidth (each end user can have more than 2.5Gbps of bandwidth), protocol transparency, security, the splitting ratio is not limited by



the splitting loss of the remote node, etc [4]. All of these will lead us to propose the WDM-PON architecture as the most feasible PON solution in Libya.

Based on the initial survey done on the Libyan market, the expected maximum bandwidth demand per application in Libya for the next five years is indicated in Table 1.

According to Table 1, the maximum downstream requirement for each home is 129.256Mbps. As a standard point of view, 155Mbps is the proposed data rate for both upstream and downstream transmission.

Table 1: The expected bandwidth demand in Libya for the next five years

Application	Bandwidth	Remark
2 Internet user (2Mbps each)	4 Mbps	"Required symmetrical Bandwidth"
2 VOIP phones	0.256 Mbps	"Required symmetrical Bandwidth"
Video phone [3]	2 Mbps	"Required symmetrical Bandwidth"
3D-computer games on demand	63 Mbps (Non-standard compression)	"Required symmetrical Bandwidth"
Streaming Video [3]	60 Mbps	Including Broadcasting, VoD and Home shopping
Total	Down Stream 129.256 Mbps Upstream 69.256 Mbps	

Under the consideration of these requirements, our aim is to propose a scalable network solution for the next generation access network in Libya. In order to choose the best solution option, Hay Al-Zohour residential area is chosen as

a case study. Hay Al-Zohour is a new residential area in Tripoli built near the airport highway. It is an apartment complex with 25 premises, and each building consists of 32 apartments, resulting in 800 end users.

### III. Case Study

In order to choose the right system, Hay Al-Zohour has been divided into four regions. The following networking options will be considered in the design of these regions: Point to Point (P2P) fiber link, GPON, WE PON and WDM PON.

Our design objective is to differentiate between these networking options. These options are briefly described as follows.

- P2P: With this option, a very high bandwidth can be delivered. However, this is a very expensive option compared with the other networking options. This is because there is a dedicated fiber from the Optical Line Terminal (OLT) at the Central Office (CO) to each ONU at the end user. Each ONU has to have its independent transceiver at the OLT; i.e., to support 32 users, 32 optical fibers are required from the OLT to end users. Moreover, the number of transceivers is 32, and each transceiver is independent from the others. Thus, the overall cost is expected to be high. Therefore, this option is not desirable.
- G PON: GPON is the current PON used in Hay Al-Zohour employing 1:64 splitting ratio (i.e., only one optical fiber can support 64 users), providing each home with 34Mbps in the downstream, and about 17Mbps for the upstream [6]. If demands increase in the next years, the splitting ratio can be decreased to 1:32, providing each user with a bandwidth of about 68 Mbps for downstream and about 40Mbps for upstream. Any further increase in the





demand will increase the number of splitters (i.e., reducing the splitting ratio to 1:16 or 1:8) and will raise the cost as well. Therefore, this option cannot be classified as the next generation PON for Libyan market.

- **WE-PON:** This option is based on transmitting several wavelengths from a Broadband Light Source (BLS) into many ONUs using the TDM technique. However, this option is better than GPON when it comes to upgradability. WE PON requires less total optical fiber length and less number of OLTs, compared with GPON with the same splitting ratio 1:32. If demands increase significantly in the future, WE PON will require much more Arrayed Waveguide Gratings (AWGs) and OLTs to support each subscriber, until WE PON reaches to a dead-end road, in which each user requires a dedicated wavelength; this is what is called WDM PON.

- **WDM PON:** In WDM PON, each building contains an AWG, enabling each user to enjoy his/her maximum demands and stopping the mass routine of upgrading, because each user can have his/her independent wavelength, enabling up to 2.5Gbps downstream and upstream. Although the same number of OLTs are required as in GPON with splitting ratio of 1:32, WDM PON can match perfectly any demands required. Also, there is no need for splitters which introduce more loss in the network. Moreover, WDM PON provides virtual P2P connectivity, protocol transparency and physical security. However, the high cost of WDM-PON equipment can be considered a major stumbling block to widespread deployment for the current time. On the other hand, as the bandwidth demand increases in the next years, there will be a significant drop in the cost of the WDM PON equipments, as shown in Figure 3. As a matter of fact, in

the United States, per-home FTTH costs have dropped in 12 years by a factor of almost 5 [8].

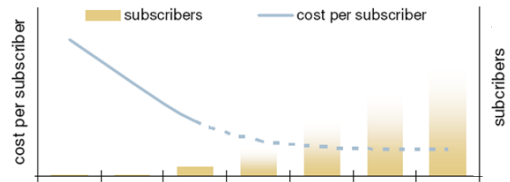


Figure 3: Number of subscribers & cost versus years [7]

Figure 4 illustrates the design of the access network in Hay Al-Zohour residential area using the previously-mentioned PON technologies.

As shown in Figure 4, WDM PON requires  $\frac{1}{4}$  feeder fiber length of that used in the dedicated fiber region, 8 times of that used WE PON region with much more scalability and the same feeder fiber as GPON region with higher bandwidth and much more scalability.

Based on the maximum number of wavelengths used in WDM PON and the nature of the area, it is found that, in order to meet the used system specifications, it is required to run 25 fiber cores (one core to each building). Each fiber core is to be demultiplexed into 32 users using AWG located inside the building.

To simplify the design, Hay Al-Zohour area is divided into 3 regions. Each region consists of 8 premises: one Optical Cable Closure Box (OCCB) is used in each region, one AWG per building, and one Access Terminal Box (ATB) per user is employed. Figure 5 shows the complete system layout.

According to the structure of Hay Al-Zohour premises, 32 channels have been assigned to each building. Each channel has



two wavelengths: one is for the upstream which uses C-band window and the other is for the downstream which uses L-band window. Both streams offer a transmission rate of 155Mbps. The proposed scheme that

performs the bidirectional transmission is the reflective scheme, which works by applying a spectral slicing with injection locked F-P LD.

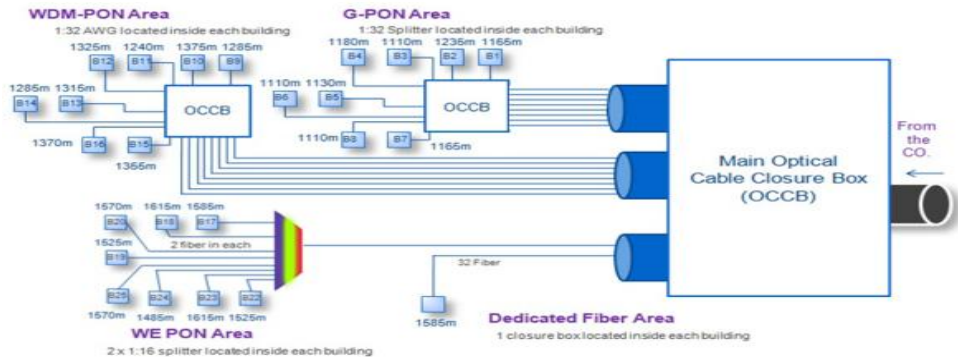


Figure 4: Choosing the right system

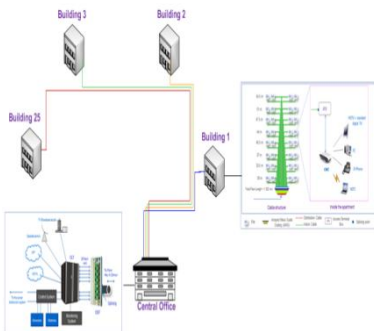


Figure 5: System Layout

In order to calculate the received power for both the ONU and OLT, the calculations have been applied to the longest fiber path which is about 1669.5 m. In order to get a BER less than  $10^{-9}$ , the injected power for both Fabry Perot Laser diodes (FP-LDs) located at the OLT and ONU has been assumed to be -14dBm, based on the assumption used in [4]. This assures that the eye diagram of the FP-LD at the ONU will be open as depicted in Figure 6.

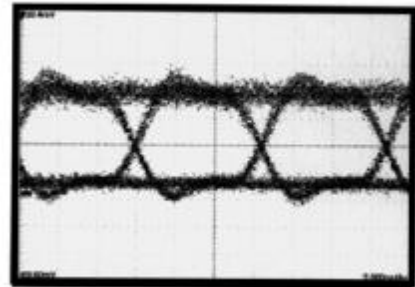


Figure 6: The eye diagram of the FP-LD at the ONU after it has been injected with a wavelength from the C- BLS [9]

Figure 7 indicates a simple sketch for the network with the parameters to be involved in our calculation.

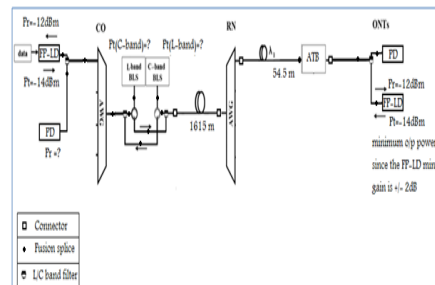




Figure 7: Simple sketch for the proposed WDM PON which indicates the equipments required to support each home by using injection locked FP-LD

▪ L-Band Power Calculations:

$$P_{BLS} = L_{Circulator} + 2 L_{Filter} + L_{AWG} + 5L_{Splice} + P_{Injected} \quad (1)$$

$$P_{BLS} = -5.65dBm$$

$$\begin{aligned} P_r &= P_{Injected} \\ &- (8 L_{Splice} + 3 L_{Connector} + 4 L_{Filter} \\ &+ 2 L_{AWG} + L_{Circulator} + \alpha * 1.6695 \\ &+ L_{Patchcord}) \end{aligned} \quad (2)$$

$$P_r = -31.317dBm$$

▪ C-Band Power Calculations:

$$\begin{aligned} P_{BLS} &= L_{Circulator} + 2 + L_{AWG} + 5 L_{Splice} \\ &+ 3 L_{Connector} + \alpha * 1.669 \\ &+ L_{Patchcord} + P_{Injected} \end{aligned} \quad (3)$$

$$P_{BLS} = -3.916dBm$$

$$\begin{aligned} P_r &= P_{Injected} - (8 L_{Splice} + 3 L_{Connector} \\ &+ 4 L_{Filter} + 2 L_{AWG} \\ &+ L_{Circulator} + \alpha * 1.6695 \\ &+ L_{Patchcord}) \end{aligned} \quad (4)$$

$$P_r = -31.234dBm$$

The survivability performance of the proposed design can also be determined by calculating the system availability. The overall unavailability of the system is given by the following equations:

$$\begin{aligned} U_{Overall} &= U_{OLT} + U_{FF} + U_{AWG} \\ &+ U_{DF} + U_{ONU} \end{aligned} \quad (5)$$

$$\begin{aligned} U_{OLT} &= U_{TRX} + U_{WDM} + U_{AWG} \\ &+ 2 U_{BLS} + U_{CD} \end{aligned} \quad (6)$$

Where:

$U_{OLT}$ : OLT unavailability

$U_{TRX}$ : Transceiver unavailability

$U_{WDM}$ : WDM filter unavailability

$U_{AWG}$ : AWG unavailability

$U_{BLS}$ : BLS unavailability

$U_{CD}$ : Bidirectional coupling device unavailability which consists of 2 circulators and 2 WDM filters.

The overall unavailability and the overall availability of the system for a single channel is  $830.8 \times 10^{-7}$  and 0.999917, respectively [10].

## IV. Conclusions

WDM-PON technology is the newest generation of fiber-based access network solutions available. It is a technology that multiplexes multiple optical carrier signals into a single optical fiber by using different wavelengths of laser light to carry different signals. Even though it provides all of the fiber-saving advantages without the limitations of TDM PON, it has a little success in commercialization. This is due to the fact that there has been no practical and low-cost solution for a WDM light source, until the ASE-injected FP-LD scheme and athermal AWG has been proposed as the best economical and practical solution.



Moreover, a qualitative overview of the need for WDM PON has been presented. Also, we have made the case for WDM PON in Libyan market by taking Hay Al-Zohour residential area as a case study in order to choose the right system for next generation access network in Libya. Furthermore, we have tested the performance of the WDM PON segment of Hay Al-Zhour design.

Finally, we believe that WDM PON is needed in Libya not just for the next five years, but this architecture can support users' overgrowing demands for more than additional 70 years from now. This is because WDM PON can be upgraded to support each end user with more than 2.5Gbps. On the other hand, other TDM PONs will not be able to handle the growing bandwidth demand since they are time dependent networks and upgrading means a night mare for carriers and service providers. This is because there is a part of network infrastructure that depends on the transmission rate before the network can be designed. If there is any upgrading process, the splitting ratio has to be decreased which means the number of the splitters will increase and accordingly increasing the cost and more wasted time will be spend on network configuration. All of these problems can be successfully avoided by the use of WDM PON.

## References

- [1] White paper, "LG-Nortel Ethernet over WDM PON technology overview technology", [http://www.profiber.cz/eshop/files/LG-Nortel\\_Ethernet\\_WDM-PON.pdf](http://www.profiber.cz/eshop/files/LG-Nortel_Ethernet_WDM-PON.pdf), accessed on June 7, 2010.
- [2] Joan Engebretson, "Get Ready for WDM-PON Emerging standards could increase PON bandwidth and help expand fiber capabilities", Article Reprint - TELLABS EMERGE, 2007.
- [3] White Paper, "WDM-PON Technologies", [http://www.ciphotonics.com/PDFs\\_Jan08/WPON\\_White\\_Paper\\_v10.pdf](http://www.ciphotonics.com/PDFs_Jan08/WPON_White_Paper_v10.pdf), accessed on June 7, 2010.
- [4] Chang-Hee Lee et al, "WDM-PON experiences in Korea", JOURNAL OF OPTICAL NETWORKING, Vol. 6, No. 5, Pages 451-464, 2007.
- [5] JimTheodoras, "Staying ahead of the access bandwidth curve with WDM-PON", <http://www.lightwaveonline.com/fttx/featured-articles/Staying-ahead-of-the-access-bandwidth-curve-with-WDM-PON-56740887.html>, accessed on June 7, 2010.
- [6] Mohamed Matoug and Najwa Shagluf, "Next Generation Access Network Fiber To The Home-GPON Technology", B.Sc. Thesis, Alfatah University, Tripoli, Libya, 2009.
- [7] Julien Vincent, France telecom, FTTH in France, presented on March 6th, 2008.
- [8] Paul E. Green, Jr., "Fiber to The Home: The New Empowerment", John Wiley and Sons, 2006.
- [9] Soo-Jin Park et al, "Fiber-to-the-Home Services Based on Wavelength-Division-Multiplexing Passive Optical Network", JOURNAL OF LIGHTWAVE TECHNOLOGY, VOL. 22, NO.11, pages 2589 – 2590, 2004.
- [10] Joon-Young Kim et al, "Protection and Fault Localization in a WDM-PON", Department of Electrical Engineering and Computer Science, Korea Advanced Institute of Science and Technology, 2008.



المؤتمر الدولي العربي الليبي الخامس للهندسة الكهربائية والإلكترونية 2010/10/26-23 طرابلس ليبيا



## A New Hardware Implementation of Manchester Line Coding

Ibrahim Khorwatt<sup>1</sup> and Nabil Naas<sup>2</sup>

(1) ALJEEL ALJADEED FOR TECHNOLOGY, Tripoli, Libya , i.khorwatt@aljeel.ly

(2) Electrical and Electronic Engineering Department, Elfatah University, Tripoli, Libya  
nabil.naas@ee.edu.ly

### *Abstract-*

Manchester encoding is a clock encoding technique used by the physical layer to encode the clock and data of a bit stream. A Manchester encoded signal contains frequent level transitions that allow the receiver to extract the clock signal and correctly decode the value and timing of each bit. Manchester encoding and decoding is usually implemented using programmable devices such as AVR and PIC. This paper presents a new hardware implementation of Manchester encoding and decoding. The new implementation is based on using familiar IC chips; such as D flip flops, shift registers, and AND gates. To verify the implementation of the new circuits, we have demonstrated that the results obtained from the real implementation exactly match the results obtained via simulation.

### I. Introduction

In order to reliably exchange digital data between two devices connected together by a transmission medium, a high degree of synchronization is required. Typically, data are transmitted bit by bit over the medium, and the timing (rate, duration, and spacing) of these bits must be the same for the transmitter and receiver [1]. To achieve this, two transmission techniques are commonly used: asynchronous transmission and synchronous transmission. However, a communication system with large amount of transmitted data usually uses synchronous transmission technique. There are two possibilities for this technique: (1) by providing a separate clock line between transmitter and receiver, or (2) by embedding the clocking information into the data signal. The second possibility can

be accomplished by using Manchester or Differential Manchester encoding.

The focus of this work is on Manchester encoding format, in which there is a transition at the middle of each bit period as shown in Figure 1. This technique has several advantages among them are: synchronization capability, no DC component, simplicity, and error detection capability.

The rest of the paper is organized as follows. In Section II, we describe the encoding circuit and elaborate on the difference between our transmitted data and Manchester encoded data. In Section III, we explain the approach behind our proposed technique for decoding the transmitted data using familiar logic gates and flip flops. Section IV presents the results of



simulating the circuits using Multisim 10, and compares the simulation results with the real measurements. Finally, Section V presents our concluding remarks, including a discussion about the advantageous and disadvantageous of the proposed technique.

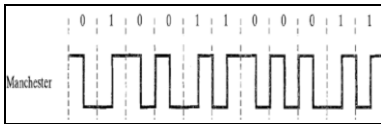


Figure 1: Manchester encoding format

Figure 2 shows the Manchester encoding circuit diagram of the transmitter used to simulate one-way transmission for eight bits of data using 8-bit static shift register, commercially known as CD4014 [2]. We can note that the clock frequency used to encode the data by an XNOR gate has a double clock frequency used to generate the data. This results in two transitions per bit of data, as shown in Figures 3 and 4.

## II. Encoding Circuit

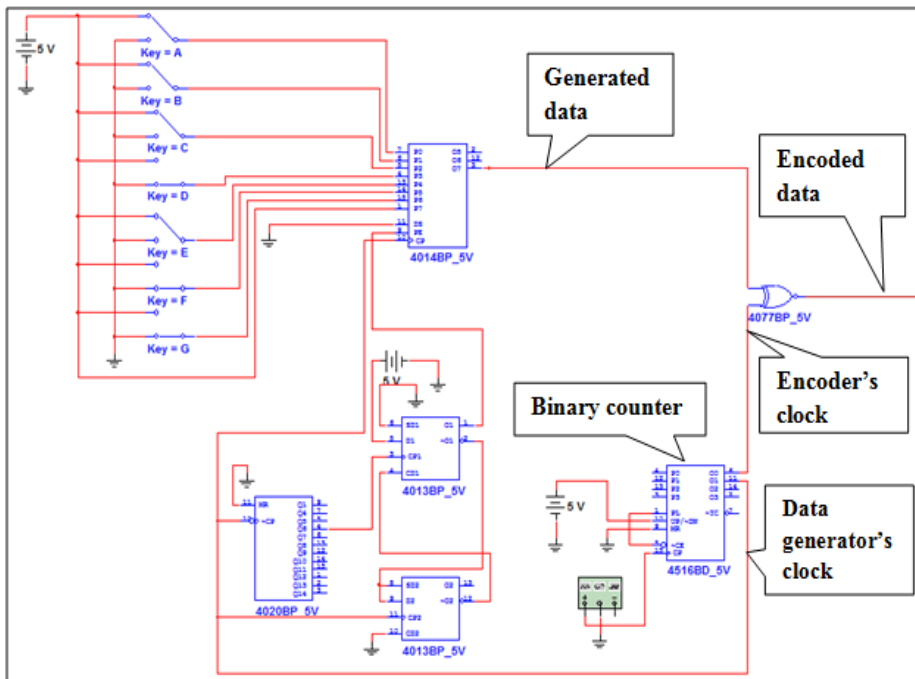


Figure 2: Manchester encoding circuit

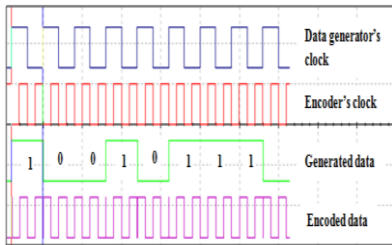


Figure 3: The encoded format after 10010111 bit pattern has been generated

Since there is a small delay between the clock frequency and the data to be encoded, as shown in the above figure, the resulted output of this circuit will not be exactly a 'Pure Manchester' but rather what we call 'Bar Manchester', as illustrated in Figure 4. However, we have made use of this output as a way to easily extract the data from Manchester using familiar gates at the decoder, leading to low complexity compared with Phase Locked Loop (PLL), Microcontrollers, or programmable devices.

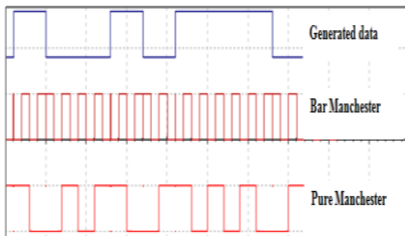


Figure 4: Representation of 10010111 bit pattern using Bar Manchester and Pure Manchester

The maximum clock frequency for this circuit is 1MHz, because the short bit duration resulted from the delay between the data and the encoder's clock will increase in width if the transmitter's clock frequency increases beyond 1MHz; therefore, it will make the decoder fails to interpret the received data accurately.

### III. Decoding Circuit

Now, since the clocking information is embedded into the encoded data stream, we can separate the clock from the original data stream using the following three stages:

#### A. Extracting the Primary Clock

The primary clock is the clock that provides the 2<sup>nd</sup> stage with a required source to decode the Bar Manchester encoded data. Figure 5 shows the circuit that performs this functionality.

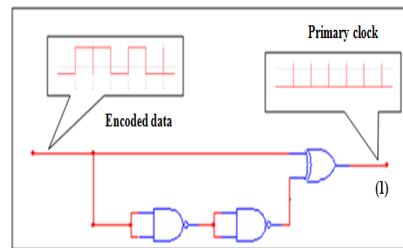


Figure 5: Extracting the primary clock from the Bar Manchester data

From the above figure, we can note that one of the XOR gate inputs is directly passing the encoded data, and the other input is passing the encoded data but with a small delay performed by two NAND gates connected in series with each other. As a result, the output is a very short pulse that can be used as a clock.

#### B. Extracting the Embedded Clock

At this stage, both the encoded data and the primary clock have to be entered into a circuit that performs the decoding process. Accordingly, we need a circuit that gives the ability of extracting the clock from Bar Manchester and it should be connected with



a feedback device in order to minimize the error resulted from the transitions in the received data. The desired circuit must have more than one output to give the flexibility of choosing the right clock, if one of its output ports does not give the correct clock. Also, the circuit should have a reset input in order to reset the chip avoiding any other errors after the desired clock has been locked. The best solution for this circuit is a shift register connected with a feed back D-flip flop (D-ff) that controls the amount of data enters the shift register through an OR

gate. Both the shift register and the D-ff work with the same primary clock. Moreover, the Master Reset (MR) for both is connected with the 4<sup>th</sup> output port of the shift register. In simulation, the best output port that produces the correct extracted clock from the shift register is the 4<sup>th</sup> output port, as shown in Figure 6, represented by (2). In real implementation, the best output port could be either the 2<sup>nd</sup> or 3<sup>rd</sup> port, depending on the clock frequency that has been employed at the transmitter.

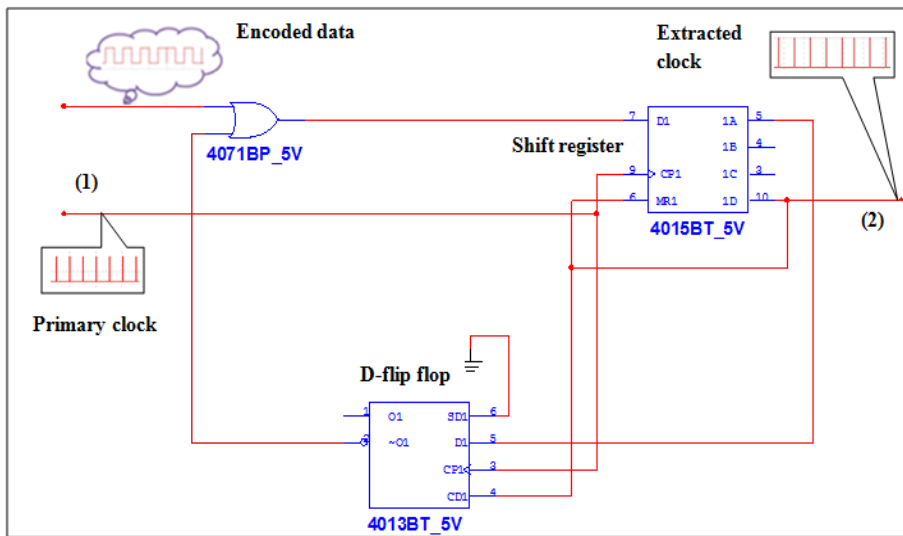


Figure 6: The circuit that extracts the embedded clock

### C. Decoding

After we got the extracted clock, we can get the original data stream, simply by using the D-ff as it has been represented by (3) in Figure 7. In real implementation, we

might have to change the output of this D-ff from  $Q^-$  to  $Q$ .

Figure 8 shows the three stages of the decoder connected all together.



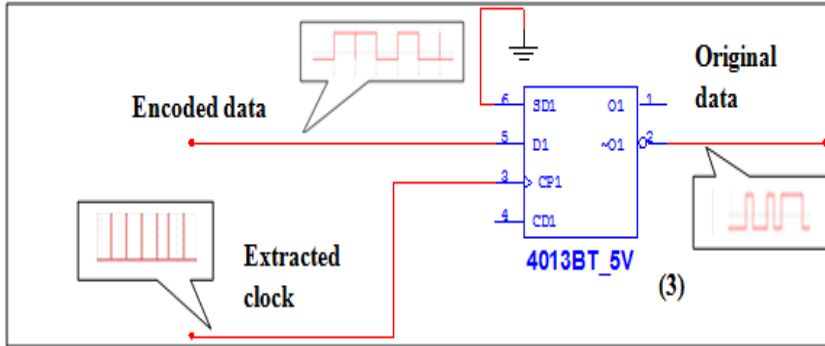


Figure 7: Decoder circuit

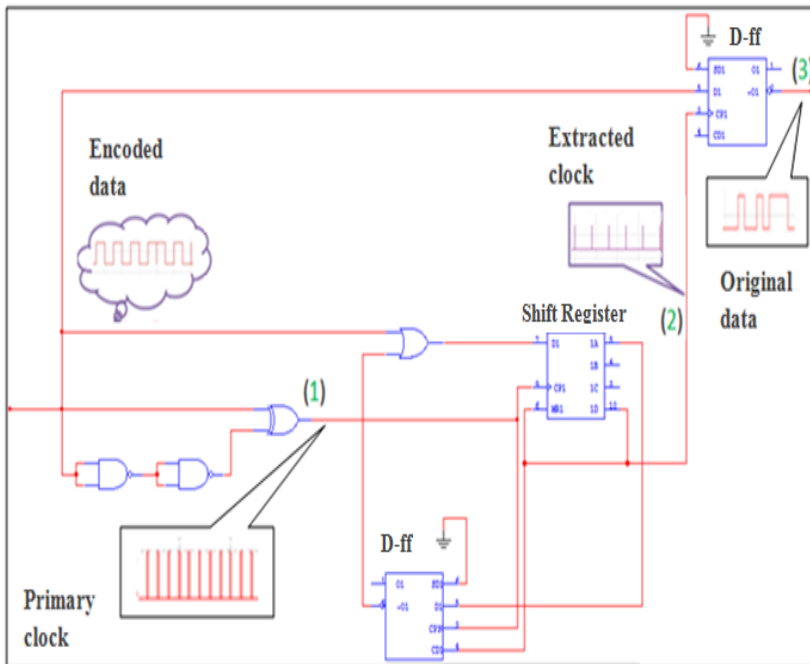


Figure 8: The full decoder circuit

#### IV. Results

The source of data to be encoded has been taken from the transmitter shown in Figure 2. We set the clock frequency to 100

KHz and adjusted the clock enable coming out from the 14-stage binary counter, commercially known as HEF4020B [3], in order to get 8 channels and a guard time equal to the time occupied by another 8



channels as a spare to transmit more data if available. The measurements using both Multisim program and real implementation are shown in Table 1.

Table 1: Comparison between the Lab and simulation measurements

Parameter	Simulation	Real
Bit Time duration ( $\tau$ )	41.131 $\mu$ sec	37 $\mu$ sec
The transmission rate (rb)	12.498 K bit/sec	13.286 K bit/sec
Idle time	321.337 $\mu$ sec	306 $\mu$ sec
Transmission time (T)	318.766 $\mu$ sec	296 $\mu$ sec

From the table, we can note that the maximum data rate that can be obtained, when 100 KHz clock frequency was applied at the transmitter is about 13 Kbit/sec. Consequently, we can get a transmission rate of about 125Kbit/sec, if 1MHz clock frequency is applied at the transmitter side. The oscilloscope output used in simulation is shown in Figure 9.

## V. Conclusions

We have proposed a new technique for line encoding and decoding of data using similar Manchester format but with two transitions per encoding bit. We have discussed how to decode data, which is encoded using this new technique by just using simple flip flops and gates and without the need for PLLs, microcontrollers or programmable devices, which results in a significant reduction in cost. Also, we have compared the simulation measurements, using Multisim program, with the measurements of the real implementation. The main finding of our results suggests that our proposed technique can be used to transmit data at maximum data rate of about 125Kbit/sec. However, due to the short pulses that are transmitted with the encoded data, we think it is difficult to apply any

digital to analogue modulation techniques on the encoded data, making it impossible to use this encoding technique for wireless communication. Nevertheless, as a future work, we do believe that we can improve this technique and make it more flexible in the near future.

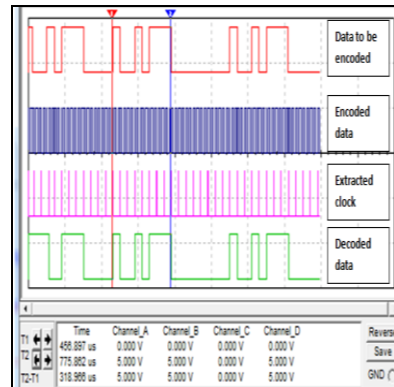


Figure 9: An oscilloscope output shows the data before/after encoding, after decoding, and the extracted clock when the data is (10010111), the used clock frequency is 100 KHz

## REFERENCES

- [1] William Stallings, "Data and Computer Communications", 7th edition, Prentice Hall, 2004, pp. 864, ISBN 0-13-1006819.
- [2]<http://www.microcontrolador.com.br/datasheets/CD4014.pdf>, accessed on June 4, 2010.
- [3]<http://pdf1.alldatasheet.com/datasheet-pdf/view/17691/PHILIPS/HEF4020B.html>, accessed on June 4, 2010.



## **CONGESTION CONTROL POLICIES FOR IP-BASED CDMA RANDOMLY EARLY DETECTION ALGORITHM (RED)**

Shaik Imam Saheb\* , Mahmoud A. Arteimi\*\*

\*Zawia Engineering College, Zawia Libya

\*\*Higher Institute of Vocational Studies Zawia -Libya

\*[shaikimamsa@yahoo.com](mailto:shaikimamsa@yahoo.com)

\*\* [mah\\_art78@yahoo.com](mailto:mah_art78@yahoo.com)

### **Abstract**

As CDMA-based cellular networks mature, the current point-to-point links used in connecting base stations to network controllers will evolve to an IP-based Radio Access Network (RAN) for reasons of lower cost due to statistical multiplexing gains, better scalability and reliability and the project growth in data applications. In this paper, we study the impact of congestion in a best-effort IP RAN on CDMA cellular voice networks. We propose and evaluate the congestion methods Drop Tail Router and RED algorithm for router control, to maximize network capacity while maintaining good voice quality. Using computer simulation on large networks results congestion level up to 50% to 60% in RED Algorithm. It is observed that computer simulation results with RED Algorithm provides better throughput as compared to computer simulation results with Drop Tail Algorithm.

### **Keywords**

### **CDMA IP-RAN RED Congestion Router**

## **1. INTRODUCTION**

Wireless access networks are more mature now days. The present wireless communication system is moving towards the IP enabled network, where the cellular services are integrated with IP network for the transmission of data. Such networks are generally termed as IP-RAN network. In this network the Transmission Control Protocol (TCP) is the most widely used method to achieve elastic sharing between end-to-end IP

flows. In these wireless access networks, the base stations are connected to radio network controller or base station controller by Point to Point links. These Links are expensive and their use imposes and ongoing cost on the service providers. In such networks reliability comes at a high price.

## 1.1 RADIO ACCESS NETWORK (RAN)

In wireless access networks the base stations and the radio network controllers are connected by point-to-point T1/E1 links [1]. These back-haul links are expensive and add to operating costs. In this point-to-point architecture, the Radio Network Controllers (RNCs) are only shared by a small set of base stations (BSs) and can contribute to significant blocking during hot spot and peak hours. So the network operator needs to appropriately scale-up the RNC capacity thereby increasing capital costs. In this architecture RNC is a single point of failure. It is highly redundant and also increases the cost of each RNC. [2]

## 1.2 IP – Based RAN

One of the effective ways to reduce these costs is to replace the point-to-point links with an IP-based Radio Access Network (IP-based RAN) [3].

Architecture IP based RAN is shown in Fig 1. and it has a number of benefits as follows

- **Scalability:** RNC capacity can be shared with a larger set of base stations. By load balancing calls across the different RNCs, call blocking and dropping can be lowered. [1]
- **Reliability:** When base stations are connected to multiple RNCs, failure of RNCs can be accommodated by transferring the calls from one RNC to another. [1]
- **Flexibility:** Point-to-Point links are expensive and cannot be shared. An IP-based RAN will benefit from statistical multiplexing gains and can also be shared with other applications as long as appropriate QoS can be ensured. [1]

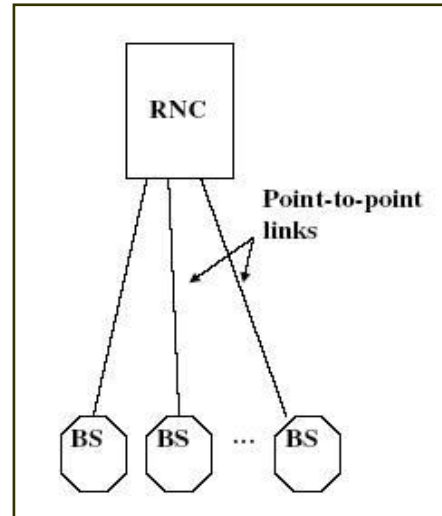


Fig 1. Current RAN

IP is expected to be the access network for next generation UMTS networks. Congestion occurs when the offered traffic exceeds the engineered IP RAN capacity. There are three approaches to control and avoid congestion.

1. The network can be over-provisioned or peak-provisioned so that congestion never occurs. This is not a practical solution because access network bandwidth is still very expensive compared to core network bandwidth.
2. One can reserve resources in the access network even though various reservation schemes have been proposed and implemented in routers. These approaches are yet to be widely deployed in current IP networks.
3. Assume a best-effort IP RAN and use properly designed policies to control and avoid congestion.[1]

## 1.3 CONGESTION IN NETWORK



Congestion in a network may occur if the load on the network i.e. the number of packets sent to the network is greater than the capacity of the network.

Congestion may occur due to several reasons such as overloading the network, burst transmission, variable bit rate transmission etc., and congestion reduces the performance of a network and to be controlled.

Congestion control refers to the mechanism or technique to keep the network load below the capacity limit.

Congestion happens in any system due to the involvement of waiting, abnormality in the flow etc.

In network congestion occurs because routers and switches have queues or buffers that hold the packets before and after processing.

- Fast sender is transmitting to slow receiver
- Buffer space on receiver is less
- Packets getting delayed at routers
- Bandwidth of the transmission media is less

For example, a router has an input queue and an output queue for each interface. When a packet arrives at the incoming interface, it undergoes three steps before departing

- The packet is put at the end of the input queue while waiting to be checked.
- The processing module of the router removes the packet from the input queue once it reaches front of the queue and uses its routing table and the destination address to find the route.

- The packet is put in the appropriate output queue and waits its turn to be sent.[3]

The two issues which result in congestion are

1. If the rate of packet arrival is higher than the packet processing rate, the input queues become longer and longer.
2. If the packet departure rate is less than the packet processing rate, the output queues become longer and longer.

### 1.3.1 CONGESTION IN IP RAN

In a wireless access network mobile devices communicate with base stations over wireless links. The base stations communicate with the rest of the voice or data network through the Access Network Controllers (ANCs) (also called Radio Network Controller, RNC, in 3G UMTS, and Base Station Controller, BSC, in CDMA2000).

A part of this network is common to both wireless voice and data traffic. The network separates only beyond the ANC where voice frames are forwarded to the MSC (PSTN) and data frames are forwarded to the Service Nodes (Internet) [9].

Each base station can communicate with hundred or more mobiles and each ANC can control several tens of base stations as shown in Fig2.

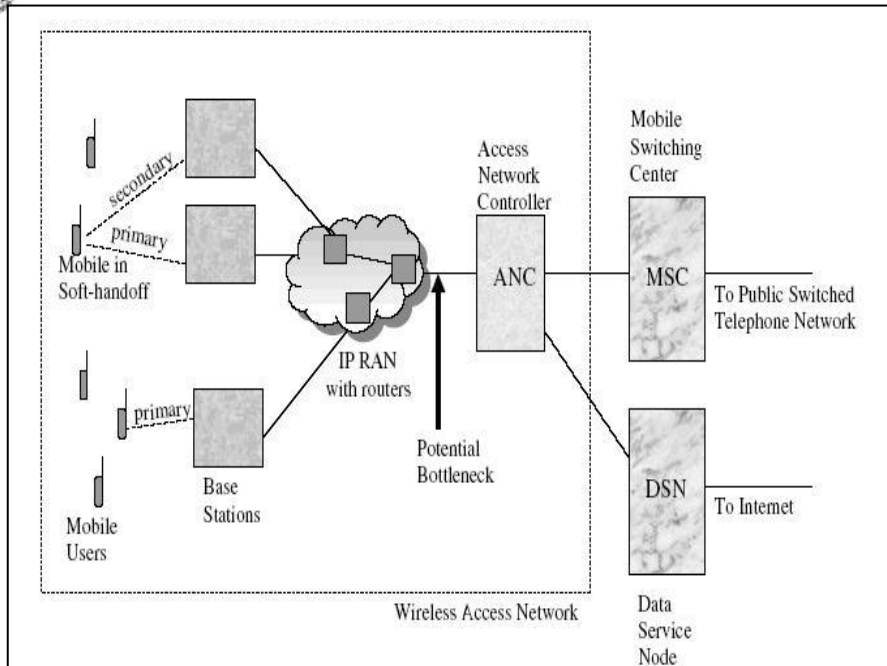


Fig 2: Several Base stations are connected

performs two main wireless functions *frame selection* and *reverse outer loop power control*

1. Frame selection exploits one of the key properties of a CDMA network soft-handoff. In soft-handoff, a mobile communicates with more than one base station simultaneously. Soft-handoff helps reduce interference on the wireless link thereby increasing CDMA capacity. When in soft-handoff, a mobile receives multiple frames in the downlink direction (also called forward link) and combines them to construct a single voice frame.
2. In the uplink direction (also called the reverse link) the ANC receives multiple frames from the mobile. It performs the frame selection function which involves selecting the frame with the best quality among the ones it receives. If the frames from all the different legs of a call in soft-handoff call do not arrive within a preset

time interval (20ms in the case of CDMA2000), the ANC forwards the current best frame to the network.[1]

In other words, a late frame is treated as if it was a dropped frame and thus, controlling delay in the access network is extremely important. Now describe the operation of the IP network between the base station and the ANC. On receiving voice frames from different mobiles, a base station aggregates several voice frames into an IP packet and sends them out towards the ANC.

Voice frames are only few tens of bytes in length. Their aggregation helps in reducing IP header overhead. Voice frames belonging to the different legs of soft-handoff are transmitted by different base stations and hence arrive at the ANC on different IP packets. On receiving IP packets from the base stations, an ANC demultiplexes the voice frames and performs frame selection and outer loop



power control functions and forwards the best voice frame uplink.

Voice frames also contain power information that is used by the ANC for outer loop power control. Therefore packet loss, and hence loss of voice frames, due to RAN congestion could result in imperfect outer loop power control.

This can cause the power consumption in a cell to be higher than its expected value and thereby reduce the overall capacity. Thus, controlling loss in the access network is very important. A bottleneck occurs during congestion as depicted in Fig. 3

## 2 ROUTER CONTROL MECHANISM

The growth of the Internet in the last decade is nothing short of an exponential one.

### 2.1 ACTIVE QUEUE MANAGEMENT

This rapid growth continues to astonish and bewilder all of us. This phenomenon has put increasing pressure on vendors to build high performance Internet Protocol (IP) routers with aggregate capacities exceeding 1 Tb/s. Also, the demand for more bandwidth with the advent of network intensive Internet applications has made router buffer management a high priority.

because the link carries the aggregate traffic of several tens of base stations. While the link will be engineered to take into account the statistical multiplexing gains of this aggregation, offered traffic could temporarily exceed the engineered capacity of the link due to hot spots or other reasons. [1]. So it requires mechanisms to respond to these temporary congestion events in a graceful manner.

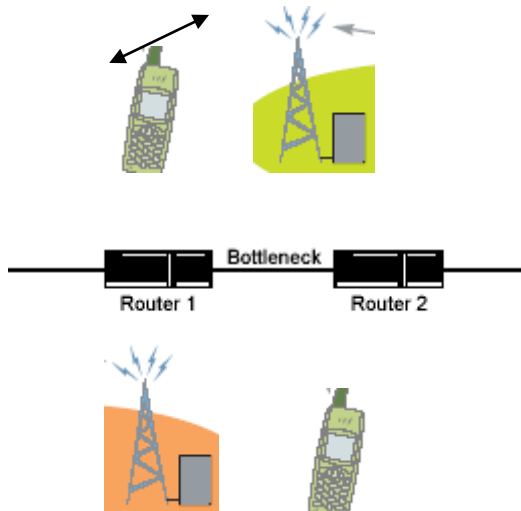


Fig 3. Network Routers Communication

Modeling TCP performance has received increasing attention during the last few years due to the benefits it offers to the networking community. Analytical TCP models enable researchers to closely examine the existing congestion control algorithms, address their shortcomings, and propose methods for their improvement. They may also be used to compare various

TCP schemes and implementations, and to determine their performance under various operating conditions. These models help examine the interactions between TCP and the queuing algorithms implemented in routers. Hence, they aid in the improvement of existing algorithms and in designing better algorithms, such as AQM techniques. Finally, such models offer the possibility of defining TCP-friendly behavior in terms of throughput for non-TCP flows that coexist with TCP connections in the same network. [6]

Internet applications, such as the World Wide Web, file transfer, Use net news, and remote login, are delivered via the Transmission Control Protocol (TCP). With an increasing number and variety of Internet and applications, congestion control becomes a key issue.

A Drop Tail queue management mechanism drops the packets that arrive when the buffer is full. This method has two drawbacks. [1]

1. This mechanism allows a few connections with prior request to dominant the queue space allowing the other flows to starve making the network flow slower.
2. Drop Tail allows queues to be full for a long period of time. During that period, incoming packets are dropped in bursts. This causes a severe reduction in throughput of the TCP flows.

## 2.2 ROUTER CONGESTION CONTROL METHODS

There are several schemes for dealing with congestion at gateway. But none of them fulfils the demand of users and consequent load on the network. Some of these are as follows.

### 2.2.1 DROP TAIL ROUTER

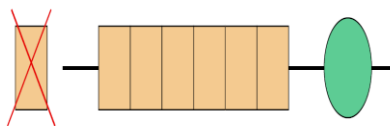


Fig 4. Drop Tail Router

In the Drop Tail queue management mechanism as shown in Fig 4, drops the packet that arrives when the buffer is full.

- FIFO queuing mechanism that drops packets from the tail when the queue overflows.
- Introduces global synchronization when packets are dropped from several connections. [8]

### 2.2.2 RANDOM DROP ROUTER

This policy intends to give feedback to users whose traffic congests on the gateway by dropping packets on a statistical basis. The key to this policy is the hypothesis that a packet randomly selected from all incoming traffic will belong to a particular user with a probability proportional to the average rate of transmission of that user. [8]



Fig 5. Random Drop Router

A key problem of this policy is that dropping a randomly selected packet as shown in Fig 5. results in users, which generates much traffic having a greater number of packets dropped compared with those generating little traffic. This policy can be Random Drop for Congestion Recovery or Random Drop for Congestion Avoidance [7]





### 3.1 DROP TAIL ROUTER WITH CDMA

In the Drop Tail queue management mechanism drops the packet that arrives when the buffer is full as shown in Fig 6.

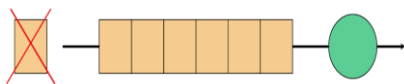


Fig 6. Drop Tail Router

FIFO queuing mechanism that drops

- packets from the tail when the queue overflows.
- Introduces global synchronization when packets are dropped from several connections.

#### 3.1.1 ALGORITHM OF DROP TAIL

1. Start
2. Checks Queue Length
3. If Number of Packets Arrived is greater than Queue Length
4. go to 7
5. else go to 6
6. En queue Arrived Packets
7. Drop Arrived Packets
8. Stop

### RED ALGORITHM WITH CDMA

#### 3.1.2 RED FUNCTIONALITY

The RED algorithm involves computing the average queue size and then comparing it to two thresholds, a minimum and maximum as shown Fig 7. If the average queue size is below the minimum threshold, the packet is not dropped and is sent to the buffer. If the average queue size is above the maximum threshold, each arriving packet is dropped. [4]

When the average queue size is between the minimum and maximum thresholds then the arriving packet is marked with a packet drop probability,  $p_a$ . This probability is a function of the average queue size, every time a packet is marked with it, then the probability that a packet is marked from a particular connection is roughly proportional to that connection's share of the bandwidth at the router [10]. Moreover this probability determines whether the packet is dropped or not. [4]

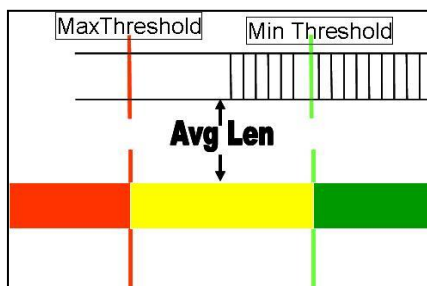


Fig 7. Red Algorithm with .Min and Max Threshold.

RED mechanism contains two key algorithms.

- To calculate the exponentially weighted moving average of the queue size, so as to determine the burstiness that is allowed in the gateway queue and to detect possible congestion.
- Algorithm is use for computing the drop or marking probability, which determines how frequently the gateway drops or marks arrival packets.

This algorithm can avoid global synchronization by dropping or marking packets at fairly evenly spaced intervals.

It can sufficiently drop or mark the ().It takes 3 packets at time.packets. It also can maintain a reasonable bound of the average



delay, if the average queue length is under control. [5]

### 3.2 RED ALGORITHM

For each packet arrival

Calculate the average queue size

$avg$

If  $minth \leq avg < maxth$

Calculate the probability

$P_a$

With probability  $P_a$ :

Mark the arriving packet

Else if  $maxth \leq avg$

Mark the arriving packet. [4]

Where  $P_a$  is Packet Drop Probability

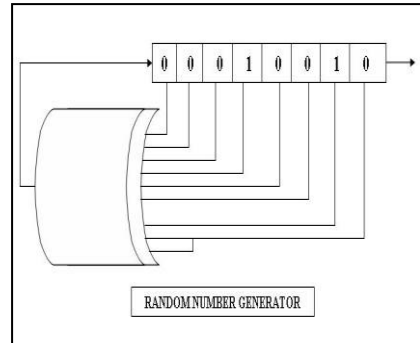


Fig 8. Random Number Generator

#### 3.2.1 IMPLEMENTATION OF RED

An overview of the system architecture for the RED buffer management scheme is as shown. The Main components of RED are given below:

- Input Interface and the Buffer
- Packet Drop Probability Unit (PDPU) [11].
- Compute Random Value Unit (CRVU).
- Random Packet Drop Unit (RPDU) [12].

#### 3.2.2 INPUT INTERFACE AND BUFFER

Input Interface consist of three users i.e. user1, user2, user3 .Input message is of 8 bit length. So to get binary form of Message, first find ASCII value using `str.getBytes ()` of each character then converted into its

binary form using `Integer.toBinaryString`

The Size of the buffer is 20,  $maxThreshold = 5$  and  $minThreshold = 15$ . [1]

#### 3.2.3 PACKET DROP PROBABILITY UNIT (PDPU)

$P_b = P_{max} * (\text{average length} - \text{minThreshold}) / (\text{maxThreshold} - \text{minThreshold})$  [1]

$P_a = P_b / (1 - \text{count} * P_b)$  [1]

Where  $P_a$  and  $P_b$  is Packet Drop Probability

#### 3.2.4 COMPUTE RANDOM VALUE UNIT (CRVU)

The Configure Random Value Unit uses a random generator function to compute a random number as shown in Fig 8. An 8 bit initial seed is used and set equal to "00010010". tests were conducted with different seeds and a seed of "00010010" produced the most unbiased random number i.e. random numbers were never repeated, a unique output for each time.



A feedback signal is computed by running an XOR process on each of 8 bits of the initial seed in the following manner:  
 $feedback \leq q(0) \text{ xor } q(1) \text{ xor } q(2) \text{ xor } q(3) \text{ xor } q(4) \text{ xor } q(5) \text{ xor } q(6) \text{ xor } q(7)$

Fig 10. Block Diagram Compute Random Number Generator

In the next step the feedback bit is concatenated with the most significant 7 bits of the initial seed:  $q \leq (feedback \& q(0 \text{ to } 6))$ . Each time the initial seed value is taken as the final seed value from the previous process. Fig 10. shows an overview of the activities in the CRVU. [1]

### 3.2.5 RANDOM PACKET DROP UNIT (RPDU)

1. Start
2. If  $(P_a > P_r)$
3. Accept the Packet
4. else if  $(P_a \leq P_r)$
5. Reject the Packet
6. Stop

#### A. Average Queue Length

Average length =  $((1-W_q) * \text{average length} + (\text{double})v.size() * (\text{double})W_q)$  [1]  
 where  $v.size()$  is the newly measured queue length and  $W_q$  is exponential weighted

#### B. RED Parameter Settings

1.  $W_q$  suggest  $0.001 \leq W_q \leq 0.005$
2. Used  $W_q = 0.3F$  for simulations
3.  $P_{max} = 0.02F$
4. Buffer Size = 20
5. "Parameter setting rule of thumb",  $maxThreshold$  at least twice  $minThreshold$ , however  $maxThreshold = 3$  times  $minThreshold$  is used. [4]
6.  $minThreshold = 05$

7.  $maxThreshold = 15$
8. average queue size i.e. average length = 0
9. Count = -1
10. RED is most effective when  $maxThreshold - minThreshold$  is larger than calculated average queue size.[4]

## 4 DROP TAIL ROUTER SIMULATION RESULTS

We show the User Interface of Transmitter and Receiver of CDMA as shown in Fig 9. The Buffer Status and Line chart of Number of packets enqueued are shown in green, Graph shows number of packets vs Buffer length in Fig 10. In Drop Tail Router Algorithm when buffer status is 100% and full the packets are dropped and give a drop message. In our results buffer status is full and line chart shows 4 packets are dropped in red color.

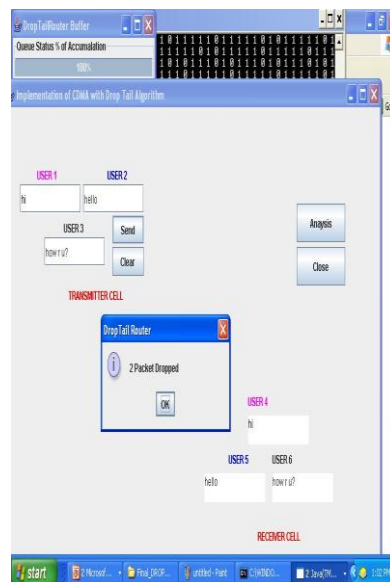


Fig 9: Drop Tail Buffer with Packet Dropping Message

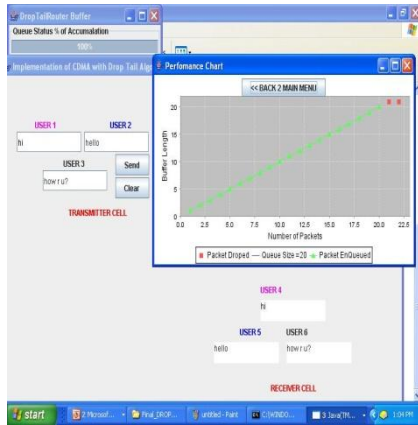


Fig10: Drop Tail Buffer with Line Chart Packet Dropping Message

## RED ALGORITHM SIMULATION RESULTS

We show user interface of Transmitter and Receiver cell of CDMA each consists of three Users namely User1, User2 and User3 at Transmitter Cell and User4, User5 and User6 at Receiver Cell as shown in Fig 11. The Buffer Status and Line Chart of Packets enqueued in green color, Graph of Number of packet Vs Average Queue Length. The Buffer Status are 35%, 30%, 25% and also it shows Packet Dropped Message as 2, 3, 3 respectively. The Buffer Status and Line Chart of Number of Packets Dropped indicate in red spot, Graph of Number of packet Vs Average Queue Length as shown in Fig 12. When the Buffer Status is 25% it shows Comparison of Congestion Level in the form of Bar Chart between Drop Tail Algorithm & RED Algorithm. Blue color bar is used to indicate congestion of due to Drop Tail Algorithm where as red color bar is used to

indicate congestion of due to RED Algorithm as shown in the Fig 13. From graph it is observed that once the buffer is Full 100% congestion occurs in Drop Tail Algorithm where as in RED Algorithm it is only 40%. Hence RED Algorithm gives better performance as compare to Drop Tail Algorithm. The Buffer Status is 25%; it shows Comparison with respect to Number of Packet Drop in Drop Tail Algorithm and RED Algorithm in the form of Bar Chart. From graph it is observed that number of packet drop is zero Drop Tail Algorithm as long as the buffer is not full. From graph it is observed that number of packet drop is maximum packet drop is eight in RED Algorithm. As RED Algorithm works on minThreshold and maxThreshold for each pack arrived average queue length is calculated. So from graph it is observed that number of packet is dropped in RED Algorithm.

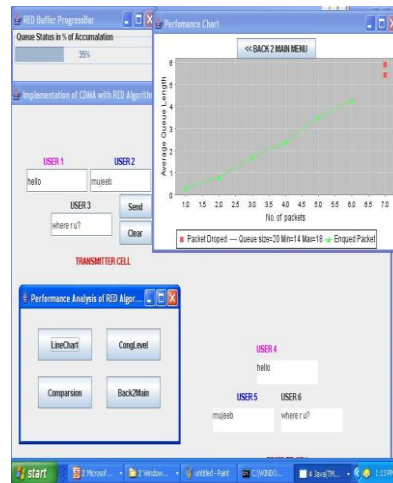


Fig 11: Red Buffer Status with Line Chart

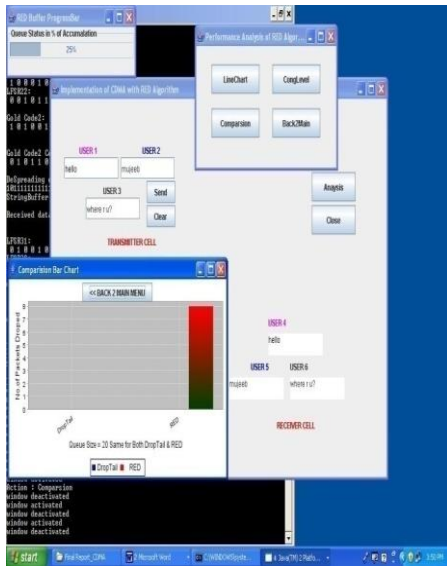


Fig 12: Comparison of Drop Tail and RED with respect to Packet Drop

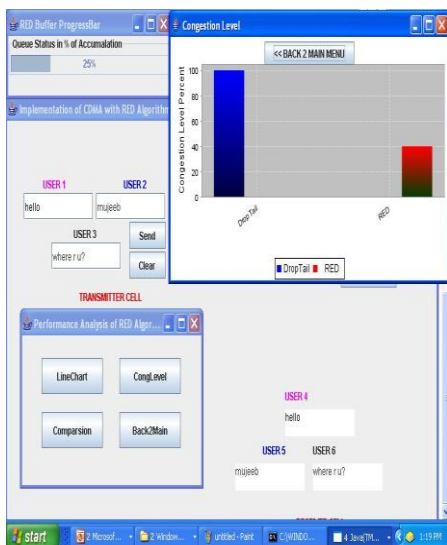


Fig 13: Congestion Level of Drop Tail and

RED

### 5. CONCLUSIONS

The present wireless communication system is moving towards the IP enabled network, where the cellular services are integrated with IP network for the transmission of data. Such networks are generally termed as IP-RAN network. In this network the Transmission Control Protocol (TCP) is the most widely used method to achieve elastic sharing between end-to-end IP flows. In these wireless access networks, the base stations are connected to radio network controller or base station controller by Point to Point links. These Links are expensive and their use imposes an ongoing cost on the service providers. In such networks reliability comes at a high price

CDMA is an important air interface technologies for cellular wireless networks. CDMA-based cellular networks mature, the current point-to-point links will evolve to an IP-based Radio Access Network (RAN). But congestion occurs when the offered traffic exceeds the engineered IP RAN capacity.

In this paper one most advanced congestion avoidance policies namely Router Control in wireless network is realized. A router is designed with Drop Tail Algorithm & the Random Early Detection Active Queue Management scheme (REDAQM) by using the features of CDMA networks to avoid congestion. Comparison is done between Drop Tail Algorithm and Random Early Detection Algorithm (RED) by taking buffer size is twenty.

Drop Tail Method works on First In First out, the Packet Drop Percentage is zero as long as the buffer is empty. Once buffer is full i.e. congestion occurs all the



in coming packets are dropped. Computer simulation result shows congestion level is 100% in Drop Tail Algorithm once buffer is full.

Random Early Detection Algorithm (RED) works on minimum, maximum threshold and average length. It avoids congestion by calculating average queue length for each packet arrived. It drops the packet depending upon calculated average queue length. Computer Simulation result shows maximum number of packet dropped in Random Early Detection Algorithm is eight & congestion level is 40%.

It is observed that computer simulation results reduced congestion level up to 50% to 60% in RED Algorithm. It is observed that computer simulation results with RED Algorithm provides better throughput as compare to computer simulation results with Drop Tail Algorithm.

In this we discuss a congestion avoidance algorithm for higher level of congestion avoidance in gateways. The threshold is calculated based on randomly generated values work can be carried on optimizing the average q-size for maximizing the throughput. The algorithm can be further enhanced with incorporation of traffic management algorithms. The work is implemented targeting TCP protocol and further works can be carried out to make it compatible with other protocols.

## 6. REFERENCES

1. Sneha Kumar Kasera, Ramchandran R, Sandra R, and Xin Wang, "Congestion Control Policies for IP-Based CDMA Radio Access Network," *IEEE Trans on mobile computing, vol4, pp.349-62, july/aug2005*.
2. Tian Busman Chon Chan, Ram Ramjee, "Connectivity Performance and Resiliency of IP-Based CDMA Radio Access Networks", *IEEE INFOCOM 2004*.
3. G. Heijenk .G. Karagiannis, V. Rexhepi, and L. Westberg "Diffserv resource management in ip-based radio access networks ," in *Proceeding of 4<sup>th</sup> International Symposium on Wireless Personal Multimedia Communications (WPMC'01)* , Aalborg, Denmark, September 2001.
4. S.Floyd and V.Jacobson, "Random Early Detection Gateways for Congestion Avoidance", *IEEE/ACM Trans.Networking, vol.1, no.4, pp.397-413, Aug1993*.
5. V.Jacobson, "Congestion Avoidance & Control", in *Processing of SIGCOMM '88*, pp.314-329, august 1988.
6. Wang, Z., and Crowcroft, J., "A New Congestion Control Scheme: Slow Start and Search (Tri-S)", *Computer Communication Review*, V.21 N.1, Jan-unary 1991, pp. 32-43.
7. Jacobson, V., "Congestion avoidance and control". In *Proceedings of ACM SIGCOMM*, pp. 314-329, 1998.
8. A. A. Akintola, G. A. Aderounmu, L. A. Akanbi and M. O. Adigun, "Modeling and Performance Analysis of Dynamic Random Early Detection (DRED) Gateway for Congestion Avoidance", *Issues in Informing Science and Information Technology*, pp 623-36 ,2001.



9. Jochen Schiller, "Mobile Communications", *Second Edition, Ch no.2, pp41-46.*
10. Vijay K. Garg, "IS-95 CDMA and cdma2000", Pearson Education, 2002.
11. Andy Miller and Michael Gulotta, "PN Generators Using the SRL Macro " , 1999.
12. E.H. Dinan, B. Jabbari, "Spreading codes for direct sequence CDMA", IEEE Communications Magazine, pp. 48-54, September 1998.



المؤتمر الدولي العربي الليبي الخامس للهندسة الكهربائية والإلكترونية 23-26/10/2010 طرابلس ليبيا





## **A SystemC-Based Design Methodology for Modelling Complex Wireless Communication Systems**

Ibrahim Aref, Nuredin Ahmed, Fernando Rodríguez-Salazar, Khaled Elgaid

E-mail: {iaref, nahmed, fernando, kelgaid}@elec.gla.ac.uk

Department of Electronics and Electrical Engineering,  
University of Glasgow, Rankine Building, Oakfield Avenue,  
Glasgow, G12 8LT, United Kingdom

### **Abstract**

SystemC is emerging as a suitable design and modelling language. It provides a consistent methodology for the design and refinement of complex digital systems.

This paper focuses on how wireless features can be incorporated into existing SystemC design methodology in order to use this methodology to model wireless systems. The SystemC modelling language currently lacks a standard framework that supports modelling of wireless communication systems (particularly the use of wireless communication channels). Three components must be investigated in order to achieve this target: the development of a system level model of a digital wireless communication channel that represents the core of any communication system, the creation of a small library of dedicated elements at system level, such as PLL (Phased Locked Loop), 8B/10B Encoder/Decoder and several communication protocols modelling, and a case study/demonstration validating wireless extension methodology. The first two parts have been modelled successful, so we now focus on modelling a flocking behaviour system and demonstrating how these parts integrate to achieve the target.

Keywords: SystemC, Modelling, Simulation, Channel, ARQ.

### **I. INTRODUCTION**

SystemC is emerging as a suitable design and modelling language. It provides a consistent methodology for the design and refinement of complex digital systems. This methodology is essential to managing complexity and enhancing designer productivity. It allows the designer to view designs at different levels of abstraction and, in particular, advocates the evaluation

of system performance early in the design cycle. It is also useful for guiding the refinement process into lower levels of abstraction. It is desirable to apply the same design methodology throughout complex systems, including any off-chip components. Surprisingly, the SystemC modelling language still lacks a standard framework that supports wireless communication systems modelling (in



particular the use of wireless communication channels).

This paper proposes to fill this gap by extending existing SystemC design methodology to include an efficient simulation of wireless systems. It proposes to achieve this by developing a system-level model of a wireless communication channel, along with a small repertoire of standard components (which can of course be replaced in a per application basis).

SystemC methodology has previously been employed to manage the complexity of the design flow process at system level. To accomplish our goal, ways of using existing SystemC methodology to model a wireless system must first be investigated. SystemC as a methodology is appropriate for modelling wireless systems because the methodology is the same for wireless and wired communication systems. Thus we can use the existing methodology to model and design wireless systems. As SystemC is a system modelling language, it has certain elements that can be used to model different systems, such as FIFO, signals, and semaphores. On the other hand, SystemC lacks elements that can be used to model and simulate wireless systems because it does not support noise links natively. Therefore, we must determine how we can make SystemC support wireless systems. To this end, we have modelled a wireless communication channel [1] that is needed to implement the wireless system using SystemC methodology; we also defined the connections (topologies). As this element was missing from SystemC, it has been designed and constructed successfully.

Moreover, some other standard components at system level that are typically required to implement wireless communication systems, such as an 8B-10B encoder-decoder, have been modelled and constructed [2]. In the final stage, a demonstration validating the methodology was needed, and was constructed by developing a small application using flocking behaviour system as a case study, which can be employed to validate the use of SystemC methodology to model wireless system. This paper thus focuses on how to achieve the final stage (case study-modelling of a flocking behaviour system), and how to integrate the three stages mentioned above to achieve the main goal.

The rest of the paper is organised as follows: section 2 gives a brief description of SystemC methodology stages and how we can model and simulate a digital system using SystemC, section 3 briefly describes how the wireless communication channel needed to extend SystemC methodology was modelled, section 4 briefly describes how 8B-10B Encoder Decoder which is a standard component is modelled successfully, section 5 presents a demonstration of a flocking behaviour system and discusses a structure in terms of a hierarchical set of behavioural modules, section 6 presents simulation results and discussion, and finally section 7 presents conclusions.

## II. SYSTEMC METHODOLOGY

SystemC methodology is employed in order to manage the complexity of the design flow process at system level. To incorporate wireless features into existing



SystemC methodology, we must first investigate how existing SystemC methodology can be used to model a wireless system. Because the methodology is the same, it can be used to design any system. Thus we can use existing methodology to model a wireless system. As a system modelling language, SystemC has certain elements, such as FIFOs, signals and semaphores [3]. The signal element behaves like a wire, which cannot be used to model a wireless system because no wireless features can be incorporated into this signal element, i.e there is no noise model that is defined to be used within the SystemC language. Thus, SystemC is missing elements and components that can be used to express and simulate wireless systems. It does not support noise links natively. Therefore, one of the specific and important elements necessary for SystemC to model wireless systems is a wireless channel model. This is necessary in order to determine how the channel will be connected to create different topologies. A. SystemC Methodology Stages The primary advantage to designing any system at the system level is having the ability to implement that system from the highest level of abstraction, i.e specifications model. From a system design methodology perspective [4, 5, 6], there are a number of intermediate models that can be defined and then used to reduce the complexity of the system design process. Using intermediate models divides the entire design into slices (small design tasks). Each task is represented by a model and has a specific design objective. Thus, each model can be simulated and the results independently

validated [7]. The methodology abstraction levels are shown in Figure (1).

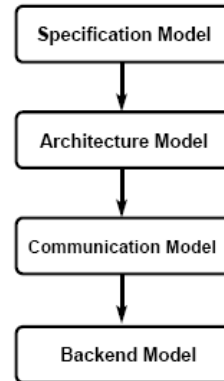


Figure 1. The Stages of the System Design Methodology.

The design flow of the system design methodology is based on the methodology stages described above. Figure(2) illustrates the block diagram of methodology design flow. The first step in designing is to capture specifications. After capturing the specifications, the next step is architecture exploration. The main purpose of this phase is to allocate system functionality into components. The system architecture is derived from the specifications. We can develop and then compare more than one option/design. Then we must estimate a metrics that will be employed to investigate system performance for these options. The next phase is known as hardware/software partitioning. In this phase, the components selected as S/W are implemented using S/W code and the other components are exported to HDL to be implemented as H/W components [8, 9].

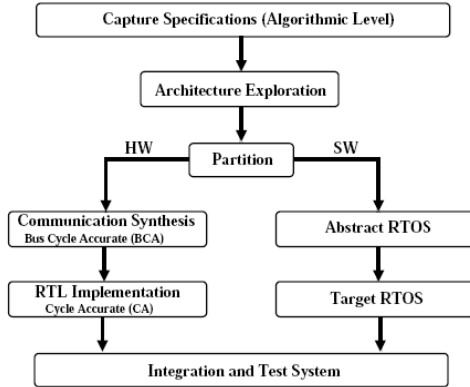


Figure 2. Methodology Design Flow.

Abstraction levels are briefly defined in the next section. Places in which wireless features could be incorporated into existing methodology were suggested. There is no change in the methodology; the only change is in the ability of the SystemC language to support the designing and modelling of the wireless system. For instance, the wireless communication channel that we modelled [1] in the first stage of this work is an important model; it is essential in designing any wireless system using SystemC methodology. We can incorporate the wireless channel model into any system. Once the channel is incorporated, we can introduce noise and communication protocols.

*1) Creating an Executable Specification Model:* The input of the design methodology is a specification model. The specification model represents the first stage of design methodology and is defined as the starting point of the system design process. At this stage, system details are highly abstracted. The main purpose of this

specification model is to define how the system is meant to behave. The system should be seen in a generalized way, without knowing if it is more suitable to model it as a wired or wireless system. If a system can be modelled either wired or wireless, we can compare between wired and wireless systems and determine which one is better.

*2) Developing an Architecture Model Using Architecture Exploration:* An Architecture model is defined as an intermediate model of the system design methodology. This stage represents the components structure of the system's architecture. At this stage, the system's functionality is mapped into components. The various parts must be defined as hardware or software. It is better to develop more than one possible design, so that comparisons can be made between them in order to determine which one is the best. In order to make this comparison, we need to evaluate performance estimation for each design, because this estimation process guides the architecture exploration.

In the case of wireless systems, other estimations, including BW and latency, are also necessary for guiding architecture exploration. This estimation can be done using modelling. A model is constructed and run in order to make the estimation. By running the simulation, we can determine BW and latency requirements. After running the simulation, the BW of the channel, the frequency, and other parameters can be estimated. In this way, an estimation of a wireless system is achieved.



3) *Communication Model*: At this stage the partition is done and communication features can be incorporated. The frequency and communication protocol for a wired or wireless system can then be specified, and noise inserted. In a wireless system, a wireless communication channel can be inserted and we may assign a value to the Bit Error Rate (BER) and insert protocol. The protocol is not part of the language; protocol is expressed in the language.

#### *B. Necessary Models*

As previously indicated, SystemC lacks elements that can be used to model and simulate wireless systems because it does not support noise links natively. Therefore a way to make SystemC support wireless systems must be established. Based on the information above, we need to address three issues in order to enable SystemC to support wireless systems:

- 1) We need to model a wireless communication channel [1] in order to implement the wireless methodology and we need to define how these will be connected (topologies).
- 2) We need to construct some standard components at system level that are typically required to implement wireless communication systems, such as an 8B-10B encoder-decoder [2].
- 3) In order to validate the methodology, we need to create a demonstration by developing a small application such as flocking behaviour system.

The first and second issues have previously been successfully modelled. This paper focuses on how to achieve the

third element (case study-modelling of a flocking behaviour system), and how to integrate the three issues mentioned above to achieve the main goal. In the next two sections, the first two elements are presented briefly, followed by a detailed description of modelling flocking behaviour.

### III. MODELLING OF A WIRELESS COMMUNICATION CHANNEL

The most important model needed to extend SystemC methodology to implementing wireless systems is a channel model. We have modelled a wireless communication channel [1] that fulfills SystemC language requirements to support wireless systems. The main aim of modeling this channel is to change SystemC to include wireless features. The model supports the setting of a different Signal-to-Noise Ratio (SNR) and different types of interference. The channel specifications support wireless features such as noise. The simplest model of digital noise is simply to consider the constructed impulsive noise, in which individual bits or packets are modified with a given probability. Though other distributions can be used to model the noise, we use exponential distribution for the sake of simplicity. The noisy digital wireless channel is modelled successfully with a preset Bit-Error-Rate (BER) for Point-to-Point (P2P) and Point-to-Multipoint (P2M) platforms based on SystemC. This channel model is what is missing in the SystemC language to support wireless systems.



#### IV. 8B-10B ENCODER DECODER

One of the standard components that modelled successful is 8B/10B. It is an 8-bit 10-bit Encoder/Decoder that is typically required to implement a wireless communication system. It is a standard model constructed to get more understanding on how we use the SystemC methodology to design and model a system. Also it is an important technique in the construction of high performance serial interfaces. In this novel work, the main objective is to develop a reusable 8B/10B IP core offering flexible interoperability, which can be used to allow efficiently prototyping of serial communication systems. Moreover, there is no body before model it at RTL level, so we have modelled it using SystemC and published on a paper[2].

#### V. A DEMONSTRATION VALIDATING WIRELESS METHODOLOGY

At this stage a demonstration must be created by developing a small application and/or test case in order to validate the methodology. The application is known as a flocking behaviour system. We must also prove that incorporating and fixing the wireless channel, wireless protocol, noise, or all of these things, early in the design methodology is very advantageous, i.e. small changes in the wireless specifications will create big changes in the system dynamics. Therefore, the system might be constructed in different ways to investigate the system over different performance parameters.

#### A. Flocking Behaviour System

Flocking is the term given to a group of particles behaving in a particular way. Each particle moves at its velocity, and all particles should be kept close to each other without colliding. Flocks can be used for explorations. In this paper the flocking behaviour system is modelled and designed based on Reynolds' three principles[10].

- **Separation:** This refers to collision avoidance. The particles always try to steer away from other particles near them.
- **Cohesion:** This is when particles move toward the average position of local flock mates.
- **Alignment:** This refers to velocity matching. The particles must match their velocity to that of other particles.

The next section illustrates how the flocking behaviour system is modelled using SystemC methodology. Initially the system is modelled at a high abstraction level of communication, i.e. the communication between particles is performed using variables. Next, the wireless communication channel previously modelled [1] is incorporated. After the insertion of the wireless channel, we can then insert the noise and investigate system performance under different conditions. This will be done in the next stage of this work.

1) *Creation of a Flocking Behaviour System Model:* This system has 24 particles. These particles are distributed in the environment. They use wireless communication to communicate with each



other. The particles should maintain stability and must stay together. They are controlled by a leader and they should converge in a certain area and be distributed around the leader's position. They can also follow the leader to a specific position. Through communication they can determine each others' location. In terms of construction, there are many ways to connect the particles. One is a ring topology illustrated in Figure (3), where particle 1 is controlled and then selected as a leader. In this stage, the system is constructed at highly abstracted level of communication; i.e communication between particles is done using variables.

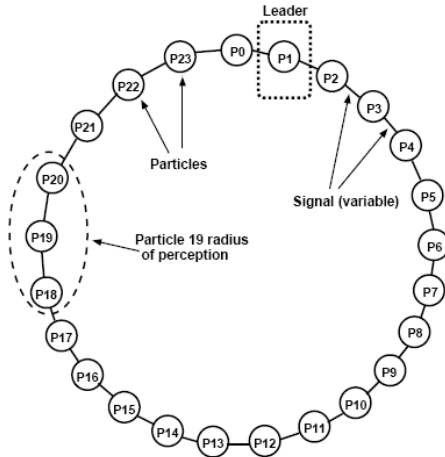


Figure 3. Flocking Behaviour System Constructed at High Abstraction Level.

‘Communication’ refers to how the particles will communicate. At this stage, the particles communicate at a highly abstracted level. The particles can ‘know’ the position of their neighbours by using communication messages. Each particle can

communicate (by transmitting and receiving messages) with the neighbours located on its radius of perception, as shown in Figure(3). In a system constructed based on ring topology, particle 1 can send its position to particle 0 and particle 2. Figure(4) shows how the particles can exchange messages.

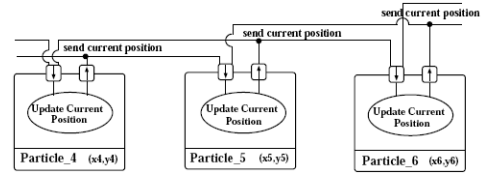


Figure 4. Transmitting and Receiving Communication Messages Between Particles.

The control algorithm of the whole system is linked to the actual transmission and implementation. Here, control refers to the stability of the system. It is represented by a proportional and derivative controller (PD controller) as shown in Figure (5). The main function of the controller is to update the acceleration and velocity of the particles using the current position of each particle and the error value that is evaluated based on the data collected in the previous clock cycle, as shown in Equations 1 and 2.

$$xacceleraton = \epsilon x * Kp + (\epsilon x - old\epsilon x) * Kd \quad (1)$$

$$yacceleraton = \epsilon y * Kp + (\epsilon y - old\epsilon y) * Kd \quad (2)$$

where:

$\epsilon x$  : current error in x direction.

$\epsilon y$  : current error in y direction.

$Kp$  : proportional gain.

$Kd$  : derivative gain.

$old\epsilon x$  : error from the last cycle in x direction.

$old\epsilon y$  : error from the last cycle in y direction.

$xacceleraton$  : current acceleration in x direction.

$yacceleraton$  : current acceleration in y direction.



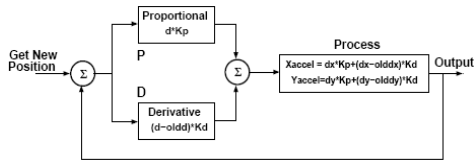


Figure 5. Particle Control System.

2) *The Particle Model Structure*: Each particle performs a simple task: transmitting its current position to the other particles located on its radius of perception (as shown in Figure(3)) and receiving other particles' positions. The particle model consists of three main elements: a transceiver that can be used to send and receive data, a PD controller used to move the particles to new positions, and an estimation process to evaluate error. The particle model state machine is illustrated in Figure(6) and the data packet format is shown in Figure(7).

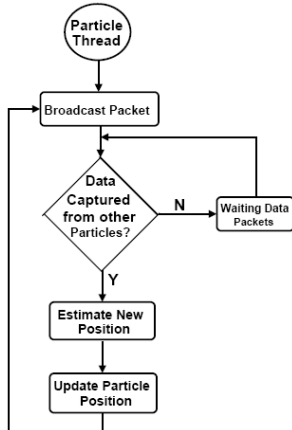


Figure 6. Particle Model State Machine.

Relative Position				Actual Position	
Pkt No.	Part. No.	relposx	relposy	xpos	ypos
2 Byte	2 Byte	2 Byte	2 Byte	4 Byte	4 Byte

Figure 7. Data Packet Format.

### 3) Insert Wireless Communication

*Channel*: To optimize system stability in terms of communication, the wireless channel model [1] is incorporated, and the stability and reliability of the system are investigated in order to get the best performance under the communication effects. Figure (8) illustrates the system diagram after inserting the wireless channel. The main advantage of inserting a wireless channel model into the system is to allow us to simulate wireless features, i.e evaluating the effects of inserting noise through the channel. Moreover, we can find the effect of the communication latency and communication BW to maintain system stability. The main objective is to prove that we can successfully use SystemC methodology with a wireless channel [1] to model a wireless communication system.

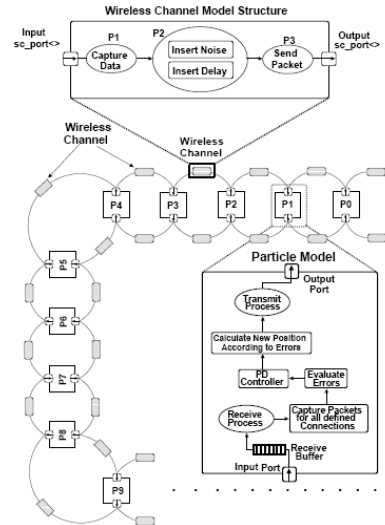


Figure 8. Flocking Behaviour System after inserting the Wireless Channel.





## VI. SIMULATION PLATFORM

In SystemC, functional verification of the modelled system is done through simulation. This process consists of applying a stimulus to the Device Under Test (DUT) and verifying the response against an expected result. At each time step in the simulation the processes in Figure(9) are applied to all particles simultaneously, and the positions and velocities of all particles at the next time step are updated accordingly. Subsequently, each particle must send its updated position to the other particles located within their radius of perception. Here the acceleration and speed are bounded based on the error value. If the acceleration or speed value is greater than the maximum level, it will be cut back to the maximum value.

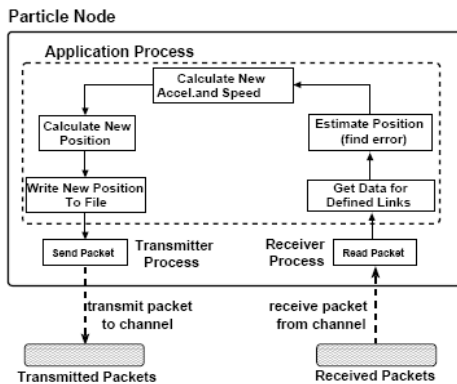


Figure 9. Data Flow within the Particle Model.

The equations of motion employed in this simulation are symmetrical because all the particles are identical. The simulation program affects the particles' movement by modifying only their acceleration; their velocity and position will be updated based on the acceleration value. The simulation

takes place on a two-dimensional axis (2D). Each particle has corresponding equations for movement on both x and y axes. The positions, velocities and accelerations of the particles are all 2D vectors (x,y).

## VII. RESULTS AND ANALYSIS

The simulation program described above was used to simulate the movements of a set of 24 particles with initial absolute positions at (0,0) and relative positions are arranged as square shape. These initial values were provided to the system by the stimulus. The particles began moving from (0,0) and distributed themselves around the leader in a uniform shape based on the initial values of their relative positions. Multiple simulations were run to optimise the model parameters, including simulation time, transmission speed, communication delay, speed and acceleration. Figure(10) shows the system behavior based on the system parameters indicated in Table(I). The system behaviour clearly shows that the particles remained in the same position structure (square) throughout the simulations. Thus it is proven that particles consistently and effectively avoid contact with one another. Figure(13) illustrates the system response curves and the converging point of the system, while the changing of particles velocities in the x direction are illustrated in Figure (14). Here the velocities are bounded based on the error value. If the velocity value is greater than the maximum level, it will be cut back to the maximum value as shown in Figure (15).



Table I: System Parameters.

Parameters	Values
No. of Particles	24
Simulation Time	250 steps
Transmission Speed	0.5 Packets/simulation step
Acceleration Range	-0.2 to 0.2
Speed Range	-1.0 to 1.0
Communication Delay	0
Proportional Gain (Kp)	0.03
Derivative Gain (Kd)	0.1

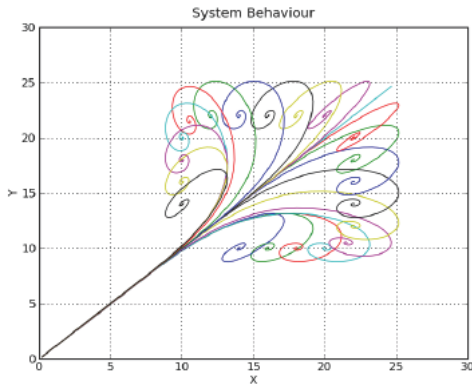


Figure 10. System Behaviour

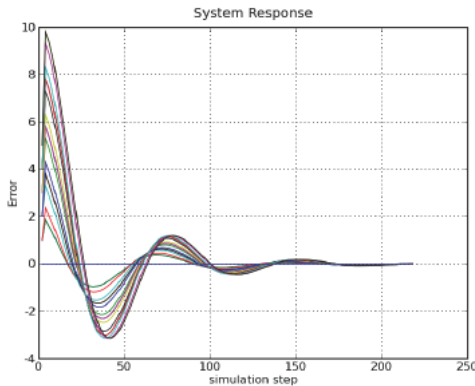


Figure 11. System Response

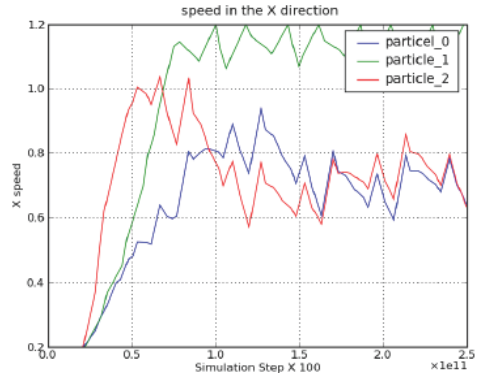


Figure 12. System Response

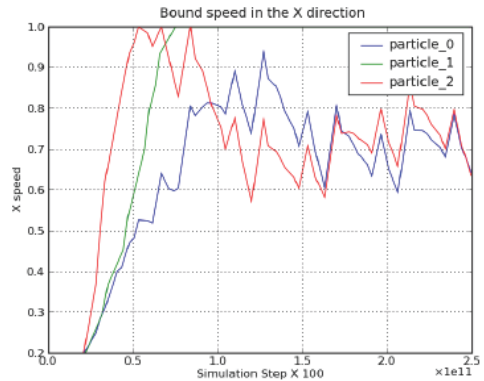


Figure 13. System Response

## VIII. CONCLUSION

SystemC has been chosen because it provides a homogeneous platform for the design and modelling of complex systems. Furthermore, as systems become more tightly integrated (for example, as in SoC) the ability to evaluate system performance in the early stages of design becomes increasingly important. This is facilitated by SystemC design methodology and by following an IPbased design.



This paper demonstrates a simple and computationally efficient way to model a wireless communication system at system level based on existing SystemC methodology. The modelling of the wireless system has been undertaken using SystemC and incorporated into a uniform design methodology, suitable for developing new technologies following SoC design methodology. The wireless channel model that was modelled before represent the main element that must be employed to incorporate wireless features. The system has been modelled successfully; positive results representing system behaviour and system dynamics were established.

This paper represents a first step towards integrating communication modelling into design modelling in the early stages of system development. The next stage of this work is to investigate the interaction between system stability and communication. Moreover, the effects of inserting noise should be investigated. A number of interesting parameters or ratios of parameters should be investigated, including transmission speed, simulation time, communication delay, number of particles, acceleration and speed. The behaviour of the system may change dramatically if these parameters are modified.

#### REFERENCES

- [1] N. Ahmed, I. Aref, F. Rodriguez, and K. Elgaid, "Wireless channel model based on soc design methodology," Fourth International Conference on Systems and Networks Communications (ICSNC), September 2009.
- [2] I. Aref, N. Ahmed, F. Rodriguez, and K. Elgaid, "Rtl-level modeling of an 8b/10b encoder-decoder using systemc," The Fifth IEEE and IFIP International Conference on Wireless and Optical Communication Networks (WOCN2008), 2008.
- [3] T. Grotker, S. Liao, G. Martin, and S. Swan, System Design with SystemC. 2002.
- [4] D. Black and J. Donovan, SystemC: From the Ground-up. first ed., 2004.
- [5] A. Ghosh, S. Tjiang, and R. Chandra, "System modeling with systemc," ASIC, 2001. Proceedings. 4th International Conference on, pp. 18–20, 2001.
- [6] T. Groetker, S. Liao, G. Martin, and S. Swan, System Design with SystemC. 2002.
- [7] D. Gajski, J. Zhu, R. Domer, A. Gerstlauer, and S. Zhao, Spec C: Specification Language and Methodology. 2000.
- [8] L. Cai and D. Gajski, "Transaction level modeling in system level design," CECS Technical Report 03-10, 2003.
- [9] L. Cai, S. Verma, and D. Gajski, "Comparsion of specc and systemc languages for system design," Technical Report, 2003.
- [10] C. Reynolds, "Flocks, herds, and schools: A distributed behaviour model," Symbolics Graphics Division - SIGGRAPH, 1987.



المؤتمر العربي الليبي الدولي الخامس للهندسة الكهربائية والإلكترونية 2010/10/26-23 طرابلس ليبيا



## Network Performance Evaluation Using Realistic Design Process

Nuredin Ahmed, Ibrahim Aref, Fernando Rodríguez-Salazar and Khaled. Elgaid  
Department of Electronics and Electrical Engineering,  
University of Glasgow, Rankine Building, Oakfield Avenue, Glasgow, G12 8LT,  
United Kingdom  
E-mail: {nahmed, iaref, fernando, kelgaid}@elec.gla.ac.uk

### Abstract

This paper presents an original development methodology for the use of SystemC to model an executable model of a wireless network system. This work demonstrates a computationally efficient way to model a wireless communication network within a system level. SystemC methodology allows the model to be reconfigurable for extensive early architectural analysis and easy re-mapping to new wireless standards and applications at numerous levels of abstraction. On the other hand network protocols have many complex concurrent and distributed characteristics, thus it is very difficult to be analysed theoretically. One of the most promising solutions to this problem is system-level modelling and simulation, which have been covered in this work. The communication nodes of the network are modelled as modules with different methods, which will reflect the Application, Transport and Data Link Control (DLC) and Physical layers (PHY) of the standard reference model of an Open Systems Interconnection (OSI/ISO). Performance results for the simulations as well as development effort are presented thus showing how this methodology is well suited to the modelling of a wireless network systems. Moreover the experiences of using SystemC design methodology to analyse the performance properties of wireless network has been presented. To our knowledge, this is the first time that the modelling of wireless communication network has been undertaken in SystemC and incorporated into a uniform design methodology, suitable for developing new technologies following the SystemC design methodology.

**Keywords:** SystemC, Modelling, Simulation, Network, Channel, ARQ, Performance Analysis.

### I. INTRODUCTION

With the advent of digital communication systems, more and more components to support new features are being integrated in a single package [1]. This trend is likely to continue, as devices

continue to incorporate an ever-growing number of components to provide interoperability with the large plethora of standards and protocols from previous and the present state of the art. It is an important issue to verify the interaction and the



integration of communication modelling into the design modelling before actually realising a system in terms of hardware and software components. Waiting until silicon is available to validate system interactions and find bugs is costly and time consuming.

The modelling of wireless communication systems is not new and has been approached in different ways. Co-simulation of analogue parts using Matlab, Simulink and SPICE are common and digital parts in HDL would be too simulation intensive for large and complex systems. Behavioural modelling has been proposed in [2], but has not been incorporated into a homogeneous design environment. Paper [2] is one of the few papers so far about modelling using SystemC. The paper shows a systematic approach to modelling and simulating an Orthogonal Frequency Division Multiplexing (OFDM) transceiver for wireless Local Area Network (LAN) using SystemC. However [1] have showed that SystemC is very useful for modelling wireless communication systems at different levels of abstraction. This paper will provide a further step towards introducing the modelling of digital wireless networking system in SystemC for structuring the earliest phases of the design process with the intention to find a feasible design before actually realising a system in terms of hardware and software components.

Network protocols for reliable transmission of data over wireless communication channels have been intensively investigated in the field of

computer science. They usually involve a subtle interaction of a number of distributed components and have a high degree of parallelism, so it is very difficult to analyse their performance characteristics by mathematical analysis [3]. The most promising solutions to this problem are the use of system-level modelling and simulation.

The novelty of this work is the modelling of a complete digital wireless networking system. All protocols needed for the performance analysis have been developed and integrated in the system for reliable data transmission at the system level of the design phases. Our methodology is based on the popular SystemC design methodology, which allows, rapid prototyping of these systems for early implementation-dependent architectural analysis, fast simulation and an excellent path to implementation with potential reuse for RTL and schematic verification. In this work a wireless communication system such as the one shown in Figure(1), which represents multiple communication nodes that exchange information through a shared communication channel has been developed and the performance properties are investigated for a number of configurations of the system parameters. The channel model [1] has been developed and carefully integrated in this network model and verified with the same methodology.

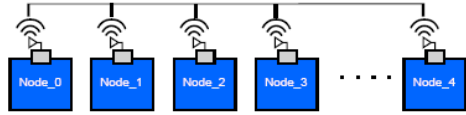


Figure 1. Block Diagram of shared channel wireless communication system consists of N nodes.

The remainder of this paper is organised as follows. Section II gives a brief description of the channel model that has been developed. Section III highlights and describes the communication node structure. Section IV introduces the CSMA development scenario which describes the implementation of the noisy digital communication channel. And also highlights the details of using that communication channel to construct a multipoint to multipoint (M2M) communication mechanism. Section V emphasises on the techniques used to measure the performance "throughput and latency" of the system with a presentation of the simulation results. Finally the conclusions are presented.

## II. CHANNEL MODEL

In this section we will introduce network model that has been used throughout this work. Wireless networks are inherently more difficult and computationally expensive to model than fixed wired networks. Wired communication links is replaced with an error-prone broadcast channel. Bit errors in wireless networks are orders of magnitudes higher than fixed wired networks and vary with the received SINR. Channel models are used at various levels of complexity to model wireless communication links. These

models may take into account the terrain, obstacles, inter-nodal interference and other physical characteristics that affect radio wave propagation. In wireless networks, it is an important consideration to determine to what extent can a pair of nodes communicate. A link quality analysis has been carried out to describe the behaviour of the communication medium between the transmitter and the receiver terminals. This is based on the free space propagation representation of the communication link in equation (1) [4], which represents signal decay as a function of distance.

$$L_{fs} = 10 \log_{10} \left( \frac{P_{tx}}{P_{rx}} \right) = 10 \log_{10} \left( \frac{G_t G_r \lambda^n}{(4\pi)^n d^n} \right) \quad (1)$$

Where the free-space propagation loss is  $L_{fs}$  (line-of-sight, in dB),  $P_{tx}$  and  $P_{rx}$  are the transmitted and received power in Watts,  $G_t$  and  $G_r$  represent the respective antenna gains and the link distance is  $d$ . The receiver sensitivity required is usually quoted in dBm, and can be computed using equation 2.

$$P_{rx} = P_{tx} - L_{fs} - \text{Fade Margin} \quad (2)$$

The general expression for propagation loss in dB with the assumption that the antenna gains are 0dB (for simple dipole antennas) and in free space (where  $n$  is assumed to have the value of 2) can be expressed as:

$$L_{fs} = P_{rx} [dB] - P_{tx} [dB] = 10 \times n \times \log_{10} \left( 4\pi \frac{d}{\lambda} \right) \quad dB \quad (3)$$



Where  $\lambda = c/f$  is the free-space wavelength at the carrier frequency (and as usual  $c$  is the speed of light and  $f$  is the frequency).

Signal reduction due to multipath fading [4], [5] is normally in the range of 20 to 30 dB and hence in practice a fade margin will be added to the power loss to account for it. We proceed to incorporate the effects of the modulation technique employed. This will allow us to estimate the bit-error probability  $P_B$  which represents the Bit Error Rate (BER) as a function of the bit energy and noise-density of the signal  $E_b/N_0$ . Figure 2 illustrates the waterfall like shape of most such curves. For the purpose of link budget analysis, the most important aspect of a given modulation technique is the signal to noise ratio necessary for the receiver to achieve a specified level of reliability in terms of  $P_B$  (BER).

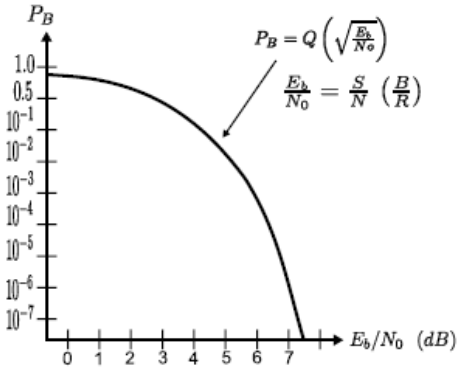


Figure 2. General shape of  $P_B$  versus  $E_b/N_0$  curve.

The probability of a bit error,  $P_B$ , is defined as:

$$P_B = Q(z) = Q\left(\sqrt{\frac{E_b}{N_0}}\right) \quad (4)$$

Where  $Q(z)$ , is called the complementary error function or co-error function. This complementary error function is numerically equal to the area under the “tail of the Gaussian”. It is closely related to the complementary error function  $erfc(z)$  and error function  $erf(z)$ :

$$erf(z) \equiv \frac{2}{\sqrt{\pi}} \int_0^z e^{-x^2} dx \quad z \geq 0 \quad (5)$$

$$erfc(z) \equiv \frac{2}{\sqrt{\pi}} \int_z^\infty e^{-x^2} dx = 1 - erf(z) \quad z \geq 0 \quad (6)$$

The Q-function is related to these functions by

$$Q(z) = \frac{1}{2} erfc\left(\frac{z}{\sqrt{2}}\right) \quad z \geq 0 \quad (7)$$

Equation (8) provides a sample BER model for a specific modulation scheme, Quadratic Phase-Shift Keying (QPSK). The BER assuming white noise AWGN is given by

$$BER = \frac{1}{2} erfc\left(\sqrt{\frac{E_b}{N_0}}\right) \quad (8)$$

Where the maximum thermal noise power within a given bandwidth  $B$  is given by  $N_0 = kTB$ .

In the radio and microwave bands, the spectral density is taken as  $N$ , for a one sided spectrum, and as  $N_0/2$  for a two side spectrum, where:  $k$  = Boltzmann’s constant,  $T$  = system temperature in Kelvins, usually





assumed to be 290K.

SNR gives the relation between the received signal power  $S$  and the noise power  $N$  as given by

$$SNR[dB] = 10 \times \text{Log}_{10} \left( \frac{S}{N} \right) \quad (9)$$

Where  $E_b/N_0$ , in equation 8 is just a normalised version of SNR [4], which can be rewritten to emphasise that  $E_b/N_0$ , is just a version of  $S/N$ , normalised by bandwidth and bit rate  $R$ , as follows:

$$\frac{E_b}{N_0} = \frac{S}{N} \left( \frac{B}{R} \right) \quad (10)$$

### III. MODELLING OF COMMUNICATION NODE

The communication nodes are the main construction units of the network system, which will communicate with each other through the communication medium modelled in section (II). The nodes of the network are modelled as modules with different methods, which will reflect the Application, Transport and Data Link Control (DLC) and Physical layers (PHY) of the standard reference model of an Open Systems Interconnection (OSI/ISO). Each node interacts with the network to send or receive data packets. Each node is assumed to have a baseband transmitter and receiver for wireless communication with other network nodes as shown in Figure 3.

Most of OSI/ISO network layers have been modelled in the communication node, because it is a wireless network and wireless communication is subject to errors. These errors will force retransmissions under certain conditions. We want to investigate

these error conditions because errors and retransmissions will add latency to the system. In addition we need to have absolute certainty that the data sent is equal to the data received. The point to model it here is to find a settle interaction between the network layers namely transport and physical layer and the network topology. So probably certain changes in the network topology and/or other network layers will imply that the transport layer which we were using does not work as it expected for the wireless. Therefore we need to find out these complex interactions, which do not mean it is always present in wired networks.

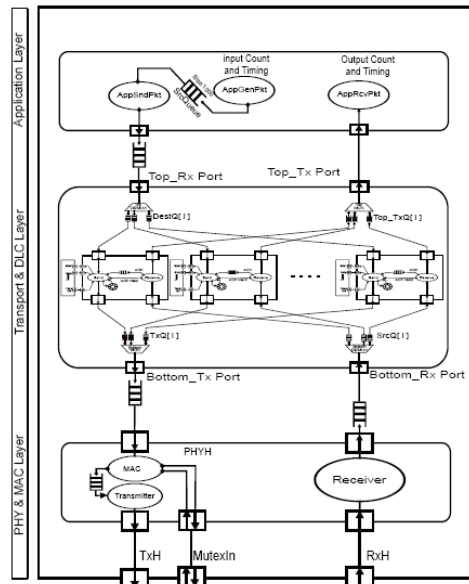


Figure 3. Conceptual model of the network communication node.



#### A. Application layer

The application layer plays a crucial role on the performance measurement of the network system. To measure the performance of the network modelled, we have included a kind of instrumentation in the application layer. The instrumentation includes a packet source process that generates packets according to an exponential distribution. And assigns packets destinations randomly and uniformly. Since most of the performance evaluation results in literature [6] have only considered a uniform distribution of packet destinations. In this distribution, the probability of node  $i$  sending a packet to node  $j$  is the same for all  $i$  and  $j$ ,  $i = j$ . The case of nodes sending messages to themselves is excluded because we are interested in packet transfers that use the network. In this work for simplicity and to match published results we model the network under the uniform traffic distribution. Yet, our methodology allows for any traffic distribution to be simulated; what is even more important, it allows for higher level applications to interact and then dynamically modify the traffic pattern used; which is something that is normally not simulated but has a very large impact on the real performance obtained in the network.

Packets generated at the application layer are equally-likely to occur at any instant of time. This packet source has been separated from the network at each node with a large source queue. Between the packet source and the source queue, packets are counted and time stamped with the start

time of each packet injected. It is important that this measurement process be placed before the source queue rather than after the queue. So that packets that have been generated by the source queue, but not yet injected into the network, are considered. And so that packet latency will include the time spent in the source queue. After the source queue another interfacing process has been implemented for sending data packets over the wireless channel through the underlying layers of the communication node. Whenever the application layer has data to be sent, it delivers it to the transport layer buffer as a data structure containing the payload or data, source and destination address.

A complementary measurement process at each receiving side of the application layer records each packet's finish time. Throughput is measured by counting the packets arriving at each receiving application process and latency is measured by subtracting the start time and the finish time for each packet. This measurement configuration enables the traffic parameters to be controlled independently of the network itself. Without the source queues, a packet source may attempt to inject a packet at a time when the network node is unable to accept any packet. In such a case, the traffic produced by the source is influenced by the network and is not the traffic pattern originally specified. Because our goal is generally to evaluate the network on a specific traffic pattern.

#### B. Transport Layer

A Transport layer provides the logical communication between application



process running on different nodes. Hence it is responsible for packet scheduling from multiple processes in different nodes. This process-to-process packet delivery is simply called transport layer multiplexing and demultiplexing. A transport layer protocol with multipoint-to-multipoint support presented in Figure (3) has been developed to allow significant performance gain in the system.

### C. Data Link Control Layer

The Data Link Control (DLC) layer is responsible for moving a data packet reliably from one node to an adjacent node over a single communication link. In our model it defines the format of the data packets exchange between the communication nodes using the High-Level Data Link Control

1) *Flow and Error Control:* As described in [7], [8] A DLC sublayer has been designed as shown in Figure(4) and the layer logic has been further detailed in a Finite State Machine (FSM) definition for reliable data transfer protocol for transmitters and receivers, this can be modelled as shown in Figure 5 and Figure 6.

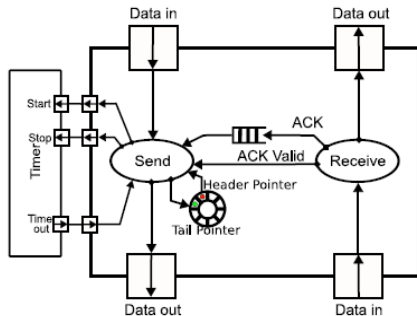


Figure 4. DLC sublayer a SystemC representation logic diagram.

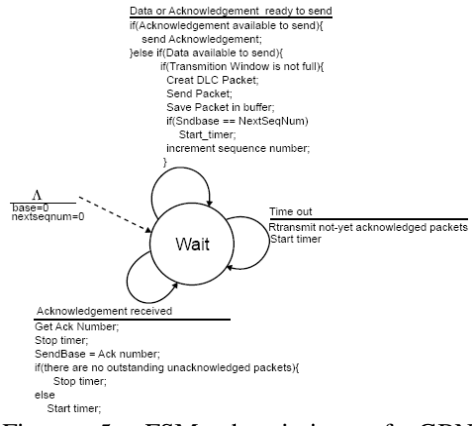


Figure 5. FSM description of GBN Transmitter.

### D. Medium Access Control Layer & Physical Layer

In this work we have integrated the functionality of the Medium Access Control (MAC) into the physical layer to reduce the processing and buffering time between the layers. The MAC and PHY layers provide medium access and transmission functions.

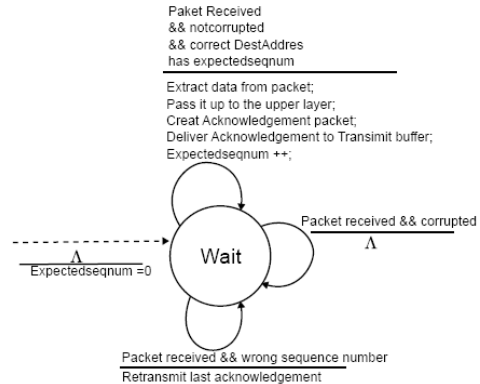


Figure 6. FSM description of GBN Receiver



In designing MAC protocols for our wireless network system, we started by adapting the existing wireless media-access control approaches and then we have developed an entirely new protocol for our wireless network. For instance, we will show in section IV, how we have developed the Carrier Sense Multiple Access (CSMA) protocol to share the communication medium among all nodes using SystemC design methodology. The main services provided by this combined layer firstly is to provide the mechanism for accessing the communication link. Secondly deciding which modulation technique will be used to generate symbols to be sent over the communication link. And thirdly perform a byte and/or bit stuffing of the packets before they are transmitted to maintain a link synchronisation.

#### IV. THE CSMA DEVELOPMENT SCENARIO

This section deals with the modelling of the nonpersistent CSMA protocol as described in [9] with additional (Go-Back-NARQ) flow and error control as described in section III-C1, and simple backoff mechanism as described in [8], [7]. Also for simplicity the CSMA channel access mechanism has been used without.

In nonpersistent CSMA, if two stations sense the medium is busy, they both immediately enter random backoff, hopefully choosing different backoff values. These random values should be different to allow one of the two stations to begin transmitting before the other in the next sense of the medium. The other will hear the medium busy and refrain from

transmitting until the first station has completed its transmission. This protocol is very effective when the medium is not heavily loaded, since it allows stations to transmit with minimum delay, but there is always a chance of stations transmitting at the same time, caused by the fact that the stations sensed the medium free and decided to transmit at once.

At the receiver node the PHY layer individual phits are received from the wireless channel module. It de-stuffs and reassembles them into a data packet and deliver it to the upper layer which is the DLC Layer. The first operation at the DLC sublayer is the packet identity check, if the packet indicates the local node address then it continues and performs an error check using CRC checksum. Once the packet received is free of errors the DLC generates an acknowledgement packet with the appropriate sequence number and passes it to the transmitting side of the node.

##### A. The Communication medium Module

At the first stage of the implementation phase, a channel model has been constructed to support contention and noncontention based wireless channel access and includes Point-to-Multi-Point (P2MP) and Multi-Point-to-Multi-Point (MP2MP) communication scenarios. One of distinct capabilities and features of the system-level modelling of SystemC is the Hierarchical channels. They are intended to model quite complex behaviors such as PCI, HyperTransport, or AMBA.

Primitive channels on the other hand are intended to provide very simple and fast communications. (e.g., `sc_signal`



provide a piece of wire behavior). To build complex system level models, SystemC defines hierarchical channels as modules that implement one or more interfaces, and serves as a container for communication functionality. An interface provides declarations of methods for accessing a given channel. No implementations or data are provided in an interface. In `sc_signal`, for example, the interfaces are defined by two classes `sc_signal_in_if` and `sc_signal_out_if`, and these define methods (e.g., `read()` and `write()`).

Separating the definition of an interface from its methods implementation, SystemC has a unique coding style in which communication is separated from behavior, a key feature to facilitate refinement from one level of abstraction to another.

Channels in SystemC create connections between module ports allowing modules to communicate. Figure (7) shows a SystemC Hierarchical channel representation. A port acts as an agent that forwards method calls up to the channel on behalf of the calling module.

Hierarchical channels are implemented as modules in SystemC: in fact, they are derived from `sc_module`. Primitive channels have their own base class, `sc_prim_channel`.

Writing hierarchical channels to support wireless behaviour is quite simple by following SystemC methodology. This section will just show the implementation of the hierarchical channel model used in this work.

The wireless channel module is responsible

for carrying the data packets to all stations and it will represent our communication medium in this network. The wireless channel module as shown in Figure (7) models the communication medium. It behaves like a multi-tap bus, where multiple nodes are connected through it. The behaviour of the link has been modelled as a wireless communication medium. In this work an external object 'mutual exclusion lock or mutex' has been used to control the access to the shared medium. The behaviour of a mutual exclusion lock as used to control access to a resource shared by concurrent processes. A mutex will be in one of two exclusive states: unlocked or locked. Only one process can lock a given mutex at one time. Whenever a node has a packet to send it tries to lock the mutex. When it locks the mutex it has access to the channel, the rest of the nodes have to wait until the node has released the channel. The other nodes may be subsequently locked by the mutex.

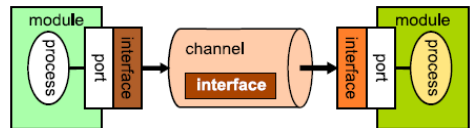


Figure 7. Hierarchical channels representation.

## V. PERFORMANCE ANALYSIS AND RESULTS

Network performance is measured in terms of latency  $L$  (the elapsed time to cross the network) and throughput  $S$  (the number of packets that cross the network per unit of time). Performance optimisation of the whole system is a crucial step in the process of design and validation of the new system. Latency is measured in time units. However, we are comparing several design



choices, the absolute value is not important. As many comparisons can be performed using simulations, latency is measured in the SystemC simulator clock cycles. Throughput is measured in bits per second or bits per clock cycles. Again, since we are comparing different design choices by simulation, and assuming that channel width is equal to a phit size, throughput can be measured in phits per clock cycles.

To provide a basic performance evaluation, it is initially assumed that the network in question will use the following important assumptions: 1- The network is deployed on an area of  $S$  square meters. The network nodes are distributed uniformly within a rectangular area  $(X, Y)$ . 2-Transmission power  $P$  is constant for all nodes. 3- For a given node its neighbour nodes will be in a circle of radius  $R$  meters, the transmission range. 4- Packets are the same size throughout the simulation. 5- The channel width is  $W$  bits and the packet length is  $L_m$  bits, the packet is broken up into  $M = L_m/W$  phits, each phit is of  $W$  bits and is transferred over the channel in one cycle unit;  $M$  is referred to as the message aspect ratio.

Our experiments concentrate on the modelling to optimise the overall performances of the protocol stack of a network rather than a local optimisation of each layer. Moreover it investigates the interaction of modelling of the whole network system under the same design methodology. Our simulations have been verified by published results [10], [8], [11]. We focused on the change in the packet size and the change in the number of nodes

to study the performance of the network. Two different packet sizes were used; 30 and 50 phits. These packet sizes were chosen to represent a short and a normal size packet, respectively, and have been used in similar studies [11], [1]. Moreover, the average latency of different packets sizes and network sizes were evaluated using the model developed in Section III, and the results are shown in Figure 8.

The average latency (y-axis) of a packet as a function of offered traffic (x-axis) and the average amount of traffic generated by each communication node in the network is shown in Figure 8. The simulation results match those curves presented in references [11], [10]. Note that the latency is tends to increase with an increased packet size. This is due to the increase in channel acquisition time due to the CSMA protocol behaviour. This is to be expected, since it is a contention based network system. It is worth noting that a single channel network saturates sooner when large packets sizes are used, than for small packets, since large decision times and large acquisition times are required. It can be seen that the network provides a small latency for all operating conditions except when the traffic is close to saturation.

The average throughput for different networks sizes and packet sizes was evaluated using the same model shown in Figure 3, and the results are shown in Figure 9. The x-axis in the figure represents the offered traffic. The y-axis gives the throughput in Mbits per second. The network throughput for 20 nodes has been shown in Figure 9. The maximum



throughput achieved was 8 for 50 phits packet size and 14 Gbits/sec for 30 phits packet size. However the throughput results should be normalised to Phits/Cycle the results present here is just to present the system throughput behaviour.

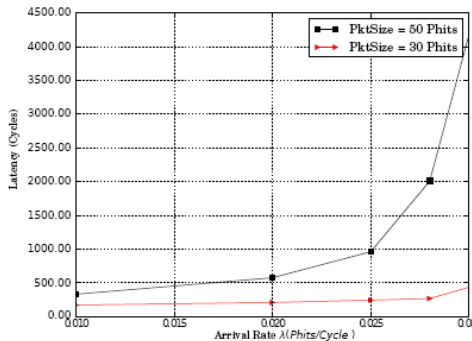


Figure 8. Model validation for different packet sizes shows communication latency versus Traffic or packet arrival rate for 16 node model.

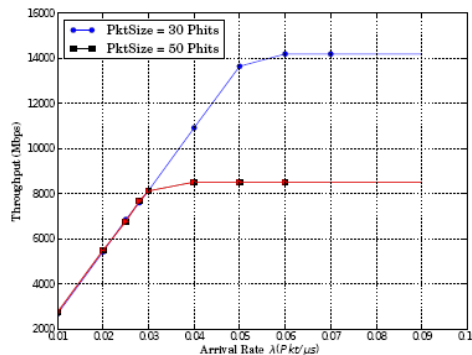


Figure 9. Throughput of the modelled network with the setting of two different packet sizes in Phits for 20 nodes.

## VI. CONCLUSION

In this paper we have addressed the modelling of contention based wireless networks using SystemC design methodology. For this purpose, we have developed a conceptual model of the network communication node and the commutation channel and verified our findings by appropriate simulations.

This work demonstrates a computationally efficient way to model a wireless communication network within a system level. The model is developed at a high level of abstraction which allows for fast simulation and early estimation, which are necessary for successful system development using the SystemC design methodology. SystemC has been chosen, as it provides a homogeneous platform for the design and modelling of complex systems. Furthermore, as systems become more tightly integrated, the ability to evaluate the system performance at early stages of a design becomes increasingly important. This is facilitated by the SystemC design methodology, and by following an IP-based design.

To our knowledge, this is the first time that the modelling of wireless communication network has been undertaken in SystemC and incorporated into a uniform design methodology, suitable for developing new technologies following the SystemC design methodology.



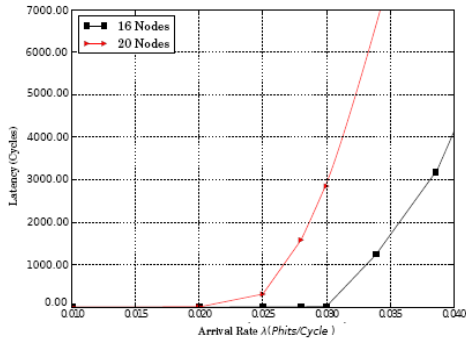


Figure 10. Latency for 16 and 20 nodes with a packet size of 30 phits

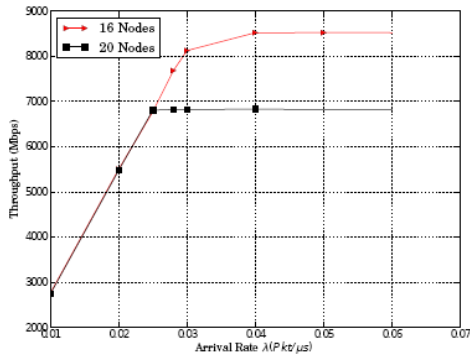


Figure 11. Throughput for 16 and 20 nodes for packet size of 30 phits.

## REFERENCES

- [1] N. A. Ahmed, I. A. Aref, F. Rodriguez-Salazar, and K. Elgaid, "Wireless channel model based on soc design methodology," ICSNC '09: Proceedings of the 2009 Fourth International Conference on Systems and Networks Communications, pp. 72-75, 2009.
- [2] M. Petrov, T. Murgan, P. Zipf, and M. Glesner, "Functional modeling techniques for a wireless lan ofdm transceiver," IEEE International Symposium on Circuits and Systems, vol. 4, pp. 3973-3973, May 2005.
- [3] D. Chkhaev, J. Hooman, and E. de Vink, "Verification and improvement of the sliding window protocol," 2003.
- [4] B. Sklar, Digital Communications: Fundamentals and Applications, 2nd ed., I. Prentice-Hall, Ed., Jan 2001.
- [5] J. Zyren and A. Petrick, "Tutorial on basic link budget analysis," Intersil Corporation, Tech. Rep., 1998.
- [6] J. Duato, S. Yalamanchili, and L. Ni, Interconnection Networks: An Engineering Approach. Morgan Kaufmann Publishers, 2003, vol. Revised Printin.
- [7] B. A. Forouzan, "Data communications and networking," McGraw Hill, 2004.
- [8] J. F. Kurose and K. W. Ross, Computer Networking: A Top-down Approach featuring the internet, 3rd ed., I. Pearson Education, Ed., 2005.
- [9] H. Saiedian, "A multi-purpose simulation project for engaging students and teaching object concepts," Computer Science Education, vol. 8, no. 1, pp. 64 - 81, Mar. 1998.
- [10] W. J. Dally and B. Towles, Principles and Practices of





Interconnection Networks, stranded  
ed. Morgan Kaufmann Publishers,  
2004.

- [11] L. Kleinrock and F. Tobagi, "Packet switching in radio channels: Part i-carrier sense multiple-access modes and their throughput-delay characteristics," Communications, IEEE Transactions on, vol. 23, no. 12, pp. 1400 - 1416, dec 1975.



المؤتمر العربي الليبي الدولي الخامس للهندسة الكهربائية والإلكترونية 23-26/10/2010 طرابلس ليبيا



## Traffic Management & QoS Scheduling in WIMAX Networks

Eng. Heba Medhat Alzegallai  
B.SC, EE Department  
hzegallai@yahoo.com

Dr. Mousa M. Mousa  
EE Department  
mousa.mousa@ee.edu.ly

### Abstract

In this paper two hybrid scheduling algorithms are considered. The first is a hybrid algorithm depends on the strict priority of the service that employs a strict priority mechanism.

The second is also a hybrid algorithm provides a more fair distribution of bandwidth among the SSs. This is also very adaptable to changing concentration of traffic. Hence the emphasis is on studying the performance of the two scheduling algorithms under different scenarios depending on the traffic mixes. The task is to find average throughput variation as function of concentration of SSs and packet delay.

### 1. Introduction

WiMAX is a cell-based technology aimed at providing last-mile wireless broadband access at a cheaper cost. The “last mile” is the final leg of delivering connectivity from the service provider to the customer. This leg is typically seen as an expensive undertaking because of the considerable costs of wires and cables. The core of WiMAX technology is specified by the IEEE 802.16 standard that provides specifications for MAC and Physical (PHY) layers. [1]

Packet scheduling is the process of resolving contention for shared resources in a network. The process involves allocating bandwidth among the users and determining their transmission order. Scheduling algorithms for a particular network need to be selected based on the type of users in the network and their QoS requirements. QoS requirements vary depending on the type of application/user. For real-time applications such as video conferencing, voice chat and audio/video streaming, delay and delay jitter are the

most important QoS requirements. Delay jitter is the inter-packet arrival time at the receiver and is required to be reasonably stable by the real-time applications.

On the other hand, for non-real time applications such as file transfer (FTP), throughput is the most important QoS requirement. Some applications, such as web-browsing and email do not have any QoS requirements. In a network, different types of applications, with diverse QoS requirements, can co-exist. A scheduling algorithm’s task in a multi-class network is to categorize the users into one of the pre-defined classes. Each user is assigned a priority, taking into account his QoS requirements. Subsequently, bandwidth is allocated according to the priority of the users as well as ensuring that fairness between the users is maintained. [1]

### 2. IEEE 802.16 Service Classes

One of the key functions of the WiMAX MAC layer is to ensure that QoS requirements for MAC Protocol Data Units



(PDUs) belonging to different service flows are met as reliably as possible given the loading conditions of the system. This implies that various negotiated performance indicators that are tied to the overall QoS, such as latency, jitter, data rate, packet error rate, and system availability, must be met for each connection. Since the QoS requirements of different data services can vary greatly, WiMAX has various handling and transporting mechanisms to meet that variety. [2]

**a. Unsolicited grant services (UGS):** This is designed to support fixed-size data packets at a constant bit rate (CBR). Examples of applications that may use this service are T1/E1 emulation and VoIP without silence suppression. [2]

**b. Real-time polling services (rtPS):** This service is designed to support real-time service flows, such as MPEG video, that generate variable-size data packets on a periodic basis. [2]

**c. Non-real-time polling service (nrtPS):** This service is designed to support delay-tolerant data streams, such as an FTP, that require variable-size data grants at a minimum guaranteed rate. [2]

**d. Best-effort (BE) service:** This service is designed to support data streams, such as Web browsing, that do not require a minimum service-level guarantee. [2]

**e. Extended real-time Polling Service (ertPS)** the IEEE 802.16-2005 standard [6] specifies an additional scheduling service called ertPS. The ertps scheduling service is designed to support real-time applications that generate variable size data packets on a periodic basis, such as VoIP with silence suppression. [2]

### 3. A QoS Service Framework

The standard IEEE802.16 has not defined the different necessary schemes to ensure that the specified QoS service can be obtained. To fill the gap between the specification of this standard and the schemes needed to provide QoS service guarantee, a solution on the framework of the QoS is as shown in Figure 1. At the BS, a few components have been proposed for ensuring the QoS guarantee. They are;

- Admission control scheme.
- Scheduling data base module.
- Uplink bandwidth allocation scheduling algorithm.
- Traffic management Table.
- Packet allocation module.

When a connection is established with the proposed QoS architecture, an application that originates at a SS establishes the connection with BS through connection negotiation. The admission control scheme will make a decision to accept or reject the new connection. Once the new connection is accepted, it will notify the Scheduling data base module that contains the detailed information about the status of all the active connections in the network. Based on this information the airlink scheduler allocates a bandwidth to each SS, and it will control the assistant modules to reach the QoS guaranteed bandwidth allocation. [3]

The traffic management enforces traffic based on the traffic specification of the connection. The packet allocation module retrieves the information from the traffic management table and generates the UL-MAP under the control of the bandwidth allocation scheduling algorithm. At each SS, there is a traffic connection classifier, which differentiates the arrival of the PDUs into different traffic streams and transmission queues. The SS will receive the UL-MAP message by MAP Parsing, Packet scheduler module selects the



appropriate packets from different queues and passes them to the fragmentation module. Fragmentation module checks to see if the packet can be fit in the transmission opportunity that is available, if not then the packet is fragmented into smaller pieces, as many fragmented packets

that can be sent in the current opportunity and the remainders are kept to be transmitted in the next time that the transmission opportunity is allocated to this SS. The interaction between modules is described in figure 1. [3]

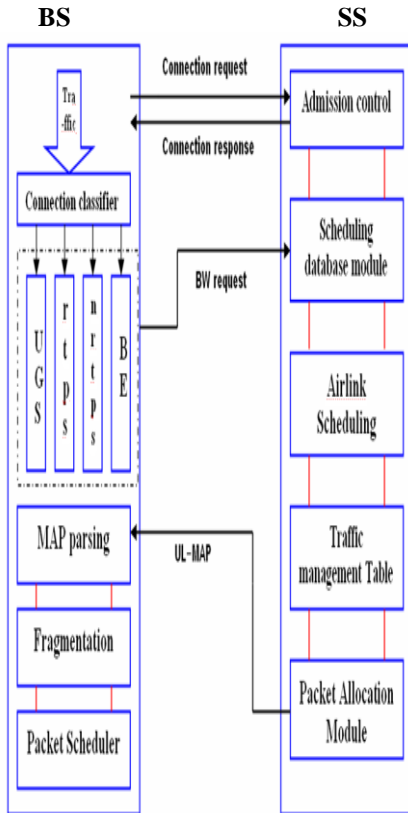


Figure 1: Structure of QoS Service Framework [4]

#### 4. WiMAX Scheduling Services

Scheduling services are the medium access control functions that define how and when devices will receive and transmit on a communication system.

The types of services that WiMAX can provide as explained earlier UGS to BE.

WiMAX systems use a grant management system to coordinate the request for new services and changes to existing services. It uses a combination of time division multiple access, polling and contention based flow control to provide specific types of services to users. Each SS to be associated with certain QoS parameters, whose values are specified by the SS upon admission into the network. These parameters are: [1]

##### a. Minimum Reserved Traffic Rate (MRTR) for the SS:

It specifies the minimum amount of data to be transported on behalf of the SS when averaged over time. MRTR rate will only be honored when sufficient data is available for scheduling.

##### b. Maximum Sustained Traffic Rate (MSTR):

Its value does not limit the instantaneous rate of the SS but it is used to police the SS to ensure that it conforms to the value specified, on average, over time.

##### c. Maximum Latency:

It specifies the maximum latency between the reception of a packet by the SS on its network interface and the forwarding of the packet to its RF interface.

#### 5. Scheduling in IEEE 802.16 Broadband Wireless Access

In the IEEE 802.16 standard, the BS and SS must reserve resources to meet their QoS requirements. i.e bandwidth.

Scheduling in IEEE 802.16 is divided into two related scheduling tasks (see Figure 2). The first task, performed at the BS is the scheduling of the airlink resources among the SSs. The second scheduler task is the scheduling of individual packets at SSs and

BS. The SS scheduler is responsible for the selection of the appropriate packets from all its queues, and sends them through the transmission opportunities allocated to the SS within each subframe.

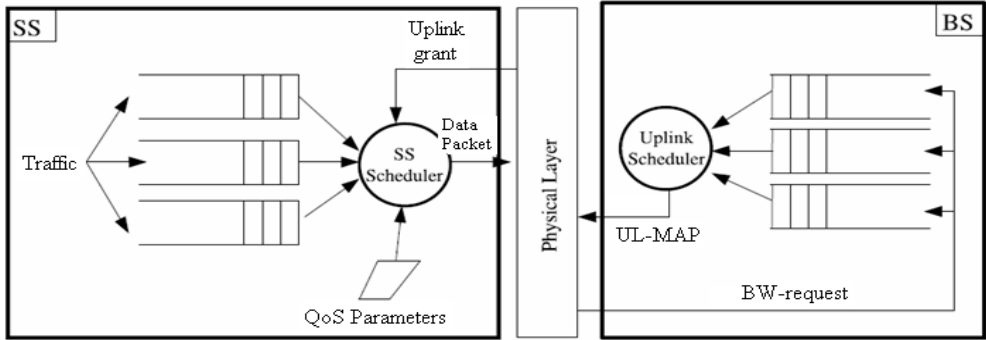


**Figure 2:** QoS function within the BS and SSs [5]

To manage the following traffic we need algorithms to control scheduling services. The scheduling algorithms are implemented at both the BS and SSs. [5, 6]

This paper is on scheduling algorithms executed at the BS for the uplink traffic, that faces challenges not faced by an algorithm for the downlink traffic, such as the queue size. An uplink algorithm at the BS has to coordinate its decision with all the SSs whereas a downlink algorithm is only concerned in communicating the decision locally to the BS. Scheduling algorithms for the uplink traffic in WiMAX are classified into three categories:

- Homogeneous scheduling algorithms
- Hybrid scheduling algorithms
- Opportunistic scheduling algorithms

Hybrid scheduling algorithms are considered for implementation as described next. [1]

## 6. Hybrid scheduling algorithms

The two hybrid algorithms selected for evaluation use different mechanisms of overall bandwidth allocation. An important aspect of hybrid algorithms is allocation of bandwidth among the traffic classes of WiMAX. The two selected algorithms perform this task in different ways are: (EDF+WFQ+FIFO) algorithm that use a strict priority mechanism for inter-class bandwidth allocation, and the (EDF+WFQ) algorithm that allocate bandwidth among traffic classes based on the number of SSs and their MRTR in each class. [1]

### a. Hybrid (EDF+WFQ+FIFO) algorithm

The hybrid algorithm uses strict priority mechanism for overall bandwidth allocation. The EDF scheduling algorithm is used for SSs of ertPS and rtPS classes, the WFQ algorithm is used for SSs of nrtPS class and FIFO is used for SSs of BE class. The Earliest Deadline First (EDF) is one of the most widely used scheduling algorithms for real-time applications as it selects SSs



based on their delay requirements. The algorithm assigns deadline to arriving packets of a SS. Since each SS specifies a value for the maximum latency parameter, the arrival time of a packet is added to the latency to form the tag of the packet. The value of maximum latency for SSs of the nrtPS and BE classes is set to infinity. [1]

**b. Hybrid (EDF+WFQ) Algorithm**

This algorithm uses the EDF scheduling algorithm for SSs of ertPS and rtPS classes and WFQ algorithm for SSs of nrtPS and BE classes. Although the mechanism of overall bandwidth distribution is not specified, but bandwidth is allocated in a fair manner. The overall bandwidth distribution is executed at the beginning of every frame, while the EDF and WFQ algorithms execute BW at the arrival of every packet. The following is the overall bandwidth allocation scheme adopted in our implementation: [1]

$$BW_{ertps,rtps} = C * \frac{\sum_{i \in ertps,rtps}^n (MRTR_i)}{\sum_{j=1}^n MRTR_j} \dots \dots (1)$$

$$BW_{nrtps,BE} = C * \frac{\sum_{i \in nrtps,BE}^n (MRTR_i)}{\sum_{j=1}^n MRTR_j} \dots \dots (2)$$

Where:

$MRTR_i$  : Minimum reserved traffic rate for connection  $i$ .

$C$ : Overall bandwidth.

$n$ : Number of connections.

**7. Performance Metrics**

**a. Average Throughput ( $\hat{R}_t$ ):**

The amount of data selected for transmission by a user per unit time.

Then we compute the average throughput ( $\hat{R}_t$ )

$$\hat{R}_t = \alpha * R_t + (1 - \alpha) * \hat{R}_{t-1} \dots \dots (3)$$

Where:  $\hat{R}_t, \hat{R}_{t-1}$  the average throughput at frame  $t$  and  $t-1$  respectively.

$\alpha$ :  $\square$  is constant factor related frame  $t$  & frame  $t-1$ , and typical value is 0.001.

**b. Average delay:**

The time between the arrival of a packet in the queue to the departure of the packet from the queue. The value is reported in milliseconds (ms) and is calculated for each SS as follows:

$$\hat{d} = \sum_{i=1}^N (f_i - a_i) / N \dots \dots \dots (4)$$

Where:  $\hat{d}$ : is the average queuing delay.

$f_i$  : is the time packet  $i$  leaves the queue.

$a_i$ : is the arrival time of packet  $i$  in the queue.

$N$ : is the number of packets.

**8. Traffic Model**

We have implemented four different traffic sources, one for each of the traffic classes. VoIP traffic is modeled for SSs of ertPS class, video streaming for SSs of rtPS class, FTP for SSs of nrtPS class and HTTP for SSs of BE class. The values of all the traffic parameters are based on one connection per SS as shown in table 1

**Table 1:** Traffic parameters for all service classes [1]

Parameter	ertps	rtps	nrtps	BE
MRTR(Kb/s)	15	64	45	1
MAX. Latency(ms)	100	150	-	-
Packet size(byte)	23	200	150	100



To study the performance of the scheduling algorithms under different Scenarios depends on the traffic mixes as given in Table 2. The experiment is conducted [7], with a total traffic rate of 4850 Kbps, of which 350Kbps is supplied by the ertPS class, 2200 Kbps is supplied by the rtPS class, 2200 Kbps is supplied by the nrtPS class and 100 Kbps is supplied by the BE class. The traffic arrival rate is calculated based on the number of symbols available in the uplink sub-frame after subtracting the preamble symbols, bandwidth request and contention request symbols. Each SS consists of one connection.

**Table 2:** Parameters of simulation (continue)

Number of SSS	42
Ratio of SS (ertps,rtps,nrtps,B E)	1:1:1:1, 3:1:1:1, 1:3:1:1, 1:1:3:1,1:1:1:3, 2:2:1:1, 2:1:2:1,2:1:1:2, 1:2:2:1, 1:2:1:2, 1:1:2:2
Modulation Technique	16QAM at 46Mb/s

## 9. Analysis of the results

### a. If Throughput is the concern

After implementing these scheduling algorithms by using a developed simulation program, it can be noted, for ertps class, as being of first priority the throughput is approximately the same on all ratios of service classes because the traffic rate for ertps is not large as shown in Figure 3.

**Table 2:** Parameters of simulation

Parameter	Value
DL:UL frame Ratio	1:1
Frame length(ms)	5
BW	20MHz
OFDM symbol duration( $\mu$ s)	44
Physical Slot	4 symbols
Number of OFDM Subcarriers	256

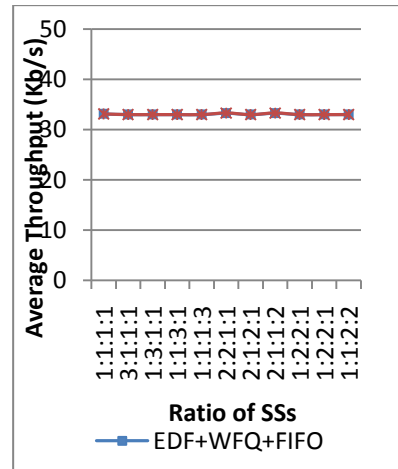


**Figure 3:** Average Throughput of ertps class per SS

For second class (rtps); when using the (EDF+WFQ+FIFO) algorithm the throughput for the ratios (1:3:1:1, 1:1:3:1, 1:2:2:1) is better than that of (EDF+WFQ) algorithm, because the reserved rate of the rtps in the second algorithm is not sufficient to all BW requested and also because rtps is of higher traffic load in these ratios as shown in Figure 4.



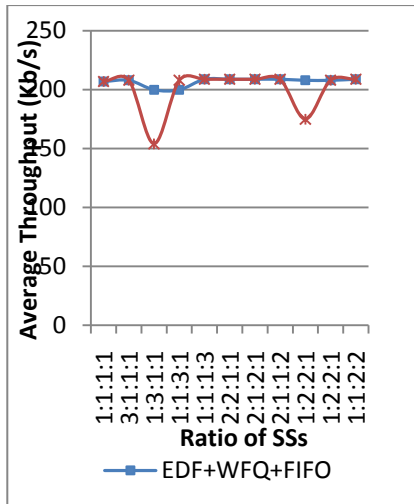


Figure 4: Average Throughput of rtps class per SS

For third class (nrtps); when using the (EDF+WFQ) algorithm the throughput for the ratios (1:1:3:1, 1:3:1:1, 1:2:2:1, 1:2:1:2) is better than that of (EDF+WFQ+FIFO) algorithm because the higher traffic of the nrtps in these ratio and the reserved rate is larger than the BW that remains to nrtps as shown in Figure 5 .

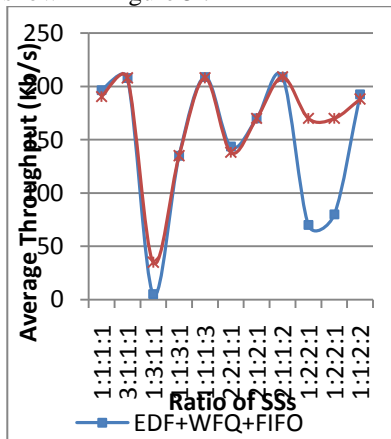


Figure 5: Average Throughput of nrtps class per SS

Fourth class (BE); which has the lowest priority, then it's obvious that for (EDF+WFQ) algorithm, the throughput for the ratios (1:1:1:1, 1:3:1:1, 1:1:3:1, 2:2:1:1, 2:1:2:1, 1:2:2:1, 1:2:1:2 1:1:2:2) is better than that of (EDF+WFQ+FIFO) algorithm as shown in Figure 6.

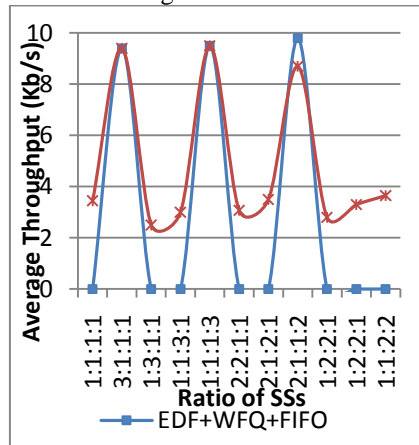


Figure 6: Average Throughput of BE class per SS

### b. If Delay is the concern

ertps, rtps classes are affected by the average delay because these services are real time services. The hybrid (EDF+WFQ) algorithm indicates a high average delay for the ertPS class when the ratios are 1:1:1:1, 2:1:2:1, 3:1:1:1 1:2:1:2 and 1:2:2:1. This behavior is due to the overall bandwidth allocation mechanism of the algorithm that allocates a small amount of bandwidth for the ertPS. The algorithm indicates a high average delay for ertPS Ss even when their concentration is high as a result of a larger number of ertps as shown in figure 7.

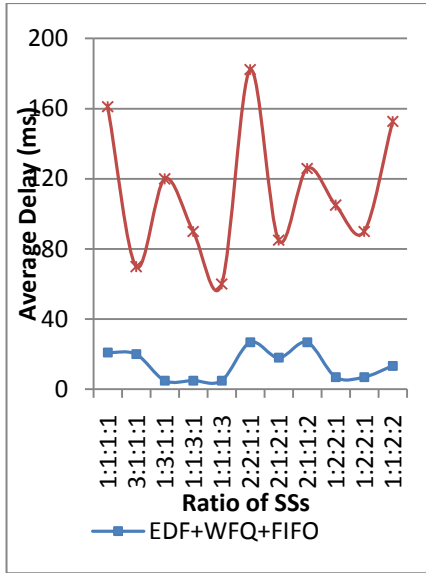


Figure 7: Average delay of ertps

Due to the high load of rtPS SSs, a large number of video packets will arrive before a VoIP packet arrives. This will result, in numerous cases, in a lower deadline assigned to video packets, even though they have a higher maximum latency.

The average delay of rtPS SSs, in most cases, under the hybrid (EDF+WFQ+FIFO) algorithms have lower delay than (EDF+WFQ) because the second algorithm is dependent on the BW reservation, then the data rate for each class is decreased based on the traffic load. Since the hybrid (EDF+WFQ+FIFO) algorithms provide high priority to rtPS SSs, all the data of rtPS SSs will be flushed out in a frame as shown in figure 8.

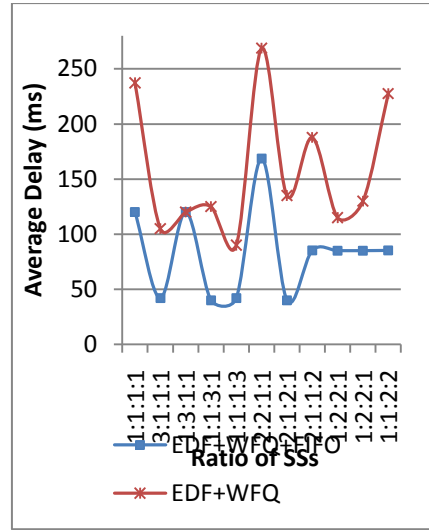


Figure 8: Average delay of rtps

### c. Summary of the results

Now if considering the ratios that give the better throughput for all services and the lowest delay; for the two algorithms these are: 3:1:1:1, 1:1:1:3, 2:1:1:2. This means that a lightly load of rtps& nrtps will give best results because of the large BW required for rtps, will starve the nrtps, and BE. However for heavy load of nrtps it causes high BW reservation of nrtps than that for others.

## 10. Conclusions

- QoS guarantee is different from type of service to another.
- Many factors are controlling QoS, where in physical layer they include; frame length, modulation technique, and parameters of OFDM; but in MAC layer they include; the ways of access to the medium that is scheduling mechanisms.



- The hybrid (EDF+WFQ+FIFO) algorithm results in the lowest average delay for ertps and rtps SSs. This algorithm provides strict priority to ertps and rtps SSs. However it does not consider the MRTR of the SSs in deciding the transmission schedule and result in a starvation of lower priority SSs. the nrtps and BE SSs will compete for bandwidth whereas in the later the nrtps SSs have strict priority over BE SSs.
  - Scheduling algorithms that employ a strict priority mechanism are not a good choice to satisfy the QoS requirements of the multi-class traffic in WiMAX.
  - The hybrid (EDF+WFQ) algorithm provides a more fair distribution of bandwidth among the SSs. This algorithm allocates bandwidth among the traffic classes in a fairer manner than preceding are also a very adaptable to changing concentration of traffic.
  - The average throughput of SSs of all classes decreases with increased concentration of SSs of that class, on the other hand when decrease the throughput the waiting time of the service packet will increase.
- [2] Xiaojing Meng, "An Efficient Scheduling For Diverse QoS Requirements in WiMAX ", Master thesis of Applied science, Waterloo University, Canada 2007.
- [3] Maode MA and Yan ZHANG , "QoS Services Provisioning at MAC Layer in WiMax Systems", Nanyang Technological University
- [4] An Analysis of the Design and Implementation of QoS over IEEE 802.16, [www-docs/cse574-06/ftp/wimax\\_qos/index.html](http://www-docs.cse574-06/ftp/wimax_qos/index.html), 12 December 2008.
- [5] Ehsan Asadzadeh Aghdaee, Quality of Service Support in IEEE 802.16 Broadband Wireless Access Networks, Master thesis of Engineering Science, Monash University October, 2006.
- [6] Dr Ahmet Sekercioglu and Professor Bala Srinivasan, Quality-of-Service support in IEEE 802.16 broadband wireless access Networks, Monash University.
- [7] Alzegallai, H.M, Traffic Management & QoS Scheduling in WIMAX Networks, B.SC, EE Department of Alfateh University, 2008.

## References

[1] Pratik Dhrona, "A Performance Study of Uplink Scheduling Algorithms in Point to Multipoint WiMAX Networks", Master thesis of Applied science, Queen's University, Canada December 2007.



المؤتمر الدولي العربي الليبي الخامس للهندسة الكهربائية والإلكترونية 2010/10/26-23 طرابلس ليبيا



## **Evaluating the Performance of IEEE802.11g in the Presence of Bluetooth Interference**

Salah'Den Saad Sasi

E-mail: [sasi\\_1984s@yahoo.com](mailto:sasi_1984s@yahoo.com)

Mobile: 0927827683 Allous Libya.

Job: Searcher in Center for Solar Energy Research and Studies.

### **Abstract**

Bluetooth Personal Area Networks (PANs) use the same 2.4 GHz ISM spectrum as IEEE 802.11b and IEEE 802.11g Wireless Local Area Networks (WLANs). The spread spectrum modulation and OFDM used by the WLANs and the frequency hopping sequence used by the PANs requires them to periodically share the same frequencies. Operation of these PANs and WLANs simultaneously in the same location is expected to become increasingly common. When WLANs and PANs are collocated, the performance of each network can be degraded by interference from the other.

In this paper, the coexistence of Bluetooth and 802.11g devices are quantified by a Matlab simulator using a conventional metrics (throughput, PER and coverage). The results show that the 802.11g throughput performance is degraded substantially in the presence of Bluetooth interference. The work carried out in this paper confirms that the interference from Bluetooth devices has a great effect on the performance of 802.11g and mitigates this effect.

### **1. Introduction**

The world has been entering the wireless revolution for a few years. Introduction of the wireless technology to our personal and business live is sure and unavoidable. Contemporary wireless systems are now more and more interesting alternative for the wireline networks. Of course they are still not so popular as the wireline solutions, but their advantages cause very big interest of the potential users.

One of the main problems for the wireless equipment producers and network operators are necessity of decreasing costs, so they try to find and use any possible cost reduction. That is the reason why most of them decided to use an unlicensed frequency bands for the transmission. At the beginning, when there were only a few wireless communication systems, it was not so big problem. However, during recent years a lot of other systems have appeared. All these actions caused general problem of using unlicensed frequency bands more and



more interferences. This problem appears especially in the 2.4 GHz band.

Bluetooth is a wireless standard designed for short range communication between different types of devices. Initially Bluetooth was created to solve a problem of replacing cables used for communication between such devices as: laptop, palmtops, PDA, cellular phone and other mobile devices. Bluetooth enable user to connect to a wide range of computing and telecommunications devices without any need of connecting cables to the devices. Bluetooth is a radio frequency specification for short range, point-to-multipoint voice and data transfer, and is the main standard for creating Wireless Personal Area Network. Bluetooth as a communication link does not offer very large data rate is 1 Mbps and it's the nominal link range is about 10 m and it can be extended to 100 m by increasing transmit power.

The foundation of mainstream WLAN products began with the original 802.11 standard developed in 1997 by the Institute of Electrical and Electronics Engineers (IEEE). That base standard continues to be enhanced through document additions that are designated by a letter following the 802.11 name, such as 802.11b, 802.11a, or 802.11g.

The family of IEEE 802.11 standards supports both infrastructure WLANs connection through access points and allows peer-to-peer communication between terminals.

The IEEE 802.11g standard for Wireless Local Area Networks will serve to replace wired LAN computer networks. 802.11g extends with payload data rates up to 54 Mbps using OFDM modulation. In this

Wireless Local Area Network, an access point radio wirelessly connects terminal devices like personal computers to each other and to the wired network. The maximum distance of terminal devices from the access point is 30 to 100 meters depending on the data rate.

### 1.1 Problem Definition

The main wireless communication systems designed for creating Wireless Personal Area Networks (i.e. Bluetooth) and Wireless Local Area Network (IEEE 802.11) use the same 2.4 GHz Industrial Scientific and Medical frequency band. This band is very popular and suitable for low cost wireless solutions and due to the global availability there is number of different systems using these frequencies for transmission. This frequency band use also many industrial devices in home environment. Such as microwave ovens and doors remote controllers, as show in figure (1).

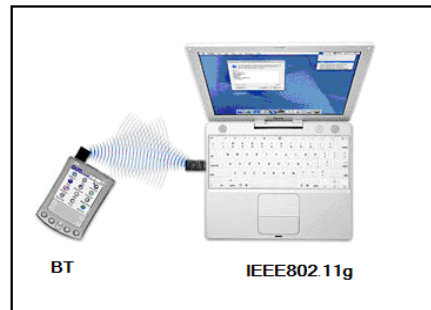


Figure (1) interference BT & IEEE 802.11g

These are complementary rather than competing technologies, and many applications require 802.11g and Bluetooth to operate simultaneously and in close proximity. Under these conditions, interference between 802.11g and Bluetooth are unavoidable.



Bluetooth devices currently designed to hop randomly over all 79 of the available hop frequencies, interference between a single Bluetooth piconet and a single 802.11g can be expected to be significant, if they are co-located and operating in the same time. This issue will be investigated in this paper in order to identify and evaluate solutions that maintain high performance of 802.11g.

## 1.2 Paper Objectives

The main goal of this study is to demonstrate that the performance of 802.11g is substantially degraded in the presence of Bluetooth (BT) interference. In order to achieve this major goal of the study, two measurable objectives listed below, have been identified.

- 1- Evaluating the performance of IEEE 802.11g without BT interference using (convention metrics PER and Throughput).
- 2- Quantifying the impact of BT interference on 802.11g data transmission using the same metrics.

## 2. Bluetooth Overview

Bluetooth is a wireless Personal Area Network (WPAN) technology designed to connect devices of different functions such as telephones, notebooks, computers (desktop and laptop), cameras, printers, coffee makers, and so on. Bluetooth technology is the implementation of a protocol defined by the IEEE 802.15 standard[1]. Bluetooth as USB is show in figure (2).



Figure (2) Bluetooth as USB.

A Bluetooth ad-hoc wireless network is called a piconet, where all data packets are exchange between one master (controlling device in the network) and each slave (The communication between the master and the slaves can be one-to-one or one-to- many) [5]. Piconets can be combined to form what is called a scatternet. A slave station in one piconet can become the master in another piconet, as shown in Figures (3 & 4) [1].

Most Bluetooth devices support a range of up to 10 meters, and speed of up to 700 Kbps for data and isochronous voice transmissions. The nominal transmission power level is specified to be 0 dBm (1mW), but can be increased to 20dBm (100 mW), if to expand its communication range up to 100m. The Bluetooth physical (PHY) layer uses FHSS PHY at a rate of 1600 hops/sec, occupying 79 different channel of 1MHz in the US. Gaussian Frequency Shift Keying (GFSK) is used as the modulation scheme in the 2.4 GHz frequency band [5].

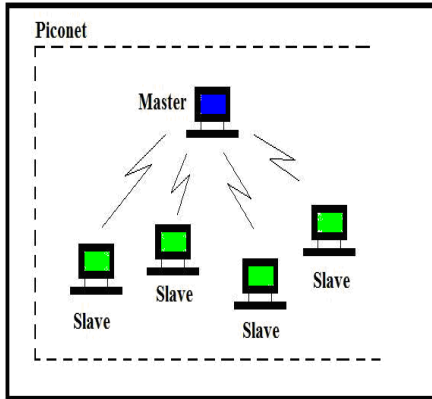


Figure (3) Bluetooth Piconet

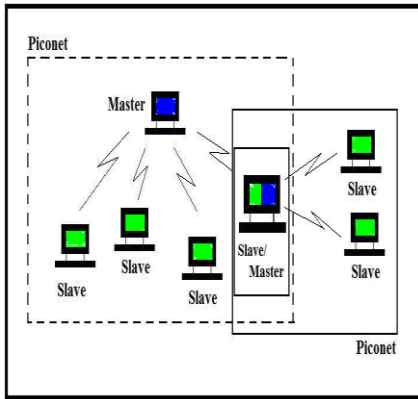


Figure (4) Bluetooth scatternet.

### 3. IEEE802.11g Overview

The IEEE 802.11g standard is a specification for Wireless Local Area Networks (WLAN), operates at data rates of 6, 9, 12, 18, 24, 36, 48 and 54 Mbps using coded Orthogonal Division Frequency Multiplexing (OFDM) in the same 2.4 GHz frequency band that operate at distances up to 100 meters. The OFDM signal occupies approximately 16 MHz of the 20 MHz channel bandwidth [4]. IEEE 802.11g as USB is show figure (5).



Figure (5) IEEE 802.11g as USB & card

An ad hoc network is a peer-to-peer network (no centralized server) set up temporarily to meet same immediate need. For example, a group of employees, each with a laptop or palmtop computer, may convene in a conference room for a business or classroom meeting. The employees link their computer in a temporary network just for the duration of the meeting.

Figure (6) suggests the differences between a WLAN that supports LAN extension and nomadic access requirements and an ad hoc WLAN. In the former case, the WLAN forms a stationary infrastructure consisting of one or more cells with a control module for each cell. Within a cell, there may be a number of stationary end systems. Nomadic stations can move from one cell to another. In contrast, there is no infrastructure for an ad hoc network. Rather, A peer collection of stations within range of each other may dynamically configure themselves into a temporary network[2].



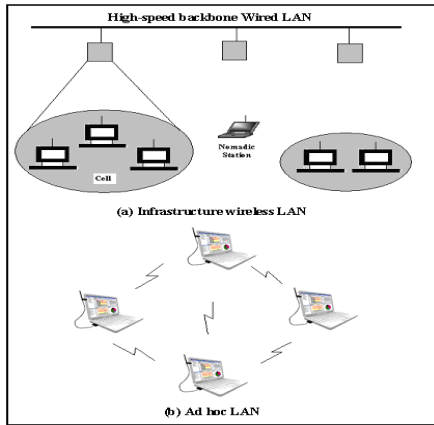


Figure (6) Wireless LAN Configurations

#### 4. Coexistence Issue between 802.11g and BT

The OFDM signal of 802.11g occupies approximately 16.5 MHz of the 20 MHz channel bandwidth. Figure (7) a shows frequency domain representation of part of the ISM band comprising 802.11g and Bluetooth signals.

For a BT transmission to disrupt the 802.11g packets there must be an overlap in frequency as well as time, as illustrated in Figure (7). The likelihood of interference depends on the bandwidth occupancy, the 802.11g packet length and the load factor of the interfering BT piconet. For a WLAN with a 16 MHz channel, the BT signal appears as narrow-band interference. The probability that both the BT and 802.11g signals overlap in frequency is roughly  $16/79 \approx 20\%$ . In the time domain, long 802.11g packets, such as 1000-byte packets, stand a higher chance of overlapping a number of BT time slots than 100-byte packets[3].

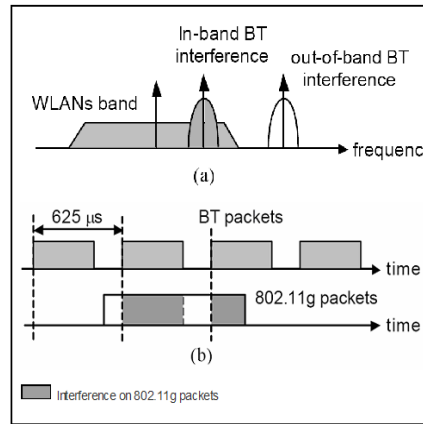


Figure (7) Interference of BT signal on 802.11g signal

(a) in frequency (b) in time.

#### 4.1 Last Study:

The first study on the performance of 802.11g WLAN in the presence of BT interference. The test setup of their experiment is shown in figure (8).

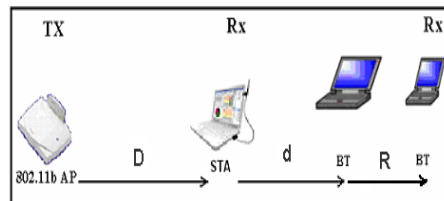


Figure (8) 802.11g Throughput with Bluetooth Interferer Test Setup.

Their results showed that the maximum Transport Control Protocol (TCP) throughput (i.e. No BT) was 18 Mbps, and then degraded to 14.5 Mbps at  $D$  equals to 30 m. when the BT device was at 2 m away from the STA i.e.  $d$  equal to 2 m, the degradation in the TCP throughput was approximately 25% when the STA was near the AP and as the distance  $D$



increase, the degradation also increases until it reached 50% when D is equal to 30 m.

As d was increased the TCP throughput was slightly improved and the degradation was between 20% and 35%. These experimental studies demonstrate that the throughput performance of 802.11b/g degrades in the presence of BT interference for a broad range of scenarios as long as the 802.11b/g device is within the range of the communicating BT devices.

It can be concluded from the previous discussion that the issue of 802.11b/g and BT interference has received significant levels of attention in both industry and academic [7].

## 5. Simulation Results

### 5.1 Introduction

This section presents a simulation study on data transmission over IEEE 802.11g in the presence of BT interference. The simulation study was divided into two tasks. The first task evaluates the performance of 802.11g without BT interference and the second task evaluates the performance of 802.11g with BT interference.

### 5.2 Simulator Overview

The block diagrams in figure (9) shows a computer-based simulator using Matlab, which was implemented to model the 802.11g PHY transmission modes with different coded-modulation and data rates ranging from 6 Mbps to 54 Mbps according to the IEEE 802.11g specifications.

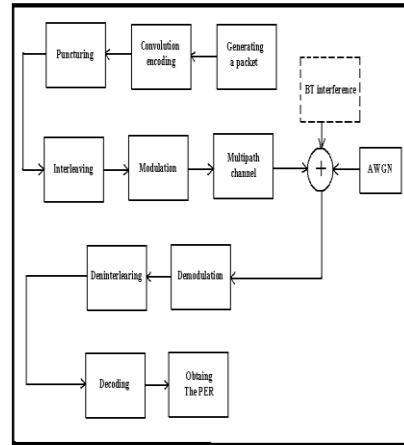


Figure (9) schematic diagram of the 802.11g WLAN simulator for data transmission with and without BT interference.

### 5.3 Performance of 802.11g without Bluetooth Interference

This section presents the results for the performance of 802.11g without BT interference.

#### 5.3.1 Experiment Scenario

In this experiment the Access point (AP) was fixed and the station (STA) was mobile in other words the distance between them was changed as shown in figure(10).

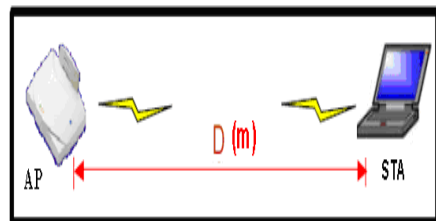


Figure (10) 802.11g Baseline Test Set-up.

Fi



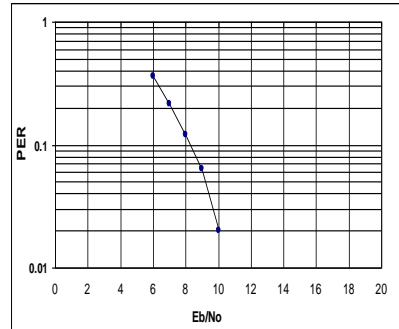
This experiment was carried out in order to calculate the minimum requirements of  $E_b/N_0$  and the corresponding maximum coverage for data transmission over 802.11g. The simulation parameters were set as shown in table (1).

Table (1) simulator parameters

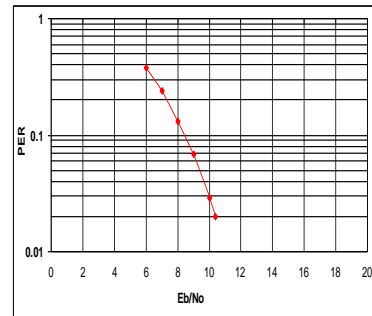
802.11g data rates	6, 12, 24 and 54 Mbps
802.11g transmission power	100 mW
802.11g packet size	100 byte
Channel rms delay spread	100 ns
Channel type	Rayleigh fading channel

### 5.3.2 Packet Error Rate (PER) Results

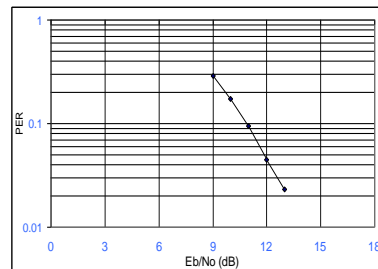
Figures (11) a, b, c and d show the simulated PER versus  $E_b/N_0$  performance of 802.11g when transmitting 100 byte packet in a multipath channel. The results display PER curves for PER values down to  $10^{-2}$  that are intended for data transmission. It can be seen from the figures that the minimum values of  $E_b/N_0$  for data rates 6, 12, 24 and 54 Mbps are 10, 10.4, 13 and 20 dB, respectively. It clear from the results that high-data rates require higher  $E_b/N_0$  values than low-data rate modes because low-data rates have more robust modulation formats.



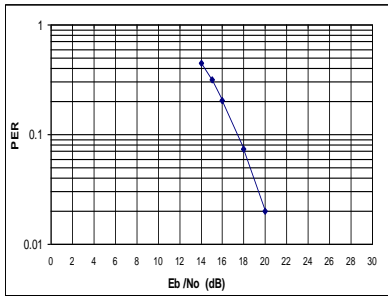
(a)



(b)



(c)



(d)

Figure (11) PER versus Eb/No for IEEE802.11g at data rates:

- (a) 6 Mbps                      (b) 12 Mbps,  
 (c) 24 Mbps                    (d) 54 Mbps

### 5.3.3 Calculation of Throughput and Coverage

Throughput is defined as the speed with which a user can send and receive data between an AP and the STA. A WLAN generally consists of an AP that connects to a wired network and STA that connect to the AP through wireless (radio) links. The Throughput is determined from equation (1).

$$\text{Throughput} = (1 - \text{PER}) * \text{Data rate} \dots (1)$$

The coverage of 802.11g is calculated from the path loss model which expressed in equation (2) a, b [6].

$$L_{\text{path}} = 20 \log (4\pi d / \lambda) ,$$

$$d \leq 8 \text{ m} \dots (2a)$$

$$= 58.3 + 33 \log (d / 8) ,$$

$$d > 8 \text{ m} \dots (2b)$$

Where,  $\lambda = 0.1224 \text{ m}$  is the free space wavelength at 2.45 GHz. The noise floor for the receiver at the STA is given by equation (3) where  $B_{\text{ofdm}} = 20 \text{ MHz}$  is the bandwidth of the OFDM receiver and  $N_F = 12 \text{ dB}$  is the receiver noise figure[4].

$$\text{Noise floor} = -174 + 10\text{Log} (B_{\text{ofdm}}) + N_F = -88.89 \text{ dBm} \dots (3)$$

The following steps are used to calculate the coverage from Eb/No requirements.

Step 1: convert Eb/No to SNR according to equation (4).

$$\text{SNR} = \text{Eb/No} + 10\text{Log} (R * N_{\text{BPSC}}) \text{ dB} \dots (4)$$

Where R= coding rate and  $N_{\text{BPSC}} =$  coded bits per sub-carrier.

Step 2: calculate the received WLAN signal power at the STA.

$$P_{\text{rx}} = \text{SNR} + \text{Noise floor} \text{ dB} \dots (5)$$

Step 3: Calculate the distance D from the path loss equation  $P_{\text{rx}}$

$$D = 8 * 10^{(20 - P_{\text{rx}} - 58.3) / 33} ,$$

$$\text{or } d > 8 \text{ m} \dots (6)$$

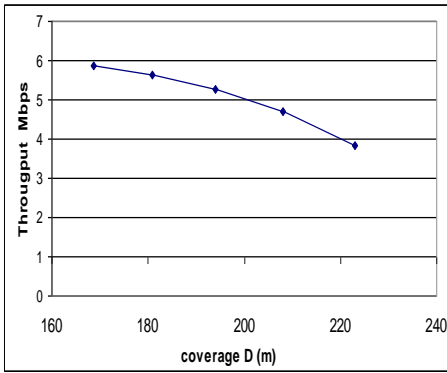
### 5.3.4 Throughput and Coverage Results

This section presents the results of the coverage performance of 802.11g at data rates 6, 12, 24 and 54 Mbps and the corresponding throughput values. Based on Eb/No and PER values, the coverage radius and the throughput was determined according to the procedure in section 5.3.2. Figures (12) a, b, c and d show throughput versus coverage radius. The results show that maximum coverage for data rates 6, 12, 24 and 54 Mbps are 170, 130, 90 and 43m respectively and the corresponding

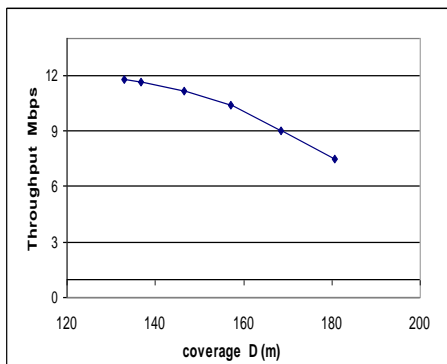


throughput vales are 5.88, 11.76, 23.45 and 52.92 Mbps.

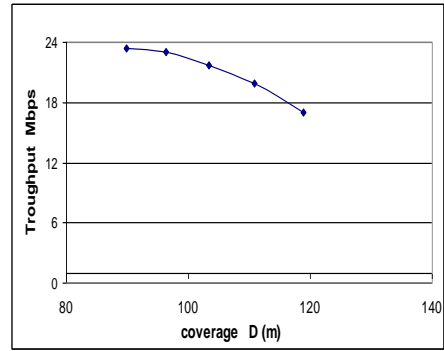
The throughput values are higher than the minimum requirement for data transmission which is 90% of the throughput. Is clear from the results that as the STA moves away from the AP, the throughput decreases and the coverage radius shrinks due to path loss and it is also clear that data rate 54 Mbps has the smallest coverage radius because of the 3/4 coding rate and 64 QAM modulation scheme.



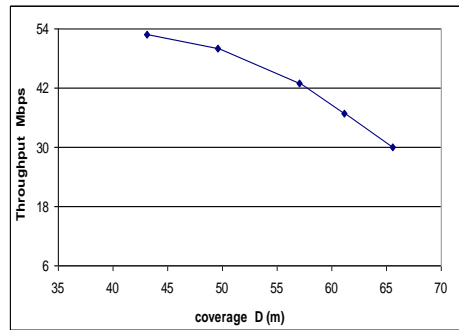
(a)



(b)



(c)



(d)

Figure (12) the throughput of IEEE802.11g at data rate:

- (a) 6 Mbps
- (b) 12 Mbps
- (c) 24 Mbps
- (d) 54 Mbps



### 5.4 Performance of 802.11g with Bluetooth Interference

This section presents a simulation study on data transmission over 802.11g in the presence of BT interference.

#### 5.4.1 Interference Scenario

In this scenario the AP is fixed, the STA is movable and the piconet devices were placed at distance  $d$  equal 9 m, and the piconet moves with its STA towards the AP until quality of service for data transmission is restored as shown in figure (13).

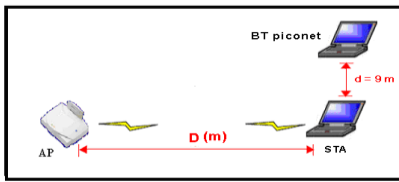


Figure (13) Interference Scenario.

The simulator parameters were set in shown in Table (2).

Table (2) simulator parameters.

Due to time constraints the effect of the BT interference on 802.11g was evaluated at data rates 6 and 12 Mbps only.

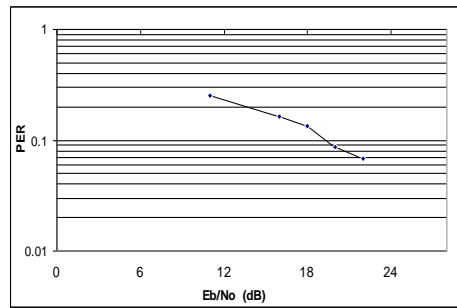
#### 5.4.2 PER Results

Figures (14)a and b show the PER results that is obtained when there is BT a device at  $d=9$  m. It can seen from these results that the PER requirements (0.068 and 0 .061) for data rates 6 and 12 Mbps respectively are obtained at higher  $E_b/N_0$  values 22 and 29 dB than that without BT interference which are (10 and 10.4 dB).

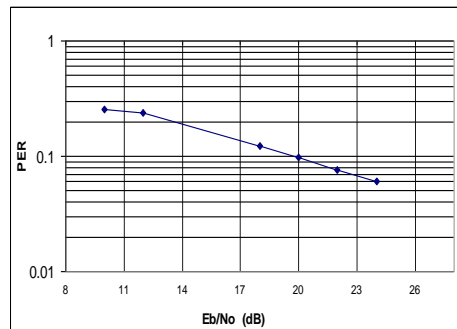
There results demonstrate that the

Data rates	6 and 12 Mbps
802.11g transmission power	100 mW
802.11g packet size	100 byte
Distance between STA and piconet	9 m
SIR	-22 and -6 dB & -18.992 and -4.992 dB

performance of 802.11g is substantially degraded due to BT interference.



(a)



(b)

Figure (14) PER versus  $E_b/N_0$  at data rate (a) 6 Mbps, (b) 12 Mbps with BT interference.



### 5.4.3 Throughput and coverage results

The proximity of a BT device to a wireless STA substantially affects the amount of interference experienced by the latter. Even though an AP transmits with a higher power than a BT device (20 dBm versus 0 dBm respectively), the AP signal power decreases rapidly with range due to path loss effects. Therefore, at the remote STA the received power from a close BT device can exceed the received power from the AP. Figure (13) shows the geographical layout of the interference scenario investigated. The path loss model used for this scenario is given in equation (2b).

To evaluate the AP coverage taking into account the BT interference effect, the minimum SIR to achieve a target PER of 10% is required, where 10% PER defines QoS operating point for non-real time data traffic.

The AP coverage as a function of distance  $d$  can be calculated as follows:

Calculate the BT signal power at the STA with  $d$  as parameter, where  $L_{path}$  is given by equation (2).

$$P_{bt} = 0 - L_{path} \quad \text{dB} \quad \dots(7)$$

Based on minimum SIR, calculate the corresponding received signal power at the STA from the AP.

$$P_{rx} = \text{SNR} + \text{Noise floor} \quad \text{dB} \quad (8)$$

$$\text{SIR} = P_{rx} - P_{bt} \quad \text{dB} \quad \dots(9)$$

$$P_{rx} = \text{SIR} + P_{bt} \quad \text{dBm} \quad \dots(10)$$

Determine the distance  $D$  from the AP to the STA for received power  $P_{rx}$ , then

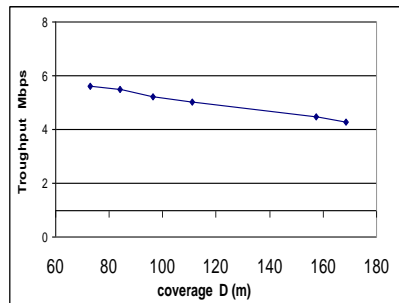
equation (6) can write  $D$  as shown in equation (11).

$$D = 8 * 10^{(20 - P_{rx} - 58.3) / 33} ,$$

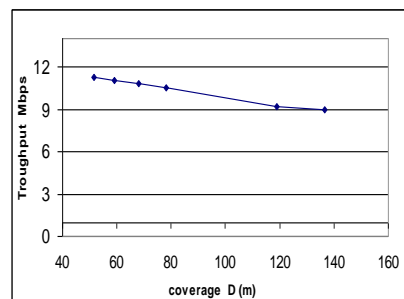
for  $d > 8 \text{ m} \dots\dots(11)$

The Throughput was calculated using equation (1).

Figures (15) a, b show the maximum coverage that can be achieved when there is a BT interference. The results show that the maximum coverage radius for data rates 6 and 12 Mbps are 73 and 51 m which is much smaller than that obtained when there is no BT interference.



(a)



(b)

Figure (15) the throughput of IEEE802.11g at data rate in the presence of BT interference (a) 6 Mbps (b) 12 Mbps



## 5.5 Summary

WLANs based on the IEEE 802.11g standard use the same 2.4GHz ISM frequency band as Bluetooth (BT). The effect of BT transmission on the station (STA) coverage of IEEE 802.11g at a different data rates are investigated as a function of the separation between the WLAN AP and STA. Results for Packet Error Rate (PER) and AP coverage are presented comparing the system performance both with and without BT interference. The results show that the BT interference has a great effect on the performance of IEEE 802.11g WLAN.

## 6. Conclusion

The robust transmission of data over IEEE 802.11g WLAN poses many challenges such as the unreliability of the wireless channel and interference from signals of other devices such as Bluetooth, cordless phones and microwave ovens.

Wireless LANs have achieved enormous growth because they allow users to gain access to network services without having to be connected by cable to backbone infrastructure. Two wireless systems that have experienced wide popularity are the IEEE 802.11g standard for WLANs and BT. Both of these systems operate in the 2.4 GHz ISM band which extends from 2.4 to 2.485 GHz. IEEE 802.g is designed to achieve operating distances between the AP and wireless STA of up to 100 m depending on the data rate used.

In this paper, the impact of Bluetooth interference on the throughput and coverage performance of IEEE 802.11g was evaluated by a Matlab simulator. Two scenarios were carried out in over to investigate the effect of BT interference on

the throughput and coverage of 802.11g. in the First scenario, the performance of 802.11g was evaluated without BT interference. The results of this experiment showed that the throughput of 802.11g at data rates 6, 12, 24 and 54 Mbps are (5.88, 11.76, 23.44 and 52.92 Mbps) respectively and the corresponding coverage values are (170, 130, 90 and 43 m) respectively. These results showed that low-data rates have better performance than high-data rates because low-data rates have more robust coding rate and modulation scheme.

In the second scenario, the impact of BT interference on 802.11g performance was investigated. The results showed the throughput and coverage performance of 802.11g was degraded substantially due to BT interference for example the coverage and throughput of 802.11g at data rate 6Mbps are (73 m and 5.58 Mbps ) and it is much long than that obtained without BT interference.

The work presented in this paper shows that the impact of BT interference on the throughput and coverage performance of 802.11g is substantial.

Finally, the paper done has demonstrated that BT interference can cause a serious degradation in performance of 802.11g.

## Reference

- 1- Andrev S.Tanebaum, computers Networks (Fourth Edition), Prentice Hall, USA ,2003, Page 372 to 378.
- 2-William stallings, Data And Computer Communications (seventh Edition),Page 547, 548.
- 3-K. K. Wong and T. O'Farrell "Co-existence of 802.11g WLANs with





Bluetooth", institute of integrated information systems, Page 1, 2.

4- Salim Abukharis and Time O'Farrell, The Effect of Bluetooth Transmission on the Access Point coverage of IEEE 802.11g, London communications symposium 2003, Page 262, 263

5- Experimental Study Co-existence of 802.11b with Alien Devices. Javier del Prado and Sunghyun Choi . Philips Research Briarcliff\_USA, Briarcliff Manor, New Your.

6-Jim Zyren , "Reliability of IEEE 802.11 Hi Rate DSSS WLANs in a High Density Bluetooth Environment", June 8, 1999, Page 3.

7- Salim Abukharis and Time O'Farrell, the coexistence of 802.11 b/g and Bluetooth: An Experimental Comparison in LoS Conditions, London communications symposium 2005, Page 152.

En. Salah'Den Sasi



المؤتمر الدولي العربي الليبي الخامس للهندسة الكهربائية والإلكترونية 2010/10/26-23 طرابلس ليبيا



## Network Security Challenges

**Eng. Khaled M. Gammo**

Email: [k.gammo@almdar.ly](mailto:k.gammo@almdar.ly)

Al-Madar Al-Jadid Co.

Tripoli- Libya

**Eng. Issa S. Gherwi**

Email: [i.gherwi@gmail.com](mailto:i.gherwi@gmail.com)

Al-Madar Al-Jadid Co.

Tripoli- Libya

**Dr. H. I. Sigiuk**

Email: [sigiuk@ee.edu.ly](mailto:sigiuk@ee.edu.ly)

Al-Fatah University

Tripoli- Libya

### Abstract

As networks grow and being interconnected with other networks, including the Internet, those networks are exposed to a greater number of security risks bringing more challenges to those who run and manage those networks. The need for integrated network infrastructure comprising voice, video, and data (all-in-one) services is evident. However, the number of potential attackers grow along with the size of the network, and the tools available to those potential attackers are always increasing in terms of sophistication.

In this paper, a survey will be given for different network attacks along with techniques used nowadays to provide required level of security, taking into consideration the challenges encountered by different organizations, and companies to secure their network. Furthermore, this paper gives a list of some recommendations and guidelines that ought to be adopted and deployed at different levels and phases to secure networks.

### 1. Introduction

Internet protocol (IP) is now considered the most promising media on which to build the new integrated services. There is an on-going integration of circuit networks and IP networks, which make operators seek ways to consolidate the security of voice and data traffic, platforms, and services in order to provide protected data and communications.

Increasing reliance on the IP, along with the explosive increase in the deployment of corporate intranets and extranets, have not only changed the way organizations do business, but also how they approach network security. For most of today's such corporate networks, it is necessary to provide connectivity between internal corporate networks and outside

world. The Internet provides a worldwide communications infrastructure allowing those organizations to provide cost-effective, worldwide connectivity to network users.

Networks might experience unauthorized access from an outside hacker or an inside attacker. This could potentially expose propriety data, adversely impact the corporation's image and reputation in the marketplace, decrease company productivity, and potentially cause the business to close if the impact is serious enough. Even if the unauthorized access does not reach this critical level, it can at the very least harm the relationships with customers and business partners, who might question the company's ability to protect confidential information. It is therefore critical that an organization take actions to



protect its confidential information from both outside attackers and those within the organization who should not gain access to classified information. For these

reasons, security has become a primary concern due to the challenges faced by the organizations at modern days' increasingly complex environments.

## 2. Type of Threats

Connecting to an outside network, the Internet for instance, introduces the possibility that outside attackers will exploit the network, perhaps by stealing network data or by impacting the network's performance (for example, by introducing viruses). However, even if a network were disconnected from any external network, security threats would still exist. The different threats that a network can face can be categorized as follows:

### 2.1 Internal Threats

Internal attacks originate from dissatisfied or unhappy inside employees or contractors. Internal attackers have some form of access to the system and usually try to hide their attack as a normal process. For instance, internal disgruntled employees have local access to some resources on the internal network already. They could also have some administrative rights on the network. One of the best means to protect against internal attacks is to implement an Intrusion Prevention system (IPS), and to configure it to scan for both external and internal attacks. All forms of attacks should be logged and the logs should be reviewed and followed up.

### 2.2 External Threats

Because external attackers probably do not have intimate knowledge of a network, and because they do not already possess access credentials, their attacks tend to be more technical in nature. For example, an attacker could perform a ping sweep on a network to identify IP addresses that respond to the series of pings. Then those IP addresses could be subjected to a port scan, in which open services on those hosts are discovered. The attacker could then try to exploit a known vulnerability to compromise one of the discovered services on a host. If the attacker gains control of the host, the attacker could use that as a jumping-off point to attack other systems in the network [1]. External threats can be further categorized into either structured threats or unstructured threats and can also occur either remotely or locally.

### 3. Attack Vectors

Attack vectors are routes or methods used to get into computer and network systems to leverage unexpected openings for misuse. Attack vectors can be generally classified as follows:

**a) Viruses:** A virus is a malicious software program or piece of code that causes an unanticipated negative event and usually is capable of causing damage to data or other programs on the infected system.

**b) Worms:** A computer worm is a self-replicating malicious software program, similar to a computer virus. Worms are viruses that can reside in the active memory of a system and are capable of self-duplicating and self-propagating from one computer system to the next over a network. Worms are often designed to exploit the file



transmission capabilities, such as e-mail found on many computer systems.

**c) Trojans:** A Trojan horse is a malicious program that pretends to be a gentle application. Trojans are seemingly harmless programs that hide a malicious activity, such as a keystroke logger that could capture all passwords or any other sensitive information entered, without the knowledge of the user.

**d) Password cracking:** Password attacks can be implemented using several methods, including brute force attacks, Trojan horse programs, IP spoofing, and packet sniffers. Generally, password attacks refer to repeated attempts to identify a valid user account or password. These repeated attempts are called brute force attacks.

**e) Buffer overflows:** Buffers are memory locations in a system that are used to store data and generally hold a predefined amount of finite data. A buffer overflow occurs when a program attempts to store data in a buffer, when data is larger than the size of the allocated buffer.

**f) IP spoofing:** An IP spoofing attack occurs when an intruder attempts to disguise itself by pretending to have the source IP address of a trusted host to gain access to specified resources on a trusted network. IP spoofing is one of the most common acts of online camouflage.

**g) Address Resolution Protocol (ARP) spoofing:** ARP spoofing occurs when an intruder attempts to disguise its source hardware address (MAC address) to impersonate a trusted host. This is one of the primary steps that aids many of the other attacks.

**h) Man-in-the-middle attack (TCP hijacking):** The man-in-the-middle (MITM), also known as a TCP hijacking attack, is a well-known attack in which an intruder intercepts legitimate communication between two points and can modify or control the TCP session without the knowledge of either the sender or the recipient of the session. TCP hijacking is an exploit that targets the victims' TCP-based applications such as Telnet, FTP, SMTP (e-mail), or HTTP sessions. An intruder can also be "inline" in an ongoing TCP session between the sender and the receiver while using a sniffing program to watch the conversation.

**i) Ping sweeps:** A ping sweep, also known as an Internet Control Message Protocol (ICMP) sweep, is a scanning technique used to determine live hosts (computers) in a network. A ping sweep, consists of ICMP ECHO requests sent to multiple hosts (one at a time, unless a broadcast IP address is used). If a given address is live, it will return an ICMP ECHO reply confirming a legitimate live host. Ping sweeps are widely used in the reconnaissance phase of the attack process.

**j) Port scanning:** Port scanning is a method used to enumerate what services are running on a system. An intruder sends random requests on different ports, and if the host responds to the request, the intruder confirms that the port is active and in listening mode. The attacker can then plan exploits to any known vulnerabilities by targeting these ports. A port scanner is a piece of software designed to search a network host for open ports. Port scanning is also one of the primary reconnaissance techniques attackers use to discover services that can be exploited.



**k) Sniffing:** A packet sniffer is software that uses a network adapter card in promiscuous mode to passively capture all

**l) Flooding:** Flooding occurs when an excessive amount of unwanted data is sent, resulting in disruption of data availability.

**m) Denial of Service (DoS):** In most cases, the objective of a DoS attack is to dispossess legitimate user access to services or resources. DoS attacks do not typically result in intrusion or the illegal theft of information, but are geared to prevent access to authorized users by means of flooding the victim with an excessive volume of packets.

Distributed DoS (DDoS) attacks amplify DoS attacks in that a large number of compromised systems coordinate collectively to flood the victim, thereby

network packets that are being transmitted across the network.

causing denial of service for users of the targeted systems [2].

In 2008, a survey was carried out by Computer and Security Institute (CSI) about a number of different sorts of computer attacks and incidents, as shown in Fig. 1, a subset of these is graphed. In particular, it shows the four categories of highest incidence, namely viruses, insider abuse, laptop theft and unauthorized access to systems. There appears to be a clear trend of lower and lower percentages of incidence being reported in these four categories over the last years. However, a glance at types of incident in Table 1 shows that only three categories showed slightly increased percentages [3].



Respondents were asked to identify the types of security technology used by their organizations. As in almost all other years, organizations use the sorts of technologies one would expect them to use, with nearly all reporting the use of firewalls and anti-virus software. A list of technologies asked about in a survey questionnaire carried out in year 2008 is shown in Table 2.

#### 4. Principles of Security

##### 4.1 The CIA Model

A simple but widely applicable security model is the confidentiality, integrity, and availability (CIA), as represented in Figure 2. These three key principles should guide all secure systems. CIA also provides a measurement tool for security implementations. These principles are applicable across the entire spectrum of security analysis - from access, to a user's Internet history, to the security of encrypted data across the Internet. A breach of any of these three principles can have serious consequences for all parties concerned [2].

##### 4.1.1 Confidentiality

Confidentiality prevents unauthorized disclosure of sensitive information. It is the capability to ensure that the necessary level of secrecy is enforced and that information

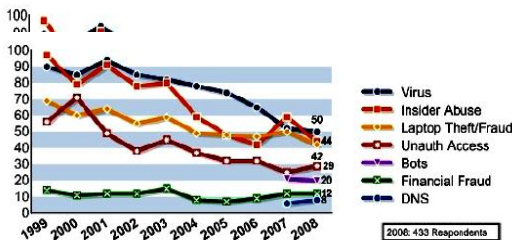


Fig.1. Types of Computer Attacks and Incidents

Table 1. Types of Computer Attacks and Incidents

Type of Attack	2004	2005	2006	2007	2008
Denial of service	39%	32%	25%	25%	21%
Laptop theft	49%	48%	47%	50%	42%
Telecom fraud	10%	10%	8%	5%	5%
Unauthorized access	37%	32%	32%	25%	29%
Virus	78%	74%	65%	52%	50%
Financial fraud	8%	7%	9%	12%	12%
Insider abuse	59%	48%	42%	59%	44%
System penetration	17%	14%	15%	13%	13%
Sabotage	5%	2%	3%	4%	2%
Theft/loss of proprietary info	10%	9%	9%	8%	9%
From mobile devices					4%
From all other sources					5%
Abuse of wireless network	15%	16%	14%	17%	14%
Web site defacement	7%	5%	6%	10%	6%
Misuse of web application	10%	5%	6%	9%	11%
Bots				21%	20%
DNS attacks				6%	8%
Instant messaging abuse				25%	21%
Password sniffing				10%	9%
Theft/loss of customer data				17%	17%
From mobile devices					8%
From all other sources					8%



is concealed from unauthorized users. When it comes to security, confidentiality is perhaps the most obvious aspect of the CIA triad, and it is the aspect of security most often attacked [2]. As example a network that provides confidentiality has the following properties:

- Use network security mechanisms (for example, firewalls and Access Control Lists [ACL]) to prevent unauthorized access to network resources.
- Require appropriate credentials (for example, usernames and passwords) to access specific network resources.
- Encrypt traffic such that an attacker could not decipher any traffic he captured from the network [1].

#### 4.1.2 Integrity

- Integrity prevents unauthorized modification of data, systems, and information, thereby providing assurance of the accuracy of information and systems. if data has integrity, one can be sure that it is an accurate and unchanged representation of the original secure information. A common type of a security attack is man-in-the-middle. In this type of attack, an intruder intercepts data in transfer and makes changes to it [2].

Examples of integrity violations include:

- Modifying the appearance of a corporate website
- Intercepting and altering an e-commerce transaction
- Modifying financial records that are stored electronically [1].

Table.2. List of Technologies used against Attacks

Technologies Used	2008
Anti-virus software	97%
Anti-spyware software	%80
Application – level firewalls	%53
Biometric	%23
Date loss prevention / content monitoring	%38
Encryption of date in transit	%71
Encryption of date at rest (in storage )	%53
Encryption security client software / NAC	%34
Firewalls	%94
Forensics tools	%41
Intrusion detection systems	%69
Intrusion prevention systems	%54
Log management software	%51
Public key infrastructure systems	%36
Server – based access control lists	%50
Smart cards and other one time tokens	%27
Specialized wireless security systems	%46
Static account /login passwords	%29
Virtualization – specific tools	%85
Virtual private network (VPN)	%65
Web / URL filtering	%61
Other	%3

- Although integrity is not well known, most sectors find it important. For example, a bank does not want all its bank accounts altered, and a university does not want students' grade results altered, and so on [6].





### 4.1.3 Availability

Availability is the prevention of loss of access to resources and information to ensure that information is available for use when it is needed. It is imperative to make sure that information requested is readily accessible to the authorized users at all times. DoS is one of several types of security attacks that attempts to deny access

to the appropriate user, often for the sake of disruption of service [2]. Here are a couple of examples of how an attacker could attempt to compromise the availability of a network:

- He could send improperly formatted data to a networked device, resulting in an unhandled exception error.
- He could flood a network system with an excessive amount of traffic or requests. This would consume the system's processing resources and prevent the system from responding to many legitimate requests. DoS is an example of this type of attacks [1].

### 4.2 Reverse Security Triad

The reverse security principles are disclosure, alteration, and disruption (DAD):

- Disclosure. Breach of confidentiality.
- Alteration. Data is modified.
- Disruption. Service/data is no longer available.

## 5. Securing Networks

### 5.1 Securing Networks' Infrastructure

A typical network infrastructure is built with devices operating at different layers, including routers (layer 3), switches (layer 2), and other equipment that provide indispensable services designed to increase the productivity of any organization [5].

Network infrastructures, however, are not only built up with routers and switches, but also with a large variety of in-line devices including, but not limited to, firewalls, Intrusion Prevention Systems (IPSs), load balancers, and application acceleration appliances. All these infrastructure devices may be subject to attacks designed to target them directly or that indirectly may affect network availability. Possible attacks include unauthorized access, privilege escalation,



Fig.2 . The CIA Triad

DoS, buffer overflows, traffic flood attacks, and much more [4].

Generally, network infrastructure devices provide multiple access mechanisms, including console and remote access based on protocols such as Telnet, rlogin, HTTP, HTTPS, and Secure Shell (SSH). The hardening of these devices is critical to avoid unauthorized access and compromise. Best practices include the use of secure protocols, disabling unused services, limiting access to necessary ports and protocols, and the enforcement of authentication, authorization and accounting (AAA) [4].

#### 5.1.1 Securing Networks at Layer 2

With the rapid growth of IP networks in the past years, high-end switching has played one of the most fundamental and essential roles in moving data reliably, efficiently, and securely across networks. The data-link layer provides the functional



and procedural means to transfer data between network entities with interoperability and interconnectivity to other layers, but from a security perspective, the data-link layer presents its own challenges. Network security is only as strong as the weakest link, and Layer 2 is no exception. Applying first-class security measures to the upper layers (Layers 3 and higher) does not benefit a network if Layer 2 is compromised [2].

The following sections introduce a variety of layer 2 attacks and, then, highlight approaches for mitigating those attacks. These strategies include best practices for securing a Layer 2 network, protecting against Virtual LAN (VLAN) hopping attacks, preventing an attacker from manipulating Spanning Tree Protocol (STP) settings, DHCP server spoofing and ARP spoofing, preventing Content Addressable Memory (CAM) table overflow attacks, and disallowing MAC address spoofing.

#### 5.1.1.1 DHCP Server Protection

Dynamic Host Configuration Protocol (DHCP) is the most widely deployed protocol for the dynamic configuration of systems over an IP network. Two of the most common DHCP attacks are the insertion of rogue DHCP servers and DHCP starvation. Rogue DHCP servers are used to provide valid users with incorrect-configuration information to prevent them from accessing the network. Also, rogue DHCP servers are used to form MITM attacks, where valid clients are provided with the IP address of a compromised system as a default gateway. DHCP starvation is another common type of attack. It consists of exhausting the pool of IP addresses available to the DHCP server for a period of time, and it is achieved by the

broadcasting of spoofed DHCP requests by one or more compromised systems in the LAN.

Best practices for securing DHCP includes server hardening and use of DHCP security features available on switches such as port security and DHCP snooping and ARP Guard Feature. This is presented in the case study in **section 6.1**.

#### 5.1.1.2 VLAN Hopping Mitigation

Many Ethernet switches can logically group ports to form a VLAN, where each VLAN is its own broadcast domain. Traffic must be routed to travel from one VLAN to another VLAN [1]. VLAN hopping attack provides a client with unauthorized access to other VLANs (without first being routed) on a switch. This type of attack can be mitigated by applying the following best common practices:

- Always use a dedicated VLAN ID for all trunk ports.
- Disable all unused ports and put them in an unused VLAN.
- Do not use VLAN 1 for anything.
- Configure all user-facing ports as non-trunking (DTP off).
- Explicitly configure trunking on infrastructure ports.
- Use all tagged mode for the native VLAN on trunks.
- Set the default port status to disable [4].

#### 5.1.1.3 Spanning Tree Protocol Protection

STP is a link management protocol, defined in the IEEE 802.1D, for bridged networks. STP provides path redundancy while preventing undesirable loops in networks consisting of multiple active paths. STP is a useful protocol but, unfortunately, the existing versions of the



protocol were conceived with no security in mind and, as a result, are both vulnerable to several types of attacks. STP does not implement any authentication and encryption to protect the exchange of BPDUs. Because of the lack of authentication, anyone can speak to a STP enabled device. An attacker could very easily inject bogus BPDUs, triggering a topology recalculation. A forced change to the STP topology could lead to a denial of service condition, or leave the attacker as a man-in-the-middle. In addition, because BPDUs are not encrypted, it is fairly simple to intercept BPDUs in transit, revealing important topology information.

STP introduces some security risks but, in topologies where a loop-free design is not possible, STP should be used along with some features that developed to address its risks. Not using STP would result in a loop becoming another attack vector.

A number of features are offered that help protect bridged networks using STP against the common attacks. The following are the recommended best practices:

- Disable VLAN dynamic trunk negotiation trunking on user ports
- Use Per-VLAN Spanning Tree (PVST)
- Configure BPDU Guard
- Configure STP Root Guard
- Disable unused ports and put them into an unused VLAN
- Implement Port Security.
- Enable traffic storm control [4].

#### 5.1.1.4 ARP Spoofing Protection

Internal network attacks are typically operated via so called ARP spoofing or ARP Poisoning attacks as shown in Figure 3 by Using fake ARP messages an attacker can divert all communication between two

machines with the result that all traffic is exchanged via his PC. By means of such as MITM attack the attacker can in particular:

- Run DoS attacks
- Intercept data
- Collect passwords
- Manipulate data
- Tap VoIP phone calls.

These ARP attacks are usually successful even with encrypted connections like SSL, SSH or PPTP. ARP spoofing protection ensures that a client on an access edge port is not able to perform a MITM attack by sending a gratuitous ARP that presents its MAC address as that associated with a different IP address, such as that of the default gateway.

Some switch vendors have devised a defense against this form of attacks that imposes very strict control over what ARP packets are allowed in to network [7].

#### 5.1.2 Securing Networks at Layer 3

Every layer of communication has its own unique security challenges. The Network Layer is especially vulnerable for many Denial of Service attacks and information privacy problems. The most popular protocol used in the network layer is IP (Internet Protocol). The following are the key security risks at the Network Layer associated with the IP:

**a) IP Spoofing:** The intruder sends messages to a host with an IP address (not its own IP address) indicating that the message is coming from a trusted host to gain un-authorized access to the host or other hosts.



**b) Routing (RIP) attacks:** Routing Information Protocol (RIP) is used to distribute routing information within networks, such as shortest-paths, and advertising routes out from the local network. RIP has no built in authentication, and the information provided in a RIP packet is often used without verifying it. An attacker could forge a RIP packet, claiming

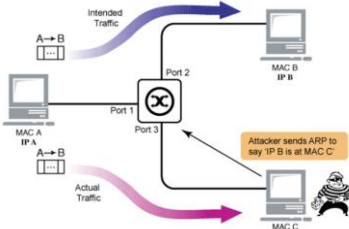


Fig. 3. ARP spoof attack

his host "X" has the fastest path out of the network. All packets sent out from that network would then be routed through X, where they could be modified or examined. An attacker could also use RIP to effectively impersonate any host, by causing all traffic sent to that host to be sent to the attacker's machine instead.

**c) ICMP Attacks:** ICMP is used by the IP layer to send one-way informational messages to a host. There is no authentication in ICMP, which leads to attacks using ICMP that can result in a denial of service, or allowing the attacker to intercept packets.

**d) PING Flood (ICMP Flood):** PING is one of the most common uses of ICMP which sends an ICMP "Echo Request" to a host, and waits for that host to send back an ICMP "Echo Reply" message. Attacker simply sends a huge number of "ICMP Echo Requests" to the victim to cause its system crash or slow down.

**Ping of Death Attack:** An attacker sends an ICMP ECHO request packet that is much larger than the maximum IP packet size to

victim. Since the received ICMP echo request packet is bigger than the normal IP packet size, the victim cannot reassemble the packets. The OS may be crashed or rebooted as a result.

**Packet Sniffing:** Because most network applications distribute network packets in clear text, a packet sniffer can provide its user with meaningful and often sensitive information, such as user account names and passwords. A packet sniffer can provide an attacker with information that is queried from the database, as well as the user account names and passwords used to access the database. This cause serious information privacy problems as well as tools for crimes [8].

Like most of the network security problems, there are no silver bullet solution to fix the problems, however, there are many technologies and solutions available to mitigate the above security problems and to monitor the network to reduce its damage if attack happens. The problems such as PING flood can be effectively reduced by deploying Firewalls and IPS at critical locations of a network to filter un-wanted traffic and from iffy destinations. By utilizing IPsec VPN at the network layer and by using session and user (or host) authentication and data encryption technologies at the data link layer, the risk of IP Spoofing and Packet Sniffing will be reduced significantly. IPV6 in combination with IPsec provides better security mechanisms for the communication at the network level and above attacks [8].

Routing protocol , which provides the information required to forward traffic through networks, the various threats against routing protocols, including peering disruption and falsifying of routing information. The best way to protect routing information on the wire is to authenticate



routing protocol packets using Message Digest Algorithm 5 (MD5) or IP Security (IPSec) signatures [9].

### 5.1.3 IDS versus IPS

Although both Intrusion Detection (IDS) and IPS devices can recognize network attacks, they differ primarily in their network placement. Specifically, although an IDS device receives a copy of traffic to be analyzed, an IPS device resides inline with the traffic.

Because the analyzed traffic does not flow through the IDS device, the IDS device is considered passive, whereas the IPS device is considered active. Both the IDS and IPS devices can send alerts to, for example, a management station. Although an IDS device can also communicate with a security appliance or router to prevent subsequent attack packets, the initially offending traffic reaches its destination. Conversely, an IPS device can drop the traffic inline, thus preventing even the first malicious packet from reaching its intended target.

In some network environments, IDS and IPS solutions complement one another. For example, an IDS device can add value to a network that already employs an IPS device by verifying that the IPS device is still operational. The IDS device might also identify suspicious traffic and send alerts about that traffic, without having the IPS device drop the traffic [1].

In-line devices in general are also subject to unauthorized access and compromise; consequently, their hardening is critical. Like any other infrastructure devices, also devices have limited resources and capabilities and as a result they are potentially vulnerable to resource exhaustion attacks as well. This sort of

attacks is designed to deplete the processing power or memory of the device. This may be achieved by overwhelming the device capacity in terms of connections per second, maximum number of connections, or number of packets per second. Attacks may also target protocol and packet-parsing with malformed packets or protocol manipulation. Security best practices vary depending on the nature of the in-line device [4].

## 5.2 Securing Applications

Applications are coded by people and therefore are subject to numerous errors. Care needs to be taken to ensure that commercial and public domain applications are up-to-date with the latest security fixes. Public domain applications, as well as custom developed applications, also require code review to ensure that the applications are not introducing any security risks caused by poor programming. This may include scenarios such as how user input is sanitized, how an application makes calls to other applications or the operating system itself, the privilege level at which the application runs, the degree of trust that the application has for the surrounding systems, and the method the application uses to transport data across the network. Poor programming may lead to buffer overflow, privilege escalation, session credential guessing, SQL injection, cross-site scripting attacks to name a few. Buffer overflow attacks are designed to trigger an exception condition in the application that overwrites certain parts of memory, causing a DoS or allowing the execution of an unauthorized command. Privilege escalation typically results from the lack of enforcement authorization controls. The use of predictable user credentials or session identifications facilitates session hijacking



and user impersonation attacks. SQL injection is a common attack in web environments that use backend SQL and where user-input is not properly sanitized. Simply put, the attack consists in manipulating the entry of data to trigger the execution of a crafted SQL statement. Cross-site scripting is another common form of attack that consists in the injection of malicious code on web pages, and that it gets executed once browsed by other users. Cross-site scripting is possible on web sites where users may post content and that fail to properly validate user's input.

Application environments can be secured with the use of endpoint security software and the hardening of the operating system hosting the application. Firewalls, IPS, and XML gateways may also be used to mitigate application-based attacks [4].

## 6. Case Study

This section is designed to draw attention to securing networks from inside attackers. Rogue DHCP server has been chosen as a real example in a real network. Followed by pointing out the necessity of using encryption techniques to prevent intruders from sniffing packets and have them analyzed.

### 6.1 DHCP Rouge Server Attack

Most clients gets an IP address from a valid DHCP server. However, a rouge DHCP server can be inserted by an inside attacker disguising itself as a DHCP server and responds to DHCP requests with a bogus IP address, which results in compromised network access.

Figure 4 shows a real simple network architecture used as an example of DHCP server attack. A client workstation is

connected to an access switch in port Fast Ethernet 1/0/2 and then connected to another Layer 3 switch through interface Fast Ethernet 1/0/1. A corporate DHCP server connects directly to the L3 switch.

To dynamically obtain IP address information, a client sends out a DHCP request. A DHCP server sees the request, and a DHCP response (including such information as an IP address, subnet mask, and default gateway) is sent to the requesting client so it has access to the network and can reach its gateway, as shown in Figure 5.

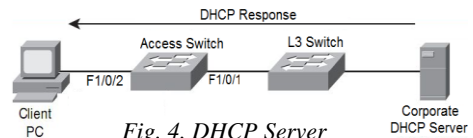


Fig. 4. DHCP Server

However, when an attacker connects a rogue DHCP server to the network, the rogue DHCP server can respond to a client's DHCP request. Even though both the rogue DHCP server and the actual DHCP server respond to the request, the client uses the rogue DHCP server's response since it reaches the client before the response from the actual DHCP server. In this scenario, the client obtained invalid IP address information from the rogue DHCP server. Consequently, the client was no longer able to access the network, nor was it able to reach its gateway, this is shown in Figure 6.

The DHCP snooping feature was enabled on the access switch to block the DHCP server spoofing attack. With this solution, the interface Fast Ethernet 1/0/1 was configured as trusted port, whereas the other ports became untrusted ports as a result of enabling DHCP snooping.





Having enabled debug in the access switch, the messages presented in Figure 7 shows the response from the corporate DHCP server, this was allowed through port Fastethernet1/0/1, whereas the DHCP rogue response from Fast Ethernet 1/0/3 was blocked, as shown in Figure 8.

The attacker's intention was preventing the client from accessing the network. Nevertheless, the consequences of attacking DHCP servers could be more serious if the attacker influences the client to send traffic to the attacker's IP address. The attacker can then capture the traffic and forward the traffic to an appropriate default gateway. Because, from the client's perspective, everything is functioning correctly, this type of DHCP server spoofing attack can go undetected for a long period of time.

### 6.2 SSH Versus Telnet

Secure Shell, commonly known as SSH, and Telnet are two network protocols that

```

Connection-specific DNS Suffix . : 
Description . . . . . : Intel(R) 82566MC Gigabit Network
Physical Address. . . . . : 00-1C-7E-42-94-26
Dhcp Enabled. . . . . : Yes
Autoconfiguration Enabled . . . . : Yes
IP Address. . . . . : 10.10.10.2
Subnet Mask . . . . . : 255.255.255.0
Default Gateway . . . . . : 10.10.10.1
Dhcp Server . . . . . : 10.10.10.10
Lease Obtained. . . . . : 21 May 2010 11:57:25
Lease Expires . . . . . : 22 May 2010 11:57:25

C:\Documents and Settings\k.ganno>ping 10.251.6.254

Pinging 10.251.6.254 with 32 bytes of data:

Request timed out.
Request timed out.
Request timed out.
Request timed out.

Ping statistics for 10.251.6.254:
    Packets: Sent = 4, Received = 0, Lost = 4 (100% loss),

```

Fig. 7. Client's IP address obtained from Rough DHCP

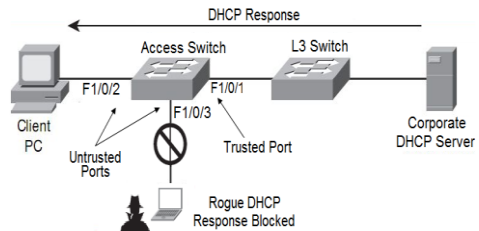


Fig. 8. DHCP Snooping

```

Connection-specific DNS Suffix . : aljadid.comp.net
Description . . . . . : Intel(R) 82566MC Gigabit Network
Physical Address. . . . . : 00-1C-7E-42-94-26
Dhcp Enabled. . . . . : Yes
Autoconfiguration Enabled . . . . : Yes
IP Address. . . . . : 10.251.6.117
Subnet Mask . . . . . : 255.255.255.0
Default Gateway . . . . . : 10.251.6.254
Dhcp Server . . . . . : 10.251.201.16
DNS Servers . . . . . : 10.251.201.15
                        10.251.201.16
Lease Obtained. . . . . : 21 May 2010 11:45:28
Lease Expires . . . . . : 29 May 2010 11:45:28

C:\Documents and Settings\k.ganno>ping 10.251.6.254

Pinging 10.251.6.254 with 32 bytes of data:

Reply from 10.251.6.254: bytes=32 time=1ms TTL=255
Reply from 10.251.6.254: bytes=32 time=1ms TTL=255
Reply from 10.251.6.254: bytes=32 time=1ms TTL=255
Reply from 10.251.6.254: bytes=32 time=1ms TTL=255

Ping statistics for 10.251.6.254:
    Packets: Sent = 4, Received = 4, Lost = 0 (0% loss),
    Approximate round trip times in milli-seconds:
        Minimum = 0ms, Maximum = 1ms, Average = 0ms

```

Fig. 5. Client's IP address information

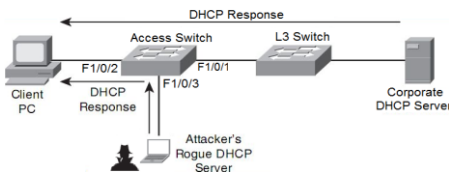


Fig. 6. DHCP Rogue Server

have been used widely at one point in time or another. They are both used to connect to remote servers in order to facilitate some sort of communications. The primary difference, which also led to one superseding the other, is in security. SSH offers security mechanisms that protect the users against anyone with malicious intent while Telnet has no security measures whatsoever, as presented below.

In Figure 9, the administrator's workstation with the IP address 10.10.10.2 uses telnet to access the router. At the same time, the inside attacker could gain access to the switch using special spoofing tools. Then, the attacker uses a sniffer, Wireshark for instance, to capture the packets between the network administrator and the router.



Since the telnet protocol sends data in clear text, it was possible for the attacker to follow the TCP stream to see

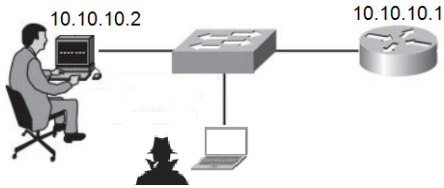


Fig. 9. The Attacked Network

all the information including username and password, as shown in Figure 10. In order to provide secure session between the administrator and the router, we enabled the SSH on the router so that the administrator should use the SSH rather than the telnet to access the router. The traffic captured by the attacker after enabling the SSH was unreadable and encrypted as can be seen in Figure 11.

## 7. Summary and Recommendations

This paper focused on the network in its entirety, and recommendations have been made where security flaws have been identified to help reinforce networks as well as to raise awareness of different types of network attacks and how challenging defending networks are.

Securing networks should be treated with the most priority. Knowing that the network is being attacked is a great advantage that will serve as a powerful tool. If network security strategy is employed correctly you should not have a major challenge with intruders. Below is some recommendations intended to strengthen networks and make it more challenging for a hacker to attack network resources.

- Data centers comprise some of the most critical assets within any organization.

Typically, applications, databases, and management servers reside in the data

Interface	IP-Address	OK?	Method	Status	Protocol
FastEthernet0/0	10.10.10.1	YES	NVRAM	up	up
FastEthernet0/1	unassigned	YES	NVRAM	administratively down	down
Loopback0	unassigned	YES	NVRAM	up	up
RI#					

Fig. 10. Telnet Session

center. For this reason, it is extremely important to have the appropriate defense mechanisms in place to protect the data center against security threats. Attacks against data center assets can result in lost business applications and the theft of confidential information.

- Keeping up with the latest security flaws and vulnerabilities.
- Physical access to your network should be closely monitored.
- Enforcing a password policy.
- Making sure that the network devices support security features and enabling those features properly.
- IPsec can be deployed within a network providing computer-level authentication, as well as data encryption.
- Application environments can be secured with the use of endpoint security software and the hardening of the operating system hosting the application. Firewalls, IPS, and XML gateway may also be used to mitigate application-based attacks.





- Use web security and mail security to protect users.
- Creating usage policy statements is recommended to outline users' roles and responsibilities with regard to security. You can start with a general policy that covers all network systems and data within your organization
- Don't wait for an attacker to find and exploit your security vulnerabilities, take the initiative by assessing the state of your network's security, and delivering advanced network testing strategies, including vulnerability scanning and penetration testing.
- During a review of your security program, you should look at the means in which you conduct your security audits. Do you have a group that is focused on auditing computers and applications for compliance with internal

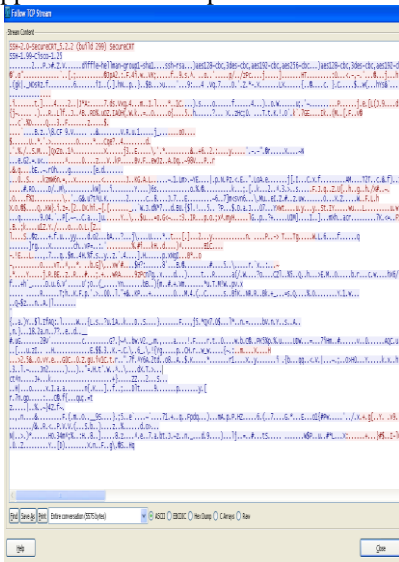


Fig. 11 Encrypted SSH Session Captured by the Attacker

standards or regulatory requirements? If so, is it separate from the operations

team? Do you have a team that is trained to help document and remediate issues that the audit finds?

- You should also check to make sure that you have deployed up-to-date antivirus software on all of your servers and clients.
- The network security team should take into consideration not only externally attack but also the inside attack.
- Last but not least, to help limit the damage of a potential security breach or system malfunction, you should always have a backup and recovery strategy in place to restore services and data in an acceptable amount of time.

### 8. References

- [1] Michel Watkins & Kevin Wallace, "CCNA Security Official Exam Guide," Cisco Press, ISBN-13: 978-1-58720-220-9, 2008.
- [2] Yusuf Bahiji, "CCIE Professional Development Series Network Security Technologies and Solutions". Cisco Press, eText ISBN 10: 0-7686-8196-0, 2008.
- [3] Robert Richardson, "Computer Crime & Security Survey".
- [4] Cisco SAFE Reference Guide, Cisco Validated Design, OL-19523-01, Aug 2009.
- [5] Omar Santos, "End to End Network Security Defense-in-Depth". Cisco Press, ISBN-10: 1-58705-332-2, 2008.
- [6] Eric Vyncke & Christopher Paggen, "LAN Switch Security". Cisco Press, ISBN-10: 1-58705-256-3, 2008.
- [7] [http://en.wikipedia.org/wiki/DHCP\\_snooping](http://en.wikipedia.org/wiki/DHCP_snooping).
- [8] <http://networkdictionary.com/security/NetworkSecurityLayer3.php>
- [9] [http://www.cisco.com/warp/public/cc/so/neo/vpn/prodlit/sfblp\\_wp.p](http://www.cisco.com/warp/public/cc/so/neo/vpn/prodlit/sfblp_wp.p)



المؤتمر الدولي العربي الليبي الخامس للهندسة الكهربائية والإلكترونية 2010/10/26-23 طرابلس ليبيا



# An Enhanced Transmission Algorithm for Cognitive Radio Network Based on Constrained Distributed Power Control

Mohamed Elalem

Electrical and Computer Engineering Department  
Ryerson University, ON, Canada, M5B 2K3

## Abstract

In order to utilize the spectrum, the FCC announced Cognitive Radio CR technology as a candidate to implement negotiated or opportunistic spectrum sharing. It has received a great attention due to the ability to improve the spectrum utilization. In such a CR network, a power control can increase the efficiency by keeping and adjusting the transmission power of the secondary user SU. In this paper, we propose an adaptive distributed power control scheme for CR networks where conventional power schemes used in cellular system are modified to be used in cognitive radio network to consider the QoS requirements of both the PU and the SU simultaneously. Since the transmission power of each SU is constrained so that the interference temperature at the primary receiver caused by all SUs does not exceed the interference tolerance of the primary user PU, the QoS requirement for the PU is always guaranteed. The simulation results, show that the proposed algorithm never exceed the interference threshold of the primary user and the priority for the primary user is always ensured .

## I. Introduction

The increasing density of competing wireless communication terminals and standards, will make the cognitive radio (CR) playing a central role in future communication systems. Since there is only a finite amount of the spectrum resource, the remaining spectrum is being exhausted and it leads to the spectrum scarcity problem. The Federal Communications Commission (FCC) indicated that not all the spectrum is in use all of the time. About

30% of the spectrum is actually in use in certain given location and at certain time [1]. This led the FCC to revisit the current fixed spectrum management policy, and proposed that unlicensed devices flexibly utilize the TV spectrum with no harmful interference[2, 3].

Power control is an essential radio resource management strategy. It aims to control the transmission power levels in such a way that acceptable quality of service for the users is guaranteed with lowest possible transmission powers. All



users benefit from the minimized interference and the preserved signal qualities. Transmitter power control is also an efficient technique to mitigate the effect of interference under fading conditions and combat the near-far problem.

Power control which has been employed for improving the link performance in cellular networks can also be applied to CR networks. However power control of CR networks is more complex, in that it should not only consider the quality of service (QoS) requirements of the secondary users but also protect the primary user communication link. Since the PU communication has priority over the SU communication, it is impossible for the SUs to share the PU channel deteriorating the link quality of the PU communication. Thus, SUs should always check the estimated interference at the primary receiver after determining their transmission power.

Choice of an appropriate power control algorithm is of prime importance, as it should aim at increasing the overall efficiency of the system.

In this paper, two conventional distributed power control algorithms, each suited for implementation under different cellular technologies, were studied and compared through simulation on the base of the performance metrics. Specifically, Distributed Constraint Power Control (DCPC) and General Distributed Constraint Power Control (GDCPC) algorithms which were studied in [4, 5]. For the distributed power control, each user controls its transmission power by itself using only local information. However, since the interference temperature at the primary receiver cannot be identified by the local information, it is difficult that the QoS requirement for the PU is guar-

anteed in the distributed power control. Thus, an additional process is needed to let the SUs recognize the interference temperature at the primary receiver [6, 7].

In this paper, we propose some modifications on the above conventional distributed power control schemes to make them applicable for cognitive radio networks without any additional process for CR networks. Specifically, the constraint for the sum of the interference induced by all SUs in the network is replaced by new one which limits the individual transmission power. Since each SU determines its transmission power within the range of the limit to protect the PU, the additional process in previous works is unnecessary in our scheme. The individual transmission power constraint and the proposed scheme are numerically derived, and the simulation results show that the suggested scheme never exceed the Interference Temperature Limit (ITL) of the primary user.

The paper is organized as follows. In section II, the system model used in this paper is introduced. Section III briefly reviews the distributed power control. In section IV, the proposed schemes are provided. In section V, the simulation and the results are analyzed. The conclusions are drawn in section VI.

## II. System Model and Assumptions

Our model consists of  $N$  secondary users distributed uniformly in a square region with an area of  $\ell \times \ell$ . As shown in Fig. 1, the primary transmitter with a transmission power  $S_p$  is located at an effective transmission coverage  $r_p$  away from the primary receiver, the effective receiving range is defined by the successful de-

coding of the TV signals. The center of the cognitive radio network is  $r$  meters away from the nearest primary receiver. Each secondary users has a transmission range of  $r_s$ . The distance from the TV station to the  $i^{th}$  secondary receiver is  $r_{ti}$  and the distance from the  $i^{th}$  secondary transmitter to the TV receiver at the border of the TV coverage area is  $r_{ri}$

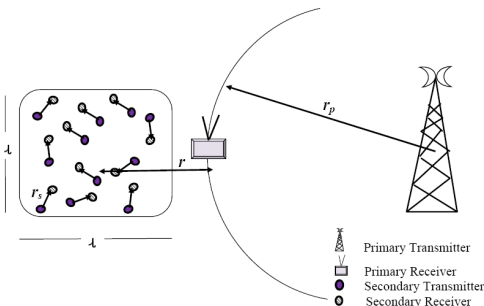


Figure 1: System model

Also assuming that the primary receiver is located at the end border of the primary transmitter coverage area (so the worst case is considered), this makes it closest to the secondary users. Further assume that the spectrum is divided into orthogonal channels. Both primary and secondary users are sharing one channel. If we assume that the primary users represent a TV channel and assuming a path loss model, that means the received power is only a function of the transmitted power and path loss, i.e., the fading effects (shadowing and small-scale fading) are omitted, the transmission power only attenuates with distance, so the channel can be expressed as:  $g(r_{ij}) = r_{ij}^{-\nu}$ , where  $r_{ij}$  is the distance between link  $j$  transmitter and link  $i$  receiver, and  $\nu$  is the corresponding path loss exponent of PU and SUs  $\nu_1$  and  $\nu_s$  respectively. Clearly ( $\nu_s > \nu_p$ ) because the primary transmit-

ter has tall antenna, while the secondary users are on the ground level so the power transmission of the SUs will attenuate faster than the PU.

Our objective is to find a certain power algorithm to adapt and adjust the transmission powers of the SUs to guarantee the  $QoS$  requirements not only for the licensed users but also for the temporary accessing users.

### III. Conventional Distributed Power Control Schemes

Interference Temperature ( $IT$ ) has been suggested by FCC [2, 8, 9] to be as a *new metric* for measuring interference at the receiver side. To compute the interference temperature for PU which is the licensee of the channel, it should be able to communicate whenever it wants. Therefore, the total amount of interference at the primary receiver caused by all SUs has to be less than a certain predefined limit; say  $\gamma_p^{th}$  which the PU can tolerate.

Now we define  $g_{p,i}$  as the channel gain from the secondary transmitter  $i$  to the primary receiver, and define  $S_i$  as the transmission power of the secondary transmitter  $i$ . The  $QoS$  requirement of the primary receiver has to satisfy the following inequality:

$$\gamma_p = \frac{(S_p/r_p^{\nu_p})}{\sum_{i=1}^N (S_i/r_{ri}^{\nu_s}) + N_o} \leq \gamma_p^{th} . \quad (1)$$

$N_o$  is the background noise. Let  $g_{i,p}$  be the channel gain from the primary transmitter to the secondary receiver  $i$  and also let  $g_{i,j}$  the channel gain from the secondary transmitter  $j$  to the secondary receiver  $i$ . The received  $SINR$  for the SU has to satisfy the following communica-

tion minimum requirements:

$$\xi_{s,i} = \frac{g_{i,i}S_i}{\sum_{j=1, j \neq i}^N g_{i,j}S_j + g_{i,p}S_p + N_o} \geq \gamma_s^{th} \quad (2)$$

where  $\gamma_s^{th}$  is certain threshold for the SUs, and Assuming the same noise power  $N_o$  for both primary and secondary users. The above equality must satisfy for all users, i.e.  $\forall i = 1 \dots N$ .

Eq.(2) can be solved for secondary transmitted power as:

$$S_i \geq \frac{\gamma_s^{th}}{g_{i,i}} \left( \sum_{j=1, j \neq i}^N g_{i,j}S_j + g_{i,p}S_p + N_o \right) \quad (3)$$

Eq. (3) gives the minimum transmitted power for the user  $i$  which is necessary to make communication with acceptable quality. Recalling the matrix notation, the linear inequality (3) can be expressed as:

$$S_i \geq \sum_{j=1}^N c_{i,j}S_j + d_i \quad (4)$$

where

$$c_{i,j} = \begin{cases} \gamma_s^{th} \frac{g_{i,j}}{g_{i,i}} & \text{if } i \neq j \\ 0 & \text{if } i = j \end{cases} \quad (5)$$

and

$$d_i = \frac{\gamma_s^{th}}{g_{i,i}} (g_{i,p}S_p + N_o) \quad (6)$$

Let  $\mathbf{C}$  be  $(N \times N)$  matrix, and  $\mathbf{D}$  be  $(N \times 1)$  one array matrix.

Defining a unit matrix  $\mathbf{I}$  with a dimension of  $N$ , we may rewrite the above inequality as:

$$(\mathbf{I} - \mathbf{C})\mathbf{S} \geq \mathbf{D} \quad (7)$$

where  $\mathbf{S}$  is the transmitted power  $(N \times 1)$  vector.

The authors in [4] show that there will be at least one non-negative power vector solution which will satisfy (7) if the maximum eigenvalue of matrix  $\mathbf{C}$  is less than one. This implies that  $QoS$  of the secondary user  $\gamma_s^{th}$  is guaranteed. This achievable solution may be written as:

$$\mathbf{S} = (\mathbf{I} - \mathbf{C})^{-1}\mathbf{D} \quad (8)$$

The object of power control is to find a solution for  $\mathbf{S}$  in (8) to specify the power distribution among the  $N$  users in the region  $\ell \times \ell$ . Since the transmitted power is practically limited to a certain value; say  $S_s^m$ , the obtained solution from the above analysis has to be bounded by  $0 < S_i \leq S_s^m, \forall i = 1 \dots N$  to make the transmission power allocation feasible. Closed form solution of power control vector  $\mathbf{S}$  has been presented in some papers, for example the authors in [10] found a solution for nonnegativity using an approach based on the Sherman-Morrison formula in linear algebra. We use here a numerical technique known as *general iterative method* described in [11] to solve this problem.

If the resulting transmission powers of Eq.(8) are within the above range, the transmission power allocation is feasible. To solve Eq.(8) distributively, a general iterative method was introduced in [4]. For the secondary transmitter  $i$ , the iterative power control method is

$$S_i(n) = \frac{\gamma_s^{th}}{g_{i,i}} \left( \sum_{j=1, j \neq i}^N g_{i,j}S_j(n-1) + g_{i,p}S_p + N_o \right) \quad (9)$$

$$S_i(n) = \frac{\gamma_s^{th}}{\gamma_{s,i}(n-1)} S_i(n-1) \quad n = 1, 2, \dots \quad (10)$$

where  $S_i(n-1)$  is the transmission power of the  $i^{th}$  secondary user terminal at the



(n-1)<sup>th</sup> iteration and  $\gamma_{s_i}(n-1)$  is its resulting SINR at that iteration. Let:

$$\beta(n) = \frac{\gamma_s^{th}}{\gamma_{s_i}(n-1)} \quad (11)$$

Because of the maximum transmission power limit, we are only interested in finding the feasible solution of the power vector, so the above iteration method should be modified into power-limited form such as

$$S_i(n) = \min(\beta(n)S_i(n-1), S_s^m) \quad n = 1, 2, \dots \quad (12)$$

The authors in [5] refer to the above power control scheme as the Distributed Constrained Power Control (*DCPC*) scheme. They concluded that the received SINR converges to  $\gamma_s^{th}$  distributively except for the cases where the maximum transmission power  $S_s^m$  is reached.

*DCPC* has a property that the power reaches the maximum level  $S_s^m$ , even if that user cannot achieve the minimum required SINR. Using maximum transmitter power may not necessarily lead to sufficient improvement of channel quality and will generate severe interference hitting other users and cause wasting of energy. This undesirable phenomenon happens more often when the system is congested.

To overcome the drawback of *DCPC* mentioned above, a Generalized *DCPC* (*GDCPC*) was introduced in [12]. The user will reduce the power to arbitrary level within the transmission power range when the user cannot achieve the required SINR, instead of necessarily using the maximum transmission power  $S_s^m$  which the *DCPC* compels to set its power to it when the algorithm can not achieve the required SINR. It is found that this

approach can save the energy consumption and decrease the interference to other users. Because the other users in the network take less interference, they can increase their transmission powers. As a result, the authors concluded that the network can support more users (more capacity) than *DCPC*. With above motivations, *GDCPC* can be represented as

$$S_i(n) = \begin{cases} \beta(n)S_i(n-1) & \text{if } \beta(n)S_i(n-1) \leq S_s^m \\ S_a(n) & \text{if } \beta(n)S_i(n-1) > S_s^m \end{cases} \quad (13)$$

where  $\beta(n)$  is given in (11) and  $S_a(n)$  is a certain power value chosen arbitrarily within the transmission power range  $0 < S_i \leq S_s^m$ . To decrease the interference, the value of  $S_a(n)$  has to be as lower as possible. If we choose  $S_a(n) = S_s^m$ , *GDCPC* is reduced to *DCPC*. When setting  $S_a(n) = 0$ , it can be interpreted as a temporary connection removal, allowing the removed user to stay on the channel and power up again in later iterations if the interference has then decreased. By setting the transmitter power to zero, the user will not waste energy on mitigating bad channel conditions and other users will benefit from lower interference. It was found in [12] that by choosing appropriate value of  $S_a(n)$  in the range of  $0 < S_i \leq S_s^m$ , the convergence of a feasible solution of the power vector is always guaranteed. The rate of convergence is related to  $S_a(n)$ . The above reference put a criteria of choosing this value in each iteration. If the power of the user  $S_i(n)$  is larger than the maximum power  $S_s^m$ , a power lower than  $S_s^m$  by the amount of the gap between the obtained power and  $S_s^m$  is used. If the user power is twice larger than the maximum power, the transmitter power is set to zero. It is important how fast the power value will



converge which is guarantee by applying this criteria.

#### IV. Proposed Distributed Power Control for Cognitive Radio Networks

To apply these approaches to the cognitive radio networks, additional processes must be executed in addition to the conventional power algorithms to grantee the new constraints and meet the requirements of the primary user. Since both DCPC and GDCPC do not consider the QoS requirement for the PU shown in Eq.(1), the solution of the above transmission power equations may go beyond the ITL of the primary receiver. So each secondary user has to execute DCPC or GDCPC taking into account the requirements for the primary users simultaneously. Each SU controls its transmission power only with the help of its local information, and no knowledge about the other secondary users's transmission power in the current network. Thus, it is unachievable that each user knows the interference temperature at the primary receiver caused by all SUs including itself. In order to address this issue, we propose three possible solutions.

The first solution is by translating the interference constraint by the sum of all SUs transmission power to the individual constraint for each connecting SU, the QoS requirement for the PU can be easily guaranteed. The QoS requirement for the PU in Eq.3 is guaranteed if the following condition:

$$g_{p,i}S_i \leq \frac{\gamma_p^{th}}{N_a}, \quad \forall i = 1, 2, \dots, N \quad (14)$$

is satisfied which means that the total interference constraint at the PU caused by

all SUs is divided equally among SUs.  $N_a$  here is the active SUs which is a subset of  $N$  i.e.  $N_a \subset N$  The transmission power constraint of the  $i^{th}$  SU which guarantee the QoS of the PU can be represented from Eq.(14) as:

$$S_i \leq \frac{\gamma_p^{th}}{N_a g_{p,i}}, \quad \forall i = 1, 2, \dots, N \quad (15)$$

Other challenges will face this analysis, which appear in Eq.(15), since each user should know the active number of SUs in the network, the ITL of the PU, and the channel gain from itself to the primary user receiver to be able to calculate its transmission power. To overcome these three challenges, let us consider them individually.

Using the ad-hoc routing protocol introduced in [13], each secondary user can find the number of terminals in the network. In the ad-hoc routing, the link information about all users belonging to the network is shared among all the nodes in the network.

In [14], the concepts of beaconing were introduced where the primary receiver transmits the beacon including the information about the beacon power and its interference temperature limit. Thus the SUs can know the channel gain from itself to the primary receiver and also the ITL of the primary receiver.

Although the constraint in (15) is sufficient to guarantee not to exceed the interference tolerance of PU, it is strong reservation and reduces the optimum utilization of the network.

The second possible solution to make the SU senses the amount of interferences produced on the PU due to the secondary users including itself is by assuming that  $r_{ri} \approx r_{rj} \approx r, \forall i \neq j$ . This assumption



is expected to be true most of the time, since typically the secondary users must reside far away enough from the TV coverage area. Under this assumption, the inequality (1) may be written as

$$\sum_{i=1}^N S_i \leq \left( r^{\nu_s} \left( \frac{S_p}{\gamma_p^{th} \cdot r_p^{\nu_p}} - N_o \right) \right). \quad (16)$$

If all secondary users those intending to transmit send their respective powers to the user  $i$ , so this particular user will be able to verify the QoS requirement of the primary users by checking the above inequality. Let

$$S_s^T = \left( r^{\nu_s} \left( \frac{S_p}{\gamma_p^{th} \cdot r_p^{\nu_p}} - N_o \right) \right)$$

denotes the total power produced by all the active CR users.

This second solution will be adapted through the simulation of this paper and will be compared with the first solution in how much the achievable capacity is in each approaches.

From Eq. 16, the maximum allowable transmitter for the user  $i$  can be expressed as

$$S_{s_i}^{max} = S_s^T - \sum_{j=1, j \neq i}^N S_j. \quad (17)$$

As we mentioned above, the cognitive radio networks introduce another constraints on the transmission power which must be enforced to each node in the secondary user's region. We modify the two conventional power algorithms explained above to new *Enhanced* ones, say: Enhanced DCPC (EDCPC), and Enhanced GDCPC (EGDCPC).

The maximum transmission power of the user  $i$  is now changed to

$$S_{s_i}^m = \min(S_s^m, S_{s_i}^{max}). \quad (18)$$

Then, transmission power of the secondary user  $i$  at the  $n^{th}$  iteration for ED-CPC can be updated as:

$$S_i(n) = \min(\beta(n)S_i(n-1), S_{s_i}^m). \quad (19)$$

This value of power will be assigned to this user as well as the condition (16) is satisfied. Here we assume that all the active cognitive users send their powers to the particular user  $i$  which has to evaluate the inequality (16) before taking the decision of assignment.

By the same way for the proposed EGDCPC scheme, the maximum transmission power constraint is enforced to each user to guarantee the QoS requirement for the PU as well as that of SUs. Thus, the maximum transmission power of the  $i^{th}$  SU is the same as that of the above EDCPC, and the updating rule of the  $i^{th}$  SU at the  $n^{th}$  iteration can be written as:

$$S_i(n) = \begin{cases} \beta(n)S_i(n-1), & \text{if } \beta(n)S_i(n-1) \leq S_{s_i}^m \\ S_{a_i} & \text{if } \beta(n)S_i(n-1) > S_{s_i}^m \end{cases} \quad (20)$$

where the value of  $S_a$  is updated as:

$$S_{a_i} = \min(S_a(n), S_{s_i}^m) \quad (21)$$

$$S_{a_i} = \min(S_a(n), \min(S_s^m, S_{s_i}^{max})).$$

The third solution introduced here is by assuming that by placing a "genie" near the primary receiver at the border of the TV coverage area [7]. The genie will monitor the interference level and inform the secondary users (such as using a beacon signal) if the interference level is too high and the QoS requirement of the primary users will be violated. One possible implementation of the genie is a secondary user that happens to locate inside the TV coverage area. Generally this solution can not be imposed on TV receiver,

and one can't enforce the licensed user to add more equipments, where there is no benefits for it behind that.

## V. Simulation Results

A simulation model is presented below to demonstrate the potential of the proposed power control method in cognitive radio systems. The cognitive radio network shown in Fig.1 is considered and the system network parameters and assumptions are given as: There are  $N = 50$  transmitting-receiving pairs of secondary users uniformly distributed in a square region of  $(1500 \times 1500)m$ . The maximum transmission power that each secondary user can provide is  $20dBm$ , and the range of the transmission of the SU,  $r_s = 500m$ . All the secondary transmitters/receivers are in the square area, and the receivers are located within the transmission range of the corresponding transmitter with a uniform distribution. The QoS requirements for them is  $3dB$ . The path loss exponent  $\nu_s$  is set to 4. The initial transmission power of each SU is randomly chosen within the range  $0 < S_i \leq S_s^m$  with a uniform distribution. Furthermore, it is assumed that the network is stationary during the power control operation. In the other side, the primary transmitter is considered as a TV station with transmission power of  $50dBW$ , and its effective coverage radius of  $r_p = 50km$  with QoS of  $\gamma_p^{th} = -100dBm$ [15]. The path loss exponent  $\nu_p$  is set to 3. The noise power  $N_o$  is the same for all CRs and set to  $-110dBm$ . The algorithm terminates after 25 iterations assuming non convergence case and so no feasible solution for that user. We varied  $r$ , which is the distance between the primary receiver and the center of the square region, from  $800m$  (the region

is very close to the primary receiver) to  $3000m$ . The interference temperature at the primary receiver is directly affected by this distance, . The longer  $r$  is, the less the PU is interfered from the SU.

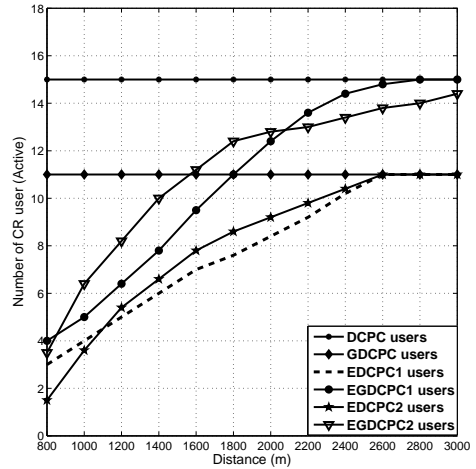


Figure 2: Number of SUs VS Distance for the different schemes

The number of secondary users those can communicate reliably for the different algorithms are shown in Fig. (2), where the subscript (1) denotes to the approach of the first solution and subscript (2) to the second solution presented in section (4). Since GDCPC decreases the interference to other users, we expect more secondary users may communicate than the DCPC case as shown in the figure. The number of users for DCPC and GDCPC are not affected by the distance because we don't consider the presence of the primary user (no CR network). For the proposed schemes, some of secondary users whose transmission power constraint to protect the primary user service is less than the required level for reliable communication. Hence the pri-

mary user should be protected first, the secondary users can't be activated in the network. As the distance  $r$  increases, the results of the proposed schemes tend to that of the conventional schemes because the channel gain  $g_{p,i}$  becomes very small and the power constraints given in Eq. (14) and (16) becomes very large. We may note that the capacity achievable by EGDCPC2 is more than that of EGD-CPC1 for distance less than 2Km, while EGDCPC1 overcome after that.

Table (1) lists the values of transmission power for the activated secondary users for each schemes.

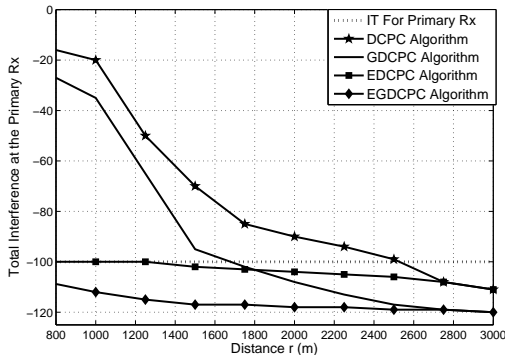


Figure 3: Interference temperature VS Distance for the different schemes

Fig. (3) shows the interference temperature at the primary receiver caused by all opportunistic communications. It demonstrates that both our schemes never exceed the threshold value  $\gamma_p^{th}$  (-100 dBm). Also here for not considering the primary existing, DCPC and GDCPC interference temperatures exceed the threshold value for short distance  $r$ . GDCPC scheme consumes less power than DCPC scheme which is generally more interference than that for GDCPC.

We can note from the figures that

these proposed algorithms are equivalent to the conventional algorithms at large enough distance, hence if all secondary transmitters satisfy interference constraint, the distance satisfies the following inequality. Such distance is found to be around 2750m.

$$r_f \geq \frac{\ell}{2} + \left( \frac{S_{s_i}^m N_a}{\gamma_p^{th}} \right)^{1/\nu_s}, \forall i = 1, 2 \dots N \quad (22)$$

## VI. Conclusion

The above analysis demonstrated an adaptation of the constrained distributed power control to be applicable for cognitive radio which share the primary users channel. We proposed algorithms that guarantee both the licensed and the secondary users's requirements. This was done by adding one more power constraint to the conventional power scheme used in cellular systems. This modified algorithm ensure the priority for the primary user and the suggested generalized algorithms is in the sense that traditional one is a special case of it. The transmission power matrix was numerically solved for feasible solutions with average number of iterations around (12).

This paper did not consider the fairness among the users to get connectivity, the algorithm allocate the powers for any user whose channel condition is good. As a future work, a kind of scheduling to achieve fairness among users will be issued regardless to the user channel condition and location.

Table 1: The feasible power solutions in (mW) at distance  $r = 2Km$



No. of CR users	DCPC mW	GDCPC mW	EDCPC mW	EGDCPC mW
1	0.0285	0.0285	0.0285	0.0285
2	0.0284	0.0284	0.0284	0.0280
3	0.0837	0.0847	0.0837	0.0137
4	0.0865	0.0895	0.0895	0.0137
5	0.0514	0.0923	0.0645	0.0137
6	0.0648	0.0824	0.0824	0.0137
7	0.0824	0.0325	0.0262	0.0137
8	0.0514	0.0644	0.0583	0.0384
9	0.0487	0.0694	0.0447	0.0280
10	0.0466	0.0955		0.0434
11	0.1037	0.1122		0.0880
12		0.1205		0.0956
13		0.1350		
14		0.1325		
15		0.1257		

#### REFERENCES

- [1] D.Cabric, S.Mishra, and R. Broderesen, "Implementation issues in spectrum sensing for cognitive radios," in *Asilomar Conference on Signals, Systems, and Computers*, 2004.
- [2] S. Haykin, "Cognitive radio: Brain-empowered wireless communications," *IEEE Trans. Selected areas in Communications*, vol. 23, no. 2, pp. 201–220, Feb 2005.
- [3] M. Marcus, "Unlicensed cognitive sharing of TV spectrum: The controversy at the federal communications commission," *IEEE Communication Magazine*, vol. 43, no. 5, pp. 24–25, May 2005.
- [4] G. J. Foschini and Z. Miljanic, "A simple distributed autonomous power control algorithm and its convergence," *IEEE Trans. Veh. Technol.*, vol. 42, no. 4, pp. 641–646, Nov. 1993.
- [5] S. Grandhi, J. Zander, and R. Yates, "Constrained power control," *IEEE Wireless Personal Communications*, vol. 13, no. 4, pp. 1332–1340, Dec. 1995.
- [6] Y. Xing and R. Chandramouli, "Qos constrained secondary spectrum sharing," *IEEE Dynamic Spectrum Access Networks*, pp. 658–661, 2005.
- [7] L. Qian, J. Attia, A. Jarosch, and C. Monney, "Power control for cognitive radio ad hoc networks," *Local and Metropolitan Area Networks, 15th IEEE Workshop*, pp. 7–12, June 2007.
- [8] P. Kolodzy, "Interfernece temprature: A metric for dynamic spectrum utilization," *International Journal of Network Management*, vol. 16, no. 2, pp. 103–113, Mar. 2006.
- [9] J. Mitola, "Cognitive radio: Making software radios more personal," *IEEE Personal Communication*, vol. 6, no. 4, pp. 13–18, Aug. 1999.
- [10] L. Zhao, W. Mark, and J. Ding, "Power distributed/allocation in multirate wideband cdma systems," *IEEE Trans. on Wireless Communication*, vol. 5, no. 9, pp. 2458–2467, Sep. 2006.
- [11] M. Geoffroy and A. Pietrus, "A general iterative procedure for solving nonsmooth generalized equations," *Computational Optimization and Applications*, vol. 31, pp. 57–67, Dec.. 2005.
- [12] F. Berggren, S. Kim, and R. Jantti, "A generalized algorithm for constrained power control with capability of temporary removal," *IEEE Trans. Veh. Communication*, vol. 50, no. 6, pp. 1604–1612, Nov. 2001.



- [13] C. Perkins and E. Royer, "Ad-hoc on-demand distance vector routing," *IEEE Mobile Computing Systems and Applications*, pp. 90–100, 1999.
- [14] S. Mangold, A. Jarosch, and C. Monney, "Operator assisted cognitive radio and dynamic spectrum assignment with dual beacons - detailed evaluation," *IEEE Communication System Software and Middleware*, pp. 1–5, 2006.
- [15] J. MacDonald and D. Ucci, "Interference temperature limits of ieee 802.11 protocol radio channels," *IEEE International Conference on Electro/Information Technology*, pp. 77–82, May. 2007.



المؤتمر الدولي العربي الليبي الخامس للهندسة الكهربائية والإلكترونية 2010/10/26-23 طرابلس ليبيا



## **A model For Estimating Systems and Cost Requirements of a Petroleum Fleet Tracking System**

Tarke B. Alhamme  
Brega Petroleum Marketing Company

Abdulkader AL. Sadek Akki  
Faculty of Engineering  
AL-Fateh university

### **Abstract**

Based on its physical and chemical properties many petroleum shipped materials classified as high risk which can adversely affect the safety of public during handling or transportation and due to many previous fatal accidents and due to potentially fuel theft and high safety and security as well as fleet management requirement. Petroleum marketing companies becomes more concerning about implementation of fleet truck tracking system. The purpose of this paper is to evaluate the best technical solution satisfying the petroleum marketing companies requirements. The evaluation where done based on potentially threaded scenarios. Two different transmission cost scenarios were calculated for different transmission interval (5 sec to 15 minutes) through satellite and terrestrial system. A statistical model software program is applied to determine the number of trucks on road at any time to calculate the required transmission bandwidth and storage data size. Finally four scenarios of cost reduction (optimistic to very pessimistic) are applied for cost benefits analysis.

### **Introduction**

The truck tracking system is a system to track the shipment of oil products across the country by equipping the trucks with wireless communication technology that provides continuous communications, vehicle position and location tracking and emergency broadcast capabilities, to identify and prevent different cases of accidents. In Libya, Brega Petroleum Marketing Company (BPMC) is responsible for store and distribute the petroleum products for whole country, from 9 depots to about 1000 gas and fuel stations and to airports and power stations, where more than 800 shipments of petroleum

material are shipped per day by road on an average of 250km per travel. The BPMC is taken as case study and data collection are based on sites survey. A sample of 3700 travels were taken from randomly selected six working days from BPMC historical travels distances data, these data are applied for statistical model software program and for cost analysis. BPMC implement tracking system for the following main goals:-

- 1- Decrease the number and reduce the risk of traffic accidents.
- 2- Increase productivity.
- 3- Improve services and reduce response time for customer.



- 4- Detect and prevent the truck hijack and fuel theft detect.

### Overview of Existing Sale and Transport Process

The BPMC oil depots supply the fuel and gas stations according to their needs of oil products all over the Libyan country. The country area is divided in two regions, west and south region, and east and middle region. Each region has separate administration (HQ) to manage of sale and transport process of oil products. A number of sale offices scattered in each region to serve the customer requirements, preparing purchase invoice and send it to its

belonging depot. Distribution department in depot process truck request to transport department to ship the material to the customer, Figure 1 shows the process of sale from source to destination. In general there are three groups of shipment carriers:-  
 1- BPMC fleet transportation. 2- Contracting transportation companies. 3- Private fleet owned by the clients, the drivers can be either owner of trucks or work on a contract basis. Due to absent of any tracking and monitoring system at present there is very little supervision and monitoring of drivers activities.

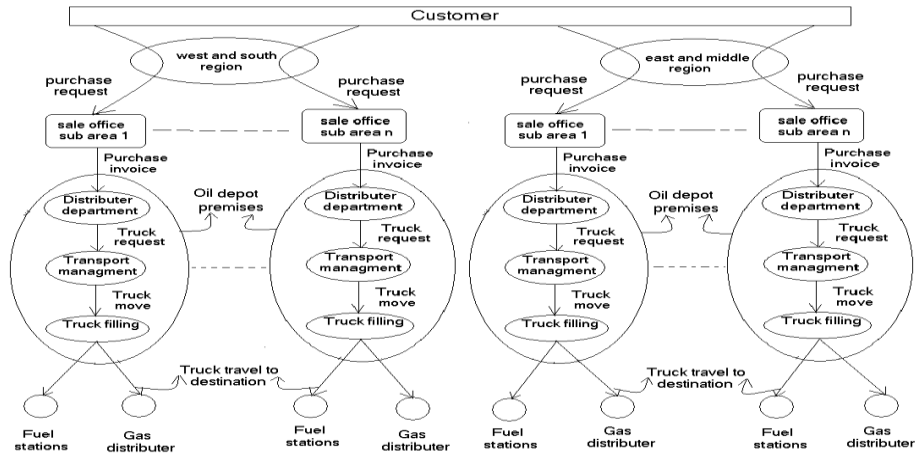


Figure 1 Sale of Oil Products from Source to Destination

### System Configuration and Information Flow

To meet the company needs and according to the dynamic of sale and transportation system of the BPMC company, three level of monitoring and

control should be implemented as shown in Figure 2. Truck receive GPS data from navigation satellites and collect and record all required data such as speed, location and direction of mobile unit and send it every certain time interval to truck tracking center





(TTC) via satellite or terrestrial system. TTC analyses the received data and store it as data base. The real time or stored data are filtered and passed to a second level of regional monitoring center, which monitor only the trucks designated to that region. Regional monitoring center filters the data and pass it to the third level of local monitor to monitor the truck belong to that depot. The first level, is TTC, TTC aggregate data from all trucks on the road and create common operating picture. TTC can analyses the data and coordinate between the two regional monitor centers. TTC receive the payload data from third level such as manifest and bill of load via private or internet network. Data from external agents such as environmental and emergency agencies support the TTC to take decision for emergency cases by passing this data to the second level to change truck route planning. The main functions of TTC are:-  
1- Receive and store planned truck routes.  
2- Provide immediate notification of emergency

incident.  
3-Direct truck calls. The second level is regional monitor center, the regional oil depots shipment travels are monitored and managed by regional monitor center. This limit the amount of data processed at TTC. Thus allow TTC to focus on more critical operation. TTC passes information related to intelligent, special events, environment issue to regional monitor center to enhance their monitor capability.

The third level is local monitor is located in each oil depot (source), tracks their own shipments. In this level all information concerning the truck travel is feed to the system. This information includes type of shipment material, destination, with trail or not etc. The information is very important to be correct for system performance. Any wrong data can cause series of problems or false of alterations. On the other hand received data such as expected time to arrive and trip time would help to increase the fleet management performance.

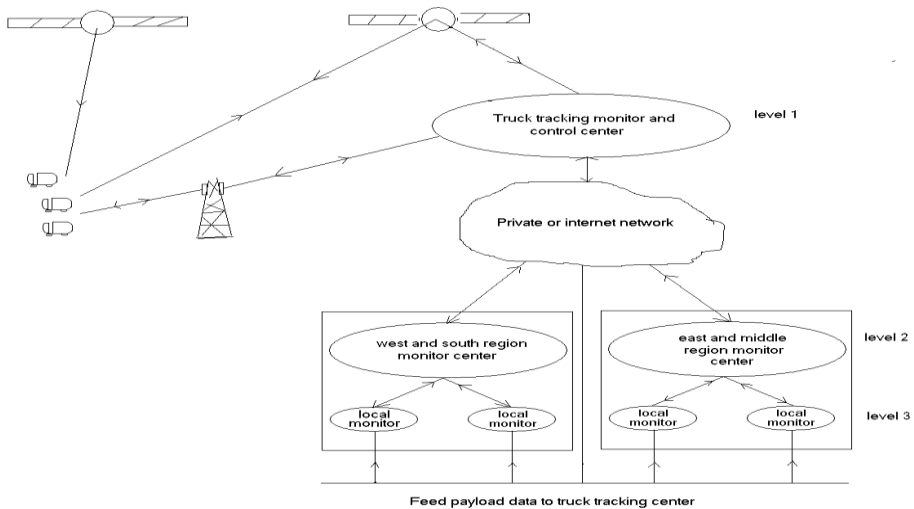


Figure 2 Truck Tracking System Levels

### Options of Technology Solutions

Several technology options are recommended for truck tracking system. The Company may be recommended to select one technology option over the other based on satisfaction of system requirements, cost, security and safety for different types of shipments. These options are: Option 1: implement wireless communication (WC), WC are usually digital mobile phone or two way radio, nearly all company long travel trucks already comply with this option. Option 2: implement WC and GPS, GPS is hamming devices that allow for the tracking of a truck and trailer (Tethered or un-tethered) without the intervention or necessarily the knowledge of driver.

Option 3: implement WC+ GPS + panic button + seals, a panic button is a device which allows a driver to signal for help in an emergency, easy to use, typically one

way signaling device and commonly silent operation. Electronic seals are devices that can detect when a cargo door or other container is opened and is used as theft deterrent and detection mechanism. Option 4: Implement WC+GPS+ Panic alter + driver ID + Truck disability, remote disability is a feature that allows for a truck to be immobilized from a location external to the truck.

### Technology Solution Evaluation

To specifically differentiate among the technology options, it is necessary to measure their performance at the whole system level. Table 1 shows the results extracted from comparison of the technology options against specific threat scenarios. These scenarios provides what would make the system better, the higher the technology option tend to provide more aids in altering of possible incidents than the lower technology option. The truck



failure in desert where no reliable wireless communication is available will force the driver to leave the truck to call for help. This is the common scenario faced by the companies in Libya, the option 2 or higher with reliable WC or SMS through satellite system can reduce the risk and waste time. The risk of traffic accident and highjack scenarios could be reduced by option 3 if driver can use panic button otherwise

option 4 could reduce the risk by sadly stop or truck disability features. For sandstorm environment as in Libya, methods of transmitting information regarding truck position would help to reduce the risk. According to scenario results and BPMC main goals and objective of the system, we could conclude that the option 3 will satisfy the company requirements.

Table 1 Comparison Of Technology Options Against Specific Threat Scenarios

Threats	options	result	Potential Cost impact	Potential life impact
Fuel theft	Option 1	Notification is not made until call from truck is made to identify the problem	The Cost of fuel	No damage
	Option 2	Notification is not made until call from truck is made to identify the problem	The cost of fuel	No damage
	Option 3	Notification is sent informing that truck trying to open fuel container emergency response	No damage	No damage
	Option 4	Notification is sent informing that truck trying to open fuel container emergency response	No damage	No damage
Truck failure	Option 1	Notification is made	No damage	No damage
	Option 2	Notification is made	No damage	No damage
	Option 3	Notification is made	No damage	No damage
	Option 4	Notification is made	No damage	No damage
sandstorm	Option 1	Truck is struck by sandstorm and Fuel is released	The cost of fuel and cleanup road	One person or more
	Option 2	Stop driver from	No damage	No damage



Threats	options	result	Potential Cost impact	Potential life impact
		continuing travel		
	Option 3	Stop driver from continuing travel	No damage	No damage
	Option 4	Stop driver from continuing travel	No damage	No damage
Traffic accident	Option 1	Will not be notified until someone calls informing about the incident	The cost of damage of truck and road, cleanup	One person or more
	Option 2	Will not be notified until someone calls informing about the incident	The cost of damage of truck and road, cleanup	One person or more
	Option 3	Will not be notified until someone calls informing about the incident	The cost of damage of truck and road, cleanup	One person or more
	Option 4	Notification is sent that truck is sadly stopped, emergency response	The cost of damage of truck and road, cleanup	Life of driver could be survived
highjack	Option 1	No one is aware if truck is on or off route.	Cost of truck and fuel	Life of several people could be at risk
	Option 2	Notification is sent that truck changed planned route and response is made	Cost of truck and fuel	Life of several people could be at risk
	Option 3	Driver may or may not be able to trigger panic button	Depend on state	Depend on state
	Option 4	Notification is sent that truck changed planned route and truck disabled	No damage	No damage



### **Network Configuration**

From the economics of transmission point of view it is recommend placing the TTC and regional centers in or near the cities which are the sources or destinations with the majority of traffic. As a result the regional monitor center is recommended to be located on Tripoli and Benghazi. The TTC is to be located also in the west and middle region. This is because due to that the overall percentage of source and destination in the west and middle region is higher than the east and south region.

### **Transmission Intervals**

A data package is considered a single transmission of data from the truck to TTC. Each transmission may contain multiple data samples. The system collect and record on truck all data once every minute and to send data to the TTC only once every certain period of time 0.5,1,5,10,15, 20, 30 minuets depending on the type of shipment material the truck is carrying and the area to be covered by the truck. It is possible to divide the region in to sub areas with different risk levels e.g. longer transmission period interval could provide sufficient coverage for local in town deliveries. The main data package structure is as follows [1]:

1- Truck ID, each truck will have a unique identifier for tracking purposes. This includes, depot (source) ID, region ID, plant ID. 2- Shipment material description: this include type of shipment. 3- Trailer connection disconnection notification, include only when trailer is disconnect. 4- Speed, latitude longitude, and direction.

### **A model For Estimating System**

**Bandwidth**Based on BPMC site survey the trucks are queued in front of depots gats each morning for loading the shipment. This queue is usually finished at time between 2:30 to 3:30 PM. So we assume the arrived time is constant and start time of loading for each loading point is random from 8 to 9 AM and the time taken for full load is about 25 minutes. Actually the service time depends on the size of truck tanks in liters and the pumping rate liter per minute which is varied with the number of trucks under load. There is in total 78 loading points in all 9 depots, the actually used number of loading points is variable from day to day, but in any case it does not exceed 40 loading points due to operation capability. There were about 800 travels per day, the go and back travel distance by each truck is random from 25 to 2300km, A sample of 3700 travels were taken from randomly selected six working days from BPMC historical recorded data in 2007 to estimate the mean and standard deviation of truck traveling distance.

### **Model Assumption**

Based on the system requirements for frequency of data transmission and type of data, the required bandwidth can be developed. The model assist in determining the number of trucks that are operating simultaneous, the model assumption are listed below.

1- The average number of shipment per day is 800. 2- Full or partial truck loads are counted as a single shipment. 3 - Multi shipment or deliveries on a single trip are counted as one shipment. 4 - Trucks that are parked are not assumed (engine turn off). 5-



Loaded or unloaded trucks will be tracked by the system for total go and back travel. 6 - The shipping distance varied widely from 5 to 2300 km. 7 - All the area of country covered by the tracking system. 8 - Shipment start time is 8 Am and last shipment is 19 Pm. 9- Driving hours per day 11 hours. 10 - 7 days work. 11- Constant driving speed (60 km/h). 12- The distance that each truck traveled was created using lognormal distribution [2] with mean of 250 km and standard deviation of 384 km. 13- Packet size 200byte, 100 byte, 500 byte. 14- 200 bytes packet size used for calculation of transmission cost[3]. 15 - The starting time of loading for each loading point is random uniform distribution from 8 Am to 9Am. 16- Frequent of transmission interval is 10, 15, 20 and 30 minutes. 17- Constant service time 20 minutes (time taken by each truck for loading the

shipment). 18- Number of loading points 40 (worst case). 19- Number of depots (sources) 9. 20- Rate of increase in travels per year 5 %, which is about 40 travels, (180.8 hours, 56 terrestrial hours and 124.8 satellite hours per day).

### Computer Added Program

The program is built using Matlab version 6, the function of the program is to calculate the peak and average number of trucks on road based on survey data and model assumption. Figure 3 shows shipment processing model. The concept of the program depends on generating 800 traveling distances and calculating the start and end time of each travel and then generates random observation time to observe the number of trucks in this time. The program is simulated for 200 days to calculate the number of peak and average truck on the road.

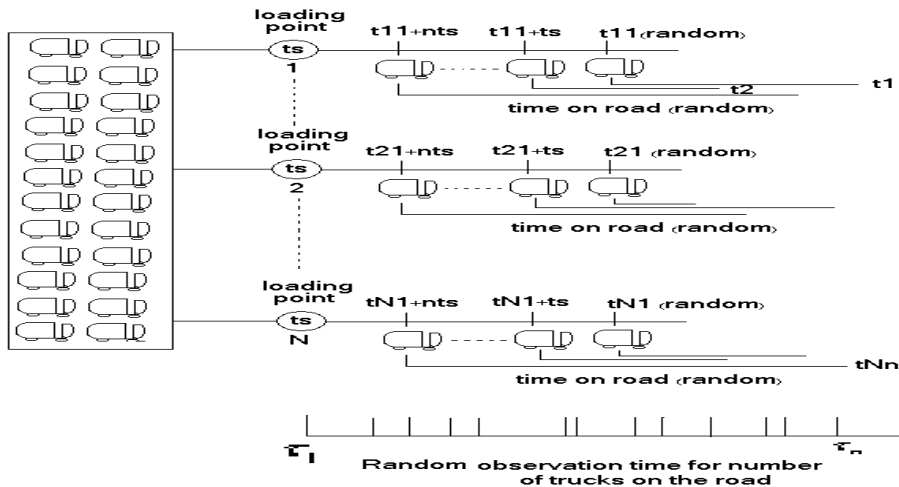


Figure 3 Shipment Processing Model



### Bandwidth Calculation

The trucks traveling distance follows lognormal distribution with average traveling distance 250km and standard deviation 384km as shown in Figure 4. The model shows that the peak number of trucks on the road at any time is 379 on the time between 2 to 3 PM and the average number of truck on road is about 153 trucks as shown in Figure 5. If every truck in progress transmitted its position to the data center at the same time and every second, it would require bandwidth of 606kbps for (200 bytes packet size) and 245kbps average BW. Also need 196Gbytes storage data for 30 days storage. Figure 6 shows the peak bandwidth required for different transmission sequences versus packet size. Since 55.75% of travels are within the city, there will be an average of 86 trucks out of 153 are on terrestrial network.

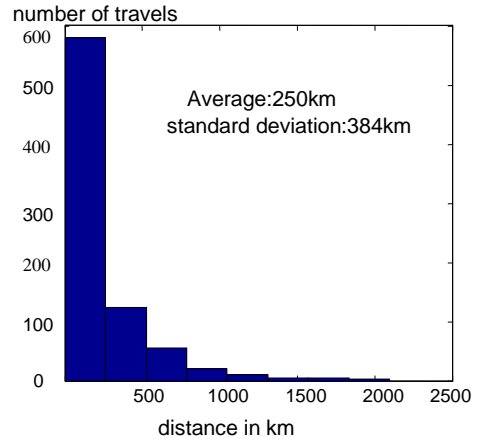


Figure 4 Lognormal Distribution of 800 Travels

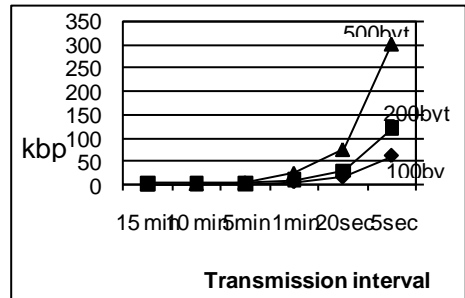


Figure 6 BW (bit rate) Required For Different Size Of Packets And Tx Intervals

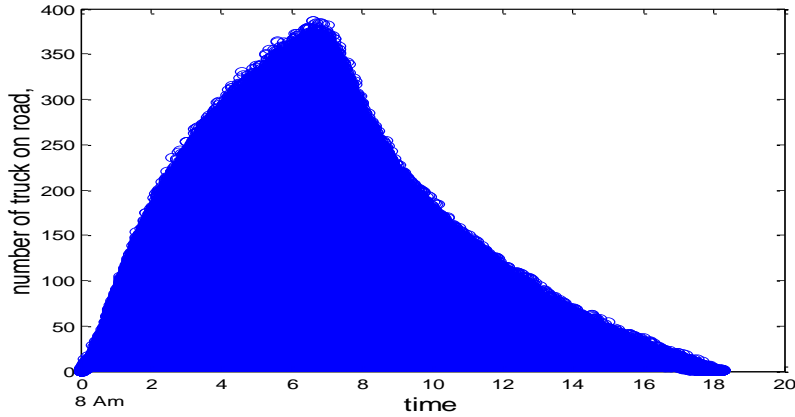


Figure 5 Truck Traveling Distribution

### Cost Estimation

The cost is divided into fixed and running cost.

1-Fixed cost,

a - Technology option cost, since the technology option 3 fulfills the requirements of BPMC system objective. The cost per unit truck for this option is to be included. The cost estimate of elements of option 3 technology is given in Table 2[3]. Assume each truck execute 2 travel per day to reflect the fact that unknown number of trucks makes one shipment per day and an unknown number of trucks makes more than two shipment per day, then the total vehicles are 400. The total cost of equipment for 400 truck is about 1.5M Libyan dinar (LD).

b- Truck tracking center cost, The cost estimate of truck tracking equipments is given in Table 3[3]. The project capital cost = tracking center equipment cost + truck equipments cost =1.89 MLD, 8% is adding

for installation, management and other expenses.

Table 2 Cost Estimation of option 3 technology

item	Cost (LD)
Global position terrestrial/ satellite (GPS)	2300
Panic button	650
Electronic seal	650
Total truck equipment	3600
Trailer tether alarm	130
Total cost per unity vehicle	3730

Table 3 Truck Tracking Center Cost

Component	Cost (LD)
Routers	30,000
Servers	20,000
O& m training	200,000
Total	250,000

2- Running cost (Annually polling cost). The cost per year to transmit tracking data





via terrestrial mobile or satellite network depends on transmission intervals and charge per call. 55.75 % of travels are within the cities, less than 120km (go & back), assumed to be covered by terrestrial communication, while 44.25 % are covered by both terrestrial and satellite. Based on the survey table of travels frequency in each distance interval, the terrestrial and satellite communication tracking hours are 1128 and 2493 hours respectively, and the total is 3621 hours per day. To calculate the cost of terrestrial and satellite communication for each transmission interval, two cost scenarios are considered to estimate the polling cost. First scenario that the cost of terrestrial SMS = 0.1 LD and satellite SMS= 0.25 LD. Terrestrial cost = number of transmission per hour  $\times$  number of terrestrial hours per day  $\times$  365 days  $\times$  cost

of terrestrial SMS. Satellite cost = number of transmission per hour  $\times$  number of satellite hours per day  $\times$  365 days  $\times$  cost of satellite SMS. The obtained cost estimation for different transmission intervals is given in Table 4. Second scenario that the cost of GSM SMS = 0.05 LD and satellite SMS= 0.125 LD. The obtained annual cost estimation for different transmission intervals of second scenario are exactly the half values given in Table 4. If only terrestrial communication is consider in both scenarios. In this case, the data store in GPS device during uncovered communication area, the data uploaded to TTC when the truck return back again to coverage area. The total cost for different communication intervals are as shows in Table 5.

Table 4 Annual Cost Estimation For Transmission Intervals (First Scenario)

Transmission intervals	Cost of Terrestrial communication (MLD)	Cost of Satellite communication (MLD)	Total cost (MLD)
5 sec	29.64	163.79	193.43
20 sec	7.41	40.95	48.36
1min	2.47	13.65	16.12
5min	0.494	2.73	3.22
10min	0.247	1.36	1.61
15min	0.164	0.91	1.07



Table 5 Annual Cost Of Only Terrestrial Communication

Communication interval	First scenario Terrestrial cost per year (MLD)	Second scenario Terrestrial cost per year (MLD)
5sec	95.16	47.58
20sec	23.79	11.89
1 min	7.93	3.96
5 min	1.59	0.795
10 min	0.793	0.396
15 min	0.529	0.264

Since that the contracting transportation companies execute about 57.5% and the BPMC execute 42.5 % of travels, the cost of transmission, will be divided between the BPMC and contractor companies according to this ratio. If we consider 15 min transmission interval, the total transmission cost for second scenario is 530,000 LD

increased by 27,000 LD every year due to increase in number of travels by 40 travels per day each year. Tracking equipment cost is about 1.89 MLD and adds 74,600 LD each year due to increase in number of truck by 20 trucks. Table 6 shows the system cost distribution over years.

Table 6 System Cost Distributed Over Years

Year	Tracking equipment cost (MLD)	Running cost (MLD)	Total cost (MLD)	Cumulative cost (MLD)
start year	0.189	0	0.189	0.189
1 <sup>st</sup> year	0.2636	0.53	0.7936	0.983
2 <sup>nd</sup> year	0.2636	0.557	0.8206	1.803
3 <sup>rd</sup> year	0.2636	0.584	0.8476	2.651
4 <sup>th</sup> year	0.2636	0.611	0.8746	3.525
5 <sup>th</sup> year	0.2636	0.638	0.9016	4.427
6 <sup>th</sup> year	0.2636	0.665	0.9286	5.356
7 <sup>th</sup> year	0.2636	0.692	0.9556	6.311
8 <sup>th</sup> year	0.2636	0.719	0.9826	7.294
9 <sup>th</sup> year	0.2636	0.746	1.0096	8.303
10 <sup>th</sup> year	0.2636	0.773	1.0366	9.34

### Cost Benefit Assumption

Based on historical data of 2007 and local Libyan market information, some

assumption is made to calculate cost, these assumptions are as follows:-



1- Truck cost 100,000 LD with 10,000 LD depreciation each year for 10 year life cycle. 2- Calculation based on 500 trucks, since now the average trucks are 400 trucks and after 10 years will be 600 trucks. The number of travels per day after 10 years is 1200, assume each truck execute 2 travels per day. 3- Average distance traveled by each truck is 182,500 km per year. 4- Engine oil change every 7500km, each change cost 82.5LD, 30 liter each change, 2.75LD/ liter. Engine oil change cost = number of changes/year  $\times$  number of liters/change  $\times$  cost/liter. 5- Fuel consumption 12%, 0.17LD/liter. Fuel cost = truck kilometers/year  $\times$  liters/km  $\times$  cost/liter. 6- Average 12 tires change every 100,000km, each tire cost 400LD. Tier change cost = number of changes per year  $\times$  number of tiers  $\times$  cost/tire. 6- 300 LD for repair or change some parts and other expenses.

### Cost Benefit Calculation

Implementation of truck tracking system, monitor speed violation, and reduce response time could significantly reduce the potential risk of life lost and catastrophic damage of flammable material and security threats [ 5]. The direct cost benefit calculation is done for 10 years, with assumption of 40 travels and 20 trucks increase each year. In the 10<sup>th</sup> year there will be 1200 travels per day executed by 600 trucks, 500 trucks on the average is applied for calculation. 72,000 LD cost of 20 trucks equipments added annually to the system tracking equipment. Since the cost saving varied from tracking system to the other due to shipment types, size, techniques, traffic, type of trucks, local market, etc. Four scenarios of cost reduction are applied as shown in Table 7.

Table 7 Percentages Of Cost Reduction

item	Scenario 1	Scenario 2	Scenario 3	Scenario 4
Percentage increase in Truck life	9 %	4 %	2 %	1 %
Driver productivity	4.7 %	2.4 %	1.2 %	0 %
Reduction in over time	22 %	10 %	8 %	5 %
Reduction in insurance	15 %	12 %	10 %	5 %
Reduction in fuel	15 %	12 %	10 %	5 %
Reduction in maintenance, tires & repair	10 %	7 %	5 %	1 %

The percentage values given in these scenarios varied from optimistic (scenario 1) to very pessimistic (scenario 4) of reduction ratios collected from different references, the parameters of reduction are as follows:

1-Fuel, fuel consumption could be reduced by many ways: a-Monitoring the truck travel could eliminate unnecessary stop, idle engine is about 30% out of total engine run time (depend on season), 3.7liters/hour average fuel consumption of idle engine [6],[7], b- Limiting driving speed. For each



1.6km/h driving speed above 100km/h fuel consumption increase by 1.5% [8].c- Reduction in mileage. Monitoring the truck travel eliminates unnecessary traveling mileage and deviation from planning route. In general fuel reduction could be from 5% to 20% [9]. 2-maintenance tires & repair, maintenance costs represent a significant portion of cost, as the traveling mileage increase the maintenance , tires & repair cost also increase and vice versa, the average maintenance cost of a truck running from (160,000 to 192,000) km could be up to 0.04LD/km[10] which, depends on local market. 3-Insurance, 10% reduction in mileage reduces crash and casualties by (12% to 20 %) and also the tracking system reduces the risk of theft [11], [3]. 4- Over time, applying tracking system could save time, from (20 to 50 minutes) per day [8] , if we assume 4 hours a day as maximum over time, that mean (8% to 22%) of over

time cost could be reduced. Reduction in over time = (reduction time/ h)× 365× overtime payment/h. 5-Driver productivity, route optimization and vehicle monitoring ensure drivers productivity, they are less likely to stop for unauthorized breaks or run up overtime costs. Estimated saving time is 5 to 20 minutes or 1.2% to 4.7% out of 7 hours per day [8]. Kilometers increase per truck = (percentage of saving time× 7hours×(driving speed/h)×365). Driver productivity = (cost per kilometer – cost per kilometer due to tracking system) × total kilometers (truck traveled kilometers due to tracking system). 6- Truck life cycle, reduction in mileage and maintenance will reflect to increase truck life cycle. Estimated increase in truck life is assumed to be from 1 week to 1 month (2% to 9% of truck depreciation). Table 8 shows the cost reduction values for four scenarios.

Table 8 Cost Reduction Of Four Scenarios

Item	Cost/year (LD)	Cost reduction Scenario 1 (LD)	Cost reduction Scenario 2 (LD)	Cost reduction Scenario 3 (LD)	Cost redu- Scenario 4 (LD)
Truck depreciation	10,000	900	400	200	100
Driver salary	3600	0	0	0	0
Driver productivity	-	1240.6	627	307	0
Over time	6000	1320	600	480	300
insurance	600	90	72	60	30
Registration and taxes	200	0	0	0	0
Fuel	3103	465	372.36	310	155.15
Maintenance, tires & repair	8265	827.5	578.6	413	82.65
Total/truck	31,768	4843.1	2649.96	1770	667.8
Total over 500 truck	15,884,000	2,421,550	1,324,980	885,000	333,900



### Breakeven Point

Overall cumulative system total cost over 10 years is (9.34MLD) was subtracted from each year cumulative reduction cost to calculate the profit and breakeven point over the years. The breakeven point occurs at the year where the cumulative reduction cost is equal or higher than total system cost (9.34MLD). After this year the BPMC will start gaining profit due to

implementation of tracking system. The breakeven point occurs at the fourth and the eighth year for scenario 1 and 2 respectively, while over 10 years of system for scenario 3 and 4 as shown in Figure 7. Figure 8 shows the cumulative profit and breakeven points for the 15 minutes using only terrestrial communication.

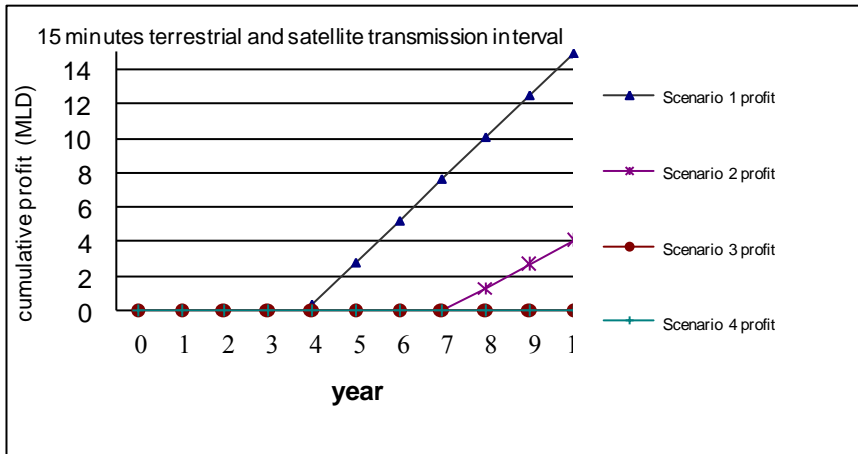


Figure 7 Cumulative Profit And Breakeven Points

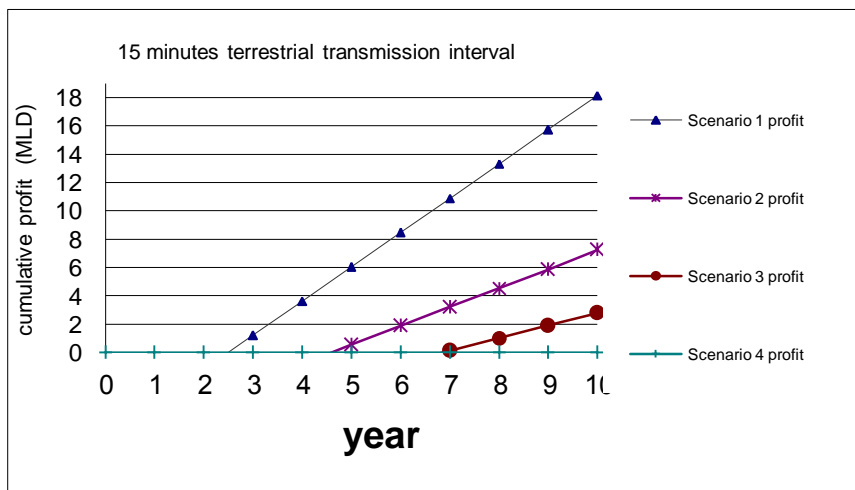


Figure 8 Cumulative Profit And Breakeven Points (15 min terrestrial).

### Conclusion

The main result from this paper shows that the fleet operation cost is very high compared with tracking system operation cost, which make the benefits of tracking system very clear even under the very pessimistic scenario. A software model program shows that the peak number of truck on road is about 379 occurring between (2 to 3 PM) with an average of 153. This peak number of vehicles will require 1Mbps bandwidth as a conservative estimate. According to the marketing companies objective of this system, the technology option number 3 (implementation of wireless communication, GPS, panic button and seals) could fulfill the BPMC requirements. The cost analysis is done for different transmission intervals, the 15 minutes communication interval where found to be more reasonable communication interval. The vehicle equipment and running cost

could be significantly reduced if only Terrestrial communication is used. The cost of terrestrial transmission is about half of satellite transmission. The 15 minutes terrestrial communication tracking system option is economical solution but the drawback of this option is the potential risk of theft and security threat during uncovered communication area.

### References

- [1] National Hazardous Material Commercial, Vehicle Tracking System Design Study. Enhancing Security on Our Nation's Roadways, University of Virginia.
- [2] Log-normal Distributions across the Sciences Keys and Clues. Eckhard Impert, Werner a. Stahel, and markus abbt, bioscience . May 2001 / vol. 51 no. 5.



- [3] National hazardous material commercial vehicle tracking system study. The university of Virginia accelerated masters program in system engineering, may 2006.
- [4] Advanced hazmat tracking decision support system A 2010 vision for hazmat vehicle. Transportation safety, APRIL 2007.
- [5] Distance-Based Vehicle Insurance as a TDM strategy, By Todd Litman Victoria Transport. Policy Institute, November 2008.
- [6] Heavy-Duty Truck Idling Characteristics, Results from a Nationwide Truck Survey. Nicholas Lutsey, Christie. Joy Brodrick, Daniel Sperling, and Carollyn Oglesby.
- [7] Institute of Transportation Studies (University of California, Davis), Evaluation of Fuel. Cell Auxiliary Power, Units for Heavy-Duty Diesel Trucks, 2002.
- [8] <http://www.gpsyourfleet.com/gps-roi-calculator.htm>.
- [9] A feasibility study department of general services, installing GPS devices on metrovehicles, Metropolitan government of Nashville and Davidson county, 2008.
- [10] New York State, Office of the State Comptroller, Establishing an Effective, Fleet Management System.
- [11] Distance-Based Vehicle Insurance, Feasibility, Costs and Benefits Comprehensive. Technical Report, By Todd Litman Victoria Transport Policy Institute, June 2008.
- [12] B.D. Ripley, stochastic simulation, Wiley, 1987.



المؤتمر العربي الليبي الدولي الخامس للهندسة الكهربائية والإلكترونية 23-26/10/2010 طرابلس ليبيا





## **Design an IP Multimedia Subsystem Client Supports Signaling Compression**

Asma Alkreak, Majdi Ashibani, Asma Elmangosh, and Fathi Ben-Shatwan  
Electrical Engineering Department  
Collage of Industrial Technology  
P.O Box 841, Misurata, Libya  
{asma\_alkreak, mashibani, a-elmangosh, fshatwan}@cit.edu.ly

### *Abstract*

The current trend in communication technologies is the support of a converged network environment in which wire and wireless access networks are integrated. This new trend known as Next Generation Networks (NGN) intend to provide multimedia communication services (voice, video and data) over standard IP-based networks, offering users various types of services anytime, anywhere using any device. IMS has been standardized as an environment for access and control multimedia session and services provision. These services can be rapidly developed, deployed, and delivered in a standardized fashion, providing operators the chance to manage rich multimedia services across NGN, and give users the prevision to access different service by a single login and the ability to negotiate the desired level of Quality of Service (QoS). IMS is standards-based and one of the key features is the use of open interfaces and functional components in both hardware and software systems to support real-time interactive services and applications. The Signaling interface between IMS components is based on the Session Initiation Protocol (SIP) and Session Description Protocol (SDP). SIP is used to initiate, modify and terminate multimedia sessions within the IMS, while SDP is used to describe the multimedia component of the session. Both SIP and SDP are text-based protocols and engineered for bandwidth rich links. The messages have not been optimized in terms of size and number of messages required for any operation.

In an attempt to overcome this problem Signaling Compression protocol (SigComp) was standardized. SigComp provides a method to eliminate this problem by offering robust, lossless compression of SIP messages. In this paper we introduce the CIT IMS client, which is an IMS client that can be used to establish multimedia sessions between IMS users through an Arabic interface. The client supports SigComp and the use of IPTV server over IMS. In this paper, we study the performance of SigComp when it is used to compress SIP/SDP session setup messages, results for both bandwidth consumption and delay time are presented for evaluating the efficacy of the compression operation.

***Keywords: IMS; NGN; Signaling Compression.***



## I. INTRODUCTION

A New Era of Seamless Content Communication is emerging. Users will have the ability to communicate and share rich multimedia content anytime, anywhere on any device. Next-generation networks (NGN) promise to provide a richer set of applications for the end user, creating a network platform that enables the rapid creation of new services. Significant progress has been made in the standardization of NGN architecture and protocols.

The IP Multimedia Subsystem (IMS) is a prime candidate as a service delivery platform for NGN, as it addresses the main characteristics of the NGN as defined by the ITU [1]. The IMS architecture facilitates new business models where various services can be provided independently of end-user access technologies, and seamlessly integrates access domains with an All-IP core. Another advantage provided by the IMS is the ability to negotiate the QoS levels of each multimedia stream which constitute the session. Briefly IMS will unify wireless and wireline networks, enable fixed-mobile convergence (FMC) and allow for a multitude of services to be developed easily and quickly. Fig. 1 shows the IMS Architecture.

IMS was originally designed by the wireless standards body 3rd Generation Partnership Project (3GPP). To ease the integration with the Internet, IMS as far as possible uses IETF (i.e. Internet) protocols such as Session Initiation Protocol (SIP) and Session Description Protocol (SDP) [2].

SIP has become the premier call control/signaling protocol for IP Communications, unseating its predecessor, H.323. Both SIP and SDP are text-based protocols and considered to be bandwidth consumer. The messages have not been optimized in terms of size and number of

messages required for any operation. In an attempt to overcome this problem Signaling Compression protocol (SigComp) was standardized [3]. Sigcomp enables compression and decompression of SIP messages to be sent across the networks, which have stringent bandwidth restrictions.

In this paper we introduce our NGN Testbed at the Collage of Industrial Technology (CIT) and the CIT IMS client, which is an IMS client that can be used to establish multimedia sessions between IMS users through an Arabic interface. The client supports SigComp and the use of IPTV server over IMS. In this paper, we study the performance of SigComp when it is used to compress SIP/SDP session setup messages, results for both bandwidth consumption and delay time are presented for evaluating the efficacy of the compression operation.

The paper is organized as follows. In Section II, we briefly describe the NGN and IMS testbed at CIT and its main components. In Section III the SigComp concept is presented; in Section IV, we give an overview of the implemented client at CIT and its main features. The performance

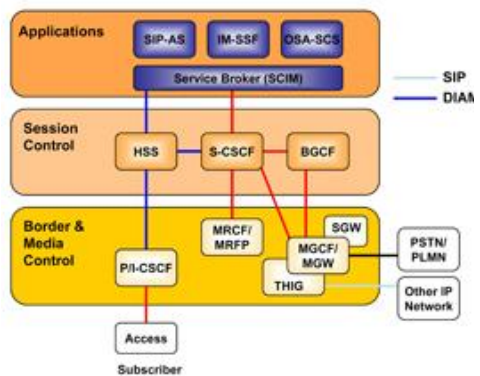


Fig. 1. The IMS Architecture.



results are presented and compared in Section V. We conclude the paper with Section VI.

## II. THE IP MULTIMEDIA SUBSYSTEM TESTBED

The 3GPP Release 6 has defined the IMS as a first instantiation of the NGN architecture in mobile networks. Since then there has been much activity in several standardisation bodies, including ETSI TISPAN, 3GPP2 and Packet Cable, to incorporate the IMS into their own specifications. Till today, IMS standards are still evolving.

The communication research group at

the Collage of Industrial Technology (CIT) has built a testbed for IMS and NGN research activities [5]. A system overview of our IMS-based testbed is shown in Fig. 2. The NGN Testbed consists of different open source program with an emphasis on communications and networks research. Some of these software are listed below:

1. The Open IMS Core: the OSIMS project of the Fraunhofer Institute FOKUS was officially launched in November 2006 [6]. The OSIMS is an open-source implementation of 3GPP's IMS standard. It consists of Call Session Control Functions (CSCFs) and a Home Subscriber Server (HSS). The Open IMS CSCFs (Proxy,

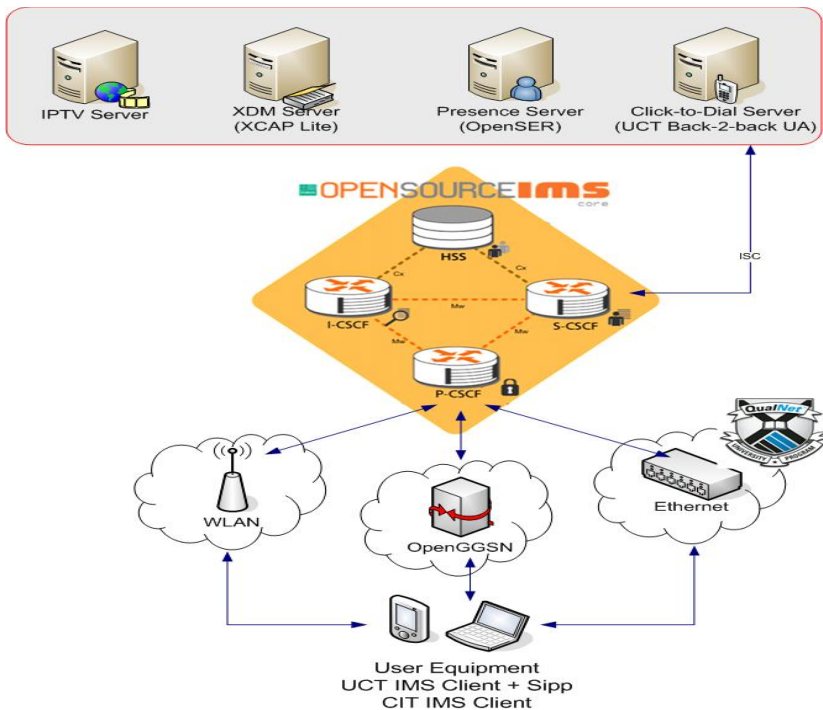


Fig. 2. The NGN/IMS Testbed at CIT.



- Interrogating, and Serving) form the central routing elements for IMS-based signaling, while the HSS manages user profiles and associated routing rules.
2. IMS Clients: mainly both UCT IMS client [7] and SIPP [8] have been used within the CIT NGN testbed. The UCT IMS client from the Communications Research Group at the University of Cape Town supports voice and video sessions with a user-friendly Graphical User Interface (GUI). SIPP is text based software provides simulation of SIP signaling.
  3. Network Emulations: used to present the transport layer. Different access network are emulated by the usage of software such as Qualnet [9].
  4. Application Servers: The Open IMS Core interfaces with multiple servers such as Security, Policy, Media, Presence, Video and Application Servers, so that fixed and wireless clients alike can establish multimedia sessions with them in a standard manner.

### III. SIP AND SIGNALLING COMPRESSION

Signaling compression (SigComp) is a mechanism for compressing and decompressing messages sent over networks in order to reduce the consumed bandwidth. SigComp is used by multimedia application protocols such as SIP. Many application protocols used for multimedia communications are text-based and engineered for bandwidth rich links.

As a result, the messages are not optimized in terms of size. For example, typical SIP messages range from a few hundred bytes up to many thousand bytes. With the planned usage of these protocols in wireless handsets, as part of 2.5G and 3G cellular networks, large message size

becomes a problem. The major components of SigComp are [4]:

- Compressor: The Compressor is the component that compresses the messages and uploads the ByteCode for the corresponding decompression algorithm to the UDVM as part of the SigComp message.
- Decompressor (UDVM): UDVM provides a mechanism to uncompress messages by interpreting the corresponding ByteCode. The UDVM can be used to decompress the output of various compressors such as DEFLATE (RFC-1951).
- State Handler: The State Handler retains information between received SigComp messages and thus, eliminates the need to send decompression instructions with each of the compressed message.

### IV. THE CIT IMS CLIENT

The communication research group at CIT had identified the need for a pure IMS client for their own research. The CIT IMS client supports:

- Voice and video calls using standard codecs.
- Instance Massaging (IM).
- Connecting to presence server, the service application is implemented by UCT.
- Connecting to Video on Demand server (VoD), the service application is implemented by UCT.
- SigComp protocol to reduce the required bandwidth in signaling.
- Arabic language interface.

Fig. 3 shows the main windows of the CIT IMS client. The CIT IME client is open-source and works under Linux operating system.



### V. PERFORMANCE RESULTS

To review the performance of our IMS client in providing its main role of establishing multimedia sessions and connecting to different service applications within the IMS Testbed. The CIT IMS client

a) *User Registration:* to use the IMS system the user must register at the IMS core first. The registration process consists of 4 SIP messages that will be send between the user and the IMS core. Table. 1 presents the size of each message before and after

shows acceptable d performance and ease of use with its friendly GUI. The Sigcomp support feature was evaluated by measuring the required signaling time with and without using this feature. The following summarizes the obtained results:

compression. The results show saving by 14.48% of the required signaling traffic to register the user with the IMS system. The messages are compressed at each side before siding over access network and recompressed at the other side.

TABLE I. SIZE OF SIP MESSAGES FOR REGISTRATION

SIP message	Size (byte)		Compression Ratio (%)
	With SigComp	Without SigComp	
<b>Register</b>	<b>586</b>	<b>777</b>	<b>24.58</b>

TABLE II.

<b>401 Unauthorized</b>	944	1046	9.75
<b>Register</b>	683	875	21.94
<b>200 OK</b>	976	1031	5.34
<b>Total</b>	<b>3189</b>	<b>3729</b>	<b>14.48</b>

b) *User Registration with signing in the precence server:* the

presence server provide users with their friends' states.



Fig. 3. The CIT IMS client.



Two more SIP messages are required to update the user state at the server. Table. II presents the presents the size of each message before and after compression. The results show saving

by 17.66% of the required signaling traffic to register the user with the IMS system and update its state at presenceserve

TABLE III. SIZE OF SIP MESSAGES FOR REGISTRATION AND CONTACT PRECENSE SERVER

SIP message	Size (byte)		Compression Ratio (%)
	With SigComp	Without SigComp	
<b>Register</b>	<b>586</b>	<b>777</b>	<b>24.58</b>
<b>401 Unauthorized</b>	<b>944</b>	<b>1046</b>	<b>9.75</b>
<b>Register</b>	<b>683</b>	<b>875</b>	<b>21.94</b>
<b>200 OK</b>	<b>976</b>	<b>1031</b>	<b>5.34</b>
<b>Subscribe</b>	<b>410</b>	<b>646</b>	<b>36.53</b>
<b>200 OK Subscription</b>	<b>692</b>	<b>837</b>	<b>17.32</b>
<b>Total</b>	<b>4291</b>	<b>5212</b>	<b>17.66</b>

c) *Session Establishing:* after registering with the IMS core, users can establish multimedia session with other online users by sending SIP invitation to the

other party. Table. III shows the required IMS messages to establish a multimedia session, and the size of each one before and after compression.

TABLE IV. SIZE OF SIP MESSAGES FOR ESTABLISH MULTIMEDIA SESSION

SIP message	Size (byte)		Compression Ratio (%)
	With SigComp	Without SigComp	
<b>Invite</b>	<b>1160</b>	<b>1313</b>	<b>11.65</b>
<b>100 Trying</b>	<b>543</b>	<b>768</b>	<b>29.30</b>
<b>180 Ringing</b>	<b>638</b>	<b>707</b>	<b>9.76</b>
<b>200 OK</b>	<b>976</b>	<b>1031</b>	<b>5.33</b>
<b>Total</b>	<b>3317</b>	<b>3819</b>	<b>13.14</b>

## VI. CONCLUSIONS

NGN/IMS is the current hot topic in the telecoms and IT industries. The main motivation of these technologies is

capability of quick and easy creation of new unprecedented services and applications. However the technology is young and there are numerous open areas for research.



Researchers need a field for validation of new ideas and applications. Open testbeds play a vital role in this context as they provide a safe testing environment for the academic and industrial parties. The Communication Research Group at the Collage of Industrial Technology (CIT) is working on improving their experience in building open testbeds, and hoping to share this experience with other national institutions.

The CIP IMS is the first IMS client supporting Arabic user interface and SigComp. The evaluation results of the client shows fine saving in the required bandwidth for signaling. Future work on the client will focus in programming a mobile version of the CIT IMS client.

Communication (ITC), 19-21/5/2008, Tripoli, Libya.

- [6] FOKUS, The Open IMS Core project. URL: <http://www.openimscore.org/>
- [7] University of Cape Town, UCT IMS Client project. URL: <http://uctimsclient.berlios.de/>
- [8] Hewlett-Packard, "IMS Bench SIPP," <http://sipp.sourceforge.net/imsbench/intro.html>, 2008,
- [9] Scalable Network Technologies: QualNet <http://www.scalablenetworks.com/products/developer.php>

#### REFERENCES

- [1] 3GPP. IP Multimedia Subsystem (IMS); Stage 2. TS 23.228, 3<sup>rd</sup> Generation Partnership Project (3GPP), December 2007.
- [2] M. Garcia-Martin, C. Bormann, J. Ott, etc., "The Session Initiation Protocol (SIP) and Session Description Protocol (SDP) Static Dictionary for Signaling Compression (SigComp)", IETF RFC3485
- [3] R. Price, C. Bormann, J. Christoffersson, etc., "Signaling Compression (SigComp)", IETF RFC3320
- [4] H. Hannu, J. Christoffersson, S. Forsgren, etc., "Signaling Compression (SigComp) – Extended Operations", IETF RFC3321
- [5] Asma A. Elmangosh, Majdi A. Ashibani, Fathi Ben Shatwan, "The Higher Institute of Industry (HII) IMS Testbed - Concepts and Architecture", The National Conference for Information Technology &



المؤتمر الدولي العربي الليبي الخامس للهندسة الكهربائية والإلكترونية 2010/10/26-23 طرابلس ليبيا





## Capacity – Coverage Product as a Tool for Dimensioning of Mixed Multi Rate Services WCDMA Mobile Networks

Ali S. Hjahaja  
LPTIC,  
Misurata, Libya.  
[alisalih\\_mis@yahoo.com](mailto:alisalih_mis@yahoo.com)

Abdulkader S. Akki  
Al-Fateh University  
Electrical & Electronic Engineering  
Department, Tripoli, Libya.  
[asakki@ltnet.net](mailto:asakki@ltnet.net)

### Abstract

This paper presents a methodology for utilizing Capacity-Coverage Product (CCP) as a tool for dimensioning and planning of single and mixed multi rate services WCDMA mobile networks. The comparison of this approach with the conventional one is performed, and advantages of this CCP approach are clarified.

### I- Introduction

The number of mobile service users has been tremendously increased during the last few years, and the types of mobile services are developed from pure voice to data and multimedia services, such as audio/video streaming, e-mail, file transfer, and web browsing. Thus there is a need to deal with mixed multi rate services, and these services have quite different requirements for their quality.

Third Generation Wide band Code Division Multiple Access (3G WCDMA) cellular mobile networks are one solution that answers this growing demand for these wireless data services. Then it needs to provide a huge capacity and wide area of coverage with acceptable quality of service.

The dimensioning and planning of mixed multi rate WCDMA mobile networks is not an easy task, this is because the random change of the service rate will cause a change in the capacity and consequently in the coverage of the network. The conventional dimensioning approach

involves a lot of steps and feedback loops.

Some of previous studies present an analytical technique for cellular planning of mobile radio networks by using hierarchical algorithm [1]. Some others are concerned with radio network dimension planning for WCDMA system using multi user detection [2].

Detailed WCDMA mobile network planning and optimization by using static simulations has been developed and derived in other studies [3].

In the last few years an evolutionary algorithm for the radio planning and coverage optimization of 3G cellular networks has been analyzed and explained [4].

Recent studies have been introduced to implement the capacity coverage product in WCDMA planning process [5].

The motivation of this paper is to implement CCP in dimensioning and planning of mixed multirate services in WCDMA cellular networks. A



comparison with the conventional planning method is to be performed.

## II- Dimensioning and Planning in Mixed Services WCDMA Network

Planning process of 3G WCDMA networks which support a lot of services and wide area of coverage is not easy task because the network must offer sufficient coverage and capacity while maintaining the lowest possible deployment costs. This needs to make feedback and adjustment on parameters estimated during the planning steps to get the optimized plan.

It is possible to facilitate this process by using mixed service capacity coverage product especially to estimate capacity and coverage.

In this section an over view on conventional method planning process will be presented first , then how can CCP be used in 3G network design will be explained.

### 1. Conventional Approach

Objectives of the planning process are to estimate the number of base station sites and their configurations, to calculate parameters of network elements and to analyze network capacity, coverage and quality of service conditions.

In this method WCDMA radio network planning process consists of three parts: dimensioning, capacity- coverage planning, and network optimization.

#### A. Dimensioning

WCDMA radio network dimensioning is a process through which possible configurations and the amount of network equipments are estimated based on operator's requirements related to the following:

- Coverage regions, area type information and propagation conditions.

- Spectrum available, subscriber growth forecast and traffic density information.
- Quality of service consists of area location probability (coverage probability), blocking probability and the end user throughput.

Dimensioning activities include radio link budget and coverage analysis, capacity estimation, and finally estimations on the amount of sites and base station hardware, radio network controllers, equipment at different interfaces, and core network elements [5].

#### B. Radio Link Budgets

In radio link budget calculations, WCDMA specific parameters are taken into account; these parameters are interference margin, fast fading margin and soft handover gain.

- *Interference margin*; the interference margin is needed in the link budget because of the loading of the cell. For coverage-limited cases a smaller interference margin is suggested because cell size is limited by the maximum allowed path loss in the link budge, while in capacity-limited cases a larger interference margin should be used.
- *Fast fading margin*; this applies especially to slow-moving mobiles where fast power control is able to effectively compensate the fast fading.
- *Soft handover gain*; handovers give a gain against slow fading by reducing the required log-normal fading margin. Soft handover gives an additional macro-diversity gain against fast fading by reducing the required  $E_b/N_0$ .

Data rates, mobile speeds, coverage requirement, terrain types and asymmetry factors are factors that must be assumed in the link budgets.



For the base station, noise figure, antenna gain, Eb/No requirement and cable loss also must be assumed.

For the mobile station maximum transmission power, antenna gain, and body loss are parameters that must be specified.

### C. Coverage Calculation Steps

The coverage estimation steps can be summarized as follows:

1. For the given parameters, calculation of the radio link budget for a chosen traffic type must be done with the maximum system load.
2. Calculate the maximum cell range for a given link budget and taking into account the propagation model for the current terrain type.
3. Calculate the number of users within the cell for a computed cell area.
4. The maximum number of subscribers that covered by each BTS can be calculated by the soft capacity equation.
5. If the number of subscribers for each cell is greater than the maximum number of users of each BTS then reduce the radius and come back to calculate a new number of users in the cell again, and if the number of subscribers for each cell is a smaller than the maximum number of users in each BTs then it is necessary to reduce the maximum system load value and then return to the beginning to give a smaller value of the maximum system load and then the cell radius will increase.
6. Taking the link budget into consideration, the cell range  $d$  can be readily calculated for a known propagation model, e.g. *Okumura-Hata* model, which is a model that is used to calculate the propagation path loss and

it is a function of the cell range  $d$  and other known parameters.

7. By knowing the cell radius, the area of the cell can be estimated and the number of BTS can be known. With the distribution of people we can estimate the number of users within the cell and the load factor equation can then be used by trial and error solution.
8. To get the actual  $d$  for the cell, the estimated value of the load factor is changed and all the above steps are repeated to get the suitable load factor. Flow chart in Figure 1 explains the steps of planning procedure in this approach.

### D. Cell Capacity Calculation

The objective of WCDMA is to meet the user requirement for innovative services such as multimedia messaging and web browsing through high speed data channels. The main target of network planning is to maximize coverage, capacity and the quality of service.

Some assumptions must be considered when we calculate the static capacity in a particular cell, these are:

- \* There are no inter-cell interference and intra-cell interferences.
- \* There is perfect power control and no limit of spreading codes.

If the voice activity gain factor  $G_v$  and the sectorization gain factor  $G_s$  are considered, then from cell capacity equation [5], we can write the following

$$N_e - 1 = G_v \cdot G_s \cdot \left( \frac{W/R}{E_b/N_o} \right) - \frac{\eta}{S} \text{ (users)..(1)}$$

where

$N_e$  is the effective number of users.

$W$  is the system chip rate.



$R$  is the service rate.

$E_b/N_o$  is the bit energy per noise power spectral density that satisfy performance requirements.

$\eta$  is the thermal noise density.

$S$  is the received signal power.

Apply the definition of *SIR* in equation (1), we get the following, [6]:

$$N_{\phi} - 1 = G_v \cdot G_s \cdot \left( \frac{W/R}{E_b/N_o} - \eta/S \right) \left( \frac{1}{1+f} \right) \text{ (users)..(2)}$$

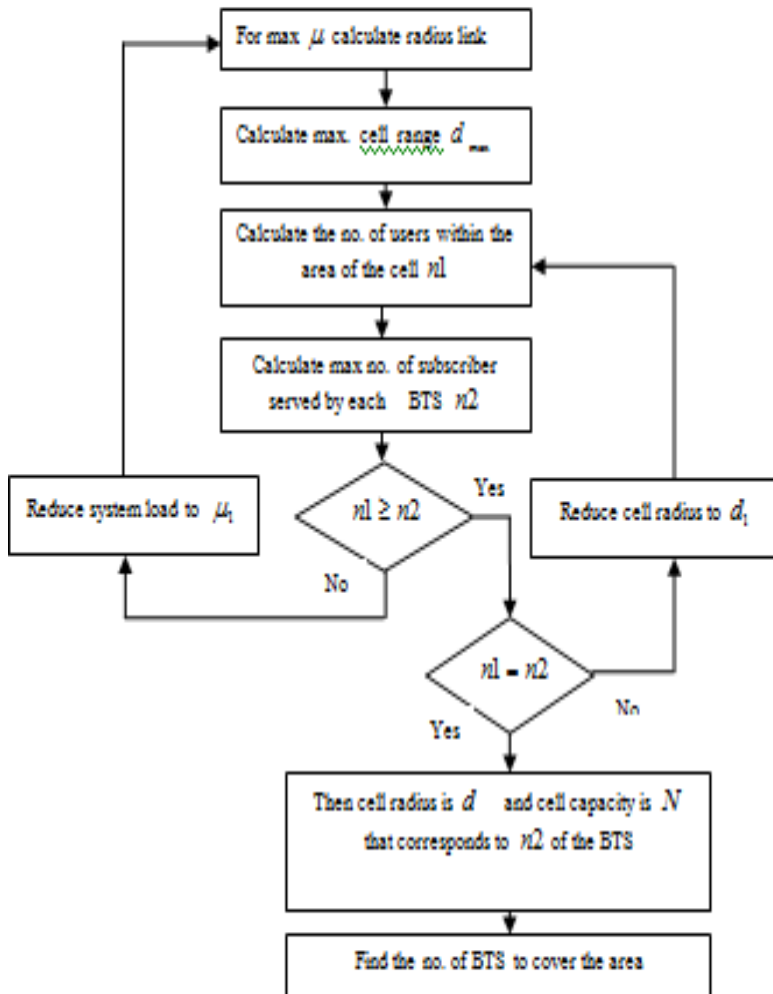


Figure 1. Planning procedure algorithm in conventional method.



where

$N_{\phi}$  is the actual number of users.

$f$  is the interference factor.

A guaranteed bit rate must be assumed to assure that all the network subscribers are to be covered by the service but that will be at the expense of the cost.

Three cases can be considered at the beginning of any design process. They are:

- *Design based on maximum required bit rate*; in this case the radius will be smaller and the number of BTS will be higher than required, then the other services will not suffer coverage problem.
- *Design based on minimum required bit rate*; in this case the cell radius will have maximum value and then the number of BTS will be minimum. The higher bit rate services will suffer coverage problem.
- *Design based on an average bit rate between the maximum and minimum bit rates*; this case will give a tradeoff between the number of BTS required and the coverage and quality requirement for other services.

## 2. CCP Implementation Approach

The mixed services capacity coverage product was obtained by multiplying capacity and coverage.

Once this product is given for specific weights of services, the capacity of the mixed services cell is calculated according to the average coverage. The coverage can be estimated based on the number of mixed users.

The steps of planning procedure in the case of CCP implementation for mixed services network are displayed by Flow chart in Figure 2 and can be summarized as:

- i. From services probabilities  $p_1, p_2, p_3$  the  $CCP_{mix}$  can be found from  $CCP_{mix}$  versus services probabilities [5].
- ii. The mixed services coverage  $d_{mix}$  can be found from the  $CCP_{mix}$  versus coverage curve that satisfies the coverage probability, Figure 3. The explanation of this curve can be found in reference [5].

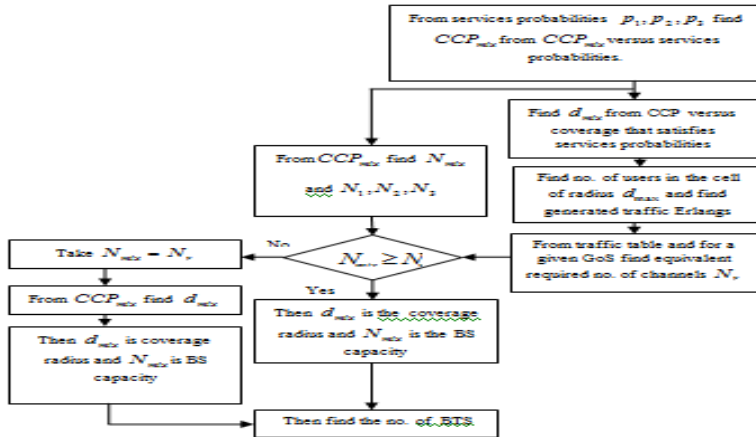


Figure 2. Planning procedure algorithm in CCP implementation method for mixed services.

- iii. Then the number of mixed users in the cell of radius  $d_{mix}$  can be estimated, consequently the guaranteed traffic in Erlang can be derived.
- iv. From the traffic table and for a given GoS, The equivalent number of channels  $N_r$  can be estimated.

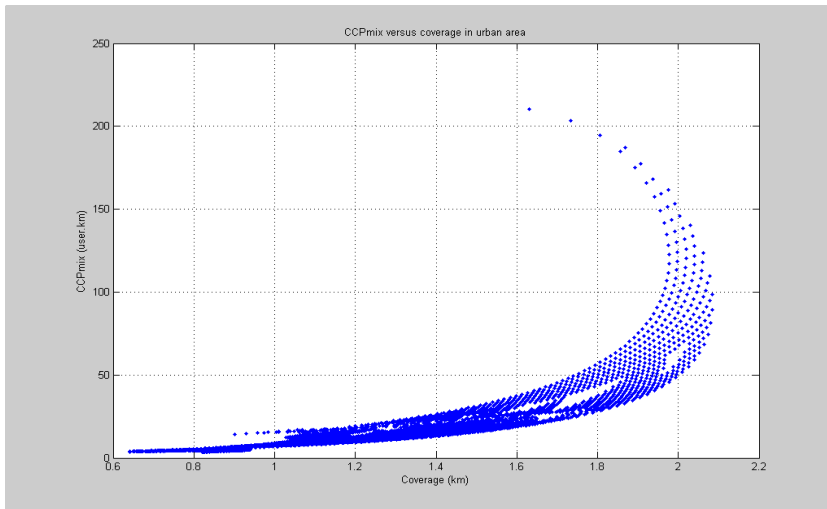


Figure 3. The relationship between  $CCP_{mix}$  and cell coverage.



- v. The number of mixed services users  $N_{mix}$  can also be found from Figure 4 for the specified services probabilities. The explanation of this curve can be found in reference [5].
- vi. If the number of active users is greater than or equal the number of channels then  $d_{mix}$  is the coverage radius and  $N_{mix}$  is the BS capacity and then the number of BTS can be found.
- vii. From services probabilities  $p_1, p_2, p_3$  the  $CCP_{mix}$  can be found from  $CCP_{mix}$  versus services probabilities [5].
- viii. The mixed services coverage  $d_{mix}$  can be found from the  $CCP_{mix}$  versus coverage curve that satisfies the coverage probability, Figure 3.
- ix. Then the number of mixed users in the cell of radius  $d_{mix}$  can be estimated, consequently the guaranteed traffic in Erlang can be derived.
- x. From the traffic table and for a given GoS, The equivalent number of channels  $N_r$  can be estimated.
- xi. The number of mixed users  $N_{mix}$  can also be found from Figure 4 for the specified services probabilities.
- xii. If the number of active users is greater than or equal the number of channels then  $d_{mix}$  is the coverage radius and  $N_{mix}$  is the BS capacity and then the number of BTS can be found.

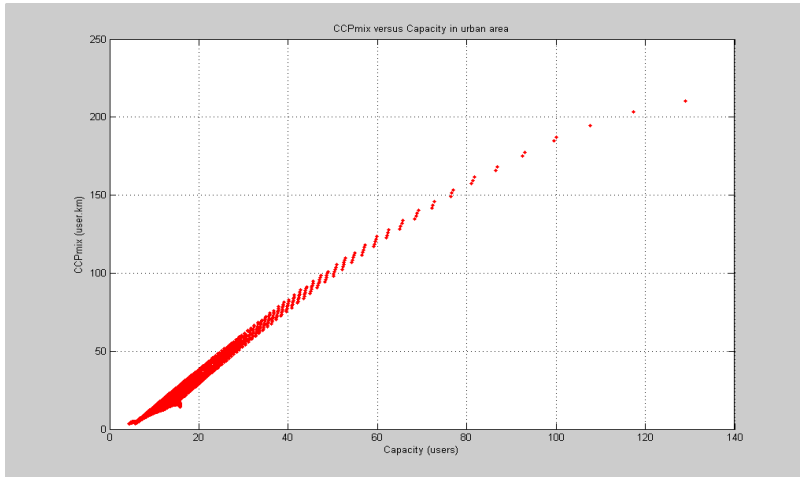


Figure 4.  $CCP_{mix}$  versus cell capacity for urban area.



- xiii.** If the number of channels is greater than the number of mixed users then take  $N_{mix} = Nr$ , and from  $CCP_{mix}$  equation we can find the cell radius  $d_{mix}$ , consequently  $d_{mix}$  can be considered as the coverage radius and  $N_{mix}$  is the BS capacity.
- xiv.** Finally, the number of BTS can be found.

### III- Comparison Between The Two Approaches

In multirate services WCDMA networks, the planning process using the conventional approach has more number of steps and complexity. Comparison with the CCP approach reveals the following:

- Number of the design or planning steps in the CCP approach is less than in the conventional approach.
- The complexity of planning process in the conventional approach is more when we compare it with the CCP approach.
- In the CCP method the optimum value of the capacity or coverage can be calculated directly and exactly and no need to make a tradeoff between bit rate and coverage.
- By specifying the percentage of each service in the mixed services we can calculate the related CCP and then we can find the capacity or the coverage of the cell directly from the CCP equations and curves.
- No need to perform feedback loop on the design steps, and the results can be obtained directly.
- WCDMA networks support several types of services, and then the percentage, data rate, bit energy per noise density, and activity factor of

each service must be specified. Now the capacity of mixed services of a cell can simply be calculated from mixed multirate services capacity equation[1]

### IV- Conclusion

The development of radio mobile networks is going towards more efficient usage of Wideband CDMA technology. The 3G denote introductions of several new services over mobile networks.

Dimensioning and detailed planning of WCDMA networks require consideration of many system performance measures, defining system parameters and requires many steps with feedback loop calculations.

In this paper the application of the mixed multirate services CCP in WCDMA cellular networks dimensioning and design steps or planning process has been presented, and compared with the conventional planning method.

A methodology and flowchart for implementing CCP as a tool to facilitate the planning process and decrease the number of design steps are explained.

### V- References

- [1] Syed Zahid Ali, "An Analytical Technique for Cellular Planning of Mobile Radio Networks", *IEEE VTC Vehicular Technology Conference 2002*, pp. 1340 - 1344 vol.3, 2002.
- [2] Zhiheng Hu, Weiwen Tang & Juebang Yu, "Radio Network Dimension Planning for WCDMA System Using Multiuser Detection", *Communications, Circuits and Systems International Conference 2004, ICCAS 2004*, PP. 467 - 470 Vol.1, 2004.





- [3] Toni Janevski, Vladimir Nikolic, "Detailed WCDMA Mobile Network Planning by using Static Simulations", *Telecommunications in Modern Satellite, Cable and Broadcasting Services International Conference 2007*, pp.175 – 178, TELSIXS 2007, November 2007.
- [4] Fangqing Gu, Hailin Liu, Ming Li, "Evolutionary Algorithm for the Radio Planning and Coverage Optimization of 3G Cellular Networks", *Computational Intelligence and Security International Conference 2009*, pp. 109 – 113 Vol.2, 2009.
- [5] Hjahaja A. Salih, "The Impact of Mixed Multirate Services on Uplink Capacity-Coverage Product in WCDMA Mobile Networks", *Ms.c. thesis Al-fateh University, Faculty of Engineering*, September 2008.
- [6] Theodore S. Rappaport, "Wireless Com -munications Principle and practice", Hall PTR, New Jersey, 1996.



المؤتمر الدولي العربي الليبي الخامس للهندسة الكهربائية والإلكترونية 2010/10/26-23 طرابلس ليبيا



## Derivation and Characteristics of the Uplink Capacity – Coverage Product of Mixed Multirate Services in WCDMA Mobile Networks

Ali S. Hjahaja  
LPTIC  
Misurata, Libya.  
[alisalih\\_mis@yahoo.com](mailto:alisalih_mis@yahoo.com)

Abdulkader S. Akki  
Al-Fateh University  
Electrical & Electronic Engineering  
Department, Tripoli, Libya.

[asakki@ltnet.net](mailto:asakki@ltnet.net)

### Abstract

This paper presents a derivation of the uplink capacity-coverage product equation for WCDMA mobile networks providing mixed multi-rate services. The effect of three scenarios of mixed multi-rate services on this CCP is studied. The impact of specific WCDMA network parameters on the capacity-coverage product is investigated.

### I- Introduction

Wide band Code Division Multiple Access (WCDMA) systems are provided to support the growing wireless communications and internet applications. High rate data services with high performance are obtained. The planning of 3G-WCDMA networks needs to take into account coverage and capacity planning. The coverage of a cell has an inverse relationship with the user capacity of the same cell.

An increase in the number of active users in the cell causes an increase in the total interference seen at the receiver. For satisfactory performance, it is necessary to increase the power required to be received from each user to maintain a certain Signal-to-Interference Ratio (SIR).

For a given maximum allowable transmission power, an increase in the required power reception will result in a decrease in the maximum distance a mobile can be from the base station thereby

reducing the coverage, this is why trade-off between coverage and capacity in WCDMA systems design is to be considered.

The multi-rate services analysis is not an easy task, because the coverage and capacity of the network will change randomly in accordance with change of the service rate. The study of this problem using CCP approach worth to be performed. So the effect of these multirate services on the CCP is to be studied for a uniform user's distribution over the coverage area.

Some of previous studies are concentrated on Coverage-Capacity Tradeoff in Cellular CDMA Systems [1]. Others are concerned with Capacity Estimation for Multi-code CDMA systems with SIR-Based Power Control [2]. Capacity Evaluation of a Mixed-Traffic WCDMA System in the Presence of Load Control is analyzed in other studies [3].



The Coverage-capacity Trade-off in Multiservice WCDMA Cellular Systems with Serial Interference Cancellation is studied and derived before [4]. The capacity coverage product in macro-cell CDMA mobile networks of single service is derived [5].

Recent studies are concerned with the impact of mixed multirate services on the uplink capacity-coverage product in WCDMA mobile networks [6]

Motivations of this paper are to expand our information about capacity and coverage of 3G WCDMA cellular networks, recognize how they are related with each other in the case of mixed multi rate services, and develop a CCP formula that may facilitate design steps. The main objectives of this paper can be summarized as follows:

- To derive the uplink capacity coverage product equation for WCDMA mobile network working on multirate services for the case of uniform user distributions and to study effect of mixed multirate services on it.
- To investigate the effect of specific WCDMA network parameters on the capacity-coverage product.

## II- Uplink CCP of Mixed Multirate Services

It is well known that in WCDMA network the capacity and coverage have inverse relationship that is the increase in one will result in decrease of the other and vice versa. Thus it is desirable to have a factor or parameter that takes care of both coverage and capacity at the same time. This factor or parameter might be multiplication, division or addition of coverage and capacity of the network.

### A. CCP Concept and Why CCP?

The multiplication of capacity and coverage is chosen based on analogy of the bandwidth-distance product parameter used in fiber optic system. With CCP we can have a view of both capacity and coverage.

Uplink capacity and coverage are related to each other in 3G WCDMA cellular networks, especially in the case of multi-rate services. Different types of services require different data-rates and received signal power levels with different amount of interference have effect directly on the cell coverage radius.

### B. System Assumptions

The main assumptions of the model are:

- The considered model is a WCDMA cellular network.
- It supports three types of users, i.e. three types of services or data rates (e.g.: voice, data and video or voice, real time data and non-real time data), [6].
- Users are distributed uniformly around the base station.
- Model coverage area is divided into hexagonal cells with a base station located at the center of each cell.
- The model services are assumed to be mixed and each service has its own activity factor, bit energy-per-noise power spectral density and transmitted power.

Three scenarios are considered in this paper. The first scenario deals with mixed traffic where voice is dominant. Equally likely of data and video traffic is considered in the second scenario. In the third scenario, voice and data services traffic have the same percentage. The three service probabilities for three scenarios are explained in Table I.



Table I. The three service probabilities for three scenarios.

Scenario/service	Voice probability ( $p_1$ )	data probability ( $p_2$ )	Video probability ( $p_3$ )
Scenario1	0.75	0.20	0.05
Scenario2	0.50	0.25	0.25
Scenario3	0.45	0.45	0.10

### C. Factors Affecting Capacity and Coverage

- *The activity factor ( $\alpha$ )* is defined as the time when the user is really active during the service processing time.
- *The power control algorithm function* is to maintain the received power from each user constant. The system capacity reduces due to imperfect power control depending on the standard deviation of power control error and the service activity factor. ( $\delta$ )
- *The sectorization gain ( $G$ )* is the capacity gain produced from dividing the cell coverage area into non-overlapping sectors. The more number of sectors per each cell, the higher capacity of the cell.
- *Interference Factor ( $f$ )* is the ratio of the other-cells interference power to own-cell interference power. It is not an easy task to calculate this factor because its value depends on several random variables. [6].

### D. Capacity Derivation and Analysis

The capacity of the cell is defined by the number of connections that can simultaneously exist with an acceptable level of mutual interference [6]. Uplink (Reverse link) capacity is limited by the

amount of interference caused by mobile units.

The system capacity of multiservice or multimedia services in a macro-cell in multi-cell environment is to be introduced. Three types of services of three data rates are considered in our model. Each service has its own activity factor, bit energy-per-noise spectral density and transmitted power. Define the following:

$S_{1i}$  is the power received at the Base Station (BS) due to the  $i$ th voice user.

$S_{2i}$  is the power received at the BS due to the  $i$ th data service1 user.

$S_{3i}$  is the power received at the BS due to the  $i$ th data service2 user.

$R_1$  is the voice service data rate.

$R_2$  is the data service1 data rate.

$R_3$  is the data service2 data rate.

$E_b/N_o$  is bit energy per noise power spectral density that satisfy performance requirements.

For the  $i$ th service user, the received

$\left(\frac{E_b}{N_o}\right)_{li}$  is given by

$$\left(\frac{E_b}{N_o}\right)_{li} = \frac{W}{R_1} \cdot \frac{S_{1i}}{\eta_o W + I_{own} + I_{other} - S_{1i}} \quad (1)$$

where

$\eta_o$  is the background noise power spectral density.

$W$  is the spreading bandwidth.



$I_{other}$  the total power received from mobiles within other cells of our network, for simplicity we call it as  $I$ .

$I_{own}$  is the total power received from mobiles within the considered cell, and it is given by

$$I_{own} = \sum_{k=1}^{N_1} \alpha_1 S_{1k} - \alpha_1 S_{1i} + \sum_{k=1}^{N_2} \alpha_2 S_{2k} + \sum_{k=1}^{N_3} \alpha_3 S_{3k} \quad (2)$$

where  $N_1$ ,  $N_2$  and  $N_3$  are the number of users of voice, data1 and data2 respectively.

$\alpha_1$ ,  $\alpha_2$  and  $\alpha_3$  are the activity factors for voice, data1 and data2 respectively.

We assume a power control mechanism is used such that the signal received for each class of service is the same. That is

$$S_{ik} = S_i \quad \text{for} \quad k = 1, \dots, N_i \quad (3)$$

thus from (2) and (3) equation (1) can be written as

$$\left(\frac{E_b}{N_o}\right)_i = \frac{W}{R_i} \cdot \frac{S_i}{\alpha_1(N_1-1)S_1 + \alpha_2 N_2 S_2 + \alpha_3 N_3 S_3 + I + \eta_o W} \quad (4)$$

Assume that the background noise  $\eta_o W$  is negligible compared to the user interference, then

$$\left(\frac{E_b}{N_o}\right)_i = \frac{W}{R_i} \cdot \frac{S_i}{\alpha_1(N_1-1)S_1 + \alpha_2 N_2 S_2 + \alpha_3 N_3 S_3 + I} \quad (5)$$

Similarly for the received  $\left(\frac{E_b}{N_o}\right)_2$  and

$\left(\frac{E_b}{N_o}\right)_3$  for the data1 user group and data2 user group.

The relation between the received signal powers of user groups is achieved [6], this means that the received signal power plus total noise power is the same for each class of service where

$$(SIR)_i = \frac{R_i}{W} \left(\frac{E_b}{N_o}\right)_i, \quad i = 1, 2, 3, \dots \quad (6)$$

To satisfy the quality requirement for various services for all user groups the received  $\left(\frac{E_b}{N_o}\right)_i$  should be greater than the

required minimum  $\left(\frac{E_b}{N_o}\right)_{im}$ , so

$$\left(\frac{E_b}{N_o}\right)_i \geq \left(\frac{E_b}{N_o}\right)_{im} \quad (7)$$

The minimum values  $\left(\frac{E_b}{N_o}\right)_{im}$  are that

required to satisfy reliability requirement  $\beta = 0.99$  for each service. That is

$$P\left[\left(\frac{E_b}{N_o}\right)_i \geq \left(\frac{E_b}{N_o}\right)_{im}\right] = \beta = 0.99 \quad (8)$$

From equation (6) and (8) the received

$\left(\frac{E_b}{N_o}\right)_i$  are limited as follows:



$$\left(\frac{E_b}{N_o}\right)_{1m} \leq \left(\frac{E_b}{N_o}\right)_1 \leq \frac{W}{R_{1r}} \cdot \frac{S_1}{\alpha_1(N_1-1)S_1 + \alpha_2 N_2 S_2 + \alpha_3 N_3 S_3 + I} \quad (9)$$

$$\left(\frac{E_b}{N_o}\right)_{2m} \leq \left(\frac{E_b}{N_o}\right)_2 \leq \frac{W}{R_{2r}} \cdot \frac{S_2}{\alpha_1 N_1 S_1 + \alpha_2 (N_2-1)S_2 + \alpha_3 N_3 S_3 + I} \quad (10)$$

$$\left(\frac{E_b}{N_o}\right)_{3m} \leq \left(\frac{E_b}{N_o}\right)_3 \leq \frac{W}{R_{3r}} \cdot \frac{S_3}{\alpha_1 N_1 S_1 + \alpha_2 N_2 S_2 + \alpha_3 (N_3-1)S_3 + I} \quad (11)$$

From these equations, the number of users  $N_1, N_2$  and  $N_3$  are upper bounded as follows:

$$\alpha_1(N_1-1)S_1 + \alpha_2 N_2 S_2 + \alpha_3 N_3 S_3 + I \leq \frac{W}{R_{1r}} \left(\frac{E_b}{N_o}\right)_{1m}^{-1} S_1 = (SIR)_{1m}^{-1} S_1 \quad (12)$$

Applying the relation between the received signal powers of the user groups, the relation between the user numbers and the required  $SIR$  is

$$\frac{\alpha_1 N_1}{(SIR)_{1m}^{-1} + \alpha_1} + \frac{\alpha_2 N_2}{(SIR)_{2m}^{-1} + \alpha_2} + \frac{\alpha_3 N_3}{(SIR)_{3m}^{-1} + \alpha_3} \leq 1 - Z_l \quad (13)$$

where

$$Z_l = \frac{I}{S_i} \cdot \frac{1}{(SIR)_{im}^{-1} + \alpha_i} \quad (14)$$

Equation (13) can be simplified as follows

$$\psi_1 \cdot N_1 + \psi_2 \cdot N_2 + \psi_3 \cdot N_3 \leq 1 - Z_l \quad (15)$$

where

$$\psi_i = \frac{\alpha_i}{(SIR)_{im}^{-1} + \alpha_i}, \quad i = 1, 2, 3, \dots \quad (16)$$

This equation specifies a capacity plane in a three dimensional space. All points  $(N_1, N_2, N_3)$  under the plane represent possible number of supportable users in voice, data1 and data2 user groups in a sector or a cell.

Since  $Z_l$  is a Gaussian random variable, then we can get the following [6]

$$\psi_1 \cdot N_1 + \psi_2 \cdot N_2 + \psi_3 \cdot N_3 + \langle Z_l \rangle + 2.33\sqrt{\text{var}(Z_l)} \leq 1 \quad (17)$$

Substituting for  $\langle Z_l \rangle$  to get

$$(1 + 0.559)(\psi_1 \cdot N_1 + \psi_2 \cdot N_2 + \psi_3 \cdot N_3) + 2.33\sqrt{\text{var}(Z_l)} \leq 1 \quad (18)$$

In general  $\text{var}(Z_l)$  is very small because  $\psi_1, \psi_2, \psi_3 \leq 1$ , so it can be neglected, then

$$(1 + f)(\psi_1 \cdot N_1 + \psi_2 \cdot N_2 + \psi_3 \cdot N_3) \leq 1 \quad (19)$$

$$\text{where } f = 0.559 \cdot [6]$$

Figure 1 clarifies how the total system resource is utilized by different users of different class service. The term  $\psi_i$  can be considered as the individual required Signal to Total Power Ratio (STPR) that corresponds to a particular rate, i.e.

$$\psi_i = \frac{\alpha_i}{\alpha_i + (SIR)_i^{-1}} = \frac{\alpha_i \cdot S_i}{\alpha_i \cdot S_i + N_o W} \quad (20)$$



This term can also be denoted as normalized bandwidth required by individual of class service  $i$ .

If loading factor  $\mu$  is defined as the ratio of the working capacity  $N$  to the pole capacity  $N_{pole}$ .

From Figure 1-b, the loading factor is given by

$$\mu = \frac{1-\rho}{1} = (1+f) \cdot \sum_{j=1}^g \psi_j N_j \quad (21)$$

$$\mu = \frac{N}{N_{pole}} \quad (22)$$

where  $g$  is the number of services in the network.

From equation (21) and equation (22), the system capacity is

$$N = \sum_{j=1}^g N_j = \mu \cdot N_{pole} = (1+f) \cdot N_{pole} \cdot \sum_{j=1}^g \psi_j \cdot N_j \quad (23)$$

$$N_{pole.mix} = \frac{\sum_{j=1}^g N_j}{(1+f) \sum_{j=1}^g \psi_j \cdot N_j} \quad (24)$$

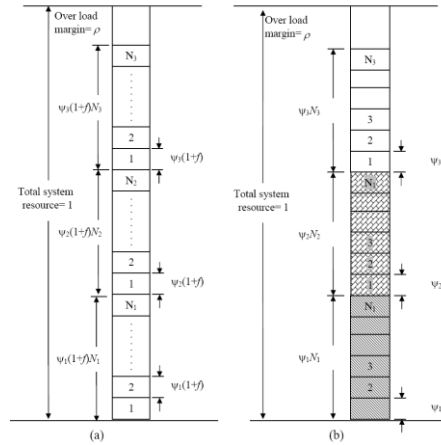


Figure1. Allocation of system resource to the users of different services. (a)Single cell in a multiple environment. (b) Isolated single cell.

By substituting the  $j^{th}$  service weight equation

$$p_j = \frac{N_j}{\sum_{q=1}^g N_q} = \frac{N_j}{N_{mix}} \quad (25)$$

and substituting for  $\psi_j$  in equation (24) the  $N_{pole.mix}$  can be written as

$$N_{pole.mix} = \frac{W}{(1+f) \sum_{j=1}^g p_j \cdot \alpha_j \cdot R_j \left( \frac{(E_b/N_o)_j}{1 + \alpha_j (E_b/N_o)_j} (R_j/W) \right)} \quad (26)$$

this coincide with the result obtained in previous work [6], then consequently the capacity  $N_{mix}$  is given by





$$N_{mix} = \mu \cdot \frac{W}{(1+f) \sum_{j=1}^g p_j \cdot \alpha_j \cdot R_j \left( \frac{(E_b/N_o)_j}{1 + \alpha_j \cdot (E_b/N_o)_j} \cdot (R_j/W) \right)}$$

(users/cell) (27)

As an example consider a system with two user groups, including voice of 12.2 kbps and data of 64 kbps. The assumed system parameters are also included in Table II.

Table II. Example of a system with three user group parameters.

Item	Symbol	Value
Bandwidth	$W$	3.84 MHz
Voice activity factor	$\alpha_1$	0.625
Data1 activity factor	$\alpha_2$	0.8
Data2 activity factor	$\alpha_3$	1
Voice data rate	$R_1$	9.6 kbps-12.2 kbps
Data1 group rate	$R_2$	64 kbps -144 kbps
Data2 group rate	$R_3$	384 kbps
Quality required for voice	$(E_b/N_o)_{req}$	(1 dB- 7 dB) (1.2- 5)
Quality required for data1	$(E_b/N_o)_{req}$	(3.5 dB) (2.2)
Quality required for data2	$(E_b/N_o)_{req}$	(1.5 dB) (1.4)

The case for three different types of services, the capacity plane is plotted in Figure 2. Each service has

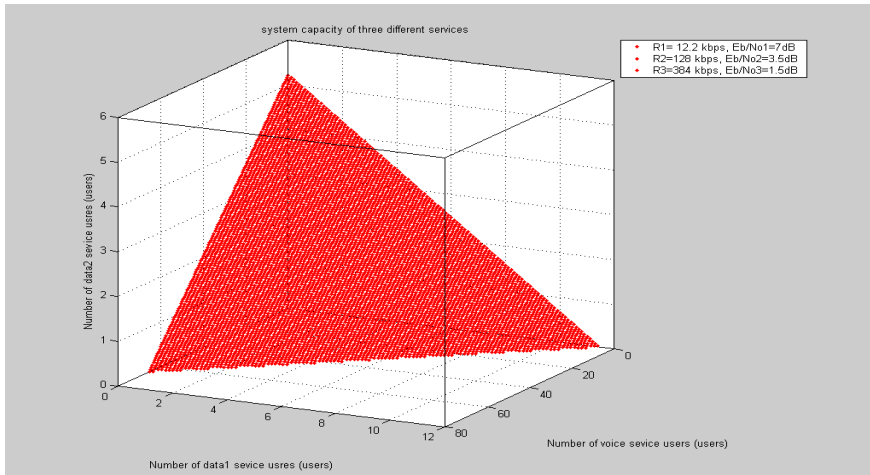


Figure 2. Capacity plane for different users, voice users, data1 and data2 users.

data rate,  $E_b/N_o$  and service activity factor. The data1 and data2 rates are 128kbps and 384 kbps,  $E_b/N_o$ 's are equal to 3.5 dB and 1.5 dB, and the activity factors are 0.8 and 1 respectively. The capacity of the

system is the volume bounded by equation (19) under the red plane. From each point in the capacity plane, the number of possible voice users, data1 users and data2 users are obtained.



### E. Total Available System Resource

It is as the total number of equivalent voice resources (or channels) that the system can support. This depends on the loading factor  $\mu$  of the system and the normalized bandwidth or resource needed for one voice user.

From equation 21, the total number of resources is given by the integer value of

$\frac{\mu}{(1+f)\psi_1}$  so equation 28 can be written as

$$\frac{\mu}{(1+f)\psi_1} = N_1 + \frac{\psi_2}{\psi_1} \cdot N_2 + \frac{\psi_3}{\psi_1} \cdot N_3 + \dots \quad (28)$$

The factors  $\frac{\psi_2}{\psi_1}$  and  $\frac{\psi_3}{\psi_1}$  are multiplication factors used to convert number of data users and video users to an equivalent number of voice users.

Thus the total number of available resources

$$= N_1 + \frac{\psi_2}{\psi_1} \cdot N_2 + \frac{\psi_3}{\psi_1} \cdot N_3 \quad \text{and these}$$

resources are to be allocated to users of different services. When these resources are utilized the cell, admission control will intervene to stop admitting new users.

### F. Coverage Derivation and Analysis

Equation (4) can be rearranged by taking into account the other interferences in details and neglecting the thermal noise term when it compared to interferences. Thus we can write the following

$$\left(\frac{E_b}{N_o}\right)_1 \left(\frac{R_1}{W}\right) = \frac{S_1}{\alpha_1(N_1-1)S_1 + \alpha_2 N_2 S_2 + \alpha_3 N_3 S_3 + f \cdot \sum_j^3 \alpha_j N_j S_j + \eta \cdot W} \quad (29)$$

$$(SIR)_i = \frac{S_i}{\alpha_i(N_i-1)S_i + f\alpha_i N_i S_i + \alpha_2 N_2 S_2 (1+f) + \alpha_3 N_3 S_3 (1+f) + \eta \cdot W} \quad (30)$$

where  $(SIR)_1 = \left(\frac{E_b}{N_o}\right)_1 \cdot \left(\frac{R_1}{W}\right)$

and

$$(SIR)_i = \frac{S_i}{\alpha_i(N_i-1)S_i + f\alpha_i N_i S_i + (1+f) \sum_{j \neq i}^g \alpha_j N_j S_j + \eta \cdot W} \quad (31)$$

from the following condition [6]

$$S_1 \cdot (SIR)_1^{-1} = S_2 \cdot (SIR)_2^{-1} = S_3 \cdot (SIR)_3^{-1} = N_o \cdot W \quad (32)$$

Then

$$S_i = N_o \cdot W \cdot (SIR)_i \quad (33)$$

also

$$(SIR)_1 \cdot [\alpha_1 \cdot [(1+f)(N_1 + N_2 + N_3) - 1] + \eta \cdot W / S_1] = 1 \quad (34)$$

Solving for  $S_1$  to get the following

$$S_1 = \frac{\eta \cdot W}{(SIR)_1^{-1} - \alpha_1 \cdot [(1+f)(N_1 + N_2 + N_3 + \dots) - 1]} \quad (35)$$

Similarly for  $S_2$  and  $S_3$ , so



$$S_i = \frac{\eta \cdot W}{(SIR)_i^{-1} - \alpha_i \cdot \left[ (1+f) \cdot \sum_{j=1}^g N_j - 1 \right]} \quad (36)$$

where  $g$  is the number of services.

The received power at the Base Station from a user  $i$  of class  $j$  service,  $S_{ij}$  is given by

$$S_{ij} = S_{Tij} - L_p(d_j) - Z \quad (37)$$

where  $S_{Tij}$  is the transmitted power of user  $i$  of  $j^{th}$  service,  $L_p(d_j)$  is the propagation path loss and  $Z$  is shadow fading.

Due to the power control mechanism  $S_{ij} = S_j$  &  $S_{Tij} = S_{Tj}$

Thus equation (37) becomes

$$S_j = S_{Tj} - L_p(d_j) - Z, \quad j = 1, 2, 3, \dots, g \quad (38)$$

To satisfy the same quality, equation (38) and (36) should be equal for the same service (taking care to equate the units), that is

$$S_{Tj} - L_p(d_j) - Z = 10 \log \left( \frac{\eta \cdot W}{(SIR)_j^{-1} - \alpha_j \cdot \left[ (1+f) \cdot \sum_{q=1}^g N_q - 1 \right]} \right) \quad (39)$$

where  $(q = 1, 2, 3, \dots, g)$  is the number of services, and

$$L_p(d_j) = a + b \cdot \log(d_j) \quad (40)$$

Substitute equation (40) in equation (39) and solve for  $d_j$  to get

$$d_j = 10^{\left( \frac{S_{Tj} - Z - a - 10 \log(\eta \cdot W) + 10 \log \left[ (SIR)_j^{-1} - \alpha_j \cdot \left[ (1+f) \cdot \sum_{q=1}^g N_q - 1 \right] \right]}{b} \right)} \quad (41)$$

Let

$$C_j = \frac{S_{Tj} - Z - a - 10 \log(\eta \cdot W)}{b}, \quad \gamma = b/10 \quad \text{and} \quad d_{oj} = 10^{(C_j)}$$

Then

$$d_j = 10^{(C_j)} \cdot 10^{\frac{\log \left[ (SIR)_j^{-1} - \alpha_j \cdot \left[ (1+f) \cdot \sum_{q=1}^g N_q - 1 \right] \right]}{\gamma}} \quad (42)$$

now, equation (3.62) can be expressed as

$$d_j = d_{oj} \cdot \left( (SIR)_j^{-1} - \alpha_j \cdot \left[ (1+f) \cdot \sum_{q=1}^g N_q - 1 \right] \right)^{\frac{1}{\gamma}} \quad (43)$$

$d_i$  is coverage radius for  $j^{th}$  service.

If  $p_j$  is the probability of occurrence of service  $j$  or its service weight, then the average coverage radius of mixed services is given by



$$d_{mix} = \sum_{j=1}^g d_j \cdot p_j \quad (\text{km}) \quad (44)$$

### G. CCP Derivation and Analysis

Now, the average capacity coverage product  $CCP_{mix}$  can be written as

$$\begin{aligned} CCP_{mix} &= N_{mix} \cdot d_{mix} \\ &= N_{polestix} \cdot \mu \cdot \sum_{j=1}^g d_j \cdot p_j \quad (\text{user.km}) \end{aligned} \quad (45)$$

If  $p_j$  is interpreted as the ratio of number of active users of  $j^{th}$  service to the total number of active users, from equation (3.45), then

$$CCP_{mix} = \sum_{j=1}^g N_j \cdot d_j \quad (\text{user.km}) \quad (46)$$

Or from equations (44), (46) & (45),  $CCP_{mix}$  can be written as follows

$$CCP_{mix} = \mu \cdot \left( \frac{W}{(1+f) \sum_{j=1}^g p_j \cdot \alpha_j \cdot R_j \left( \frac{(E_b/N_o)_j}{1 + \alpha_j (E_b/N_o)_j (R_j/W)} \right)} \right) \cdot \sum_{j=1}^g d_j \cdot p_j \quad (\text{user.km}) \quad (47)$$

Figures 3 & 4 explain the effect of services weights on  $CCP_{mix}$  which is defined by equation (47). Each point in the sketched regions represents the average CCP of specific three values of service weights.

The empty spaces in the regions represent impossible combination of the service mix probabilities. That is the cases where equation  $p_1 + p_2 + p_3 \neq 1$ . The numerical parameters values which are used in equation (47) are given in Table III.

Table III. Parameters of the three types of services.

Service/Parameter	Voice-service	Data-service	Video-service	Notes
R (kpbs)	12.2	144	384	
S (dBm)	21	21	21	
Eb/No(dB)	5	1.5	1	
$f$	0.55	0.55	0.55	Omni directional antenna
$\alpha$	0.375	1	1	
$\mu$	0.75	0.75	0.75	
$\delta$	1	1	1	Perfect power control
Gs	1	1	1	Omni directional antenna

### II. Effect of Some Parameters on CCP

changing of several parameters values are performed on the CCP equation in order to see the behavior of  $CCP_{mix}$  curves of specific services weights when those parameters are implemented.

The relationship between  $CCP_{mix}$  and bit energy per noise density (*system performance*  $E_b/N_o$ ) for different scenarios in urban areas are shown in Figure 5.  $CCP_{mix}$  decreases as the system performance increases for the three scenarios. High  $CCP_{mix}$  values are seen when the mixed traffic contains large number of voice users

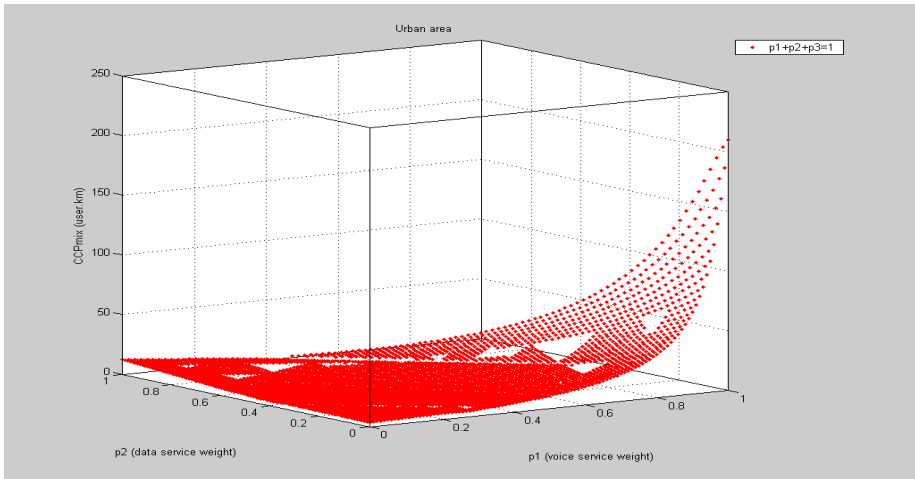


Figure 3. Effect of voice and data service weights on  $CCP_{mix}$ .

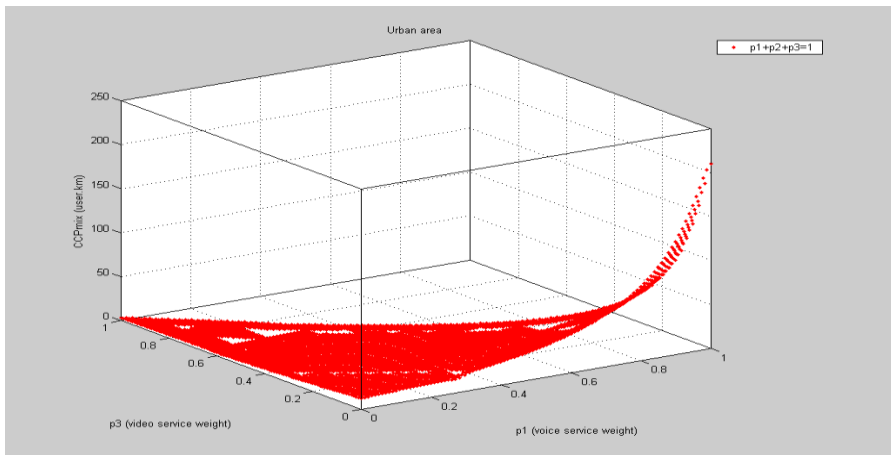


Figure 4. Effect of voice and video service weights on  $CCP_{mix}$ .

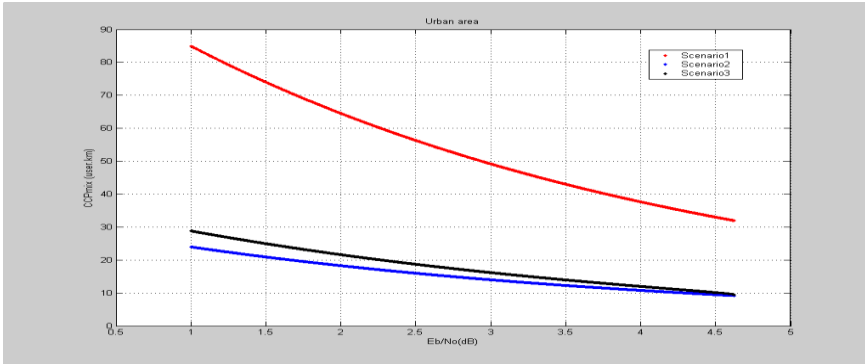


Figure 5. Impact of Eb/N0 on  $CCP_{mix}$  for different scenarios.

scenario1 with low system performance.

Effect of Mobile transmit power on  $CCP_{mix}$  is explained in Figure 6. So, as the mobile power increases,  $CCP_{mix}$  value increases for the three mixed services scenarios. In the case of scenario2 (users of

video services are relatively high), low  $CCP_{mix}$  values were displayed and its rate of increase is low. On the other hand for scenario1, (voice dominant case), the rate of increase of CCP versus transmit power is high.

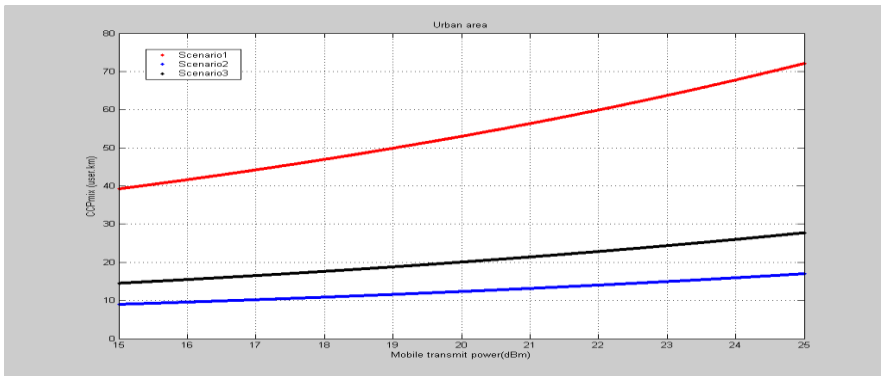


Figure 6.  $CCP_{mix}$  versus mobile transmit power for different scenarios.



### III. Conclusion

The demand for wireless mobile Internet access is driven by the continuing emergence of new multimedia services and applications, such as instant messaging, real-time media streaming, peer-to-peer file transfer, interactive gaming, etc.

In WCDMA cellular networks, the capacity and coverage are the most important issues especially in the mixed rate services because of they are dependent of each other and they are related to the type of service in the coverage area.

In this paper capacity and coverage formulas for mixed rate services in WCDMA cellular networks are developed, the total available system resource is calculated, and then a capacity coverage product formula for mixed rate services is derived and analyzed and three scenarios were assumed.

The effect of some parameters, such as type of environment, system performance, mobile transmit power ...etc. on mixed services CCP are studied.

### IV. References

- [1] Venugopal V. Veeravalli, and Andrew Sendonaris, "The Coverage Capacity Tradeoff in Cellular CDMA Systems" *IEEE Transactions On Vehicular Technology*, Vol. 48, NO. 5, Sep. 1999.
- [2] Duk Kyung Kim, and Dan Keun Sung, "Capacity Estimation for a Multicode CDMA Systems with SIR-Based Power Control", *IEEE Transactions On Vehicular Technology*, VOL. 50, NO. 3, MAY 2001.
- [3] Andrea Abrardo, Giovanni Giambene, , and David Sennati, "Capacity Evaluation of a Mixed-Traffic WCDMA System in the Presence of Load Control", *IEEE Transactions On Vehicular Technology*, VOL. 52, NO. 3, MAY 2003.
- [4] Zaher Dawy, sasa Davidovic, and Alexander Seegar, "The Coverage-capacity Tradeoff in Multiservice WCDMA Cellular Systems with Serial Interference Cancellation", 1536-1276/06, *IEEE Transactions On Wireless communications*, VOL.5,NO. 4, APRIL 2006.
- [5] Al-alem Mohamed, "Capacity-Coverage Product in a Macrocell CDMA Mobile Networks", *Ms.c. thesis Al-fateh University, Faculty of Engineering*, June 2007.
- [6] Hjahaja A. Salih, "The Impact of Mixed Multirate Services on Uplink Capacity-Coverage Product in WCDMA Mobile Networks" , *Ms.c. thesis Al-fateh University, Faculty of Engineering*, September 2008.



المؤتمر الدولي العربي الليبي الخامس للهندسة الكهربائية والإلكترونية 2010/10/26-23 طرابلس ليبيا





## DATA EMBED IN H.264 VIDEO COMPRESSION

<sup>1</sup>Tarik .F. Idbeaa , <sup>1</sup>.kasmiran Jumari, <sup>2</sup> Salina Abd. Samad, <sup>3</sup> Ali abdulgader

Computer & Network Research Group  
Faculty of Engineering & Built Environment

Department of Electrical, Electronic & Systems Engineering  
University Kebangsaan Malaysia (UKM)

43600 Bangi Selangor, Malaysia

<sup>1</sup>tidbeaa@yahoo.com, <sup>1</sup>kbj@eng.ukm.my, <sup>2</sup>salina@eng.ukm.my, <sup>3</sup>aa752006@yahoo.com

### Abstract

Digital video steganography has attracted much research interest in recent years in some applications. In this paper, a method of embedding secret text messages in video sequences using steganography technique based on the H.264 video coding standard. In recent years, H.264 uses to be anew advanced video compressed standard, but to this date, very few steganography schemes have been designed for it. This is mainly due to its complexity and compression efficiency, which presents a major challenge for all video steganography approach. It provides high compression efficiency and compression quality, compress the standard for compressed video of new generation. In this context, Block Index and Sub-band modulation coefficient embed in quantized AC coefficients of I frame is used. The system implemented in this work provides robust H.264 video compression constant, without significantly affecting the overall bit rate and quality of the video stream. The results indicate that the algorithm can be implemented steganography fast and efficiently and effect vision and peak signal to noise ratio (PSNR) of video sequences are almost unaffected after decoding.

**Keyword:** Video Compression, H.264, MPEG-4, Data hiding

### 1. Introduction

Nowadays, Internet and digital media applications are rapidly growing which made the requirement of secure transmission of data also increased. In the field of data security, various techniques have been implemented and proposed. Data Hiding is considered one of these techniques that are used to embed data in side different media like image, video or audio. It hidden mes

sages in such a way that no one apart from the sender and intended recipient even realizes there is a hidden message. The method proposed in this paper, is based on increasing the amount of the data which will be embed inside H.264 video. H.264 [1] is the newest international video coding standard providing many techniques to improve the



coding efficiency of intra and inter frames. This technique, which is used in the proposed method, increases the dependence of the neighbouring blocks. The H.264/AVC standard is designed to have high compression efficiency [2]. It has good performance in low bite rate applications and has experienced widespread adoption within this few years. Experimental results are provided to show that this H.264 steganography implemented scheme can improve both the imperceptibility and the robustness under attacks. Our paper proposes a novel high capacity reversible image data hiding scheme using a prediction technique based on the benefits of the verity of H.264 motion-compensation. All the required stages to hide data will be concentrated in the use of inter prediction section that at the encoding process of the H.264 standard.

## 2. Previous Work

The early approaches were proposed for video data hiding yet Image watermarking techniques extended to video by hiding the message in each frame independently [3]. Methods such as Spread spectrum are used, where the basic idea is to distribute the message on a wide range of frequencies of host data. Transform domain is generally preferred for hiding data since, for the same robustness as for the spatial domain; the result is more pleasant to the human visual system (HVS). For this Indeed, the DFT (Discrete Fourier Transform), the DCT (Discrete Cosine Transform) and DWT (Discrete Wavelet Transform) domains are commonly used [4-5]. Recent video data hiding techniques are considerate on characteristics generated by the video compression standards. Motion vector systems have been proposed for MPEG algorithms [6-7]. Motions vectors are

calculated by the video encode in order to remove temporal redundancies between frames. In these methods the original motion vector is replaced by another local optimal motion vector for maximum embed a. Only few data hiding algorithms considering the properties of H.264 standard [8-9] have recently appeared in the open literature. In [8] a subset of the  $4 \times 4$  DCT coefficients is modified in order to achieve a robust watermarking algorithm for H.264. In [9] the blind algorithm for copyright protection is based on the intra prediction mode of the H.264 video coding standard. In [9] some skipped macroblocks are used to embed data.

## 3. Proposed Method

In this paper, the process of hiding data based on PPM module (Proposed Prediction Module). The PPM will use the inter prediction in its scenario. So when a frame enters the mentioned module, decision will take place by the algorithm, deciding whether to use the frame for hiding data or not. If so, the algorithm will choose the macroblock competitor and perform the motion estimation on them. The encoder will choose a specific block type as it mapped and decision will also be based on the hiding bounds. These issues are considered very important factors and are the keys to finish the hiding and extracting of data in correct manner. They are represented as the assigning of the frame and the block numbers and the numbers of the blocks that will be using for hiding the entered data. Figure 1 show the implemented system associated with H.264 standard encoding.

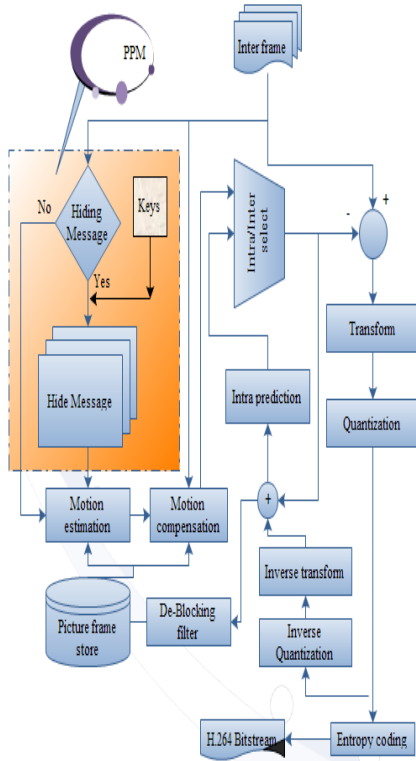


Figure 1: Block diagram of the proposed scheme

Since H.264 standard based up on 7 different types of blocks (i.e.  $16 \times 16$ ,  $16 \times 8$ ,  $8 \times 16$ ,  $8 \times 8$ ,  $8 \times 4$ ,  $4 \times 8$ ,  $4 \times 4$ ) as it appears in figure 2, this will increase its application efficiency. The reason is that the motion estimation is applied on each of this block types.

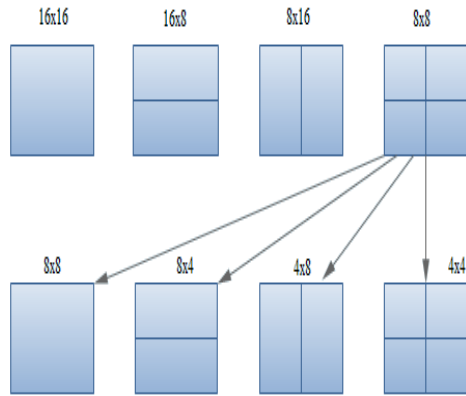


Figure 2: Different types of blocks used in H.264 standard

The motion estimation aims at finding the “closest” macroblock (best match) in the previously coded frame for every macroblock of the current input frame. Then each macroblock is motion compensated. In this implemented scheme, the idea based on assigning a binary code to every block type (2 bits/ block). For example ( $16 \times 16 = 00$ ,  $16 \times 8 = 01$ ,  $8 \times 16 = 10$ , and  $8 \times 8 = 11$ ). The embedding message of size 10KB will be converted into a binary numbers. These binary numbers will be separated into pairs of bits and mapped into macroblock as the example of figure 3 then motion compensated.

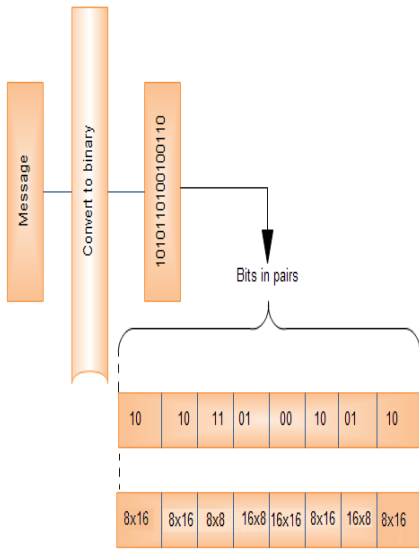


Figure 3: Message mapped into block types

Once the hiding arena gets finished, then the encoding process would normally perform. The entropy encoded coefficients, together with its side-information (prediction mode, quantization parameters, motion vector information, etc.) are transmitted to a Network Abstraction Layer (NAL) for transmission or storage.

#### 4. System Results

The proposed algorithm was implemented, tested and results reported. H.264 /AVC reference software is used as benchmark to implement our algorithm. The algorithm has applied on City standard test sequence and PSNR is chosen to represent video quality. In our case, the PSNR was used not for measuring the quality for the whole video frames but it was only calculated for Inter frames because the message is inserted

into these frames only. The PSNR is defined as follows:

$$PSNR = 10 \log_{10}(255^2 / MSE) \quad (1)$$

where  $MSE$  denotes the mean square error between the original  $M_{(u,v)}(i,j)$  and embedded samples  $M'_{(u,v)}(i,j)$  in pixel domain .

$$MSE = \frac{1}{256} \sum_{i=1}^{16} \sum_{j=1}^{16} (M_{(u,v)}(i,j) - M'_{(u,v)}(i,j))^2 \quad (2)$$

Visual quality is another factor that has used as visual indicator for the measuring frame quality. Figure 4, demonstrate the PSNR of the inter frames has not affected by the implemented method.

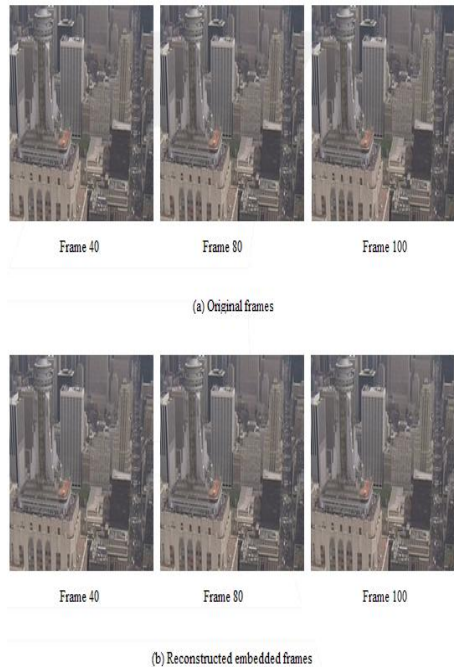


Figure 4: Original frames and reconstructed embedded frames.



Figure 5 shows that the *PSNR* values of the whole selected frames are not much different from the normal H.264 video and shows how the performance of the proposed scheme varies with different block sizes. The *PSNR* Variation was approximately only 0.11 dB and after calculating the average of the *PSNR* for all the tested sequences, we found differences were very low percentage.

The experimental results show that the *PSNR* of all marked images is in range from 38 to 43 dB and show that the embed-

ded data remains invisible, since no visual distortion can be revealed.

Although in the description of the method only 4 types of blocks (16x16, 16x8, 8x16, and 8x8) were used for embedding and detecting data, other block sizes could be easily used. The reason of choosing the four types of blocks instead of one block type is to increase the efficiency of the implemented algorithm when the situation requires hiding more information.

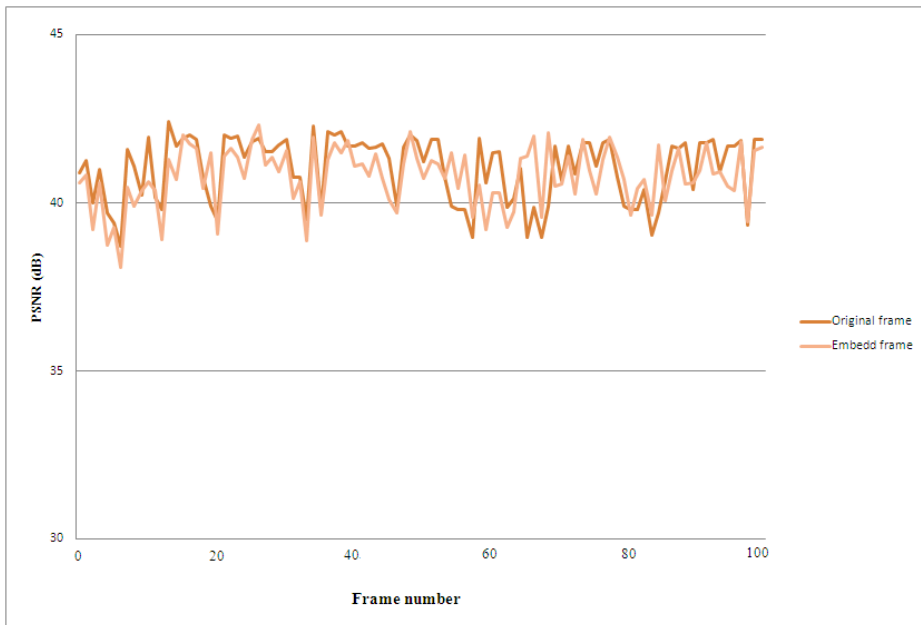


Figure 5: *PSNR* of the inter frames



## 5. Conclusions

A robust algorithm of hiding data into H.264 video stream rapidly was proposed in this paper. PPM is considered as a simple way to implement and it introduces a higher data security performance and higher embedding capacity. PPM has applied to H.264 encoding process. By comparing between the original and constructed used frames, the quality in both (Human visual system and Mathematical expression) indicated how our proposed scheme is useful with no much affection on video quality over encoding stage and this scheme is very computational efficient during water-mark embedding and extraction and the embedded data not lead to increasing the bit-rate of H.264 bit-stream too many. Another advantage can be obtained from PPM; message can be extracted directly from the encoded video stream without the need of the original host video sequence.

## Acknowledgements

The authors would like to acknowledge the support from Department of Department of

- [5] H.Liu, J.Huang, Y. Q. Shi(2005). "Used Video Data Hiding Robust to MPEG Compression and Frame Loss", *Int.Journal of Image and Graphics* Vol.5 No.1, pp. 111-134.
- [6] J. Zhang, J. Li, L. Zhang(2001). "Video Watermark Technique in Motion Vector", *Proc. of XIV Symposium on Computer Graphics and Image Processing*, pp.179-182.
- [7] D.-Y. Fang, L.-W. Chang.(2006). "Data Hiding for Digital Video with Phase of Motion Vector", *IEEE Proc. Int. Symposium on Circuits and Systems, IS-CAS 2006*.
- [8] M. Noorkami, M. Mersereau. (2006). "Towards Robust Compressed-Domain Video Watermarking for H.264",

*Electrical, Electronic & Systems Engineering* for this work and also thank the anonymous reviewers for their constructive comments.

This project is supported by University Grant fund UKM-OUP-ICT-36-182/ 2010.

## References

- [1] VTG050.(2003). "Advanced Video Coding, Final Committee Draft", ITU-T Rec. H.264/ISO/IEC14496-10.
- [2] I.E.G. Richardson. (2004). "H.264 and MPEG-4 video compression", Wiley, Chichester .
- [3] J. J. Chae, B. S. Manjunath. (1999). "Data Hiding in Video", *IEEE Proc. Int.Conf. On Image Preccessing*, pp.243-246.
- [4] V.Fotopoulos, A. N. Skodras . (2003) "Transform Domain Water-marking: Adaptive Selection of the Watermark's Position and Length", *Proc. Visual Communications and Image Processing, VCIP2003*.  
*Proc.SPIE*, Vol. 6072, pp. 489-497, 2006.
- [9] D. Proefrock, H. Richter, M. Schl auweg, E. Mueller.(2005). "H.264 /AVC Video Authentication Using Skipped Macroblocks for an Erasable Watermark", *Proc. SPIE Vol. 5960*, pp. 1480-1489.
- [10] A. K. Bhaumik, M. Choi, R.J. Robles, M.O.Balitanas.(2009) "Data Hiding in Video" *International Journal of Database theory and Application* Vol. 2, No. 2.

## NOMENCLATURE

PSNR Peak Signal to Noise Ratio  
MSE Mean Square Error



## HIGH SECURE DATA HIDING WITHIN MPEG-4 COMPRESSED VIDEO

<sup>1</sup>Tarik .F. Idbeaa , <sup>1</sup>kasmiran Jumari, <sup>2</sup> Salina Abd. Samad, <sup>3</sup> Ali abdulgader

Computer & Network Research Group

Faculty of Engineering & Built Environment

Department of Electrical, Electronic & Systems Engineering

University Kebangsaan Malaysia (UKM)

43600 Bangi Selangor, Malaysia

<sup>1</sup>tidbeaa@yahoo.com, <sup>1</sup>kbj@eng.ukm.my, <sup>2</sup>salina@eng.ukm.my, <sup>3</sup>aa752006@yahoo.com

### Abstract

The Steganography is about embedding a secret data into different media. It has emerged as an important sub-discipline of data embedding methods. Although it usually applied to still images in the past, it is very popular in recent years for video. Since recent video data hiding techniques are focused on the characteristics generated by video compressing standards, a higher secure steganography method for MPEG-4 standard using Bit Plane Complexity Segmentation (BPCS) algorithm is proposed in this paper. The reason of selecting such video cover in this approach is the huge amount of data that can be hidden in different types of frames image because The MPEG-4 standard has three types of frames: I-frame, P-frame and B-frame. Security information is embedded into the host video at I-Frame meanwhile the BPCS can achieve high embedding rates with low distortion based on the theory that noise-like regions in an image's bit-planes can be replaced with noise-like secret data without significant loss in image quality.

This approach will invent high secure data hidden within frames which are randomly selected. The experiment results show the success of the hidden data within select frame and the extraction of data from the frames sequence and are also indicate the efficiency of applying scheme to compressed video steganography with high security features.

**Keyword:** Video Compression, H.264, MPEG-4, Data hiding

### 1. Introduction

Steganography is the art and science of hiding messages. . It is distinct from encryption, because the goal of encryption is to make a message difficult to read while

the goal of steganography is to make a message altogether invisible [6, 7]. The hidden message could be vary secret or privet information that not be allowed to be viewed by the public or might be from people who wish to evade surveillance,

especially by governments. This includes people who have reason to fear punishment for expressing their political ideas, as well as terrorists. The word steganography is derived from the Greek words "steganos" and "graphein", which mean "covered" and "writing". Comparing with the old traditional hiding methods where the hiding of data involved techniques such as disappearing ink or microdots, modern steganography involves hiding data in computer files since the computer gives more flexibility and accurately when is working with different media such as Text, Image, Sound, and Video [2]. It is fairly easy to hide a secret message in a graphic file without obviously altering the visible appearance of that file but the point is that the limitation of the data that could be hidden. In other words, Just a limited amount of data could be hidden inside still image file. In recent years, most of the researchers in this filed are focusing their work on hiding data within Video files. The reason of that is the possibility of hiding a large amount of data within frames instead of using one still image.

In this paper, steganography algorithm method based on the bit plane complexity segmentation is presented. The presented method used to embed secret information in Video file. In our case, a method of hiding data for video data in AVI format at MPEG-4 compress standard is presented and results recorded. The reason of chosen such Technique is that the MPEG-4 standard is considered as the most efficient and popular standard for the video data communication [1].

The rest of the paper is organized as follows. In section II, the concept of the bit-plane complexity algorithm is introduced. It will also include some facts that have been

reported from using such algorithm over the steganography applications. The chosen algorithm and the implemented system will be described in section III. All the obtained results and discussions presented in section IV. The last two sections V and VI will present the conclusions and future work referring to the results presented in this paper.

## 2. Bit-Plane Complexity Segmentation (BPCS)

Bit-Plane Complexity Segmentation Steganography is considered one of the most techniques that are still being used in term of image and video steganography [3, 5]. In such technique, a large amounts of data where it is possible to be embed in sill images or video frames. A bit plane is a data structure created from all the bits of a certain position of each binary digit, with precise location saved and the Fig 1. Shows the position (0, 0) from bit plane 2 is bit 2 from pixel (0, 0) in the image.

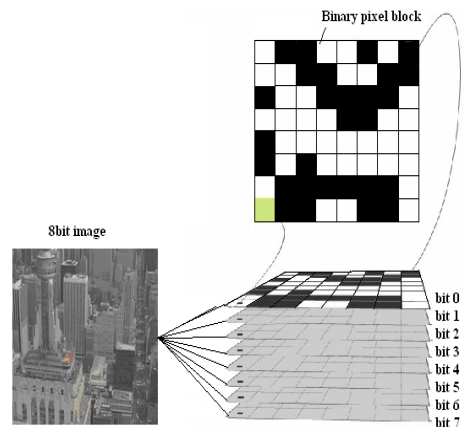


Figure 1: the position (0, 0) from bit plane 2 is bit 2 from pixel (0, 0) in the image.





Studies have shown that the optometry human visual system is very good at identifying anomalies in areas of uniform color, but less able to see them in visually complex areas. When an image is little decompose in aircraft, the complexity of each region can be measured. Areas with a low complexity, such as single color or simple shapes appear as uniform areas with very little change from one to zero. In the case of defining a coherent scale of complexity, the normalizing such that a solid color with a complexity of 0 and the checkerboard pattern (the most complex possible region) has a complexity of 1 is required in this situation. Each a bit-plane region with a complexity above a selected threshold is considered as random noise and replaced by 8 bytes of data.

In assessing applications for BPCS steganography, it is instructive to note that different digital watermarks in two fundamental ways [4]. The first is that the colors (eg 24-bit) images, a large capacity for integration. The second difference is that BPCS steganography is not robust to even small changes in the image. This can be seen as a good thing in applications where a user might have ignored an embedded image. All changes, such as cropping, sharpening or lossy compression, would "destroy evidence" and unusable for later retrieval. Extraction of integrated information requires a deliberate attempt by a knowledgeable user on an image intact. The lack of robustness is the fact that a malicious user can not change the embedded information without the knowledge of personalization settings.

BPCS steganography applications are not limited to those relating to confidentiality. For such applications, the presence of embedded data and software for mining and processing can be normalized to a common

set of parameters. An example is a digital photo album, where information about an image such as date and time of capture, exposure settings and scene content can be integrated into the image.

### 3. System Implementation

Since the steganography concepts are based mainly on the idea of embedding and extracting stages, the implemented system introduced in this frame work also supports those steps to hide the secret data and avoiding interlopers and gatecrashers to detect such information. In our proposed approach, a number of procedures should be followed to hide the secret data successfully. Fig 2 shows the embedding phase of the implemented system.

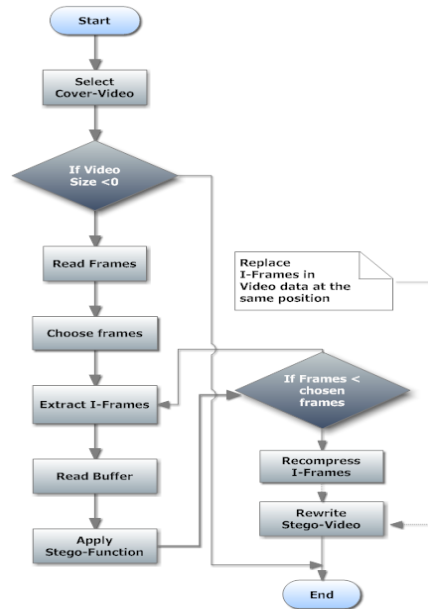


Figure 2: Embedding phase diagram



As we have mentioned, our proposed system will focus on MPEG-4 as the compressor and AVI as the type of video data to embed secret information in it. All I-Frames should be extracted and decompressed from the compressed video before getting start with hiding process. Not all frames have been used in this approach, we modify a function that can select I-Frame randomly and saves its sequence number in the video data. This will give more robust and secure technique for data hiding concept. We have chosen three blocks from each I-Frame to hide data in. Selecting blocks depending on the amount of data that to be hide in one frame and also to the color information reduction. All I-Frames will compress back again after the blocks to be used for hiding data are selected and the stego-Function has applied.

At the detection phase that extracts the secret message from the host video data which is illustrated in Fig. 3 below. All the I-Frames will need to be extracted first. Choosing of the carrier bocks will be trough referencing blocks that have kept /saved by our implemented function. Once the blocks are assigned, the Extracting function will take place. After this step, all the I-frames will compress again.

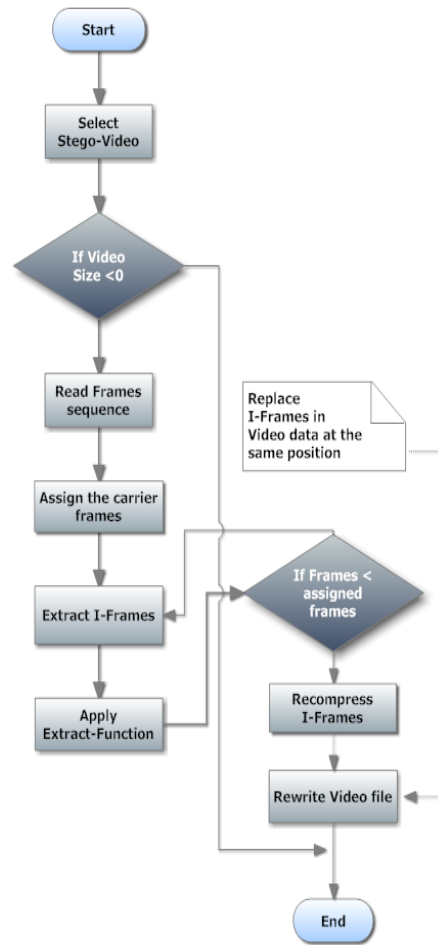


Figure 3: Extracting phase diagram

#### 4. Experimental Results

Thirty image frames have taken from the TV show video named "miss\_am" and used in all our experiments. The obtained results are very logical and convinced. This decision is made based on quality of the carrier frames. Figures 4 & 5 represents video frames before and after hiding process. By considering the Human Visual

system as an indicator to measure the quality, we notice that all used frames are still with the perfect condition and almost no much difference appeared among original and embedded frames. The reason is related to the using of Y component (luminance) to hide data in and avoiding further decreasing color information (Cb, Cr).



Figure 4: Frames before embedding



Figure 5: Frames after embedding

The mathematical expression has also approved that our proposed algorithm is very useful. The PSNR values for all used frames has illustrate in the figure 6.

$$PSNR = 10 \log_{10} (255^2 / MSE) \quad (1)$$

where  $MSE$  denotes the mean square error between the original  $M_{(u,v)}(i,j)$  and embedded samples  $M'_{(u,v)}(i,j)$  in pixel domain .

$$MSE = \frac{1}{256} \sum_{i=1}^{16} \sum_{j=1}^{16} (M_{(u,v)}(i,j) - M'_{(u,v)}(i,j))^2 \quad (2)$$

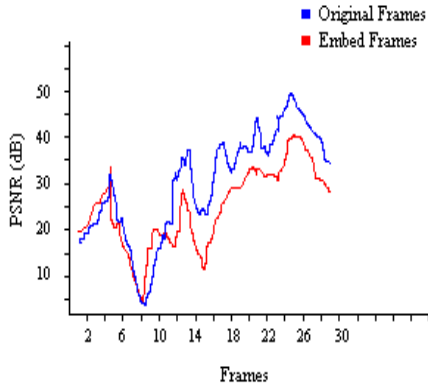


Figure 6: PSNR of the inter frames

## 5. Conclusion

In this paper, a method of hiding a secret data using the BPCS algorithm is presented. The proposed approach is basically focused on the use of AVI video data that had compressed using MPEG4 standard. The idea behind this is to investigate the efficiency of applying BPCS algorithm over such file format. In our presented method, data is separated and embed in different blocks with a Varity collection of frames. The obtained results show and guarantee a large amount of data could be hiding using this technique. The reason is related to the number of chosen blocks to hide message in and selected I-frames.

## Acknowledgments

The authors would like to acknowledge the support from Department of Department of Electrical, Electronic & Systems Engineering for this work and also thank the anonymous reviewers for their constructive comments.

This project is supported by University Grant fund UKM-OUP-ICT-36-182/2010.

## References

- [1] A.M. Alattar, M.U. Celik, E.T. Lin: Evaluation of Watermarking Low Bit-rate MPEG-4 Bit Streams. Proceedings of the SPIE International Conference on Security and Watermarking of Multimedia Contents V, Santa Clara, CA (2003).
- [2] Digital Watermarking: A Tutorial Review S.P.Mohanty, 1999.
- [3] E. Kawaguchi, M. Niimi. "Modeling Digital image into informative and Noise-Like Regions by a Complexity Measure", *7th European-Japanese Conference on Information Modeling and knowledge Bases*, 1997.
- [4] Jeremiah Spaulding, Hideki Noda , Mahdad N. Shirazi , Michiharu Niimi, Eiji Kawaguchi DICTA2002: Digital Image Computing Techniques and Applications, Melbourne, Australia; Jan(2002).
- [5] M. Niimi, H. Noda, E. Kawaguchi. "A Steganography Based on Region Segmentation by Using Complexity Measure". *Trans. Of IEICE, Vol. J81-D-II, No. 6, pp. 1132- 1140*, 1998.
- [6] Ross J. Anderson and Fabien A.P. Petitcolas, "On the limits of steganography," *IEEE Journal on Selected Areas in Communications (J-SAC)*, Special Issue on Copyright & Privacy Protection, vol. 16 no. 4, pp 474-481, May 1998.
- [7] T Mrkel, JHP Eloff and MS Olivier ."An Overview of Image Steganography," in *Proceedings of the fifth annual Information Security South Africa Conference*, 2005

## Nomenclature

PSNR Peak Signal to Noise Ratio

MSE Mean Square Erro



## **Errors monitoring and solutions via simulation of an operational DWDM Transmission system**

**Name: Najia M.Gaboa**  
**e-mail:nagia\_86@yahoo.com**

**Name: Mousa M.Mousa**  
**e-mail:mmousa@ltnet.net**

### **Abstract**

In this paper the optimization of DWDM system performance is discussed through simulation by monitoring and adjusting the power level at each individual wavelength. This is done by locating the resulted errors.

In the paper also, a consideration of how to know the errors in this system at any part, and to propose solutions for such problems

### **1. Introduction**

Dense wavelength division multiplexing (DWDM) is a technology that puts data from different sources together on an optical fiber, with each signal carried at the same time on its own separate light wavelength. Using DWDM, up to 80 (and theoretically more) separate wavelengths or channels of data can be multiplexed into a light stream transmitted on a single optical fiber. Each channel carries a TDM signal. In a system with each channel carrying 2.5Gbps, up to 200 billion bits can be delivered a second by the optical fiber. DWDM as one of WDM technology, but Due to small interval (1nm~10nm order) between adjacent wavelengths, it is called DWDM. At present, the practical DWDM system works in 1550nm window for the purpose of using the gain spectrum feature of the EDFA to directly amplify the composite optical wavelength signals. To meet the horizontal compatibility between systems, the central wavelength of the optical channel must accord with G.692

standard. In the DWDM system, each optical channel can bear different customer signals, such as SDH signal, PDH optical signal and ATM signal. Due to unique advantages of fiber communication and its networking technologies for accommodating multi-service and broadband requirements, high speed SDH system, N\*2.5Gbit/s DWDM system and N\*10Gbit/s DWDM system become majority and backbone of the core network.[1]

Implementing DWDM systems involves maximizing the rate of transmitted information, while minimizing the limitations of the existing physical network. Accounting for potential problems in the design and installation of DWDM systems is necessary because of the many performance imperfections of current optical components.[ 2]

Testing and troubleshooting single-wavelength systems in the field can be accomplished by monitoring a few well-



defined parameters. For example, optical power loss, or attenuation, has always been a key factor in the performance of fiber-optic links, and portable optical loss test sets have been developed to measure this loss in the field. Instruments with optical time domain reflectometric capabilities have been developed to locate faulty elements in a link. As system sophistication has grown, so has the significance of optical return loss, especially in the CATV field, where source-laser instability caused by reflected energy can have serious effects on signal quality. Field instrumentation has been developed to monitor this parameter as well. All this test equipment is still required in a DWDM environment—but with characteristics adapted to the much more stringent needs of WDM systems.[3] Basic test equipment to test power, dispersion, OSNR, and other spectral content are necessary for installing and maintaining a WDM network. The recommended basic test equipment includes optical power meters, attenuators, optical spectrum analyzers (OSAs), and optical time domain reflectometers (OTDRs). [4] In this paper a DWDM network is simulated by using visual basic v.06 program to measure Eb/No and calculate BER under many changes on stated parameters to know these changes effect, and to explain such effect.

## 2. Configuration of Network under Test

The network in figure (1) consists of four sites in addition to the company site, to be of a ring configuration, through this ring information are sent from company site to any site.

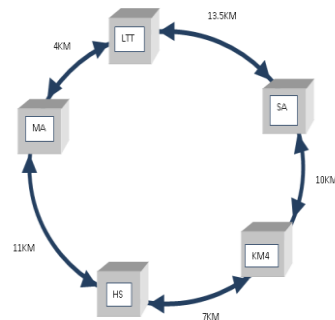


Figure (1) DWDM Ring Network for LTT Company [5]

## 3. Traffic at any Site

The bands for wavelengths that are sent from company site to any site are given in the table (1).

Table (1) Traffic at any site [5]

Site	Traffic
LTT company	RR band( $\lambda_1, \lambda_2, \lambda_3, \lambda_4, \lambda_5, \lambda_6, \lambda_7, \lambda_8$ ), RB band( $\lambda_{12}, \lambda_{15}, \lambda_{17}, \lambda_{18}$ ) and BR band ( $\lambda_{25}, \lambda_{26}, \lambda_{27}, \lambda_{28}$ ).
Alzawia street (SA)	RR band ( $\lambda_1, \lambda_2, \lambda_3, \lambda_4$ )
KM4	RB band ( $\lambda_{12}, \lambda_{15}, \lambda_{17}, \lambda_{18}$ )
Hey Senaie (HS)	BR band ( $\lambda_{25}, \lambda_{26}, \lambda_{27}, \lambda_{28}$ )
Maidan Algazier (MA)	RR band ( $\lambda_5, \lambda_6, \lambda_7, \lambda_8$ )

Where :

- RR band: Red Red band
- RB band: Red Blue band
- BR band: Blue Red band

## 4. Monitoring

The DWDM simulated ring network given in figure (1) is monitored using Visual Basic v6.0 program measuring output power level (dBm), for wavelengths transmitted from the LTT company site to the other four sites as given by table (1)



measuring  $E_b/N_0$  (dB), checking of devices if wavelengths have losses out of range, and testing if having BER large ( $> 10^{-4}$ ), and how to process the resulted errors from transmitted wavelengths.

### 5. Signal Flow in Ring Network [5]

#### a. Signal flow in LTT company site

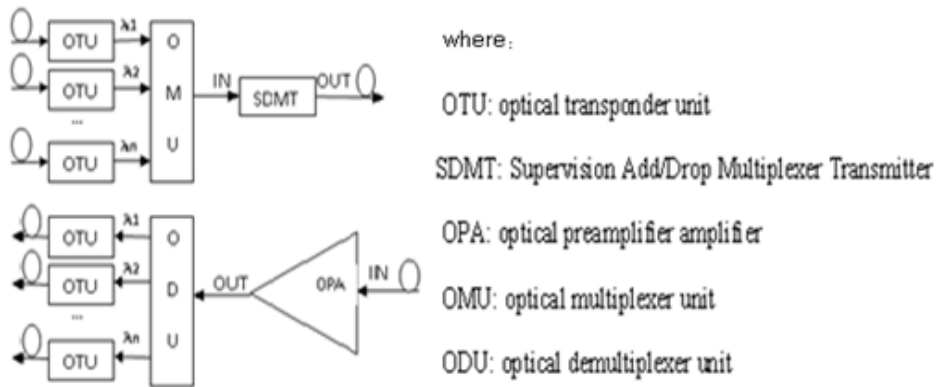


Figure (2) Signal Flow in Company Site [5]

Table (2) The value of losses [5]

<b>1. For the wavelengths insensitive OMU, the insertion loss &lt; 4dB.</b>
<b>2. Insertion loss of the OP &lt; 5dB.</b>
<b>3. Insertion loss of the ODU &lt; 6dB.</b>
<b>4. Insertion loss of the OAD &lt; 4dB.</b>
<b>5. Insertion loss of the SDMT &lt; 2dB.</b>
<b>6. Insertion loss of the OGMD &lt; 2dB.</b>

The wavelengths for transmission pass through OTU, OMU and SDMT. The wavelengths for receiver pass through OPA, ODU and OTU, as in figure (2). Table (2) presents the losses for some of the components.

#### b. Signal Flow at Any Site in the Ring Network (figure 1)

The wavelengths for transmission pass through OPA, OTU, OAD, OGMD6C and SDMT and wavelengths for receive pass through OPA, OGMD6C, OAD and OTU. As shown in figure (3).



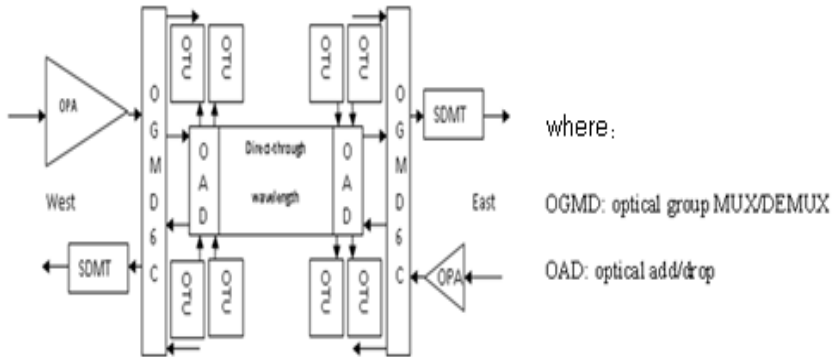


Figure (3) Signal flow at any of the four sites in the ring network [5]

## 6. Error analysis

The simulated DWDM given in figure(1) using visual basic v6.0 program is connected to measure output power level (dBm) for wavelengths ( $\lambda_1$ ) and ( $\lambda_3$ ) to consider changed loss, data rate for wavelengths and gain, and how this change affect BER?.

### 6.1 Results of Program

Figure (4) describes the simulated DWDM system.

In this simulation we measure  $E_b/N_0$  for  $\lambda_1$  and  $\lambda_3$  in many cases and under various changes of these parameters; insertion loss, gain and data rate. The results are given in tables (3), (4) for  $\lambda_1$  and  $\lambda_3$  respectively. The relationship between these parameters and  $E_b/N_0$  are as shown in figures (5), (6), (7), (8), (9) and (10).



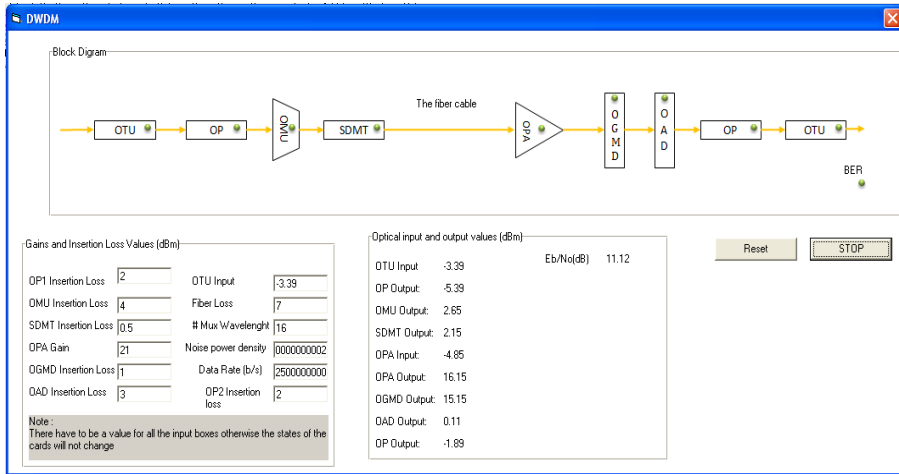


Figure (4) Result for  $\lambda 1$  [6]

Table (3) Results of the simulation of Eb/No & BER for  $\lambda 1$

Case	Parameters set fixed	Changed input parameter(s) & values	Eb/No (dB)	BER calculated	
1	Insertion loss, data rate and gain	Non of parameters is changed	11.12	3.6258E-007	
2	Data rate & gain	One parameter: insertion loss	3dB	8.12	3.1607E-004
			4dB	7.12	0.0013
			5dB	6.12	0.0042
3	Gain is fixed	Two parameters: Insertion loss & Data rate	3dB, 2Gb/s	10.089	~0
			4dB, 1.5Gb/s	10.84	8.3830E-007
			5dB, 1Gb/s	12.6	1.6120E-009
4	Data rate	Two parameters: Insertion loss & Gain	3dB, 19 dB	6.62	0.0024
			4dB, 17dB	4.12	0.0231
			5dB, 15dB	4.12	0.0231
5	Insertion loss & gain	Data Rate	2Gb/s	12.089	~0
			1.5Gb/s	13.34	5.0573E-011
			1Gb/s	15.1	8.6390E-016



Table (3) continued

6	Insertion loss	Two parameters: Data Rate & Gain	2Gb/s,19dB	10.09	6.2216E-006
			1.5Gb/s,17dB	9.34	3.3995E-005
			1Gb/s,15dB	9.1	5.5316e-005
7	Insertion loss & Data rate	Gain	19dB	9.12	5.3169E-005
			17dB	7.12	0.0013
			15dB	5.12	0.0108

Figure (5) Eb/No VS Insertion Loss for  $\lambda_1$

Figure (6) Eb/No VS Data Rate for  $\lambda_1$

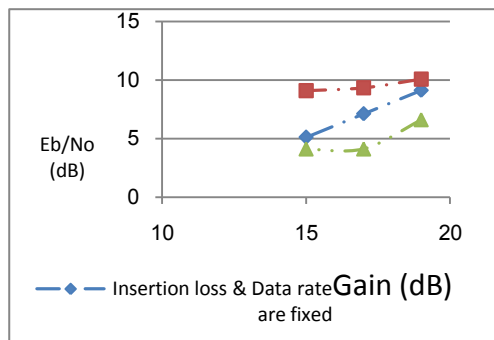
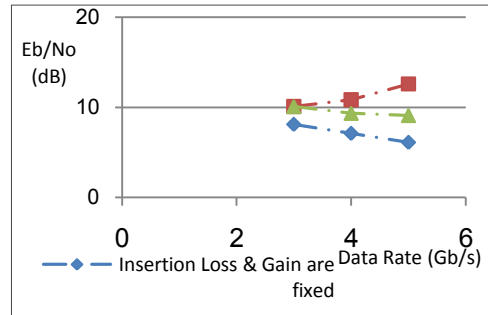
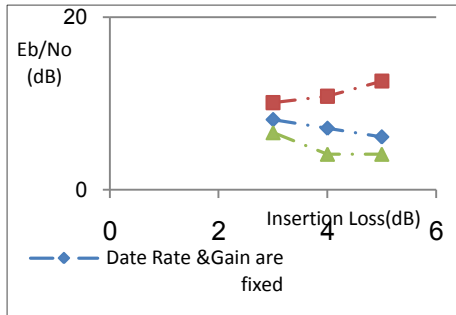


Figure (7) Eb/No VS Gain for  $\lambda_1$



Table (4) Results of the simulation of Eb/No & BER for  $\lambda_3$

Case	Parameters set fixed	Changed input parameter(s) & values	Eb/No (dB)	BER calculated	
1	Insertion loss & data rate, gain	Non of parameters is changed	14.79	8.3114E-015	
2	Data rate& gain	One parameter: insertion loss	3dB	11.79	3.8939E-008
			4dB	10.79	9.6838E-007
			5dB	9.79	1.2694E-005
3	Gain	Two parameters: Insertion loss & Data rate	3dB,500Mb/s	14.8	7.7451E-015
			4dB,400Mb/s	10.77	1.0254E-006
			5dB,100Mb/s	19.79	~0
4	Data rate	Two parameters: Insertion loss & Gain	3dB,19 dB	9.79	1.2694E-005
			4dB,17dB	6.79	0.0020
			5dB,15dB	3.79	0.0287
5	Insertion loss & gain	Data Rate	500Mb/s	17.8	~0
			400Mb/s	18.77	~0
			100Mb/s	24.79	~0
6	Insertion loss	Two parameters: Data Rate & Gain	500Mb/s, 19dB	15.8	2.7828E-018
			400Mb/s, 17dB	14.77	9.5668E-015
			100Mb/s, 15dB	18.79	~0
7	Insertion loss & Data rate	Gain	19dB	12.79	6.9967E-010
			17dB	10.79	9.6838E-007
			15dB	8.79	1.00E-004

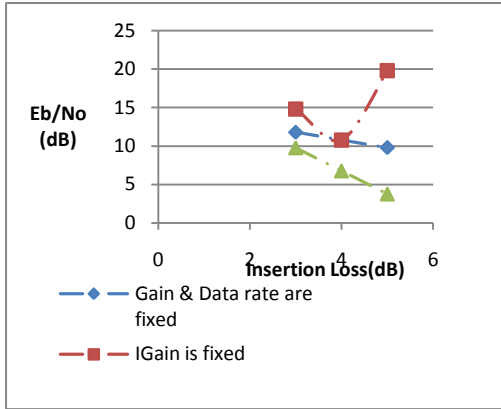


Figure (8) Eb/No VS Insertion Loss for  $\lambda_3$

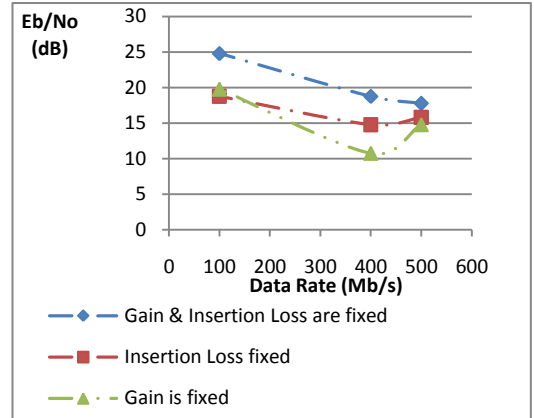


Figure (9) Eb/No VS Data Rate for  $\lambda_3$

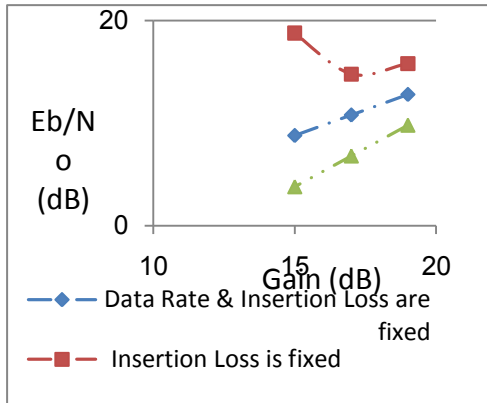


Figure (10) Eb/No VS Gain for  $\lambda_3$

## 6.2 Analysis of Results

From figures(5),(6),(7),(8),(9) and (10) it can be noted that Eb/No is affected by three parameters that is gain, insertion loss and data rate as follows:

- When insertion loss only is changed as shown in figure (5) and (8) it can be noted that Eb/No is decreased when insertion loss increased by 1dB, this change implicate an increase of BER.
- When data rate only is changed as shown in figure (6) and (9). Eb/No

is increased if data rate is low for  $\lambda_3$  and  $\lambda_1$ .

- When gain is changed as shown in figure (7) and (10), Eb/No is decreased when gain is decreased by 2dB and this change implicate an increase of BER.

When both insertion loss and gain are changed as shown in figures (5),(7),(8) and (10), Eb/No is decreased when insertion loss increase and gain is decrease.

- When both insertion loss and data rate are change as shown in figures (5), (6),(8) and (9), Eb/No is increased when insertion loss increase and data rate is decrease because low of data rates implicate a decrease of BER.
- When both data rate and gain are changed as shown in figures (6),(7),(9) and (10), Eb/No is decreased when date rate is decrease.

From above analysis it is noted that, the changes of the main system parameters eg. Gain, data rate and insertion loss individually or as



combination of any two at a time implicate an increase in the value of BER and hence the errors, where in some errors this increase of BER exceeds the allowable minimum threshold value set as  $10^{-4}$ . These results are possible by only simulating an operational network in order to avoid interruption of service continuity. Having the above the resulted errors can be treated as given next.

### 7. Proposed Solution

In this section solutions for problems that result in an increase of BER are given:

- a. When insertion loss is changed this problem can be processed by choosing to have high quality devices or reduce the loss by repeatedly check the devices to make sure that the insertion loss doesn't exceed the allowed range; in addition to knowing other causes that increase losses.
- b. In case gain is decreased, this problem can be processed by adding amplifiers but this solution

implicate an increase of the cost, therefore a solution might is to find a balance between cost and performance.

- c. In case data rate, BER is decreased when transmit the load at high data rate load, it is proposed to divide up such load into segments to be sent simultaneously or sequentially.

### 8. conclusion

- In our work we study the performance of DWDM system and flow of signal from the company site to other sites in an operational network. BER is increased by losses resulted from the operational DWDM system and affected by three parameters. Value of BER is calculated under changes of these parameters and found that insertion loss and gain are the parameters that has the greater effect as shown in figures (5), (8).

### 9. References

- [1] "DWDM Principle Training Manual", <http://www.support.zte.com.cn>, 1/8/2009.
- [2] <http://www.measurement/training/troubleshooting-dwdmNetworks>, 12/8/2009.
- [3] <http://www.iec.org/online/tutorials/dwdm-test/topic01.html>, 15/9/2009.

- [4] Ashwin Gumaste & Tony Antony, "DWDM Network Designs and Engineering Solutions", Cisco Press, 2003, 30/9/2009.
- [5] "Libya Telecom Technology Company (LTT Company)", 2008.
- [6] Gapoa, N.M., & Al-Kahili, A.A., "Study & Simulation of DWDM Ring Network", B.SC, EE Department of Al-Fateh University, 2009.



المؤتمر الدولي العربي الليبي الخامس للهندسة الكهربائية والإلكترونية 2010/10/26-23 طرابلس ليبيا



## **LTE versus WiMAX Technology Study and Simulation**

Noura Nazir Daadaa  
Communication Engineer  
Email: [nouradaadaa@gmail.com](mailto:nouradaadaa@gmail.com)

### **1. Abstract**

Worldwide Interoperability for Microwave Access (WiMAX) and Long Term Evolution (LTE) are new Wireless communication technology provide users with high data rate and easy way to sharing information everywhere and at any time.

The importance of these technology comes because the needs for high speed And increasing of subscribers numbers. LTE is the 4<sup>th</sup> generation and complementary for WiMAX technology which is 3.5G.

The main target of this paper is to make an overview study of LTE and WiMAX, make comparison between both systems requirements and features then using MATLAB program, both LTE and WiMAX are simulated and the performance of the two Technologies are compared.

These include the relation between throughputs vs. Signal to Noise Ratio (SNR), and Block Error Rate (BLER) vs. SNR. Then the advantages and capabilities of each system is to be presented.

### **1.1 Introduction**

LTE is the 4<sup>th</sup> generation and complementary for WiMAX technology which is 3.5G. In this section we are going to give a brief introduction about development in wireless technology.

### **1.2 Evolution from 1G to 4G Technology**

1G refers to analog cellular system and became available in the 1980s.

2G denotes initial digital systems, introducing services such as short messaging and lower speed data SMS and GPRS.

CDMA2000 and GSM are the primary 2G technologies, although CDMA2000 is sometimes called a 3G technology because it meets the 144 kbps mobile throughput. EDGE also meets this requirement. 2G technologies became available in the 1990s. [8]

3G requirements were specified by the ITU as part of the International Mobile



Telephone 2000 (IMT-2000) project, for To provide 144 kbps of throughput at mobile speed, 384 kbps at fixed speed and 2 Mbps in indoor environments The

which digital networks had following Table 1.1 summarizes the generations

**Table 1.1** Wireless Evolutions

Generation	Requirements	Comments
1G	Analog technology	Deployed in 1980's, simple system.
2G	Digital technology	First digital system, deployed in 1990,new services implemented such as SMS and low data rate
3G	ITU's IMT-2000 required 144 kbps mobile, 2 Mbps indoors	Primary technologies include CDMA2000 EV-DO and UMTS-HSPA. WiMAX now an official 3.5G technology.
4G	ITU's IMT-Advanced requirements include ability to operate in up to 40 MHz radio channels and with very high spectral efficiency.	No technology meets requirements today. IEEE 802.16m and LTE Advanced being designed to meet requirements.

### 1.3 WiMAX EE802.16 Standards

IEEE 802.16 is a series of Wireless Broadband standards authored by the IEEE (Institute of Electrical and Electronics Engineering).

IEEE 802.16 (formerly 802.16.1) - Air interface for 10 to 66 GHz, also known as Local Multipoint Distribution Service. It was approved in December 2001. It delivered a standard for point to multipoint Broadband Wireless transmission in the 10-66 GHz band, with only a line-of-sight (LOS) capability.

So the need for more coverage area and high reliability drive them to develop these standards [2].

OFDMA is a multi-user OFDM that allows multiple accesses on the same

IEEE 802.16.2 - Coexistence of broadband wireless access systems this can also classified in to:

- 1- IEEE 802.15 Personal Area Network (PAN) coverage around 1m.
- 2- IEEE 802.11 Wireless Local Access Network (WLAN) coverage around 10-100m.
- 3- IEEE 802.16 Metropolitan Area Network (MAN) coverage 1-10 KM.

Channel (a channel being a group of evenly spaced sub carriers).

WiMAX uses OFDMA, extended OFDM, to accommodate many users in

The same channel at the same time, we have here two types of Duplexing included





in OFDMA: FDD/TDD and Multiple Access Method:

TDMA/OFDMA.

FDD (Frequency Division Duplexing) Uses One Frequency for the Downlink, and a Second Frequency for the Uplink.

TDD (Time Division Duplexing) uses the same frequency for the Downlink And the Uplink. This can be shown in

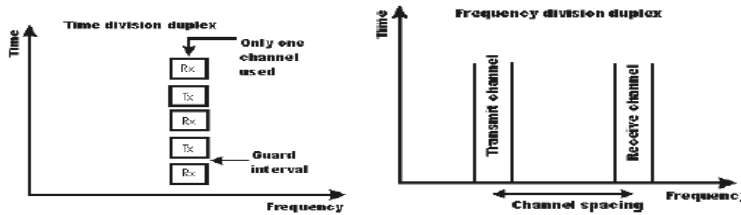


Figure 1.1

Most WiMAX implementations either on licensed or license-exempt bands will most likely use TDD. The reasons are TDD uses half of FDD spectrum hence saving the bandwidth, TDD system is less complex

and thus cheaper, And WiMAX traffic will be dominated by asymmetric data. [4] In Table 1.2 below you will find WiMAX standards properties of each one as: [1], [3]

Table 1.1 WiMAX development

	802.16	802.16 2004	802.16e 2005
<b>Frequency band</b>	10-66 GHz	2-11 GHz	2-11 GHz for Fixed, 2-6 GHz for mobile
<b>Coverage scope</b>	Outdoor antenna	Outdoor antenna	Outdoor/indoor antenna
<b>Cell radius</b>	1.5-4.5 Km	4.5-7.5 Km depends on antenna gain and Pt	1.5 to 4.5 Km
<b>Transmission scheme</b>	Single carrier only	Single carrier, 256 OFDM or 2048 OFDM	SC, 256 OFDM scalable 128,512,1024 2048 sub carrier
<b>Modulation</b>	QPSK, 16 QAM and 64 QAM	QPSK, 16 QAM and 64 QAM	QPSK, 16 QAM and 64 QAM
<b>Cross data rate</b>	32 – 134.4 Mb/s	1-75 Mb/s	1-75 Mb/s
<b>Multiplexing</b>	Burst TDM, TDMA	Burst TDM, TDMA, FDM, FDMA	Burst TDM, TDMA, FDM, FDMA
<b>Channel BW</b>	20, 25, 28 MHz	1.75, 3.5, 7, 14, 25, 5, 10, 15, 8.75 MHz	1.75, 3.5, 7, 14, 25, 5, 10, 15, 8.75 MHz



## 1.4 OFDMA based WiMAX

Orthogonal Frequency Division Multiple Access (OFDMA) and Scalable OFDMA (SOFDMA) both

Flexible extensions to the classical OFDM. The SOFDMA (Simpler OFDMA) is used for the transmission in WiMAX. The most important features are: [3]

1-OFDMA facilitates the system to allocate a varying number of sub carriers to each user, flexible sub channeling of the bandwidth.

2-FDMA and TDMA are applied as multiple access technologies SOFDMA allows adjusting the number of carriers to the transmission channel bandwidth.

3- Minimization of the frequency selective impacts by spreading sub carriers of a user over the entire channel spectrum.

4- Coverage improvement by introducing Adaptive Antenna Systems (AAS) and Multiple Input Multiple Output (MIMO) technology.

5-Introduces high-performance coding techniques such as Turbo Coding and Low-Density Parity Check (LDPC), enhancing security and NLOS performance.

6- Increase system gain by use of denser sub-channelization, thereby improving indoor penetration.

Sub channeling means that instead of transmitting on all sub channels, it is Possible to allocate to a single user only a few and even a single sub channel.

Efficiency Carrier separation is a synonym for carrier spacing or carrier stepping. It is the distance between adjacent sub carriers in the Frequency Domain [3] this could be shown in the Figure 1.2

As a consequence, the equivalent transmission bandwidth for this user will be a portion of the total bandwidth, thus enhancing the link budget. Trade-off between throughput at cell edge and maximum uplink data rate [3]

There are different modulation types used in WiMAX:

PSK, FSK, ASK etc ....

The basic principle of OFDMA is a dedicated carrier spacing in the Frequency Domain. A modulated carrier in Frequency Domain is a sinc x function. The Peak of the sinc x function is the spot on frequency axis where modulation and demodulation takes place.

In OFDMA an exemplary carrier  $f_1$  – peak of the sinc x function – is placed in such a manner on the frequency axis that it has its zero crossings where all other sinc x functions have their peaks. That way it does not disturb the peaks of the other carriers. [3] [1]

In return, the peak of carrier  $f_1$  is not affected by any other carriers, since they have their zero crossings where carrier  $f_1$  has its peak.

In non-OFDMA systems the interference between the carriers is excluded by a guard band between them. With the help of the intelligent placement of the carriers in OFDM, a guard band is obsolete and can be reused for data sub-carriers.

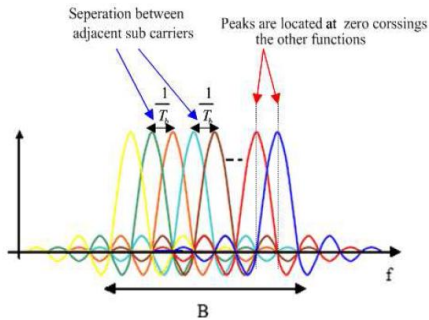


Figure 1.2 OFDMA

FFT sizes — Fast Fourier Transformation sizes point out how often a channel is sampled in the frequency domain. Thus the FFT size corresponds to the number of the sub carriers in the channel. [3] [1]

To cover multiple bandwidths with a similar sub carrier spacing, four FFT sizes are possible in 802.16(e):

- 128
- 512 for 3.5, 5 MHz channelization
- 1024 for 7, 8.75, 10MHz

## 1.5 Slot and Frame Structure

The WiMAX PHY layer responsible for slot allocation and framing over the air . The minimum time-frequency resource that can be allocated by a WiMAX system to a given link is called a slot.

Each slot consists of one sub channel over one, two, or three OFDM symbols, depending on the particular sub channelization scheme used.

A continues series of slots assigned to a given user is called that user's data region, scheduling algorithms could allocate data regions to different users, based on demand, QoS requirements, and channel conditions.

Figure 1.3 shows an OFDMA and OFDM frame when operating in TDD mode. The frame is divided into two sub frames:

- 1- A downlink frame followed by an uplink frame after a small guard interval.
- 2- The downlink-to-uplink-sub frame ratio may be varied from 3:1 to 1:1 to support different traffic profiles.

TDD allows for a more flexible sharing of bandwidth between uplink and downlink. The downside of TDD is the need for synchronization across multiple base stations to ensure interference-free coexistence.

Paired band regulations, however, may force some operators to deploy WiMAX in FDD mode [1].

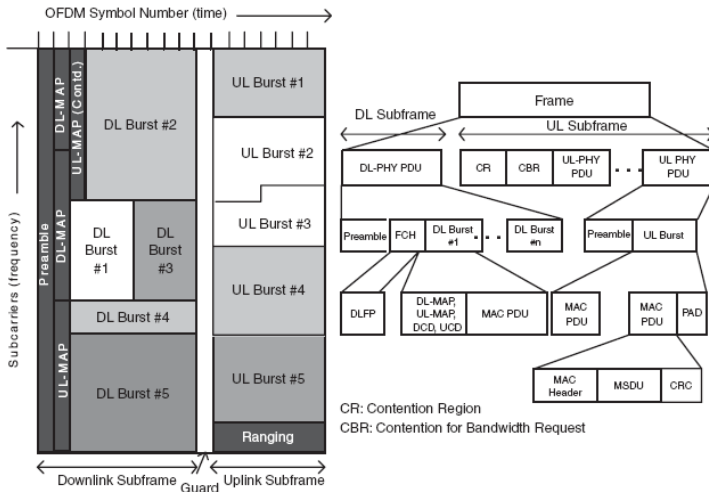


Figure 1.3 TDD Frame structure for mobile WiMAX

The downlink sub frame begins with a downlink preamble that is used for physical-layer procedures, such as time and frequency synchronization and initial channel estimation.

The downlink preamble is followed by a frame control header (FCH), which provides frame configuration information, such as the Mobile Application Part (MAP) message length, the modulation, and coding scheme, and the usable sub carriers. MAP messages include the burst profile for each user, which defines the modulation and coding scheme used in that link. Since MAP contains critical information that needs to reach all users, it is often sent over a very reliable link, such as BPSK with rate 1/2 coding and repetition coding.

When there are a large number of users with small packets (e.g., VoIP) for which allocations need to be specified. WiMAX is quite flexible in terms of how multiple users and packets are multiplexed on a In the downlink, a short preamble can be inserted at the beginning of each burst. It is

single frame. A single downlink frame may contain multiple bursts of varying size and type carrying data for several users.

The frame size is also variable on a frame-by-frame basis from 2 ms to 20 ms, and each burst can contain multiple concatenated fixed-size or variable-size packets or fragments of packets received. From the higher layers. At least All WiMAX equipment will support only 5 ms frames. [1] [5]

The uplink sub frame is made up of several uplink bursts from different users. A portion of the uplink sub frame is set aside for contention-based access that is used for a variety of purposes. [1]

To handle time variations, WiMAX optionally supports repeating preambles more frequently.

In the uplink, short preambles, called midambles, may be used after 8, 16, or 32 symbols.



estimated that having a mixable every 10 symbols allows mobility up to 150 kmph. [1], [5]

A transmission frame as shown in Figure 1.4 is the basic unit for data transport. It is anchored in the MAC layer of the 802.16 standard; a transmission frame has the following basic properties [3]:

1- Lasts for a certain time (number of symbols) — around 5ms.

2- Each transmission frame allocates logical resources to the users.

3- Each frame has a downlink and an uplink sub frame wherein only downlink or uplink data is transmitted

4- Each sub frame has a schedule called MAP that contains information about the location of the data inside the corresponding sub frame.

5- Each connection in the frame is characterized by the number of sub channels and by the number of symbols that are allocated to that connection.

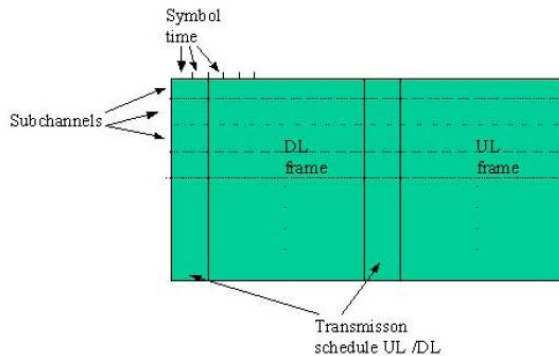


Figure 1.4 Transmission Frame Structure

## 1.6 WiMAX NW architecture

This section describes the WiMAX Access Network for release W3MR1 in Alcatel-lucent. WiMAX Access Network architecture is very similar to UMTS and GSM Technologies. However, the core network does have some new elements, which can be integrated into the existing core.

The WiMAX Forum's Network Working Group (NWG) has defined

- 1- Radio Access Network (RAN)
- 2- Core Network (CN).

So these network elements will be described in details below

First let's consider RAN part which consists of the following

The overall reference architecture of a WiMAX (RAN/CORE)

The WAN is composed of two networks:



## I. Mobile Subscriber Station

The terms MSS, Mobile Subscriber Station (SS) or Customer Premise Equipment, (CPE) all means the user equipment.

## II. BS stands

A WiMAX Base Station provides wireless Internet access to MSS, The Base Station conveys Internet protocol (IP) data between the MSS and the Internet or Services GW by implementing the WiMAX air Interface. This provides an equivalent DSL path to the subscriber for Internet connection and Voice over IP (VoIP) communication. WiMAX Base station (WBS) provides its geographical coordinates using GPS.

## III. WiMAX Access Controller

The WiMAX Access Network Controller (WAC) bundles, controls WBS's network elements. WAC traffic is handled by IP protocols with the rest of the network (Internet, Core Network, Corporate Network, etc...). It plays a vital role during the authentication and the authorization of the user. Based upon the result of authentication, it may allow the user to access the Network, access some limited local services or deny the access. [3], [6]

## IV. Operation and Maintenance Center

Provides a centralized management function for all the elements belonging to the WiMAX access network.

The Operation and Maintenance Center is responsible for:

- 1- Performance Counters
- 2- Alarms

## 3- Network Statistics of the WAN.

The main offered functionality is the management of the following entities like: Topology, Transport, Software, Equipment, Radio and Security [3], [6]

After that let's move to find the main components for Core Elements:

## I. Dynamic Host Configuration Protocol (DHCP)

A DHCP server manages the allocation of IP configuration info by automatically assigning IP addresses to systems configured to use DHCP.

The range to allocate the address depends on the general rules defined by the Operators or related to the external network to be reached through the WAC. Two DHCP servers are required for resiliency purpose [6]

One DHCP server is handling the network elements IP allocation, and the other one allocates IP to the MSS connected to the system.

## II. Domain Name Server (DNS)

This DNS is used to translate names into IP address. The DNS data are gathered into zones. A zone is called primary, when it is the reference for the other secondary zones. The secondary DNS zones are regularly synchronized on the primary zone. The DNS is used to resolve names belonging to foreign PLMN(s). In addition it Allows products from foreign PLMNs to resolve names belonging to the HPLMN. [3]

## III. Network Time Protocol (NTP)

The main WiMAX network elements (like WAC, WBS, DHCP ...) in all the network



need to be synchronized (for charging reports, logs, events ...)

The NTP servers are used to ensure time synchronization. A NTP master server connected to a reference time source by wire or radio acts as a clock reference for all other entities running a NTP client. Each entity system clock is updated with the NTP server system clock. [3]

#### **IV. Authentication, Authorization and Accounting (AAA) Server**

The AAA server is responsible to ensure

- 1- Authentication: that refers to the confirmation that a user who is requesting services is a valid user of the network services requested
- 2- Authorization that refers to the granting of specific types of service (including "no service") to a user, based on their authentication, what services they are requesting, and the current system status.
- 3- Accounting that refers to the tracking of the consumption of network resources by users. This information may be used for management, planning, billing, or other purposes.

#### **V. Home Agent (HA)**

The Home Agent (HA) is in charge of handling the Mobile IP protocol. Each MSS has a static IP address that is stored in the HA. Since the MSS can move around, it might be physically attached to another than the home network.

Usually that means that it has another IP address. Therefore the mobile IP Protocol provides two IP addresses per MSS — a static and a dynamic one. All data from the backbone is sent to the static one. The HA

tracks the mapping of the static home IP address to the dynamic one.

It redirects/tunnels the packets to the dynamic IP address so that the MSS actually receives the data. [3]

### **2. LTE Standards**

Long Term Evolution (LTE) in abbreviation means is new technology Offers high data rate and speed to the end users (costumers), the 3GPP (LTE) represents a major advance in cellular technology. LTE is designed to meet the needs for high-speed data and media transport the development of this technology comes because of many needs and challenges that could be summarized as below:

- 1- 2G Started years ago with GSM Mainly voice and no other services except SMS, MMS and others.
- 2- 2.5G Adding Packet Services to GSM system like GPRS, EDGE
- 3- 3G Adding 3G Air Interface UMTS, this achieved in non urban areas where the land line telephones are not Available, 3G Supports of 2G/2.5G Access.
- 4- It is complimentary of WiMAX technology
- 5- 4G or Long Term Evolution (LTE) Main target is significantly increases data throughput, cell edge, bit rates, reduced latency and many other features [3]

LTE/SAE Long term evolution /System Architected Evolution shall further enhance the 3GPP community with respect to mobile and fixed services, providing data rates beyond 100 Mbps. [1] [2]

LTE/SAE suites for re-farming of the GSM bands and deployments in upcoming allocations, utilize common technologies for different Modes like (FDD, TDD...), in



different frequency bands, with different bandwidths.

## 2.1 OFDMA and SC-FDMA based LTE

Downlink based on OFDMA Orthogonal Frequency Division Multiple Access (OFDMA) offers improved spectral efficiency, capacity and modulation are like QPSK, 16QAM and 64QAM schemes or other supported (Adaptive modulation and coding usually up to 64-QAM in ALU system )

Uplink based on (SC-FDMA) Single Carrier-Frequency Division Multiple Access is technically similar to OFDMA but is better suited for uplink from hand-held devices (battery power considerations), modulation also are BPSK, QPSK, 8PSK and 16QAM schemes or other supported. [5] [3]

So we can summarize these results:

- 1- SC-FDMA saving BW
- 2- SC-FDMA symbol contains M “sub-symbols” that represent the modulating data. It is the parallel transmission of multiple symbols that creates the undesirable high Peak to Average Ratio (PAR) of OFDMA.

By transmitting the M data symbols in series at M times the rate, the SC-FDMA occupied bandwidth is the same as multi-carrier OFDMA but, crucially, the PAR is the same as that used for the original data symbols.

As the number of subcarriers M increases, the PAR of OFDMA with random modulating data approaches Gaussian noise statistics but, regardless of the value of M, the SC-FDMA PAR remains the same as

that used for the original data symbols. [10] [8]

## 2.2 Slot and Frame Structure

TDD Frame structure below in Figure 2.1 shown, Sub-frames consist of either an uplink or downlink transmission or a special sub-frame containing the downlink and uplink pilot timeslots (DwPTS and UpPTS) separated by a transmission gap guard period (GP). [8]

Generally we have 10 sub frames; each sub frame has 2 slots, with over all total duration 10 ms.

The allocation of the sub-frames for the uplink, downlink, and special sub-frames is determined by one of seven different configurations.

Sub-frames 0 and 5 are always downlink transmissions, sub-frame 1 is always a special sub-frame, and sub-frame 2 is always an uplink transmission. The composition of the other sub-frames varies depending on the frame configuration. [10]

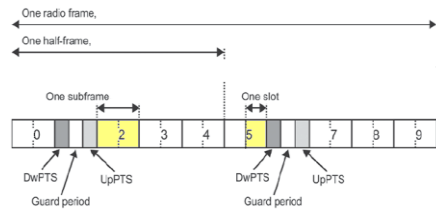


Figure 2.1 TDD Frame Structures [10]

## 2.3 LTE Network architecture

Usually known to build an Evolved packet system (EPS), this can be divided in to 2 main parts:

- 1- Evolved UMTS Terrestrial Radio Access Network E-UTRAN
- 2- Evolved packet core (EPC)





E-UTRAN working as RAN (Radio access network) part in other network, EPC working like PSCN (packet switch core network).

EPC consists of 4 Main parts which are:

- 1- MME (Mobility management Entity)
- 2- S-GW (Serving GW)
- 3- PDN-GW (Packet data NW GW)
- 4- HSS (Home subscriber server)

The most important 2 parts are MME and S-GW, they together works as PDSN or SGSN (parts in UMTS network) they also works as MSC in 2G [13]

MME works as Serving GPRS Support Node gateway (SGSN-GW), and S-GW works as Data Gateway, to manage the data in and out going from the NW. These previous 2 node manage subscriber like Authorize, Authenticate, setup, barriers and other. [13]

The HSS is the evolution of HLR in 2G, it's like a subscriber data base, and it consists of subscriber information, what subscriber allowed doing, PGW represents IP architecture, its function as HA (home agent).

While R-UTRAAN represents RAN, and EPC represents core network and responsible for all packet services, IMS is very important to support voice over IP, in other means support IP Multimedia System. So we call it Service Voice NW. [13]

## 2.4 Inter Networking between LTE and other technologies

The existence networks can be upgraded to be internetworking with LTE so the following Networking schemes are possible [4] [6] [2]

1. LTE over WiMAX Network.
2. LTE over 3G Network.
3. LTE over WCDMA Network

## 4. LTE over GSM Network

This means that it is the treatment of the above internetworking with other access technology is not considered in this paper.

The Figure 2.2 below shows the abbreviation of LTE network

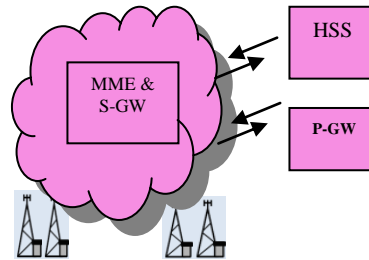


Figure 2.2 LTE architecture

## 3. Simulation

In this chapter, the main target is to simulate and study the behaviour of both LTE and WiMAX technology in the air interface. And to compare both Technologies under different air-condition. (Note that all simulation procedure done for DL in the UE side)

Let's now describe each LTE and WiMAX simulators one by one.

Now the basic variables adjusted but not limited are:

1. SU-SISO.
2. Number of End user is 1.
3. Number of base station is 1.
4. Bandwidth 5 and 10 MHz.
5. Channel type AWGN.
6. Simulated transmitted bits 10 000 bits.
7. Cycle prefix =  $\frac{1}{4}$ .
8. AMC (Adaptive modulation and coding) according to Channel Quality Indicator (CQI) as:
  - From (CQI 1) to (CQI 6) QPSK



- From (CQI 7) to (CQI 9) 16-QAM
- From (CQI 10) to (CQI 15) 64-QAM

Where CQI Channel Quality Indicator is a measurement of the communication quality of wireless channels .

### 3.1 Throughput vs. SNR with 5 and 10 MHz

The relation between LTE and WiMAX throughput summarized if Figures 3.1 and 3.2 for 5 and 10MHz bandwidth. Both are Adaptive coding and modulation AMC, WiMAX Throughput in saturation mode when SNR exceed 9dB, and the maximum throughput could get for user is around 5 Mb/s, while in LTE throughput Increases when SNR increase so that the maximum throughput could get from LTE is around 20Mb/s under 18dB then the throughput goes in saturation mode. LTE gives better bitrates under the same condition compared to WiMAX.

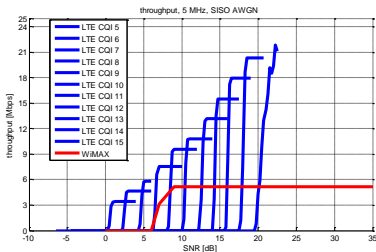


Figure 3.1 LTE and WiMAX throughput vs. SNR in 5 MHz BW

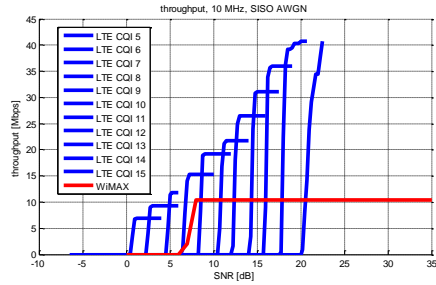


Figure 3.2 LTE and WiMAX throughput vs. SNR in 10 MHz BW

### 3.2 BLER vs. SNR with 5 and 10 MHz

Also in this part, BLER vs. SNR in both LTE and WIMAX were merged together in one Figure for both cases 5 and 10MHz shown in Figures 3.4 and 3.5 as:

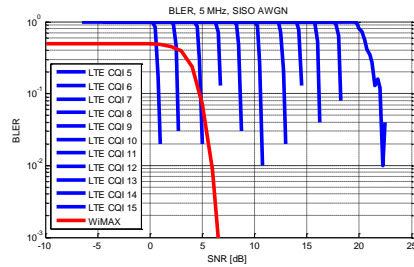


Figure 3.4 LTE and WiMAX BLER vs. SNR for 5MHz

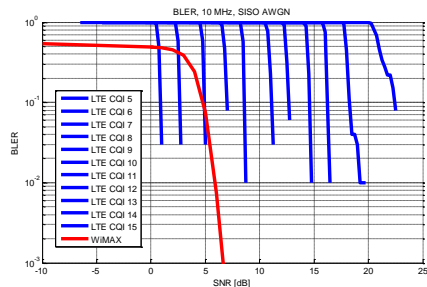


Figure 3.5 LTE and WiMAX BLER vs. SNR for 10MHz



**We can conclude from the simulation these points:**

I. for LTE and WiMAX, when we doubled the BW, the throughput increase clearly. If

Practically the SNR must be higher than this value but theoretically we had Very good speed in LTE compared to WiMAX. And also for the BLER: WiMAX is better than LTE from Block error rate because we get lower error.

This because the modulation type and coding rate in LTE is greater than WiMAX standardization, the probability of falling error increase. But under this bad condition LTE still better than WiMAX. This could compare when BW is 10 MHZ, at SNR is 20 dB and higher, maximum throughput for:

**Table 3.1** comparison between LTE and WiMAX

	WiMAX	LTE	Comments
<b>Network Architected</b>	IP based, BS	IP based eNodeB	Both reduced number of nodes compared to 2G/3G.
<b>Services and reach voice</b>	Packet Data , VOIP	Packet Data , VOIP	LTE high quality video conferencing
<b>Mobility Km/h</b>	Mobility full with less 120	Mobility full with target up to 320	LTE more flexible
<b>Theoretical peak data rates: DL UL</b>	(MIMO 2x 2)  75 Mbps 25 Mbps	(MIMO 2x 2)  172 Mbps 57 Mbps	LTE reaches higher data rate with same MIMO schemes (326.4 MB/s when 20MHz BW and 4x4 MIMO)
<b>Access Technology</b>	OFDMA in both UL and DL	DL- OFDMA and UL SC-OFDMA	SC-FDMA reduces PAPR by ~5 dB → UL improvements
<b>Channel BW</b>	1.25, 3.5, 5, 7, 8.75, 10, 14, 15, 20, 28 MHz	1.25, 2.5, 5, 10, 15, 20 MHz	Both very flexible
<b>Spectrum</b>	Licensed & unlicensed, 2.3, 2.5, 3.5 & 5.8 GHz	Licensed, IMT-2000 Bands (in Appendix )	LTE available at preferred low Frequency Bands _ Coverage Advantage
<b>Duplex Mode</b>	TDD + FDD	FDD + TDD TDD focus	TDD requires Synchronization, FDD can be asynchronous.
<b>MIMO &amp; Antennas</b>	BS: 1, 2, 4 ; MS: 1,2 Closed + open Loop	eNodeB: 1, 2, 4 ; UE: 2 Closed + open Loop	LTE working assumption is 2 DL Antennas p.UE
<b>Networking</b>	Need new NW to be built	Runs as evolution for existing NW infrastructure	LTE has a crucial advantage and more economics

we now take for 5 MHz bandwidth at 20 dB SNR, the maximum throughput:

1. In WiMAX we can get around 5.2 Mb/s
2. In LTE we can get under bad condition in CQI 15 around 17.5 Mb/s.

1. WiMAX is around 10.3 Mb/s.
2. in LTE around 30 Mb/s. So LTE in this case is better than WiMAX.

II. In both technology, throughput better while we increase the Bas Station bandwidth.

So after implementing comparison between LTE and WiMAX using MATLAB we can summarize the Comparison between them as shown in Table3.1:



#### 4. Conclusion

1. WiMAX is a wireless technology, could be fixed and mobile, offer high data rates in both uplink and downlink and uses OFDMA access technology in both, AMC modulation, HARQ, MIMO and limited Transmitter diversity (open diversity).
2. LTE is newest wireless technology , offers higher data rate compared to WiMAX , AMC modulation , used both OFDMA and SC-OFDMA , HARQ, MIMO and (opened/closed diversity), improved spectral efficiency with scalable bandwidth and allow operators to offer advanced services and higher performance for new wider bandwidth.
3. They are both 4G technologies designed to move data rather than voice and all IP networks based.
4. As for speed, LTE can offer higher than the current generation of WiMAX.
5. The crucial difference is that WiMAX requires a new network to be built but LTE runs on an evolution of the existing GSM infrastructure. This means that LTE may have a crucial incumbent Advantage.

#### 5. Future work

There is another Evolution known as LTE Advanced, it's the second release for LTE today. LTE-A helps in integrating the existing networks, new networks, services and terminals to suit the escalating user demands. Coordinated base stations, scheduling, MIMO, interference management and suppression will also require changes on the network architecture.

#### 6. References

- [1] Fundamental of WiMAX understanding broadband wireless networking by Jeffery Andrews and Rays Mohamed 2007
- [2] WiMAX Standardization, FujiTSU laboratories, LTD/michiharu nakamura.pdf 2008
- [3] WAN System introduction .pdf based on IEEE 802.18e standards, ALU W3 release 2007
- [4] Migration to LTE/SAE for a word LTE biasness Development.pdf, Dallas, January 2009, Nokia Siemens NW,
- [5] WiMAX vs. LTE Technology and performance comparison.pdf, Zoin hadad and peretz shekalim, Runcom, 30/10/2008
- [6] LTE overview .pdf, white paper 2007, Ericson.
- [7] LTE Q&A from (GSMA) mobile broadband 2007.
- [8] Overview of 3GPP LTE phy. Layer, white paper, by Dr. Wes McCoy and Jim zyren
- [9] LTE standards (standards for 3GPP) ALU, 2009
- [10] 3GPP/LTE system overview, product development and test challenges, Agilent technology, 10 June 2009.



## Computer Aided Design of 1x2 Optical Power Splitter

MOHAMMAD SYUHAIMI AB-RAHMAN<sup>1</sup>, FOZE SALEH ATER<sup>1</sup>, KASMIRAN JUMARI<sup>1</sup>, RAHMAH MOHAMMAD<sup>2</sup>

Spectrum technology Research Division (SPECTEC)  
Faculty of Engineering & Built Environment  
Department of Electrical, Electronic and Systems Engineering  
University Kebangsaan Malaysia(UKM)<sup>1</sup>, 43600 Bangi, Selangor MALAYSIA  
Universiti Teknologi Mara (UiTM)<sup>2</sup>  
syuhaim@vlsi.eng.ukm, aterfoze@yahoo.com, kbj@vlsi.eng.ukm.my,  
rahmah@technologist.com

**Abstract:** - In this paper, an optimum design of 1x2 optical power splitter is presented. The influence of the width of waveguide has also been examined. We showed that the output power is improved when the width increases for single mode transmission. In addition, at specified values the core and cladding refractive indices, approximately 50% input-to output power ratio is achieved at the output.

**Key-Words:** - Optical power splitter, optimum design

### 1 Introduction

Optical devices are very important components for photonic and optoelectronic optical applications due to their simple structure, low loss and wide optical bandwidth. These structures in term of splitter or coupler provide optical power splitting or combining respectively [1]. Optical splitters find application in optical fiber networks particularly for broadcast optical signal distribution. The preferred device for such applications is the fused tapered optical fiber coupler [2]. However, these devices suffer from high reflection and radiation loss due to branching complexity. It is known that the radiation loss increases with branching angle, and it may be quite significant if the angle exceeds specified value. Thus, in order to keep the loss low by using small branching

angles, long structures are necessary. Though, these are generally undesirable because of the size of structures needed. Consequently, optimum design in term of geometrical dimensions is necessary to improve overall performances, like optical losses and output power division ratio.

In this paper, equal power divider (splitter) is designed. The influence of the width ( $w$ ) of optical channel waveguide on the output power dividing ratio at specified values of core ( $n_{core}$ ) and cladding ( $n_{cladd}$ ) refractive indices and waveguide length is investigated in details. Further, optimum values of  $w$ ,  $n_{core}$ ,  $n_{cladd}$  are obtained that give approximately 50% output power dividing ratio.

### 2 The optimum design

Schematic view of the device used in this



paper is shown in Fig.1. In principle, the waveguide is designed with length,  $L=500\mu\text{m}$ , core  $n_{\text{core}}=1.5$ , and cladding  $n_{\text{cladd}}=1.48$  refractive indices. Moreover, the wavelength is considered to be  $1.55\mu\text{m}$ . This is the most promising wavelength for optical communications, because of the minimum attenuation in optical fiber. The branching angle of our device is estimated to be  $\alpha=0.1^\circ$ . Generally the branching angle should be fixed small in order to decrease the excess loss due to the effective up tapering of the branches and to ensure that the optical splitter adiabatic, i.e. the local super mode does not couple to higher-order-modes. The width of waveguide is changed in order to investigate its influence on the output power dividing ratio.

A beam propagation method (BPM) is used in order to get the desired output. Figs 2a through 2c show respectively the simulation results for normalized output power of the propagating optical beam inside the proposed structure for  $w=2, 4$  and  $6\mu\text{m}$ . As shown in Fig. 2a the output power decreases as the length increases due to increasing of transmission loss. In addition, it can also be noted that output power decreases quit sharply through the optical branching region due to scattering losses. The scattering loss in general can be decreased by adjusting the branching angle (not included here). Instead, the overall loss can be improved by increasing the waveguide width further to 4 and  $6\mu\text{m}$  as shown in Fig 2b and c.

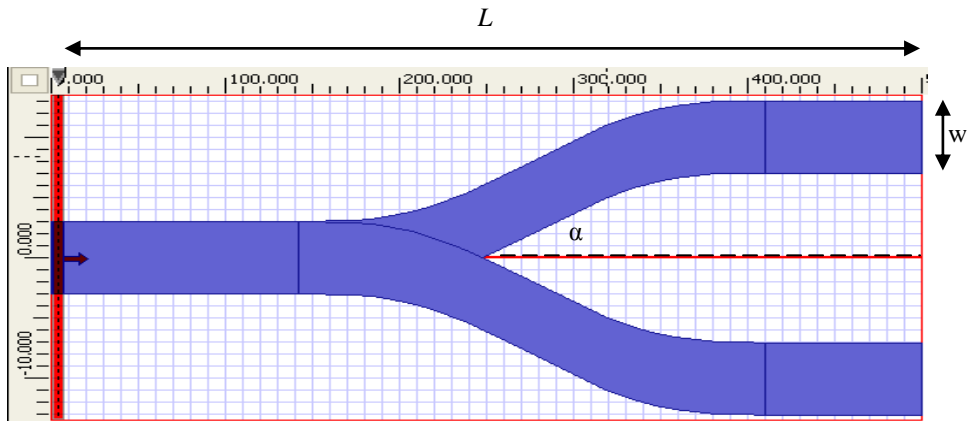


Fig. 1 Schematic view of 1x2 optical power splitter.

From the other hand, decreasing the  $n_{\text{cladd}}$  to 1.35 would lead to improve the output power as shown in Fig. 3a. Moreover, approximately 50% of the input power is obtained with equal power dividing ratio which accords to the symmetric structure. Fig 3b depicts the topographical map of

optical field which is basically the electric field(E) in the electromagnetic waves derived by Maxwell's Equations. Finally, Fig 3c depicts E which varies with the dimensions of our designed optical splitter.



### 3 Conclusion

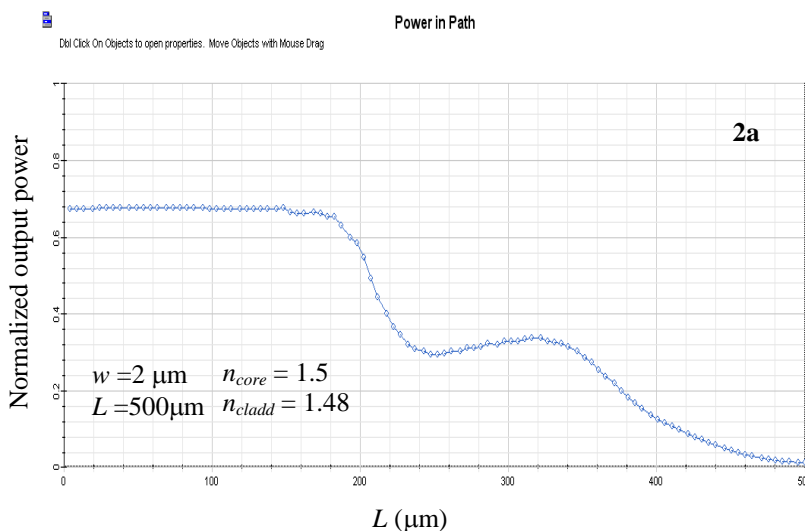
We have presented an optimum design for 1x2 optical power splitter devices. The proposed structure uses an optimum values for the dimensions and refractive indices of the core and cladding of the waveguide. We have examined the influence of the width of waveguide on the output power. When the width increases, the output power increases correspondingly. Further increase in the width may improve the output power slightly but the device may support multimode transmission. Moreover, the output power was improved significantly when the refractive index of the cladding was decreased from 1.48 to 1.35 giving approximately 50% of the input power at the output branches.

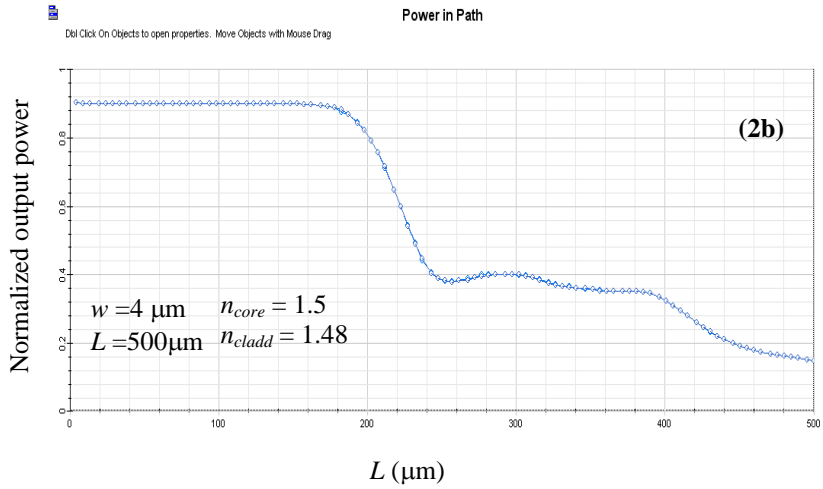
### Acknowledgement

This work is sponsored by Universiti Kebangsaan Malaysia (UKM) through UKM-AP-ICT-17-2009.

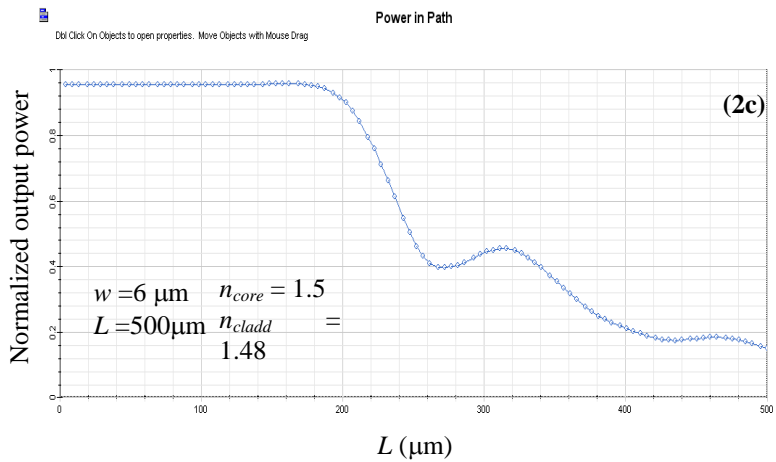
### References:

- [1] N. GROSSARD, J. HAUDEN, H. PORTE, Low-loss and stable integrated optical Y-junction on lithium Niobate modulators, European Conference on Integrated Optics, ThG08, 2007.
- [2] R. A. BETTS, F. LUI, and S. DAGIAS, Wavelength and polarization Insensitive optical splitters fabricated in K<sup>+</sup> /Na<sup>+</sup> ion-exchanged glass, IEEE Photon. Technol. Lett., vol. 2, no. 7, 1990.
- [3] Y. S. YONG, A. L. Y. LOW, S. F. CHIEN, A.H. YOU, H. Y. WONG, Y. K. CHAN, Design and analysis of Equal power divider using 4-branch waveguide, IEEE Journal of Quantum Electronics, Vol. 41, No.9, 2005
- [4] M. H. IBRAHIM, N. M. KASSIM, A. B. MOHAMMAD, M. K. CHIN, S. Y. LEE, Polymeric optical splitter based on multimode interference mechanism, 4th IEEE Student Conference on Research and Development (SCORED 2006), Shah Alam, Selangor, Malaysia, 2006.
- [5] OptiBPM, Waveguide design software, Version 9.





(a)



(b)



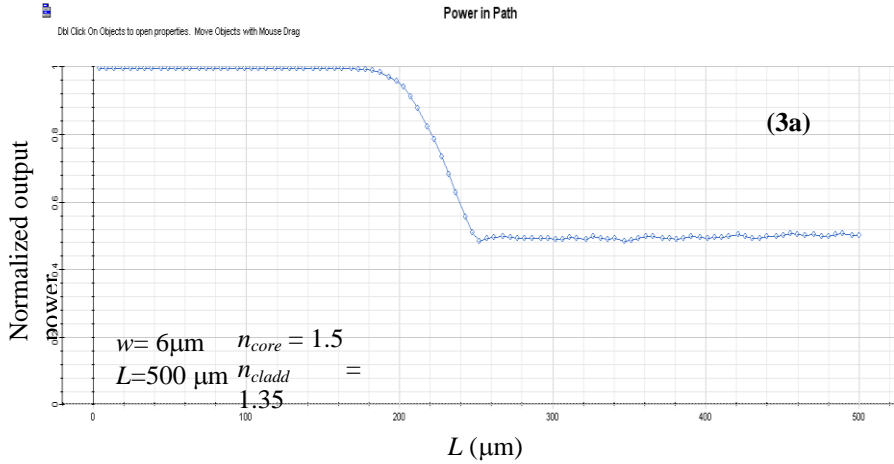
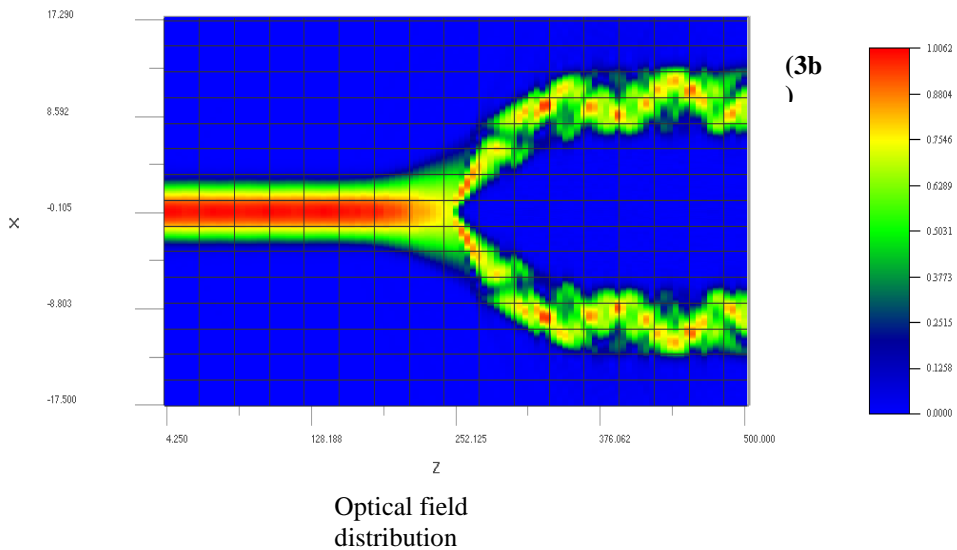


Fig 2 Normalized output power of the propagating optical beam inside the proposed structure of 1x2 optical splitter for the two branches for  $L = 500 \mu\text{m}$  and  $w =$  (a) 2 , (b) 4 and (c)  $6 \mu\text{m}$ . (d)



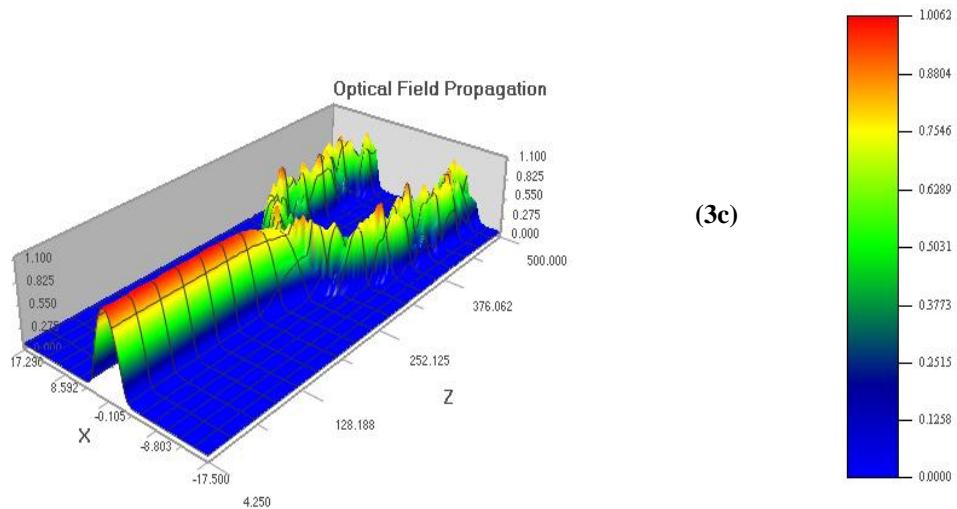


Fig 3 (a) Normalized output power of the propagating optical beam (b) and (c) The Top graphical map and 3D graphical representation of optical field respectively for  $n_{cladd} = 1.35$ .



## Paper NO. 102067

### PERFORMANCE OF ADAPTIVE MULTIUSER DETECTION IN DS/CDMA RECEIVER

\* Satyanand Singh  
Assistant Professor  
Aurora's Scientific Technological and Research  
Academy, Hyderabad.  
techno\_satya@yahoo.com

Sanjay Kumar Tripathy  
Lecturer, Department of communication and  
Software Engineering,  
Civil Aviation Higher Institute, Asbia  
Libya

#### 1.ABSTRACT

CDMA technology has the potential to provide a significant improvement in the capacity of cellular mobile radio systems compared with FDMA and TDMA systems. However, the improvement is dependent upon the effectiveness of the power control system, especially on the up-link. In absence of power control, a base station would receive a much stronger signal from a mobile that is geographically close to it than from a mobile that is farther away. The consequence is a dramatic decrease in system capacity. This is the so-called near-far problem. The Near-Far problem in the Direct-Sequence Code-Division Multiple-Access communication field has drawn a lot of attention. The focus of this paper is on the multi-user interference rejecting capability of the so-called adaptive DS/CDMA receiver. The receiver uses a chip-matched filter followed by an adaptive equalizer structure. It allows the users to adjust to the interference and the noise. The Qualitative results of this receiver and the conventional receivers are compared and this receiver is shown to have lower BER. Also by inspecting the BER results with and without the power control, it can be concluded that this receiver is resistant to Near-Far effect.

#### Note:

**This paper is included in the conference program but not published because the revised copy after introducing the reviewed comments did not arrive in the specified Time**



المؤتمر العربي الليبي الدولي الخامس للهندسة الكهربائية والإلكترونية 23-26/10/2010 طرابلس ليبيا



## Improved 3G System using MIMO in Rayleigh Fading Channels

Mohamed Aziz and Xian Yang.

School of Electronics & Electrical Engineering University of Bath-UK.

Email: m.aziz@bath.ac.uk

### ABSTRACT

WCDMA is the heart of the third generation (3G) mobile communication networks which supports multimedia communications. In WCDMA there is no need for frequency planning as the case for the second generation system (2G). However, WCDMA system is an interference-limited system making it difficult to support large numbers of users. Also, problems still arise in terms of QoS and call dropping in high interference channels, which opens the 3G system for investigation and research. In this paper we propose a MIMO/WCDMA system that mitigates the wireless channel effects and enhance QoS as well as the capacity of the system. To investigate the 3G system performance using MIMO (Multiple Input Multiple Output) diversity scheme and STBC 2\*2 algorithm in real environment, channel effects were added through Rayleigh fading and AWGN. By analyzing the results achieved, significant improvements can be made including high quality multimedia services and improved QoS with larger capacity transmission. The proposed system can also be used as a platform for the 4th generation system.

**Keywords:** WCDMA, 3G, MIMO, Rayleigh Fading Channel.

### 1. INTRODUCTION

The third generation (3G) system developed to provide high bit rate communications with multimedia capability. It utilizes a mobile radio and network access scheme which enables the transmission of high-speed data [1]. The Wideband Code Division Multiple Access (WCDMA) is one such efficient and flexible radio access technology adopted in 3G system [2]. Based on Direct-Sequence Code Division Multiple Access (CDMA) algorithm, WCDMA can support mobile voice, images, data and video

communications at up to 2 Mbps [3]. Although, in theory, the WCDMA system can greatly increase information transmission ability, it still encounters problems in the delivered QoS and call dropping, i.e. also known as cell-breathing. This is due to the interference limitation of the WCDMA multiple access system. However, this limitation can be alleviated by using proper techniques to mitigate the channel effects and interference problem in 3G systems. The MIMO technique is one of such strategies that can be implemented in order to increase channel capacity and reduce interference [7, 8, 9].



Hence, in this paper we are proposing the use of the MIMO/WCDMA system to improve the existing performance of the 3G system and also as a proposal for the next generation mobile networks. The following points highlight the importance and contributions of this research:

- WCDMA mobile system is designed to support a large variety of multimedia services for mobile users with different quality of service (QoS) requirements. There are four different categories of QoS: conversational, streaming, interactive and background [2]. Each class has different specifications of QoS such as delay, data speed, and bit error rate [4]. However, data traffic quality is related to interference levels. This investigation will help to analyze the QoS requirements on WCDMA system and suggests an improved method to enhance the system resilience to interference.
- WCDMA utilizes the technology of code division multiple access to enable all users to share the same bandwidth simultaneously. So the system capacity and traffic quality are related to interference levels. The blocking occurs when either there are no spreading codes available or the noise level exceeds the requirement of service quality [5]. In this paper, the influence of interference will be analyzed and the scheme to improve system capacity will be proposed.

- It is also necessary to improve the performance of WCDMA system in order to provide a better platform for the next generation mobile systems and to provide more integrated services and applications with higher capacity [6].

The rest of this paper is divided into the proposed system model for MIMO/WCDMA, the simulation results and discussion and finally the conclusion.

## 2. SYSTEM MODEL

The proposed WCDMA system generally contains three parts: transmitter, receiver and MIMO module. The transmitter generates the transmission signal and spreads it into wideband signal, while the receiver recovers the signal and transfers it to the baseband. The MIMO system introduces the space diversity to the WCDMA system by applying multiple antennas at the transmitter and receiver. Moreover, the simulated propagation channel in the wireless system is also modelled in MIMO part. In order to analyze the MIMO performance properly, an additional factor is developed to show the capacity increment brought about by the MIMO utilisation.

### A. WCDMA transmitter

The transmitter of a WCDMA uplink channel is shown in Figure 1. The signal at the receiver undergoes three stages: modulation, spreading and scrambling.

In order to transmit the information and control bits together, the WCDMA system utilizes the QPSK modulation scheme



which can provides two orthogonal channels. Then the Orthogonal Variable Spreading Factor (OVSF) code is generated simultaneously to spread the bits into the wideband channel. At this stage, each user is assigned to a unique orthogonal spreading code. This is then followed by the scrambling process. All the users in the same cell share the same scrambling code. The purpose of applying scrambling code is to distinguish the users in different cell. Afterwards, the data is transmitted through the MIMO system frame by frame. The receiver acquires the signal through MIMO interface and processes the data in the reverse order to that of the transmitter.

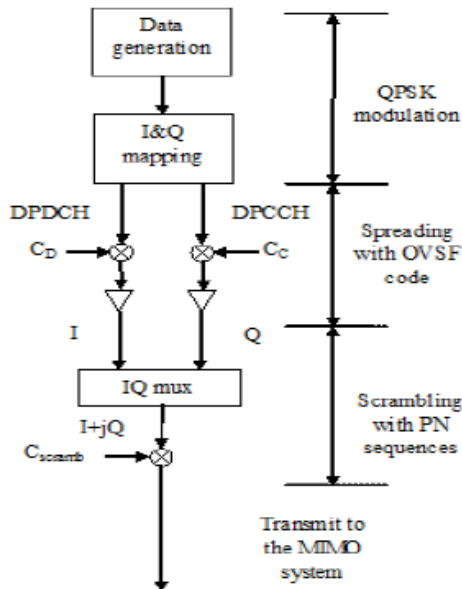


Figure 1: WCDMA transmitter block diagram for uplink channel.

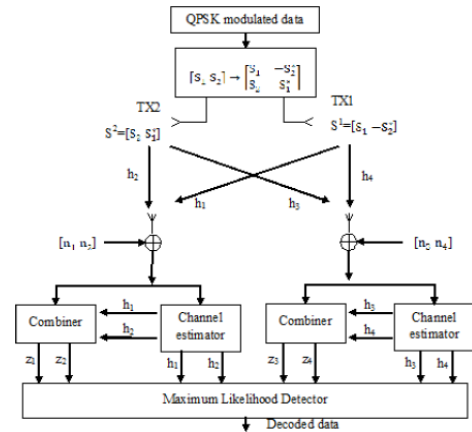


Figure 2: Block diagram of MIMO system

### B. MIMO System Model

The MIMO model involves channel simulation and antenna diversity. Figure 2 illustrates the block diagram of the MIMO scheme. The MIMO system receives the data from WCDMA transmitter, and applies the Space-Time Block Codes (STBC) scheme to encode the QPSK modulated signal.

By introducing the STBC 2\*2 scheme, the encoder takes the block of two symbols  $S_1$  and  $S_2$  in each encoding operation and gives it to the transmit antennas according to the code matrix [7],

$$S = \begin{bmatrix} S_1 & -S_2^* \\ S_2 & S_1^* \end{bmatrix} \quad (1)$$

The column represents the two symbols transmitted at the same time, while the row shows two symbols transmitted at the same antenna. Assuming the fading coefficient of antenna\_1 and antenna\_2 is defined as  $h_1$  and



$h_2$ , two received symbols can be expressed by:

$$r_1 = h_1 s_1 + h_2 s_2 + n_1 \quad (2)$$

$$r_1 = -h_1 s_2^* + h_2 s_1^* + n_2 \quad (3)$$

where  $h_1$  and  $h_2$  are channel matrices which represent the Rayleigh fading channel,  $n_1$  and  $n_2$  are Additive White Gaussian Noise with zero mean and unit variance.

At the receiver the Rayleigh fading channel matrices  $h_1$  and  $h_2$  are recovered. The combiner combines the signal as follows [8]:

$$z_1 = h_1^* r_1 + h_2 r_2^* = (\alpha_1^2 + \alpha_2^2) s_1 + h_1^* n_1 + h_2 n_2^* \quad (4)$$

$$z_2 = h_2^* r_1 - h_1 r_2^* = (\alpha_1^2 + \alpha_2^2) s_2 - h_1 n_2^* + h_2^* n_1 \quad (5)$$

Where  $\alpha_1 = h_1^* h_1$ , and  $\alpha_2 = h_2^* h_2$ .

The received signals are then passed to the Maximum Likelihood Decoder, which minimize the following decision metric.

$$\left| r_1 - h_1 s_1 - h_2 s_2 \right|^2 + \left| r_2 + h_1 s_2^* - h_2 s_1^* \right|^2 \quad (6)$$

Afterwards, the symbols are decoded and the last step of MIMO system is to examine the BER improvement of STBC 2\*2 scheme. The bit error rate of the MIMO system is compared to the bit error rate achieved without MIMO for proper comparison.

### 3. SIMULATION MODEL

In the simulation model, the WCDMA transmitter where  $h_1$  and  $h_2$  are channel matrices which and receiver are implemented first. Bit error rate represent the Rayleigh fading channel,  $n_1$  and  $n_2$  are

calculation is the main method to test the system performance. Only when the BER of the decoded signal at the receiver is zero, i.e. the system is fully functional, the channel effects can be introduced to the system. The application of MIMO scheme is the key improvement or addition to the previous system design. The Rayleigh channel and AWGN effects are added to the system in the MIMO stage.

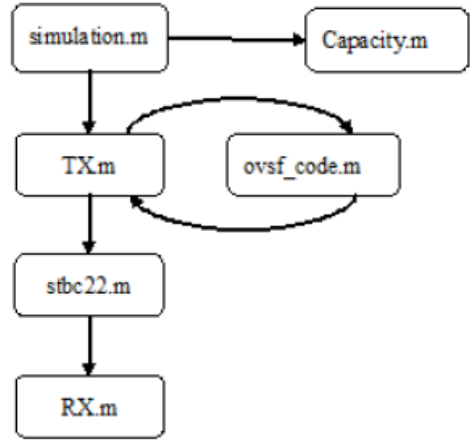


Figure 3: Blok diagram of system simulator model.

The basic simulation block diagram is shown in Figure 3. The whole system is divided into four parts: transmitter, MIMO, receiver and capacity analysis, which are denoted by the MATLAB files TX.m, stbc22.m, RX.m and Capacity.m. The MATLAB file simulation.m provides a user interface to run the model.





#### 4. SIMULATION RESULT AND DISCUSSION

In this section, the simulation results are presented and analyzed. The simulation shows the system performance of WCDMA uplink channel. The results are discussed in mainly two aspects: the attributes of WCDMA and the improvements of WCDMA with the assistance of the MIMO interface. However, the main method to evaluate the system performance is through the BER measurements at the receiver.

##### A. WCDMA system characterisation without MIMO

The WCDMA system can provide different transmission rates, by which the SF varies for different traffic streams. Hence, the system performance resulted from different SF will be discussed in details. Furthermore, the interference limitation of multiple access method will also be explained by the simulation results.

##### - Interference restriction of WCDMA (SNR)

The effect of the rising number of users on the overall system performance is shown in Figure 4 below. The WCDMA utilizes the DSSS scheme which can support multiple users to transmit the signal simultaneously. This attribute of the WCDMA system raises the problem of multiple access interference. It is clear from Figure 4 that the increasing number of user results in larger accumulated BER.

##### - Spreading Factor effects

In Figure 5, the effects of using different spreading factors on the BER are illustrated. In the simulation, three mobile users are introduced to transmit signal at the same time with the spreading factor of 4, 8, and 16 respectively. 38400/SF symbols are transmitted by each user. Moreover the recovered data is compared with the original data generated at the transmitter. The receiver then calculates the BER of the signal which is corrupted by the Rayleigh fading channel.

In Figure 5, the BER is examined by various SNR. The signal to noise ratio ranges from 0 to 20dB. The maximum BER is obtained when the SNR equals to zero.

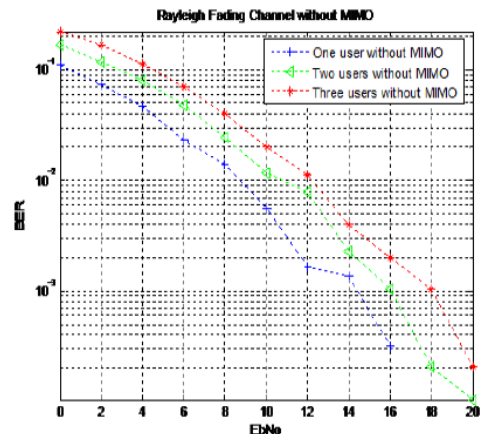


Figure 4: Simulation results of Rayleigh fading channel.

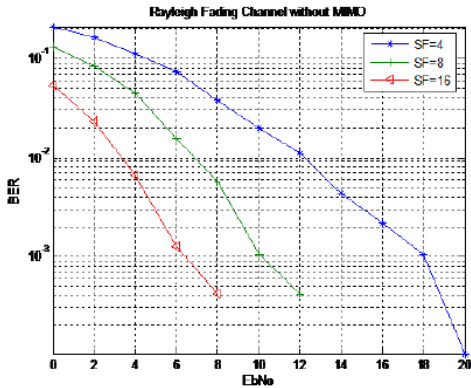


Figure 5: The simulation results due to different SF.

Table 1 below, indicates the value of BER resulted from different SF application. It is clear that the user with higher SF has much fewer errors than the others. The BER equals to zero for ‘User One’ when SNR equals to 10 dB, while the BER for ‘User Two’ can only reaches to zero when SNR is equal to 14 dB, this is equivalent to saving 4dBs of signal power. When SNR is 2dB, for example, the BER with SF 16, 8 and 4 is 0.023333, 0.084375 and 0.16323 respectively. Therefore the BER is highly reduced when SF increases. On the other hand, from a design perspective, if the system is designed to achieve the bit rate of 0.001, the SNR of ‘User-1’ is 6 dB, while the SNR of ‘User-2’ and ‘User-3’ approximates to 10 dB and 18 dB, respectively. It can be concluded that the spreading factor is a very important value in the WCDMA system. The SF can influence the system performance and transmitted signal power greatly.

SNR\User	User 1: SF =16	User 2: SF =8	User 3: SF =4
0	0.05375	0.13021	0.2124
2	0.0233333	0.084375	0.16323
4	0.0066667	0.044792	0.11365
6	0.00125	0.015625	0.073125
8	0.00041667	0.005625	0.037917
10	0	0.0010417	0.02
12	0	0.00041667	0.011042
14	0	0	0.004375
16	0	0	0.0021875
18	0	0	0.0010417
20	0	0	0.00010417

Table 1: The simulation results due to different SF.

### B. WCDMA system with MIMO

The key contribution to the WCDMA in this section is introducing the MIMO interface to combat the fading effects of the channel and analyse the mathematical requirements of the system. The simulated results will show the advantages of applying antenna diversity to the system. The aspect of BER reduction will be taken into consideration. The improvement in capacity due to MIMO system will also be presented and discussed.

#### - BER reduction

In order to test the ability of MIMO system to suppress BER and improves capacity, the system simulates one user transmission. The modulated data of the user is transmitted over Rayleigh fading channel. The total number of symbols generated in the simulation is 38400 symbols. Figure 6 shows the BER reduction brought about by the MIMO system. It is clear that the STBC 2\*2 scheme can reduce



the channel effect to a significant degree.

With the increase in SNR we notice and large improvement in the system performance, which is significant in terms of the BER improvement.

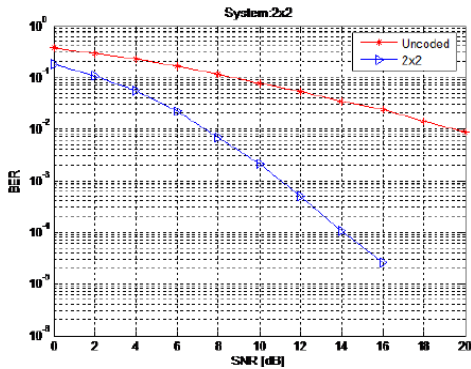


Figure 6: The BER improvements of MIMO system.

#### - BER and capacity

After observing the advantages of introducing MIMO to reduce BER and increase capacity [9], the next step is to discuss these two factors together. From Figure 7 below, when the BER of about 0.022 is achieved, the SNR of the uncoded (SISO) system is 16dB, while the SNR of the MIMO system is only 6dB. Therefore, in this case, the saving in signal power is about 10 dB, which is a significant improvement in performance. Not only the power is saved, the inter-channel interference can also be reduced. With the reduced SNR of 10 dB, the increased capacity can be roughly calculated as:

$$C = \log_2(1+10) = 3.4594 \text{ b/s/Hz} \quad (7)$$

Thus, the increase in capacity can

be used to transmit other information bits or allow more users and services. So it can be concluded that applying MIMO is a good choice to improve WCDMA system capacity and performance.

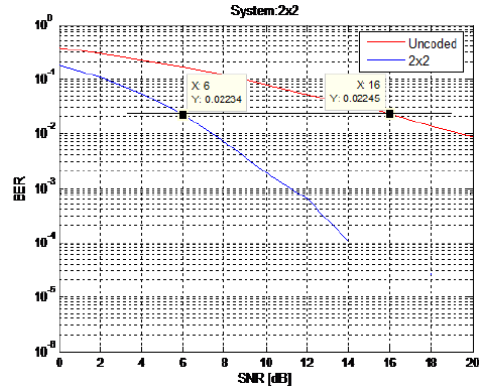


Figure 7: BER of MIMO system

#### 5. CONCLUSION

The 3G system utilizes WCDMA multiple-access method to support multiple wireless users simultaneously in the same frequency bandwidth. The general schemes of WCDMA system including duplex, modulation and spectral spreading techniques are adopted to build the simulation platform. The proposed WCDMA system is assisted with the MIMO scheme which guarantees better QoS, i.e. lower BER, and improved capacity of the system. By analyzing the simulation results, it is clear that the channel effects are mitigated by the STBC 2\*2 scheme as shown above in Figures 6 and 7. The BER resulted from the MIMO system is much smaller than the SISO (Single Input Single Output) system. Moreover, the capacity improvement brought by the



MIMO scheme further proves the advantage of introducing diversity to the WCDMA system. Hence, the proposed MIMO/WCDMA system can provide and improved service and is suitable for the next generation mobile networks.

## 6. REFERENCES

- [1] SIMTH, C. AND COLLINS, D., 2006. 3G Wireless Networks. 2nd ed. McGraw-Hill Professional.
- [2] HOLMA, H. AND TOSKALA, A., 2004. WCDMA for UMTS: Radio Access for Third Generation Mobile Communications. 3<sup>rd</sup> ed. John Wiley and Sons.
- [3] BEDELL, P., 2005. Wireless Crash Course. 2<sup>nd</sup> ed. McGraw-Hill Professional.
- [4] ALQAHTANI, S. A. AND MAHMOUD, A. S., 2006. Radio Resource Management with Dynamic Behaviour for 3G and Beyond Wireless Networks with Heterogeneous Traffic. 14th IEEE International Conference on Networks. September 2006. Singapore.
- [5] OWEN, R. et al., 2000. Uplink WCDMA capacity and range as a function of inter-to-intra cell interference: theory and practice. IEEE 51st Conference Proceedings of Vehicular Technology. pp. 298 - 302 vol.1. Tokyo.
- [6] MUNOZ, M. AND RUBIO, C.G., 2004. A new model for service and application convergence in B3G/4G. Wireless Communication, 11(5),pp.6-12.
- [7] KUHN, V., 2006. Wireless communications over MIMO channels: applications to CDMA and multiple antenna systems. Chichester: Wiley.
- [8] JANKIRAMAN, M., 2004. Space-time codes and MIMO systems. Artech house publishers.
- [9] DRIESSEN, P.F AND FOSCHINI, G.J., 1999. On the capacity formula for multiple input-multiple output wireless channels: a geometric interpretation. IEEE Transactions on Communications, 47(2).



## Performance Study of Forward Error Correction Codes for long bursty IPTV traffic over Wireless AWGN Channels

Manar Sami Arif , Mohamed Hadi Habaebi, Yousef Hwegey

Department of Computer Engineering, Alfatah University, Tripoli, Libya  
[amged\\_20072003@yahoo.com](mailto:amged_20072003@yahoo.com) ; [habaebi@ieee.org](mailto:habaebi@ieee.org); [y\\_hwegey@yahoo.com](mailto:y_hwegey@yahoo.com)

**Abstract**— Powerful Forward Error Correction (FEC) codes are usually used over digital video broadcast (DVB) networks . IPTV uses a base video layer &enhancement layer. In IPTV the slight variation between consecutive frames gets propagated, and amplified in future P or I-frames, The I-frame has the highest dependency where corruption of an I-frame will result in error propagation through all the frames in the Group of Pictures (GOP). This phenomena motivates the development at fine - granulated FEC Scheme in the application layer at the frame level (GOP) rather than the packet level. In this paper, we study the use of power full Reed Solomon (RS) codes at the video source layer to improve the Internet Protocol Television (IPTV) performance over DVB-T channel. Protecting the I-frames separately resulted in better picture quality and less packet loss ratio in comparison to current schemes used in DVB-T standard The use of double RS encoding and interleaving for the I-frame in the application layer reduces the Bit Error Rate (BER) and provides a good Average Peak- Signal- to -Noise- Ratio (PSNR) with small system Signal to Noise Ratio (SNR).

Keywords-component:-MBEG-4, IPTV, video frame, GOP, Reed-Solomon.

### I. INTRODUCTION

In the digital television service is delivered using the IP protocol over a network infrastructure. It covers both live TV (broadcasting) as well as stored video (Video on Demand). The playback of IPTV requires either a personal computer or a "set-top -box" connected to a TV. Video content is typically compressed using either a MPEG-2 or a MPEG-4 codec and then sent in an MPEG transport stream delivered via IP Multicast in case of live TV or via IP Unicast in case of Video on Demand [1]. The video stream is up linked to the service provider's satellite in DVB format, or over terrestrial links to DVB-H /DVB-T units .

Video compression algorithms are based on exploiting spatial and temporal redundancy present in a sequence of frames. Spatial redundancy

means that different parts in a frame are correlated whereas temporal redundancy means that neighboring frames are correlated. Digital video formats define a hierarchy of data types to represent the material. For block based schemes, the video sequence is typically divided into a series of Group of Pictures (GOP). Each picture is made up of slices, which contain macro-blocks (MB) of four blocks each. A block is typically 8x8 pixels. A Group of Pictures (GOP) is a set of pictures in



contiguous display order. MPEG4 supports three types of pictures: I-frames, P-frames and B-frames. Intra frames (I-frames) are compressed using intra frame coding, without the need to reference to another picture. Predicted frames (P-frames) are coded with reference to the nearest previously coded picture (either I or P frame), using a motion-compensated prediction mechanism. Bidirectional predicted frames (B-frames) use both Prediction and future I or P fairness as reference for motion estimation and compensation. Each picture is divided into slices. Slice is a horizontal strip of macro blocks within a frame, slice is divided into macro blocks[3],[5-7]. Recently IPTV is introduced over WLAN and WIMAX networks and delayed to be broadcasted over satellite networks .Wireless channels are error-prone in nature and backward/forward error correction code (ARQ/FEC), are necessary to support the QOS levels associated with IPTV traffic .In fact , practically IPTV traffic requires 2-

layer FEC code (application & link ) layer in order to minimize the channel effect[2]. For example , IPTV over Wimax used Raptor codes for application layer in conjunction with RS codes for the link layer together with ARQ techniques .The main traditional distribution method for broadcast television uses coaxial cables for the distribution of the television broadcasts. These television broadcasts are analogue and are affected by propagation losses. This traditional form of television is gradually being replaced by distribution over IPTV networks and other methods of digital video broadcasting (DVB) that provided either via cable (DVB-C), satellite (DVB-S) or terrestrial (DVB-T). This paper ,utilize the IP networks for the distribution of television content . The performance comparison of RS codes with interleaver code in the application layer and RScore with convolution codes in the physical layer were considered for the DVB-T standard system.

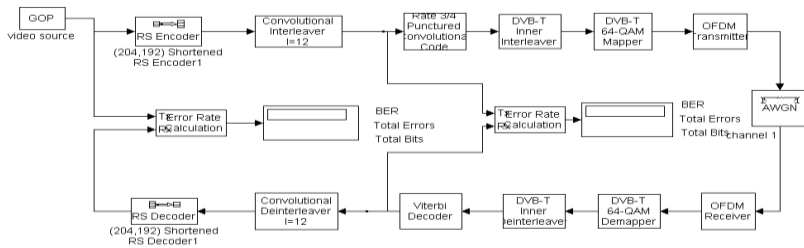


Figure 1. Block diagram of the transmitter and receiver of simulated digital video broadcast – terrestrial(DVB-T)system

video streams up to 3-Gbps without any retransmissions is proposed in [14]. New features of the mmWave system incorporates: (i) UEP (unequal error protection) where different video bits (MSBs (most significant bits) and LSBs(least significant bits) ) are protected

differently, (ii) a multiple-CRC to determine whether MSB or/and LSB portions are in error, (iii) RS code swapping (RSS), an error concealment scheme which can conceal some errors in video pixels. Simulations using real uncompressed HD images indicate that the proposed mm



Wave system can maintain good average PSNR (peak-signal-to-noise-ratio) under poor channel conditions, achieving what is generally accepted as a good picture quality with PSNR values greater than 40dB.

The next section introduces the simulated DVB-T system, and introduce the proposed source coding used for I-frame.

## II. SYSTEM MODEL AND PROPOSED FEC SCHME

Digital Video Broadcasting – Terrestrial ( DVB-T) is defined as the functional block of equipment performing the adaptation of the baseband TV signals from the output of the MPEG- 4 transport to the terrestrial channel characteristics. Since the intention of this paper is to highlight the FEC performance for IPTV traffic over DVB-T channel, we shall concentrate on explaining the error correction codes used in the simulator. Other details will be ommitted for space limitation and can be found in [10] and [11].

### A. DBV-T System Model

Modulation of digital data is insufficient to ensure error free communication. Therefore, redundancy needs to be added to the data bits so that the receiving end can recover from errors by correcting them. Forward Error Correction (FEC) is implemented in our system in four phases: Application Layer (AL-FEC) for MPEG-4 stream source, Physical layer Randomization, Forward Error Correction and Interleaving.

Fig.1 shows a block model of a communication system that is simulated in MATLAB environment. Before the coding an energy dispersal process is applied: the data at the baseband interface is combined with the bit stream of a pseudorandom

noise generator to achieve a flat power-density spectrum. This Randomization stage of error correction ensures that there is a high level of entropy in the data. In other words, the probability of occurrence of a '0' is the same as that of a '1', locally and over a long range. The bits issued from the randomizer are fed to the FEC block.

The Link layer Forward Error Correction block consists of two layers – an outer Reed-Solomon code and an inner Convolutional code. Reed Solomon codes are block codes that

are good for correcting burst errors. Convolutional codes are good for correcting random errors. Together, the combination effectively corrects most errors caused by the hostile wireless channel. The outer error protection is implemented with a byte-oriented block code. For each block, i.e. the TS packet constituted by 188 information bytes, 16 error correcting bytes are calculated and appended to that packet. To achieve this, a Reed-Solomon (204, 188,  $t = 8$ ) shortened code is used, derived from the original systematic Reed-Solomon (255, 239,  $t = 8$ ) code. After the coding process, convolutional byte-wise interleaving is applied to the error protected packets. An outer convolutional interleaver rearranges the bytes of the packets in order to facilitate the correction of long burst errors. A Viterbi decoder is used at the receiving end to decode data and correct errors.

A second level of error correction, denoted as inner coding, is subsequently applied. In particular, a punctured convolutional coding with code rate  $m/n$ , i.e. the ratio between number of useful bits,  $m$ , and number of useful plus redundancy bits,  $n$ , is applied to the input binary sequence. Therefore,  $n-m$  redundancy bits for error correction are added to each group of  $m$  useful bits. The system allows for a range of punctured convolutional codes, based on





a mother convolutional code of rate 1/2 with 64 states [10].

An inner interleaver follows the inner error protection; it consists of block based bit-wise interleaving and block-based

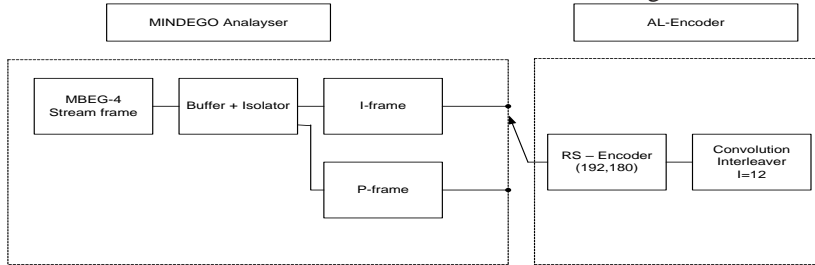


Figure 2. Source Coding For MBEG-4 Traffic At The Application Layer

symbol interleaving. In the bit-wise interleaving process the input is demultiplexed into  $v$  sub-streams, where  $v = 2$  for QPSK,  $v = 4$  for 16-QAM, and  $v = 6$  for 64-QAM. Each sub-stream is then processed by a separate bit interleaver where 126 successive input bits are grouped into one block and are then interleaved within this block. The purpose of the symbol interleaver is to map  $v$  bit words onto the 1512 (2K mode) or 6048 (8K mode) data carriers per OFDM symbol, where each OFDM symbol is constituted by the sequence of the 1705 or 6817 data symbols of the corresponding active subcarriers. The symbol-wise interleaver acts on blocks of 1512 or 6048 data symbols by changing their sequence. The result on the DVB-T signal is frequency interleaving inside an OFDM symbol [11]. This interleaving process is defined as a two-step permutation. The first ensures that neighboring data bits are mapped onto non-adjacent OFDM carriers. This ensures that if a deep fade affects a bit, its neighboring bits are likely to remain unaffected by the fade, and therefore FEC is sufficient to correct the effects of the fade. The second step maps adjacent bits onto less or more significant constellation bits. This makes

detection accurate and long runs of low reliability bits are avoided.

After the data bits are interleaved, they are entered serially into a data modulator with the option of Gray coded QPSK, 16-QAM and 64-QAM. The following modulation and coding rates are supported: 1/2, 2/3, 3/4, 5/6, and 7/8. For the purpose of our performance simulation, the 64-QAM with rate = 1/2 is used only in this paper in conjunction with the varied Additive White Gaussian Noise (AWGN) wireless channel. Noise described by the Gaussian model is characterized by a Gaussian probability density function and a constant power spectral density, independent on frequency. AWGN plays a fundamental role in all the experimental tests mandated to emulate communication channel background noise. It degrades slowly the quality of a digital communication system as its power level ( $N$ ) relative to the signal level ( $C$ ) increases, causing a reduction of the carrier-to-noise ratio ( $C/N$ ) at receiver input. The main parameter of the AWGN is in fact the noise power in the frequency bandwidth of interest, i.e. the bandwidth of the transmission channel. The relevance of its effect on the performance of DVB-T systems mainly depends on the power level





exhibited; if a given threshold value is not exceeded negligible effects are experienced.

#### A. Proposed AL-FEC Scheme

Before the passing the MPEG-4 stream to the DVB-T LINK/PHY blocks, the data is processed at the application layer (AL) video source itself (see figure 2). An application layer frame isolator is used for the MPEG-4 transport video frame to separate the I-frame and P-frame hex streams in MB extracted using the Mindego Analyzer (more on this later). This process facilitates the encoding for any separate IPTV frame stream alone in order to test the performance of the FEC code on the overall system performance.

It is then followed by a AL-FEC Reed-Solomon encoder that uses block length of 192 and a payload of 180 bytes where  $t=8$ . The encoded stream is processed using a convolutional

Interleaver of rate  $I=1/2$  block. See figure 2 for details. The source stream video is made of group of picture which are of 1 I-frame and 9 P-frame sequence. Frames are extracted individually from each GOPs in a hex format. The following scenarios were devised for the simulation in order to evaluate the extra protection proposed for the base video layer that produces the IPTV frames .

**Scenario 1:-** standard DVB-T with Two layer (outer and inner FEC encoding) protection as described above in section A is applied to two GOPs chosen from the trace Mindego Analyzer [12] (GOP 1 and GOP10). The separation between them is only used to allow the I-frame content to build up as is always the case with the beginning and ending of any movie frame sequence. Hence frame  $I^1$  is smaller than frame  $I^{10}$

**Scenario 2:-** Proposed AL-FEC is applied to the I-frame stream only before being

combined with the P-frame stream to form the GOP ( $I = 1$  frame,  $P = 9$ frames) and forward it to the standard DVB-T simulator. The GOP is assembled back together into a *IPPPPPPPP* format only after being applied to the RS (192,180) and the interleaver.

**Scenario 3:-** Proposed AL-FEC is applied to the GOP stream without separation. This allows both I and P stream types to be encoded using the (RS+Interleaver) block. The GOP is assembled together into a *IPPPPPPPP* format before being applied to the RS (192,180) and the interleaver.

### III. PERFORMANCE METRICS

The measurement technique often used to evaluate video quality is by computing the peak signal to noise ratio or PSNR. The PSNR is computed by taking the root mean square (RMS) value of the differences (errors) of the original and the received video frames, often normalized to be expressed in dB. PSNR measurements are often used to compare the quality loss of a video codec compared to a raw video footage, but can also be used to compute the quality loss due to packet loss.

A PSNR ratio of 34dB and higher is required for television broadcast; lower than 30dB is not acceptable anymore and anything below 20dB can be considered unwatchable. We use the Peak Signal-to-Noise Ratio (PSNR) as the objective measure of the quality of a reconstructed video frame  $R(x, y)$  with respect to the uncompressed video frame  $F(x, y)$ . The larger the difference between  $R(x, y)$  and  $F(x, y)$ , or equivalently, the lower the quality of  $R(x, y)$ , the lower the PSNR value . Let  $N_x$  and  $N_y$  denote the resolution in pixels of the source video[4],[8].



$$RMSE = \sqrt{\frac{1}{N_x \cdot N_y} \sum_{x=0}^{N_x-1} \sum_{y=0}^{N_y-1} [F(x, y) - R(x, y)]^2} \quad (1)$$

The video frame quality as PSNR can be calculated from the RMSE as

$$PSNR = 20 \log_{10} \left( \frac{255}{RMSE} \right) \quad (2)$$

The measured PSNR indicates the difference between the transmitted and received video frames.

#### IV. MINDEGO ANALYZER

The Mindego Analyzer [12] is a software tool that analyze the contents, compliance, and construction of MPEG-4 media data. The software is designed for technical professionals who handle MPEG-4 files and bit streams. Each picture is comprised of several macro block (MB) data that can be transmitted in one of several coding types, depending upon the slice-coding type. The MB Bits display the bit count distribution per macro block on the grayscale. Three types of slices are supported by MBEG-4.

- I slices are intra-frame encoded. All macro blocks in the slice are coded without referring to other pictures in the video sequence.
- P slices are predictive and refer to prior coded pictures.
- B slices are b-predictive and are coded in a manner that allows some macro blocks to use a weighted average of two distinct prediction values.

All slice of MB is represented in hex/binary data format. We have used the Mindego analyzer to extract the frames individually from each GOP in hexadecimal format.

#### V. SIMULATION RESULT

In order to evaluate the performance of the different coding schemes over the video frame sequence, the BER and PSNR are considered as the key performance metrics used in this study. Matlab simulator shown in fig.1 was designed and built to investigate the performance of the different coding scheme scenarios considered in this paper. Each frame has a 320 width \* 240 height dimensions. MBEG-4 pictures are divided into one or more slices and each slice of the picture has a specific type (intra, predictive, bi-predictive). A picture may contain more than one type of slice, but a given type can be interpreted from the slice information. In this simulation work a 20 GOP frame sequence from the movie, shown in fig.3&4 is simulated. The stream is a sequential, progressing picture by picture, so it may take some time to progress through a lengthy stream. Nevertheless, if a picture contains only I slices, it can be concluded that the picture is of type I.



Figure .3 snapshot of example video frame simulated



Figure .4 video stream



The Macro block bit distributions are used for getting information of each frame separately. Only representative results are discussed in this paper. Fig.5 shows the performance of the IPTV traffic BER over the adaptive white Gaussian noise (AWGN) channel for all different coding schemes versus the  $E_b/N_0$ . As illustrated, standard DVB-T performance is worse than the 2 proposed AL-FEC protected scenarios in terms of required  $E_b/N_0$ . Nevertheless, very little difference observed between protecting the I-frames only or protecting the whole stream. This is an interesting result as one can reduce the coding overhead if only protecting the I-frame stream. This is confirmed by the PSNR results in Fig. 6 for the average PSNR vs. BER performance. The advantage of protecting the video at the base layer out performs the standard DVB-T with a margin of over 6dB justifying the use of extra protection at the source. And, interestingly enough, protecting the I-frame stream only scenario is not far behind the fully protected stream scenario, in terms of average PSNR performance. However, GOP 10 performance is obviously better than GOP 1. This is due to the location of GOP 1 in the stream as the video sequence has just started and not much data is available in the I-frames produced by the video source. As the video frame progressed to GOP 10, I-frame size was very large and the benefit of video source protection becomes apparent.

Fig.7 shows the instantaneous PSNR performance over time for the 3 simulated coding scenarios. Note that the AWGN channel does not present a strong challenge against either of the simulated cases. In fact, the least protected standard DVB-T stream does not produce much fluctuation into the the PSNR and none of the scheme

proposed has fluctuated below the 35 dB threshold.

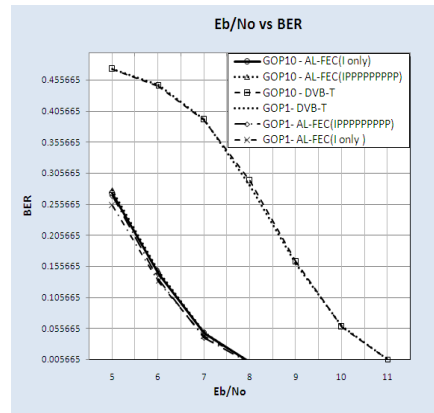


Figure.5 Channel average BER versus  $E_b/N_0$  performance.

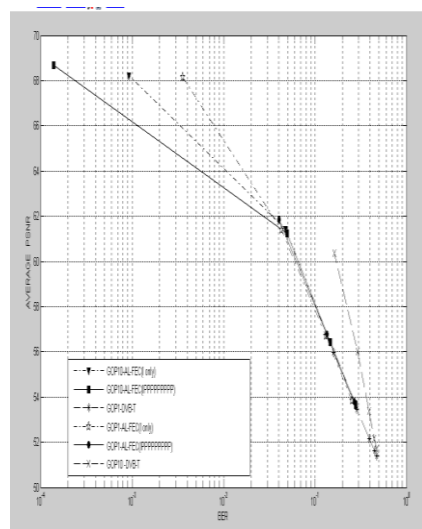


Figure.6 average PSNR for three scenarios Studied.

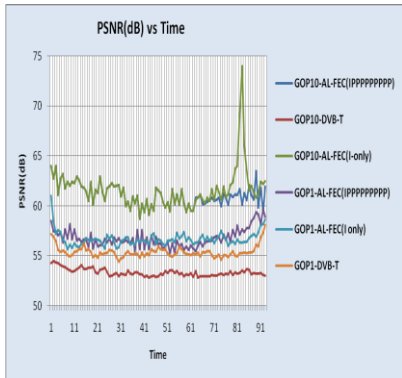


Figure.7 Stream Instantaneous PSNR overtime.

## VI. CONCLUSION

All of the goals as set forth in this paper have been achieved. The verifications have been met as shown in fig(5), (6) and fig(7), and the requirements have been completed. The simulations show the performance of the different coding schemes and the best the performance of the different coding schemes and the best performance is achieved for the case when the protection using one Reed Solomon encoders and one interleaver in application layer with stander DVB-T. That is when full protection to  $11, p10$  frame and  $p1, p10$  frame and the second pest using one RS and interleaver to frame  $11$  and  $110$  only without RS and interleaver to  $p$  to  $gop1, p$  to  $gop10$  frame in application layer this reduce processing time.

## REFERENCES

- [1] IoanVlad Uilecan, Chi Zhou "Framework for Delivering IPTV Services over WiMAX Wireless Networks"
- [2] Kim, S. Kim, and J. Heo, "Performance Analysis of Forward Error Correcting Codes in IPTV", IEEE Transactions in Consumer Electronics, vol. 54, No.2, May 2008.
- [3]"Using MPEG-4 Technology in Networked Video Surveillance Systems" Version 1.0 July 2005
- [4] Seeling, P. Reisslein, M. Fitzek, " Offse Distortion Traces for Trace-Based Evaluation of Video Quality after Network Transport".Dept. of Electr. Eng., Arizona State Univ., Tempe, AZ, USA, Fitzek,2005 IEEE
- [5] G.eert Van, T. David, and Martin Reisslein" Traffic and Quality Characterization of Single-Layer Video Streams Encoded with the H.264/MPEG-4 Advanced Video Coding Standard and Scalable Video Coding Extension".
- [6] P. Seeling, M. Reisslein, and B. Kulapala, "Network performance evaluation with frame size and quality traces of single-layer and twolayer video: A tutorial," IEEE Communications Surveys and Tutorials Third Quarter 2004.
- [7] "MPEG2Tool: A toolkit for the study of MPEG-2 video transmission over ATM based networks," Department of Electrical Engineering, University of Pennsylvania, Tech. Rep., 1996.
- [8] H. Singh, Jisung Oh, ChangYeul Kweon, Xiangping Qin, Huai-Rong Shao, and Chiu Ngo,Samsung Electronics "A 60 GHZ Wireless Network for EnablingUncompressed Video Communication" Samsung Electron., San Jose,
- [9] J. Shin, J. W. Kim, and C.-C. J. Kuo, "Quality-of-service mapping mechanism for packet video in differentiated services network," IEEE Transactions on Multimedia, vol. 3, no. 2, pp. 219-231, June 2001



- [10] *ETSI EN 300 744*, “Digital Video Broadcasting (DVB); Framing structure, channel coding and modulation for digital terrestrial television,” v. 1.5.1, June 2004.
- [11] U. Ladebusch, C.A. Liss “Terrestrial DVB (DVB-T): A Broadcast Technology for Stationary Portable and Mobile Use,” *Proc. of the IEEE*, Vol. 94. NO.1, January 2006.
- [12]” Mindego Analyzer 4600” MPEG-4 Media Analysis And Verification Software November, 2005
- [13] Michael Luby, Thomas Stockhammer, and Mark Watson “Application Layer FEC in IPTV Services” Digital Fountain Inc., Fremont, Communications Magazine, IEEE, may 2008
- [14] H. Singh, Huaning Niu, Xiangping Qin, Huai-rong Shao, ChangYeul Kwon,”Supporting Uncompressed HD Video Streaming without retransmissions over 60GHz Wireless Networks”



المؤتمر الدولي العربي الليبي الخامس للهندسة الكهربائية والإلكترونية 2010/10/26-23 طرابلس ليبيا



## Session-Based Misbehaviour Detection Framework for Wireless Ad hoc Network

Taraq Fahad  
Email: t.fahad@gmail.com

### Abstract

Data packet dropping misbehaviour is a serious threat in ad hoc networks. The motivation of such behaviour is either to take illegal advantage and preserve resources (selfish) or to intentionally cause harm (malicious) to some victims. Most of the existing solutions to solve such misbehaviour rely on the watchdog technique, which suffers from many drawbacks, particularly when using the power control technique. To overcome this problem with a moderate communication overhead, this paper introduces a new Session-based Misbehaviour Detection Framework (SMDF) for detecting misbehaving nodes that drop data packets in wireless ad hoc network. It consists of three components, the detection component in which each node monitors its direct neighbours with respect to forwarding data packets of a traffic session in the network, and the Decision component, in which direct neighbouring nodes decide whether the monitored node misbehaved or not and finally the isolation component where the guilty node will be penalized. Simulations results shows that SMDF is scalable and able to detect the misbehaviour with high accuracy as at low communication overhead and low energy consumption compared to the existing approaches in stationary ad hoc networks.

### 1. Introduction

Nowadays we witness an exceptional growth of wireless communications. One type in particular has huge interest from both research and commercial sides, which is called wireless Ad hoc Network. It is a group of autonomous mobile nodes or devices connected through wireless links without the support of a communications infrastructure. Nodes can be static e.g. sensors network or freely mobile.

Due to the infrastructure-less feature, all networking functions must be performed by the nodes themselves. Particularly, packets

sent between distant nodes are expected to be relayed by intermediate nodes, which act as routers and provide the forwarding service. The

forwarding service is closely related to the routing. It consists of correctly relaying the received packets from node to node until reaching their final destination, following routes selected and maintained by the routing protocol. These services (routing and data forwarding) together are at the core of the network layer.

The nature of wireless ad hoc network makes cooperation among nodes essential for the system to be operational. In some ad



hoc network applications, such as battlefield or rescue operations, all nodes belong to a single authority (in the application layer point of view) and have a common goal, e.g. soldiers in a military unit or rescuers in a rescue team. For this reason, nodes are cooperative by nature. However, in many commercial applications, such as networks of cars and provision of communication facilities in remote areas, nodes typically do not belong to a single authority and do not pursue a common goal. In such networks, forwarding packets for other nodes is not in the direct interest of anyone, so there is no good reason to trust nodes and assume that they always cooperate. Indeed, nodes try to preserve their resources, and particularly their batteries.

To take this constraint in charge many power-aware routing protocols have been proposed, but none of these solutions eliminate the problem due to the complex nature of the network. As a result, users will be permanently worried about their limited batteries, which may lead the nodes to behave selfishly. A selfish node regarding the packet forwarding process is the one that takes advantage of the distributed forwarding service and asks others to forward its own packets, but would not correctly participate in this service. This misbehaviour represents a potential danger that threatens the quality of service, as well as one of the most important network security requirements, namely the availability. In this paper we introduce a new low cost Session-based Misbehaviour Detection Protocol (SMDP) to monitor data forwarding, and detect packet dropping nodes in MANET. Our solution takes advantage of a cross-layer design, and exploits information related to the session layer that makes its control packet transmissions proportional to sessions,

which reduces the communication overhead. At the end of a session, each forwarder node shows to its neighbours the number of packets it received from each other during the session, as well as the total sent, by sending a special packet we call Forwarding Approval Packet (FAP). Mechanisms to ensure authentication of such information and to prevent nodes from denying receptions of data packets are used. Nodes then collaboratively analyze the FAPs, and judge one another.

The rest of the paper is organised as follows. Section 2 discusses related work including some of the detection mechanisms proposed in literature so far. Section 3 describes the new protocol with an illustrative example. Section 4 provides a simulation study of the solution, followed by a summarized comparison with related work in section 5 and some discussions about the solution limitations in section 6. Finally, section 7 concludes the paper.

## 2. Related Work

There are two main approaches to dealing with node misbehaviour in MANET [1] [2]. The first approach tries to give a motivation for participating in the network function. A typical system representing this approach is Nuglets [3]. The authors suggest introducing a virtual currency called Nuglets that is earned by relaying foreign traffic and spent by sending its own traffic. The major weakness of this approach is the demand for trusted hardware to secure the currency. SPRITE [4] has a major advantage in comparison with [3], as it does not require any tamper-resistant hardware. In this solution, virtual money is considered as credits and is not held in packets. However, SPRITE relies on central





authority to manage credits, which is not practical in MANET.

Most of the existing work in the field of node misbehaviour concentrates on the second approach which is detecting and excluding misbehaving nodes. Marti et al [5] propose a system which uses a watchdog that monitors the neighbouring nodes to check if they actually relay the data the way they should do. Then a component called pathrater will try to prevent paths which contain such misbehaving nodes. As indicated in the paper, the detection mechanism has a number of severe weaknesses such as its failure to correctly detect the misbehaviour in cases of collisions, partial collusion, and power control employment.

The power control technique has been used by many routing protocols proposed after the watchdog's proposal in the field of power consumption optimization, e.g. [11]. By using the power control technique, nodes in MANET can preserve their power, by only transmitting packets from one node to another using controlled power according to the distance separating them from each other. For example, in the watchdog, when node C is closer to node B than A, and when B transmits packets using controlled power according to the distance separating it from C, A could not overhear B's forwarding, and may accuse it wrongly.

There are other reputation approaches that use the watchdog mechanism in their monitoring component. CORE [6] and CONFIDANT [7] are two examples of such observation approaches. In CORE [6] nodes' observations are propagated beyond the neighbourhood, but only the positive observations. Not propagating negative observations would prevent the vulnerability of propagating rumours aiming DoS attacks, but this way the experience of

others gets unused. In contrast, CONFIDANT [7] propagates negative observations beyond the neighbourhood, while considering the rumours problem and taking measures to mitigate it at the trust manager component. Further, CONFIDANT with its modified Bayesian approach for reputation gives less and less importance to past observations, which allows redemption in contrast to CORE which gives more importance to past observations. Nonetheless, in both CORE and CONFIDANT the monitoring component inherits all of the watchdog problems. Moreover, the isolation is performed unilaterally by each node, which might result in false accusation. As when a node isolates unilaterally another and denies forwarding packets for it (punish it), other neighbours would consider its behaviour illegal.

The probing approach first proposed by Awerbuch et al. [8] could be viewed as a combination of route and node monitoring. It uses the end-to-end Acknowledgement (ACK) to monitor routes, and improves it by adding a dichotomic probing phase to detect the appropriate selfish nodes whenever a route becomes suspicious. Iterative probing [2] is more effective but allows to merely detect the link including the selfish node and has high overhead. On the other hand, unambiguous probing [2] deals with the node detection issue, by suggesting utilising the promiscuous monitoring at the predecessor of the suspicious link. This would have inevitably the watchdog's (promiscuous monitoring) problems.

Two-hop ACK [9] allows to detect the selfish nodes and not only unreliable routes, and it enables the usage of the power control technique with no detection problem, contrary to promiscuous

monitoring solutions. However, the major drawback of this solution is the significant overhead it generates, although the authors provide further reduction using random acknowledgement approach [9]. A review of existing solutions is described in [10].

### 3. The New Proposed Solution Overview

Our solution to the misbehaviour problems in MANET is a new Session-based Misbehaviour Detection framework (SMDF) [14]. It consists of three new components integrated together to detect and deal with nodes Misbehaviour in MANET. The first and most important component of the framework is the novel detection component. For this component we have developed a novel Session-based Misbehaviour Detection Protocol (SMDP) [15, 13, 14]. The second component of the new framework is the decision component [14] which will judge whether the nodes misbehave intentionally or not. The third and final component of our framework is the isolation component which will penalize nodes who are judged to have misbehaved. Figure 1 above shows our framework SMDF and its components.

#### 3.1 Detection Component

In our approach [13] each node in the route session monitors all of its direct neighbours (i.e. neighbours within a one hop communication), and checks whether they correctly forward packets. We define a session as the continuous traffic sent from the source node to the final destination node. The routing protocol has to be aware of the beginning and the end of each session. This has been done through cross-layer collaboration between the session layer and the network layer, shown in figure

2. Cross-layer is a paradigm in wireless network architecture design that takes into accounts the dependencies and interactions among layers, and supports optimisation across traditional layer boundaries [16]. In our framework it means the exchange of information between the session layer and the network layer. As a result, our protocol has two components, a session component and a network component.

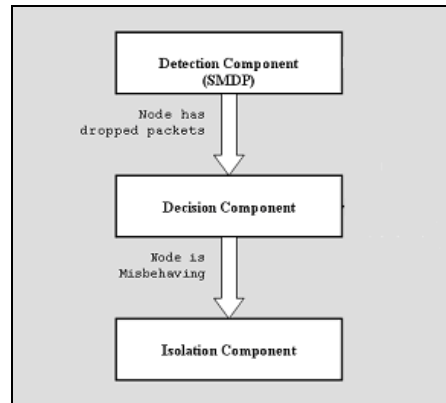


Figure1. Session-Based Protocol's Framework

The first one informs the second about the beginning and the end of sessions. All the other operations are performed by the network component. In our solution (SMDP) [13] we monitor nodes only after the end of the session contrary to all of the other existing approaches such as [5, 7, 1, 6, 17,18, 9] where monitoring happens immediately after the node sent packets to its successor to forward them further in the network. By using sessions based approach we will save a considerable amount of communication overhead and subsequently reduce the cost.

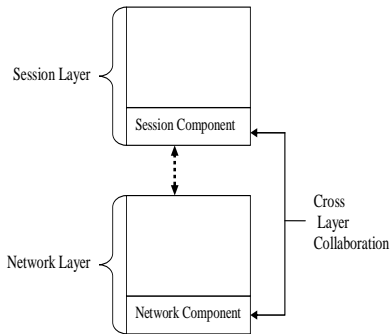


Figure2. Session-Based Protocol's Framework

After the end of each session, each node included in a path used by the session (apart from the originated source node and the final destination node) sends two *cryptographically signed* (i.e. using asymmetric encryption) packets. One to its successor containing the number of packets it has sent to it, we denote by NPS, and the other one to its predecessor containing the number of packets it has received from it, denoted NPR. The source node will send only the number of packets it has sent NPS to its successor, and the final destination node will send only the number of packets it has received NPR from its predecessor. NPR and NPS contain the sequence number of their sender, which is a number maintained by each node and monotonically increased (by 1) after including it in a packet. This prevents using an NPS or NPR more than once. After sending and receiving this information, each node builds and broadcasts to all of its one-hop neighbours a Forwarding Approval Packet (FAP) shown in figure 4-3, which is divided into SENT/RECEIVED fields. Each field involves one neighbour participating in the session, and contains the following attributes:

$T_{ij} / R_{ij}$  : Number of packets node ' i ' has sent/received to/from neighbor 'j'.

$id_{T_{ij}} / id_{R_{ij}}$  : Node identification number (ID) of the sender/receiver node.

$S_{T_{ij}} / S_{R_{ij}}$  : A node signature for authentication.

$m_j$ : The sequence number of node j.

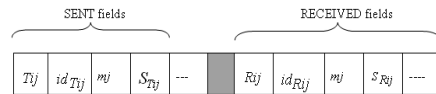


Figure3. The Forwarding Approval Packet (FAP)

Note that contrary to almost all the other solutions, our new framework can work independently of the routing protocol, as it does not need to know the two-hop neighbor to monitor its successor. It does it locally with its neighbours.

### 3.2 SMDF Detection Component

After receiving a Forwarding Approval Packet FAP (described previously) broadcasted from its one hop neighbour, our detection component through our Session-based Misbehaviour Detection Protocol (SMDP) will start working. Each node checks the authentication of each  $T_{ij}$  and  $R_{ij}$  in the FAP using digital signature. It also checks that none of the sequence number has already been used. For this it keeps the last sequence number of each other node, so that the new received number should be greater than the previous one. Any failure in one of the previous verifications results in considering the appropriate number of packets to be zero, meaning do not accept such information.



If there are no packets dropped the following equation holds:

$$\sum_{i \in I} T_{ij} = \sum_{i \in I} R_{ij} \quad (1)$$

Thus far, nodes are assumed to not deny the sending and the reception of packets, and accordingly they correctly send the NPS and notably NPR packets, and include all the receptions in the FAPs as well. Now we deal with situations where selfish nodes lie. Assume that there is no more than one such a node in a neighbourhood, and we do not consider collusions. Finally, we point out that we are dealing with selfish nodes, but not with malicious attackers. If a well-behaving node does not receive NPR or NPS from a neighbouring node, it simply leaves the corresponding signature field empty in the FAP it sends. The neighbours receiving such a packet with an empty signature assume that either the node of the appropriate field or the FAP sender is misbehaving. They keep their IDs for further investigations. This will be enhanced in the following.

We first deal with the situations where nodes do not lie, and all the required signatures are put in the FAP. From equation (1) we consider the following:

$$\sum_{i \in I} T_{ij} = T \quad \& \quad \sum_{i \in I} R_{ij} = R$$

If  $R-T=0$  then the node is forwarding packets correctly. Otherwise,  $(R-T)$  packets has been dropped.

Now we treat the cases where a FAP's SENT field regarding some node, for example  $X$  lacks a signature. Lack of a signature in a RECEIVED field is of no impact if the sender of the FAP has

correctly forwarded packets and shows proofs (signatures in the SENT fields). The previous sums ( $T$  and  $R$ ) are calculated as before, and if  $R-T > 0$ , this number  $(R-T)$  of packets will be considered dropped. But in addition, the node will not be immediately considered forwarding the  $T$  packets. In fact, either  $X$  is denying the reception of packets, or the sender of the FAP has dropped packets and is lying. The two nodes' IDs as well as the appropriate number of packets (claimed in the SENT field that lacks a signature) are safeguarded in what we call the suspicious set. Later, if one of these two nodes will be considered as suspicious in another experience, it will be charged of dropping packets (both in the first and the second experiences), and the innocent's id will be released from the suspicious set.

We have used Bayesian approach for our new decision stage. Our new proposed Bayesian approach is similar to that used in [12] but using SMDP as the monitoring component. The monitor allows the neighbouring nodes to decide whether each monitored node in the session has forwarded packets correctly or not. Therefore, when a monitoring node notices that some packet has been dropped over a link it should not directly accuse the monitored as misbehaving, since this dropping could be caused by collisions or channel conditions. Therefore, a threshold of tolerance should be fixed.

In the Bayesian approach, well behaving of nodes improves their reputation, whereas intentional or unintentional packet dropping decreases it. Since misbehaving is usually exception rather than the norm, information exchange in our solution is limited to negative impressions. It is simpler and



creates no overhead when nodes well-behave, as [12].

Each node A thinks that each other node B misbehaves with a probability  $\theta$ , which is a random variable estimated by a Beta distribution  $Beta(a, b)$  described above. Initially with no prior information,  $\theta$  is assumed uniform in  $[0, 1]$ , which is identical to  $Beta(1, 1)$ . As observations (that follow a Bernoulli distribution with a parameter  $\theta$ ) are made,  $a$  and  $b$  are updated as follows:

$$a = a + (R - T), b = b + T$$

Where  $R$  is the number of packets received by the monitored node (as a router), and  $T$  is the number of packets forwarded by it during the session, as mentioned in our detection component. The previous sums ( $T$  and  $R$ ) are calculated as before in our detection component, and if  $R - T > 0$ , this number ( $R - T$ ) of packets will be considered dropped.

After as many observations as the decision could be made ( $\theta$  could be approximated by the mathematical expectation  $E(Beta(a, b))$ ), the node will be judged. This is denoted by the decision (or stationary) point, while the number of observations is expressed by  $a + b$ . Upon reaching this point, B will be accused of misbehaving as soon as:

$$E(Beta(a, b)) > E_{\max}$$

Note that:  $E(Beta(a, b)) = a / (a + b)$ .

$E_{\max}$  could be fixed to 0.5 (i.e. 50% of misbehaviour), or for more efficiency it should be estimated empirically for each network [12]. In mathematical estimation methods, the decision (stationary) point is

the one upon which the difference between two subsequent observations could be negligible. One usual choice is that fulfilling the following condition:

$$Var(Beta(a, b)) < \varepsilon$$

Such that  $Var$  is the mathematical variance and  $\varepsilon$  is a very small positive.

Note that:

$$Var(Beta(a, b)) = \frac{a \times b}{(a + b + 1) \times (a + b)^2}$$

However, this choice is inappropriate here, since  $Var(Beta)$  is not monotonous with  $a + b$ . We use the following variance like function, which is indeed decreasing with  $a + b$  [12]:

$$Max\left(\frac{b}{(a + b) \times (a + b + 1)}, \frac{a}{(a + b) \times (a + b + 1)}\right)$$

When enough observations with regard to a given monitored node are collected such that the judgment point is reached, the monitoring node will accuse the monitored one as soon as the estimated probability ( $E(Beta(a, b))$ ) exceeds the configured maximum tolerance threshold, i.e.  $E(Beta(a, b)) > E_{\max}$ .

$$E(Beta(a, b)) > E_{\max} \iff \frac{a}{a + b} > E_{\max} \iff a > \frac{b \times E_{\max}}{1 - E_{\max}}$$

This latter  $\left(\frac{b \times E_{\max}}{1 - E_{\max}}\right)$  represents the tolerable number of packets a node is allowed to drop without being accused. This maximum tolerable threshold is proportional to  $b$ , the number of packets forwarded. The more a node forward packets, the more its tolerable



threshold increases. Forwarding packets after unintentional or intentional droppings that do not result in an accusation would decrease  $E$ , which allows redemption. This redemption could not be possible when setting the tolerable threshold to a fixed number of packets. In our SMDF the redemption is just before decision. A node that forwards packets will need much more packets to be dropped before being accused compared to the one that does not forward, so it is like the forwarding redeems its dropping. However, there is no redemption after the decision.

In [19], every node periodically broadcasts in its neighbourhood its view of  $\theta$  regarding all the other nodes. Nodes use these information (known as second hand information) to update their own opinion on nodes' behaviour. To decide about the acceptance of the provided information, each node performs complicated tests on the trustworthiness of the provider. The problem with this proactive solution is that it causes an increase in the amount of overhead generated, even if nodes well-behave. Our approach is rather reactive, thus no such information are exchanged. Indeed, each node performs monitoring separately and informs the others as soon as a misbehaving node is approved, as we will see in the next section with more details.

### SMDF Isolation Component

Our Isolation Component used the social sciences principle that a person that accuses another of misconduct must show proof. One possible way to prove the accusation is to get observers against the accused person. In order to mitigate false detections and false accusations vulnerability, we have used Observation-Based Protocol very

similar to that used in [12]. In this protocol, a node that detects and accuses another as misbehaving must approve its accusation before taking any measure against it. It should not isolate the assumed misbehaving unilaterally, because this could result in false detections against it. However, it could avoid routing its own packets through this node.

Isolating a misbehaving node in MANET required two actions. First, not to route packets through it, to avoid losing them; second, do not forward packets for it, in order to punish it. For example, node A that judges some other node B as misbehaving should not isolate it unilaterally, but must ensure its isolation by all nodes. This is because when A unilaterally isolates B, the others could consider A as misbehaving when they realize that it does not forward packets for B.

The way that our proposed Observation-Based Protocol work is describe as follow: Upon detection, the detector informs nodes in its neighbourhood about the dropper (the accused), and asks for observers by broadcasting an Observation REQuest (OREQ) packet. It also puts the detected node ID in a special set called a *suspicious set*. Each node receiving the OREQ investigates the issue as follows:

The packets recipient immediately sends a *signed* Observation REPLY (OREP) packet to the accuser if the accused node's misbehaving expectation is close to  $E_{max}$ , or the number of control packets considered dropped is close to the configured maximum threshold. Also if its suspicious set includes the accused node. Otherwise, when it has not enough experience with the accused node (B), and if B is its neighbour



then it asks the successor of this latter whether it has received packets forwarded from it, by sending an ACCusation REQuest ACREQ packet (using a route that does not include B). But first, in order to avoid false accusations, the investigator should ensure that the accuser has really sent a packet to B to be forwarded to the appropriate successor. The node also should check whether B has sent the accuser an ACK just after overhearing the data, to ensure that the former has really received the packet and that the latter is not impersonating it. If B's successor has not recently received any packet *forwarded* from B, it sends a *signed* ACREP (ACCusation REPlY) packet to the investigator, then this latter testifies for the accusation and sends the accuser a signed Observation REPlY- OREP packet. The signature of the packets prevents their spoofing, thus no node could testify using the ID of another.

The accuser node has to collect ' $S$ ' different signatures to approve its accusation. Theoretically,  $S-1$  is the maximum number of misbehaving nodes that could exist at any time. In practice, however, it is hard to determine such a number, so it should be fixed to strike a balance between efficiency and robustness. Setting  $S$  to a high value increases the robustness of the protocol against false detections and rumours, but decreases its efficiency regarding true detections. On the other hand, a low value of  $S$  allows high detections, but opens the vulnerability of rumours and increases the unintentional false detections (false positives), since  $S$  nodes could collude to accuse maliciously (respectively wrongly) any node.

Once the accuser collects  $S$  valid signatures, it broadcasts an Isolation Packet (ISOP) including all signatures through the network to isolate the guilty. This broadcast is not performed until a node is detected and approved as misbehaving. Apart from the monitoring stage, our solution requires no overhead as long as nodes well behave, as no opinions are exchanged periodically. This gives our solution the advantages of being a reactive one, unlike the other reputation-based solutions that were presented before.

## 4. Simulation Study

### 4.1 Simulations Parameters

To study the effect of node misbehaviour on MANET and to assess the performance of the proposed detection protocol, we have developed a GloMoSim-based [20] simulation study. We have simulated a network of 100 nodes, located in an area of  $2500 \times 2000 \text{ m}^2$  where nodes are deployed randomly for 1800 seconds of simulation time. To generate traffic we have used five Constant Bit Rate (CBR) sessions between five pairs of remote nodes, each consists of continually sending a 512 byte data packet each second. On each hop, each data packet is transmitted using a controlled power according to the distance between the transmitter and the receiver.

Table 1 shows the important simulation parameters that have been used in our simulation. These parameters are typical for MANET simulations (see e.g.[21]) and are used for all following simulations. For the results of the simulation to be meaningful, it is important that the model on which is based the simulator matches as closely as possible the reality. Various examinations,





such as [22], show significant divergences between different simulators that demonstrate an identical protocol. Therefore, the results obtained from the simulations should be evaluated appropriately.

Parameter	Value
Number of Nodes	100
Area X (m)	2500
Area Y (m)	2000
Traffic Model	Constant Bit Rate (CBR)
Sending Rate (Packets/S)	1.0
Packet Size (Byte)	512
Simulation Time (S)	1800
Node Placement	Random
Mobility	None

Table 1: Simulation parameters

## 4.2 Simulation Metrics

We evaluate our proposed SMDF using the following six metrics:

- **Packet delivery ratio:** This is the percentage of sent data packets actually received by the intended destinations over the submitted packets.
- **Overhead:** This is the amount of control-related transmissions (control packets including FAPs) measured in bytes, and generated during each session in the network. We count the amount of the actual control packets in bytes instead of

the number of packets, because it reflects the real amount of overhead, as you might have small number of packets that generates huge amounts of bytes and vice versa.

- **True Positive Detection Rate:** The rate of true dropping detection, when nodes correctly detected dropping packets.
- **False Positive Detection Rate:** The rate of false dropping detection, when nodes wrongly accused of misbehaviour, when in fact they are not.
- **Power Consumption Rate:** The average amount of power consumed by the nodes during the simulation.
- **Scalability:** How scalable the new protocol is if the network number of nodes increased.

## 4.3 Simulation Results

### 4.3.1 Evaluation of the Effect of Node Misbehaviour on MANET Packet Delivery Ratio

In order to study how node misbehaviour affects a MANET performance, we have done a number of simulations where we modelled a varying number of selfish nodes. In order to compare the affect of node misbehaviour in the network, we first run the simulation without selfish nodes (i.e. all of the nodes in the sessions are behaving correctly and forwarding packets as required from them without any dropping). Next, we run the simulation and in this case we have injected the network with selfish nodes that misbehave by not forwarding packets they received from other nodes. We have varied the number of selfish nodes from 1 to 20 nodes of the total number of





nodes, which is 100. Figure 4 shows the results of these simulations. It is obvious that this number has a significant effect on the rate of packets that are successfully delivered in the network. In this simulation we have used DSR routing protocol, the selfish node has not been detected by DSR and no countermeasures are taken.

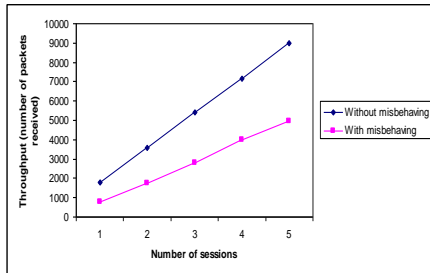


Figure 4: Node Misbehaviour Effects on MANET's Throughput

#### 4.3.2 Evaluation of the Effect of Packet Dropping Attack in MANET

In this simulation we are targeting to simulate and study the affect of packet dropping attack in MANET. Unlike the previous simulation in figure 4 where the dropping rate fixed to 50%, in this simulation the dropping rate varies form 0% to 100%. We simulated 20 nodes launching this attack by different rate of dropping as shown in figure 5. It can be seen from figure 5 that when the dropping rate of the attacker is low, the throughput (i.e. number of packet received) is high. As the dropping rate increased the throughput is severely affected until it reaches 0 as the attacking nodes increased their dropping rate to 100%. This clearly shows the affect of such attack on the performance of MANET and wireless sensor network. The result shows that the more number of such malicious nodes inside the network the more the harmful impact on the reliability, and that the decline is dramatic.

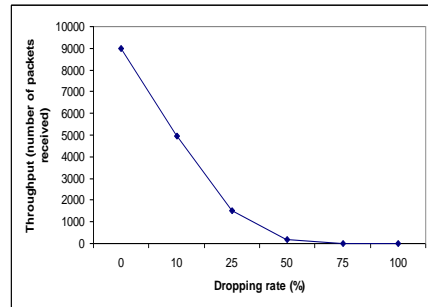


Figure 5: The Effect of Packet Dropping Attack on Throughput in MANET

#### 4.3.3 Comparison With Existing Approaches for True Positive Detection Rate

Having seen true detection positive rate results for our SMDF, we are now comparing it with other mechanisms. Figure 6 depicts a comparison between our proposed SMDF and the Watchdog [5] and Random Two Hop ACK [9]. We have used the same simulation parameters mentioned before and run the simulations using each protocol separately (i.e. WD then Random Two Hop ACK). In addition, as in our SMDF simulation case we have set the POWER CONTROL parameter to YES in order to see how the other two protocol perform. The result shows that our proposed SMDF outperformed Watchdog, which suffers from a sharp fluctuation between (98% - 100%), whereas SMDF remains constant at 100%. On the other hand, SMDF has as same true detection rated as the random Two Hop ACK.

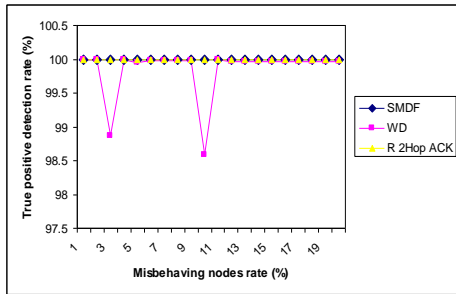


Figure 6: Comparison of True positive detection vs. Misbehaving rate

#### 4.3.4 Comparison With Existing Approaches for False Positive Detection Rate

As we have done in the true detection positive rate comparison, we have compared our SMDF False Positive Detection Rate result with the Watchdog and the Random Two Hop ACK. Figure 7 shows clearly the considerable advantages of SMDF over both the Watchdog and the Random Two Hop ACK in keeping the false detection rate steady at 0% level. As the highest false detection rate was produced by the Watchdog which was between (35% - 75%), the Random Two Hop ACK performed better than the Watchdog as it fluctuates around 20%.

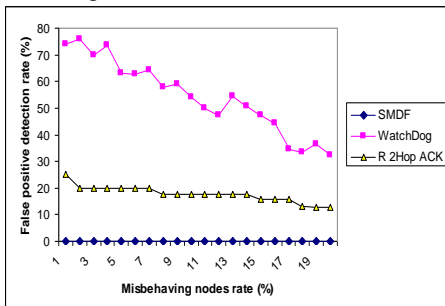


Figure 7: Comparison of False positive detection vs. Misbehaving rate

#### 4.3.5 Comparison of SMDF vs. Optimised SMDF with Sessions Aggregation and Two-Hop ACK

In this scenario we compare the overhead produced previously by SMDF in table 2 to the optimised SMDF and Two-Hop ACK. The optimised SMDF uses sessions aggregation approach presented earlier. When using this approach, nodes that are involved in more than one session could wait a certain time until all sessions end before sending the FAP to their direct neighbours. The results (reported in table 2) show a significant reduction in the amount of communication overhead produced by the aggregated SMDF in comparison with that in non-aggregated SMDF. Both versions clearly outperform Random Two-Hop ACK.

Sessions	Overhead Amount (Byte Per Session)				
	1	2	3	4	5
SMDF	724	1088	1512	2012	2028
Optimised SMDF	724	1022	1096	1436	1450
R 2 Hop ACK	11260	13300	20520	42800	43860

Table 2: Comparison between SMDF and R 2Hop ACK (Overhead)

#### 4.3.6 Comparison With Existing Approaches for (Power Consumption)

Having seen the SMDF power consumption results in previous section, we now compare them with the Watchdog and Random Two Hop ACK results. The comparison results in figure 9 shows that our SMDF clearly outperforms both the Watchdog and Random Two Hop ACK in saving energy with less power consumption. There is a very small difference between the Watchdog and Random Two Hop ACK, with slight advantages to Watchdog. This could be due the huge amount of overhead that the Random Two Hop ACK generates.

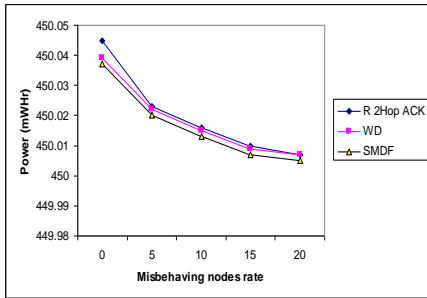


Figure 9: Comparison of power consumption of SMDF with existing approaches

### 4.3.7 Comparison with Existing Approaches for Scalability

Our proposed protocol SMDF has already been evaluated using 100 nodes, which is higher than 50 nodes average used in many other existing mechanisms evaluated using simulation. Since the scalability property is one of the desired characteristics especially in wireless sensor network, we have increased the number of nodes to 500 and the terrain to  $3500 \times 3000 m^2$  and measure the true/false positives. The main difference between small and large networks is the average path lengths (e.g. 3-4 hops in small network vs. 8-13 hops in large network). We have increased the network sessions from 5 to 50 sessions to reflect the increase in the number of nodes. It can be seen from figure 10 that SMDF is scalable and still has the highest true positive detection rate at 100%. Figure 11 shows that SMDF has the lowest ever false positive detection rate at 0% compared with the WD and Random 2 Hop ACK.

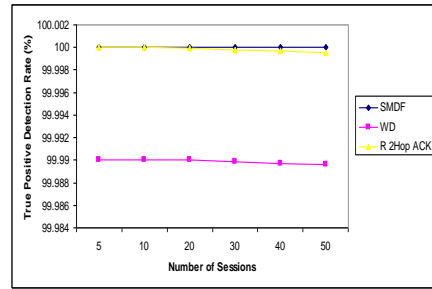


Figure 10: Comparison of True Positive Detection Rate (Scalability)

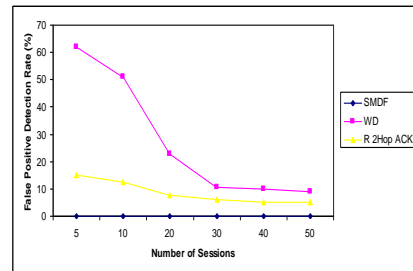


Figure 11: Comparison of False Positive Detection Rate (Scalability)

## 5 Comparison with Related Work

As mentioned before, the main objective of our misbehaviour detection framework is to provide a set of components and mechanisms that can detect and eliminate misbehaviour at low energy and communication overhead cost but with high accuracy. The problem of node misbehaviour in MANET has been treated by many research groups, and many mechanisms have been proposed. Our framework shares some similarities with prior work carried out in other projects. In this section we compare our framework with these works.

The first and most famous mechanism in misbehaviour detection in MANET is the



Watchdog [5]. We have compared our SMDF results with the Watchdog results on five of our six different metrics using simulation, and found that SMDF outperform the Watchdog in four of these metrics. The five metrics are true positive detection rate, false positive detection rate, power consumption rate and scalability. Where as the Watchdog has lower overhead than SMDF. Nonetheless, all of the other Watchdog drawbacks including partial dropping do not exist in our SMDF, which is the gain we obtain from our extra but low overhead.

There are many other detection mechanisms especially the reputation mechanisms such as [7 18, 6, 17, 1] using the watchdog as their main monitoring component. Consequently, they inherit all the drawbacks that the watchdog suffers, even though their other system components are efficient. This gives our SMDF clear advantages over all of the mechanisms that adopting the watchdog concept in their detection system.

We have also compared our framework with the other types of mechanism that do not use the watchdog as their monitoring component. The most recent solution of these is the Random Two-Hop ACK [9]. Our comparison through simulation showed us that our SMDF outperforms the Random Two-Hop ACK in four of our six simulation metrics. These matrices are communication overhead, false positive detection Rate, power consumption rate and scalability. Although, we have similar true positive detection rate as the Random Two-Hop ACK. However, through our simulation comparison we noticed that the Random Two-Hop ACK can often detect the full dropping case more than the partial one.

Our framework evaluation and comparison with other existing mechanisms shows it performs better and has novel aspects that do not exist in other mechanisms.

We completed our detection approach with decision and isolation component using mechanisms of [12] to make a complete solution. The major advantage of our solution compared to [12] is at the monitoring component as the latter use Random Two-Hop ACK.

## 6 Discussion

Whilst the SMDF solves an interesting problem with some novel aspects there remains several shortcomings. This section outlines these problems.

Waiting until the end of all sessions to check node misbehaviour reduce the communication overhead considerably as we have seen in the simulation results. However, it will increase the delay before detection. It is a trade-off issue as reducing the cost is more valuable and important than increasing the waiting time. In some application such as video streaming, it is important to detect misbehaviour immediately as it occurred and not wait until the end of all sessions involved in the network. This shortcoming can be reduced by fixing a timeout to the sessions waiting instead of waiting for the end independently of the period, if not all the session terminate upon the timeout only the closed sessions will be aggregated and another timeout will be set for the remaining ones.

The Session-based Misbehaviour Detection Framework (SMDF) we proposed in this work assumes that nodes only drop data packets and not control packets. If the nodes drop the control packets, the SMDF



can not detect them, as it only deals with data packets dropping. The increased amount of control packets is not preferable due to the overhead they generate. However, moderate number of control packets is important, and as such, dropping them will affect the performance of the network. Selfish nodes drop both data and control packets whereas malicious node targeting only data packets. This make our solution directly applicable in the context of malicious nodes but needs to be completed with some mechanism for control packets monitoring to comprehensively deal with selfish nodes.

We intentionally examine the situation when MANET is stationary, as this was the main target investigation of this research. Our solution is suitable for most applications of wireless sensor networks. However, it is possible to have mobile sensor nodes. Dealing with mobility represents an open perspective to our work. In our SMDF Decision component we have used a fixed threshold of tolerance in which node will be judged as misbehaving after exceeding it. This is fine for a stationary MANET and static WSN scenarios. However, it is more efficiency to use variable threshold which can change according to the network topology and scenarios. The threshold can be also estimated empirically for each network by first, making simulations with no misbehaving and calculate the threshold at each node for different scenarios that estimate the network. Then, retrieving the maximum value in all scenarios from the decision point and then consider it final threshold.

In some application such as the battlefield or the rescue operations there is no need to

run all of the three components in every node. For example isolating and punishing such nodes would not be beneficial. In this case there is no need for the isolation component and it need to be switch OFF. Therefore, deciding when to turn components ON/OFF is another challenge that needs to be resolve. One suggestion is to add a separate component with *intelligent* decision capability to SMDF in order to deal with such situation. More efficient suggestion would be to add to each component of SMDF this intelligent capability to decide itself when and where to function according to the network and nodes status.

For the purpose of evaluation and comparison with other approaches we have used simulations techniques. Performance evaluation through simulations is helpful but will not reflect the reality 100%. It will thus be fascinating to see the actual performance of our complete SMDF framework by integrating every component that it consisted of. By doing that we could measure new parameters that will add more understanding of the reality and that can not be performed clearly through simulations. Once the above tasks have been completed successfully, it would be interesting to implement the complete model in an experimental test-bed to see its practical feasibility. This task appears feasible in the near future as the price of advanced sensors and handheld devices are already decreasing gradually.

## 7 Conclusion

The main direction of our work has been to look for an effective approach that can satisfy our initial requirements. The result is a new low cost framework entitled Session-based Misbehaviour Detection Framework



(SMDF). It consists of three components, the detection component, the decision component and the isolation component. The most important contribution is the detection component that contains our novel Session-based Misbehaviour Detection Protocol SMDP to detect selfish or malicious nodes that drop packets partially or completely to launch either black-hole or data dropping attacks. For the decision component we have integrated an existing Bayesian approach to decide whether the node deliberately misbehaved or not [12]. For the Isolation component, we have used an existing approach [12] and used an Observation-Based Protocol to isolate misbehaving nodes. It uses neighbouring observation experience to isolate misbehaved nodes.

We analysed and evaluated the proposed schemes by simulation techniques. Our evaluation was focused on six important parameters, namely packet delivery ratio, overheard, true positive detection rate, false positive detection rate, power consumption rate and scalability. By comparing our results to those of other mechanisms available on literature, we showed that our solution has low cost in terms of communication overhead than other approaches. We showed also that our framework has the lowest false positive detection rate amongst other approaches, and that it has highest value of True positive detection rate compared with other approaches. Our evaluation also showed that our solution has lower energy consumption rate compared with other existing approaches. The experiments showed also that our framework is scalable and can work with higher number of nodes, especially in wireless sensor networks. It is important to emphasise that though the

proposed framework was developed for stationary MANET and static wireless sensors network, the ideas by this framework are still extendable for other mobile wireless networks.

To achieve the grand vision of pervasive computing where applications are enhanced through tools such as wireless sensors and integrated using mobile ad hoc networks many problems need to be solved. However, remarkable progress has been made in the last decade and we believe our SMDF contribution, addressing fairness within MANET, will help make a step toward this future.

## 7. References

- [1] H Yang, H Y. Luo, F Ye, S W. Lu, and L Zhang. *Security in mobile ad hoc networks: Challenges and solutions*. IEEE Wireless Communications, 2004. **11**(1): p. 38-47.
- [2] Frank Kargl, Andreas Klenk, Stefan Schlott, and Michael Weber. *Advanced Detection of Selfish or Malicious Nodes in Ad Hoc Networks*. in *1st European Workshop on Security in Ad-Hoc and Sensor Networks (ESAS 2004)*. 2004. Heidelberg, Germany.
- [3] Buttyan, L. and J.-P. Hubaux, *Stimulating Cooperation in Self-Organizing Mobile Ad Hoc Networks*. ACM/Kluwer Mobile Networks and Applications, 2003. **8**(5).
- [4] S. Zhong, J. Chen, and Y. R. Yang, "SPRITE: A simple, cheat-proof, credit-based system for mobile ad-hoc networks. in *The 22nd IEEE INFOCOM'03*, San Francisco, CA, USA, April 2003.
- [5] S. Marti, T. Giuli, K. Lai, and M. Baker, *Mitigating routing misbehaviour in*



*mobile ad hoc networks*. Mobile Computing and Networking, 2000: p. 255-265.

[6] Michiardi, P. and R. Molva. *CORE: a collaborative reputation mechanism to enforce node cooperation in mobile ad hoc networks*. in *Communication and Multimedia Security*. 2002. Portoroz, Slovenia: Kluwer Academic.

[7] Buchegger, S. and J.-Y.L. Boudec. *Performance Analysis of the CONFIDANT Protocol: Cooperation Of Nodes - Fairness in Distributed Ad-hoc Networks*. in *IEEE/ACM Workshop on Mobile Ad Hoc Networking and Computing (MobiHOC)*. 2002. Lausanne.

[8] B. Awerbuch, D. Holmer, C. Nita-Rotaru, and H. Rubens. *An on-demand secure routing protocol resilient to byzantine failures*," in ACM Workshop on Wireless Security (WiSe), Atlanta, Georgia, USA, September 2002.

[9] D.Djenouri and N.Badache. *Cross-layer Approach to Detect Data Packet Droppers in Mobile Ad-hoc Networks*. In Proceeding of the first International Workshop On Self-organized systems IWSOS'06, Passau, Germany, 2006.

[10]D. Djenouri, L. Khelladi, and A.N. Badache, "A survey of security issues in mobile ad hoc and sensor networks", *Communications Surveys & Tutorials*, IEEE, 2005, 7(4): p. 2- 28.

[11] S. Doshi and T. Brown, *Minimum Energy Routing Schemes for a Wireless Ad Hoc Network*, *IEEE INFOCOM'02*, New York City, USA, 23–27 June 2002.

[12] D. Djenouri and N. Badache, "Struggling Against Selfishness and Black Hole Attacks in MANETs" Accepted in the *Journal of Wireless Communications and Mobile Computing (WCMC)*, Wiley & sons Publisher (to appear in 2008), available online at:

<http://www3.interscience.wiley.com/cgi-in/jissue/77502232>).

[13] T. Fahad, D. Djenouri, and R. Askwith "On Detecting Selfish Packet Droppers in MANET: A Novel Low Cost Approach", The Third IEEE International Symposium on Information Assurance and Security IAS'07, pp 56-61, Manchester, UK, August 2007.

[14] T.Fahad, D.Djenouri, R.Askwith, M.Merabti "A New Low Cost Sessions-Based Misbehaviour Detection Protocol (SMDP) for MANET", 21st IEEE International Conference on Advanced Information Networking and Applications Workshops Proceedings (AINAW'07), Niagara-falls, pp. 882-887, Ontario, Canada, May 2007.

[15]: T. Fahad and R. Askwith. "A Node Misbehaviour Detection Mechanism for Mobile Ad-hoc Networks", in *The Seventh Annual Postgraduate Network Symposium (PGNet 2006)*, Liverpool, UK, 2006

[16]: Conti, M.; Gregori, E.; Maselli, G. Improving the performability of data transfer in mobile ad hoc networks. The 2<sup>nd</sup> IEEE International Conference on Sensor and Ad Hoc Communications and Networks (SECON 2005), Santa Clara, CA, Sept 26–29, 2005.

[17]: Miranda, H.; Rodrigues, L. *Friends and foes: preventing selfishness in open mobile ad hoc networks*. The 23<sup>rd</sup> IEEE International Conference on Distributed Computing Systems (ICDCS 2003), Providence, RI, May 19–22, 2003; 440–445.

[18]: Q. He, D. Wu, and P. Khosla. "SORI: A Secure and Objective Reputation-Based Incentive Scheme for Ad Hoc Networks", in *IEEE Wireless Communications and Networking Conference WCNC 2004*, Atlanta, GA, 2004.





[19]: Buchegger, S.; Le-Boudec, J.-Y. A robust reputation system for p2p and mobile ad-hoc networks. 2nd Workshop on the Economics of Peer-to-Peer Systems, Berkeley, CA, June 4–5, 2004.

[20]: X. Zeng, R. Bagrodia, and M. Gerla, "Glomosim: A library for the parallel simulation of large-scale wireless networks," in *The 12th Workshop on Parallel and distributed Simulation. PADS'98*, Banff, Alberta, Canada, May 1998, pp. 154–161.

[21]: Broch, D.B. Johnson, and D.A. Maltz, "The dynamic source routing protocol for mobile ad hoc networks. Internet draft", 2004, IETF, URL: <http://www1.ietf.org/mail-archive/web/ietf-announce/current/msg02559.html>.





## An Improved Scheduling Scheme of UL-Traffic in PMP WiMAX Network: an Analytical Model and its Evaluation

Khaled M. Shalghum  
Faculty of Technical Engineering  
Mesalata-Libya  
Email: [kmsshalgoum@yahoo.com](mailto:kmsshalgoum@yahoo.com)

Hasein I. Sigiuk  
Faculty of Engineering, Alfateh University  
Tripoli-Libya  
Email: [sigiuk@mwc.ly](mailto:sigiuk@mwc.ly)

**Abstract** – IEEE802.16 as a wireless MAN broadband access standard, defines a flexible QoS mechanism in MAC layer for wild variety classes of services. However, it does not define specific scheduling algorithm of UL-traffic, which is becoming the research hot spot in resent years. In this paper, a modified scheduling algorithm is developed on the features of services defined in IEEE802.16d, including UGS, rtPS, nrtPS, and BE services. An analytical model is derived and evaluated under different loading conditions for the proposed scheme, and it is compared with a related scheme which we have proposed and published.

**Keywords-** *Broadband Wireless Access, IEEE 802.16, UL-Scheduling Algorithms, Performance Evaluation.*

### I. INTRODUCTION

Broadband is a transmission facility where bandwidth is wide enough to carry multiple voice, video or data channels simultaneously. Broadband Wireless Access (BWA) is capable for providing high speed network access to a broad geographic area with rapid flexible deployment at low cost. Other advantages of BWA are high scalability, lower maintenance and upgrade costs [1].

The IEEE802.16 standard was developed to produce high performance BWA systems. The standard specifies a Wireless MAN air interface for fixed point to multi-point BWA systems. A Wireless MAN consists of at least one radio Base Station (BS) and one or more Subscriber Station

(SS) with a fixed point to multi-point topology [2].

In spite of the WiMax standard specifies the request-grant mechanisms and the traffic types (voice, video and data), it leaves the question open that how to use the scheduling mechanism of these services, thus make it available for providers and vendors to innovate in this area.

Scheduling algorithms serve as an important component in any communication network to satisfy the QoS requirements, such as: delay, fairness, complexity, etc. Uplink scheduling algorithm have not standardized in IEEE802.16 protocol.

In this paper, a modified scheduling algorithm is presented, where an analytical model is derived and evaluated with



different types of traffic under balanced and unbalanced traffic scenarios.

The basic architecture of PHY and MAC layers in IEEE802.16d standard is introduced in Section II. In section III, the system model and the related works for the proposed scheduling algorithm are presented. The assumptions made for the analytical model of the proposed scheme are presented in section IV. Section V gives some numerical results with discussions for different scenarios. Finally the paper ends with a conclusion in section VI.

## II. PHY AND MAC IEEE802.16 STANDARD

In WiMax, time is divided into frames, each of them, in turn, is composed of a fixed number of slots. At the start of each frame, the BS schedules the uplink and downlink grants in order to meet the negotiated QoS requirements. On the uplink, the BS determines the number of time slots for which each SS will be allowed to transmit in an uplink subframe. This information is broadcast by the BS through the uplink map message (UL-MAP) at the beginning of each frame. The UL-MAP contains an Information Element (IE) per SS, which includes the transmission opportunities for each SS, and the time slots in which a SS can transmit during the uplink subframe. The BS scheduling module determines the IEs by using the bandwidth request message sent from the SSs to the BS. On the downlink, the BS is the only one that transmits during a downlink subframe. Data packets are broadcast to all SSs and an SS only listens in on the packets destined for it.

There are four types basic services described in the standard. Named respectively as follows: Unsolicited Grant

Service (UGS): such as VoIP applications; Real-Time Polling service (rtPS): such as video applications; Non-Real-Time Polling Service (nrtPS): such as the file transfer protocol applications; Best Effort (BE): such as the e-mails, and add the Extend Real-Time Polling Service in IEEE802.16e. This paper is based on the first four classes of services which supported by IEEE802.16d protocol (fixed WiMAX network) [3].

## III. SYSTEM MODEL

### A. RELATED WORK :

In [4,5], the authors proposed a MAC scheduling algorithm for IEEE802.16 protocol by applying a reservation priority access control (RPAC) scheme, with two versions I and II. The proposed algorithm is evaluated using FDD allocation scheme under balanced traffic conditions in [4], and unbalanced traffic condition in [5]. The main ideas behind the RPAC scheme employed for version I and II are summarized below:

- **RPAC-I scheme:** For any  $p, q \in \{1, \dots, P\}$  such that  $p < q$ , and  $p, q$  represent the classes of services and  $P$  is a class number which has the lowest priority, all class- $p$  messages are transmitted before any messages of class- $q$ , independent of which station it belongs to. For the messages belonging to the same class but in distinct stations, the order of the transmissions is according to the order in which the stations access the channel (first station 1 and the last station  $M$ ). For messages in the same station with the same class of priorities, the transmissions occur by order of arrival.
- **RPAC-II scheme:** For any  $i, j \in \{1, \dots, M\}$  such that  $i < j$ , where  $i, j$  represent the station order number in the



list, all the messages in station  $i$  are transmitted before any messages in station  $j$ , independently with respect to other nodes traffic priority class. In any terminal, the messages are transmitted in accordance with their priority classes and in order of arrival, in the case of belonging to the same class; that is, at each station, the priority discipline HOL (Head-Of-the-Line) is applied, with the highest priority assigned to class 1 and the lowest assigned to class  $P$ .

From the obtained results in [4, 5], it is found that the RPAC-I scheme gives better differentiation between classes of services than RPAC-II scheme, with respect to average waiting-time per class. However, first scheme (RPAC I) has suffered from some degree of unfairness in the access to the media amongst network SSs, especially if most traffic intensity offered from one class or one SS.

In this paper, the proposed algorithm (modified RPAC-I scheme) is presented and evaluated under different loading conditions to improve the degree of fairness among stations.

#### **B. PROPOSED ALGORITHM :**

Our scheduling algorithm is proposed for UL-transmission (from SSs to BS), as follows:

For any  $p, q \in \{1, \dots, P\}$  such that  $p < q$ , and  $p, q$  represent the classes of services and  $P$  is a class number which has the lowest priority, all class- $p$  messages are transmitted before any messages of class- $q$ , independent of which station it belongs to. For the messages belonging to the same class but in distinct stations, the order of the transmissions is according to the order of arrival and the order in which the stations access the channel, (message 1 from SS # 1, message 1 from SS # 2, up to message 1 from SS #  $M$ , then message 2 from SS # 1, message 2 from SS # 2, ..... and so on for other messages and stations), as shown in Fig.(1).

Fig.(2) shows the transmission stages needed to transmit the  $k^{\text{th}}$  class- $p$  message from station  $i$  using the proposed scheme together with the developed flow chart.

### **IV. MODEL ASSUMPTIONS AND ANALYSIS**

#### **A. MODEL ASSUMPTIONS :**

To analyze the performance of the proposed scheme, the system model has to take into considerations the following assumptions:

- The system considered has one BS and  $M$  ( $M \geq 1$ ) client stations (SSs), each of which has an infinite buffer-size and is already associated with the BS.



- All subscriber stations (SSs) are within the range of the BS.
- Different stations are not limited to be in the line of sight of each other.

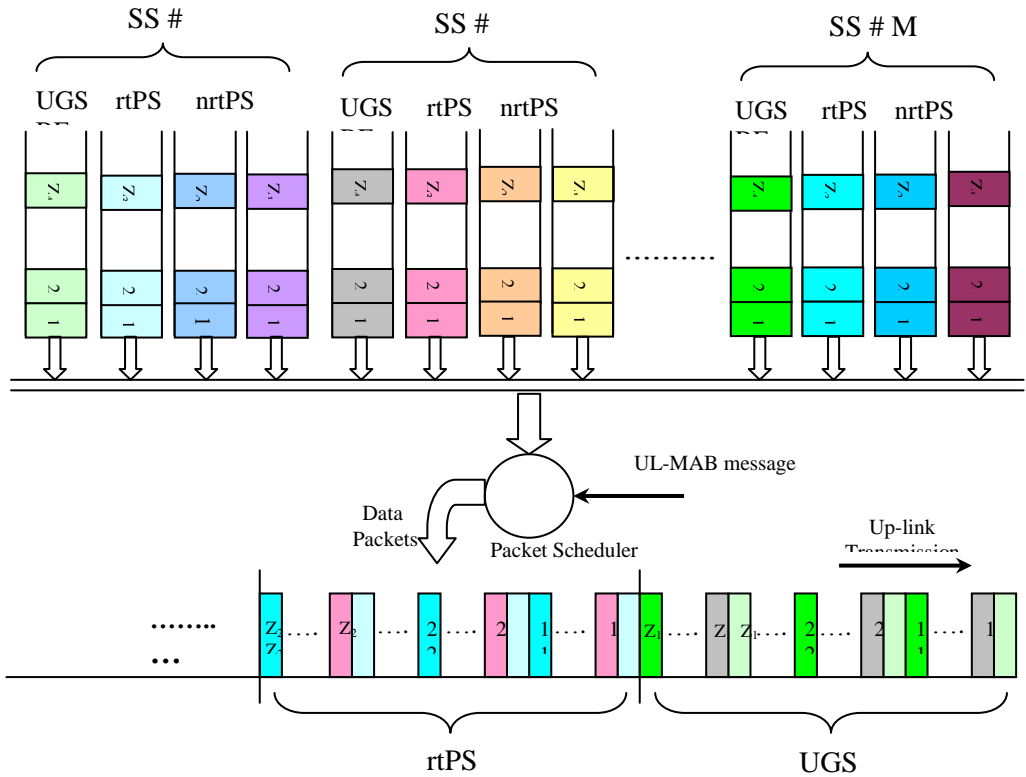


Fig.(1) The proposed algorithm for UL-transmission.

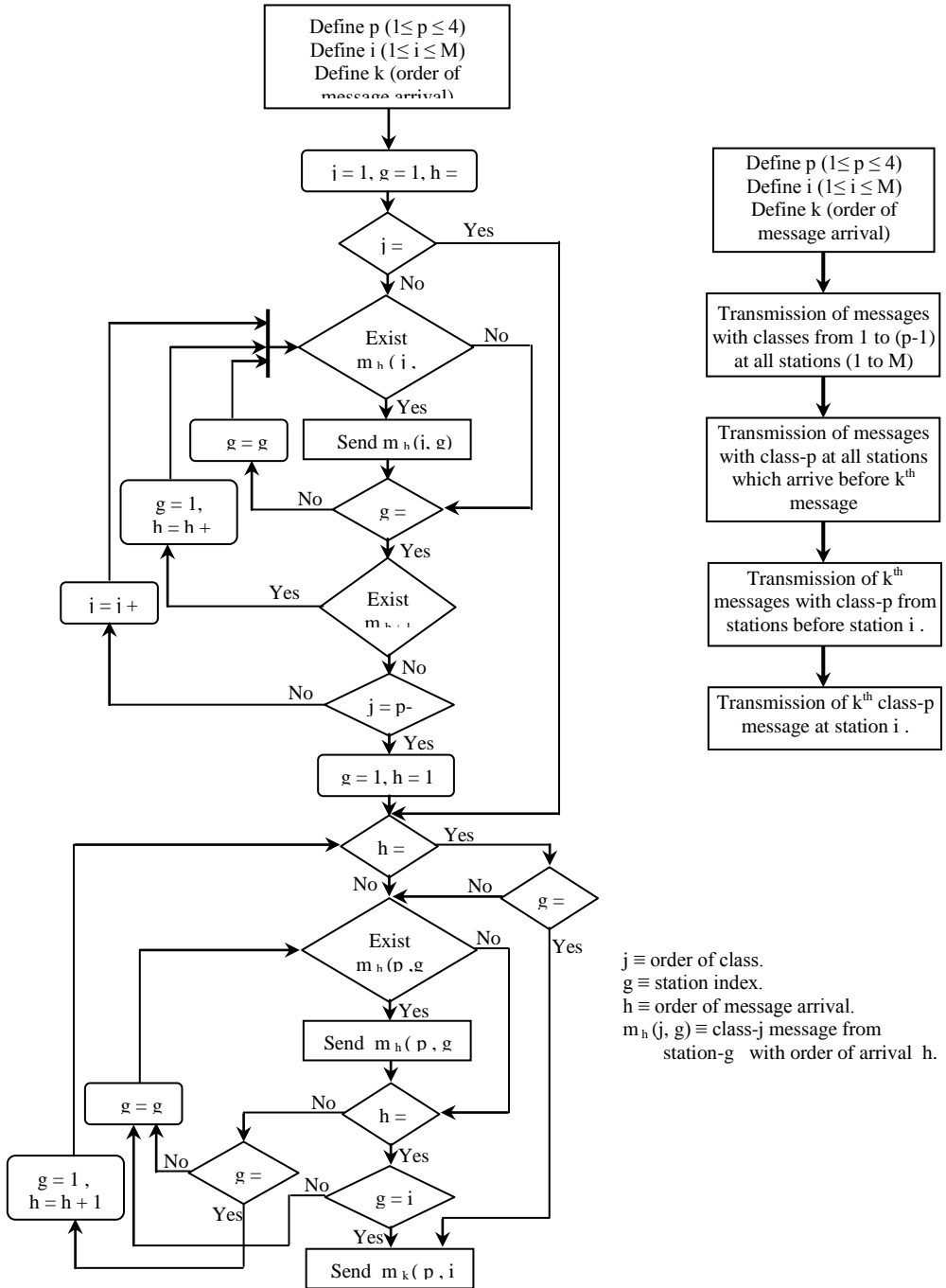


Fig. (2) Transmission stages for  $k^{\text{th}}$  class- $p$  message from station  $i$  using the proposed algorithm.

- The communication channel is assumed to



be completely synchronized by the BS.

- The transmission channel is assumed to be error free.
- At each station, the arrival of messages is characterized by a Poisson process.
- The number of packets in each message of class-p in the station  $i$  is independent and identically distributed.

By assuming that, the channel is fully synchronized by the BS. Thus, time is subdivided into equal-length segments, the duration of each segment ( $\tau$  seconds) called time slots. The start of message transmissions across the channel must be synchronized with the beginning of a time slot.

At each of the  $M$  stations, the arriving messages belong to one out of  $P$  different priority classes. We assume that, class-1 messages have the highest priority and class- $P$  have the lowest.

For each  $i \in \{1, \dots, M\}$  and  $p \in \{1, \dots, P\}$ , we assume that the number of class-p messages arriving to terminal  $i$  during the  $n^{\text{th}}$  time slot is a sequence of independent and identically distributed (i.i.d.) random variables, governed by a Poisson distribution with average  $\lambda_i^p$  (messages/slot), independent of the arrival processes of other classes. In general, the message generated at each station is composed of a random number of packets, such that  $B_{n,i}^p$  is the number of packets contained in the  $n^{\text{th}}$  class-p message arriving to station  $i$ , with mean  $b_i^p$  and second moment  $b_{2,i}^p$ .

### B. MESSAGE WAITING-TIME ANALYSIS :

Messages are assumed to arrive at the end of slots. Let  $W_{n,i}^p$  represent the waiting-time for the  $n^{\text{th}}$  class-p message arriving to

station  $i$ , measured in slots. Hence,  $W_{n,i}^p$  is the total number of slots elapsed since the arrival of the  $n^{\text{th}}$  class-p message at station  $i$  until the start of the slot in which transmission of this message is initiated. The following additional random variables are defined:

$Z_{n,i}^p \equiv$  number of class-p messages buffered at station  $i$  at the beginning of the  $n^{\text{th}}$  cycle.

$N_{n,k,i}^p \equiv$  number of class-p messages arriving at station  $i$  during the  $k^{\text{th}}$  slot of the  $n^{\text{th}}$  cycle.

$N_{A,i}^p(k) \equiv$  a random variable governed by the same distribution as the number of class-p messages arriving to station  $i$  during the  $k^{\text{th}}$  slot.

$B_{n,k,i}^p \equiv$  number of packets contained in the  $k^{\text{th}}$  class-p message transmitted by station  $i$  during the  $n^{\text{th}}$  cycle.

$Y_{n,i}^p \equiv$  queue size of class-p messages at terminal  $i$  during the  $n^{\text{th}}$  cycle.

$N_i^p(Y_{n,i}^p) \equiv$  total number of class-p messages transmitted at station  $i$ , during the  $(n+1)^{\text{th}}$  cycle, given  $Y_{n,i}^p$ .

$W_i^p(Y_{n,i}^p) \equiv$  sum of the waiting-time components of all class-p messages served at station  $i$ , in the  $(n+1)^{\text{th}}$  cycle, given  $Y_{n,i}^p$ .

We have

$$N_i^p(Y_{n,i}^p) = Z_{n+1,i}^p \quad (1)$$

$$W_i^p(Y_{n,i}^p) = D_1 + D_2 + D_3 + D_4 \quad (2)$$

$D_1 \equiv$  the overall delay of class-p messages arriving to terminal  $i$  during  $L_n$  ( where  $L_n$  is the length of  $n^{\text{th}}$  cycle), from their instants of arrival to the instant of termination of  $L_n$  (recall that arrivals occur at the end of slots), then:



$$D_1 = \left[ N_{n,1,i}^p (L_n - 1) + N_{n,2,i}^p (L_n - 2) + \dots + N_{n,(L_n-1),i}^p \right]$$

$D_2 \equiv$  the total waiting, of all  $Z_{n+1,i}^p$  messages, due to the all reservation intervals of M slots, and the allocation start time ( $T_{st}$ ) (round-trip delay + processing time), then:

$$D_2 = (L_n^R + L_n^{st}) Z_{n+1,i}^p$$

$D_3 \equiv$  (stage-1 delay in Fig. (2)), the time that all  $Z_{n+1,i}^p$  messages must wait due to all transmissions from classes 1 to (p-1), at all stations (1 to M), then:

$$D_3 = \left\{ \sum_{j=1}^{p-1} \left[ \sum_{g=1}^M \left( \sum_{k=1}^{Z_{n+1,g}^{st}} B_{n+1,k,g}^j \right) \right] \right\} Z_{n+1,i}^p$$

$D_4 \equiv$  (stage-2 and stage-3 delays in Fig.(2)), the total time that all  $k^{th}$  class-p messages must wait due to all class-p transmissions at all stations (1 to M) with order of arrive from 1 to (k-1), plus the  $k^{th}$  class-p transmissions at stations 1 to (i-1), then:

$$D_4 = \sum_{g=1}^{i-1} B_{n+1,1,g}^p + \left( \sum_{g=1}^M B_{n+1,1,g}^p + \sum_{g=1}^{i-1} B_{n+1,2,g}^p \right) + \dots + \left( \sum_{g=1}^M B_{n+1,1,g}^p + \dots + \sum_{g=1}^M B_{(n+1,Z_{n+1,i-1}^p-1,g)}^p + \sum_{g=1}^{i-1} B_{(n+1,Z_{n+1,i}^p,g)}^p \right)$$

Then, applying a Markov Ratio Limit Theorem (MRLT) [2], we obtain:

$$\bar{W}_i^p = \frac{E^* \left[ W_i^p \left( \underline{Y}_{n,i}^p \right) \right]}{E^* \left[ N_i^p \left( \underline{Y}_{n,i}^p \right) \right]} \quad (3)$$

Where  $E^* \left[ N_i^p \left( \underline{Y}_{n,i}^p \right) \right]$  and  $E^* \left[ W_i^p \left( \underline{Y}_{n,i}^p \right) \right]$  are the steady-state averages of (1) and (2) respectively.

$$E^* \left[ N_i^p \left( \underline{Y}_{n,i}^p \right) \right] = E^* \left[ Z_{n+1,i}^p \right] = \lambda_i^p E(L) \quad (4)$$

Where  $E(L) = \lim_{n \rightarrow \infty} E(L_n)$

By taking the steady-state average of (2), and with substitution into (3), the average waiting-time of class-p messages at terminal i will be given by:

$$\bar{W}_i^p = M + E \left[ T_{st} \right] - \frac{1}{2} + \left( i - 1 - \frac{M}{2} \right) b_i^p + \left[ \frac{(1 + M \rho_i^p)}{2} + \sum_{j=1}^{p-1} \sum_{g=1}^M \rho_g^j \right] \frac{E \left[ L^2 \right]}{E \left[ L \right]} \quad (5)$$

Where  $\rho_i^p = \lambda_i^p b_i^p$  is the traffic in the terminal i due to the messages of class-p,  $E \left[ T_{st} \right] = \lim_{n \rightarrow \infty} E \left[ L_n^{st} \right]$ ,  $E \left[ L \right]$  and  $E \left[ L^2 \right]$  are the first and second steady-state moments of  $n^{th}$  cycle length  $L_n$ . The length of the  $n^{th}$  cycle is  $L_n = L_n^R + L_n^{st} + L_n^T$ , where  $L_n^R$  is the length of the  $n^{th}$  reservation interval,  $L_n^{st}$  is the allocation start time of the  $n^{th}$  cycle, and  $L_n^T$  is the size of the  $n^{th}$  transmission interval. We assume that  $L_n^R = M$  (where M is the number of SSs in the network) with duration of  $M\tau$  seconds. We have (see [2] for more details).

$$E \left[ L_n \right] = E \left[ L_n^R + L_n^{st} + L_n^T \right] = M + E \left[ L_n^{st} \right] + \sum_{p=1}^P \sum_{i=1}^M \rho_i^p E \left[ L_{n-1} \right] \quad (6)$$

Then, making  $\rho = \sum_{p=1}^P \sum_{i=1}^M \rho_i^p < 1$  and taking the limits (with  $n \rightarrow \infty$ ) in both sides of the above equation, we obtain:

$$E \left[ L \right] = \frac{M + E \left[ T_{st} \right]}{1 - \rho} \quad (7)$$

In a similar way, through a recursive equation for  $E \left[ L_n^2 \right]$  and assuming  $\rho < 1$ , then:



$$E[L^2] = \frac{1}{1 - \sum_{p=1}^P \sum_{i=1}^M (\rho_i^p)^2} \left\{ M^2 + E[T_{st}] + 2M E[T_{st}] + 2\rho(M + E[T_{st}]) + \sum_{p=1}^P \sum_{i=1}^M \lambda_i^p b_{2,i}^p \right\} E[L] + \left\{ \sum_{p=1}^P \sum_{i=1}^M \sum_{\substack{j=1 \\ j \neq i}}^M \rho_i^p \rho_j^p + \sum_{p=1}^P \sum_{q=1}^P \sum_{i=1}^M \sum_{\substack{k=1 \\ q \neq p}}^M \rho_i^p \rho_k^q \right\} E^2[L] \quad (8)$$

Finally, substituting expressions of  $E[L]$  and  $E[L^2]$  in (5) we have a closed expression for the mean waiting-time of class- $p$  messages at terminal  $i$  under the proposed algorithm.

## V. NUMERICAL RESULTS

To evaluate the level of differentiation obtained with the proposed scheme, we considered two distinct scenarios, where in each scenario there is a differentiated probability between four classes of traffic ( $P = 4$ ), as shown in Table I.

**Table I, Traffic Scenarios Used**

Classes of services	Scenario 1	Scenario 2
UGS	60%	10%
rtPS	20%	10%
nrtPS	10%	20%
BE	10%	60%

From equation (9), we can plot the , as average waiting-time versus station index shown

To simulate the proposed scheme presented here and compare it with the **RPAC-I** scheme, which was modeled and simulated in [4, 5], under balanced and unbalanced traffic conditions, we assume that:

- (a) **Balanced case:** there are 10 stations ( $M=10$ ), each station shares with a traffic percentage ( $\rho_i = \rho/10$ ), and each station contributes with its traffic class according to Table I.
- (b) **Unbalanced case:** similarly  $M=10$ , but 82% of the traffic from station "4" and the remaining 18% of the traffic from other stations (2% from each SS), each SS has traffic type as illustrated in Table I.

We assume that the number of packets in each message of class  $p$  in the station  $i$  is constant with average  $b_i^p = 5$  and  $b_{2,i}^p = 25$ , for each  $p = 1, 2, 3, 4$ ; and  $i = 1, \dots, 10$ . So, the average waiting-time in the queue for the station  $i$  is given by:

$$\bar{W}_i = \sum_{p=1}^4 \frac{\lambda_i^p}{\lambda_i} \bar{W}_i^p \quad (9)$$

Where  $\lambda_i$  represents the average number of messages arriving to station  $i$ :

$$\lambda_i = \sum_{p=1}^P \lambda_i^p$$



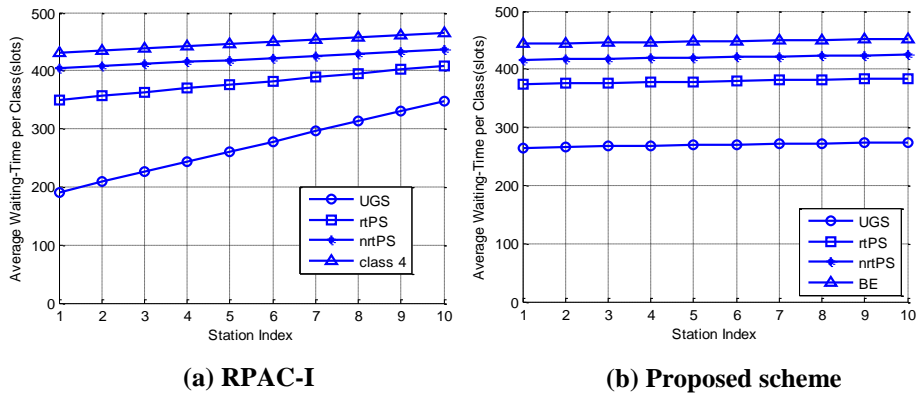


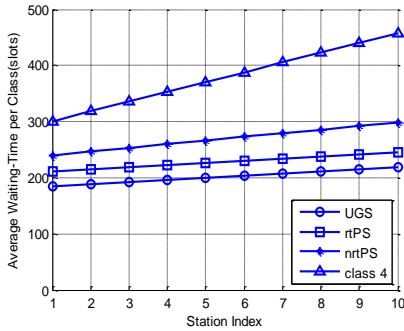
**Fig.(3) Average waiting-time vs. station index in Scenario-1 under**

in Figures (3), (4), (5) and (6) for the two schemes, the RPAC-I and the proposed

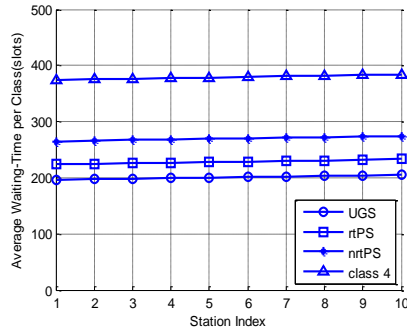


algorithm, both for under balanced and unbalanced traffic conditions, with overall traffic intensity ( $\rho=0.9$ ).

From Fig.(3)-a and Fig.(4)-a, for the balanced traffic case and for the same class of service traffic, the RPAC-I scheme shows

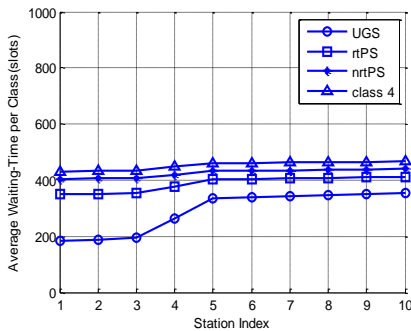


(a) RPAC-I

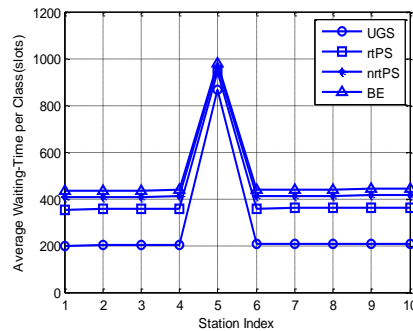


(b) Proposed

Fig.(4) Average waiting-time vs. station index in Scenario-2

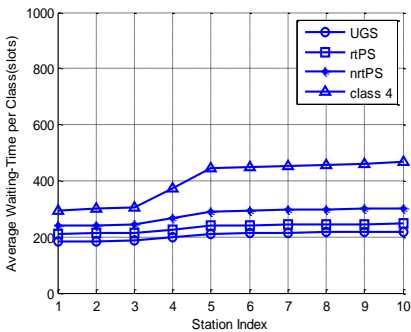


(a) RPAC-I

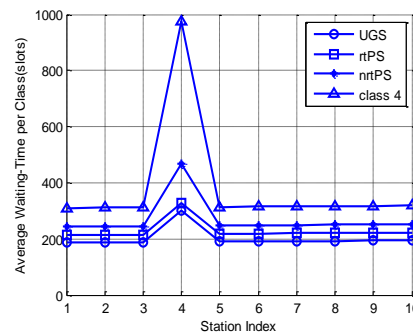


(b) Proposed

Fig.(5) Average waiting-time vs. station index in Scenario-1



(a) RPAC-I



(b) Proposed

Fig.(6) Average waiting-time vs. station index in Scenario-2 under unbalanced



some degree of difference in the average waiting-time in the queue among stations, this can be clearly noticed between stations with high traffic intensity. This behavior is improved using the proposed model as shown in Fig.(3)-b and Fig.(4)-b. From these Figures, we can notice that the proposed scheme managed to decrease the degree of unfairness in waiting times required to access the network, among stations transmitting at the same class of service.

As shown in Fig.(5)-a and Fig.(6)-a, for a given traffic intensity of class-p, messages using RPAC-I scheme under unbalanced traffic case, one can observe that there is some degree of unfairness between stations, this can be clearly noticed nodes located before and after node "4" , this degree of unfairness between stations increases as the traffic intensity of a given class of service increases. This behavior also is improved using the proposed model as shown in Fig.(5)-b and Fig.(6)-b.

From these Figures, we can notice that, the degree of unfairness is decreased in the waiting-times for stations to access the network. And we can observe that, the average waiting-time increases with respect to stations which have high traffic intensity and decreases with stations which have low traffic intensity.

## VI. CONCLUSIONS

In this paper, an UL-scheduling algorithm is proposed which supports the IEEE802.16d standard, and it incorporate traffic scheduling function with message based priority. Moreover, an analytical model is derived for the average waiting-time for different traffic scenarios, under the assumptions of Poisson arrivals and general distributions of message lengths.

The proposed model is managed to improve the degree of unfairness among stations that was reported in [4, 5] for RPAC-I scheme. The improvement introduced by the proposed scheme is noticed for both balanced and unbalanced traffic conditions.

## REFERENCES

- [1]. IEEE802.16, IEEE Standard for Local and Metropolitan Area Networks - Part 16: Air Interface for Fixed Broadband Wireless Access Systems, IEEE Std. 802.16, Oct. 2004.
- [2]. Khaled M. Shalghum, "Performance Evaluation of a MAC Reservation Scheme for Multimedia Traffic in WiMAX", Master Thesis, Electrical and Electronic Eng. Dep., Alfatah University, Tripoli-Libya, 2008.
- [3]. Hui-Lian Wa, Jun Gu, and Ya-Ping Deng, "Dynamic Frame Scheduling Scheme for IEEE802.16 Broadband Wireless Networks", IEEE communication conf., 2009.
- [4]. K. M. Shalghum, H. I. Sigiuk and K. A. Khalfalla, "Performance Evaluation of IEEE802.16 Protocol Using FDD Allocation Scheme", Mosharaka International Conf. on Comm., Propagation and Electronics (MIC-CPE 2008), IEEE Comm. Society, Jordan, Amman, March 2008.
- [5]. K. M. Shalghum, H. I. Sigiuk and K. A. Khalfalla, "Performance Evaluation of IEEE802.16 Using a Modified Reservation Scheme Under Different Loading Conditions", IEEE-3<sup>rd</sup> International Conf. on Information & Comm. Technologies: from Theory to Applications (ICTTA'08), Damascus, Syria, April 2008.



المؤتمر الدولي العربي الليبي الخامس للهندسة الكهربائية والإلكترونية 23-26/10/2010 طرابلس ليبيا



## Linkmeter – The Swiss Army Knife of Radio Relay

Per Thorvaldsen, Net designer, Nera Networks, [pt@nera.no](mailto:pt@nera.no)

### Abstract

In conventional radio relay systems one of the most challenging tasks for radio engineers is to find the cause and nature of transmission errors when they occasionally occur. Is it fading, interference or equipment error? Nera Networks has developed a novel PC based tool, Linkmeter, which extracts information from the radio elements and presents graphs making it easy to identify possible problems.

### 1. Introduction

Radio relay systems are mainly used to provide backhaul data transmission or to provide capacity to cellular networks. The popularity and widespread use of radio relay is due to its flexibility, low cost and fast deployment. Figure 1 shows a typical network for a mobile operator.

With Nera Networks Evolution radios it is possible to create networks with capacities ranging from a couple of megabits per second to 1.6 gigabits per second depending on configuration and number of available channels. The transmission type may be PDH, SDH, Ethernet or a scalable combination.

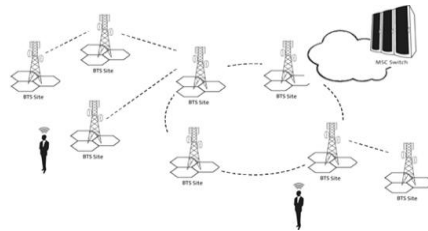


**Figure 1 Radio relay network**

To manage and monitor the performance of large microwave networks, Nera Networks has an application called NetMaster. This product performs the usual FCAPS (Fault, Configuration, Accounting, Performance and Security) and is excellent for getting an overall view and status of the network. In Figure 2 a typical NetMaster scenario is shown.

One challenge with management systems when transmission errors occur is that they are often flooded with alarms so that the root cause of a problem is not easily found.

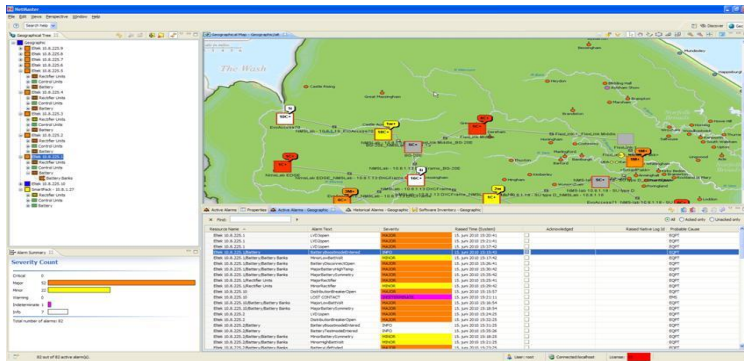


Figure 2 NetMaster management system

. To make it simpler to analyse fault situations on individual paths Nera Networks has developed a PC based software called Linkmeter. This software correlates various input level statistics and errors, making fault finding easy. As an example, Figure 3 shows the statistics of a measurement done on an overwater path in Norway. Notice the blue spikes at -65 dBm and -80 dBm that indicate error pulses at these input levels

Most ideas come as a result of the hardship of work. In the nineties, I laboured a lot over endless alarmlists looking for the possible cause of errors in a myriad of consequential alarms. Could there be a simpler way? The main challenges concerning radio relays are fading, possible inference or equipment related errors. What is common for all three is that they all generate bit errors, but at different receiver input levels. That could be exploited!

## 2. The Linkmeter - a novel idea

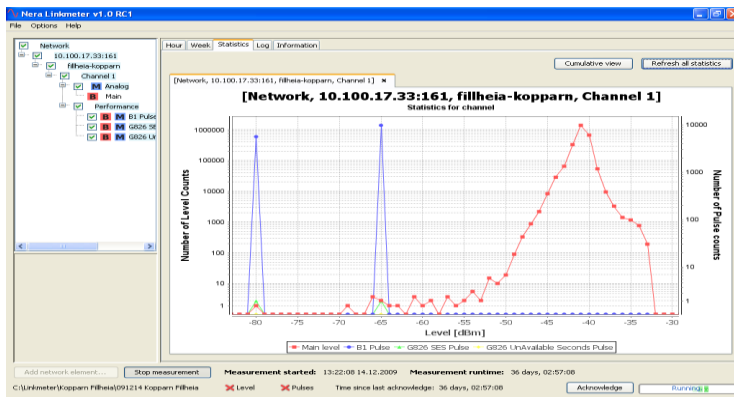


Figure 3 Long term measurement with Linkmeter



By making and presenting statistics correlating between bit errors and input levels it would be possible to separate the three phenomena's with a glance. If all the errors occur at input levels below the radio threshold, outage is due to fading. If the errors start at an input level above the radio threshold, the most likely cause is interference. This new degraded threshold may be used to calculate the strength of the interference. If errors are a consequence of equipment problems, they will appear at all input levels.

Hence, three very distinct and labour-saving graphs would easily reveal the cause of the transmission errors and immediate action could be taken to solve the problem.

### 3. Extracting information

The Evolution radio elements can be addressed by using SNMP (Simple Network Management Protocol). It is possible to extract inventory information, receiver input levels and performance data. The data is renewed every second and hence this becomes the fastest measurement sampling rate. Since SNMP is a part of the Internet suite of protocols it is possible to extract information from radio relays anywhere in the world as long as a VPN (Virtual Private Network) connection is established between the radio relay and the monitoring PC.



**Figure 4 Nera Networks Evolution at work**

Linkmeter exploits the inventory information to create a logical tree structure of the Evolution radio element. The radio may have up to four different directions and each direction can have one or more channels. The channels may have space and/or frequency diversity and in addition have various transmission formats like PDH, SDH or Ethernet.

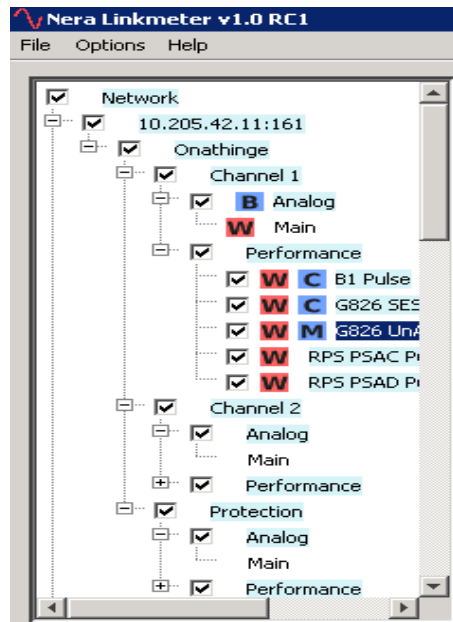


**Figure 5 The logical tree of a 2+1 radio**



The Linkmeter can analyse more than one element. In fact the number of elements it can measure is only limited by the amount of memory in the PC. Measuring more than one element at the same time makes it possible to compare different radio relay paths.

#### 4. Linkmeter functionality and GUI

The main purpose of Linkmeter is to make radio relay fault finding easy. By displaying time series and correlated statistics graphically the cause of errors can effortlessly be found. The GUI (Graphical User Interface) has been designed to achieve that goal.

The GUI is divided into three different views. The left view contains the logical tree (see Figure 5). This tree is used to choose desired measurements and to select what is to be presented.

The largest view which is to the right is used for the graphs and the log. The different graphs are selected using tabs. There are two graphs used for time series: one of them shows the measured values for the last hour and the other one shows measurements for the last week. The weekly time series has a resolution of five minutes and shows the maximum, minimum and average value in each five minute interval.

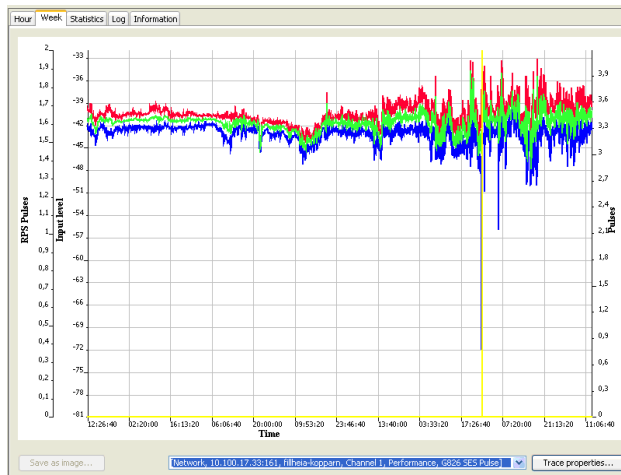


**Figure 6 A week of measurements having errors due to multipath fading**

The Statistics graphs show the accumulated correlated measurements in each channel and also the effects of space and frequency diversity if applicable. The type of errors

correlated with the input level may be selected using the logical tree.



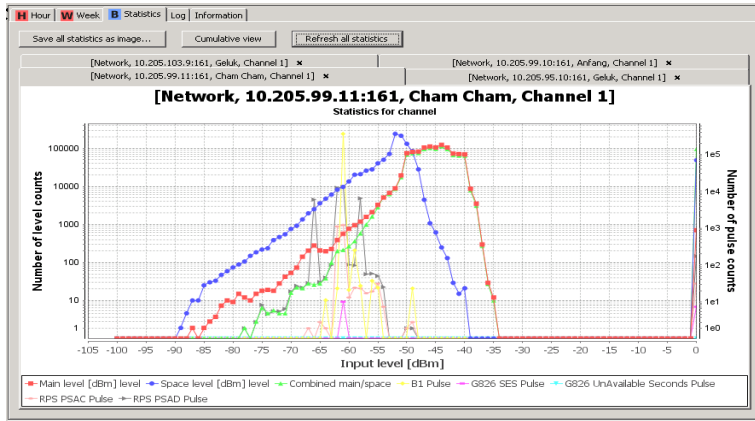


Figure 7 Correlated statistics of a space diversity channel in an African desert

The Log window shows all the measured values that are written to files. The interval between successive measurements, the highest resolution being 1 Hz, and the size of the logs is set by the user. Every time a log is completed, statistics logs are also written to file. All files have a format that makes them readable in Excel or other spreadsheets.

In the latest version of Linkmeter, it is also possible to look at measurements off-line. Recorded data is read from file and periods that have either low input level and/or errors are highlighted. By using a sliding time bar, the period of interest may be selected and the graphs will show data from the desired period. This off-line function is very useful when reports are made after measurements.

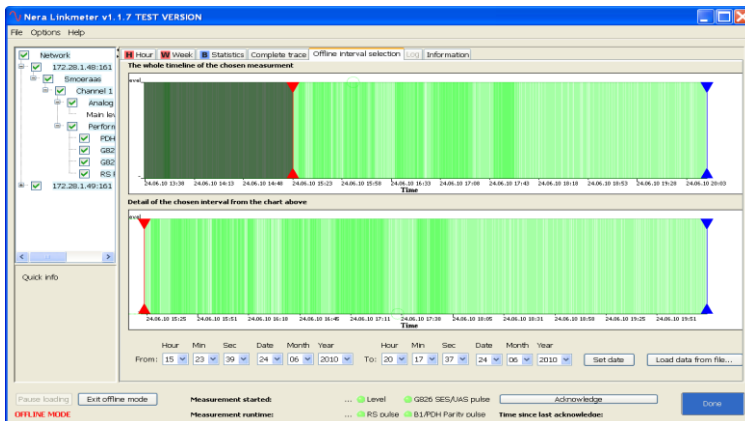


Figure 8 Off-line interval selection



The lower view in the GUI contains measurement related data like Linkmeter runtime, errors or low input levels since last acknowledge and the time elapsed since last acknowledge.

Linkmeter has been nicknamed the Swiss Army knife of radio relay since we, as time has elapsed, have found many more applications for Linkmeter than initially thought of. Let us start by looking at the error scenarios that Linkmeter was made to reveal and explain.

## 5. Linkmeter in action

### 5.1 Fading

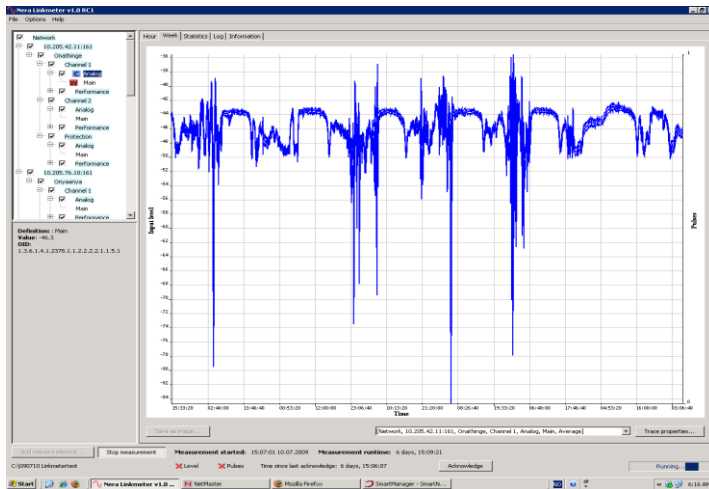


**Figure 9 Multipath in Namibia. Notice the diurnal effect**

For small percentages of the time radio relays are susceptible to fading. This fading is mainly of two types – multipath due to layering of the atmosphere or rain when the radio frequency is above 10 GHz. Multipath fading is predominant on long paths over

flat, hot and humid areas and rain fading in places with high rain intensity. Nera Networks radio relays are scattered all over the globe so it is likely that some of them will experience fading in one way or the other.

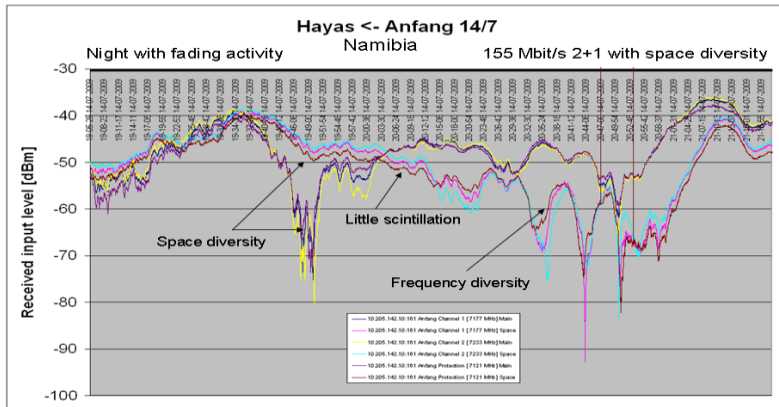


Figure 10 An evening in Namibia with heavy fading but no errors. Diversity works

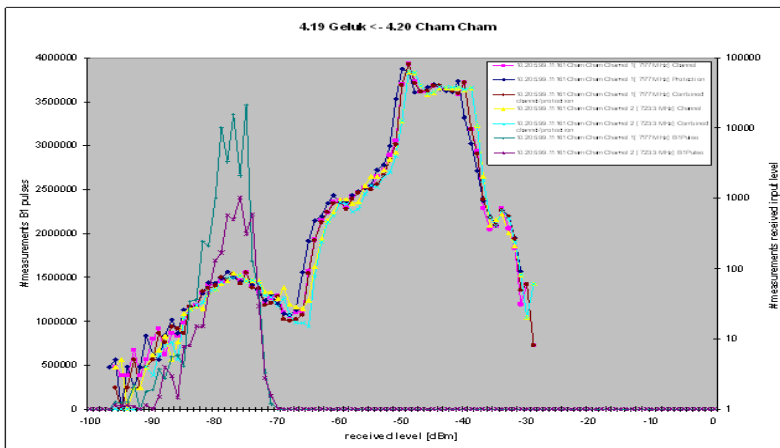


Figure 11 No errors above the threshold of -70 dBm i.e. fading related

If there is a difficult path, Linkmeter can measure it to check if all errors that occur are fading related. In that case, there will be

no errors above the input level threshold in the correlated statistics.

## 5.2 Interference

Since interference varies with time it may be hard to detect. It usually drowns in



concurrent fading activity on the victim path. With Linkmeter interference is easily

detected since errors will occur up to the “new” threshold given by the strength of the interference. In the figure below a long term measurement on a path shows occasional interference with accompanying errors.

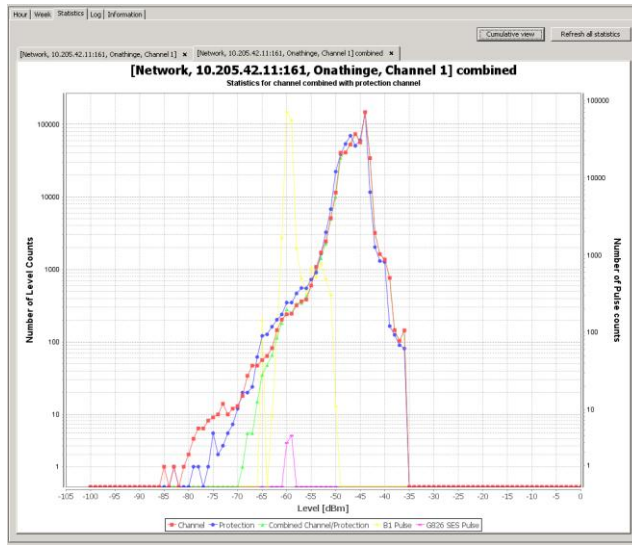


**Figure 12 Errors appearing around -60 dBm due to interference**

If one suspects that a network has interference problems, Linkmeter hourly time series may be used to find the interferer. At the victim site, one listens for interference by turning off the transmitter of one of the channels at the opposing site. By doing so, one can look at the fading activity on the path, see how the interference varies and by turning the

transmitter on again, see the errors the interference produces. When interference is detected on a channel, the transmitters of all possible interferers in the network are turned off. By turning them on again one at the time the strongest interferers can be found and action taken to get rid of the problem.

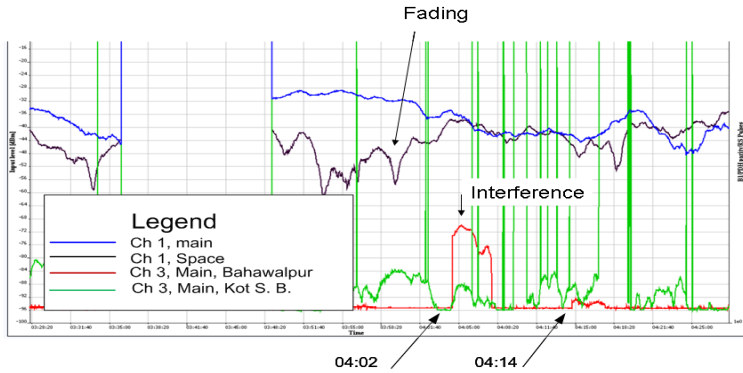


Figure 13 Fading together with interference give low S/N and errors

### 5.3 Equipment error

Some types of equipment malfunction like, for instance oscillator problems, may affect the transmission quality from time to time. These problems are typically not correlated

with the input level. By using Linkmeter these failures may be found by observing that the transmission errors happen at any input level.

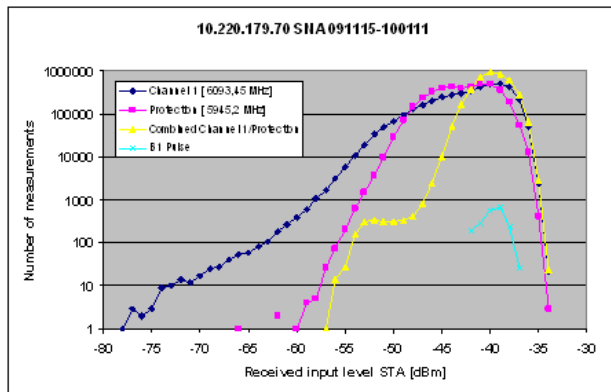


Figure 14 Errors occurring around the nominal level of -40 dBm

### 5.4 Improving diversity

Since Linkmeter has made propagation measurements so easy, it opens up new possibilities to test some old rules of thumb. For example, Nera Networks some twenty years ago improved system quality by

increasing the space diversity distance on some desert paths in Botswana. With the increased antenna separation there was diffraction loss on the lowest antenna during daytime but when there was ducting at night the lowest antenna became unobstructed and the system performance was improved.



Meeting the same challenge now in Namibia, we decided to try the old trick once more, but this time measure the effect.

On one side of the difficult desert path we kept the original space diversity distance and on the other side we increased it by 10 meters.

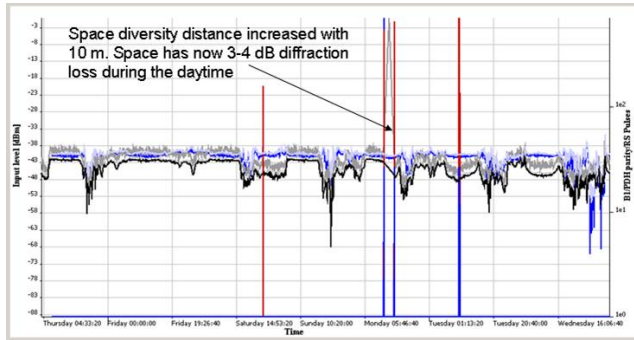


Figure 15 Input level before and after increasing space diversity

As seen from Figure 15 showing the diurnal time series, the diffraction loss disappears in the evening and comes back the next morning. This should give potential for

space diversity improvement, but the statistics from both sides of the path provide evidence of the contrary. The site with least space diversity is performing best

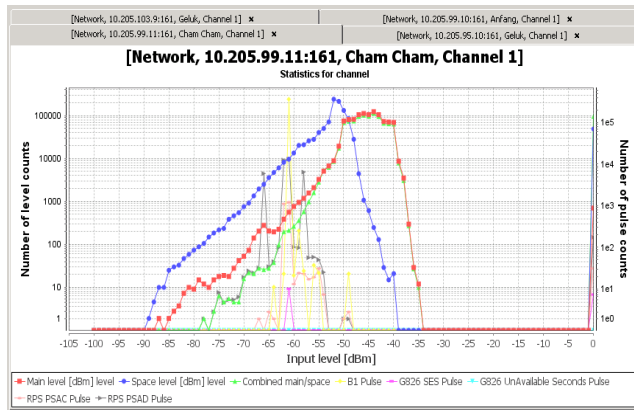


Figure 16 Errors and low combined input level on the site with increased space diversity

This conflicts with our expectations and may be explained by having too low fading margin or that we have not measured long

enough. In any event, the results are both interesting and experience building.

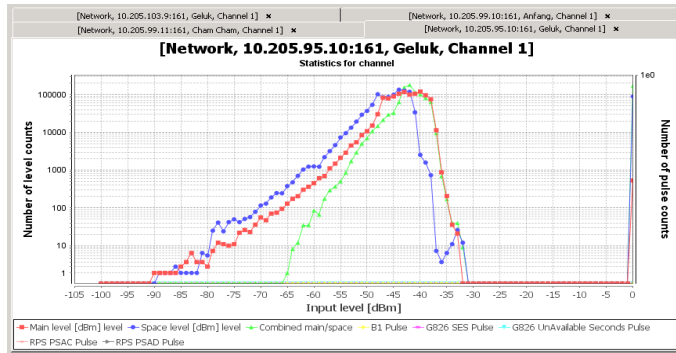


Figure 17 Better performance on the site with the original space diversity distance

### 5.5 Improving prediction

Earlier, due to the complexity and high cost involved with measurements, we always focused on measuring challenging paths. With Linkmeter there is now a, so to say, democracy when it comes to performance measurements. Linkmeter can measure any path – long or short, north or south –

without any budget or toil. That is what we do and will, in the long run, improve and strengthen our capabilities in performance prediction at various places on earth. Linkmeter are currently running on paths all over the world - from the longest overwater path (243 kilometres) in Equatorial Guinea to a 15 kilometres short path on the plains of the USA.

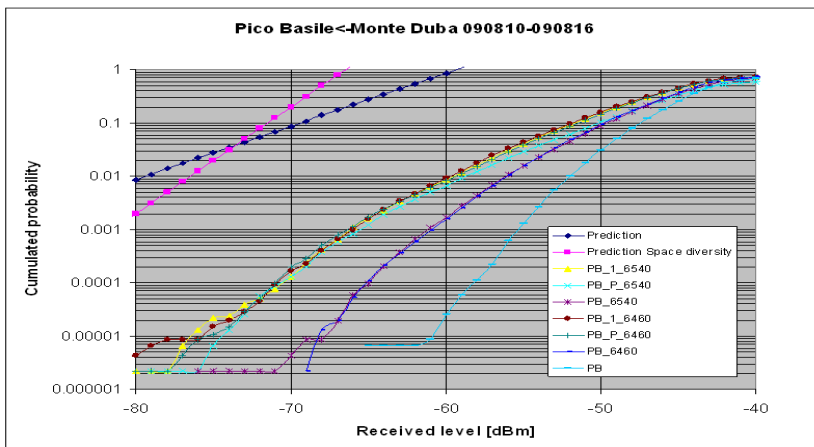


Figure 18 The 243 km over-water path shows excellent diversity performance

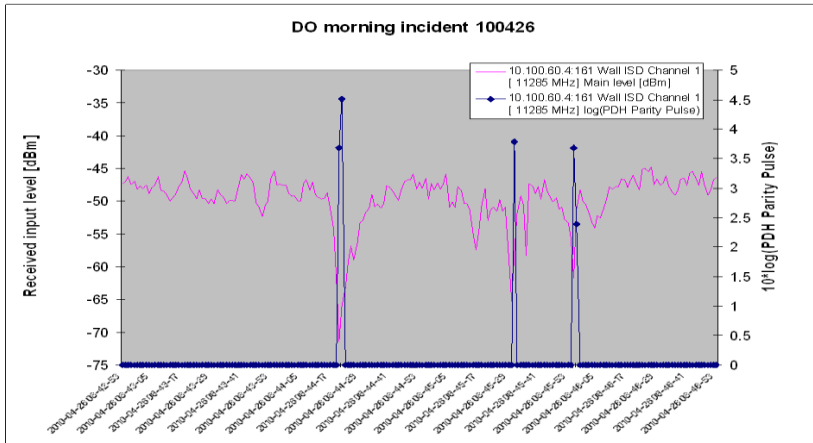


Figure 19 Heavy multipath fading giving errors on a 15 km path. Astonishing!

### 5.6 Checking models

In Recommendation ITU-R P.530-12 [1] a new model for calculating the outage due to sleet (wet snow) has been introduced. Due to the fact that parts of Norway experiences such weather conditions in the winter time,

we decided to do a long term measurement of a 43 kilometres, 1+0, 13 GHz, 155 Mbit/s link shooting over the Trondheimsfjord which has paramout sleet occurrence in the country. The measurement started in the autumn of 2009 and will be carried out for years to come.

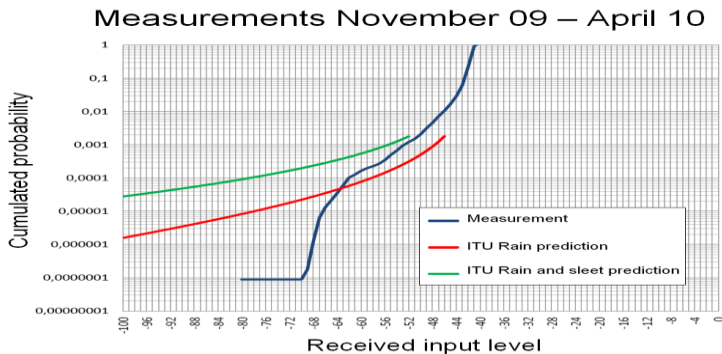


Figure 20 Rain and sleet measurements





The graph shows that the measurement has deeper fades than predicted with only rain, but more shallow fades than predicted taking both rain and sleet into account.

### 5.7 Commissioning

Since Linkmeter can measure possible errors and exclude causes such as fading or interference, it has become a handy toll during Site Acceptance Tests of the Evolution radios. Linkmeter runs for a couple of days and if the Evolution performs error free, papers are signed and the Evolution delivered.

At one such commissioning in the North Sea the input levels varied greatly, but there were no accompanying bit errors. The customer complained and it was decided to do measurements for a period of time. By averaging the input levels within a one hour window, we observed that the input levels varied in step with the tide. The tide changed the sea reflection point and hence the input level. Having proved this, our customer accepted this as normal behavior and had no more fears that this should cause any outage on the radio path.

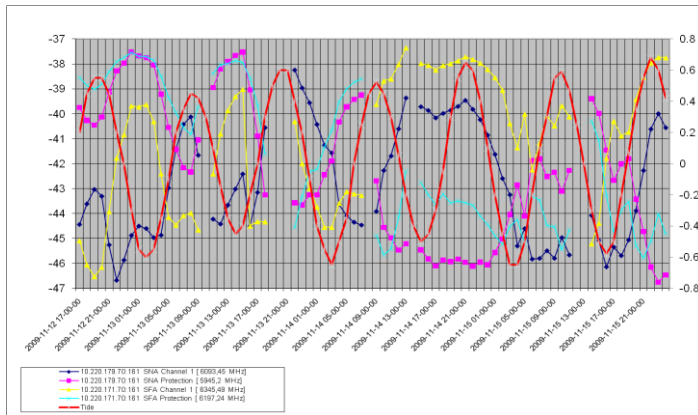


Figure 21 Fading caused by tide

### 5.8 Hardware problems

Even though the purpose of Linkmeter was to find causes of trans-mission errors, it can also be used to identify various intermittent hardware problems.

### 6. The future

Well, the future is already coming into shape. Some of the features of Linkmeter have been introduced directly into the Evolution radio elements i.e. the radio

elements themselves now generate correlated statistics. The benefit is highly increased measurement sampling rate, reduced management communication between the elements and a central unit and more importantly, the statistics can be run on all installed elements. As a result of this we will, over time, generate an enormous database of the performance of radio relay paths all over the world. Data collected in this fashion can then be used to improve the accuracy of performance prediction.

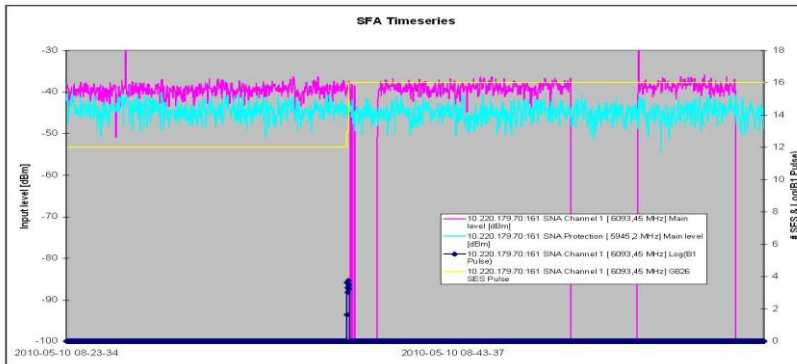


Figure 22 Loose cable on the main channel

Linkmeter itself will also be continuously improved. Currently we are looking at adding the S/N (Signal to Noise ratio) as a parameter for simpler detection of interference that varies with time. After having implemented the S/N function, the next natural step is to introduce a spectrum analyser function into Linkmeter to measure interference in the operating sub-

bands. Having a function like that, it is possible to detect and avoid channels that from time to time are littered with noise.

## 7. Conclusion

Linkmeter started as a novel idea to efficiently find the true cause of transmission errors. By the use of correlated statistics and graphs that are easy to interpret, the errors can be divided into three categories – fading, interference or equipment error.

As presented in the paper, Linkmeter can do much more than this and has truly become the Swiss Army knife of radio relay.

## 8. Acknowledgements

The Linkmeter software has been developed by Nera Networks with the aid of students from Bergen University College. We would like to thank the Bergen University College and especially the students Øystein Taskjelle, Espen Steine and Hans-Even Ramsevik Riksem for their valuable contribution.

## 9. References

Recommendation ITU-R P.530-12  
Propagation data and prediction methods required for the design of terrestrial line-of-sight systems



## ***Chapter II***

# **Electromagnetic and Microwave Engineering**



المؤتمر العربي الليبي الدولي الخامس للهندسة الكهربائية والإلكترونية 23-26/10/2010 طرابلس ليبيا



## Measurements of Electromagnetic Radiation from mobile phone base stations in Tripoli

Fatima A. Ashkal  
Altahadi University  
[fatmaaa07@yahoo.com](mailto:fatmaaa07@yahoo.com)

Ibrahim M. Saleh  
AL-fateh University  
[ibrahim.saleh@ltnet.net](mailto:ibrahim.saleh@ltnet.net)

### Abstract

There is a substantial advancement in the world's wireless communications, therefore communication antennas were installed in places where people live or work, in addition numerous base station antennas installed on homes and schools. As other countries, Libya has substantial growth in use of mobile communication services; therefore, it is very important to conduct a study to measure the radiation levels from mobile base stations where young people live or spend part of their daily life near these base stations. The measurements will give information on radio wave exposure levels from base stations in the mobile communication networks, and compare the radiation levels with limit values prescribed in International Commission on Non-Ionizing Radiation Protection for exposure levels.

There is no study up to now affirm that the electromagnetic radiations emitted by mobile base station antennas cause adverse health effects specially when emitted within limited levels that issued by international guidelines.

The aim from this work is to investigate the radiation power from mobile base stations by measuring the power density of selected base station on schools of local communication networks in Tripoli.

The measurement of radiated power density from mobile phone base station antennas conducted on seven schools on which mobile phone base stations installed; and then compare the measured data with ICNIRP guidelines, to ensure power radiation level radiated by base station antennas over these schools is within the level of radiation permitted by ICNIRP guidelines.

The measurements conducted using two types of measurement devices, and can be noted from measurements and from obtained results that all values of power densities was less than the international guidelines

**Key words:** EM radiation , base station radiations, EM hazard

### 1- Introduction

The radiation of electromagnetic waves is very important in science and technology, but its effects on health and environment are very important subjects that had been studied by specialized persons as many people are concerned about the health effects of electromagnetic radiation. The

main objective was the useful use of electromagnetic radiations, as well as, minimizing the possible effects which following the exposing to these radiations. Therefore, there is a great attention to study these possible effects, to know what is the best use of electromagnetic radiation without any health concerns. Many studies



has been conducted which are concerned about the possibility of adverse health effects arising from exposure to radiation from mobile base stations.

Due to the expanding of mobile phone networks in Libya many mobile base station antennas has been installed on roof of many schools where students spend some times, and other places where people live for the whole day long. The question rise out of this is the radiation level of the power radiated by base stations over schools; are within the level of radiation permitted by the international health organization or not?. Therefore, it is necessary to measure the level of radiated power from these stations.

Many measurements in many developed countries have been conducted to verify that the power radiated by base station antennas complies with international guidelines. Some of these studies that have been done are:

- 1- In Canada a survey of five Vancouver schools, conducted in response to parental concerns about safety, showed levels of radiofrequency radiation many times below established safety limits. The maximum level at the schools with PCS (Personal Digital Cellular) antenna across the street was  $1620 \mu W/m^2$ ,  $25600 \mu W/m^2$ ,  $2250 \mu W/m^2$ , whereas the Canadian safety limit is  $10 W/m^2$  [1].
- 2- In the UK, the NRPB (National Radiological Protection Board) took measurements at 118 locations of public access near base stations and found that the maximum exposure was 0.023% of their guidelines [2].
- 3- In 2001, the Radio communications Agency of the UK Department of Trade and Industry measured RF

energy levels at 100 schools that had mobile phone base stations on (or near) them. The maximum RF level measured at any school was less than 1% of the ICNIRP standard [3].

- 4- A 2000 survey of GSM (Global System of Mobile ) base stations by the Australian Radiation Protection and Nuclear Safety Agency found that public exposures to RF energy were less than 0.1% of their standard [3].

## 2- International exposure guidelines

There are national and international safety guidelines for exposure of the public to the RF energy produced by mobile phone base station antennas. The most widely accepted standards are those developed by the Institute of Electrical and Electronics Engineers and American National Standards Institute (ANSI/IEEE), the International Commission on Non-Ionizing Radiation Protection (ICNIRP), and the National Council on Radiation Protection and Measurements (NCRP) [3].

There are differences between the standards. ANSI/IEEE, ICNIRP and FCC all use the same general approach to setting safety guidelines. However, there are differences in the physics models used by the different groups, and hence there are slight differences in the final numbers. A number of countries have their own regulations for public exposure to RF energy from mobile phone base station antennas. While most of these regulations follow the same patterns and rationales used by ANSI/IEEE and ICNIRP, they do differ. A summary of reference levels for exposure of the public are given in Table (1).



Table (1) reference levels for occupational exposure to electromagnetic fields

guideline	Frequency range	Power density $\mu W / cm^2$
ICNIRP	400-2000MHz	f/200
United Kingdom	0.8-1.55GHz	41f <sup>2</sup>
	1.55-300GHz	100
USA	300-1500MHz	f/150
	1.5-100 GHz	10
Canada	300-1500MHz	f/150
	1.5-100 GHz	10
Japan	300-1500MHz	f/150
	1.5-300 GHz	50*f
China	30-3000 MHz	0.4
Russian	0.3-□ 300GHz	0.10 (0.25 <sup>h</sup> )
Bulgaria	0.3-300GHz	10,0**
Turkey	400-2000MHz	f/ 200
Taiwan	400-2000MHz	f/200
Italy	3-3000 MHz	1

Where: h for rotating, and scanning antenna.

\*\* In the presence of ionizing radiation and /or high temperatures ( above 28°C) maximal permissible exposure should be not more than  $1 w / m^2$

### 3- Methodology of measurements

To assure the validity of the measurements, in this work using the EM power density is carefully designed and controlled, the elements of this methodology include the following:

- Measurements have been made at a number of different
- locations around the base stations.
- The exact measurement position was recorded using a GPS receiver and meter.
- The measurements were repeated at each point three times over three days in each school.

e. The measurements were repeated at each point three times along one day in different times in each school.

f. The measurements were repeated in different dates to ensure the readings.

#### 3-1 Site selection

Measurements were made at sites where people live, work, or has frequent access. The sites were selected which has the highest number of antennas on rooftop. People are rarely exposed to the main beam, because of close proximity to the mobile phone mast in question, or due to shielding by buildings. Measurements have



been taken at seven sites in Tripoli, and these measurements have been made at a number of different locations around base station, inside buildings and rooftops and court-yards. The selected schools are:

- 1- Ibn Haitham School at Nufliyin in Tripoli.
- 2- Attasadi School at Gergaresh (Antiquity Avenue) in Tripoli.
- 3- Atifaq Jerba School at Gurji in Tripoli.
- 4- Ali Annaffati School at Tajura in Tripoli.
- 5- AL Entelaka School at Arada in Tripoli.
- 6- Shohadaabomelyana School at Tariq sur (behind the Islamic museum) in Tripoli.
- 7- Azzahf Al-Mostamer School at Ghut shaal in Tripoli.

### 3-2 Instrumentation

We have selected two different types of instruments to measure the radiation power density, one of them capable of measuring the total power density in its measuring range. The other is to measure the power

density of each signal-radiated frequency. These instruments are as following:

- a. Power meter "RF Field Strength Meter ".This meter detects the electric field of radio and microwaves (RF) from 0.5MHz to 3GHz, and expresses the field strength as power density from 0.001 to 200 microwatts/cm<sup>2</sup>.
- b. Power meter "Sagem OT 290"for all cellular frequencies to ensure that the measurements are meaningful and accurate.

### 3-3 Technical data of the base stations

The base station antennas that were installed by the two only mobile phone operators in Libya AL-Madar and Libyana companies, over the selected sites consist of sector dipoles antennas each cover an angle of 120°. Operators have provided us with the technical data of macrocellular base stations at the seven sites (all sites are shared by the two operators Libyana and AL-Madar except one, Shohadaabomelyana School) i. The data include the radiated powers, beam characteristics of sector antennas, and powers radiated by dish antennas. Table (2) shows the height of the antennas for all the base stations.

Table (2) Height of the different floor of schools

school	Height of first floor	Height of second floor	Height of rooftop	Height of antenna
Ibn Haitham	420cm	840cm	1260cm	2410cm
Attasadi	420cm	840cm	1260cm	2050cm
Atifaq Jerba	420cm	-	840cm	1720cm
Ali Annaffati	420cm	840cm	1260cm	2410cm
AL Entelaka	420cm	840cm	1260cm	2410cm
Shohadaabomelyana	420cm	840cm	1260cm	2700cm
Azzahf Al-Mostamer	420cm	840cm	1260cm	2310cm





#### 4 Measurements of power density

The measurements of power density is carried out in the period between 8-8-2006 to 19-8-2006 and repeated in the period 1-4-2007 to 5-4-2007 to ensure the measurements.

##### 4-1 Measurements using RF Field Strength Meter

The RF field strength meter used in our measurements can measure the power density of all mobile phone base stations and all radio and microwaves (RF) from 0.5MHz to 3GHz at the site. The data are presented as function of the radial distances directly to the base station antennas irrespective of whether the path was obstructed by walls, roofs etc. The measurements were conducted using the RF field strength meter, in different locations in the same elevation and different elevation, and different times.

##### 4-1-1- Measurements under antenna tower in different days

The measurements were done for the previous seven selected schools and repeated along three days; Figure (1) shows the power density levels on rooftop for all schools at three days.

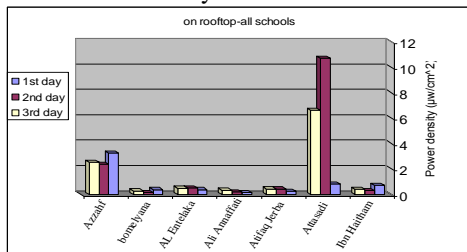


Figure (1) Power density level under the tower

From Figure (1), we can see that the radiation power density on rooftop of

Attasadi School was the highest; Azzahf AL-Mostemer School is second.

Figure (2) shows the power density levels at second floor for all schools at three days.

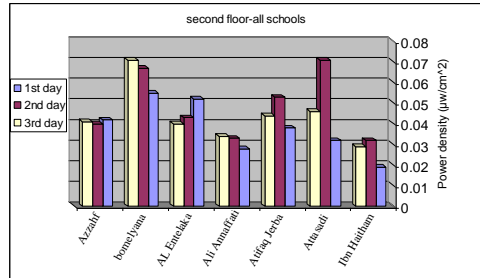


Figure (2) Power density level under the tower

From Figure (2) we can see that the radiation power density at second floor of Attasadi School and Shohadaabomelyana School were the highest.

Figure (3) shows the power density levels at first floor for all schools at three days.

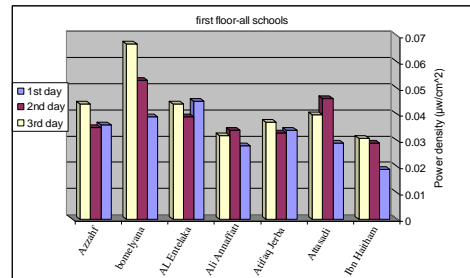


Figure (3) Power density level under the tower

From Figure (3), we can see that the radiation power density at first floor of Shohadaabomelyana School was the highest.

Figure (4) shows the power density levels at ground floor for all schools at three days.

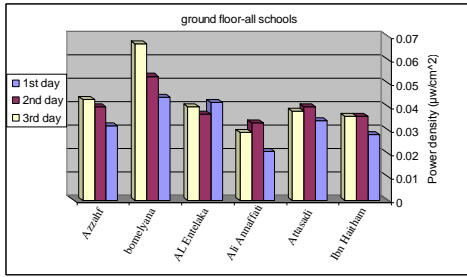


Figure (4) Power density level under the tower

From Figure (4-11) we can see that the radiation power density at ground floor of Shohadaabomelyana School was the highest.

#### 4-1-2- Measurements under tower in different times of day

To help understanding the radiation level through the school hour we have measured the radiation power density in early morning about 9:00 o'clock and at 11:00 o'clock and at 1:00 o'clock. The measurement was conducted for the following schools:

- Attasadi School at 1-4-2007.
- Atifaq Jerba School at 2-4-2007.
- Ali Annaffati School at 3-4-2007.
- AL Entelaka School at 4-4-2007.
- Azzahf Al-Mostamer School at 5-4-2007.

The measurements were conducted on the rooftop and floors under the antennas in three different times.

Figure (5) shows the level of radiated power density on the rooftop for the previous schools:

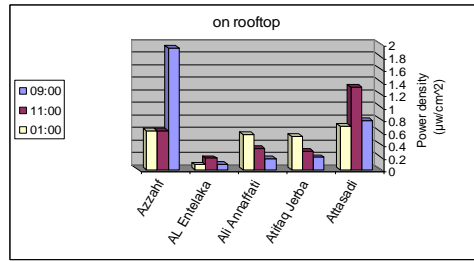


Figure (5) Power density radiation level on rooftop

From Figure (5) it can be seen that the maximum value of measured power density on rooftop in Azzahf AL-Mostamer School. Figure (6) shows the level of radiated power density in the second floor for the previous schools:

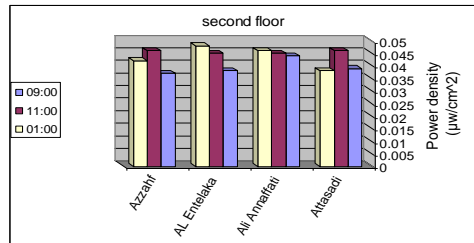


Figure (6) Power density radiation level in second floor

From Figure (6) it can be seen that the value of measured power density in these schools approximately are in the same level in the second floor where it is not in the same levels in the rooftop. And it is same for the first and ground floors, that is clear from Figures (7) and (8).

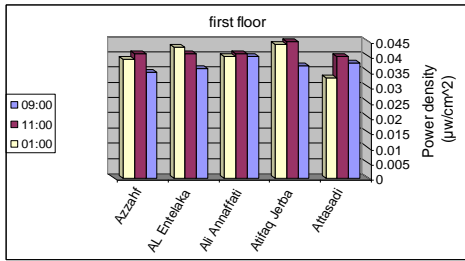


Figure (7) Power density radiation level in first floor

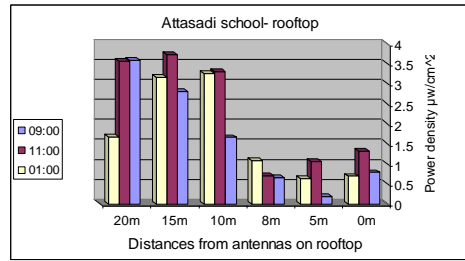


Figure (9) Power density level on rooftop

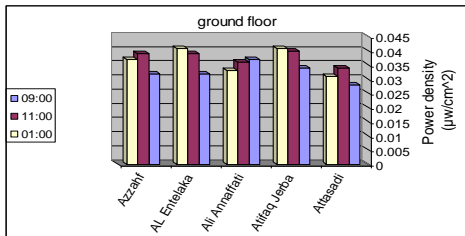


Figure (8) Power density radiation level in ground floor

### 4-1-3- Measuring on rooftop at different distances from antennas

The measurements had been conducted on rooftop at different distances from antennas for the following schools:

- Attasadi School at 1-4-2007.
- Atifaq Jerba School at 2-4-2007.
- AL Entelaka School at 4-4-2007.
- Azzahf Al-Mostamer School at 5-4-2007.

The two worst cases will be presented:

- Attasadi school: the locations in which power measured, was in the east of antennas with distances shown in Figure (9), and it is noted that the power density increased by increasing the distance. It can be seen from the figure that the power density during midday is higher than that at early morning, and more away from the antenna up to same distance.

- Azzahf AL-Mostemer School: the measurements were done west of the antennas at different distances and at different time, Figure (10) shows the power density variation at different distances and time. It can be also shows from figure that the power densities increased by increased distances.

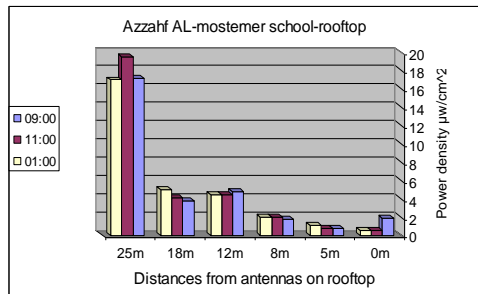


Figure (10) Power density level on rooftop

### 4-1-4- Measurements at ground level

The measurements had been done at ground level at different distances from antennas projection in the following five schools:

- Attasadi School.
- Atifaq Jerba School.
- Ali Annaffati School.
- AL Entelaka School.
- Azzahf Al-Mostamer School.

The two worst cases will be presented.

Figures (11) and (12) show the level of radiated power density increased with distances then decreased after 40m in



Attasadi school then increased, in Azzahf AL-Mostemer school the level of measured power densities increased with distances then decreased after 60m.

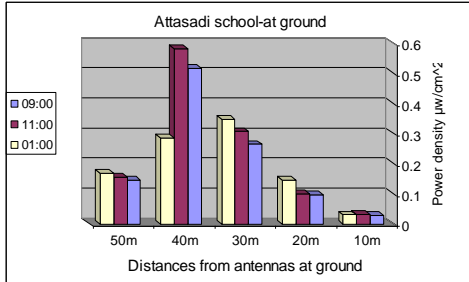


Figure (11) Power density level at ground

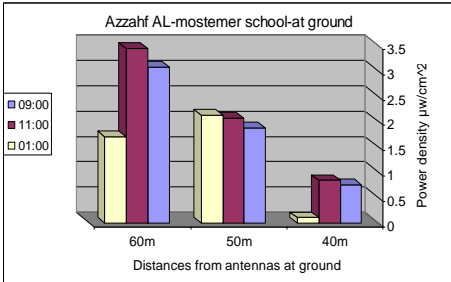


Figure (12) Power density level at ground

#### 4-1-5- Measurements of the power density on rooftop at different directions

To know the radiated level at different directions of antennas we measured the power density at all directions of antennas at the same distance. The measurement was done for the following schools:

- Attasadi School.
- Atifaq Jerba School.
- Ali Anaffati School.
- AL Entelaka School.
- Azzahf Al-Mostamer School.

The two worst cases will be presented.

- Attasadi School: Figure (13) shows the power density variation at three directions at 8m. At this school, the

level of radiated power density in the south is the highest.

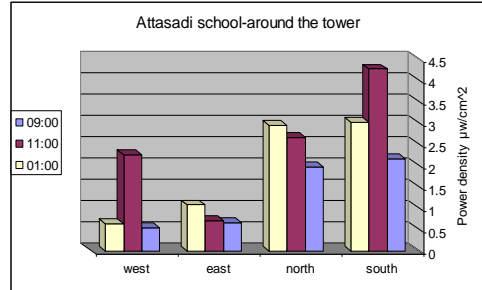


Figure (13) Power density level around the tower

- Azzahf Al-Mostamer School: Figure (14) shows the power density variation at all directions at 8m. At this school, the level of radiated power density in the south is the highest.

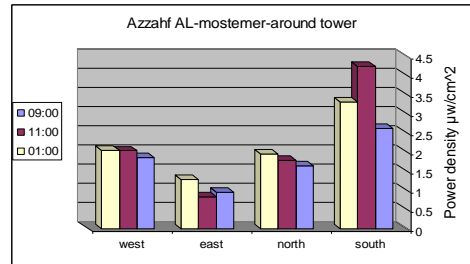


Figure (14) Power density level around the tower

#### 4-2 Measurement of power density using Sagem OT 290

To help compare the measurements done by RF field strength meter we used another type of power density measuring device (SAGEM OT 290) this devices measure the level of signals in dBm. The measurements by this meter have been taken at the two worst cases (Azzahf Al-Mostamer School and Attasadi School), as there two sites has the most number of antennas.

Figure (15) shows the power radiation level on rooftop and at different floors below for Azzahf AL-Mostemer and Attasadi Schools.

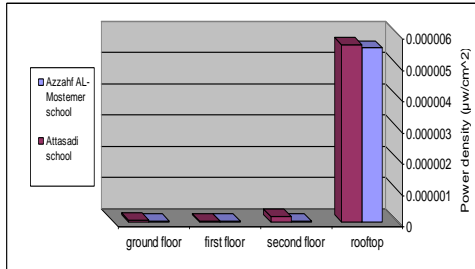


Figure (4-36) Power density level under the tower

#### 4- Results and discussion

It can be noted from conducted measurements and from all results that all values obtained of power densities was less than the international guidelines and the highest measured value is only 5.68% of ICNIRP reference level

It can be also noted that the power density under antennas decreased dramatically in the lower floors; in all schools, and the maximum level that measured was on rooftop under tower in Attasadi School and Azzahf AL-Mostemer School. While in lower floors, the power density was minimum and it was approximately constant through repeating the measurements.

The level of power density increased by increasing distances on rooftop in all schools, with distance until it reach the ground level after 50-200m away from the base station; depending on the height and title of the antenna. And the power density level increased by explicit increasing in west direction in Azzahf AL-Mostemer School. It is possible due to the existence of TV transmitters in the west of Azzahf AL-Mostemer School is one of reasons which rise the value of total power density.

When measuring the radiation power density at ground, it can be noted that the power density increased by increasing distance and then it starts to decrease with distance and the presence of other structures may shield or reflect the RF signals. In the Azzahf Al-Mostamer School, the power density level increased by explicit increasing in west direction the power density level was maximum in the west of Azzahf Al-Mostamer School. In addition, when studying location of this school we note that it is situated near TV transmitter and nearby other base stations.

Table (3) shows the maximum power density level on the rooftop and lower floors for all seven schools, and it can be noted that the power density levels are less than the ICNIRP limits.

Table (3) Maximum power density level

School	Max power density( $\mu\text{w}/\text{cm}^2$ )			
	rooftop	Second floor	First floor	Ground floor
Ibn Haitham	0.746	0.032	0.031	0.036
Attasadi	10.734	0.071	0.046	0.040
Atifaq Jerba	0.537	-	0.053	0.037
Ali Annaffati	0.617	0.046	0.041	0.037
AL Entelaka	0.505	0.052	0.045	0.042
Shohadaabomelyana	0.484	0.071	0.067	0.067
Azzahf Al-Mostamer	2.554	0.064	0.041	0.043



In comparison of these measurements with the ICNIRP limits, it can be said that the highest ratio between the measured power density and the ICNIRP reference level was in the Azzahf Al-Mostamer School on rooftop south of antennas at 8m .

## 5- Conclusion

In this paper, the measurement of radiated power density from mobile phone base station antennas for seven schools in Tripoli city was conducted during the period 8-8-2006 to 19-8-2006 and repeated during the period 1-4-2007 to 5-4-2007; to ensure the safety level of the radiation in comparison with adopted standard that we compare the radiation level to its reference level we adopted ICNIRP standard.

The measurements conducted using two types of measurement devices, the highest level of measured radiation using RF field strength meter was on the rooftop of Azzahf AL-Mostemr School, and the level of radiation is only 5.68% of ICNIRP standard. In comparison with the measurement conducted in Canada a survey of five Vancouver schools, the maximum RF level measured at any school was 0.036% of the ICNIRP standard, it is

157.78 times of maximum power density obtained from conducted measurements. In comparison of our results with the measurement conducted in UK, the maximum RF level measured was in the range 0.002-2% of the ICNIRP standard, it is 2840-2.84 times of maximum power density obtained from conducted measurements.

And by using Sagem OT 290 the highest level of measured radiation was on the rooftop of Attasadi School south of the tower 8m, and the level of radiation is only 0.332% of ICNIRP standard.

## 6-References

- 1- "Radiation Standards and Measures", 13-Sep-1998.  
<http://ntrg.cs.tcd.ie/mobile/SAR.html>
- 2- Global System for Mobile Communication (GSM).  
<http://www.iec.org/online/tutorials/gsm>
- 3- Juhn Korhonen, "Introduction to 3G Mobile Communications", second edition, Artech House, 2003.
- 4- Electromagnetic Fields (EMF) Protection.  
[http://www.who.int/docstore/peh-emf/EMFStandards/who-0102/Europe\\_uk.htm](http://www.who.int/docstore/peh-emf/EMFStandards/who-0102/Europe_uk.htm)



## Effect of sand and dust storms on CDMA coverage signal in southern Libya

Esmaeil Mohamed Abuhdima<sup>1</sup>, Ibrahim Mohamed Saleh<sup>2</sup>

<sup>1</sup> General post and telecommunication company, <sup>2</sup> Al-Fateh university

<sup>1</sup>[ismaeil666@hotmail.com](mailto:ismaeil666@hotmail.com), <sup>2</sup>[ibrahim.saleh@ltnet.net](mailto:ibrahim.saleh@ltnet.net)

Tripoli - Libya

### Abstract

The propagation of Electromagnetic waves in millimeter band is severely affected by rain and dust particles in terms of attenuation and de-polarization. There is a growing interest in the effect of dust particles on the propagation of microwaves. This is brought by the increasing number of terrestrial and satellite links in those regions that encounter dust and/or sand storms. Computations of these effects require knowledge of electrical properties of the scattering particles and climate conditions of the studied region. Libya has a large area and it is counted as a country having desertification climatic. Wireless communication networks and CDMA coverage stations has been installed in the southern part of Libya, where there are dust and sand storms that may affect the microwave signal propagation. When microwaves and millimetre waves pass through a medium containing precipitations like sand and dust particles, the signals get attenuated through absorption and scattering of energy out of beam by the sand and dust particles. The main object of this paper is to study the effect of sand and dust storms on wireless communication, such as microwave links and CDMA signal coverage, in the southern region of Libya (Sebha, Ashati, Obari, Morzok, Ghat) by determining the attenuation. The result showed that there are some consideration that has to be taken into account in the communication power budget.

*Keywords*—Attenuation; Scattering; Transmission Loss

### I. Introduction

In the course of increasing data transformation of wireless communication systems, embodied in Microwave links and GSM network system surroundings. These systems are actually influenced by climate circumstances. The performance of service of many applications, for example cellular telephones, public service radio, pagers, broadcast television, radio stations, and

differential GPS transmitters, CDMA and WiMax networks, that require RF or microwave propagation from point to point very near the earth's surface, depends on many factors such as area of coverage, and climate conditions. The millimeter waves bands are in the short wavelengths range; unfortunately, the shorter the wavelength the more attenuation will be induced by absorption and scattering due to rain drops, dust and sand particles in the radio path.



The attenuation caused by sand and dust particles is one of the major problems in the utilization of microwave and millimeter wave bands for terrestrial and space communication. The attenuation and phase shift constants for a medium with dust or/and sand particles depends on the frequency, visibility, maximum particles-size, complex permittivity, shape of the scattering particles, concentration, and orientation relative to the wave polarization, also the attenuation of electromagnetic waves due to dust is predominantly function of the moisture content of the particles .

Libya is considered as desertification country, in the last few years many problems in wireless communication networks have been recorded in windy and sandy days in the southern part of Libya; No scientific reason has been given for these problems. Wind storms may continue for days, reducing visibility to just tens of meters or as little as few meters. The main object of this paper is to study the effect of dust and sand storms on wireless communication such as microwave links and CDMA signal coverage in the southern region of Libya (Sebha- Ashati, Obari, Morzok), where the effect of the dust and sand on the microwave links in this area has not been studied before, neither the effect of the humidity on the complex permittivity nor the antenna height on the visibility, whereby its effect on both attenuation and cross-polarization constants in this region.

## II. The Dielectric Constant of Dust and Sand

Knowledge of the dielectric constant of particles suspending or precipitating in the atmosphere is of importance in radio communication and radio meteorology. In

desert and semi-desert regions dust and sand storms are frequently encountered and it is therefore of interest to investigate the dielectric constant properties of these particles [1].

A number of models are available to estimate the dielectric constant of a sand and dust samples. Where dielectric constant of mixture ( $\epsilon_m$ ) depends on the complex dielectric of the substance ( $\epsilon_i$ ) and its relative volume ( $V_i$ ).the complex permittivity of the composite component can be calculated using the Looyenga equation as given by [2].

$$\epsilon_m^{1/3} = \sum_{i=1}^n V_i \epsilon_i^{1/3} \dots\dots\dots (1)$$

Where:  $\epsilon_m$  is the complex dielectric constant of the mixture.  $\epsilon_i$  is the complex dielectric constant of the  $i^{\text{th}}$  substance.  $V_i$  is the relative volume of the  $i^{\text{th}}$  sample from the volume of the total sample. The permittivity of materials at microwave frequencies is  $\epsilon = \epsilon' - j\epsilon''$ , where  $\epsilon'$  is referred to the dielectric constant and  $\epsilon''$  is the dielectric loss factor. The complex permittivity also depends on frequency of operation and moisture content. In general, the moisture cause increase of both real and imaginary parts of the complex permittivity which depend on chemical composition of dry soil samples [3].

## III. Visibility during Dust Storms

A measure of severity of a dust storm that is used in meteorology is visibility; needless to mention that visibility decreases with increasing intensity of dust in a storm. It is found that visibility is related to the mass of dust per cubic meter of air by[1].





$$M = C/V^\gamma \dots\dots\dots(2)$$

$$V^\gamma = Vo^\gamma \left[ \frac{h}{h_o} \right]^b \dots\dots\dots (6)$$

where *M* is the mass of dust in kilograms, *V* is the visibility in kilometres, and *C* and  $\gamma$  are constants that depend on the distance from the point of origin of the storm, type of soil and climatic conditions at the origin. The following values are applicable to conditions in Libya :  $C = 2.3 \times 10^{-5}$  and  $\gamma = 1.07$  From measurements of dust concentration and visibility the following empirical relationship between visibility *V* (in km) and mass density  $\rho$  (in gm/cm<sup>3</sup>) has been obtained [1]:

$$\rho = \frac{C}{\nu \times V^\gamma} \dots\dots\dots(3)$$

Where  $\nu$  is the relative volume occupied by particles (m<sup>3</sup> of particles /m<sup>3</sup> of air). The visibility during dust and/or sand storms increases as the height is increased, [4] , arrived at the following empirical relation for the variation of dust or/and sand mass concentration (M,kg/m<sup>3</sup>) with height(h, meter).

$$M = \frac{a}{h^b} \dots\dots\dots (4)$$

Where (a) and (b) are constants that vary a little from one year to another. They depend on the climatic conditions, meteorological factors and particle size distribution of the dust and sand [3].

By substituting for *M* from eq. (2) into eq. (4), then visibility can be written as:

$$V^\gamma = \frac{C \times h^b}{a} \dots\dots\dots (5)$$

Let the visibility at some reference height *h<sub>o</sub>* to be *Vo* , thus (3-5) yields

#### IV. Measurements and Analysis

The Southern part of Libya was chosen as the study region of measuring the impact of dust and/or sand storms on the wireless communication systems such as mobile phone and microwave links, because the region is famous as desert climate and fast wind filled with dust from time to time. Climate information for the region of study, was obtained from weather stations, and more information was obtained from people living in the area, they cleared that frequent interruption and fluctuation in mobile phone signals occurs during strong wind. From data recorded by the surveillance system of CDMA during dust storms, it turned out that locations which get fluctuations sometimes experience signal link disconnections between stations or low coverage signals. Nine places were chosen for collecting the sand and dust they are (Albeder, Dleame, Labide, Sebha Air port, Ramlat Zelaf, Bergen,Agar, Gota, Algorda ), which covers the area of study. The collected samples have to be analysed and companied with the climate conditions to estimate the factors which are needed for calculating the effect of dust storms on CDMA networks and microwave links. In this work all the samples are collected at the nine sites, during different times of the year, on the roofs of the building near the communication towers or from plastic cans which were placed in the towers at a height of 13m.



#### 4-1 Meteorological data for the regional study

The region of study is located between three meteorological stations namely Sebha , Obari and Ghat; the metrological data of the sites were selected from the Libyan centre of metrology.

The collected meteorological data obtained for a period of 30-years (from 1971 up to the end of 2000) from three recording stations, the monthly average relative humidity, Max. Temp.(C), Min. Temp.(C), Wind Speed Km/h and Rainfall Q.mm. From the data mention above the following summary can be pointed out:

- The highest average temperature recorded from 20 to 40 C°.
- The highest average percentage of humidity was recorded from 20 to 51%.
- The wind speed recorded from 10 to 22 km/h.
- The proportion of rainfall recorded from 0 to 3.4 mm.
- The maximum temperature recorded 45 C°.
- The maximum rate of humidity was recorded about 60%.

#### 4-2 Analysis of the samples

For this study some analysis is needed for samples such as particle size distribution, average density and chemical composition, which are used to compute the dielectric constant and attenuation factors. There are two Libyan laboratories and labs, available to carry out the analysis of the samples (Industrial Research Centre and Libyan Petroleum Institute in Tripoli), where the results as shown in table (1), and table (2) as follows:

Table (1.a) Chemical Analysis of Samples

S No.	SiO <sub>2</sub>	Fe <sub>2</sub> O <sub>3</sub>	Al <sub>2</sub> O <sub>3</sub>	CaO	MgO
1	97.58	0.35	0.32	1.14	0.2
2	96.77	0.26	0.32	1.98	0.2
3	91.17	0.66	1.91	2.55	0.2
4	87.34	2.41	2.55	4.83	1.02
5	81.32	2.89	5.72	3.97	1.22
6	89.62	0.69	3.19	1.99	1.02
7	81.48	2.32	5.08	5.11	1.22
8	91.34	1.46	1.27	2.28	0.82
9	82.25	2.74	3.16	6.49	0.81

Table (1.b) Chemical Analysis of Samples

S No.	Na <sub>2</sub> O	K <sub>2</sub> O	Mn	Zn
1	0.13	0.03	-	0.005
2	0.13	0.03	-	0.001
3	0.34	0.19	0.024	0.004
4	0.11	0.07	0.04	0.01
5	0.52	0.82	0.024	0.037
6	0.44	0.3	0.026	0.03
7	1.01	0.32	0.024	0.006
8	0.24	0.14	0.012	0.004
9	0.79	0.31	0.052	0.004

Table (2) PSD and density of Samples

Sample No.	PSD	Density (g/cm <sup>3</sup> )
1	Sand	2.5426
2	Sand	2.56857
3	Dust	2.6138
4	Sand	2.62714
5	Dust	2.4202
6	Dust	2.9232
7	Dust	2.4732
8	Dust	2.5425
9	Dust	2.4764

Where the average density of all samples equal to 2.5764 g/m<sup>3</sup>.



### 4-3 Calculation of the Complex Permittivity for Samples

By using the results presented in tables (1), and (2), which represent the relative volume of the  $i^{th}$  sample from the volume of the total sample. The complex permittivity of each substance is given in table (3) and equation (1) can be used to estimate the complex permittivity of each sample [2], by using computer program, where the results are given in table (4).

Table (3) Complex Permittivity of Substances

Compound	$\epsilon' - j \epsilon''$
SiO <sub>2</sub>	4.43-j0.04
Al <sub>2</sub> O <sub>3</sub>	12.66-j1.31
Fe <sub>2</sub> O <sub>3</sub>	16.58-j0.93
CaCO <sub>3</sub>	8.22-j0.12
MgCO <sub>3</sub>	5.03-j0.17
CaSO <sub>4</sub>	5.01-j0.08

These values are given in reference [6], the curves showed a small changes in the permittivity( $\epsilon_r$ ) for the frequency range between 0.3-24 GHz, accordingly the variation is considered as small in the lower frequency band.

Table (4) the Complex Permittivity of each Sample

Samples No.	complex permittivity
1	5.0384 - j 0.0509
2	5.4851 - j 0.0562
3	5.4801 - j 0.0694
4	7.5929 - j 0.1140
5	6.7899 - j 0.1296
6	5.4003 - j 0.0787
7	7.4707 - j 0.1344
8	5.5713 - j 0.0704
9	8.3078 - j 0.1329

The Complex Permittivity of all samples from table (4) equal to 6.3485 - j 0.0929.

### 4-4 Estimate of Air Relative Humidity

The complex permittivity depends on moisture contents in samples, S. M. Sharief [5] arrived at the following empirical relation for the variation of complex permittivity with relative humidity.

$$\epsilon' = 6.3485 + 0.04H - 7.78 \times 10^{-4} H^2 + 5.56 \times 10^{-6} H^3 \dots (7)$$

$$\epsilon'' = 0.0929 + 0.02H - 3.71 \times 10^{-4} H^2 + 2.76 \times 10^{-6} H \dots (8)$$

Where H is the air relative humidity (percentage).

### 4-5 Calculate the attenuation Constant

In this study, the same expression obtained by Samir I. Ghobrial [1] was used, and the analysis based on the work of Maxwell Garnett was also used. Also the effect of the height (height of towers) on the visibility thereby its effect on both the attenuation constants in this region as follows:

$$\alpha = \frac{2.46 * 10^5 * \nu}{\lambda} * \left[ \frac{\epsilon''}{(\epsilon' + 2)^2 + \epsilon''^2} \right] \dots (9)$$

$$\nu = \frac{C}{\rho * V_o^\gamma \left( \frac{h}{h_o} \right)^\gamma} \dots (10)$$

Where  $\nu$  is the relative volume occupied by particles ( $m^3$  of particles /  $m^3$  of air) C and  $\gamma$  are constants that depend on the distance from the point of origin of the storm, type of soil and climatic conditions at the origin. The following values are



applicable to conditions in Libya,  $C=2.3 \times 10^{-5}$ ,  $\gamma = 1.07$ ,  $\lambda$  is the wavelength (in meters),  $V_0$  is the visibility at  $h_0$ ; its minimum value about 4m,  $h_0=2m$  is the reference height,  $\epsilon'$  &  $\epsilon''$  are the values obtained from the average complex permittivity of the samples collected in the studied region is equal to 6.3485 and 0.0929 respectively and  $\rho$  is the average measured density of the samples collected in the studied region is  $2.5764 \text{ gm/m}^3$ , where the results are as follows:

Figures (1), (2) and (3) showing the relation between attenuation per km and visibility at  $h=20m$  in the region of study for humidity 0%, 60% and 100%.

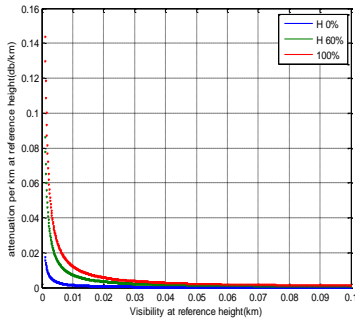


Fig.( 1) Attenuation per km at  $h=20m$  and for

$f=0.9GHz$

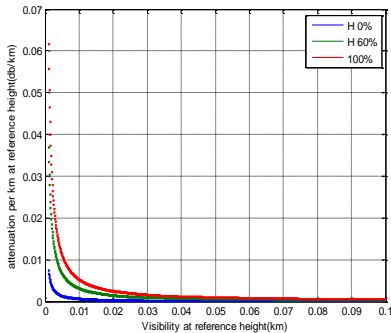


Fig. (2) Attenuation per km at  $h=20m$  and for,  $f= 2.1GHz$

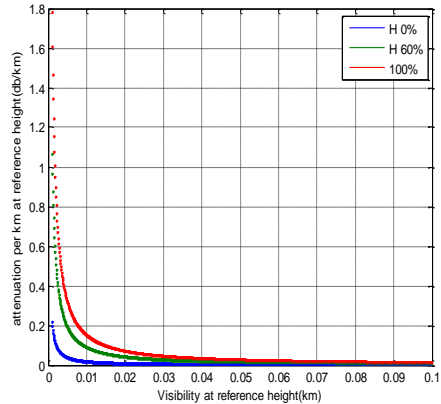


Fig.( 3) Attenuation per km at  $h=20m$  for  $f=26GHz$

### 5. Conclusions

The effect of dust and sand storms on CDMA coverage signal and microwave signal propagation in southern part of Libya were investigated. It was found that the major constituents of sample are  $\text{SiO}_2$ ,  $\text{CaO}$ ,  $\text{Al}_2\text{O}_3$ , and  $\text{Fe}_2\text{O}_3$ . Where the Silicon dioxide has the major influence on the real part of the permittivity of dust. On the other hand aluminium oxide has the greatest effect on the imaginary part.

It was also found that the average of density and complex permittivity of samples in Southern region are equal to  $2.5764 \text{ gm/m}^3$ ,  $6.3485-j0.0929$  respectively and the attenuation constant of the region of study is equal to  $0.2412 \text{ dB/km}$ .

The CDMA Signal coverage attenuation, due to dust storms with visibility of 4m (worst case), and with a humidity equal to 0 % and 60% is negligible for cells, while the attenuation at  $H=100\%$  is serious and the Microwave Signal attenuation due to dust storms with visibility equal 4m (worst case) at  $H=0\%$ ,  $H=60\%$  and  $H=100\%$  is serious. We recommended that an



experimental study should be conducted by using special instrument devices to record the power signals between stations especially in studied area , during dust and/or sand storms, to get the real losses, and compare it with the attenuation factor of this study.

## 6. References

- [1]-S.I Ghobrial and S.M Sharief; ‘‘ Microwave Attenuation and Cross-Polarization in Dust Storms ‘‘, IEEE Trans on Ant. and prog. , VOL .AP-35, No.4, 1987, PP 418-425.
- [2]- S.I Ghobrial and S.M Sharief;’’X-Band Measurement of the Dielectric Constant of Dust ‘‘, Proc.Ursi commission F 1983 Symposium. Louvain .Belgium .June 1983, PP143-147.
- [3]- S.I Ghobrial and S.M Sharief;’’Measurement of the Dielectric Constant of Dust at 8.3 GHz’’, National Radio Science Meeting, University of New Mexico , Albuquerque, USA,1982.
- [4]- S.M Sharief; ‘‘Performance of Earth-Satellite Links During Dust Storms at the X-Band’’, SES Journal, VOL.40, No.33, 1993, PP 14-19
- [5]- Sami M. Sharif, "Clutter and backscatter cross-section of dust storms at x-band", Sudan engineering society journal, June 1997, vol. 44 No. 35.
- [6]- A.J Ansari, B.Sc, M.Sc, and B.G. Evans, B.Sc, Ph.D., C. Eng., M.I.E.E., " Microwave propagation in sand and dust storms", IEEPROC, Vol. 129, Pt. F, No. 5, OCTOBER 1982.



طرابلس ليبيا 23-26/10/2010 المؤتمر الدولي العربي الليبي الرابع للهندسة الكهربائية والإلكترونية



## **MEMS Printed mm-wave Antennas for G-band Applications**

Adel Emhemmed, Ian McGregor, Khaled Elgaid

*Department of Electronics and Electrical Engineering, University of Glasgow  
Glasgow, United Kingdom*

[adel@elec.gla.ac.uk](mailto:adel@elec.gla.ac.uk)

*Abstract*— This paper presents a novel low pull-down voltage MEMS switch integrated with elevated patch antenna on a high dielectric substrate GaAs for G-band applications. The proposed antenna is composed of MEMS switch loaded on CPW stub, CPW feed line, air-bridge, and an elevated patch. The antenna topology effectively creates a low-substrate dielectric constant and undesired substrate effects can be eliminated, since the antenna substrate is essentially air which the lowest possible dielectric constant. This will increase the radiation efficiency, gain, and the radiation bandwidth. The antenna is also used a cantilever beam MEMS switch to reduce the actuation voltage. The simulation and measurement data have shown high performance reconfigurable antenna with low pull-down voltage of 12.5volt and approximately 10GHz tunability.

### **1-Introduction**

The growing global demand for broadband wireless communication services motivates the need for new antenna structures with high gain, large bandwidth, small size, and controlled operating bandwidth at ever higher frequencies. G-band frequencies (140GHz-220GHz) have been experiencing resurgence in popularity recently as many systems have been allocated or are proposing to use frequencies within this operating band. These systems have intensified the demands for integrated antennas with high performance and for reconfigurable antennas with low tuning voltage. These demands are very challenging for antenna design

due to the requirements of different substrate properties and for different operation bands. These two considerations are summarised below.

**1) Different substrate property requirements:** Printed antennas are widely used as they are good candidates for on-wafer integration. However, there are different substrate requirements in terms of dielectric constant and thickness from the rest of the integrated circuits. More specifically, for the rest of the RF components, a high dielectric constant and thin substrate are commonly used for the sake of compactness and thermal dissipation. However, printed antenna designs prefer thick substrates with low dielectric constant to achieve



a wider bandwidth and undisturbed radiation patterns, and reduce any undesired coupling between the various elements in array configurations. This conflict can either lead to a hybrid integration solution or both antennas and other RF parts to be built on the same substrate with an intermediate dielectric constant which therefore yields suboptimal component performance instead of the best performance for each part. To integrate printed millimetre-wave antenna directly with MMICs, the antenna has to be designed on a high dielectric substrate. However, design of antennas on such substrates is generally avoided, as substrate thickness becomes large compared with  $\lambda/4$  at millimetre-wave regimes. This results in a strong moding effect and high dielectric loss due to surface wave excitation which in turn leads to lower efficiency, reduced bandwidth, degraded radiation patterns and undesired coupling between the various elements in array configurations [1-4]. This has limited printed antenna application in broadband modules and they are difficult to successfully apply at millimetre-wave frequencies. A reduction in surface waves is very important in millimetre-wave antenna design for it not only improves the efficiency of the antenna but also weakens the side-lobe level which is produced by surface wave diffraction

around the antenna substrate.

As micromachining technology is developed, it increasingly offers an alternative scheme to simultaneously satisfy the demands of the antenna and circuitry as it can allow the use of the same substrate for both functions without performance degradation. Several techniques have been reported to synthesize a localized low dielectric constant environment and thus reduce the surface wave excitation. These include: (a) using bulk micromachining to etch a portion or complete section of the substrate material underneath and around the radiating element [5, 6]; (b) using an electromagnetic band-gap (EBG) structure [7, 8]; (c) elevating the radiator element above the substrate using a membrane or using posts to lift the radiator into the air [9-11]. Still other techniques have been introduced in order to overcome the narrow bandwidth of the printed antennas. These techniques include using multiple-radiator resonators, modified radiator shape, stacking substrates and coupling through aperture and proximity coupled antennas [12, 13]. All these referenced results achieved improved performance compared with conventional printed millimetre-wave antennas on relatively high dielectric constant substrates. On the other hand, a process such as etching the substrate and fabricating the membrane can be





very difficult to establish in order to obtain high yield. Also, most of these approaches are not fully compatible with MMIC processes or package processing and can consume large amounts of precious chip area.

## **2) Need for different operation bands:**

A single antenna that can support multiple communication services would allow a wireless device with multiple wireless applications to utilise a single antenna element to transmit and receive signals at different frequencies bands. By only having a single antenna element, the space required for antennas on the device is significantly reduced. To meet the need for multi-band millimetre-wave applications, a choice could be made from the following three types of antennas: (a) a single antenna showing multi-resonance characteristics for the required frequencies; (b) a very broadband antenna to cover all required frequencies; (c) a reconfigurable antenna to operate at required frequency points. Both a multi-resonance antenna and a very broadband antenna suffer interference from signals operating in unused covered bandwidths, whereas using a reconfigurable printed antenna design overcomes this problem and it can be controlled at required frequency band without changing the whole dimension and structure of the antenna

[14]. Many techniques have been developed for the design of reconfigurable printed antennas to get multiple-band operation without use of additional radiators. These techniques tune the antenna bandwidth by controlling the antenna parameters - either by using solid state switches (diodes, transistors) or using MEMS (Micro-electromechanical Systems) switches [15, 16]. With these techniques, only the desired frequency bands or one band is in use at a time, this can decrease the level of the interfering signals and thus decrease the need for separate filtering. However, tuning the antenna operation band by using solid state switches at deep millimetre-wave frequencies limits the antenna efficiency, due to the high insertion losses [14, 17] of the devices. MEMS (Micro-Electro-Mechanical System) switches have been introduced as a prime candidate to replace the conventional solid state switches, since they offer high isolation, very low insertion loss, high linearity, and the MEMS actuator does not require any special epitaxial layers as in the case of diodes.

Even though MEMS switches have been shown to give very good performance, current implementations still suffer from a high actuation voltage - restricting their integration with MMICs. In order to lower the actuation voltage of the MEMS



switch, three different routes can be followed. These are: (a) increasing the area of actuation; (b) diminishing the gap between the cantilever and bottom electrode; (c) designing a structure with a low spring constant. In the first case, the area can only be increased by so much before compactness becomes a prevailing issue. In the second case, the isolation (parasitic plate capacitance) associated with the RF signal restricts the value of the gap. The third route is the one with the most flexibility, since the design of the springs does not considerably impact the size, weight, and performance of the antenna [9, 17, 18]. There are many variations of cantilever beam geometry that can be used to lower the effective spring constant of the MEMS switches. Therefore, the cantilever beam structure can be considered to provide very low values of spring constant in a compact area as well as providing high cross-axis sensitivity between vertical and lateral dimensions [19].

Although there is much work to be found in the literature on printed antennas and frequency reconfigurable antennas at microwave frequencies, very little information can be found in the literature at G-band (140GHz to 220GHz). The design of patch antenna on high dielectric substrates, working at G-band and possessing high performance, full compatibility with

MMICs and which can be tuned for different bands using low actuation voltage RF-MEMS switches still remains a challenging task. This paper will provide characterization of such antennas - something which has not yet been done for this type of antenna.

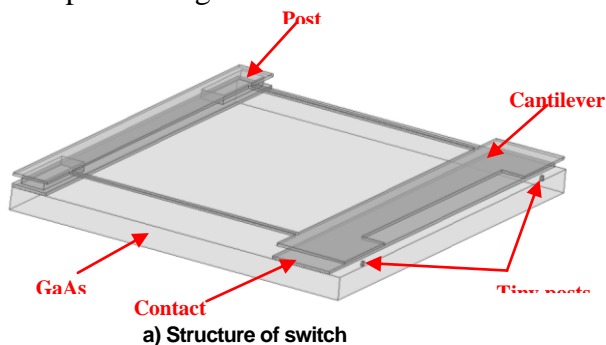
## 2- MEMS Switch Design

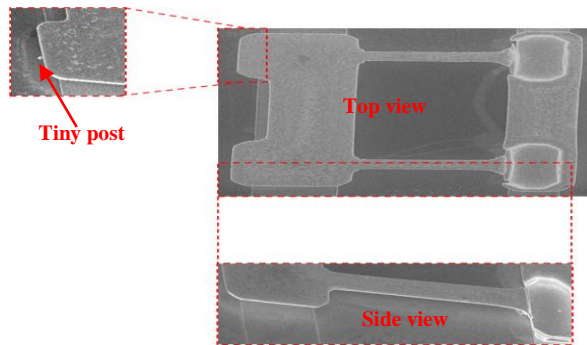
In this paper cantilever beam MEMS switch has been designed and fabricated in order to lower the pull-down voltage and solve the stiction problem. Fig. 1 shows the structure of MEMS switch which was used to tuning the elevated patch antenna.

The switch structure has a movable top cantilever beam which consists of a contact pad and two non-meandered suspensions connected with two supporting posts from one side at the input signal line. The other side is elevated above the bottom output signal line. The contact pad connects RF signal lines and enables actuation when a DC voltage is applied. The area of contact pad is a more limited variable than others because the larger contact pad, the lower the insertion loss, but also the poorer the Off-state electrical isolation because of the increased capacitive coupling between the contacts pads. This capacitance can be reduced by increasing the air gap, but this increase in the gap also increases the pull-down voltage because the same gap distance also determines the actuation capacitance.

Also, the increase in the pad area increases the overall mass of the cantilever beam and thus the switching time of the MEMS switch. Many switches with different contact pad area have been fabricated and their electrical and mechanical performance tested. The switch with  $3175\mu\text{m}^2$  contact pad area was chosen to be integrated with the elevated patch antenna. It is large enough to provide lower pull-down voltages, good isolation and minimize the contact resistance - avoiding any ohmic heating due to passing a large DC or RF signal; hence the cantilever beam with  $2\mu\text{m}$  thickness of gold was used. When there is no DC voltage applied, the cantilever beam will be in the up position where the contact pad does not allow the RF signal to directly pass through the switch. The cantilever beam can be pulled down to the bottom contact by applying a DC voltage - creating a short circuit that allows the RF signal to pass through

the switch. If the DC voltage is then reduced, the cantilever beam releases back up (typically at a lower voltage than the actuation voltage). The geometry of cantilever beam in this design was chosen to produce the lowest possible pull-down voltage. Also, the gold was chosen as switch material since it provides a low Young's Modulus of  $57\text{GPa}$ . However, reduction of the spring constant  $k$  might cause more stiction problems during operation. Therefore, in this design, we propose a simple integrated way to prevent the stiction problem using two tiny posts located on the substrate at the free end of the cantilever beam. These tiny posts will limit the downward motion of the contact pad and maximize the mechanical restoring force without significant effect on pull-down voltage. This solution should be effective no matter what the actual cause of stiction is.





b) SEM photo of fabricated switch.

Fig. 1 cantilever beam MEMS switch configuration

The calculated pull-down voltage was  $14.8\text{ volt}$ , which agrees very well with the measured value of  $12.5\text{ volt}$  with an actuation current on the order of  $1\text{ mA}$  which corresponds to a power consumption of  $12.5\text{ mw}$ . It requires zero power to maintain the switch in either the Off-state due to the nature of the electrostatic actuation. Fig. 2 shows I-V measurements of the proposed switch, this measurement was done using an on-wafer DC probe station. The switch Off-state capacitance and contact resistance have been calculated based on the

measured dimensions and were approximately  $9.54\text{ fF}$  and  $0.615\Omega$ , respectively. This results in high electrical isolation of  $-32.4\text{ dB}$  and low insertion loss of  $0.053\text{ dB}$  at  $200\text{ GHz}$ . This is a spectacular performance not attained by any MEMS switch at G-band. The proposed switches utilize physical contact of metal with low contact resistance to achieve low insertion loss when actuated, so it can be operated at G-band frequencies with isolation defined by the coupling capacitance of the electrodes when the switch is open.

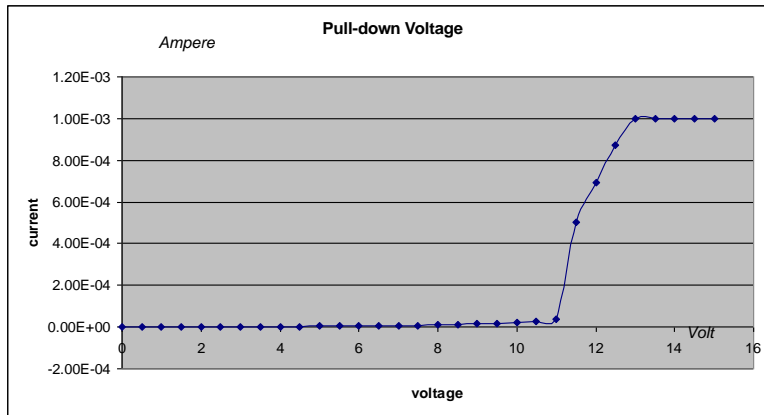


Fig. 2 actuation voltage vises the current of the MEMS switch

### 3- Antenna Design

To reduce the dielectric substrate loss, the rectangular patch is elevated above a CPW ground plane by  $13\mu\text{m}$  height of gold posts. By elevating the patch, antenna topology effectively will create a low dielectric substrate since the antenna substrate is essentially air, which is the lowest possible dielectric constant. This will help increase the radiation efficiency, gain, and the bandwidth. In order to decide appropriate dimension of the antenna and optimum design, investigation was performed by simulation software HFSS. For this design the rectangular patch dimensions are  $L \times W = 746\mu\text{m} \times 806\mu\text{m}$  with  $13\mu\text{m}$  height and  $2\mu\text{m}$  thickness. The patch is fed by a gold feeding post which connected to a CPW feed line on gallium arsenide (GaAs) substrate. The feeding post is placed in the middle of the width of the patch to avoid the excitation of the

orthogonal  $TM_{01}$  mode. To tuning the elevated patch antenna at desired frequency, the feeding post must be located at that point on the patch where the input impedance is equal to  $50\Omega$  at the resonant frequency. The antenna ground plane has to be large enough to reduce diffraction of the edges for reducing ripples in the main pattern and backward radiation, and to shield the antenna from the underlying elements and vice versa. Hence, for this design, the ground plane dimensions were chosen as  $W_s \times L_s = 1.5\text{mm} \times 2.03\text{mm}$  with  $1.2\mu\text{m}$  thickness of gold to reduce the antenna ohmic losses.

Reconfigurability of the operating frequency of the patch antenna is achieved by loading the antenna feed line with a variable reactive load. The MEMS reactive load is a CPW stub on which MEMS switch is placed to

change the state of the stub from open circuit to short circuit, or in the other words from capacitance reactive load to inductance reactive load. Changing the imaginary part of the antenna input impedance lead to tuning the resonance frequency of the antenna. The tuning range of the antenna can be controlled by adjusting the length of the stub at short and open circuit and connected position from the antenna patch. The length and position of the CPW stub were optimized using HFSS simulation software. The stub length is  $0.14mm$  when the switch is in the up-state while  $0.047mm$  when the switch is in down-state, and it is located at  $0.46mm$  from the patch feeding post. The cantilever beam MEMS switch which has been discussed in section 6.6 was used to tune the antenna resonant frequency. The states of the MEMS switch, hence the loading reactance, can be changed

by the dc actuation voltage applied between the dc contact pads and switch cantilever beam. Thus, the CPW stub with MEMS switch provides a variable reactance input impedance, resulting in tuneability in the resonant frequency. Fig. 3 shows reconfigurable antennas integrated with MEMS switch which connected with CPW feed to tune the operating frequency.

The antenna was designed and simulated using the Ansoft HFSS simulator, which is based on the finite element technique. A waveport at the antenna input terminal was used for the simulation with meshing at  $\lambda/4$  to obtain higher simulation resolution. The simulation was carried out using Dual Intel Xeon 3.20GHz Quad Core and 64 GB DDR2 800 MHz Quad Channel FBD Memory PC platforms.

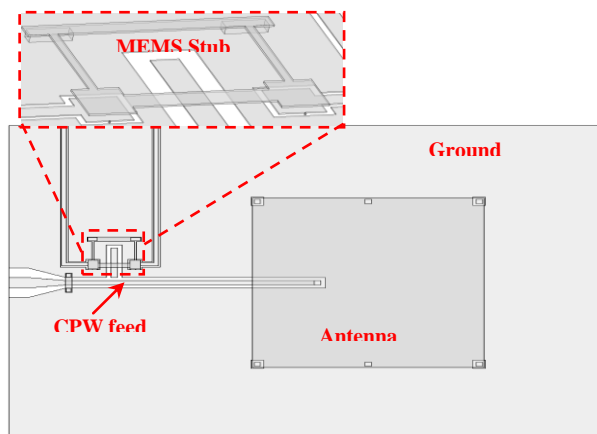


Fig. 3 the configuration of rectangular elevated patch antenna design

#### 4- Fabrication

The antenna fabrication was based on a standard III-V MMIC airbridge technology. The antenna has three levels of height, the first level consists of the ground plane and dc switch pads, then cantilever beam of MEMS switch was elevated by  $3.5\mu\text{m}$  gold posts, and finally the patch was elevated by  $13\mu\text{m}$  gold posts. The antenna was fabricated on a  $630\mu\text{m}$  thickness SI GaAs substrate with a dielectric constant of 12.9. The height of the MEMS switch and patch above the substrate can be varied as required for optimum antenna performance by changing the thickness of the photoresist layers, which is used in the airbridge process. This can be used to further enhance the patch bandwidth

when we cannot change the substrate thickness for the sake of the rest of the module circuits.

Three steps were required to realize the antenna structures. First the ground plane and dc switch pads were defined by e-beam exposure and development of a  $1.5\mu\text{m}$  thick layer of PMMA followed by electron beam evaporation and lift-off of a  $50\text{nm}/1.2\mu\text{m}$  thickness nichrome/gold layer. The second and third steps employ photolithography and electroplating techniques to form the suspended airbridge structures at two other levels. Fig. 4 shows an SEM image of the completed antenna.

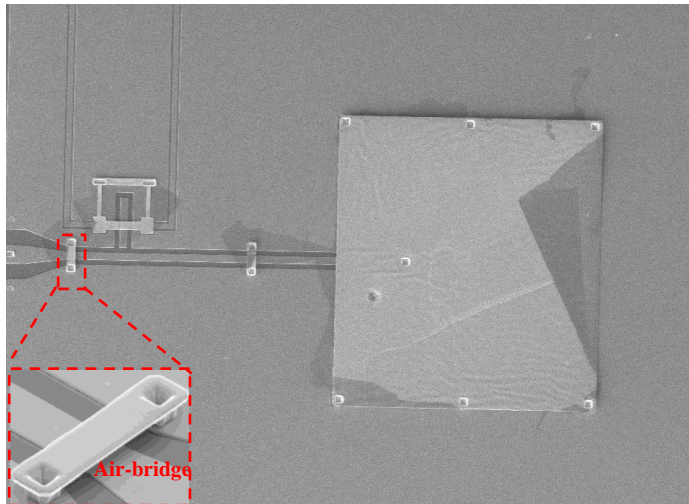


Fig. 4 SIM photo of fabricated reconfigurable antenna



## 5- Results

The proposed antenna is designed using an Ansoft HFSS simulator, and the fabricated antennas were characterized using an Agilent PNA Vector Network Analyzer and  $140\text{GHz}$  to  $220\text{GHz}$  OML heads and in wafer dc prop station. The resonant frequency of the antenna when the MEMS switch is in the up-state occurs at  $173\text{GHz}$  with good matching of  $22\text{dB}$  and bandwidth of  $5\text{GHz}$  from  $171\text{GHz}$  to  $176\text{GHz}$ . As the height of the cantilevers moves down to short the stub at  $12.5\text{volt}$  pull-down voltage, the resonant frequency shifts to  $184\text{GHz}$  with excellent matching of  $36\text{dB}$  and with nearly the same bandwidth as in the off-state. Fig. 5 and Fig. 6 show the simulation and the measurement return loss of the reconfigurable antenna at different switch states. The antenna radiates broadside for the two resonances and changing the reactance input impedance does not cause any adverse effect on the radiation patterns. Also, the dc connection between the top and

bottom plates does not have a significant effect on the performance since it is separately connected.

Proposed antenna demonstrates a broadside radiation pattern over its bandwidth. The maximum antenna gain is  $1\text{dB}$  when the switch at off-state while is  $1.3\text{dB}$  when the switch at on-state. Fig. 7 shows 3-D simulated radiation pattern for the antenna gain at Off and On state of MEMS switch.

Although the CPW stub increases the antenna dimensions significantly, it is a simple way of loading the elevated patch antenna with a MEMS switch without a significant effect on the antenna performance. Therefore, it can be concluded that the proposed antenna configuration in this paper offers significant improvements in the reconfigurable antenna performance at G-band region.



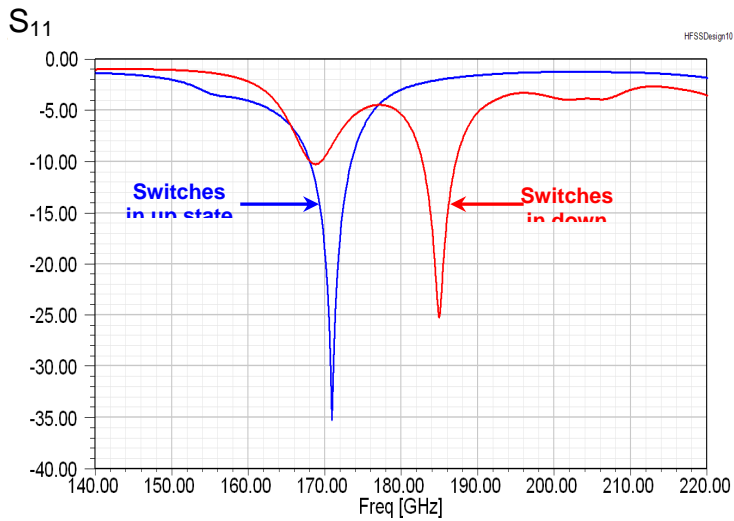


Fig.5. Simulated results of return loss at different switch states.

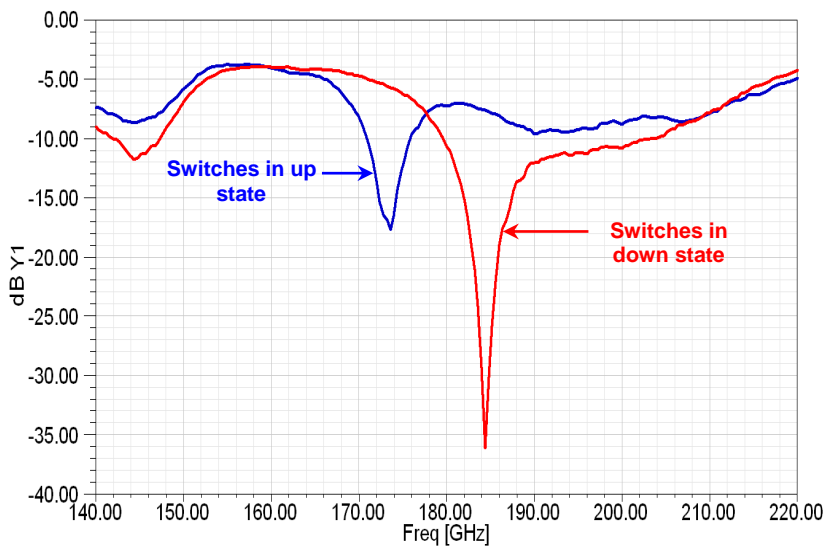


Fig.6. measured results of return. at different switch states

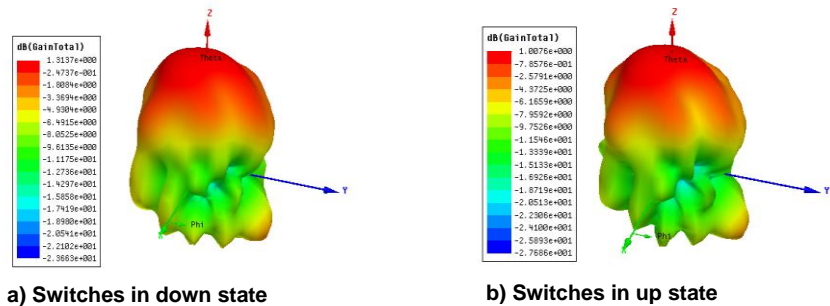


Fig. 7 3-D simulated radiation pattern (Gain dB).

## 6- Conclusion

The antenna scheme offers an easy method to integrate antenna with other MMICs, eliminate the most undesired substrate effects and maximize antenna performance on high dielectric substrates. Also, because there is no needing for additional transition, therefore a single chip wireless mm-wave system including the antenna can be achieved with a very compact size, low cost, and high performance. Further, because the CPW feed line is formed on the substrate and the radiating patch is lifted on the air, therefore the radiating patch and the feed line can be optimized separately like aperture coupled antenna.

## 7- References

- [1] D. Pozar, "Consideration for Millimetre Wave Printed Antennas," IEEE Transactions on Antennas and Propagation, vol. AP-31, 1983.
- [2] K. Hettak, G. Delisle, and M. Boulmalf, "A novel integrated antenna for millimeter-wave personal communications systems," Antennas and Propagation, IEEE Transactions on, vol. 46, pp. 1757-1758, 1998.
- [3] L. B. Lok, C. J. Hwang, H. M. H. Chong, K. Elgaid, and I. G. Thayne, "Measurement and modeling of CPW transmission lines and power dividers on electrically thick GaAs substrate to 220GHz," in Infrared, Millimeter and Terahertz Waves, 2008. IRMMW-THz 2008. 33rd International Conference on, 2008, pp. 1-2.
- [4] K. Elgaid, I. G. Thayne, G. Whyte, J. Martens, and D. Culver, "Parasitic Moding Influences on Coplanar Waveguide Passive components at G-Band Frequency," in Microwave Conference, 2006. 36th European, 2006, pp. 486-488.
- [5] I. Papapolymerou, R. Franklin Drayton, and L. P. B. Katehi,



- "Micromachined patch antennas," *Antennas and Propagation, IEEE Transactions on*, vol. 46, pp. 275-283, 1998.
- [6] G. P. Gauthier, A. Courtay, and G. M. Rebeiz, "Microstrip antennas on synthesized low dielectric-constant substrates," *Antennas and Propagation, IEEE Transactions on*, vol. 45, pp. 1310-1314, 1997.
- [7] L. Yoonjae, L. Xuesong, H. Yang, Y. Shoufeng, J. Evans, and C. G. Parini, "Low-Profile Directive Millimeter-Wave Antennas Using Free-Formed Three-Dimensional (3-D) Electromagnetic Bandgap Structures," *Antennas and Propagation, IEEE Transactions on*, vol. 57, pp. 2893-2903, 2009.
- [8] Y. Lee, X. Lu, Y. Hao, S. Yang, R. Ubic, J. R. G. Evans, and C. G. Parini, "Directive millimetre-wave antenna based on freeformed woodpile EBG structure," *Electronics Letters*, vol. 43, pp. 195-196, 2007.
- [9] R. E. Jackson and R. Ramadoss, "MEMS Based Electrostatically Tunable Circular Microstrip Patch Antenna," in *Wireless and Microwave Technology Conference, 2006. WAMICON '06. IEEE Annual, 2006*, pp. 1-4.
- [10] L. Hyung Suk, K. Jeong-Geun, H. Songcheol, and Y. Jun-Bo, "Micromachined CPW-fed suspended patch antenna for 77 GHz automotive radar applications," in *Wireless Technology, 2005. The European Conference on*, 2005, pp. 249-252.
- [11] K. Jeong-Geun, L. Hyung Suk, L. Ho-Seon, Y. Jun-Bo, and S. Hong, "60-GHz CPW-fed post-supported patch antenna using micromachining technology," *Microwave and Wireless Components Letters, IEEE*, vol. 15, pp. 635-637, 2005.
- [12] K. R. Girish Kumar, *Broadband Microstrip Antennas: Artech House antennas and propagation library Inc.*, 2003.
- [13] G. P. Gauthier, J. P. Raskin, L. P. B. Katehi, and G. M. Rebeiz, "A 94-GHz aperture-coupled micromachined microstrip antenna," *Antennas and Propagation, IEEE Transactions on*, vol. 47, pp. 1761-1766, 1999.
- [14] G. Liu, C. L. Law, M. J. Rajanik, and H. Yang, "A switchable MEMS antenna for 38/60 GHz millimeter wave communications," in *Microwave and Millimeter Wave Technology, 2004. ICMMT 4th International Conference on*, *Proceedings, 2004*, pp. 86-89.
- [15] J. Zhang, A. Wang, and P. Wang, "A Survey on reconfigurable antennas," in *Microwave and Millimeter Wave Technology, 2008. ICMMT 2008. International Conference on*, 2008, pp. 1156-1159.
- [16] D. Langoni, M. H. Weatherspoon, E. Ogunti, and S. Y. Foo, "An overview of reconfigurable antennas: Design, simulation, and optimization," in *Wireless and Microwave Technology Conference, 2009. WAMICON '09. IEEE 10th Annual, 2009*, pp. 1-5.
- [17] B. A. Cetiner, J. Y. Qian, H. P. Chang, M. Bachman, G. P. Li, and F. De Flaviis, "Monolithic integration of RF MEMS switches with a diversity antenna on PCB substrate," *Microwave Theory and Techniques, IEEE Transactions on*, vol. 51, pp. 332-335, 2003.



- [18] E. Erdil, K. Topalli, M. Unlu, O. A. Civi, and T. Akin, "Frequency Tunable Microstrip Patch Antenna Using RF MEMS Technology," *Antennas and Propagation, IEEE Transactions on*, vol. 55, pp. 1193-1196, 2007.
- [19] G. M. Rebeiz and J. B. Muldavin, "RF MEMS switches and switch circuits," *Microwave Magazine, IEEE*, vol. 2, pp. 59-71, 2001.



## Design and Simulation of a Single Feed Multi-band Dual Polarized Microstrip Patch Antenna

Mohamed A. Elmansouri

*Electrical and Computer Engineering Department, University of Colorado at Boulder  
Boulder, Colorado, USA*

*Mohamed.Elmansouri@colorado.edu*

**Abstract**— In this work, two models of a single feed multi-band stacked microstrip patch antenna are presented. The first model is a double layer, triple band stacked patch antenna with circular polarization for operation in GPS 1223 MHz and 1575 MHz bands and linear polarization for operation in 2400 MHz (Bluetooth band), and the second model is a triple layer, quad band stacked patch antenna working with circular polarization for operation in GPS 1223 MHz and 1520 MHz bands, and with linear polarization for operation in 1800 MHz (GSM band) and 2400MHz bands. The simulation results, which are obtained by using HFSS and FEKO, show that the proposed antennas meet the requirement of the circular polarization operation in the suggested bands. The impedance matching bandwidth ( $<-10$  dB) and the gain requirements for all bands are achieved. The parametric study has been done to optimize the antenna using HFSS. Furthermore, the detailed comparison between the HFSS and FEKO are introduced to show the features of each simulator to help the antenna designer to choose the best tool to simulate this kind of geometry.

### I. INTRODUCTION

The microstrip antenna is very popular in wireless and satellite communication because it has many advantages such as lightweight, conformability, low costs and the fact that it is simple to manufacture. One of the important subjects that attract microstrip antenna designers in recent days is multi-frequency different polarization operation. Achieving multi-frequency operation using microstrip antennas have been reported in literature [1,2]. Multilayered aperture coupled microstrip antennas have been proposed in [3,4]. A dual-feed triple bands microstrip antenna

for GSM and GPS operation is reported in [5]. A triple-layer patch antenna capable of triple-frequency operation is proposed in [6,7]. A double layer microstrip patch with single feed and optimum axial ratio is introduced in [8]. However, none of these references has reported an antenna combining quad-frequency with dual linear polarization and dual circular polarization operation or double layer stacked patch antenna with triple band operation. In this report, we present double and triple layer stacked patch antenna with a single coaxial feed support triple and quad bands dual polarization operations. The optimum parameters of the proposed antenna are obtained using the full wave EM numerical tools HFSS and FEKO.



## 2-ANTENNA MODELS DESIGN

Microstrip antenna with multi-frequency operation has been achieved by several techniques: the use of multilayer stacked patches, a rectangular patch with a pair of narrow slots placed close to the patch's radiating edges, a square patch with a rectangular notch [1], a rectangular patch loaded with shorting pins and slots, a rectangular patch fed by an inclined coupling slot [7], etc. Stacked patches are easier to achieve multi-band operation than other approaches, and they can be optimized to work in different polarization modes by analyzing the parameters of the multilayer structure.

### A. *Prototype Model: Double Layer Model*

The double-layer structure of the proposed antenna is shown in Fig. 1.a. The lower and upper patches are designed in order to get the circular polarization in the 1223MHz and 1575MHz bands respectively. A circularly polarized EM-wave is generated when an antenna radiates two orthogonal field components having equal amplitude with a quadrature phase difference between them. Several geometrical configurations of microstrip patch antennas can provide such dual orthogonal field components with proper excitation of the patch cavity. Normally two orthogonal field components are excited in the patch cavity using dual orthogonal feeds and splitting input microwave power in various ways [8]. This method generally gives a large AR-bandwidth. However, the external power divider increases the size and complexity of the system; thus preference is given to single-feed circularly polarized microstrip antennas. A perturbed symmetrical patch cavity of square, supports two orthogonal modes, which can be excited with a single feed [2]. This concept is used here to design

the lower and the upper patches. The square patch with diagonally opposite truncated corners is designed using the formulas in [9] to achieve the circular polarization at 1223MHz and 1575MHz bands. The common feed technique is used to feed the stacked antennas. The feed probe of the coaxial line extends completely through the lower patch, passes through the hole in the lower patch, and connects to the upper patch. In this case, patches are in series with each other. At the resonant frequency of the lower patch, the upper patch looks basically like a short circuit. This short effectively connects the probe directly to the lower patch metallization. Conversely at the resonant frequency of the upper patch, the lower patch appears as a short circuit and thus connects the ground plane to the lower patch [9]. This approach of feeding works well when the upper patch is the smaller of the two to ensure that there is little coupling between the patches via the fringing fields at the edges. The upper patch is connected to the ground plane by using a shorting pin in order to enhance the impedance matching and the axial ratio bandwidths at 1575MHz band. The size of the used ground plane is  $80 \times 80 \text{ mm}^2$ . Layers' material is low cost FR4 ( $\epsilon_r = 4.4, \tan\delta = 0.02$ ). The dimensions as shown in Fig.1 are  $L_1 = W_1 = 54\text{mm}$ ,  $L_2 = W_2 = 45.5\text{mm}$ ,  $c_1 = 9.6\text{mm}$ ,  $c_2 = 6\text{mm}$ ,  $H_1 = 3.3\text{mm}$ ,  $H_2 = 1.6\text{mm}$ ,  $(x_1, y_1) = (15\text{mm}, 1\text{mm})$ ,  $(x_2, y_2) = (0, 0.5\text{mm})$ ,  $d = 4.4\text{mm}$ .

### B. *The second model: Triple Layer model*

To achieve the quad band operation another FR4 layer and microstrip patch printed on the top of it are added above the two layers of the prototype design. The third patch is a meandered patch designed to achieve the operation in 1800 MHz band [1]. In this



model, the feed probe is connected to the third patch as shown in Fig. 1.b. The shorting pin remains in the same position. The dimensions of the third patch, new dimensions of the other patches and feed position are shown in the optimization section below.

### C. Optimization

Prototype model has many parameters that must be optimized to achieve the required specifications. The optimization process is based on the FEM simulator, HFSS. The optimization process started with parametric studies to find the effect of each parameter on the antenna impedance matching bandwidth, axial ratio 3dB bandwidth, gain and the radiation patterns at each band. We found that the feed position is critical parameter to achieve the circular polarization operation with the best impedance matching bandwidth; the optimized location of the coaxial feed probe is shown in Fig. 1. Increasing the height of the first and second substrate increases the impedance matching bandwidth; on the other hand, it reduces the axial ratio bandwidth. Increasing the height of the third substrate reduces the impedance matching bandwidth ( goes  $> -10$  dB) for the first and second band of operation. The largest patch is in the first layer (1223MHz), then the second one (1575MHz) finally the smallest one (1800 MHz) at the top. The antennas should be arranged in that way to reduce the coupling between the patches. The truncated corners dimensions ( $c_1, c_2$ ) affect sharply the axial ratio bandwidth and the slightly the impedance matching bandwidth and the gain of the antenna. The shorting pin position affects the axial ratio bandwidth and impedance matching bandwidth; the optimized position of the shorting pin is the near zero fields point on the patch #2 where

the shorting pin won't affect the original performance of the second patch largely, and simultaneously it will enhance the performance of the antenna. The size of the ground plane can be reduced 13% with slight effect on the antenna parameters. We run HFSS about 620 times to reach the optimized dimensions of the antenna and the other parameters which are  $L_1 = W_1 = 54mm$ ,  $L_2 = W_2 = 45.5mm$ ,  $L_3 = 38mm$ ,  $W_3 = 32mm$ ,  $w_s = 2mm$ ,  $l_s = 20mm$ ,  $c_1 = 9mm$ ,  $c_2 = 5.8mm$ ,  $H_1 = 3.3mm$ ,  $H_2 = 1.4mm$ ,  $H_3 = 1.3mm$ ,  $(x_1, y_1) = (15mm, 1mm)$ ,  $(x_2, y_2) = (0, -1mm)$ ,  $d = 4.4mm$ .

### 3- RESULTS AND DISCUSSION

The proposed models have been studied using HFSS and FEKO. fig. 2 shows the simulated return loss for the double and triple layer models. The results show that both models have a good 10-dB impedance matching bandwidth that meets the operation requirements at the suggested bands. The 3-dB axial ratio bandwidth for 1223MHz and 1575MHz bands for the double layer model, and 1223 MHz and 1525 for triple layer model are shown in fig. 3. 22 MHz bandwidth is achieved for the lower band and 16MHz for the upper band for both models. This bandwidth as in [5,6] is quite enough for the GPS functionality at these bands. The results are summarized in table 1 and table 2.

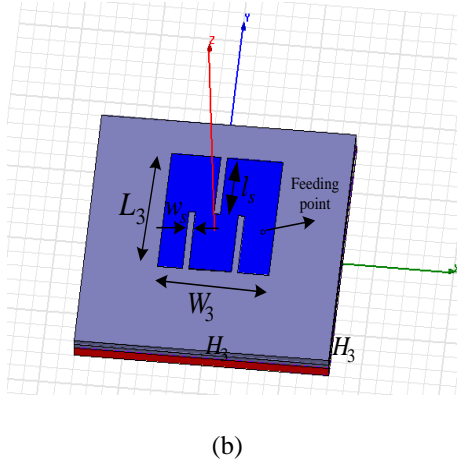
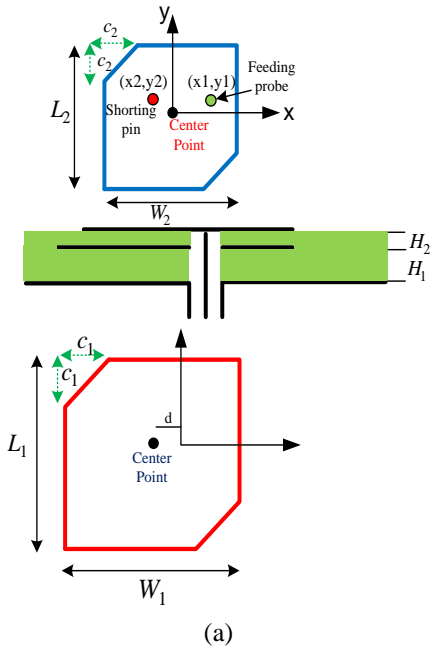


Fig.1: the geometry of the proposed antennas: (a) the configuration of the prototype model (double layer), (b) the geometry of the third patch as designed in HFSS

The RHCP and LHCP gain radiation patterns for  $f=1223\text{MHz}$ ,  $1575\text{MHz}$  for the first model, and for  $f=1223\text{MHz}$ ,  $1520\text{MHz}$

for the second model are shown in fig. 4. The co-polarization and cross polarization radiations patterns are plotted and shown in figures 5 and 6 at  $f=1800\text{MHz}$  for the second model (triple layer) and at  $f=2400\text{MHz}$  for the first and second model (triple layer model). The figures show that the cross-polarization level of the antenna models at these frequencies below -14dB except for  $f=1223\text{MHz}$  for the double layer model is about -5dB. The antenna models produce good RHCP radiation in broadside direction for the GPS bands. The gain of the double layer antenna is about 2.5dBi, 1.8dBi for 1223MHz band, 1575MHz respectively, and 3.5dBi, 2dBi for the triple layer model. In addition, it is 3dBi at  $f = 2400\text{MHz}$ , and 2.2dBi at  $f = 1840\text{MHz}$ . The max gain of the  $f = 1840\text{MHz}$  radiation pattern is at  $\theta = 70^\circ$ . The future work will include the enhancing (clear) the radiation pattern of this band.

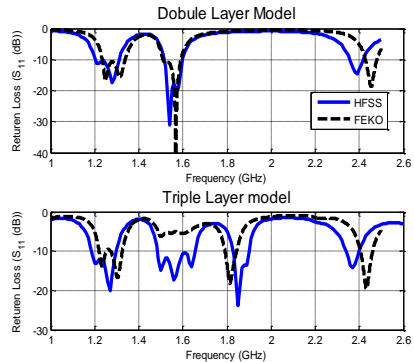


Fig.2: Simulated return loss of the proposed models



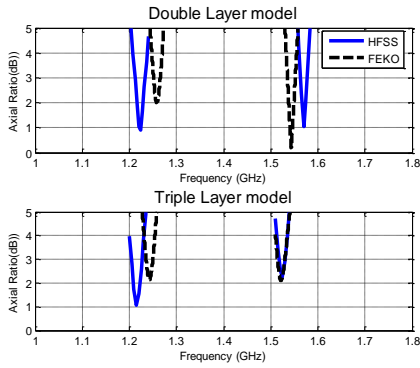
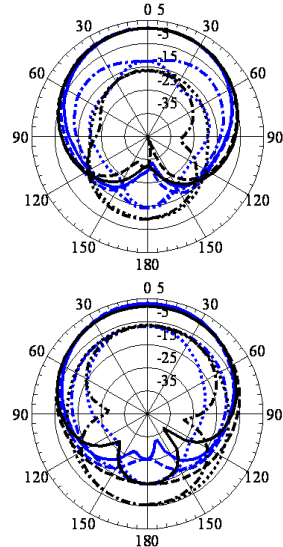
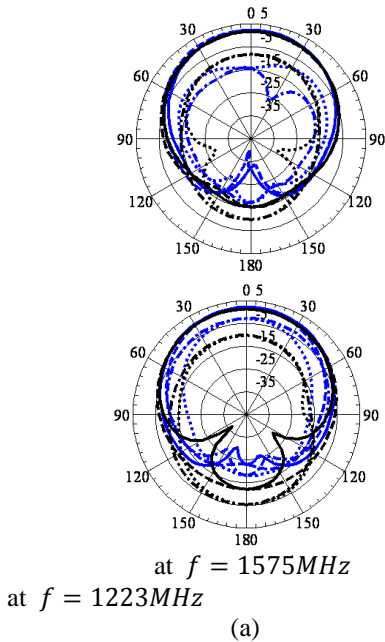


Fig.3: Simulated axial ratio at the broadside  $\theta = 0^\circ$  of the proposed models



at  $f = 1520\text{MHz}$  at  $f = 1223\text{MHz}$   
(b)

Fig.4: Simulated radiation patterns of the antenna: (a)-double layer model, (b)-triple layer model, at the GPS bands. (Blue lines: HFSS, Black:FEKO). (—) Gain-right,  $\phi = 0^\circ$ ; (---) Gain-right,  $\phi = 90^\circ$ ; (.....) Gain-left,  $\phi = 0^\circ$ ; (-.-.-) Gain-left,  $\phi = 90^\circ$ ;

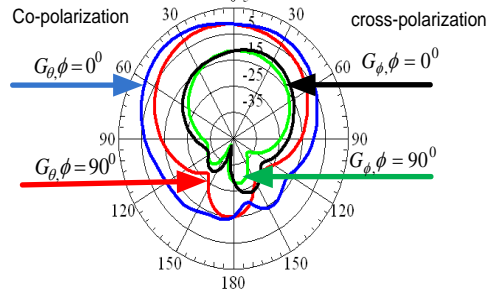


Fig.5: HFSS Simulated radiation patterns of the antenna at  $f = 1840\text{MHz}$

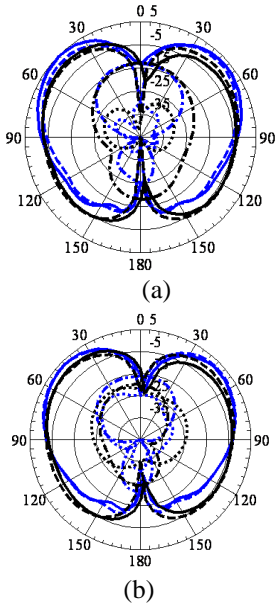


Fig.6: Simulated radiation patterns of the antenna at = 2380MHz : (a)-double layer model, (b)-triple layer model. (Blue lines: HFSS, Black:FEKO). (—)  $G_{\theta}$  co-polarization,  $\phi = 0^{\circ}$  ;(----)  $G_{\theta}$  co-polarization,  $\phi = 90^{\circ}$  ; (.....)  $G_{\phi}$  cross-polarization,  $\phi = 0^{\circ}$  ;(-.-.-)  $G_{\phi}$  cross-polarization,  $\phi = 90^{\circ}$

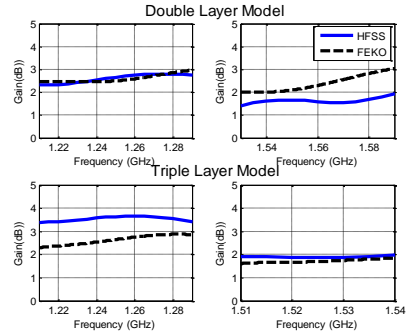


Fig.7: Simulated gain of the two models versus the frequency at  $\theta = 0^{\circ}$

Table 1: the performance of the first model

	First Band (1223M Hz)	second Band (1575M Hz)	Third Band (2400M Hz)
Impedance BW	100MHz	90MHz	65MHz
Polarization	Circular	Circular	Linear
Axial ratio BW	22MHz	16MHz	

Table 2: the performance of the second model

	First Band 1223MHz	Second Band (1525MHz)	Third Band (1800MHz)	Fourth Band (2400MHz)
Impedance BW	105MHz	180MHz	72MHz	66MHz
Polarization	Circular	Circular	Linear	Linear
Axial ratio BW	22MHz	15MHz		

In general, the results show a good agreement between HFSS in FEKO in most cases. The differences between the results especially for the triple layer model came from an inadequate meshing size that has been chosen to simulate the problem in

FEKO. We choose relatively large mesh size to overcome the memory requirements.

Also, we used wire segment model to feed the structure in FEKO, which is not a perfect model for coaxial feed. In addition to that, the differences between the core methods of these simulators, and pre and post processing engines in each one introduce differences between the results. In



our case, we consider the results of HFSS as more accurate results.

#### 4-THE EFFECT OF THE SHORTING PIN

Several structural parameters are important to enhance the performance of the antenna; one of them is the shorting pin that is shown in Fig.1.a. The effect of the shorting pint on the performance of the proposed model is discussed in this section.

The significance of the shorting pin in enhancing the impedance bandwidth for the second band of the triple layer model is demonstrated in Fig. 8

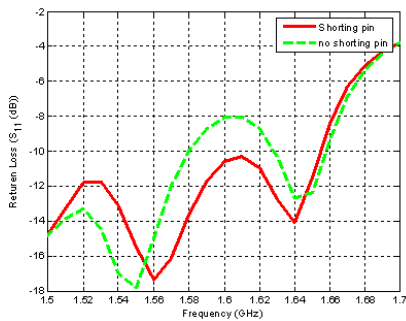


Fig.8:The effect of the shorting pin of the triple layer antenna performance

The impedance bandwidth is reduced when we remove the shorting pint. Furthermore, the axial ratio bandwidth is reduced 3MHz at 1223,1525MHz bands, and at 1223MHz band impedance BW is slightly reduced. The presence of the shorting pint isn't significant, yet it helps reasonably to enhance the performance of the antenna at different bands.

#### 5- HFSS vs. FEKO OR (FEM vs. MOM)

HFSS and FEKO are two of the most efficient EM simulators in the recent time. They prove the capability of the simulation of complex geometries, and they introduced results which are in excellent agreement with the measured results, so the question that we are trying to solve here which

simulator is the best. Absolutely, we cannot introduce a general answer because the performance (run time, memory, and accuracy of the solution) of each simulator is different from case to case; this performance depends on the type of the problem, the complexity of the geometry, and the contents of this geometry. In fact, when we compare between HFSS and FEKO we compare between the two computational EM techniques that represent the core of these simulators, which are Finite Element method (FEM) and Method of Moments (MOM). The good comparison between these methods is introduced in [10]. The applications, advantages, and disadvantages of these methods are the main points that make the differences between FEKO and HFSS; for instance, Green's function for the free space (open or exterior problems: e.g. radiation and scattering problems) can be easily calculated and implemented for the MOM solution which makes FEKO is more convenient and accurate to simulate this kind of problems from many comparison points; On the other hand, the Green's functions for multi-layers and dielectric structures are complicated and need more time to calculate from the numerical point of view (more calculations, more run time, more memory, more errors) which makes HFSS (FEM) is better for this kind of geometries. In table 3, we introduce a comparison between FEKO and HFSS from the numerical aspects in CEM point of view

The comparison in table 3 demonstrates that the HFSS (FEM) has a better performance comparing to FEKO (MOM) in analysis of these structures. The first order basis function and direct solver is used to get values shown in table 3 for HFSS



Table 3: Comparison between FEKO and HFSS

	Double Layer Model		Triple Layer Model	
	HFSS	FEKO	HFSS	FEKO
Run time	3min.	27min	5min.	58mi
Memory	320M B	369M B	455M	705M B
#. of triangles	110	2562	111	3689
# of tetrahedrons	14272	0	18353	0
# of Basis function		6944		9600

. If we increased the order of the basis function to the second order for the double layer model simulation the run time increases to 9min and the memory increases to 700MB (53%). The grid size is critical parameter from the memory point of view when you are dealing with FEKO; to illustrate, if we decrease the grid size for the triple layer model simulation from  $\lambda/13$  to  $\lambda/14$  the memory requirement in this case increases to 1015MB (44%). The type of matrix in FEM and MOM makes a significant difference in CPU time and the memory required for process. The FEM matrix is large as we can see from the table 3 ( # of tetrahedrons) ,yet it is sparse which can be efficiently stored, and easily solved; In contrast, the MOM matrices are dense and ill-conditioned matrices which are in some cases need long time to solve. Furthermore, the excitation modelling in MOM is a problem; in some cases, we need to use approximate model (as in our case). The comparison we introduced here is not general but it is related to our problem. In the other problems analysis may you will get completely different results.

## 6- CONCLUSION

In this work, two models for a single feed multi-band stacked patch antenna with circular and linear polarization have been designed and simulated by using HFSS and FEKO. The results show that the double layer model supports triple band operation with dual right hand circular polarization at two GPS bands and vertical polarization at 2400MHz (Bluetooth band). Furthermore, they show that the triple layer stacked patches support a quad band operation with dual circular polarization operation at the GPS bands, and dual linear polarization operation at 1800MHz (GSM band) and 2400MHz bands. As a part of this work, a detailed comparison between HFSS and FEKO from CEM's prospective is introduced. The comparison shows that HFSS (FEM) performance in analysis this kind of geometry is better than FEKO (MOM) from different aspects.

## 7-REFERENCES

- [1] Kin-Lu Wong, *Compact and Broadband Microstrip Antennas*, John Wiley & Sons, Inc., New York, 2002.
- [2] R. Garg, P. Bhartia, I. Bahl and A. Ittipiboon, *Microstrip antenna design handbook*, Artech House, Norwood, MA, USA, 2001.
- [3] F. Croq and D.M. „Pozar,” Microstrip Antennas Using Aperture Coupled Parallel Resonators", IEEE Trans. Ant. and Propag., vol.40, no.11, ppl367-1374, November 1992.
- [4] X.H. Yang and L. Shafai, "Muitifrequency Operation Technique for Aperture Coupled Microstrip Antennas", APSymp., pp 198-1201, 1994.



- [5] Min Sze Yap, Lenna Ng and Sheel Aditya, "A Triple Band Antenna for GSM and GPS Application", IEEE ICICS-PCM, vol.2, ppl1 19-1123, December 2003.
- [6] Sho Yuminaga and Yoshihide Yamada, "A Triple-layer Patch Antenna Capable of Triple-frequency Operation", IEEE Antennas and Propagation Society, AP-S International Symposium (Digest), vol.4, ppl38-141, June 2003.
- [7] Qiu Jinghui, Li Hongmei, Yang Caitian and Li Wei;, " A Triple-Frequency Circularly Polarized Microstrip Patch Antenna", [Microwave Symposium Digest, 2006.](#)
- [8] Nasimuddin, K. P. Esselle, and A.K.Verma, " Optimization of stacked microstrip antenna for circular polarization, " in Proc. WARS2006 Conf., Sydney, Australia. Feb. 15- 17, 2006.
- [9] Robert A. Saintai, "CAD for *Microstrip Antennas* for. Wireless Applications", Artech House, Norwood, MA, USA.
- [10] R. Garg, Analytical and Computational Methods in Electromagnetics, Norwood, MA: Artech House, 2008.





## Design of UWB Tapered Slot Antenna for Extracting Metallic Objects Late Time Responses

Ali Atiah, N. Bowring and A. Albarbar

*Electrical and Technology Department  
Manchester Metropolitan University*

UK

[aliattia1@gmail.com](mailto:aliattia1@gmail.com)

**Abstract:** The detection of human body worn concealed metallic objects based on the late time response (LTR) method is one of the great challenges.

Successful LTR extraction to identify the target signature and its correct interpretation requires UWB antenna, which can cover the frequency of the fundamental (lowest) complex natural resonance (CNR) of the target(s) under detection. A flat gain UWB tapered slot antenna with operating bandwidth of 0.25-3GHz to cover the lowest CNR frequencies designed and fabricated. Antenna tests made in an anechoic chamber to provide complete back scattering and signal radiation control. The results showed that the fabricated antenna has relative flat gain from about 0.3GHz to just over 3GHz with distortion less narrow pulse transmission.

### I. INTRODUCTION

The standoff detection of on-body concealed objects is one of the great challenges. Achieving UWB antenna that is capable to have non-resonant (flat) gain across all frequencies in the desired spectrum is a key role for the successful detection of on-body concealed metallic objects, such as guns and knives. In fact, to achieve an impulse response of on-body concealed weapon(s), the weapon(s) need to illuminate in the far field region by a very narrow pulse, equivalent to a UWB

frequency sweep. As the pulse propagates through the concealed objects, Omni directional reflections and scattering occur at the interfaces. Of particular interest are the aspect independent resonance(s) and their associated dampening which measured by receiving UWB antenna, the amplitude and phase of such backscatter is aspect dependent relative to the linear polarisation. For an accurate detection system with high resolution and dynamic range, the transmitting/receiving UWB antenna should be flat gain (non zeros resonant) as much as possible, distortion



less pulse transmission and reception and directive with high-radiation efficiency.

Tapered slot antennas (TSA) have been widely used in different radar applications, especially the Vivaldi antenna that was first brought out by Gibson in 1979 [1] that's have been recently widely investigated and developed by many researchers and institutions [2-5]. Several excellent TSAs with improved antenna parameters involving dual exponentially tapered slot antenna [6], dual elliptically tapered antipodal slot antenna [7], antipodal exponentially tapered slot antenna [8], dual V-type linear taper slot antenna [9], is optimized for issuing ultra-wideband (UWB) applications and millimetre-wave detection systems. Practically, on the frequency range 0.25–3GHz, none of the improved TSAs has non-resonant flat gain around 10 dBi that is indispensable for successful standoff concealed weapon detection based on back scattering late time response by covering all of the basic frequencies of common interested objects. Two specific Vivaldi antennas studied and investigated in [10]. Regrettably, antenna gain characteristics are not available. The ridged horn antenna [11] shows high antenna gain with ultra-wide bandwidth, but it does not meet none resonate demand to cover the fundamental CNR of the target(s) under detection. Instead, TSA arrays [12] usually achieve 10-dBi or higher antenna gain covering the frequency of interest. However, compared with the single tapered slot antenna element, antenna array is more difficult not only with its larger size due to the extra feeding

networks but also it is harder to design and fabricate. Most of the compact UWB antennas presented in the literature exhibit omni directional radiation patterns with comparatively low gain and an impulse response with observable distortion [13]. These types of UWB antennas are convenient for short-range indoor and outdoor communication applications. However, for radar systems, used for the detection of weapons concealed under clothing, upon the human body or within carried bags at standoff distance, a flat gain directional antenna and VSWR around unity is advantageous.

In addition, the required UWB antenna must be able to pass very narrow distortion less monocycle time pulse to cover the fundamental CNR frequencies of the target(s) under detection, equivalent to a flat (non-resonant) response in the frequency domain. This criterion is required to enable effective deconvolution of the antenna response from the received scattered signal, which is essential to enable successful extraction of CNR modes. Nevertheless, having a less than desirable antenna response, may lead to have unauthentic resonances as any antenna resonance could contribute to mask concealed on-body objects. The bandwidth must be sufficiently wide to cover all of the basic frequencies of the most common firearms.

In this paper, a compact UWB antenna exponentially tapered slot with a bandwidth of the operating frequency 0.25 to 3GHz is developed. This operating bandwidth chosen to cover the fundamental CNR



modes of most firearms and to give a fine enough time resolution to resolve these CNR, and to minimize clutter from the human subjects and other objects in the surveillance area.

## II. ANTENNA DESIGN

For the 0.25-3GHz with flat gain operation bandwidth a tapered slot antenna TSA was developed and optimized as successfully used for radar applications. The presented TSA antenna will be used in concealed on-body weapon detection. The detection system includes identical TSA antennas, one used to transmit a sharp UWB pulse while the rest receive the back scattering signal. The proposed antenna fabricated on the FR4 epoxy substrate with 0.5-oz copper and dielectric constant 2.33. A top view of the designed antenna illustrated in Figure 1.



Figure 1. Shape the top of the designed antenna.

The design objective is to obtain a UWB antenna with non-zeros resonant frequency as any antenna resonant can mask the very important aspect independent late time response of objects concealed on the human body. The exponential taper profile is

determined by the opening rate and two points  $p_1(x_1, y_1)$  and  $p_2(x_2, y_2)$ .

$$y = c_1 e^{Rx} + c_2 \quad (1)$$

Where,

$$c_1 = \frac{y_2 - y_1}{e^{Rx_2} - e^{Rx_1}} \quad (2)$$

$$c_2 = \frac{y_1 e^{Rx_2} - y_2 e^{Rx_1}}{e^{Rx_2} - e^{Rx_1}} \quad (3)$$

$c_1, c_2$  are constants and  $R$  is the opening rate of the exponential taper.

Note that  $(y_1, x_1)$  and  $(y_2, x_2)$  are the coordinates of the origin and end of flare curve, respectively and the taper length  $L = x_2 - x_1$ .

An exponentially tapered slotline rather than an elliptically antipodal tapering structure exploited to make the antenna simulation and optimization easier. The width  $W$  of the proposed antenna controls the lowest operation frequency, which is set at  $0.47\lambda$ , where  $\lambda$  is the free space wavelength at 0.25 GHz. The length  $\lambda$  could affect the front-to-back ratio of the radiation patterns at the lowest frequency band, which is set at around  $0.4\lambda$ . The antenna is excited with a Gaussian monocycle pulse in the time domain and is optimized and simulated using the electromagnetic FTD solver *CST microwave studio* transient solver mode which helped to reveal the most critical antenna areas to reduce cavity resonance and to ameliorate their related transmitted and received amplitudes. The excited monocycle pulse has maximum amplitude at a frequency 0.75 GHz, which carefully selected to excite basic CNR for most common firearms [14].

### III. SIMULATION AND DISCUSSIONS

An optimum antenna achieved by the adjustment of the following parameters: flare angle, cavity radius and throat width to reduce the antenna ringing as much as possible.

The ultra wideband antenna designed according to the mentioned procedure and it is manufactured using FR4 epoxy ( $\epsilon_r = 2.33, h = 0.125\text{cm}$ ) as substrate. The taper rate was 0.18cm and radial stub angle( $\theta$ ) =  $105^\circ$ . The radiating microstrip is in the bottom layer of the substrate whereas the ground plane is printed on the top of it. The validity of the proposed design methodology is verified using the CST *microwave studio transient solver* simulator which is based in finite integral technology. The antenna is located in the  $x$ - $y$  plane, E-plane of the antenna is in the  $x$ - $z$  plane ( $\varphi = 0^\circ$ ) and  $H$ -plane is in the  $y$ - $z$  plane ( $\varphi = 90^\circ$ ). Antenna measurements made in anechoic chamber. The simulated and measured 10dB return loss bandwidth extends from 0.25GHz to 4GHz covering the required UWB of 0.25 to 3GHz. As shown in Figure 2, the simulated results closely resemble the measured result confirming the design procedure of the antenna.

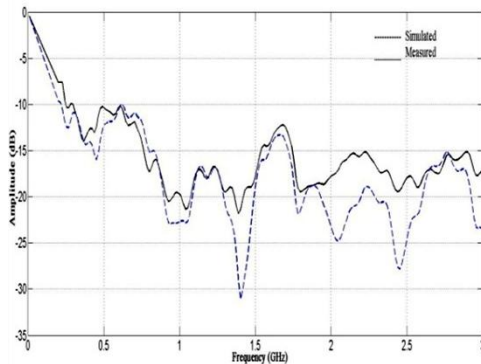


Figure 2 Measured and simulated S11 return loss.

It is very critical that the gain across the operating bandwidth to be high and comparatively flat, resulting in an around unity VSWR across the broadband spectrum specifically in the affected frequencies, leading to the improvement to excite resonances needed for on-body weapon detection. Both the measured and simulated figures show that the antenna gain of the designed antenna achieves these requirements, as illustrated in Figure 3 and Figure 4.

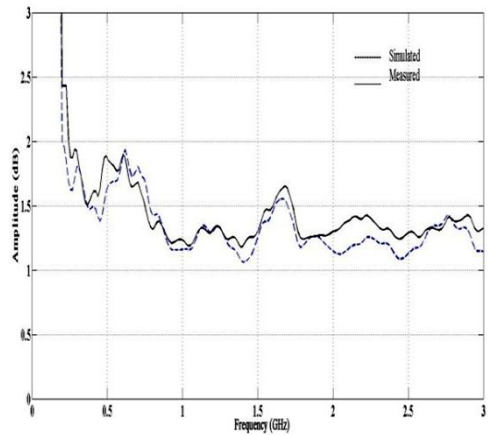


Figure 3 Measured and simulated VSWR.

The far-field radiation patterns of the antenna were calculated by using the software CST microwave studio. These far field results are presented in Figure 5 for the frequencies 0.7GHz and 1.5GHz. The antenna achieves directive properties with an average front-to back ratio which is greater than 10 dB across the whole band, making it convenient for standoff detections applications.

The time domain performance of the presented antenna was measured as well. Two identical co-polarized antennas were faced to each other cross a distance of 50 cm; the measured results are illustrated in Figure 6.

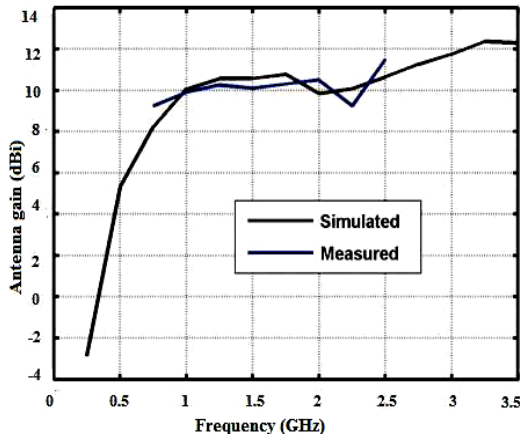
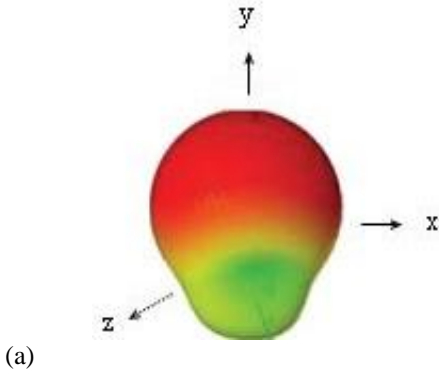
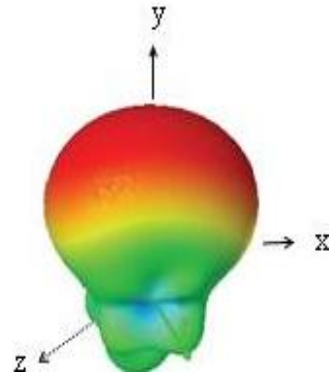


Figure 4 Measured and simulated antenna gain.

The excited pulse and the obtained pulse are normalized with respect to their peak values. The figure shows that the time pulse of the antenna is 0.7 nanoseconds. The pulse distortion happens at the 0.16 level with respect to the peak level of 1, which is almost negligible. The results show that the optimized antenna improves distortion less narrow pulse which makes it an excellent radiator for the application of a detection system with high resolution.



(a)



(b)

Figure 5 Simulated three-dimensional far field radiation pattern (a) 0.7GHz and (b) 1.5 GHz,

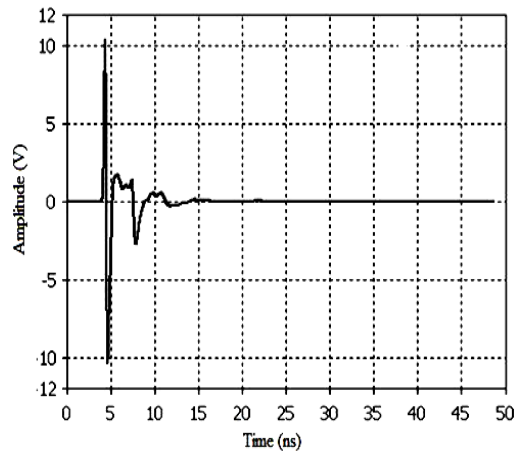


Figure 6 Measured impulse response.

#### IV. CONCLUSIONS

The design of ultra wideband tapered slot antenna for use in concealed weapon detection has been introduced. Detection of concealed on-body weapons is limited by antenna response as any antenna ringing could mask very important aspect independent scattering related to the



concealed object signature. An approach is described based on relatively flat gain antenna across the operating bandwidth. Simulated and measured antenna characteristics illustrate that the developed antenna has relative flat gain cross proposed band from 0.25GHz to more than 3GHz. The time domain of the antenna has been studied as well. It has been illustrated that the presented antenna could send and receive very narrow pulses in a distortion less manner to meet the requirements of successful concealed weapon detection based on the late time response scattered from the illuminated objects. More work has to be done in the next months to minimize or even to block the forced back scattering early time response.

#### REFERENCES

- [1] Gibson, P. J., "The Vivaldi aerial," *Proc. 9th European Microwave Conference*, pp.101–105, 1979.
- [2] Gazit, E., "Improved design of the Vivaldi antenna," *IEE Proceedings: Microwaves, Antennas and Propagation*, Vol. 135, No. 2, pp.89–92, 1988.
- [3] Yngvesson, K. S., D. H. Schaubert, T. L. Kollberg, T. Thungren, and J. F. Johansson, "End fire tapered slot antennas on dielectric substrates," *IEEE Transactions on Antennas and Propagation*, Vol. 33, No. 12, pp. 1392–1400, 1985.
- [4] Kim, S. G. and K. Chang, "Ultra wideband exponentially-tapered antipodal vivaldi antennas," *IEEE Antennas and Propagation Society, AP-S International Symposium (Digest)*, Vol. 3, pp. 2273– 2276, 2004.
- [5] Janaswamy, R. and D. H. Schaubert, "Analysis of the tapered slot antenna," *IEEE Transactions on Antennas and Propagation*, Vol. 35, No. 9, pp. 1058–1065, 1987.
- [6] Ponchak, G. E., J. L. Jordan, and C. T. Chevalier, "Characteristics of double exponentially tapered slot antenna (DE TSA) conformed in the longitudinal direction around a cylinder," *IEEE Antennas and Wireless Propagation Letters*, Vol. 6, pp. 60–63, 2007.
- [7] Langley, J. D. S., P. S. Hall, and P. Newham, "Balanced antipodal Vivaldi antenna for wide bandwidth phased arrays," *IEE Proceedings Microwaves Antennas and Propagation*, Vol. 143, No. 2, pp. 97–102, 1996
- [8] Qing, X. M., Z. N. Chen, and M. Y.W. Chia, "Parametric study of ultra-wideband dual elliptically tapered antipodal slot antenna," *International Journal of Antennas and Propagation*, 2008.
- [9] Cheng, Y. J., W. Hong, and K. Wu, "Design of a monopulse antenna using a dual V-type linearly tapered slot antenna (DVL TSA)," *IEEE Transactions on Antennas and Propagation*, Vol. 56, No. 9, pp. 2903–2909, 2008.
- [10] Mehdi-pour, A., K. M-Aghdam, and R. Faraji-Dana, "Completed dispersion analysis of Vivaldi antenna for ultra wideband applications," *Progress In Electromagnetics Research, PIER 77*, pp. 85–96, 2007.
- [11] Abbas-Azimi, M., F. Arazm, J. Rashed-Mohassel, and R. Faraji Dana, "Design and optimization of a new 1–18 GHz double ridged guide horn antenna," *Journal of Electromagnetic Waves and Applications*, Vol. 21, No. 4, pp. 501–516, 2007.



- [12] Yang, Y., Y. Wang, and A. E. Fathy, "Design of compact Vivaldi antenna arrays for UWB see through wall applications," *Progress In Electromagnetic Research*, PIER 82, pp. 401–418, 2008.
- [13] Chen, F. C. and W. C. Chew, "Time-domain ultra-wideband imaging radar experiment for verifying super-resolution in nonlinear inverse scattering," *Journal of Electromagnetic Waves and Applications*, Vol. 17, No. 9, pp. 1243–1260, 2003.
- [14] D. Andrews; N. Bowring; N. Rezgui; M. Southgate; E. Guest; S. Harmer and Ali Atiah, "A multifaceted active swept millimeter-wave approach to the detection of concealed weapons" *SPIE security and defense conference*, Cardiff, UK, Sept. 2008.



المؤتمر الدولي العربي الليبي الرابع للهندسة الكهربائية والإلكترونية 2010/10/26-23 طرابلس ليبيا



## **Study of the Performance of Multi-Band Planar Inverted F (PIF) Antennas in the Presence of Human Head and Hand Using Full-Wave Modeling Techniques**

Mohamed A. Elmansouri, and Ibrahim M. Saleh

Electrical and Electronic Engineering Department

Al-Fateh University, Tripoli, Libya

E-mail: mansori82@yahoo.com, Ibrahim.saleh@ltnet.net

### **Abstract**

In this paper, the performance of dual, triple, and quad-band PIFAs, analyzed in free space in a previous work [1], have been evaluated in presence of human head and hand models. The effect of proximity of the user on the input reflection coefficient, radiation pattern, and radiation efficiency of the antennas have been studied in details using different full-wave modeling techniques which are FDTD, FIM, FEM, and MOM. The results are compared and analyzed.

### **1. Introduction**

Interaction of mobile phone antennas with human body has great consideration in cellular communications. The user's body, especially head and hand, influence the antenna voltage standing wave ratio (VSWR), gain and radiation patterns. Furthermore, thermal effect, when tissues exposed to unlimited electromagnetic energy, can be a serious health hazard, so standard organizations have set exposure limits in terms of the specific absorption rate (SAR). This paper focuses on the evaluation of the performance of the modern PIFAs in the presence of simple models of human head and hand. Four-tissue head model and two-tissue hand model are included as part of the simulation geometries of the finite difference time

domain (FDTD), finite element method (FEM), finite integration method (FIM), and method of moments (MOM) simulation models to study the effect of the proximity of the user on the reflection coefficient, radiation pattern, and radiation efficiency of the planar inverted-F antennas proposed in [1],[2], and [3].

### **2. Human Head and Hand Models**

Fig.1.a demonstrates the used four tissues spherical model. It consists of four scaled sphere which are inserted into each other. The spheres are terminated by a brick on both sides. The size of head model is: 150 x 180 x 180 mm<sup>3</sup> Fig.2.b shows the model tissues: Skin with thickness =0.75 mm, Fat with



thickness =1.5 mm, Bone with thickness =4.35mm, and Brain thickness =136.8 mm. Table 1 presents values of relative permittivity, conductivity, and density of tissues.



Fig.1: Four -tissue spherical head model used in this simulation (a) -3D front view (b) mesh view in FDTD.

Table 1: Relative Permittivity, Conductivity, and Mass Density of spherical Model tissues at several frequencies [4]

Frequency (MHz)	Brain		Skull		Fat		Skin	
	$\rho = 1030kg / m^3$		$\rho = 1850kg / m^3$		$\rho = 1100kg / m^3$		$\rho = 1100kg / m^3$	
	$\sigma$ (S/m)	$\epsilon_r$	$\sigma$ (S/m)	$\epsilon_r$	$\sigma$ (S/m)	$\epsilon_r$	$\sigma$ (S/m)	$\epsilon_r$
920	0.7738	45.72	0.2452	16.59	0.0515	5.46	0.873	41.30
960	0.7886	45.57	0.2524	16.53	0.0525	5.45	0.886	41.11
1800	1.153	43.54	0.4317	15.56	0.0784	5.349	1.185	38.87
1900	1.2038	43.37	0.4561	15.46	0.0823	5.330	1.224	38.71
1965	1.2377	43.26	0.4720	15.40	0.0846	5.331	1.251	38.61
2000	1.2562	43.21	0.481	15.37	0.0859	5.327	1.265	38.56
2100	1.310	43.05	0.506	15.28	0.0898	5.317	1.308	38.43
2400	1.4814	42.62	0.5861	15.01	0.1023	5.285	1.441	38.06
5300	3.758	38.92	1.485	12.89	0.260	5.01	3.290	35.53

Hand model and dimension is shown in Fig.2. It is similar to a typical hand model used in the literature [5], [6]. The models consists of two tissues, bone surrounded by muscle. it modeled mainly the palm, while

the fingers were very short [Fig.2.a]. The model was symmetric, i.e., the short fingers wrapped both the chassis edges similarly, and the shape of the model was identical in all  $xy$  cuts.



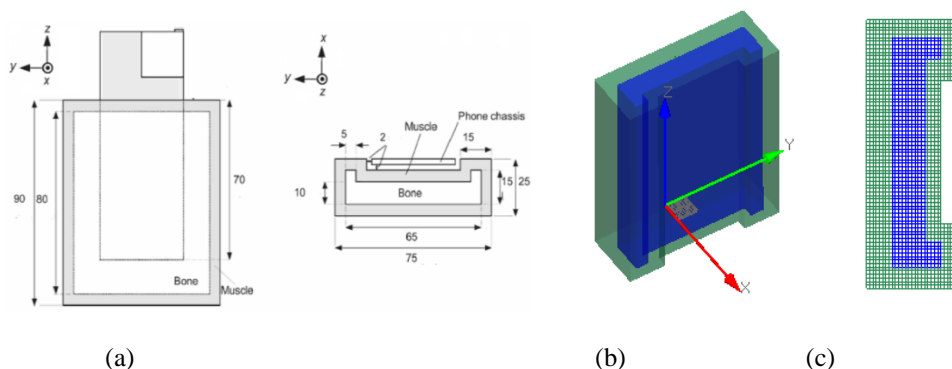


Fig.2: Hand Model: (a) dimensions and its position [5] (b) 3D-view, (c) Upper view

Table 2 presents values of relative permittivity, conductivity, and density of hand model tissues

Table 2: Relative Permittivity, Conductivity, and Mass Density Hand model tissues at several frequencies [5]

Frequency (MHz)	Bone		Muscle	
	$\rho = 1850kg / m^3$		$\rho = 1050kg / m^3$	
	$\sigma$ (S/m)	$\epsilon_r$	$\sigma$ (S/m)	$\epsilon_r$
920	0.3447	20.745	0.976	55.91
960	0.3542	20.663	0.991	55.82
1800	0.5882	19.341	1.389	54.44
1900	0.6198	19.213	1.448	54.30
1965	0.6407	19.13	1.487	54.21
2000	0.6521	19.086	1.509	54.17
2100	0.6851	18.963	1.572	54.035
2400	0.7875	18.61	1.775	53.64
5300	1.937	15.79	4.592	49.71

### 3. Results and Discussion

The chosen dual, triple, and quad-band PIFAs are analyzed at two positions as shown in Fig.3; at the position#1, the interaction between the antennas and the head model are simulated at the different distances ( $D=3mm$  and  $D=7mm$ ) to demonstrate the effect of the distance between the antenna and the head on the

amount of the interaction.

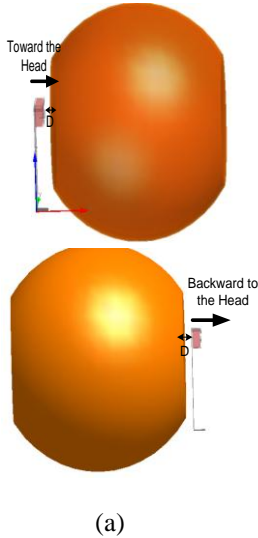


Fig.3:(a)-Antenna Positioned toward to spherical head model (position 1), (b) Antenna Positioned backward to spherical head model (position 2)

Fig.4 shows the simulated reflection coefficient of the dual-band PIFA in presence of human head and hand; the results show that in the lower and higher bands, this antenna haven't reach the impedance matching criteria ( $S_{11} < -6\text{dB}$ ) when antenna is positioned toward the head model (Position 1) and the antenna chassis surrounded by the hand model, and it works fine at the other cases. Fig.5 shows the simulated reflection coefficient of the studied triple-band PIFA at different simulation cases, the results describe the changing of return loss in vicinity of different head models and hand model at different position of the antenna, they show that when the antenna is positioned at  $D=3\text{mm}$  from the head model the return

loss is more affected than when the antenna is positioned at  $D=7\text{mm}$ , the effect on the amplitude of the  $S_{11}$  is changing from case to case and from band to band. In most cases, the second band of return loss curve is less affected than the other bands. This antenna will cover the operation at EGSM900 band only if the antenna installed at the backward position in mobile phone case, if it directed to the user it will work only at this band if the distance between antenna and the head is more than 7mm. At the second band the antenna doesn't meet the operation requirement of the GSM1900 (PCS) when the antenna is located in position 1 with  $D=3, 7\text{mm}$  from the head model and hand model is included in simulation. At the higher band (Bluetooth or WLAN802.11g), the antenna won't work properly; the simulation results show the antenna covers partially in some cases the frequency band of WLAN802.11g. The results of simulated reflection coefficient of the studied quad-band PIFA, shown in Fig.6, indicates that the antenna will not work in the lower band (EGSM900) because the bandwidth requirements at this band hasn't achieved. At the higher band the antenna covers the operation at (GSM 1800, GSM 1900, UMTS and Bluetooth or WLAN 802.11g); the GSM 1800 band is partially covered in some simulation cases. A good agreement is achieved between the different numerical techniques. Tables 3, 4, and 5 show the radiation efficiency of the studied antennas at different frequencies. The simulated radiation pattern of the studied antennas at different band in presence of the human head and hand models are shown in Figures 7-11.



Table 3: Radiation efficiency of dual-band antenna at different frequencies

Case	Freq.=920MHz	Freq.=1900MHz
Free Space	100%	100 %
Spherical Model at D=3mm (Position 1)	12 %	18.06 %
Spherical Model D=7mm (Position 1)	19.43 %	29.22%
Spherical Model with Hand D=3mm (Position 1)	9.36%	9.6 %
Spherical Model D=3mm (Position 2)	26.66 %	34.35 %
Spherical Model D=3mm (Position 2) with hand	5.07 %	7.07 %

Table 4: Radiation efficiency of triple-band PIF antenna at different frequencies

Case	920MHz	1900MHz	2400MHz
Free Space	<b>100%</b>	<b>100%</b>	<b>100 %</b>
Spherical at D=3mm (Position 1)	15.14%	24.94 %	14.57 %
Spherical D=7mm (Position 1)	24.07%	32.43 %	19.40 %
Spherical with Hand D=3mm (Position 1)	11.84%	11.33 %	12.13 %
Spherical D=3mm (Position 2)	29.92 %	38.13 %	63.82 %
Spherical D=3mm (Position 2) with hand	5.3 %	10.64 %	11.32 %

Table 5: Radiation efficiency of quad-band PIF antenna at different frequencies

Case	920MHz	1900MHz	2100MHz	2400MHz
Free Space	100%	100%	100%	100 %
Spherical at D=3mm (Pos # 1)	7.32 %	4.98 %	7.98 %	6.15 %
Spherical D=7mm (Pos # 1)	9.84 %	12.61 %	15.31%	25.68 %
Spherical with Hand D=3mm (Pos# 1)	7.41%	2.62 %	3.49 %	3.52 %
Spherical D=3mm (Pos # 2)	33 %	33.51 %	44.77%	60.63 %
Spherical D=3mm (Pos# 2) with hand	9.89 %	26.45%	38.12 %	51.22 %

The radiation efficiency of the studied antennas are assumed to be 100% in free space; so the effect of presence of human head and hand on the radiation efficiency of the antennas can be demonstrated. The results show that the antenna's efficiency degrades highly in presence of the head and hand models in position#1. In position#2, the antennas have a better performance in case of presence the head model only

except in the case of quad-band antenna. The results also indicate that the back-radiation amounts of the studied antennas are quite similar. The gain of the studied antennas reduces in presence of the human head and hand models. The amount of reduction is different from case to case and from band to band as can be seen from the simulated gain radiation pattern figures.



#### 4. Conclusion

This paper studies the performance of the multi-band PIFAs in the presence of the human head and hand. The study shows that the reflection coefficient, antenna's gain, and the radiation efficiency are highly affected by the presence of human head and hand. The radiation efficiency and the antenna's gain are more affected than the input reflection coefficient. The degradation of the radiation efficiency and the reduction of the PIFA's gain depend on the distance between the antenna and the head, the position of the antenna on the mobile phone chassis, and the position of the hand on the mobile phone chassis. The results show a good agreement between the used numerical techniques.

#### 5. References

- [1] M. Elmansouri, "Interaction between Human Head and Modern Cellular Communication Systems Antennas" master's thesis, Dept. Electrical and Electronic Eng., Al-Fatah University, 2008.
- [2] D. Sim and Seong-Ook, "A Triple Band Internal Antenna: Design and performance in Presence of the Handset Case, Battery, and Human Head" *IEEE Transactions on Antennas and Propagation*, Vol.47 No.3 pp.658-666 August 2005.
- [3] Y. Xin Guo, M.Y.W.Chia and Z.N.Chen "Miniature Built-In Quad-Band Antennas for Mobile Handsets" *IEEE Antennas and Wireless Propagation Letters*, Vol.52, No.8 ,pp 1936-1944 ,August 2004.
- [4] Y. Xin Guo, and M.Y.W.Chia "Compact Internal Multiband Antennas for Mobile Handsets" *IEEE Antennas and Wireless Propagation Letters*, Vol.2, pp143-146 ,2003.
- [5] M. Popovi'c., Q. Han, and H. Kanj, "A parallel study of SAR levels in head tissues for three antennas used in cellular telephones: monopole, helix and patch," *Springer Earth and Environmental Science*, Vol. 25, No. 2-4, 215-221, December 2005.
- [6] M. A. Jensen and Y. Rahmat-Samii, "EM interaction of handset antennas and a human in personal communications," *IEEE Transactions on Antennas and Propagation*., vol. 83, pp.7-17, Jan. 1995.
- [7] J. T. Rowley and R. B. Waterhouse, "Performance of shorted microstrip patch antennas for mobile communications handsets at 1800 MHz," *IEEE Transactions on Antennas and Propagation*., vol. 47, pp. 815-822, May 1999.

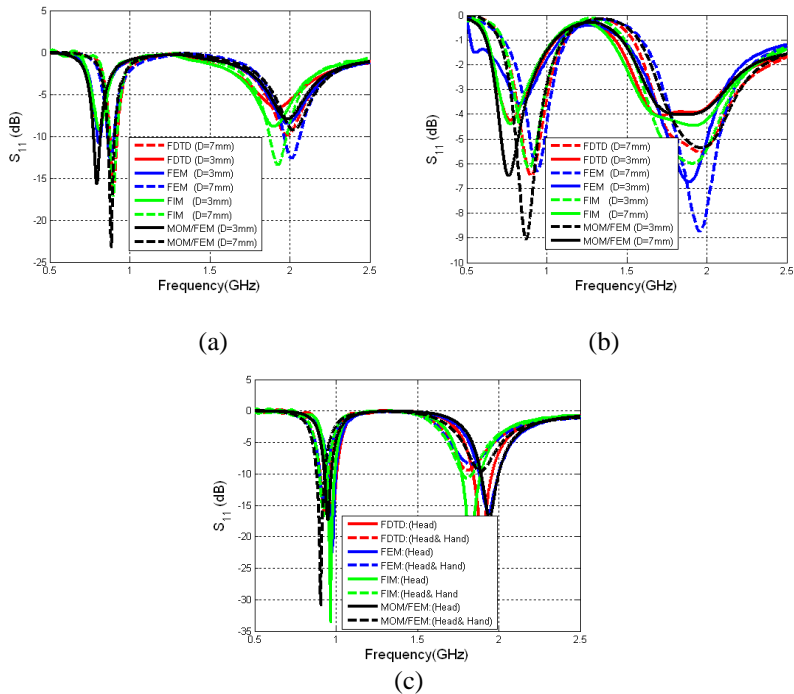
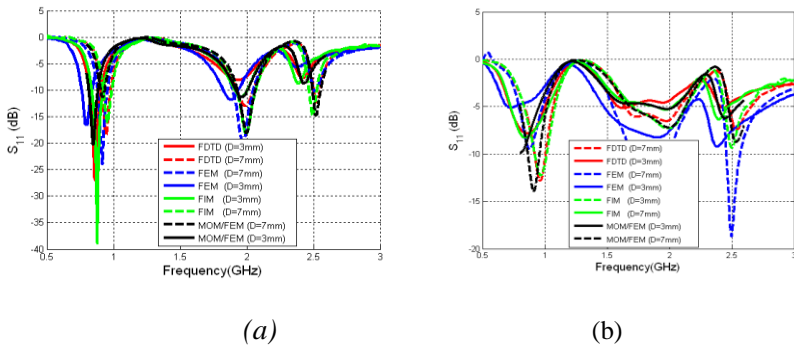


Fig.4: Simulated Return Loss of studied dual-band PIFA in (a)- presence of spherical model of human head only (position1), (b)- in presence of spherical model of human head (position1) and simple hand model, and (c)- in presence of spherical model of human head (position2) and simple hand model at  $D = 3\text{mm}$ . ((Head only): solid line, (Head & Hand): dashed line).



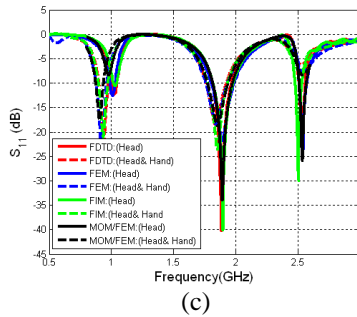
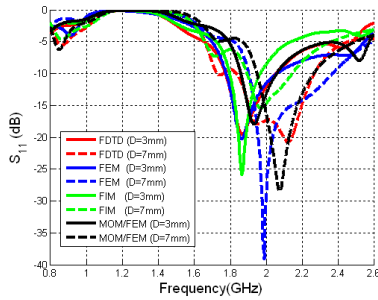
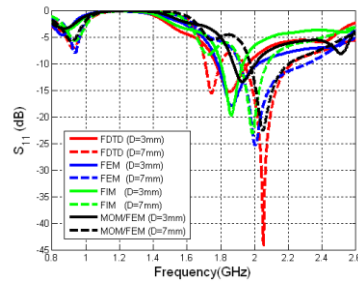


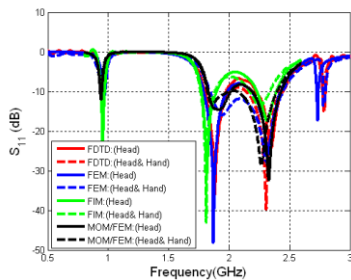
Fig.5: Simulated Return Loss of studied triple-band PIFA in (a)- presence of spherical model of human head only (position1), (b)- in presence of spherical model of human head (position1) and simple hand model, and (c)- in presence of spherical model of human head (position2) and simple hand model at  $D = 3\text{mm}$ . ((Head only): solid line, (Head & Hand): dashed line).



(a)

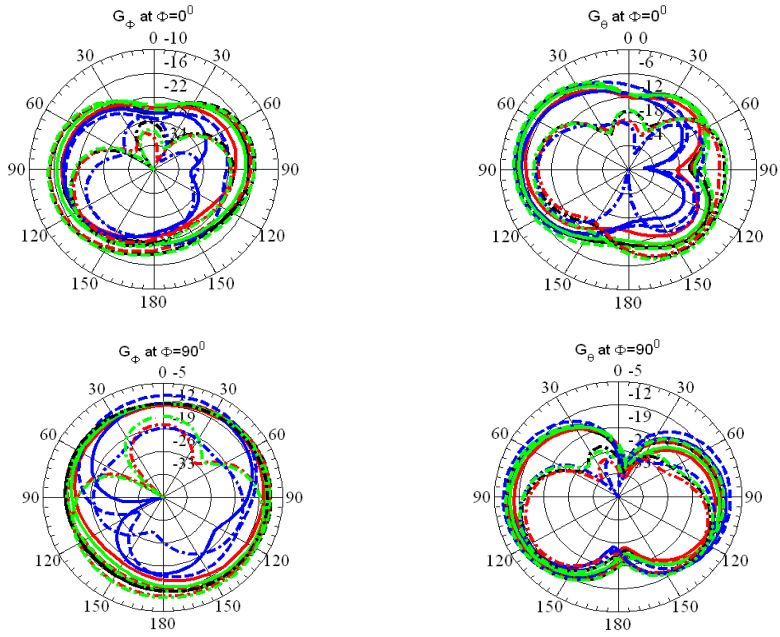


(b)

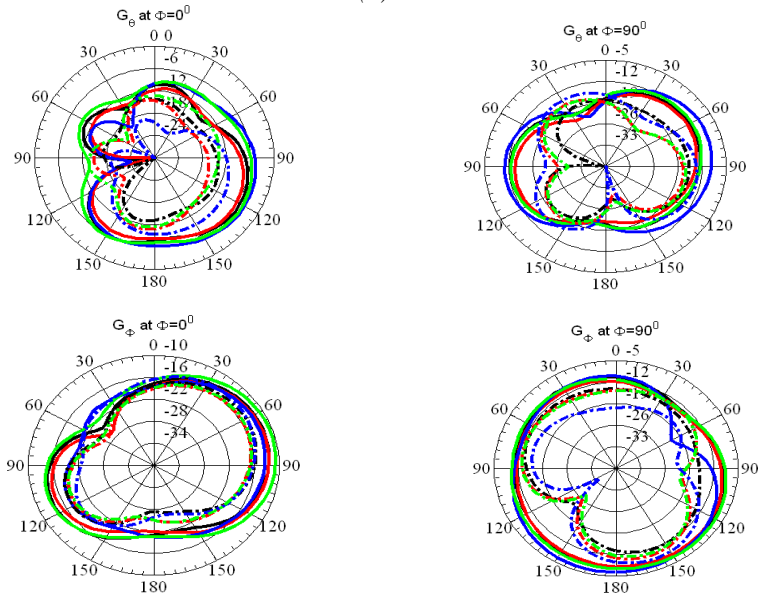


(c)

Fig.6: Simulated Return Loss of studied quad-band PIFA in (a)- presence of spherical model of human head only (position1), (b)- in presence of spherical model of human head (position1) and simple hand model, and (c)- in presence of spherical model of human head (position2) and simple hand model at  $D = 3\text{mm}$ . ((Head only): solid line, (Head & Hand): dashed line).



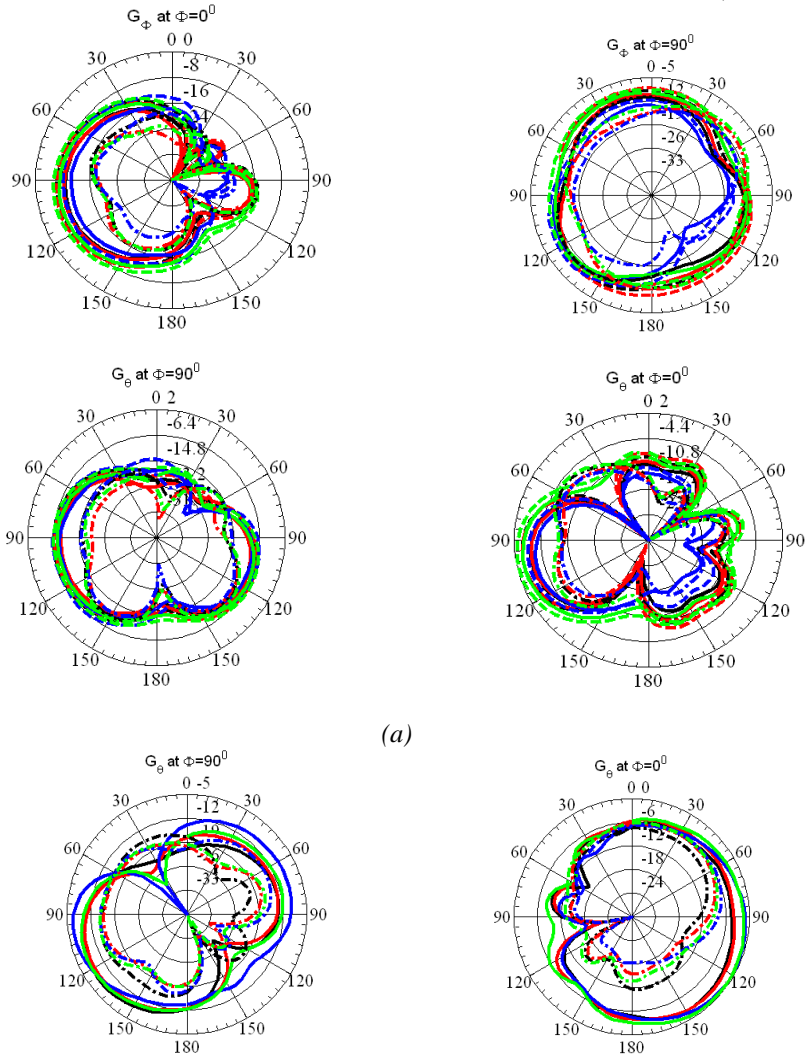
(a)



(b)

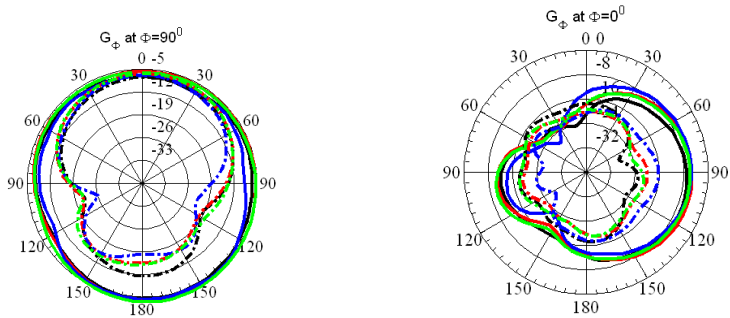


Fig.7: simulated radiation pattern ( $G_\theta$ ,  $G_\phi$ ) at  $\phi = 0^\circ$  (x-z) plane and  $\phi = 90^\circ$  (y-z) plane of the dual-band PIFA at frequency=920MHz, (solid line) : 3mm from spherical head model ((a)-position 1, (b)-position 2), (dashed-dotted line (-.-)) :3mm from spherical head model ((a)-position 1, (b)-position 2)in presence of hand model. (red line :FDTD, blue line : FEM , Green line :FIM, Black line :MOM/FEM)



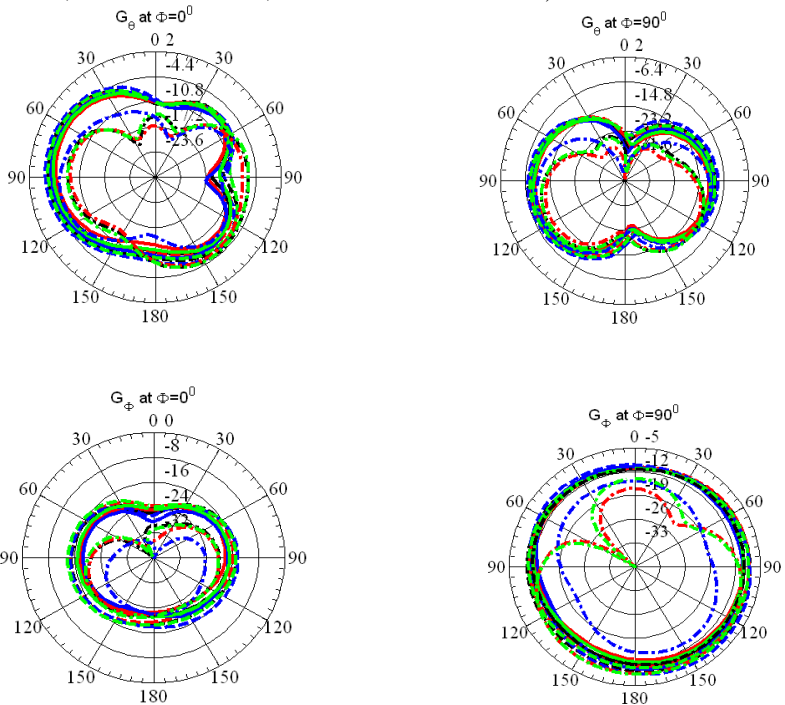
(a)



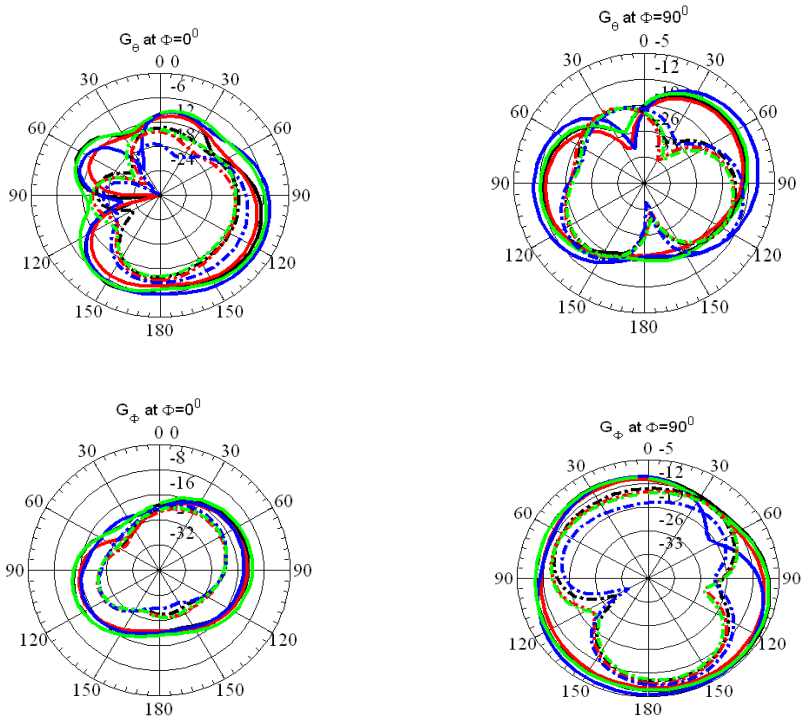


(b)

Fig.8: simulated radiation pattern ( $G_\theta, G_\phi$ ) at  $\phi = 0^\circ$  (x-z) plane and  $\phi = 90^\circ$  (y-z) plane of the dual-band PIFA at frequency=1900MHz, (solid line) : 3mm from spherical head model ((a)-position 1, (b)-position 2), (dashed-dotted line (-.)) :3mm from spherical head model ((a)-position 1, (b)-position 2)in presence of hand model. (red line :FDTD, blue line: FEM , Green line :FIM, Black line :MOM/FEM)

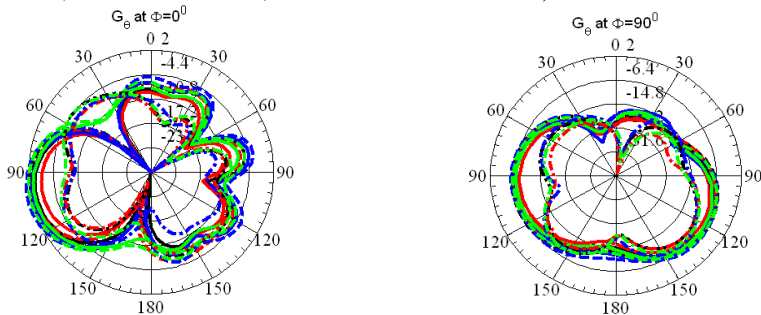


(a)



(b)

Fig.9: simulated radiation pattern ( $G_\theta, G_\phi$ ) at  $\phi = 0^\circ$  (x-z) plane and  $\phi = 90^\circ$  (y-z) plane of the triple-band PIFA at frequency=920MHz, (solid line) : 3mm from spherical head model ((a)-position 1, (b)-position 2), (dashed-dotted line (-.)) :3mm from spherical head model ((a)-position 1, (b)-position 2)in presence of hand model. (red line :FDTD, blue line: FEM , Green line :FIM, Black line :MOM/FEM)



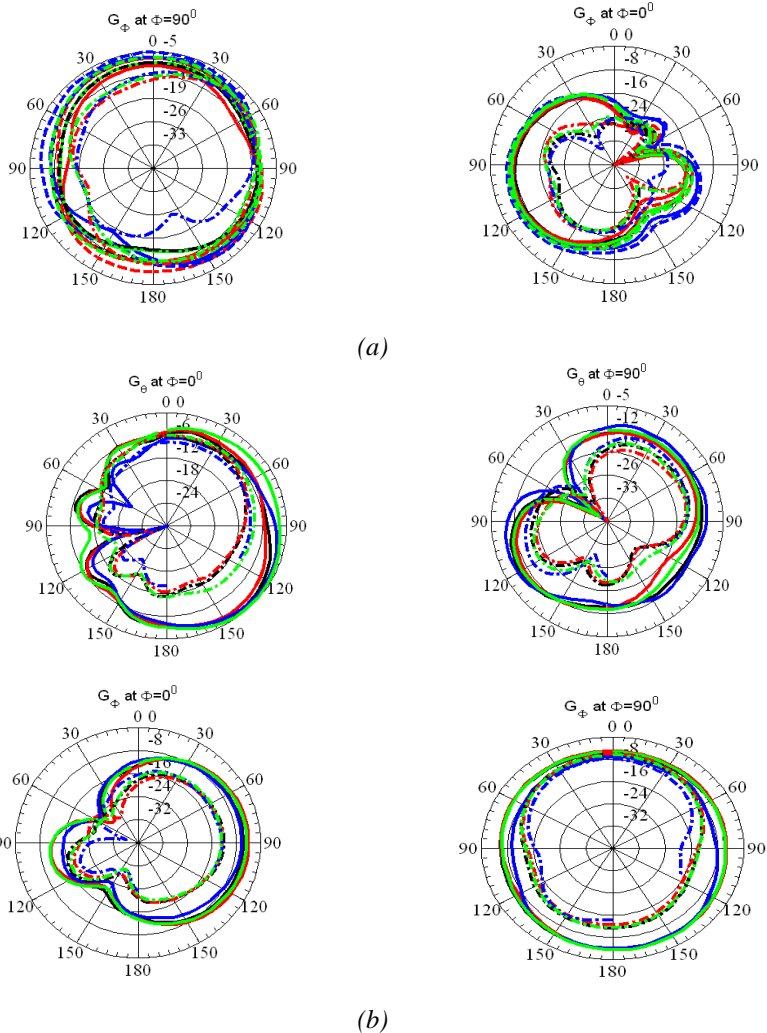
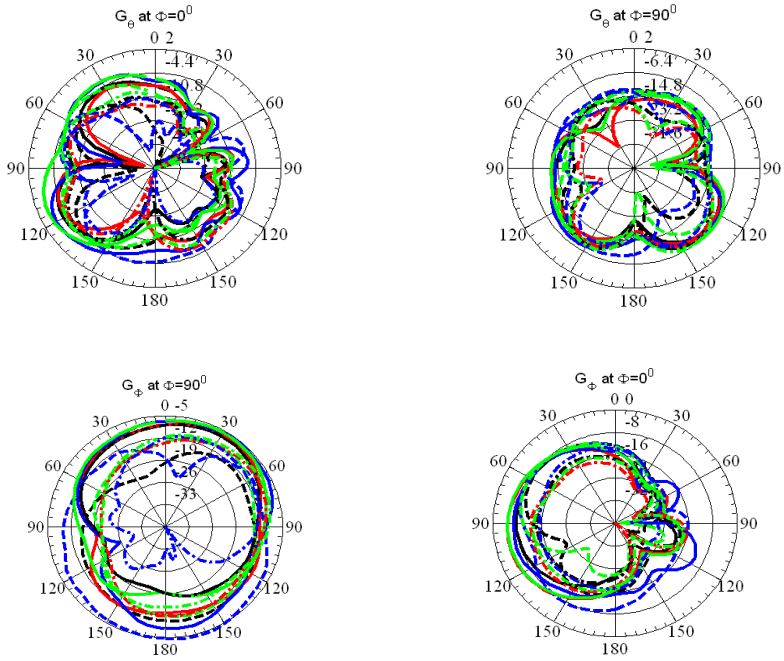
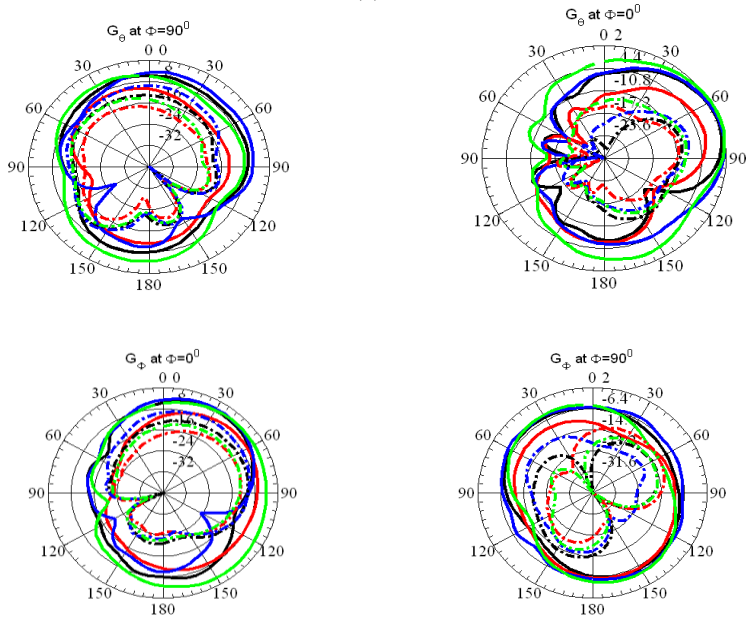


Fig.10: simulated radiation pattern ( $G_{\theta}$ ,  $G_{\phi}$ ) at  $\phi = 0^{\circ}$  (x-z) plane and  $\phi = 90^{\circ}$  (y-z) plane of the triple-band PIFA at frequency=1900MHz, (solid line) : 3mm from spherical head model ((a)-position 1, (b)-position 2), (dashed-dotted line (-.)) :3mm from spherical head model ((a)-position 1, (b)-position 2)in presence of hand model. (red line :FDTD, blue line: FEM , Green line :FIM, Black line :MOM/FEM)



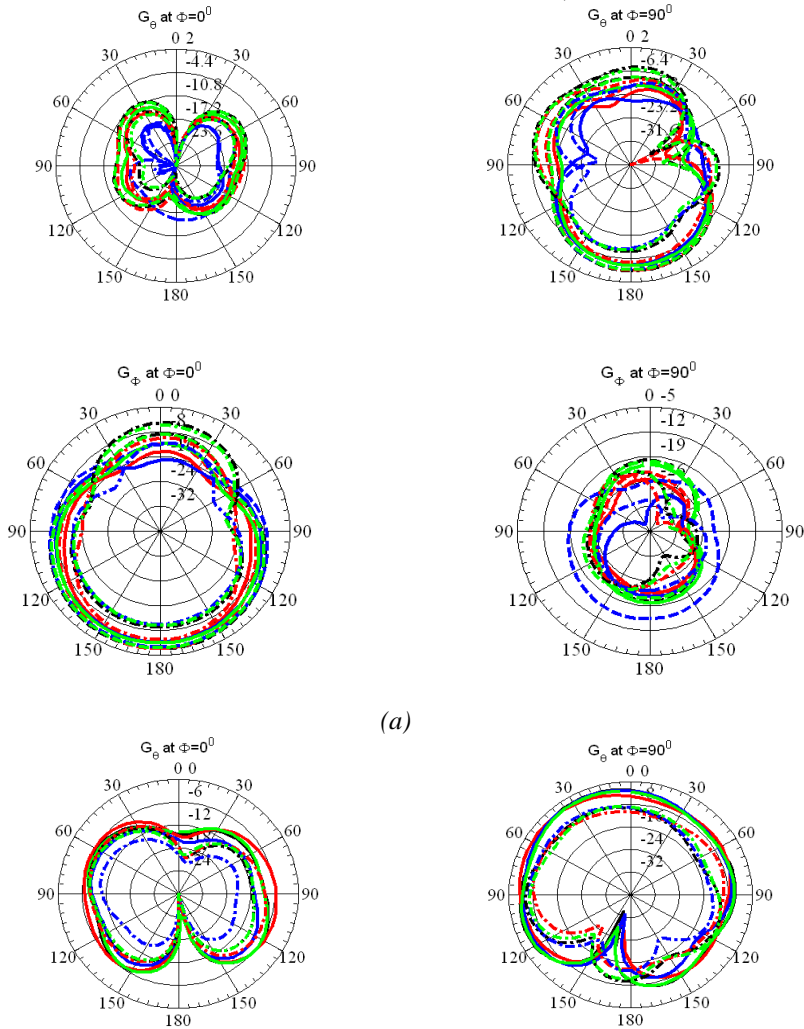
(a)

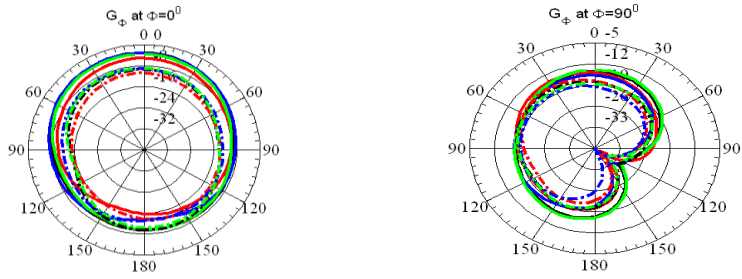


(b)



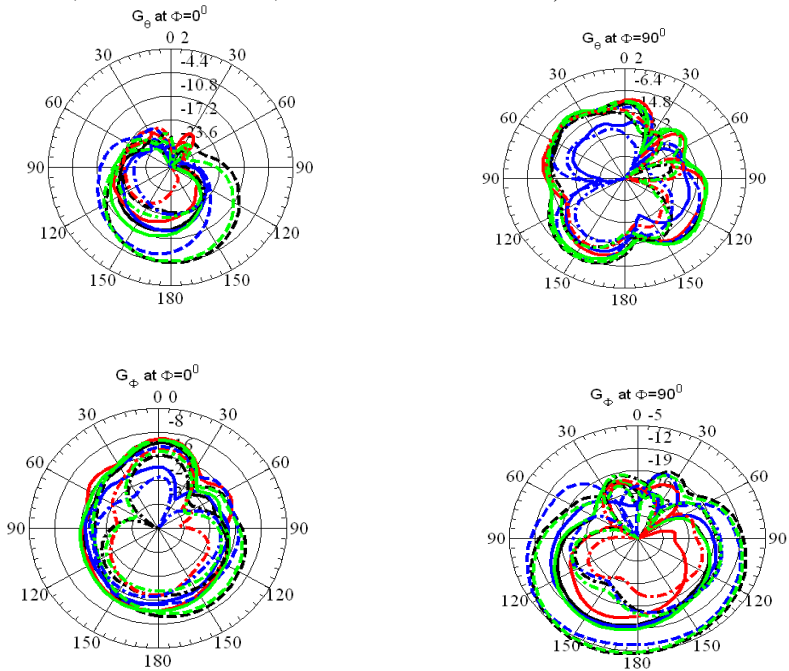
Fig.11: simulated radiation pattern ( $G_\theta, G_\phi$ ) at  $\phi = 0^\circ$  (x-z) plane and  $\phi = 90^\circ$  (y-z) plane of the triple-band PIFA at frequency=2400MHz, (solid line) : 3mm from spherical head model ((a)-position 1, (b)-position 2), (dashed-dotted line (-.)) :3mm from spherical head model ((a)-position 1, (b)-position 2)in presence of hand model. (red line :FDTD, blue line: FEM , Green line :FIM, Black line :MOM/FEM)





(b)

Fig.12: simulated radiation pattern ( $G_\theta, G_\phi$ ) at  $\phi = 0^\circ$  (x-z) plane and  $\phi = 90^\circ$  (y-z) plane of the quad-band PIFA at frequency=920MHz, (solid line) : 3mm from spherical head model ((a)-position 1, (b)-position 2), (dashed-dotted line (-.)) :3mm from spherical head model ((a)-position 1, (b)-position 2)in presence of hand model. (red line :FDTD, blue line: FEM , Green line :FIM, Black line :MOM/FEM)



(a)

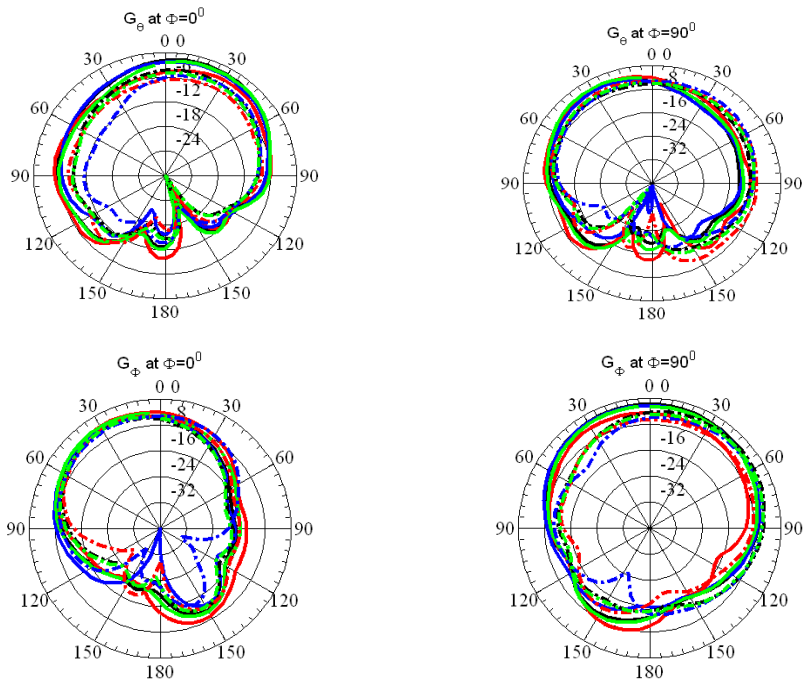
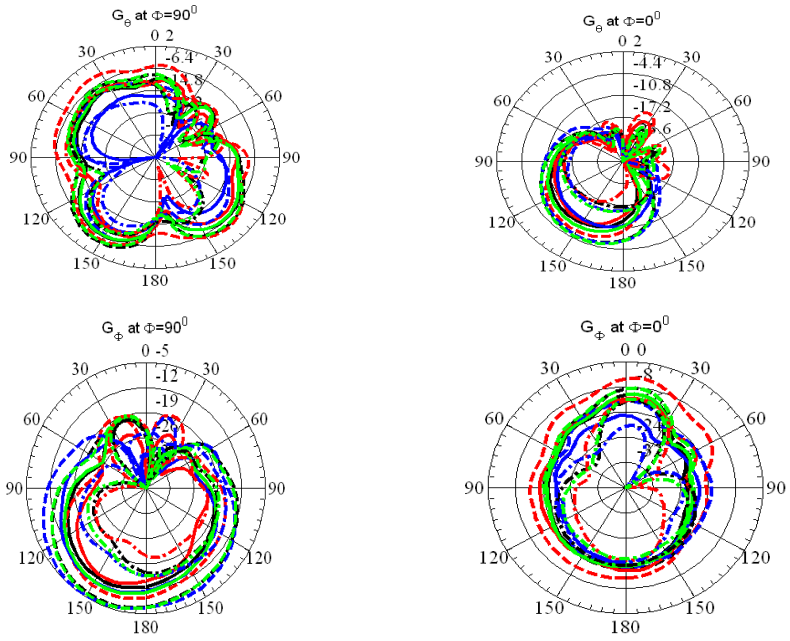
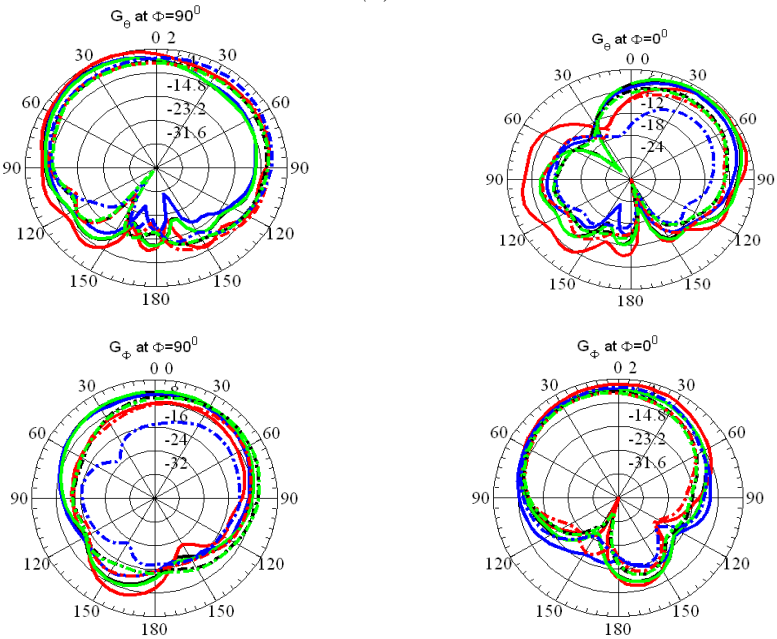


Fig.13: simulated radiation pattern ( $G_\theta$ ,  $G_\phi$ ) at  $\phi = 0^\circ$  (x-z) plane and  $\phi = 90^\circ$  (y-z) plane of the quad-band PIFA at frequency=1900MHz, (solid line) : 3mm from spherical head model ((a)-position 1, (b)-position 2), (dashed-dotted line (-)) : 3mm from spherical head model ((a)-position 1, (b)-position 2)in presence of hand model. (red line :FDTD, blue line: FEM , Green line :FIM, Black line :MOM/FEM).



(a)

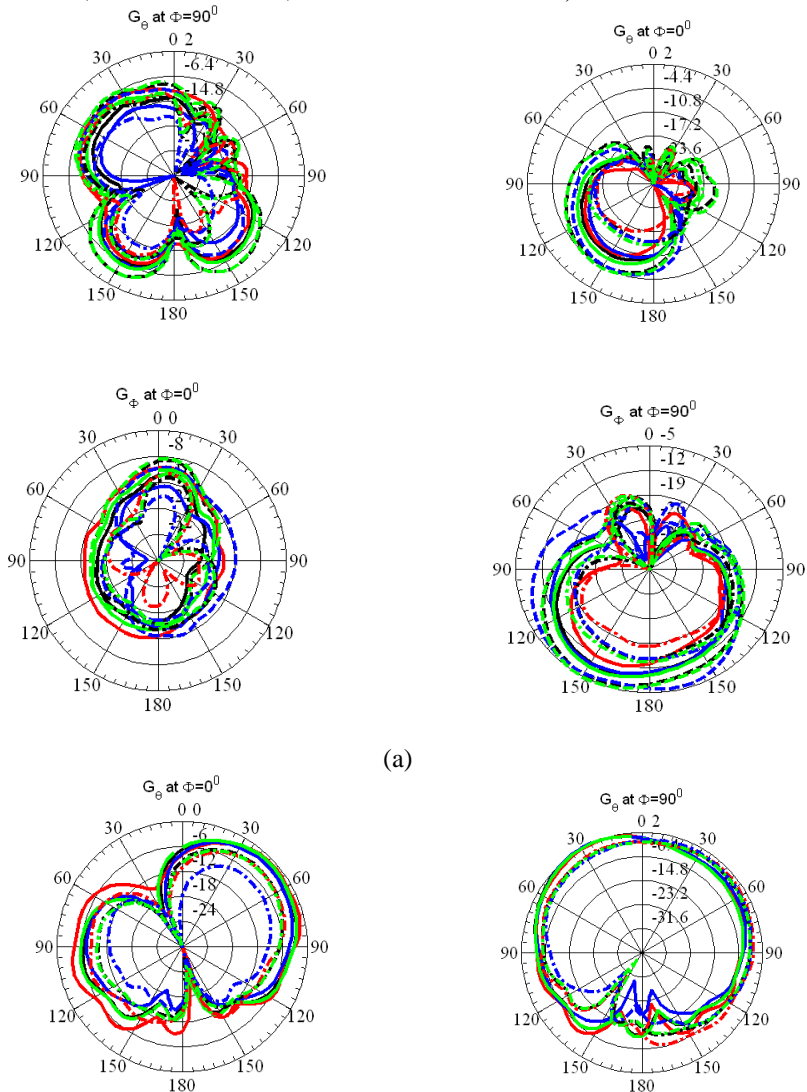


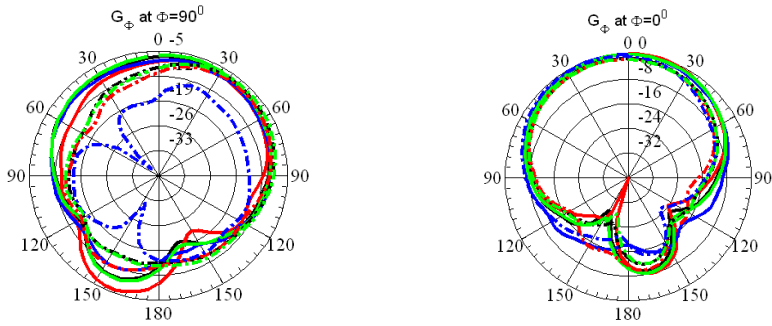
(b)





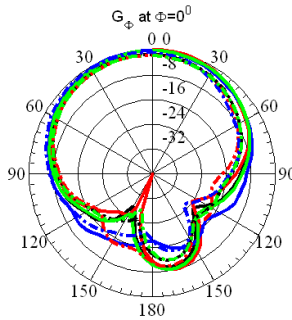
Fig.14: simulated radiation pattern ( $G_\theta, G_\phi$ ) at  $\phi = 0^\circ$  (x-z) plane and  $\phi = 90^\circ$  (y-z) plane of the quad-band PIFA at frequency=2100MHz, (solid line) : 3mm from spherical head model ((a)-position 1, (b)-position 2), (dashed-dotted line (-.)) :3mm from spherical head model ((a)-position 1, (b)-position 2)in presence of hand model. (red line :FDTD, blue line: FEM , Green line :FIM, Black line :MOM/FEM)





(b)

Fig.15: simulated radiation pattern ( $G_\theta, G_\phi$ ) at  $\phi = 0^\circ$  (x-z) plane and  $\phi = 90^\circ$  (y-z) plane of the quad-band PIFA at frequency=2100MHz, (solid line) : 3mm from spherical head model ((a)-position 1, (b)-position 2), (dashed-dotted line (-.)) :3mm from spherical head model ((a)-position 1, (b)-position 2)in presence of hand model. (red line :FDTD, blue line: FEM , Green line :FIM, Black line :MOM/FEM)



(b)

Fig.15: simulated radiation pattern ( $G_\theta, G_\phi$ ) at  $\phi = 0^\circ$  (x-z) plane and  $\phi = 90^\circ$  (y-z) plane of the quad-band PIFA at frequency=2400MHz, (solid line) : 3mm from spherical head model ((a)-position 1, (b)-position 2), (dashed-dotted line (-.)) :3mm from spherical head model ((a)-position 1, (b)-position 2)in presence of hand model. (red line :FDTD, blue line: FEM , Green line :FIM, Black line :MOM/FEM)



# Study of the Performance of Multi-Band Planar Inverted F (PIF) Antennas in Free Space Using Computational Electromagnetic Methods

Mohamed A. Elmansouri<sup>(1)</sup>, and Ibrahim M. Saleh\*<sup>(1)</sup>

(1) Electrical and Electronic Engineering Department  
Al-Fateh University, Tripoli, Libya

E-mail: mansori82@yahoo.com, Ibrahim.saleh@ltnet.net

## Abstract

In this paper, the performance of dual, triple, quad, and hexa -band PIFAs have been evaluated in free space using four different full-wave electromagnetic numerical techniques. The impedance matching bandwidth, radiation pattern, and gain of these antennas have been computed using FDTD, FIM, FEM, and MOM. The results are compared with the published measured results to check the accuracy of the simulations.

**Key words:** antenna performance, radiation, computational electromagnetic

## 1. Introduction

Recently, the planar inverted F antenna (PIFA) has been widely used as mobile phone antenna because the advantages that it has over the other kinds of the cellular phone antennas. PIFAs offer two major advantages: They are easy to place fully within the housing of a mobile phone, and have reduced backward radiation towards the user's head. Other advantageous features of PIFAs are the inexpensive manufacturing, simplicity in structure and low profile. Also, no additional matching networks are needed because the matching is achieved by varying the feed location and the length of the patch, and multi-band operation can be achieved by including certain considerations in the antenna design. This paper investigates modern multi-band PIFAs introduced in [1],[2],[3], and[4] in

term of impedance matching bandwidth and return loss, gain and radiation pattern using Finite Difference Time Domain Method (FDTD) [5,6], Finite Element Method(FEM) [7,8], Finite Integration Method (FIM) [9,10], and Method of Moments (MOM) [11,12]. The simulation results are compared to measurement results to demonstrate the abilities of these methods to solve and simulate this kind of antenna geometry.

## 2. Studied Antennas' Geometries

Fig.1.a describes the dual-band PIFA structure. The antenna comprises a folded radiating patch in the first layer, a ground plane in the second layer, a supporting foam in-between, a short circuited strip, and a feed strip. The patch is connected to the ground plane via a vertical short-circuited strip and is fed via a feed strip connected to a 50  $\Omega$  transmission line etched on the back



of the ground plane. The folded PIFA is spaced from the ground plane by a dielectric substrate of foam. At the first layer, the long bent portion of the antenna is tuned to have a relatively low band resonance frequency, such as 900 MHz, and the short part of the antenna is tuned to have a high band resonance frequency, such as 1800 MHz. The ground plane has dimensions of length 80 mm, and width 36 mm. The dielectric constant of foam is around 1.07. The dimensions of the dual band antenna are

$$L_1 = 36mm, L_2 = 15mm, L_3 = 15mm,$$

$$g_1 = 2mm, g_2 = 1mm, W_1 = 16mm,$$

$$W_2 = W_3 = W_4 = W_5 = W_6 = W_7 = W_8 = 4mm,$$

$$W_f = W_s = 3mm, d_1 = 7mm,$$

$H = 8mm$  [1]. Fig.1.b depicts the studied triple-band PIFA, the antenna is mounted on a ground plane of dimensions 80 mm x 36 mm. The antenna comprises a main plate in the top layer, a ground plane in the bottom layer, two folded arms in-between, a short-circuited strip, and a feed strip. The structure is supported by foam. The main plate is directly shorted to the ground plane by means of the shorting strip and fed via a feed strip connected to a 50Ω transmission line etched on the back of the ground plane. A rectangular slit is made in the main patch to divide it into two parts so as to generate a dual-frequency characteristic. By adding only arm 2 triple band operation can be achieved. The antenna has dimensions of

$$L_1 = L_{31} = 36mm, L_{11} = 1mm,$$

$$L_{21} = 33mm, W_1 = 16mm,$$

$$W_{11} = 11mm, W_{21} = 7mm,$$

$$W_{12} = W_{32} = 3mm, G_{11} = 2mm,$$

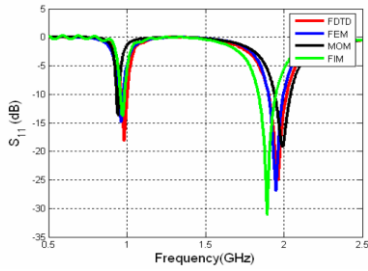
$$H = 9mm, H_{31} = 4mm, D_1 = 1mm,$$

$$D_2 = 2mm, F_1 = 9mm$$
 the widths of shorting pin and feed strip are 3mm [2].

The quad-band PIF antenna photo and its dimensions are shown in Fig.1.c. The radiating element is mounted on a ground plane of size 40 mm x 110 mm. The thicknesses of the radiating element and the ground plane are 0.2 mm and 0.3 mm, respectively. The narrower parasitic patch is shorted with a strip of thickness 0.2 mm, the width being the same as the width of the parasitic patch: 2 mm. The other two shorting strips have thicknesses of 0.5 mm. The capacitive load of the driven patch has the height of 5 mm, and the capacitive load of the narrow parasitic patch is 4 mm high. The widths coincide with the widths of the patches where the vertical capacitive loads are added. The substrate is an air layer with a thickness 7.0 mm [3]. The hexa-band antenna for DCS/PCS/IMT2000/UMTS/ISM/WLAN applications is shown in Fig.1.d. The overall size of the radiating element with a thickness of 0.2 mm and made entirely of metal is  $19 \times 10 \times 5mm^3$ . It is installed on a FR ( $\epsilon_r = 4.6$ ) substrate with volume of

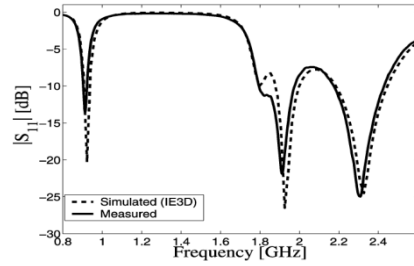
$45 \times 70 \times 1mm^3$ , which is considered to be the ground plane of a practical mobile handset. A 50Ω coaxial line is used to feed the antenna. Specifically, two folded feed lines are placed between the radiator patch and the feed point. The optimized height of the proposed antenna is 5 mm, which is suitable for practical mobile handsets. The dimensions are shown in Fig.1.d. In addition, the design parameters are  $L_1 = 3mm, L_2 = 7.9mm, L_3 = 5mm, L_4 = 4.8mm, L_5 = 10mm, L_6 = 5mm, L_7 = 14mm, L_8 = 29mm, W_1 = 6.2mm,$



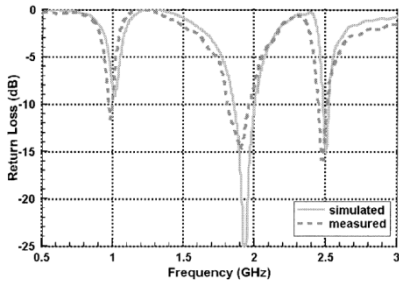


(b)

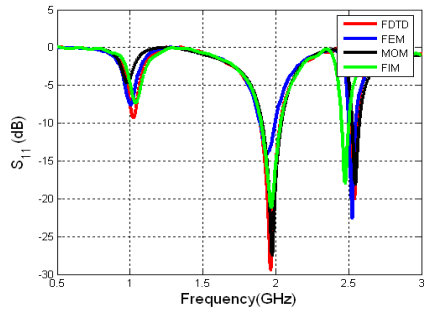
Fig.2: (a) Measured [1] and (b) simulated return loss results of the dual-band PIFA



(a)

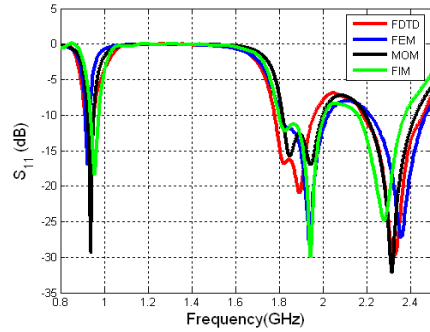


(a)



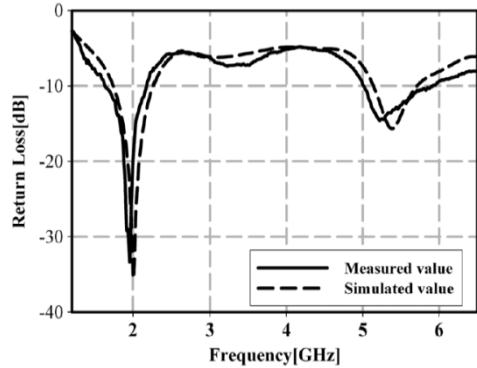
(b)

Fig.3: (a) Measured [2] and (b) simulated return loss results of the triple-band PIFA



(b)

Fig.4: (a) Measured [3] and (b) simulated return loss results of the quad-band PIFA



(a)

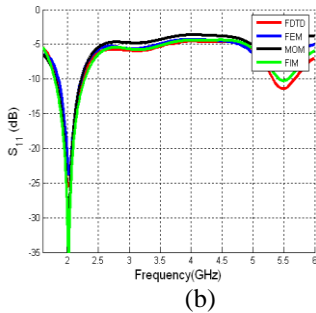
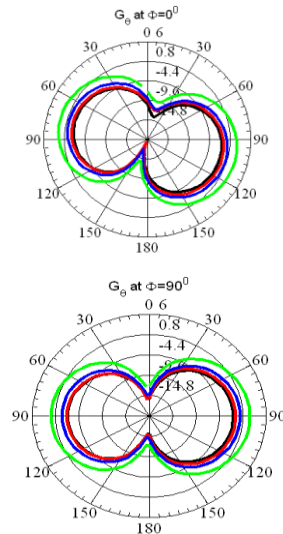


Fig.5: (a) Measured [4] and (b) simulated return loss results of the hexa-band PIFA

The measured bandwidths for -6 dB return-loss are 76 MHz (942–1018 MHz) for the lower band and 239 MHz (1752–1991 MHz) for the upper band for the dual-band PIFA. For the triple-band PIFA, the measured bandwidths are 68 MHz (945–1013 MHz) at the low band, 260 MHz (1765–2025 MHz) at the first high band, and 130 MHz (2420–2550MHz) at the second high band. The measured impedance bands with -6dB matching criteria are 893–933 MHz (bandwidth 43 MHz) and 1.765–2.508 GHz (bandwidth 743 MHz); the higher frequency band covers the PCS (1880–1990 MHz), UMTS (1900–2200 MHz), and ISM (2400–2480 MHz) bands. For the hexa-band PIFA the measured bandwidth ( $S_{11} < -6$  dB) is about 32% from 1.6 to 2.21 GHz at the lower frequency band covering the DCS (1710–1880 MHz), PCS (1750–1870 MHz), IMT-2000 (1885–2200 MHz), and UMTS (1920–2170 MHz) bands. Also, for the higher resonance frequency (5.3 GHz), the measured impedance bandwidth is enough to cover the required operating bandwidths of the ISM (5725–5850 MHz) and WLAN (5150–5875 MHz) bands. A satisfactory agreement between

the measurements and simulations has been achieved. The used numerical methods show similar performance especially at low frequency band where an excellent agreement has been achieved. The radiation pattern of the studied antennas at x-z and y-z planes for different operation bands are shown in Figures 6,7,8 and 9. The FDTD (red curves), FEM (blue curves), FIM (green curves), and MOM (black curves) show an excellent agreement in the most cases. The maximum realized gain of the dual-band antenna at  $f = 920$  MHz is 1dB, and 2.7 dB at  $f = 1900$  MHz. For the triple-band PIFA, the maximum simulated gain of the antenna at  $f = 920$  MHz is about 1 dBi, at  $f = 1900$  MHz is 3dBi and at  $f = 2400$  MHz is 5 dBi. The maximum simulated gain of the quad-band PIFA at  $f = 920$  MHz is about 5.4dBi, at  $f = 1900$  MHz is 3dBi, at  $f = 2100$  MHz is 4 dBi and at  $f = 2400$  MHz is 5 dBi, and it is at  $f = 1900$  MHz is 4dBi, at  $f = 2000$  MHz is 2dBi, and at  $f = 5300$  MHz is 5 dBi for the hexa-band PIFA.



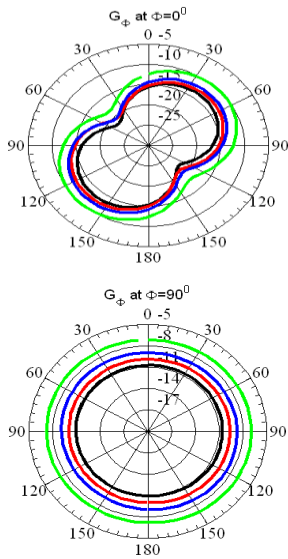


Fig.6.a : Simulated radiation pattern ( $G_\theta, G_\phi$ ) at  $\phi = 0^\circ$  (x-z) plane and  $\phi = 90^\circ$  (y-z) plane of the dual-band PIFA at frequency=920MHz

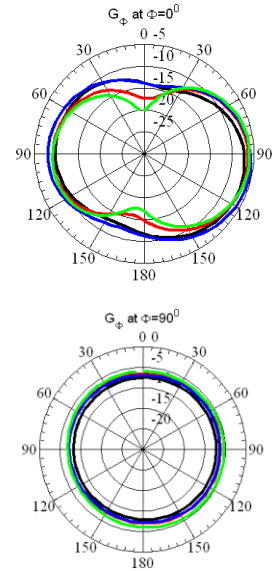
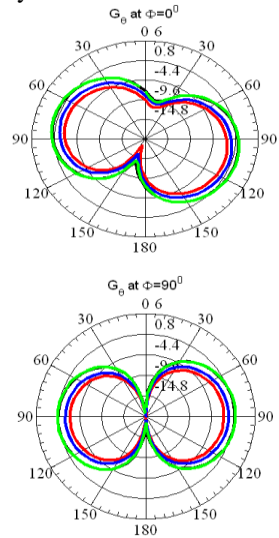
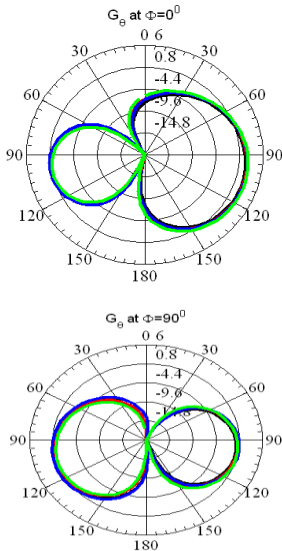


Fig.6.b: simulated radiation pattern ( $G_\theta, G_\phi$ ) at  $\phi = 0^\circ$  (x-z) plane and  $\phi = 90^\circ$  (y-z) plane of the dual-band PIFA at frequency=1900MHz





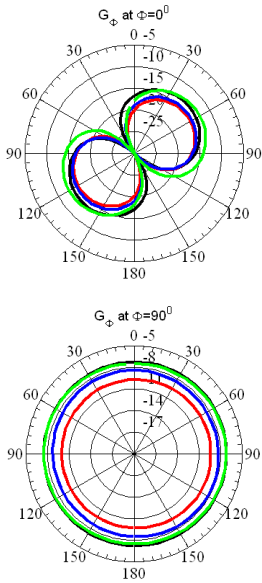


Fig.7.a: simulated radiation pattern ( $G_{\theta}, G_{\phi}$ ) at  $\phi = 0^{\circ}$  (x-z) plane and  $\phi = 90^{\circ}$  (y-z) plane of the triple-band PIFA at frequency=920MHz

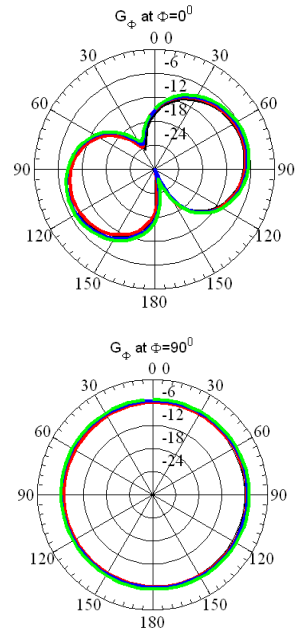
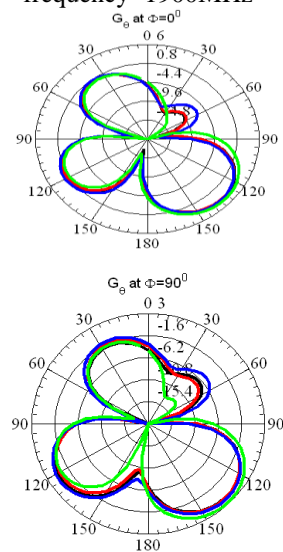
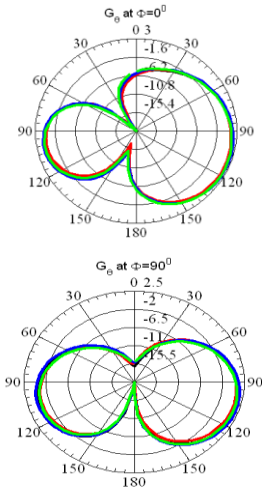


Fig.7.b: Simulated radiation pattern ( $G_{\theta}, G_{\phi}$ ) at  $\phi = 0^{\circ}$  (x-z) plane and  $\phi = 90^{\circ}$  (y-z) plane of triple-band PIFA at frequency=1900MHz



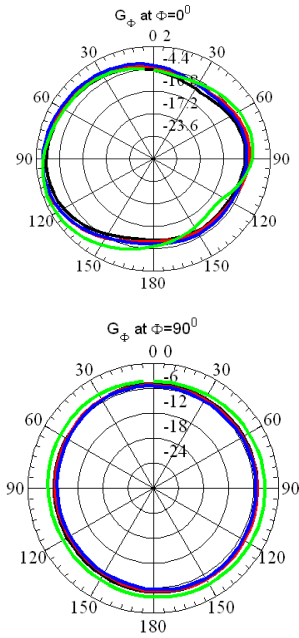


Fig. 7.c: Simulated radiation pattern ( $G_{\theta}$ ,  $G_{\phi}$ ) at  $\phi = 0^{\circ}$  (x-z) plane and  $\phi = 90^{\circ}$  (y-z) plane of triple-band PIFA at frequency=2400MHz

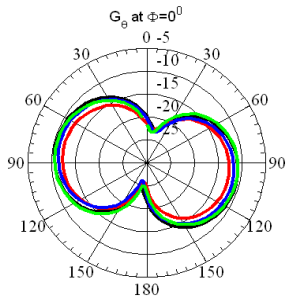
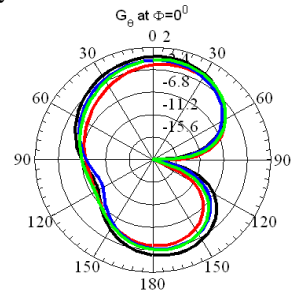


Fig.8.a: Simulated radiation pattern ( $G_{\theta}$ ,  $G_{\phi}$ ) at  $\phi = 0^{\circ}$  (x-z) plane and  $\phi = 90^{\circ}$  (y-z) plane of quad-band PIFA at frequency=920MHz



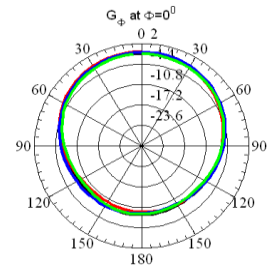
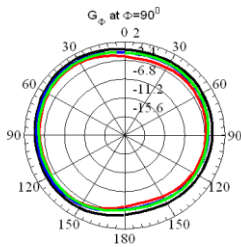
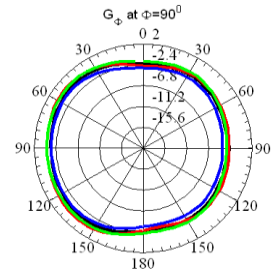
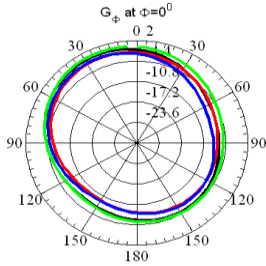
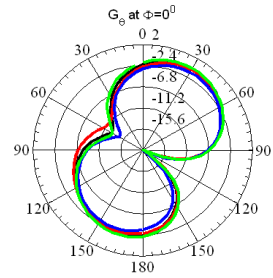
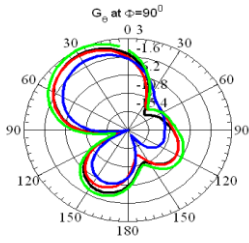
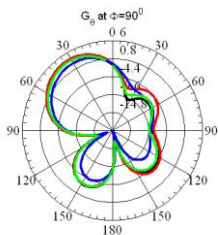


Fig.8.b: Simulated radiation pattern ( $G_{\theta}$ ,  $G_{\phi}$ ) at  $\phi = 0^{\circ}$  (x-z) plane and  $\phi = 90^{\circ}$  (y-z) plane of quad-band PIFA at frequency=1900MHz

Fig.8.c: Simulated radiation pattern ( $G_{\theta}$ ,  $G_{\phi}$ ) at  $\phi = 0^{\circ}$  (x-z) plane and  $\phi = 90^{\circ}$  (y-z) plane of quad-band PIFA at frequency=2100MHz



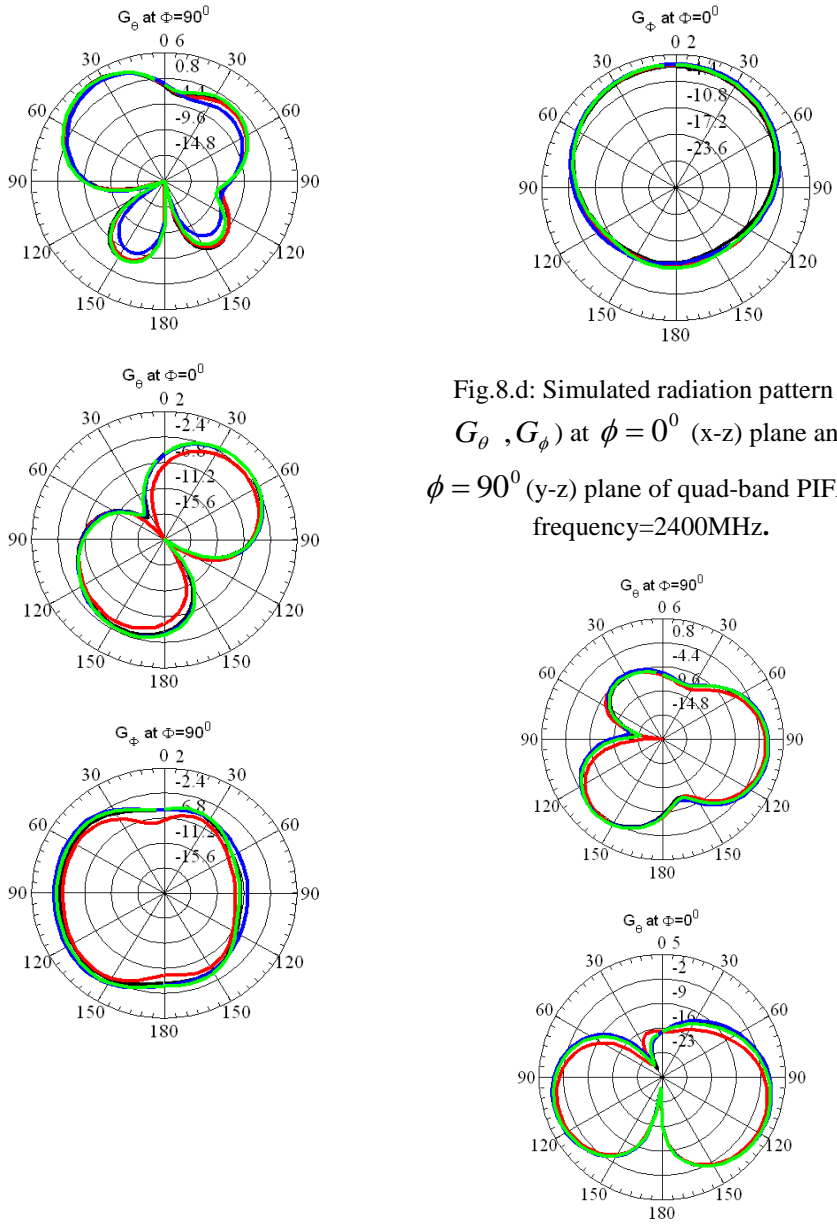


Fig.8.d: Simulated radiation pattern ( $G_\theta$ ,  $G_\phi$ ) at  $\phi = 0^\circ$  (x-z) plane and  $\phi = 90^\circ$  (y-z) plane of quad-band PIFA at frequency=2400MHz.

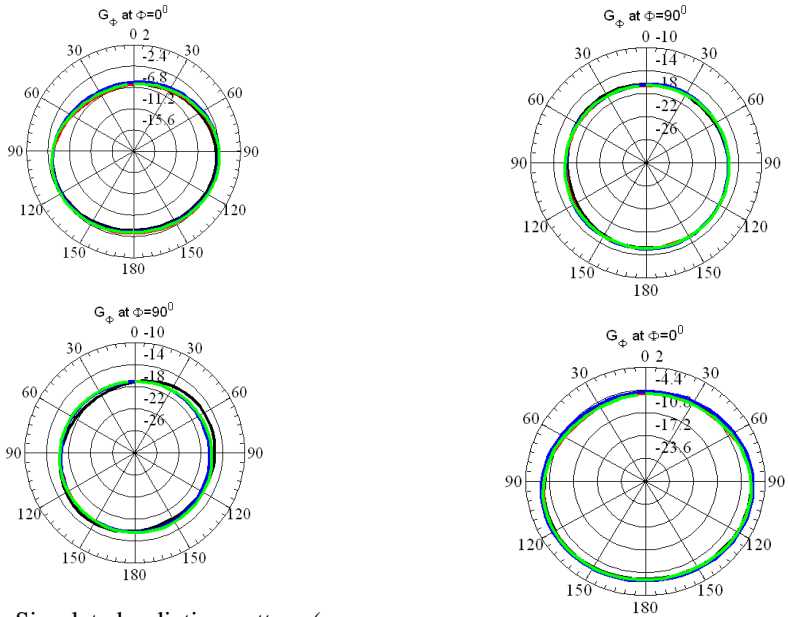


Fig.9.a: Simulated radiation pattern ( $G_{\theta}$ ,  $G_{\phi}$ ) at  $\phi = 0^{\circ}$  (x-z) plane and  $\phi = 90^{\circ}$  (y-z) plane of hexa-band PIFA at frequency=1900MHz

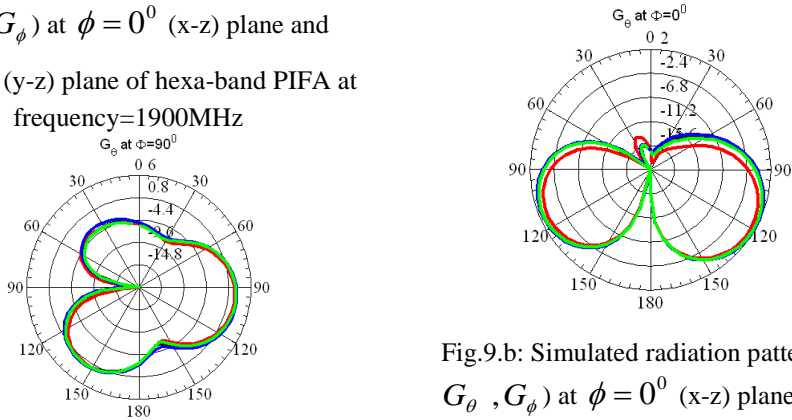


Fig.9.b: Simulated radiation pattern ( $G_{\theta}$ ,  $G_{\phi}$ ) at  $\phi = 0^{\circ}$  (x-z) plane and  $\phi = 90^{\circ}$  (y-z) plane of hexa-band PIFA at frequency=2000MHz

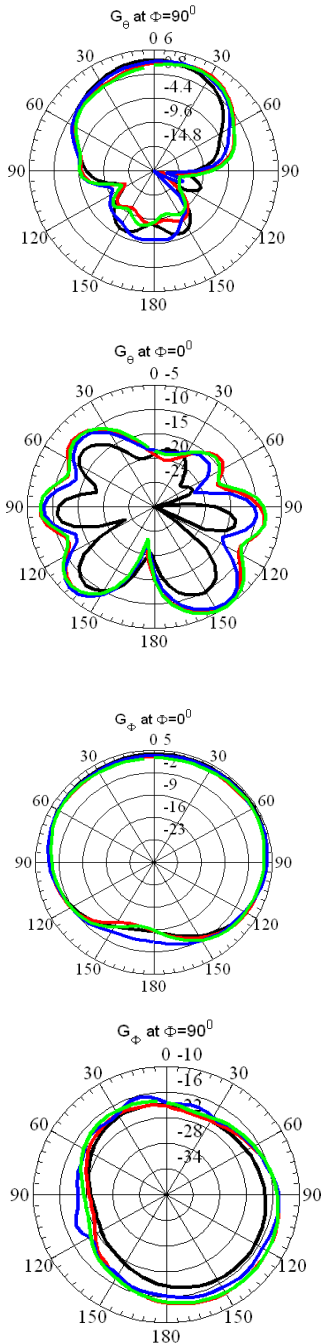


Fig.9.c: Simulated radiation pattern ( $G_{\theta}$ ,  $G_{\phi}$ ) at  $\phi = 0^{\circ}$  (x-z) plane and  $\phi = 90^{\circ}$  (y-z) plane of hexa-band PIFA at frequency=5300MHz

#### 4. Conclusion

In this paper, the performance of four modern planar inverted-F antennas has been studied using FDTD, FEM, FIM, and MOM. The return loss and the radiation pattern of the antennas have been calculated. The results show a good agreement between the measurements and simulation results and also show an excellent agreement between the used full-wave modeling techniques. Furthermore, the results showed that the studied antennas are suitable to be used as mobile phone antenna form the size and the performance point of views. The paper demonstrates that the full-wave modeling techniques are excellent tool to analyze PIFAs effectively from the time and cost point of views. Further research will include the effect of the presence human hand and head on the performance of the chosen antennas.

#### 5. References

- [1] D. Sim and Seong-Ook, "A Triple Band Internal Antenna: Design and performance in Presence of the Handset Case, Battery, and Human Head" *IEEE Transactions on Antennas and Propagation*, Vol.47 No.3 pp.658-666 August 2005.
- [2] Y. Xin Guo, M.Y.W.Chia and Z.N.Chen "Miniature Built-In Quad-Band Antennas for Mobile Handsets" *IEEE Antennas and Wireless Propagation Letters*, Vol.52, No.8 ,pp 1936-1944 ,August 2004.



- [3] Y. Xin Guo, and M.Y.W.Chia  
“Compact Internal Multiband  
Antennas for Mobile Handsets”  
*IEEE Antennas and Wireless  
Propagation Letters*, Vol.2, pp143-  
146,2003.
- [4] M. Karkkainen “Meandered Multiband  
PIFA With Coplanar Parasitic  
Patches” *IEEE Microwave and  
Wireless Components Propagation  
Letters*, Vol.2. No.10 October 2003.
- [5] M.Sadiku, “ Numerical Techniques in  
Electromagnetic” , CRC press,1999.
- [6] XFDTD, FDTD-Based  
Simulator,Ver.6.3.[online]. Available  
:<http://www.remcom.com> April 2010.
- [7] J. Jin, “ *The Finite Element Method in  
Electromagnetics.* ” Wiley-Interscience,  
New York, NY, 1993.
- [8] High Frequency Structure Simulator  
(HFSS) FEM-Based Simulator (HFSS),  
Ver.11 [online]. Available  
:<http://www.Ansoft.com>.
- [9] T. Weiland, “A discretization  
method for the solution of  
Maxwell’s equations for six-  
component fields,” *Electronics and  
Communications AEU*”, Vol. 31, No.  
3, 116–120, 1977.
- [10] Computer Simulation Technology  
(CST) Microwave Studio Ver. 8.2  
FIM Base Simulator [online].  
Available :<http://www.cst.com>.
- [11] Harrington,“ *Field Computations by  
Moment Method*”, MacMillan, 1993.
- [12] FEKO, MOM-Based Simulator Ver  
5.2 [online]. Available  
:<http://www.feko.com>.



المؤتمر الدولي العربي الليبي الخامس للهندسة الكهربائية والإلكترونية 23-26/10/2010 طرابلس ليبيا





## ***Chapter III***

# **Computer Systems, Networks and Software Engineering**



المؤتمر العربي الليبي الدولي الخامس للهندسة الكهربائية والإلكترونية 23-26/10/2010 طرابلس ليبيا



## On the efficiency of test cases in mutation testing

**Elfurjani Sassi Mresa**

Department of Electrical and Electronic Engineering, Al Fateh University, Tripoli, Libya.

Email: mresa@ee.edu.ly

**Ali Mohamed Okok**

Department of Electrical and Electronic Engineering, Al Fateh University, Tripoli, Libya.

Email: okok@ee.edu.ly

**Hussein S. Elbuaeshi**

Department of Computer Science, Al Fateh University, Tripoli, Libya.

Email: huselb@hotmail.com

**Abstract**—Mutation testing, although powerful, is an expensive testing method due to the high cost of executing mutants against numerous test cases. Automatic test case generators greatly reduce the cost of test case generation but at the expense of excessive test set sizes. This paper investigates methods by which the number of test cases can be reduced at the same time maintaining test effectiveness. Improved approaches for test data generation and identification of equivalent mutants are given and shown empirically to result in a substantial reduction in cost.

KEY WORDS: Mutation testing, Test data generation, Equivalent mutants, Mutant execution

### I. INTRODUCTION

Mutation analysis, originally proposed by DeMillo [1], is a fault-based technique for testing software. The basic problem is to find a set of test cases that will find all the faults that are at all likely to be present in a given program. To do this, the program is deliberately seeded with faults. The program containing a seeded

fault is called a mutant. The tester's task is then to produce a set of test cases that can

detect all these faults. In this way, mutation analysis allows the tester to evaluate and improve the quality of the test data [2].

The precise method used for mutation analysis may vary according to the order in which certain activities are done. Figure.1 shows the activities performed in this paper and outlines a basic mutation analysis procedure.

When the program  $P$  is presented for mutation analysis an initial set of mutants may be produced. If an initial set is produced then they can be used to guide the generation of candidate test cases which is done in the next step. Test cases can be produced manually or with the aid of a test case generator. Once a candidate test set has been assembled, the correctness of the program  $P$  is verified for each test. If an error is found then  $P$  is corrected and the entire procedure must start again. Once the correctness of  $P$  has been established for every test in  $T$  then the evaluation of  $T$  can begin. A test case kills a mutant if it causes the mutant to produce an incorrect output. Clearly, the more mutants a test set kills, the better the test set. Note that it is not necessary

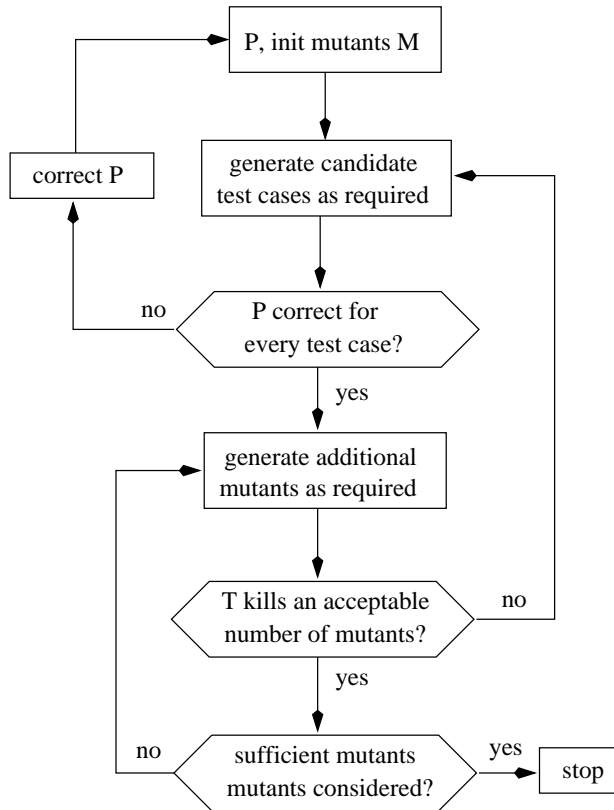


Fig. 1. Outline of mutation analysis procedure

to consider all the possible mutants to a program at once. An incremental approach allows the tester to control the number of mutants considered in line with the available budget.

If the test set evaluation shows the test set to be wanting i.e. it does not kill or distinguish sufficient mutants, additional test cases or additional mutants must be obtained. Again, test cases can be produced manually or with the aid of a test case generator. The repeated uses of a test case generator, however, are typically much less effective, and manually generated test cases are usually required to kill the last few

mutants that contain faults that are not easily manifested.

Note that although the flowchart in Figure.1 establishes the correctness of  $P$  on a test set before evaluating that test set, correctness can be established later. In this situation, a test case is said to distinguish a mutant if it causes the mutant to produce an output that differs from the output of  $P$ . The correctness of  $P$  on each such test case must of course be established later. Clearly, if at this stage an error is found in  $P$  then the entire procedure must recommence from the beginning.



## II. THE COST OF MUTATION ANALYSIS

Mutation analysis is a complex activity involving both manual and automated activities. The generation of mutants, for example, is readily automated but this automation is not without its indirect cost. Automated mutant generators, because they make syntactic modifications to a program  $P$ , produce a proportion of equivalent mutants. These are not mutants at all but programs that differ from  $P$  only at the lexical level. There exists no general algorithm for the detection of these equivalent mutants and so it must be done by the tester. Test data generation can also be automated but that too is not without its indirect cost. Ideally, the tester is looking for effective test cases. These are test cases that kill a number of mutants that are not killed by any other candidate test case. The best that a typical automated test generator can do is to produce test cases that cause the mutant to execute the statement in the program that contains the fault. There is no guarantee that such a test will distinguish the mutant and typically, the tester must generate some test cases manually.

Mutation analysis is generally regarded as a costly testing method [3], [4], [5]. The major part of this cost resides in performing the following activities:

- Test data generation.
- Mutants execution.
- Identification of equivalent mutants.

Various proposals have been made to reduce this cost. Some proposals are concerned with reducing the number of mutants considered, either by random elimination [6], [7] or by more systematic elimination of certain kinds of fault [8]. This paper explores the way in which the cost of mutation testing is influenced by the way in which mutation analysis is conducted. The way that both of the test data and mutation

operators are generated and applied as well as the sequence in which test activities are performed, may have a significant impact on the resultant cost. In comparison to mutant reduction, little work has been done in this area. These factors and how they may effect the cost of mutation testing will be discussed in the following sections.

## III. TEST DATA GENERATION

Test data generation is the process of generating a set of test inputs which satisfies a given testing criterion. In mutation testing, this criterion is the ability to differentiate the test program from all of its generated mutants. It can be a very labour and a time-consuming task to generate a mutation adequate test data set, in that a tester repeatedly interacts with a mutation system to examine remaining live mutants and hand-crafts tests that kill them.

DeMillo and Offutt [9] have produced a constraint-based automatic test data generator, called “Godzilla”. The Godzilla tool generates test data designed specifically to kill mutants of the test program. It represents the conditions necessary to kill each mutant as a system of mathematical constraints and attempts to solve these constraints to generate a test case that targets the mutant. There are three types of constraints considered by the Godzilla tool: “reachability” requires that the fault containing statement is executed; “necessity” requires that the mutant state after some execution of the statement containing it can be distinguished from that of the program under test; and “sufficiency” requires that the final state of a mutant (at the output) differs from that of the original program. Godzilla explicitly generates test cases to satisfy the reachability and necessity conditions. A more detailed description of how Godzilla generates test



cases and a discussion on its limitations are given in [10]. This paper is concerned with measuring the mutant killing rate of the test data generated by Godzilla, and its effect on the resultant cost. Alternative approaches to increase the cost-effectiveness of generated test data are suggested.

Experimental results from using Godzilla [10], [9] show that it can produce test data that is almost adequate. This means that the tester has to generate only a few test cases by hand and thus substantially reducing the total time taken to produce an adequate test set. Although Godzilla is able to generate test cases far faster than a human, it unfortunately generates many more test cases than a human tester does. It generates almost<sup>1</sup> one test case for every mutant. The majority of these test cases, however, are ineffective because they kill only mutants that have already been killed by other test cases that are executed earlier in the mutation process. As a result, only a small percentage of the Godzilla generated test cases are actually required for killing a set of mutants.

An experiment was conducted to measure the effectiveness of test cases generated by Godzilla for a sample of programs. An effective test case with respect to a test set, is one that kills at least one mutant that has not been killed by some other test case.

The experiment was conducted using the Mothra mutation system. A suite of four Fortran-77 programs was used. The four programs have been chosen to cover a range of different applications<sup>2</sup>.

<sup>1</sup>When two mutants result in identical constraints, only one test case is generated.

<sup>2</sup>Descriptions of the programs together with their source listings are available from the author.

In this experiment, all the Mothra mutation operators were used to generate mutants, Godzilla was used to generate test cases, and then mutants were executed against the generated test cases. The same procedure was repeated on all programs. Table I shows the results of this experiment. The first three columns show the program name, the number of source lines, and the number of generated mutants. The 4th column labelled "Gen. TCs" is the total number of test cases generated by Godzilla. The last three columns are the number of test cases that were found to be effective, their percentage of the total generated test cases, and the mutation adequacy score achieved.

Clearly, from the above results, although Godzilla is effective at producing test cases for killing mutants, it is very inefficient. The number of test cases that are typically generated by Godzilla is much more than necessary. In fact, the vast majority of the generated test cases are redundant. On average, only less than 1.5% have been found to be effective.

Godzilla produces test cases very quickly and so the cost of Godzilla's inefficiency is not in the time taken to generate test sets. The cost incurred in using large test sets comes from the time required to execute each test case on each mutant. Each redundant test case must be applied to all the live mutants before it can be identified as redundant and discarded. In addition to this cost in machine time is the cost of examining the outputs of the mutant and the test program on these test cases. Large inefficient test sets impose unacceptable demands on computing and human resources.

DeMillo and Offutt [10], have suggested that the expensive task of comparing a test case output with the expected output is left until it has been applied to all mutants,



Program	Source Lines	Gen. Muts	Gen. TCs	Eff. TCs	Eff. TCs%	Adq. Score
FINDCNT	40	1879	1076	15	1.39	1.000
SORT	21	879	852	7	0.82	1.000
BANKER	44	2972	2444	63	2.58	0.984
MInv	53	4092	2241	14	0.62	0.987
Average	39.5	2456	1653.25	24.75	1.35	0.993

TABLE I  
STATISTICS OF GODZILLA GENERATED TEST DATA

ignoring any test cases that do not kill any mutants.

In this way, all test cases that are ineffective at killing any mutant can be identified and removed automatically before their outputs need to be examined. However, although this approach may significantly reduce the amount of time required for doing manual tasks, since the tester is required to examine the output of effective test cases only, it does not reduce the machine time overhead. Redundant test cases still need to be executed on mutants before they can be identified and ignored. This wasteful computation, however, typically represents the major amount of the total machine time required. This is, as shown Table I, due to the high percentage of redundant test cases generated.

#### A. Improved approaches to generating test data

This paper presents two studies that investigate the effects of reducing the amount of test data on both the mutation adequacy score and mutation cost. The four programs of the previous experiment are used in both studies.

1) *Random selection of a small proportion of the automatic test data:* In the first

experiment, only small proportions of the test data generated by Godzilla are applied. After applying Godzilla to generate test data to kill all mutants of a test program, small proportions, 2% and 5% of the generated test data are randomly selected, and applied to program mutants. Table II shows the average results of three trials performed. The first three columns show the program name, the number of generated mutants and the total number of test cases generated by Godzilla. The middle three columns, labelled “All”, “2%”, and “5%”, are the adequacy scores of all, 2%, and 5% of the generated test cases respectively. The last two columns are the reduction factors in mutant execution times<sup>3</sup> with respect to the time needed for the complete set of generated test cases.

The results of this experiment show that almost the same adequacy score can be obtained using only 2% of the test data generated by Godzilla, at a substantially reduced cost. On average, the amount of time spent executing mutants has been reduced by a factor of nearly 30 for only 2% loss in adequacy; showing a large reduction in mutation cost. These results suggest that the

<sup>3</sup>All measurements are in cpu-time units.



Program	Gen. Muts	Gen. TCs	Adequacy Score			Speedup Factor	
			Test cases applied			2%	5%
			All	2%	5%		
FINDCNT	1879	1076	1.000	0.980	0.987	23.04	13.09
SORT	879	852	1.000	0.990	1.000	31.50	15.75
BANKER	2972	2444	0.984	0.943	0.961	33.75	14.76
MInv	4092	2241	0.987	0.977	0.977	31.16	13.89
Average	2456	1653.25	0.992	0.972	0.981	29.86	14.37

TABLE II  
STATISTICS OF GODZILLA GENERATED TCs: USING SMALL PERCENTAGES

mutant killing rates of Godzilla's generated test cases drop sharply after the first 2% of tests, and therefore, manual generation of test cases to kill the remaining mutants, is likely to be a more cost-effective alternative.

2) *Removing unstable mutants*: The second experiment investigates the effects of the unstable mutants, those that can be easily killed by almost any test case, on the effectiveness of Godzilla's generated test data and hence, on the overall cost of mutation testing. Allowing Godzilla to generate test cases to kill unstable mutants, which typically represent a high percentage of the total generated mutants, is likely to result in generating a large number of ineffective test cases. Avoiding the generation of these test cases, may significantly reduce the execution time required with no accompanied loss in the mutation adequacy score.

In this experiment, before initiating Godzilla to generate test cases, one test case was applied to all program mutants to kill all unstable mutants before resorting to Godzilla. Table III shows the average results of three trials. The first three columns show the program name, the number of generated mutants and the number of equivalent mutants. The 4th and 5th columns, labelled "Muts Killed" and "Adq. Score",

are the number of mutants killed, and the achieved adequacy score after applying one manually-generated test case. The 6th, 7th and 8th columns with the labels "Gen. TCs", "Size%" and "Total Score", show the number of test cases generated by Godzilla for the remaining live mutants after applying the initial test case, their percentage of that generated without a manual test case being applied, and the total adequacy score respectively. The last column is the reduction factor in test case generation and mutant execution times with respect to the time needed without an initial test case.

The results of this experiment show that applying one test case, possibly manually-generated, before initiating Godzilla, will significantly reduce the number of generated test cases with no loss in testing strength. On average, the size of the generated test cases has been reduced to only 24% of that generated in previous experiments. This has resulted in 4.17 times reduction in the machine time required to generate and execute test cases. The 4th column of the table shows that, on average 80% of the total generated mutants are killed after applying the first test case. It is interesting to note that this coincides with other empirical results





Program	Gen. Muts	Eqv. Muts	Manual (1st_tc)		Godzilla			Speedup Factor
			Muts Killed	Adq. Score	Gen. TCs	Size%	Total Score	
FINDCNT	1879	112	1376	0.77	259	24	1.000	2.94
SORT	879	98	746	0.95	117	14	1.000	4.02
BANKER	2972	156	1511	0.53	1077	44	0.984	3.06
MInv	4092	330	3615	0.96	282	13	0.987	6.68
Average	2460	174	1812	0.80	433.8	24	0.993	4.17

TABLE III  
STATISTICS OF GODZILLA GENERATED TCs: AFTER APPLICATION OF FIRST TEST CASE

reported elsewhere, [11].

It is evident, from the results of the experiments above, that the test data size, is of a significant influence on the number of mutant executions required and hence, on the overall cost of mutation testing. More importantly, however, these results show that the current use of an automatic test data generator, Godzilla, results in a more expensive mutation testing than necessary. Only a small percentage of the total processing time is actually required. The major amount of time is wasted on processing ineffective test cases.

Two approaches have been presented to reduce the cost-overhead of using Godzilla to generate test data. The first approach, requires that only a small randomly selected proportion of the test data generated by Godzilla, is used for mutation testing. Using only 2% of the test data has been shown to give a 30 times reduction in mutation execution cost for only a 2% loss in adequacy. If 5% of the test data is used a 15 times reduction in mutation execution cost was obtained for only 1.1% loss on testing strength.

In the second approach, automatic test generation is delayed until the unstable mutants have been eliminated. In this approach

there is no loss of adequacy but using the experimental programs, it has been possible to obtain a 4 times reduction in machine time required to generate and execute test cases. Both approaches are able to produce a substantial reduction in mutation cost.

Examinations of the generated test cases, however, show that there is still a large proportion of redundant test cases. One possible way for reducing this redundancy and subsequently further reduce the cost of mutation testing is to combine the two approaches. In this, after the application of the first, possibly manually-generated, test case to kill unstable mutants, Godzilla is used, as was done in the second experiment, to generate test cases for the remaining live mutants that have not been killed by the first test case. However, rather than applying all the test cases generated by Godzilla, a small randomly selected proportion of the generated test cases are applied.

The results of the previous experiments indicate that there is still the potential to make a significant reduction in mutation cost by focusing on developing better approaches for generating test data alone.



#### IV. MUTANT EXECUTION

The execution of mutant programs against test data, is the dominant factor in the computational cost of mutation testing. The amount of processing required to execute each mutant against at least one, and potentially many, test cases is large, even for small programs. It remains unclear, however, how to measure this cost accurately. The difficulty arises because the cost is dependent not only on the number of mutants and the test cases, but also on the rate at which mutants are killed. For example, if all the mutants of a program are killed by the first few test cases, then the test size has little influence on the cost and the cost is mainly influenced by the number of mutants. On the other hand, for less effective test sets, many mutants might need to be executed on all the test cases, and the cost would then be proportional to the test set size as well as the number of mutants.

A cost model may be developed as follows. Initially, each mutant is executed once on the first test case. Only a proportion of these mutants survive to be executed on the second test case. Assume that there are  $m$  mutants generated and  $\eta$  test cases. Let  $p_i$ , where  $i = 1, \dots, \eta$ , be the proportion of the total number of generated mutants that are executed with test case  $i$ . Then  $p_1 = 1$ , and  $0 \leq p_i \leq 1$ , for  $i = 2, \dots, \eta$ . Each  $p_i$  depends of course on the set of mutations and the test set.

$$E = mp_1 + mp_2 + \dots + mp_\eta = m \sum_{i=1}^{\eta} p_i \quad (1)$$

One strategy for developing a cost model is to assume each test is equally effective i.e. all tests have the same killing rate  $\alpha$ . In this case, the number of mutants alive before the  $i$ th test is the number alive before the  $i - 1$

test less those that died during the  $i - 1$  test.

$$\begin{aligned} mp_i &= mp_{i-1} - \alpha mp_{i-1} \\ p_i &= p_{i-1}(1 - \alpha) \\ p_i &= (1 - \alpha)^{i-1} \text{ using } p_1 = 1 \end{aligned}$$

The number of mutant executions,  $E$ , given  $\eta$  tests is therefore:

$$E = m \sum_{i=1}^{\eta} p_i = m \sum_{i=1}^{\eta} (1 - \alpha)^{i-1} \quad (2)$$

Choi and Mathur [12] have reported that, in general, if  $m$  is the number of mutants generated,  $\eta$  is the number of test cases, and  $\alpha$  is the test case effectiveness— the probability that an arbitrary test case from the test data set kills a mutant, then the average number of mutant executions  $E$  can be computed as:

$$E = \frac{m(1 - (1 - \alpha)^\eta)}{\alpha} \quad (3)$$

This is essentially the same model as  $1^4$ .

From Equation (1), it can be seen that as the test case effectiveness,  $\alpha$ , tends to 1,  $E$  tends to  $m$ . For a relatively ineffective test set, however,  $\alpha$ , tends to 0, and  $E$  tends to  $\eta \times m$ .

Notice that the above model, shown in Equation (1), ignores the differences in,  $\alpha$ , between test cases. If  $m$  is the total number of mutants and  $K$  is the number of mutants killed when executed against a test set containing  $\eta$  test cases, then  $\alpha$  is the proportion of mutants  $m$  that is killed by one test case, and it is defined as:

$$\alpha = \frac{K}{\eta \times m} \quad (4)$$

<sup>4</sup>This can be shown by using  $\frac{1}{1-x} = 1 + x + x^2 + x^3 + \dots + x^{n-1} + \frac{x^n}{1-x}$



In practice, however,  $\alpha$  is not the same for all test cases. In fact, the mutant killing rate of test cases may vary largely depending on the order in which they are applied.

Using the average value of  $p_i$ , for  $i = 1, \dots, \eta$ , Equation (2) can be rewritten in a simpler form, as shown in Equation (3).

Let  $p_a$  be the average value of  $p_i$ ,  $i = 1, \dots, \eta$ , i.e.,  $p_a = 1/\eta \sum_{i=1}^{\eta} p_i$ , where  $p_a \leq 1$ , and  $p_a = 1$  in the unlikely case that no test case kills any mutant. Equation (2) can be rewritten as follows:

$$E = m \sum_{i=1}^{\eta} p_i = m \times \eta \times p_a \quad (5)$$

For large  $\eta$ , that is  $\eta \gg m$ ,  $p_a$  tends to the proportion of mutants that are not killed by any test case from the  $\eta$  test cases.

This shows that the number of mutant executions, or the computational cost of mutation testing, is proportional to the product of the number of test cases and the number of mutants. In general, however, the number of mutant executions,  $E$ , are bounded by  $m \leq E \leq m \times \eta$ .

The majority of program mutants, however, are often killed after applying the first few test cases. Table IV shows the results of an experiment that investigates mutants killing rate against applied test inputs. The experiment has been performed on the same suite of programs used in the previous experiments. The first five columns show the program name, the numbers of generated and equivalent mutants respectively, the average number of test cases of three generated mutation-adequate test data sets, and the average number of test cases that have been found to be effective. The next four columns, labelled “1st”, “2nd”, “3rd”, and “4th”, are the average percentages of mutants killed by the first four test cases. The last column is the percentage of mutants

killed by all remaining test cases.

The results of this experiment show that the first test case applied typically kills a high percentage of the total mutants. On average, it has been found to kill around 76% of the total mutants. As described in [10], this high killing rate is probably due the existence of a large number of unstable mutants. The situation thereafter changes, and the mutant killing rate becomes lower and lower as more test cases are applied. With the exception of the BANKER program case, the mutants killing rate is very small after the first few test cases.

The apparent difference in the mutant killing rate for the BANKER program, and hence the relative large size of effective test cases required to kill all its mutants is due to the limited domain of its possible outputs. BANKER is a function program unit with output restricted to one of the two logic values. Naturally, it is more difficult to distinguish mutants of programs of this type than other programs with large output domains.

The results of this experiment have been used to compute the average percentage of the total mutants that have been executed against each test case. Tabulation of the computed results are shown in Table (V).

Clearly, the results, shown in Table (V), show a considerable difference, in the percentages of mutants executed against test cases, between different programs. This suggests that probably a large number of similar experiments, on different collections of programs, may be required before good estimates to the percentages of mutants executed against test cases can be made. However, the results of this experiment may provide a crude estimates to the variables  $p_2, p_3, p_4$ , and  $p_5, \dots, p_{\eta}$  in Equation (2). The values of  $p_2 = 0.24, p_3 = 0.13, p_4 = 0.12$ , and  $p_i \leq 0.1$ , for  $5 \leq i \leq \eta$ , as shown



Program	Gen. Muts	Eqv. Muts	Gen. TCs	Eff. TCs	Total mutants killed %				
					T e s t C a s e s				
					1st	2nd	3rd	4th	5th-Last
FINDCNT	1879	112	1076	15	82.00	08.20	01.30	04.30	≤ 04.20
SORT	879	98	852	7	95.50	02.70	00.80	00.25	≤ 00.80
BANKER	2972	156	2470	71	32.50	29.50	03.30	00.96	≤ 33.70
MInv	4092	330	2260	18	95.70	00.30	00.70	00.08	≤ 03.30
Average	2456	174	1698	28	76.40	10.20	01.50	01.40	≤ 10.50

TABLE IV  
STATISTICS OF TEST CASES AND MUTANT KILLING RATE

Program	Gen. Muts	Eqv. Muts	Gen. TCs	Eff. TCs	Total mutants executed %				
					T e s t C a s e s				
					1st	2nd	3rd	4th	5th-Last
FINDCNT	1879	112	1076	15	100	18.0	09.8	08.5	≤ 04.20
SORT	879	98	852	7	100	04.5	01.8	01.0	≤ 00.75
BANKER	2972	156	2470	71	100	67.5	38.0	34.7	≤ 33.70
MInv	4092	330	2260	18	100	04.3	04.0	03.3	≤ 03.22
Average	2460	174	1698	28	100	23.6	13.4	11.9	≤ 10.50

TABLE V  
STATISTICS OF THE NUMBER OF MUTANT EXECUTIONS

in the last row of Table (V), are the average obtained values. Using these values, the cost model in Equation (2) can be rewritten as

$$E = m + 0.24m + 0.13m + 0.12m + m \sum_{i=5}^{\eta} p_i \quad (6)$$

where  $(0 < p_i \leq 0.1 \text{ for } i = 5, \dots, \eta.)$

#### V. IDENTIFICATION OF EQUIVALENT MUTANTS

The identification of equivalent mutants is the process of examining program mutants and identifying all mutants that are functionally equivalent to the test program, those that

always produce the same output, on every input, as the test program.

The identification of equivalent mutants is the most human-intensive activity in mutation testing. It is therefore a time-consuming step, and generally regarded as one of the greatest expenses in current mutation systems [2], [10], [13]. Moreover, it is a very difficult task and requires a detailed knowledge of the test program and its mutants.

It is difficult, however, to measure how much effort is required to identify equivalent mutants in practice. The cost of this activity and how much it contributes to the total cost may depend upon many factors. Other than the tester experience and the complexity of



the program, they depend on the way and the stage at which this activity of identifying equivalent mutants is performed. For example, are equivalent mutants identified at several stages, by applying one mutation operator at a time, or all at one go by applying all mutation operators together? Irrespective of the choice of mutation strategy, does the search for equivalent mutants take place before or after test cases are applied?

Ideally, all equivalent mutants should be identified at an early stage in the testing process, before test cases are applied. This prevents performing wasteful computations on equivalent mutants, and therefore reduces mutants execution time. For large size test data set, a substantial amount of time may be saved. However, this reduction in mutants execution time may be far outweighed by the tedious and time-consuming task of examining all mutants for equivalence. Leaving this activity until all test cases are applied on mutants, is likely to make the task of examining equivalent mutants much easier for the tester, since the majority of mutants are typically killed before he or she needs to examine them.

A more cost-effective approach, is to limit the process of identifying equivalent mutants to one mutation operator only. A single mutation operator is applied and the resultant mutants are executed on a few generated test cases. The tester then examines the remaining mutants for equivalence. Once all equivalent mutants of that operator have been identified, more test cases are added, if necessary, to kill any remaining mutants. The process is repeated with the next operator until all mutation operators have been applied. Notice that mutants generated by each mutation operator are executed on all previously generated test cases before adding new test cases is considered. The

advantages of concentrating on one type of mutant at a time, in identifying equivalent mutants, are:

- Reducing the total number of examined mutants.

Ideally, where a mutation-adequate test data for the test program can be generated automatically, the mutants that have to be examined for equivalence are limited to equivalent mutants only. In practice, however, automatic test data generators do not, in general, generate mutation adequate test data, and therefore, the number of mutants that have to be examined for equivalence may be considerably larger than the number of equivalent mutants. The total number of mutants examined for equivalence depends on the quality of the test data applied. The more effective the test data at killing mutants the less the number of mutants that the tester has to examine for equivalence. The total number of examined mutants can be reduced by reducing the number of non-equivalent mutants that need to be examined. The incremental improvement in the quality of the test data generated, by focusing on killing all mutants of one operator at a time, is likely to reduce the number of non-equivalent mutants that have to be examined for subsequently applied operators.

- Reducing the cognitive effort required to identify equivalent mutants.

Typically, knowledge of some aspect of the program, will allow the tester to eliminate not one but several equivalent mutants. Ideally, these mutants should be examined together before the knowledge that the tester may have acquired about the program has been



forgotten. These set of equivalent mutants so identified, are likely to belong to the mutations of the same operator. Therefore, presenting all mutants, that need to be examined for equivalence, which belong to one mutation operator, at one time, is likely to reduce the time and effort required to examine them. For example, consider the absolute value insertion operator (*abs*), being applied on the statement  $x:=x+y$  and that, on examining the mutant  $x:=abs(x)+y$ , the tester gathered the knowledge that  $\{x, y\} \in \mathbb{N}$ . This gathered knowledge, would allow the tester to identify all the mutants  $x:=x+abs(y)$ ,  $x:=abs(x+y)$ ,  $x:=zpush(x)+y$ ,  $x:=x+zpush(y)$ , and  $x:=zpush(x+y)$  as equivalent, with no effort, had they been presented together.

An additional advantage of using this approach is that it reduces wasteful computations on equivalent mutants. Identifying an equivalent mutant early in the testing process will exclude it from being executed on the test cases applied later in the process, and hence, the time overhead spent on executing equivalent mutants is reduced.

## VI. CONCLUSIONS

The paper reports on the three major activities that contribute to the cost of mutation analysis; test data generation, mutant execution, and identification of equivalent mutants. It is noted that the cost of these activities may be significantly influenced by the way in which mutation analysis is conducted. That is, the way that both of the test data and mutation operators are generated and applied as well as the sequence in which test activities are performed, may have a significant impact on the resultant cost.

Experiments measuring the efficiency of a constraint-based automatic test data generator, called “Godzilla” [10], [9] show that although Godzilla is effective at producing test cases for killing mutants, it is very inefficient. The number of test cases that are typically generated by Godzilla is much more than necessary. In fact, the vast majority of the generated test cases are redundant. On average, only less than 1.5% have been found to be effective. However, although the time required to generate test data automatically is small, the wasteful computation of executing a large number of redundant test cases on mutants, before they can be identified as redundant and ignored, and the process of examining the outputs of a program on these test cases is very time consuming.

The paper presents two approaches to improve the efficiency of using the Godzilla test data generator. The first approach is based on selecting randomly only a small proportion 2-5% of the test data generated by Godzilla. The second approach is to kill unstable mutants, by applying one test case to all program mutants, before resorting to Godzilla.

Experiments with these approaches have shown a substantial reduction in mutation cost. The first approach, using only 2% of the test data generated by Godzilla, has been shown to give, on average, 30 times reduction in mutation execution cost for a 2% loss in adequacy. Increasing the percentage of test cases used to 5% of the test data generated by Godzilla, has shown to give 15 times reduction in mutation execution cost for only a 1.1% loss in adequacy. The second approach has been shown to result in the same adequacy as full mutation with 4 times reduction in machine time required to generate and execute test cases.



Examinations of the generated test cases, however, show that there is still large proportion of redundant test cases. One possible way for reducing this redundancy and subsequently reduce further the cost of mutation testing is to combine the two approaches. After the application of the first, possibly manually-generated, test case to kill unstable mutants, Godzilla is used to generate test cases for the remaining live mutants that have not been killed by the first test case. However, rather than applying all the test cases generated by Godzilla, a small randomly selected proportion of the generated test cases are applied.

The execution of mutant programs against test data, represents the dominant factor of the computational cost required in mutation testing. An approximate formula for computing the run time complexity of mutation analysis is presented. The formula presented in this paper differs to that reported by Choi and Mathur [12], in that their model treats all test cases to have the same mutant killing rate. In practice, however, the mutant killing rate of different test cases is not the same. The results of experiments conducted on a range of different programs have indicated that the first applied test case typically kills a high percentage of the total mutants. On average, it has been found to kill around 76% of the total mutants. The situation thereafter changes, and the mutant killing rate becomes lower and lower as more test cases are applied.

The cost model presented in this paper is based on an empirical investigation of the relation between the mutant killing rate of test cases and the order in which they are applied. Although a large number of similar experiments, on different collections of programs, may be required before good estimates can be made, the cost model pre-

sented in this paper provides a fairly reasonable estimation of the cost profile of mutant execution. The profile shows that the first few test cases have the highest execution cost. However, for a relatively ineffective test data set, the major part of the total mutant execution time is spent on executing ineffective test cases and it is here that the greatest savings can be made.

The identification of equivalent mutants is the most human-intensive activity in mutation testing. It is therefore a time-consuming step, and generally regarded as one of the greatest expenses in current mutation systems [2], [10], [13]. Moreover, it is a very difficult task and requires a detailed knowledge of the test program and its mutants. Ideally, all equivalent mutants should be identified at an early stage in the testing process, before test cases are applied. This prevents performing wasteful computations on equivalent mutants, and therefore reduces mutants execution time. For large size test data set, a substantial amount of time may be saved. However, this reduction in mutant execution time may be far outweighed by the tedious and time-consuming task of examining all mutants for equivalence. Leaving this activity until all test cases are applied on mutants, is likely to make the task of examining equivalent mutants much easier for the tester, since the majority of mutants are typically killed before he or she needs to examine them.

A cost effective approach that has been suggested in this paper, is to limit the process of identifying equivalent mutants to one mutation operator only. A single mutation operator is applied and the resultant mutants are executed on a few generated test cases. The tester then examines the remaining mutants for equivalence. Once all equivalent mutants of that operator have been identi-





fied, more test cases are added, if necessary, to kill any remaining mutants. The process is repeated with the next operator until all mutation operators have been applied. Notice that mutants generated by each mutation operator are executed on all previously generated test cases before adding new test cases is considered. The advantages of this approach are that it reduces the total number of examined mutants and the effort required to identify equivalent mutants and is likely to reduce wasteful executions of equivalent mutants.

## VII. FUTURE WORK

There are several potential extensions to the work presented in this paper. The results of the experiments presented in Section III show that there is still the potential to make a significant reduction in mutation cost by focusing on developing better approaches for generating test data alone. One possible way may be is to adopt an incremental approach in generating test data. In that, rather than treating the generation of test data and mutant execution as two separate activities, individual test cases are generated, as required, in the light of the results provided by previously applied test cases. This can be done simply by executing live mutants on each generated test case before the generation of the next test case is considered. At the stage where it becomes difficult for the automatically generated test case to kill any more mutants, the tester might consider examining the remaining live mutants for equivalence, and then move to manual test cases. This is likely to result in avoiding redundancy in the test cases generated, and subsequently avoiding the wasteful resources spent in executing redundant test cases on mutants and examining the output of a program on these test cases.

Another possible approach is to use partitioning. In this approach, mutants are partitioned according to their execution path constraints, and a representative set of mutants, one from each partition, is used to guide the test generation process. In that, rather than generating a test case for each mutant and executing it on all live mutants, regardless of whether the test case satisfies the necessary path constraint for a mutant, a test case is generated for one mutant only in each partition. This test case is then applied only to the mutants of the same partition. In this way, test cases are not applied to mutants where mutant death is less likely, and therefore, every test case is likely to have a reasonably high mutant killing rate.

Evaluating of the mutation run time cost model, given by Equation (1) in Section V, against a wide range of large programs may show to what extent the cost profile varies according to program.

## REFERENCES

- [1] R. DeMillo, R. Lipton, and F. Sayward, "Hints on test data selection: help for the practising programmer," *IEEE Computer*, vol. 11, no. 4, pp. 34–41, 1978.
- [2] R. DeMillo, D. Guindi, K. King, W. McCracken, and A. Offutt, "An extended overview of the Mothra software testing environment," in *Proceedings – Second workshop on software testing, verification and analysis*. IEEE, July 1988, pp. 142–151.
- [3] B. Choi, A. Mathur, and B. Pattison, "PMothra: scheduling mutants for execution on a hypercube," in *Proceedings of the ACM SIGSOFT 89: Third Symposium on Software Testing, Analysis and Verification (TAV3)*. New York, NY, USA: ACM, December 1989, pp. 58–65.
- [4] S. Weiss and V. Fleishgaker, "Improved serial algorithms for mutation analysis," in *Proceedings of the 1993 International Symposium on Software Testing and Analysis ISSTA 1993*. New York, NY, USA, 1993, pp. 149–158.
- [5] I. M. Duncan, "Strong mutation testing strategies," Ph.D. dissertation, Department of Computer Science, University of Durham, 1993.





- [6] A. Acree, "On mutation," Ph.D. dissertation, School of Information and Computer Science, Georgia Institute of Technology, 1980.
- [7] A. Mathur and W. Wong, "Reducing the cost of mutation testing: an empirical study," Department of Computer Sciences, Purdue University, Technical Report SERC-TR-138-p, 1993.
- [8] A. Mathur, "Performance, effectiveness, and reliability issues in software testing," in *Proceedings of the 15th annual International Computer Software and Applications Conference COMPSAC*, Tokyo, Japan, September 1991, pp. 604–605.
- [9] R. A. DeMillo and J. Offutt, "Constraint-based automatic test generation," *IEEE Transactions on Software Engineering*, vol. 17, no. 9, pp. 901–910, September 1991.
- [10] R. DeMillo and J. Offutt, "Experimental results of automatically generated adequate test sets," *ACM Transactions on Software Engineering and Methodology*, vol. 2, pp. 109–127, April 1993.
- [11] T. Budd, "Mutation analysis of program test data," Ph.D. dissertation, Yale University, New Haven CT, 1980.
- [12] B. Choi and A. Mathur, "High performance mutation testing," *Journal of Systems and Software*, vol. 20, pp. 135–152, 1993.
- [13] A. Offutt, "Investigations of the software testing coupling effect," *ACM Transactions on Software Engineering and Methodology*, vol. 1, pp. 3–18, Jan 1992.



المؤتمر الدولي العربي الليبي الخامس للهندسة الكهربائية والإلكترونية 2010/10/26-23 طرابلس ليبيا



## Evaluating the Testability of VLSI Systems from X-Machines Formal Specification

Elfurjani Sassi Mresa

Department of Electrical and Electronic Engineering, Al Fateh University, Tripoli, Libya.  
Email: mresa@ee.edu.ly

*Abstract*—In recent years, growing system complexity and shrinking time-to-market requirements have resulted in a strong need for new design methods and tools. In order to keep pace with the increased system complexity, designers must work at a higher level of abstraction. Depending on the abstraction level (namely, the number of details used to model the system) different concerns can be addressed and solved. At each step of the design process, the key to cope with complexity is to model the systems, only with the minimum number of details needed. Abstraction hides complexity and accelerates design process[1]. This paper discusses the use of X-machines, which are general models of computation, in the specification of VLSI systems. The elementary theory of X-machines is briefly described, but the bulk of the paper is concerned with the testability aspects of VLSI systems. The ultimate hope is that by using X-machines to produce a high level specification, enough information can be obtained to indicate the parts of the design which might be difficult to test and hence assessing design testability at an early stage in the design process.

An abstract X-machine does not provide enough information to the system designers to adopt a suitable design methodology to make more testable designs. There is no procedural method to follow in implementing a system from its given X-specification and hence, a number of different design styles with different testability measures can be implemented for the same specification. In this paper, however, we will show that X-machine specifications might be beneficial if they are used as a pre-design phase to other conventional hardware specification languages. They can provide useful information to the lower level

hardware designers about the complexity of the required design, the functions which might be implemented with some shared hardware and the areas which have feedback loops and may therefore cause testability problems.

### I. X-MACHINES

X-machines were introduced by Samuel Eilenberg[2], as a general model of computation. The concept of an X-machine is further described by Mike Holcombe[3] and Gilbert Laycock[4]. Essentially an X-machine can be thought of as a Finite State Machine with one important exception, the labels of the arcs are functions that operate on a fundamental data type <sup>1</sup> called, X. The formal definition of an X-machine is presented in the following section.

#### Definition

The style of definition we use here is due mainly to Holcombe[3] and Laycock[4].

An X-Machine,  $\mathcal{M}$ , is a 10 tuple:

$$\mathcal{M} = (X, \phi, Q, F, Y, Z, \alpha, \beta, I, T)$$

Where:

- $X$  is the fundamental data set to be processed by the machine.
- $Y$  and  $Z$  are the input and output sets respectively. The data types of these sets might not directly match the type of the fundamental data set  $X$  and therefore,

<sup>1</sup>Actually the labels could be relations in theory, in practice we usually use functions.



some encoding and decoding might be needed before and after the processing is performed.

- $\alpha$  and  $\beta$  are the input and output relations respectively. They are used to convert the input and output sets into and from the fundamental data set  $X$ :

$$\alpha : Y \longleftrightarrow X$$

$$\beta : X \longleftrightarrow Z$$

- $Q$  is a finite set of states. A single state  $q \in Q$  usually represents a group of related states in a lower level specification.
- $\phi$  is the type of  $\mathcal{M}$ , a set of relations on  $X$ :

$$\phi : \mathbb{P}(X \longleftrightarrow X)$$

$\phi$  represents the set of relations or functions which operate on the fundamental data set  $X$ .  $\phi$  can be infinite set, although only a finite number of the set members will actually be used in any particular machine.

- $F$  is the 'next state' function  
 $F : Q \rightarrow (\phi \rightarrow \mathbb{P} Q)$   
 $F$  is often described by means of a state transition diagram.
- $I$  and  $T$  are the sets of initial and terminal states respectively.  $I \subseteq Q, T \subseteq Q$ .

Intuitively, the control structure of this model which determines how the processing is performed is very similar to the state transition graph of a Finite State Machine. However, this similarity is concerned with the control of processing and not with the type of processing that the machine performs. Nevertheless, this similarity is very useful and allows us to apply familiar techniques for machine analyses which have proved to be very successful.

In the following sections, we will illustrate by an example how an X-machine can be used to specify a digital system and how we might assess the testability of that

system.

## II. EXAMPLE: COFFEE MACHINE CONTROLLER

The Coffee Machine Controller is used to control the operation of an automatic coffee vending machine. It continually checks the current inputs applied to the coffee machine by both the customer and the machine environment parameters and consequently, generates the appropriate signals which control the machine. The block diagram and the state diagram of the controller is shown in Figure 1 and Figure 2 respectively.

### A. Description.

- 1) In the initial state the machine waits for some money to be inserted (all drinks cost 15p).
- 2) Only three coins (5p,10p and 20p), are accepted by the machine.
- 3) When the sum of the inserted coins exceeds the required amount, the change is returned to the user and a selection can then be made. If there is no change available in the machine, the user will be advised to insert exact money only.
- 4) Finally, the selected drink is dispensed and the machine returns to its initial state. If the selected drink is not available, however, the machine does not respond to the user request and it waits for another selection to be made.

### B. Specification using X-machines

The diagram in Figure 3 shows how the coffee machine controller can be modelled by an X-Machine. A suitable definition of the fundamental data type  $X$  which represents the data set upon which the machine operates is as follows:

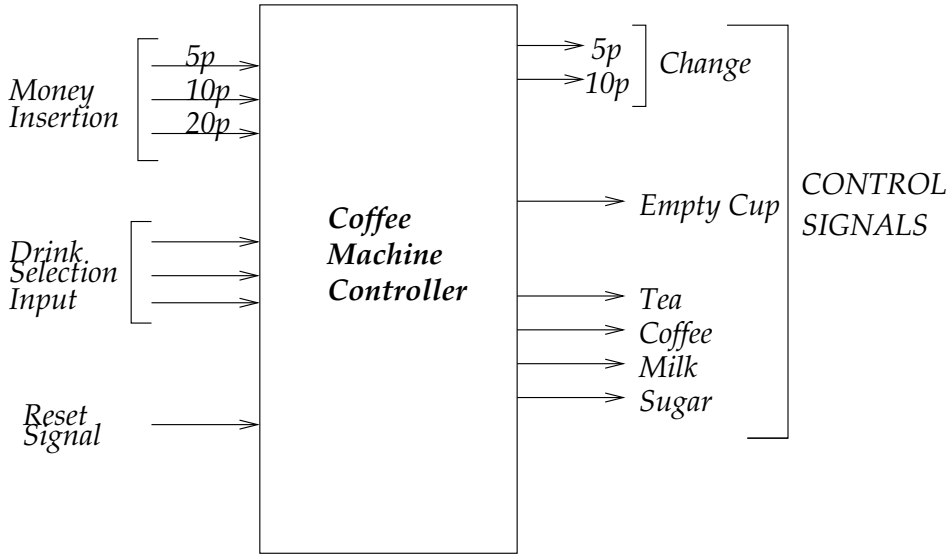


Fig. 1. Block Diagram

Given that:

$TENS ::= present \mid absent$   
 $SELECTAVAIL ::= available \mid notavailable$   
 $DRINKAVAIL ::= empty \mid notempty$   
 $SELECT ::= BTS \mid BTnS \mid WTS \mid WTnS \mid BCS \mid BCnS \mid WCS \mid WCnS$

Where the elements of the set  $SELECTAVAIL$  indicate whether the selected drink is available, and the elements of the set  $DRINKAVAIL$  indicate whether the machine is empty. Each of the elements of the set  $SELECT$  represents a specific item selected by the customer, these elements are described below:

$BTS$  : Black tea with sugar  
 $WTS$  : White tea with sugar  
 $BTnS$ : Black tea no-sugar  
 $WTnS$ : White tea no-sugar  
 $BCS$  : Black coffee with sugar  
 $WCS$  : White coffee with sugar

$BCnS$ : Black coffee no-sugar  
 $WCnS$ : White coffee no-sugar

CoffeeMachine

$X : \mathbb{Z} \times TENS \times \mathbb{Z} \times SELECTAVAIL \times DRINKAVAIL \times SELECT \times \mathbb{Z} \times \mathbb{Z}$

$\forall (count5, ten, total, selectAvail, drinkAvail, select, retFives, retTens) \in X$   
 $\Rightarrow count5 \geq 0 \wedge$   
 $total \in \{0, 5, 10, 15, 20, 25, 30\} \wedge$   
 $retFives \in \{0, 1, 2, 3\} \wedge$   
 $retTens \in \{0, 1\}$

Where:

- $count5$  is an integer value representing the number of 5p coins currently in the machine.
- $ten$  is either *present* or *absent* to indicate whether any 10p coins are available in the machine.
- $total$  is initially zero at the first cycle.

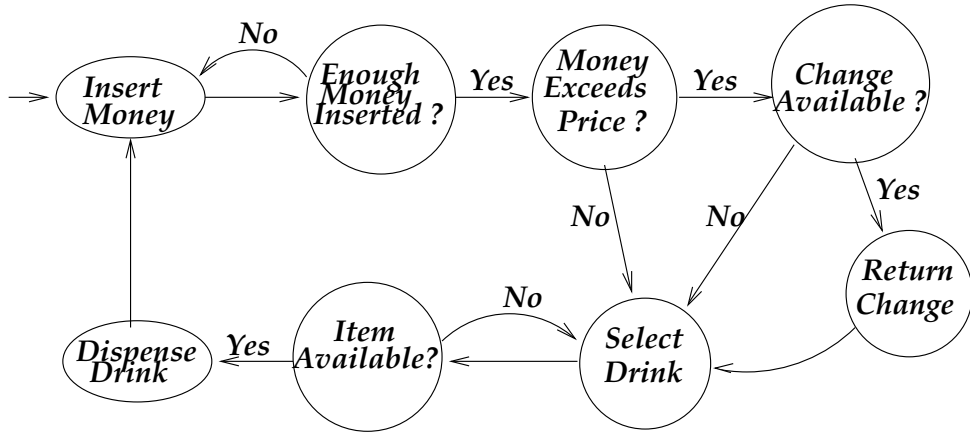


Fig. 2. State Diagram

It can be one of the integer values  $\{0, 5, 10, 15, 20, 25, 30\}$ . Each element of this set represents the total amount of money inserted by the customer at a particular state.

- *drinkAvail* is either *empty* or *notempty* to indicate the machine state.
- *selectAvail* is either *Yes* or *No* to indicate whether the selected drink is available.
- *select* represents a specific item selected by the customer.
- *retFives* is an integer value and represents the number of 5p coins to be returned to the customer.
- *retTens* is an integer value and represents the number of 10p coins to be returned to the customer.

### C. Interactive Inputs

$$\begin{array}{|l}
 y_1 : \mathbb{Z} \times \mathbb{Z} \times \mathbb{Z} \\
 \hline
 y_1 \in \{(3, 0, 0), (1, 1, 0), (0, 2, 0), \\
 (0, 0, 1), (1, 0, 1), (0, 1, 1)\}
 \end{array}$$

Where  $(a, b, c)$  represents the number of 5p, 10p and 20p coins, respectively.

$$| \quad y_2 : \text{SELECT}$$

### D. Transition Functions:

The X-machine will be carrying out computations on the fundamental data set  $X$ , which will represent the flow of data from the input to the output.

Initially the values of *count5*, *ten*, *selectAvail* and *drinkAvail* are assumed to be set during the first cycle, they represent system environment parameters<sup>2</sup>.

$$\begin{array}{l}
 (-, -, 0, -, \text{empty}, -, 0, 0) \xrightarrow{f^0} \\
 (-, -, 0, -, \text{empty}, -, 0, 0)
 \end{array}$$

$$\begin{array}{l}
 (-, -, \text{total}, -, \text{notempty}, -, 0, 0) \xrightarrow{f^1} \\
 (-, -, \text{total} + 5, -, \text{notempty}, -, 0, 0)
 \end{array}$$

$$\begin{array}{l}
 (-, -, \text{total}, -, \text{notempty}, -, 0, 0) \xrightarrow{f^2} \\
 (-, -, \text{total} + 10, -, \text{notempty}, -, 0, 0)
 \end{array}$$

$$\begin{array}{l}
 (-, -, \text{total}, -, \text{notempty}, -, 0, 0) \xrightarrow{f^3} \\
 (-, -, \text{total} + 20, -, \text{notempty}, -, 0, 0)
 \end{array}$$

$$\begin{array}{l}
 (-, -, 15, -, -, 0, 0) \xrightarrow{f^4} \\
 (-, -, 15, -, -, 0, 0)
 \end{array}$$

$$\begin{array}{l}
 \text{count5} > 0 : \\
 (\text{count5}, -, 20, -, -, \text{retFives}, 0) \xrightarrow{f^5} \\
 (\text{count5} - 1, -, 20, -, -, \text{retFives} + 1, 0)
 \end{array}$$

<sup>2</sup>The symbol  $-$  is used for an arbitrary constant.

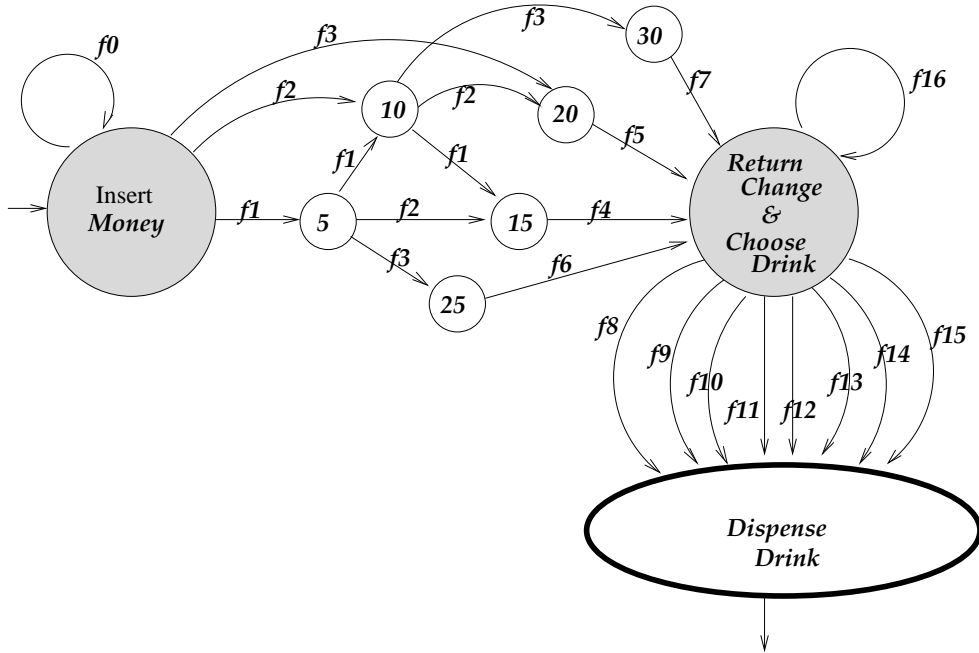


Fig. 3. Specification of the Coffee Machine Controller using an X-Machine

$$\begin{aligned} (0, -, 20, -, -, -, 0, 0) &\xrightarrow{f^5} \\ (0, -, 20, -, -, -, 0, 0) & \end{aligned}$$

$$\begin{aligned} (-, present, 25, -, -, -, 0, retTens) &\xrightarrow{f^6} \\ (-, x, 25, -, -, -, 0, retTens + 1) & \end{aligned}$$

$$\begin{aligned} count5 > 1 : \\ (count5, absent, 25, -, -, -, retFives, 0) &\xrightarrow{f^6} \\ (count5 - 2, absent, -, 25, -, -, retFives + 2, 0) & \end{aligned}$$

$$\begin{aligned} (1, absent, 25, -, -, -, retFives, 0) &\xrightarrow{f^6} \\ (0, absent, 25, -, -, -, retFives + 1, 0) & \end{aligned}$$

$$\begin{aligned} (0, absent, 25, -, -, -, 0, 0) &\xrightarrow{f^6} \\ (0, absent, 25, -, -, -, 0, 0) & \end{aligned}$$

$$\begin{aligned} count5 > 0 : \\ (count5, present, 30, -, -, -, retFives, retTens) &\xrightarrow{f^7} \\ (count5 - 1, x, 30, -, -, -, retFives + 1, retTens + 1) & \end{aligned}$$

$$\begin{aligned} (0, present, 30, -, -, -, 0, retTens) &\xrightarrow{f^7} \\ (0, x, 30, -, -, -, 0, retTens + 1) & \end{aligned}$$

$$\begin{aligned} count5 > 2 : \\ (count5, absent, 30, -, -, -, retFives, 0) &\xrightarrow{f^7} \\ (count5 - 3, absent, 30, -, -, -, retFives + 3, 0) & \end{aligned}$$

$$\begin{aligned} (2, absent, 30, -, -, -, retFives, 0) &\xrightarrow{f^7} \\ (0, absent, 30, -, -, -, retFives + 2, 0) & \end{aligned}$$

$$\begin{aligned} (1, absent, 30, -, -, -, retFives, 0) &\xrightarrow{f^7} \\ (0, absent, 30, -, -, -, retFives + 1, 0) & \end{aligned}$$

$$\begin{aligned} (0, absent, 30, -, -, -, 0, 0) &\xrightarrow{f^7} \\ (0, absent, 30, -, -, -, 0, 0) & \end{aligned}$$

$$\begin{aligned} (-, -, x, available, -, y, -, -) &\xrightarrow{f^8} \\ (-, -, 0, z, -, BTS, -, -) & \end{aligned}$$

$$\begin{aligned} (-, -, x, available, -, y, -, -) &\xrightarrow{f^9} \\ (-, -, 0, z, -, BTnS, -, -) & \end{aligned}$$

$$\begin{aligned} (-, -, x, available, -, y, -, -) &\xrightarrow{f^{10}} \\ (-, -, 0, z, -, WTS, -, -) & \end{aligned}$$

$$\begin{aligned} (-, -, x, available, -, y, -, -) &\xrightarrow{f^{11}} \\ (-, -, 0, z, -, WTnS, -, -) & \end{aligned}$$

$$\begin{aligned} (-, -, x, available, -, y, -, -) &\xrightarrow{f^{12}} \\ (-, -, 0, z, -, BCS, -, -) & \end{aligned}$$

$$\begin{aligned} (-, -, x, available, -, y, -, -) &\xrightarrow{f^{13}} \\ (-, -, 0, z, -, BCnS, -, -) & \end{aligned}$$



$$\begin{aligned} &(-, -, x, \text{available}, -, y, -, -) \xrightarrow{f14} \\ &(-, -, 0, z, -, \text{WCS}, -, -) \end{aligned}$$

$$\begin{aligned} &(-, -, x, \text{available}, -, y, -, -) \xrightarrow{f15} \\ &(-, -, 0, z, -, \text{WCnS}, -, -) \end{aligned}$$

$$\begin{aligned} &(-, -, -, \text{notavailable}, -, -, -, -) \xrightarrow{f16} \\ &(-, -, -, \text{notavailable}, -, -, -, -) \end{aligned}$$

$$\begin{aligned} &(-, -, -, -, -, \text{WTS}, x, y) \rightarrow (\text{WhiteTeaSugar}, x, y) \\ &(-, -, -, -, -, \text{WTnS}, x, y) \rightarrow (\text{WhiteTeaNoSugar}, x, y) \\ &(-, -, -, -, -, \text{BCS}, x, y) \rightarrow (\text{BlackCoffeeSugar}, x, y) \\ &(-, -, -, -, -, \text{BCnS}, x, y) \rightarrow (\text{BlackCoffeeNoSugar}, x, y) \\ &(-, -, -, -, -, \text{WCS}, x, y) \rightarrow (\text{WhiteCoffeeSugar}, x, y) \\ &(-, -, -, -, -, \text{WCnS}, x, y) \rightarrow (\text{WhiteCoffeeNoSugar}, x, y) \end{aligned}$$

### E. Input/Output Relations

Input Relation:

$$\alpha : Y \longleftrightarrow X$$

The initial state is:

$$(-, -, 0, -, -, -, 0, 0)$$

Output Relation:

$$\beta : X \longleftrightarrow Z$$

Given that:

$$\begin{aligned} \text{DISPENSEDRINK} ::= & \text{BlackTeaSugar} \\ & | \text{BlackTeaNoSugar} \\ & | \text{WhiteTeaSugar} \\ & | \text{WhiteTeaNoSugar} \\ & | \text{BlackCoffeeSugar} \\ & | \text{BlackCoffeeNoSugar} \\ & | \text{WhiteCoffeeSugar} \\ & | \text{WhiteCoffeeNoSugar} \end{aligned}$$

Where the elements of the set *DISPENSEDRINK* represent all the drinks which can be dispensed by the machine, the output of our model is defined as follows:

$$\begin{array}{|l} \hline \text{Output} \\ \hline Z : \text{DISPENSEDRINK} \times \mathbb{Z} \times \mathbb{Z} \\ \hline \forall (\text{dipenseDrink}, \text{retFives}, \text{retTens}) \in Z \\ \Rightarrow \text{retFives} \in \{0, 1, 2, 3\} \wedge \\ \text{retTens} \in \{0, 1\} \\ \hline \end{array}$$

The coding relation  $\beta$  describes how data processed by the machine is decoded into a suitable output format. The applications of  $\beta$  on the *CoffeeMachine* data set ( $X$ ) are listed below:

$$\begin{aligned} &(-, -, -, -, -, \text{BTS}, x, y) \rightarrow (\text{BlackTeaSugar}, x, y) \\ &(-, -, -, -, -, \text{BTnS}, x, y) \rightarrow (\text{BlackTeaNoSugar}, x, y) \end{aligned}$$

### III. MODIFIED VERSION OF PREVIOUS EXAMPLE

We will, for the sake of argument, modify the specification presented in the previous example to introduce a feedback loop. We will show that this loop has a significant impact on the design complexity and consequent testing.

In Figure 4 the state diagram given in the previous example for the coffee machine controller has been altered to incorporate a new feature in the design. This new feature gives the customer the option to reclaim his money if the selected drink is not available.

#### A. Specification using $X$ -machines

Given that:

$$\text{RETMONEY} ::= \text{yes} \mid \text{no}$$

Which is a new member added to the original definition of the *CoffeeMachine* state. It represents another interactive input.

A suitable definition of the fundamental data type  $X$  which represents the data set upon which the machine operates is:

$$\begin{array}{|l} \hline \text{NewCoffeeMachine} \\ \hline X : \mathbb{Z} \times \text{TENS} \times \mathbb{Z} \times \text{SELECTAVAIL} \times \\ \text{DRINKAVAIL} \times \text{SELECT} \times \text{RETMONEY} \times \\ \mathbb{Z} \times \mathbb{Z} \\ \hline \forall (\text{count5}, \text{ten}, \text{total}, \text{selectAvail}, \text{drinkAvail}, \\ \text{select}, \text{retMoney}, \text{retFives}, \text{retTens}) \in X \\ \Rightarrow \text{count5} \geq 0 \wedge \\ \text{total} \in \{0, 5, 10, 15, 20, 25, 30\} \wedge \\ \text{retFives} \in \{0, 1, 2, 3, 4, 5, 6\} \wedge \\ \text{retTens} \in \{0, 1, 2\} \\ \hline \end{array}$$



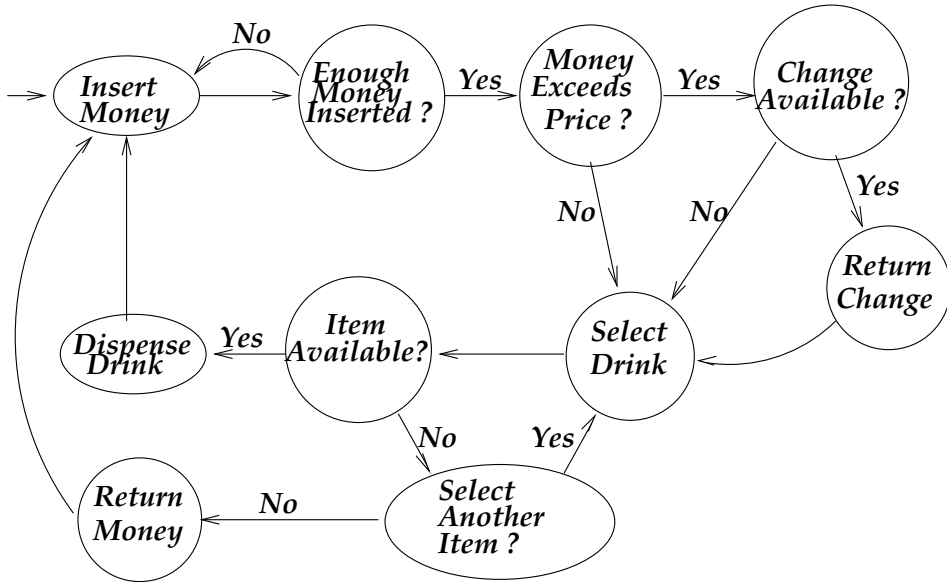


Fig. 4. Modified State Diagram

Where:

- *retMoney* is a member of the set *RETMONEY*. It is input by the customer to indicate whether the money is to be returned, if the selected drink is not available.

### B. Transition Functions

The transition functions  $f1, f2, \dots, f16$  which operate on the fundamental data set are very similar to those shown in the previous example.

The new introduced transition functions are given below:

$$\begin{matrix} (-, -, -, \text{notavailable}, -, -, -, -, -) \\ (-, -, -, \text{notavailable}, -, -, -, -, -) \end{matrix} \xrightarrow{f16}$$

$$\begin{matrix} (-, -, -, x, -, y, \text{no}, -, -) \\ (-, -, -, x, -, y, z, -, -) \end{matrix} \xrightarrow{f17}$$

$$\text{count5} > 0 : \begin{matrix} (\text{count5}, \text{present}, x, y, z, w, \text{yes}, \text{retFives}, \text{retTens}) \end{matrix} \xrightarrow{f18}$$

$$(\text{count5} - 1, v, 0, y, z, w, u, \text{retFives} + 1, \text{retTens} + 1)$$

$$\begin{matrix} (0, \text{present}, x, y, z, w, \text{yes}, -, \text{retTens}) \\ (0, v, 0, y, z, w, u, -, \text{retTens} + 1) \end{matrix} \xrightarrow{f18}$$

$\text{count5} > 2 :$

$$\begin{matrix} (\text{count5}, \text{absent}, x, y, z, w, \text{yes}, \text{retFives}, -) \\ (\text{count5} - 3, \text{absent}, 0, y, z, w, u, \text{retFives} + 3, -) \end{matrix} \xrightarrow{f18}$$

$$\begin{matrix} (2, \text{absent}, x, y, z, w, \text{yes}, \text{retFives}, -) \\ (0, \text{absent}, 0, y, z, w, u, \text{retFives} + 2, -) \end{matrix} \xrightarrow{f18}$$

$$\begin{matrix} (1, \text{absent}, x, y, z, w, \text{yes}, \text{retFives}, -) \\ (0, \text{absent}, 0, y, z, w, u, \text{retFives} + 1, -) \end{matrix} \xrightarrow{f18}$$

$$\begin{matrix} (0, \text{absent}, x, y, z, w, \text{yes}, -, -) \\ (0, \text{absent}, 0, y, z, w, u, -, -) \end{matrix} \xrightarrow{f18}$$

### IV. EVALUATION OF TESTABILITY

X-machines are considered to be an appropriate formalism for the specification and analysis of arbitrary systems [3][4]. The main advantage possessed by the X-machine notation, other than its general applicability and simplicity, is that it allows a clear distinction between the control aspects of the





and (c) respectively.

In general, the complexity of the system implementation increases with the number of loops in the X-specification diagram. Furthermore, the larger the sets of states that lie within these loops, the more complex the system is likely to be. This is due to the simple fact that every loop in the X-specification diagram typically translates into one or more feedback loops in the hardware design. The appearance of feedback loops in a hardware design would almost always imply an increase in the complexity of both of the operation and testability of the hardware blocks which exist within these loops. Naturally, the size of the hardware blocks which would be effected by the feedback loops in the hardware design increases with the length of the loops in the X-specification diagram.

To summarise, we can say that loops in the X-specification diagram imply an increase in both of the hardware components and sequentiality in the hardware design. This has an important effect on both of the cost and the testability of the ultimate design.

From the X-specification diagrams of the Coffee Machine Controller and its modified version given in Figure 3 and Figure 5, it can be seen that the modification made in the specification requirement of the original system has resulted in a modified version with a different X-specification diagram. The difference between the two X-specification diagrams given in Figure 3 and Figure 5 is illustrated by the inclusion of the extra components

shown by the dashed line rectangle shown in Figure 7.

The existence of the loop indicated by *fl6* and *fl7* in Figure 7 as one of the extra components, although it is a simple loop between only two states, can have a considerable effect on the hardware design. From the two hardware designs of the original Coffee Machine Controller and its modified version given in Figure 8 and Figure 10 respectively, it can be seen that the later involves more hardware components. It also has two feedback loops indicated by *FB1* and *FB2* in Figure 10 and consequently, both of the hardware cost and testability are affected.

- 2) Transition functions with the same labels identify the same operations being performed by the system at different states. Although it is not always possible, these transition functions, especially if they appear in succession, might be implemented with the same hardware components. Moreover, it might also be possible to make partial or total use of these components in implementing other transition functions of a similar operation nature. This decision has an important impact on the hardware complexity and consequent testability. To illustrate this point, consider the X-specification diagram for our coffee machine controller shown in Figure 3. *fl* is used several times in the specification. It may be possible to implement several applications of *fl* using the same components of hardware, i.e. the application of *fl* in state *InsertMoney* may be implemented with the same hardware as the application in state 5 and state 10.

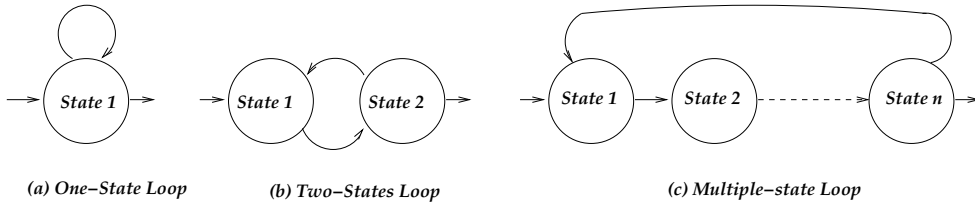


Fig. 6. Types of Loops

This is in fact done in the designs shown in Figure 8 and Figure 10. All the applications of  $f1$  in the mentioned states are implemented using the same block of hardware. The same is done for  $f2$  and  $f3$ . The hardware blocks used, are labelled A, B and C for  $f1$ ,  $f2$  and  $f3$  respectively.

- 3) In contrast to the situation described above, if there exist two or more distinct transition functions which have identical behaviour on a subset of the data set  $X$ , where  $X$  is the fundamental data set upon which the machine operates, then this would suggest that these transition functions might be implemented in such a way as to share some hardware. For example, In our model presented in the previous section, the two transition functions  $f7$  and  $f18$  behave identically on some parts of the data set  $X$  and consequently; most of the hardware components involved in their implementation were shared.

$$\begin{aligned}
 & \text{count5} > 0 : \\
 & (\text{count5}, \text{present}, 30, -, -, -, \text{retFives}, \text{retTens}) \xrightarrow{f7} 4) \\
 & (\text{count5} - 1, x, 30, -, -, -, \text{retFives} + 1, \text{retTens} + 1) \\
 & (0, \text{present}, 30, -, -, -, 0, \text{retTens}) \xrightarrow{f7} \\
 & (0, x, 30, -, -, -, 0, \text{retTens} + 1) \\
 & \text{count5} > 2 : \\
 & (\text{count5}, \text{absent}, 30, -, -, -, \text{retFives}, 0) \xrightarrow{f7} \\
 & (\text{count5} - 3, \text{absent}, 30, -, -, -, \text{retFives} + 3, 0) \\
 & (2, \text{absent}, 30, -, -, -, \text{retFives}, 0) \xrightarrow{f7} \\
 & (0, \text{absent}, 30, -, -, -, \text{retFives} + 2, 0)
 \end{aligned}$$

$$\begin{aligned}
 & (1, \text{absent}, 30, -, -, -, \text{retFives}, 0) \xrightarrow{f7} \\
 & (0, \text{absent}, 30, -, -, -, \text{retFives} + 1, 0) \\
 & (0, \text{absent}, 30, -, -, -, 0, 0) \xrightarrow{f7} \\
 & (0, \text{absent}, 30, -, -, -, 0, 0) \\
 & \text{count5} > 0 : \\
 & (\text{count5}, \text{present}, x, y, z, w, \text{yes}, \text{retFives}, \text{retTens}) \xrightarrow{f18} \\
 & (\text{count5} - 1, v, 0, y, z, w, u, \text{retFives} + 1, \text{retTens} + 1) \\
 & (0, \text{present}, x, y, z, w, \text{yes}, -, \text{retTens}) \xrightarrow{f18} \\
 & (0, v, 0, y, z, w, u, -, \text{retTens} + 1) \\
 & \text{count5} > 2 : \\
 & (\text{count5}, \text{absent}, x, y, z, w, \text{yes}, \text{retFives}, -) \xrightarrow{f18} \\
 & (\text{count5} - 3, \text{absent}, 0, y, z, w, u, \text{retFives} + 3, -) \\
 & (2, \text{absent}, x, y, z, w, \text{yes}, \text{retFives}, -) \xrightarrow{f18} \\
 & (0, \text{absent}, 0, y, z, w, u, \text{retFives} + 2, -) \\
 & (1, \text{absent}, x, y, z, w, \text{yes}, \text{retFives}, -) \xrightarrow{f18} \\
 & (0, \text{absent}, 0, y, z, w, u, \text{retFives} + 1, -) \\
 & (0, \text{absent}, x, y, z, w, \text{yes}, -, -) \xrightarrow{f18} \\
 & (0, \text{absent}, 0, y, z, w, u, -, -)
 \end{aligned}$$

The hardware shared by both of the transition functions  $f7$  and  $f18$  can be indicated by all those components which are injected in a direct or indirect way by the output of the OR-gate labelled "W" in Figure 10.

More than one specification with different levels of complexity can be used for the same functionality and therefore; it is not always possible to relate operations used by X-machine specification to specific hardware components. For example, a different specification could have been used for the transfer functions  $f5$  -

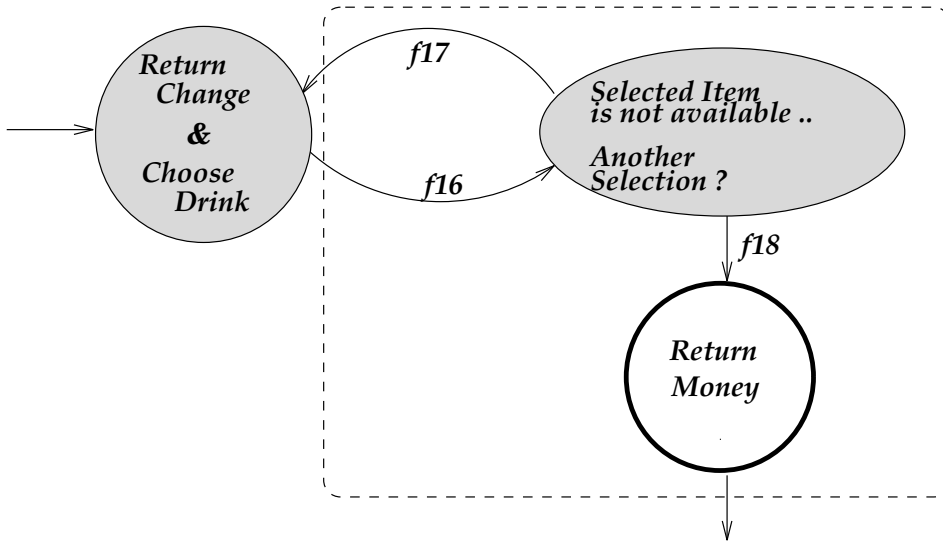


Fig. 7. Diagram illustrating the extra components in the X-specification diagram of the modified version

$f7$  shown in the first example. The values of  $retFives \in \{0, 1, 2, 3\}$  and  $retTens \in \{0, 1\}$ , which are initially set to 0, could have been simply set to specific values within their corresponding data sets rather than using the more complicated '+' operation. The transfer function  $f7$  could have been specified as follows:

$$\begin{aligned}
 &count5 > 0 : \\
 &(count5, present, 30, -, -, -, 0, 0) \xrightarrow{f7} \\
 &(count5 - 1, x, 30, -, -, -, 1, 1) \\
 &(0, present, 30, -, -, -, 0, 0) \xrightarrow{f7} \\
 &(0, x, 30, -, -, -, 0, 1) \\
 &count5 > 2 : \\
 &(count5, absent, 30, -, -, -, 0, 0) \xrightarrow{f7} \\
 &(count5 - 3, absent, 30, -, -, -, 3, 0) \\
 &(2, absent, 30, -, -, -, 0, 0) \xrightarrow{f7} \\
 &(0, absent, 30, -, -, -, 2, 0) \\
 &(1, absent, 30, -, -, -, 0, 0) \xrightarrow{f7} \\
 &(0, absent, 30, -, -, -, 1, 0) \\
 &(0, absent, 30, -, -, -, -, 0) \xrightarrow{f7} \\
 &(0, absent, 30, -, -, -, -, 0)
 \end{aligned}$$

Although  $f18$  behaves identically to  $f7$  on the data variables  $retFives$  and  $retTens$ , the '+' operation used in  $f18$  could not have been avoided. This is because the initial values of  $retFives$  and  $retTens$  in the latter case are unknown. It is accidental that we chose to use the '+' operation in our specification of the transfer functions  $f5-f7$ , which allowed us to see the behaviour similarities between  $f7$  and  $f18$  shown in (3). Had we chosen the above form in specifying  $f7$ , these similarities would have not been noticed.

X-machine models represent a very high level of specification. The structure of state transition diagrams of X-machine specifications masks a model of considerable computational power, due to the fact that the functions labelling the arcs can be of a compound nature, i.e. many different simple operations can be performed in every transition from one state to another. Indeed they



can be of arbitrary complexity. There is no procedural method to follow in implementing a system from its given X-specification and hence, a number of different design styles with different testability measures can be implemented for the same specification. This can be clearly seen by the two different designs of our Coffee Machine Controller given in Figure 8 and Figure 9. Although, both designs were made for the same specification, they have completely different design styles and consequently; different testability measures. This means that different techniques would be used to assess and enhance the testability of each of these circuits.

## V. CONCLUSIONS

X-machine specifications can be useful for design and testing, in terms of conveying the dynamics and the complexity of the required design. X-machine specifications, because they are completely functional, do not provide the block structure information that is useful for assessing testability.

However, this high level of specification can be of good value if it is integrated as a pre-design phase to other lower level hardware description languages such as VHDL. The use of X-specification model as an early phase in the design process can give some feedback to the lower level hardware designer about the complexity of the required design, the functions which might be implemented with some shared hardware and more importantly, the areas which need extra care in their implementation, so that testability problems can be reduced.

## REFERENCES

- [1] K. Bogdanov, M. Holcombe, F. Ipate, L. Seed, and S. Vanak, "Testing methods for x-machines: a review," *Formal Aspects of Computing*, vol. 18, pp. 3–30, 2006.
- [2] S. Eilenberg., "Automata, languages and machines," *Academic Press*, vol. A, no. 1, NewYork 1974.
- [3] M. Holcombe, "X-machines as a basis for dynamic system specification," *Software Engineering Journal*, vol. 2, March 1988.
- [4] G. Laycock, "Introduction to x-machines," Department of Computer Science, University of Sheffield, Sheffield, UK, Research Report CS-93-13, 1993.
- [5] R. Pang, "Formal specification and functional verification of vlsi systems," MSc. Thesis, Department of Computer Science, University of Sheffield, Sheffield, UK, 1992.
- [6] L. J. Morell, "A theory of fault-based testing," *IEEE Transactions on Software Engineering*, vol. 16, no. 8, pp. 844–857, August 1990.
- [7] E. J. Weyuker, "The evaluation of program-based software test data adequacy criteria," *Communications of the ACM*, vol. 31, no. 6, pp. 668–675, June 1988.
- [8] E. J. Weyuker and T. Ostrad, "Theories of program testing and the application of revealing subdomains," *IEEE Transactions on Software Engineering*, vol. 6, no. 3, pp. 236–246, May 1980, .



APPENDIX

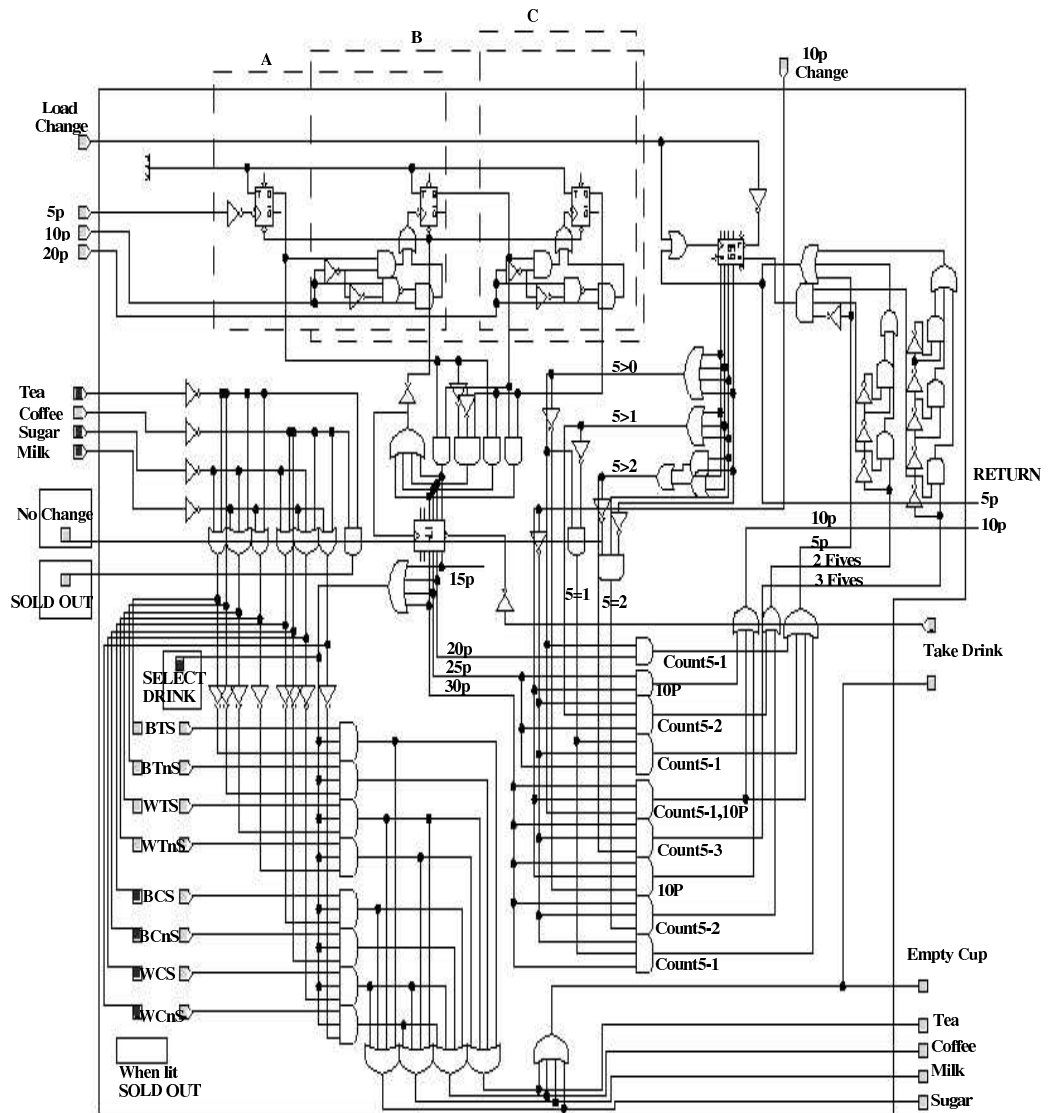


Fig. 8. A Design for the Coffee Machine Controller

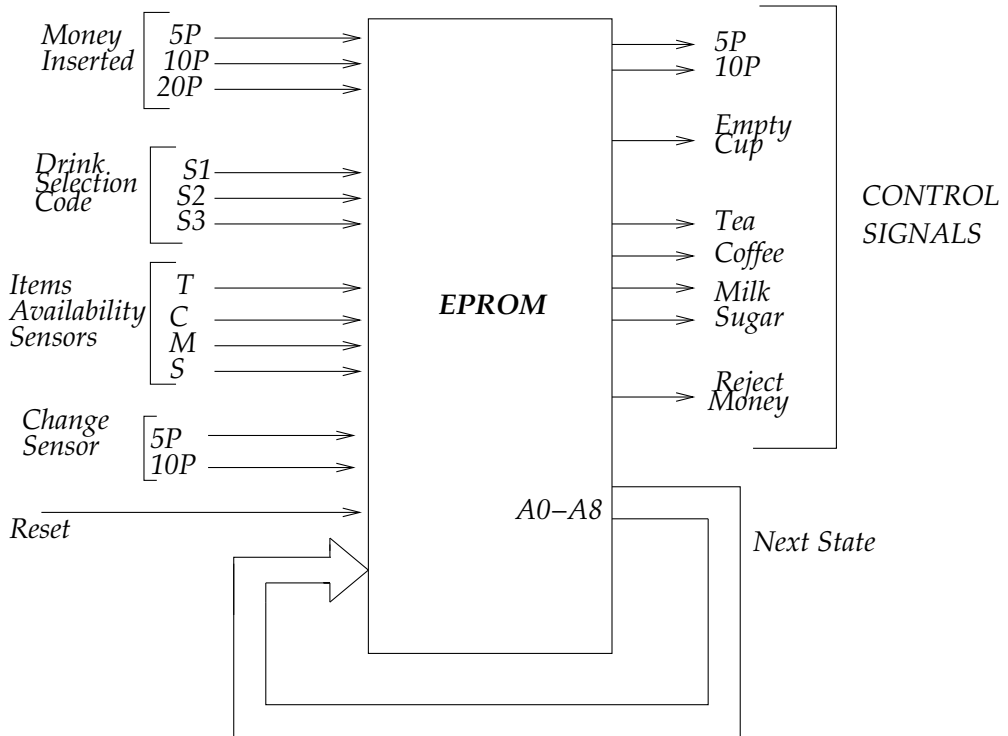


Fig. 9. A Different Design for the Coffee Machine Controller



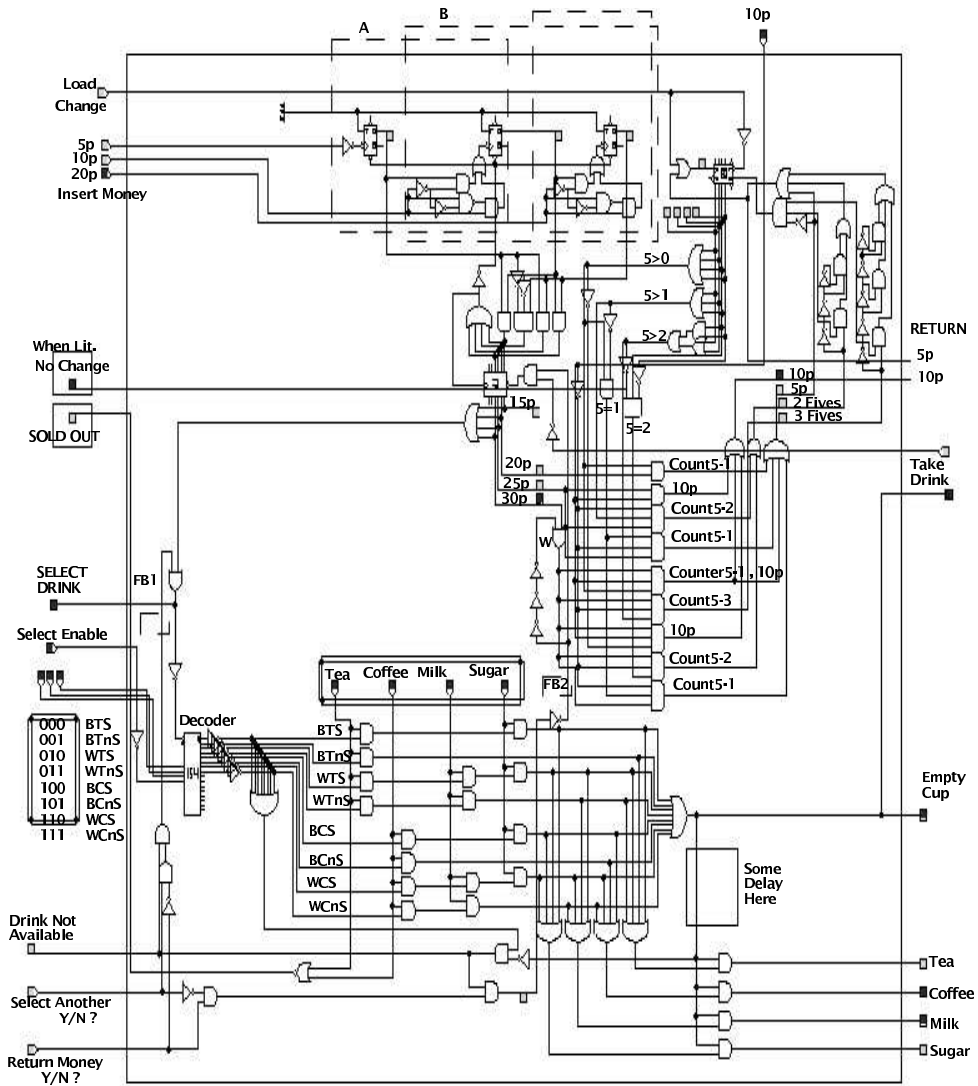


Fig. 10. A Design for the Modified Version of the Coffee Machine Controller



المؤتمر الدولي العربي الليبي الخامس للهندسة الكهربائية والإلكترونية 2010/10/26-23 طرابلس ليبيا



## Time Efficient Extension of Exponential Index

Seema Verma

AIM & ACT, Banasthali University, Banasthali (INDIA) – 304022

[Seemaverma3@yahoo.com](mailto:Seemaverma3@yahoo.com)

Rakhee

Mathematics Group, Birla Institute of Technology & Sciences,

Pilani (INDIA) – 333031

[Rakhee.bv@gmail.com](mailto:Rakhee.bv@gmail.com)

Savita Kumari \*

Computer Engineering, Faculty of Engineering College, Zawia (Libya)

Mobile No. 0917200671, E- mail: savita\_gandas@yahoo.com

Mahmoud A. Artemi

Higher Institute of Vocational Studies, Zawia (Libya)

[mah\\_art78@yahoo.com](mailto:mah_art78@yahoo.com)

**Abstract-** Wireless broadcasting has emerged as an excellent and scalable way to disseminate information to massive number of clients equipped with hand held devices. In practice, wireless broadcast faces challenge from issues like timely delivery of data, error free quality of service, low battery capacity and limited bandwidth. Different applications need to curb out different challenges. Exponential indexing is recently been popular as parameterized and distributed index scheme to reduce access time and energy consumption. Here, in this paper we address an issue where error free timely delivery of information is major concern. Such state of affairs generally appears in an in-house environment where recharging of battery is not a serious concern. We have proposed a Data Replicated Exponential Index (DR-EI) which is extension of exponential index to get advantages of data replication to reduce access latency. Here, energy consumption is not considered as a serious concern and hence access latency minimization can only be discussed with out enunciating tune time. The DR-EI is found to have lesser access latency than exponential index in specific situations.

**Key words:** mobile computing; wireless broadcast; exponential indexing; access latency; data replication.

### I. INTRODUCTION

In recent years, the use of wireless technology devices has been growing at an exponential rate; the standard for timely access of global information is also

changing. The recent advancement in mobile network, data dissemination and retrieval strategies, server and client architectures, services and applications have spurred an unprecedented emergence of



various techniques that de facto gives a new generation wireless environment. Most people are now able to access information located in wired networks anywhere and anytime using portable size wireless computing devices like notebooks, tablet PCs, personal digital assistants (PDAs) and GPRS-enabled cellular phones, laptops, palmtops which are powered by small batteries. These portable computing devices communicate with a central stationary server via a wireless channel and become the integral part of the existing distributed computing environment. These mobile clients can have an access to database information systems located at the static network while they are traveling and this type of computing is known as *wireless computing* or *mobile computing*.

Wireless computing provides database applications with useful aspects of wireless technology and subset of mobile computing that focuses on querying central database servers is referred as to *wireless databases*. Mobile service providers have established a number of information services that includes weather information or weather forecast services, news, stock indices information, foreign exchange rates, election results, tourist services, airlines, railways schedules etc. With the introduction of mobile computing, mobile client can have a higher flexibility in accessing the information from different locations with varying network connectivity.

The major shortcoming with broadcast data items in a wireless environment is that data are accessed sequentially. The increasing number of broadcast items causes

mobile clients to wait for larger time before receiving desired data item. Consequently, dependence of mobile devices on rechargeable batteries, which has limited capacities, is also another drawback of wireless data retrieval. The rate of increase in the chip density is much higher than the rate of increase of battery capacity. Also, due to ever increasing demand for mobile information services, huge numbers of operators providing services come in to fray which cause large data broadcast rate causing deterioration in quality of services. In order to overcome these drawbacks and improve system performance, it is necessary to visualize two performance matrices viz: *access time* and *tune time*. Former is related with retrieval delay of data while later is associated with energy consumption during data retrieval. Since these parameters are at odds to each other so can not be reduced to great extent simultaneously, but a trade off between two can be set for better system performance.

In a mobile environment queries can be classified into two categories *traditional queries* and *location-dependent queries*. The queries invoke in traditional wired environment are *traditional queries*, while when these are transmitted over a wireless communication network, called *location-dependent queries*. However, queries on wireless database have much more complexity, which does not exist in traditional wired databases. It is realized that location-dependent queries will soon become common and of great interest. Consequently, providing efficient and effective mobile information services that cover both traditional queries and location-



dependent queries will be highly desirable. The process of queries retrieval in wireless environment can be performed in two ways (i) pull or on demand mode and (ii) push or broadcast mode. On-demand queries are those where the client initiates the query and sends it to the server. The server processes the query and sends the result back to the client. In broadcast-based queries, the server broadcasts the data items periodically over one or more broadcast channel. Mobile clients tune to it and select data items of interest and capture it. With broadcast-based queries, a mobile client is able to retrieve information without wasting power to transmit a request to the server. Also it supports a large number of users at a time and the number of users in a cell or high information down loading rate does not affect query performance. It is effective despite a large number of user's retrieving data simultaneously. The behavior of the broadcast-based information system is unidirectional which means the server disseminates a set of data periodically to a multiple number of users. With this mechanism, the requests from the clients are not known a priori. These novel features of broadcast approach makes it popular among professionals engaged in data management.

The emergence of ubiquitous and small mobile devices along with the development of fast, reliable and accessible network has helped to advance research in pervasive computing area. The various data broadcast management techniques like indexing; scheduling and broadcast along parallel channels pivot this development. Broadcast data can be managed in various ways. The broadcast in which a data item is placed

once on a single broadcast channel is called *flat broadcast* and a broadcast in which a single data item appear more than once is called *skewed broadcast*.

The behavior of broadcast system is unidirectional and cyclic hence mobile client need only tune-in to channels. For effective data broadcast tree based and signature based, approach are used. Tree based approach gives the exact time of arrival of data so that mobile client can go to doze mode and save considerable amount of battery power; while signature based approach use signature to examine data object, which result in saving access time. Further, different application scenario demands minimization of different parameters. In an in-house environment where battery can easily be recharged or devices can be connected to direct power supply, only access time minimization is sufficient and in remote area where device has to depend on previously charged battery tune time needs a control. In some applications both parameters needs a trade off.

This paper envisages a situation where access time has high priority and a worse tune time can be accepted. We are intending to extend the existing exponential index to facilitate it with data replication at bucket level. The repetitions of data over broadcast channel fasten the data retrieval process and exponential index reduces the index overhead. We will propose Data Replicated Exponential Index (DR-EI) which is extended version of exponential index to toil better in specific situation. The rest of this paper is organized as follows. Section II,



introduces the background and gives related work on topic. In section III, proposed model along with its index structure and data access protocol is discussed. Section IV, evaluates its performance theoretically as well as it present simulation results carried out at different parameter values. Section V, finally concludes the paper and cite direction for further research in this field.

## II. BACKGROUND

The propose of broadcast disks by Acharya et. al. [1] in which hot data items are allocated more frequently than cold data items on disc from which average access time decrease; enunciate new paradigm in mobile computing. Amar and Wong describe the architecture of teletext broadcast cycles system considering data access probability [2]. Selective tuning is best possible way to reduce power consumption in single channel environment. A (1, m) indexing and distributed indexing method were developed to efficiently replicate and distributed the index tree in broadcast by Imielinski and Viswanathan and Badrinath [3] which is further extended for skewed broadcast by them [4]. Various Indexing and scheduling techniques to effectively manage data have been discussed in literature. Yee et. al. develops efficient strategy of data allocation on multiple channels [5]. Hsu et.al. considered data access frequency while allocating data and index over channels [6]. A parameterized distributed index is proposed by Xu et. al. (2004) to reduce index load on channel by forming index on per chunk basis [7]. Xu et. al. (2004) extended it for error resilient

case to improve data retrieval in fault ridden environment [8]. Seifert and Hung have developed FlexInd to increase flexibility of access tune trade off in exponential index [9].

Our work is further extension of exponential index considering data access frequency by replicating data buckets to propose a model with reduced error and access time for unambiguous applications. Proposed model called DR-EI is discussed in detail in forthcoming section.

## III. DATA REPLICATED – EXPONENTIAL INDEX (DR – EI)

This section presents an extension of parameterized and distributed exponential indexing scheme to allow it to index replicated data. We are discussing data management in an environment where only data retrieval time is major concern and energy consumption is least bothered. This situation generally occurs in offices, class rooms and train where battery of mobile device can easily be recharged or a direct power supply can be inputted. For this it is sufficient to adjust the access latency and derivation for tune time can be left to avoid the lengthening of paper. The proposed extension for data replicated exponential index called DR - exponential index (DR – EI) can serve better in such scenario.

### A. Preliminaries

In exponential Index two parameters I and r are tunable to adjust access latency and tune time. DR – EI takes data access frequency in to account and allows the data to replicate at bucket level (logically basic unit of data transfer in broadcast) according



to access frequency. The bucket containing hot data (most demanded data) appears more times than bucket containing cold data (least demanded data) on broadcast channel. A critical bucket access frequency is decided by broadcast scheduler based on bucket access statistics gathered by it during last day, week or months time. Each data is assigned a number called bucket replication factor (BRF). BRF may be defined as below:

Definition BRF: - If  $P_c$  is critical bucket access frequency and  $P_i$  is demand frequency for  $i^{\text{th}}$  bucket at present than

$$BRF_i = \lfloor \frac{P_i}{P_c} \rfloor \quad \forall i \in t$$

where  $t$  is the numbers of data bucket with out replication, is called BRF for  $i^{\text{th}}$  data bucket. It gives number of times data bucket appear on broadcast cycle.

DR-EI differs from original exponential index in two aspects:

- Instead of two parameter  $I$  and  $r$  in original, it can be tune on three parameter  $I$ ,  $r$  and BRF hence become more flexible.
- In later data buckets access pattern is taken in to consideration and buckets are allowed to replicate on broadcast channel hence client get access gain from data repetition as well as missed data can be accessed without waiting for next

broadcast resulting in easy data access with less error.

### B. Index Structure

The exponential index naturally replicates the index and DR-EI replicates the data buckets. We have considered here data transmission over single channel only because multichannel is similar to single channel with bandwidth splitting. Different data items have different access probabilities because all data are not equally demanded. According to Zipf distribution of demand probability it follow 80/20 rule i.e. 80 % client demand, 20% data and vice versa. In DR-EI all data items are sorted according to their access probabilities. There can be two types of buckets in broadcast one with index, containing index and some data according to available space and other with out index explicitly containing data. These data are filled in buckets as per available space. The buckets including replicated are adjusted on broadcast channel as shown in figure1. All buckets are divided in to data chunks. A *data chunk* is a group of data buckets. The first bucket of each chunk contains an index entry and data in remaining part. It is wisely to develop index at chunk level instead of bucket level to reduce index overhead.

The index entry consists of global index and local index. Global index indices the coming data chunk and local index indices the bucket(s) with in chunk. Global index have two fields distint (distance to end of data bucket indexed by index entry) and mkey (maximum key value). Now, each bucket is assigned a weight called BRF according to its demand. The data buckets



are replicated as many times as BRF in sequence. Figure 1 show index structure of DR-Exponential Index with  $I=2$ ,  $r =2$  and BRF ranging 1-3, where  $r$  is term called index base as in exponential index. Since  $r$  affects only the tune time and have no effect on access time, hence we are not paying attention to it [7].

### Access Protocol

The access protocol for initial data buckets is similar to exponential index [7] but for later replicated buckets is different. The access protocol to get data with attribute value 'K' is as follows:

- (i) Tune in to the broadcast channel and get pointer to the bucket containing index.
- (ii) Tune in again to the beginning of designated data bucket. Search its global index from top to bottom.
- (iii) If  $\text{initial\_distint} < K < \text{mkey}$  than tune in to  $\text{initial\_distint}$  and follow step (ii) else search local index, get the pointer to data.
- (iv) If required data is corrupt or missed than continue to search global index of next bucket:
  - If a link found there than follow the step (ii) and (iii).
  - Else wait for next broadcast and follow step (ii).

### IV. PERFORMANCE EVALUATION

We theoretically analyze the performance of DR-EI to evaluate the time efficiency and compare it with exponential index for same number of data. In DR – EI there are three tunable parameters:  $I$ ,  $r$  and BRF. Since we are interested only in access latency management which is exclusively

independent of  $r$  [7]. So  $I$  and BRF need to be adjust to achieve shorter data access time.

### A. Theoretical Analysis

This sub-section is devoted to theoretical analysis of DR – EI. Let there are  $N$  data items and for simplicity considering all data items of equal size. Initially there are  $t$  buckets available for  $N$  data items. Various symbols used while synthesizing the model are shelled in table 1.

The bucket with index contains less data than bucket without index by an amount equal to index load.

Therefore,  $B' = B - S_0$

Let  $b = \{b_1, b_2, b_3, \dots, b_t\}$  be set of data buckets containing data without replication with  $P = \{p_1, p_2, p_3, \dots, p_t\}$  as set of their access probabilities and the set  $R$  of BRF's for all buckets

Table 1: Symbols for various parameters

Symbol	Parameter
$N$	Number of data items to be broadcasted
$B$	Capacity of data bucket with out index
$B'$	Capacity of data bucket with index
$I$	Number of buckets in data chunk
$t$	Number of data buckets containing data without replication
$R_i$	BRF for $i^{\text{th}}$ bucket
$C$	Number of data chunks in broadcast cycle
$S_0$	Index overhead in first bucket of chunk



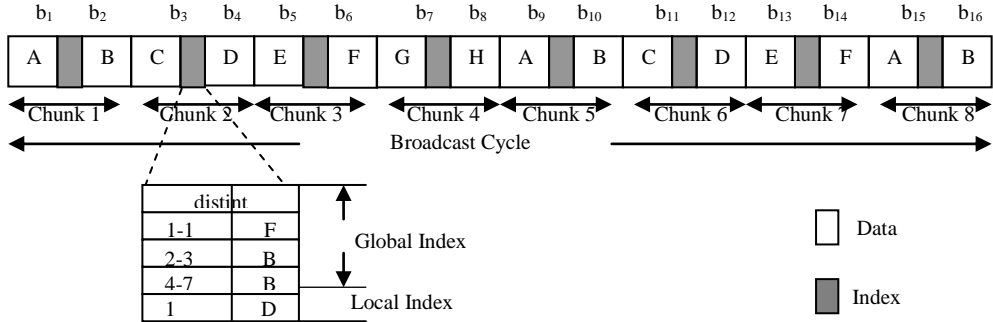


Figure1. : Example of DR – Exponential Index (I=2, r=2, BRF = 1-3)

$R = \{R_1, R_2, R_3, R_4, R_5, R_6, R_7, R_8\}$  with  $R_i$  as BRF for  $i^{th}$  item. A data chunk consists of one bucket with index entries and remaining  $(I-1)$  buckets with out index entry, it can hold  $[B(I-1)+B']$  data items. Therefore, number of chunks formed from non-

$$C' = \frac{N}{B(I-1)+B'}$$

replicated buckets is

The total number of buckets in broadcast

$$F = \sum_{i=1}^{i=t} R_i$$

cycle is. Out of these buckets  $F-t$  are replicated. Hence, number of chunks formed from

$$C'' = \frac{F-t}{I}$$

replicated buckets is

$$C = C' + C'' = \frac{N}{B(I-1)+B'} + \frac{(F-t)}{I}$$

Total number of chunks in broadcast cycle  
The average access latency consists of initial probe in chunk and half of the length of broadcast cycle. In DR – EI some buckets appears more than once on broadcast channel, such buckets can be accessed with

shorter latency. The  $i^{th}$  bucket can be accessed with  $\frac{IC}{R_i}$  times. The effective broadcast length is

$$L = \frac{1}{t} \left( \frac{IC}{R_1} + \frac{IC}{R_2} + \frac{IC}{R_3} + \dots + \frac{IC}{R_t} \right)$$

$$AverageAccessTime = \frac{I}{2} + \frac{L}{2} = \frac{I}{2} + \frac{IC}{2t} \left( \frac{1}{R_1} + \frac{1}{R_2} + \frac{1}{R_3} + \dots + \frac{1}{R_t} \right)$$

Consider a specific example where  $P = \{0.19, 0.18, 0.13, 0.13, 0.12, 0.12, 0.7, 0.6\}$  and  $t=8$  considering critical access probability  $P_c = 0.6$ , the set R of BRF for all buckets becomes

$$R = \{3, 3, 2, 2, 2, 2, 1, 1\}$$

$$F = 16 \text{ and } t = 8 \text{ Hence } C = \frac{N}{B(I-1)+B'} + \frac{8}{I}$$

Here, in this example

$$AverageAccessTime = \frac{I}{2} + \frac{7}{24} IC$$

The average access latency calculated here can be used as general formula for 16 bucket broadcast system with out serious consequences for any number of data item and chunk size.



## B. Results

This section compares the model presented in section IV (A) for DR-EI with exponential index presented in [7] for specific example mentioned there. For calculation different parameters are set as mentioned in table 2.

Table2: Values of different parameters for results

Parameter	Value	Parameter	Value
B	20-110	$S_0$	14
I	1-10	N	300-1200

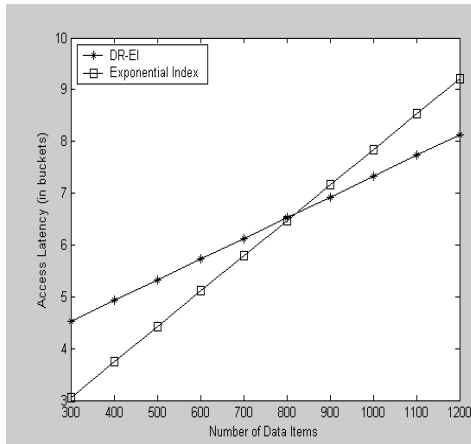


Figure 2: Effect of number of data on latency (I=2, B=80)

Number of data items and chunk size are two important factors to affecting the time performance of DR-EI. The number of data in broadcast is important for comparing normalized performance of two broadcast designs. The comparison of DR-EI with exponential index presented in [7]

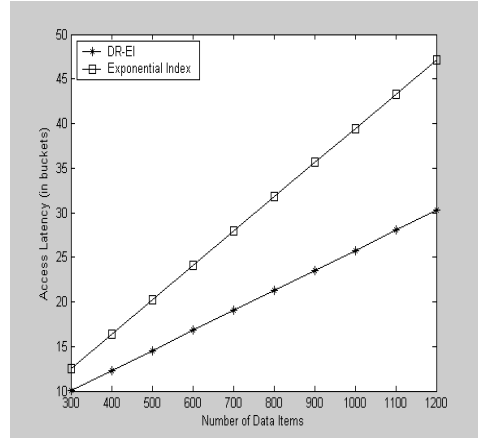


Figure 3: Effect of number of data on latency (I=2, B=20)

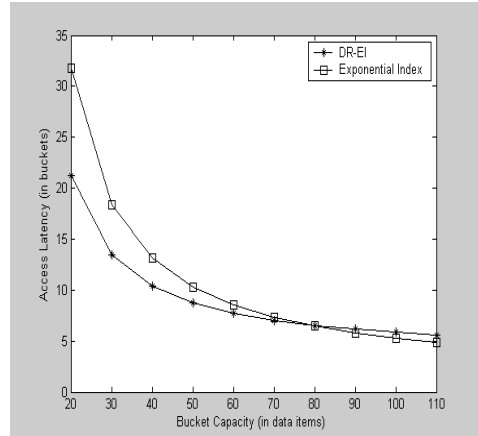


Figure 4: Effect of bucket capacity on latency (I=2, N=800)

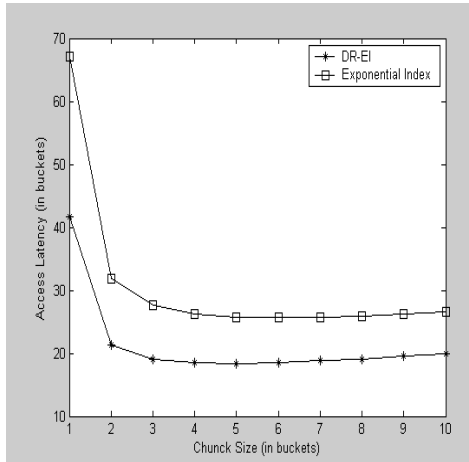


Figure 5: Effect of chunk size on latency for chunk size  $I=2$  and bucket capacity with out index,  $B = 80$

items is shown in figure 2. Figure depicts that for  $N > 800$  data items on broadcast and a bucket capacity of 80 our design performs better. Hence, DR-EI is improved extension of exponential index for  $N > 800$ . The comparison between these design at  $B=20$  and  $I=2$  is presented in figure 3. It clearly shows that for small bucket capacity DR-EI is an all time good extension.

Figure 4, shows the variation of access latency with bucket capacity. It reveals that with  $N=800$  and  $I=2$  DR-EI is good bidder than exponential index up to  $B < 80$  item after that later is slight good. At  $B=20$  our results are much better. For checking dependence of access latency on chunk size we choose  $N=800$  (practically sufficient) and  $B=20$  items. Comparison is shown in figure 5, which show that for any chunk size DR-EI has advantage over exponential index. Comparison results reveal that for  $N$

$> 800$  items,  $B < 80$  items DR-EI is profitable extension of exponential index.

## V. CONCLUSION

Wireless communication is application specific and faces various challenges in practice. Instead of combating all challenges collectively, it would be judicious to face them on application specific pattern. In this research we have addresses an issue faced in an in-house environment where energy consumption is less concerned and timely retrieval of data is key point. In such situation it would be prudent to go for minimizing access latency with tolerable tune time. We have extended exponential index to propose a new parameterized distributed indexing, for latency specific environment, called DR-EI. The proposed model is analyzed for specific situation. The results of analysis model calculated for values of parameter settings contained in table 2 are presented in section IV (B). We have found that for  $N > 800$  items,  $B < 80$  items and arbitrary chunk size DR-EI performs better than popular exponential index [7]. As buckets get repeated, it gets lesser error from corrupted data and easy access to missed data without waiting for next broadcast cycle.

From this discussion it is clear that for large data items on broadcast, small bucket capacity and arbitrary chunk size DR-EI is preferable index strategy, which gets benefit from bucket replication. Further, data management considering error probability for individual data item and access tune trade off is matter to further explore. Extension of this to multichannel will be



effective in maintaining pace with modern trend of multichannel broadcast.

Mobile Data Management (MDM 2002), pp. 87-93, 2002.

#### REFERENCES

- [1] S. Acharya, R. Alonso, M. Franklin and S. Zdonik, "Broadcast Disks: Data Management for Asymmetric Communication Environments," In Proceedings of ACM Sigmod, pp.199-210, 1995.
- [2] M. H. Ammar and J. Wong, "The Design of Teletext Broadcast Cycles," Performance Evaluation 5(4):235-242, 1985.
- [3] T. Imielinski, S. Viswanathan and B.R. Badrinath, "Energy Efficient Indexing on Air," Proceedings of the ACM SIGMOD Conference, pp.25-36, 1994.
- [4] T. Imielinski, S. Viswanathan and B.R. Badrinath, "Data on Air: Organization and Access," IEEE Transaction on knowledge and Data Engineering, 9(3) May/June 1997.
- [5] W.G. Yee, S.B. Navathe, E.Omiencinski, and C. Jermaine, "Efficient Data Allocation over Multiple Channels at Broadcast Servers," IEEE Transaction on Computers 51(10), 1231-1236, 2002.
- [6] C. H. Hsu, G. Lee, and A. L. P. Chen, "Index and data allocation on multiple broadcast channels considering data access frequencies," in Proceedings of 3rd International Conference on Mobile Data Management (MDM 2002), pp. 87-93, 2002.
- [7] J. Xu, W.C. Lee, and X. Tang, "Exponential Index: A Parameterized Distributed Indexing Scheme for Data on Air," MobiSys 2004, pp. 153-164, 2004.
- [8] J. Xu, W-C. Lee, X. Tang,, Q. Gao, and S. Li, "An Error- Resilient and Tunable Distributed Indexing Scheme for Wireless Data Broadcast," IEEE Transaction on Knowledge and Data Engineering, Vol. 18, No. 3, 392 - 404, 2006.
- [9] A. Seifert, J. Hung, "FlexInd: A Flexible and Parameterizable Air-Indexing Scheme for Data Broadcast Systems," EDBT 2006, LNCS 3896, pp. 902-920, 2006.



## Self Checking Hardwired Control Unit Using CED Technique

Ezdihar A. Elowhechee

Ali H. Maamar

Faculty of Electronic Technology

Beni Waled

ali\_h\_maamar@yahoo.com

### Abstract

As digital systems grow more and more complex, it is becoming highly desirable to have systems with concurrent error detection, or the capability of self-checking. That means the ability to verify automatically whether there is any fault in the system or not. The concurrent error detection could be achieved using redundancy; it may be hardware, time, or information redundancy. From the reliability point of view, the control unit, is usually the most critical part of the system, since it plays the central role in correct functioning of the whole system. Therefore, providing the control unit with the properties of self-checking is very important.

This paper presents the design and implementation of a self-checking Hardwired control unit, using Berger code. The control unit will be designed and implemented using Active HDL 7.2 language

### Introduction

The advances in VLSI/ULSI technology have made possible many changes not only in processor architecture but also in the amount of hardware that can be integrated into a chip, makes it possible to include the entire system in a single chip. Although increased scales of integration offers many advantages, these complex circuits are more susceptible to transient and intermittent faults, these faults are the most frequently occurring faults in digital systems, it has been reported [1][2][3] that 90% of VLSI system failures are due to intermittent faults. Unfortunately the characteristics of this type of faults, namely random occurrence and short duration, render standard test strategies ineffective. The detection of these types of faults necessitates the use of a test strategy which

continuously monitors the operation of the circuit and compares it with some known reference. This approach is usually referred

to as Concurrent Error Detection (CED). One method of implementing CED is through the use of information Redundancy or coding techniques. Amongst all of the separable codes used in CED schemes, Berger code [4] is the least redundant separable code capable of detecting all unidirectional errors. This paper investigates the use of Berger code as a means of incorporating CED into a self checking control unit.

From the reliability point of view, the control unit, is usually the most critical part of the system, since it plays the central role in correct functioning of the whole system.



Therefore, providing the control unit with the properties of self-checking is very important.

### Berger Code:

Berger code is a separable and unordered code, it is separable because the information bits and the check bits (check symbol) in the codeword are separate, it is an unordered code as it is not possible to change one codeword into another codeword by simply changing either 1's to 0's or 0's to 1's, this means that the code can detect all unidirectional errors. The codeword of the Berger code is formed by appending the check bits to the information bits, the check bits of the code is the binary representation of the number of 1's (or the complement of the number of 0's) in the information bits, the number of check bits  $k = \lceil \log_2 (I + 1) \rceil$ , where  $I$  is the number of bits in the information bits (data word), the number of bits in the codeword  $n = I + k$  bits. If the number of information bits in a codeword is  $I = 2^k - 1$ ,  $k \geq 1$  then the code is known as a Maximal Length Berger code; otherwise it is known as a Non Maximum Length Berger code.

For example, if  $I = 7$  and  $k = 3$ , it is Maximal Length Berger code because  $I = (2^k - 1)$ , whereas  $I = 6$  and  $k = 3$  is Non-Maximal Length Berger code because  $I \neq (2^k - 1)$ .

### The Control unit

1. Instruction Register which used to hold the instruction (op-code) fetched from the RAM to be executed, the size of the instruction register depends on the number of instructions that the system can performed.

The control unit is the main component that directs the system operations by sending control signals to the data path. These signals control the flow of data within the CPU and between the CPU and external units such as memory and I/O.

Basically there are two types of control units: micro programmed and hardwired controllers. In micro programmed control, the control signals associated with operations are stored in special memory units inaccessible by the programmer as control words. A control word is a microinstruction that specifies one or more micro-operations. A sequence of microinstruction is called a micro program, which is usually stored in a ROM.

In a hardwired implementation, the control unit is essentially a combinatorial circuit. Its input logic signals are transformed into a set of output logic signals, which are the control signals. This approach is examined in this section.

Figure(1) is a block diagram showing the internal organization of a hardwired control unit. The Input to the controller consists of the 4-bit op-code of the instruction currently contained in the Instruction Register and the negative flag from the accumulator. The controller's output is a set of 16 control signals that go out to the various registers and to the memory of the computer, in addition to a HLT signal that is activated whenever the leading bit of the op-code is one. The control unit is composed of the following function units:

2. An instruction decoder to decode the op-code, in other words it selects only one instruction according to the op-code.
3. A ring counter which provides a sequence of consecutive signals that cycle continuously, and synchronized by the

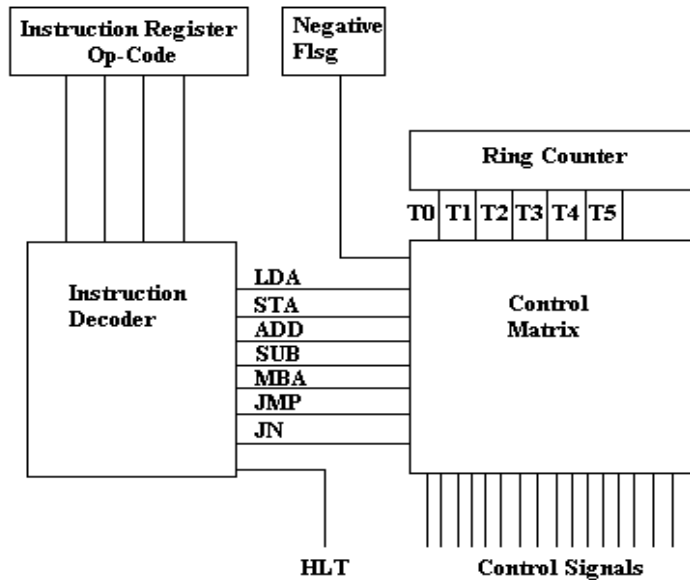


system clock. The number of signals or the size of the ring counter depends on the number of cycles needed to execute the longest instruction or op-code. In this paper only six signals ( T0, T1.... T5 ) are needed.

4. The control matrix, which receives timing signals from the ring counter, the instruction to be executed from the instruction decoder, and flags from status register, then it generates the proper sequence of control signals. These signals are feed to all other units in the processor

that involved in the execution of the current instruction.

As we have seen, the controller causes instructions to be executed by issuing a specific set of control signals at each beat of the system clock. Each set of control signals issued causes one basic operation (micro-operation), such as a register transfer, to occur within the data path section of the computer. In the case of a hardwired control unit the control matrix is responsible for sending out the required sequence of signals.



### Self Checking Hardwired Control Unit

Classical approaches for designing self-checking control unit are based on either duplication, or application of specific error detecting codes. Latter techniques provide error detection for the FSM's next-state logic, by encoding the states with a special property. In [5], the FSM states are encoded using an m-out-of-n code. FSM encoding employed in [6,7,], is achieved providing a state assignment in which each state is at a constant Hamming distance from its

have been taken in the past to design self-checking sequential circuits with lower area overhead in respect to duplication. In [1,2], a monitoring machine is used in order to monitor the states of the original machine. This technique is effective for Error-detection techniques for controllers can mainly be classified into two categories. The first category relies on checking the

controller outputs only using the same techniques as applied to data paths, whereas



the second type of techniques focuses on the more challenging

problem of observing the state transitions and the control flow. Here, a number of approaches has been published ranging from state coding based on error detecting codes to monitoring the control flow by on-chip signature analyzers or special monitoring machines [8,9]. Usually, these techniques lead to considerable hardware overheads, performance degradations or large error-detection latencies. In particular their impact on the circuit speed is not tolerable for many applications, where powerful techniques like pipelining and massive parallelism as well as innovative computing algorithms improve the maximum speed of the data path but require highly complex control units at the same time. As a straightforward solution techniques for finite state machine decomposition, which are often applied for the synthesis of high performance controllers, can be combined with the above mentioned error-detection schemes [9]. The technique presented in this paper is simple, instead of full duplication of the control unit, only some extra hardware (self checking hardware) is added to the control unit to detect the errors. The self checking hardwired control unit, Figure 2, consists of the following blocks: Step Code Generator (SCG), Berger Code Check Symbol Generator (BCCSG), and Two Rail Checker (TRC).

**Step Code Generator (SCG)** receives its inputs from the instruction register (the opcode) and the ring counter. The output of the SCG is the Berger code check symbol for the control signals generated from the control matrix. For example if the instruction to be executed is LDA, then the SCG generates the check symbol of the signals generated by the control matrix at

T0, then T1 and so on. The check symbol generated by the SCG will be compared with the actual check symbol generated by the CSG.

**Berger Code Check Symbol Generator (BCCSG):** The Berger Code Check Symbol Generator receives its inputs from the control matrix, and produces the Berger code check symbols for the control signals generated by the control matrix.

#### **Two Rail Checker (TRC)**

TRC is used to compare two complementary code words. The checker determines whether the Berger check symbol of the signals that generated by the control matrix and the check symbols generated by the Step Code Generator (SCG) circuit are match. If match then no error detected and the control signals should be allowed to pass and performed, but if not match then an error signal is activated and the operation should be halted



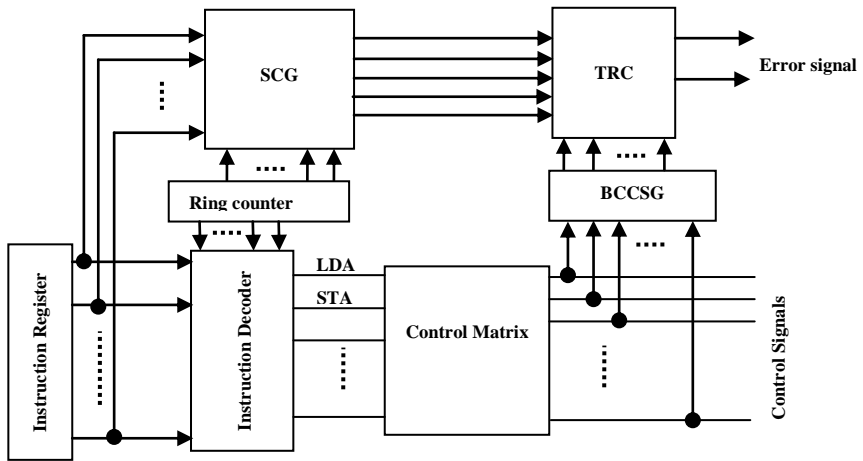


Figure 2. Self Checking Hardwired Control Unit

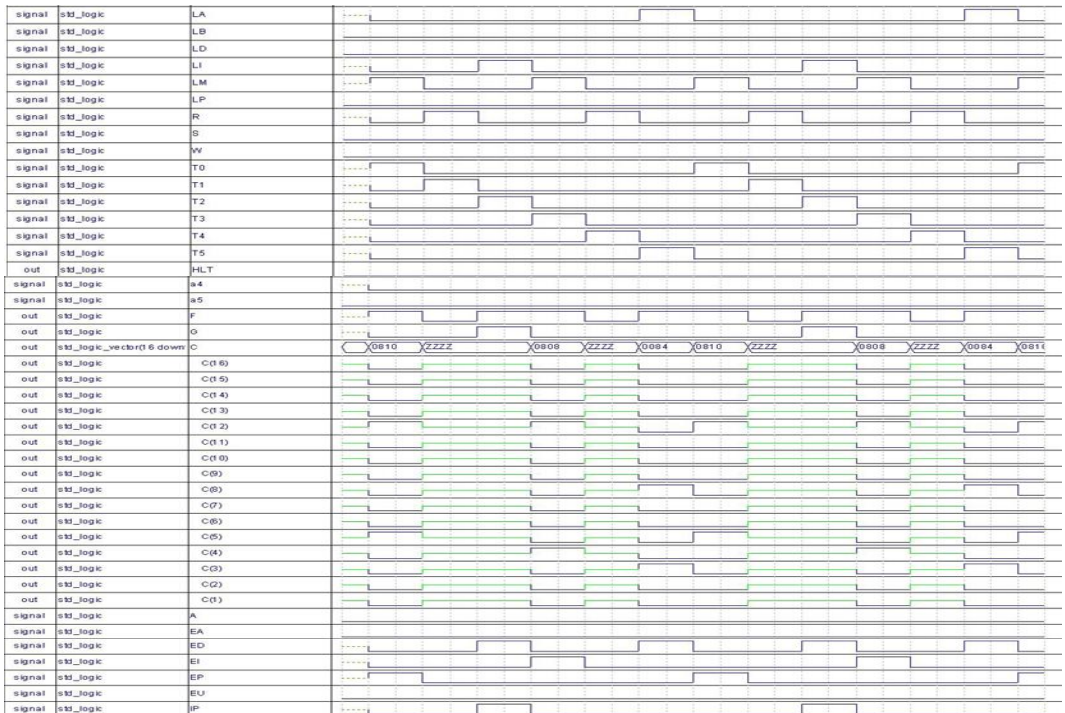


Figure 3. Simulation wave forms

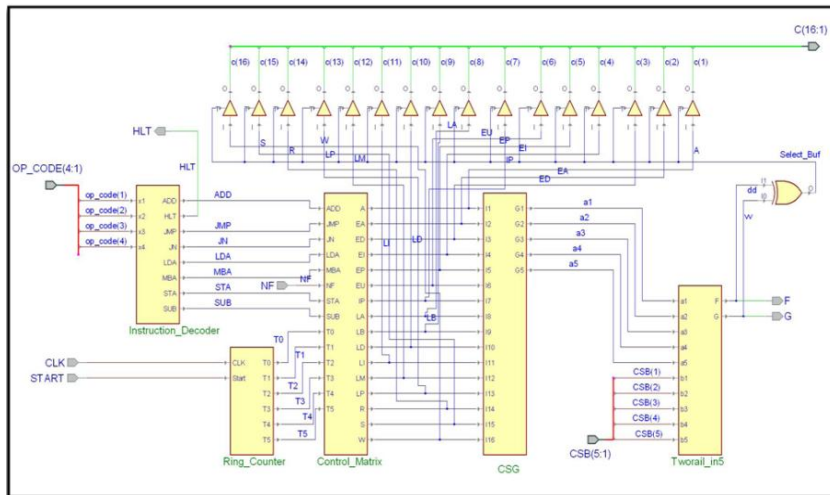


Figure 4. Self checking Hardwired control Unit Implementation

### Conclusion

The self checking Hardwired control unit was designed and simulated using HDL simulation package figure (3,4), and the following conclusion points can be concluded :

Self checking increases the cost of the system, the cost is Hardware and Time, depends on the type of redundancy used. In Information redundancy, the cost is both Time and Hardware, and it depends on the code used. Berger code is suitable for self checking control unit, as the hardware needed to implement the code is less than the hardware needed for hardware redundancy.

The hardware used to design self checking control unit in this work is less than duplication.

### References:

[1] N. K.Jha, S. Gupta, "Testing of Digital Systems", Cambridge University Press 2003.  
[2] Parag K. Lala, "Self Checking and Fault tolerance digital Design",Morgan Kaufmann Publisher, 2001.

[3] J. B Clary, R. A. Sacane, "Self-Testing Computers", IEEE computers, Vol. no.10,October 1979, pp. 49-50.

[4] J.M. Berger, " A note on error detection codes for Asymmetric Channels " , Information and Control, vol. 4, March 1961, pp68 – 73

[5] M. A Marouf, A. D. Friedman, "Design of Self Checking Checker for Berger Codes", Proc. Int. Symp. Fault Tolerant computing, 1978, PP. 179-184.

[6] L. Guibas and F. Liang, "Systolic stacks, queues, and Counters," inProc. Conf. Advanced Res. VLSI, MIT, Cambridge, 1982.

[7] C. Mead, L. Conway, "Introduction to VLSI Systems", Addison Wesley Publishing Company, Second Printing, 1980.

[8] Niraj K. Jha, "Design and Synthesis of Self checking VLSI Circuits", IEEE Transaction on Computer Aided Design Of Integrated Circuits and Systems, Vol. 12, No.6, June 1993, pp. 878-887.

[9] Lala Parag k., "Digital Circuit Testing and Testability", Academic Press, 1997..



## **Double data buffer design approach in 64-bit PCI-X Master/Target bus for high speed embedded systems and PC servers**

**G. Sumathi** Faculty of Engineering, Nalla Malla Reddy Engineering College, Hyderabad, Andhra Pradesh, India, Tel: +91-9000537597  
sumathigujja@yahoo.in

**V. Kumara Swamy,**  
Faculty of Engineering, Dept. of EE, Sirte University, Sirte, Libya,  
[Tel:+218917084428](tel:+218917084428) / Fax: +2185465461,  
ksvarkuti@yahoo.com

**Prabhu G Benakop, Senior Member, IEEE,**  
Director, Aurora Technological Research Institute, Hyderabad,  
Andhra Pradesh, India, Tel: +91-9866666651,  
pgbenakop@ieee.org

### **ABSTRACT:**

The Peripheral Component Interface-Extension (PCI-X) is a high speed bus structure, the new PCI extension, became a real standard for embedded systems as well as for PC servers. PCI-X increases PCI's bandwidth potential, especially for burst transactions. Compaq, HP, and IBM developed it. The PCI-X includes behavioral models like master, target, and arbiters. The 64-bit PCI-X master/target core is designed so that user interface can operate at any clock speed independent of the PCI bus speed. The user interface clock and PCI-X bus clock can be synchronous or asynchronous to each other. The PCI-X core utilizes double write buffer for write posting in both the master and target directions. The double data buffer design approach allows data access by the user interface and the PCI interface simultaneously and independent from each other. Thus the data transfer takes place at a faster speed in PCI-X compared to PCI bus. In this paper, we achieved higher speed and optimized transistor count compared to the other bus structures available for data transfer. This paper discusses overview of

architectural design, master write buffer design, target read buffer design, target write buffer design, and master read buffer design, configuration registers design, overall design and their simulation results and proves that the double data buffer design approach enhances the speed of PCI-X Master/target

**Keywords:** PCI, PCI-X, Master, Target, Buffer, and Controller



## 1.0 Introduction

A bus is basically a collection of wires which is responsible for interconnecting the various components of a microcomputer together in order to allow the exchange of data between these components. Devices operating on a bus can be divided into three categories, i.e.,

Bus masters, Bus slaves and intelligent slaves as shown in figure1. Bus masters are devices capable of initiating any bus cycle (memory read/write, port addressing, etc.). Bus slaves are devices which are not capable of initiating a bus cycle but merely responding to it. Intelligent slaves have their own intelligent controlling devices but do not assert control over the bus.

## 2.0 PCI BUS

It is a high performance bus for interconnecting Chips, expansion boards, and processor/memory Subsystems. It is originated at Intel in early 1990s. Standard method of interconnecting chips on a board. PCI was used in personal computers in 1994 for the Intel's 486 processor.

### 2.1. PCI Specifications:

1. PCI 1.0, which was merely a component-level specification, was released on June 22, 1992.
2. PCI 2.0, which was the first to establish standards for the connector and motherboard slot, was released on April 30, 1993.
3. PCI 2.1, released on June 1, 1995, allows for 66 MHz signaling at 3.3 volt signal voltage (peak transfer rate of 533 MB/s), but at 33 MHz both 5 volt and 3.3 volt

signal voltages are still allowed. It also added transaction latency limits to the specification

4. PCI 2.2 Power rails to provide 3.3 volt *supply* voltage are now mandatory.
5. PCI 2.3 permits use of 3.3 volt and universal keying, but does not allow 5-volt keyed add-in cards.
6. PCI 3.0 is the final official standard of the bus, completely removing 5-volt capability.
7. Mini PCI is a form factor of PCI 2.2 for use mainly inside laptops
8. Card Bus is a PC card form factor for 32-bit, 33 MHz PCI
9. Compact PCI uses Euro card-sized modules plugged into a PCI backplane.
10. PC/104-Plus is an industrial bus that uses the PCI signals lines with different connectors.

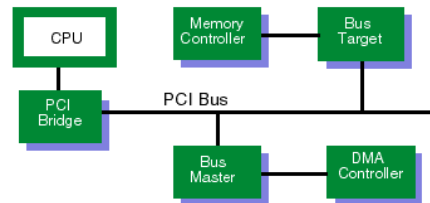


Fig1. Block diagram of PCI bus system

Master function is to initiate PCI memory and IO read/write, automatic transfer of control between master and target, restart on target retry and disconnect. Target Function is to perform Memory or IO read/write, Configuration read/write, and supports high speed bus request. Arbiter Function is to arbitrate between multiple bus masters on the PCI bus and implementing rotating priority and fixed priority.

### 3.0. PCI-X Bus and its specifications

PCI-X is a high-performance variant of 64-bit PCI designed for servers. PCI-X adapters and slots are backward-compatible with 32-bit PCI slots and adapters.

1. PCI-X 1.0 increased the maximum signaling frequency to 133 MHz (peak transfer rate of 1066 MB/s) and revised the protocol.
2. PCI-X 2.0 permits a 266 MHz rate (peak transfer rate of 2133 MB/s) and also 533 MHz rate (4266 MB/s — 32× the original PCI bus), expands the configuration space to 4096 bytes, adds a 16-bit bus variant (allowing smaller slots where space is tight), and allows for 1.5 volt signaling

It is a 64-bit PCI-X bus, supports for 32/64-bit data transfer. It fully supports PCI and PCI-X protocol and is designed for PLD implementations. It is an efficient user interface for different types of user devices. The user interface and PCI interface runs at different clock speed. It includes data buffer and synchronization logic to bridge the two clock domains. It automatically detects of PCI and PCI-X bus systems. It consists of combined bus master and target functions. Master initiates PCI-X memory and IO read/write, automatic transfer restart on target retry and disconnect. Target performs memory or IO read/write, Configuration read/write and Split transaction operations.

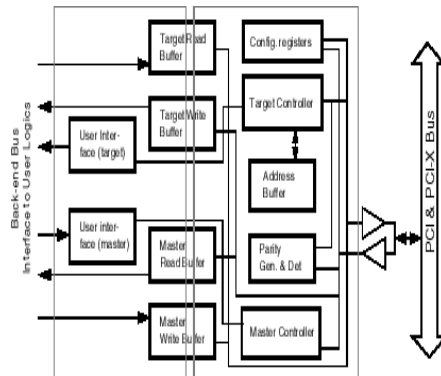


Fig 2. Architecture of 64-bit PCI-X Master/Target

PCI-X master/target can operate in both PCI mode and PCI-X mode as shown in figure2. It provides easy integration with other user logic, supports PCI version 2.2 and PCI-X version1.0. User interface can operate at any clock speed independent of PCI bus speed. PCI-X utilizes double data write buffer for write operation in both the master and target direction. Double data buffer design allows data access by the user interface and the PCI interface simultaneously and independent from each other. During master operation, the controller is capable of initiating memory or I/O read and writes upon user requests. Burst size is specified by the user for each transaction. During target operation, master target core monitors the target device signal on PCI-X bus and transfer data to the user logic. All types of transfer terminations such as retry, disconnect and split response are handled by PCI-X. The target controller is capable of handling memory and IO accesses on the PCI and PCI-X bus. Configuration register read and write transactions are supported locally by the bus target without assistance from the user logic. Memory and I/O write to the target are posted in the write buffer before they



are transferred to the user. Memory and I/O read are handled as delay read on PCI bus and as split transaction on PCI-X bus. The user interface allows the user to control the characteristics of access.

#### 4.0. Architectural Design

In this section of paper, the concentration is on design of interface for various blocks of 64-bit PCI-X Master/Target. Configuration register as shown in figure3, has first written with control word of 8-bits based on configuration read/write signal. The output of this register is the user request signal for various operations as per user choice.



Fig 3 Interface of Configuration Register  
The Master Controller will receive the user request input and generates the control signals for Memory or IO read/write operations, receive/transmit mode, target retry and disconnect signals shown in fig4.

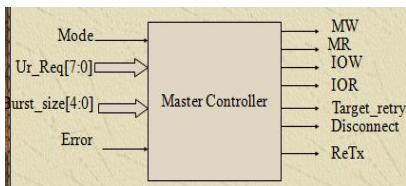


Fig 4 Interface of Master Controller

If transmit mode is selected, 64 bit data is written in to master write buffer as shown in fig 5

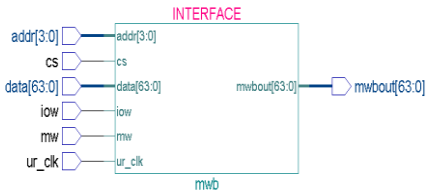


Fig 5 Interface of Master Write Buffer

Then at the target, target read buffer reads the data from master write buffer for the user connected at the target end shown in fig6. This is the data flow from Master to target as shown in fig2. Here target acts as slave.

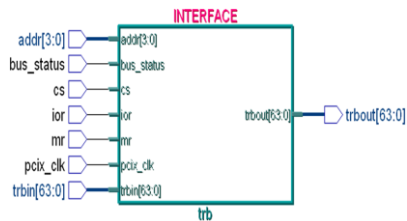


Fig 6 Interface of Target Read Buffer  
When target wants to transmit data, then master transfers the control to the target and target will hold the function of master. Thus the user request is given to the target controller from configuration register. Target controller checks for bus status whether bus is free or busy. If bus is free and target is ready for data transfer, then it will generate memory or IO read/write control signals shown in fig7.

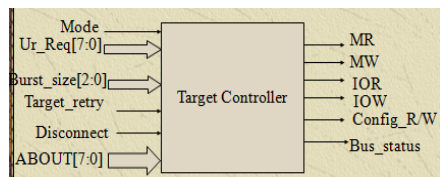


Fig 7 Interface of Target Controller



Data is written in to target write buffer when chip select is enabled shown in fig8.



Fig 8 Interface of Target Write Buffer

Master read buffer reads data from target write buffer when bus status is active shown in fig9. This operation completes the dataflow from target to master end user.



Fig 9 Interface of Master Read Buffer

Parity generation and detection module generates parity during transmission and detects parity during reception as shown in fig10 .

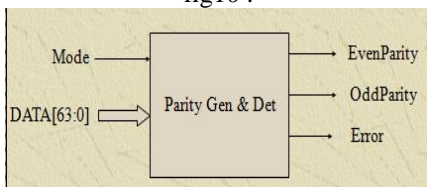


Fig 10 Interface of Parity Generation and Detection

Address buffer (fig11) stores the address location of data stored.

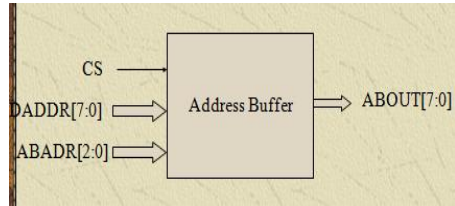


Fig 11 Interface of Address Buffer

### 5.0. Results and Discussion

The PCI-X includes behavioral models like master controller, target controller, data and address buffers and parity generation and detection modules. All these modules are programmed using Verilog HDL and simulated using ModelSim EDA Tool from Mentor Graphics. Configuration register gives control word also called as user request to the master/ target controller based on which is transmitting the data.

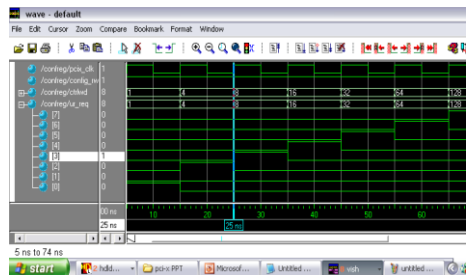


Fig 12 Configuration Register Simulation Result

Read/write buffers are designed in both the directions of data transfer from master to target and target to master.

Observe the data written in to master write buffer in different locations as shown in fig13.



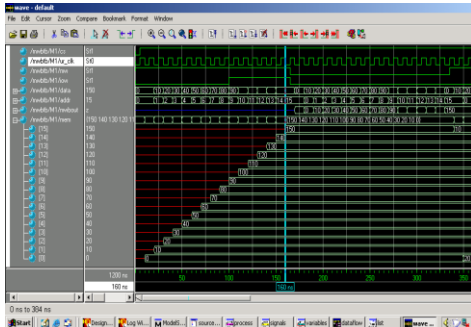


Fig 13 Master Write Buffer Simulation Result

Target read buffer s reading the same data from output of the master write buffer shown in fig14 and fig15. Thus it completes data transfer from master to target.

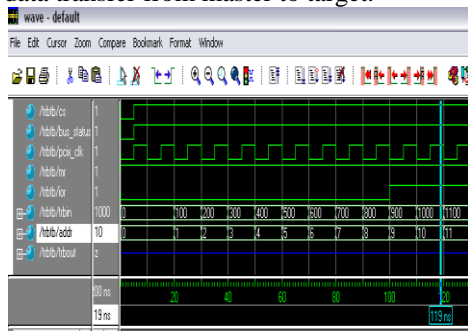


Fig 14 Target Read Buffer Simulation Result

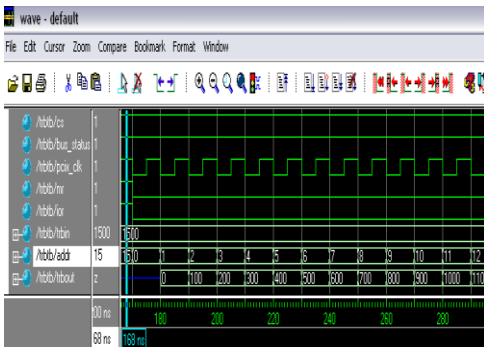


Fig 15 Target Read Buffer Simulation Result Continued

Now the data transfer taking place from target to master shown in fig16 to fig17.

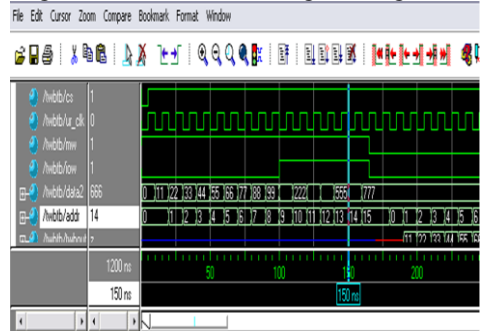


Fig 16 Target Write Buffer Simulation Result

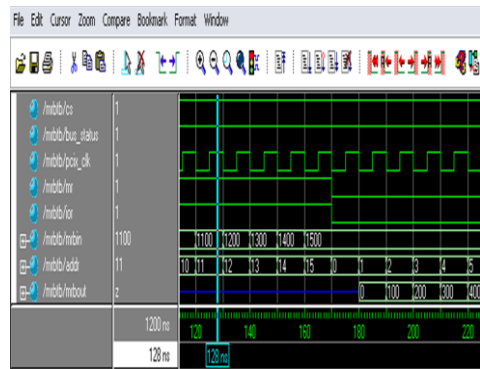


Fig 17 Master Read Buffer Simulation Result

This is bidirectional data transfer independent of each other with the double data buffer design approach.

## 6.0. Conclusion

The 32/64-bit PCI-X master/target core is designed so that user interface can operate at any clock speed independent of the PCI-X bus speed. The user interface clock and PCI-X bus clock can be synchronous or asynchronous to each other. The PCI-X core utilizes double data buffer





for write posting in both the master and target directions. The double data buffer design approach allows data access by the user interface and the PCI interface simultaneously and independent from each other. Thus the data transfer takes place at a faster speed in PCI-X compared to PCI bus. In this paper, the PCI-X with double data buffer design approach has achieved twice the speed (266MHz) compared to the design speed (133MHz) achieved in PCI-X without double data buffer design approach. The Simulation tool used is ModelSim and the synthesis tool is Leonardo Spectrum from Mentor Graphics.

#### **Related work:**

1. Altera is implementing Compaq's PCI-X bus controller, as a core for its FPGAs. This Altera PCI-X MegaCore function was originally implemented by Compaq in multiple ASICs. It implements a 64-bit master/target PCI-X interface, but supports both 32-bit and 64-bit operation. PCI-X able to work at both the PC system I/O bus level and at the system bus level. Drive capability is expected to reach five to seven boards.
2. In-silicon has announced a PCI-X design package, TymeWare. This package integrates a PCI-X bus controller with a bus test environment. The core is made up of synthesizable RTL blocks that can be used for ASIC or FPGA development of a PCI-X bus controller. The PCI-X development environment includes both PCI 2.2 and PCI-X behavioral models (master, target, and arbiters) and a protocol/timing monitor.
3. DCM Technologies also supplies a PCI-X bus controller core, the Corex-V10 PCI-X. This core comes in a netlist version that supports 133-MHz, 64-bit PCI-X operation. In fact, DCM is pushing the core controller's 133-MHz operation as an enabler for high-bandwidth Gigabit Ethernet.
4. Agilent—Its E2929A PCI-X Exerciser and Analyzer supports 32-/64-bit with bus rates to 133.4-MHz operation. It consists of a PCI-X Protocol Checker, a PCI-X Analyzer, a PCI-X Exerciser and a C-API Interface, and PPR (software). Its PCI-X protocol checker verifies 53 PCI-X protocol implementation rules. The tester also provides the option to link a logic analyzer to the PCI-X signals for deeper signal analysis. It comes with a ready-to-use library of stress tests. The E2929 is a short PCI formfactor card.
5. Catalyst—Its TA700 PCI/PCI-X Analyzer and Exerciser supports 32-/64-bit, 66-MHz bus operation. It has a 750-MHz timing analyzer and a 10-GHz (100-ps) set-up and hold timing violations detector. It has automated PCI Device Compliance test and verification. This unit can be controlled from the PCI-X bus itself by the system host. Additionally, the PCI-X tester card has an auxiliary PCI expansion connector on top for accepting a PCI device
6. VMEtro—Its PBT-615 PCI-X Bus Analyzer and Exerciser supports 32-/64-bit operations with speeds up to 100-MHz (sampling rate). It has a 500-MHz Timing Analyzer with a 16 Msample trace buffer. It also supports PCI at rates up to 66-MHz operation. It is a short PCI formfactor card. It connects to a host PC via a front panel connector with USB or RS-232 serial connections.



### **Technical Papers:**

1. PCI-X Moves Out  
Tech OnLine Publication  
Date: Jun. 9, 2000
2. PCI-X 2.0: The Next Generation  
of  
Backward-Compatible PCI  
Sujith Arramreddy and Dwight  
Riley Server Works and Compaq
3. 64-bit PCI-X Master/Target  
Eureka Technologies

### **References**

- Web Sites:** [www.in-silicon.com](http://www.in-silicon.com)  
[www.dcmtech.com](http://www.dcmtech.com)  
[www.eurekaTech.com](http://www.eurekaTech.com)



## **Add On System on a Programmable Chip (SOPC)**

A.A.Badi\* and A.H.Infis\*\*

EE Department, Faculty of Engineering, Al-Fateh University, Tripoli, Libya.

\*Email: [abubaker.badi@gmail.com](mailto:abubaker.badi@gmail.com) \*\*Email: [ali\\_infis@yahoo.com](mailto:ali_infis@yahoo.com)

### **ABSTRACT**

System On a Programmable Chip (SOPC) is a modern-day technology that has emerged to enable designers to utilize a large Field Programmable Gate Array (FPGA), that contains both memory and logic elements along with an intellectual property (IP) processor cores, such as Altera's Nios II and Xilinx's MicroBlaze processors to implement a computer and custom hardware for system-on-a-chip (SOC) applications. For projects requiring a hardware implementation, the FPGA-based SOPC approach is easier, faster and more economical in low to medium quantity production [1].

One of the applications of SOPC is in the digital image processing which needs both high memory capacity and high processing speed. Ben Atitallah et. al. [2] built a SOPC system that uses core processor working on 50 MHz clock frequency connected to a real time digital camera. They found that 18.4% of the image sampling period would be necessary for Camera and VGA transfer and 81.6% for the real-time processing algorithms.

In this paper a SOPC system design will be introduced to implement some image processing algorithms based on Altera's Cyclone II FPGA. Here the image will be read from a Secure Digital (SD) card which is connected to parallel input/output (PIO) ports controlled by a 32-bit Nios II soft-core processor with 100 MHz clock frequency, the data comes from PIO ports of SD card will be stored into Synchronous Dynamic Random Access Memory (SDRAM), which help processing being faster, then the original and the processed image will be displayed on Video Graphic Array (VGA) monitor .

---

### **1. Introduction**

Altera Co provides a SOPC Builder system development tool, which is a powerful platform for composing memory-mapped systems based on processors, peripherals, and memories that may be internal or external to the FPGA. Many types of IP components for use with SOPC Builder are

available from Altera and third-party vendors. In addition to these off-the-shelf SOPC Builder-ready components, the user can also create his/her own custom peripheral and connect it to the system by importing it into the SOPC Builder. So the user can easily connect custom peripheral



to an SOPC Builder-generated system in the same manner as commercially available SOPC Builder components [3].

Altera's Nios II is a soft-core processor, defined in a hardware description language, and available as an IP component in SOPC Builder. It uses existing programmable logic elements from the FPGA to implement the processor logic which can be implemented in Altera's FPGA devices by using the Quartus ® II

CAD system; figure 1.1 shows the block diagram of Nios II processor core.

Altera offers three types of Nios II processors [4].

- *Nios II/f* "fast" core which is designed for fast performance.
- *Nios II/s* "standard" core which is designed for small size while maintaining performance.
- *Nios II/e* "economy" core which is designed to achieve the smallest possible core size.

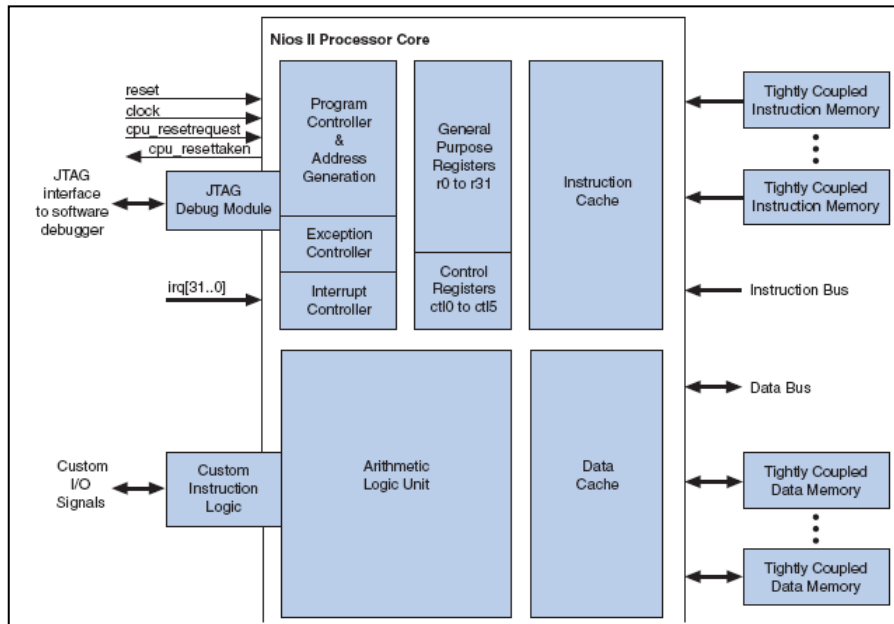


**Fig 1.1 Nios II Processor Block Diagram**

The embedded application program (software) for the processor is typically written in C or C++ and compiled using a

Nios II® Integrated Development Environment (IDE) compiler tools.



The FPGA device that the SOPC system will be implemented on is Altera's Cyclone II FPGA, which is installed on DE2-70 educational board. DE2-70 board contains more hardware components which can be

connected to the FPGA, such as two 32 MB SDRAM, 2 MB SSRAM, 8 MB Flash memory, VGA Monitor connector, Serial COM connector, SD card port and other components as shown in figure 1.2 [5].

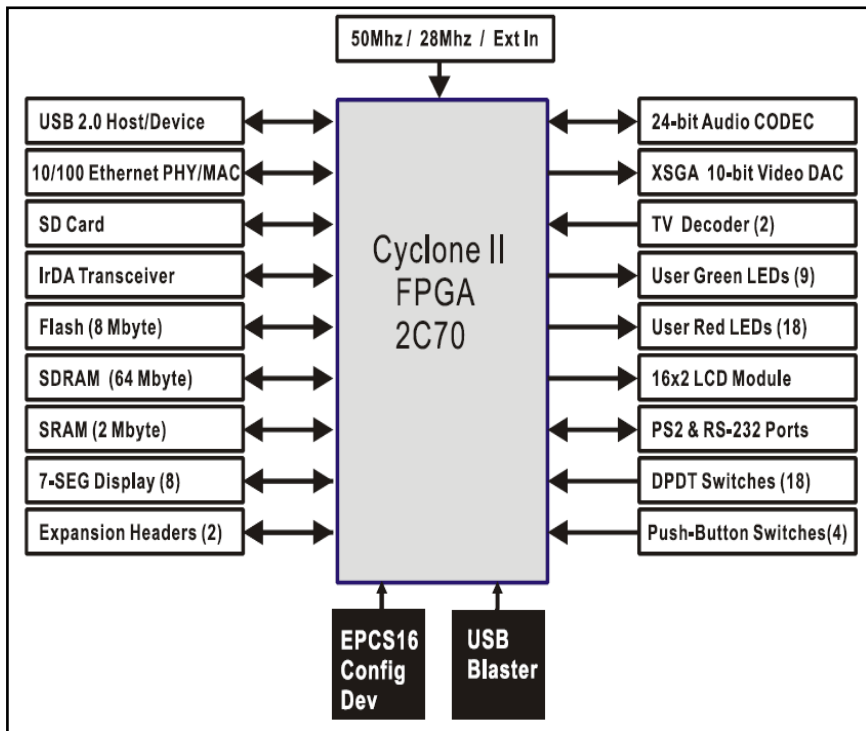
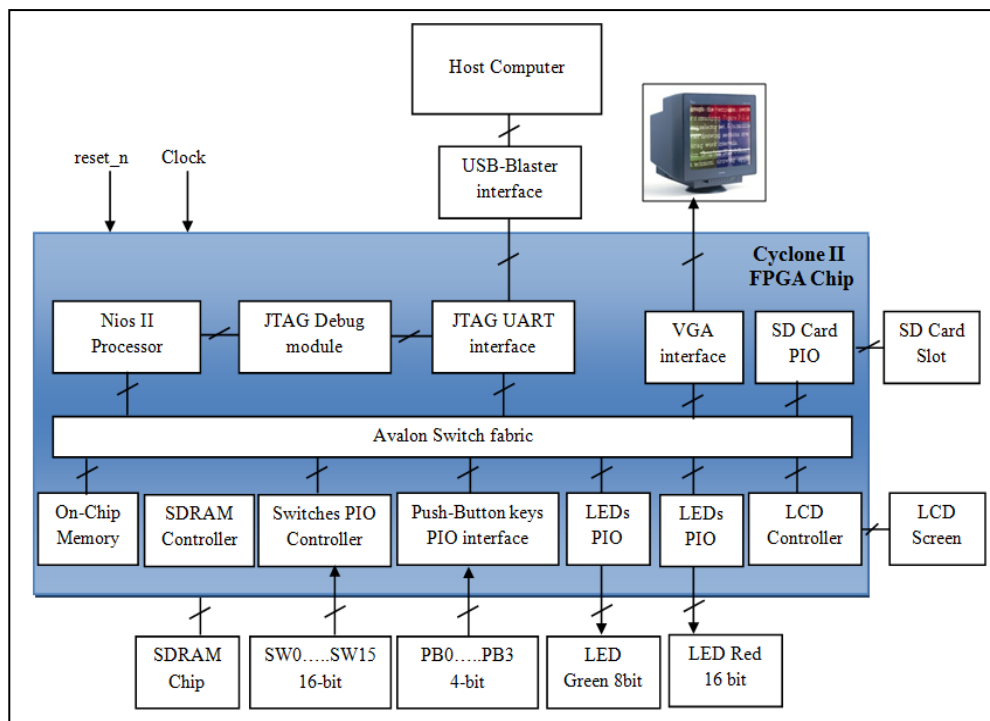


Fig 1.2 Block Diagram of DE2-70 board

## 2. Add on SOPC Clock frequency signals

DE2-70 board includes two oscillators that produce 28.86 MHz and 50 MHz clock signals. Both two clock signals are connected to the FPGA that are used for

clocking the user logic. The Add on SOPC design block diagram which is shown in figure 2.1, works on 100 MHz clock frequency, so a Phase-Locked Loop (PLL) must be used to get the needed clock frequency.



**Fig 2.1 Block Diagram of Nios II system implemented on the DE2-70 board**

"**The Phase-Locked Loop (PLL)** is a closed-loop frequency-control system that compares the phase difference between the input signal and the output signal of a voltage-controlled oscillator (VCO). The negative feedback loop of the system forces the PLL to be phase-locked. PLLs are widely used in telecommunications, computers, and other electronic applications. The PLL can be used to generate stable frequencies, recover signals from a noisy communication channel, or distribute clock signals throughout SOPC design." [6]. the PLL block diagram is shown in figure 2.2. Cyclone II FPGA

supports 4 PLLs, in our design we'll use 3 PLLs, the first one is to control the system clock frequency to 100 MHz, the second one is to control the SDRAM chip clock to 100 MHz with phase shift lagged 3 n sec and the last one to control the VGA chip clock which is needs 25 MHz for resolution  $480 \times 640$  pixels. All these PLLs can be found as an IP megafunction core which is called ALTPLL. The ALTPLL megafunction related to Cyclone II FPGA supports four different clock feedback modes, each mode allows clock multiplication and division, phase shifting, and duty-cycle programming.

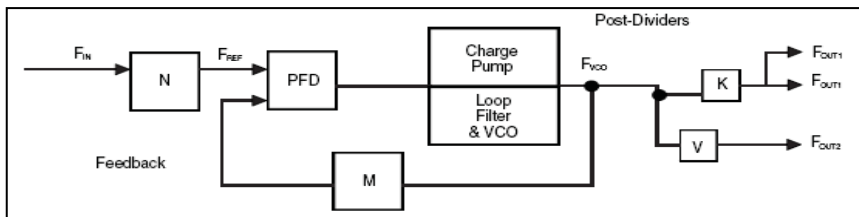


**Fig 2.2 PLL Block Diagram.**

### 3. SD Card Interface

Secure Digital (SD) is a non-volatile memory card format developed by Panasonic, SanDisk and Toshiba for use in portable devices, such as digital cameras, handheld computers, notebook computers, PDAs, GPS receivers and mobile phones. As has been said in the introduction DE2-70 board supports a SD card port which allows an SD card to be connected to the FPGA-based design on this board, facilitating access to potentially large amounts of data. To use a SD card in DE2-70 board, the data must be in files that can be accessed by File Allocation Table 16 (FAT16) file format, data is saved into bins called clusters, and each cluster has an ID number that can range from 2 to 65520. A file is created by filling a cluster with data, and setting a flag to indicate in which cluster the next set of data for the file is located. This is a reasonably simple scheme and has been in use for a long time. The SD card interface driver in this design works with an SD card that must be formatted so that each cluster contains 2048 bytes of data. So the allocation unit size is 2048 bytes, and therefore it can be formatted to match these specifications in Microsoft Windows using the format command, for example if the SD card is inserted into drive

D, so the format command can be written as [7]: -  
format D:/FS:FAT/A:2048/V:SDCARD.

### 4. SDRAM Controller

The SDRAM chip manufactured by Integrated Silicon Solution, Inc (ISSI) is IS42S16160B, so when SDRAM controller has been chosen from SOPC builder the exact timing parameters must be selected so as to match what is written in datasheets [8].

### 5. VGA Controller

The DE2-70 board includes a 16-pin D-SUB connector for VGA output. The VGA synchronization signals are provided directly from the Cyclone II FPGA, and the analog data signals red, green, and blue (RGB) are obtained from the Digital to Analog Converter (DAC) ADV7123 triple 10-bit high-speed video chip manufactured by Analog Devices, Inc [9].

The timing specification for VGA synchronization and RGB data depends on the requested resolution, in this SOPC design the resolution for VGA (60 Hz) configuration is  $640 \times 480$  pixel, so the frequency must be 25 MHz and the timing specification for synchronization is shown in table 1. The timing of the horizontal synchronization (*hsync*) shown in figure



5.1, where an active-low pulse of specific duration time ( $a$ ) is applied to the  $hsync$  input of the monitor, which signifies the end of one row of data and the start of the next. The data (RGB) inputs on the monitor

must be off (driven to 0 V) for a time period called the *back porch* ( $b$ ) after the  $hsync$  pulse occurs, which is followed by the display interval ( $c$ ).

Table 1 VGA Timing Specification

Format	Pixel Clock (MHz)	Horizontal (in Pixels)				Vertical (in Lines)			
		Active Video	Front Porch	Sync Pulse	Back Porch	Active Video	Front Porch	Sync Pulse	Back Porch
640x480, 60Hz	25.175	640	16	96	48	480	11	2	31

During the data display interval the RGB data drives each pixel in turn across the row being displayed. Finally, there is a time period called the *front porch* ( $d$ ) where the RGB signals must again be off before the next  $hsync$  pulse can occur.

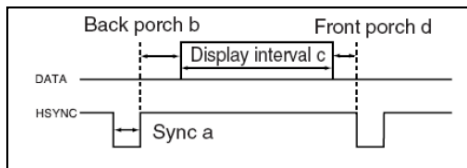


Fig 5.1 VGA horizontal timing specification

The timing of the vertical synchronization ( $vsync$ ) is the same as shown in Figure 5.1, except that a  $vsync$  pulse signifies the end of one frame and the start of the next, and the data refers to the set of rows in the frame (horizontal timing).

## 6. PIO ports Interfaces

In this SOPC design some PIO ports interfaces are included to perform some tasks when needed. The PIO IP core can be configured as input, output, both input and output or as bidirectional (Tri-State) ports,

with different data width starting from 1 to 32 bits per port. The PIO's can also be used to generate an optional Interrupt Request (IRQ) signal for input ports, to interrupt the CPU when any unmasked I/O pin is logic true. The input PIO hardware in DE2-70 board includes Double Pole Double Throw (DPDT) Switches and Push Buttons switches. The output includes LED's and seven segment display, finally the bidirectional I/O present in expansion header represent General Purpose Input Output (GPIO).

## 7. Implementation Results

- The resource usage summary for this implementation is shown in table 2.
- Figure 7.1 shows the logic array block (LAB) schematic for logic elements (LEs) and figure 7.2 shows LAB schematic for wide signals.
- The Nios II cpu clock Timing Analyzer Summary is shown in table 3.





**Table 2 Analysis & Synthesis resource usage summary.**

FPGA Family (Cyclone II)		
FPGA Device (EP2C70F896C6)		
Resource	Usage	Percentage
Total logic elements (LEs)	8211/ 68416	12%
Total combinational functions	7280/ 68416	11%
Dedicated logic registers	4976/ 68416	7%
Total reg's	5178	---
Total pins	411/ 622	66%
Total memory bits	183232/115200	16%
Embedded Multiplier 9-bit elements	4/300	1%
Total PLLs	3/4	75%

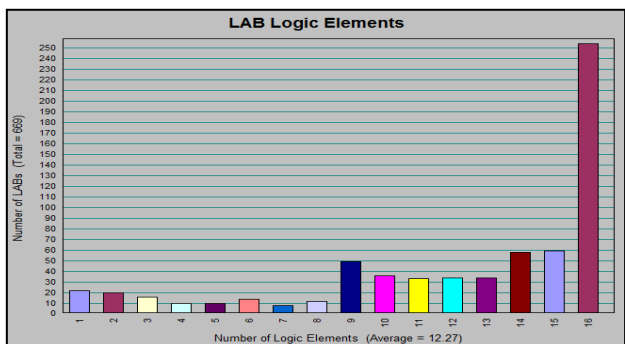


**Fig 7.1 LAB Logic Elements.**

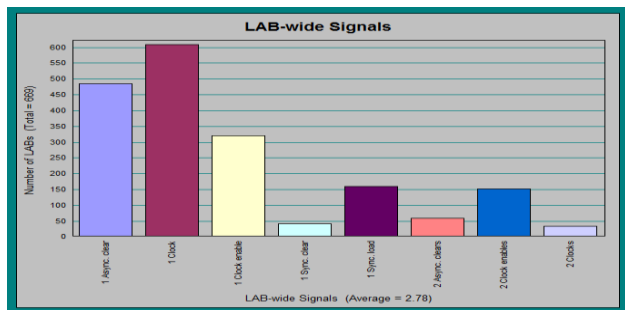


**Fig 7.2 LAB wide signals.**



**Table 3 Nios II cpu clock Timing Analyzer Summary**

Path Number :	5
Type:	Clock Setup: 'ADD_ON_SOPC:ADD_ON_SOPC_Instance pll:the_pll altpllpll:the_pll altpll:altpll_component _clk0'
Slack :	0.299 ns
Required Time :	100.00 MHz ( period = 10.000 ns )
Actual Time:	103.08 MHz ( period = 9.701 ns )
From :	ADD_ON_SOPC:ADD_ON_SOPC_Instance cpu:the_cpu A_ctrl_shift_rot
To :	ADD_ON_SOPC:ADD_ON_SOPC_Instance cpu:the_cpu cpu_nios2_oci:the_cpu_nios2_oci cpu_nios2_oci_dbrk:the_cpu_nio
From Clock :	ADD_ON_SOPC:ADD_ON_SOPC_Instance pll:the_pll altpllpll:the_pll altpll:altpll_component _clk0
To Clock	ADD_ON_SOPC:ADD_ON_SOPC_Instance pll:the_pll altpllpll:the_pll altpll:altpll_component _clk0
Failed Paths	0

## 8. Conclusion & further work

Based on re-configurable technology (FPGA, NIOSII soft core processor), a powerful SOPC design prototype platform for digital image processing was designed in order to support HW/SW co-design and partitioning. The steps of the processing algorithms is to transfer the raw data image that is stored into SD card to SDRAM, then by using synchronous static ram (SSRAM) as a buffer through Avalon Memory Mapped interface the original and processed image will be displayed on the VGA monitor. The system is implemented

on (FPGA) and it only uses 66% of the IOBs, 12% of the LEs, which's run on 100 MHz clock frequency that's sufficient to make the processing faster and reliable. The images can also be stored and read from the flash memory chip that is installed into the board, but when we use the flash the images must be stored in row-zip files and must be programmed before running the system, while the SD card can be inserted, removed or changed at any time when the system is running i.e. (more flexible than using that flash memory chip). Further work is going



on real-time digital video processing algorithms based on FPGA.

## 9. References

[1] JAMES O.HAMBLEN, TYSON S.HALL, MICHAEL D.FURMAN. "Rapid Prototyping of Digital Systems Quartus® II Edition". Springer 2006.

[2] A. Ben Atitallah, P. Kadionik, F. Ghozzi, P.Nouel, N. Masmoudi, Ph.Marchegay. "Real-Time Video System Design Based on the NIOS II Processor and  $\mu$ CLinux" In IP / SoC: IP Based SoC Design Conference France (2005) [hal-00183047 - version 1].

[3] Quartus II Development Software Literature, <http://www.altera.com/literature/lit-qts.jsp>. Apr -2010.

[4] Nios II Processor Reference Handbook, <http://www.altera.com/literature/lit-nio2.jsp> . Apr-2010.

[5] Altera DE2-70 Board user Manual , <http://www.terasic.com.tw/cgi-bin/page/archive.pl?Language=English&CategoryNo=53&No=226&PartNo=4>, Apr-2010.

[6] Phase-Locked Loop (ALTPLL) Megafunction User Guide. [www.altera.com/literature/ug/ug\\_altpll.pdf](http://www.altera.com/literature/ug/ug_altpll.pdf). Apr-2010.

[7] Altera University Program Secure Data Card IP Core. [ftp://ftp.altera.com/up/pub/Altera\\_Material/QII\\_9.0/University\\_Program\\_IP\\_Cores/Me](ftp://ftp.altera.com/up/pub/Altera_Material/QII_9.0/University_Program_IP_Cores/Me)

[mory/SD Card Interface for SoPC Build er.pdf](#). Apr-2010.

[8] Integrated Silicon Solution, Inc "256-MBIT SYNCHRONOUS DRAM datasheet", <http://www.issi.com>. Apr-2010.

[9] CMOS, 240 MHz Triple 10-Bit High Speed Video DAC (ADV7123) datasheet, <http://www.analog.com>. Apr-2010.



المؤتمر الدولي العربي الليبي الخامس للهندسة الكهربائية والإلكترونية 2010/10/26-23 طرابلس ليبيا



## التأكيد الجزئي في منهجية هندسة المتطلبات Partial Validation in Requirements Engineering Methodology

قسم الحاسب الآلي /كلية العلوم /جامعة الفاتح  
قسم الحاسب الآلي /كلية العلوم /جامعة الفاتح

د. مصطفى عبد العال  
أ. محمد بن زاهية

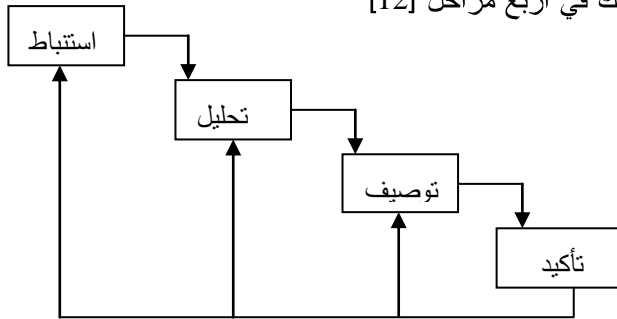
### مستخلص

تزخر أدبيات هندسة المتطلبات بالطرق المستخدمة في تأكيد المتطلبات (بمعنى التأكد منها) قبل الاعتماد عليها في تصميم المنظومات البرمجية. وواضح من هذه الأدبيات ومن خبرة العاملين والباحثين في هذا المجال عدم الارتياح لمرحلة تأكيد المتطلبات كمرحلة أخيرة تأتي بعد استنفاد الطرق واستثمار الوقت وبذل الجهد في جمعها وتحليلها وصياغتها. لأن اكتشاف الخطأ والخلل بعد كل ذلك يكون مكلفاً. لذلك نقدم في هذه الورقة تعديلاً في منهجية هندسة المتطلبات تجعل عمليات التأكد مصاحبة لجميع المراحل والطرق المستخدمة في هذه المنهجية من بدايتها، ليتسنى اكتشاف الخلل مبكراً وإكساب المتطلبات درجة كافية من الجودة في مراحل مبكرة. واقتراحنا لذلك تطبيق طريقة " التأكيد الجزئي " في كل مرحلة على حده بل وفي كل جزء من المرحلة.

- (1) استنباط / تجميع المتطلبات Elicitation
  - (2) تحليل المتطلبات Analysis
  - (3) توصيف المتطلبات Specification
  - (4) التأكيد من المتطلبات Verification and Validation (V&V)
- ويمكن توضيح ذلك بالشكل التالي ( 1 ) :

I - مقدمة :  
تهتم هندسة المتطلبات Requirement Eng بالطرق والأدوات التي تؤدي أو تساعد على تحديد المتطلبات ذات الجودة العالية التي يمكن الاعتماد عليها في إعداد منظومات برمجية تنال رضا المستخدمين.

وعادة ما يتم ذلك في أربع مراحل [12] وهي :



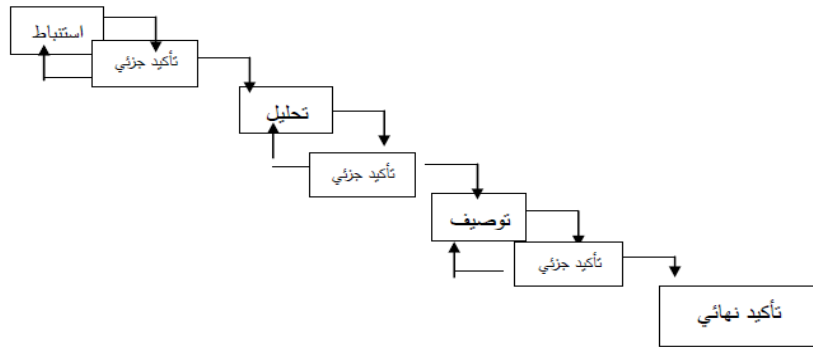
شكل [ 1 ] مراحل هندسة المتطلبات /النموذج التسلسلي



ومتيسرة ومعبرة تماماً على جميع مراحل الدورة الحياتية. كذلك هنا فإن نتيجة تأكيد المتطلبات النهائية لا تكون مجدية ومثمرة إلا إذا سبق ذلك تأكيداً جزئياً خاصاً بكل مرحلة من المراحل المذكورة أعلاه ، بل وفي كل خطوة من خطوات كل مرحلة . وواضح من نموذج الشكل (1) أنه إذا كانت نتيجة التأكيد سلبية في أحد بنود المتطلبات فإن الأمر يستدعي المراجعة والتعديل ابتداءً من المرحلة الأولى ثم متابعة التعديلات إلى المراحل التالية وهو أمر معقد ومكلف. لهذا نرى ضرورة تعديل هذه المنهجية وتنفيذ أعمال التأكيد في كل مرحلة من المراحل على حدة لتكون عملية التأكيد الواردة في المرحلة الأخيرة عملية استكمالية ومتيسرة كما هو موضح في شكل (2)

والمقصود بالتأكيد الوارد في المرحلة الأخيرة هو التحقق من والمصادقة على بنود المتطلبات التي تم جمعها ( استنباطها ) وتحليلها وتوصيفها ( صياغة مواصفاتها ) وأنها حقا تمثل البنود الفعلية التي يجب أن يتم تصميم المنظومة البرمجية على أساسها وقد وضعت جمعية IEEE [1] معايير لذلك وهي أن تكون متطلبات صحيحة وواضحة وكاملة ومتناسقة...الخ.

غير أن التأكيد كمرحلة أخيرة في منهجية هندسة المتطلبات تعتبر مهمة شاقة ومعقدة وغير دقيقة وغير مجدية. وهذا ما يشبه مرحلة التوثيق النهائي في منهجية هندسة البرمجيات. فقد أتضح أنه من الضروري أن تتم أعمال التوثيق الجزئية في كل مرحلة على حدا بل وفي كل خطوة من خطوات المرحلة الواحدة لتكون مرحلة التوثيق النهائية استكمالية



شكل [ 2 ] النموذج التسلسلي بالتأكد الجزئي

دوراً جوهرياً. أي أننا في هذه الورقة سنركز على طرق التأكيد الجزئي في المرحلة الأولى.

ولتوضيح التأكيد الجزئي موضوع هذه الورقة نكتفي بالتركيز على عمليات التأكيد الجزئي الخاص بمرحلة الاستنباط والتجميع التي تتولد فيها جميع بنود المتطلبات والتي يلعب فيها أصحاب الأدوار الرئيسية Stakeholders



تزداد في المراحل اللاحقة. والجدول التالي يوضح التكاليف النسبية لتصحيح الأخطاء: جدول التكاليف النسبية.

المرحلة	تكاليف تصحيح الخطأ
المتطلبات	1-2
التصميم	5
البرمجة	10
الاختبار	70
الصيانة	500

ولقد ركز أغلب العلماء على التأكيد الكلي للمتطلبات وخصوصاً استخدام طريقة V&V. فقد ذكر Bryan [ 8 ] أن التأكيد يقلص تكاليف المنظومة ويحسن مستوى الأداء وشدد هذا العالم على أن تأكيد المتطلبات ليس من الأشياء التي يمكن تأجيلها أو تأخيرها إلى مرحلة متأخرة من المشروع.

. وبخصوص التأكيد الكلي باستخدام V&V ، فقد ذكر العالم Tran [ 9 ] إن ذلك أصبح ضرورة ملحة خصوصاً في البرمجيات التي أصبحت أكثر تعقيداً. وخلاصة القول إن الأدبيات المتوفرة على كثرتها إلا أنها تختص بطرق التأكيد كمرحلة نهائية ( شكل ( 1 ) ) مع التعرض كثيراً إلى عدم الارتياح لذلك باعتبار أن التأكيد لا يحتمل التأخير إلى هذه المرحلة. ومن ذلك أنت فكرة هذه الورقة التي تتعلق بالتأكد المبكر والمصاحب لجميع المراحل والطرق المستخدمة في هندسة المتطلبات.

### ( III ) طرق جمع واستنباط المتطلبات:

بما أن هذه الورقة تركز على التأكيد الجزئي الخاص بمرحلة استنباط المتطلبات، رأينا لتسهيل ذلك أن نقدم في هذه الفقرة ملخصاً للطرق المستخدمة في الاستنباط والتي يمكن

### ( II ) نبذة تاريخية:

أوضح العالم Cleland Huang [2] أن التأكد من جودة المتطلبات يجب أداءه في جميع مراحل إعداد البرمجيات وشدد على مرحلة المتطلبات بصفة خاصة.

إن الوصول إلى متطلبات ذات جودة ليس بالأمر الهين واليسير فقد تعرض العالم Kazmierczak [ 3 ] لذلك واستشهد بمشروع Airbus فذكر سلباً إدماج مرحلتَي المتطلبات والتصميم في مرحلة واحدة . أما العالم Boehm [ 4 ] فقد ذكر أن مشروع TRW كانت به 85% من الأخطاء سببها عدم جودة المتطلبات بينما الأخطاء البرمجية لم تتعدى 15% وهذا يظهر مدى أهمية التأكيد من المتطلبات مبكراً في مراحل المشروع البرمجي. إن الخلل في بنود المتطلبات من أهم أسباب فشل المشاريع البرمجية حيث ذكر العلماء Hofmann و Lehner [ 5 ] أن الحصول على متطلبات صحيحة من أصعب وأهم عناصر المشروع البرمجي وأن في أحد التجارب على التأكيد اتضح أن المشاريع البرمجية الناجحة يكون المجهود المبذول فيها على النحو التالي:

40% جمع المتطلبات

35% توصيف المتطلبات

25% التأكيد مشتملاً V&V

أما العالم Sommerville [ 6 ] وهو يعتبر من أشهر علماء هندسة البرمجيات فقد ذكر أن أخطاء المتطلبات ترفع من تكلفة البرمجيات بحوالي 100 ضعف عند اكتشافها متأخراً في مرحلة البرمجة وسانده Kotony [7] حيث ذكر أن الدراسات بينت أن أخطاء المتطلبات مكلفة لأنها تؤثر مباشرة على تصاميم المنظومة المراد إعدادها وأن تكلفة تصحيح هذه الأخطاء



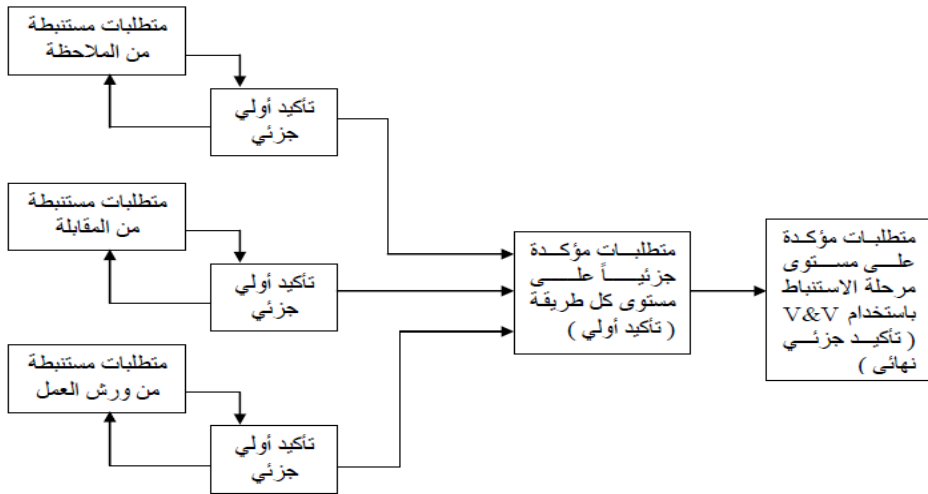
(3) المقابلة الشخصية Interview  
وتكون هذه الطريقة مجدية خاصة في المؤسسات التي يتواجد فيها ذوي خبرة بالمنظومات في المجال المطلوب ميكنته ، وفي الحالات التي تستوجب استطلاع رؤية الإدارة العليا (الزبون) وتوقعاتها من المنظومة المطلوبة.

تصنيفها وفقاً لبيئة العمل السائد في بلادنا حسب ما يلي [ 14 ]:

- 1) الملاحظة Observation  
ويمكن من خلالها تطبيق طرق مثل:  
جمع العينات Sampling وتعليمات المستخدم User instructions  
ومخططات حالة الاستخدام Use case diagram والسيناريوهات Scenarios.

(VI طرق التأكيد الجزئي :  
يجدر أن نوضح أن التأكيد الجزئي الخاص بمرحلة جمع واستنباط المتطلبات لا ينتظر إلى نهاية هذه المرحلة بل لابد من تطبيقه على كل طريقة تم استخدامها في هذه المرحلة لاستنباط بنود المتطلبات كما هو موضح في شكل (3):

- 2) ورشة العمل Workshop  
ويمكن أن يندرج تحتها طرق أخرى مثل: إثارة الأفكار Brainstorming والمتطلبات التفصيلية Detailed requirements والنموذج التجريبي Prototyping.



شكل [3] النموذج التسلسلي بالتأكيد الجزئي الأولي

أي أن هناك تأكيد جزئي أولي يتم على مستوى كل طريقة، ثم تأكيد جزئي نهائي يتم على مستوى المرحلة. وأهم طرق التأكيد الجزئي الأولي فهي:

- 1 المراجعة غير الرسمية Walkthrough
- 2 الفحص Inspection





شبيهة بالتطبيق المطلوب. ويتم فحص كل بند من المتطلبات وفقاً لقائمة الفحص التي تم إعدادها مسبقاً (Check List). ويفضل مشاركة الزبون أو المستخدم خاصة الذي لعب دوراً في جمع المتطلبات. وبهذا تكون قائمة المتطلبات في نهاية الجلسات أكثر تنقيحاً وأعلى جودة.

### 3) التحقق Verification [ 11 ]

التحقق هو إجراء عملية التأكيد عن طريق المواد والوثائق التي تم جمعها ( استنباطها ) وتصنيفها ووضع الأسبقيات لتنفيذها & Classify Prioritize والتي تم التحقق منها مسبقاً بواسطة المراجعة غير الرسمية والفحص. ويفضل أن يقوم بهذا الاختبار استشاري مستقل ويمكن أن يقوم به مهندس المتطلبات التابع لفريق التطوير. ويتم التحقق هنا (من خلال الوثائق فقط) من أن هذه المتطلبات فعلاً مقتبسة من الاحتياجات الفعلية المتعلقة بالزبائن بالإضافة إلى أهمية التأكد من مرجعية كل بنود المتطلبات و أولويتها، وأن التوثيق صالحاً للاستخدام في المراحل التالية.

### 4) المصادقة Validation [11]

ويتم عن طريق ما يعرف بالعرض التجريبي Prototype وهي طريقة تحقق وتأكيد عملي (على جهاز الحاسوب) على المتطلبات المنقحة جزئياً بواسطة الطرق السالفة الذكر وهنا يُفضل الاستعانة بخبرة استشاري مستقل، ويحضر جلسة العرض التجريبي مهندسي المتطلبات والزبون والمستخدم لمعرفة أي نواقص أو تناقضات أو أخطاء أو

والتي يجدر تنفيذها على مستوى كل طريقة تم استخدامها في جمع المتطلبات مثل المقابلة الشخصية والملاحظة وغيرها. أما طرق التأكيد الجزئي النهائي الخاص بهذه المرحلة فهي (V&V):

### 3 التحقق Verification.

### 4 المصادقة Validation.

وهذه لا يمكن تنفيذها بحكم تكلفتها وطول إجراءاتها إلا على مستوى نهاية المرحلة أي بعد جمع واستنباط جميع المتطلبات التي تم تأكيدها أولاً على المستوى الجزئي، وتسمى "تأكيد جزئي نهائي" كما في الشكل (3).

وفيما يلي نبذة عن كل من هذه الطرق الجزئية :

### 1) المراجعة غير الرسمية

#### [10] Walkthrough

هذه الطريقة عبارة عن جلسة ( أو عدة جلسات ) غير رسمية وغير منتظمة بين محلل النظم الذي قام بجمع واستنباط جزء معين من المتطلبات وبين زملائه من فريق العمل من أجل كشف أي أخطاء أو نواقص أو تناقضات أو غموض في المتطلبات. وهذه الجلسات تكون عفوية وقصيرة ويتم تكرارها لحين الوصول إلى متطلبات شبه خالية من الأخطاء والنواقص والتناقضات والغموض .

### 2) الفحص Inspection [10]

وهي عبارة عن جلسة أو مجموعة جلسات رسمية ( غير عفوية ) منتظمة بين محلي النظم وفريق فحص متمرس ذو خبرة في كشف الأخطاء. ويستعين هذا الفريق عادة بقائمة من أخطاء تطبيقات سابقة



الدقيقة للمتطلبات بين جهة المستفيد  
وجهة التطوير.

( V ) مثال تطبيقي للتأكيد الجزئي :

في هذا المثال نتناول كيفية تحديد وظيفة  
معينة من وظائف قسم الحسابات الجارية  
بالمصرف. فمحلل النظم يبدأ بمقابلة  
شخصية مع موظف الشباك حول  
استفسارات زبائن المصرف عن  
حساباتهم. كان جواب موظف الشباك أن  
الزبائن يكثرون من الاستفسار عن  
أرصدتهم. وقد تم وضع قصاصة لذلك  
فيما يلي عينة منها:

غموض في المتطلبات. كما يمكن  
اقتراح أي متطلبات جديدة خصوصاً  
بعد التوضيح العملي والمرئي  
للإمكانيات والوظائف والخيارات .  
وفائدة العرض التجريبي أنه يحول  
المتطلبات الغير ملموسة ( على  
الورق ) إلى متطلبات واقعية ملموسة  
يمكن التأكد من صحتها مباشرة على  
جهاز الحاسوب. وهذا ما يعرف  
بطريقة المصادقة وهي بالتأكيد ترفع  
من مستوى الفهم المشترك للمعاني

رقم الحساب : \_\_\_\_\_ الرصيد \_\_\_\_\_

الزبائن يسألون عن مرتبات ، وآخرين يسألون  
عن صكوك تم إيداعها للتحصيل عن طريق  
المقاصة، لهذا تم اقتراح نموذج أخر يفى بهذه  
الأغراض وهو كالاتي :

طبعاً محلل النظم سيستخدم طرق أخرى ومنها  
ملاحظة على أرض الواقع ومن خلال مراقبة  
تعامل الزبائن مع الشباك وجد أن بعض

رقم الحساب : \_\_\_\_\_  
تاريخ آخر صك : \_\_\_\_\_ قيمة آخر صك : \_\_\_\_\_  
تاريخ آخر مرتب : \_\_\_\_\_ قيمة آخر مرتب : \_\_\_\_\_  
الرصيد الحالي : \_\_\_\_\_

أعمال أخرى. كما أن هناك زبائن تجار  
قد يستفسرون على مجموعة صكوك تم  
إرسالها للمقاصة، وقد تم تطوير النموذج  
وفقاً لذلك. طبعاً هناك بعض التحسن  
ولكن عند الاستعانة بخبير استشاري له  
خبرة في منظومات المصارف واحتياجات  
مختلف أنواع العملاء أقترح النموذج  
التالي:

وللتحقق من هذا النموذج قام محلل النظم  
بعرض هذا النموذج على زميل أخر وهو  
محلل نظم لعمل مراجعة غير رسمية  
Walkthrough وقام هذا الأخير بتعديل  
طفيف في هذا النموذج وهو أن كثير من  
الزبائن لديهم أكثر من مرتب حيث



رقم الحساب :	_____	الاسم :	_____
<input type="checkbox"/>	الرصيد الحالي :	_____	
<input type="checkbox"/>	آخر رواتب :	_____	العدد: _____
<input type="checkbox"/>	آخر صكوك مقاصة:	_____	العدد: _____
<input type="checkbox"/>	آخر حوالات :	_____	العدد: _____
<input type="checkbox"/>	آخر إيداعات نقدية:	_____	العدد: _____
<input type="checkbox"/>	آخر سحبوات نقدية:	_____	العدد: _____
<input type="checkbox"/>	آخر صكوك مصدقة صادرة:	_____	العدد: _____
<input type="checkbox"/>			
<input type="checkbox"/>			
<input type="checkbox"/>			

النموذج أكثر تكلفة. هذا بالنسبة لبند بسيط من بنود المتطلبات فما بالك بقائمة المتطلبات الطويلة والمعقدة والمتداخلة.

### خاتمة

إن الفكرة الرئيسية في هذه الورقة البحثية هي استحداث طريقة "التأكيد الجزئي" وتنفيذها على أي جزء من المتطلبات وتصحيح أخطائها واستكمال نواقصها والتخلص من تناقضاتها وتوضيح ما يكتنفها من غموض في مرحلة مبكرة من قبل أصحاب الأدوار الرئيسية في المنظومة Stakeholders. فبدلاً من تأجيل التأكيد إلى المرحلة النهائية، نبدأ بالتأكيد الجزئي للمتطلبات المستنبطة من كل طريقة من طرق المرحلة الأولى، ونتبعه بالتأكيد الجزئي النهائي ( على مستوى كل مرحلة ) وقبل الشروع في المراحل

فيختار الزبون المعلومة المطلوبة بوضع إشارة ( ✓ ) في المربع مع تحديد العدد الذي يدل مثلاً على آخر مرتب أو آخر مرتبين أو ثلاثة أو غير ذلك . وبالتالي تقوم المنظومة بعرض نتائج هذا الاستعلام بالتفصيل.

ويلاحظ هنا أن إجراءات التحقق التي تمت جزئياً لهذه الوظيفة قد أدت إلى تطوير العينة من القصاصات التي تم جمعها من موظف الشباك إلى النموذج الشامل الذي تم تطويره بسهولة ابتداء من خطوة الملاحظة Observation، إلى خطوة المراجعة غير الرسمية Walkthrough، إلى رأي الخبير. ولو أن خبير المتطلبات المصرفية قد أعطى رأيه في المرحلة الأخيرة بعد برمجة المنظومة بالكامل لكان تعديل



- [5] Lehner, Hofmann, "Requirement Engineering as a Success Factor in SW Projects", IEEE Software, 2001
- [6] IAN Sommerville, "Requirement Engineering Processes", Software Engineering", 7<sup>th</sup> edition 2004
- [7] Kotony, G., Sommerville, I. " Requirement Engineering Processes and Techniques", John Wiley and Sons, 2000.
- [8] Bryan Chojnowski, Reglera : " Software Validation Turning Concepts into Business Benefits", MD & MI 2008.
- [9] E. Tran, " Verification & Validation and Certification", Carnegie Mellon University, Spring 1999.
- [10] D.P. freedman and G.M. Weiberg, "Handbook of Walkthrough, Inspection and Technical Reviews."
- [11] Andriole Stephen , " Software Validation & Verification & Testing and \Documentation", Princeton, N.J. : Petro Cell; books, 1986.
- [12] مصطفى عبد العال وإمحمد بن زاهية . " تكييف منهجيات هندسة المتطلبات للحصول على متطلبات جيدة لتطوير المنظومات البرمجية " المؤتمر الوطني لتقنية المعلومات والاتصالات 2008

التالية التي يجدر أن تخضع بالمثل إلى "التأكيد الجزئي". وهذا بدوره يقطع بنا شوطاً هائلاً من التنقيح والتنقية والوصول إلى متطلبات ذات جودة عالية في فترة مبكرة جداً. وبالتالي تكون مرحلة التأكيد النهائية على مستوى منهجية هندسة المتطلبات مرحلة تأكيد شمولية ومنتيرة ومجدية. والهدف دائماً أن نتفادى أكثر ما يمكن من تكلفة التعديلات التي تتناسب بزيادة مطردة مع وقت إثارتها وخاصة عند اكتشافها في مراحل متأخرة من تحديد المواصفات أو أثناء التصميم والتطوير البرمجي أو ربما خلال الاختبارات أو التشغيل الحقيقي.

## المراجع

- [1] IEEE standard glossary of software engineering.
- [2] Cleland Huang, "Software Requirement", DePual University, 2004
- [3] Kazmierczak, "Requirement Engineering", University of Melbourne, 2003
- [4] B. Boehm, "Software Engineering Economics", Prentice Hall, 1981



## Branch folding technique for all branch instructions

A. H. Infis  
Electrical & Electronic Engineering Dep.  
Faculty of Engineering  
AlFateh University  
Email [Ali\\_infis@yahoo.com](mailto:Ali_infis@yahoo.com)

S. A. Elfandi  
Computer Engineering Dept.  
Faculty of Engineering  
Alfateh University  
Email [Saelfandi@yahoo.com](mailto:Saelfandi@yahoo.com)

### Abstract

Branch instructions makes up 15 to 25% of the total program instructions[1] and in reality they are overhead for the program because they do not contribute to the actual processing. furthermore they may cause an extra delay "branch penalties" over that required to execute them due to the pipeline nature. Several techniques have been proposed to reduce branch penalties including branch predictions and the use of branch target buffer BTB [1], [3],[4]. Branch prediction techniques can only reduce branch penalties to some extent and the use of BTB can reduce the branch penalties to zero in some cases and can effectively eliminate all unconditional branches "branch folding". A technique for folding backward conditional branches for embedded systems is proposed by [2]. In this paper we present a hardware technique to fold all kinds of branch instructions and therefore increase processor performance by up to 25%. Our approach require modification of the BTB structure and triplicating the execution stage of the processor's pipeline.

### 1\_Introduction

Control hazard caused by branch instructions is one of the main problems for pipelined processors because of the difficulty to decide which instruction to follow the branch instruction until the branch instruction is executed and the branch condition is evaluated. The problem

solution to fold all kinds of branch instructions provided that they are separated by at least three non-branch instruction. The idea can be explained by referring to the basic five stage MIPS processor. To simplify the idea we will assume that we will have three pipelines PL1, PL2, and PL3. Each one is exactly similar to the basic five stage MIPS processor. Normally only pipeline one is working until we hit a

gets harder with increasing pipeline length especially when the branch instruction takes longer to execute. Several software and/or hardware solutions to the control hazard problem exist in literature but none of these solutions manage to fold all kinds of branch instructions. In this paper we present a hardware

branch instruction. when we hit a branch instruction, the branch instruction will be given to pipeline PL1, and with the help of a branch target buffer BTB we will give the instruction just after the branch to pipeline PL2, and the branch target instruction to pipeline PL3. All three pipelines will then be allowed to work in parallel until the branch instruction finish execution. At that time we will of course know whether PL2



or PL3 is the correct one. At this moment the correct pipeline (PL2 or PL3) will be selected to be the main pipeline to continue execution. The net effect is that branch instruction execution will not contribute to the program execution time because it is executed in parallel with the other two alternative program flow. In the following sections we will describe the necessary hardware modification to the basic MIPS so that it achieves branch folding and show how it works.

## 2\_The Data Path:

The solution to the branch folding problem requires the following hardware modifications:

1. Tripling the execution unit "EX" stage so that the branch

instruction, the instruction following the branch, and the branch target instruction can all be executed in parallel.

2. Modify the decoding stage so that all three instructions can be decoded simultaneously.
3. Modify the BTB so that when accessed by the PC of the branch instruction it gives the code for the instruction just after the branch instruction, and branch target instruction. Each of these two instruction codes is to be given to one of the two extra execution units mentioned above after being all decoded simultaneously.

The block diagram for the new basic 5 stage MIPS processor is given in figure 1 below.

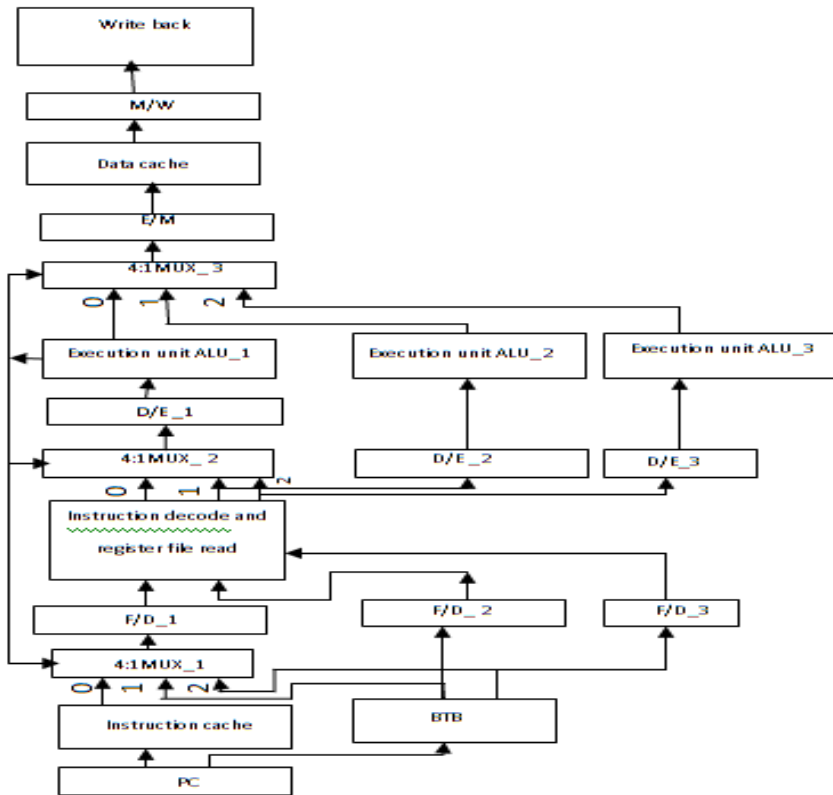


**Figure 1 Block diagram for the basic modified MIPS**

The basic idea for the branch target buffer is that it is now an associative memory which is indexed by the least significant bits of the program counter and is used to store the code of the instruction just after the branch instruction, and the code of the target instruction. That is if the input PC is an address for a branch instruction the BTB should produce the code for the instruction just following the branch instruction, and the code for the target instruction. Further more if PC is the address for the first or second instruction

following the branch address, the BTB will produce the code for the first or second instruction following the branch instruction and the branch target instructions respectively. If the PC is neither branch address nor an address for the first or the second instruction following the branch (BTB miss), the BTB will produce a no operation code.

The given data path in figure 1 above can be considered to be consisted of three pipelines PL1, PL2, and PL3. All three



pipelines share the same hardware in the Decode, Memory, and Write back stages. PL1 gets its instructions from the instruction cache and uses Execution unit ALU-1 in the execution stage. It is considered the main pipeline. PL2 gets its instruction from the BTB and uses Execution unit ALU\_2 to execute the instruction that is just after the branch instruction. PL3 however, gets its instruction from the BTB and uses Execution unit ALU-3 to execute the branch target instruction. At the end of the branch execution either PL2 or PL3 will have the correct set of instructions that should be allowed to continue depending on whether the branch is taken or not taken. In either case the correct pipeline PL2 or PL3 will be selected and passed to the main pipeline PL1 using the multiplexers (MUX\_1, MUX\_2, and MUX\_3). Execution flow will then continue from there. Note that the instruction to be fetched from the instruction cache after the branch is resolved is either the fourth instruction after the branch instruction or the third instruction after the target instruction depending on the branch outcome not taken or taken respectively. This means that the Data Path must take this fact into consideration by either loading PC with  $PC+4*4$  if the branch instruction is not taken or load PC with the target address calculated by the branch address+  $3*4$  (we assumed here that the instruction code is 4 bytes long). The latter case can actually be taken care of by the compiler but the former case may require adding another MUX at the PC input.

### 3\_CPU operation

When a new PC value is loaded into the program counter the instruction cache will generate the instruction code which will

then be loaded into the F/D\_1. At the same time if the instruction is a branch instruction, the code of the instruction just after the branch will be loaded into F/D\_2, and the code of the target instruction will be loaded into F/D\_3. On the next cycle all three instructions (coming from F/D\_1, F/D\_2 and F/D\_3) will be decoded simultaneously and their results (register values) will be loaded into D/E-1, D/E\_2 and D/E\_3 respectively. On the next clock cycle Execution unit ALU\_1, Execution unit ALU\_2, and Execution unit ALU\_3 will execute the three instructions coming from D/E\_1, D/E\_2 and D/E\_3 respectively.

At the end of execution (of all three instructions) we will have two cases to consider; that is either the branch instruction (executed by ALU\_1) is not taken or taken. For the first case the Execution unit ALU\_1 should command MUX\_1, MUX\_2, and MUX\_3 to select input 1 and therefore the execution flow will go sequentially starting from the instruction just after the branch. For the second case when the instruction executed by the Execution unit ALU\_1 is a taken branch, Execution unit ALU\_1 should command MUX\_1, MUX\_2, and MUX\_3 to select input 2. In this case the execution flow will go from the target instruction. In both cases and after selecting the correct set of instructions to fill the Decode, Execute, and Memory stages, the MUX's return to select input 0 and be prepared for a second branch instruction. It may be clear that the data path cannot handle two consecutive branches if they are separated by less than three instructions.





### 3.1\_Space timing diagram example:

To see how the CPU works let us see how the following program sequence would be executed on the given data path. As it can be seen from the space timing diagram

figure 2 the sequence of instruction consists of eleven instructions I1 to I11. Instruction I3 is a conditional branch instruction (BEQ L). Instruction I8 is the target address (labeled L).

clock INS	1	2	3	4	5	6	7	8	9	10
I1	F I\$	D	E ALU-1	M	W					
I2		F I\$	D	E ALU_1	M	W				
I3 BEQ L			F I\$	D	E ALU_1 END TAKEN BRANCH					
I4			F BTB	D F/D_2	E ALU_2					
I5				F BTB	D F/D_2					
I6					F BTB					
I7										
L: I8			F BTB	D F/D_3	E ALU_3	M MUX_3	W			
I9				F BTB	D F/D_3	E ALU_1 MUX-2	M	W		
I10					F BTB	D F/D_3 MUX-1	E	M	W	
I11						F	D	E	M	W

Figure 2 space timing diagram for the case of taken branch

In figure 2 we assume that the branch instruction is a taken branch. In clock pulse 1 instruction I1 get fetched from the instruction cache (I\$). In clock pulse 2 I2 gets fetched from I\$ while I1 gets decoded. Instructions I1 and I2 will continue their journey through the rest of the pipeline and will finish on clock pulse 5 and 6 respectively. In clock pulse 3, the branch instruction I3 gets fetched and the BTB will give the code for I4 (the instruction just after the branch) and the code for

instruction I8 (target instruction). The instructions I3, I4, and I8 will all go in parallel through the decoding and executing stages through pipelines PL1, PL2 and PL3 as explained before (see sec. 3). At the end of clock pulse 5, the branch instruction (I3) ends its execution and it become known if the branch condition is satisfied or not. Note that the target instruction address (its PC value) will also be calculated in this stage. In figure 2 assume that the branch is taken, therefore at the end of clock pulse 5,



Execution unit ALU\_1 (the one that execute the branch instruction) will force Instructions I8, I9, and I10 to enter their Memory, Execution, and Decoding stages of pipeline PL1 through the multiplexers as explained before (see sec.3). The next instruction to be fetched in clock pulse 6 is I11 (target instruction +3 see sec.2).

If the branch instruction is not taken however, the Execution unit ALU\_1 will force Instruction I4, I5, and I6 to enter their Memory, Execution, and Decoding stages of pipeline PL1 through the multiplexers as explained before (see sec.3). The next instruction to be fetched in clock pulse 6 is now I7 (The branch instruction address+4 see sec.2). Note that we are neglecting any data hazed which can obviously be solved using data forwarding [1].

It can be seen that the space timing diagram given in figure 2 is representative of all kinds of conditional branch instruction. For conditional branches, however pipeline PL2 must get a NOP instruction because there is no reason for executing the instructions following the unconditional branch instruction.

#### 4\_Conclusion:

In this paper we show that it is possible to fold all kinds of branch instruction provided that they are separated by at least 3 non branch instructions. This will of course increases the CPU performance. To see how let us take an example. Assuming that we have a program of 1000 instructions with 200 branch instructions, and that the clock frequency of a 5 stage CPU is 100MHZ. If the program executes on a machine without branch folding, the execution time would be given by  $(5+999)*.01=10.04$  micro sec. with the proposed enhancement all branch instructions will effectively be eliminated

and therefore the number of instruction will be 800 and the execution time will be about  $(5+799)*.01=8.04$  micro second. This means performance improvement of about 20%. The drawback of our design is that branch instruction should not be separated by less than 3 instruction is not series one and it can be taken care of by an optimized compiler. The extra hardware is another drawback but it is also not series one because the hardware cost is continuously going down and with this enhancement there is no need for all branch prediction hardware which is to some extent comparable to the proposed hardware.

#### 5\_references:

1. L. Hennessy and D. A. Patterson "computer architecture A quantitative approach", Forth edition, Morgan Kaufmann, 2007.
1. L. Hwang Lee, J. Scott, B. Moyer, and J. Arends ", Low cost branch folding for embedded application with small tight loops", IEEE international symposium on microarchitecture, Haifa, Israel, November 16-18, 1999.
2. K. M. Kavi, "Branch Folding For Conditional Branches", Internal report, Department of Electrical and computer Engineering, The University of Alabama in Huntsville.
3. D. R. Ditzel, and H.R. Mclellan, "Branch Folding in CRISP microprocessor: reducing branch delay to zero" proceedings of the 14th annual international symposium on coputer architecture, p. 2-8, june 2-5,1987.



## Investigation of the coupling-effect in fault-based software testing

Elfurjani Sassi Mresa

Department of Electrical and Electronic Engineering, Al Fateh University, Tripoli, Libya.

Email: mresa@ee.edu.ly

**Abstract**—One of the hypotheses upon which mutation testing is based is the coupling-effect. This states that, in a given program, a test set that detects simple faults is sensitive enough to detect more complex faults. The hypothesis does not define simple or complex faults but in the few studies that have been done on the coupling effect [1], [2], [3], complex faults have always been considered to be combinations of simple faults. In contrast, this paper considers the coupling effect between programs that contain simple faults of different kinds. The paper reports the results of extensive experiments that support a more general form of the coupling effect hypothesis. Specifically, a test data set that can reveal certain sets of simple faults in a given program is likely to be able to reveal not only more complex faults but also sets of different types of simple faults. This result is further evidence for the effectiveness of fault-based testing. This paper also investigates the subsumption relation between the 22 mutation operators used in the Mothra mutation system. The results show that full mutation is much more expensive than is probably necessary, and that most of the mutation operators used in the Mothra mutation system do not contribute to the effectiveness of mutation testing. Out of the entire set of mutation operators used in the Mothra tool, only few operators are likely to be sufficient for achieving full mutation adequacy.

**KEY WORDS:** fault-based testing, Mutation testing, coupling-effect, simple faults, complex faults

### I. INTRODUCTION

Mutation analysis, originally proposed by DeMillo *et al* [4], is a fault-based technique for testing software. Fault-based testing techniques are based on the notion of testing for specific kinds of faults, and one distinctive feature of fault-based testing techniques is their ability to demonstrate the absence of specific faults from the test program. This unique feature provides quantitative indicators to help the tester predict the reliability of a program.

The basic idea of mutation testing is to make many small changes, one at a time, to a given program to generate a collection of variants, so-called ‘mutants’. Then, an attempt is made to provide test data which distinguishes each mutant from the original program. If a test that distinguishes a mutant is also successful, i.e. produces the correct output when applied to the program under test, the test is said to kill the mutant and consequently is able to detect the fault that produced the mutant. After execution on a successful test, a mutant may remain alive for one of two reasons:

- Equivalent mutant— the mutant program is functionally equivalent to the original program, hence cannot be killed by any test case.
- Inadequate test data— the mutant is not equivalent but the test data set failed to distinguish the mutant from the original



program.

Clearly, there is a very large number of faults a given program can exhibit. To restrict the number of mutations that need to be examined, mutation testing relies on two assumptions (i) the competent programmer hypothesis[5], and (ii) the coupling effect[4]. The former hypothesis is the assumption that competent programmers, working conscientiously with adequate tools, tend to write programs that are either correct, or contain at most a few simple faults.

The coupling effect states that a test data set which distinguishes all programs with simple faults is capable of distinguishing a much larger class of programs with more complex faults[1], [5], [3], [6], [7]. The meaning of coupling-effect depends on the definitions of simple and complex faults. Mutation analysis regards a simple fault as a single syntactic change to a source statement[3] and a complex fault is typically regarded as a combination of two or more simple faults.

This paper reports extensive experiments that consider a far more general interpretation of the coupling effect hypothesis. Rather than considering coupling between simple and complex faults it considers coupling between different kinds of simple faults. The results of these experiments not only support the coupling effect hypothesis but show its role to be more important than has been claimed previously. It shows that a test data set that can reveal a specific type of fault is in practice capable of revealing other types of faults. This paper also investigates the subsumption relation between the 22 mutation operators used in the Mothra mutation tool. The results show that most of these mutation operators are redundant, and only a few operators are likely to sufficient for achieving full mutation adequacy.

The structure of this paper is as follows: Section 2 reviews previous work on the coupling effect; Sections 3 and 4 describe the experiments done and Section 5 presents the results; the conclusions are presented in the final section.

## II. PREVIOUS INVESTIGATIONS OF THE COUPLING EFFECT

Morell[2] has reported several theoretical results on fault-based testing and coupling. Morell does not define simple and complex faults but considers faults in general. In Morell's terms, two mutants, each containing a fault, are said to be coupled for a given test if each is individually distinguished by the test, but the mutant containing both faults is not distinguished by the same test; one fault effectively masks the other. Morell's results on coupling show that there is no algorithm for determining if two mutations couple. The results of Morell's study[2] also gives a probabilistic argument to show that for any given pair of non-equivalent mutations, there are relatively very few test cases for which the two mutations couple.

The coupling effect hypothesis is difficult to verify empirically because of the huge number of faults that would need to be considered. In addition, it is not clear how to distinguish between "simple" and "complex" faults[2], programs, and test generation methods.

In the few empirical studies that have been done on mutation coupling effect[1], [3], complex faults were modelled by inducing multiple mutations into the program.  $n$ -order mutations are mutations that are created by combining  $n$  mutations in a single program.

Lipton and Sayward [1] performed an experiment to investigate the mutation coupling effect. This was done by taking a



test set that is adequate with respect to the 1-order mutants of a given program, and measuring the effectiveness of this set against higher-order mutants generated for the same program. Lipton and Sayward' used one program only for their experiment. They generated a mutation adequate test set for the program, and executed this test set on 21,100 2-order mutations of the program. Offutt[3] generated 500,000 2-order mutants for the same program and so 21,000 is but a small proportion. Nevertheless, every non-equivalent 2-order mutant was killed by the test set. The experiment was repeated with 3000 3-order and 3000 4-order randomly generated mutants and again all the 3-order, and 4-order non equivalent mutants were killed. In this experiment, only a small percentage, however, of the 3 and 4-order mutants were generated.

Offutt[3] repeated Lipton and Sayward' experiment on a collection of 4 programs. In Offutt's experiment, all connected 2-order mutations were generated for all programs. An  $n$ -order mutation is considered connected if there is an execution path that reaches all the  $n$  mutations introduced. Clearly faults in unconnected mutations cannot couple and were not considered. Each 2-order mutation was executed against those test cases that caused both of the mutated statements to be executed. Since the number of 3-order mutants is so huge, 3-order mutations were generated for two programs only. The results of Offutt's experiment show that test data that is developed to kill 1-order mutations is very successful at killing higher-order mutants. The important implication of the results reported in[1] and[3] is that, when using mutation testing, one can focus on 1-order mutants and ignore higher-order mutants with practically no loss in testing quality.

In all these empirical studies, however, complex faults have always been considered to be combinations of simple faults. The results obtained from all these studies[1], [2], [3] have all shown that coupling between such faults is very rare in practice. Although it has been convincingly demonstrated that coupling is rare, and that higher-order mutants can be ignored, it is by no means clear that this factor alone explains the effectiveness of fault-based testing.

### III. TERMINOLOGY AND DEFINITIONS

In what follows,  $P$  denotes a program under test.  $M_A$  denotes the set of all mutants generated by applying the complete set of mutation operators to  $P$ . A test case that when applied to a mutant produces an output distinct from the output of the test program  $P$  is said to kill that mutant. The set of mutants from the set  $M$  killed by any test case in the set of test cases  $t$  is denoted by  $killedBy(M, t)$  so that  $\forall t \bullet killedBy(M, t) \subset M$ . A mutant is an equivalent-mutant if it is functionally equivalent to the original program; otherwise it is non-equivalent.  $M_e$  and  $M$  denote all the equivalent and non-equivalent mutants in  $M_A$  respectively so that  $M_e \cup M = M_A$ . A set of test cases  $T$  that can kill all mutants in  $M$ , i.e.  $killedBy(M, T) = M$ , is called mutation adequate test data set with respect to program  $P$ . The set of all mutants produced by applying the mutation operator  $i$  to the program  $P$  is denoted by  $M_{ia}$ . The corresponding sets of equivalent and non-equivalent mutants in  $M_{ia}$ , are denoted by  $M_{ie}$  and  $M_i$  respectively. A set of test cases that kills all non-equivalent mutants ( $M_i$ ), i.e.  $killedBy(M_i, T_i) = M_i$ , is called  $i$ -adequate and is denoted by  $T_i$ .

The strength of an operator seeks to measure in general terms the contribution made

by the mutants of this operator to the assembly of a test set that is mutation adequate for the mutants of all operators.

**Definition:** The strength of a mutation operator  $i$ ,  $S_i$ , w.r.t. a given set of mutants and  $i$ -adequate test set  $T_i$ , is measured, as given in Equation (1), by the number of mutants from  $M$  killed upon the execution of the test data set  $T_i$  relative to the total number of mutants in  $M$ . # denotes the size of a set.

$$S_i = \frac{\#killedBy(M, T_i)}{\#M} \quad (1)$$

The empirical partial strength of a mutation operator  $i$  over another operator  $j$  seeks to measure the contribution made by the mutants of operator  $i$  to the assembly of a test set that is mutation adequate for the mutants of operator  $j$ .

**Definition:** The partial strength of a mutation operator  $i$  against another operator  $j$ ,  $S_{i,j}$ , w.r.t. a given set of mutants and test set, is measured, as given in Equation (2), by the relative adequacy of a test data set  $T_i$  to kill mutants from the set  $M_j$ . A score of 1 indicates that, using  $T_i$ , the mutation operator  $i$  subsumes the mutation operator  $j$ .

$$S_{i,j} = \frac{\#killedBy(M_j, T_i)}{\#M_j} \quad (2)$$

Note that the value of these measures depends on the test program, the type and occurrences of the constructs used, and consequently, the applicability of different mutation operators and the test data. intuitively, a set of test cases is non-redundant if the removal of any test from the set decreases its mutant killing power.

**Definition:** A set of test cases  $t$  is said to be non-redundant with respect to a set of mutants  $M$  if for every test set  $t'$ ,  $t' \subset t$  implies  $killedBy(M, t') \subset killedBy(M, t)$ .

Note that an adequate non-redundant test set  $T_i$  for  $M_i$  may not be the minimal adequate test set over all possible test sets. In all of the following definitions,  $T$  and  $T_i$  are restricted to be non-redundant test sets. The reason for removing redundant test cases from the generated test data sets is that the presence of redundant test cases in  $T$  or  $T_i$  may bias the results and lead to overestimated strength measurements.

However, much consideration was given to the selection of the programs used in this study so that their effect on the calculation of these measures is minimised. This was done by selecting the programs such as to cover a range of different applications. Furthermore, in each program, it was ensured that all the operators being investigated, that is all the mutation operators used in Mothra, with the exception of *dsa* operator, are applicable. The decision to exclude data statement alterations operator (*dsa*) from this investigation was motivated by its infrequent use in practice and non-applicability in most programming languages other than Fortran.

The empirical subsumption relation between two mutation operators seeks to measure the contribution made by the mutants of one operator to the assembly of a test set that is mutation adequate for the mutants of the other operator. Subsumption is a convenient term for 100% partial strength. For example, a mutation operator  $i$  is said to empirically subsume another operator  $j$  if test cases assembled to achieve adequacy for the mutants of  $i$  are adequate for the mutants of operator  $j$ .

Table I lists the complete set of mutation operators used by the Mothra mutation tool[8]. Detailed descriptions can be found in [9]. Each mutation operator is represented by a three-letter acronym. Referring to Table I, the Mothra mutation operators can be



Mut. Op.	Description
<b>aar</b>	array reference for <b>array</b> reference replacement
<b>abs</b>	<b>absolute</b> value insertion
<b>acr</b>	array reference for <b>constant</b> replacement
<b>aor</b>	arithmetic <b>operator</b> replacement
<b>asr</b>	array reference for <b>scalar</b> variable replacement
<b>car</b>	constant for <b>array</b> reference replacement
<b>cnr</b>	comparable array <b>name</b> replacement
<b>crp</b>	constant <b>replacement</b>
<b>csr</b>	constant for <b>scalar</b> variable replacement
<b>der</b>	<b>DO</b> statement <b>END</b> replacement
<b>dsa</b>	<b>DATA</b> statement <b>alterations</b>
<b>glr</b>	<b>GOTO</b> label replacement
<b>lcr</b>	logical <b>connector</b> replacement
<b>ror</b>	relational <b>operator</b> replacement
<b>rsr</b>	<b>RETURN</b> statement replacement
<b>san</b>	statment <b>analysis</b>
<b>sar</b>	scalar variable for <b>array</b> reference replacement
<b>scr</b>	scalar for <b>constant</b> replacement
<b>sdl</b>	statement <b>deletion</b>
<b>src</b>	<b>sour</b> ce constant replacement
<b>svr</b>	scalar <b>variable</b> replacement
<b>uoi</b>	<b>unary</b> operator insertion

TABLE I  
MOTHRA MUTATION OPERATORS

divided into three broad classes, depending upon whether they effect operands, operators or statements as a whole[9]. These classes are statement analysis (*san*, *sdl*, *rsr*, *glr* and *der*), predicate and domain analysis (*abs*, *aor*, *ror*, *lcr*, *uoi*, *crp*, and *dsa*), and coincidental correctness (*svr*, *aar*, *acr*, *asr*, *car*, *csr*, *sar*, *scr*, *src*, and *cnr*). Each class corresponds to a particular kind of tests. For example, by constructing test cases that kill mutants generated by the statement analysis class, the tester performs traditional statement analysis tests (testing that all statements are executed and that every

statement is not redundant, for example). The predicate and domain analysis class can be used to create test data to exercise all predicate boundaries and data domains. Using the coincidental correctness analysis class provides test data that, as might be expected, attempts to eliminate coincidental correctness errors. Under this kind of error, the outcome of a test is as expected but the fact that the outcome is correct is a coincidence, a fault is present but not revealed by the test. For example, the statements  $a + 2$ ,  $a * 2$  and  $a ** 2$  will all produce the same result for  $a = 2$ .





#### IV. THE EXPERIMENT

The objective of the experiment reported in this paper is to measure the partial strength of every mutation operator used in the Mothra mutation system[8] over all other operators. The experiment also investigates the subsumption relation that may exist between various mutation operators.

##### A. Experimental Programs

The experiments used a sample of 4 programs, Brief descriptions of which are given below<sup>1</sup>.

**FINDCNT** This program is a modified version of **FIND** subroutine developed by DeMillo, Lipton, and Sayward [4] for partitioning an integer array. The original program was modified and renamed **FINDCNT**. This modified version, in addition to the function of the original program, it counts the elements of the input array that lie within a specific range and stores the result in a variable.

**SORT** This program[10] executes a selection sort using a pointer. It takes as input an array  $X$ . The array  $X$  is sorted, smallest to largest, and is not destroyed. The program was modified such that the squares of all elements of array  $X$  are computed and stored, according to their values, in ascending order in an array  $Z$ .

**MInv** This program[10] computes the inverse of the square  $N$  by  $N$  matrix  $A$ . If the matrix has no inverse, the program terminates.

<sup>1</sup>Source listings of all the programs are available from the author.

**BANKER** This function[11] is a deadlock avoidance algorithm for processes competing for resources.

##### B. Adequate test set generation

In this study, the automatic test data generator tool, Godzilla[12], was used to generate as many of the required test cases as it was able to; before resorting to generating test cases by hand. The method used to generate mutation adequate test data in this study, however, differs than that used in all previous studies. Methods used in previous studies[13], [3], [14], [15], [11] do not guarantee non-redundant test sets. Test sets are generated sequentially by including any test case that kills any as yet unkilled mutant. A test case is discarded if it does not distinguish at least one non-equivalent mutant. If a test case is retained there is no attempt to establish if the previous test cases are still necessary since once a new test case is included, previously included test cases may become redundant.

To avoid any affects on the results of this investigation that may be caused by redundant test cases, the same algorithm, developed by the author in [16] for generating non-redundant test sets, is used in this investigation. Figure 1 shows the redundancy elimination algorithm. A rigorous description of this algorithm can be found in[16].

##### C. Experiment method

For each of the programs selected for the experiment, the following steps were performed.

- 1) Each mutation operator  $i$ ,  $i=1, \dots, 21$ , was applied to  $P$ , to identify the sets of mutants  $M_{i_a}$ , and the corresponding sets of non-equivalent mutants  $M_i$ , hence also the sets  $M_A$  and  $M$ .



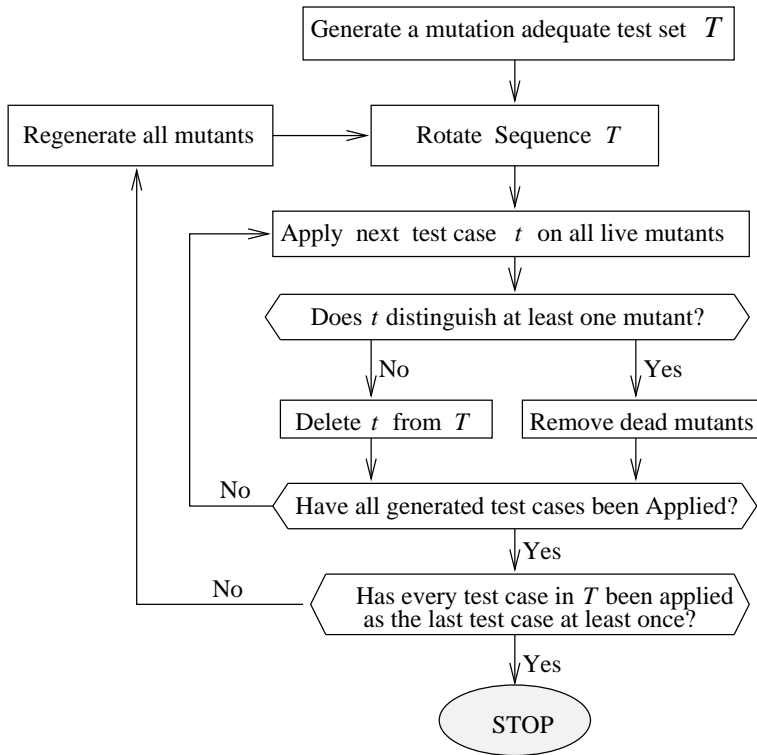


Fig. 1. Flow chart for eliminating redundancy from a mutation adequate test set

- 2) A mutation-adequate non-redundant test set  $T$  was generated for program  $P$ .
- 3) For each set  $M_i, i=1, \dots, 21$ , adequate non-redundant test data set was generated. In an attempt to eliminate any bias that could be introduced in the generation of a particular test data set, a sample of 31 randomly generated adequate non-redundant test data sets,  $T_i^1, T_i^2, \dots, T_i^{31}$ , was generated for each mutation operator  $i$ .
- 4) For each mutation operator used in the Mothra mutation system  $i, i=1, \dots,$

21:

The partial strength of the mutation operator  $i$  over all other operators  $j$ , where  $j=1, \dots, 21$  and  $j \neq i$ , was calculated as the mean partial strength over 31 trials.

$$S_{i,j} = \frac{\#killedBy(M_j, T_i)}{\#M_j}$$

where  $\#killedBy(M_j, T_i) = \frac{1}{31} \sum_{j=1}^{31} \#killedBy(M_j, T_i^j)$

The overall partial strength of each mutation operator over other operators was then computed as the average value obtained for all four programs.



## V. RESULTS AND ANALYSIS

### A. The partial strength

The results obtained from the partial strength experiment is shown in Table II. All data in this table are rounded to two digits. Table II shows the average partial strength of each mutation operator (average over 31 trials), used in the Mothra mutation system, over every other mutation operator, for all of the experimental programs, FIND-CNT, SORT, MInv and BANKER. In this table, the partial strength of each mutation operator appearing in the first column, with respect to each other operator listed along the top row, is given in the corresponding row-column intersection. The symbol ‘—’ indicates 100% partial strength. From the obtained results, the following observations can be made:

- Previous results on the strength of individual mutation operators[16] have shown that  $T_i$  will kill many mutants other than  $M_i$  but have not shown if these other mutants belong to only a few operators or are spread over all operators. From the results shown in the Table II it can be seen that the partial strength of each mutation operator over all other operators, i.e., the average strength of a test set that is adequate for one mutation operator on other operators, is quite high. It is important to note that a conservative approach was adopted in measuring mutation operators’ partial strength. The decision in this experiment to use non-redundant test data sets, led to test data sets 50% smaller than what would normally have been generated in practice. As a consequence, test sets generated in practice would normally be of a higher mutant killing rate than the test sets used in this experiment.

- The partial strength of a mutation operator over other operators has been found to be more influenced by the program under test than the test cases used. However, there is a little variation in the ranking of mutation operators, in terms of their partial strength, between different programs. For example, the mutation operators *uoi*, *svr*, and *abs*, in respective order, are found to be of the highest partial strength, and *lcr* is of lowest partial strength in almost all programs. This suggests that partial strength relation between various mutation operators is to some extent a robust property.
- The partial strength of mutation operators measured for the BANKER program is relatively much lower than that obtained for the other programs FIND-CNT, SORT, and MInv. This is due to the fact that BANKER is a function program unit where its outputs are restricted to one of the two logic values; 0 and 1, and such programs with high domain/range ratio typically have a high information loss and are generally more difficult to test[17], [18], [19], [20].
- The results show that, among the Mothra mutation operators, the unary insertion operator *uoi* has the highest partial strength over all other operators and is essential for achieving full mutation coverage in all experimental programs. Other operators that have a relatively high partial strength are *abs*, *svr*, *acr*, *crp*, *scr*, *asr*, *ror*, *aor*, and *csr* in respective order. The results also show that the logical connector replacement operator *lcr* is of the lowest partial strength. Other mutation operators with a relatively low partial strength are *rsr*, *san*, *sar*, *der*, *glr*, *car*, *src*, *cnr*, *aar*,



and *sdl*.

The conclusion that can be reached from these results is that the average partial strength of mutation operators, over a number of programs and large number of test sets, is very high. i.e, a test set generated to detect one type of fault is expected to reveal a much broader class of faults. This provides strong evidence of the coupling-effect hypothesis in a more general sense, and thus increases our confidence in fault-based testing as viable technique for software testing.

Table III shows the average standard deviation percentage of the partial strength of mutation operators (over 31 trials) for all experimental programs. This table show that the average standard deviation of the partial strength of a mutation operator on other operators has been found to be relatively small. In fact, the standard deviation of mutation operators' partial strength is even much smaller with the exclusion of the BANKER program. An interesting observation, however, is that the partial strength of mutation operators that are of high strength relative to full mutation, like *uoi*, *svr*, *abs* and *acr* [16] for example, are the least effected by the program under test or the test cases used.

### B. Empirical subsumption between mutation operators

1) *Subsumption hierarchy*: The average subsumption hierarchies for all mutation operators used in the Mothra mutation system, for all experimental programs (over 31 trials), are shown in Figure 2. This figure is deduced from the corresponding average partial strength results shown in Table II. In this figure, an arrow from a mutation operator *i* to another mutation operator *j* on the subsumption graph, resembling a '—'

on the partial strength table, indicates that operator *i* subsumes operator *j*. A mutation operator that does not have a parent operator, is not subsumed entirely by any other operator and may therefore be essential for achieving full mutation adequacy. The subsumption relation between mutation operators, however, is almost transitive, i.e. a mutation operator at any level on the hierarchy graph subsumes all of its child operators that lie below that level on the graph. Violations of the transitive relation are indicated by dotted lines. A dotted line between two operators indicates that the particular operator at the lower end of the line is not entirely subsumed by the operator at the higher end of the line. Labelled arrows apply only to operators attached to arrow.

From analysis of the subsumption relation graphs, deduced for each of the experimental programs, and the average mutation operators' subsumption hierarchy, for all programs (over 31 test trials), shown in Figure 2, the following observations can be made:

- The subsumption relation between mutation operators varies to some extent with the test program. This is due to the influence of the test program and test data on mutation operators' strength[16]. For some mutation operators, however, the subsumption power is slightly influenced by the test program. For example, the mutation operators that have a high subsumption power, appearing at the top of the subsumption graphs, like *uoi* and *abs*, and the mutation operators that have a low subsumption power, appearing at the bottom of the subsumption graphs, like *der* and *lcr* are the least effected by the test program.
- The results show that, for all experimental programs, only a few muta-



Mean	aar	abs	acr	aor	asr	car	cnr	crp	csr	der	glr	lcr	ror	tsr	san	sar	scr	sdl	src	svr	uoi
aar	—	82	89	98	95	99	99	88	94	—	93	—	92	98	97	99	91	90	96	94	92
abs	98	—	96	—	98	99	99	95	99	—	99	—	97	—	—	98	96	97	—	98	96
acr	99	90	—	—	96	—	—	94	97	—	97	—	96	99	99	99	98	94	—	97	95
aor	94	80	86	—	92	93	94	84	91	99	88	99	90	97	97	94	89	89	94	92	89
asr	99	92	95	—	—	—	—	95	—	—	99	—	97	—	99	99	97	98	98	99	97
car	98	82	87	96	94	—	99	83	92	—	81	—	92	97	97	99	87	89	94	93	90
cnr	98	81	86	95	93	99	—	84	93	—	93	—	91	98	97	98	88	89	94	92	90
crp	99	90	96	—	98	99	—	—	97	—	98	—	98	—	—	98	99	94	—	97	97
csr	—	89	94	—	98	99	99	92	—	—	99	—	96	—	—	99	95	99	—	98	96
der	95	78	85	94	90	95	94	83	90	—	87	98	90	96	96	95	88	87	93	90	88
glr	97	86	90	—	96	97	98	90	96	—	—	—	94	—	99	96	92	93	95	95	93
lcr	94	80	86	94	89	95	94	84	88	—	85	—	90	95	95	95	88	87	93	89	88
ror	98	89	93	—	97	98	99	93	97	—	99	—	—	—	—	98	94	95	99	97	96
tsr	96	82	88	99	94	96	97	86	94	—	98	—	91	—	99	96	89	90	94	94	92
san	96	86	90	98	94	95	97	88	94	99	98	—	94	—	—	96	92	92	97	94	92
sar	99	84	90	98	95	—	99	87	93	—	94	99	93	98	97	—	92	91	96	94	92
scr	99	92	97	—	98	99	—	97	98	—	98	—	97	—	—	98	—	96	—	98	96
sdl	99	89	91	—	97	97	99	91	97	—	66	—	96	99	99	98	92	—	97	98	95
src	97	86	90	99	95	97	97	89	96	—	95	—	94	99	99	97	93	92	—	95	92
svr	—	92	95	—	99	99	—	96	—	—	—	—	97	—	—	99	96	—	—	—	98
uoi	99	91	97	—	99	—	—	98	99	—	—	—	99	—	99	99	99	97	98	99	—

TABLE II  
AVERAGE PARTIAL STRENGTH BETWEEN MUTATION OPERATORS (ALL PROGRAMS)



S.D.	aar	abs	acr	aor	asr	car	cnr	crp	csr	der	glr	lcr	ror	rsr	san	sar	scr	sdl	src	svr	uoi
aar	—	4	4	4	3	1	2	4	3	3	3	1	3	1	1	1	3	2	2	3	3
abs	1	—	1	2	1	1	2	4	1	1	1	0	2	0	0	1	2	1	0	1	2
acr	1	4	—	2	2	1	1	3	2	0	2	0	3	1	1	1	2	2	1	1	2
aor	7	8	6	—	6	8	9	7	6	2	12	3	8	3	2	7	5	6	3	6	6
asr	1	3	2	1	—	1	1	3	1	1	1	0	2	0	0	1	2	1	0	1	1
car	2	5	6	6	3	—	3	6	3	4	15	1	4	2	2	1	5	3	4	3	4
cnr	3	4	6	5	3	2	—	6	3	5	2	1	3	1	1	2	4	3	5	4	4
crp	1	3	2	2	1	1	0	—	2	0	1	0	1	0	0	1	1	1	0	1	1
csr	1	3	3	2	1	1	2	4	—	0	1	0	2	0	0	1	2	1	0	1	2
der	8	6	7	7	6	7	9	5	6	—	13	3	7	2	2	7	5	5	3	6	6
glr	5	5	4	2	4	6	6	5	4	4	—	0	2	0	0	5	4	2	2	4	4
lcr	12	9	7	8	10	10	14	8	10	4	14	—	13	15	5	11	7	8	4	8	9
ror	3	4	3	2	3	3	3	5	3	1	1	0	—	0	0	3	3	2	2	4	3
rsr	5	6	4	4	4	6	7	5	4	1	1	0	6	—	0	4	4	5	3	4	4
san	6	6	5	6	5	6	7	5	6	6	2	0	5	0	—	5	5	5	4	5	5
sar	2	4	5	5	3	1	3	7	3	3	2	2	3	1	1	—	5	2	3	3	3
scr	1	3	1	0	2	1	1	3	1	0	1	0	2	0	0	1	—	1	0	1	2
sdl	3	5	3	3	2	4	3	4	2	1	1	1	2	0	0	3	2	—	1	2	3
src	3	4	4	3	3	4	5	5	2	0	2	0	3	1	1	3	3	1	—	3	3
svr	1	4	3	1	0	1	1	3	0	0	0	0	2	0	0	1	2	0	0	—	2
uoi	0	4	1	1	0	0	0	2	1	2	0	0	1	0	1	0	2	1	2	0	—

TABLE III  
PARTIAL STRENGTH BETWEEN MUTATION OPERATORS: THE AVERAGE STANDARD DEVIATION % (OVER 31 TRIALS) FOR ALL PROGRAMS



tion operators are actually required to achieve a full mutation adequacy. The set of mutation operators sufficient for achieving full mutation adequacy are *uoi*, *abs*, *acr*, *crp*, and *scr*. Notice that the *uoi* mutation operator has been found to be essential, for achieving full mutation adequacy, for all programs.

- The average mutation operators' subsumption hierarchy, for all programs (over 31 test trials), shown in Figure 2, shows that, for all programs considered, the mutation operators *uoi*, *abs*, *acr*, *crp*, *scr*, *asr*, *ror*, *svr*, and *sar* are the only operators that may contribute to the quality of mutation assembled test data. Each of the remaining mutation operators *lcr*, *rsr*, *san*, *der*, *glr*, *car*, *src*, *cnr*, *csr*, *aar*, *aor*, and *sdl* is subsumed by one or more of the above mutation operators and is therefore very likely to be redundant. In fact, the mutation operators *ror*, *svr*, and *asr* are also redundant, since each of these operators is subsumed by one or more operators in all the subsumption relation graphs. The reason that they are shown with no parent operators in Figure 2 is that none of these operators is subsumed entirely by the same operator in all the three programs.
- Function programs are more difficult to test and often requires many more operators, to achieve a subsumption cover, than other programs with lower domain/range ratio. This suggests that mutation analysis may not be a cost-effective technique to consider when testing function program units. Nevertheless, the rank of mutation operators w.r.t. their subsumption power is reasonably consistent.

In this paper, however, a mutation oper-

ator is identified as redundant only if it is subsumed by at least one operator and this is the same operator for all the programs considered, and for all 31 trials of each program. This is a very stringent requirement, and only few of the mutation operators, *uoi*, *abs*, *acr*, *crp*, *scr*, *ror*, *svr*, *asr*, and *csr* that are identified as non-redundant in Figure 2, are likely to be sufficient for achieving a full mutation adequacy. The majority are likely to be redundant for the following reasons:

- The identification of a mutation operator being redundant is based on whether the operator is subsumed entirely by one operator only. The case where a mutation operator may be subsumed jointly by two or more other operators has not been considered. This is likely to result in a much smaller set of mutation operators that are identified as redundant with respect to the stringent criteria than the actual redundant set in practice with a typical program. Consider, for example, the *uoi* mutation operator. The average partial strength of the *uoi* operator, as shown in Table II, over all other operators, except for the *abs*, is greater than or equal to 0.96, a very high percentage. This means that the *uoi* mutation operator alone will leave a very small percentage, (0.0–0.04%), of the mutants of all mutation operators alive. Now, consider the operators, *abs*, *acr*, *crp*, and *scr* in the respective order. Each of these mutation operators, as shown in Table II, also has a very high partial strength against all other mutation operators. However, the results of the subsumption experiment show that considering the individual subsumption power of each mutation operator alone, the mutation operators *uoi*, *abs*, *acr*,

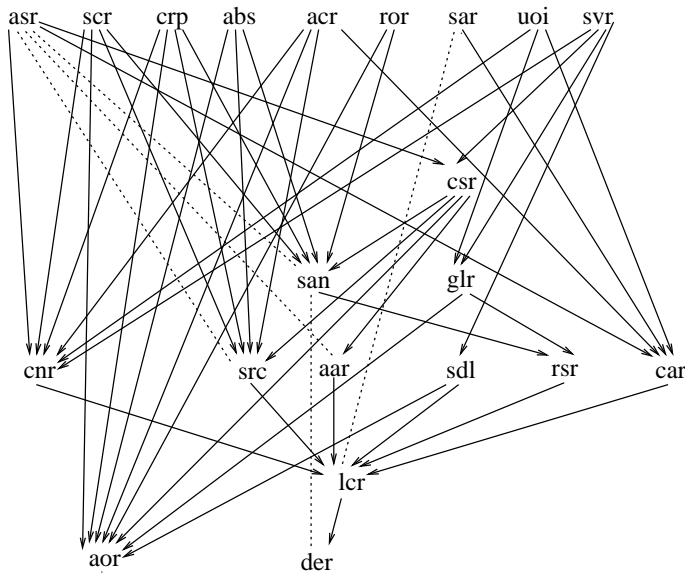


Fig. 2. Average of mutation operators' subsumption hierarchy (all programs)

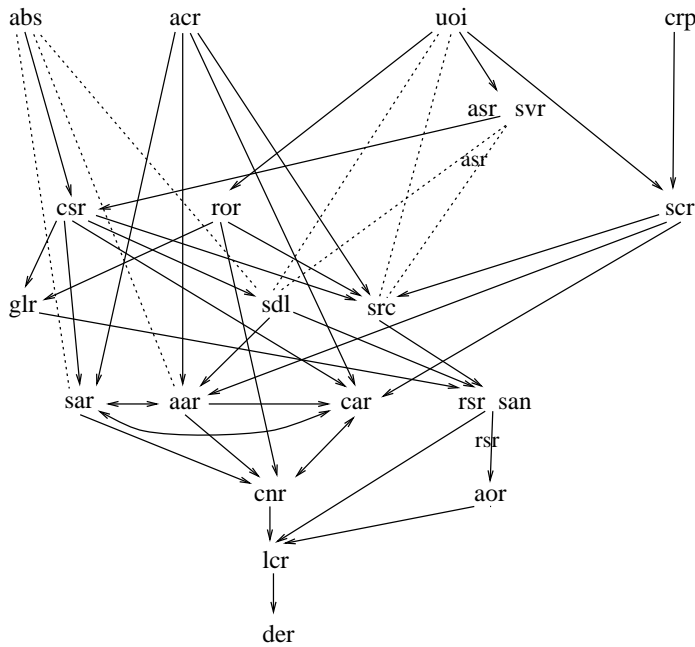
*crp*, and *scr* are sufficient to subsume all other mutation operators, and hence achieving a full mutation coverage for almost all the experimental programs. This suggests that, considering the cumulative subsumption power of a few selected mutation operators over each of the remaining operators, these few, if selected from the set *uoi*, *abs*, *acr*, *crp*, and *scr* are likely to subsume all other mutation operators and are therefore the only operators necessary to achieve a full mutation coverage.

- The identification of a mutation operator being redundant is based on whether the mutation operator is 100% subsumed. Mutants that are almost subsumed, are not considered to be redundant. Figure 3 shows the average subsumption relation between mutation

operators for the three experimental programs FINDCNT, SORT, and MInv, with a subsumption threshold of 99%. This figure shows that only 4 mutation operators, in contrast to 9 operators in Figure 2, are sufficient to achieve a subsumption cover for the 22 mutation operators used in the Mothra mutation system.

- The decision in this experiment to use non-redundant test data sets, is likely to result in test data sets of much smaller sizes than what would have been normally generated in practice. As a consequence, test sets generated in practice would normally be of a higher mutant killing rate than the test sets used in this experiment.

To summarise, the data indicates that of the 22 mutation operators used in the Mothra



Labelled arrows apply only to operators attached to arrow.

Fig. 3. Average of mutation operators' subsumption hierarchy (all programs) (99% Subsumption)

mutation system, the five mutation operators *uoi*, *abs*, *acr*, *crp*, and *scr* in that order are the most important mutation operators, and are likely to be sufficient to achieve full mutation adequacy. A plot graph showing the strength against the relative cost, and the preference of using each of the five mutation operators is shown in Figure 4.

## VI. CONCLUSIONS AND FUTURE WORK

The results reported in this paper support the coupling effect hypothesis in a far broader sense than has been previously studied [1], [2], [3]. The coupling effect hypothesis states that test data sets that detect simple types of faults are sensitive enough

to detect more complex types of faults. In all previous studies[1], [2], [3], however, complex faults have always been considered to be combinations of simple faults. In addition, the test data used were such that they were able to kill each component of the complex fault. The definition of complex faults to mean multiple mutations is a rather restrictive definition. The main concern in these previous studies was to investigate masking between simple software faults and not coupling in general. i.e., to examine whether simple faults considered by a mutation system mask each other, and although the results reported from these investigations have convincingly demonstrated that mask-



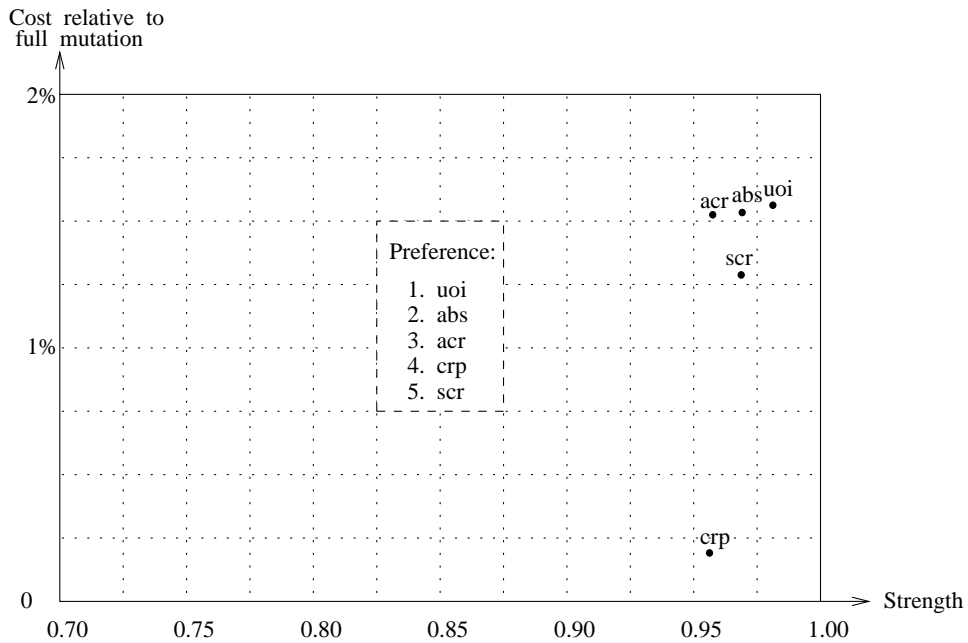


Fig. 4. The subset of mutation operators sufficient for full mutation coverage

ing is rare, it is still by no means clear that this factor alone explains the effectiveness of fault-based testing. In contrast, this paper considers a far more general interpretation for complex faults to mean other faults of different types.

The results of the experiments reported in this paper show that different types of faults are coupled in the sense that a test set generated to detect one type of fault is very effective at detecting faults of different type. The experiments have been performed on 21 mutation operators used the Mothra mutation system[8]. In these experiments, a sample of 31 non-redundant mutation adequate test set has been generated for each mutation operator, and mutants generated by each of the other 20 operators were executed

on each of these test sets. The results of this experiment show that the average strength of a test set that is adequate for one mutation operator  $i$ , on other operators  $j$ , is very high. In fact, test sets that are mutation adequate for some mutation operators like  $uoi$ ,  $abs$ ,  $svr$ , were found to be almost adequate with respect to all other mutation operators. The results also show that the strength of an operator against other operators is very little influenced by the test cases used. Clearly, the results of these experiments support a very general form of the coupling effect hypothesis and suggests that a test data set that can reveal one type of faults in a given program is actually capable of revealing a much broader class of different types of faults in the same program. This goes a long



way towards explaining the effectiveness of mutation testing.

An important result that can be reported in this paper is that focus to detect simple faults, faults that can be fixed by a single change in an expression or program statement, is an effective approach for testing software. In mutation testing for example, a test case that can reveal a simple fault that is introduced by simple syntactic change to an expression or a statement in the test program is likely to be of high quality, and is expected to reveal a high percentage of other faults that may occur in the same statement or execution path of that fault. The domain of test cases that would cause a single simple fault in the test program to manifest itself at the program output is often small, and therefore, the requirement to detect a single simple fault in a program forces the tester to generate a sensitive test case that would be difficult to generate otherwise. The results obtained from the experiments reported in this paper provides an empirical evidence that supports this, and show that test sets that are generated to detect a simple type of fault is in practice capable of detecting other types of faults.

The results of the subsumption experiment support the results obtained from earlier studies[21], [11] to suggest a considerable amount of redundancy in the mutation operators used in the Mothra tool. Specifically, the results indicate that most of the mutation operators used in the Mothra mutation system do not contribute to the quality of mutation assembled test data. Only 5 mutation operators are likely to be sufficient to subsume the entire set of the Mothra mutation operators. The 5 mutation operators are *uoi*, which inserts unary operators in front of expressions, *abs*, which forces each arithmetic expression to take on

the value 0, a positive value and a negative value, *acr*, which replaces constants by array references, *crp*, which emulates domain perturbation testing and *scr*, which replaces constants by scalar variables. From the results of the author's work on establishing the cost and strength of all mutation operators used in the Mothra mutation tool[16], these 5 operators when applied incrementally account to only 6.2% of the total cost required in previous implementation of mutation testing. This result is a major step forward towards making mutation testing a viable technique.

The results of the experiments performed to establish the partial strength and subsumption power of various mutation operators also show that among all the mutation operators used in the Mothra mutation tool[8], The *uoi* mutation operator is likely to be the most useful operator to use in practice not only because of its high subsumption power over all other operators but also it has been found to be essential for achieving full mutation adequacy in all of the experimental programs considered. Another important observation that can be made from the results reported in this paper is that programs types that have small output domain like function programs have typically a high information loss and therefore mutation analysis may not be a cost-effective technique to consider when testing programs of this type.

The results reported in this paper are very encouraging to software testers and researchers in the sense that by focusing on a restricted class of faults, one can have a high expectation to detect a much broader class of other faults as well. This increases confidence in fault-based techniques as viable approach for software testing, not only because of the types of faults it is guaranteed



to eliminate, but probably more importantly for the many other types of faults it is likely to detect.

## REFERENCES

- [1] R. Lipton and F. Sayward, "The status of research on program mutation," in *Digest for the workshop on software testing and test documentation*, December 1978, pp. 355–373.
- [2] L. J. Morell, "A theory of fault-based testing," Ph.D. dissertation, Department of Computer Science, University Maryland, College Park, 1984, technical Report TR-1395.
- [3] A. Offutt, "Investigations of the software testing coupling effect," *ACM Transactions on Software Engineering and Methodology*, vol. 1, pp. 3–18, Jan 1992.
- [4] R. DeMillo, R. Lipton, and F. Sayward, "Hints on test data selection: help for the practising programmer," *IEEE Computer*, vol. 11, no. 4, pp. 34–41, 1978.
- [5] A. Acree, T. Budd, R. DeMillo, R. Lipton, and F. Sayward, "Mutation analysis," School of Information and Computer Science, Georgia Institute of Technology, Technical Report GIT-ICS-79/08, 1979.
- [6] B. Choi and A. Mathur, "High performance mutation testing," *Journal of Systems and Software*, vol. 20, pp. 135–152, 1993.
- [7] S. Weiss and V. Fleyshgakker, "Improved serial algorithms for mutation analysis," in *Proceedings of the 1993 International Symposium on Software Testing and Analysis ISSTA 1993*, New York, NY, USA, 1993, pp. 149–158.
- [8] R. DeMillo and E. Spafford, "The Mothra software testing environment," in *Proceedings of the 11th NASA Software Engineering Laboratory workshop*. Goddard Space Center, December 1986.
- [9] K. King and A. Offutt, "A fortran language system for mutation based software testing," *Software – Practice And Experience*, vol. 21, no. 7, pp. 685–718, July 1991.
- [10] G. Borse, *Fortran 77 and numerical methods for engineers*. PWS-KENT, 1991.
- [11] A. Offutt, G. Rothermel, and C. Zapf, "An experimental evaluation of selective mutation," in *Proceedings of the 15th International Conference on Software Engineering*, Baltimore, MO, May 1993, pp. 100–107.
- [12] R. A. DeMillo and J. Offutt, "Constraint-based automatic test generation," *IEEE Transactions on Software Engineering*, vol. 17, no. 9, pp. 901–910, September 1991.
- [13] A. Mathur and W. Wong, "An empirical comparison of data flow and mutation-based test adequacy criteria," *Software Testing, Verification and Reliability*, vol. 4, no. 1, pp. 9–31, Mar 1994.
- [14] A. Offutt and S. Lee, "An empirical evaluation of weak mutation," *IEEE Transactions on Software Engineering*, vol. 20, no. 5, pp. 337–344, May 1994.
- [15] A. Offutt, J. Pan, K. Tewary, and T. Zhang, "An experimental evaluation of data flow and mutation testing," *Software – Practice And Experience*, vol. 26, no. 2, pp. 165–176, February 1996.
- [16] E. Mresa and L. Bottaci, "Efficiency of mutation operators and selective mutation strategies: An empirical study," *Software Testing, Verification and Reliability*, vol. 9, no. 4, pp. 205–232, December 1999.
- [17] J. Voas, L. Morell, and K. Miller, "Predicting where faults can hide from testing," *IEEE Software*, vol. 8, no. 1, pp. 41–84, March 1991.
- [18] J. Voas, "PIE: a dynamic failure-based technique," *IEEE Transactions on Software Engineering*, vol. 18, no. 8, pp. 717–727, August 1992.
- [19] J. Voas and K. Miller, "The revealing power of a test case," *Software Testing, Verification and Reliability*, vol. 2, pp. 25–42, Mar 1992.
- [20] J. Voas and K. Miller, "Semantic metrics for software testability," *Journal of Systems and Software*, vol. 20, pp. 217–225, 1993.
- [21] A. Mathur, "Performance, effectiveness, and reliability issues in software testing," in *Proceedings of the 15th annual International Computer Software and Applications Conference COMPSAC*, Tokyo, Japan, September 1991, pp. 604–605.



المؤتمر الدولي العربي الليبي الخامس للهندسة الكهربائية والإلكترونية 2010/10/26-23 طرابلس ليبيا



## ***Chapter IV***

# **Electronic Devices and Systems**



المؤتمر العربي الليبي الدولي الخامس للهندسة الكهربائية والإلكترونية 23-26/10/2010 طرابلس ليبيا



## ANALYSIS, OPTIMIZATION AND DESIGN OF NEGATIVE DIFFERENTIAL RESISTANCE GALLIUM ARSENIDE FET VOLTAGE-CONTROLLED OSCILLATORS

Vladimir Vasily Ulansky<sup>1</sup>, Hassan Mohamed Elsherif<sup>2</sup>,  
Mustafa Fituri Abusaid<sup>3</sup>, and Sali Faisal Ben Suleiman<sup>4</sup>

<sup>1,2,3,4</sup>Electrical and Electronic Engineering Department, Faculty of Engineering,  
Al Fateh University, Tripoli, Libya, e-mail: vulanskyi@yahoo.com

**Abstract-** This paper presents a comparison of five proposed negative differential resistance (NDR) GaAs voltage-controlled oscillators (VCOs) for UHF applications. The VCO circuits are based on the classical BJT current mirrors (CMs). The mathematical models of the proposed VCOs are developed and the start-up condition is determined. The VCOs comparison is conducted using a figure of merit, which is dependent on the phase noise, total harmonic distortion and power consumption. The VCOs characteristics were simulated by ADS 2008 program. The designed and implemented 275.8-MHz oscillator draws 4.2 mA from a 3.3 V power supply and generates low-noise low-distortion signal.

### 1. Introduction

The VCOs are critical building blocks in all modern communication transceivers and synthesized radio frequency signal generators. A considerable amount of publications has been devoted to a GaAs FET microwave oscillators [1] – [6]. Most of these oscillators have the Colpitts or the Clapp topology.

These oscillators are related to the class of negative impedance oscillators having negative real part in the input impedance [6], [7], [8]. Another class of microwave oscillators is based on the tunnel and Gunn diodes [9], [10], which have an NDR region in the  $N$ -type  $I$ - $V$  characteristics. Locating

the operating point in the NDR region results in creating a negative resistance induced into the tank circuit for compensating its losses. The  $N$ -type  $I$ - $V$  characteristics can be obtained artificially by using an electronic circuit, which generally consists of a FET with negative gate source voltage and a CM [11]. This paper analyses five GaAs FET VCOs with different BJT CMs. The VCOs performance characteristics are simulated by ADS 2008 program. By using the proposed figure of merit (FOM) the best configuration is selected. The theoretical







$$V_{CC1} = V_{IN} \frac{R_1 + R_2}{R_2} \quad (1)$$

transistor  $Q_1$  is cut off. This region is indicated by curve OA in Fig. 2. At about voltage  $V_{CC1}$ , transistor  $Q_1$  turns ON and enters ohmic region because  $V_{DS}$  is very small, where  $V_{IN}$  is the CM input voltage which turns it ON and  $V_{DS}$  is the voltage between drain and source of  $Q_1$ .

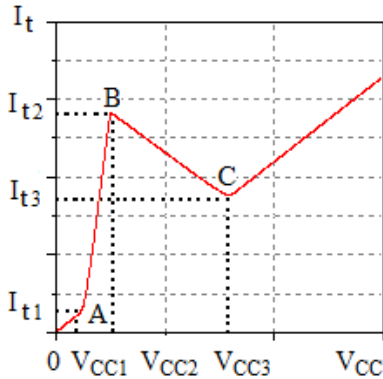


Fig. 2. Typical  $I$ - $V$  characteristics of the VCO circuit

Since  $Q_1$  operates in the ohmic region then

$$V_{DS} < V_{GS} - V_P \quad (2)$$

where  $V_{GS}$  is the gate-source voltage of  $Q_1$  and  $V_P$  is the pinch off voltage of  $Q_1$ .

Applying the Kirchoff voltage law to the circuit of Fig.1 gives

$$V_{CC} = V_{IN} + V_{DS} + I_1 R_1 \quad (3)$$

$$V_{IN} + V_{DS} - I_2 R_2 = 0 \quad (4)$$

$$I_1 = I_2 + I_{IN} \quad (5)$$

where  $I_{IN}$  is the CM input current.

From (3), (4) and (5) we find that

$$V_{DS} = V_{CC} \frac{R_2}{R_1 + R_2} - I_{IN} (R_1 \parallel R_2) - V_{IN} \quad (6)$$

Combining (6) with equation

$$V_{CC} = V_{IN} + V_{DS} - V_{GS}$$

we find that

$$V_{GS} = -\frac{V_{CC} R_1}{R_1 + R_2} - I_{IN} (R_1 \parallel R_2) \quad (7)$$

Applying the KCL to the node  $a$  in the circuit of Fig.1, the terminal current  $I_t$  can be found as

$$I_t = \frac{I_{IN} R_2}{R_1 + R_2} + I_{OUT} + \frac{V_{CC}}{R_1 + R_2} \quad (8)$$

where  $I_{OUT}$  is the CM output current.

The current  $I_{OUT}$  is a function of the input current  $I_{IN}$ .

Substituting  $V_{DS}$  and  $V_{GS}$  from (6) and (7) into (2) we obtain that in the ohmic region of  $Q_1$

$$V_{CC} < V_{IN} - V_P$$

As  $V_{CC}$  is increased further, transistor  $Q_1$  enters the saturation region where

$$V_{DS} \geq V_{GS} - V_P \quad (9)$$

Substituting  $V_{DS}$  and  $V_{GS}$  from (6) and (7) into (9) results in the following inequality

$$V_{CC} \geq V_{IN} - V_P$$



The threshold voltage  $V_{CC2}$  is in the vicinity of the boundary between the ohmic and saturation regions of  $Q_1$ , that is

$$V_{CC2} \approx V_{IN} - V_P \quad (10)$$

Thus, the  $I$ - $V$  characteristic has a positive slope between voltages  $V_{CC1}$  and  $V_{CC2}$ . From equations (1) and (10) follows that for reducing the interval of power supply voltages, where the  $I$ - $V$  characteristic has positive slope, the CM input voltage,  $V_{IN}$ , must be as small as possible. As  $V_{CC}$  is increased further, the current  $I_{IN}$ , which is the drain current of  $Q_1$ , decreases due to increasing the negative voltage  $V_{GS}$ . And this drop in current  $I_{IN}$  exceeds the rise in current  $I_2$ . Hence, the terminal current  $I_t$  begins to decrease as the voltage  $V_{CC}$  is raised.

This is negative resistance region shown in Fig.2 as line BC.

As  $V_{CC}$  is increased further, eventually the decrease in currents  $I_{IN}$  and  $I_{OUT}$  becomes equal to the increase of current  $I_2$ , that is

$$\frac{dI_t}{dV_{CC}} = \frac{R_2}{R_1 + R_2} \times \frac{dI_{IN}}{dV_{CC}} + \frac{dI_{OUT}}{dV_{CC}} + \frac{dI_2}{dV_{CC}} = 0$$

Since  $dI_2/dV_{cc} = 1/(R_1 + R_2)$ , then

$$\frac{dI_2}{dV_{CC}} = \frac{1}{R_1 + R_2} = -\frac{R_2}{R_1 + R_2} \times \frac{dI_{IN}}{dV_{CC}} - \frac{dI_{OUT}}{dV_{CC}}$$

Assuming for simplicity that  $I_{OUT} = I_{IN}$  in last equation gives

$$\frac{dI_{IN}}{dV_{CC}} = -\frac{1}{R_1}$$

Thus, the threshold voltage  $V_{CC3}$  is very much dependent on the value of resistor  $R_1$ . The smaller values of  $R_1$  correspond to the greater values of  $V_{CC3}$ . This voltage,  $V_{CC3}$ , is shown as the valley point C in Fig. 2.

Any further increase of  $V_{CC}$  results in increasing the terminal current  $I_t$ . For  $V_{CC} > V_{CC3}$ , the current  $I_t$  is due to the current  $I_2$  and the decreasing currents  $I_{IN}$  and  $I_{OUT}$ . The currents  $I_{IN}$  and  $I_{OUT}$  become zero when the gate-source voltage,  $|V_{GS}|$ , of transistor  $Q_1$  exceeds the corresponding pinch-off voltage,  $|V_P|$ , that is

$$|V_{GS}| = V_{CC}R_1/(R_1 + R_2) \geq |V_P|$$

and finally

$$V_{CC} \geq |V_P|(R_1 + R_2)/R_1 \quad (11)$$

From (11) follows that

$$V_{CC3} < |V_P|(R_1 + R_2)/R_1 \quad (12)$$

Supposing  $R_1 \ll R_2$ , we obtain from (12) that

$$V_{CC3} < |V_P|(R_2/R_1)$$

The last inequality shows that the valley voltage,  $V_{CC3}$ , is also dependent on the pinch-off voltage  $V_P$  and the resistance  $R_2$ .

#### 4. VCO Circuits

The VCO of Fig. 1 can be implemented with different CMs. As is well known [12], the CMs have different input voltage ( $V_{IN}$ ), output resistance ( $R_O$ ), dependence of  $I_{OUT}$  versus  $I_{IN}$ , and bandwidth. These



parameters may affect the VCO operation. That is why the performance characteristics of the VCOs with different CMs will be compared by using the proposed FOM. Figure 3 shows the VCOs with the most frequently used CMs. These CMs were chosen regarding circuit simplicity, accuracy, and proximity their characteristics to the ideal values. The simplest configuration is shown in Fig. 3(a). It uses a simple current mirror (SCM) [12]. For this VCO configuration equations (8) and (10) are represented as

$$I_t = I_{IN} \frac{R_2}{R_1 + R_2} + \frac{I_{IN}}{1 + \frac{2}{\beta_F}} + \frac{V_{CC}}{R_1 + R_2} \quad (13)$$

$$V_{CC2} = V_{EB} - V_P \quad (14)$$

where  $\beta_F$  is a  $p-n-p$  transistor current gain. To reduce the dependence of the terminal current  $I_t$  versus  $\beta_F$ , the SCM with beta helper (SCMB) [12] is used in the VCO circuit of Fig. 3(b). For this VCO circuit it can easily be proved that

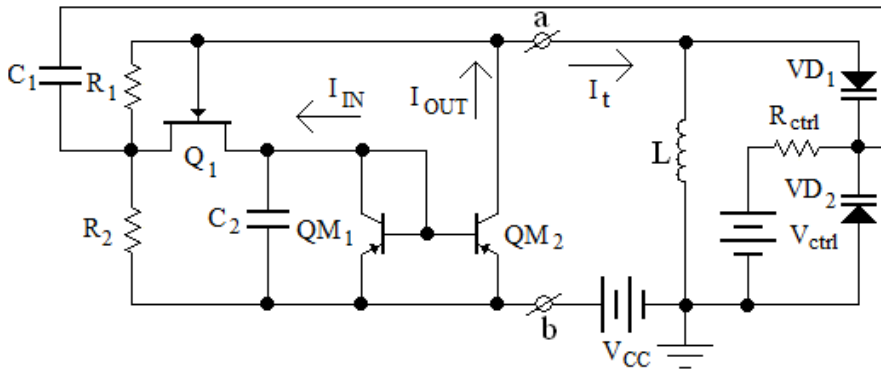
$$I_t = I_{IN} \frac{R_2}{R_1 + R_2} + \frac{I_{IN}}{1 + \frac{2}{\beta_F(\beta_F + 1)}} + \frac{V_{CC}}{R_1 + R_2} \quad (15)$$

$$V_{CC2} = 2V_{EB} - V_P \quad (16)$$

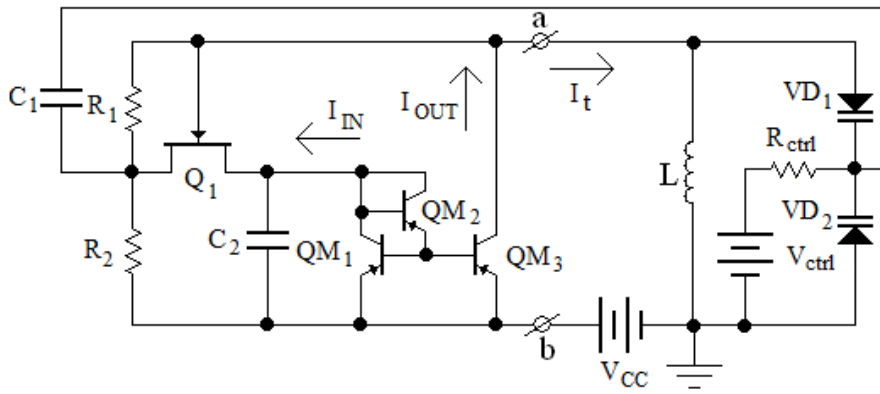
Comparing (16) with (14), we find that the threshold voltage  $V_{CC2}$  is increased by one diode drop in the circuit of Fig. 3(b).

The VCO circuit with the cascode current mirror (CCM) is shown in Fig. 3(c). As is well known [12], the CCM achieves much higher output resistance compared to the SCM and SCMB. It can easily be shown that equation (8) is now represented as

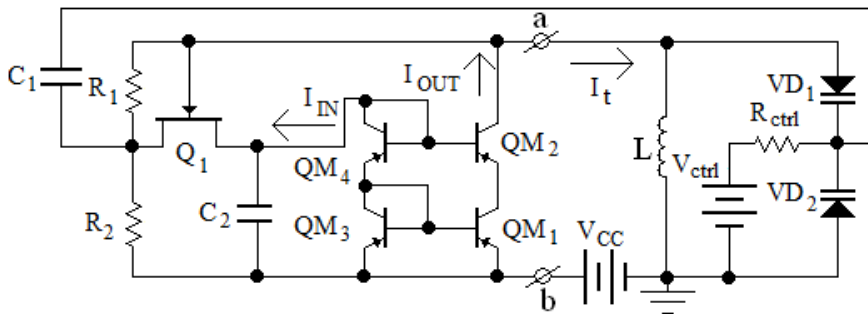
$$I_t = I_{IN} \frac{R_2}{R_1 + R_2} + I_{IN} \left( 1 - \frac{4\beta_F + 2}{\beta_F^2 + 4\beta_F + 2} \right) + \frac{V_{CC}}{R_1 + R_2} \quad (17)$$



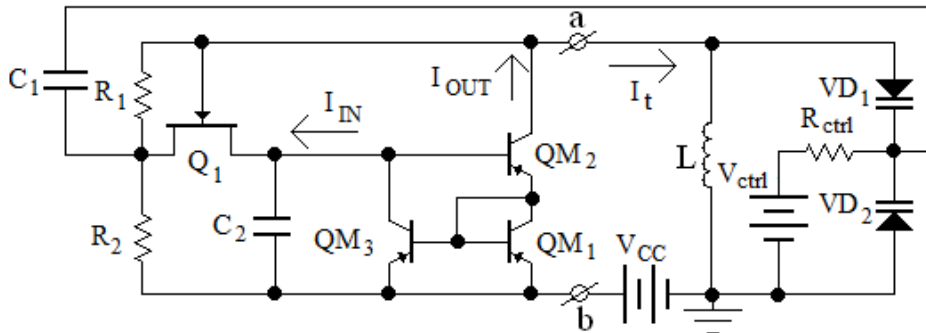
(a)



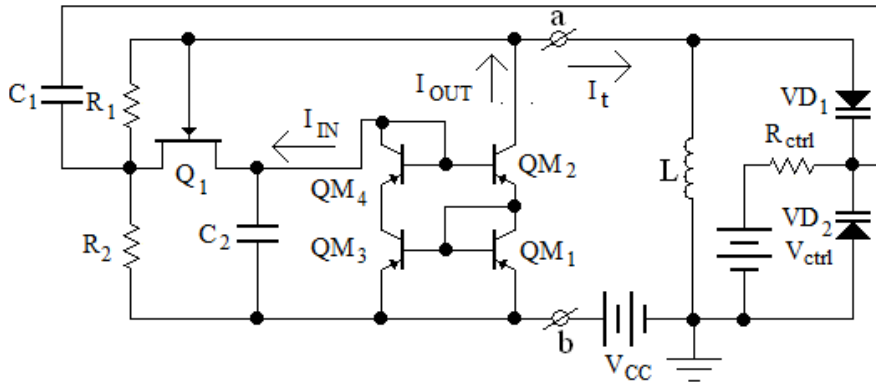
(b)



(c)



(d)



(e)

Fig. 3. VCO circuits: (a) with SCM, (b) with SCMB, (c) with CCM, (d) with WCM, (e) with IWCM

Since  $V_{IN} = 2V_{EB}$ , the threshold voltage  $V_{CC2}$  is calculated by equation (16).

The basic Wilson current mirror (WCM) has in contrast to the CCM, much less dependence of  $I_{OUT}$  from  $\beta_F$  and

approximately the same output resistance [12]. The VCO with incorporated WCM is shown in Fig. 3(d). The terminal current,  $I_t$ , is given by

$$I_t = I_{IN} \frac{R_2}{R_1 + R_2} + I_{IN} \left( 1 - \frac{2}{\beta_F^2 + 2\beta_F + 2} \right) \left( 1 + \frac{V_{CEM1} - V_{CEM3}}{V_A} \right) + \frac{V_{CC}}{R_1 + R_2} \quad (18)$$

where  $V_{CEM1}$  and  $V_{CEM3}$  are the collector-emitter voltages of transistors  $QM_1$  and  $QM_3$ ,  $V_A$  is the Early voltage.

As in the case of the VCO with CCM, the threshold voltage  $V_{CC2}$  is given by (16).

In Fig. 3(e) is shown the VCO with improved Wilson current mirror (IWCM). Introduction of a new diode-connected transistor  $QM_4$  equalizes the collector-emitter voltages  $V_{CEM1}$  and  $V_{CEM3}$  [12], so that equation (18) is now represented as

$$I_t = I_{IN} \frac{R_2}{R_1 + R_2} + I_{IN} \left( 1 - \frac{2}{\beta_F^2 + 2\beta_F + 2} \right) + \frac{V_{CC}}{R_1 + R_2} \quad (19)$$

It should be pointed out, that if  $\beta_F \rightarrow \infty$  then the terminal current, as it follows from (14), (15), (17), and (19), reduces to

$$I_t = I_{IN} \left( 1 + \frac{R_2}{R_1 + R_2} \right) + \frac{V_{CC}}{R_1 + R_2} \quad (20)$$

Since current  $I_{IN}$  is the drain current of transistor  $Q_1$ ,  $I_{IN} = I_D$ , then (20) can be rewritten as

$$I_t = I_D \left( 1 + \frac{R_2}{R_1 + R_2} \right) + \frac{V_{CC}}{R_1 + R_2} \quad (21)$$

From (21) follows that for large values of  $\beta_F$  ( $\beta_F \gg 1$ ) the terminal current,  $I_t$ , depends only on the resistor values, power



supply voltage and drain current of GaAs transistor  $Q_1$ .

For case when  $R_2 \gg R_1$  equation (21) reduces to

$$I_t \approx 2I_D + \frac{V_{CC}}{R_1 + R_2} \quad (22)$$

As seen from (21) and (22), the drain current,  $I_D$ , must be modeled in terms of circuit parameters for calculating the terminal current,  $I_t$ .

## 5. DC Drain Current Modeling

### 5.1. Analytical Modeling

For the purpose of modeling the GaAs FETs, many models are available. The following three models are the most

$$I_D = \beta \left\{ \left[ \frac{V_{CC}R_1}{R_1 + R_2} + I_D(R_1 \parallel R_2) \right] + V_P \right\}^2 \times \left\{ 1 + \lambda \left[ \frac{V_{CC}R_2}{R_1 + R_2} - V_{IN} - I_D(R_1 \parallel R_2) \right] \right\} \times \tanh \left\{ \alpha \left[ \frac{V_{CC}R_2}{R_1 + R_2} - V_{IN} - I_D(R_1 \parallel R_2) \right] \right\} \quad (24)$$

As in the case of the Curtice approximation, drain current of  $Q_1$  is a nonlinear function of the Curtice model parameters and the VCO circuit parameters. The voltage  $V_{IN}$ , included to equation (24), is determined as  $V_{IN} = V_{EB}$  for the VCO circuit of Fig. 3(a) and as  $V_{IN} = 2V_{EB}$  for the rest of the VCO circuits. The current  $I_D$  as a function of  $V_{CC}$  can be found numerically by solving the nonlinear equation (24). Then, by substituting  $I_D$  into equation (21), the terminal current  $I_t$  can be calculated.

The Statz static model is a modification of the Curtice model by means of replacing the hyperbolic tangent function with a polynomial approximation. In the saturation

popular with computer aided design tools: the Curtice, the Statz, and the TOM (TriQuint's Own Model) [13].

The Curtice model defines the drain current in the saturation region with respect to the drain-source and gate-source voltages as follows [14]:

$$I_D = \beta(V_{GS} - V_P)^2(1 + \lambda V_{DS}) \tanh(\alpha V_{DS}) \quad (23)$$

where  $\beta$ ,  $\lambda$ , and  $\alpha$  are the model parameters;  $\beta$  is the transconductance,  $\alpha$  is the tanh constant, and  $\lambda$  is the channel length modulation coefficient.

Substituting  $V_{DS}$  and  $V_{GS}$  from (6) and (7) into (23) gives

region the Statz drain current equation is given by [15]

$$I_D = \frac{\beta(V_{GS} - V_P)^2(1 + \lambda V_{DS})}{1 + B(V_{GS} - V_P)} \quad (25)$$

$$I_D = \frac{\beta \left[ \frac{V_{CC}R_1}{R_1 + R_2} + I_D(R_1 \parallel R_2) + V_P \right]^2}{1 - B \left[ \frac{V_{CC}R_1}{R_1 + R_2} + I_D(R_1 \parallel R_2) + V_P \right]} \times \left\{ 1 + \lambda \left[ \frac{V_{CC}R_2}{R_1 + R_2} - I_D(R_1 \parallel R_2) - V_{IN} \right] \right\} \quad (26)$$



As in the case of the Curtice approximation, the drain current,  $I_D$ , is found numerically by solving equation (26) and, then, the terminal current  $I_t$  is calculated by using equation (21).

where  $B$  is the doping profile parameter. Substituting  $V_{DS}$  and  $V_{GS}$  from (6) and (7) into (25) finally results in the following equation:

$$I_D = \frac{I_{DO}}{1 + \delta I_{DO} V_{DS}} \quad (27)$$

where

$$I_{DO} = \beta(V_{GS} - V_P)^2 \quad (28)$$

The parameter  $\delta$  in equation (27) is used for modeling the decreased drain conductance at low gate-source biases.

Substituting  $V_{DS}$  and  $V_{GS}$  from (6) and (7) into (27) and (28) results in the following equations:

$$I_D = \frac{I_{DO}}{1 + \delta I_{DO} \left[ \frac{V_{CC} R_2}{R_1 + R_2} - I_D (R_1 \parallel R_2) - V_{IN} \right]} \quad (29)$$

$$I_{DO} = \beta \left[ -\frac{V_{CC} R_1}{R_1 + R_2} - I_{IN} (R_1 \parallel R_2) - V_P \right]^2$$

Again, substituting  $I_D$  from (29) into (21) the terminal current,  $I_t$ , can be calculated.

### 5.2. Simulation Results

In order to evaluate the validity of the VCO  $I-V$  characteristics analytical modeling, some simulations were made. All simulations were carried out using Agilent's ATF-33143 PHEMT and

The TOM is popular because it fits the  $dc$  behavior of a GaAs FET accurately. The exponent in the expression  $(V_{GS} - V_P)^2$  is changed from a constant 2 to the variable  $Q$ , so that the drain current is represented as [16]

BFT92W  $p-n-p$  BJTs for the IWCM. The resistor values of  $R_1$  and  $R_2$  were selected to be 0.25k $\Omega$  and 2k $\Omega$  respectively.

The simulated by MULTISIM the  $I-V$  characteristics of the VCO are shown in Fig. 4 by a thin line. The thick line in the NDR region corresponds to the theoretical approximations made by using the Curtice and Statz models, and the TOM. As seen from Fig. 4, a very good agreement exists between the simulated and the theoretical results in the NDR region of the VCO  $I-V$  characteristics.

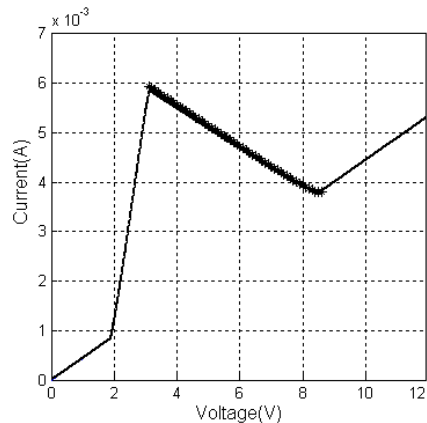


Fig. 4. The VCO  $I-V$  characteristics: thin line corresponds to the simulated characteristics; thick line corresponds to the theoretical characteristics

Therefore, any of the three obtained equations (24), (26) and (29) can be used for modeling the drain current of transistor  $Q_1$  in the NDR region of the VCO  $I-V$  characteristics.

## 6. Start-up Condition

Since the VCO operating point is selected in the NDR region, the VCO electronic circuit can be represented as a small-signal negative resistance ( $R_{neg} < 0$ ), which is connected in parallel with the tank circuit as shown in Fig. 5, where  $r_L$  and  $r_{var}$  are, respectively, the coil and the varactor diode  $ac$  resistance,  $i_1$  and  $i_2$  are, respectively, the current in the inductive and capacitive branches.

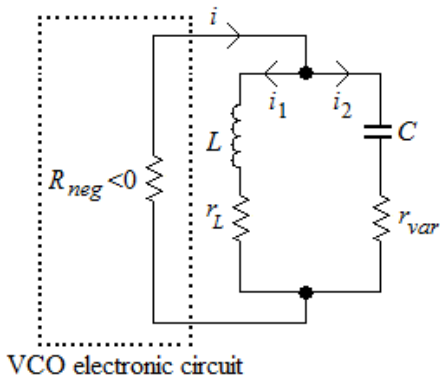


Fig. 5. The VCO tank circuit with a small-signal negative resistance created by the electronic circuit

The capacitance  $C$  is represented as

$$C = \frac{C_{V1}C_{V2}}{C_{V1} + C_{V2}} + C_{par} \quad (30)$$

where  $C_{V1}$  and  $C_{V2}$  are the capacitances of varactors  $VD_1$  and  $VD_2$ , and  $C_{par}$  is the parasitic capacitance of the VCO electronic circuit including the inter-connect capacitance.

The negative differential resistance is defined as

$$R_{neg} = \left( \frac{dI_t}{dV_{CC}} \right)^{-1} \quad (31)$$

where the terminal current,  $I_t$ , is determined by equation (21).

For determining the start-up condition, we write the following Kirchoff's equations for the circuit of Fig. 5:

$$u_R + \frac{1}{C} \int i_2 dt + i_2 r_{var} = 0 \quad (32)$$

$$L \frac{di_1}{dt} + r_L i_1 = \frac{1}{C} \int i_2 dt + r_{var} i_2 \quad (33)$$

$$i_1 + i_2 = i \quad (34)$$

where  $u_R$  is the voltage across  $R_{neg}$ .

Combining the set of equations (32)-(34) results in the following differential equation:

$$\frac{d^2 u_L}{dt^2} + \frac{L + Cr_{var}r_L - C|R_{neg}|(r_L + r_{var})}{LC(r_{var} - |R_{neg}|)} \times$$

$$\frac{du_L}{dt} + \frac{r_L - |R_{neg}|}{LC(r_{var} - |R_{neg}|)} \times u_L = 0 \quad (35)$$

where  $u_L$  is the voltage across inductor  $L$ .

Eq. (35) can finally be represented as

$$\frac{d^2 u_L}{dt^2} + a_1 \frac{du_L}{dt} + a_2 u_L = 0 \quad (36)$$

where

$$a_1 = \frac{L + Cr_{var}r_L - C|R_{neg}|(r_L + r_{var})}{LC(r_{var} - |R_{neg}|)} \quad (37)$$





$$a_2 = \frac{r_L - |R_{neg}|}{LC(r_{var} - |R_{neg}|)}$$

Equation (36) describes the voltage  $u_L(t)$  across the coil. As is well known [17], the amplitude of voltage  $u_L(t)$  will rise if coefficient  $a_1 < 0$ . From (37) follows that the denominator of coefficient  $a_1$  is negative because in most of practical cases  $|R_{neg}| \gg r_{var}$ . Therefore, to make coefficient  $a_1$  negative, the numerator in equation (37) must be positive, that is

$$L + Cr_{var}r_L - C|R_{neg}|(r_L + r_{var}) > 0 \quad (38)$$

After some manipulations inequality (38) is represented as

$$|R_{neg}| < \frac{L}{C(r_{var} + r_L)} + r_{var} \| r_L \quad (39)$$

If varactors  $VD_1$  and  $VD_2$  are matched then  $C_{V1} = C_{V2} = C_V$  and equation (30) reduces to

$$C = 0.5C_V + C_{par} \quad (40)$$

In this case, the total losses in two varactors are given by

$$r_{var} = 2r_V \quad (41)$$

Substituting (40) and (41) into (39) results in the following start-up condition:

$$|R_{neg}| < \frac{L}{(0.5C_V + C_{par})(2r_V + r_L)} + (2r_V \| r_L)$$

The values of resistors  $R_1$  and  $R_2$  are selected to satisfy the derived start-up condition.

### 7. Figure of Merit

A figure of merit defines a quantity used for comparing the performance of different VCOs. The FOMs are most helpful for the VCO designers since they combine the most important performance characteristics in one integrated function. The well-known FOMs include such VCO characteristics as phase noise and power consumption [18], [19]. Unfortunately, these FOMs are not sensitive to the total harmonic distortion (THD) of the generated sinusoidal signal, which is a measure of the VCO energy at harmonics of the oscillation frequency. The FOM used in this paper in addition includes the THD, because experimentally it was found that an improvement in phase noise can be reached at the expense of increasing the power of higher harmonics.

The FOM is defined as

$$FOM = -10 \log L_N(\Delta f) + 20 \log \left( \frac{f_o}{\Delta f} \right) -$$

$$10 \log \left( \frac{P_{dis}}{1mW} \right) - 20 \log THD$$

where  $L_N(\Delta f)$  is the single-sideband phase noise at an offset frequency  $\Delta f$  from the central frequency  $f_o$  with a measurement bandwidth of 1 Hz,  $P_{dis}$  is the VCO power dissipation in mWs,  $THD$  is the total harmonic distortion of the VCO output signal. Greater values of the FOM represent better VCO performance. The FOM is a modification of the FOM proposed in [20].



### 8. Simulation Results

In order to select the best VCO topology out of the five shown in Fig. 3, each VCO topology was simulated by ADS 2008 program. A pseudomorphic hetero-junction FET NE3210S01 with  $L=0.2\mu\text{m}$  and  $W=160\mu\text{m}$  was used in all VCOs. The selected FET has super low noise figure of 0.35dB at  $f=12\text{GHz}$ . The current mirrors were built using a  $p-n-p$  BJT BFT92W. The SMV1104-34 hyperabrupt junction varactors were used in the VCO tank circuits. The varactor capacitance is about 6.5pF at 1V and 2.1pF at 6V reverse diode voltage. A 10-nH ACT AIC1210 series SMT inductor was also used in all VCO tank circuits.

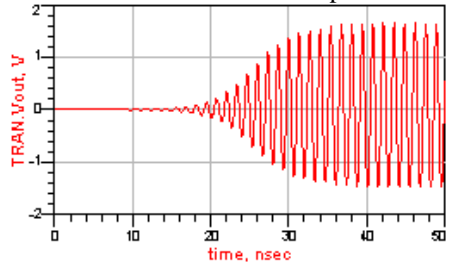
The values of resistors  $R_1$  and  $R_2$  were chosen to be 0.15kΩ and 2kΩ respectively. The  $dc$  operating point was selected in the NDR region with  $V_{CC}=3\text{V}$  for all VCO circuits. The values of capacitors  $C_1$  and  $C_2$  were adjusted for each VCO configuration in such a way that they provided the following condition:

$$\max_{C_1, C_2} \{ -(L_N)_{dB} - (THD)_{dB} \}$$

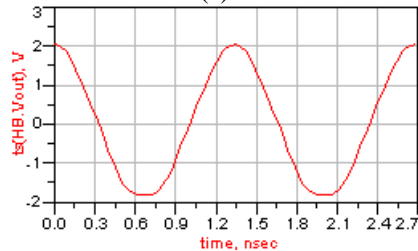
The simulation results are summarized in Table 1. Each VCO circuit was simulated for two different values of the varactor control voltage,  $V_d=2\text{V}$  and  $V_d=12\text{V}$ . The phase noise was simulated at 1-MHz offset frequency from the carrier for each VCO circuit. For illustration purposes, below, are shown the simulation results for VCOs only with SCM and IWCM.

Figure 6(a) shows the simulated transient and Fig 6(b) the steady-state waveform of the VCO with SCM under 2V control voltage applied to the cathodes of the contrary connected varactors. Figure 6(c) shows the amplitude spectrum. In Fig. 6(d)

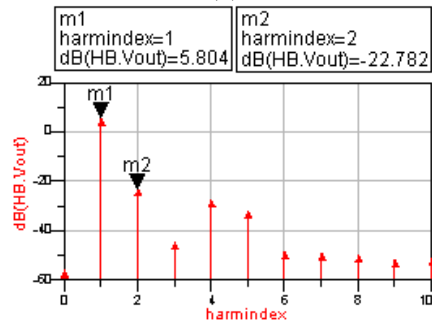
are shown the phase and amplitude noise of the simulated waveform. As seen from Fig. 6(d), the amplitude noise level at offset frequency 1MHz is 35dBc less than the phase noise level. So the main contributor to the NDR VCO noise is the phase noise.



(a)



(b)



freq	HB.Vout
0.0000 Hz	0.002 / 0.000
749.8 MHz	1.951 / 0.621
1.500 GHz	0.073 / -5.822
2.250 GHz	0.006 / 11.424
2.999 GHz	0.042 / -7.107
3.749 GHz	0.026 / -155.011
4.499 GHz	0.004 / 114.174
5.249 GHz	0.004 / 161.843
5.999 GHz	0.003 / 168.699
6.749 GHz	0.003 / 173.769
7.498 GHz	0.003 / 73.101

(c)

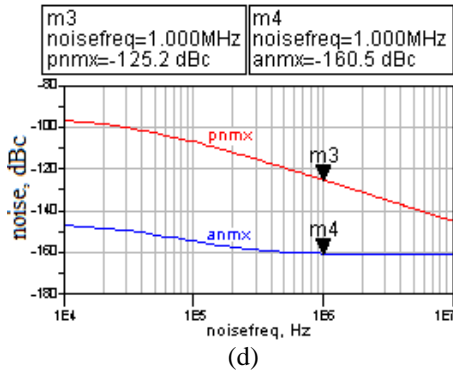
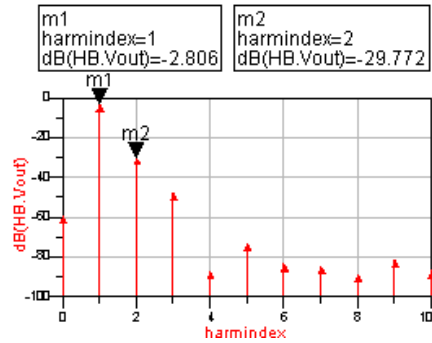
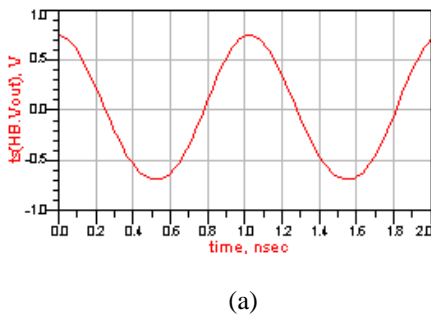


Fig. 6. The VCO with SCM when  $V_{CC}=2V$ ,  $C_1=8.2pF$ ,  $C_2=4.7pF$ : (a) transient response, (b) steady-state response, (c) amplitude spectrum, (d) phase noise and amplitude noise

In Fig. 7 are shown the simulation results for the VCO with SCM when  $V_{CC}=12V$ . Comparing the simulation results shown in Fig. 6 and 7, we can see that the phase noise is less at  $V_d=2V$ , but the THD is less at  $V_d=12V$ . The simulation amplitude is greater at  $V_d=2V$ .



freq	HB.Vout
0.0000 Hz	0.001 / 0.000
969.5 MHz	0.724 / 0.742
1.939 GHz	0.032 / 28.706
2.909 GHz	0.004 / 163.480
3.878 GHz	4.385E-5 / 69.236
4.848 GHz	2.291E-4 / -12.836
5.817 GHz	6.853E-5 / 69.946
6.787 GHz	6.021E-5 / 147.979
7.756 GHz	3.815E-5 / -99.001
8.726 GHz	8.494E-5 / 10.303
9.695 GHz	4.677E-5 / -18.193

(b)

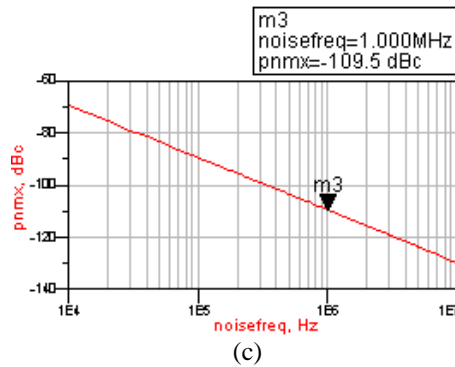
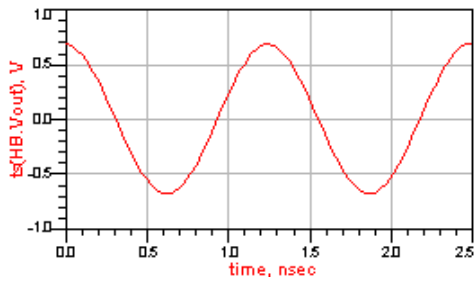
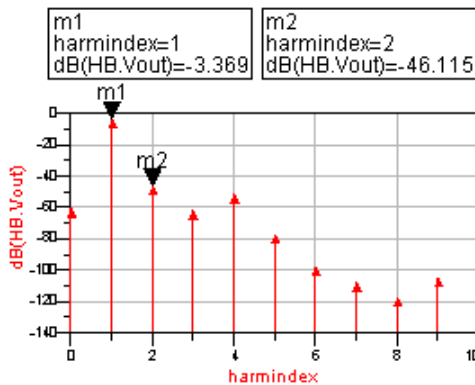


Fig. 7. The VCO with SCM when  $V_{CC}=12V$ ,  $C_1=8.2pF$ , and  $C_2=4.7pF$ : (a) steady-state response, (b) amplitude spectrum, (c) phase noise

The simulation results for the VCO with IWCM at  $V_d=2V$  and  $V_d=12V$  are shown in Fig. 8 and 9, respectively.

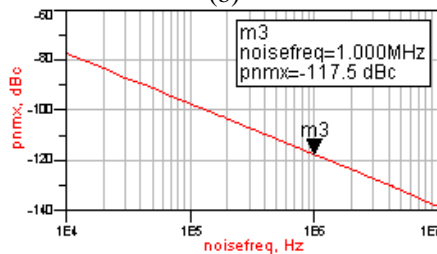


(a)



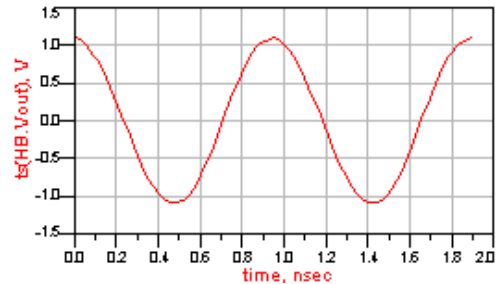
freq	HB.Vout
0.0000 Hz	9.532E-4 / 0.000
804.8 MHz	0.678 / 0.475
1.610 GHz	0.005 / 43.754
2.415 GHz	8.521E-4 / -18.219
3.219 GHz	0.003 / 19.729
4.024 GHz	1.453E-4 / 144.277
4.829 GHz	1.327E-5 / -179.066
5.634 GHz	3.645E-6 / 49.307
6.439 GHz	1.356E-6 / 10.598
7.244 GHz	5.607E-6 / -13.320
8.048 GHz	5.521E-6 / 171.502

(b)

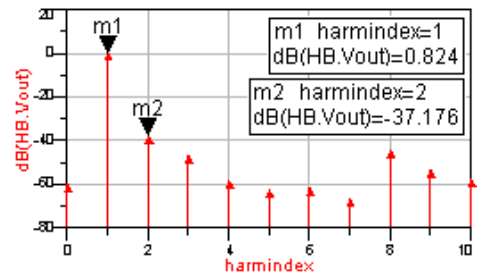


(c)

Fig. 8. The VCO with IWCM when  $V_{CC}=2V$ ,  $C_1=4.7pF$ ,  $C_2=39pF$ : (a) steady-state response, (b) amplitude spectrum, (c) phase noise



(a)



freq	HB.Vout
0.0000 Hz	0.001 / 0.000
1.056 GHz	1.099 / 0.585
2.112 GHz	0.014 / 94.946
3.168 GHz	0.005 / 174.556
4.224 GHz	0.001 / -52.378
5.280 GHz	7.513E-4 / 132.979
6.336 GHz	8.382E-4 / -133.088
7.392 GHz	4.791E-4 / 62.964
8.448 GHz	0.006 / -31.353
9.504 GHz	0.002 / 36.789
10.56 GHz	0.001 / 170.189

(b)

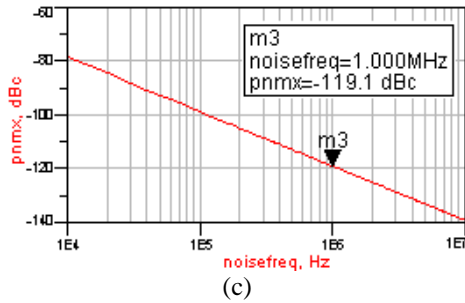


Fig. 9. The VCO with IWCM when  $V_{CC}=12V$ ,  $C_1=4.7pF$ ,  $C_2=39pF$ : (a) steady-state response, (b) amplitude spectrum, (c) phase noise

As seen from Table 1, the VCO with IWCM has the best performance. It has the

largest value of FOM and what is important this value is almost constant in the tuning frequency band. The VCO with WCM has the same performance as that with IWCM at  $V_d=2V$ , but less performance at  $V_d=12V$ . The worst performance has the VCO with SCMB. The VCO with CCM has the widest tuning frequency range, the smallest THD

value at  $V_d=2V$ , and the smallest power consumption.

Table 1. Summary of VCO optimization

VCO Type	$f_{o \min}$ (MHz) ( $V_d=2V$ )	$f_{o \max}$ (MHz) ( $V_d=12V$ )	$\Delta F$ (MHz)	$L_N$ (dBc)		$P_{dis}$ (mW)	THD%		FOM (dBc)	
				$V_d$ (2V)	$V_d$ (12V)		$V_d$ (2V)	$V_d$ (12V)	$V_d$ (2V)	$V_d$ (12V)
SCM	749.8	969.5	219.7	-125.4	-109.5	23.5	4.55	1.65	196	191
SCMB	725.9	916.1	190.2	-124.8	-110.4	21.4	6.40	6.06	193	181
CCM	837.7	1152	314.3	-110.4	-115.6	19.7	0.74	5.69	199	189
WCM	807.8	1107	299.2	-117.3	-119.4	20.3	0.84	2.80	204	198
IWCM	804.8	1056	251.2	-117.5	-119.1	20.6	0.87	1.48	204	203

The VCO with SCM has the smallest phase noise level at  $V_d=2V$ . The VCOs with WCM and IWCM have almost the same phase noise levels.

It should be pointed out that if the THD was not used in the FOM, like in [18], [19],

the VCO with SCMB would be better than the VCO with IWCM at

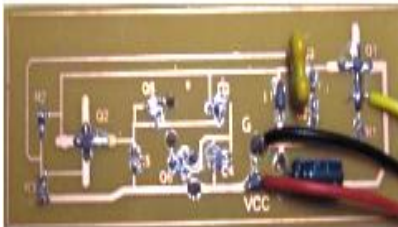
$V_d=2V$  because  $FOM_{SCMB} = 169dBc$  is less than  $FOM_{IWCM} = 164dBc$ . Thus the



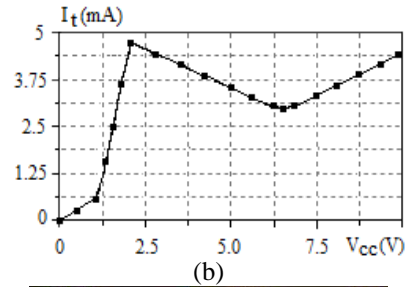
worst VCO could be the best if the THD was not taken into account.

## 9. Experimental Results

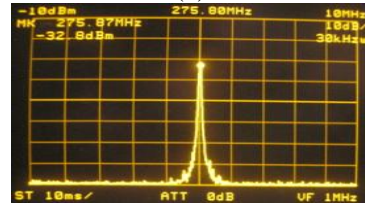
The NDR oscillator circuit with IWCM and output buffer was designed and implemented as shown in the photograph of Fig. 10(a). The values of the SMT resistors  $R_1$  and  $R_2$  were, respectively, selected to be  $270\Omega$  and  $2k\Omega$ . NEC's NE3210S01 Hetero-Junction FET was used as an InGaAs transistor. The IWCM was constructed using four BFT92  $p-n-p$  transistors. A  $22nH$  SMT inductor ELJRFN2 was selected. The ceramic SMT capacitors of  $2.2pF$  were used instead of varactors. The capacitors  $C_1$  and  $C_2$  were set to  $4.7pF$  and  $470pF$ , respectively. The measured  $I-V$  characteristic is shown in Fig. 10(b). The operating point was selected in the NDR region at  $V_{CCQ}=3.3V$  with  $I_{tQ}=4.2mA$ . The oscillator was connected to a spectrum analyzer R4131C (Advantest) through a buffer circuit. The photograph of the power spectrum is shown in Fig. 10(c). The measured output power is  $-32.8 dBm$  with  $20dB$  probe attenuation,  $4.5dB$  buffer insertion loss and  $8.5dB$  connecting cable loss. The measured oscillation frequency is  $275.8MHz$ .



(a)



(b)



(c)

Fig. 10. Practical implementation of the NDR oscillator circuit with IWCM: (a) printed-circuit board; (b) oscillator  $I-V$  characteristics; (c) output power spectrum over  $10MHz$  span and  $RBW=30kHz$

The measured frequency is about two times less than the theoretical value because of the parasitic capacitance of the printed circuit board and the buffer input capacitance.

## 10. Conclusions

A comparative analysis of the NDR VCO with five different CMs was presented. The generalized VCO circuit was described and the break points defining the NDR region on the  $I-V$  characteristic were determined. The terminal current was analytically modeled in terms of a CM input and output current for each VCO circuit. The FET drain current was modeled by the Curtice and Statz models, and the TOM. From comparing the theoretical modeling of the NDR region with the Spice simulation follows that all three nonlinear GaAs FET models show a very good



agreement between the simulated and the theoretical results. The start-up condition was derived for the NDR VCOs. It allows selecting the VCO components for reliable start-up on the stage of VCO designing. A new FOM was proposed for selecting the VCO with the best performance. This FOM is sensitive to the VCO phase noise, power consumption, tuning frequency range, and harmonic distortions. The VCOs with five different CMs were simulated and the performance characteristics were determined. By calculating the FOM for each VCO topology it was found that the best performance possessed the VCO with IWCM. A 275.8-MHz InGaAs FET oscillator with IWCM was designed and implemented. It draws 4.2 mA from a 3.3 V power supply and generates low-noise signal.

### References

- [1] U. L. Rohde, A. K. Poddar, and G. Bock, "The design of modern microwave oscillators for wireless applications", John Wiley & Sons, Inc. 2005, 561p.
- [2] A. Grebennikov, "RF and microwave transistor oscillator design", John Wiley & Sons, Inc. 2007, 441p.
- [3] R. Ludwig, P. Bretchko, and G. Bogdanov, "RF circuit design: theory and applications", 2<sup>nd</sup> edition, Pearson Prentice Hall, 2009, 704p.
- [4] M. Odyniec, "RF and microwave oscillator design", Artech House, Inc., 2002, 411p.
- [5] F. Ellinger, "Radio-frequency integrated circuits and technologies", Springer, 2007, 507p.
- [6] Z. D. Schwartz and G. E. Ponchak, "1 GHz, 200 °C, SiC MESFET Clapp oscillator", *IEEE Microwave and Wireless Component Lett.*, vol. 15, no. 11, pp. 730-732, Nov. 2005.
- [7] J.-H. Conan Zhan, K. Maurice, J. Duster, and K. V. Kornegay, "Analysis and design of negative impedance LC oscillators using bipolar transistors", *IEEE Transactions on Circuits and Systems-I: Fundamental Theory and Applications*, vol. 50, no. 11, pp.1461-1464, Nov. 2003.
- [8] V. V. Ulansky, M. F. Abusaid, and I. A. Machalin, "Mathematical modeling of voltage-controlled oscillators with the Colpitts and Clapp topology", *Electronics and Control Systems*, no. 1(19), pp. 82-90, 2009, ISSN 1990-5548.
- [9] Irving M. Gottlieb, "Practical oscillator handbook", Elsevier, 1997, 292p.
- [10] S. S. Gorbatov, A. A. Semenov, D. A. Usanov, A. N. Sorokin, and V. Yu. Kvasko, "Magnetic frequency tuning of the microwave Gunn diode oscillator", *Izvestiya Vysshih Uchebnyh Zavedenyi: Radioelektronika*, 2009, vol. 52, no. 3, pp. 77-80.
- [11] V. V. Ulansky, H. M. Elsherif, and M. F. Abusaid, "A voltage-controlled oscillator based on BJT Wilson current mirror", 4<sup>th</sup> LAICEEE, vol. 1, pp. 455-469, March 2006.
- [12] P. R. Gray, P. J. Hurst, S. H. Lewis, and R. G. Meyer, "Analysis and design of analog integrated circuits", 4<sup>th</sup> Edition, John Wiley & Sons, Inc. 2001, 875p.
- [13] "Converting GaAs FET models for different nonlinear simulators", AN1023, *California Eastern Laboratories*, April 2003.
- [14] W. R. Curtice, "A MESFET model for use in the design of GaAs integrated circuits", *IEEE Trans. Microwave Theory Tech.*, vol. MTT-28, 1980, pp. 448-456.



- [15] H. Statz, P. Newman, I. Smith, R. Pucel, and H. Haus, "GaAs FET device and circuit simulation in PSPICE", *IEEE Trans. Electron Devices*, vol. ED-34, 1987, pp. 160-169.
- [16] A. McCamant, G. McCormack, and D. Smith, "An improved GaAs MESFET model for SPICE", *IEEE Microwave Theory Tech.*, vol. MTT-38, pp. 822-824.
- [17] N. V. Zernov, V. G. Karpov, "Theory of radio engineering circuits", 2<sup>nd</sup> edition, Energy (in Russian), 1972, 816p.
- [18] H. Jacobsson, S. Gevorgian, M. Mokhtari, et al., "Low-phase-noise low-power IC VCOs for 5-8-GHz wireless applications", *IEEE Trans. Microwave Theory Tech.*, vol. 48, no. 12, pp. 2533-2539, Dec. 2000.
- [19] P. Andreani, X. Wang, L. Wandt, and A. Fard, "A study of phase noise in Colpitts and LC-tank CMOS oscillators", *IEEE J. Solid-State Circuits*, vol. 40, no.5, pp. 1107-1118, May 2005.
- [20] V. V. Ulansky, H. M. Elsherif, and E. M. Elmabrouk, "Optimization of nanoscale NMOS VCO for Bluetooth applications", *Proceedings of 7<sup>th</sup> International Conference "AVIA 2006"*, pp. 12.9-12.12.





## OPERATIONAL AMPLIFIER VOLTAGE-CONTROLLED OSCILLATORS WITH RESISTIVE AND CAPACITIVE FEEDBACK

Vladimir Vasily Ulansky<sup>1</sup>, Hassan Mohamed Elsherif<sup>2</sup>,

Mustafa Fituri Abusaid<sup>3</sup>, and Munira Abdalla Bengashier<sup>4</sup>

<sup>1,2,3,4</sup>Electrical and Electronic Engineering Department, Faculty of Engineering,  
Al Fateh University, Tripoli, Libya, e-mail: vulanskyi@yahoo.com

*Abstract* – Two low noise low distortion operational amplifier (OPA) voltage - controlled oscillators (VCOs) with minimum number of components are presented. The first VCO topology is based on the OPA negative impedance converter and the second VCO uses a unity gain OPA buffer with a feedback capacitor. The fabricated oscillator circuits operate at, respectively, 273.58 MHz and 203.65 MHz. Measurement results demonstrate a single sideband phase noise of -119dBc/Hz and -130 dBc/Hz at a 500kHz offset, and the total harmonic distortion (THD) of 2.2% and 1.3%, respectively.

### 1. INTRODUCTION

The VCOs are widely used in modern communication and instrumentation systems. The use of an OPA as an active device in the VCO circuits has the following advantages: it is a complete amplifier with high input impedance and low output impedance;

the required voltage gain is obtained by using maximum two gain-setting resistors; the positive feedback is easily introduced around the OPA; the VCO design is considerably simplified because of easy biasing. However, OPA VCOs of the Colpitts and Hartley topology require a relatively high voltage gain to start-up the oscillation [1], [2]. This

The tank circuit is also connected at the non-inverting input. This topology is called a VCO with capacitive feedback. Both proposed VCO topologies can operate at much higher frequencies compared to the

reduces maximum operating frequency due to the limited gain-bandwidth product of used OPA. In this paper two OPA VCO topologies are proposed, analyzed, and designed. The first VCO topology is based on the OPA circuit with negative input resistance observed at the non-inverting input of the OPA [3]. This negative resistance compensates the losses in the VCO tank circuit connected to the non-inverting input. Such topology is called a VCO with resistive feedback.

The second VCO topology is based on a unity gain OPA buffer with a feedback capacitor connected between the output and the non-inverting input of the OPA [4].

Colpitts and Hartley VCOs. The analysis, simulation and design of the two proposed VCO circuits are described. Each oscillator was implemented to provide a printed circuit board (PCB) solution with an ultra

wide band (1.5GHz) low noise OPA LMH6624. Measured results for these VHF oscillator circuits allow a number of complicated implementation issues to be enlightened including an exhibition of a buffer circuit importance. In addition to illustrating a number of new circuit solutions, this paper concludes with some new views regarding RF bands where proposed VCOs can be used.

## 2. RESISTIVE FEEDBACK VCO

### 2.1. Architecture

The proposed VCO circuit with resistive feedback is shown in Fig. 1(a).

The tank circuit is represented by the inductor  $L$  and two contrary connected varactors  $VD_1$  and  $VD_2$ . Resistor  $R_c$  isolates the dc control line from the VCO tank. Resistor  $R_a$  is the feedback resistor; it connects the OPA output to the non-inverting input. The resistors  $R_1$  and  $R_2$  are the voltage gain setting resistors.

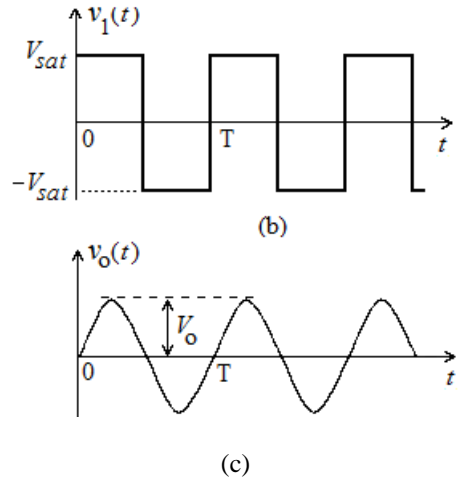
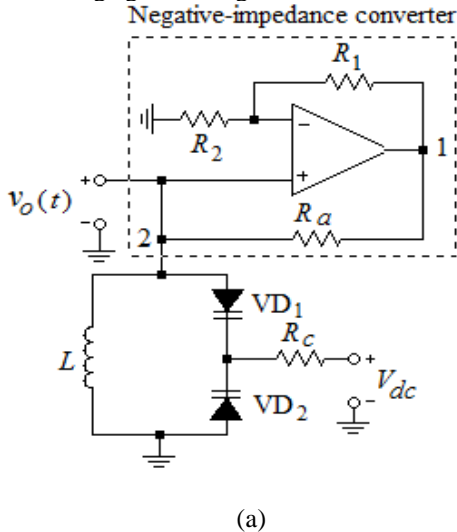


Figure 1. (a) Schematic of the VCO with positive resistive feedback, (b) waveform at node (1), (c) waveform at node (2)

Assuming the OPA is ideal and cutting wire to the tank circuit, the input impedance at node 2 is given by [3]

$$Z_{in} = R_a / (1 - A_V) \quad (1)$$

where  $A_V$  is the voltage gain of the non-inverting amplifier,  $A_V = 1 + R_1/R_2$ .

From (1) follows that if  $A_V > 1$  then  $Z_{in} < 0$ . Having negative input resistance, the electronic part of the VCO can compensate the losses of the tank circuit.

Assuming the OPA is ideal, the voltage time diagrams at nodes 1 and 2 are shown in Fig. 1 (b) and (c). As seen from Fig. 1(b), the OPA output voltage (node 1) is a square waveform with maximum amplitude  $V_{sat}$ , where  $V_{sat}$  is the OPA saturation voltage. This voltage is fed back through resistor  $R_a$  to the tank circuit producing a current,

which is rich with the harmonics of the fundamental frequency,  $f_0$ . Since the equivalent impedance of the tank circuit has maximum at the resonant frequency  $f_0$  and decreases very fast to the left and to the right from  $f_0$ , then only first harmonic of the current flow will create a significant voltage drop across the tank circuit. The other harmonics will be filtered out. Thus, the voltage at node 2 is a sinusoidal waveform as shown in Fig. 1(c). Since for the practical VCOs the slew rate is limited, the voltage at node 1 can be a trapezoidal waveform or a triangular waveform as shown in Fig. 2(a) and (b), but the voltage at node 2 remains a sinusoidal waveform. The shape of voltage in Fig. 2(a) corresponds to an OPA with a moderate slew rate. The pulses of such voltage have visible rise and fall times, but the slew rate is still sufficient for saturation of the OPA output.

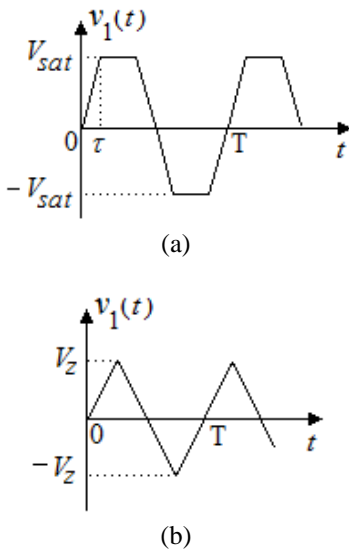


Figure 2. Typical waveforms at the OPA output (node 1): (a) - trapezoidal, (b) - triangular

The shape of voltage in Fig. 2(b) corresponds to an OPA with low slew rate, which is not sufficient for saturating its output, therefore  $V_z < V_{sat}$ .

## 2.2. Description

The ac equivalent circuit of the VCO is shown in Fig. 3(a). Since the input resistance of the non-inverting OPA circuit ( $R_{in}$ ) is extremely large and the output resistance ( $R_o$ ) is very small due to the advanced characteristics of modern OPAs and negative voltage-series feedback through  $R_1$  and  $R_2$  they can be neglected as shown in Fig. 3(b).

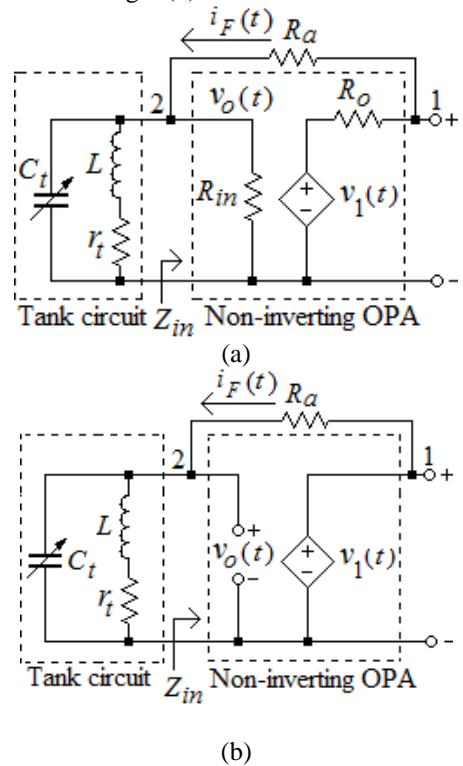




Figure 3. AC equivalent circuit of the VCO with real (a) and ideal (b)  $R_{in}$  and  $R_o$

In Fig. 3, the capacitance  $C_t$  and resistance  $r_t$  represent the total tank circuit capacitance and ac resistance

$$C_t = 0.5C_V + C_{par}$$

$$r_t = r_L + 2r_v$$

where  $C_V$  is the capacitance of one varactor,  $C_{par}$  is the total parasitic capacitance of the VCO,  $r_L$  is the ac resistance of the coil, and  $r_v$  is the ac resistance of one varactor. The current  $i_F(t)$  represents the ac current through the positive feedback resistor  $R_a$ .

A simplified ac equivalent circuit of the VCO is shown in Fig. 4, where a series to parallel transformation of the ac loss resistance is performed. The resistance  $R_a$  in the positive feedback path is reflected to the non-inverting input as the negative resistance

$$R_{neg} = Z_{in} = \frac{R_a}{1 - A_V} < 0$$

This resistance  $R_{neg}$  compensates the losses in the tank circuit represented by the loss resistance  $R_p$ . The voltage  $v_o(t)$  is a sinusoidal signal that can be represented as

$$v_o(t) = V_o \sin(\omega_0 t + \varphi_0)$$

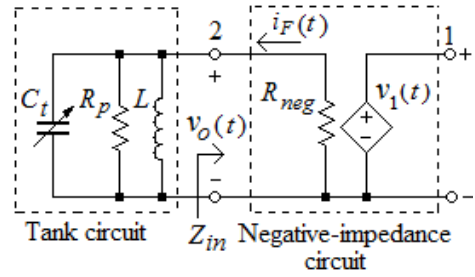


Figure 4. Simplified ac equivalent circuit of the VCO

Where  $V_o$ ,  $\omega_0$ , and  $\varphi_0$  are, respectively, the amplitude, frequency and initial phase of the output voltage. The average power consumed by the negative resistance is negative

$$P_{neg} = \frac{V_o^2}{2R_a} (1 - A_V) < 0 \quad (2)$$

Therefore the negative resistance is an electric energy source that can be replaced with an ac current source as it will be shown later. The energy losses in the VCO tank circuit are computed as follows:

$$P_r = \frac{V_o^2}{2R_p} \quad (3)$$

If  $|P_{neg}| > P_r$ , the VCO starts to oscillate. This is the start-up condition of the VCO. Substituting  $P_{neg}$  and  $P_r$  from (2) and (3) into the last inequality gives

$$R_1/R_2 > R_a/R_p$$

The value of  $R_a$  is usually less than  $R_p$ . Therefore, in practical applications the required voltage gain is usually in the range

of 1 to 2. The small voltage gain required for oscillation in the resistive feedback VCO results in a significant increase of the maximum possible oscillation frequency ( $f_{0\max}$ )

$$f_{0\max} \leq GBP/A_v$$

compared to the OPA Colpitts VCO [1], where  $GBP$  is the gain-bandwidth product of the OPA.

From the ac equivalent circuit of Fig. 3(b) follows that the VCO circuit can be represented as a parallel connection of the non-inverting OPA circuit and the feedback circuit (resistor  $R_a$ ). Therefore, both of these circuits can be represented as two parallel connected two port networks as shown in Fig. 5(a). The  $y$ -parameters in the circuit of Fig. 5(a) are defined as follows:

$$y_{11f} = y_{22f} = 1/R_a$$

$$y_{12f} = y_{21f} = -1/R_a$$

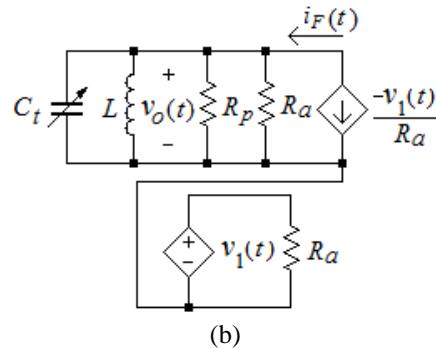
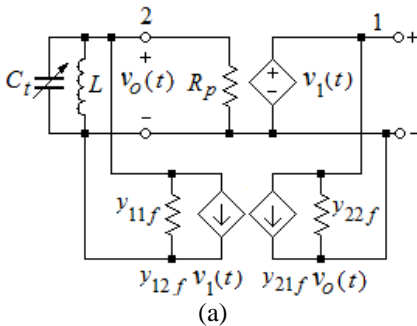


Figure 5. (a) VCO ac model with a  $y$ -parameter model of feedback voltage-shunt circuit. (b) Unilateral ac model of the VCO with positive feedback incorporated as  $y_{11f}$  and  $y_{22f}$  loading and  $i_F(t)$  generator

The  $y$ -parameter model of the feedback network can be simplified because under normal feedback network operation we expect the  $y$ -parameter  $y_{21f}$  is negligibly small. This is indeed true because the feedback network is used for transmitting the signal from node 1 to node 2 but not vice versa. Assuming  $y_{21f} = 0$ , the unilateral ac model of the VCO is shown in Fig. 5(b).

To find the amplitude of the VCO output voltage  $V_o$ , the periodic voltage  $v_1(t)$  can be approximated by the Fourier series. Consider, for example, the triangular waveform shown in Fig. 3(b). For this waveform the Fourier series is represented as

$$v_1(t) = \frac{8V_z}{\pi^2} \sum_{n=1,3,5,\dots}^{\infty} \frac{1}{n^2} \sin \frac{n\pi}{2} \sin n\omega_0 t$$



where  $V_z$  is the amplitude of the waveform shown in Fig. 3(b) and  $n$  is the harmonic number.

The current  $i_F(t)$ , flowing through the tank circuit as shown in Fig. 5(b), can also be represented by a Fourier series

$$i_F(t) = \frac{v_1(t)}{R_a} = \frac{8V_z}{R_a \pi^2} \sum_{n=1,3,5,\dots}^{\infty} \frac{1}{n^2} \sin \frac{n\pi}{2} \sin n\omega_0 t \quad (4)$$

From (4) the amplitude of the first harmonic of  $i_F(t)$  is found as

$$I_{F1} = \frac{8V_z}{R_a \pi^2}$$

Since only the first harmonic of the current  $i_F(t)$  creates a significant voltage drop across the tank at resonance, the amplitude of the sinusoidal voltage is found as a product of the current amplitude  $I_{F1}$  and the loaded tank circuit equivalent resistance, which is  $R_p \parallel R_a$ . Thus, we have

$$V_o = I_{F1} (R_p \parallel R_a) = \frac{8V_z}{\pi^2} \left( \frac{R_p}{R_p + R_a} \right) \quad (5)$$

It can easily be shown that the oscillation amplitude across the tank for the square (Fig. 1(b)) and trapezoidal (Fig. 2(a)) waveforms at node 1 (Fig. 1(a)) are computed by the following formulas:

$$V_o = \frac{4V_{sat}}{\pi} \left( \frac{R_p}{R_p + R_a} \right),$$

$$V_o = \frac{4V_{sat}}{\pi} \left( \frac{\sin \frac{2\pi\tau}{T}}{\frac{2\pi\tau}{T}} \right) \left( \frac{R_p}{R_p + R_a} \right)$$

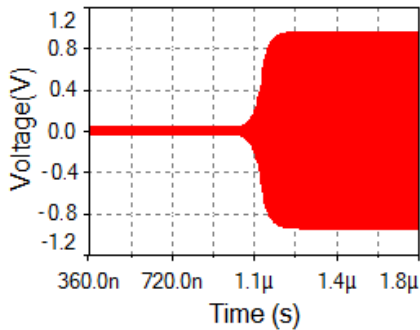
where  $\tau$  is the rise time for the trapezoidal waveform. From the last two equations follows that the oscillation amplitude cannot exceed the voltage level of  $4V_{sat}/\pi$ .

### 2.3. Simulation

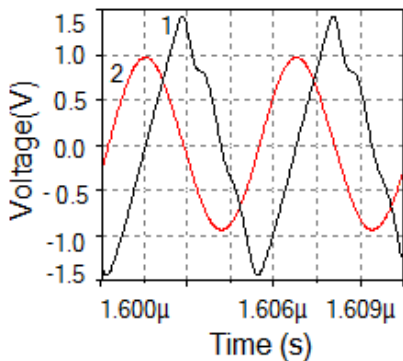
SPICE simulations are performed for the VCO circuit shown in Fig. 1(a) with a wideband low-distortion OPA 643U (Burr-Brown). It has the gain-bandwidth product of 800MHz and input capacitance of 2.5pF. The voltage gain setting resistors  $R_1$  and  $R_2$  were set to 0.47k $\Omega$  and 1k $\Omega$ , respectively, resulting in  $A_V=1.47$ . The positive feedback resistance,  $R_a$ , is 8.2k $\Omega$ . Two varactors BBY62 (Philips) are used to change the VCO frequency from 190.159MHz to 259.737MHz when the dc voltage  $V_{dc}$ , applied through  $R_5=10k\Omega$  to the varactor cathodes, is changed from 3V to 20V. A single varactor capacitance is varied from  $C_{V_{max}} \approx 10.7pF$  to

$C_{V_{min}} \approx 2.4pF$ . The inductor value is 100nH with loss resistance of 1 $\Omega$ .

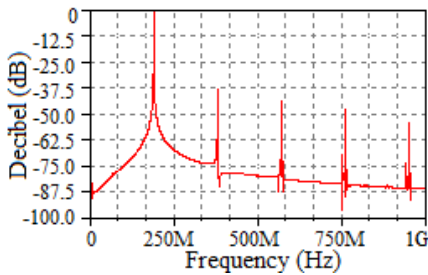
Simulation results for  $V_{dc}=3V$  are shown in Fig. 6.



(a)



(b)



(c)

Figure 6. Simulated VCO waveforms at  $V_{dc}=3V$ : (a) starting-up waveform; (b) triangular voltage at node 1 and sinusoidal voltage at node 2; (c) output voltage spectrum with RF=122.07kHz

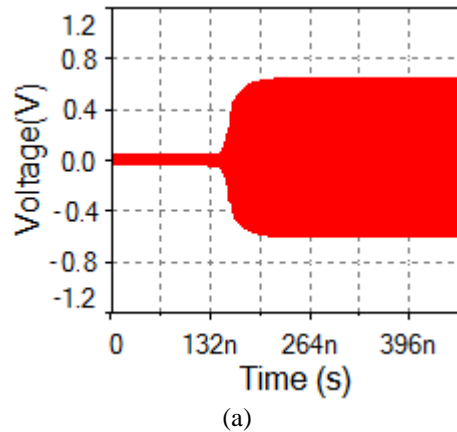
The VCO starting-up waveform is shown in Fig. 6(a). As seen, the output voltage

amplitude reaches the steady-state level in approximately  $1.25\mu S$ .

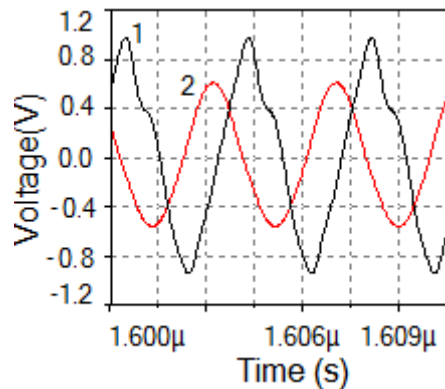
From Fig. 6(b) follows that the voltages at nodes 1 and 2 are, respectively, a triangular waveform with amplitude  $V_z = 1.42V$  and a sinusoidal waveform with amplitude  $V_o = 0.96V$ . The oscillation frequency is

$f_{0min} = 190.159MHz$  The output voltage spectrum with resolution frequency (RF) of 122.07kHz is shown in Fig. 6(c). The total harmonic distortion (THD) is 2%.

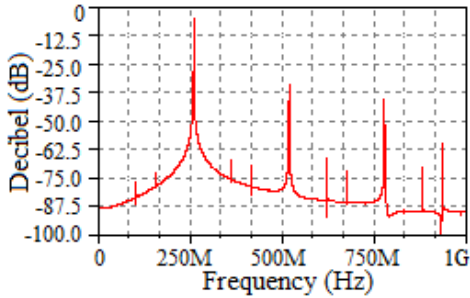
The simulated results at  $V_{dc}=20V$  are depicted in Fig. 7.



(a)



(b)



(c)

Figure 7. Simulated VCO waveforms at  $V_{dc}=20V$ : (a) starting-up waveform at node 2; (b) triangular voltage at node 1 and sinusoidal voltage at node 2; (c) output voltage spectrum with  $RF=122.07kHz$

The VCO starting-up waveform is shown in Fig. 7(a). As seen, the oscillated voltage amplitude reaches the steady-state level within approximately 220ns. From comparing the starting-up waveforms shown in Figures 6(a) and 7(a) follows that at  $V_{dc} = 20V$  the settling time is about 6 times less than at  $V_{dc}=3V$ . This happens because the characteristic impedance of the VCO,  $\sqrt{L/C_t}$ , is increased from  $113\Omega$  at  $V_{dc}=3V$  to  $164\Omega$  at  $V_{dc}=20V$ .

The waveforms at nodes 1 and 2 (see Fig. 1(a)) are shown in Fig. 7(b).

The amplitudes of the triangular and sinusoidal waveforms are reduced to 1.13V and 0.51V, respectively. The oscillation frequency is  $f_{0max} = 259.737MHz$

The calculated negative power is  $P_{neg} \approx -7.5\mu W$  and the power dissipated by the tank circuit is  $P_r \approx 4.9\mu W$ .

So  $|P_{neg}| > P_r$ , and the start-up condition is satisfied.

The output voltage spectrum is depicted in Fig. 7(c). The THD is 5.2%, which is considerably greater than 2% value at  $V_{dc}=3V$ . This fact requires additional explanation. Indeed, analyzing the output voltage spectrums shown in Figures 6(c) and 7(c) we can see that the noise voltage between the multiples of the fundamental frequency is about  $5 \div 10dB$  less for the case of  $V_{dc}=20V$  compared to the case of  $V_{dc}=3V$ . Thus, there is a trade-off between the THD and noise voltage of the VCO. When the characteristic impedance,  $\sqrt{L/C_t}$ , increases the noise voltage decreases while the THD increases.

The simulated tuning characteristic of the VCO is shown in Fig. 8. As seen, a tuning range of 36.6% is achieved.



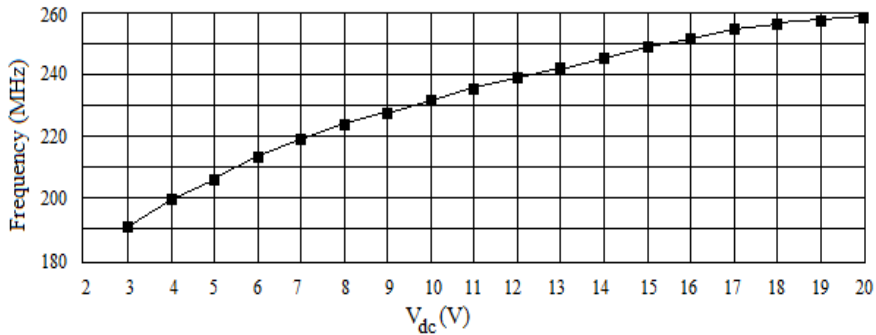


Figure 8. Simulated frequency tuning characteristic of the resistive feedback VCO

### 2.4. Experimental Results

A resistive feedback oscillator was implemented with an ultra low noise ( $0.92 \text{ nV}/\sqrt{\text{Hz}}$ ) wideband (1.5GHz) operational amplifier LMH6624 as shown in Fig 9. The supply dc voltage was  $\pm 5\text{V}$ .

The measurements of oscillation frequency and output power spectrum were performed using an R4131C (Advantest) spectrum analyzer. For reducing the effect of the connecting cable and spectrum analyzer input capacitance a unity gain buffer was connected to the oscillator output. As shown in Fig. 9(a), resistor  $R_2$  was removed from the oscillator circuit providing a required voltage gain. The output power spectrums are shown in Fig. 10(a) and (b).

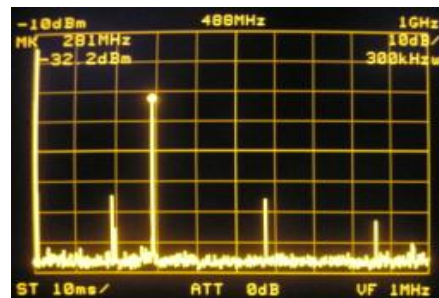
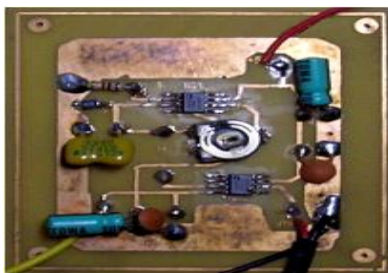
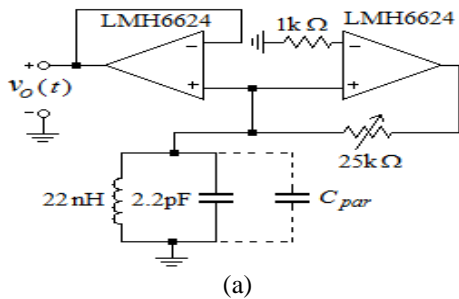
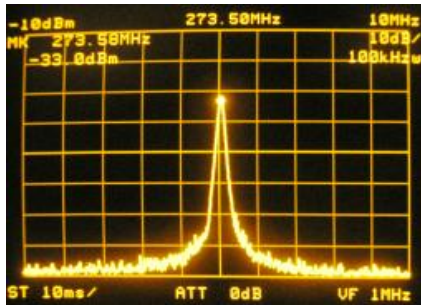


Figure 9. Resistive feedback test oscillator: (a) circuit diagram, (b) PCB photograph

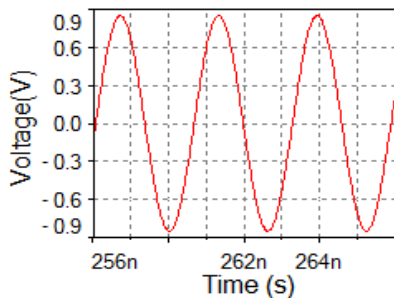


(b)

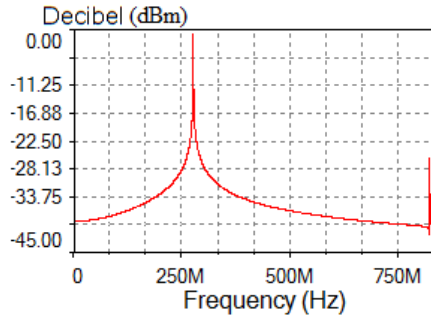
Figure 10. Output power spectrum of the resistive feedback oscillator over 1GHz span and RBW=300kHz (a), and 10MHz span and RBW=100kHz (b)

The spectrums were measured with 1GHz and 10MHz span, and 300kHz and 100kHz resolution bandwidth (RBW), respectively. The measured oscillation frequency is 273.58MHz. The measured output power is -33dBm with 20dB probe attenuation and 12dB buffer insertion loss. The phase noise is -119dBc/Hz at a 500kHz offset. The estimated value of THD is 2.2%.

The oscillator circuit of Fig. 9(a) was simulated by MULTISIM 11 as shown in Fig. 11. To obtain the same oscillation frequency the parasitic capacitance was set to 5.5pF. As seen from Fig. 11(a) and (b), the amplitude and power of simulated signal at node 2 are 0.85V and -1dBm, respectively. The simulated value of the THD is 0.27%.



(a)



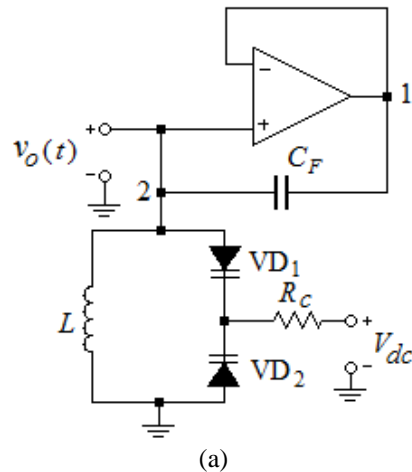
(b)

Figure 11. Simulated resistive feedback oscillator waveforms: (a) sinusoidal voltage at node 2; (b) output power spectrum with RF=122.07kHz

### 3. CAPACITIVE-FEEDBACK VCO

#### 3.1. Architecture

The capacitive feedback VCO circuit diagram is shown in Fig. 12(a).



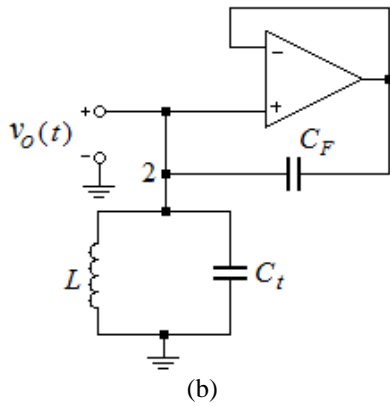


Figure 12. VCO with capacitive feedback: (a) schematic, (b) simplified schematic

As seen from Fig. 12(a), the VCO circuit comprises minimum number of components and provides maximum possible frequency of oscillation, which is theoretically equal to the unity gain bandwidth of the selected OPA.

### 3.2. Description

For simplicity of analysis the two varactors are replaced by the equivalent capacitance  $C_t$  as shown in Fig. 12(b).

The waveforms at nodes 1 and 2 have the same shapes as in Fig. 1 (b) and (c), and Fig. 2 (a) and (b). The voltage-shunt feedback presentation of the VCO ac equivalent circuit is shown in Fig. 13(a).

As seen from Fig. 13(a), the capacitor  $C_F$  provides a voltage-shunt feedback and can be modeled by the y-parameters in the same manner as in Fig. 5(a).

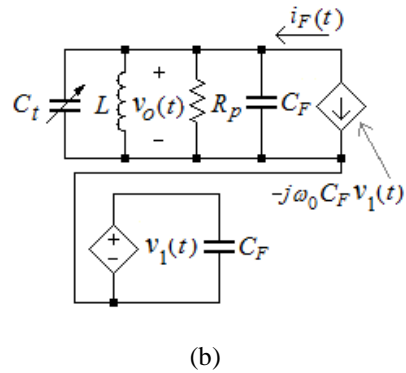
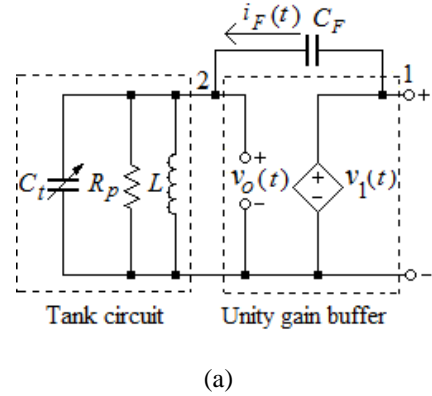


Figure 13. (a) AC equivalent circuit of the capacitive feedback VCO, (b) unilateral ac model of the VCO

The y-parameters are defined as follows:

$$y_{11f} = y_{22f} = j\omega_0 C_F,$$

$$y_{12f} = y_{21f} = -j\omega_0 C_F$$

The feedback current generator,  $y_{12f}V_1(t)$ , is given by

$$y_{12f}V_1(t) = -j\omega_0 C_F V_1(t) = -i_F(t) \quad (6)$$

Assuming  $y_{21f} = 0$ , the unilateral ac model of the capacitive feedback VCO



is shown in Fig. 13(b), where the admittances  $Y_{11f}$  and  $Y_{22f}$  are, respectively, incorporated into the left and right part of the circuit. As seen, the oscillation will start if the ac current source  $i_F(t)$  compensates the energy losses in the VCO tank circuit. From (6) follows that the amplitude of the feedback current  $i_F(t)$  is directly proportional to the value of  $C_F$  and the phase of  $i_F(t)$  leads the phase of  $V_1(t)$  by  $90^\circ$ . By choosing the value of  $C_F$  two conditions must be satisfied: the value of  $C_F$  must not be too small, otherwise the energy generated by the incorporated ac current source will not be sufficient for compensating the energy losses in the VCO tank circuit; the value of  $C_F$  must not be too large, otherwise this capacitor will shunt the controlled voltage source  $V_1(t)$ .

From the circuit of Fig. 13(b) the oscillation frequency is found as

$$f_0 = 1 / (2\pi \sqrt{L(C_t + C_F)})$$

The oscillation amplitude is determined for the case of the square wave voltage  $V_1(t)$  shown in Fig. 1(b). The periodic voltage  $v_1(t)$  is represented by the complex exponential Fourier series

$$v_1(t) = \frac{1}{2} \sum_{m=-\infty}^{\infty} V_{1,m}^* \exp(jm\omega_0 t)$$

where  $V_{1,m}^* = V_{1,m} \exp(j\varphi_m)$  is the complex amplitude of the  $m$ -th harmonic of the voltage at node 1,  $V_{1,m}$  and  $\varphi_m$  are, respectively, the amplitude and the initial

phase of the  $m$ -th harmonic. The amplitude of the  $m$ -th voltage harmonic is determined as follows:

$$V_{1,m} = \frac{4V_{sat}}{m\pi} \sin^2 \frac{m\pi}{2}, m=1,2,\dots \quad (7)$$

The feedback current  $i_F(t)$  is also represented by the complex exponential Fourier series

$$i_F(t) = \frac{1}{2} \sum_{m=-\infty}^{\infty} I_{F,m}^* \exp(jm\omega_0 t)$$

where  $I_{F,m}^* = I_{F,m} \exp(j\phi_m)$  is the complex amplitude of the  $m$ -th current harmonic,  $I_{F,m}$  and  $\phi_m$  are, respectively, the amplitude and the initial phase of the  $m$ -th harmonic of  $i_F(t)$ . Taking into account (6) and (7), we obtain

$$I_{F,m}^* = j\omega_0 C_F V_{1,m} = \omega_0 C_F V_{1,m} e^{j\frac{\pi}{2}} = \quad (8)$$

$$\frac{4V_{sat}\omega_0 C_F}{m\pi} \sin^2 \frac{m\pi}{2} \exp \left[ j \left( \varphi_m + \frac{\pi}{2} \right) \right]$$

As seen from (8), the  $m$ -th harmonic of  $i_F(t)$  leads the  $m$ -th harmonic of  $v_1(t)$  by  $\frac{\pi}{2}$ , i.e.  $\phi_m = \varphi_m + \frac{\pi}{2}$ . Since only the first harmonic of  $i_F(t)$  having the complex amplitude

$$I_{F,1}^* = j\omega_0 C_F V_{1,1}^* = \frac{4V_{sat}\omega_0 C_F}{\pi} \times \exp \left[ j \left( \varphi_1 + \frac{\pi}{2} \right) \right]$$

creates a significant voltage drop across the tank circuit at resonance, then the voltage



complex amplitude across the tank is given by

$$V_0^* = I_{F,1}^* R_p = \frac{4V_{sat}\omega_0 C_F R_p}{\pi} \times \exp\left[j\left(\varphi_1 + \frac{\pi}{2}\right)\right] \quad (9)$$

It follows easily from (9) that the amplitude of the sinusoidal voltage across the tank is

$$V_0 = \frac{4}{\pi} V_{sat}\omega_0 C_F R_p \quad (10)$$

and the initial phase of this voltage leads the initial phase of  $v_1(t)$  by  $90^\circ$ .

It can be shown that the oscillation amplitude across the tank for the trapezoidal (Fig. 2(a)) and triangular (Fig. 2(b)) waveforms at node 1 (see Fig. 12(a)) are, respectively, represented by the following equations:

$$V_0 = \frac{4V_{sat}C_F R_p \sin \omega_0 \tau}{\pi \tau} \quad (11)$$

$$V_0 = \frac{8V_z \omega_0 C_F R_p}{\pi^2} \quad (12)$$

where  $\tau$  is the rise time for the trapezoidal waveform. As seen from (10) - (12), the amplitude of the generated sinusoidal voltage is directly proportional to  $C_F$  and  $R_p$ . As it also follows from (10) and (11), the oscillation amplitude can exceed the voltage level of  $4V_{sat}/\pi$ , which cannot be exceeded by the resistive feedback, the Colpitts, or the Hartley OPA oscillator [1].

### 3.3. Simulation

SPICE simulations are performed with wideband, low-noise, voltage-feedback

OPA CLC 426AJP (National Semiconductor). It has gain-bandwidth product of 230MHz and input capacitance of 2pF. A 19.4nH RF coil and two BBY62 varactors are used in the VCO tank circuit. The selected value of  $C_F$  is 1.2pF. The control dc voltage,  $V_{dc}$ , is applied through  $R_S=10k\Omega$  to the varactor cathodes and varied from 0V to 20V to change the VCO oscillation frequency from 295.212MHz to 457.976MHz. It should be pointed out, that the VCO frequency range significantly exceeds 230MHz, which is the bandwidth of the selected OPA with unity voltage gain.

Simulation results for  $V_{dc}=0V$  are shown in Fig. 14. As it follows from Fig. 14(a), the steady-state level is reached in approximately  $0.41\mu S$ . The voltage amplitudes at nodes 1 and 2 are shown in Fig. 14(b). As seen, the amplitude of the triangular voltage,  $V_z=0.22V$ , is much less than the amplitude of the sinusoidal voltage,  $V_0=2.35V$ . Returning back to Fig. 6(b) we find that for the resistive feedback VCO the ratio of  $V_z$  to  $V_0$  is opposite:  $V_z > V_0$ . This fact can also be observed from comparison of equations (5) and (12). From (5) is seen that  $V_0$  cannot be greater than  $V_z$ . But from (12) follows that  $V_0$  is not limited. Thus, the capacitive feedback VCO is inherently more effective than the resistive VCO in terms of the frequency bandwidth and generated voltage amplitude. The output voltage spectrum is shown in Fig. 14(c). The 1<sup>st</sup> harmonic is 7.4dB, the 2<sup>nd</sup> is -36dB, and the 3<sup>rd</sup> is -64dB resulting in the THD value of only 0.79%.

Simulation results for  $V_{dc}=20V$  are shown in Fig. 15. As seen from Fig. 15(a), the time required to reach the steady-state level is



approximately 216nS. The voltage amplitudes at nodes 1 and 2 are shown in Fig. 15(b). Again, the amplitude of the triangular voltage,  $V_z=0.19V$ , is significantly less than the amplitude of the sinusoidal voltage,  $V_0=1.45V$ . The output voltage spectrum is shown in Fig. 15(c). The 1<sup>st</sup> harmonic is 3.2dB, the 2<sup>nd</sup> is -35dB, and the 3<sup>rd</sup> is -41dB. The THD value is 1.8%.

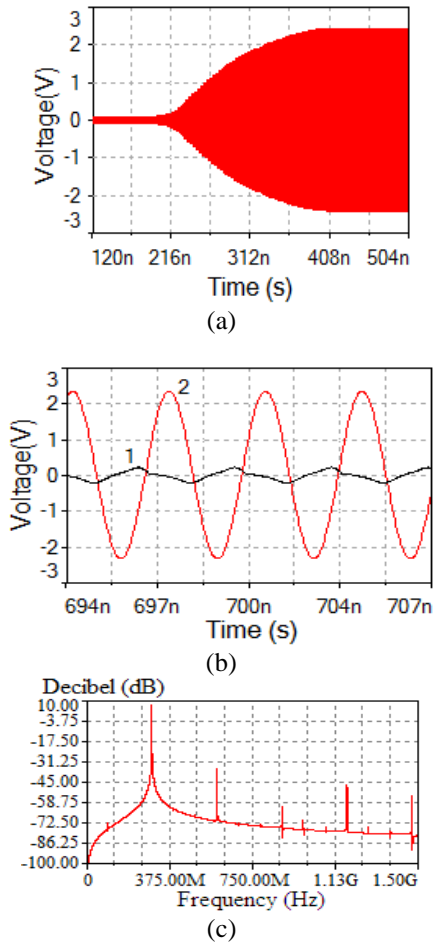


Figure 14. Simulated VCO waveforms at  $V_{dc}=0V$ : (a) starting-up waveform; (b)

triangular voltage at node 1 and sinusoidal voltage at node 2; (c) output voltage spectrum with  $RF=183.105kHz$

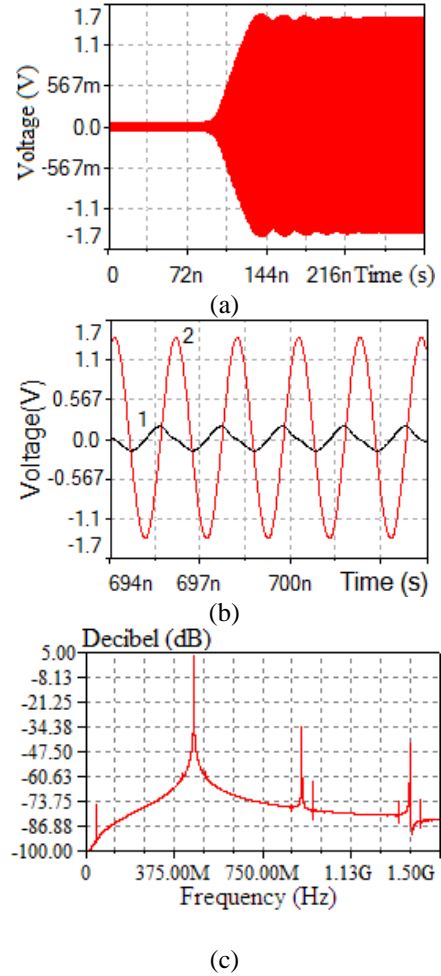


Figure 15. Simulated VCO waveforms at  $V_{dc}=20V$ : (a) starting-up waveform; (b) triangular voltage at node 1 and sinusoidal voltage at node 2; (c) output voltage spectrum with  $RF=183.105kHz$



Comparing the voltage spectrums simulated for the resistive feedback (Fig.6(c) and Fig. 7(c)) and the capacitive feedback (Fig. 14(c) and Fig. 15(c)) VCOs at  $V_{dc,min}$  and  $V_{dc,max}$ , one can conclude that the THD and noise voltage level are more dependent on the dc control voltage for the resistive

feedback than for the capacitive feedback VCO. This is one more advantage of the capacitive feedback VCO.

In Fig. 16 is shown the simulated frequency tuning characteristic of the capacitive feedback VCO. As can be seen the tuning range is 55%.

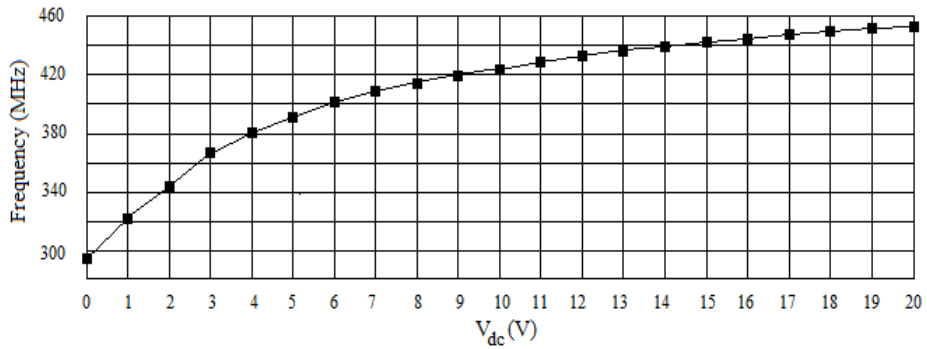
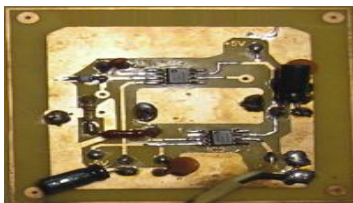
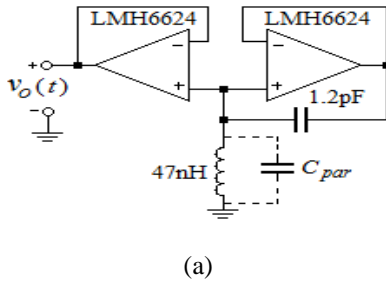


Figure 16. Simulated frequency tuning characteristic of the capacitive feedback VCO



### 3.4. Experimental Results

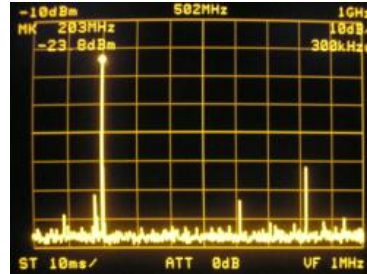
A capacitive feedback oscillator was also implemented with an ultra low noise wideband OPA LMH6624 as shown in Fig 17. The supply dc voltage was  $\pm 5V$ . The oscillation frequency and output power spectrum were measured by using the same spectrum analyzer R4131C (Advantest) as in the case of the resistive feedback oscillator. The unity gain buffer was also connected to the oscillator output for isolating the tank circuit from the measuring equipment. The photographs of the power spectrums are shown in Fig. 18. The measured oscillation frequency is 203.65MHz. The measured output power is -23.8dBm with 20dB probe attenuation and 12.8dB buffer insertion loss. The phase noise is -130dBc/Hz at 500kHz offset from the carrier. The estimated value of the THD is 1.3%.



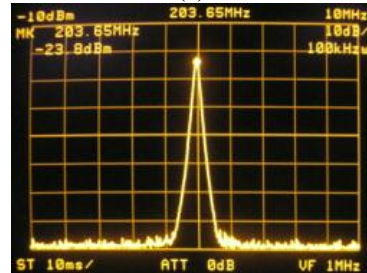
(b)

Figure 17. Capacitive feedback test oscillator: (a) circuit diagram, (b) PCB photograph

Comparing the power spectrums shown in Fig. 10 and 18 we can conclude that the capacitive feedback oscillator generates less noisy and less distorted sinusoidal voltage than the resistive feedback oscillator.



(a)



(b)

Figure 18. Output power spectrum of the capacitive feedback oscillator: (a) over 1 GHz span and RBW=300kHz, (b) over 10MHz span and RBW=100kHz

In Fig. 19 are shown the simulation results for the oscillator circuit of Fig. 17(a). The same oscillation frequency was obtained with  $C_{par}=3.4pF$ .



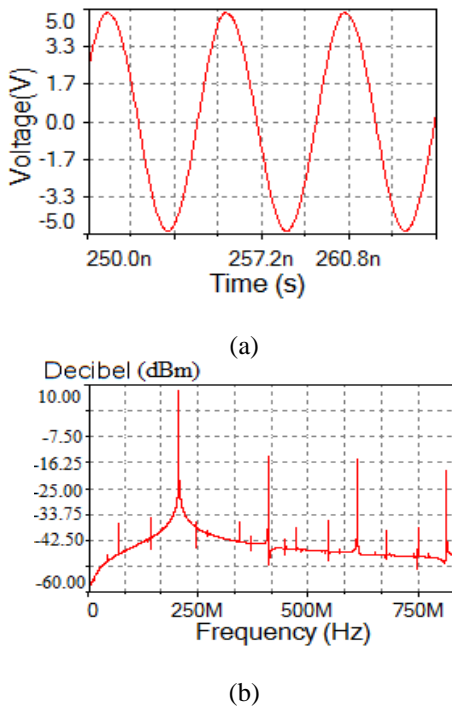


Figure 19. Simulated waveforms of the capacitive feedback oscillator:  
 (a) sinusoidal voltage at node 2;  
 (b) output power spectrum with RF=122.07kHz at node 2

From Fig. 19 follows that the amplitude and power of simulated signal at node 2 are 5V and 9dBm, respectively. The simulated value of the THD is 0.9%.

#### 4. CONCLUSIONS

In this paper we have presented two operational amplifier VCO architectures. Highly accurate ac equivalent circuits of the VCOs have been developed, providing a practical insight into the negative impedance generation mechanism. For both VCOs the analytical equations were derived for computing the output voltage amplitudes.

The proposed VCOs have a number of unique properties. Firstly, the tank circuit is connected at the non-inverting input of the operational amplifier having extremely high input resistance. Therefore, the tank circuit is not shunted by the active element as it is in the Colpitts and Hartley VCOs. Secondly, the VCOs comprise small number of circuit components and by using low-noise operational amplifiers can provide the level of internal phase noise approaching to the tank circuit phase noise, which is the minimum. Thirdly, since the voltage follower gain is equal to unity, the maximum oscillation frequency is theoretically equal to the unity gain bandwidth of the operational amplifier for the capacitive feedback VCO. Fourthly, the oscillation amplitude of the capacitive feedback VCO can exceed the operational amplifier saturation voltage that cannot provide any other known operational amplifier oscillator circuit.

Two practical operational amplifier oscillators have been demonstrated. Both of them were implemented with an ultra low noise ( $0.92\text{ nV}/\sqrt{\text{Hz}}$ ) wideband (1.5GHz) operational amplifier LMH6624. For reducing the parasitic capacitance effect of the connecting cable and spectrum analyzer a unity gain buffer was connected to the oscillator output. The phase noise of -119dBc/Hz and -130dBc/Hz at 500-kHz offset at 273.58MHz and 203.65MHz carrier frequency was achieved for the resistive and the capacitive feedback oscillator, respectively. The total harmonic distortion was, respectively, 2.2% and 1.3%.

#### REFERENCES

- [1] V. V. Ulansky, I. A. Machalin, O. P. Tkalich, "Analysis and Design of Voltage-Controlled Oscillators



- Using High-Speed Operational Amplifiers*”, Proceedings of the National Aviation University, Kiev, № 3 (14), 2002, pp.171-178.
- [2] M. M. Jakas, “*LC Sine-Wave Oscillators Using General-Purpose Voltage Operational-Amplifiers*”, Int. J. of Electrical Eng. Education, Vol. 44, No. 3, September 2007, pp. 244-248(5), Manchester University Press.
- [3] T. H. Lee, “*The Design of CMOS Radio Frequency Integrated Circuits*”, 2<sup>nd</sup> Ed., 2007, Cambridge University Press.
- [4] V. V. Ulansky, I. A. Machalin, “*Low-Noise Voltage-Controlled Oscillators Based on Operational Amplifier Voltage Followers*”, Information Protection, Kiev, №2, 2004, pp. 62-70.



## Effect of the driver parameters on the switching losses of the IGBT switch at high frequency applications

H. Abo-Zied  
Omar al Muktar University  
Faculty of engineering,  
Elect. Eng. Dept.  
Al-bieda, Libya  
yassmen1@yahoo.com

F. Al-Abdaly  
Omar al Muktar University  
Faculty of engineering,  
Elect. Eng. Dept.  
Al-bieda, Libya  
elabdli@hotmail.com

### Abstract

Electric energy with high frequency ( $>100\text{kHz}$ ) and high power ( $>100\text{kW}$ ) is required in many types of processing metallic materials like surface tempering, heating, melting, tube welding and others. The frequency depends strongly on the technological process, for future technological development, a frequency up to 500 kHz is attractive. At high frequency applications as induction heating, the switching losses of the IGBT switch are very high. The IGBT losses are totally dominated by the turn-off losses. The switching performance of an IGBT module depends upon the drive circuit characteristics and external dc loop inductance. So, the present paper study by the Pspice simulation results, the influence of the IGBT driver parameters as positive gate voltage, negative gate voltage and gate resistance on the IGBT switching losses during the operation of H bridge inverter containing two IGBT modules at high power high frequency (400 KHz). Also the influence of the temperature on the IGBT Losses is covered. From this study, the optimum values of the IGBT driver parameter, which give minimum IGBT switching losses, was cleared.

### Introduction

The insulated gate bipolar transistor (IGBT) is popularly used in high power, high frequency power-electronic applications such as pulse width modulated (PWM) inverters. At high switching frequencies, switching losses constitute a significant portion of the device power dissipation. The IGBT can change its switching properties through the gate drive, so designing a proper gate drive is extremely important to the performance of the IGBT. So-called the "best performance" of the IGBT is different by application, which means the design of the gate drive

must be different depending on the application of each IGBT.

In order to obtain the optimum performance from the IGBT, it is of foremost importance to design a gate drive that is suited for the application. As such, this paper intends to discuss the characteristics of IGBT and some issues to consider in designing a gate drive as well as providing necessary information in designing an application system to help engineers who design systems using IGBT. In order to do so, one must select a device that satisfies the ideal conditions as much as possible, and then the optimum gate

drive must be designed for the system to realize the best performance. The positive gate bias voltage, gate resistance, max gate current, drive layout, and drive power rating are some of the basic parameters necessary in designing a gate drive. It is necessary to understand each of the parameters as well as the characteristics of IGBT switching in order to design a gate drive. This study examines characteristics of IGBT and gate drive parameters; discuss the relationships between the two, and some issues to consider in designing a gate drive.

### IGBT switching losses in high frequency applications

To study the influence of the IGBT gate driver parameters on the IGBT switching performance, an inverter-module will be simulated using PSpice programmer. The maximum output power rating of the inverter is mainly limited by the IGBT losses. So, the turn-off losses must be decreased.

A different Spice-model of the IGBT transistor will be used as switching devices. The IGBT module equipped with the fastest, thinner transparent emitter NPT type chips. The schematic system diagram of the voltage-fed type series load-resonant inverter, which will be simulated in PSpice, is shown in Fig. (1). The switching performance of an IGBT module depends upon the switching frequency and the drive circuit characteristics. Most important are the switching transients and losses within a module. So, the influence of these parameters on the switching losses, diode recovery, switching voltage transients, short-circuit operation and  $dv/dt$  during the operation of the inverter at high frequency and high power will be discussed in detail.

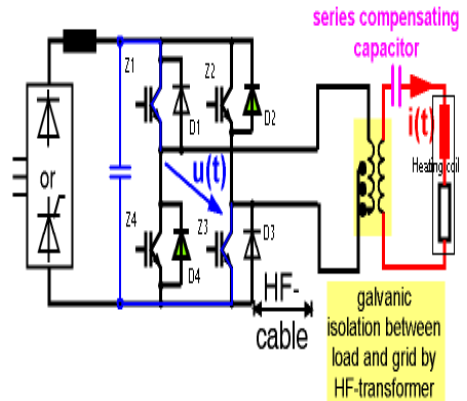


Fig.(1) A series resonant inverter generator

There are three steps to decrease the switching losses. These steps are: using a suitable IGBT, using high-speed IGBT devices and using soft switching technology such as resonant switching.

#### 1) Using a suitable IGBT

The switching losses of the IGBT depend on its characteristics. It is found that IGBTs though having the same data sheet rating, IGBTs can have very different properties depending on the manufacturer's philosophy and this gives IGBTs different behavior [1]. This is because there are two types of the IGBT manufacturers philosophy. The first is the devices from manufacturers using low carrier lifetime and high bipolar emitter efficiency, such as Toshiba. The second is the devices which having the same data sheet ratings both in current, voltage and switching speed from manufacturers using high carrier life time and low bipolar emitter efficiency like Siemens devices.

#### 2) Using a high speed IGBT

The switching losses of the IGBT depend on the switching time. So, the direct



and simple method to decrease the switching losses at high frequency applications is by using the high speed IGBT available today [2].

### 3) Using soft switching technology

At very high frequency applications, the switching losses are very high even though when high-speed IGBT switches are used. So, soft switching technology such as resonant must be used in high frequency high power inverters. In this study, the series resonant inverter is used.

At very high frequency 400KHz, even for selecting suitable IGBTs, using very fast IGBTs available today and using series resonant as soft switching technology, the switching losses of the IGBT switch are still very high and the IGBT losses are totally dominated by the turn-off loss. This is because the tail current lasts for several microseconds, and thus it represents the main source of the turn-off losses [2-5]. Also, the switching performance of an IGBT module depends upon the drive circuit characteristics and the external dc loop inductance. So, the influence of the IGBT driver parameters as positive gate voltage, negative gate voltage and gate resistance on the IGBT switching losses will be explained in the following parts in detail to reach the optimum IGBT driver parameters. This study is during the operation of H bridge inverter containing two IGBT modules (FF200R12KS4) at high power high frequency. Thus, a voltage-fed series resonant modular IGBT converter system for high power high frequency induction heating applications can be proposed at reasonable cost and minimum IGBT switching losses.

### Simulation of switching transients

To study the influence of the IGBT gate driver parameters on the IGBT switching performance, an inverter-module will be simulated using PSpice programmer. A Spice-model of the Eupec FF200R12KS4 transistor will be used as switching devices. The FF 200 is a 1200V, 200A IGBT module equipped with the fastest, thinner transparent emitter NPT type chips from Infineon technologies.

The simulation results at  $f = 400\text{KHz}$  are shown in Fig.(2) and Fig.(3), where

$$V_{dc} = 600V,$$

$V_{ge} = +15V \dots to \dots -15V$ . Figure (2)

shows the waveforms of the gate signals voltage, the collector currents of the IGBT Z1 and Z4, and the load current. Figure (3) shows the switch waveforms. From these results, the total energy losses are 6.5mJ and the turn-off losses are 5.5mJ. This means that the turn-off losses are equal about 85% of the total losses and the  $dV_{ce}/dt$  at turn-off is equal 4.8KV/us. It can be seen from Fig. (3) that the tail-losses are the dominant ones because the tail current continues and does not reach to zero instantaneously. So, the dead time between the upper and lower transistor is very important and very critical. There occurs an overlapping conduction of both transistors in one arm. The lower IGBT Z4 is gated "on" during the turn-off process of the upper IGBT Z1. Therefore, a transient "shot through" happens as shown in Fig. (2), where the current through the upper IGBT during its turn -off process increases temporarily. During the "shot through" the peak losses occur as shown in Fig. (3). And this leads to very high turn-off losses. If the dead time increases, the output power will decrease and if the dead time decreases, the



turn-off losses will increase. So, the dead time must be selected to give optimum solution. For this work, 100 ns is optimum solution to give minimum turn-off losses (the simulation results were calculated at different values of the dead time 50ns, 100ns, 150ns, and 200ns)

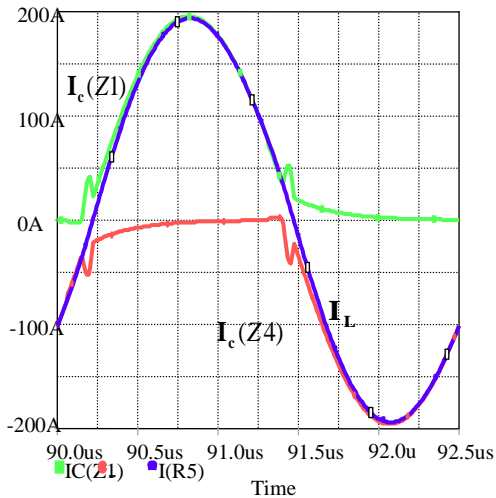
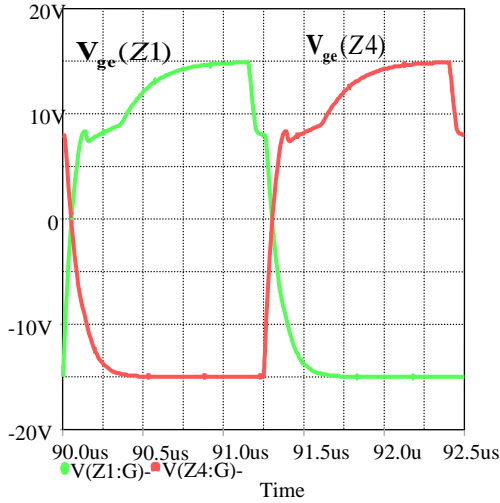


Fig. (2) The waveforms of the gate signals voltage, the collector currents of the IGBT

Z1 and Z4, and the load current at f= 400KHz

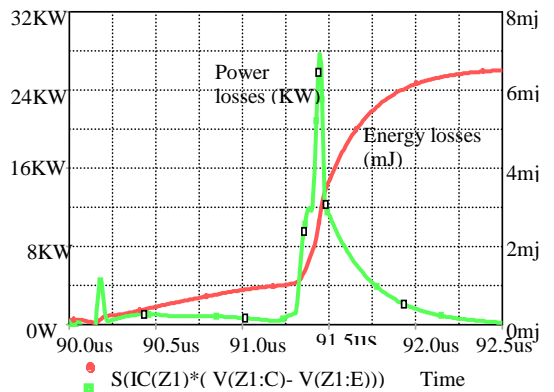
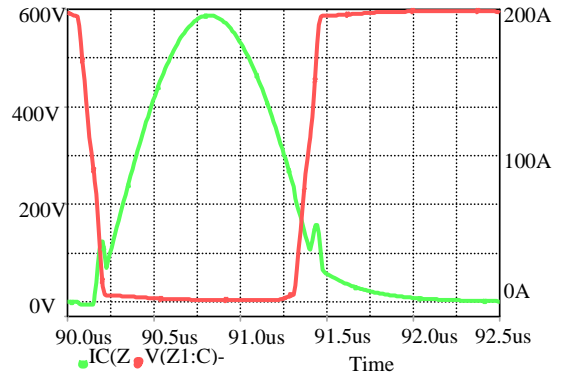
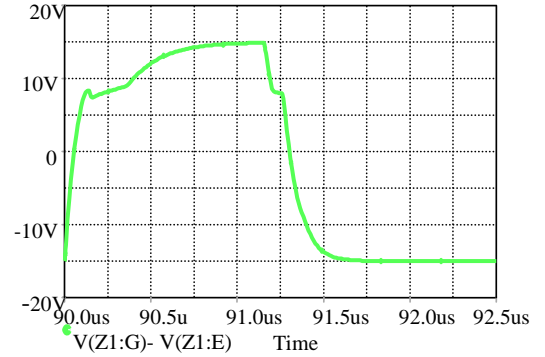


Fig.(3) The switch waveforms at F = 400 KHz



### Driver parameters

From the above results, at high frequency, the switching losses of the IGBT are very high and the IGBT losses are totally dominated by the turn-off losses. IGBTs are voltage controlled devices and require gate voltage to establish collector-to-emitter conduction. Recommended gate drive circuitry includes substantial on and off biasing as shown in Fig. (4) [6].

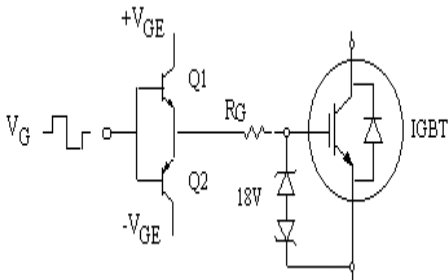


Fig.(4): Typical gate drive circuitry

### Influence of the negative part of the gate signal ( $V_{GE} (-)$ ) on the switching losses

A +15V positive gate drive is normally recommended to guarantee full saturation and limit short circuit current [7-8]. A negative voltage bias is used to improve the IGBT immunity to collector-to-emitter  $dv/dt$  injected noise and reduces turn-off losses as shown in Fig.(5) and Fig.(6). These figures shows the transient waveforms of the gate voltage, collector current, and collector-emitter voltage, switching losses and the energy losses for one period for two cases of the gate voltage. The first one is, the negative bias voltage is -10V and the second, negative bias voltage is -15V.

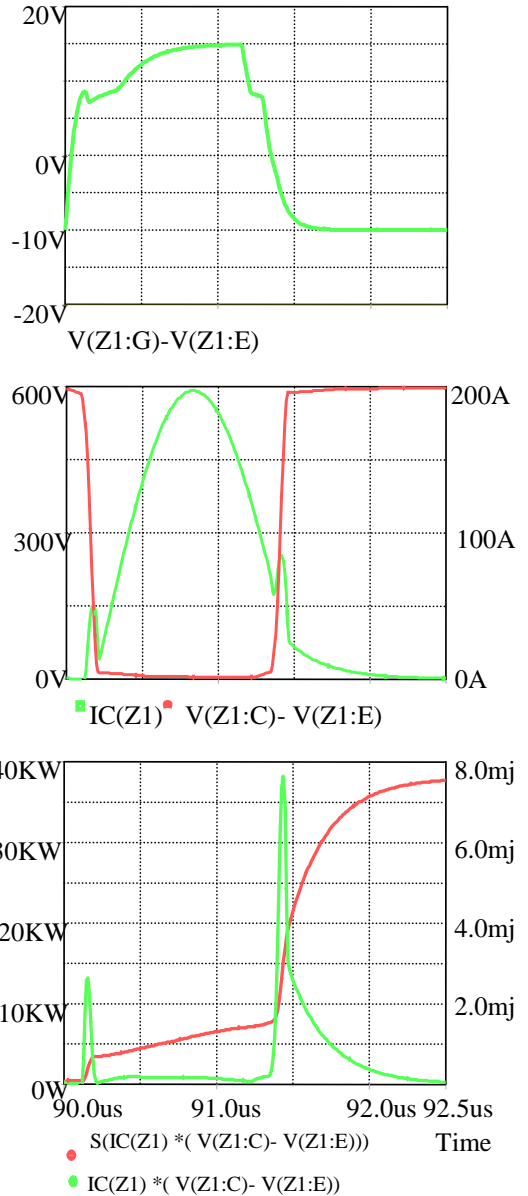


Fig.(5) Simulation result for:  
 Eupec FF 200R12KS4,  $V_{dc}=600$  V,  
 $f = 400$  KHz,  $R_g= 3\Omega$

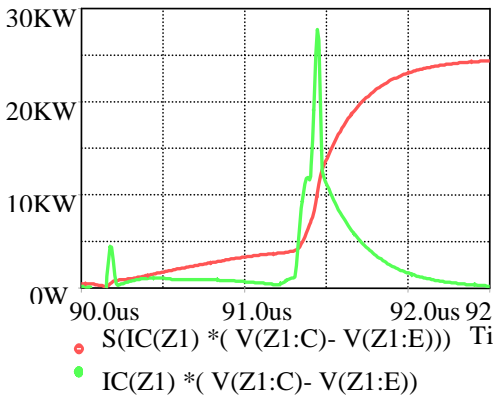
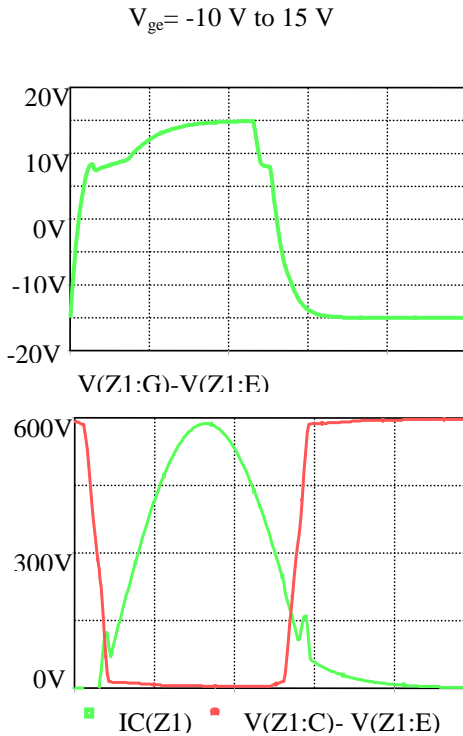


Fig.(6) Simulation result for:  
 Eupec FF 200R12KS4,  $V_{dc}=600 \text{ V}$ ,  
 $f = 400\text{KHz}$ ,  $R_g = 3\Omega$   
 $V_{ge} = -15 \text{ V to } 15 \text{ V}$

From this study, the turn off losses are decreased when the negative bias of the gate voltage is increased as shown in Fig. (7). Also, from this figure, the turn-off losses are found to vary little when the value of the negative bias voltage lies between  $-12\text{V}$  to  $-15\text{V}$ .

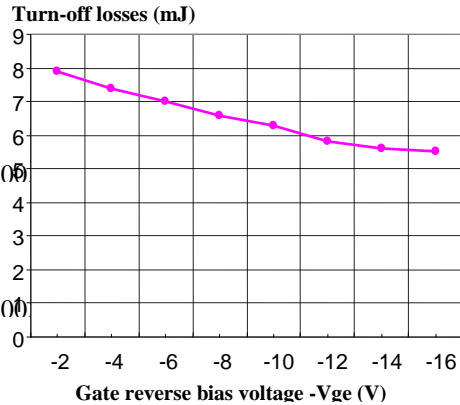


Fig.(7) Effect of negative bias on turn-off losses at  $V_{dc}=600 \text{ V}$ ,  $f = 400\text{KHz}$ ,  $R_g = 3\Omega$

### Influence of the positive part of the gate signal (VGE (+)) on the switching losses

Although a +15 V positive part of the gate drive is normally recommended to guarantee full saturation and limit short circuit current, at high frequency, the turn-off loss is very large [9]. The turn-off losses can be decreased by decreasing the positive part of the gate voltage as shown in Fig. (8). Figure (8) shows the influence of the positive part of the gate signal on the IGBT switching and conduction losses during the operation of H bridge series resonant inverter containing two IGBT modules (FF200R12KS4) when  $V_{dc} = 600\text{V}$ ,  $f = 400\text{KHz}$ , and  $R_g = 3\Omega$ . However, by reducing the positive part of the gate





voltage, the conduction losses increase as shown in Fig. (8). Also, the short circuit current increases by reducing the positive part of the gate signal. So, this solution is, however, in direct conflict with reduction of the conduction losses and short circuit current. A compromise needs to be made to satisfy the circuit performance criteria. For our study, the positive parts of the gate voltage must not be less than +12V; this value is optimum for our inverter (Fig. (8)).

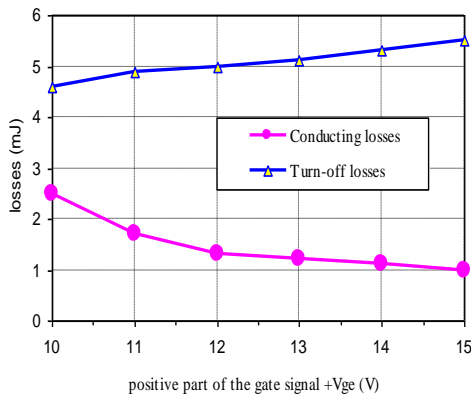


Fig.(8) Effect of positive part of the gate driver voltage on the losses at

$$V_{dc} = 600V, f = 400KHz, R_g = 3\Omega$$

### Influence of the gate resistance on the switching losses

The value of the gate resistance has a significant impact on the dynamic performance of IGBTs. A smaller gate resistance charges and discharges the IGBT input capacitance faster reducing switching times and switching losses and improving immunity to  $dv/dt$  turn-on. Figure (9) shows the influence of the gate resistance on the IGBT turn-off losses during the operation of H bridge series resonant inverter containing two IGBT modules (FF200R12KS4) when  $V_{dc} = 600V$ ,  $f =$

400 KHz, and  $V_{ge} = +15V$  to  $-15V$ . It can be seen that, the turn-off losses are found to vary little with the gate resistance. When the gate resistance increased from  $1.5\Omega$  to  $3\Omega$ , the turn-off losses increased by 20%. The bipolar stage of the IGBT exhibits tailing current at turn-off due to the stored minority carriers in the transistor base region which must be allowed to recombine and cannot be removed through the gate. However, a small gate resistance can lead to oscillations between the IGBT input capacitance and the parasitic lead inductance. Also, reducing the gate resistance is in direct conflict with reduction of the over voltage and the higher gate resistance is recommended for the snappier device to reduce the overshoot at turn-off. So, a compromise needs to be made to satisfy the circuit performance criteria. For our application (400 KHz, 600V, 200A), the value of the gate resistor must not be higher than  $1\Omega$ .

The critical factor that determines the limits of the safe operation during turn-on, is the transient over voltage developed across the diode as it recovers and hence, also, across the anti-parallel IGBT. The peak diode recovery voltage must be constrained within the rated voltage, by setting appropriate limits on the operating conditions of the module. The peak diode recovery voltage depends upon the dc supply voltage, the dc loop inductance, and the peak diode reverse recovery current in combination with the diode's recovery  $di/dt$ . The peak reverse recovery current and recovery  $di/dt$  themselves depend upon the diode junction temperature, the initial amplitude of the diode forward current and the rate of increase of the IGBT current ( $di_c(on)/dt$ ). The rate of increase of the



IGBT current ( $di_c(on)/dt$ ) can be controlled by setting the value of the gate resistance in combination with the amplitude of  $V_{ge}$  during the turn-on. Very low values of series gate resistance, besides producing high diode recovery voltage transients, could give rise to unacceptable ringing during recovery. The stray inductance and parasitic capacitance form a resonant circuit that will be set into damped oscillation. The electrical noise thus produced could interfere with control and protection circuits. The reduction of the problem is simple either to reduce the gate drive voltage or to increase the series gate resistor. This solution is, however, in direct conflict with the reduction of the switching losses. During turn-on, as mentioned in the previous section, diode recovery  $di/dt$  combined with the dc loop inductance produces a recovery voltage transient. This recovery voltage transient needs to be limited to at least the rated breakdown voltage of the diode and the IGBT in parallel with it. A trade-off between this voltage overshoot and the turn-on losses is necessary. It is important that the dc loop inductance is kept as low as possible.

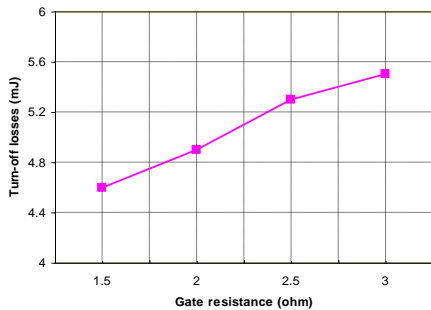
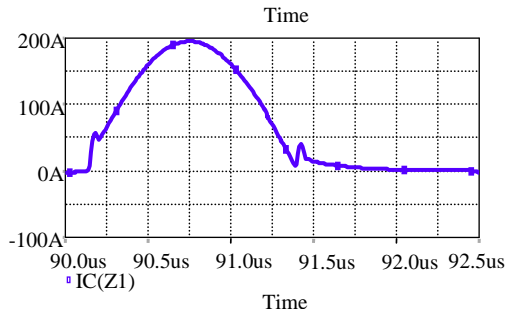
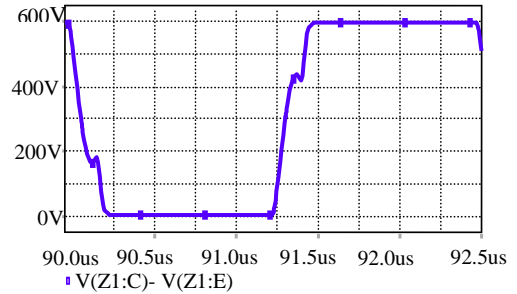


Fig.(9): Effect of gate resistance on the turn-off losses at  $V_{dc} = 600V$ ,  $f = 400KHz$ ,  $V_{ge} = +15V$  to  $-15V$

### Effect of the temperature on the switching losses

From the above discussion, when the series resonant inverter operates at  $f = 400KHz$  and  $V_{dc} = 600V$ , the IGBT driver parameters are  $V_{ge} = +12V$  to  $-12V$ ,  $R_g = 1\Omega$ , and the dead time between the upper and lower IGBT transistors in the same leg is equal 100ns to reach the optimum switching losses (i.e. minimum switching losses). Figure (10) and Fig.(11) show the simulation results at optimum IGBT driver parameters (i.e. minimum switching losses) for two cases, at  $25^\circ C$  and  $125^\circ C$ .



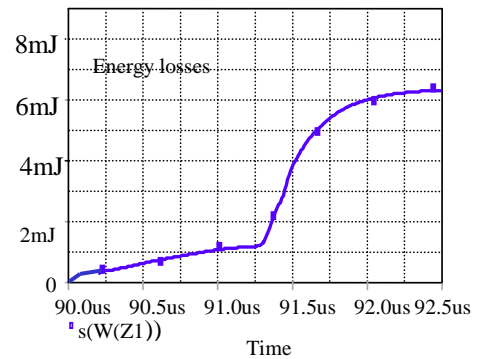
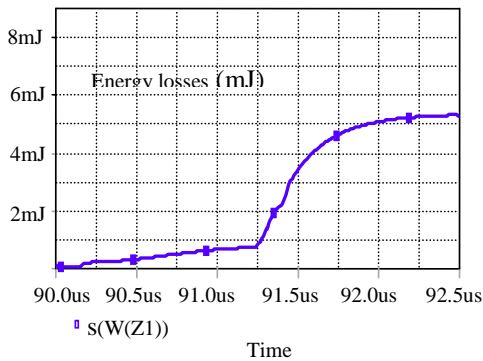
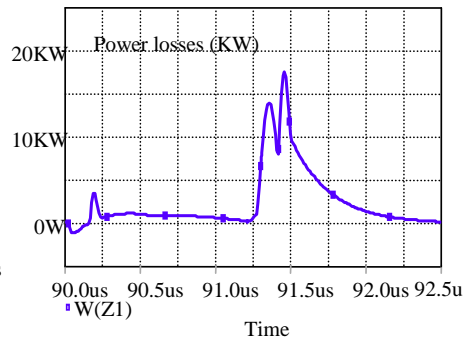
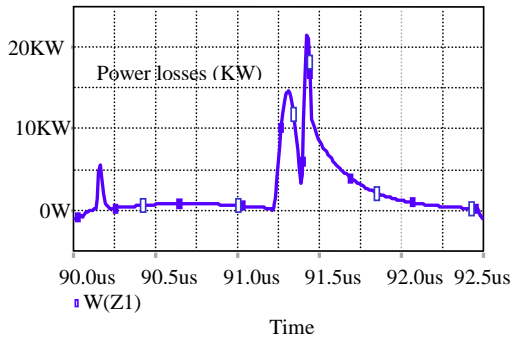
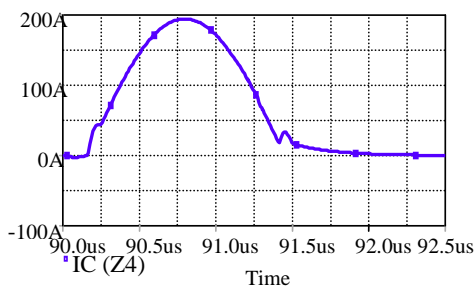
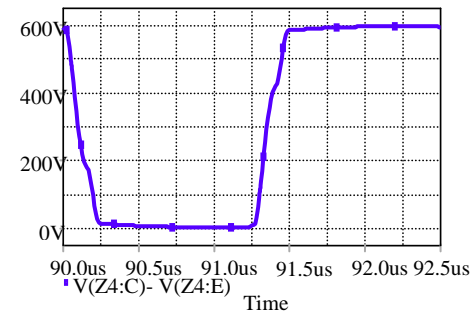


Fig (10) The simulation results at  $t = 25^{\circ}\text{C}$

Fig.(11) The simulation results at  $t = 125^{\circ}\text{C}$



Almost all electrical characteristics of IGBTs are dependent on the chip temperature. At rising temperature, avalanche breakdown voltage will increase and the blocking current will, also, increase. Hence the blocking power dissipation and the forward-on stage losses will increase, and turn-on, turn-off time will increase. In other words, turn-on and turn-off losses will increase. Also, threshold voltage will decrease. The total energy losses at  $25^{\circ}\text{C}$  and  $125^{\circ}\text{C}$  were equal to 5.3mJ and 6.4mJ respectively. This means that, the total energy losses at  $125^{\circ}\text{C}$  increased by 21%. The turn-off losses at  $125^{\circ}\text{C}$  increased by 16% and the conduction losses increased by 50%.



## Conclusions

Most important are the switching transients and losses within a module. At high frequency, the switching losses of the IGBT switch are very high and the IGBT losses are totally dominated by the turn-off losses. The switching frequency strongly affects the switching losses of the IGBT. When the switching frequency increases from 100KHz to 400KHz, the total energy losses increased from 4.8mJ to 6.5mJ for one period at the same conditions. The switching losses strongly depend on the driver parameters, and the device temperature.

The turn-off losses decreases by nearly 17 %, when the positive part of the gate voltage decreases from +15V to 10V. However, the conduction losses increase by 150 %. So, the positive parts of the gate voltage must not be less than +12V.

The value of the gate resistance must not be higher than  $1\Omega$ , because the transistor can not reach saturation during the turn-on, and the conduction losses will increase, especially, when the positive parts of the gate voltage is low.

## References

- [1] J. K. Johansen, F. Jensen and T. Rogne "Characterization of high power IGBT's with sinewave current", IEEE Transactions on Industry Applications, Vol. 30, No. 5, September/October 1994, PP. 1142-1148.
- [2] Ulrich Schwarzer and Rik W. De Doncker, "Power losses of IGBT in an inverter prototype for high frequency inductive heating applications", IECON'01, the 27<sup>th</sup> Annual Conference of the IEEE Industrial Electronics Society, 2001, PP. 793-798.
- [3] A. Okuno, S. Shirakawa and M. Nakaoka "Latest developments of voltage-fed resonant high frequency inverter with load resonant frequency tracking scheme for induction heating", IEE 1998, Power electronics and variable speed drives, 21-23 September 1998, PP. 152-157.
- [4] W. Berkan, A. Michalski, S. Serafin and K. Zymmer, "50 KHz, 25 KW frequency converter with IGBT for induction heating", PEMC' 94, Warsaw, Poland, 20-22 September 1994, PP. 537-542.
- [5] A. D. Rajapakse, A. M. Gole, and P. L. Wilson, "Approximate Loss Formulae for Estimation of IGBT Switching Losses through EMTP-type Simulations", International Conference on Power Systems Transients (IPST'05), Montreal, Canada, June 19-23, 2005, paper No. IPST05 - 184.
- [6] International Rectifier application note AN-937, AN-990 "Application characterization of IGBTs", Power Designers, copyright 2001 International Rectifier, PP. 1-20.
- [7] Gary Aw, "IGBT Gate Drivers in High-Frequency Induction Cookers", Power Systems Design Europe, www.powersystemsdesign.com, December 2007.
- [8] Dusan Graovac and Marco Purschel, "IGBT Power Losses Calculation Using the Data-Sheet Parameters", Published by Infineon Technologie AG, 85579 Neubiberg, Germany, January 2009.
- [9] H. Robert, "Intelligent IGBT - Drivers with Exceptional Driving and Protection Features", EPE 2009 - Barcelona ISBN: 9789075815009 P.1, 2009.



## ***Multi-chip modules (MCM) factors***

Assia A. Hanzaz and Abdelsalam Ambarek

**Abstract-** New electronic systems for automotive/industrial/medical/aerospace will continue to challenge both packaging engineers and technology due to the increased performance requirements, higher densities and limited space available. This challenge mandates the use of unique packaging techniques such as multi-chip modules (MCM). MCM is advanced technology in this time its categories depends on the substrate. An MCM combines high performance ICs with common substrate structure that provides mechanical support for the chips and multiple layers of conductors to interconnect them. The feature of MCMs is the complex substrate structure that is fabricated using multilayer ceramics, polymers, silicon, metals, glass ceramics, laminates, etc. This paper provides a factors of different Multi-Chip Module (MCM) types. The criteria which are looking at study are: Dimension properties, Electrical properties, Mechanical properties and Thermal properties.

**Keywords:** Microelectronic technologies, MCM technology, martial characteristic.

### **I. Introduction**

The expanding market for high-density electronic circuit layouts calls for multi-chip modules (MCMs) to be able to meet the requirements of fine track and gap dimensions in signal layers, the retention of accurately defined geometry in multilayers, and high conductivity to minimize losses. Multi-chip module technologies fill this gap very nicely; however there are many factors such Dielectric constant,

dissipation factor, CTE and others must be taken at mind before application used.

The multi-chip module (MCM) is a single electronic package containing more than one integrated circuit (IC) die. Depending on substrate MCM can be categorized into three types: Laminated Substrates MCM (MCM-L), Multilayer Ceramic Technology (MCM-C) and Thin Film MCM Technology (MCM-D). Dimension properties, Electrical properties,



Mechanical properties and Thermal properties must be known before any use at manufacturing or application.

## II. Electrical line parameters

Figure (1) shows physical parameters for transmission line of MCM types [4], the transmission line parameters (electrical line parameters) are shown in table (1).

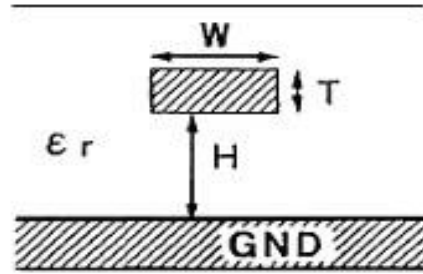


Fig. 1. Physical parameters for transmission line

TABLE 1 ELECTRICAL PARAMETERS OF MCM TYPES

Specification $s$	H $\mu\text{m}$	W $\mu\text{m}$	T $\mu\text{m}$	R $\Omega/\text{cm}$	C $\text{nF}/\text{cm}$	L $\text{nH}/\text{cm}$	Zo $\Omega$
MCM-L	200	200	35	0.05	1.2	3.9	60
MCM-C	200	125	25	0.5	2.7	4.1	40
MCM-D	10	25	3	2	1.2	3	50

## III. Dimension properties

The dimensions differ at each type which is a challenge for designer engineer and MCM

technology. Table (2) gives the dimension properties comparison of MCM types.



TABLE 2 DIMENSION PROPERTIES COMPARISON OF MCM TYPES

	MCM-L	MCM-C	MCM-D
<b>Line width</b> (□m)	<i>Typical</i> :50-300 Epoxy-glass :50-150 Cu/Epoxy :75-150	<i>Typical</i> : 50-150 Thick film :100- 125 HTCC: 100-200 LTCC: 50- 150	<i>Typical</i> : 10- 35 Polyimide: 15 Si: 10-30
<b>Line Pitch</b> (□m)	<i>Typical</i> : 150- 600 Epoxy-glass :100- 1000 Cu/Epoxy :150- 300	<i>Typical</i> : 100- 800 Thick film :120- 375 HTCC: 100-500 LTCC: 100-500	<i>Typical</i> : 25- 75 Polyimide: 25-60 Si : 30- 60
<b>via diameter</b> □□m)	<i>Typical</i> : 90- 300	<i>Typical</i> : 75- 200 HTCC : 100- 200 LTCC : 100- 200	<i>Typical</i> : 10- 30
<b>Via size</b> □□m)	<i>Typical</i> : 200	<i>Typical</i> : 100-125	<i>Typical</i> : 10-50 Polyimide: 30-50 Si : 15-30
<b>via Pitch</b> (□m)	<i>Typical</i> : 1270 -2540	<i>Typical</i> : 200 HTCC : 225- 625 LTCC : 225- 625	<i>Typical</i> : 30-100
<b>Pad size(mm)</b>	4	5	3
<b>Pad Pitch</b> (mm)	6	10	4
<b>Average number of layers</b>	6-10	>50	4-6
<b>Resolution in lines and spaces</b>	lowest which is currently being limited to 25 -50 μm	intermediate resolution	highest Due to the thin film processes.



Note:

- ◆ There are many values from many fabrication companies are different, here the average at summary.
- ◆ The pad size and pitch in the table here are a maximum.
- ◆ In MCM-L the smaller vias and fine lines compared to PWB (Printed wired board) allow more signal lines to be routed between the pads, thereby reducing the overall number of layers required.
- ◆ One of MCM-L disadvantages is the vias are drilled and plated and in many fabrication processes incorporate large capture pads that can cause noticeable signal-

contaminating wave front reflections.

- ◆ In MCM-C high number of layers increase wiring density.
- ◆ MCM-D has been the solution for integrated high density packaging due to its superior line resolution and higher inputs/outputs (I/O) density compared to MCM-C and multi-chip module-laminate (MCM-L) technologies [1].

If we take the minimum value at range of dimension and draw the curve shown at figure (2), it gives the light of the difference between the three types of MCM. {Note they measured by ( $\mu\text{m}$ )}. We see from figure (2) the MCM-D is the best one at Miniaturization

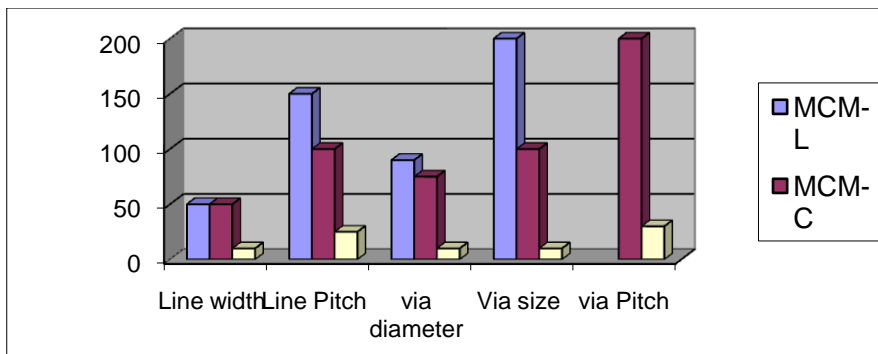


Fig.2. Dimension comparison between the three type of MCM





#### IV. Electrical properties

The electrical properties are differed from type to type and from material to other, this give us the limited at electronic applications, as example dielectric constant is low especially at high frequencies thus give good

performance as same as in dissipation factor. The parameters shown in *table (3)* give the electrical performance of each type for MCM technology with materials used.

TABLE 3 ELECTRICAL PROPERTIES COMPARISON OF MCM TYPES

	MCM-L	MCM-C	MCM-D
<b>dielectric constant (<math>\epsilon_r</math>) from 1MHz- 10 GHz</b>	FR-4 : 4.40- 4.80 Epoxy-glass* :2.8- 4.5 Cu/Epoxy :4.8 Polyimide : 4-4.6	Thick film :6.3- 9.2 Thick film on Alumina: 4.5- 9 HTCC: [Al <sub>2</sub> O <sub>3</sub> : 9-9.5, AlN: 8.6] LTCC: 5- 9 [glass ceramic:7.4]	Alumina : 9.9 Polyimide: 2.8- 10 BeO : 6.3 Si :3.8
<b>Dissipation Factor (tan<math>\delta</math>) from 1MHz- 10 GHz</b>	FR-4 : 0.020- 0.025	HTCC: [Al <sub>2</sub> O <sub>3</sub> :0.0002- 0.0006, AlN: 0.0001-0.0005] LTCC: 0.009- 0.0002 [glass ceramic: 0.0011]	Alumina: 0.0001- 0.0002
<b>Resistivity (<math>\Omega.cm</math>)</b>	<8000	> 10 <sup>14</sup> all type of ceramic	> 10 <sup>14</sup>
<b>Dielectric thickness (<math>\mu m</math>)</b>	75- 100	100-300	5- 20
<b>Clock rate</b>	<100 MHz @ 2002** >100 MHz @2004 =150MHz @ 2005	> 25MHz @ 2002 Thick film : 7 GHz @ 2004 Thick film on Alumina: 40 GHz @ 2005 LTCC: 77GHz @ 2005 Low loss: 98GHz @ 2005	> 120 MHz @ 2002 > 20 GHz @ 2003 50 GHz @ 2004 100 GHz @ 2005

\* Epoxy/glass with different developed material itself

\*\* The year



Note:

- ◆ At MCM-L the moisture sensitivity of materials and high crosstalk noise are two disadvantages must taken in the account.
- ◆ MCM-C is preferred alternative when Large number of embeddable passives, RF coupler, Filters, large number of IC's are often built into ceramic MCMs.
- ◆ High-temperature co-fired ceramic multi-chip modules (MCM-Cs, HTCC) exhibit the lowest routing density of the available MCM options and employ a substrate material with a high dielectric constant ( $\epsilon_r=8-10$ ) which results in long propagation delays and higher levels of crosstalk.
- ◆ MCM-D is highest performance, good electrical proprieties and excellent technical parameters (crosstalk, reflexions).
- ◆ In MCM-D termination resistors and de-coupling capacitors may be integrated in the substrate with high quality integrated passives.
- ◆ MCM-D has very good high frequency properties. It used for high-frequency circuits requiring thin-film

inductors or controlled impedance lines [1].

☒ **Frequency state in MCM**

High frequency property is one of important benefit of MCM technology. MCM-L is poor at high frequency; high-performance processors ( $>1$  GHz) is challenging the limits of FR-4, but Ceramic technologies are used in microwave circuits , we can take these material as a brief:

*MCM-C:*

*Thick film on alumina* up to about 40 GHz

*LTCC* up to about 77 GHz

*MCM-D:*

*Thin film technology* up to about 100 GHz for advantages of low loss and excellent dimensional stability.

The use of MCM-L (by FR-4) is limited by its high losses in the microwave frequency range as well large variations in dielectric constant from manufacturer to manufacturer. MCM-C made with LTCC technology have been shown to have lower losses than MCM-L made with conventional organic FR-4 laminate technology. *Figure (3)* illustrates the curves of these materials.



### Mechanical properties

Mechanical properties give the users the force of the technology chosen. *Table (4)* gives the mechanical properties comparison of MCM types.

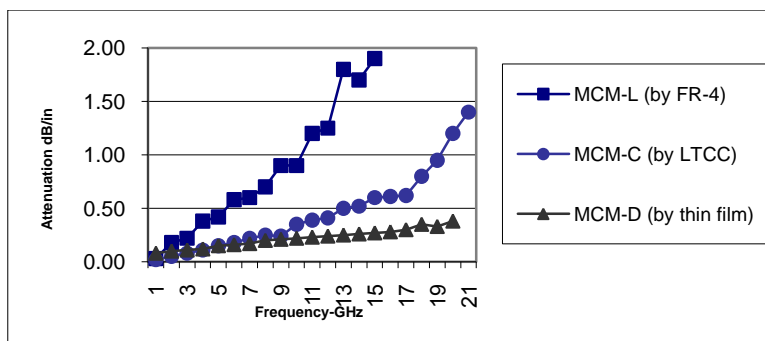


Fig. 3. Comparative of MCM types from Attenuation view.

TABLE 4 MECHANICAL PROPERTIES COMPARISON OF MCM TYPES

	MCM-L	MCM-C	MCM-D
<b>Thermal Conductivity (W/m<sup>0</sup>C)</b>	0.2- 0.3	Thick film : 20-26 HTCC: 25-160 [ AIN :160 , Al2O3:25] LTCC: 2	3.6- 25.1
<b>Coefficient of Thermal Expansion CTE (ppm/<sup>0</sup>C)</b>	10-15	Thick film: 6.4 HTCC: 6-7 HTCC [AIN : 4.8, Al2O3: 6.5- 7.6] LTCC: 3-8 LTCC [glass ceramic :3.5- 7.5, Al2O3: 7.1]	6.4- 7.1
<b>Density (g/cm<sup>3</sup>)</b>	1.7	Thick film: 3.92 HTCC: 3.3 HTCC [AIN : 3.2-3.3,	3.8- 3.9



		Al <sub>2</sub> O <sub>3</sub> : 3.3- 4.0] LTCC: 2.57-3.9 LTCC [glass ceramic:2.5-3.1]	
<b>Flexural Strength (MPa)</b>	N/A	Thick film: 200- 400 HTCC: 420 HTCC [AlN : 340- 450, Al <sub>2</sub> O <sub>3</sub> :480- 520] LTCC: 210 LTCC[glass ceramic:230-280]	90

Note:

- ◆ The need for matched CTE's (Coefficient of Thermal Expansion) between the active device and the package substrate is important, as this is low and matching to substrate, the quality is increased. CTE is differed from material to material which enters to make MCM .For same material CTE is change due to the change in temperature degree. For MCM-L the high significant CTE mismatch between substrate and die material is
- ◆ one of disadvantages which must taken in the account.

- ◆ For MCM-C the mechanical properties is differed from Thick film to co-fired ceramic technologies.
- ◆ High thermal conductivity to handle a wide range of heat dissipation requirements is important thing at heat dissipation. The thermal conductivity of Alumina 100 times MCM-L (FR-4) , LTCC 10 times FR-4. HTCC is high which is the best at heat dissipation[1].
- ◆ MCM-D has □very good mechanical properties.

The important two factors of Mechanical properties are Thermal Conductivity TC (W/m<sup>0</sup>C) and Coefficient of



Thermal Expansion CTE ( $\text{ppm}/^{\circ}\text{C}$ ), the comparison of three types is drawn at the curve as shown in figure (4).

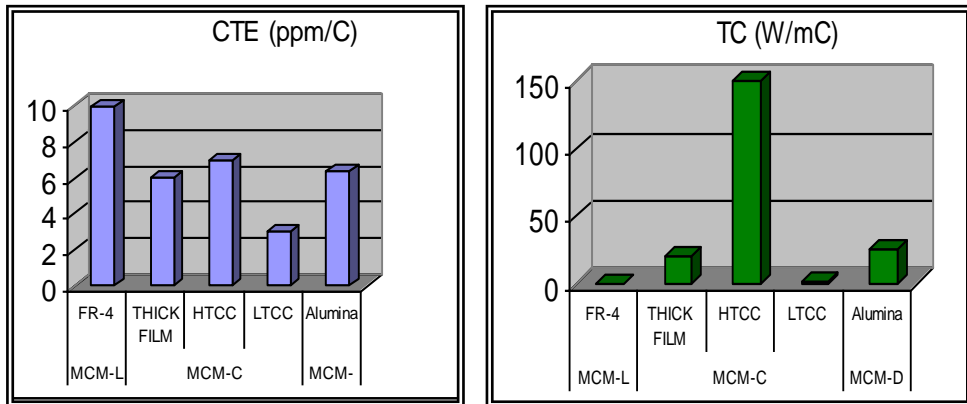


Fig.4. TC and CTE comparison of MCM types

## V. Thermal properties

Table (5) gives the thermal properties comparison of MCM types as important thing in comparative study

TABLE 5 THERMAL PROPERTIES COMPARISON OF MCM TYPES

	MCM-L	MCM-C	MCM-D
<b>Thermal Coupling</b>	It is the best laminated onto the surface of the thermoelectric cooler and is thus offering a cost-effective manufacturing technology.	Al <sub>2</sub> O <sub>3</sub> is not offering sufficient thermal coupling for the necessary temperature Stabilization AlN is selected but expensive.	Ceramic not guarantee efficient, but Si & Polymer is better.



	<b>MCM-L</b>	<b>MCM-C</b>	<b>MCM-D</b>
<b>Thermal conductivity</b>	Poor <i>This need complex cooling design .</i>	Good <i>Better than MCM-L</i>	Good
<b>Thermal stability</b>	Medium	Good <i>depend on ceramic type used</i>	Good
<b>Thermal Expansion</b>	High <i>May cause problem when attaching large Si Chips</i>	Low	Excellent
<b>Thermal dissipation</b>	Medium	High	High <i>By Polyimide is better.</i>

Note:

- ◆ MCM-C (by HTCC) has Thermal performance characteristics superior to MCM-L and MCM-D.
- ◆ Copper slugs and cutouts are used in MCM-Ls for direct heat transfer. This degrades interconnection density.
- ◆ Due to substrate material characteristics, for some applications MCM-C forces the designers to choose between relative levels of

thermal and electrical performance, such; HTCC has excellent thermal performance with modest electrical characteristic, while LTCC reverses these attributes.

- ◆ MCM-C is better electrical and thermal conductivity than MCM-L but Lower wiring density than MCM-D.

## VI. Conclusion

Characteristics such as surface chemistry, overall tolerances, coefficient of thermal expansion (CTE) and substrate flatness are important factors at any application. The user should consider all of those factors and



others, including potential toxicity issues and availability of suppliers in order to achieve the greatest cost advantages and best performance for their application. MCM is advanced technology nowadays there are complication with other technology to improve reliability and work of many devices.

### References

- [1] Assia A Hanzaz "Comparative study of multi-chip module types" Thesis at Gar Younis university, July 2007
- [2] [Ferro Corporation, website: http://www.ferro.com](http://www.ferro.com) visited at : Mar 2009
- [3] IBM Corporation, website : <http://www.ibm.com> visited at : Feb 2009
- [4] Takashi Okada and Toshio Sudo "Characterization of Net Configurations for Multichip Modules" IEEE Electronic Components and Technology Conference, pp 32-37, July 1994.
- [5] Michael Weinhold, David J. Powell "Alternatives to FR4" Advanced Fibers

Systems ,website: <http://www.Dupont.com> , visited : Jun 2006

[6] Choma Jr., J., et al. "Multichip Module Technologies" *The VLSI Handbook. Ed. Wai-Kai Chen* . CRC Press LLC, 2000.

### Authors' information

1- Assia Abdeslam hanzaz

Born at CasaBlanca/ Morocco 1981

She got B.Sc degree at Electrical and Electronic Engineering (Communication) form university of Omar AlMukhtar university at 2003.

She got M.Sc at Electronic Engineering at 2007.

Now she is a Lecturer at Electrical and Electronic Engineering college/ Omar Al-Mukhtar university- Libya

*E'mail:* [engassia@yahoo.com](mailto:engassia@yahoo.com)

2- Abdelsalam Ambarek

Born at BENGHAZE /Libya 1948

He got BSc degree at Electrical and Electronic Engineering from Libya

He got MSc and PhD from United Kingdom from Manchester University.

Now he is a Doctor at Electrical and Electronic Engineering College/ Gar Younis university-



المؤتمر الدولي العربي الليبي الخامس للهندسة الكهربائية والإلكترونية 2010/10/26-23 طرابلس ليبيا





## **Fabrication and Comparison of Micro Thin Films for Development of High Performance Hydrogen Sensors**

**M. M. Jamshidi, K. Alshaltami and F. Akkari**

*Department of Electronic Engineering, Institute of Technology Tallaght, Dublin 24, Ireland*

### **Abstract**

In this research we describe the fabrication and testing of two types of thin films for the study of hydrogen sensors. Individual thin films of pure palladium and alloy of palladium-silver are fabricated on silicon oxide substrates using a vacuum evaporation technique. In this process, the surface area and the thickness are kept constant for both the fabricated thin films. The electrical resistance and sensing properties of the structures in conjunction with 5% hydrogen concentration at room temperature are obtained from the Resistance-Time and Sensitivity –Time characteristics respectively and the results are compared and discussed. The thin film made with Pd-Ag alloy shows the better response to sensitivity and reversibility to hydrogen.

**Keywords:** Hydrogen sensor, Pd and Pd-Ag micro thin films, Resistance and Sensitivity responses

### **Introduction**

Hydrogen is a promising potential fuel for use in machinery and transport and can be converted into electricity in fuel cells. It also is already in use in medicine and space exploration as well as in the production of industrial chemicals and food products. Safety is the most important issue when using hydrogen. An explosive mixture can form if hydrogen leaks into the air from a tank or valve reaches the limit of 4.65% at room temperature [1]. Therefore, it is important and encouraging to fabricate hydrogen sensors with high sensitivity, high accuracy, small size and low cost.

Moreover, today the focus of sensor development is based on research into new devices and materials, which provide increased sensitivity, selectivity and stability. Among the various types of hydrogen sensors that have been explored including metal oxide semiconductor sensors, thermoelectric sensors, Schottky diode sensors, fiber optic sensors, and electrochemical sensors, many employ metal palladium as the active sensing material due to its unique property of strong interaction with H<sub>2</sub> gas.

The absorption of molecular hydrogen by metal palladium to form Pd–H hydride can cause physical properties changes including



mass, volume and electric resistance, all of which can be used to signal the  $H_2$  partial pressure changes. Nevertheless, although pure palladium-based hydrogen sensors can give good  $H_2$  sensitivity, there are some drawbacks associated with the use of pure palladium metal. The response time ranging from several to more than 10 minutes for Pd-sensors is too slow to allow real-time monitoring of flowing gas streams [2]. To overcome these problems, the sensing material has been modified by introducing a second metal to make a mixed metal film of palladium for  $H_2$  sensing.

In the past years, mixed thin films of palladium with other metals have shown to be more suitable for hydrogen sensing, due to their good physical and mechanical strength, resistance toward other chemicals, and lower consumption of noble metal to reduce the fabrication cost. The interaction of palladium and several palladium alloys to hydrogen gas, such as Pd–Cr, Pd–Cu, and Pd–Al were studied [3] and found that the electrical resistance of many palladium-rich substitution systems was dependent on the absorbed hydrogen amount of the metal phase. Thereafter, many research groups reported Pd alloys as  $H_2$  sensing materials although further improvement is still required with respect to selectivity, sensitivity and lifetime of the sensors [4, 5, 6, 7, and 8].

Here, we study the hydrogen sensing performance of Pd and Pd-Ag alloy thin films. For this, square shape micro thin films are fabricated using the vacuum evaporation technique, and their change of electrical resistance in conjunction with 5% hydrogen is measured as the sensing signal. The sensing signal of Pd-Ag alloy shows a better performance than the one of pure Pd.

## Experimental

### Fabrication process

The Pd and Pd-Ag alloy micro thin films were fabricated on the silicon oxide ( $SiO_2$ ) substrate by vacuum evaporation. Prior to the fabrication, P type silicon wafer was cleaned using a solution of 5 part water ( $H_2O$ ), 1 part 27% ammonium hydroxide ( $NH_4OH$ ) and 1 part 30% hydrogen peroxide ( $H_2O_2$ ). The temperature of the solution was brought to  $80^\circ C$  and the silicon wafer was soaked in the solution for 15 minutes, and then was dried with hot air. To ensure that the silicon wafer was electrically insulated, a thin layer of 200nm silicon oxide was created on the surface of the wafer. For this, the wafer was placed in the quartz boat and was loaded into a HITECH thermal furnace with a temperature of  $450^\circ C$ . The temperature was gradually increased to  $1100^\circ C$  when a low flow rate of  $20\text{ cm}^3/\text{min}$  oxygen was circulated to the furnace for 3 hours.

The produced  $SiO_2$  substrate was then allowed to perfectly cool down at room temperature before the evaporation process was started. Note that, the blue colour on the surface of the silicon wafer after heating indicates the existence of  $SiO_2$  layer. Individual thin films of Pd and Pd-Ag alloy with the ratio of (77-23)% were deposited onto  $SiO_2$  substrates using an Edwards E306 vacuum evaporation machine. This system was equipped with a thin film monitoring unit, which could measure the film thickness during the evaporation process. The pumping system evacuated the chamber to a vacuum of  $10^{-5}$  to  $10^{-6}$  Torr and a shutter was used between the heating source and the substrate holder for careful deposition of the thin films.



With this arrangement thin films of Pd and of Pd-Ag alloy were deposited onto SiO<sub>2</sub> substrates at room temperature. Both the thin films were fabricated with the surface area of 1cm<sup>2</sup> and the thickness of 210nm for comparison toward the hydrogen effect.

## Measurement process

Prior to the measurement, the electrical contacts were made on the two corners of each square shaped thin film with two single strand non-resistive copper wires using the silver adhesive paste. To dry the contact points the sample was allowed to rest overnight at room temperature. The surface composition and uniformity of the thin films were examined using an Olympus PME3 Microscope equipped with a PC giving a magnification of 1 to 500. Figure 1 shows the basic experimental arrangement for the measurements.

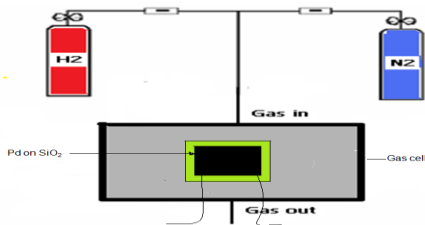


Figure1. Schematic diagram of the hydrogen sensing measurements

A 12cm<sup>2</sup> by 6cm height rectangular gas cell was specially designed and constructed from steel and a clear plastic top. To maintain the gas flow an inlet and outlet were installed into the cell for the connection of pipes. The gas supply was made of one (5% H<sub>2</sub> - 95% N<sub>2</sub>) cylinder and one (pure N<sub>2</sub>) cylinder, which were connected to the gas cell by steel pipes and

shut off valves. A constant low flow of nitrogen was subjected into the cell as the gas carrier, to create a base line. With this set up, the gas flow from the nitrogen base can be changed to the hydrogen concentration in nitrogen. Note that individual gas flow into the cell was controlled with flow meters. Individual thin film was placed and secured in the cell and its change of resistance was measured through the contact wires at each 10 seconds as a signal for 5% hydrogen concentration. The reversibility of the sensor performance was evaluated by switching the gas line from the hydrogen to nitrogen concentration. To measure the instant change of the thin film resistance at different times with high accuracy, a HP34401A Multi-meter was used.

## Results and Discussions

In general, the required thin films for gas sensors should be fabricated from semiconductor or conductor materials so their resistance can be easily measured with the gas concentration. Moreover, for high sensitivity and reduced response time the thin film sensor must be made as thin as possible.

The magnitude of response (*S*) to hydrogen gas is defined as [9]:

$$S\% = (R - R_0) * 100 / R_0$$

(1)

$$\Delta R = (R - R_0)$$

Where **R** is the resistance of the thin film under H<sub>2</sub> concentration and **R<sub>0</sub>** is the resistance before the introduction of hydrogen into the system.

The sensing performance of a deposited square shape micro thin film of Pd on the SiO<sub>2</sub> substrate at room temperature is examined with 5% hydrogen. In this way,



the resistance of the film is measured every 10 second with hydrogen. Figure 2 shows the response time of sensitivity for Pd thin film. In this,  $\Delta R/R_0$  is approximately 2% at 20 seconds and is 16% when the recovery starts to occur. The speed of the response is tremendously low in comparison with the speed of response for the Pd-Ag thin film sensor. Figure 3 shows the change of resistance with time for Pd thin film at 5% hydrogen concentration. The rise of the film resistance from around 3.2 to 3.7 $\Omega$  is achieved for the maximum absorption of hydrogen by the Pd thin film surface. Note that, the response and recovery times are defined as the time required to achieve 90% of the signal change for the adsorption and desorption of hydrogen respectively [10].

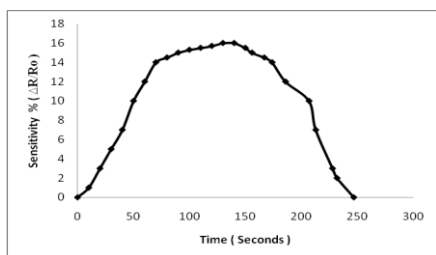


Figure 2. Response time of the pure Pd thin film at 5% hydrogen concentration at room temperature

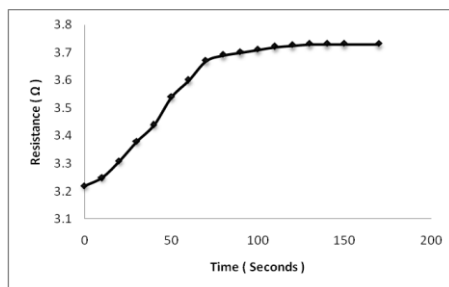


Figure 3. Rise of resistance with time for the pure Pd thin film at 5% hydrogen concentration at room temperature

For the fabricated thin film of Pd-Ag alloy with the ratio of (77-23)% on the SiO<sub>2</sub> substrate, the resistance is measured against the time towards the hydrogen concentration under the same condition as for the pure Pd thin film, and the response time is found. In figure 4 the response curve shows that, the value of  $\Delta R/R_0$  for the Pd-Ag thin film sensor is approximately 4% at 20 seconds with the hydrogen concentration. This value indicates that, the speed of response for the Pd-Ag alloy film is about twice the speed of response for the pure Pd thin film sensor. At around 14% sensitivity the recovery phase starts. The time for recovery is about 80 seconds, which is close to the value reported in the past [9]. When the recovery time is complete the curve returns to the same baseline after the gas is switched back to N<sub>2</sub>. The response time curve shows a sharp and good reversibility obtained by the Pd-Ag thin film. Figure 5 shows that, the electrical resistance of the thin film increases from 4.35 to 5 $\Omega$  with time in contact with 5% hydrogen. The speed of this change of resistance is nearly twice faster than for the pure Pd thin film. Furthermore, our results clearly show that, the resistance of the Pd-



Ag alloy thin film has a higher dependency to the absorption of the hydrogen molecules by the film surface than the resistance of the pure Pd thin film. Both thin films were re-examined after three months and the results showed reasonable reliability and performance.

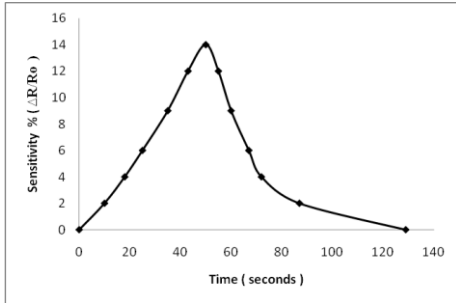


Figure 4. Response time of the Pd-Ag alloy thin film at 5% hydrogen concentration at room temperature

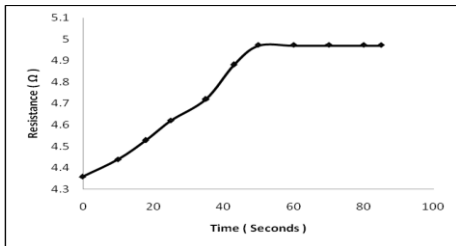


Figure 5. Rise of resistance with time for the Pd-Ag alloy thin film at 5% hydrogen concentration at room temperature

## Conclusions

The resistance of each thin film sensor is increased due to its surface interaction with the hydrogen molecules. The speed of the sensor performance depends on how fast

this interaction can occur. Similarly once the hydrogen is flushed out of the gas cell, the thin film resistance starts decreasing until it reaches its original value. The results show that, the speed of response for the Pd-Ag sensor is approximately twice that for the pure Pd film sensor. Both sensors showed some lack of performances after repeat testing over a period of time. This is due to the cracking and contracting of the Pd element in each film in contact with hydrogen. By increasing the evaporation time or changing the physical shape of the thin film this problem can be remedied. The Pd-Ag thin film on the SiO<sub>2</sub> substrate showed a reasonable operation and can be a suitable choice for sensing the hydrogen leakage at room temperature. Moreover, the results indicate the possibility of further improving the sensitivity and reliability of the Pd-Ag thin film by altering the substrate temperature for each sample, design of the thin film, ratio of Pd-Ag alloy, evaporation period and finally use of annealing at different temperatures and period of times after the evaporation process.

## Acknowledgements

The authors would like to thank the personnel of the microelectronic fabrication lab of the Institute of Technology Tallaght and the department of physics lab at Trinity College Dublin for their kind assistance and advice in using the experimental devices.

## References

- [1] T. Xu, M. P. Zach, Z. L. Xiao, D. Rosenmann, U. Welp, W. K. K. Kwok and G. W. Crabtree, *Appl. Phys. Lett.*, **86** (2005), p 203104.



- [2] D.B. Wolfe, J.C. Love, K.E. Paul, M.L. Chabiny and G.M. Whitesides, *Appl. Phys. Lett.* **80** (2002), pp. 2222–2224.
- [3] K. Baba, U. Miyagawa, K. Watanabe and Y. Sakamoto, *J. Mater. Sci.* **25** (1990), pp. 3910–3916.
- [4] R.C. Hughes and W.K. Schubert, *J. Appl. Phys.* **71** (1992), pp. 542–548.
- [5] Y.T. Cheng, Y. Li, D. Lisi and W.M. Wang, *Sens. Actuators B, Chem.* **30** (1996), pp. 11–16.
- [6] L. Huang, H. Gong, D.K. Peng and G.Y. Meng, *Thin Solid Films* **345** (1999), pp. 217–221.
- [7] P. Kumar and L.K. Malhotra, *Mater. Chem. Phys.* **88** (2004), pp. 106–109.
- [8] S. Nakano, S. Yamaura, S. Uchinashi, H. Kimura and A. Inoue, *Sens. Actuators B Chem.* **104** (2005), pp. 75–79.
- [9] M. Wang and Y. Feng, *Sens. Actuators B Chem.* **123** (2007), pp. 101–106.
- [10] K. Gleeson and E. Lewis, *J. Phys. conf. series* **76** (2007), p. 012004.



## Structure and temperature dependent behavior of Cd-Zn-Fe-O system

M.M.BenOmran<sup>a</sup>, M.A.Sefannaser<sup>b</sup>

*Department of Physics, Faculty of Science Alfateh University, Lybia*

*e.mail<sup>(a)</sup> Mahmudomran@yahoo.com*

*mhslemg@gmail.com<sup>(b)</sup>*

**Abstract:** Samples of the type  $Cd_yZn_{1-y}Fe_2O_4$  ;( $y = 0.0, 0.1, 0.2$ ) were prepared by conventional ceramic method. The X-ray measurements was done for all studied samples. The lattice parameter ( $a$ ) and x-ray density ( $D_x$ ) were determined at different (Cd) substitutions. Ac-conductivity ( $\sigma_{ac}$ ) was measured at temperature range from 308K up to 698K and at fixed frequencies (100,1K,10K,100K,2MHz). The X-ray diffraction analysis showed that all studied samples have a single phase and cubic spinel structure. The lattice parameter ( $a$ ) is found to increase with  $Cd^{2+}$  ion concentration . The samples are found to have measured densities in the range (91-95%) of x-ray density. The values of the x-ray density are higher than measured density ( $D_m$ ). The x-ray density increases with increasing ( $Cd^{2+}$ ) ion content. The ( $\sigma_{ac}$ ) increases as temperature increases for all studied samples. The behavior of conductivity with temperature shown two regions; frequency dependent region (I) (at relative low temperatures) and frequency independent region (II) (at relative high temperatures) separated by transition point ( $T_t$ ). The transition point ( $T_t$ ) increases with increasing ( $Cd^{2+}$ ). The activation energy in region (II) is higher than that in region (I). In region (I) the activation energy decreases with increasing frequency and in region (II) the activation energy has one value approximately corresponding to the change in frequencies.

### 1-Introduction

Ferrites are used in wide range of ac technological application, especially in core transformers, recorder heads, etc. [1] Due to their magnetic and electrical properties. Very useful information on the behavior of localized electric charge carriers can be obtained from the frequency and temperature dependence of the ac conductivity. The ac conductivity is one of the most important properties for ferrites which markedly depends on the preparation conditions , sintering time and temperature, quantity and type of additives [2].

### 2-Experimenta

Samples of the compositions ( $Cd_yZn_{1-y}Fe_2O_4$ );( $y = 0.0, 0.1, 0.2$ ), were prepared by Ceramic Method. Presenting of the mixture was done in an electric furnace at  $750C^\circ$  for five Hours. After this step at least partial formation of the ferrite takes place. The powder was pressed using stainless steel die in to disc-shaped Samples 12cm, the disc-shaped were pressed at  $3.5 \times 10^8 Pa$  by hydraulic press.

A final sintering of the pressed samples was made at 1200C° for Four hours by using programming digital furnace and then they were slowly cooled to room temperature. The sintered samples are coated (electroded) with silver paint in both sides and inserted between the two wires in samples holder and Then support these wires by drips of silver paint.

One disc-shaped sample of each composition was ground To a very fine powder to be used in X-ray Diffraction analysis .The powder should be ground extremely fine to produce accurate Relative line intensities. The X-ray Diffraction of samples was made Using an PW1800 X-ray Diffractometer (Cu-K $\alpha$ -radiation,  $\lambda=1.54060\text{\AA}$  , 30mA , 40Kv ) . The lattice parameter (a) was determined for all compositions using the relation [3]:

$$d=a/(h^2+k^2+l^2)^{0.5} \quad (1)$$

were d is the interplanar distances calculated according to Bragg's formula [3]:

$$n\lambda=2d\sin(\theta) \quad (2)$$

The density of the samples was determined by using the relation:

$$\text{Density}(D_m)=[\text{Weight}(W)/\text{Volume}(V)] \quad (3)$$

The weight was determined using a digital balance and the volume was calculated by measuring the samples dimensions.

X-ray density (Theoretical density),  $D_x$ , was calculated from the Relation [3]:

$$D_x = (8M)/(NV) \quad (4)$$

Were (M) is the molecular weight, (N) is Avogadro's number and (V) is the unit lattice volume ( $a$ )<sup>3</sup>.

The A.C conductivity are measured for all the samples in the temperature range 308k up to 698k in the selected frequencies (100, 1K, 10K, 100K, 2MHz) by using (RC-Circuit) as in fig1.

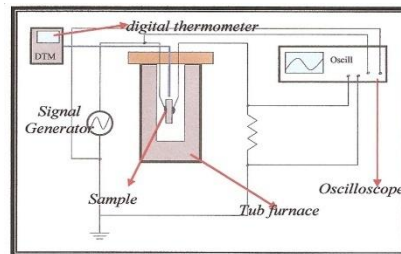


Fig (1) circuit diagram of ac electrical conductivity measurements

The ac electrical conductivity is determined from following relations:

$$\sigma = 1 / \rho \quad (5)$$

$$\rho = Z A / l \quad (6)$$

Were: ( $\sigma$ ) Electrical conductivity, ( $\rho$ ) Electrical resistivity, (Z) Impedance, (A) Area of sample, (t) Thickness.

### 3-Results and discussion

X-ray diffraction analysis for the studied samples of the general formula  $Cd_yZn_{1-y}Fe_2O_4$  ;(y = 0.0,0.1,0.2) are shown in Fig2.

The x-ray pattern show the existence of spinel structure with the reflection planes; (111), (220), (311), (222), (400), (422), (511), (440), (533), (642), (731). It is found that for the samples, the single phase spinel structure was constructed as compared with Inorganic Crystal Structure Database (ICSD), reference code: (56453) for sample Zn-ferrite.



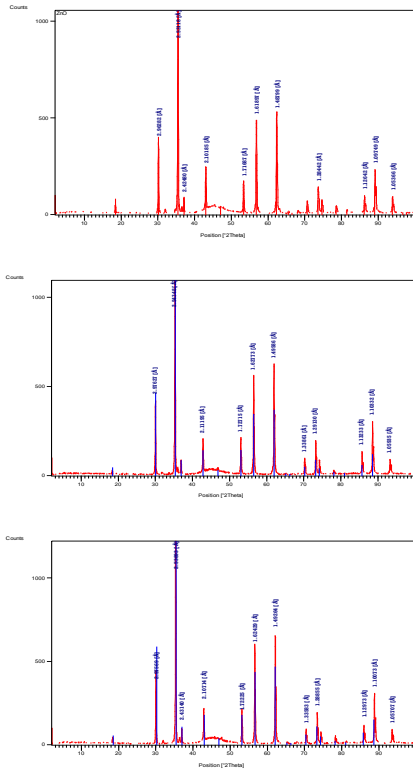


Fig (2) X-ray diffraction patterns for ,a-  $ZnFe_2O_4$ , b-  $Cd_{0.1}Zn_{0.9}Fe_2O_4$ , c-  $Cd_{0.2}Zn_{0.8}Fe_2O_4$ .

The values of lattice parameter is plotted against the composition (x) as shown in Fig 3 for  $Cd_yZn_{1-y}Fe_2O_4$ . The figure show that the lattice parameter increases with increasing  $(Cd^{2+})$  ion content. The behavior is attributed to larger ionic radius of  $(Cd^{2+})$  ion; ( $r_{Cd}= 0.97\text{\AA}$ ) than  $(Zn^{2+})$  ion ;( $r_{Zn}=0.74\text{\AA}$ ).

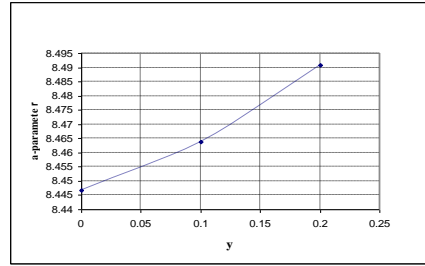


Fig (3) variation of a-parameter ( $\text{\AA}$ ) with composition for system Cd-Zn ferrite.

The relative x-ray density ( $D_x$ ) and the relative measured density ( $D_m$ ) are summarized in table (1). The samples are found to have measured densities in the range (91-95%) of x-ray density. The value of the relative x-ray density( $D_x$ ) is higher than relative measured density( $D_m$ ). This is attributed to the existence of pores which depend on the sintering conditions, kind of additions and radius of ion.

The relative x-ray density increases with increasing content of  $(Cd^{2+})$  ion as shown in fig (4).

Table (1) measured Density, X-ray Density.

Sample	Thick (mm)	Area $\times 10^{-6}$ ( $m^2$ )	W (g)	$D_x$	$D_m$
$ZnFe_2O_4$	1.82	12.51	1.14	5.31	5.01
$Cd_{0.1}Zn_{0.9}Fe_2O_4$	1.82	12.49	1.11	5.38	4.88
$Cd_{0.2}Zn_{0.8}Fe_2O_4$	1.82	12.50	1.17	5.43	5.14

$D_x \rightarrow$  X-ray Density,  $D_m \rightarrow$  measured Density.

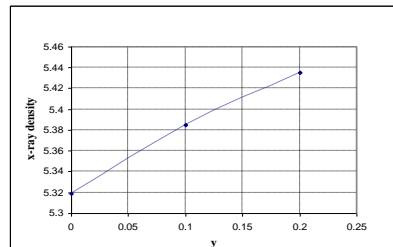


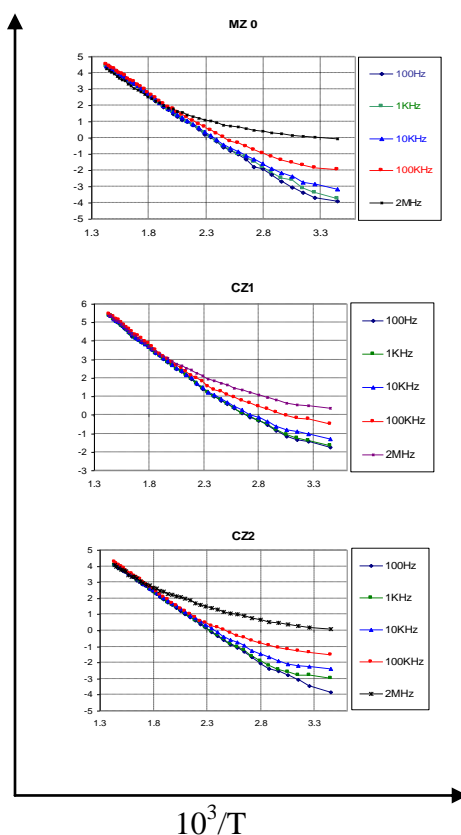
Fig (4) variation of X-ray density ( $g/cm^3$ ) with composition for system Cd-Zn ferrite.



This behavior related to the replacement of ( $\text{Cd}^{2+}$ ) with atomic weight; ( $M_{\text{Cd}}=112.41\text{g/mol}$ ) and density; ( $D_{\text{Cd}}=8.642\text{g/cm}^3$ ) by ( $\text{Zn}^{2+}$ ) ion with atomic weight ; ( $M_{\text{Zn}}=65.37\text{g/mol}$ ) and density; ( $D_{\text{Zn}}=7.14\text{g/cm}^3$ ).

The results of the a.c conductivity ( $\sigma_{\text{ac}}$ ) was measured at five different frequencies (100, 1K, 10K, 100K, 2MHz) for  $\text{Cd}_y\text{Zn}_{1-y}\text{Fe}_2\text{O}_4$ ; ( $y = 0.0, 0.1, 0.2$ ). The Arrhenius's plot for all compositions is shown in Fig (5).

From Arrhenius's plot we can obtain that, each composition has Negative Temperature Coefficient Resistors behavior (NTCR) . It is clear that ( $\sigma_{\text{ac}}$ ) increases as temperature increases. This can be attributed to the semi conducting behavior of the studied ferrite samples and It can be seen that , the a.c conductivity increases with increasing frequency . The studied samples exist two regions; frequency dependent region-(I) at relative low temperatures and frequency independent region-(II) at relative high temperatures separated by transition point ( $T_t$ ).



Fig(5) Arrhenius's plot for samples  $\text{ZnFe}_2\text{O}_4$ (MZ0),  $\text{Cd}_{0.1}\text{Zn}_{0.9}\text{Fe}_2\text{O}_4$ (CZ1),  $\text{Cd}_{0.2}\text{Zn}_{0.8}\text{Fe}_2\text{O}_4$ (CZ2).

At temperature ( $T_t$ ) the conductivity becomes frequency Independent. This behavior was observed earlier for Cu-Cr ferrites[4], Ni-Sb ferrites[5], Ni-Mg ferrites[6] and Ni-Zn ferrites[7]. In the frequency dependent region (I) the a.c conductivity Increases with increasing frequency for all samples. The values of temperature ( $T_t$ ) for all studied samples are tabulated in table (2).



Table (2) Composition Dependence of transition temperature ( $T_i$ ).

Sample	$T_i$ (k)
ZnFe <sub>2</sub> O <sub>4</sub>	498 k
Cd <sub>0.1</sub> Zn <sub>0.9</sub> Fe <sub>2</sub> O <sub>4</sub>	518 k
Cd <sub>0.2</sub> Zn <sub>0.8</sub> Fe <sub>2</sub> O <sub>4</sub>	558 k

From table we can obtain that the temperature ( $T_i$ ) increases with increasing Cd<sup>2+</sup> ion content.

The values of activation energy in frequency dependent region (I) and frequency independent region (II) are determined from Arrhenius's equation[8]:

$$\ln(\sigma T) = \ln(\sigma_0) - (E/KT) \quad (7)$$

and the values of activation energy for ZnFe<sub>2</sub>O<sub>4</sub> are tabulated in table (3), Cd<sub>0.1</sub>Zn<sub>0.9</sub>Fe<sub>2</sub>O<sub>4</sub> in table(4) and Cd<sub>0.2</sub>Zn<sub>0.8</sub>Fe<sub>2</sub>O<sub>4</sub> in table(5).

Table (3) Variation of Activation Energy with frequency for ample ZnFe<sub>2</sub>O<sub>4</sub>.

f(Hz)	Region I (RT-498k)	Region II (498k-698k)
100Hz	0.35313ev	0.44386ev
1KHz	0.33591ev	0.44023ev
10KHz	0.30724ev	0.43006ev
100KHz	0.24253ev	0.42115ev
2MHz	0.1112ev	0.36646ev

Table (4) Variation of Activation Energy with frequency for ample Cd<sub>0.1</sub>Zn<sub>0.9</sub>Fe<sub>2</sub>O<sub>4</sub>.

f(Hz)	Region I (RT-518k)	Region II (518k-698k)
100Hz	0.30033ev	0.40315ev
1KHz	0.29428ev	0.40462ev
10KHz	0.27151ev	0.40671ev
100KHz	0.21891ev	0.39992ev
2MHz	0.17300ev	0.38430ev

Table (5) Variation of Activation Energy with frequency for ample Cd<sub>0.2</sub>Zn<sub>0.8</sub>Fe<sub>2</sub>O<sub>4</sub>.

f(Hz)	Region I (RT-558k)	Region II (558k-698k)
100Hz	0.36027ev	0.401187ev
1KHz	0.33767ev	0.39589ev
10KHz	0.29921ev	0.40290ev
100KHz	0.24156ev	0.39677ev
2MHz	0.15266ev	0.32668ev

From tables we can see that the activation energy in region (II) is higher than that in region (I) for all studied samples This behavior was observed earlier for Cu-Cr ferrites[4] and Ni-Sb ferrites[5]. In region (I) the activation energy decreases with increasing frequency and In region (II) the activation energy has one value



approximately corresponding to the change in frequencies (100Hz, 1KHz) and at frequencies (f) when  $2\text{MHz} > f > 10\text{KHz}$  the decreasing in activation energy becomes clear but very small for all studied samples. Table (5) Variation of Activation Energy with frequency for sample  $\text{Cd}_{0.2}\text{Zn}_{0.8}\text{Fe}_2\text{O}_4$ .

#### 4-conclusions

The results of this study can be summarized as follows:

- 1-The compounds ( $\text{Cd}_y\text{Zn}_{1-y}\text{Fe}_2\text{O}_4$ ); ( $y = 0.0, 0.1, 0.2$ ) have a cubic spinel structure.
- 2-The lattice parameter increases with increasing ( $\text{Cd}^{2+}$ ) ion content and the value of the relative x-ray density is higher than relative measured density.
- 3-The relative x-ray density increases with increasing content of ( $\text{Cd}^{2+}$ ) ion content.
- 4-A.C conductivity increases as temperature increases; each composition has Negative Temperature Coefficient Resistors behavior (NTCR).
- 5-The behavior of conductivity with temperature shown two regions; frequency dependent (region-(I)) at relative low temperatures and frequency independent (region-(II)) at relative high temperatures separated by transition point ( $T_i$ ).
- 6-The activation energy in region (II) is higher than that in region (I) for all studied samples.

#### References

- [1] Introduction to Magnetic Materials, B.D.CULLITY, (1972).
- [2] Modern Ferrite Technology, ALEX. GOLDMAN 2ed, (2006).

- [3] Elements of X-RAY Diffraction, B .D .Cullity, 2ed, (1978).
- [4] M.A.Ahmed, M.A.Elhiti, M.M.Mosaad, S.M.Attia, (J.Mag.Mag.Mat) , 146, 84-88, (1995).
- [5] M.A.Ahmed, M.A.Elhiti, M.K.Elnimr, M.A.Amer, (J. Mag.Mag. Mat), 152, 391-395, (1995).
- [6] M.A.El-Hiti, (J.Mag.Mag.Mat), 164,187-196, (1996).
- [7] A.M.Abdeen, (J. Mag.Mag. Mat), 185, 199-206, (1998).
- [8] Introduction to Ceramics (Part2), Kingery, (1963).



# APPLICATION OF ELECTRIC FIELD ON THE MOLECULAR ORIENTATION OF A FERROELECTRIC LIQUID CRYSTAL MIXTURE STUDIED BY FTIR SPECTROSCOPY

<sup>a</sup>M. M. JAMSHIDI, <sup>b</sup>O. PANARINA AND <sup>a</sup>F. AKKARI

<sup>a</sup>Department of Electronic Engineering, Institute of Technology Tallaght, Dublin 24, Ireland

<sup>b</sup>Department of Electronic and Electrical Engineering, University of Dublin, Trinity College, Dublin 2, Ireland

## ABSTRACT

The molecular orientational behaviour for a homogeneously aligned cell of a ferroelectric liquid crystal mixture in Smectic C\* (SmC\*) phase is investigated using FTIR spectroscopy. This paper studies the main molecular mechanism and structure of the mixture. For this, the polarisation dependence of the absorbance for the core carbonyl (C=O) and phenyl (C=C) stretching bands for various stages of the electrically induced transformation of the sample structure is analysed until the complete unwinding of helix is formed. The angular shift of the absorbance profile for core carbonyl and phenyl bands is found to be dependent on the applied field and its value is found as the DC voltage is altered across the liquid crystal cell. The effects of ionic separation and hysteresis are found to be the cause for the existence of a non-zero value in apparent tilt angle at zero applied voltage. The value of the dichroic ratio and polarisation angle for both the core carbonyl and phenyl groups are calculated and the key results are explained and discussed.

Keywords: ferroelectric liquid crystal mixture, FTIR spectroscopy, switching

## INTRODUCTION

The absorbance profiles of each stretching vibrational band are studied and their characteristics in relation to the orientation of the molecules are discussed.

The apparent tilt angle for each molecular group is also found and their values as a function of the applied electric field are

given. FTIR spectroscopy is an efficient technique for investigating the orientational

behaviour of the various parts of the molecules in a liquid crystal cell [1, 2]. It is known that in bookshelf geometry the direction of the long molecular axis is fixed relative to the smectic layer normal by the application of a constant electric field. This

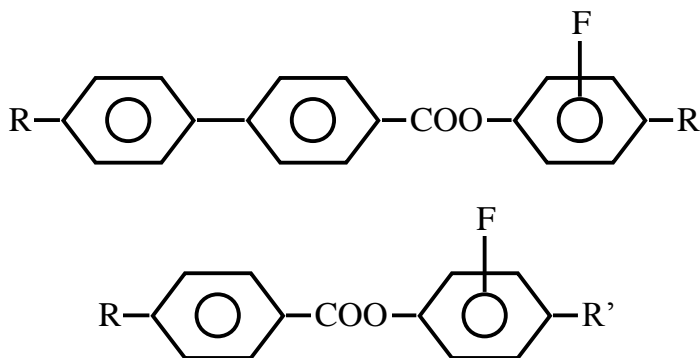


voltage across the cell causes distortion and an eventual unwinding of the helicoidal structure. However the molecular director can be switched to a new but opposite sense when the sign of the applied field is altered. In this arrangement the molecular director is parallel to the plane of the cell windows [3]. The intermolecular interactions can influence the frequency and the shape of the vibrational bands under investigation. This leads to a better understanding of the molecular behaviour for switching in SmC\* phase. Furthermore, absorption profiles obtained from these selected bands as a function of the polarizer rotation angle together with their rotational motion can be studied in greater details. Generally for chiral materials the origin of ferroelectricity lies in the average biased rotation of the molecules about their long axis. The biased

rotation and the permanent dipole moment located near the chiral centre give rise to the spontaneous polarisation. Note that, for this material due to the low percentage of the dopant the effect of chirality is considerably low and also the location of the chiral centre in the structural formula is not known. We focus our attention on the characteristics of the phenyl and the core carbonyl groups in order to study the main behaviour of the molecules.

## EXPERIMENTAL

The material (SCE8) used in this investigation is a ferroelectric liquid crystal mixture synthesised by Merck Ltd [4]. The structural formula and the phase transition temperatures in °C are as follows:



Smectic C\* phase → 59 → Smectic A\* phase → 79 → Nematic phase → 100 →  
Isotropic

This material is a mixture of two components and two substituents R and R'. One component is a chiral dopant with ~ 5% and the other is a matrix which is not chiral. R and R' represent the alkyl chains in the molecules. R represents heptyloxy, octyloxy and dodecyl chains in the ratio 1.9, 2.7 and 1.0. R' represents pentyl,

heptyl and octyloxy chains in the ratio 3.75, 1.0 and 1.25 respectively.

Sample was aligned between the two transparent CaF<sub>2</sub> windows with inner surfaces coated with conductive indium tin oxide (ITO). For planar alignment ITO surfaces were spin coated with polyvinyl alcohol (PVA) and after drying, the surfaces were rubbed in anti-parallel



directions on a velvet rail. In this way the surfaces become grooved and hence, during the cell filling with liquid crystal, molecules will lie approximately along the direction of the grooves. Mylar spacer of thickness  $6\mu\text{m}$  was used between the two  $\text{CaF}_2$  windows for obtaining a fixed sample thickness. The cell was filled with capillary effect at a temperature above the isotropic phase, i.e.  $>100^\circ\text{C}$ , and examined for the alignment using polarising microscope. The structure of the cells used in this study is shown in Fig. 1(a).

Measurements were carried out by recording the polarised IR spectra as a

function of the polarisation angle for different DC voltages across the cell in  $\text{SmC}^*$  phase. For this investigation the absorption peaks at  $1737\text{ cm}^{-1}$  for the core carbonyl stretching ( $\text{C}=\text{O}$ ) and at  $1605\text{ cm}^{-1}$  for phenyl ring stretching ( $\text{C}-\text{C}$ ) vibrations have been analysed. The polarisation angle is fixed to be zero when the axis of the polarizer is parallel to the smectic layer normal. A Bio-Rad FTS60A spectrometer with a  $2\text{ cm}^{-1}$  resolution with an averaging over 16 scans is used. The wire grid polarizer is rotated with a computer controlled device with a capability of a rotational step by 2 degrees

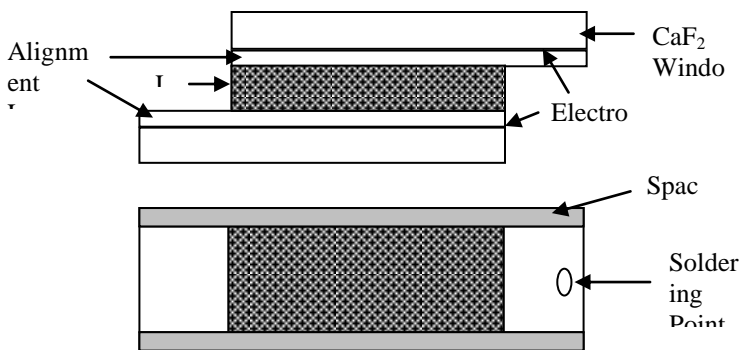


Figure 1(a). Structure of the experimental cell shows the side and plan views

## RESULTS AND DUSCUSSION

Fig. 1(b) illustrates the absorbance versus frequency for two vibrational bands that have been investigated. The angle of polarisation for  $0^\circ$  and  $90^\circ$  represents parallel and perpendicular spectra with respect to the smectic layer normal. The selected bands correspond to the molecular vibrations of the core carbonyl ( $\text{C}=\text{O}$ ) at the frequency of  $1737\text{ cm}^{-1}$  and the phenyl ( $\text{C}-\text{C}$ ) vibrations at frequency of  $1605\text{ cm}^{-1}$ .

The polarisation angle is defined as the angle between the layer normal and the electric vector of the infrared beam. In  $\text{SmA}^*$  phase the long molecular axis is essentially parallel to the smectic layer normal and therefore lies along the rubbing direction of the cell windows. Fig. 1(b) displays the differences between absorbance peaks at  $0^\circ$  and  $90^\circ$  polarisation angles which represent a higher degree of orientation for the phenyl rather than for the core carbonyl group in  $\text{SmC}^*$  phase at an applied voltage of  $+12\text{V}$ . The small shift of



frequency between peak positions for core carbonyl group seen in Fig. 1(b) can be addressed to the existence of dopant in the compound.

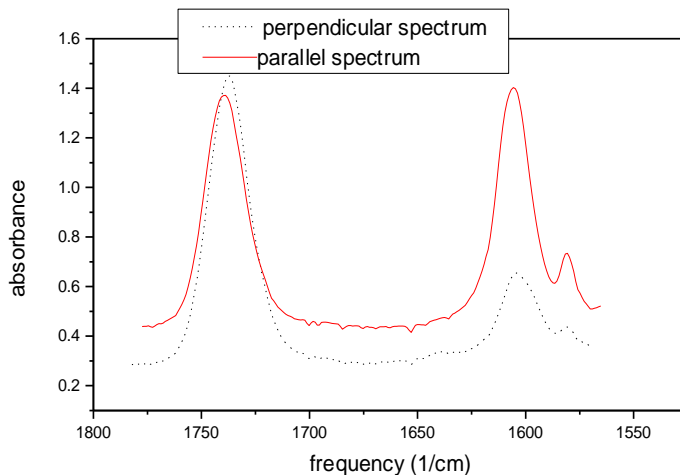


Figure 1(b). Absorbance as a function of vibrational frequency ( $\text{cm}^{-1}$ ) for which DC applied voltage across the cell is +12V.

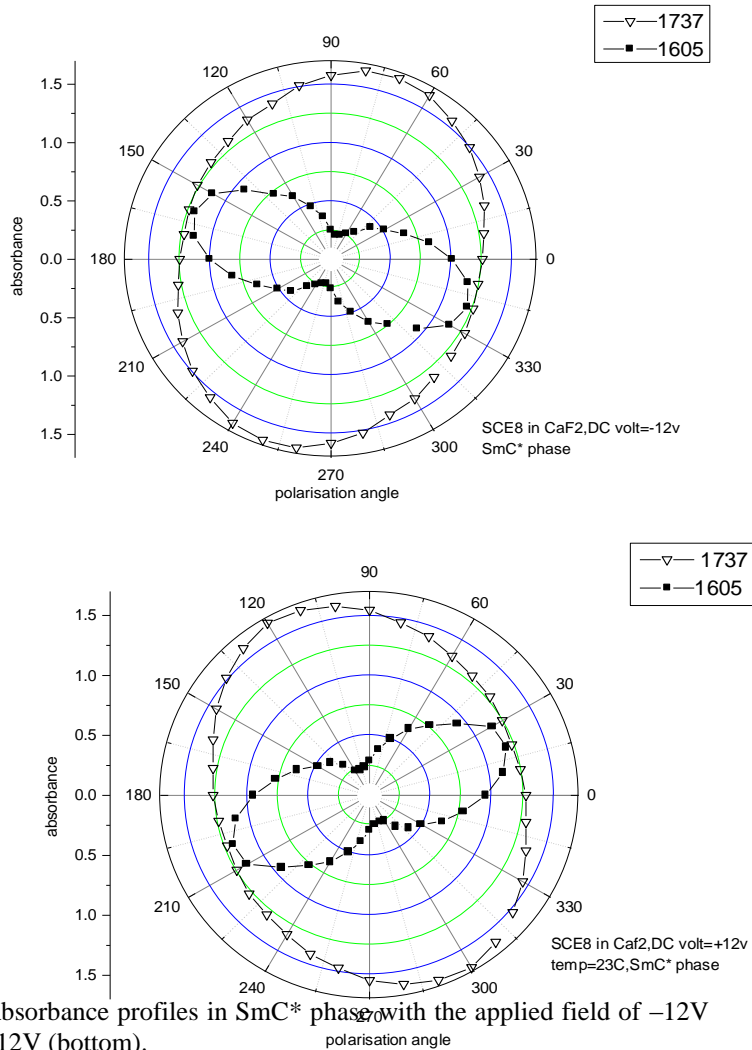
Plot shows two absorption band intensities at  $1737 \text{ cm}^{-1}$  (C=O) and  $1605 \text{ cm}^{-1}$  (C-C) for two polarisation angles, dash line  $\Omega = 90^\circ$  and full line  $\Omega = 0^\circ$ .

Polar plots of the absorbance profiles  $A(\Omega)$  for the two bands in SmC\* phase with bias voltage at +12 and -12V are shown in Fig. 2. It is noted that, in SmA\* phase the maximum absorbance ( $A_{\text{max}}$ ) for the phenyl ring profile occurs when the maximum polarisation angle ( $\Omega_{\text{max}}$ ) is approximately

$0^\circ$  or  $180^\circ$ , whereas for the core carbonyl profile  $A_{\text{max}}$  is situated at  $90^\circ$  or  $270^\circ$ .

Molecular orientation is expressed in terms of the average direction of the molecular director. If this director is not collinear with the transition dipole moment then  $A_{\text{max}}$  does not occur for which  $\Omega_{\text{max}}$  has a zero value [5].





In SmC\* phase, we find that both phenyl and core carbonyl profiles show angular changes with the applied voltage. The direction of the angular motion is the same for both profiles for any sign of the applied electric field. Fig.3 clearly shows that both profiles rotate with smaller polarisation angles when the sign of the applied DC voltage is negative. The angle of rotation is

approximately equivalent to the optical tilt angle with respect to the polarisation axis. Furthermore, we notice the value of  $\Omega_{max}$  for these absorbance profiles does not change in the same manner as the polarity of the applied field changes with respect to zero voltage position. This is expected to be due to the effect of the hysteresis within the cell, see Fig. 3.

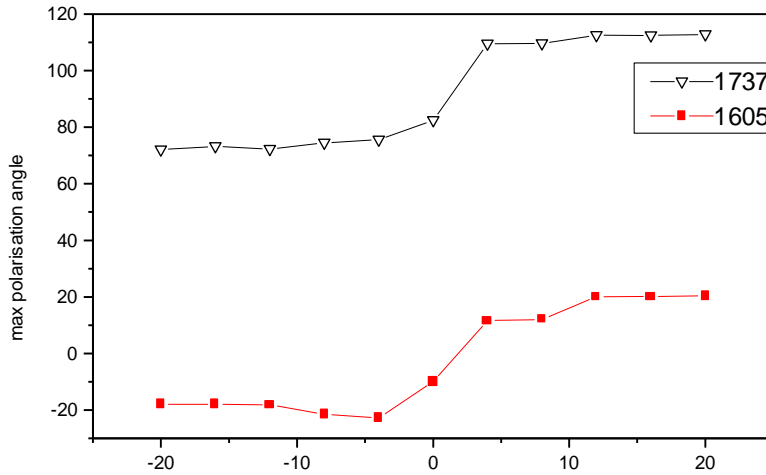


Figure 3. Voltage dependence of  $\Omega_{\max}^{\text{DC volt}}$  for core carbonyl and phenyl groups.

The dependence of the tilt angle on the applied voltage in the range of -12 to +12V is shown in Fig. 4. In this range of voltages the unwinding of the helical structure in

FLC takes place [6]. However for both polarity of voltages >12V, the helix has been completely unwound and the apparent tilt angle is the same.

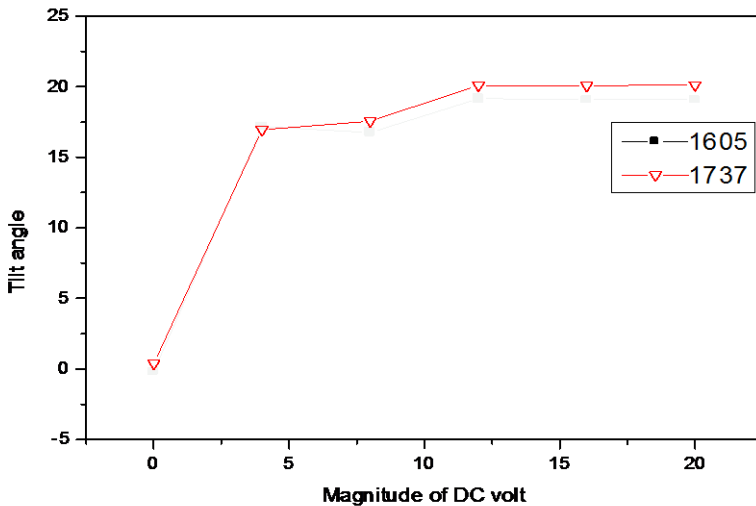


Figure 4. Tilt angle as a function of the magnitude of applied voltage for core carbonyl and phenyl groups.

Jang et.al [2] shows that the variation of the absorbance profile for various bands

depends on the degree of bias and on the polar angle of the transition dipole moment



with respect to the molecular axis. The absorbance as a function of the angle of polarization is given by the following formula [2, 7]:

$$A(\Omega) = -\log(10^{-A_{\max}} + (10^{-A_{\min}} - 10^{-A_{\max}}) \sin^2(\Omega - \Omega_{\max})) \quad (1)$$

In equation (1),  $A_{\max}$  and  $A_{\min}$  are obtained when the electric vector of the polarised infrared beam is parallel and perpendicular to the transition dipole moment respectively,  $\Omega$  is the angle of polarisation and  $\Omega_{\max}$  is the polarisation angle to the direction at which  $A_{\max}$  occurs.

The dichroic ratio ( $D_r$ ) for a single absorbance profile can simply be defined as:

$$D_r = A_{\max} / A_{\min} \quad (2)$$

Table 1. Angular shift ( $\Delta\Omega_{\max}$ ) for various applied voltages for the phenyl and the carbonyl groups.

DC	-20	-16	-12	-8	-4	0	+4	+8	+12	+16	+20
volts											
C-C	-18°	-18°	-	-	-22.7°	-9.96°	11.66°	12°	20.1°	20.2°	20.2°
phenyl			18.	21.							
			2°	5°							
C=O	72.14	72.23	72.	74.	75.6°	82.44°	109.5°	109.6°	112.5°	112.4°	112.4°
core	°	°	3°	48°							

Fig. 5 shows dichroic ratio versus biased voltage. It can be seen that  $D_r$  of phenyl ring is dependent on the applied electric field in the range of -12 to +12V and is different in its response to fields of different polarities (i.e.  $D_r = 4.16$  at 0 voltage, 4.44 at +12V and 4.61 at -12V DC). From this we can infer that prior to the completion of unwinding process by the application of DC

In this investigation the absorbance profiles of the core carbonyl (C = O) and phenyl ring (C-C) for various applied voltages are fitted to equation (1) and the values of  $A_{\max}$ ,  $A_{\min}$  and  $\Omega_{\max}$  are obtained.

Table 1 shows the angular shift ( $\Delta\Omega_{\max}$ ) of the maximum absorbance for various voltages across the cell for the phenyl and the core carbonyl bands.

Fig. 3 also shows the variation of angular shift ( $\Delta\Omega_{\max}$ ) as the bias voltage across the cell increases from -20 to +20V. Fig. 4 displays the change in tilt angle obtained, from the values of  $\Omega_{\max}$  as the polarity of the applied voltage changes at any particular value for both phenyl (C - C) and core carbonyl (C = O) groups.

field; the molecular orientation is dependent to the degree to which the helix is disturbed. Once the helix is unwound, the orientation stays constant for both positive and negative voltages; therefore the value of dichroic ratio stays unaffected at higher voltages [6, 7]. For a thinner cell of thickness 4 $\mu$ m, distortion of the helix at the same voltage can be stronger.

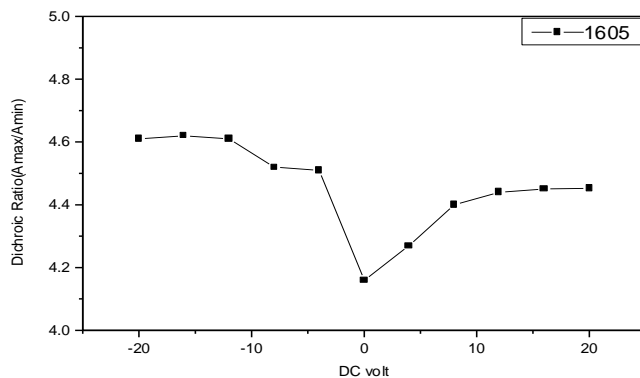


Figure 5. Dichroic ratio as a function of applied voltage for phenyl band (C – C).

The surface effect tends to align the molecules on the surface better than in the bulk for a thinner sample. Therefore surface effect also plays a vital role in fixing the position of the molecular director [8].

Fig. 6 shows that  $D_r$  for the core carbonyl group has a low value  $\approx 1.33$  in comparison with the phenyl ring and is nearly independent of the bias voltage, see Figs. 5 and 6. This indicates that orientation of the

core carbonyl group does not change dramatically by the application of electric field. However, for both groups, the rotation of absorbance profile show differences with respect to zero polarisation axis when positive and negative field is applied. Again this interesting phenomenon is expected to be due to the existence of the hysteresis related to the internal electric field produced by the ions when the polarity of the field is altered.

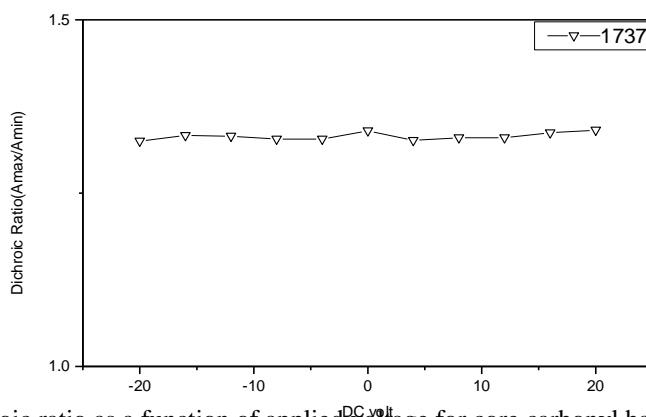


Figure 6. Dichroic ratio as a function of applied voltage for core carbonyl band (C = O).



Using a polarising microscope, the cell shows strips with the applied field at saturated values. This is a consequence of a bookshelf structure present in the cell [9, 10]. We found that the dichroic ratio is dependent on the difference between the values of  $A_{\max}$  and  $A_{\min}$  and ultimately on the shape of the absorbance profile.

Fig. 7 shows the dichroic ratio versus DC voltage for  $\text{CH}_2$  asymmetric vibration at

$2926 \text{ cm}^{-1}$  and  $\text{CH}_2$  symmetric vibration at  $2856 \text{ cm}^{-1}$ . From this figure, it is evident that for voltages greater than 8V, the dichroic ratio stays nearly constant. This result also shows that, the orientation of the  $\text{CH}_2$  group is approximately similar to that of the phenyl group, having however a lower value of dichroic ratio [10].

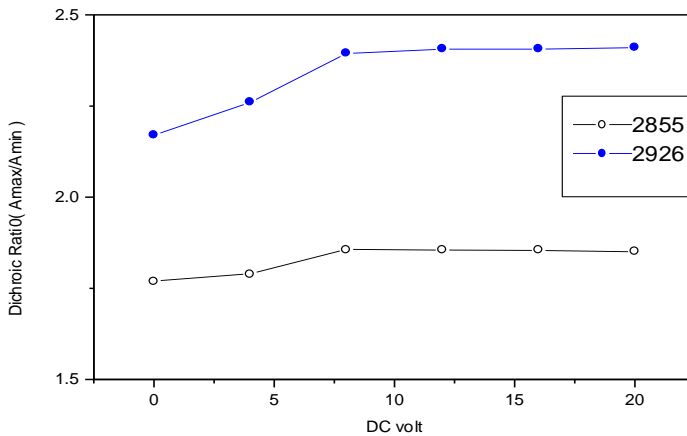


Figure 7. Dichroic ratio as a function of applied DC voltage for  $\text{CH}_2$  symmetric vibration at  $2855 \text{ cm}^{-1}$  and  $\text{CH}_2$  asymmetric vibration at  $2926 \text{ cm}^{-1}$ .

Fig. 8 displays  $\Omega_{\max}$  versus DC voltage for four stretching bands. From this we can confirm that prior to the application of voltage,  $\Omega_{\max}$  for phenyl group was found to be  $-9.96^\circ$  with respect to the axis of the polarisation. This indicates that the helix

was already disturbed due to the surface stabilization of the liquid crystal cell and the possible hysteresis effect. In this case for the cell, the helical pitch is usually large in comparison with the thickness of the cell.

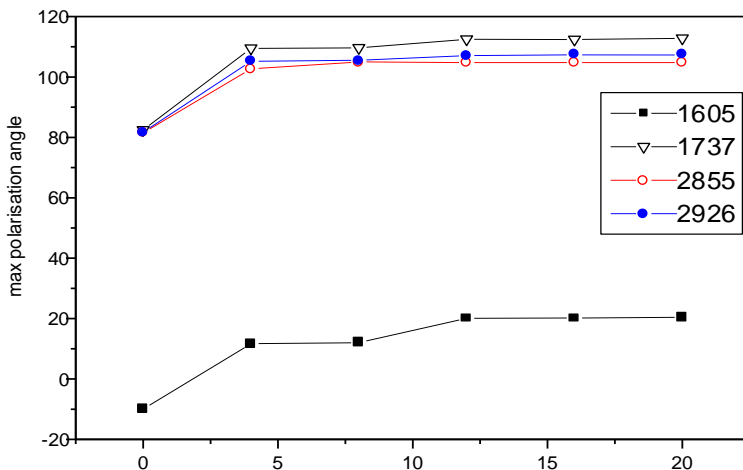


Figure 8. Maximum polarisation angle ( $\Omega_{\max}^{\text{DC volt}}$ ) as a function of applied voltage for phenyl, core carbonyl and  $\text{CH}_2$  groups.

Fig. 8 also shows the higher magnitude of  $\Omega_{\max}$  versus DC voltage for phenyl group rather than for  $\text{CH}_2$  group. Thus, angle of rotation around the Z axis for phenyl group is larger than for  $\text{CH}_2$  group, although the rotation of the  $\text{CH}_2$  group follows the same motion as the phenyl group. From the dependencies of dichroic ratio and the apparent tilt angle on the applied field for phenyl and core carbonyl groups of this mixture, the following conclusions are drawn.

## CONCLUSIONS

Polarised infrared spectroscopy is found to be an efficient technique for investigation of the localized orientation of the various molecular segments. We find that for chiral smectic C phase the rotation of the both phenyl (C - C) and core carbonyl (C = O) absorbance profiles are unidirectional as the value of the applied voltage is altered across the area of the cell. The angular rotation is also different with respect to the polarisation axis as the polarity of the field changes in the range of -12 to +12V. The

hysteresis effect was found to be the reason for this angular difference. The ionic separation effect is the cause for this hysteresis effect. The internal electric field produced by the ions causes a non-zero value in apparent tilt angle at zero applied field. The values obtained for the dichroic ratio under the applied biased voltage with two different polarities indicate that the orientation of the molecules depend on the degree to which the helix is disturbed by this voltage. At higher voltages when the helix is completely unwound, molecules exhibit symmetrical orientation with respect to the zero volt position. The surface stabilized liquid crystal is one of the main causes for the disturbance of the helix prior to the application of bias voltage across the area of the cell. A further increase in the dichroic ratio with the application of DC voltage for phenyl group associates with a deformation of the helix and a presence of the chevron structure in the cell. As the applied field of both polarities reaches to saturated values, the helix is unwound and the chevron structure is converted into a bookshelf structure. At this time the



molecules are tilted within their smectic layers and making a maximum apparent tilt angle with respect to the layer normal. The direction of the tilt depends on the polarity of the applied field. At this stage the spontaneous polarisation ( $P_s$ ) reaches to its maximum value. We find that the  $\text{CH}_2$  group follows the same direction as the phenyl group when the same polarity of electric field is applied to the cell. Although its orientation also shows similarity with the orientation of the phenyl rings but has a lower value of dichroic ratio.

### ACKNOWLEDGEMENTS

We thank the Laboratory's personnel of the Trinity College and the Institute of Technology Tallaght for their kind assistance and advice during the experimental work for this research.

### REFERENCES

1. K.H.Kim, K Ishikawa, H.Takezoe and A.Fukuda, *Phys. Rev.E.*, **51**,2155 (1995).

2. W.G.Jang, C.S.Park, J.E.Maclennan, K.H.Kim and N A Clark, *Ferroelectrics*, **180**,213-225 (1996).
3. A.Kocot, G.Kruk, R.Wrzalik and J.K.Vij, *Liquid Crystals*, **12**,1005-1012 (1992).
4. Merck Ltd, West Quay Rd, Pool, BH15 1IIX, UK.
5. J.K.Vij, A.Kocot, G.Kruk and R.Wrzalik, *Liquid Crystals*, **237**,337-350 (1993).
6. T.S.Perova, Y.P.Panarin and J.K.Vij, *Ferroelectrics*, **180**,105-115 (1996).
7. A.Kocot, R.Wrzalik and J.K.Vij, *Liquid Crystals*, **21**,147 (1996), A.Kocot, R.Wrzalik, B.Orgasinska, T.Perova, J.K.Vij and H.T.Nguyen, *Phys. Rev.*, **59**, 551-555 (1999).
8. M.Brunet and N.Isaert, *Ferroelectrics*, **84**,25 (1988).
9. V.P.Vorflusev, Yu.Panarin, S.A.Pikin and V.G.Chigrinov, *Liquid Crystals*, **14**,1055-1060 (1993).
10. A.A.Sigarev, J.K.Vij, A.W.Hall, S.J.Cowling and J.W.Goodby, *Phys. Rev.*, **76**, 051707 (2007)



المؤتمر الدولي العربي الليبي الخامس للهندسة الكهربائية والإلكترونية 2010/10/26-23 طرابلس ليبيا





## Design, Fabrication and Testing of Micro fluidic Devices for Medical Applications

Ahmad Benkhial<sup>1\*</sup>, Anna Tsigara<sup>1</sup>, Eithne Dempsey<sup>2</sup>, Fathi Akkari<sup>3</sup>

<sup>1</sup> MiCRA/CREATE Group, ITT Dublin.

<sup>2</sup> CREATE, Dept. Science, ITT Dublin.

<sup>3</sup> CREATE, Dept. Electronic Engineering, ITT Dublin.

\* [Ahmad.benkhial@ittdublin.ie](mailto:Ahmad.benkhial@ittdublin.ie)

### Abstract

The development of miniaturized analytical systems is a subject that has been arousing a great deal of interest of the scientific community in the area of analytical chemistry [1]. In the area of biological and electrochemical analysis and research, the demand is not only on miniaturized cells/devices working area; it is also directed towards providing minimum analytes for tests and analysis. The rapidly advancing field concerning minimizing test solution is better known as Microfluidics. Microfluidic devices have emerged as effective platforms for handling small samples and integrating multiple processes required for lab-on-a-chip (LOC) experiments [2]. One of the most known procedures in making Microfluidic channels is Soft lithography using polydimethylsiloxane (PDMS), it allows one to fabricate complex microfluidic devices easily and at low cost. This work describes the construction and characterization of an electrochemical reaction within a fluidic channel between two electrodes a working electrode and a reference electrode, these two electrodes making a simple microsensor. The resulting changes in the electrical characteristics of the analyte in the sensor were investigated using cyclic voltammetry technique. A new generation of flow-through microsensor of three electrodes with a micro-fluidic channel will also be presented. In the new microsensor, PDMS was used to fabricate the microfluidic channels while the three electrodes (working, reference and auxiliary) were fabricated on insulating substrates using noble metals. The three electrodes are the platform of a Micro-electrochemical sensor. The work will show how even simple devices that are inexpensive and relatively easy to fabricate can be useful tools.

### 1. Introduction

Thin-film technology has been widely utilized in the development of integrated and miniaturised electrochemical sensors. Devices based on thin-film technology combined with electro-chemical detection provide plenty of advantages over other technologies because of small sample volume, reliability and low cost.

A major focus in this work was initially given to the electrochemical characterization and fabrication of miniaturised two-electrode thin film electrochemical sensors (devices). Xin-Xia Cai *et al* used the two electrode system as an electrochemical micro-sensor and considered it perfectly acceptable for the measurement of current/voltages where only a small current density is passed, and it is ideal



for micro electrode studies (where  $i < \mu\text{A}$ ) [3]. Jiang, Liying *et al* [4] indicated in a further work that a thin-film electrode in the two electrode system using potassium ferricyanide as a mediator can be used for measuring the concentration of haemo-globin.

The drawback of the use of the two-electrode system, as addressed by Angel E. Kaifer and Marielle-Gómez Kaifer, is that the passage of current, which is caused by the prevalent nonequilibrium conditions, polarizes the electrodes and displaces them from their equilibrium potentials. This creates a particularly acute problem with the reference electrode. Once the potential of the reference electrode shifts from its equilibrium value, meaningful potentials

in such a cell may not be measured [5].

The first solution to the problem mentioned by Angel E. Kaifer and Marielle-Gómez Kaifer, was to use reference electrodes with a very large surface area in order to maintain low current densities and thus, minimize the polarization of these electrodes. This approach was employed in this work.

In the main part of this work, unlike commonly employed three electrode system, a two electrode thin film electrochemical device was studied. The two electrodes employed were Platinum disk working electrode in a micro-scale ( $0.049 \text{ m}\mu^2$ ) and a thin film pseudo Ag/AgCl reference electrode in a mini-scale ( $32 \text{ m}\mu^2$ ), a 'face to face' configuration micro-sensor was fabricated by means of semiconductor technology. The structure of the two facing electrodes microsensor mimics the idea of fluidic channel as the two electrodes were bonded with a spacer between them. This spacer created a channel into which the analyte was injected.

Voltammograms for the two electro-de microsensor were interpreted using potassium (ferri/ ferrocyanide) as a model one-electron redox compound in order to investigate the low volume electro-chemical characterization of the micro-sensor with an Ag/AgCl pseudo reference. The sensor was subsequently applied to glucose detection.

Although the arrangement of this two electrode microsensor provides a meaning of microfluidic channel but it lacks the ability of performing a continuous monitoring. Therefore, it was our desire to make a new arrangement that can fulfil our aim of producing a full device capable of performing a continuing glucose monitoring, creating a prototype of an implantable sensor.

The new prototype is a three electrode microsensor with (working, reference and counter) electrodes integrated with a microfluidic channel. We will briefly demonstrate the fabrication procedure of this microsensor at the end of this work and show the continuous monitoring experiment setup.

## 2. Experimental

### 2.1 Reagents

A p-doped (Bor) 3 inches single-crystal silicon wafer (University Wafers, Boston) with  $\langle 100 \rangle$ -orientation, specific resistance of  $>10 \text{ }\Omega\text{cm}$  and thickness of  $380 \pm 5 \text{ }\mu\text{m}$  and four inch  $750 \text{ }\mu\text{m}$  thick borosilicate glass wafers were used. The positive photoresist, (Microposit S1818) primer (Microposit primer), the developer (Microposit 351) and negative epoxy based photoresists SU8- 5 were purchased from Chestech Ltd, England. Testbourne Limited, England provided the chromium and silicon dioxide ( $\text{SiO}_2$ ) sputtering targets, the silver evaporation slugs, platinum wires and the tungsten evaporation filament



baskets. All the remaining reagents were purchased from Sigma-Aldrich Ireland.

## 2.2 Apparatus

The oxidation of the silicon wafer was accomplished using a Birlec Model C oven (Hi-Tech). Spin coating was performed using a Laurell Technologies spin processor model number WS-400 B-6NPP-lite. A yellow line MST Basic C and TC1 hotplate enabled the soft-baking of the photoresists. Mentor Graphics® IC layout station and Linkcad and AutoCAD package were used for designing the photomasks of the two and three electrode microsensors. Exposure was carried out using a Quintel Mask Aligner Model Q4000. Physical vapour depositions (Evaporation and sputtering) were carried out within an Edwards Auto 500 chamber and PVD75 Kurt J Lesker vacuum system. Electrochemical analyses were performed using a CHI Model EQCM analyser. Deionised water was produced by a Purelab Prima ELGA.

## 2.3 Summary of fabrication (Two electrode system)

The microsensor under consideration was a two electrode electrochemical thin film device with a working electrode and pseudo reference/counter electrode. The two electrodes were fabricated on two individual substrates, and then bonded in a face to face arrangement with a 2mm PDMS spacer.

For the fabrication of both electrodes, a p-doped (Bor) 3" single-crystal silicon wafers with <100>-orientation, specific resistance of  $>10 \Omega\text{cm}$  and thickness of  $380 \pm 5 \mu\text{m}$  was used. As an initial fabrication step, an RCA clean was performed on the wafers to remove any contamination. Subsequently a 125 nm

$\text{SiO}_2$  layer was grown onto the silicon substrate by means of thermal wet oxidation.

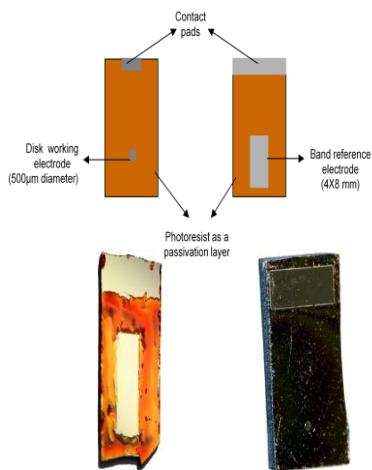
A bilayer of Cr/Pt with an estimated thickness of 20:20 nm was then deposited onto the  $\text{SiO}_2$ . Up to this stage the two substrates of both electrodes were treated together. In order to complete the fabrication of the working electrode, a successive evaporation of Pt was continued until a 150 nm thickness layer was achieved. This was followed by an RF sputtering of a  $\text{SiO}_2$  layer of 100 nm thickness. To realize the contacts for the microsensors, it was required to pattern the wafer by means of photolithography.

The exposed areas produced by photolithography were displaying a  $\text{SiO}_2$  layer. In order to expose the Pt layer underneath, the wafer was post-baked on a hotplate and then dipped in HF to remove the exposed  $\text{SiO}_2$  layer.

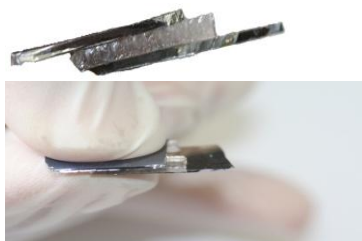
In the case of the band pseudo reference/counter electrode a layer of 300 nm Ag was evaporated on top of the Cr/Pt bilayer after the first three steps, followed by a photolithography stage to form the required structure.

After these steps were completed, the whole wafer was cut into single chips. Each chip consists of one working electrode with its contact pad, and one pseudo reference/counter electrode.

In order to form the Ag/AgCl, the Ag layer for the pseudo reference/counter electrode was chloridised; a drop of 0.1 M of iron chloride ( $\text{FeCl}_3$ ) was applied to the silver layer for approximately 5 seconds. The electrode was then washed and dried. Finally the two electrodes were bonded together. Figure 1 shows the shape of the two electrodes and the micro sensor.



(a)



(b)

**Figure 1:** (a) The two electrode WE 500µm in diameter and pseudo RE 4X8 mm with spacer of (2mm) virtual view (b) the actual sensor (digital photos).

#### 2.4 Electrochemical measurements

Cyclic voltammetry has proven to be a powerful diagnostic tool for characterizing many electrochemical systems. Using this powerful analysing technique, our microsensors were investigated.

The electrochemical tests were carried out using 0.1 M potassium chloride (KCl) and 6mM potassium ferricyanide  $K_3[Fe(CN)_6]$ . The micro-sensor was connected to a potentiostat, and cycled between -0.3V to 0.5 V. A potentiostat and an electrochemical workstation (CHI Model EQCM) were used to perform the cyclic voltammetry.

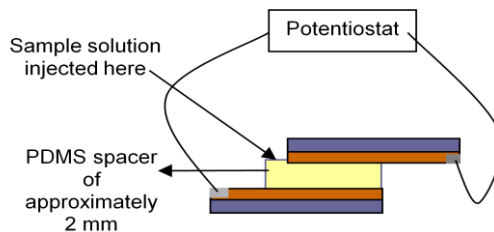


**Figure 2:** The two electrode system electrochemical test setup.

### 3. Results and Discussion

#### 3.1 Surface characterization

Surface examination with SEM (Scanning Electron Microscope) was performed to quantify the quality of the working electrodes fabricated. Figure 3 shows an example of a 500 µm diameter Pt working electrode disk examined under SEM.

Better information was obtained by the Energy Dispersive X-ray (EDX) analysis of the elements existing in the window represented in Figure 4. The lower the accelerating voltage the shallower the X-ray penetrates the surface layers of the sample. Therefore since the aim was to examine the top surface layer of the electrode, the accelerating voltage of the examination was held at 6 keV to avoid detecting underlying layers.

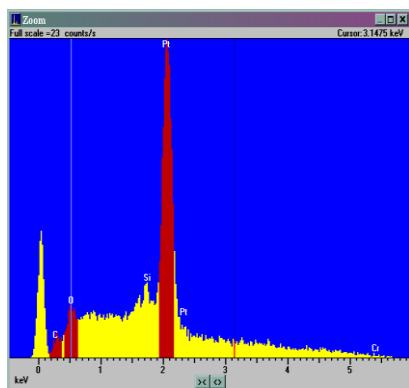
The highlighted elements (C, O<sub>2</sub>, Pt) targeted by the EDX, representing the working electrode WE disk (Pt) while the (C, O<sub>2</sub>)

representing the composition of the photoresist surrounding the electrode

disk.



**Figure 3:** SEM photograph of 500 μm diameter Pt disk working electrode, at 200



magnification and 20kV accelerating voltage.

**Figure 4:** Energy Dispersive X-ray Analysis (EDX) or Histogram of the surface components (range 0-6 keV).

### 3.2 Electrochemical characterisation

As mentioned in a previous section, in order to characterise the microsensors an electroactive species of potassium ferricyanide  $K_3Fe(CN)_6$ , was added to the KCl electrolyte and used for the electrochemical characterisation. the test solution was 6 mM  $K_3Fe(CN)_6$ , in 0.1 M PBS buffer and 0.1 M KCl and the potential range employed for the test was from -0.3 to 0.5 Volts

Figure 5 shows overlaid cyclic voltammograms of the microsensor cycled in the 10 mV/sec -100 mV/sec range.

According to the Randles-Sevcik equation (1) there should be a direct relationship between peak current  $I_p$  and the square root of (scan rate  $\nu$ ), electrode size  $A$ , square root of (diffusion coefficient  $D$ ), concentration of analyte  $C$  and  $n$  (number of electron involved in the redox reaction).

$$I_p = 2.687 \times 10^5 n^{\frac{3}{2}} A D^{\frac{1}{2}} C \nu^{\frac{1}{2}} \quad (1)$$

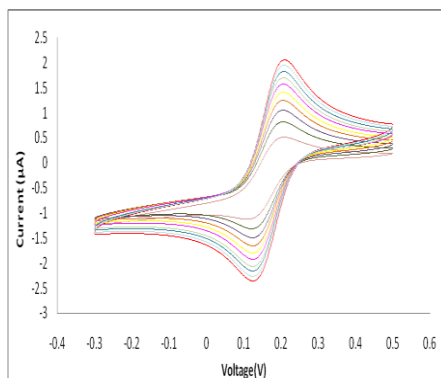


**Figure 5:** Cyclic voltammograms of different scan rates using two electrodes microsensors



cycled in the characterization solution between -0.3 and 0.5 V vs Ag/AgCl, range of scan rate is from 10 mV/sec -100 mV/sec.

For a diffusion controlled system, a linear relationship between  $I_p$  and the square root of the scan rate  $\nu$  should be obtained. In figure 6 the plot of the peak currents against the square root of scan rate is displayed with a clear linear relationship observed.

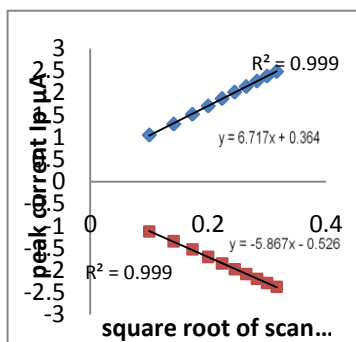


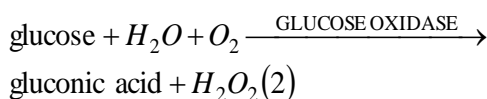
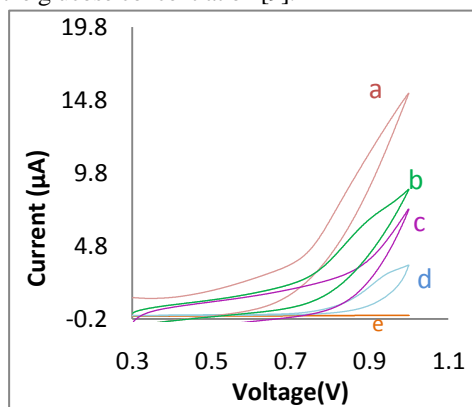
**Figure 6:** Anodic and cathodic peaks current recorded by ‘face to face’ 500µm WE device (2 mm spacer) versus square root of scan rate.

### 3.3 Glucose detection using the two electrode microsensor

A typical biosensor is composed of a biological recognition element, a trans-ducer and a signal processing system. Typically the working electrode of a microsensor acts as the transducer. The biological recognition element is usually a receptor, protein, antibody or enzyme which is immobilised upon the working electrodes surface [8]. The introduction of any of these biological recognition elements enables electrochemical

data to be retrieved from non-electroactive compounds.

Glucose sensing is one of the most studied biosensor applications and is common among microfabricated sensors in the field of clinical analytes detection. Generally speaking, the enzyme “glucose oxidase” is mostly employed in this application. In the presence of oxygen, glucose oxidase acts as a catalyst oxidising and the glucose produces gluconic acid and hydrogen peroxide. The measurement of either the oxygen consumption or hydrogen peroxide production provides electrochemical data on the glucose concentration [9].



In this section a glucose measurements using a two electrode system was reported. A basic biosensor was tested using a fresh solution of 5 mg glucose oxidase + 20 mg of bovine serum albumin + 0.1M PBS. 50 µl of the glucose oxidase based solution was added to 10 µl of 2.5 % glutaraldehyde. A drop of the prepared solution was dispensed over the working electrode of the microsensor and allowed to evaporate at room temperature (22 °C). The device and immobilised enzyme were

stored in a PBS buffer at 4 °C overnight to equilibrate. The modified device was cycled in a 0.1 M KCl solution containing various glucose concentrations (1 to 7 mM). A scan rate of 10mV/s and a potential window between 0.3 and 1.0 V were employed. The slow scan rate allowed sufficient time for the H<sub>2</sub>O<sub>2</sub> to diffuse through the biological element. An anodic potential window was used as the oxidation of hydrogen peroxide occurs at 0.7 V versus an Ag/AgCl reference electrode.

In the presence of glucose, a typical catalytic oxidation current was observed. Under the optimal experimental conditions, the catalytic current produced was proportional to the glucose concentration as observed in Figure 7.

**Figure 7:** The catalytic electrooxidation response of 500µm ‘face to face’ device glucose biosensor cycled in (a) 7, (b) 5, (c) 3, (d) 1 and (e) 0 mM of glucose.

The catalytic oxidation current was linearly proportional to the glucose concentration in the range of 0 mM to 7 mM glucose as plotted in Figure 8.

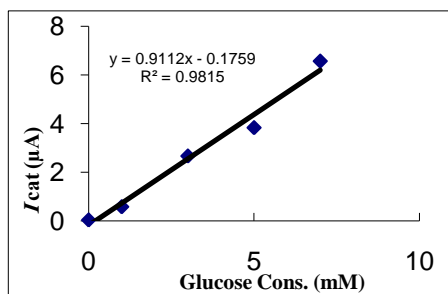


**Figure 8:** Catalytic current increase versus glucose concentration, the device was cycled in a 0.1 M KCl solution containing glucose concentration range from (1 to 7 mM), at scan rate of 10 mV/s and a potential window between 0.3 and 1.0 V.

#### 4. Microfabrication Summary (three electrode system)

Following is a brief summary of the microfabrication procedure with a flow chart (Figure 10) and a general layout of the total system.

Prior to processing the silicon wafer underwent pre-treatment in an RCA cleanser and a HF dip to remove all surface contaminants. A 125 nm thick SiO<sub>2</sub> layer was thermal grown to electrically isolate all subsequent metallic thin films. The wafer was prepared for photolithography # 1 with the application of positive photoresist. The photoresist was softbaked, where it was heated to approximately 59 °C. The wafer was exposed to UV light through photomask # 1 which altered the chemical structure of the resist, increasing its solubility in 20 % v/v NaOH. A Cr and Pt metallic thin films of 20nm and 150nm respectively were deposited by RF sputtering and resistant heated thermal evaporation respectively. Once the Pt thickness was achieved a covering step took a place; a tape was used to cover both the counter and working electrodes for all the sensors on the wafer, this was to allow for the Ag deposition to the reference electrodes. A 250 nm of Ag was deposition to the reference electrodes inside a vacuum system using chamber resistant heated thermal evaporation. Lifting-off the unnecessary metallic and photoresist parts was accomplished in an ultrasonic acetone bath followed by another bath in a very high concentrated NaOH solution. At this point the fabrication of the counter, reference and working electrodes, contact pads and interconnections was completed. Photolithography # 2 was responsible for the passivation of the whole system. The passivation was needed for two reasons; first is to prevented galvanic corrosion of the metals multilayers and second is to delineate the





device's active area. An epoxy negative photoresist (SU8-5) was applied, softbaked, aligned, exposed to UV light through mask # 2, hardbaked and developed. If the wafer was passed mask #2 successfully it was progress to be integrated with a PDMS slap. This slap has an in-wall channel. The top side of the channel was opened with two openings on both top-ends of the channel (inlet and outlet), this was followed by a pouring of an uncured layer of PDMS and allowed it to cure overnight

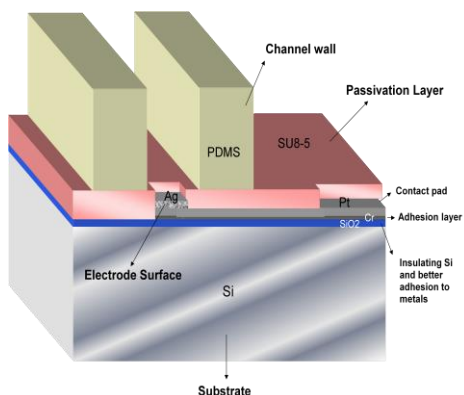
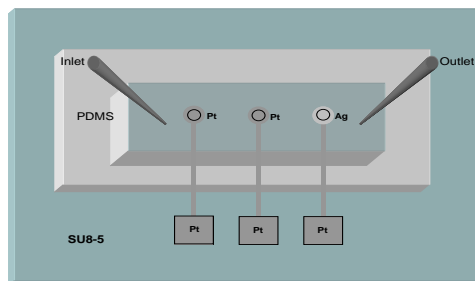


**Figure 9:** (a) top view of the device, (b) cross secti-onnal view of the device.

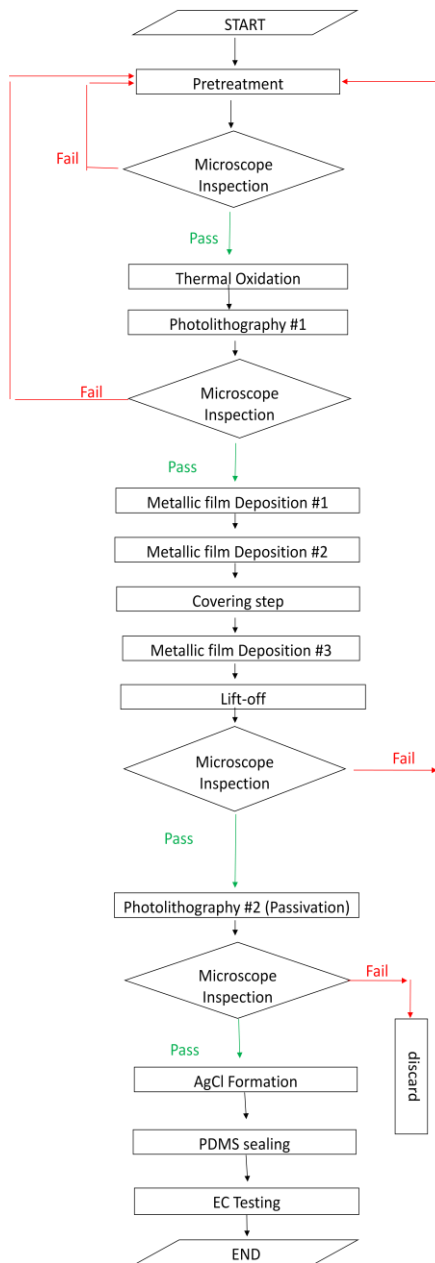


**Figure 10:** flowchart outlining the procedural steps entailed in the fabrication of the microfluidic Microsensor



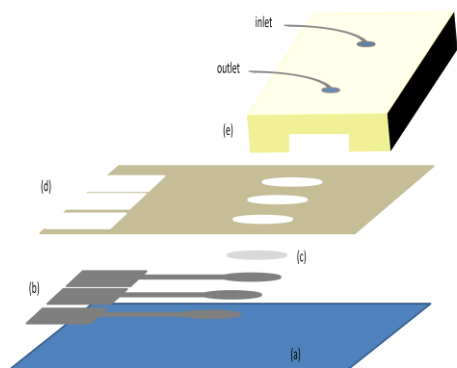


**Figure 11:** Exploded view of  $\mu$ -fluidic a microsensors, (a) silicon, (b) Cr/Pt, (c) Ag (d)SU8-5 and (e) PDMS

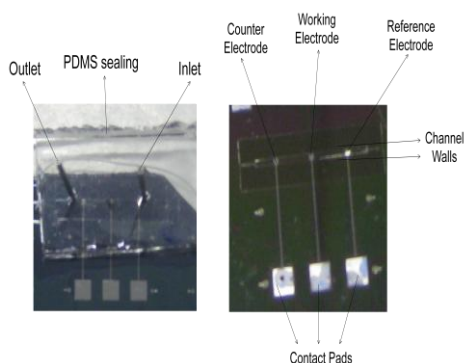


**Figure 12:** Components of the  $\mu$ -fluidic microsensors represented on the actual chip (each in position). The left photo shows the chip in final shape prior the electro-chemistry test.

### 5. Continuous Monitoring test setup

The completed microfluidic sensor was connected to a peristaltic pump (Ismatec model PCI) through the metallic needles. The flow rate was initially adjusted to  $49.9\mu\text{L}/\text{min}$  and a Phosphate buffer solution flow through the

microsensor was monitored for approximately an hour for ensuring the systems sealing properties. Testings were also performed in variable flow rates between  $43\mu\text{L}/\text{min}$  –  $250\mu\text{L}/\text{min}$ . The current application for this sensor is continuous glucose monitoring, but it can be used for many more medical diagnostic, biological and environmental applications.

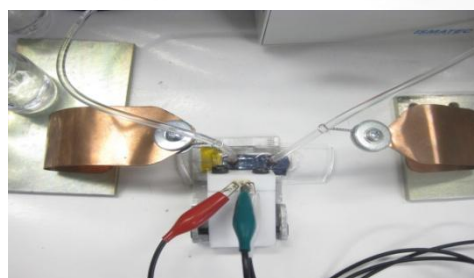


**Figure 13 :** shows the setup of the electrochemistry test ,in the pictures (peristaltic pump, tubing, tubing holder, chip holder and triple clips of the Potentiostat).

### 6. Conclusion

In this work a simple two electrode microsensors was fabricated and successfully employed for glucose detection. It was illustrated that the ‘face to face’ con-figuration of this microsensors creates a fluidic channel into which the analyte sample can be injected. While we are pleased with the results achieved



with this microsensor, we are looking with more expectation towards the next microfluidic sensor presented at the end of this work. The new system is now insured for fluids flow sealing (water tight sealed) and ready to be used as a complete sensor. With further miniaturizing the electrodes and the fluidic channel, the analyte sample required to fill the new micro fluidic channel will be in a volume of tens of nano litres compare to hundreds of micro litres required for the current two electrode sensor.

### Acknowledgment

The two electrode system work was sponsored by the TECHNOLOGY SECTOR RESEARCH STRAND III GRANT. While Enterprise Ireland sponsored the three electrode Micro-fluidic microsensor project under the Applied Research Enhancement Programme (ARE). All the work was executed in the laboratory facilities of both Electronic Engineering and Science departments in the Institute of Technology Tallaght (ITT Dublin).

### References

[1] Rodrigo A. B. da Silva; Edimar G. N. de Almeida; Adriano C. Rabelo; Abílio T. C. da Silva; Lucas F. Ferreira; Eduardo M. Richter. J. Braz. Chem. Soc. vol.20 no.7 São Paulo 2009.  
[2] Pedro A. Quinto-Su, Hsuan-Hong Lai, Helen H. Yoon, Christopher E. Sims, Nancy L. Allbritton, and Vasana Venugopalan, Lab Chip. 2008 March; 8(3):408-414.  
[3] Xin-Xia Cai, Jonathan M. Cooper, Norbert Klauke, Andrew Glidle, Li Cui, Da-Fu Cui, International Journal of Nonlinear Sciences and Numerical Simulation, 3, 2002, 173-176.  
[4] Jiang, Liying; Liu, Chunxiu; Li, Huaqing; Luo, Xianbo; Wu, Yirong; Cai, Xinxia, Journal of Nanoscience and Nanotechnology, Volume 5, Issue 8, 2005,1301-1304.

[5] Marek Orlik, Journal of Electroanalytical Chemistry 434, 1997, 139-152.  
[6] Lin-Chi Chen and Kuo-Chuan Ho, Electrochimica Acta, Volume 46, Issues 13-14,2001,2159-2166.  
[7] Angel E. Kaifer, Marielle Gómez-Kaifer, Supramolecular Electrochemistry, Wiley-VCH,Weinheim,1999.  
[8] Hiroaki Suzuki, Taishi Hirakawa, Satoshi Sasaki and Isao Karube, Sensors and Actuators B: Chemical, Volume 46, Issue2,1998,146-154  
[9] Atsunori Hiratsuka, Kazunori Ikebukuro, Isao Karube, Ken-ichi Kojima, Hiroaki Suzuki and Hitoshi Mugaruma, Analyst, 126, 2001, 658 – 663.  
[10] Brian R Eiggans, Chemical Sensor and Biosensor,Wiley,2002.  
[11] J. Raba and H.A. Mottola, Glucose oxidase as an analytical reagent, Critical Reviews in Analytical Chemistry, 25, 1995,1-42.  
[12] John Alden, Computational Electrochemistry, Thesis from Oxford University1998.  
[13] P. T. Kissinger and W. R. Heineman, Laboratory Techniques in Electroanalytical Chemistry, 2<sup>nd</sup> edition, Marcel Dekker, New York, 1996.  
[14] Marek Orlik, Journal of Electroanalytical Chemistry 575, 2005, 281-286.  
[15] Steven Holdcroft and B. Lionel Funt, Journal of Applied Electrochemistry, Springer Netherlands, Volume 18, Number4,1988,619-624.  
[16] Junjie FEI, Yunhua WU, Xiaobo JI, Jing WANG, Shengshui HU and Zhiqiang GAO, Analytical Sciences,19, Issue9,2003,1259.  
[17] Rónán O'Reilly, Development of Integrated Microsensors using Thin Film Microfabrication Technology, Thesis from ITT Dublin, 2007.  
[18] Feeney R.; Kounaves S.P., Electrochemistry Communications, 1, Issue 10, 1999, 453-458.



## **Implementation of a digital design flow for DPA Secure WDDL Cryptoprocessor using Blowfish algorithm**

**V. Kumara Swamy**

Sirte University, Faculty of Engineering, Dept. of EE, Sirte-Libya  
Tel:0917084428/ Fax: +218-5465461 Email:ksvarkuti@yahoo.com

**Prabhu G Benakop, Senior Member, IEEE,**

Director, Aurora Technological Research Institute, Hyderabad,  
Andhra Pradesh, India, Tel:+91-9866666651 Email:pgbenakop@ieee.org

**B. Sandeep,**

Faculty of Engineering, M.V.S.R. Engineering College, Hyderabad,  
Andhra Pradesh, India  
Email:sandeep\_bee437@yahoo.com

### ***Abstract:***

This paper incorporates security into cryptoprocessor at hardware level against side channel attack namely Differential Power Analysis (DPA). The attacker can gain information by monitoring the power consumption, execution time, electromagnetic radiation, and other information leaked by the switching behavior of digital Complementary Metal Oxide Semiconductor (CMOS) gates. This paper presents a digital design flow to create secure power-analysis-attack-resistant ICs. The design flow starts from a normal design in a hardware description language such as Verilog HDL and provides a direct path to a SCA-resistant implementation. The basis for the power analysis attack resistance is the power dissipation of the IC during various operations. The power dissipation is proportional to the number of transactions of the output signal. With Wave Dynamic Differential Logic (WDDL) style, the number of output transactions is maintained constant and thus the power dissipated by the Integrated circuit is maintained constant irrespective of operation.

In addition to the regular steps in digital IC design flow (logic design, logic synthesis, place & route, stream out, and verifications), this paper include two additional steps, namely cell substitution and interconnect decomposition. The cell substitution is to replace the conventional CMOS gates by WDDL gates. It presents WDDL logic by which the sides channel attack namely Differential Power Analysis (DPA) can be disabled. Experimental results have demonstrated that the secure digital design flow is a functional technique to resist side-channel power analysis. A cryptoprocessor that executes Blowfish, a symmetric block cipher has been considered for the design and its verification. It successfully protects a prototype Blowfish Encryption Standard Integrated Circuit (IC). The cryptoprocessor using Blowfish algorithm with WDDL style has been designed for the key size of 448 bits and plain text of 64 bits. Blowfish algorithm has 16 rounds, requires 9 clock cycles per round and it requires 18 clock cycles per byte encrypted which are best performance figures



compared to RC5,DES, IDEA, and Triple-DES algorithms. The code for the implementation has been written in Verilog HDL. The functional verification has been done using ModelSim 5.5 simulation package. The synthesis of the design is done using the Xilinx WebPack 7.1.

**Keywords:** SCA, CMOS, DPA, WDDL, VLSI and IC

## I. Introduction:

Security is an important aspect for any crypto-processor. The more the security, more would it find applications [3]. A hacker can indulge in any form of attack to extract the information from the communication link or any IC. One form of attacks namely Side-channel attacks have emerged which pave a smooth path for the hackers to gain the confidential information about an IC by continuously monitoring the secondary information of an IC such as power dissipation, timing properties, electromagnetic radiation, etc [1,4]. The main side channel attack that is worth considering is differential power analysis wherein the hacker tries to attack an IC or any small-embedded system by analyzing the power dissipation of the system and by performing series of operations to extract the secret information of the IC. Especially crypto processor that is involved in executing cryptography algorithm is more vulnerable to such side channel attacks.

## II. Power Analysis:

The power consumption of traditional standard cells and logic is dependent on the signal activity. When the output of the logic gate makes a 0 to 1 transition, a current comes from the power supply and charges the output capacitance. On the other hand, when the output sees a 1 to 0, a 0 to 0, or a 1 to 1 transition, no or only a limited amount of power (due to short circuit or

leakage) is consumed from the power supply. This is the fundamental reason why information is leaked through the power supply and why power attacks are possible [1]. Power Analysis can be of two categories namely Simple Power Analysis and Differential Power Analysis [2, 5]. These two mechanisms are explained in detail as following [3]:

### i) Simple Power Analysis (SPA):

In this analysis, the power dissipated for each cryptographic operation is calculated which can yield information about the device's operation or key material. The power varies for each reading depending on the nature of the instruction or operation executed by the microprocessor or a crypto processor. Analyses can be made with the help of the visible differences between the readings taken. Many of the cryptographic units, to be tested were found vulnerable to this Simple Power analysis.

### ii)Differential Power Analysis (DPA):

This analysis is quite complex when compared to the former one and is harder to prevent. It comprises statistical analysis to obtain information about the key. The power traces obtained are classified into two sets depending on a guess function and then the calculation of differences of the



two sets. The differential trace, if containing peak, would hint that the guess function is fairly correct and the key can be disclosed [5].

Therefore it becomes an important task to obtain a constant power dissipation mechanism that can disable the Differential Power Analysis [10,11] scheme and provide security to an IC against it.

### **III. Constant power consuming logic style:**

There exists many different logic styles namely Voltage Mode Logic (VML), Current Mode Logic (CML), Sense Amplifier Based Logic (SABL), etc. But each has its own pros and cons. The decisive drawback of CML is its static power consumption when the gate is not processing any data. VML has to satisfy two more conditions to provide constant power dissipation like one switching event per signal transition and constant capacitance charge. SABL suffers from large clock load [1]. These factors compel one to opt for any other logic style like Dynamic Differential Logic (DDL). This logic involves a clock signal for the functioning of the gates, hence the name dynamic. It is termed differential because both the true and false outputs of the gate are used.

### **Wave Dynamic Differential Logic (WDDL):**

WDDL logic can be implemented with static CMOS logic. Static CMOS standard cells are combined to form secure compound standard cells, which have a reduced power signature. WDDL has many advantages. It can be readily implemented from an existing standard cell library. The design flow is fully supported with accurate

EDA library files that come directly from the vendor. WDDL also results in a dynamic differential logic with only a small load capacitance on the pre-charge control signal and with the low power consumption and high noise margins of static CMOS [1].

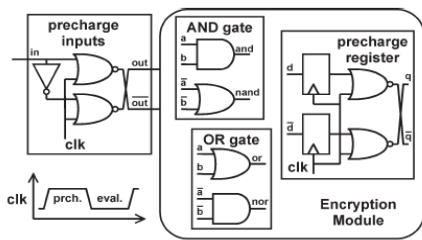
### **Advantages of WDDL logic style are as follows**

A major advantage is that, it can be incorporated by the common EDA tool flow. No special design rules are involved in the interconnection of WDDL gates.

A WDDL gate consists of a parallel combination of two positive complementary gates, one calculating the true output using the true inputs, the other the false output using the false inputs. A positive gate produces a zero output for an all zero input. The AND gate and the OR gate are examples of positive gates. A complementary gate, sometimes also referred to as a dual gate, expresses the false output of the original logic gate using the false inputs of the original gate. The AND gate fed with true input signals and the OR gate fed with false input signals are two dual gates. Fig 1 shows the WDDL AND gate and the WDDL OR gate. In the evaluation phase, each input signal is differential and the WDDL gate calculates its differential output. In the precharge phase, the inputs to the WDDL gate are set at 0. This puts the output of the gate at 0. A module in WDDL precharges without distributing the precharge signal to each individual gate. During the precharge phase, the input vector of the combinatorial logic is set at all 0s. Each individual gate will eventually have all its inputs at 0, evaluate its output to 0, and pass this 0 value to the next gate. One could say that



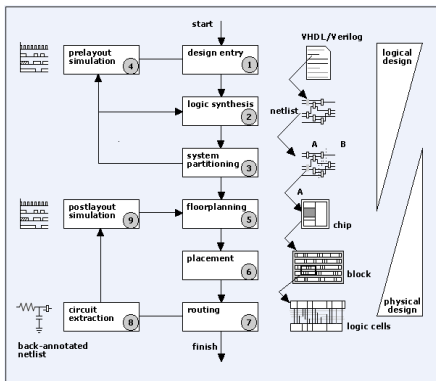
the precharge signal travels over the combinatorial logic as a 0-wave, hence, WDDL. There are several ways to launch to precharge wave. In Fig., a precharge operator is inserted at the start of every combinatorial logic tree, i.e., the inputs of the encryption module and the outputs of the registers. They produce an all-zero output in the precharge phase (clk-signal high) but let the differential signal through during the evaluation phase (clk-signal low).



WDDL: Precharge wave generation.

Fig 1 WDDL Precharge and evaluation Phase

In addition to the regular steps in an IC design (logic design, logic synthesis, place



& route, stream out, and verifications), one can recognize two additional steps, namely “cell substitution and interconnect decomposition”. The cell substitution  
Fig 2 Digital Design Flow

procedure modifies the gate level description. The differential netlist is obtained by replacing each gate by its WDDL counterpart. This means that each net is duplicated, made differential, and connected to the differential pin. The inverters are also removed; the inversions are implemented by switching the nets [1].

#### IV. Blowfish Algorithm:

WDDL can be implemented for any logic design. Since the discussion moves around crypto processors, it would be wise to consider a cryptographic algorithm called Blowfish, which is a 64-bit block cipher presented by Bruce Schneier: a software programmer in C, and is a suggested replacement for DES (Data Encryption Standard). DES was the standard cryptographic algorithm for more than 19 years, but it is now accepted that its key size is too small for present usage.

Blowfish is a fast algorithm and can encrypt data on 32-bit microprocessors at a rate of one byte every 26-clock cycles. The algorithm is compact and can run in less than 5KB of memory. It has a variable-length key block cipher of up to 448 bits. Although a complex initialization phase is required, the encryption of data is very efficient on microprocessors. It suits applications where the key does not change often, for example, a communication link or automatic file encryptor.

#### Analysis of Blowfish Algorithm:

Blowfish is a symmetric block cipher that encrypts data in 8-byte (64-bit) blocks. The algorithm has two parts, key expansion and data encryption. Key expansion



consists of generating the initial contents of one array (P-array), namely, eighteen 32-bit sub-keys, and four arrays (the S-boxes), each of size 256 by 32 bits, from a key of at most 448 bits (56 bytes). The data encryption uses a 16-round Feistel Network

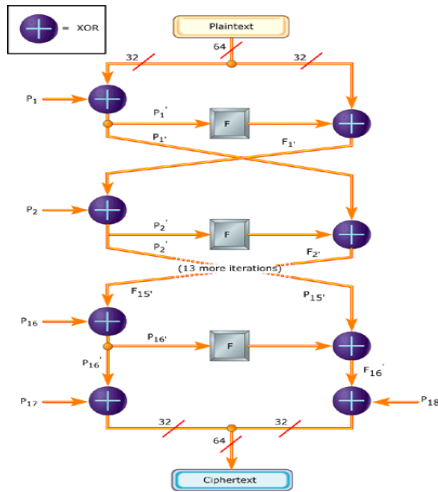


Fig 3 Block diagram of Encryption algorithm

The encryption algorithm shown in fig 3 can be defined by the following pseudo code:

$$\begin{aligned} &\text{For } i = 1 \text{ to } 16 \text{ do} \\ &RE_i = LE_{i-1} \oplus P_i; \\ &LE_i = F[RE_i] \oplus RE_{i-1}; \\ &LE_{17} = RE_{16} \oplus P_{18}; \\ &RE_{17} = LE_{16} \oplus P_{17}; \end{aligned}$$

The variables  $LE_i$  and  $RE_i$  refer to the left half of the data after round  $i$  has completed. Decryption is easily derived from the encryption algorithm. In this case, the 64-bits are initially assigned to two one-word variables  $LD_0$  and  $RD_0$ . We use variables  $LD$  and  $RD$  to refer to the left and right half of the data after round  $i$ . The decryption process as with most block ciphers,

involves using keys in reverse order. The algorithm can be defined as follows:

$$\begin{aligned} &\text{For } i = 1 \text{ to } 16 \text{ do} \\ &RD_i = LD_{i-1} \oplus P_{19-i}; \\ &LD_i = F[RD_i] \oplus RD_{i-1}; \\ &LD_{17} = RD_{16} \oplus P_1; \\ &RD_{17} = LD_{16} \oplus P_2; \end{aligned}$$

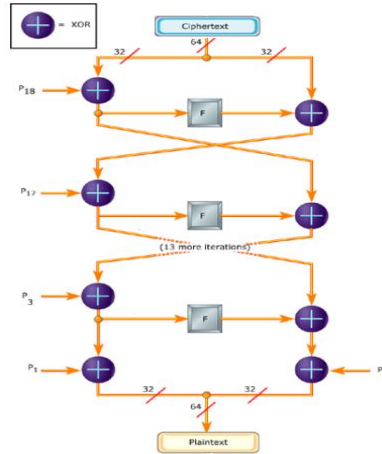


Fig 4 Block diagram of Decryption algorithm

The encryption and the decryption processes are described as shown above in the block diagrams. The Feistel Function block can be shown as follows:

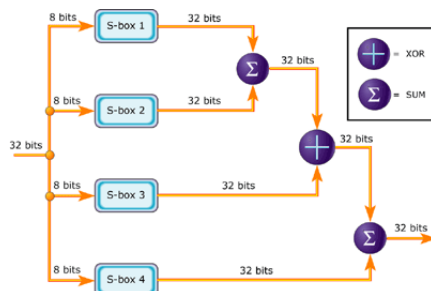


Fig 5 Block diagram of Function Block

The different modules of the algorithm like Substitution Boxes, Feistel Function





Blocks, Exclusive-OR gates, Adder circuits are implemented using WDDL so that when all these components are integrated to execute the cryptographic algorithm, we can obtain constant power dissipation.

## V. Results & Discussions:

Different logic gates and modules of the design have been implemented in WDDL and have been simulated to verify the same number of transitions for any input combination shown as follows:

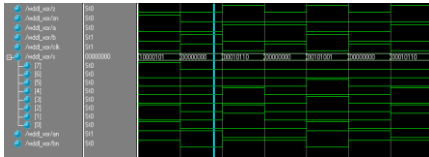


Fig 8 WDDL XOR Gate Simulation Result:

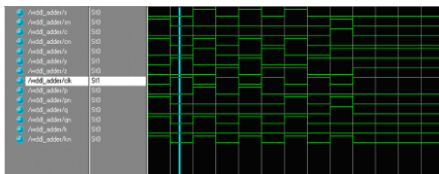


Fig 9 WDDL Full Adder Simulation Result:

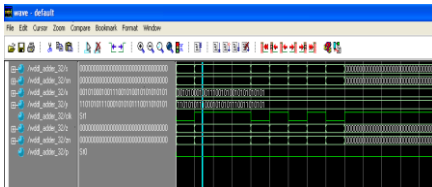


Fig 10 WDDL 32 Bit Parallel Adder Simulation Result:

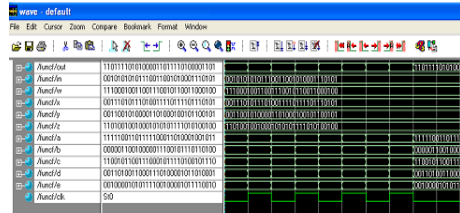


Fig 11 Function Block Simulation Result: Function ‘F’ is used to create ‘confusion’ to thwart cryptanalysis based on statistical analysis. ‘Confusion’ seeks to make the relationship between the statistics of the cipher text and the value of encryption key as complex as possible. One advantage of this model is that the round function F does not have to be invertible, and can be very complex.

## S-BOX 1:

A substitution box (or S-box) is a basic component of symmetric key algorithm used to obscure the relationship between the plaintext and the cipher text. In general, an S-box takes some number of input bits,  $m$ , and transforms them into some number of output bits,  $n$ : an  $m \times n$  S-box, implemented as a lookup table. Fixed tables are normally used, as in the Data Encryption Standard (DES), but in some ciphers the tables are generated dynamically from the key; e.g. the Blowfish and the Twofish encryption algorithms. Advantage of key-dependent S-boxes is that since they are not fixed, it is impossible to analyze the S-boxes ahead of time to look for weakness. The four S-boxes are initialized in order using the bits of the fractional part of constant  $\Pi$  after the initialization of P-array. After the encryption of a 64-bit block of all zeros, the S-boxes are also updated after the update process of P-array.



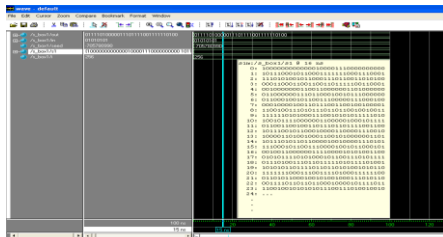


Fig 12 Substitution Box (S-BOX) Simulation Result:

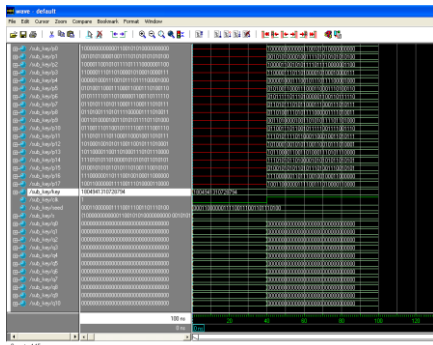


Fig 13 Sub Key Generation Unit Simulation Result:

The sub-key generation unit expands the given 448-bit key into 18 sub-keys, each of 32 bits, so that they can be used at different stages in the algorithm. The subkey generation process is designed to preserve the entire entropy of the key and to distribute that entropy uniformly throughout the subkeys. It is also designed to distribute the set of allowed subkeys randomly throughout the domain of possible subkeys. The entire key is stored in an Array of 14 elements  $K_1$  to  $K_{14}$  each of 32-bit.

The sub-keys are stored in P-array  $P_1$  to  $P_{18}$ . The leftmost 32 bits of fractional part of  $\Pi$  become  $P_1$  and so on.

$P_1 = 243F6A88$ ,  $P_2 = 85A308D3$  and so on.

Then bit wise XOR of the P-array and K-array is performed reusing the words from K-array as needed shown as follows  $P_1 = P_1 \wedge K_1 \dots P_{15} = P_{15} \wedge K_1 \dots P_{18} = P_{18} \wedge K_4$ . A 64-bit block of all zeros is encrypted using current P and S arrays and the P-array is updated with the output of encryption.

From the above obtained results it is evident that irrespective of the input combination, the number of signal transitions tends to remain same leading to constant power dissipation and number of clock cycles required is only 9 compared to all other algorithms. Thus blowfish is a high-speed and more secured algorithm against Differential power analysis compared to the algorithms given in the table no.1

Table no.1: Speed Comparison of Blowfish Algorithm with others

Algorithm	Clock cycles Per round	Number of rounds	Number of clock cycles per byte encrypted
Blowfish	9	16	18
RC5	12	16	23
DES	18	16	45
IDEA	50	8	50
Triple-DES	18	48	108

## VI. Conclusion:

Since the power dissipation of a circuit depends upon the signal activity, it is sufficient that the same number of signal transitions is maintained for every input combination so that power dissipation would remain constant thereby resulting in resistance against Differential Power Analysis (DPA). This is very much possible



by implementing the design in WDDL. But it is to be noted that the circuit size might increase three folds to provide security against DPA.

## REFERENCES

- [1] Kris Tiri, Member, IEEE, and Ingrid Verbauwhede, Senior Member, IEEE “A Digital Design Flow for Secure Integrated Circuits”, IEEE Transaction on Computer-Aided Design of Integrated Circuits and Systems, Vol. 25, No. 7, July 2006.
- [2] Jean-Jacques Quisquater, Math RiZK “Side Channel Attacks” October 2002.
- [3] P. Kocher, J. Jaffe, and B. Jun, “Differential power analysis,” in *Proc. Advances Cryptology (CRYPTO)*, Santa Barbara, CA, 1999, vol. 1666, pp. 388–397.
- [4] S. Chari, C. S. Jutla, J. R. Rao, and P. Rohatgi, “Towards sound approaches to counteract power-analysis attacks,” in *Proc. Advances Cryptology (CRYPTO)*, Santa Barbara, CA, 1999, vol. 1666, pp. 398–412.
- [5] K. Tiri, M. Akmal, and I. Verbauwhede, “A dynamic and differential CMOS logic with signal independent power consumption to withstand differential power analysis on smart cards,” in *Proc. Eur. Solid-State Circuits Conf. (ESSCIRC)*, Florence, Italy, 2002, pp. 403–406.
- [6] P. Kocher, R. Lee, G. McGraw, A. Raghunathan, and S. Ravi, “Security as a new dimension in embedded system design,” in *Proc. 41st Design Automation Conf. (DAC)*, San Diego, CA, 2004, pp. 753–760.
- [7] S. Ravi, A. Raghunathan, and S. Chakradhar, “Tamper resistance mechanisms for secure, embedded systems,” in *Proc. 17th Int. Conf. Very Large Scale Integration Design (VLSID)*, Mumbai, India, 2004, pp. 605–610.
- [8] E. Oswald, S. Mangard, and N. Pramstaller, “Secure and efficient masking of AES—A mission impossible?” IACR Cryptology ePrint Archive, Santa Barbara, CA, Rep. 2004/134, Jun. 2004.
- [9] S. Mangard, T. Popp, and B. Gammel, “Side-channel leakage of masked CMOS gates,” in *Cryptographers’ Track—RSA Conf. (CT-RSA)*, San Francisco, CA, Feb. 2005, pp. 351–365.
- [10] K. Tiri and I. Verbauwhede, “Securing encryption algorithms against DPA at the logic level: Next generation smart card technology,” in *Proc. Cryptographic Hardware and Embedded Systems (CHES)*, Cologne, Germany, 2003, vol. 2779, pp. 125–136.
- [11] K. Tiri and I. Verbauwhede, “A logic level design methodology for a secure DPA resistant ASIC or FPGA implementation,” in *Proc. Design, Automation and Test Eur. Conf. (DATE)*, Paris, France, 2004, pp. 246–251.
- [12] “A VLSI design flow for secure side-channel attack resistant ICs,” in *Proc. Design, Automation and Test Eur. Conf. (DATE)*, Munich, Germany, 2005, pp. 58–63.
- [13] K. Tiri and I. Verbauwhede, “A dynamic and differential CMOS logic style to resist power and timing attacks on security IC’s,” IACR Cryptology ePrint



Archive, Santa Barbara, CA, Rep. 2004/066, Feb. 2004.

[14] K. Tiri and I. Verbauwhede, "Place and route for secure standard cell design," in *Proc. Smart Card Research and Advanced Application IFIP Conf. (CARDIS)*, Toulouse, France, 2004, pp. 143–158.

[15] K. Tiri, D. Hwang, A. Hodjat, B. Lai, S. Yang, P. Schaumont, and I. Verbauwhede, "AES-based cryptographic and biometric security coprocessor IC in 0.18- $\mu\text{m}$  CMOS resistant to side-channel power analysis attacks," in *Symp. Very Large System Integration (VLSI) Technology and Circuits*, Kyoto, Japan, Jun. 2005, pp. 216–219.

[16] N. Pramstaller, F. Gürkaynak, S. Häne, H. Kaeslin, N. Felber, and W. Fichtner, "Towards an AES crypto-chip resistant to differential power analysis," in *30th Eur. Solid-State Circuits Conf. (ESSCIRC)*, Leuven, Belgium, Sep. 2004, pp. 307–310.

[17] E. Hess, N. Janssen, B. Meyer, and T. Schuetze, "Information leakage attacks against smart card implementations of cryptographic algorithms and countermeasures—A survey," in *Proc. Eurosmart Security Conf.*, Marseille, France, 2000, pp. 55–64.



المؤتمر الدولي العربي الليبي الخامس للهندسة الكهربائية والإلكترونية 2010/10/26-23 طرابلس ليبيا



## Effect of Input Matching Network on Class-E RF Power Amplifier Performance

*Firas Mohammed Ali Al-Raie*

*Department of Electronic Engineering, The Polytechnic Higher Institute, Yefren*

*E-mail: firas@ieee.org*

### Abstract

Class-E power amplifiers are very efficient which makes them attractive in modern wireless mobile communication systems. There are several techniques and approaches developed solely to design the output load networks of such amplifiers to shape the RF power device's output voltage and current for minimum power loss. However, little attention is brought to the design of the input matching network and to the device bias conditions with their effects on the overall circuit performance. This paper attempts to discuss these topics through a systematic design and simulation approach of a typical 5W class-E power amplifier operating at 150 MHz.

### 1. Introduction

Several methods have been developed for the design of the load network for class-E RF power amplifier. Among those are the shunt capacitance [1], shunt inductance [2], finite DC feed inductance [3], and parallel circuit [4] techniques. The most popular configuration is the shunt capacitance technique due to its simplicity and designability, which means that when the amplifier is built as designed, it works as expected [1].

The schematic diagram of the class-E power amplifier with shunt capacitance configuration is presented in Figure 1. In this circuit  $L_G$  and  $L_D$  represent the gate and drain bias RF chokes respectively,  $C_B$  is a DC blocking capacitor,  $C_{b1}$  and  $C_{b2}$  are bypass capacitors,  $V_{GG}$  is the gate bias voltage,  $V_{DD}$  is the drain supply voltage,  $C$  is the capacitor shunting the active device  $Q_1$ ,  $L_o$  and  $C_o$  constitute a series resonant circuit tuned at the operating frequency, and

$R$  is the optimum resistance seen by the load network for the required output power. The active device  $Q_1$  (power MOSFET in this case) operates as an ON/OFF switch.

In class-E power amplifier circuit, efficiency is maximized by minimizing power dissipation in the active device, while providing the desired output power. The circuit can be arranged so that high drain voltage and high drain current don't exist at the same time.

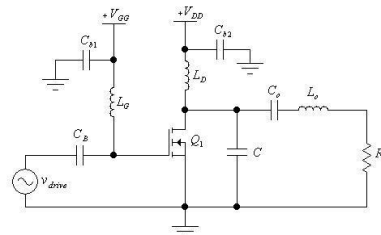


Figure 1: Typical Class-E Power Amplifier with Shunt Capacitance Configuration



For idealized class-E power amplifier operation, it is necessary to provide the following optimum conditions for the drain voltage  $v_D(t)$  across the power MOSFET just prior to the start of the device's ON state at the moment  $t=T$ , where  $T$  is the period of the input driving signal [5]:

$$v_D(t) \Big|_{t=T} = 0 \quad (1)$$

$$\frac{dv_D(t)}{dt} \Big|_{t=T} = 0 \quad (2)$$

Equations (1) and (2) state that the drain voltage should be zero at the turn-on moment, and that the slope of this waveform is zero at the same moment.

## 2. Load Network Design Equations

The load network of class-E power amplifier is not intended to provide a conjugate match to the transistor output impedance. Design equations for the load network elements ( $C$ ,  $C_o$ ,  $L_o$ , and  $R$ ) can be derived by writing time domain equations for the voltage  $v_D(t)$  at the drain of the RF power MOSFET when it is OFF, and the current  $i_D(t)$  passing through the RF device when it is ON. A set of simultaneous differential equations can be formed according to the necessary conditions (1) and (2) and solved to determine the network elements [6].

Nathan Sokal, the inventor of this amplifier, has developed explicit form equations to calculate the values of the network elements at any output power and loaded quality factor  $Q_L$ . These equations are formulated as [7]:

$$R = 0.5768 \left( \frac{V_{DD}^2}{P_{out}} \right) \left( 1 - \frac{0.451759}{Q_L} - \frac{0.402444}{Q_L^2} \right) \quad (3)$$

$$C = \frac{1}{5.44658\omega R} \left( 1 + \frac{0.91424}{Q_L} - \frac{1.03175}{Q_L^2} \right) + \frac{0.6}{\omega^2 L_D} \quad (4)$$

$$C_o = \frac{1}{\omega R} \left( \frac{1}{Q_L - 0.104823} \right) \left( 1 + \frac{1.01468}{Q_L - 1.7879} \right) - \frac{0.2}{\omega^2 L_D} \quad (5)$$

$$L_o = \frac{Q_L \cdot R}{\omega} \quad (6)$$

where  $P_{out}$  is the required output power, and  $\omega$  is the operating frequency.

The value of  $Q_L$  can be selected based on a trade-off between operating bandwidth and harmonic distortion of the output signal.

## 3. Typical Class-E Power Amplifier Design

For the clarification of the goals of this paper, a power amplifier circuit has been designed and simulated using a commercial microwave CAD program. Design specifications of the amplifier are to achieve an output RF power of 5W from an input driving level of 0.5W, and drain efficiency of more than 65% at an operating frequency of 150MHz.

The following sections describe a step-by-step design procedure with the simulated results obtained from the Agilent's ADS microwave circuit analysis program.

### 3.1 RF Power Device Selection and Characterization

The first step of the amplifier design procedure is the selection of the RF power transistor. For this design, the Motorola's power MOSFET MRF134 has been chosen. This device is capable of delivering 5W at 400MHz with a typical power gain of more than 10dB. It operates from a 28V DC supply and has a typical drain-to-source breakdown voltage of 65V.



The RF transistor library of the computer program ADS contains a SPICE model for this transistor which simplifies the simulation process. The simulated input DC characteristic ( $I_D$  versus  $V_{GS}$ ) of the power MOSFET is shown in Figure 2 with  $V_{DS} = 28V$ . It can be shown from this curve that the gate threshold voltage  $V_{GS(th)} = 3V$ . On the other hand, Figure 3 presents the simulated output DC characteristic ( $I_D$  versus  $V_{DS}$ ) at several gate voltages. The drain ON resistance  $R_{D(on)}$  can be estimated from Figure 3 as  $12.5 \Omega$ . This relatively large value of  $R_{D(on)}$  will cause a reduction in amplifier's efficiency due to the dissipated power at the drain during the ON period of the power device.

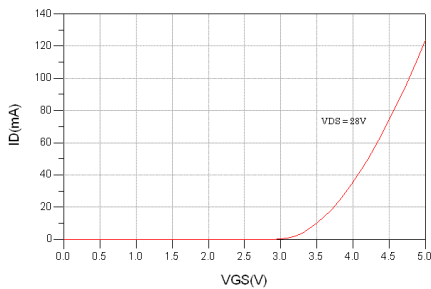


Figure 2:  $I_D$  versus  $V_{GS}$  for the MRF134 Power MOSFET

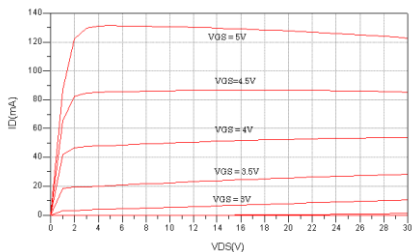


Figure 3: Simulated Drain DC Characteristics of the MRF134 Power MOSFET

### 3.2 Calculation of the Load Network Elements

The design procedure begins by calculating the component values of the load network using equations (3) to (6). For output power  $P_{out} = 5W$ , operating frequency  $f = 150MHz$ , loaded quality factor  $Q_L = 5$ , and drain power supply  $V_{DD} = 28V$ , the calculated values of the elements of the load network are:

$$R = 80\Omega, C = 3pF, C_o = 3pF, \text{ and } L_o = 430nH.$$

The output capacitance of the RF device,  $C_{out}$ , is measured as  $9.7 pF$  from the device data sheet. This means that it is greater than the required value of the shunt capacitance. The excess value of  $6.3 pF$  should be tuned out by part of the drain bias RF choke.

### 3.3 Design of the Output Matching Network

An output matching network is needed to transform the  $50\Omega$  amplifier impedance into the required load resistance which is set to be  $80\Omega$ . This network has been designed with the aid of an immittance Smith chart, and takes a T-section configuration as shown in Figure 4.

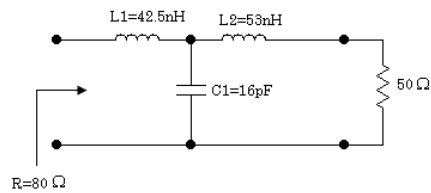


Figure 4: Configuration of the Output Matching Network

In addition to the transformation function of the output matching network, it can be used to reduce the harmonic content of the output RF signal. Figure 5 shows the



simulated input return loss of this network, while Figure 6 presents its insertion loss.

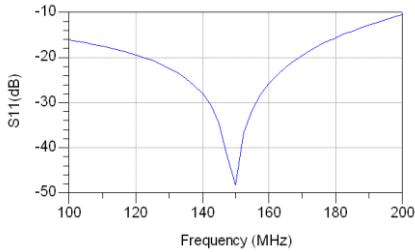


Figure 5: Input Return Loss of the Output Matching Network

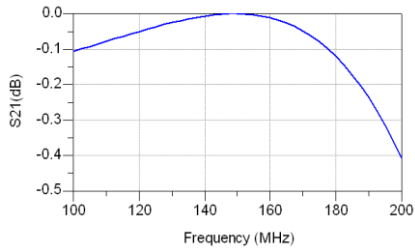


Figure 6: Insertion Loss of the Output Matching Network

### 3.4 Design of the Biasing Network

The biasing network consists of the drain and gate RF chokes, bypass capacitors, DC blocking capacitors, in addition to the gate and drain bias voltages. For 50% duty cycle operation, the transistor is biased at the threshold point, which means that  $V_{GG} = V_{GS(th)} = 3V$ . This actually corresponds to class-B mode.

Based upon the previous calculations, the schematic diagram of the amplifier circuit is shown in Figure 7.

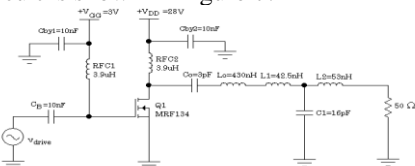


Figure 7: The Designed Class-E Power Amplifier without the Input Matching Network

### 3.5 Amplifier Performance Simulation

The designed amplifier circuit has been simulated using ADS 2006A. With a single tone input signal of 0.5W power level and an operating frequency of 150MHz, the RF device's drain voltage and current are sketched as depicted in Figure 8. As shown from this plot, the peak values of drain voltage and current don't exist simultaneously which minimizes the device's power loss. However, at the ON time of the RF signal, the drain voltage is about 3.5V due to the ON resistance at the drain,  $R_{D(on)}$ . This may degrade the overall efficiency of the circuit. During the OFF interval of the RF signal, a negative current flows through the power MOSFET's output capacitance  $C_{out}$ .

In Figure 9 the output signal waveform is sketched, while its spectrum is displayed in Figure 10. It is obvious that the harmonic level is acceptable due to the filtering effect of the load and matching networks.

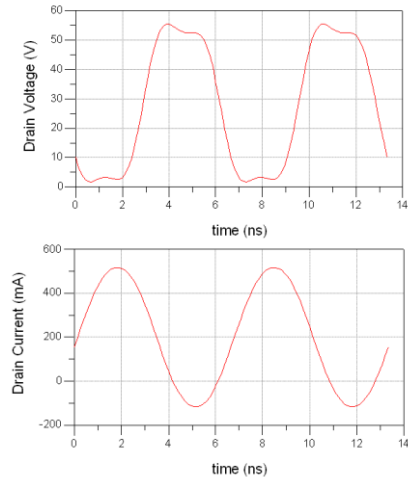


Figure 8: Simulated Drain Voltage and Current Waveforms of the Power MOSFET



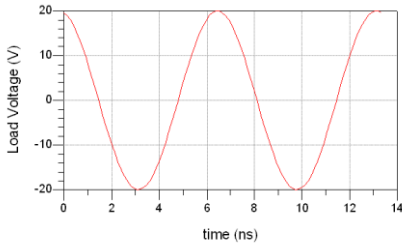


Figure 9: Simulated Waveform of the Load Voltage

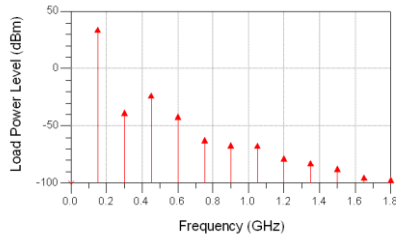


Figure 10: Power Spectrum of the Output Signal

In order to display the power amplifier's performance characteristics, a sweep of the input power level has been carried out from 10dBm to 30dBm at the operating frequency. Figure 11 shows a sketch of the output power versus input power. The output power is obtained from:

$$P_{out} = \text{real}(0.5V_L \cdot I_L^*) \quad (7)$$

Where  $V_L$  and  $I_L$  are the peak values of the fundamental components of load voltage and current respectively.

The output power is about 36dBm at an input level of 27dBm.

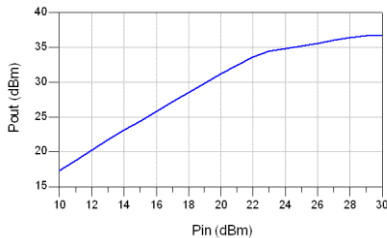


Figure 11: Amplifier Output Power versus Input Power

Figure 12 presents the operating power gain of the amplifier,  $G_p$  versus input power. The power gain is calculated from:

$$G_p \text{ (dB)} = P_{out} \text{ (dBm)} - P_{in} \text{ (dBm)} \quad (8)$$

It is noticed that the power gain is about 9.0dB at an input power level of 27dBm.

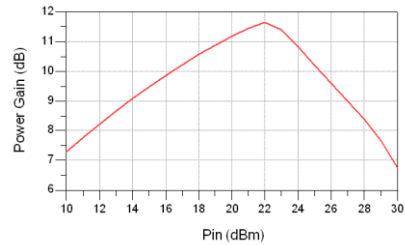


Figure 12: Power Gain versus Input Power

Finally, Figure 13 displays a sketch of the amplifier's DC to RF efficiency with input power. The amplifier efficiency is about 71.1% at an input power of 27dBm.

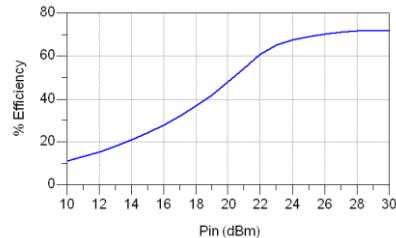


Figure 13: Simulated Efficiency versus Input Power

The efficiency of the amplifier circuit has been evaluated from:

$$\eta = \frac{P_{out}}{P_{dc}} \quad (9)$$

Where  $P_{dc}$  is the DC power consumed by the RF device and is obtained from:

$$P_{dc} = V_{DD} \cdot I_{DD} \quad (10)$$

$I_{DD}$  is the DC component of the drain current.



### 3.6 Input Matching Network Design

The input matching network can be designed to match the large signal input impedance of the RF power device with the 50 Ω source impedance. Therefore, the large signal input impedance of the RF transistor should be estimated at the nominal input power, operating frequency, and bias voltages with the existence of the load and output matching networks. The large signal input impedance of the power transistor consists of two parts, resistance  $R_{in}$  and reactance  $X_{in}$ :

$$Z_{in} = R_{in} + jX_{in} \quad (11)$$

$R_{in}$  and  $X_{in}$  can be estimated from:

$$R_{in} = \text{real}(V_{in} / I_{in}) \quad (12)$$

$$X_{in} = \text{imag}(V_{in} / I_{in}) \quad (13)$$

Where  $V_{in}$  is the fundamental component of the input voltage at the gate of the MOSFET, and  $I_{in}$  is the fundamental component of the current entering the gate of the transistor.  $I_{in}$  can be estimated using a current probe with the aid of ADS simulation capabilities. Figure 14 shows a sketch of the large signal input impedance of the power device versus input power.

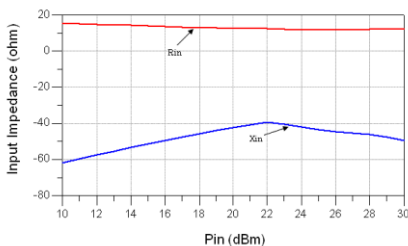


Figure 14: Variation of the Large Signal MOSFET Input Impedance with Input Signal Level

As shown from the plot in Figure 14, the input impedance is capacitive. At an input power of 27dBm (0.5W), the input

impedance is approximately 12-j45 Ω. The input matching network can thus be designed to match this value with the 50 Ω source impedance. An immittance Smith chart has been used to construct an L-section matching network graphically. Figure 15 presents the final power amplifier circuit after incorporating the input matching network.

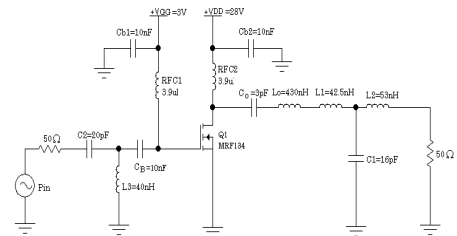


Figure 15: The Designed Class E Power Amplifier after Adding the Input Matching Network

There is no doubt that the input matching network improves the net input power delivered to the RF device. The amplifier circuit was simulated again after adding the input matching circuit using ADS. The output power of the circuit is displayed in Figure 16 with a sweep of input power from 10 to 30dBm. As shown from Figure 16, there is a slight increase in output power being 38.8dBm for an input power of 27dBm. The power gain is plotted in Figure 17, and becomes equal to 9.8dB at the nominal input power. The DC to RF efficiency is sketched in Figure 18 versus input power. The efficiency becomes 71.8% at an input power level of 27dBm. However, no attempts have been made to optimize the component values of the input matching network for better performance characteristics.

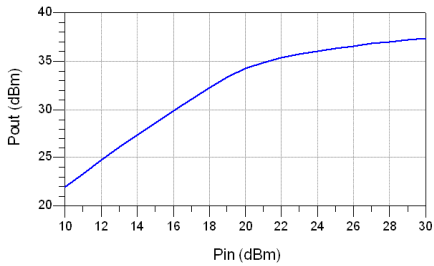


Figure 16: The Simulated Output Power versus Input Power for the Final Amplifier

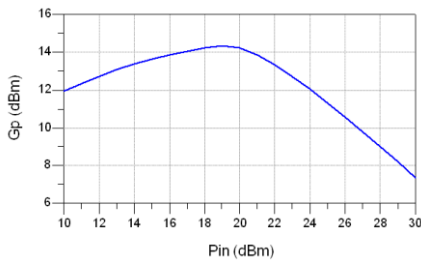


Figure 17: Operating Power Gain versus Input Power

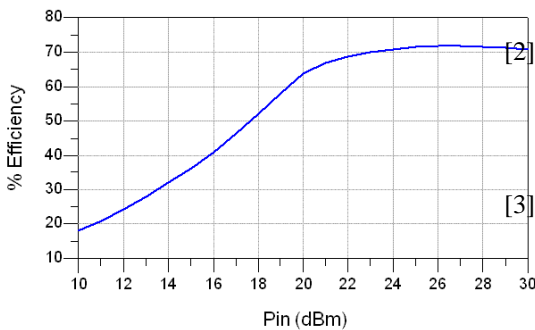


Figure 18: Efficiency versus Input Power

#### 4. Conclusion

The performance of Class E RF power amplifier with traditional shunt capacitance load network has been studied thoroughly. It was shown that the high efficiency operation of such amplifiers is determined mainly by the output load network. However, with an accurate and proper

design of the input matching network, the performance characteristics of the amplifier can be improved. This paper has put and discussed the main guide lines for synthesizing the input matching circuits for this type of RF amplifiers.

#### Acknowledgement

I would like to express my deep gratitude to *Dr. Andrei Grebennikov*, of Bell Labs, Ireland, for his continuous technical support and useful suggestions in high efficiency power amplifier analysis, and also for providing me with some technical papers and e-books in the field of RF power amplifiers.

#### References

- [1] N.O. Sokal and A.D. Sokal, "Class E- A New Class of High-Efficiency Tuned Single-Ended Switching Power Amplifiers", *IEEE J. Solid-State Circuits*, Vol. SC-10, June 1975, pp. 168-176.
- [2] M.K. Kazimierczuk, "Class E Tuned Power Amplifier with Shunt Inductor", *IEEE J. Solid-State Circuit*, Vol. SC-16, February 1981, pp. 2-7.
- [3] R.E. Zulinski and J.W. Steadman, "Class E Power Amplifiers and Frequency Multipliers with Finite DC-Feed Inductance", *IEEE Trans. Circuits and Systems*, Vol. CAS-34, September 1987, pp. 1074-1087.
- [4] A. Grebennikov, "Switched-Mode RF and Microwave Parallel-Circuit Class E Power Amplifiers", *Int. J. RF and Microwave Computer-Aided Eng.*, Vol.14, Jan/Feb 2004, pp. 21-35.
- [5] A. Grebennikov, "Load Network Design Techniques for Class E RF and



Microwave Amplifiers", *High Frequency Electronics*, Vol. 3, July 2004, pp. 18-32.

- [6] A. Grebennikov and N.O. Sokal, *Switchmode RF Power Amplifiers*, Elsevier Inc., 2007, Chapter 5.
- [7] N.O. Sokal, "Class-E RF Power Amplifiers", *QEX*, Jan/Feb 2001, pp. 9-19.



**Paper NO. 102420**

## **Bipolar Junction Transistor: Process Fabrication and characterization Technology**

Osama S Hammad<sup>1\*</sup>, Othman Sidek<sup>2</sup>, Kamarul Azizi Ibrahim<sup>3</sup>, and M.A.H.Qa'eed<sup>3</sup>

<sup>1\*</sup>School of Electrical and Electronic Engineering, Universiti Sains Malaysia. <sup>2</sup>Collaborative Microelectronic Design Excellence Center Engineering Campus. <sup>3</sup>Nano-Optoelectronics Research and Technology Laboratory School of Physics and Universiti Sains Malaysia (USM), 11800 Minden, Penang, MALAYSIA

\* Author to whom correspondence should be addressed. (E-mail: Osama<sup>1\*</sup>hammad762008@yahoo.com)

### **Abstract:**

The great success of semiconductor industry has been driven by the advancement in transistor technology in its early era. The industry could improve the performance of their products by shrinking the transistor dimensions and integrating more transistors. However, this strategy is becoming less effective, as the transistors demanded substantial interconnections between them, and the speed of integrated circuit products are being dominated by interconnections. Innovations are necessary in the interconnection technology to overcome the barriers. Furthermore, fabrication thin-film silicon on insulator of bipolar junction transistor (TFSOI-BJT) is the subject of this paper. More specifically, we have worked in two domains: the main part of the work was to fabricate Bipolar Junction Transistor on Silicon on Insulator. While the second part was the technological solid source diffusion which is PhosphPlus/BoronPlus of a process to manufacture base and emitter transistor. This paper focuses on selective solid source diffusion of in-situ PhosphorusPlus/BoronPlus doped silicon on insulator (SOI) alloys intended for this application. Experiments were carried out to study electrical properties of the in-situ doped layers with emphasis on maximizing the active carrier concentration. Active phosphorus and boron levels were obtained.



The diffusion layers were used to fabricate two pn junctions back to back. Junctions were fabricated to create heavily doped region suffered from band to band tunneling, which is expected regardless of the junction formation technique. While in, Junctions fabricated to create lightly doped region exhibited behavior equivalent to best junctions.

**Keywords:** Bipolar junction transistor (BJT), pn junction diode, boronplus, and hophoursplus

**Note:**

**This paper is included in the conference program but not published because the revised copy after introducing the reviewed comments did not arrive in the specified Time**



## "Study The Effect of Thermal and Chemical Treatment on the Electrical behaviour for Edri Zone Sands

N. A. Abdulgader<sup>1</sup>, M.M. Ben Omran<sup>2</sup>, A.Y. Okasha<sup>3</sup>, A.H.Osman<sup>4</sup> and Y.A.Soliman<sup>5</sup>.

<sup>1</sup>Physics Department, Nasser Nations University, Tarhuna-Libyan

<sup>2</sup>Physics Department, University of Al-Fateh, Tripoli- Libyan

<sup>3</sup>Physics Department, Almergap University, Khomes-Libyan

<sup>4</sup> Physics Department, University of SEBHA, Sebha- Libyan

<sup>5</sup>Industry Research Center, IRC, Tripoli Libyan

Email : [nabdulgader7@hotmail.com](mailto:nabdulgader7@hotmail.com)

### **Abstract**

Quartz and silica sands are one of the most important materials for some advanced applications when they are present in pure form and good quality. Sources of the material are available in many sites in Libya, especially in Edri zone. The received material may include fine graded mixtures of sand, silt, and clay as well as organic or other deleterious or undesirable materials. So, the quality and gradation of sand are very important, therefore, it is necessary to remove clay lumps or oversize material, binder and sometimes filler or blends.

Three samples taken from Edri area southwest of Libya. Mamunitat sandstones have been treated with different chemical and physical processes. Samples were thermally treated at some selected temperature. Crushing, grinding and the grain-size distribution for each sample were carried out. Using X-Ray diffraction analysis (XRD), the lattice constants for each sample were calculated to identify the purity of the quartz sands. The x-ray measurements confirmed that all samples have hexagonal structure.

A-c and d-c conductivities of the samples as a function of temperature and at fixed frequency of 50Hz were measured by using ohmic technique, also the activation energy was determined to investigate the main physical-chemical changes due to these treatments.

### **Introduction**

While apparently simple, the composition of silicon dioxide, SiO<sub>2</sub>, represents in fact, a series of polymorphous modifications. Owing to its crystalline structure this oxide takes a special position among native oxides. The crystalline structure of silicon

dioxide is actually connected directly with that of silicates. For This reason some authors consider this mineral belong to the silicates group.



Silicon dioxide  $\text{SiO}_2$  is commonly called Silica, and it is widely found as sandstone and quartzite.<sup>[1]</sup> It is the starting material for production of silicate glasses and ceramics. Silica is one of the most abundant oxide materials in the earth's crust. It can exist in an amorphous form or in a variety of crystalline forms.<sup>[1]</sup>  $\text{SiO}_2$  has a high melting point. Crystalline silica exists in seven different forms or polymorphs, four of which are extremely rare. The three major forms are: quartz, cristobalite, and tridymite. They are stable at different temperatures.<sup>[2]</sup> Within the three major forms, there are subdivisions<sup>[3]</sup>, each of which has different structure at high and low temperatures. Geologists distinguish, for example, between alpha and beta quartz, noting that at 573 °C, quartz changes from one form to the other. Each of these

### **Experimental**

#### **Instruments**

- a- X-ray diffractometer Bruker axS D5005.
- b- Function generator (G F 10-100KHz )

#### **Chemical and physical processes:**

Three samples taken from Edri area southwest of Libya. Mamunitat sandstones have been treated with different chemical and physical processes as shown in the table (1) below. The received material may include fine graded mixtures of sand, silt, and clay as well as organic or other deleterious or undesirable materials. To achieve high purity, the used sand often has to go through extensive physical and chemical processing. This involves acid washing with different acid concentrations to remove contaminated impurities and mostly soluble ions in the sand as well as from the surface of the individual

subdivisions is stable under different thermal conditions.<sup>[4]</sup>

There are two methods for purification of silica from ores. One of them is the acid processing and the other alkali processing. We have used the first one in the purification of our samples.<sup>[5]</sup> after that the samples were heat treated.

Using X-Ray diffraction analysis (XRD), the lattice constants for each samples were calculated according to the suitable choice of the crystal

Structure. Variations of a-c conductivity at low frequency with temperature were recorded. Besides the activation energy was determined to investigate the main physico-chemical changes due to these treatments and to decide on the usability of these sands for some applications.

c- Digital multimeter model 3800d

d- Digital Voltmeter model HP

quartz grains. Samples were thermally treated at 650°C for 4 hour and also subjected for cooling modes. Crushing, grinding and the grain-size distribution for each samples were carried out.





**Table 1 summarises all the samples details**

No	Sample name	Colour of sample	Type of treatment
1-	NS9	White	Original sample as received
2-	NS1	White	Thermally treated at 650 °C for 4 hour
3-	NS3	White	Acid washed for 1 hour, 30 °C

**XRD and Preparation of samples for electrical conductivity measurements**

The specimens ( NS1, NS3 and NS9 ) are received in the powder form and then put compact form in a hardened steel die "with 15mm in diameter and 1-2 mm in thickness" by a pressure of  $(1.5 \times 10^8 \text{ pa})$  held for 60 seconds. For studying the electrical conductivity, the specimens in the two pellets form are electroded by using the silver past, painted in The tow opposite faces and inserted between the two wires in samples holder and then support these wires by drips of silver paint.

Using Ohmic Technique the conductivity measurements of three samples were carried out.

The a.c conductivities are measured for all the samples in the temperature range 325K-449K in the fixed frequency 50Hz.

The circuit used for electrical measurements is illustrated in the Fig. 1. The current (I) passing through the sample of thickness d and cross-sectional area A, is determined from the potential difference

$(V_R)$  measured between the terminals of a standard resistance (R) using Ohm's law<sup>[2]</sup>:

$$I = \frac{V_R}{R} \tag{1}$$

$$R = \rho \frac{d}{A} = \frac{d}{\sigma A} \tag{2}$$

were  $\rho$  is the resistivity and the conductivity is the  $\sigma$

$$\sigma = 1/R \cdot d/A \tag{3}$$

The conductivity  $\sigma$  varies with temperature exponentially as

$$\sigma = \sigma_o \exp^{-E_{act}/kT} \tag{4}$$

Where  $\sigma_o$  is the constant.

$E_{act}$  is the activation energy, (eV)

k is the Boltzmann constant

T is the absolute temperature in Kelvin

then



$$Ln\sigma = Ln\sigma_o - \frac{E_{act}}{k} \frac{1}{T} \quad (5)$$

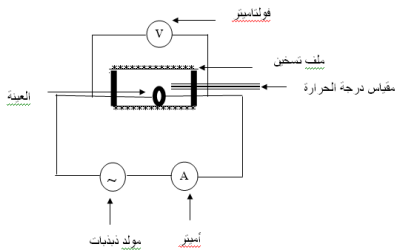


Fig. 1. The circuit used for a.c conductivity measurements.

## Results and discussion

### (A)-X-Ray diffraction analysis (XRD)

X-ray diffractometer (Bruker) type D5005 was used to study the crystal structure and to determine the lattice constant for each sample. The measurements were carried out at room temperature (25°C). The target of the machine was copper with wave length 1.5406 Å [7,8], and Ni filter. For each sample

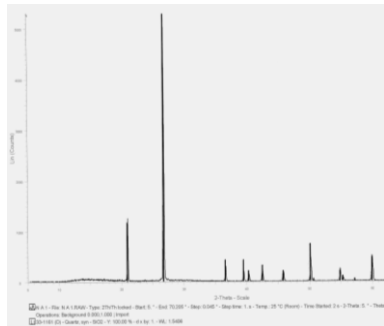


Fig. (2) XRD spectra for Sample( NS1 )

the measurement was repeated at least three times with different intensities, as shown in (Figures1-4). The XRD- spectra of all samples are almost the same, never the less the lattice constants for each sample were determined. The crystal structure of the all sample was found to be hexagonal one. The XRD- results are combatable with those found in literature [7,8]. The volume of the primitive cell is found to be 112.3(Å)<sup>3</sup> approximately, this result agree very well with the volume of standard SiO<sub>2</sub> material, and also with the of V.J. Hurst et al, [9].

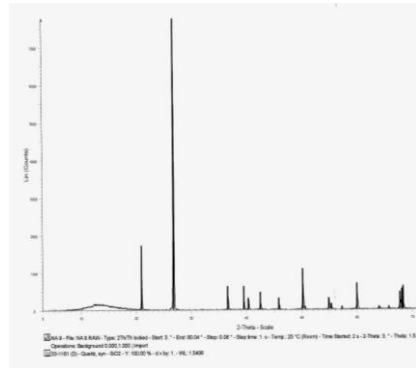


Fig. ( 1 ) XRD spectra for sample (NS9)

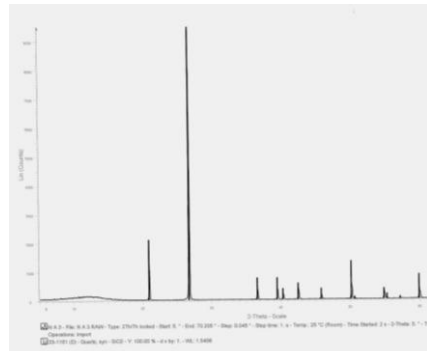
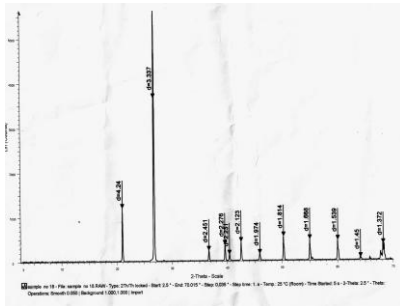


Fig. (3) XRD spectra for sample(NS3)



**Fig. (4 ) XRD spectra for standard sample of SiO<sub>2</sub>**

**(B) Electrical conductivity Measurements**

the three samples prepared for the electrical conductivity are crystalline in structure. In the present investigation of the electrical conductivity for the three different Specimens (thermal treatment NS1), (Chemical treatment NS3), (Specimen as received NS9) all samples are crystalline in structure.

**Table 2 The Electrical conductivity and activation energy for group of samples with different treatments**

<i>Specimen</i>	<b>Conductivity <math>\sigma</math> ( S m<sup>-1</sup> )</b>	<b>E<sub>act</sub></b>
<i>NS1<sub>DC</sub></i>	$\sigma$ (325K) = 36786×10 <sup>-9</sup>	<b>E<sub>act</sub>=(361-389K) =0.8 eV</b>
	$\sigma$ (361K) =42351×10 <sup>-9</sup>	
	$\sigma$ (389K) =266456×10 <sup>-9</sup>	
<i>NS3<sub>DC</sub></i>	$\sigma$ (296K) =66×10 <sup>-9</sup>	<b>E<sub>ac</sub> (388-423K) =1.611 eV</b>
	$\sigma$ (388K)=430×10 <sup>-9</sup>	
	$\sigma$ (423K) =12626×10 <sup>-9</sup>	
<i>NS9<sub>DC</sub></i>	$\sigma$ (305K)=242327×10 <sup>-9</sup>	<b>E<sub>ac</sub> (371-379K) =2.43 eV</b>
	$\sigma$ (371K) =90279×10 <sup>-9</sup>	
	$\sigma$ (379K) = 468066×10 <sup>-9</sup>	<b>E<sub>ac</sub> (379-393K) =0.286 eV</b>
	$\sigma$ (393K) =605836×10 <sup>-9</sup>	
<i>NS3<sub>AC</sub></i>	$\sigma$ (293K) = 1333×10 <sup>-9</sup>	<b>E<sub>ac</sub> (423-449K) =0.403 eV</b>
	$\sigma$ (423K) =14557×10 <sup>-9</sup>	
	$\sigma$ (449) =27821×10 <sup>-9</sup>	

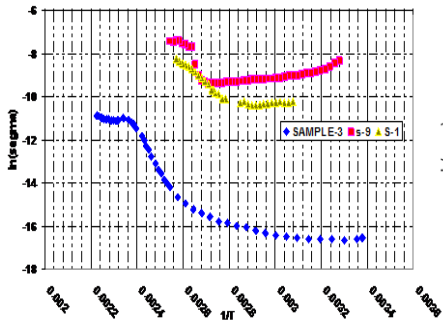


Fig. (5) the conductivity for samples (NS1,NS3,NS9) using DC measurements.

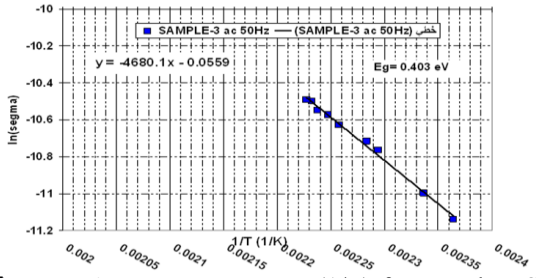


Fig. (8)  $\ln \sigma$  Versus  $(1/T)$  for sample NS3 at range of temperature (423-449K) measured at 50Hz A.C

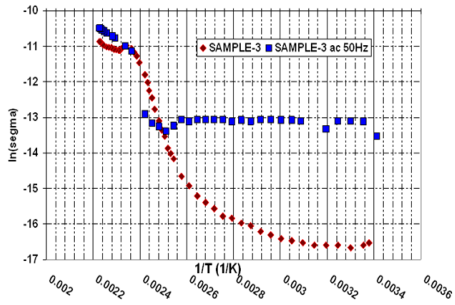


Fig. (6) the conductivity for sample NA3 measured Dc and Ac-50Hz

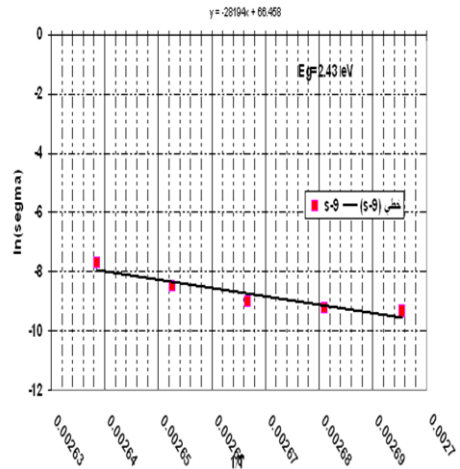


Fig. (9)  $\ln \sigma$  Versus  $(1/T)$  for sample NS9 at range of temperature (371-379K) measured at DC

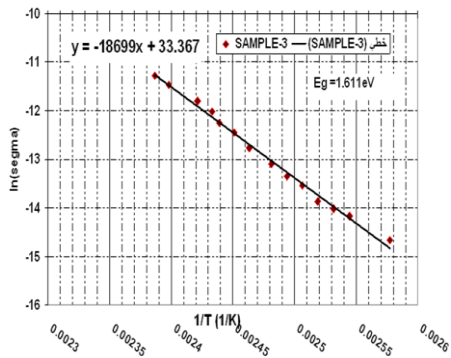


Fig. (7)  $\ln \sigma$  Versus  $(1/T)$  for sample NS3 at range of temperature (388-423K) measured at DC

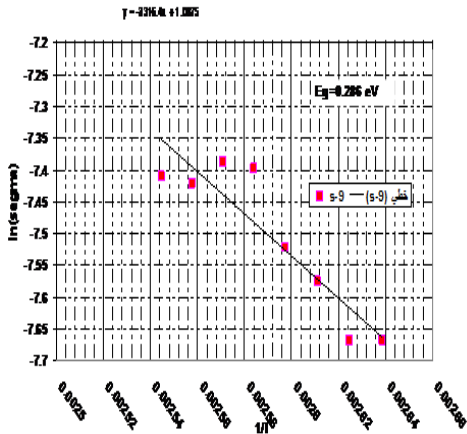


Fig. (10)  $\ln \sigma$  Versus  $(1/T)$  for sample NS9 at range of temperature (379-393K) measured at DC

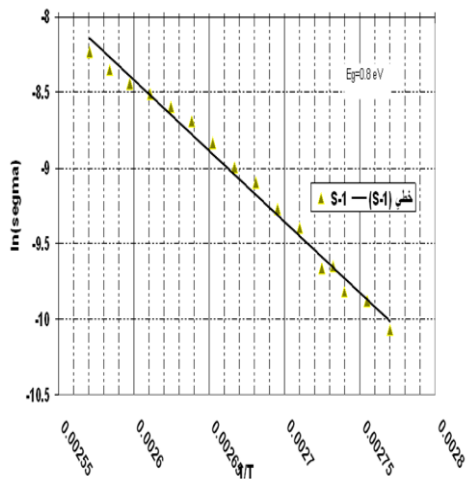


Fig. (11)  $\ln \sigma$  Versus  $(1/T)$  for sample NS1 at range of temperature (361-389K) measured at DC.

The conductivity measurements of the three samples (NS1, NS3, and NS9) were carried out. The d.c conductivity for three samples

(NS1, NS3, and NS9) was carried. From Fig. (5) it is clear that the values of the conductivity at room temperature decrease for treated specimen compared with the normal sample.

This behavior is attributed to the decreasing in impurities at the surface of the samples, and the decreasing was higher for chemical treatment specimens, and also the transition point is much higher for the normal sample (NS9).

The Fig.(6) shows the conductivity for sample NS3 measured at (dc) and (ac) (50Hz) . Its clear from the figure that the frequency is causes the increasing of the conductivity at room temperature, and also the transition point is higher.

Fig. (5) and Fig.(6) show the d.c-conductivity variation with temperature in the 388 up to 423K for the sample NS3. This variations indicate that the sample NS3 exhibit a semiconductor behavior.

Using equation (5) the activation energy was obtained for the sample NS3 to be 1.611 eV as shown in Fig, (7) at d.c hand the measurement. On the other activation energy at a.c (50Hz) measurements for the same sample gave a value of 0.403 eV as shows Fig.(8).

The activation energy for the sample NS9 was detected to be 2.43 eV from d.c conductivity measurements using equation No (5), and to be 0.286 eV from a.c conductivity measurements. These results are obtained from Fig. (9) and Fig. (10). of the sample at range of temperature (371-379K) using equation (5), and to be Fig (9). the activation energy at d.c measurements for the same sample at range of temperature (379-393K ) is gave a value of 0.286 eV as shows in Fig.(10).



The activation energy was obtained for the sample NS1 to be 0.8 eV as shown in Fig, (11) at d.c measurement.

The above mentioned results for the d.c and a.c conductivity were shown in table (2).

### Conclusion:

The physical and chemical treatments did not affect the samples. It is hard to differentiate between the samples according to the lattice constants result which are obtained from the XRD measurements. No X-rays reflections seemed to be coming from the planes perpendicular to the c-axis. Thus the c-axis is a symmetry axis for all the samples. results are combatable with those found in literature.

Conductivity measurements indicate that the effect of acid processing decrease the conductivity, besides the heat temperature treatments decrease the conductivity more. This may be due to the effects of impurities and size grain.

### References

- 1-J.D. Lee, Concise Inorganic Chemistry, Fifth Edition, Chapman & Hall, London, UK, p430, (1990).
- 2- Donald R. Askeland, The Science and Engineering of Materials, second SI Edition, Chapman & Hall, London, UK, (1990).
- 3- Crystalline Silica Primer

Staff, Branch of Industrial Minerals  
U.S. Department of the Interior  
Manuel Lujan, Jr., Secretary  
U.S. Bureau of Mines  
T S Ary, Director

5-M.Takemori, Hydrometallurgical  
Methods for Extraction and purification of  
silica, Minerals Engineering, Vol.6. No.3,  
pp. 279-290, (1993).

6-Levinson. L.M. " Electronics ceramics  
properties, Devices & application, 9 Marcel  
Dekker inc (1988).

7 - J. Holzer and G. McCarthy, North  
Dakota state University, USA, (1990)

8- Natt. Bur. Stand. (us) Monogro 25, 201  
113 (1983)(R.L. Barns, 1972)Parrish, 1960

9- V.J. Hurst et at, Regional variation in  
the cell dimension of metamorphic quartz,  
American Mineralogist, V.66,pp. 204-  
212,( 1981).

10- R.L. Barns, A strategy for rapid and  
accurate (p.p.m) measurement of Bonds's  
method, (1972). In Kurt F.J. Heinrich, Ed.,  
Advances in X-rays Analysis, Vol. 15, PP.  
330-338, Plenum Press, New York.

12-W. Parrish, Results of the I.U.Cr.  
precision lattice parameters project. Acts  
Crystallographica,13, PP.838-849 (1960).

13-N.Abdulgader, et at, ((Study of physical  
properties and Chemical treatment for Edri  
zone sands for use in Semiconductors  
advanced

applications)) The 3<sup>rd</sup> National  
Conference in Basic Sciences,(2009)  
Gharian, Libya



## Conception study of different material used for MMI–WDM demultiplexer in C-L bands

Monia Najjar<sup>1,2</sup>, Sami Triki<sup>1</sup>, Houria Rezig<sup>1</sup>

<sup>1</sup> High school of engineering (ENIT), SysCom Laboratory, PB 37, Tunis 1002, Tunisia

<sup>2</sup> High institut of computer sciences (ISI), Elmanar, Ariana 2080, Tunisia

[monianajjar@yahoo.fr](mailto:monianajjar@yahoo.fr)

### *Abstract*

Our paper presents generalized modeling to investigate different materials to simulate wavelength demultiplexer. The combination of Si, SiO<sub>2</sub>, BK7 and polymer for MMI demultiplexer is investigated. The theoretical studies of different models are presented in a general formalism considering the essential parameters of demultiplexer such as: MMI width, effective indexes, coupling length, rib height ...etc. Rib waveguide is considered as the main modeling component and 2D-BPM-effective index method as principal technique of simulation. The numerical results show that BK-7-Si-BK-7 combination can give a compact dimension and excellent performance to separate the wavelength 1550 nm and 1585 nm band C and band L, respectively. The MMI performance can be ameliorated by modifying the structure (using S bend waveguide or double MMI).

Keywords: MMI width, effective indexes, coupling length, rib height, 2D-BPM-effective index method, BK7-Si-BK7

### **1. Introduction**

The most important required to any suitable material to be used in the integrated optics application is:

1. Homogeneous to get rid from refractive index variation.
2. Transparent at the working wavelength.
3. Linear to avoid birefringence effects.
4. Low impurity level which acts as scatter or absorption centers to increase power loss.
5. Chemically stable to not be effected by the fabrication processes.
6. Good adherence both at the surface and between them so as allow obtaining shift structures. Moreover, their thermal expansion coefficients must be as close as possible in order to avoid cracking during the fabrication process.

Many materials that can be suitable for integrated optical device silicon and polymer are of special because, in addition to optical function, they can combine electronic control units on the same silicon waveguide and the silicon substrate waveguide. The silicon substrate guarantees chemical stability, high surface quality, low cost and good thermal conductivity. For active devices such as Lasers detectors based on III-V semiconductors materials, modulators, hybrid integration on the common light wave circuits (PLCs) is the technology of today although recently GaAs material grown on silicon wafer by



using a novel concept with intermediate buffer oxide has been demonstrated which may soon lead to totally monolithic integrations. Waveguide devices and Silica-based channel waveguides are main candidates for integrated communication circuit. These components have to be compatible with optical fibers, exhibit low attenuation for the whole 3<sup>rd</sup> optical communication window around 1,55  $\mu\text{m}$  and be fabricated by using low temperature processing [1].

Polymeric materials offer many distinct properties compared to other materials, it can be deposited directly on any kind of substrates, and this is advantageous over other optical waveguide materials such LiNbO<sub>3</sub>, III-V materials and SiO<sub>2</sub>. On the other hand, polymers are attractive to be used due to their compatibility with Si and GaAs fabrication processes, ease of fabrication, and low cost. Such properties are important factors for the practical implementation of complex, high-density interconnects and optical circuits [2].

High refractive index difference waveguides in general and specially Silicon-on-insulator (SOI) waveguides [3] are very promising for realizing dense photonic integrated circuits (PICs) [4]. They allow an extreme minimization of PICs due to their ability to realize, ultra small bend and high optical insulation between adjacent waveguides [5,6]. The particular advantage of SOI waveguides that it has a potential for monolithic integration with electrical and mechanical structure and it uses the mature silicon processing technology. SIO waveguides technology is also useful for directly fiber coupled circuits, where the single mode behavior of large SIO ridge waveguide [5] can be exploited. Such waveguides are used

for realizing waveguide gratings, MMI couplers and wavelength multiplexers. The SIO core fabricated by a silicon material ( $n=3.5$ ) surrounded by some cladding materials, such as deposited oxide, thermal oxide or air, that have refractive index typically between 1 and 2. Therefore, the silicon core always has a very high index difference with respect to the cladding where a thin cladding layer is demanded to isolate the core from its surrounding structures.

This work can be considered as a generalization of some investigations already proposed in literature. In particular, the combination of Si, SiO<sub>2</sub>, BK7 and polymer materials for MMI demultiplexer is investigated. In section II the theoretical studies are presented in a general formalism considering the essential parameter of MMI demultiplexer such as: MMI width, effective indexes, coupling length, rib height ...etc. In section III, a number of numerical results are shown and discussed including comparisons between different combination. The parametric study is based on 2D-BPM-effective index method.

## 2. Component analysis

The MMI demultiplexers analyzed in this work is simulated by using three layers rib waveguide. The Rib waveguide can be single-moded with both width and height clearly below 10 $\mu\text{m}$ . The thickness of the silicon layer is H within the rib and h is the core thickness (With certain H and h the width W of the rib is limited by a single mode condition [7,8]:

$$\frac{W}{H} < 0,3 + \frac{h/H}{\sqrt{1-(h/H)^2}} \quad (1)$$





On the other hand, propagation of higher order vertical modes is prevented by choosing:

$$\frac{h}{H} < 0,5 \quad (2)$$

The MMI demultiplexer can be designed by using monomode input and output waveguides and multimode waveguide as a main zone which guarantees the wavelength separation based on mode coupling. The structure performance can be ameliorated by modifying the simple MMI model; adding other multimode waveguides or using output S curve waveguides [Fig. 1].

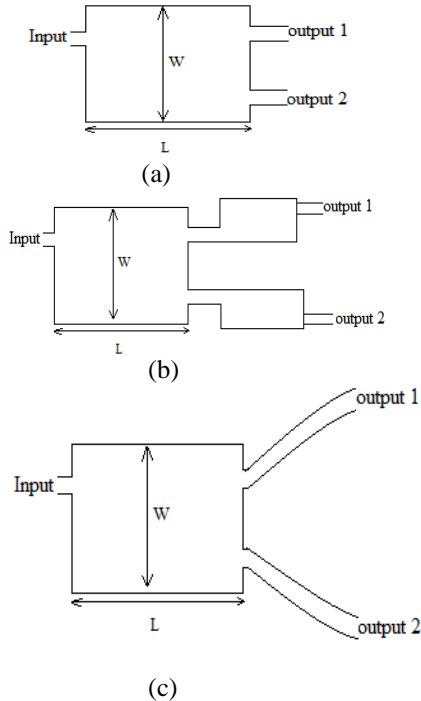


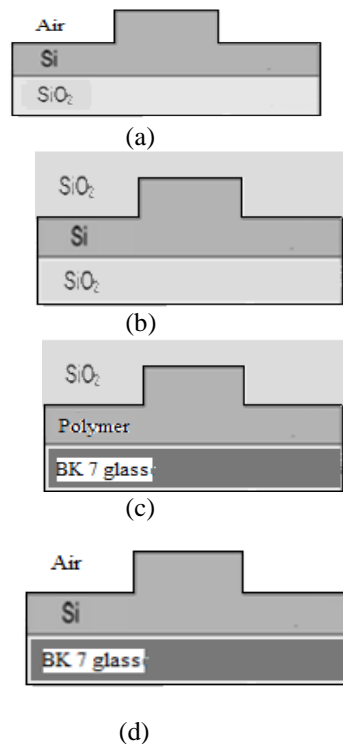
Figure 1: The proposed MMI demultiplexers

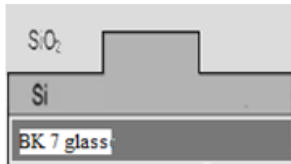
- a) Simple MMI model
- b) Double MMI model
- c) Simple MMI model with S curve.

The different models are simulated by using BPM-2D and effective index methods. The structures are modeled on the base of rib waveguide which characterised by H, h, W and the refractive index of different layers (core cladding and subtrait).

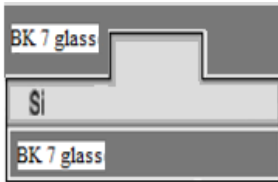
### 3. Results and discussion

In this work some demultiplexers are studied by using a combination of different materials used in the literature as Si, SiO<sub>2</sub>, BK7 and polymer. The different structures are presented in the following figure.





(e)



(f)

Figure 2 : The combinaison of different materiels used to modelise MMI demultiplexer.

By using the shown waveguides (fig.2) in the MMI demultiplexer, the parameters H and h have an anormeus effect on the width and length of demultiplexer which are effected by the effective index of the 2-D model . Table 1 shows the effective indexe of different structures for the two wavelengths 1550 nm and 1585 nm which will be demultiplexed by the proposed device.

Table 1. Effective index of different modeles.

MMI model	$N_{eff1}(1550)$	$N_{eff1}(1585)$	$N_{eff2}(1550)$	$N_{eff2}(1585)$
a	3,4995	3,4957	3,4709	3,4660
b	3,4958	3,4996	3,4712	3,4662
c	1,5352	1,5345	1,5203	1,5194
d	3,4995	3,4957	3,4709	3,4660
e	3,4958	3,4996	3,4712	3,4662
f	3,4996	3,4958	3,4712	3,4663

However the chosen model, the MMI width and MMI length of demultiplexer must be carfully calculated to enssur a small dimention and an excelent performance.

Therefore, the necessary condition to separate two wavelengths such that  $\lambda_1$  (band C) in the first output and  $\lambda_2$  (band L) in the second output ( $\lambda_1 < \lambda_2$ ) is:

$$L_{MMI} = pL_{\pi,\lambda_1} = (p + q)L_{\pi,\lambda_2} \quad (3)$$

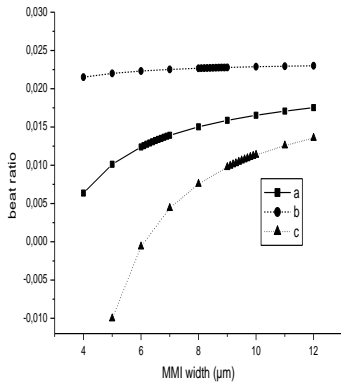
Where  $L_{\pi,\lambda_i}$  is the beat length for wavelengths  $\lambda_i$ , p is a positive integer and q is an odd integer. As it is known the beat ratio  $L_{\pi}$  increases as the wavelength decreases. Therefore, the device length minimizing is one of the most important parameter to optimize the structure composition. Then p and q should be as small as possible.

The optimum values of p and q can be determined from the following curves which present the variation of the beat ratio

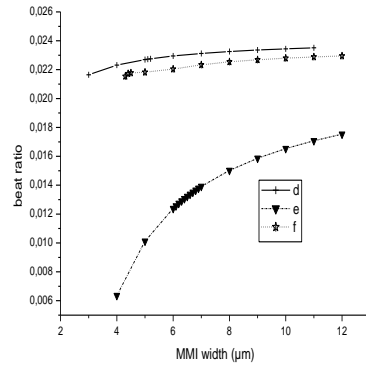


$(\frac{L_{\pi\lambda_1}}{L_{\pi\lambda_2}} = 1 + \frac{q}{p})$  as a function of MMI

width for different model [10].



(a)



(b)

Figure 3: Beat ratio variation versus MMI width.

(a) Models a, b and c.

(b) Models d, e and f.

From the above curves we can calculate the dimension ( $L_{MMI}$  and  $W_{MMI}$ ) of the proposed models. The results are resumed in the following table.

Table 2. The performance of different models

model	$W_{MMI}(\mu m)$	$L_{MMI}(\mu m)$	Insertion loss for $\lambda=1550nm$	Insertion loss for $\lambda=1585nm$	Extinction loss for $\lambda=1550nm$	Extinction loss for $\lambda=1585nm$
a	13730	6,7	1,33518	0,98748	8,63874	9,36619
b	12057	8,4	2,14803	2,15703	15,86975	22,0483
c	18722	9,8	0,59854	0,48398	4,88502	4,58847
d	13730	6,7	1,33518	0,98748	8,63874	9,36619
e	12057	8,4	2,14803	2,15703	15,86975	22,0483
f	4227	5,1	1,88542	1,43569	21,5362	19,1768

The results show that same values are obtained for models a,b,d and e respectively. It means that when we replace silicon dioxide layer by BK7 glasse no change can accurate and same dimensions

and performance are resulted. The only advantage that BK-7 is more suitable for practical implementation. The last model (BK



7-Si-BK7) can considered as the most important one because of the small dimension and the excellent performance. Moreover, these dimensions are ameliorated by using S bend waveguide and double

MMI structure. The BK7-Si-BK7 model is presented in table 3.

Table 3. Comparison between S-bend and double MMI structures

	S bend waveguide		Double MMI	
	1550nm	1585nm	1550nm	1585nm
Insetion loss(dB)	1,92	1,56	2,509	1,64
Extinction loss(dB)	23,93	22,13	19,45	31,04

## Conclusion

Different materials are investigated to simulate wavelength demultiplexer based on rib wave guide. The combinations of Si, SiO<sub>2</sub>, BK7 and polymer are effected to simulate different layers of MMI demultiplexer. The theoretical models are presented in a general formalism considering the essential parameter of demultiplexer such as: MMI width, effective index coupling length, rib height ...etc. The simulations are based on 2DBPM- EIM methods which show that BK7-Si-BK7 waveguide can give a compact dimension ( $\cong 4\text{mm}$ ) and excellent performance. Moreover, the results can be ameliorated by modifying the MMI

structure (using S bend waveguide, double MMI). The MMI demultiplexer is characterized by two main parameters, extinction loss and insertion loss. Therefore, the optimum extinction loss is 31dB (double MMI) and insertion loss 1,56 dB (S bend).

## References

- [1] M. C. Oh, H. J. Lee, M. H. Lee, J. H. Ahn, S. G. Han and H. G. Kim, "Tunable wavelength filters with Bragg gratings in polymer waveguides", *Appl. Phys. Lett.*, vol. 73, pp.2543-2545, 1998.
- [2] D. Chen, H. R. Fetterman, A. Chen, W. H. Steier, L. R. Dalton, W. Wand and Y. Shi, "Demonstration of 110GHz electro-optic polymer modulators", *Appl. Phys. Lett.*, vol. 70, pp.3335-3337, 1997.
- [3] Timo A., Milko H., Päivi H. And Matti L., "Development of silicon-on-Insulator waveguide technology" invited paper, edited by Yakov Sidorin, Ari Tervonen, Proceedings of SPIE 5355, pp 81-95, 2004.
- [4] Jalali B., "Silicon-on-Insulator photonic integrated circuit (SIO-PIC) technology" SPIE Proc. Proceedings of SPIE 2997, pp. 66-71, 1997.
- [5] Hosomi K., Katsuyama T. "A dispersion compensator using coupled defects in a photonic crystal" *IEEE J. Quantum electron* vol. 38, pp. 825-829, 2002.



- [6] S. Yliniemi, T. Aalto, P. Heimala, P. Pekko, K. Jefimovs, J. Simonen, T. Uusitupa, "Fabrication of photonic crystal waveguide elements on SIO", Proceedings of SPIE 4944, pp. 23-31, 2003.
- [7] R. A. Soref, J. Schmidtchen, K. Petermann, "Large single mode rib waveguides in GeSi-Si and S-on-SiO<sub>2</sub>" *IEEE J. Quantum electron*, vol. 27, pp 1971-1974, 1991.
- [8] D. An, Z. Xhi, L. Sun, J. M. Taboada, Q. Zhou, X. Lu, R. T. Chen, S. Tang, Hua Zhang, W. H. Steier, A. Ren and L. R. Dalton, "Polymeric electro-optic modulator based on 1x2 Y-fed directional coupler", *Appl. Phys. Lett*, vol. 76, pp.1972-1974, 2000.
- [9] M. Hikita, Y. Shuto, M. Amano, R. Yoshimura, S. Tomaru, and H. Kozawaguchi, "Optical intensity modulation in a vertically stacked coupler incorporating electro-optic polymer", *Appl. Phys. Lett.*, vol. 63, pp.1161-1163, 1993.
- [10] M. Najjar, S. Triki, H. Rezig "Conception and simulation of wavelength demultiplexer for C and L bands based on MMI structure" *J. of optical commu*, vol. 30, pp.12-15, 2009.



المؤتمر الدولي العربي الليبي الرابع للهندسة الكهربائية والإلكترونية 2010/10/26-23 طرابلس ليبيا



# ***Chapter V***

## **Information and Communication Technology**



المؤتمر العربي الليبي الدولي الخامس للهندسة الكهربائية والإلكترونية 23-26/10/2010 طرابلس ليبيا





## Semantic-Based Semi-Automatic Web Service Composition

Abdaladhem Albreshne<sup>#1</sup>, Jacques Pasquier<sup>\*2</sup>

*#Computer Department, Fribourg University  
Switzerland*

<sup>1</sup>abdaladhem.albreshne@unifr.ch

*\* Computer Department, Fribourg University  
Switzerland*

<sup>2</sup>jacques.pasquier@unifr.ch

**Abstract**—The presence of software systems in every aspect of our life results in increased requirements and expectations addressed by new development projects. The domain of home computing constitutes a typical example of an environment which is characterized by complex requirements with regard to context awareness, intelligent assistance, autonomy, dynamic discovery, dynamic service composition, and easy services management for end users. This work aims to propose an approach based on semantic description and ontologies in order to discover and compose services in a home changing environment. Furthermore, our goal is to offer a partial automation of web service composition, with a human controller. We propose to enable customers to select and configure available services to meet their requirements and reach a specific goal.

### 1 Introduction

Over the past several years, a range of industry languages and frameworks solutions have been realized to enable web service composition. Among these, Business Process Execution Language for Web Services (BPEL4WS) [1] is probably the most prominent. It provides a language for web service composition where the flow of processes and the bindings between services are known a priori. These approaches are of purely syntactical nature. There are still

challenges in the web service composition field which need to be addressed and investigated. For example, there is a general lack of methodology and tools which enable the semi-automatic composition and analysis of web services taking into account their semantic and behavioural properties. Even though a lot of work has been done in the field of semi-automatic composition [2-3], there still remain problems. These are mainly related to the question how to help non-expert users to achieve goal oriented service composition. An



essential issue is how available semantic services can collaborate and use domain knowledge and user inputs to help achieving semi-automatic service composition for dynamic adaptation to changing business requirements.

We propose an approach which uses domain information and semantic to define a specific environment. Our main objective is to offer non-expert users who tend to not know in advance how to achieve their goals, an assistant mechanism to obtain optimized solutions to compose web services in a way that meets their changing requirements. To attain this objective, we propose to users generic process templates. These templates are oriented toward users' goals. A process template defines a workflow which is composed of several activities with specific functions (semantic description of participating web services) linked with control flow, structured activities (loops, If statements, sequences, etc.), and user preferences that need to be involved in the process. The proposed process template is used to define the services types and to offer a suitable decision at each step of the composition depending on the process goal, user choices and the current situation. The end user configures and customizes these generic templates according to his current requirements, preferences and environmental context. We explain

our work in more detail in Section 3.1.

## 2 Motivating Scenario

In this section we explore the presented approach through a case study realized in the field of home environment.

### Home Energy Saver Scenario

Thomas home is a home equipped with diverse web enabled sensors and actuator devices such as light switches, home heating system, air-conditioners, shower indicator, temperature sensors, curtains and windows controllers and door controllers, etc. Thomas controls his home environment in a way that allows him to save energy and to adapt his environment to his habits and live conditions.

Daily observation shows that total energy consumption can be minimized by 1) **Reducing wastage**: lighting, heating and air-conditioning (HVAC), and other systems can be turned off when not needed. 2) **Reduced lighting levels** (dimming): a light can be operated at less than 100% when full light is not needed. 3) **Shower time**: limiting the shower time can economise energy. There is no need to have hot water for the shower when the user is outside for hours. The developer has used the recommendations described above in order to create a generic energy saver process template for the final user.



Thomas consults the menu of his automation system which proposes several composition scenarios. He chooses the “Energy Saver Plan” which is a generic predefined process plan. Figure 1 illustrates the Energy Saver Plan workflow. The tool suggests him different options, step by step, and in each step he can define his preferences. The following steps resume the scenario interaction between the system and the final user:

- At first, the system discovers available services (devices, sensors) and understands their functions.
  - Then, the system selects the services that are potentially involved in the energy saver process. The system detects a heating system, three air-conditioners, four room lamps, two entrance overhead lights and an external temperature sensor.
  - The system starts configuring the energy saver plan by asking the final user to take a decision about the involved services as following:
    - What is the interior comfort home temperature when you are at home?
    - Select from the given list which entrance overhead lights to turn on at night.
    - Choose which air conditioners you like to turn on.
- Set the shower timer.
  - Adjust the preferred temperature for each air conditioned room.
- After having finished asking the user about services and his preferences, the process is now configured to meet the user’s requirements and the system is able to create a final process. The defined activities in the process are bound to concrete web services and the data flow in the process is assigned. The process is ready to be executed.

This scenario demonstrates that there is a need to help the final user in a changing environment where services are not known at design time. It shows that decisions sometimes could not been taken without the end-user involvement. It is a challenging problem to search and select the concrete services and involve users to adjust them in order to achieve the desired goal. So as to overcome this lack of flexibility, we propose to develop a framework as a prototype, consisting of an intuitive user tool that allows users to create and run on their home device customized programs that implement the intended smart home tasks. Additionally, this tool needs to be aware of the context in which the composition and invocation of the available web services (devices, sensors) occur.

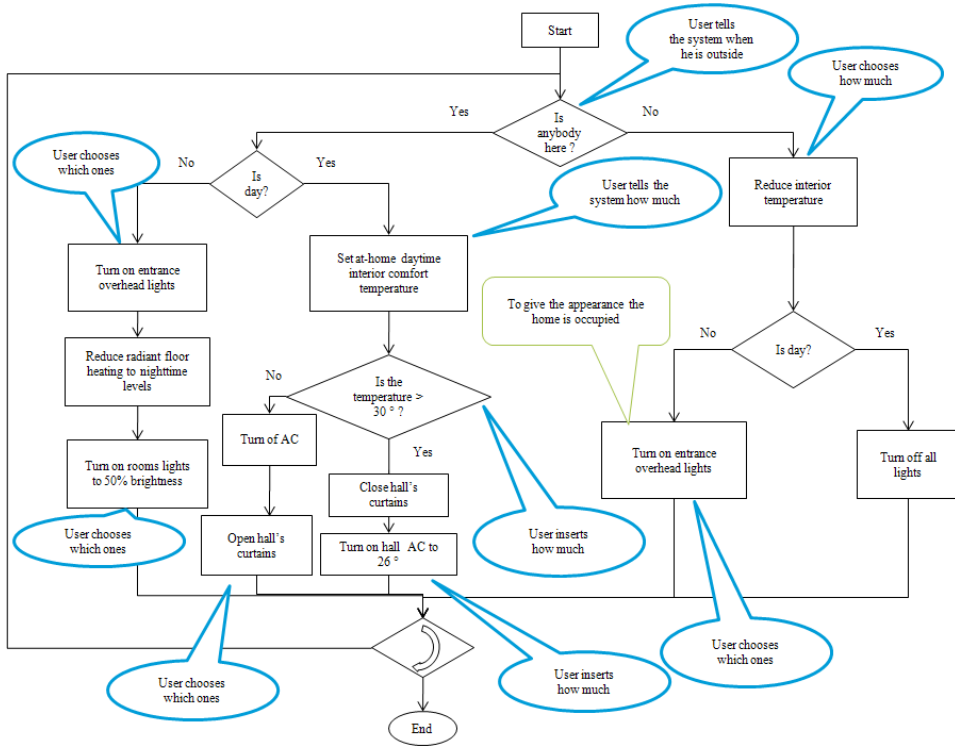


Figure 1 Home Energy Saver Workflow

### 3 Semi-automatic Service Composition Approach

In general, there are several kinds of service composition. The traditional approach is called *manual composition* where users program and tell the system what to do during all the composition process development steps. Processes are defined using a process execution language like BPEL. Many plug-ins for tools like Net-Beans [4], JOpera [5] are available to enable

manual composition. The problem with such an approach is that it demands too much knowledge on the part of the user and it becomes more and more difficult with the explosion of web services resources.

The second approach is called *automatic composition* (without human involvement). It is used when the requestor has no process model but has a set of constraints and preferences. It is based on finding



services for executing predefined abstract processes. The tools try to discover the available web services that semantically match as much as possible the user's needs [6]. Several approaches for automatic service composition have been introduced [7], including solutions based on Hierarchical Task Network (HTN), Golog [8], Artificial Intelligence (AI) planning or Rule-Based planning [7, 9-10]. However, automatic composition is still viewed as a task of high complexity because of the rapid proliferation of available services to choose from and the composition result risks to differ from the user's original goal.

The third approach is called *semi-automatic or interactive composition*. We work in this direction. In this kind of composition, the system usually helps users to find, filter and integrate automatically the desired services by matching the users requests with the available services. Moreover, it enables end users to intervene continuously during the composition process. Some efforts like OWL-S [11], METEOR-S [12] use semantic description of web services to help improving the discovery and composition processes. We believe that the semantic of the provided services could be used by tools or systems to guide the user to limit the available choices and to define his preferences to finally reach the composition goal.

### 3.1 Goal Oriented Service Composition Approach

The composition of web services is difficult when one is using exclusively the WSDL [13] descriptions with a composition language like BPEL, since each description lacks the semantic description of services' properties and capabilities as well as some non-functional attributes, such as service name, service type or service location. To be able to describe the services, semantic web languages like the Ontology Language for Web Services (OWL-S), and the Web Services Modeling Ontology (WSMO) [14] have been proposed. They introduce an additional level of abstraction. Instead of a syntactic description of a web service, a declarative description of the service's functionalities is given.

Our approach uses web services and semantic web service technologies like OWL-S to facilitate the discovery, as well as the semi automatic composition of web services. We propose an assistance mechanism for the semi-automatic composition of services where the composition is gradually generated by using a declarative oriented generic composition plan. It is not up to the user to tell the system what to do but rather to establish and negotiate about goals and how to accomplish them. At each composition step, the system could propose to the user which new service can be added to the composition and which kind of actions can be taken. Further



possibilities are filtered based on the current context, the composition objective and user preferences.

To validate our approach, we want to develop an interactive service composition smart home prototype that assists non-expert users to compose and generate goal oriented composition plans in which the system is able to provide suggestions and direct the control flow in a step by step style. Depending on the composition goal, context and the user's preferences, the system selects the suitable services and which available decisions could be taken.

However, several challenges need to be addressed in order to build our system: for instance, lack of a generic process language which would facilitate the orchestration of semantic web services, a need to involve user preferences and context-awareness in the process, the requirement to build a process design tool based on semantic and ontology and finally the question of how services discovery can be optimized. We provide principles for the underlying software architecture which make it easier to create such a system. In the next Section, we explore those challenges in more detail and present our framework.

### 3.2 Proposed Framework

In the following, we give an overview of our framework for semi-automatic web service composition. As shown in Figure 2, the user can choose a recommended generic process template from the process repository. The generic process template acts as a configurable module. It defines the semantic of the participating activities, control flow and conditional branches. There are several ways to write process templates. For example, PEBL4SWS [1] is an extension of BPEL that allows to create a semantic process and then generate an executable one. OWL-S can be used as well to execute the process. Our framework is not restricted to these languages. If none of these solutions corresponds to our requirements, we can propose our own language. The Process Generator component captures the semantic activities' characteristics in the process template and sends it to the Service Discovery Engine as service query. Web services are usually published in registries (Discovery Engine). Consumers can request available services by a keyword-based search engine (e.g. expedia.com, google.com) or by looking it up in a web services registry (e.g. UDDI – Universal Description, Discovery and Integration Registry) [15].

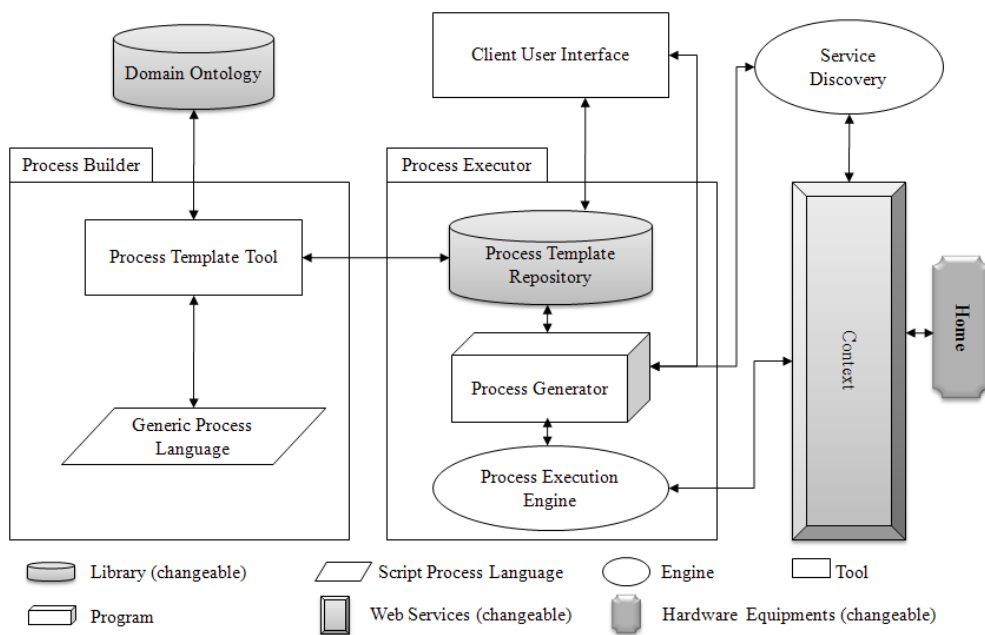


Figure 2 Semi-automatic Service Composition Framework

Improving service discovery involves adding a semantic research mechanism. The requestor can provide the inputs and outputs of the required service. Then the discovery process in the registry will find any service which matches these semantic requirements. Several semantic discovery algorithms have been proposed like [6]. In our framework, service discovery is based on services' semantic description and their relation with the domain ontology.

After Services have been discovered by the Service Discovery Engine, the user binds all desired activities and defines his preferences according to

the activities configuration requirements which can be involved in the generic process or can be declared separately in another format. When a service is put into the composition, the information about input, output, preconditions and effects (IOPE) of this service is checked automatically to assure that all needed input data are provided, all operations can be executed and all links are established. The process now can be converted into an executable process by the Process Generator. The Process Execution Engine component has the capability to execute the generated process using an execution language such as BPEL4WS



or OWL-S API. In the next section, we explain briefly the role of our framework components.

### 3.3 System Architecture

The proposed architecture (See Figure 3) supports the construction and execution of semi-automatic service

composition. The system architecture is based on three categories of components: Service Discovery Component, Process Building Components, and Process Configuration & Execution Components.

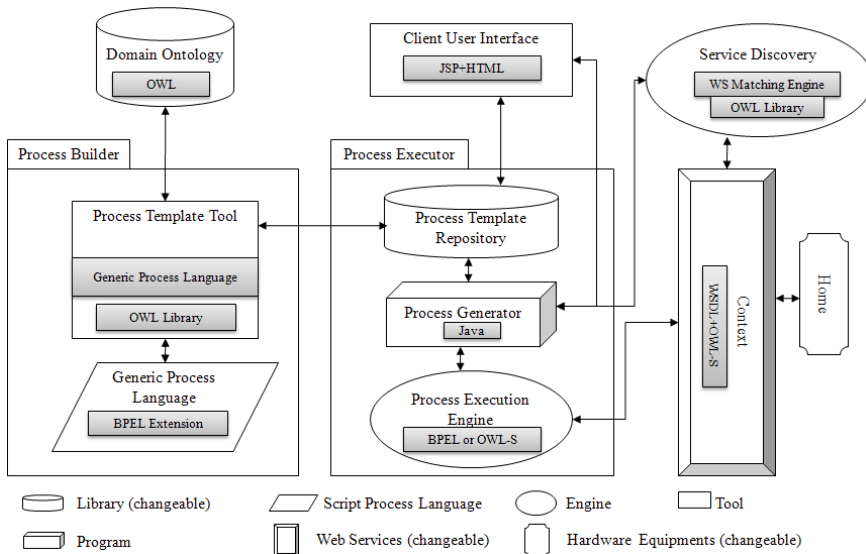


Figure 3 – Semi-automatic Service Composition Architecture

#### 1. Service Discovery Component

The providers publish their web services on a web services registry.

- [Service Discovery]: The Service Discovery & Registry has registry, discovery and selection functions. It uses a matching engine to find the requested services by comparing their semantic

descriptions with the available registered services.

#### 2. Process Building Components

The process developer uses a graphical design tool in order to build a generic process template. He uses a published domain ontology which is related to a



specific organization to describe participating activities semantically.

- [**Domain Ontology Library**]: stores the detail information of a specific domain like services or devices. The domain ontology is defined using the OWL language.
- [**Process Template Design Tool**]: a graphical composition tool. It lets the expert user create a generic process template by defining the workflow of services according to the composition goal. It uses the capabilities of the domain ontology in order to provide the user with a task abstraction of the complexity of whatever lays underneath. The tool includes various libraries such as BPEL4SWS or OWL-S and OWL.
- [**Process Template Repository**]: contains abstract services composition templates. These composition templates define the capabilities and functionalities of needed services as well as the conditions and requirements that must be applied to achieve the composition goal.

### 3. **Process Configuration and Execution Components**

The Client uses the client interface to configure a process template that matches her goal and provides her preferences. Then the process can be executed. The following components allow realizing this objective:

- [**Client User Interface**]: a graphic tool which handles the communication between the end-user and the platform. It lets the user choose a template process in order to achieve a specific goal. Then the user configures this process according to her preferences. The tool will present the available choices at each step according to the proposed plan. After process configuration, the process is executed by the execution engine.
- [**Process Generator**]: handles the process configuration and converts the generic process into an executable one.
- [**Execution Engine**]: has the capability to execute the generated process. It uses an execution language such as BPEL4WS or OWL-S API [16].

### 4 **Related work**

On the one hand, a range of industry solutions have been realized to enable web service composition. Among these, the Business Process Execution Language for Web Services (BPEL4WS). These approaches only address the syntactical aspects of web services. On the other hand, there are efforts which go in a different direction. They aim to establish standards enabling the syntactic and semantic description and composition of Web Services. For instance, the Ontology Web Language for Services (OWL-S [17]) has triggered significant



research efforts to build frameworks and tools which allow the composition of semantically annotated Web Services.

Artificial Intelligence (AI) approaches for web service composition focuses on automatically generating a plan of a composite service that satisfies users given goals [9-10, 18]. We propose an alternative approach which involves users in the composition process, including the selection of components and their configuration.

[19] Proposes a system which informs the user about issues to be addressed in the current workflow. It is limited by the fact that the composition assistant occurs during the design phase. Consequently, it does not enable users to discover and then choose concrete services which meet their requirements. On the contrary, the user interaction methods and tools proposed by [2, 20] capture the user's intentions in an interactive and continuous manner during the whole composition process. These systems utilize the semantics of the available services to guide the user and limit the available choices. Nevertheless, they do not guide the user to reach the objective of the composition.

[21] Proposes a goal description language for automatic web service composition (GDL4WSAC). The latter describes the goals to be achieved and the corresponding constraints

unambiguously. Its limitations are that it fits developers more than end-users, since the goal must be predefined and since there is no way for users to intervene during the composition. [22] proposes a semantic-based ontology language (OWL-T) used to formulate business demands in terms of structured task templates. An automatic composition method is used to transform task templates into executable processes. Neither in the composition process nor in services selection the user is involved.

[23] Proposes a web service composition framework SWSCF which is based on semantic and has the ability to integrate services according to application domain semantics and dynamic business requirements. A hierarchical activity mechanism (AI technique) enables this framework to dynamically decompose business requirements. This helps to identify suitable semantic process templates.

Task Computing approach [24] exposes the functionality found in smart environments (i.e. networked devices, web services) as semantic web services, which in turn the user can discover and arbitrarily compose. It focuses namely on dynamic service discovery as well as service publishing and management.

## 5 Conclusion

The contribution of this work is: First, proposing a semantic-based

framework which offers flexibility to integrate services and reinforces the human-computer collaboration paradigm. Second, we use the semantic descriptions and ontologies to provide an assistant mechanism to obtain optimized solutions to compose services in a way that meets user's changing requirements.

Some key features of our approach are:

- defining a generic process template to describe semantic activities for goal oriented composition
- using a semantic matchmaking mechanism to discover and select the suitable services that conform to semantic activities defined in the process template
- enabling users to adjust the process, where the process template acts as a configurable module for user preferences and requirements.
- enabling end-users to choose concrete services to be invoked according to their changing business requirements.
- Providing context awareness through a context discovery module.
- providing an ontology-based tool that enables semantic-based, goal oriented, semi-automatic service composition.
- providing a process execution engine, which has the capability to execute the generated process.

## 6 Future Work

In order to have a good evaluation of our approach, we are currently working on our smart home prototype. Several challenges need to be addressed in order to build our system: for instance, a generic process languages which facilitate the orchestration of semantic web services, a need to involve user preferences and context-awareness in the process, as well as building a process design tool based on semantic.

## 7 References

- [1] IBM. (2002, 11.05.2010). Business Process Execution Language for Web Services version 1.1. Available: <http://www.ibm.com/developerworks/library/specification/ws-bpel/>
- [2] B. Parsia, et al., Semi-automatic composition of Web Services using Semantic Descriptions. Angers, France: Web Services: Modeling, Architecture and Infrastructure Workshop in Conjunction with ICEIS, 2003.
- [3] B. Steffen, et al., "Semantic Web Service Composition for Service-Oriented Architectures," presented at the 10th IEEE Conference on E-Commerce Technology, Washington, USA, 2008.
- [4] NetBeans.org. (2007, 11.05.2010). NetBeans IDE 6.1 SOA Pack Documentation. Available: <http://netbeans.org/kb/61/soa/index.html>



- [5] JOpera. (2010, 12.05.2010). JOpera for Eclipse. Available: <http://www.jopera.org>
- [6] F. Benedikt, et al. (2008, 02.02.2010). Hybrid OWL-S Web Service Matchmaker. Available: <http://www-ags.dfki.uni-sb.de/~klusck/owls-mx/index.html>
- [7] H. Li, et al., "Automatic Composition of Web Services Based on Rules and Meta-Services," presented at the 11th International Conference on CSCW in Design, Melbourne, Australia, 2007.
- [8] S. Narayanan and S. A. McIlraith, "Simulation Verification and Automated Composition of Web Service," presented at the 11th International World wide Web conference, Hawaii, USA 2002.
- [9] I. Paik and D. Maruyama, "Automatic Web Services Composition Using Combining HTN and CSP," presented at the 7th IEEE International Conference on Computer and Information Technology (CIT 2007), Aizu-Wakamatsu City, Fukushima, Japan, 2007.
- [10] X. Li and C. Wu, "Research on OWL-S Service Automatic Composition Based on Planning," Wuhan, China 2009.
- [11] W3C. (09.05.2010). OWL-S: Semantic Markup for Web Services. Available: <http://www.w3.org/Submission/OWL-S/>
- [12] LSDIS. (2005, 06.03.2010). METEOR-S: Semantic Web Services and Processes. Available: <http://lsdis.cs.uga.edu/projects/meteor-s/>
- [13] W3.org. (2001, 10.05.2010). Web Services Description Language (WSDL) 1.1. Available: <http://www.w3.org/TR/wsd1>
- [14] W. W. W. Consortium. (2005, 11.05.2010). Web Service Modeling Ontology (WSMO). Available: <http://www.w3.org/Submission/WSMO/>
- [15] OASIS. (2004, 10.04.2010). UDDI Spec Technical Committee Draft. Available: [http://www.uddi.org/pubs/uddi\\_v3.htm](http://www.uddi.org/pubs/uddi_v3.htm)
- [16] Mindswap. (2010, 12.05.2010). OWL-S API. Available: <http://www.mindswap.org/2004/owl-s/api/>
- [17] DAML. (2009, 07.05.2010). DAML Services. Available: <http://www.daml.org/services/owl-s/>
- [18] K. Srividya, et al., "Automatic Composition of Semantic Web Services," presented at the IEEE 2007 International Conference on Web Services (ICWS), Salt Lake City, USA, 2007.
- [19] K. Jihie, et al., "An Intelligent Assistant for Interactive Workflow Composition," presented at the 9th international conference on Intelligent user

- interfaces, Madeira, Portugal, 2004.
- [20] E. Sirin, et al. (2004). Composition-driven Filtering and Selection of Semantic Web Services.
  - [21] M. Lin, et al., "Goal Description Language for Semantic Web Service Automatic Composition," presented at the IEEE, Symposium on Applications and the Internet, Washington, USA, 2005.
  - [22] V. X. Tan and H. TSUJI, "OWL-T Ontology-based Task Template Language for Modeling Business Processes," presented at the Fifth International Conference on Software Engineering Research, Management and Applications, Busan, South Korea, 2007.
  - [23] J. Hu, et al., "SWSCF: A Semantic-based Web Service Composition Framework," Journal of Networks, ACADEMY PUBLISHER, vol. 4, pp. 290-297, 2009.
  - [24] R. Masuoka, et al., "Semantic Web and Ubiquitous Computing - Task Computing as an Example-," Maryland, USA, 2004.



المؤتمر العربي الليبي الدولي الخامس للهندسة الكهربائية والإلكترونية 2010/10/26-23 طرابلس ليبيا



## **ICT from a Student's Perspective A study based on Al Jabal Al Gharby University**

Taher Omran Ahmed, C. Prasanna Ranjith, Osama Ali Mahdi  
Faculty of Science, Al Zintan, Al Jabal Al Gharbi University  
Gharyan, Libya

[tahar.ahmed@jgu.edu.ly](mailto:tahar.ahmed@jgu.edu.ly), [lectcs@gmail.com](mailto:lectcs@gmail.com), [osama\\_haba@yahoo.com](mailto:osama_haba@yahoo.com)

### **Abstract**

In the last two decades, technology has made information available at no difficulty. With computers and Internet technologies, more people can now have access to more information more quickly than ever before. ICTs are accepted as very vital, for both teachers and students. ICTs provide links - between students themselves, between students and teachers and between the administration and the students. They also facilitate access to knowledge. Presently, the use of ICTs varies from one university to another, with certain universities promoting a wider use of ICTs, and others provide very limited access to ICT.

The objective of this paper is to examine, from a student's perspective, how ICTs should be used within the university. It will suggest solid proposals, acquired mainly from discussions with students in selected faculties of the University of Al Jabal Al Gharby, and by conducting a variety of debates among students and teachers of the university.

This paper's approach will be pragmatic. It will bring to light those aspects of ICTs that students look ahead to have at university, explicitly: a comprehensive university website, computer training, courses on how to search for information with ICTs and E-learning. Finally, the funding of ICTs will also be examined.

### **Introduction**

The world we live is not more different from a decade before. Technology is rising significantly. In the past years, technology has made information, once a scarce resource, abundant. With computers and Internet technologies in particular, more people can now have access to more information more quickly than ever before. Moreover, the exponential growth in access to information has led to a corresponding exponential growth in the production of new information, and this has forced us to

rethink our notions of what we need to learn and how we should learn it.

The costs of these technologies had been falling continuously and as this happens, the capabilities of the technologies had been increasing steadily<sup>[1]</sup> and they are being applied more to various sectors of economies and societies.

The confluence of computing, audio visual and telecommunication technologies on the one hand [3] and the spectacular advance in digital compression technology



[4]., during the last two decades have drastically transformed the way information is accessed and assimilated on a global scale. People communicating now, have powers of transmitting and receiving information, undreamed of even ten years ago.

Libya boasts the highest literacy rate in the Arab world, and the UN's Human Development Index, which ranks standard of living, social security, health care and other factors for development, places Libya at the top of all African countries [2].

Government reform plans in developing ICT infrastructure in Libya and incorporating ICT in education as key components in its overall development plans [2].

Educational institutions also agree that they must move smartly with the technology-driven changes. Learners must develop three foundational skills:

1. How to find information.
2. How to determine if what is found is relevant to task.
3. How to determine if the relevant information is accurate.

Attainment of these three foundational skills sets the parameters for the use of ICT in education institution. The integration of ICT in the teaching and learning process is one of the most practical interventions towards educational improvement.

### **Project scope**

Recent study on ICT higher education focussed on the nature and extent of innovation in teaching practice in tertiary ICT education [1].

This current paper has the broad aim of scoping the issues and challenges facing ICT education and the initial exercise was

to consult with students and faculty members who directly benefit from ICT. This paper reports on the findings from that consultation process mainly with Al Jabal Al Gharbi University which we suppose will suit to the majority of universities in Libya.

### **Objectives**

The general objective of this study is to determine the use of ICT in the Al Jabal Al Gharbi University education system and to determine what should be the use of ICTs at University.

### **Method**

The consultation process included surveys and interviews of a broad range of academicians and students. Those consulted included Deans and Heads of Departments, Students of different faculties and of different discipline, teachers of other Nationals as well as tutors.

Forums and debates were held in the premises of Faculty of Science, Al Jabal Al Gharbi University, Al Zintan involving few teachers and students.

Two types of Questionnaires were prepared for teachers and students respectively. The questionnaires are attached in *annexure 1 & 2*.

### **Results and discussion**

Findings from the consultation process have been distilled into the following issues and challenges which are briefly summarised.

### **University Website**

Every university now has its website. Quality of the website differs from one another. A website should contain detailed *administrative* and *academic information* [2], as well as access to job search facilities





and electronic notice boards. Students strongly agree that a complete website must provide general practical information, such as

- Course listings
- Important dates
- Timetables
- University organisational charts
- Telephone and e-mail directory, etc.

The availability of *administrative information* on the university's website is a good way to improve transparency at university. It assures that all students obtain the same information on the many possibilities such as additional courses, conferences, and so on. This is the kind of information that students often find difficult to obtain because they do not know whom to ask.

Students also need to find proper *academic information* on the university's website. It is therefore very important that each department have its own web pages to provide students with the following information:

- Outlines of courses
- Reading lists
- Past exam papers
- Latest publication of articles and books
- Conference announcements in their own area of study.

All professors' email addresses should be available on the university's website. This can prove very useful for students if they need to contact their teachers.

### **Electronic Noticeboards**

The principle of electronic notice-boards is simple: it consists of a webpage which

students, teachers and administrative staff can access via a password. This type of forum facilitates the exchange of news, proposals, questions and advice and can save students, faculty and administrators time by asking and answering questions publicly in one location.

### **Computer training**

Fundamental modules on the use of ICTs should be made available for those students who need or wish to improve their computer skills. More advanced computer training should be made available as well. The use of word processors or other software (such as PowerPoint or Excel) is now a requirement for graduate students wishing to type their own projects and assignments.

Collecting information about the capability of students in use of ICT applications is difficult [2]. One approach is to ask students to rate themselves in terms of their own skills.

In general, the students in our sample reported good skills with different applications. The highest abilities were with e-mail with which many students reported being able to use without help. A slighter lower ability to use word processing was reported.

Majority of the respondents indicated that they would need some help' in using power point slides and the highest percentage of students reporting that they had never used the applications like Access and other database software.

### **Search for information with ICTs**

All the students of university are expected to know how to find information in the mass of knowledge. This implies that they would benefit from courses on how to search for information with ICTs.



Two fundamental things should be considered:

1. Sessions on how to use the electronic resources of the library and
2. On how to search for information on the Internet.

During the first weeks at university, students should be compelled to attend sessions on how to use the library's digital catalogue and electronic resources. Students should be made aware that their university's library is going to be one of their principal sources of knowledge during their university years.

It would also be wise to develop the concept of courses on how to search for information on the Internet. The Internet is for students a marvellous way to access knowledge. At the click of a mouse, nearly any information is accessible on the Net. This is very useful to prepare exercises, papers, oral presentations, or assignments. But the wonderful possibilities of the Internet are still not fully exploited by all students.

What the students need to know is

1. *How to make the best use of the Internet, and*
2. *How not to waste time when searching for information.*

Students should be educated on how best to search for information on the Net: where to look and how. Specifically, on which sites, and with which web searchers [2]. They should know how to formulate their inquiries and be acquainted with more complex techniques such as Boolean research. Such courses are essential for navigating efficiently in the numerous sites, pages and documents available on the Internet, and universities should consider

making them compulsory. Advanced sessions on how to search for specialised information would also be useful, especially in certain disciplines.

### **E-Networks between universities and students**

ICT should not only be used within each university but also between universities. Exchanges between universities have always existed, even in the early stages of universities. The Web represents a powerful means of facilitating exchanges between students, teachers and researchers from different universities around the world. In that they provide an irreplaceable framework for deeper cooperation and greatly facilitate the sharing of mutual experiences ICTs should be encouraged at university.

To conclude, e-networks prevent the waste of time and money and allow material and intellectual resources to be exploited more efficiently.

One question remains: who should be in charge of creating e-networks?

### **Netiquette**

Although ICTs should be promoted at university, they must not become a trouble [4]. One cannot but advise a reasoned use of e-mails. The main danger concerning the use of e-mails is the development of e-mail pollution or "spam", which occurs when someone sends an e-mail for any reason, whatever its importance. Students should be made aware that they have to send e-mail only for relevant reasons.

Another idea to promote good netiquette would be the development of courses on how to use information. Related to netiquette is the problem of plagiarism from online sources. With so many websites, it is difficult for a teacher to notice plagiarism.



In order to avoid plagiarism, some teachers have already abandoned the idea of having students writing essays at home. They prefer students to write their papers during the courses, after having prepared them at home.

### **E-learning**

Education in Libya is free to everyone from elementary school right up to university and post-graduate study, at home or abroad. Schools and universities are positioned throughout the country [1].

Studying at university has no substitute. It is more important to have pedagogical learning methodology. It implies interaction between teachers and students and among students themselves. For instance, it is much more difficult for a teacher to transmit his/her passion about a subject via e-mails than through lively tutorials.

E-learning should nevertheless be more widely available. Distance learning is undoubtedly necessary for students who cannot attend a traditional classroom course, such as those who work, suffer from an illness or live abroad.

It should also be possible for a student to register, with permission, for a course offered electronically by another university. This kind of e-learning implies one-off agreements between universities. Such a scheme is difficult to implement because it requires the administration and the teachers, who are already very busy. But this type of e-learning could be advantageous for students in order to specialise in the areas which interest them most.

Some forms of e-learning can also complement traditional methods of learning. For example, it can be useful for graduate students to test themselves by means of multiple-choice questionnaires

before taking an exam. This opportunity could be explored.

### **Financing the use of ICTs at university**

There is no doubt that the use of ICTs is very expensive for universities. The acquisition, installation and maintenance of computers is costly, and so is the design and maintenance of websites. The library's electronic catalogue and digital library represent a whole other cost structure.

A useful way to reduce costs linked to the use of ICTs is to require the help of students and teachers. Students are willing to contribute to the improvement of their lives at university. They often look forward to being more involved in the activities of the university, and many of them would agree to spend a few hours explaining to students how to use a computer, how to create web pages and so on. To begin with, student representatives could be in charge of circulating a list of all students' e-mail addresses at the beginning of each term.

Another idea would be to have private sponsors. Sponsors can pay for the design of the university's website in exchange for the presence of their brands on the home page, and they can also provide computers.

It is important to recall that the use of ICT is not always a financial burden for universities. It can in fact help reduce administrative costs. Thanks to the existence of a website, one can suppose that the administrative staff have to answer fewer phone calls and can devote their time to more productive tasks. ICTs can also simplify many administrative tasks, such as registration.

### **Conclusion**

Throughout this paper, various proposals have been made. It would be impossible to implement them all, but at



least they show which aspects of the use of ICTs students are eager to see developed.

It has been demonstrated here that the use of ICTs at university is essential. A university which does not use them risks lagging behind the other universities in terms of attractiveness towards not only students, but also towards teachers and researchers.

Nevertheless, if ICTs are necessary at university, their use should not be seen as a solution. The aim is not to have students spending their whole day sitting in front of a computer screen. ICTs are an effective way to improve the lives of students, teachers, researchers and administrators: their use at university is not an end but a valuable means.

## References

- [1] UNDP (2000), "Human Development Report 2000", United Nations Development Programme.
- [2] "ICT in Education in Libya" - by *Amr Hamd*, June 2007 - SURVEY OF ICT AND EDUCATION IN AFRICA: Libya Country Report, Libya.
- [3] UNESCO (1996) "Learning : The Treasure within Report to UNESCO of the International Commission on Education for the Twenty-first century"
- [4] The crisis in ICT education: An academic perspective - Tony Koppi, Fazel Naghdy, Joe Chicharo Faculty of Informatics University of Wollongong – ASCILITE 2008, Melbourne.



## Annexure – 1

### Al Jabal Al Gharbi University Form for Students

Name: \_\_\_\_\_(Optional)

Class: \_\_\_\_\_

Faculty: \_\_\_\_\_

1. Have you visited your university's Web Site? Yes  No

**If YES**..Please answer to the following:

Does your University Web Site provide the following information?

- |                                    |     |                          |    |                          |
|------------------------------------|-----|--------------------------|----|--------------------------|
| 2. Important dates                 | Yes | <input type="checkbox"/> | No | <input type="checkbox"/> |
| 3. Course Listings                 | Yes | <input type="checkbox"/> | No | <input type="checkbox"/> |
| 4. University Organisational Chart | Yes | <input type="checkbox"/> | No | <input type="checkbox"/> |
| 5. Maps                            | Yes | <input type="checkbox"/> | No | <input type="checkbox"/> |
| 6. Telephone Directory             | Yes | <input type="checkbox"/> | No | <input type="checkbox"/> |
| 7. E-mail Directory                | Yes | <input type="checkbox"/> | No | <input type="checkbox"/> |
| 8. Job Search                      | Yes | <input type="checkbox"/> | No | <input type="checkbox"/> |
| 9. Electronic Notice Board         | Yes | <input type="checkbox"/> | No | <input type="checkbox"/> |

1. Can you use this software without anybody's assistance?

- |                   |     |                          |    |                          |
|-------------------|-----|--------------------------|----|--------------------------|
| a. Word Processor | Yes | <input type="checkbox"/> | No | <input type="checkbox"/> |
| b. Excel          | Yes | <input type="checkbox"/> | No | <input type="checkbox"/> |
| c. PowerPoint     | Yes | <input type="checkbox"/> | No | <input type="checkbox"/> |

2. Do you have an E-mail Id? Yes  No

3. Do you know how to search for a study material on the WEB?  
Yes  No

4. Have you used a Digital Library? Yes  No

5. How many computers are there in your department? \_\_\_\_\_

6. How many computers in your department have internet? \_\_\_\_\_

7. How often you visit Internet? \_\_\_\_\_

8. How would you think ICT can help in studies?

- \_\_\_\_\_
- \_\_\_\_\_
- \_\_\_\_\_
- \_\_\_\_\_
- \_\_\_\_\_



## Annexure – 2

Department of Computer Science  
Faculty of Science, Al Zintan  
Al Jabal Al Gharbi University  
Form for Teachers

Name : \_\_\_\_\_ (Optional)

Department : \_\_\_\_\_

Faculty : \_\_\_\_\_

1. Have you visited university's Web Site?

Yes   
No

**If YES**..Please answer to the following:

Does University Web Site provide the following information?

- |                                    |                              |                          |
|------------------------------------|------------------------------|--------------------------|
| 1. Important dates                 | <input type="checkbox"/> Yes | <input type="checkbox"/> |
| No                                 |                              |                          |
| 2. Course Listings                 | <input type="checkbox"/> Yes | <input type="checkbox"/> |
| No                                 |                              |                          |
| 3. University Organisational Chart | <input type="checkbox"/> Yes | <input type="checkbox"/> |
| No                                 |                              |                          |
| 4. Maps                            | <input type="checkbox"/> Yes | <input type="checkbox"/> |
| No                                 |                              |                          |
| 5. Telephone Directory             | <input type="checkbox"/> Yes | <input type="checkbox"/> |
| No                                 |                              |                          |
| 6. E-mail Directory                | <input type="checkbox"/> Yes | <input type="checkbox"/> |
| No                                 |                              |                          |
| 7. Job Search                      | <input type="checkbox"/> Yes | <input type="checkbox"/> |
| No                                 |                              |                          |
| 8. Electronic Notice Board         | <input type="checkbox"/> Yes | <input type="checkbox"/> |
| No                                 |                              |                          |

2. How often do you use the following ICT resources in your class room?



- a. Internet and WWW       Daily    Weekly    Monthly    Never
- b. E-mail                       Daily    Weekly    Monthly    Never
- c. Video Conferencing       Daily    Weekly    Monthly    Never
- d. Word Processing            Daily    Weekly    Monthly    Never
- e. Power Point                 Daily    Weekly    Monthly    Never
- f. Spread Sheets               Daily    Weekly    Monthly    Never
- g. Desk Top Projectors       Daily    Weekly    Monthly    Never
- h. Educational Software       Daily    Weekly    Monthly    Never
- i. CD-ROM (eg.,Encarta)     Daily    Weekly    Monthly    Never

3. If you don't use specific ICT resource, please state your reasons:

- a. Internet and WWW
  - Inaccessible when needed    Unfamiliar    Expensive
- b. E-mail
  - Inaccessible when needed    Unfamiliar    Expensive
- c. Video Conferencing
  - Inaccessible when needed    Unfamiliar    Expensive
- d. Word Processing
  - Inaccessible when needed    Unfamiliar    Expensive
- e. Power Point
  - Inaccessible when needed    Unfamiliar    Expensive
- f. Spread Sheets
  - Inaccessible when needed    Unfamiliar    Expensive
- g. Desk Top Projectors
  - Inaccessible when needed    Unfamiliar    Expensive



- j. Educational Software  
 Inaccessible when needed  Unfamiliar  Expensive
- k. CD-ROM (eg.,Encarta)  
 Inaccessible when needed  Unfamiliar  Expensive

4. What do you think about ICT?

- a. I'd like to use ICT but they are unavailable      Agree  
Disagree
- b. I'm afraid to use computers      Agree  
Disagree
- c. ICT help me getting information for teaching      Agree  
Disagree
- d. I know only the basics of ICT      Agree  
Disagree
- e. I know ICT but do not know to use it      Agree  
Disagree
- f. I manage information effectively with ICT      Agree  
Disagree
- g. I find ICT to be time consuming      Agree  
Disagree
- h. ICT makes my work easier      Agree  
Disagree
- i. Students get distracted because of Technology      Agree  
Disagree
- j. Computers are usually slow when used in teaching      Agree  
Disagree
- k. ICT motivates students to learn easily      Agree  
Disagree
- l. I cannot find anything relevant for my subject      Agree  
Disagree
- m. Computers are usually slow when used in teaching      Agree  
Disagree
- n. I have no proper skills to use ICT in my classroom      Agree  
Disagree

5. Have you ever participated in ICT TRAINING?





Yes No

6. Please indicate your answers to the following:

- |  |       |          |
|--|-------|----------|
| a. I'm interested to learn about using ICT             | Agree | Disagree |
| b. I feel ICT training is not useful to my teaching    | Agree | Disagree |
| c. ICT training may be useful to teach my subjects     | Agree | Disagree |
| d. I need ICT skills for my student's benefit          | Agree | Disagree |
| e. I don't see the need to learn about ICT             | Agree | Disagree |
| f. I'm interested but there's no time for me           | Agree | Disagree |
| g. I'm interested but there is no one to give training | Agree | Disagree |
| h. I think no one in my faculty bothers to use ICT     | Agree | Disagree |
| i. I feel I have adequate skills in using ICT          | Agree | Disagree |

7. If you have any suggestions or if you would like to tell us something about "Using ICT in classroom", please write below:

8. We will be following up this survey with in-depth interviews and forums with selected students and teachers of our university. If you are interested please provide us with your willingness and E-mail Id:

I am interested, please contact me E-mail:

I am sorry.

**Thank you very much for your assistance in this survey.**

Faculty of Science, Al Zintan.

Al Jabal Al Gharbi University, Libya



المؤتمر العربي الليبي الدولي الخامس للهندسة الكهربائية والإلكترونية 2010/10/26-23 طرابلس ليبيا



## Mobile Banking using USSD

Abdulkhalic H.Ashour  
Almadar Al-Jadid company  
e-mail: a.ashour@almadar.ly

### 1. Abstract

This paper describes the design and implementation of this integrative customer-centric MP system named WATABA. The four main mobile payment technologies, WAP, NFC, SMS and USSD were evaluated to compare their performance. The evaluation process involved a team of experts and six criteria. The evaluation results provided conclusive evidence that USSD is the most suitable technology for building the mobile payment system. The data also gave us good insights about the concern for security and privacy. The mobile payment (MP) system was sponsored and built by two partners, Almadar Communications and Bank of Commerce and Development (BCD). In the first phase of the system launch customers are offered the following MP services: buy telecom voucher, money transfer, telecom account top up, utility bill payment and shopping. There are plans to make this MP system a national one by including all commercial banks and mobile network operators in the country.

### 2. Introduction

In recent years leading commercial banks began offering credit card services to their customers. Although no data have been published to show the extent of acceptance of this initiative, observation of the market indicates that credit card usage in Libyan is confined to a handful of hotels, restaurants and retail shops catering mainly to foreign travelers and cash withdrawal from Auto Teller machines (ATM).

This seemingly un-warm welcome of credit cards by consumers and merchants alike is not a sign of indifference or total refusal of this powerful B2C tool, it rather reflects the need for parallel improvement

in other aspects of a modern economy. It requires the presence of all key elements to build the foundation of a successful operation. In this case, banks need to do more than simply offering credit cards to their customers, they need to put out a major marketing campaign to educate the public about the benefits to both business and customer in using the new tool, providing incentives and equipment i.e. Point Of Sale (POS) to merchants, work with internet providers to improve the quality of service and expand high speed internet coverage, deal with regulators to build public confidence and trust and so on. Building of these features require collective efforts and investment from various



agencies and may take a long period of time perhaps several years to accomplish.

This business reality has led the author to carefully examine other payment options, crystallizing his thoughts in ideas to formulate this project. The search process focused on electronic payment (E-Payment) as an alternative medium of exchange in B2C transaction. The E-Payment environment consists of these basic elements:

- 1- A core banking system that holds customer accounts and processes E-Payment transactions.
- 2- Computers that store customers account information in electronic format.
- 3- Point of sale (POS) systems enabled to read account information and build a transaction.
- 4- Data Communication network to connect POS to the core banking system.

Currently in Libya there are more than five million mobile phone users [1] which represent a very high level of penetration in the society. This reality makes mobile phones the best candidate for electronic payment. A mobile phone is an electronic device that converts speech into digital signals at one end and communicates these signals as a stream of binary digits through the network to the other end. Mobile phones also have built-in information storage capabilities. These features of mobile phones satisfy items 2,3 and 4 of the 4 basic elements of the E-Payment environment discussed above. This careful examination of mobile phone features and

E-Payment elements shows clearly the great potential this device offers as an alternative system of E-Payment.

### **The Hypothesis**

The mobile phone may serve as a practical payment tool in the Libyan consumer market. The foregoing assumption simply, clearly and concisely stated represents the hypothesis of the project.

Although the Libyan consumer market, is becoming more dynamic and growing at a rapid rate, it is still lagging in many features key to a modern market. The task of improving this situation may not be quick or easy. This task requires among other things major investments to modernize the banking industry, regulations to protect public interests and assure safety and security, building the supporting infrastructure, etc.

### **Project Objectives**

The project aims at providing the Libyan market with a safer and more convenient alternative method of payment. The mobile payment system was based on Unstructured Supplementary Service Data (USSD) utilizing generic features of the technology supported by all makes and models of mobile phones available in the market as well as mobile network operators. The proposed MP system offers many mobile payment services including, telecom top up, utility bill payment, money transfer, shopping, ticketing, couponing and other services. The new system is expected to facilitate business transactions and remove restrictions and limitations experienced in traditional payment methods (see Figure 1).



## Project Structure

Once the project proposal was carefully discussed and analyzed for adoption in the Libyan market, the next step was to select the proper technology to use to build the system. After this step, the proposal was introduced to prospective sponsors; Almadar Communications, a major mobile network operator in the country; and BCD, a well established private bank in Libya. The two companies approved the proposal and accepted to co-

sponsor the project. Following this enthusiastic approval by the co-sponsors, the project was designed, built, tested and commissioned. Several mobile payment services were implemented and offered to mutual customers of Almadar and BCD. The author was directly involved in every step of the project. It is very important to point out that the entire project was designed, built, tested and commissioned by Libyan engineers and experts.

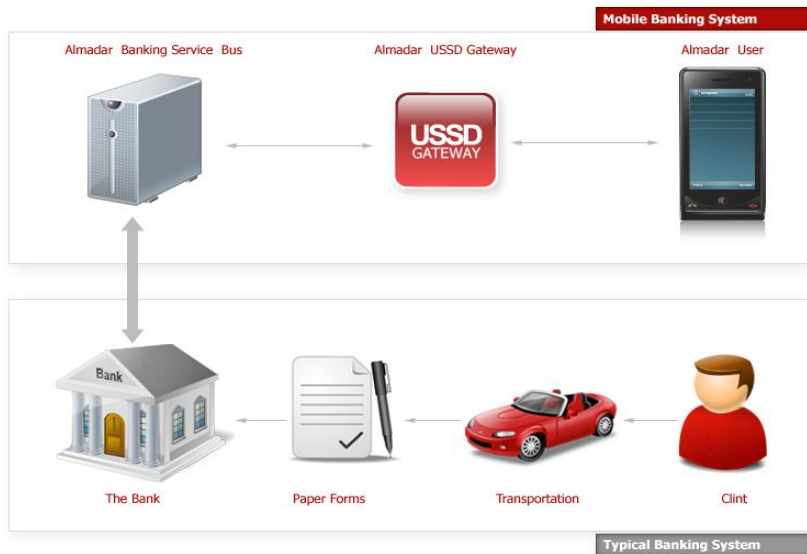


Figure 1 Mobile Payment vs. Paper Payment System



### **3.0 Mobile Payment Systems (MP System)**

A mobile payment is defined as any payment initiated, authorized and completed with at least one mobile device, i.e. mobile phone [2]. The present mobile technology offers these two MP routes or scenarios:

#### **3.1 Direct MP Scenario**

In this option a mobile phone is used to access a credit account either phone credit at a Mobile Network Operator (MNO) or a bank account credit directly via Short Message Service (SMS) or USSD but not through internet as intermediary.

#### **3.2 Indirect MP Scenario**

In this scenario the mobile phone is used just to access mobile internet then following traditional business of e-shopping and e-payment.

These scenarios indicate that a mobile payment service provider (MPSP) falls in one of these three categories:

1. Mobile network operator (MNO)
2. Financial services provider (FSP) such as banks and credit card companies
3. Specialized intermediary

While banks / FSP and MNO operate on their existing infrastructure and customer base, a specialized intermediary operators MP as its core business and has to build the

required infrastructure and customer base from scratch. Thus, its revenue model is rather complex and difficult as it has to finance itself completely from the MP revenues while banks and MNO can simply generate additional revenues from their MP business. The indirect MP system described above relies on internet and WAP/HTTP capable mobile phones as well as GPRS infrastructure at MNO side which require substantial investments and time. This scenario also suffers from issues related to e-security.

The search for a MP solution that offers better e-security, uses existing infrastructure with nominal additional investment, does not rely on internet as intermediary and available for every owner of a mobile phone in the market, has led the author to the newly developed USSD-based direct MP platform supported by MNO in conjunction with FSP, i.e. bank accounts. This interactive USSD technology constitutes the backbone of this project. The improved security in this system is due to the direct connection between mobile phone and the core banking unit. The solution offered involves mobile phones, mobile network and a banking legacy system.

#### **4.0 Techniques used to build MP systems**

Mobile payment developments have been quite uneven throughout the world. One major difference of the various mobile



payment platforms initiated is the technology deployed in the process. The main wireless technologies that can enable mobile payment systems are briefly discussed herein:

#### 4.1 WAP

Wireless Application Protocol (WAP) is basically a suite of communication protocols for the wireless and mobile devices designed to access the internet independent of manufacturer and Vendor. WAP bridges the gap between the mobile phone and the internet world and offers the ability to deliver a wide range of mobile value-added services to subscribers.

WAP applications are written in Wireless Markup Language (WML), which is a subset of Extensible Markup Language (XML).

A WAP-Enabled system consists of three major parts: WAP gateway, HTTP Web Server and WAP device, a WAP-Enabled mobile phone, therefore in the WAP technique a WAP device uses GPRS Service of the mobile network operator to access WAP pages of banks or e-sellers and conduct a transaction [3].

Mobile payment services over WAP are very much limited to Europe and the US markets where advanced technologies exist in the customer base [3]. In other markets, including the Libyan mass market, lagging in advanced technology, i.e. dependable and widely available high speed internet, WAP based mobile payment service will at best be an inefficient business venture.

This in addition to the fact that more than 53% of mobile phones currently in use in Libya are not WAP devices [4] which

means that a WAP based MP service will be unavailable to these customers.

#### 4.2 NFC

Near Field Communication or NFC, is a Short-Range high frequency Wireless Communication technology which enables the exchange of data between devices over a very short distance. To a certain degree, NFC is the fusion of a contactless smart card (RFID, Radio Frequency Identification) and mobile phone. One important feature of NFC is that mobile phones are capable to act as RFID tags or readers. This feature creates opportunity to make innovative applications especially in ticketing and couponing [5]. The "Pay-Buy Mobile" project launched by the GSM Association (fourteen mobile operators are part of the initiative) targeted 900 million mobile users with a common global approach using NFC [5].

In this platform bank account and or Credit Card data are stored securely in the mobile phone and Communicated "Waived" to the POS via built-in NFC (Exactly Like Bluetooth).

In this case, NFC mobile phones come at an added cost to the Consumer. Moreover, NFC based mobile payments needs the exact infrastructure required for credit card processing (POS, reliable data communication infrastructure) which needs huge investment to build. Although the communication range of NFC is limited to a few centimeters, NFC alone does not ensure secure communications, and offers no protection against eavesdropping [6].



### 4.3 SMS

SMS is a text communication service which employs standardized communications protocols that allow the exchange of short text messages between phone devices. The short messages (maximum 160 characters) are stored and forwarded to their destinations by SMS Centers (Store – and – forward – Mechanism).

Although SMS technology is supported by all types of mobile phones and GSM networks, it is subject to high levels of message loss and delay. This session-oriented deficiency is caused by the lack of interactive characteristic tools needed to complete multi-event transactions of mobile commerce, i.e. Authentication, request, confirmation, etc. SMS based mobile payment services also suffer from security issues, because the SMS text follow insecure transmission route [7].

### 4.4 USSD

The Unstructured Supplementary Service Data (USSD) is a unique GSM feature that enables data transmission sessions between mobile phone and external applications transparently. It uses the same Radio Network resources as SMS but USSD has its own gateway to interface platforms that host external applications. USSD is a generic built-in feature of GSM supported by all types of mobile phones and mobile networks.

The technology is highly efficient as it consumes very small radio network resources and because of its flash nature USSD offers an added element of data privacy [6].

### 5.0 Evaluation of M-Payment Technologies

As it has been described in the preceding section there are four main techniques, WAP, NFC, SMS and USSD, that can be used to build a mobile payment system. Each of these technologies has its limitations, advantages and drawbacks. In order to determine the best suited technology to use for building the project a simple evaluation test was conducted to compare their performance. The evaluation test involved several experts and a set of criteria. The selection of experts was based on their knowledge and experience in these technologies. The evaluation criteria submitted to the experts were:

1. Infrastructure Cost: The network infrastructure cost consists of two main components, namely the price of technology and the cost of implementation.
2. M-Phone Capability: This criterion refers to the mobile phone compatibility with the technology and the need for customer investment in technology capable device. SMS and USSD are generic and work well with standard mobile phones, while WAP and NFC require GPRS or NFC enabled mobile devices.
3. Transaction Cost: This includes the cost of operation and maintenance of network infrastructure.

Cost is certainly an important criteria to consider in building a M-Payment operation since profitability of the business is





directly linked to the different costs [8].

4. Ease of use: This criteria refers to the degree of knowledge and effort required on the part of the customer to consummate a transaction.
5. Security and Privacy: This represents the different security and privacy features the technology already embeds to safeguard customer privacy and security.
6. Session Support: This criteria refers to compatibility and speed of the payment process.

All of these criteria as well as others have been proposed and used by other workers to evaluate mobile payment technologies [8,9].

The experts of the related areas were provided with evaluation forms and given an equal amount of time (45 minutes) to complete their evaluation. They began the evaluation process by grading the criteria according to their proportional relevance on a percentage scale and then grading the performance of the separate technologies for each criterion based of the following scale:

Excellent = 9, Very Good =7, Good =5, Satisfactory =3 and Poor =1.

At the end of the evaluation period the scoring forms were collected and analyzed.

**Table 1** shows the six criteria proportional scores in percentage and corresponding weights. The weight was calculated as follows:

$$\text{Weight} = \frac{\text{Sum Of Scores in \%}}{\text{Total Percentage}}$$

Total Percentage = 500%

One very interesting observation about the table is the proportionally large weight given to the criterion, security and privacy. It is more interesting to note that this criterion weight is greater than the combined weight of criterion 1 and 3, the cost to build the network infrastructure plus the cost of operation and maintenance of the M-Payment system. The experts were more or less united in placing security and privacy at greater priority than all other criteria.

**Table 2** shows the evaluation results for the four technologies. The data was analyzed using very basic statistical procedures to compute the average and weighted average for each criteria.

$$\text{Average} = \frac{\text{Sum Of Scores}}{\text{Number of Experts}}$$

Number of Experts = 5

Weighted average = Average x weight

Then the final average and weighted average scores for each technology were calculated:

Technology Average Score =

$$\frac{\text{Sum Of Criteria Average}}{\text{Number Of Criteria}}$$

Number Of Criteria

Number of Criteria = 6

Technology weighted average score = Sum of criteria weighted Average



**Table 1: Criteria Weights**

Exp ert	Criteria Score %						Tot al
	Netw ork Cost (1)	Phone Capab ility (2)	Consum ption of Resource s (3)	Ease of Use (4)	Secur ity + Priva cy (5)	Sessi on Supp ort (5)	
1	15	5	15	5	50	10	100
2	20	5	20	10	40	5	100
3	25	15	15	10	30	5	100
4	4	20	20	30	25	1	100
5	20	12	15	13	20	15	100
Sum %	84	57	85	68	170	36	500
Wei ght	0.168	0.114	0.170	0.136	0.340	0.072	1.00

Where (1), (2), etc. refer to criteria numbers as describe above.



**Table 2: Technology Evaluation Scores (W. Average = Weighted Average)**

Technology	Expert	Criteria Score						Total
		Network Cost (1)	Phone Capability (2)	Consumption of Resources (3)	Ease of Use (4)	Security + Privacy (5)	Session Support (5)	
WAP	1	5	5	5	3	5	9	
	2	5	3	1	3	1	7	
	3	5	5	3	5	5	9	
	4	5	5	3	5	7	9	
	5	9	7	3	3	7	9	
	SUM	29	25	15	19	25	43	
	Average	5.8	5	3	3.8	5	8.6	
W.Average	0.974	0.570	0.510	0.517	1.700	0.619	4.89	
NFC	1	1	1	9	9	5	9	
	2	1	1	7	9	3	9	
	3	1	1	9	9	3	1	
	4	1	1	9	9	3	5	
	5	3	1	9	9	1	9	
	SUM	7	5	43	45	15	33	
	Average	1.4	1	8.6	9	3	6.6	
W.Average	0.235	0.114	1.462	1.224	1.020	0.475	4.53	
SMS	1	9	9	7	5	7	5	
	2	9	9	5	5	3	1	
	3	9	9	7	7	3	1	
	4	9	9	5	7	3	7	
	5	9	9	7	5	3	1	
	SUM	45	45	31	29	19	15	
	Average	9	9	6.2	5.8	3.8	3	
W.Average	1.512	1.026	1.054	0.789	1.292	0.216	5.89	
USSD	1	9	9	9	9	9	9	
	2	9	9	9	7	9	3	
	3	9	9	7	9	9	9	
	4	9	9	7	7	9	9	
	5	9	9	9	9	9	9	
	SUM	45	45	41	41	45	39	
	Average	9	9	8.2	8.2	9	7.8	
W.Average	1.512	1.026	1.394	1.115	3.060	0.562	8.67	



After figuring each technology weighted average score the sample standard deviation, S, was calculated applying the following statistical equation:

$$s = \sqrt{\frac{1}{n-1} \sum_{1}^n (x_1 - \bar{x})^2}$$

Where

$X_1$  Weighted average score of sample 1

$\bar{X}$  Mean of weighted average scores

$$\bar{X} = \frac{X_1 + X_2 + X_3 + X_4}{n}$$

$$\bar{X} = \frac{4.89 + 4.53 + 5.89 + 8.67}{4} = 6.00$$

$$s = \sqrt{\frac{1}{3}((4.89 - 6.00)^2 + (4.53 - 6.00)^2 + (5.89 - 6.00)^2 + (8.67 - 6.00)^2)}$$

2. the following tasks:

$$S = 1.87$$

The weighted average score for USSD is greater than one standard deviation from the mean. This reveals that the weighted average score of USSD is significantly higher than WAP, NFC and SMS technologies. These results indicate that USSD is the best suited technology to use to build a M-Payment system in Libya

## 6.0 Project Implementation

### 6.1 Technical Aspects n=4; Number of Samples

The project design architecture involves intricate three way communications and interconnections between the mobile device, USSD network and the core banking unit. Figure 5 shows the MP system architecture. The MP system implemented comprehends the following Functional Blocks:

1. The USSD Gate Way (GW) at Almadar network terminal to interconnect the mobile device and the Core Banking System (CBS) at BCD across mobile network. This component of the system performs

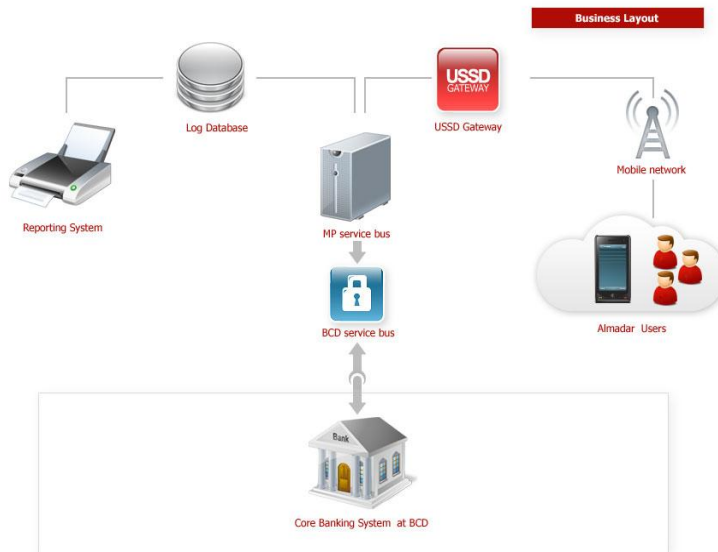


**Figure 2 MP system architecture**

- a. Interactive real time response between the mobile phone and the core banking system.
- b. Service menu management (structure and management)
- c. User access management (only subscribed customers access the service)
3. The Mp system bus controls data flow between CBS, subscribers and the transactions controller.
4. The Log Data Base Logs all of the customer service requests both successful and unsuccessful
5. The reporting tool manages and controls fraud attempts.
6. The BCD service bus controls traffic flow between MP service bus and CBS.
7. The Core Banking System (CBS) at BCD holds the customer account information and provides data flow between both sides. The data goes via encrypted tunnel using IPSec algorithm over a



8. private Point-to-Point Ethernet connection to further enhance security.

### 6.3 Services Implemented

Once installation was completed many trial runs were made to test the system performance and readiness. The following services were then implemented and offered to mutual customers of Almadar and BCD in phase 1 of the project:

1. Buy Telecom Voucher (Madar, LTT, Libyana, Thuraya, GPTC, Marhaba Int. CC)
2. Money Transfer (MT) from one BCD account to another BCD account or to cash (Post Office, BCD desk).
3. Direct Top up of prepaid accounts.
4. Shopping (hotels, clinics, food, grocery, fuel,.. etc)
5. Utility Bills payment, e.g. electricity and telephone (Predefined Accounts)

### 7.0 Description of Service Procedures

To use the MP system the customer must first obtain a Personal Identification Number (PIN). Upon dialing the service code (\*123#) a welcome message prompts the user to enter his PIN number. If the PIN number is valid the user will be presented with the main service menu that has six options to choose from. The service map of the system is a given in [10]. From this menu the user can select any service. The description of each service procedure is presented in [10].

### 7.0 Total Cost Of Ownership (TCO)

The cost of ownership of the mobile payment project may be very small for both partners because both companies have their

established infrastructures to support the project without the need for much capital investment. The TCO for the partners is may be different since neither company provided any actual values for their costs to be a part owner of the project. For Almadar, in addition to the existing USSD GW, the backbone of the mobile payment system, they installed few hardware items and developed the MP service bus and the reporting tool software in-house by their own team of experts and engineers. Therefore no extra investment was involved. For BCD, they used their existing core banking system plus a small investment in developing the interface kit. The fact that neither Almadar nor BCD had to make any serious investment played a major roll in their decision to co-sponsor the project and the speedy implementation of the mobile payment system. Basically, they figured that there is little or no risk in sponsoring the project and perhaps that is the reason for the absence of an elaborate economic feasibility study for the project.

### 7.1 Revenue Model

This revenue model is based on estimates and assumptions which may change when the project is officially launched. Revenues are generated from service fees and perhaps other sources. Customers may pay for the mobile payment services based on one of these plans:

**Plane 1:** A 1% charge on every payment transaction amount

**Plane 2:** A fixed service fee per transaction

**Plane 3:** A flat annual subscription fee per service

**Plane 4:** A Combination of plan 3 + Plan 1 or plan 3 + Plan 2



The partners have their different operation and maintenance costs. For example, Almadar incur cost of providing the following:

1. Dedicated secure interactive USSD procedural call menu
2. Customer Help Desk
3. Operation and maintenance of the network infrastructure

Since neither Almadar nor BCD provided any figures for their expected operation and maintenance costs, it is exceedingly difficult to assign values to these costs at this time. We can only assume that the partners will split the system revenues. Here a number of scenarios are possible; perhaps one scenario is 20/80, 20% Almadar, 80% BCD to offset their respective costs and generate some profit. Of course the partners seek to increase their customer base by attracting more customers to the mobile payment system.

In this scenario and based on success history of mobile payment systems in other markets [11,12] we can conservatively estimate that 50,000 customers will sign-up for the service in the first year at an annual average spending of 500 LYD per customer, and that all customers will select Plan 4 (combination of plan 3 and plan 2) and , that the fixed annual subscription is 15 LYD.

Therefore revenues can be calculated as follows:

First Year Revenue:

Number of Customers = 50,000

Annual Subscription Fee = 15 LYD Per Customer

Annual Subscription Revenues = 50,000 x 15 = 750,000 LYD

Transaction Fee = 1%

Annual Average Spending = 500 LYD

Transaction Revenues= 50,000 x 500 x  $\frac{1}{100}$   
=2500,000LYD

Total Annual Revenues=750,000 + 250,000  
= 1,000,000 LYD

If we assume further that in the second year the service attracts 500,000 customers at an annual average spending of 1000 LYD per customer, then the revenues will be 12,500.000 LYD. Keep in mind that the number of mobile phone accounts in Libya is greater than 5,000.000 accounts of which Almadar has 43% share.

## 7.2 Return On Investment (ROI) Analysis

With all investment figures missing and unavailable it is impossible to calculate the ROI or to make valuable ROI analysis. Since the amount of capital investment in the project per Sa is very small and negligible we can assume it is zero. In such case any revenue realized from the service is acceptable as a return on investment. The calculations made in the previous section represent an estimation of these revenues.

## 8.0 summary and conclusion

From the project work that has been completed, we can conclude that:

1. The wide penetration and personal nature of mobile phones can make mobile payment solutions applicable for a variety of services in Libya.
2. Mobile payment may become the most practiced e-payment solution in the B2C market in Libya because it accommodates market



conditions and national economic practices.

3. USSD is significantly better technology to use for building a mobile payment system in Libya.
4. The concern for security and privacy is much greater than the concern for any other criteria used to evaluate mobile payment technologies.
5. The cost of ownership of the USSD-based MP system is very small because the system was built almost entirely on already existing infrastructure and technologies.
6. Early indication of public demand for the services implemented (WATABA Services) is strong and very promising.
7. WATABA Services offered can be expended to cover more payment transactions as more retailers and businesses sign up to accept the services.
8. WATABA provides sufficient security measures to begin using the system with the opportunity to enhance security at a later date and small investment.

Although the mobile payment services implemented are a big step forward in a market starved for alternative methods of payment, the system need to be developed further to reach a much larger segment of the population. Therefore, the following set of recommendations must be considered by all parties interested in building a more national mobile payment system in Libya.

1. Commercial banks must take serious steps to modernize their

information technology (IT) infrastructure and to build core banking systems capable of accommodating MP services.

2. Telecom operators must provide a more reliable and more secure data communications infrastructure to permit banks to interconnect their branches and build a central core banking applications necessary for modern banking services.
3. Telecom operators must also provide infrastructure for building a national ATM switch board to interconnect participating banks.
4. The government must provide cyber laws and regulations to govern mobile payment services and transactions.

The benefits of mobile payment services may prove to be of great value to commerce and the national economy in general.

## 10.0 References

- [1] General Telecom Authority Unpublished Report, (2008), General Telecom Authority, Tripoli, Libya.
- [2] Andy Dornan, (2000), The Essential Guide to Wireless Communications Applications, From Cellular Systems to WAP and M-Commerce, pp.315, Prentice Hall Publisher.
- [3] Dale Bulbrook, (2001), WAP : A Beginners Guide, pp. 319, McGraw-Hill Osborne Media Publisher.
- [4] Almadar Unpublished Internal Report, (Feb.2010), Almadar Aljadeded Co., Tripoli, Libya.





- [5] Visa and SK Telecom to Launch mobile payments, (2007), Card Technology Today 19 (2), p. 6.
- [6] Gerhard P. Hancke, (2008), Eavesdropping Attacks on High-Frequency RFID Tokens, p. 100-113, 4th Workshop on RFID Security.
- [7] E. Valcourt, J. Robert and F. Beautieu, (2005), Investigating mobile payment: supporting technologies methods and use, IEEE international conference on wireless and mobile computing, networking and communications, vol 4, p. 29-36.
- [8] Jan Ondrus and Yves Pigneur, (2006), A Multi-stakeholder Multi-criteria Assessment Framework of Mobile Payments: An Illustration with the Swiss Public Transportation Industry, 39th Annual Hawaii International Conference on System Sciences, IEEE Computer Society.
- [9] Y. Chou, C. Lee and W. Chung, (2004), Understanding m-commerce payment systems through the analytic hierarchy process, Journal of Business Research, 47, p.1423-1430.
- [10] A.Ashour, "USSD based mobile payment in Libya ", M.Sc . thesis, May,2010.
- [11] Olga Marawczynski, (2007), Innovations in Mobile Banking: The case of M-Pesa, First National Consultative form on Microfinance, Khartoum, Sudan
- [12] P.Y.K Chau and S. Poon, (2003), Octopus: and e-cash payment system success story, communications of the ACM 46 (9), p. 129-133



المؤتمر العربي الليبي الدولي الخامس للهندسة الكهربائية والإلكترونية 23-26/10/2010 طرابلس ليبيا



## Cross-Layer Routing Protocol for Wireless Sensor Networks

Khaled Daabaj<sup>i</sup>, Shubat Owhida<sup>ii</sup>, Yousef Daabaj<sup>iii</sup>

<sup>i</sup>School of IT, Murdoch University, Australia, khdaabaj@hotmail.com

<sup>ii</sup>Dept. of Computer Eng., Alfateh University, Tripoli, Libya, s.owhida@yahoo.com

<sup>iii</sup>School of IT, Eccles College, Manchester, England, UK, yousefdaabaj@hotmail.com

### ABSTRACT

Wireless Ad hoc sensor networks require a highly dynamic, adaptive routing scheme to deal with the high rate of topology changes. Besides that, energy consumption rate need to be consistently distributed among sensor nodes, and efficient utilization of battery power is essential. If only the link reliability metric is considered in the routing scheme, it may create a long hops route, and the high quality paths will be frequently used. This leads to shorter lifetime of the high quality routes; thereby the entire network's lifetime will be significantly minimized. This paper presents a cross-layer and reliable load balancing routing (RLBR) protocol for ad hoc sensor networks by integrating routing information from different layers. The RLBR scheme aims to redistribute the relaying workload and the energy usage among relay sensor nodes to achieve balanced energy dissipation, thereby maximizing the functional network lifetime. The proposed routing protocol was tested and benchmarked against the TinyOS-2.x based implementation of MintRoute routing protocol on an indoor testbed comprising 20 Mica2 motes and low power listening (LPL) link layer provided by CC1000 radio. The proposed routing scheme consumes less energy for communications while reducing topology repair latency and achieves better connectivity and communication reliability in terms of end-to-end packets delivery performance.

*Keywords-wireless sensor networks; reliable routing; energy balancing; cross-layer protocol.*

### I. INTRODUCTION AND MOTIVATIONS

Wireless Sensor Networks (WSNs) provide the ability to collect information cheaply, accurately and reliably over both small and vast physical regions. Unlike other large data network forms, where the ultimate I/O interface is a human being, WSNs are about collecting data from unattended physical environments. Therefore, reliable and energy efficient routing is a key issue in WSNs deployments. From energy efficiency standpoint, the existing TinyOS-based routing protocols [6] for wireless sensor

networks (WSNs) are steadily improving for forming a reliable tree-based data gathering but they are still inferior over custom solutions concerning energy consumption [17][18][19]. In other words, these protocols are reliability-oriented but unaware of the energy status of relaying sensor nodes and do not explicitly apply energy balancing in their routing schemes; thereby diverting load to sensor nodes with low energy capacity. As a result, this paper focuses on balanced energy dissipation routing scheme for lifetime maximization by taking the advantage from reliability-oriented routing



schemes and traditional energy-aware routing schemes.

Since the communications overheads are the major energy consumer during a sensor node's operation, the proposed routing scheme a simple but reliable routing algorithm, aims to cause minimal communication overheads for network configuration and multihop data dissemination. Although the main objective of a cross-layer load balancing routing is the efficient utilization of network resources, the literature [1][19][20][22] lacks such protocols that take jointly link reliability and energy-wise metrics into account with load balancing. There is no doubt that a better distribution of load leads to the more efficient use of bandwidth, which means that there is less contention and consequently less energy is consumed, but it is not self-contained for achieving complete energy efficiency. WSNs are not necessarily energy-homogeneous, and there is thus insufficient information about the sensor nodes' load tasks to enable the energy-wise selection of the paths. The current load of a given sensor node can be used to estimate the potential dissipation of energy but it does not contain a record of past activities and the residual energy level of the sensor node remains hidden.

Recent studies on energy efficient routing in multihop wireless sensor networks (WSNs) have shown great reliance on radio link quality in the path selection process. If sensor nodes along the routing path and closer to the base station advertise a high quality link to forwarding upstream packets, these sensor nodes will experience a faster depletion rate in their batteries. This results in a topological routing hole or network partitioning [19]. Our paper presents an empirical study on how to improve energy efficiency for reliable multihop communication by integrating additional useful information from different

layers: e.g., residual energy level, link quality, and hop count. The proposed approach aims to balance the workload among relay nodes to achieve a balanced energy usage, thereby maximizing the functional network lifetime. The experiments are based on a prototype real-network, Mica2 (MPR400) sensor network platform, from Crossbow Technologies Inc [5].

Although the majority of WSN-related research activities have used network simulators to demonstrate the benefits of employing various routing algorithms, simulations have limitations in emulating real low power WSN characteristics. Therefore the work done in this paper has been conducted on a real-world WSN by taking in account the inconsistent behavior of wireless signal propagation, and how the real sensor device's behavior affects a routing protocol's performance or even a device's rate of energy consumption. In low-power WSNs, the unreliability of the links and the limitations of all resources bring considerable complications to routing. Even in the presence of static nodes, the channel conditions vary due to multipath fading effects [14]. Furthermore, sensor nodes are typically battery-powered, and ongoing maintenance may not be feasible: the progressive reduction of the available residual power needs to be considered as a crucial factor in the parent selection process to control nodes' energy drain for the extension of the lifetime of the individual nodes and for the achievement of energy balancing in the entire network. The testbed network is constructed using 30 identical Mica2 sensor nodes with a single perimeter stationary base station.

The proposed routing scheme allows a child sensor node dynamically searches for a new reliable parent node with more residual energy. This dynamic adaptation strategy can alleviate the energy-hole



problem [10][23]. The experimental work done in this paper aims to improve the indoor performance evaluation of the proposed routing scheme by extending the experiments to outdoor, and simulations on larger networks in its future work. The remainder of the paper is organized as follows. In section II, the related work is introduced. Section III presents the proposed routing scheme. Section IV describes briefly the implementation platform, Experiment methodology and testing setup. The experimental results are illustrated in section V. Finally, Section VI concludes the paper and outlines the future work.

## II. RELATED WORK

Since the wireless links in low-power WSNs are not stable, the reliability-oriented routing protocols for WSNs purely rely on either Channel State Information (CSI) from broadcast control traffic or delivery cost estimates from unicast traffic using the ETX link metric [21]. The earlier common form of CSI, the Received Signal Strength Indicator (RSSI), used to be considered a predictor of link quality of some platforms such as Mica2 CC1000 RF transceiver [7][8]. The RSSI has early been recognized as a good predictor of link quality; specifically, it has been shown that the RSSI, if higher than the sensitivity threshold, about -87dBm, correlates very well with the packet reception rate [18,19]. As for link estimation by means of delivery cost estimates, the ETX link metric is proposed in [21]; the idea is to estimate the total number of transmissions needed to get a packet across a link, and use the route with the minimum ETX. ETX has been shown to be very robust, especially on top of an Automatic Repeat Request (ARQ) scheme [19] which strengthens low quality links. However, using ARQ scheme in the link layer, the child sensor node will retransmit the unacknowledged packet and degrade the network throughput. The traditional way of

estimating the ETX relies on link symmetry assumption. While this may be reasonable in mobile ad hoc networks (MANETs) due to mobility, it is not accurate in typical WSN deployments where packets losses on the direct and reverse channel are not correlated even though sensor nodes are static.

The observations in [2][3][4][17][19][22] states that it is vital to use link layer acknowledgments to evaluate the ETX metric. For example, MintRoute [17] experiences the asymmetric link problem inappropriately as child sensor nodes might not get their packets acknowledged from their current parents albeit maximum number of successive transmission failure is reached. The proposed load balancing scheme solves the asymmetric link problem by using active bidirectional monitoring of link status and switching to a new valid parent when exceeding a threshold of maximum successive transmission failures, and puts the old invalid parent into blacklist to avoid switch oscillation.

Since the data rate in WSNs is typically low, route messages do not need to be exchanged frequently and the rate of route message exchanges is very low as in MintRoute. In terms of energy dissipation cost, this helps MintRoute to reduce its energy consumption in low data rates. However, MintRoute is more expensive at high data rates. Also MintRoute takes a long time to convey the topological changes to the whole network (i.e., due to node failure or damage); during this period, many packets are routed through optimal paths, which consume additional energy and thus offsets the benefit of energy balancing in reliability-based routing schemes. Hence, the proposed distributed routing algorithm considers the acceleration of route message exchange rate for propagating the topological changes. Although MintRoute protocol balances the traffic load with



occasional switches of nodes' parents which is a direct consequence of the Minimum Transmissions (MT) metric, MintRoute protocol does not explicitly apply a metric that considers workload balancing. Hence, the proposed algorithm is proposed to address load balancing in energy efficient manner by maintaining a reliable set of valid parent nodes in the routing table to allow sensor nodes to quickly find a new parent upon parent loss due to the existing of node failure or routing hole.

### III. CROSS-LAYER ROUTING SCHEME

The proposed routing scheme is a hybrid, reactive and proactive, designed to

adaptively provide enhanced balanced energy usage on reliable routes and to employ ready-to-use neighborhood routing tables in order to allow sensor nodes to quickly find a new parent upon parent loss due to link degradation or run-out of energy. The RLBR scheme is built on the ongoing work stated in [24][25][27]. As shown in figure 1, the scheme uses Channel State Information (CSI) and residual energy capacity with other locally overheard parameters, e.g., aggregation load, sensor node-*id*, and tree-level, to form a cost function for selecting the most reliable and energy-efficient route towards the base station.

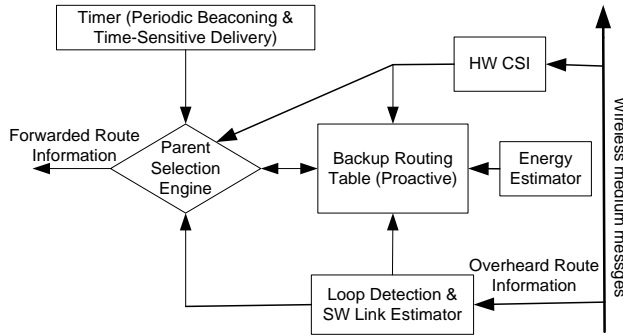


Figure 1. Routing Scheme Overview

The routing tree is a directed acyclic graph which relays packets towards the base station over multiple paths. The routing tree is built by assigning a *level number* to each sensor node depending on its distance (e.g., number of hops) to the base station, and delivers sensing data packets from higher-level to lower-level sensor nodes. The base station is at *level 0*. Each sensor node at level *i* can select a valid parent from its level *i* or from lower level *i-1* towards the base station. The valid parent is selected by the routing metrics used in the routing cost function, i.e., link quality, residual energy, hop-count, aggregation load or latency. Obviously, any

path from source sensor nodes to the base station is the most efficient path in the resulting routing tree. The routing tree starts with the easily-constructed shortest path tree, and then allows each sensor node to pick a new parent node if it appears to provide better routing cost with a higher link quality. Using the broadcast nature of the contention-based wireless medium, a sensor node can easily observe its neighborhood by receiving and overhearing periodic beacon packets which initially originate by the base station.

In *route maintenance phase*, the value of routing metric is to be used first from the



routing table, and then to select a valid parent on a route  $r_j$  from multiple available routes according to the metric values. Based on link reliability as a primary cost metric, it can be assumed that a given number of sensor nodes are distributed arbitrarily and each node  $n_i$  sends a packet at a given transmitting rate and has a multihop route  $r_j$  of  $hc_{ni,rj,b}$  hops to the base station  $b$ .  $hc_{ni,rj,b}$  is the hop count of the route  $r_j$  between  $n_i$  and  $b$ , which is greater than or equal *zero*. If sensor node  $n_i$  can't reach the base station  $b$ ,  $hc_{ni,rj,b}$  is set to *infinity*. In view of that, the probability of relaying a packet

originated at node  $n_i$  is expressed in equation 1, which is the *probability*  $P_{ni,rj,b}$  of relaying a data packet towards the base station  $b$  through the selected route  $r_j$ . Where  $lq_{ni,r,ni+1}$  is the link quality between sensor node  $n_i$  and its current parent (upstream neighbor node)  $n_{i+1}$  along route  $r_j$ . In other words,  $P_{ni,r,b}$  counts for the readiness of node  $n_i$  of forwarding a packet based on its residual energy capacity level  $e_{ni}$  and link quality  $lq_{ni,r,ni+1}$  to its intended upstream neighbor node  $n_{i+1}$  that receives the packet and relay it towards the base station  $b$ .

$$P_{ni,rj,b} = \begin{cases} \prod_{hc_{ni,rj,b}} P_{ni,rj,ni+1}(lq_{ni,rj,ni+1}, Pow_{ni,rj,ni+1}^{rx}), & \text{if } 0 < hc_{ni,rj,b} < \infty \\ 0, & \text{if } hc_{ni,rj,b} = \infty \\ 1, & \text{if } hc_{ni,rj,b} = 0 \end{cases} \quad (1)$$

If the base station is unreachable,  $P_{ni,rj,b}$  is approaching zero as the cost or route  $r_j$  in terms of hop count  $hc_{ni,rj,b}$  is perpetuating to infinity. Otherwise,  $P_{ni,rj,b}$  is normalized to one and the cost  $hc_{ni,rj,b}$  is zero; this means that no packets are being sent or relayed by sensor node  $n_i$ .

#### IV. EXPERIMENTAL EVALUATION

##### A. Implementation Platform

Considerable advances have been made in recent years in hardware [5] and software [6] for building wireless sensor networks. The implementation was based on real world testbed of wireless sensors nodes, specifically the UC Berkeley's Mica2 motes which are popular due to their tiny architecture, open source development and commercially available from Crossbow@ Technology [5] with TinyOS operating system [6]. Mica2 (MPR400CB) mote is a low-power sensor device whose low cost can be attributed to its lack of limited resources. Mica2 was built with an 8-bit, 7.3828MHz Atmel® ATmega 128L

processor, 128 kilobytes (KB) of in-system program memory, 4KB of in-system data memory, and 512KB of external flash (serial) memory for measurements storage [7]. Mica2 mote uses a low powered radio "Chipcon SmartRF CC1000 transceiver" which is a single-chip very low power radio frequency transceiver. CC1000 has 23 different digitally programmable output radio power levels ranges from -20dBm to +5dBm and linear RSSI (received signal strength indicator) to measure the strength of the received signal. [8].

Since these limited resources seem unfit for computationally expensive or power-intensive operations and communications are much more expensive than computation on wireless sensor devices, explicit energy saving techniques are necessary to extend battery lifetime as much as possible [4]. Furthermore, to ensure effective data gathering by sensor networks in indoor or outdoor environments, there are problems such as the ability of network sensor nodes to function correctly in such environments; and maximizing the length of time the



network is able to deliver data before nodes' batteries are exhausted.

### B. Experiment Methodology

In this sensor network experiment, source nodes transmit data packets at the nominal rate to any nodes that can hear it. Receiving nodes forward the data to the base station depending on the local information that have been maintained in the node's neighbor table, so the most energy efficient path is selected. The work in this paper considers the following assumptions: the testbed network is a homogeneous sensor network; all nodes are identical with the same resources and initially with the same residual power; the network topology is static unless occurring of obstacles or node failures; the base station is fixed and the communications pattern is many-to-one; single radio channel; omni-directional whip antenna, and event-driven sensing mode.

### C. Testing Setup

TinyOS was used as the development environment in this work, which is an event-driven operating system intended for sensor networks with limited resources. The testing environment was conducted indoor and was done on a network of 20 Mica2 sensor nodes with one perimeter base station used to collect messages sent within the network. To limit the transmission range, the motes were placed directly on the ground and to determine the distance which provides a reliable delivery rate but minimizes the possibility of a mote transmitting further than to adjacent motes; motes closer to the base station were placed at varied distances and the delivery rate recorded. Then, the distance that provided a successful packet delivery rate was used which is calculated as the total number of packets received successfully divided by the total packets transmission epochs.

In indoor environment, where the radio behavior is irregular, the radio power was initially reduced to the minimum output power setting -20dBm (10 $\mu$ W), and variable in-between spaces to provide a one-hop reliable delivery rate and to minimize opportunistic reception. The source sensor nodes generate packets, while the network operates for a given epoch; the number of messages received by the base station was recorded. The Mica2 motes were labeled with numbers and placed in predetermined locations. The base station mote was placed on the MIB520 Mote Interface Board which powered by an AC power supply and attached to a laptop.

## V. EXPERIMENTAL RESULTS

Although the WSN is positioned in indoor environment with very limited ambient noise, multihop WSN has several challenges which represent in: the wireless link failures that limit the number of traversed packets that can be in flight concurrently from source to destination due to unreliable wireless transmission at each hop and MAC protocol contention problems from hidden nodes and/or exposed nodes; the physical-layer properties that may constrain the throughput achievable over a multihop route; end-to-end reliable delivery of data requires each packet to traverse one or more intermediate hops from the source sensor node towards the base station. This empirical research in the context of WSNs has given a good understanding of the complex and irregular behavior of low-power indoor wireless channels.

### D. Route Reliability

The RSSI values seem to descending fluctuate as the distance between sensor nodes increase. Although the indoor experiment is performed with stationary sensor nodes, the RSSI values of Mica2's





CC1000 radio have a tendency to fluctuate as shown in figure 2 where the values presented are average values from the packets that are received and do not imply a steady link with fixed packet size. It was

observed that within short distances of few meters, the RSSI were generally stronger with a small packet loss. For longer distance, at 10 meters, the link quality has a bit stronger RSSI readings.

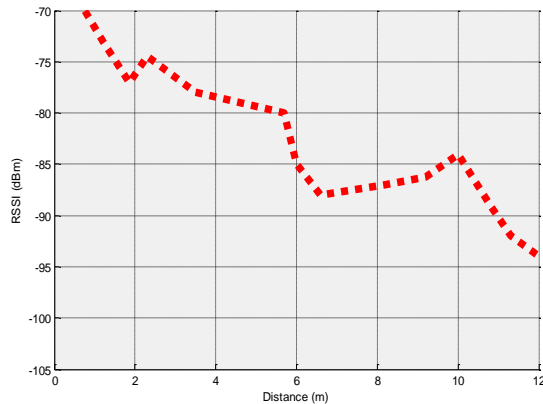


Figure 2. RSSI Indoor Measurements

However, the RSSI readings follow an exponential diminishing while the successful packet reception ratio is still high; after approximately 12 meters of distance with low RF power and mote are placed on the ground, the signal is noisier and its strength deteriorates to the minimum receive sensitivity of the CC100 transceiver which is about -98dBm [7]. This extreme sensitivity can be interfered by another oscillator from an adjacent Mica2 node. A distance of at least 65cm should be maintained between adjacent mica2 nodes to avoid local oscillator interference. However, at low transmission power levels, the sensor nodes are still able to communicate with each other. Using CC1000 RF chip's RSSI independently may not be adequate indicator of the link quality for reliable connectivity; even with high RSSI there might be severe interference. The link quality need to be computed based on bit or packet error.

The experience with the experimental work done has revealed several underlying issues that stem from the properties of the reliability-oriented cost-based routing layers, specifically, MintRoute combined with the resource constraints of the mote platform. Those issues include energy efficiency, long-term link estimations, count-to-infinity and routing loops. The RLBR scheme considers the suitable countermeasures to address these issues. During the parent selection process, MintRoute uses the link quality estimations with the surrounding neighbors together with cumulated route quality estimation to the base station, and the hop count metric included in the route updates is completely ignored. This can lead to undesirable results in MintRoute, when a sensor node has optimal routes with two or more neighbors with the same best link quality. MintRoute will then arbitrarily choose one of them as its new parent node using its default minimum transmissions (MT) metric, which results optimal route that could be in



some direction faraway from the base station and in the worst case in the opposite direction of where the base station is located. This results in an undesirable routing problem, e.g., routing hole. The natural occurrence of suboptimal routes is taken into account by the RLBR scheme when performing parent selection by adopting, for instance, the tree-level number in terms of the least number of hops is used as a tie breaker; this advantage does not apply for MintRoute. In MintRoute, only next packets transmission may probably reduce the already perceived link quality, which makes the selective forwarder look less attractive.

In other words, the parent selection process in MintRoute is merely based on link quality. When the link quality degrades, neighboring sensor nodes will choose other sensor nodes with a better link quality. For example, creating routing holes in MintRoute is straightforward due to purely relying on the best link quality. When a sensor node has the base station as one of its neighbors, the sensor node will not automatically choose it as its parent.

Instead, it will choose the neighbor with the best link quality. To be selected, a sensor node must have both a good send and receive quality. To get a high send quality, the high value must be included in a route update sent by the relay sensor node that caused a routing hole. To get a high receive value, this relay sensor node will have to keep sending packets to prevent the decaying of the receive value by the sensor node. The number of packets that might be lost also lowers the receive quality.

Figure 3 shows an example of how routing in MintRoute picks sensor node 14 as a parent for node 16 instead of node 19 and constructs the optimal route through sensor node 14 even though node 14 is in the opposite direction of where the base station is located. In figure 3, sensor nodes 11, 13 and 16 select node 14 as their parent with best link quality using optimal routes that purely based on link quality estimations using MT metric. This leads MintRoute to cause a routing hole to the downstream child nodes at node 14. As a result, MintRoute is deemed to be unstable in packets transmission to be efficient.

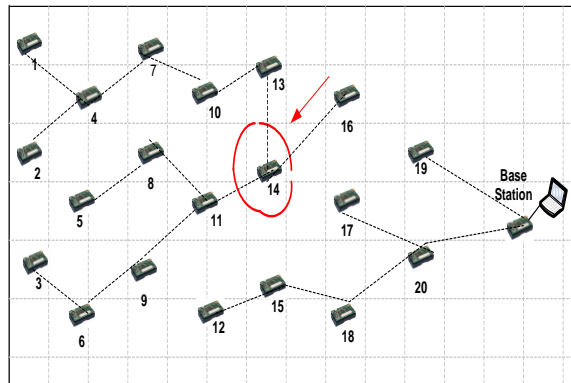


Figure 3. Status of Routing Hole in MintRoute

#### E. End-to-End Packet Delivery

In multihop indoor WSN, the achieved packet delivery performance may be

inferior than it should be for several reasons at different layers. At the MAC layer, specifically the B-MAC used on Mica2 motes, CSMA-based MAC protocol



backoff waiting times at each wireless sensor node could cause a packet to be lost before it has been transmitted if a sensor node senses a busy wireless channel for a maximum number of times.

In this situation, the sensor node will simply discard the packet and move on to the next packet. Besides that, packet loss due to link failures or collisions leads to a high rate of link layer retransmissions; thereby resulting in a low packet reception ratio (*PRR*) and inversely a high packet loss ratio (*PLR*). As a consequence of packet retransmissions, a considerable amount of the energy is spent for repairing lost transmissions and re-establishing asymmetric links.

At the physical layer, indoor environment surrounding, and the orientation of Mica2 motes and their antennas have unconstructive effect on packet delivery performance. In addition, high signal strength is a necessary but not a sufficient condition for good *PRR*, especially when a higher transmission power is used, conceivably due to the effect of Multipath Rayleigh Fading Channel (MRFC) [14]. Furthermore, there is a number of factors cause a packet to be corrupted and thereby packet is to be considered lost or not received at all at the destined recipient. A packet may be lost due to errors in the wireless transmission, signal degradation caused by multi-path fading, packet drop due to channel congestion, faulty mote hardware, and packet collision due to the hidden node problem [13]. In

addition to this, packet loss probability is also affected by signal-to-noise and distance between the transmitter and receiver. As a result, predicting the source of the packet loss is complicated and unclear in terms of the hardware. In addition, this indoor experimental testbed indicates that low-power radio connectivity is imperfect and non-uniform, even in ideal settings.

A packet loss due to link failures is the most common in WSN channels. When data aggregation is enabled, a single link failure will result in a sub-trees of aggregated values being lost. If the failure is close to the base station, the influence on the resulting aggregate can be significant. Figure 4 shows the impact of link failures on packet reception ratio at the base station for the RLBR scheme and MintRoute. Although link failure rate is very low, a small percentage of sent packets are lost due to packet collisions and halted acknowledgements.

Figure 5 shows the multihop routing overhead in terms of how the reception rate for both protocols decreases as the number of hops increases for a constant transmission rate of 7Kbits per seconds. MintRoute performs poorly in the small-scale deployed testbed topology due to the limitations of its route searching and maintenance compared to RLBR. This leads to a prediction that MintRoute also cause a lower end-to-end transfer rate in large-scale WSN with large number of hops between the source sensor node and the base station.

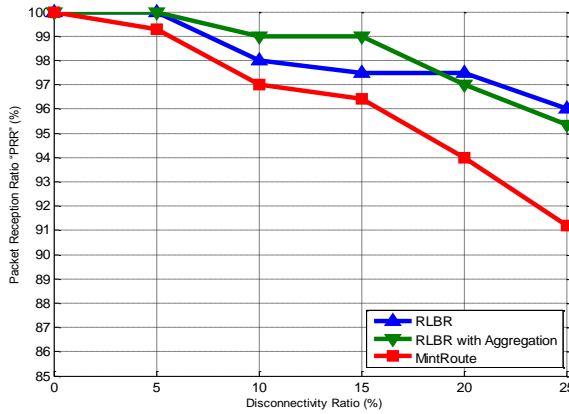


Figure 4. Average PRR vs. Link Failure

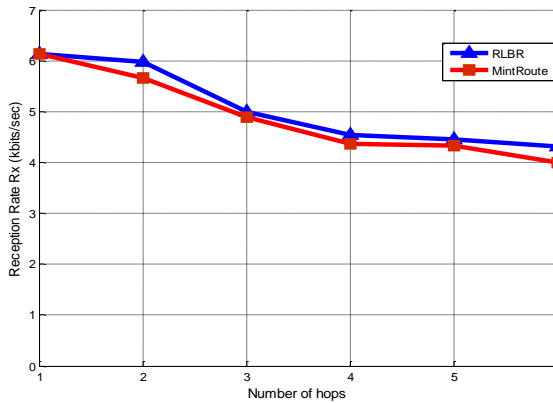


Figure 5. Throughput vs. Hop Count

As an overall, the RLBR scheme outperforms MintRoute owing to its lighter traffic as a result of data aggregation, which leads to fewer packet collisions. But when the link failure rate starts to increase above about 20%, the packet reception ratio (PRR) in the RLBR scheme with aggregation is lower than without aggregation due to data aggregation along the routing path or outdated data packets and that each packet contains more aggregated packets being lost. On average, without data aggregation, most sent packets are successfully delivered

by greater than 95% and the packet loss is lower in the RLBR scheme even though the link failure rate increases.

#### F. Average Dissipated Energy

Failed packets reception that may result from packet collision or link failure requires packet retransmission to be successfully received at the destined recipient. Figure 6 shows the total dissipated energy consumption required for retransmissions due to packet loss or link failures. Since the



RLBR scheme has the feature of employing the implicit acknowledgements strategy as stated in [26] for less communication overhead, packet transmission is less than that in MintRoute. The fewer packets sent results the less energy consumed for packet receiving, overhearing, and failed packet retransmission. In addition, the total dissipated energy for packet transmission is still much lower in the proposed routing scheme than in MintRoute even though the RLBR scheme requires only 0.48% of computation overhead for parent selection

overhead. On average, the RLBR scheme saves around 35% on energy consumption for communication less than MintRoute. MintRoute keeps transmitting route message, e.g., control packets, at constant periods [17] and the beaconing rate doesn't adjust with topological changes. In terms of energy, the non-adaptive beaconing followed by MintRoute consumes additional energy and is not energy efficient particularly on fixed indoor testbed that doesn't experience high rate of link failures.

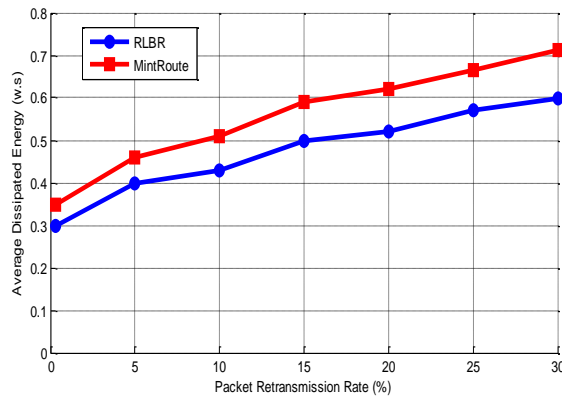


Figure 6. Average Dissipated Energy due to Link Failures

## VI. CONCLUSION AND FUTURE WORK

Since the wireless links in low-power WSNs are not stable, and the loss of packets happens frequently in communications, the link quality metric is mainly used by most reliability-oriented routing protocols to select the optimal link. However, WSNs are mainly powered by AA batteries and the resources are limited. If the reliability of communication is purely deemed as a routing cost metric, a number of sensor nodes will be exhausted quickly. Consequently, this number of dead sensor nodes is extremely essential to the lifetime of the entire network, if these important nodes fail to relay packets, the network's

functionality will be ruined. In other words, If only the link reliability metrics are considered in WSNs, it may create a long hops route, and the high quality paths will be frequently used. This leads to shorter lifetime of the high quality routes; thereby the entire network's lifetime will be significantly minimized. In indoor experiment, MintRoute protocol improperly assumes that links has stable with independent packet losses and uses this assumption to derive link quality estimations inaccurately based on long-term link estimations.

Therefore, on the basis of reliability metrics, a reliable, energy efficient, and load balancing routing is a key issue for



maximizing functional lifetime of the low-power WSNs. As an overall, the proposed routing scheme, RLBR, can achieve an overall average of over 35% energy savings over the standard network layer currently provided by TinyOS-2.x. MintRoute and achieves better connectivity and communication reliability in terms of end-to-end packets delivery performance. Finally, the RLBR scheme performs well as it shows a high success rate of packet delivery and moderate energy consumption.

Maximising the network lifetime is the subject of ongoing work on outdoor wireless sensor network testbed comprising IEEE802.15.4 compliant sensor nodes, i.e., TelosB that built with the CC2420 radio and provides a much more reliable RSSI/LQI/bit error patterns. Also comparisons using scalable simulations are being addressed in order to validate the experiments.

#### REFERENCES

- [1] S. Singh, C.S. Raghavendra, and J. Stepanek, "Power-aware broadcasting in mobile ad hoc networks," in Proceedings of the 10th IEEE International Symposium on Personal, Indoor and Mobile Radio Communications (PIMRC'99), September 1999, pp. 22–31.
- [2] A. Cerpa, J. Wong, M. Potkonjak, and D. Estrin, "Temporal Properties of Low Power Wireless Links: Modeling and Implications on Multi-Hop Routing," In Proceedings of the ACM/IEEE Fourth International Conference on Information Processing in Sensor Networks (IPSN'05)", Los Angeles, CA, USA, April 2005.
- [3] R. Fonseca, O. Gnawali, K. Jamieson, and P. Levis, "Four-Bit Wireless Link Estimation," In proceedings of the Sixth Workshop on Hot Topics in Networks (HotNets-VI), Atlanta, GA, USA, November 2007.
- [4] A. Cerpa, J. Wong, L. Kuang, M. Potkonjak, and D. Estrin, "Statistical Model of Lossy Links in Wireless Sensor Networks," In Proceedings of the 6th ACM international Symposium on Mobile Ad Hoc Networking and Computing", Urbana-Champaign, IL, USA, May 2005.
- [5] Crossbow Technology, Inc., <http://www.xbow.com>
- [6] TinyOS Community Forum, <http://www.tinyos.net>
- [7] Crossbow Tech. Inc., Mica2 wireless measurement system datasheet, [http://www.xbow.com/products/Product\\_pdf\\_files/Wireless\\_pdf/MICA2\\_Datasheet.pdf](http://www.xbow.com/products/Product_pdf_files/Wireless_pdf/MICA2_Datasheet.pdf)
- [8] Cipcon CC1000 Single Chip Very Low Power RF Transceiver, <http://focus.ti.com/lit/ds/symlink/cc1000.pdf>
- [9] G. Anastasi, A. Falchi, A. Passarella, M. Conti, and E. Gregori, "Performance measurements of motes sensor networks," In Proceedings of the 7th ACM International Symposium Modeling, Analysis and Simulation of Wireless and Mobile Systems, 2004, p.p. 174-181.
- [10] K. Daabaj, M. Dixon, T. Koziniec, "Avoiding Routing Holes in Wireless Sensor Networks", in Proceedings of the World Congress of Engineering and Computer Science (WCECS'09), San Francisco, CA, USA, October 2009, pp. 356-361.
- [11] K. Schwieger and G. Fettweis, "Power and Energy Consumption for Multi-Hop Protocols: A Sensor Network Point of View," Vodafone Chair Mobile Communications Systems, Dresden University of Technology, Germany.
- [12] Crossbow Technologies Inc., MPR-MIB Users Manual, [http://www.xbow.com/support/support\\_pdf\\_files/mpr-mib\\_series\\_users\\_manual.pdf](http://www.xbow.com/support/support_pdf_files/mpr-mib_series_users_manual.pdf)
- [13] A. S. Tannenbaum, Computer Networks, Prentice Hall PTR, 4 edition, 2003.
- [14] L. Zhou; S. Zhou; Y. Yao, "Multipath Rayleigh Fading Channels in the Low SNR Regime," In Proceedings of the IEEE International Conference on Communications (ICC'06), Volume 3, June 2006, p.p. 1404 – 1409.



- [15] J. Hill, R. Szewczyk, A. Woo, S. H. D. Culler, and K. Pister, "System architecture directions for networked sensors," In Proceedings of the 9th International Conference on Architectural Support for Programming Languages and Operating Systems (ASPLOS'00), November 2000.
- [16] C. Intanagonwiwat, R. Govindan, and D. Estrin, "Directed diffusion: A scalable and robust communication paradigm for sensor networks," In Proceedings of the ACM/IEEE International Conference on Mobile Computing and Networking (MobiCom'00), Boston, MA, USA, August 2000, pp. 56–67.
- [17] A. Woo, T. Tong, and D. Culler, "Taming the Underlying Challenges of Reliable Multihop Routing in Sensor Networks", in the Proceedings of the 1st ACM International Conference on Embedded Networked Sensor Systems (SenSys'03), Los Angeles, CA, USA, November 2003.
- [18] Tinyos multihoplqi collection protocol, "MultiHopLQI",  
<http://www.tinyos.net/tinyos-1.x/tos/lib/MultiHopLQI/>.
- [19] O. Gnawali, R. Fonseca, K. Jamieson, D. Moss, and P. Levis, "Collection Tree Protocol," In Proceedings of the 7th ACM Conference on Embedded Networked Sensor Systems (SenSys'09), 2009.
- [20] Rahul C. Shah , Jan M. Rabaey, "Energy Aware Routing for Low Energy Ad Hoc Sensor Networks," In Proceedings of Wireless Communications and Networking Conference (WCNC), March 2002.
- [21] D. De Couto, D. Aguayo, J. Bicket, and R. Morris, "A High-Throughput Path Metric for Multi-Hop Wireless Routing," In the 9th Annual International Conference on Mobile Computing and Networking (MobiCom'03), San Diego, CA, USA, 2003.
- [22] K. Srinivasan, P. Dutta, A. Tavakoli, and P. Levis, "Understanding the Causes of Packet Delivery Success and Failure in Dense Wireless Sensor Networks," Stanford University Technical Report 2006.
- [23] K. Daabaj, M. Dixon, T. Koziniec, "LBR: Load Balancing Routing for Wireless Sensor Networks," IAENG Transactions on Engineering Technologies, Volume-4, American Institute of Physics (AIP), Melville, NY, July 2010.
- [24] K. Daabaj, M. Dixon, T. Koziniec, "Experimental Study of Load Balancing Routing for Improving Lifetime in Sensor Networks", In the Proceedings of the fifth International Conference of Wireless Communications, Networking and Mobile Computing (WiCOM'09), Beijing, China, September 24-26, 2009, p.3471-3474.
- [25] K. Daabaj, M. Dixon, T. Koziniec, "Reliable Load-Balancing Routing Algorithm For Wireless Sensor Networks," In Proceedings of the 19th International Conference on Computer Communications and Networks (ICCCN'10) Workshop on Wireless Mesh and Ad Hoc Networks (WiMAN'10), Zurich, Switzerland, August 2-5, 2010.
- [26] Q. Cao, T. He, L. Fang, T. Abdelzaher, J. Stankovic, S. Son, "Efficiency Centric Communication Model for Wireless Sensor Networks," In Proceedings of the IEEE International Conference on Computer Communications (IEEE INFOCOM'06), 2006.
- [27] K. Daabaj, M. Dixon, T. Koziniec, P. Cole, "Reliable Routing Scheme for Indoor Sensor Networks," In proc. of the 21st Annual IEEE International Symposium on Personal, Indoor and Mobile Radio Communications (PIMRC2010), Istanbul, Turkey, September 26–29, 2010.



المؤتمر العربي الليبي الدولي الخامس للهندسة الكهربائية والإلكترونية 23-26/10/2010 طرابلس ليبيا





## **E-health Service: Critical Issues and Emerging Concepts**

Mosbah Ageal, Asma Elmangosh, Majdi Ashibani, and Fathi Ben-Shatwan

Electronics Engineering Department

Collage of Industrial Technology

P.O Box 841, Misurata, Libya

{mosbah.ageal, a-elmangosh, mashibani, fshatwan}@cit.edu.ly

### **Abstract:**

Information technology (IT) plays an important role in making healthcare a more accessible, high quality, cost effective, sustainable and safe service for citizens. Patients subjected to critical health crises such as the brain strokes, heart attacks or any accident often lose their life because of delayed succor. In such cases the first few minutes after the accident are really crucial for the patient's life. Libya covers large geographical area, people living in rural areas do not have central hospitals in their area, and they can't get emergent specialist care when they need it. The medical sector is the most important area in which recent technological development in communication networking has been applied. By the use of variant applications such as medical databases, electronic health records, and routing text/audio/video/photo medical information, E-Health services may be supported in underserved locations, such as rural health center, ambulances, ships, airplanes as well as home environments. E-health service includes many types of services such as remote diagnosis, remote monitoring, monitoring the patient in the ambulance, and remote assistance.

Due to its real-time nature, e-health systems must provide Quality of Service (QoS) support, in order to provide a pervasive, valuable and fully reliable assistance to patients with risk abnormalities. Next Generation Networks (NGN) provides different wire and wireless technologies such as WiMAX, WiFi, GSM, GPRS, and Fixed/Mobile CDMA Broadband wireless. In this paper we define the networking requirements to support E-health services provisioning using the available communication networks in Libya, and the required NGN infrastructure for E-health to be implemented in the country. This paper focuses on studying the possibility of exploiting the current available access network technologies in Libya as a case study to implement e-health services, explaining the technical inhibitors in the current infrastructure and how to overcome these inhibitors to provide a fully reliable E-health service by proper manners.

### **I. INTRODUCTION**

The medical sector is the most important area in which recent technological development in communication networking

has been applied. With the worldwide deployment of mobile and wireless networks, the wireless infrastructure can support many current and emerging



healthcare applications. E-health services are becoming an increasingly important part of modern medicine.

In an effort to reduce healthcare costs more emphasis is being placed on providing community care for both chronic and acute illnesses. In the last few years, developments in telemedicine have greatly expanded the depth and range of homecare services that can be provided. These include management of chronic illnesses such as diabetes, heart failure and renal failure, acute illnesses such as pneumonia, and also convalescence and recovery after operations and acute illnesses.

Any E-health system consists of three phases [1], as illustrated in Fig. 1:

1. collection information phase, includes the body devices and sensors which used to extracting the patient's information like temperature and blood pressure.
2. data transfer phase, where the collected information is carried by the network to hospital. Health care advices might be returned to patients by the network as well.
3. monitoring phase, occurs at hospitals and medical centers, by analysis the extracted information and response by replaying warning or notice signal.

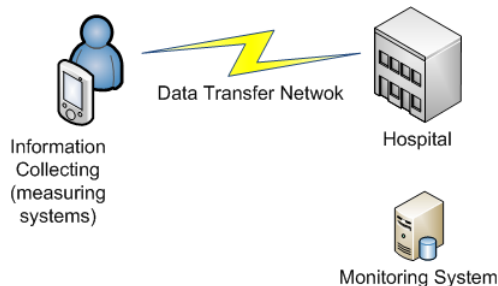


Figure 1. E-health system.

In this paper we will focus on the data transfer phase, and its readiness in Libya to support E-health systems.

In E-health, a key requirement for telecommunication to be successfully applied to homecare is an adequate telecommunications infrastructure. With the rapid development of NGN, the wire and wireless network infrastructure can support many healthcare applications. This could fulfill the vision of wide range healthcare applications to anywhere, anytime, and any-device, removing the location and time constraints.

The remainder of this paper is organized as follows. Section II reviews related work in providing health care using electronic manner. Section III analyses the issues of the current E-health services in depth. Section IV presents the related network technologies. Section V demonstrates the current telecommunication infrastructure in Libya and possibility the implementation, and finally section VI concludes this paper.

## II. RELATED WORK

Despite the numerous researches and proposals of telemedicine, the E-health platforms were introduced only in the last few years. The WEIRD Project was started in June 2006, based on WiMAX "Worldwide Interoperability for Microwave Access" technology [3]. The project aims to develop an infrastructure filling the gap between broadband network and applications, one of the main outcomes of his project is a mobile E-health system allowing the enforcement of Quality of Service (QoS) resource reservation policies onto underlying broadband networks. In fact WEIRD infrastructure is able to map application QoS requirements making the most of the features available in each broadband access technology, especially wireless.

TEBID project [4] aims to introduce a mobile part of wider system of biodata monitoring. Mobility and a smart design of the health monitoring equipments contribute to patient/client lifetime advanced quality of life, early disease detection, and then enhanced healthcare level.

WIH European project[5] aiming to support the day-by-day activities of doctors and nurses within an hospital ward by providing a tool for workgroup collaboration and wireless access to the patient's clinical records. WIH is currently being used within three hospital wards, in Italy, Spain and Germany, where the medical personnel is connected by an IEEE 802.11 wireless LAN.

The first successful implementation in industry of a mobile E-health service was in the United States of America (USA). The service was announced on 13 October, 2008 by InfoLogic. This mobile health service was limited to selected hospitals in the USA [2].

### III. CRITICAL ISSUES FOR PROVIDING E-HEALTH SERVICES

Providing E-health service impose strict requirements on the network technologies due to the critical nature of the medical applications. This raises many challenges related to the implemented network technologies, the main challenging issues includes:

- **QoS Support**

QoS provisioning is inherent to the patient's information when processed in the network, the importance of the collected information is necessarily distinct, and so the network must prioritize the transmission of critical data when occurs a sudden clinical change in the patient. For example, in patients with cardiac diseases, heart activity information is more important than body temperature data. Also, depending on the patient's clinical condition, the priority assigned to a vital signal can change dynamically. For instance, glucose data might be assigned a low priority when readings are in the normal range, but a higher priority might be reassigned to it when readings indicate hypo or hyper glycemia. Most current network architecture only offers best-effort service and not support for QoS, which is limitative for emergency support. In the E-health network, the QoS provision is required to assist critical cases conveniently. This will enable, for instance, guaranteed bandwidth to higher priority streams for an efficient data delivery.

In order to counter this behavior a few NGN technologies were designed to complement the IP (Internet Protocol) infrastructure to it capable of handling traffic with different QoS needs. These technologies are including the Differentiated Services (DiffServ), Integrated Service (IntServ) and Multi Protocol Label Switching (MPLS). DiffServ was designed to be scalable

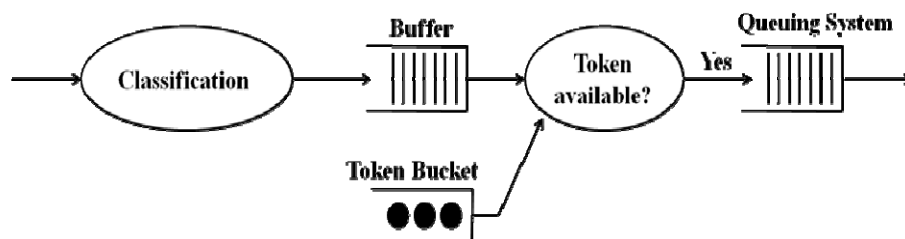


Figure 2. DiffServ Router Packet classification.



Table 1. Classification of E-Health Qos Requirements [7]

Application Type	Required Throughput	Small Delay	Small Jitter
Teleconsultation	High	Yes	Yes
Telediagnostic	High	Yes	No
Telemonitoring	Low	No	No
Teleeducation	High	No	No
Access to DB	Low/ High	No	No

service differentiation architecture for the Internet. It achieves scalability by classifying and possibly conditioning traffic streams on the edge of the network, according to their requirements as shown in Fig(2) [6].

QoS mechanisms are usually deployed in networks to guarantee consistent service levels concerning certain parameters, such as packet loss ratio, data transmission delay, jitter, and guaranteed bandwidth. These are traditional QoS parameters used to characterize the performance of communication infrastructure, Table (1) describes the requirements of some E-health services in term of QoS parameters and shows the distinctness between them. So, as described above, the network must priorities the data and then assigning the high priority (high QoS level) to the critical data.

- **Context awareness**

The term context refers to any information that can be used to characterize the situation of an entity. An entity is a person, place, event, or object that is considered relevant to the integration between a user and an application, including the user and the application themselves e.g., context can be

information related to patient status, speed, or location.

Context-aware medical networks can overcome many issues, through performing appropriate content adaptation. So, when a patient's clinical state turn from a non-critical situation into a critical one, a context change occurs and consequently the healthcare network should adapt its performance requirements to the new situation. For instance, higher monitoring activity and lower delay transmission of the vital signals might be required when the patient's clinical situation changes from non-critical to critical. Hence, healthcare networks should provide QoS facilities for e-emergency services, since these clearly demand for high reliability, guaranteed bandwidth, and short delays [8].

The location of doctor or hospital is important factor to save the patient's live. So, it better, if the telemedicine system enables discovering and tele-consultation with a doctor located within shortest distances. This helps incase the patient is advised to travel to the nearest hospital.

Implementing a context-aware E-health system requires key issues to be addressed. For example, key issues are the way the context is represented internally, how context information is combined with E-



health system and application state, where context is stored and what are the relevant data structures and algorithms. Other aspects to consider are, *e.g.*, how frequently context information have to be consulted, what is the overhead of taking context into account and how this overhead can be reduced. The method to extract context information from an environment and the fallback solutions in case an environment does not provide such information and the option to use historical context information are also of interest. Finally, how to perform the fusion of different context information and how to better exploit context information for adapting wireless transmission are important future research areas [4].

- **Mobility Support:**

To ensure that quality care delivered efficiently any time and any place requires ready access to patient records and expertise from remote sources such as specialists and online databases, and mobile wireless technology can enable this support. So, the patients can carry devices that assist them to stay in constant communication with their organizations, friends, family, and advisors [9].

An ambulance, which is moving through different e-health domains (areas that include static or mobile type of nodes), supporting different E-health applications the connectivity between the monitoring applications with the medical data source may be assured by the different wireless technologies [10].

Some limitations and challenges related to mobility are still under research. In general, using wireless technologies to provide wide

coverage for an entire rural region can still be economically difficult due to the high cost of setup and maintenance of infrastructure. Another important issue, when the mobile user rooming between base stations in case of rooming within same technologies or between heterogeneous technologies, this is raises many issues related to QoS management like: inter domain QoS management, QoS level matching, and handover issues as described below.

- **Handover in Heterogeneous Access Network technologies**

The purpose of handover was introduced in order to achieve the uninterrupted communication of a communication session. The handover process is one of the most complex functions to support the mobility. Since it ensure the continuity of connection through heterogeneous access network technology [10].

In some cases, the mobile node would prefer to perform the handover in heterogeneous networks. For example, if the user is currently in an ongoing video session handled by a mobile phone and in the same session its device detects the presence of a WiMAX network is available, considering just cost and bandwidth reasons, the obvious selection is to handover to the WiMAX detected, this is called anticipated handover. On the other hand, unanticipated handover does not include the preferences of the access network technologies. The handover can be sorted to two types, vertical and horizontal handover, a handover performed when a user moves from one base station to another using the same access network technology is called horizontal. While, a horizontal handover performed when a user moves



from one access network technology to the different one. Performing the handover raises many challenges and still open area for research. For example, loses connectivity due to the change of base station due to connection is lost for a short period, and the affect of connection losses on the QoS provisioning.

#### IV. RELATED TECHNOLOGIES

##### • Access Network Technologies:

The main strict requirement of the E-health service is a broadband connectivity, through the NGN there is rapidly evolving around the globe with both fixed line (e.g. Asynchronous Digital Subscriber Line - ADSL) and wireless (e.g. Wi-Fi, WiMax, and HSxPA) connections [11]. In fact, the suitable wireless technology for the E-health service is WiMAX, since its new version IEEE 802.16e standard supports many features like QoS, mobility, and inexpensive. Some issues and challenges related to WiMAX are still open for research. In general, using WiMAX base stations to provide wide coverage for an entire region can still be economically infeasible due to the high cost of setup and maintenance of the base stations. However, the previews access network technologies are usually only available in urban and suburban areas. Telemedisition for patients living in isolated areas is a highly desirable goal, and could potentially be provided through the use of satellite communications. This is an attractive networking solution for the provision of medical information and services since satellites offer worldwide coverage and a variety of data transfer rates.

##### • IP Multimedia Subsystem (IMS)

The IP Multimedia Subsystem (IMS) standardized by the Third Generation Project Partnership (3GPP) to offer multimedia services over an Internet Protocol (IP) based infrastructure [12]. It's a prime candidate as a service delivery platform for NGN, the IMS defines a control layer on top of IP-based fixed and mobile networks that enables seamless provisioning of multimedia services riding over the control layer [13].

IMS aims to make Internet technologies, such as presence service, Short Message Service (SMS), Multimedia Messaging Service (MMS), IP-based services such as IPTV, instant messaging, push to talk, Web browsing, VoIP and video conferencing available to everyone from any location over any access network technology supporting the integration of different services. so in the future people will use every single device and every network to connect using a different services as shown in Fig. 3, the important advantage of the IMS is supporting fixed mobile convergence (FMC) and legacy networks, another important advantage of the IMS is supporting the rooming (handover) between the access networks, so the patient can rooming seamlessly between the fixed and the mobile or between any two networks in the same session without interrupting the session. Regarding QoS, The IMS takes care of synchronizing session establishment with QoS provision so that users have a predictable experience. So, in the future, IMS will be playing an important role to provide E-health services over any technology.





## V. CASE STUDY: E-HEALTH IN LIBYA

The public health sector is the main health services provider in Libya. Health care including preventive, curative and rehabilitation services are provided to all citizens free of charge by the public sector. Almost all levels of health services are decentralized. The health care delivery system operates on three levels [14]:

1. The first level consists of the Primary health care units (which provide curative and preventive services for 5,000 to 10,000 citizens); Primary health care centers (serve from 10,000 to 26,000 citizens); and polyclinics, staffed by specialized physicians

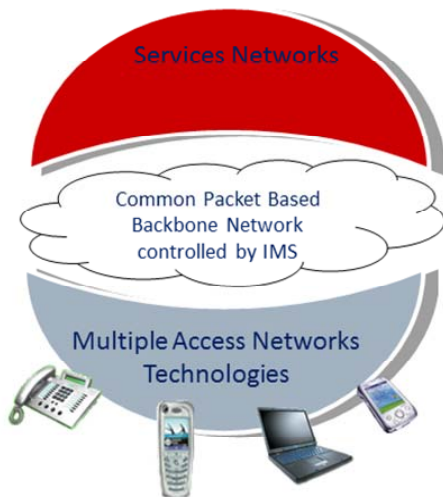


Figure. 3. Access independent and services integration.

and containing laboratories as well as radiological services and a pharmacy. These polyclinics serve

approximately 50,000 to 60,000 citizens.

2. At the second level, there are General hospitals in rural and urban areas where care is provided to those referred from the first level.
3. The third level comprises of tertiary care specialized hospitals. "located in Tripoli (the capital) and Benghazi (the second largest city in Libya)."

A growing private health sector is emerging although currently it has a limited role. The government has decided to encourage the expansion of private clinics and hospitals. As well, serious attempts are being made to introduce the family physician practice along with the necessary rules and regulations. Health insurance is also being considered. All charges for the private sector are out-of-pocket due to the absence of health insurance. The small but growing private health sector continues to be hampered by the lack of an overall policy approach to the sector from the health authorities [14].

With these facts about Libyan demography and health care system in mind, it is clear that the main obstructions to provide high quality health care to all citizens come from the high population distribution over wide land area. Patients from rural and small cities need to travel long distance to obtain sophisticated health care at specialized hospitals.

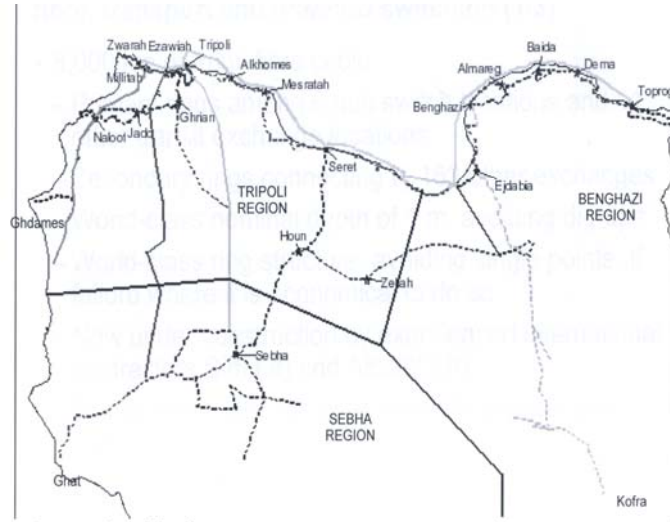


Figure. 4. The Libyan NGN project.

In 2008, Libya's national incumbent Libyan Post Telecommunications and Information Technology Company (LPTIC) announced its plans to put in place a fibre Next Generation Backbone Network (NGBN) and that pilot projects will extend IP delivery at a local level. Its implementation of the NGBN is split into two phases and between the eastern and western part of the country at a total cost of EUR 160 million. The first phase of the project is to roll out 8,000 kms of fibre to link all of the cities of Libya. Most of the cable has to be laid across rocky ground. The second phase involves putting in the transmission equipment. This work is carried out at two levels: the first level concerns the transmission equipment for the backbone infrastructure and the second level concerns the routers to link the small and medium-sized towns.

Libya Telecom & Technology (LTT), Libyan Internet service provider, launched its first commercial WiMax wireless network, with WiMax coverage, including mobile WiMax, in 18 cities. The operator's new system, which has initial capacity for 300 000 subscribers, began signing up business and residential customers in the beginning of 2009. The project is worth almost USD 60 million. In May 2009, the company awarded a contract to an equipment vendor to provide it with a FTTH network. Under the deal, a provider will roll out an FTTH network, covering 800 apartment buildings on the Airport Road in Alzohor District, Tripoli, in the first phase, and expanding the network coverage to other districts in the second phase. Fig. 4 presents the NGN project in Libya. The deployment will enable LTT to offer more stable and more advanced broadband services for end users. The





network will be the first commercial FTTH project in Libya.

Presently Kingston University- UK is proposing the Medi-Health project with the cooperation with other associations. The College of Industrial Technology (CIT) is a partner in this project as a researcher. The mHealth initiative aims to drive the transformation potential of mobile technology by bringing together the diverse range of healthcare, education and industry across all stakeholders chain. This project aims to bridge this gap by a combination of mobile and healthcare offering tremendous benefits with viable mobile health care service permitting healthcare professionals to remotely assess, diagnose and treat patients whilst the patients are free to continue with daily life activities. The project concept allows patients and nonpatients to monitor their physical condition and obtain advice and information at anywhere and anytime. Thus, the mHealth services enable convenience and improved quality of life for patients.

The Medi-Health system project could impact the health care system in Libya by providing patients with easy accessibility of health care providers, improvements in the patient-doctor relationship, reduce of expanses, and efficiency of time and effort. Health care providers are expected to advance from the Medi-Health system, as they can improve the efficiency of their time and effort, since most of the time spent with the patients in the clinic could be saved using a way of telecommunication.

Also specialist doctors will be able to deliver health medical advice and diagnosis to patients in other far town.

## VI. CONCLUSIONS

In this paper we addressed the design issues and technologies to implement E-health services over NGN. We have seen the important of implementing E-health service in Libya. The NGN project and other access network currently working in Libya are highly promising, however more work is needed to provide added-value services to network's users, taking advantage of the Libyan NGN infrastructure.

## REFERENCES

- [1] P. Gioannis, "WiMAX against unexpected Health problems: Automatic prevention and Assistance," TELE-INFO '08, Turkey, May 27-30, 2008.
- [2] J. Oladosu, et.al, "Framework for a Context-Aware Mobile E-health Service Discovery Infrastructure for Rural/Suburban Healthcare," [www.jatit.org](http://www.jatit.org), 2009.
- [3] G. Martufi, et.al, "Extending WiMAX to New Scenarios: Key Results on System Architecture and Testbeds of the WEIRD project," EUMOB 2008, Finland, July 7-9, 2008.
- [4] M. Martini, "Wireless Broadband Multimedia Health Services: Current Status and Emerging Concepts," 2008.
- [5] R. Hudec, M. Vestenický, "The m-health terminal for collecting and



- transmission of biodata,” Slovak, 2010.
- [6] S. Mignanti, et.al, “WEIRD – Real Use Cases and Applications for the WiMAX Technology,” Consumer Communications and Networking Conference, IEEE CCNC 2008.
- [7] D.J. Vergados, et.al, “Applying Wireless DiffServ for QoS Provisioning in Mobile Emergency Telemedicine. IEEE Communications Society subject matter experts for publication in the IEEE GLOBECOM 2006 proceedings, 2006.
- [8] O. Gama, “Quality of Service in Wireless e-Emergency: Main Issues and a Case-study,” Portugal, 2010.
- [9] N. Archer, “Mobile eHealth: Making the Case,” Canada, 2010.
- [10] A. Zvikhachevskaya, et.al, “Quality of Service consideration for the wireless telemedicine and e-health services,” WCNC, Malaysia, 2009.
- [11] V. Pasiak, et.al, “E-health Performance Assessment of an Interactive Satellite Network Infrastructure,” The Journal on Information Technology in Healthcare 2006, Greece.
- [12] 3GPP TS 23.228, “IP Multimedia Subsystem (stage 2),” 2006.
- [13] Open Source IP Multimedia Subsystem Core, [www.openimscore.org](http://www.openimscore.org).
- [14] World Health Organization (WHO), “Health Systems Profile- Libya “, 2007.



## **Complex Event processing – TIBCO simplifying Business**

Azmath Ali Shaik

Faculty of Engineering - Beniwalid  
7th October University, Misurata, Libya  
e-mail: azmathsk@yahoo.com

### **Abstract**

Nowadays enterprises are more complex than ever. Different processes take place all over the world and events are flying through the enterprise IT systems. These systems have grown from standalone applications that were able to handle a certain aspect within an enterprise to an enterprise wide IT system that provides a coupling between the different IT applications.






These enterprise wide IT systems are widespread across large enterprises and generate many events that flow through the enterprise system layers. The events feed other applications or services which generate new events on their turn. We can truly speak about an event-cloud that hangs within an enterprise. Because of this event-cloud the event-flow of an enterprise IT system becomes non transparent and difficult to understand.

A new innovation is arising that can help tackle this problem: Complex Event Processing. With CEP it is possible to correlate events and detect complex situations. This white paper deals with a number of CEP related questions. The first part describes surrounding concepts that help understanding what CEP really is about. The second part introduces a general CEP language with other technologies. The third part introduces commonly used CEP design patterns and the fourth part talks about TIBCO CEP.



## 1 Introduction

### Glossary

Name	Description
BAM	Business Activity Monitoring
BI	Business intelligence
BPM	Business Process Management
BPMG	Business Process Management Group
CEP	Complex Event Processing
CRM	Customer Relationship Management
DSL	Domain Specific Language
EDA	Event-Driven Architecture
ERP	Enterprise Resource Planning
ESB	Enterprise Service Bus
ESP	Event Stream Processing
EQL	Event Query Language
PUB/SUB	Publish / Subscribe
XML	Extensible Mark-up Language
SOA	Service-Oriented Architecture
	Complex Event Processing Engine
	In-Memory Cache with Windows
	Incoming, Outgoing, or Intermediate Event Streams
	A Continuous query, registered with the process
	A relational database
FSM	simple finite state machine
RTC	Rete Network Construction
BW	BusinessWorks
RETE	Based Rules Engine
RMS	Rules Management Server
DM	Decision Manager



## 1.1 Overview

Concept of EP evolved in 90s (1989 – 95) and coined by Prof David Luckham (<http://complexevents.com>)

“Complex event processing is a technology for extracting information from message-based systems.”

A complex event processing (CEP) system enables organizations to process distributed business events and identify opportunities or threats. Business events may be tracked individually, such as a stream of stock trades, or correlated with other events, producing derived or “complex” events often called “situations.”

Complex Event Processing (CEP) is a technology for low-latency filtering, correlating, aggregating, and computing on real- world event data an emerging network technology that creates actionable, situational knowledge from distributed message-based systems, databases and applications in real time or near real time

Complex event processing software allows you to process and analyze multiple streams of high-volume, high-speed business and system events, and to uncover opportunities and threats as they happen -- not after the fact

Can be applied to extracting and analyzing information from any kind of distributed message-based system. It facilitates to develop from the Rapid concepts of Causal event modelling, Event patterns and pattern matching, and Event pattern maps and constraints. Solve wide variety of

Enterprise monitoring and Management problems, from low level network management To high level enterprise intelligence gathering

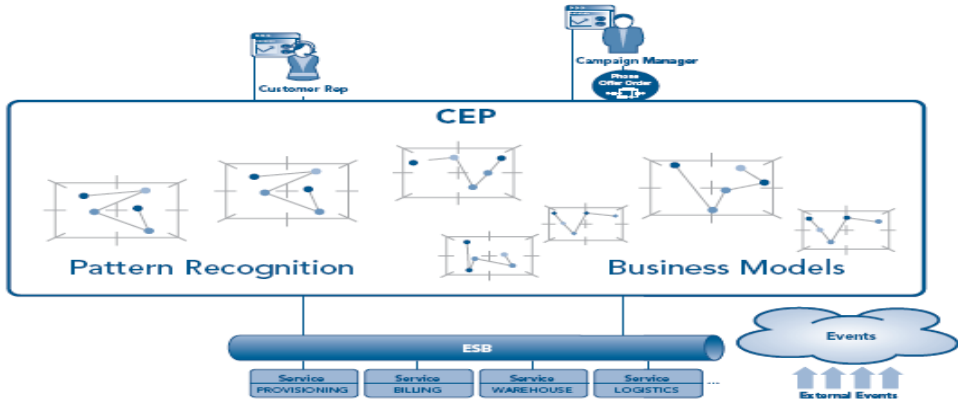


**Figure 1: Complex Event Processing in Distributed Systems**

## 2 Context

### 2.1 Purposes

CEP can be used to serve many purposes. In this paragraph the most relevant purposes of CEP are introduced and briefly explained:

- Event-Driven Architectures
- Enterprise Application Integration
- Business Process Management, and
- Business Activity Monitoring

#### 2.1.1 CEP and Event-Driven Architectures

Event-Driven Architecture (EDA) is a software infrastructure that by nature is very loosely coupled. The main idea behind EDA is that a large software system consists of many small components that all have their own function. The communication

between the components is done by using events. An event can be seen as a notification, which tells other components that a certain 'job' is done. Because events are very important within an Event-Driven Architecture also the handling and routing of events is very important.

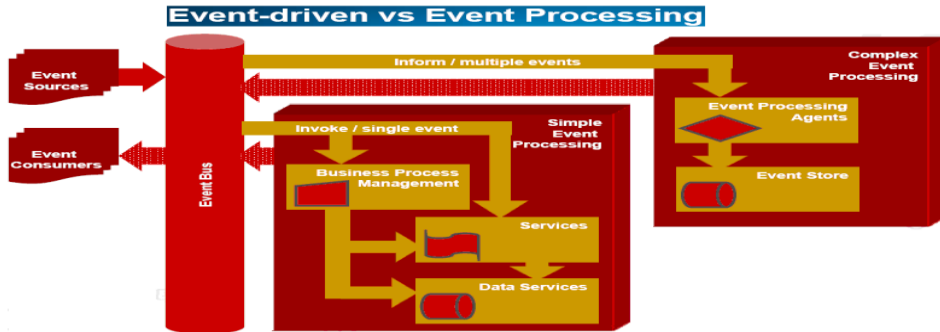


**Figure 2: Event-Driven vs Event Processing**

CEP correlates multiple messages within given time frames. EDA is an architectural approach to model information systems from a business event perspective. EDA differs from SOA by its focus

CEP is a technique to process message streams. These messages do not need to represent business events. A business event is something that happens (change of state) where your business has planned to react upon in a predefined way. A business event is represented by a message, but not all messages are representations of business events. CEP is about messages, EDA is about business events

EDA is CEP at the business level. The business can be seen as a complex event processor which holds states, reacts on state changes and correlates business events



**Figure 3: CEP, EDA and SOA**

CEP can be used to implement EDA. CEP is a very powerful addition to EDA, as it can detect complex situations in real-time.

SOA puts services at the centre of the model and EDA does so with business events. The SOA-approach tends to result in a synchronous communication style and the EDA-approach in an asynchronous communication style.

#### 2.1.2 CEP and Enterprise Service Bus

To integrate old and new, service-oriented architecture (SOA) needs an infrastructure that can connect any IT resource, whatever its technology or wherever it is deployed. To be flexible, it needs an infrastructure that can easily combine and re-assemble services to meet changing requirements without disruption. And to be dependable, it needs an infrastructure that is robust and secure.

This infrastructure is the enterprise service bus (ESB).

An ESB is software infrastructure that simplifies the integration and flexible reuse of business components within a service-oriented architecture. An ESB provides a dependable and scalable infrastructure that

connects disparate applications and IT resources, mediates their incompatibilities, orchestrates their interactions, and makes them broadly available as services for additional uses.



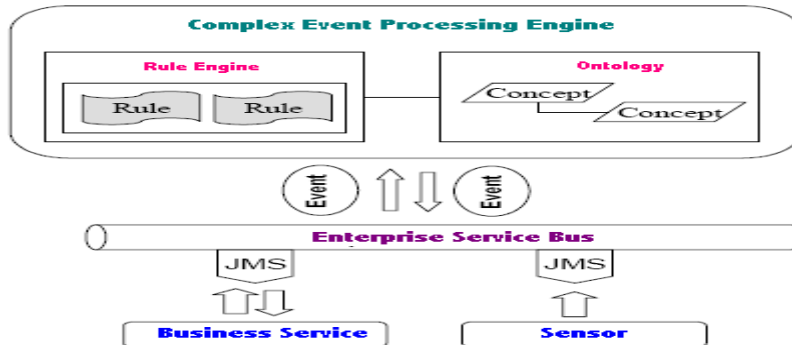


Figure 4: CEP with ESB

ESB provides the communication backbone to federate event-driven services in a loosely coupled fashion as shown in above figure. The CEP engine continuously evaluates changes in the state against patterns of interest that impact the business.

## 2.2 Event receiving

Events are the main ingredient for a CEP engine. It is of great importance that all events of interest are received by the CEP engine; otherwise defined situations will never be detected. The CEP engine can be connected to the enterprise IT system in different ways, depending on the type of connection used within the enterprise IT system.

## 3 Commonly Used Design Patterns

A design pattern in architecture and computer science is a formal way of documenting a solution to a design problem in a particular field of expertise.

Some fundamental CEP design patterns that appear repeatedly in CEP applications, listed below in order of complexity, from the simplest to the most sophisticated.

These basic patterns may be thought of as building blocks that can be combined to create complete application

### 3.1.1 Filtering

#### 3.1.1.1 Context

Filtering Events Based on Event Attributes

#### 3.1.1.2 Problem

Filtering is ubiquitous in CEP applications. Here are some examples:

- Trading: a filter may be used to filter out all trades where the volume is too small, or all trades that do not refer to particular stock symbols.
- Click-stream analysis: a filter may be used to capture the trades that originate from a certain set of IP addresses.
- Sensor network: a filter may be used to capture sensor readings where values fall outside of the normal range.



### 3.1.1.3 Solution

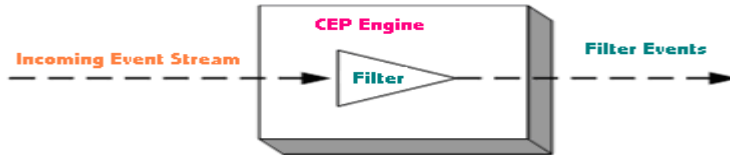


**Figure 5: Filtering**

The above diagram depicts a simple filter query. The query subscribes to one stream, evaluates a specified logical condition based on event attributes, and, if the condition is true, publishes the event to the destination stream. For example, an application monitoring a stream of purchase orders may filter out all orders where the condition is  $\text{Priority} \neq \text{'High'}$  and  $\text{Amount} < 100000$ .

This example presents the simplest kind of filter, where events are evaluated one by one, and where the query condition only involves the attributes of one event. It is also possible to construct many other more complex filters, for example, filters that compare events to other events in the same stream, or in another stream, or compare events to a computed metric.

For instance, a filter might capture orders where the purchase amount is larger than the previous purchase amount, or purchase amounts that are larger than the average for the previous day. Such relatively more complex queries are discussed later in this document.

### 3.1.2 In-memory caching

#### 3.1.2.1 Context

Caching and Accessing Streaming and Database Data in Memory

#### 3.1.2.2 Problem

In-memory caching is used in every non-trivial CEP application. Here are a few examples:

- **Trading:** in a trading application, the cache may hold the values of recent trades, recent orders, or recent news events, coupled with the relevant historical and reference information.
- **Click-stream analysis:** a typical application may hold the recent clicks and searches performed by the users, coupled with the relevant historical and reference information.
- **Network security:** A typical application may hold recent events from firewalls, intrusion detection systems, and other devices, coupled with the relevant historical and reference information.



### 3.1.2.3 Solution

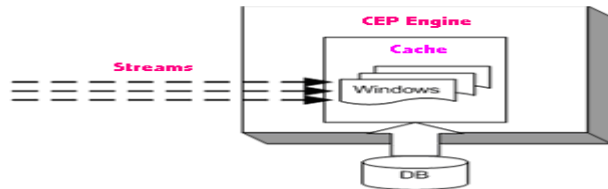


**Figure 6: In-memory caching**

In-memory data caching is the foundation of most CEP design patterns. The cache typically stores two kinds of data:

- Recent events from one or more streams
  - Recent events are typically stored in windows. A window is an object, similar to an in-memory database table. However, a window can manage its state automatically, by keeping and evicting certain events according to its policy. For example a window policy might specify: KEEP 1000 ROWS PER Id. This window maintains 1000 rows for each ID value, and expires old rows, as necessary.
- Data from one or more database tables
  - Just as streaming events can be cached in memory; it often makes sense to cache data from a relational database, so that different kinds of operations may be performed on this data more efficiently. This cache is typically managed according to the Least Recently Used (LRU) algorithm, or by explicit invalidation.

**Note:** that, although we are describing an in-memory cache here, many applications require this cache to be persistent. This means that, if a machine that hosts the CEP engine fails, the data kept in windows is not lost. This functionality is even more important when the window holds not just the last few seconds', but minutes', hours', days', and even weeks' worth of events.

### 3.1.3 Aggregation over windows

#### 3.1.3.1 Context

Computing Statistical Metrics over Various Kinds of Moving Windows

#### 3.1.3.2 Problem

Windows-based computations are used in a wide variety of applications. For example:

- Trading: it is often necessary to compute "one minute bars" the average, maximum, minimum, and/or closing price within each one-minute interval.
- Click-stream analysis: it is often useful to compute the number of visitors who click on a particular link within a specified time interval.



- System management: applications may compute maximum and minimum CPU usage, memory, and Disk I/O utilization for each machine, within a specified time interval.

### 3.1.3.3 Solution

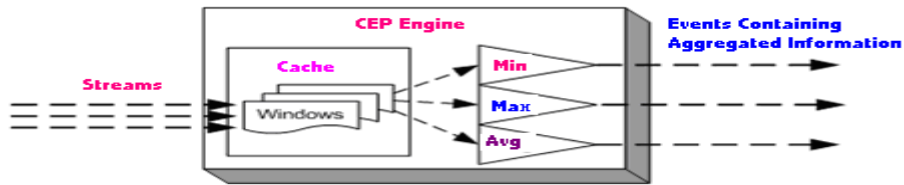


Figure 7: Aggregation over windows

This pattern does not merely keep events in memory, but uses the stored values to compute various statistics. A typical example here would involve computing a running average over a sliding window. (As we have seen in the previous example, a window is an object that holds a set of events in memory):

This design pattern comes in quite a few flavours, differing along the following dimensions:

- The kinds of aggregators computed, these include running averages, sums, counts, minimum, maximum, standard deviation, user-defined aggregators, and so on.
- The kinds of windows used These include time-based and count-based windows, sliding and jumping (tumbling) windows, windows that keep the specified number of largest or smallest elements, and so on.

- Output frequency: continuous vs. periodic In the case of continuous output (also called "tick-by-tick" output) each incoming event updates the calculated expression, and an output event is produced. With periodic output, the calculated expression is updated continuously, but is published only periodically, for example, every ten seconds. Note that, in both cases, the expression is computed incrementally, that is, the entire window is not rescanned on each incoming event.

### 3.1.4 Database lookups

#### 3.1.4.1 Context

Accessing Databases to Retrieve Historical or Reference Context for Incoming Events

#### 3.1.4.2 Problem

This design pattern is widely applicable. For example:



- Trading: a trading application may look up historical price for a stock, or certain information about an order, or certain rules and regulations stored in a database.
- RFID application: an application may look up information about a palette or case, identified by its tag ID, or information about the reader that reported the tag. An application may also check where the object should be located, according to the plan stored in the database, and compare this location to the actual location of the object.
- Network security: when deciding how serious an alert is, it may be necessary to refer to other alerts related to the same IP address.

### 3.1.4.3 Solution

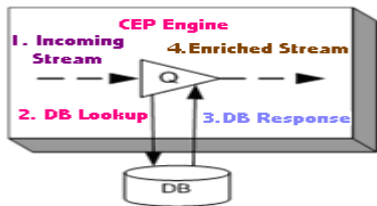


**Figure 8: Database lookups**

While there are applications that deal exclusively with real-time events, most useful applications refer to historical data or reference data to enrich the incoming events.

The following diagram shows how:

- An event comes into the system.
- The engine issues an SQL request to the database and passes a key (from

the event) as a parameter to the database query.

- The database returns a result.
- The engine combines the result with data from the event, and forwards the enriched event to the next query for further processing.

### 3.1.5 Database Writes

#### 3.1.5.1 Context

Sending Raw or Derived Events to a Relational Database

#### 3.1.5.2 Problem

This design pattern cuts across a wide range of applications, such as:

- Trading: writing 1 minute bars (maximums, minimums and the closing price for each one-minute interval) into the database.
- Click-stream analysis: storing the raw click-stream history, together with derived data, in the database.
- Network security: storing new relevant security events in the database.



### 3.1.5.3 Solution

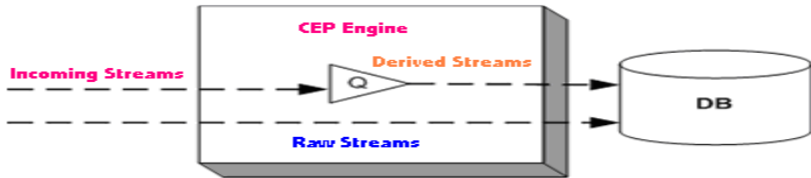


**Figure 9: Database Writes**

A relational database can manage very large volumes of data for very long periods of time, and it also supports a number of interfaces that other applications can use to retrieve the data. This design pattern illustrates the complementary nature of databases and CEP engines.

**Note:-** that, if the database must store large volumes of events, this design pattern may call for a number of advanced techniques, such as batching, asynchronous writing (to avoid blocking), queuing (to handle spikes), concurrent writes, writing via native database interfaces, and so on.

### 3.1.6 Event pattern matching

#### 3.1.6.1 Context

Complex Time-Based Patterns of Events across Multiple Streams

#### 3.1.6.2 Problem

Event patterns occur naturally in situations where complex behaviour is tracked, such as:

- Fraud detection: fraud patterns are often described as a sequence of events, in one or more streams. For example, in financial services,

many fraud patterns involving traders and brokers include events, such as the broker taking an order from the customer and emailing the trader, the trader issuing a certain trade and, perhaps, calling another trader, the other trader waiting for certain market events then issuing another transaction, and so on.

- Business process monitoring: many instances of business process failures may be described as patterns. For example, an application may initiate a certain sequence of steps, some of which complete normally, while others encounter problems because of another application.
- Network security: network attacks are often sophisticated, and involve a number of events. For example, an attacker may send a certain sequence of packets to certain ports, then try to authenticate across a number of servers and applications, send another sequence of packets, and so on.



Tracking and preventing such attacks, especially distributed denial of service attacks; involve the monitoring of a large number of patterns.

### 3.1.6.3 Solution

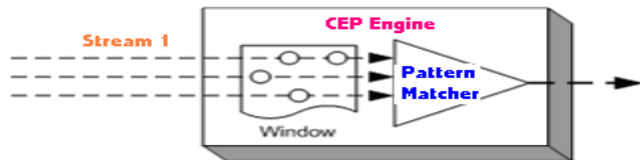


Figure 10: Event pattern matching

The continuous joins, discussed in the Correlation pattern, are quite powerful, but some tasks make the use of multiple joins very cumbersome. Suppose we want to be notified if, within a 10 minute interval, event A occurs, followed by event B, followed by either event C or D, followed by the absence of event E, with all events relating to each other in some way. While such an event pattern can be tracked with a combination of inner and outer joins, it is often desirable to have a more direct way of expressing such time-based relationships. The diagram below depicts a similar pattern with four events in three streams

Most interesting event patterns involve a number of relationships among events:

- A followed by B Event B occurs after event A.
- A and B both events A and B occur, in either order.
- A or B Either A or B (or both) occur.
- Not A Event A does not occur.

Some of the most interesting patterns involve "negative" events, in which the pattern-matching criteria are met when a specified event does not occur within the specified time interval. For example, when tracking a process based on requests and responses, it may be important to know when a response does not occur within a specified time period from the request, or when a response occurs without first being preceded by a request.

### 3.1.7 Hierarchical Events

#### 3.1.7.1 Context

Processing, Analyzing, and Composing Hierarchical (XML) Events

#### 3.1.7.2 Problem

Hierarchical events are applicable wherever complex behavior and processes are tracked. For example:

- Order processing:



- RFID applications: an RFID-tagged pallet may contain a number of RFID-tagged cases, each of which may contain a number of RFID-tagged items. Hierarchical events are typically necessary to model such containment directly.
- News feed and RSS monitoring: hierarchical events often arise in these applications.

### 3.1.7.3 Solution

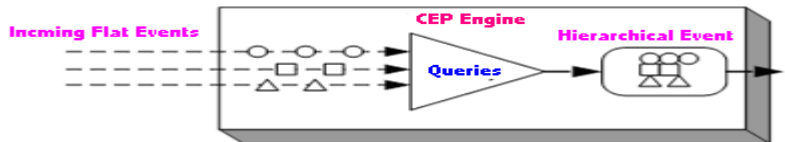


Figure 11: Hierarchical Events

Most simple CEP applications analyze flat events. A flat event is similar to a row in a database table: it has a fixed number of fields, corresponding to the columns of the table. Flat events provide sufficient functionality for many applications, but other applications deal with events that are more complex. For example, a Purchase Order event may contain a list of the ordered items. Such hierarchical events appear more often in CEP applications, especially with the rise of XML and SOA.

This diagram depicts the design pattern where a complex event is created out of a number of simple events:

The following operations may be performed on hierarchical events:

- Decomposing hierarchical events
  - A complex, hierarchical event may need to be decomposed into simpler

events. For example, it may be necessary to know the items that make up a purchase order.

- Correlation across hierarchical events
  - It may be necessary to know, for example, if two or more purchase orders contain the same item.
- Composing a hierarchical event
  - For example, it may be necessary to compose a purchase order from a list of items.

### 3.1.8 Dynamic Queries

#### 3.1.8.1 Context

Submitting Parameterized Queries, Requests, and Subscriptions Dynamically.

#### 3.1.8.2 Problem

Dynamic queries come up in many applications, especially those that





involve large numbers of business users.  
Here are some examples

- Trading environments: every trader can enter their subscriptions, as described above.
- Enterprise portals: every user of an enterprise portal, from the CEO down, can subscribe to different queries. Again, parameterization is important here: while the CEO may register interest in incoming purchase orders over one million dollars, a sales manager may want to know about all purchase orders for their territory.
- Fraud detection and other machine learning applications: machine learning applications in a CEP environment must dynamically adjust both the queries and parameters, in response to ever-changing external conditions.

### 3.1.8.3 Solution

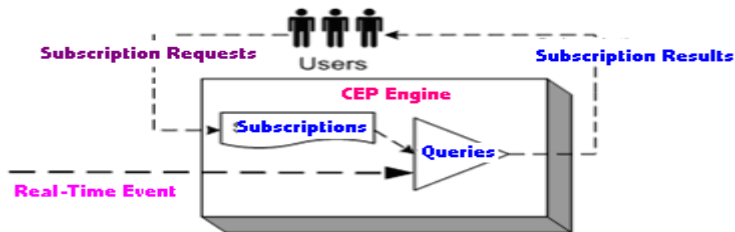


Figure 12: Dynamic Queries

Many CEP discussions revolve around the subject of continuous queries, that is, queries registered with a CEP engine and triggered by the arrival of data.

Dynamic queries come in several flavours':-

- Dynamic registration of continuous queries
  - In many applications, the ability to register continuous queries programmatically, without restarting the server, is important.



- Request/response queries
  - Request/response queries analyze streaming data, but these queries return results only upon explicit request from a user. Often the query itself is pre-registered with the engine, and its execution is triggered by a message on a separate "request" stream.
- Subscription queries
  - Subscription queries are similar to request/response queries, as these queries are instantiated by an explicit command. However, while request/response queries produce a single response immediately, subscription queries register interest in certain events, and the responses are streamed to subscribers. The diagram illustrates how the engine keeps a list of subscriptions from users, and dispatches the results of queries to the right subscriber:

#### 4 TIBCO Complex Event Processing

TIBCO BusinessEvents™ software helps organizations identify and address developing situations and trends by correlating massive volumes of data about discrete events and applying predefined rules to identify situations that require a response. BusinessEvents is then able to adapt running processes, initiate new processes and notify people when human intervention is necessary.

#### 4.1 Overview

TIBCO BusinessEvents can be described as a CEP engine. The Features of TIBCO BusinessEvents are:-

- Definition of Channels for capturing events
- Definition of the business objects and relationships between them - ontology
- Mapping of events to business objects providing overall context
- Capability to recognize patterns of events including the temporal dimension
- Ability to aggregate event patterns into higher order event patterns
- Modelling of state transitions with timing expectations showing the expected lifecycle of objects
- Detection of the absence of an event
- Execution of rules enabling response to exceptional circumstances, alerts and notifications as well as initiation of business processes

The below figure shows TIBCO CEP Solution overview

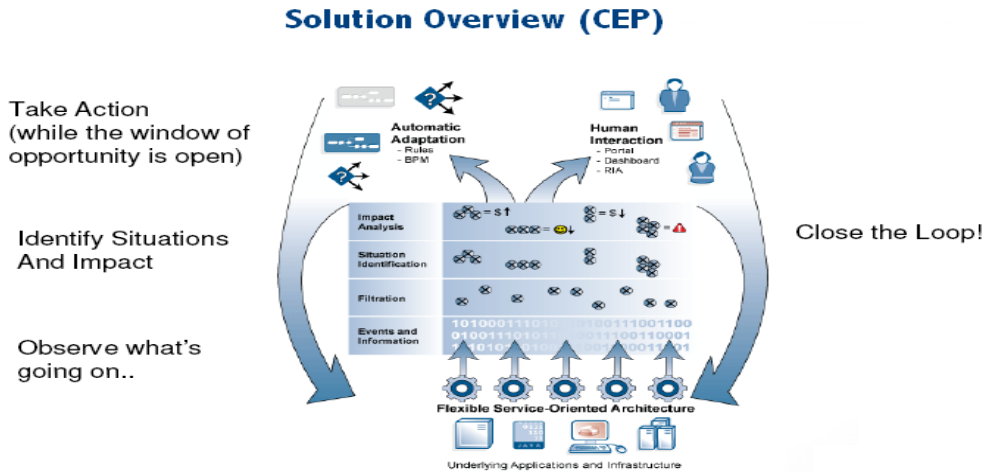


Figure 13: TIBCO CEP Solution

## 5 Conclusions

### 5.1 Key capabilities

To summarize, event processing, and in particular TIBCO CEP provides the capability for businesses to

- Track
- Trace, and correlate events
- To process events for trends and patterns
- Finally to predict the impact of identified situations

Rapid action can then be taken to prevent or minimize damage from threats to businesses – such as a customer not receiving a product on time resulting in a cancelled order.

The same is true on the upside. A positive situation can be capitalized upon rapidly and effectively –such as an emerging trading pattern or customer up-sell opportunity. Situations can also be analyzed to improve the underlying business processes and applications.

### 5.2 Benefits

To summarize the key benefits TIBCO CEP provides for businesses to

- Accelerates response to threats and opportunities by automatically identifying obscure but important relationships between seemingly unrelated events before they result in situations that impact customer experience or the bottom line.



- Improves resource allocation and problem resolution by helping organizations prioritize situations that require the most urgent attention based on a sophisticated analysis of likely outcome and secondary or indirect impacts.
- Applications include service assurance, fraud detection, logistics, compliance and security, among others.

### 5.3 Recommendations

#### When do you need CEP?

The best strategy is to ask that question now and identify the first CEP projects. Almost every enterprise application can take advantage Complex Event Processing. Given below are some examples.

Banking Domains can use it for :

- 
- Fraud detection
- ATM monitoring and control
- Improve operational efficiency E.g. One a/c of a customer for loan, banking, credit cards and monitoring each one of them as single entity.
- Customer service assurance
- Real-time risk management , Etc

In Insurance:-

- Coordinate and monitor for various partner agencies.
- Operational efficiency, E.g. faster claim processing.

- Detect fraudulent cases.

Telecom Domain:-

- Network management
- SLA management
- OSS/BSS systems
- Location-based services

Security Domain:-

- Algorithmic trading
- Detect the trends to minimize the risks and act faster in case of opportunity.
- Fraud detection

Others like Health Care, Public Sector/Government, Retail/ Supply Chain, Energy, Web, Entertainment, Travel etc.

#### References:-

- [1] Botella P., Burgués X., Carvallo J.P, Franch X and Quer C. 2003. 'Towards a Quality Model for the Selection of ERP Systems'. Component-Based Software Quality. Methods and Techniques. LNCS 2693, Springer Verlag, 225- 246.
- [2] Franch X. and Carvallo J.P. 2003. 'Using quality models in software package selection'. IEEE Software, 20(1): 34-41.
- [3] Losalvio F., Ortega D. and Pérez M. 2003. 'Towards a Standard EAI Quality Terminology'. Proceedings of the 23<sup>rd</sup> International Conference of the Chilean Computer Science Society (SCCC'03).



- [4] Themistocleous M. 2004. 'Justifying the decisions for EAI implementations: a validated proposition of influential Factors'. The journal of Enterprise Information management. Vol. 17. No. 2, 85-1004.
- [5] Business Process Execution Language for Web Services, Version 1.1, 5 May 2003, BEA Systems, Inter-national Business Machines Corporation, Microsoft Corporation, SAP AG, Siebel Systems.
- [6] Bussler, c.: B2B Integration Springer Verlag, 2003



المؤتمر العربي الليبي الدولي الخامس للهندسة الكهربائية والإلكترونية 23-26/10/2010 طرابلس ليبيا



## Medical Images Compression using Wavelet Transform and Neural Networks: Assessment of Reconstruction Quality Based on the Structural Information

Ali A. Elrowayati<sup>1</sup>, Jamal R. Elbergali<sup>2</sup>,

1: Misurata University, 2: Higher Institute of Industry Misurata

[arwyate@yahoo.com](mailto:arwyate@yahoo.com), [jelbergali@yahoo.com](mailto:jelbergali@yahoo.com)

### ABSTRACT

In this paper, we propose a novel method of encoding a medical image and develop a tool capable of improving the quantification of quality Medical image. The method incorporates the wavelet transform and neural network to achieve significant improvement in medical image compression performance. To reduce the computational effort a new neural system which is called wavelet back propagation neural networks has been introduced.

The traditional peak-signal-to-noise-ratio PSNR measure is mainly focused on the pixel-by-pixel difference between the original and compressed images. Such metric is improper for subjective quality assessment, since human perception is very sensitive to specific correlations between adjacent pixels. In this paper, we present a structural similarity method to measure the visual quality of compressed medical images. The results show that the proposed approach succeeded to improve high performance in terms of compression ratio and reconstruction quality. The results show the structural similarity method has high correlation with human judgment in assessing reconstructed medical images.

**Keywords:** images compression, wavelets, neural networks, wavelet networks, Error sensitivity, human visual system HVS, image quality assessment, Structural SIMilarity SSIM.

### I . Introduction

Image compression plays a critical role for telemedicine or tele-browsing applications. It is desired that either single image or sequences of images be transmitted over computer networks at large distances so as that they could be used in a multitude of purposes. Especially when

concerning medicine, where even today a big part of a radiologist's work is to make a diagnosis and to evaluate potential methods of treatment from X-ray photographs, extremely high demands are obviously made on the quality and resolution of a digital X-ray image.



Medical diagnostic data produced by hospitals increase exponentially. In an average-sized hospital, many tera or  $10^{15}$  bytes of digital data are generated each year, almost all of which have to be kept and archived [1]. Therefore, compression of medical image data is a crucial question, as well as image retrieval. Thus, our aim is to find an appropriate procedure that is able to represent the information contained in a digital image with fewer bits. In information theory this approach is usually called source encoding. Therefore, they have to be used carefully, especially in medical field: compressed images have to lead to the same diagnosis than the original ones.

There are two main families for image compression: lossless image compression techniques and lossy ones. Lossless algorithms guarantee a perfect reconstruction of every pixel, but they have the disadvantage of being limited in term of compression rate. Lossy techniques allow larger compression rates, while introducing some distortion in reconstructed images. In order to improve compression rates, we are interested in the second family of techniques. In this paper, we propose a novel method of encoding an image using both the wavelet transform and neural network to achieve significant improvement in medical image compression performance. We investigate the optimal implementation of the discrete wavelet transform DWT that is at the heart of the JPEG2000 image compression standard. A lifting approach is used as method that offers computational advantages over the traditional convolution approach. We focus

on the biorthogonal 9/7 wavelet filters of the JPEG2000 lossy coder [2].

In addition, new soft computing technologies such as neural networks are being developed for image compression. Parallelism, learning capabilities, noise suppression, transform extraction, and optimized approximate functions are some main reasons that encourage researchers to use artificial neural networks as an image compression approach. Although there are no significant work on neural networks that can take over the existing technology but there are some admissible attempts. Research activities on neural networks for image compression do exist in many types of networks such as Multi-Layer Perceptron MLP, Hopfield, Self-Organizing Map. Among these methods, the MLP network which usually uses Back-Propagation BP training algorithm provides simple and effective structures. It has been more considered in comparison with other artificial neural network ANN structures [11].

Wavelet Networks WNs were introduced by Zhang and Benveniste [1,2] in 1992 as a combination of artificial neural networks and wavelet decomposition. WNN employ wavelets as the activation functions, recently have been researched as an alternative approach to the neural networks with sigmoidal activation functions, which has been used in BP neural network.

The combination of wavelet theory and neural networks has led to the development of WNNs. The 25% largest coefficients wavelet subband that product from first stage DWT are divided into





vectors, which are projected onto a subspace using a WNN. The number of coefficients required to represent the vector in the subspace is less than the number of coefficients required to represent the original vector, resulting in data compression.

The organization of this paper is as follow. Section II describes briefly the LDWT used in this paper. Section III focuses on the BP neural network. Section IV gives an overview of the approach of WBPT and AWPBPT. Section V gives an overview of Compressed Image Quality Assessment. Section VI discussed the experimental results are shown. Finally the paper concludes in Section VII.

## **II LIFTING SCHEME DISCRETE WAVELET TRANSFORM**

Discrete wavelet transform DWT can be efficiently used in image coding applications because of its data reduction capabilities. Unlike the case of Discrete Cosine Transform DCT which based on cosine functions, DWT has some properties, making it a better choice for image compression than DCT, especially for image on higher resolutions. The entire image is transformed and compressed as a single data object rather than block by block (as in DCT based system such as JPEG Standard) allowing a uniform distribution of compression error across the entire image.

Wavelet theory [2] has provided a promising hope for image processing applications because of its flexibility in representing images and its ability in taking into account human visual system characteristics. It is mainly used to

decorrelate the image data, so the resulting coefficients can be efficiently coded. It also has good energy compaction capability which results in a high compression ratio. A wavelet transform decomposes an image into a set of different resolution sub-images, corresponding to the various frequency bands. This gives better re-representation of images with localization in both the spatial and frequency domains. This advantage is desirable in image compression, and it is not possible in both Fourier and Discrete Cosine Transforms which give good localization in one domain at the expense of other. A wavelet transform can also be viewed as a special case of multi-rate filter bank with dyadic tree decomposition. Wavelet transforms are multiresolution decompositions that can be used to analyze signals and images. They describe an image by the power at each scale and position edges can be located very effectively in the wavelet transform domain. For image processing applications, one can use the hierarchical wavelet decomposition by Mallat [3]. The G and H filters are applied to the image in both the horizontal and vertical directions, and the filter outputs sub-sampled by a factor of two, generating three orientation selective high-pass sub-bands, GG, GH, HG, and a low-pass sub-band HH. The process is then repeated on the HH band to generate the next level of the decomposition, and so on.

The wavelet transform, in general, produces floating point coefficients. Although these coefficients can be used to reconstruct an original image perfectly in theory, the use of finite precision arithmetic and quantization results in a lossy scheme.



Recently, reversible integer wavelet transforms that transform integers to integers and allow perfect reconstruction of the original signal have been introduced [4]-[5]. In [6], Calderbank et al. introduced how to use the lifting scheme presented in [7], where Sweldens showed that the computational complexity of convolution based bi-orthogonal wavelet transforms can be reduced by implementing a lifting-based scheme as shown in Fig. 1. Note that only the composition part of wavelet transform is depicted in Fig. 1 because the reconstruction process is just the reverse version of the one in Fig. 1. The lifting-based wavelet transform consists of splitting, lifting, and scaling modules and the wavelet transform is treated as prediction error de-composition. It provides a complete spatial interpretation of DWT. In Fig. 1, let  $X$  denote the input signal and  $X_{LI}$  and  $X_{HI}$  be the decomposed output signals, where they are obtained through the following three modules of lifting-based 1D-DWT:

(1) **Splitting:** In this module, the original signal  $X$  is divided into two disjoint parts, i.e.,

$x_e(n) = x(2n)$  and  $x_o = x(2n + 1)$  that denotes all even-indexed and odd indexed samples of  $X$ , respectively.

(2) **Lifting:** In this module, the prediction operation  $P$  is used to estimate  $x_o(n)$  from  $x_e(n)$  and results in an error signal  $d(n)$  which represents the detail part of the original signal. Then we update  $d(n)$  by applying it to the update operation  $U$  and the resulting signal is

combined with  $x_e(n)$  to estimate  $s(n)$  which represents the smooth part of the original signal.

(3) **Scaling:** A normalization factor is applied to  $d(n)$  and  $s(n)$ , respectively. In the even indexed part is multiplied by a normalization factor  $K_e$  to produce the wavelet subband  $X_{LI}$ . Similarly in the odd-index part, the error signal  $d(n)$  is multiplied by  $K_o$  to obtain the wavelet subband  $X_{HI}$ .

Compared with the traditional convolution based wavelet transform, the Lifting Discrete Wavelet Transform LWDT scheme has several advantages: First, it makes optimal use of similarities between the high pass and low pass filters, the computation complexity can be reduced by a factor of two. Second, it allows a full in-place calculation of the wavelet transform. In other words, no auxiliary memory is needed [7].

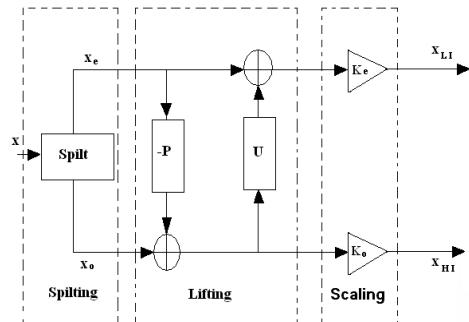


Fig. 1: The lifting-based wavelets transform.

DWT is applied on an image in order to reduce the inter pixel redundancy. As a



result of decomposition, most of the coefficients with high frequency low scale region are either zero or in close proximity to zero. Hence, most of significant coefficients can be extracted and coded by applying strategies such as designing a JPEG like quantization table [8] or applying thresholding. Thresholding parameter value is chosen intuitively based on experimentation and satisfactory visual effect of reconstructed image as reported in [9]. Donoho and Johnstone [10] have given a formula for thresholding parameter  $\lambda$  in the form of universal thresholding which takes into account the number of total coefficients and standard deviation of coefficients. The significance of coefficients is directly related to its magnitude as well as their subbands after wavelet decomposition.

In our approach, bottleneck structure WNNs employing wavelets as the activation. WNNs are feed forward neural networks using wavelets as an activation function.

The 25% largest coefficients wavelet sub band that product from LDWT are divided into vectors.

### III Back-Propagation Neural Networks

The compression of images by Back-Propagation BP Networks is investigated by many researchers. One of the first tries in using this approach was done in [11], in which the authors proposed a three layer BP network for compressing images. In their method original image is divided into blocks and fed to input neurons, compressed blocks are found at the output of the hidden layer and the de-compressed blocks are restored in the neurons of output

layer. This implementation was done on the NCUBE parallel computer and the simulation results showed that this network could achieve a poor image quality even for trained images in 4:1 compression ratio [11]. As in [13] pointed out, none of the results in using single network are so good as the result that could be achieved by taking average of image blocks and using their values as the indicator of blocks. Because of these poor results achieved by using one simple BP network, several authors tried to improve the performance of this neural network-based compression technique. One of these efforts was hierarchical neural networks [11] which extended BP network by adding two more hidden layers to it. This extension will exploit the correlation between blocks in an image in addition to the correlation between pixels among a block. This method had some improvements in Signal to Noise Ratio SNR of reconstructed image, but this improvement is not so considerable.

### IV Wavelet Back-Propagation

BP neural network is now the most popular mapping neural network. But it has few problems such as trapping into local minima and slow convergence. Wavelets are powerful signal analysis tools. They can approximately realize the time frequency analysis using a mother wavelet. The mother wavelet has a square window in the time-frequency space. The size of the window can be freely variable by two parameters. Thus, wavelets can identify the localization of unknown signals at any level. Activation function of hidden layer neurons in standard BP neural network is a sigmoidal function. In traditional wavelet



networks wavenets, the position and dilation of the wavelets are fixed and the weights are optimized [6]. To design wavelet back propagation WBP neural network we substitute hidden layer sigmoidal activation function of BP with Morlet wavelet [7]:

$$M(t) = \cos\left(\frac{t-b}{a}\right) \exp\left(-0.5\left(\frac{t-b}{a}\right)^2\right) \dots (1)$$

The parameters  $a$  and  $b$  of the wavelets activation function can be optimized by the least mean squares LMS, sensed by minimizing a cost function or the energy error function.

To minimize energy error function, we use the method of steepest descent, which requires the gradients  $\frac{\partial E}{\partial w}$ ,  $\frac{\partial E}{\partial b}$ ,  $\frac{\partial E}{\partial a}$  for updating the incremental changes to each particular parameter of Adaptive Wavelet Neural Network AWNN,  $w$ ,  $b$  and  $a$  respectively.

$$\Delta w = -\frac{\partial E}{\partial w}, \Delta b = -\frac{\partial E}{\partial b}, \Delta a = \frac{\partial E}{\partial a} \dots (2)$$

Thus each parameters  $w$ ,  $b$ , and  $a$  of the network is updated in accordance with the rule:

$$w(n+1) = w(n) + \mu_w \Delta w \quad (3)$$

$$a(n+1) = a(n) + \mu_a \Delta a \quad (4)$$

$$b(n+1) = b(n) + \mu_b \Delta b \quad (5)$$

Where  $\mu$  is the adaptive learning rate parameter.

Typical topology of proposed AWNN is shown in Fig.2.

Applying the LDWT on images does not reduce the amount of the data to be compressed. A common way to reduce the

number of bits required for the compression phase is to quantize the coefficients.

According to Shannon's rate distortion theory, vector quantization of signals reduces the coding bit rate significantly compared to scalar quantization. The wavelet coefficients are divided into vectors, which are projected onto a subspace using an AWNN.

The number of coefficients required to represent the vector in the sub-space is less than the number of coefficients required to represent the original vector, resulting in data compression.

AWBP neural network can be directly applied to LDWT coefficients. The simplest neural network structure for this purpose is illustrated in Fig. 2. This network has three layers; input, hidden and output layer. Both the input and output layers are fully connected to the hidden layer and have the same number of neurons,  $N$ .

Quantization can be achieved by allowing the value of the number of neurons at the hidden layer  $K$  to be less than that of neurons at both input and output layers  $K \leq N$  (It's called bottleneck structure WNN). As in most quantization methods, the input coefficients are divided apart into blocks. For example with  $8 \times 8$ ,  $4 \times 4$  or  $16 \times 16$  elements. These block sizes determine the number of neurons in the input/output layers which convert to a column vector and fed to the input layer of network; one neuron per element. With this AWBP neural network, compression is conducted in training and testing phases as follow.



#### IV.1. Training Processes

Like all other training processes, in this phase a set of medical image samples are selected and decomposed at different scales using wavelet transform to obtain bi-orthogonal wavelet representation of the image to train the network via the wavelet-back propagation learning rule. We have modified back propagation learning rule, during training stage the weights, dilations and translations parameters, are iteratively adjusted to minimize the network error.

For compression purpose, the target pattern in the output layer neurons of the network will be same as the input pattern. The compression is represented by the hidden layer which is equivalent to compress the input into a narrow channel. Training samples of blocks are converted into vectors and then normalized into [0, 1]. In accordance with the structure of wavelet neural network shown in Fig. 2, the operation for adjusting weights for compressing and de-compressing can be described as the following equations [14].

$$H_j^{in} = \sum_{i=1}^N V_{ij} X_i$$

$$h_j = f(H_j^{in}); 1 \leq j \leq K \quad \dots (6)$$

$$\hat{X}_i^{in} = \sum_{j=1}^K W_{ji} h_j$$

$$\hat{X} = g(\hat{X}_i^{in}); 1 \leq i \leq N \quad \dots (7)$$

In the above equations,  $f$  and  $g$  are the activation functions which can be linear or nonlinear.  $V_{ij}$  and  $W_{ji}$  represent the

weights of compressor and de-compressor, respectively. This transform provides optimum solution for linear narrow channel and minimizes the mean square error between original and reconstructed coefficients. In addition, it maps input samples into a new space where all samples in the new space are de-correlated; this fact led to better compression. The training process of the neural network structure in Fig. 2. is iterative and is stopped when the weights converge to their true values. In real applications the training is stopped when the error of (4) reaches to a threshold named ( $\mathcal{E}$ ), or maximum number of iterations limits the iterative process.

$$Err = \frac{1}{2} \sum (x_k - \hat{x}_k)^2 \quad (8)$$

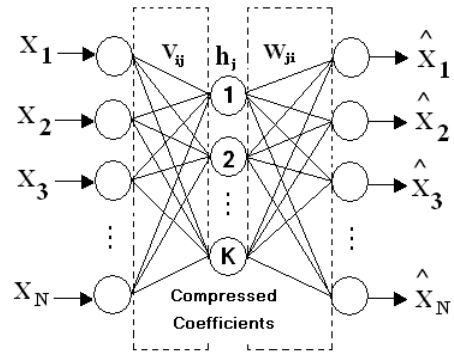


Fig. 2: Bottleneck structure neural network.

#### IV.2. Test Processes

When training is completed and the coupling parameters are adjusted, the test coefficients are fed into the AWBP neural network and quantized coefficients are obtained in the outputs of hidden layer. These outputs must be quantized to the desired number of bits. If the same number



of bits is used to represent input and hidden neurons, then the Compression Ratio  $CR$  will be the ratio of number of input to hidden neurons. For example, to compress a coefficient block of  $8 \times 8$ , 64 input and output neurons are required. In this case, if the number of hidden neurons are 16 and coefficient block of size  $8 \times 8$ , the compression ratio would be  $64:16=4:1$ . In general, the compression ratio of the basic network illustrated in the Fig. 3, for coefficients with  $n$  blocks is computed as (9), [14].

$$CR = \frac{nNB_i}{nKB_h} = \frac{NB_i}{KB_h} \quad (9)$$

Where  $B_i$  and  $B_h$  are the number of bits needed to code the output of input and hidden layers, respectively. In this equation  $N$  and  $K$  are the number of neurons in the input and hidden layers, respectively.

In dequantizer, the quantized coefficients are converted to a version similar to original coefficients by applying the hidden to output layer de-compression with adjusted parameters on outputs of hidden layer. Then the reconstruction process is just the reverse version of the one LDWT.

## V. Compressed Image Quality Assessment

Any imaging system must be judged on the quality of the images it produces. For medical imaging systems the images must be diagnostically useful, that is capable of leading to the detection and identification of an abnormality and its interpretation so as to determine its cause, and obtained at an acceptable dose to the patient.

In order to be able to design useful compression systems as well as assess their performances, we need to define a measure of quality of the compression systems. As pointed out, a lossy compression introduces distortions in the decompressed image at higher compression ratio. It is possible to classify image quality criteria in two types of image quality criteria that are used for evaluation of image quality, subjective and quantitative or objective. It is said to be subjective if the quality is evaluated by humans. The use of human analysts, however, is quite impractical and may not guarantee objectivity. The assessment is not stationary, depending on their feelings. Moreover, the definition of distortion highly depends on the application, i.e. the best quality evaluation is not always made by people at all. In the objective measures, the distortion is calculated as the difference between the original image, and the reconstructed image by a predefined function. It is assumed that the original image is perfect. All changes are considered as occurrences of distortion, no matter how they appear to a human observer.

### V.1 Subjective Measures

The subjective criteria use rating scales such as goodness scales, such as Table I.

The scale ranging of goodness criteria rates image quality is from excellent to unsatisfactory. A training set of images is used to calibrate such a scale. It is useful in applications such as image coding, where the encoding process introduces degradation in the output image [19].



**Table I.** Image Goodness Scale

Goodness Scale	Weighting Rate
Excellent	5
Good	4
Fair	3
Poor	2
Unsatisfactory	1

If several observers are used in the evaluation process, then the mean rating or mean opinion score MOS, which is defined as [19]

$$MOS = \frac{\sum_{k=1}^n s_k n_k}{\sum_{k=1}^n n_k} \quad (10)$$

Where  $s_k$  the score associated with the  $k$ th rating,  $n_k$  is the number of observers with this rating, and  $n$  is the number of grades in the scale.

Other image quality assessment is quantitative measures that can be divided into two error metrics, the Mean Square Error MSE and the Signal to Noise Ratio SNR. The MSE is the cumulative squared error between the output and the original image, whereas SNR is a measure of the error. The mathematical formulae for the two are

$$\text{Error: } E = F - \hat{F} \quad (11)$$

Where  $F$  is the original image and  $\hat{F}$  reconstructed image.

$$MSE = E / (\text{Size of Image}) \quad (12)$$

$$SNR = 20 \log \left( \frac{F}{\sqrt{MSE}} \right) \quad (13)$$

These measures are mainly focused on the pixel-by-pixel difference between the original and output images. The measure of

MSE or PSNR gives a value Digital on degradation, but not describes the type of degradation. Moreover as is often noted in the [Geisler 1995], [Watson, 1997], [Watson, 2000], it represents not quite the quality perceived by observers humans, especially in cases of high rates of compression. Between two degraded images of the same original image, one that has a value of PSNR significantly higher may correspond to a quality Visual significantly lower. Such metric is improper for subjective quality assessment. [20]

### V.2. Structural Similarity Based Image Quality Assessment

It is widely believed that the statistical properties of the natural visual environment play a fundamental role in the evolution, development and adaptation of the human visual system (HVS). Structural similarity is presented as an alternative design philosophy for quantitative image quality assessment methods. This is different from and complementary to the typical HVS-based approaches, which usually calculate signal difference between the distorted and the reference images, and attempt to quantify the difference “perceptually” by incorporating known HVS properties. The basic form of SSIM is where the comparison between the reference and test medical images is broken down into three different comparisons: luminance, contrast, and structural compare-sons. The luminance comparison  $l(x, y)$  between a reference image  $X$  and a test image  $Y$  is describe by [20]





$$l(x, y) = \frac{2\mu_x\mu_y}{\mu_x^2 + \mu_y^2} \quad (14)$$

Where  $\mu_x$  and  $\mu_y$  denote the mean values of the images X and Y, respectively, the contrast comparison is defined as

$$c(x, y) = \frac{2\sigma_x\sigma_y}{\sigma_x^2 + \sigma_y^2} \quad (15)$$

Where  $\sigma_x$  and  $\sigma_y$  are the standard deviations of X and Y, respectively. The structural comparison is given by

$$s(x, y) = \frac{\sigma_{xy}}{\sigma_x\sigma_y} \quad (16)$$

These local similarities are expressed using simple, easily computed statistics, and combined together to form local SSIM:

$$\begin{aligned} \text{SIM}(x, y) &= l(x, y)c(x, y)s(x, y) \\ &= \frac{4\mu_x\mu_y\sigma_{xy}}{(\mu_x^2 + \mu_y^2)(\sigma_x^2 + \sigma_y^2)} \end{aligned} \quad (17)$$

In order to alleviate the problem of stability and improve the correlation between the objective and subjective measures, Wang et al. [20] proposed the structural similarity index SSIM. The SSIM has been defined as follows [20]:

$$\text{SSIM}(x, y) = \frac{(2\mu_x\mu_y + C_1)(2\sigma_{xy} + C_2)}{(\mu_x^2 + \mu_y^2 + C_1)(\sigma_x^2 + \sigma_y^2 + C_2)} \quad (18)$$

$$C_1 = (K_1L)^2, \quad C_2 = (K_2L)^2$$

Where  $L$  is the dynamic range of the pixel values (255 for 8 bit images), and  $C_1$

and  $C_2$  are small positive constants. At every pixel (i, j), a local SSIM index,  $\text{SSIM}(i, j)$  is de-fined by evaluating the mean, standard deviation and covariance on a local neighborhood  $N_{i,j}$ , around that pixel. The overall image quality is measured by the mean SSIM MSSIM index given by

$$\text{MSSIM} = \frac{1}{M} \sum_i \sum_j \text{SSIM}(i, j) \quad \dots (19)$$

Where  $M$  is the total number of local SSIM indexes.

The SSIM indexing algorithm is quite encouraging not only because it achieves good quality prediction accuracy in the current tests, but also be-cause of its simple formulation and low complexity implementation.

## V EXPERIMENTAL RESULTS

We are interested in methods lossy compression based LWDT because their properties are interesting. Indeed, the LWDT combines good spatial relationships and frequency, with reduced the computation complexity and memory saved.

In addition, we use WBP neural network for second stage to improve high performance in terms of compression ratio and reconstruction quality.

In the following experiments, our data set consist of 200 medical images (X-ray, MRI, Ultra Sound and CT) taken from the database image of the National Cancer Institute- Misurata.





We present the encoding results of 512 x 512 sizes, 8bit or 12bit resolution. Fig. 3 shows some sample images of data set. For first stage, we take 100 different images and applied LDWT on them. In the second stage, we use the 25% largest coefficients that have been produced from first stage to fed AWBP neural network.

The bi-orthogonal 9/7-tap filters for DWT are proven to offer excellent coding performance [12]. The bit per pixel is 0.25 and compression ratio is 75% for first stage, stage the 25% largest coefficients are divided into vectors, which are fed onto a neural network as in Fig.2.

We compare the cross distortion and cross-image performances of different quality on an image database compressed by proposed method.

The bit rates were in the range of 0.0625 to 0.19 bits/pixel, and were chosen depend on compression ratio.

Subjects viewed the images from comfortable seating distances (this distance was only moderately control-led, to allow the data to reflect natural viewing conditions) by physicians specializing or radiologist and were asked to provide their perception of quality. Mean opinion scores MOS were then computed for each test image, after removing outliers (most subjects had no outliers).

We compare the MOS, SNR and MSSIM for different testing medical images, as on table I.

**Table I:** Compression results by Wavelet lifting scheme and Adaptive Wavelet Back Propagation Networks for X-ray chest image (4) in Fig. 3 after 1000 Iterations.

Input Hidden layers	bbp	SNR (db)	CR%	MOS
64-49	0.19	4.56	81.00	good
64-36	0.10	4.56	90.00	good
64-16	0.0625	4.57	93.75	Very good

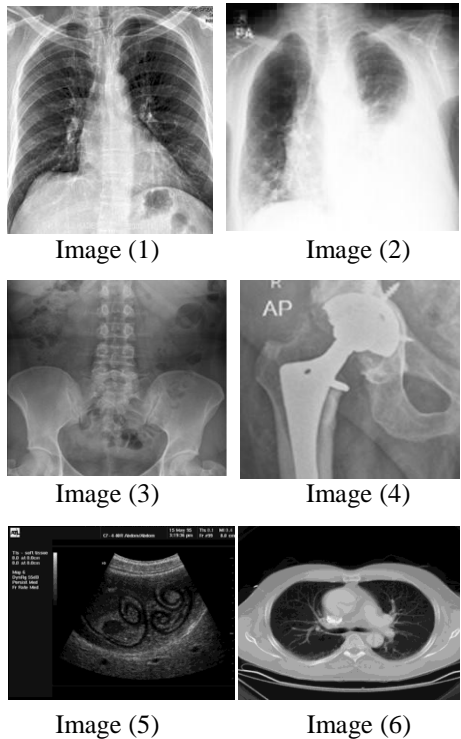


**Fig. 3:** Some sample images of the training / testing sets.



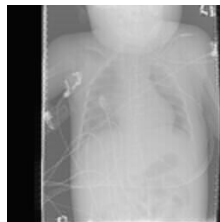
The SNR and MSSIM measurement results are given in the figure (4) obviously; SNR performs very poorly in this case. The MSSIM values exhibit much better consistency with the qualitative visual appearance.



Image(2)  
CR=93.75%  
MOS=Fair  
SNR=4.57db  
MSSIM= 0.841



Image(4)  
CR=93.75%  
MOS= good  
SNR=6.50db  
MSSIM= 0.9906



Image(7)  
CR=93.75%  
MOS=good  
SNR= 5.4243 db  
MSSIM= 0.864



Image(5)  
CR=93.75%  
MOS=POOR  
SNR=4.5604db  
MSSIM= 0.564

**Fig. 4:** Comparison of image fidelity measures for samples of test images.

We observe that the SSIM index is better in capturing such poor quality regions. The compressed image supplies acceptable perceived quality as shown in

figure (4). In fact, although the visual quality is better than its absolute error map or SNR .

The SSIM index maps deliver better consistency with perceived quality measurement.

## VI CONCLUSION

Medical Image Compression has been achieved using the proposed AWBP neural network approach. Comparison between the numerical results obtained by AWBP neural network with the corresponding ones obtained by the standard BP neural network reveals the better performance generality of AWBP neural network. It was shown that the use of vector quantization to quantize the values at the hidden layers of the neural networks provides better performance than using scalar quantization.

Our proposed system shows that the AWBP neural network approach succeeded to improve high performances in terms of compression ratio and reconstruction quality, especially for rates of compression lower than 75%.

In this work, we summarized and recalled the classical approach for assessing the quality image-based sensitivity. We reminded outlines its limitations for the assessment Medical image quality. We proposed the use of a structural similarity alternative for the design quality metrics image.

The value of the concept of structural similarity is shown through the SSIM index and we have proved it helps to better evaluation of image quality.



Finally, note that the SSIM index can be used to optimize design of image compression algorithms.

## VII References

- [1] Kim Y and Pearlman WA, " Stripe-based SPIHT lossy compr-ession of volumetric medical images for low memory usage and uniform reconstruction quality," Proc of Int Conf on Image Processing 2000, vol .3, pp. 652-655.
- [2] Rioul and M. Vetterli, "Wavelet and signal Processing," IEEE SP Magazine, pp. 14 – 37, October 1991
- [3] S. Mallat, "A theory for multi-resolution signal decomposition; The wavelet representation," IEEE Trans. Pattern Anal. Mach. Intell., vol. 11, pp. 674- 693, 1989.
- [4] Said A and Pearlman WA, " An image multiresolution representation for lossless and lossy compression," IEEE Trans on Image Processing 1996, vol .5, pp. 1303-1310.
- [5] Dewitte S and Cornelis J, " Loss-less integer wavelet transform," IEEE Signal Processing Letters 1997, vol..4, pp.158-160.
- [6] Calderbank AR, Daubechies I, Sweldens W, and Yeo BL, "Wavelet transforms that map integers to inte-gers," Appl Comput Harmon Anal 1998, vol .5, pp 332- 369.
- [7] Sweldens W, " The lifting sche-me: A custom-designconstruction of biorthogonal wavelets," Appl Com-put Harmon Anal 1996; 3(2), pp. 186-200.
- [8] Ricardo de Queiroz, C. K. Choi, Young Huh, and K. R. Rao, "Wavelet transform in a JPEG-like image cod-er", IEEE Trans. On Circuit and Systems for Video Technology, vol. 7, pp. 419-424, April 1997.
- [9] Eduardo Morales, Frank Y. Shin, "Wavelet coefficients clustering using morphological operations and pruned quadtrees," Pattern Recognition , Elsevier, vol. 33, no. 10, pp. 1611-1620, 2000.
- [10] D. Donoho, I. Johnstone, G. Kerkyacharian, and D. Picard, "Density estimation by wavelet thresholding," Technical Report Stan-ford University, 1993.
- [11] Shaou-Gangmlaou, Shih-Tse ch-en, Shu-Nien chao" Wavelet-based lossy-to-Lossless Medical Image Co-mpression using dynamic VQ And SPIHT Coding," , Biomedical Engin-eering Application ,Basis & Comm-unication., Vol. 15 No. 6,pp. 235-242, December 2003
- [12] N.Sonehara, M.Kawato, S.Miya-ke, K.Nakane," Image compression using a neural network model', Inter-national Joint Conference on Neural Networks, Washington DC, 1989.
- [13] R. Baron. Contribution à l'étude des réseaux d'ondelettes, Thèse de doctorat, Ecole Normale Supérieure de Lyon, Février 1997.
- [14] G. Lekutai, "Adaptive Self-Tun-ing Neuro Wavelet Network Cont-rollers," Ph.D thesis, Virginia Polyt-echnic Institute and State University, The Electrical Engineering Depart-ment, 1997.
- [15] Q. Zang, Wavelet Network in Nonparametric Estimation. IEEE Tra-ns. Neural Networks, 8(2):227-236, 1997
- [16] Q. Zang and A. Benveniste, Wa-velet networks. IEEE Trans. Neural Networks, vol. 3, pp. 889-898, 1992.



- [17] P. Goupillard, A. Grossmann, and J. Morlet, "Cycle-Octave and Re-lated Transforms in Seismic Signal Analysis," *Geoexploration*, vol.23, pp. 85-102 ,1984.
- [18] Hadi Veisi, Mansour Jamzad , "A Complexity-Based Approach in Image Compression using Neural Networks," , *International Journal of Signal Processing* 5;2 © www.waset.org Spring 2009. 4, April 2004.
- [19] A. K. Jain, *Fundamentals of Digital Image Processing*, Prentice-Hall, Inc., USA, 1989.
- [20] Zhou Wang, Alan Conrad Bovik, Hamid Rahim Sheikh and Eero P. Simoncelli." Image Quality Assess-ment: From Error Visibility to Structural Similarity", *IEEE Trans. Image processing*, vol. 13, NO.



## Overview of Cloud Computing Technology

Abubaker M. F. Abushofa

Department of Electrical & Electronic Engineering,

Faculty of Engineering, Al-Fateh University

Email: [abushofa@ee.edu.ly](mailto:abushofa@ee.edu.ly)

### Abstract

Cloud computing represents a paradigm shift in the delivery architecture of information services. Companies such as Google, Yahoo, Amazon, and others have built large, purpose-built architectures to support their applications and taught the rest of the world how to do massively scalable architectures to support compute, storage, and application services.

Cloud computing is about moving services, computation and/or data—for cost and business advantage—off-site to an internal or external, location-transparent, centralized facility or contractor. By making data available in the cloud, it can be more easily and ubiquitously accessed, often at much lower cost, increasing its value by enabling opportunities for enhanced collaboration, integration, and analysis on a shared common platform.

Cloud computing can be divided into three areas; Software-as-a-Service (SaaS), Platform-as-a-Service (PaaS) and Infrastructure-as-a-Service (IaaS).

This overview paper presents some of the key topics related to the emerging technology of cloud computing and summarizes the fundamental issues of cloud computing to help readers to assess the applicability of cloud computing to their application areas.

### 1. Introduction

Cloud computing is a computing paradigm, where a large pool of systems are connected in private or public networks, to provide dynamically scalable infrastructure for application, data and file storage. With the advent of this technology, the cost of computation, application hosting, content

storage and delivery is reduced significantly.

Cloud computing is a practical approach to experience direct cost benefits and it has the potential to transform a data center from a capital-intensive set up to a variable priced environment.



The idea of cloud computing is based on a very fundamental principal of “reusability of IT capabilities”[1]. The difference that cloud computing brings compared to traditional concepts of “grid computing”, “distributed computing”, “utility computing”, or “autonomic computing” is to broaden horizons across organizational boundaries.

Figure 1 illustrates the three principle components of a cloud model. This figure reflects the proportions of IT mass as it relates to cost, physical space requirements, maintenance, administration, management oversight, and obsolescence.

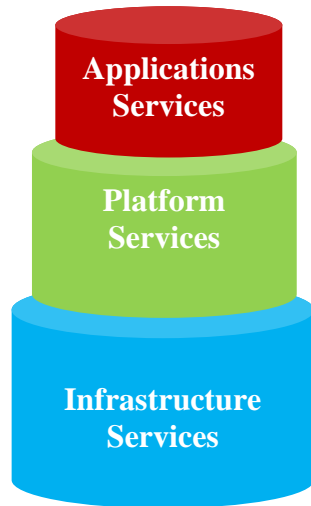


**Figure 1:** Cloud anatomy.

The rest of the paper is organized as follows. Cloud computing models are discussed in section 2. Section 3 presents

some understanding of public and private clouds. Cloud computing benefits are stated in section 4. Section 5 discusses the challenges of cloud computing. Finally, conclusion is drawn in section 6.

## 2. Cloud Computing Models

Cloud Providers offer services that can be grouped into three categories[2].

- i. **Software as a Service (SaaS):** In this model, a complete application is offered to the customer, as a service on demand. A single instance of the service runs on the cloud & multiple end users are serviced. On the customers' side, there is no need for upfront investment in servers or software licenses, while for the provider, the costs are lowered, since only a single application needs to be hosted & maintained. Today SaaS is offered by companies such as Google, Salesforce, Microsoft, Zoho, etc.
- ii. **Platform as a Service (Paas):** Here, a layer of software, or development environment is encapsulated & offered as a service, upon which other higher levels of



service can be built. The customer has the freedom to build his own applications, which run on the provider's infrastructure. To meet manageability and scalability requirements of the applications, PaaS providers offer a predefined combination of OS and application servers, such as LAMP platform (Linux, Apache, MySQL and PHP), restricted J2EE, Ruby etc. Google's App Engine, Force.com, etc are some of the popular PaaS examples.

iii. **Infrastructure as a Service (IaaS):**

IaaS provides basic storage and computing capabilities as standardized services over the network. Servers, storage systems, networking equipment, data centre space etc. are pooled and made available to handle workloads. The customer would typically deploy his own software on the infrastructure. Some common examples are Amazon, GoGrid, 3 Tera, etc.

3. **Understanding Public and Private Clouds**

Enterprises can choose to deploy applications on Public, Private or Hybrid

clouds. Cloud Integrators can play a vital part in determining the right cloud path for each organization.

3.1. **Public Cloud**

Public clouds are owned and operated by third parties; they deliver superior economies of scale to customers, as the infrastructure costs are spread among a mix of users, giving each individual client an attractive low-cost, "Pay-as-you-go" model. All customers share the same infrastructure pool with limited configuration, security protections, and availability variances. These are managed and supported by the cloud provider. One of the advantages of a Public cloud is that they may be larger than an enterprises cloud, thus providing the ability to scale seamlessly, on demand.

3.2. **Private Cloud**

Private clouds are built exclusively for a single enterprise. They aim to address concerns on data security and offer greater control, which is typically lacking in a public cloud. There are two variations to a private cloud:

- **On-premise Private Cloud:** On-premise private clouds, also known as internal clouds are hosted within one's own data center. This model provides a



more standardized process and protection, but is limited in aspects of size and scalability. IT departments would also need to incur the capital and operational costs for the physical resources. This is best suited for applications which require complete control and configurability of the infrastructure and security.

- **Externally hosted Private Cloud:** This type of private cloud is hosted externally with a cloud provider, where the provider facilitates an exclusive cloud environment with full guarantee of privacy. This is best suited for enterprises that don't prefer a public cloud due to sharing of physical resources.

### 3.3. Hybrid Cloud

Hybrid Clouds combine both public and private cloud models. With a Hybrid Cloud, service providers can utilize third party Cloud Providers in a full or partial manner thus increasing the flexibility of computing. The Hybrid cloud environment is capable of providing on-demand, externally provisioned scale. The ability to augment a private cloud with the resources of a public cloud can be used to manage any unexpected surges in workload.

## 4. Cloud Computing Benefits

Enterprises would need to align their applications, so as to exploit the architecture models that Cloud Computing offers. Some of the typical benefits are listed below:

### i. Reduced Cost

There are a number of reasons to attribute Cloud technology with lower costs. The billing model is pay as per usage; the infrastructure is not purchased thus lowering maintenance. Initial expense and recurring expenses are much lower than traditional computing.

### ii. Increased Storage

With the massive Infrastructure that is offered by Cloud providers today, storage & maintenance of large volumes of data is a reality. Sudden workload spikes are also managed effectively & efficiently, since the cloud can scale dynamically.

### iii. Flexibility

This is an extremely important characteristic. With enterprises having to adapt, even more rapidly, to changing business conditions, speed to deliver is critical. Cloud computing stresses on getting applications to market very quickly, by using the most appropriate building blocks necessary for deployment.





## 5. Cloud Computing Challenges

Despite its growing influence, concerns regarding cloud computing still remain. In our opinion, the benefits outweigh the drawbacks and the model is worth exploring. Some common challenges are:

### i. Data Protection

Data Security is a crucial element that warrants scrutiny. Enterprises are reluctant to buy an assurance of business data security from vendors. They fear losing data to competition and the data confidentiality of consumers. In many instances, the actual storage location is not disclosed, adding onto the security concerns of enterprises. In the existing models, firewalls across data centers (owned by enterprises) protect this sensitive information. In the cloud model, Service providers are responsible for maintaining data security and enterprises would have to rely on them.

### ii. Data Recovery and Availability

All business applications have Service level agreements that are stringently followed. Operational teams play a key role in management of service level agreements and runtime governance of applications. In production environments, operational teams support:

- Appropriate clustering and Fail over.
- Data Replication.
- System monitoring (Transactions monitoring, logs monitoring and others).
- Maintenance (Runtime Governance)
- Disaster recovery.
- Capacity and performance management.

If, any of the above mentioned services is under-served by a cloud provider, the damage & impact could be severe.

### iii. Management Capabilities

Despite there being multiple cloud providers, the management of platform and infrastructure is still in its infancy. Features like „Auto-scaling“ for example, is a crucial requirement for many enterprises [3]. There is huge potential to improve on the scalability and load balancing features provided today.

### iv. Regulatory and Compliance Restrictions

In some of the European countries, Government regulations do not allow customer's personal information and other sensitive information to be physically located outside the state or country [4-6]. In order to meet such requirements, cloud providers need to setup a data center or a storage site exclusively within the country



to comply with regulations. Having such an infrastructure may not always be feasible and is a big challenge for cloud providers.

With cloud computing, the action moves to the interface — that is, to the interface between service suppliers and multiple groups of service consumers. Cloud services will demand expertise in distributed services, procurement, risk assessment and service negotiation — areas that many enterprises are only modestly equipped to handle.

## 6. Conclusion

Cloud platforms don't yet offer the full spectrum of an on-premises environment. For example, business intelligence as part of the platform isn't common, nor is support for business process management technologies such as full-featured workflow and rules engines. This is all but certain to change; however, as this technology wave continues to roll forward.

Cloud platforms aren't yet at the center of most people's attention. The odds are good, though, that this won't be true five years from now. The attractions of cloud-

based computing, including scalability and lower costs, are very real. If you work in application development, whether for a software vendor or an end user, expect the cloud to play an increasing role in your future. The next generation of application platforms is here.

## References

- [1] Neil Turner , Cloud Computing: A Brief Summary, Lucid Communications Limited, September 2009.
- [2] David Chappell, A Short Introduction to Cloud Platforms, an Enterprise-Oriented View, David Chappell & Associates, August 2008.
- [3] <http://www.microsoft.com/windowazure/windowsazure/> (1/7/2010).
- [4] Srinivasa Rao, Nageswara Rao and Kusuma Kumari, Cloud Computing: An Overview, Journal of Theoretical and Applied Information Technology, 2005.
- [5] Frank Gens, Robert P Mahowald, Richard L Villars, *IDC Cloud Computing 2010 - An IDC Update*, Sep 2009 - Doc # TB20090929, 2009.
- [6] David Bradshaw, *Western European Software-as-a-Service Forecast, 2009–2013*, Apr 2009 - Doc # LT02R9, 2009.



## The Impact of WiMAX Security on the System Performance

Abubaker M. F. Abushofa\* and Alferjani S. M. Mahmud  
Department of Electrical & Electronic Engineering,  
Faculty of Engineering, Al-Fateh University  
\* Email: abushofa@ee.edu.ly

### Abstract

With the exploding growth of wireless communication in recent years, security issues in wireless networks also become a growing concern. Security requirements for wireless networks are similar to those for wired networks. However, wireless networks are inherently less secure compared to their wired counterparts due to the lack of physical infrastructure. Therefore, special attention should be paid to the security of wireless networks. Security goals for wireless networks can be summarized as follows. Privacy or confidentiality is fundamental for secure communication, which provides resistance to interception and eavesdropping. Message authentication provides integrity of the message and sender authentication, corresponding to the security attacks of message modification and impersonation. Anti-replay detects and disregards any message that is a replay of a previous message. Non-repudiation is against denial and fabrication. Access control prevents unauthorized access.

In this paper we concentrated on the mobile WiMAX IEEE802.16e, and its related features and technologies. We proposed a security system module to evaluate the impact of the security measures on system performance in terms of authentication cost, delay, and the effect of security measures on the scanning time before initiating handover. This is all attributed to some assumptions and scenarios such as, system mobility, arrival rates, and traffic pattern.

### 1. Introduction

Security requirements for wireless networks are similar to those for wired networks. However, wireless networks are inherently less secure compared to their wired counterparts due to the lack of physical infrastructure. Therefore, special attention should be paid to the security of wireless networks. Security goals for wireless networks can be summarized as follows. Privacy or confidentiality is fundamental for secure communication, which provides resistance to interception and eavesdropping. Message authentication provides integrity of the message and

sender authentication, corresponding to the security attacks of message modification and impersonation. Anti-replay detects and disregards any message that is a replay of a previous message. Non-repudiation is against denial and fabrication. Access control prevents unauthorized access.

In order to achieve efficient authentication, challenge/response authentication mechanism based on secret keys is widely used in wireless networks [1]. However, the credentials of the Mobile Station (MS) are encrypted and transmitted hop-by-hop for remote verification among

authentication servers in challenge/response authentication. This remote transmission and encryption/decryption of credentials increases the overhead of communications, thus influences many system performance parameters such as authentication cost, delay, arrival rate, and call dropping probability, system utilization, due to extended waiting time. e.g. transmission time, processing time, key generation time, etc. Therefore, the tradeoff between security service and system performance should be concerned in different scenarios, because users have different preferences on security and performance from time to time.

## 2. Security model

In this paper, we analyze the impact of security mechanisms such as authentication, encryption/decryption on system performance quantitatively. First, we propose a system model, which concentrates on mobile WiMAX components. This model is highly consistent with many WiMAX Base station (BS) networks in which each group is controlled by Access Service Network (ASN) with one or more ASN controlled by CSN, [2-7]. This consistency guarantees that our analysis is applicable in realistic mobile WiMAX environments. Second, we classify the handoff authentication type and security levels with regard to the nature of security, i.e., information secrecy, data integrity, confidentiality and resource availability, and study the effects of security mechanisms on system performance at different security levels. Third, while we focus on mobile WiMAX, we recognize the highly important parameter such as handover. System performance parameters that we investigate in this paper include authentication cost, delay, and arrival rates of requests and scanning time, all of which are considered in combination with important network

parameters such as mobility and traffic patterns.

## 3. System modeling

We consider a generic system model for WiMAX network with respect to the security and system performance. In which the security is defined with regard to security levels, and the system performance that are evaluated with authentication cost, delay and scanning time. The modeling system depends on two main aspects. One is to describe the handover authentication interaction between autonomous communication entities i.e. BSs, ASNs, CSNs networks; the other is to illustrate the encryption/decryption and key generation within the network. The system model is depicted in Figure 1.

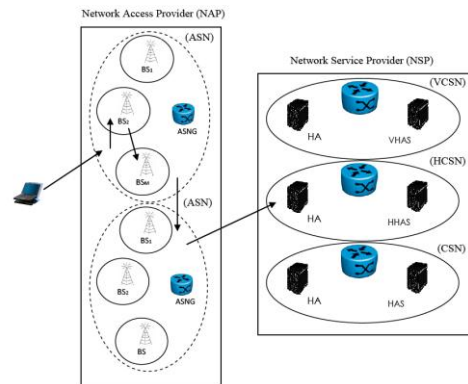


Figure 1: System model of secure handover authentication in WiMAX network.

- |  |   |
|--|---|
| <b>MS:</b> mobile Station                | <b>HAS:</b> Home Authentication Server    |
| <b>BS:</b> Base Station                  | <b>VAS:</b> Visitor Authentication Server |
| <b>ASN:</b> Access Service Network       | <b>HA:</b> Home Agent                     |
| <b>CSN:</b> Connectivity Service Network | <b>NAP:</b> Network Access Provider       |
| <b>VCSN:</b> Visitor CSN                 | <b>NSP:</b> Network Service Provider      |
| <b>HCSN:</b> Home CSN                    |   |

In this model, there are a number of M autonomous wireless BSs networks. Each one or group of BSs allocated in the Access Service Network (ASN) domain connected with ASN Gateway (ASNG). Furthermore,



all the ASNs are connected together to the Connectivity Service Network (CSN), included in central authentication servers in the Connectivity Service Network (CSN) domain. The Local Authentication Server (LAS) takes charge of authentication for visiting MSs within same ASN that subscribe services in current ASN domain. The Home Authentication Authorization and Accounting server (HAAA) is responsible for the authentication of the MSs that subscribe services in current CSN domain. The trust relationships between these LASs and HAAA are maintained through a (CSN), while its relationship reasonable for the authentication of MS with contact Home Agent (HA) server to take information about its MS. Here, a BS is a function unit that can control and transmit data for MSs with established security associations SAs. An LAS controls the authentication in the ASN domain with number of M of BS in the same ASN. The LAS also shares an SA with it that is trusted by and connected with the HAAA, HA of foreign mobile users.

#### 4. Performance analysis

We categorize the performance metrics into security and system performance parameters. The security parameter is represented by security levels, at which different levels of protection are provided. Meanwhile, we consider authentication cost, delay, arrival rates, and handover scanning time as the system performance metrics for evaluation.

#### 5. Security levels classification

The gap between the performance and security analysis demands quantization of security for the engineering researches. Therefore, the concept of security level

becomes widely used for security evaluation [8]. The classification of security levels in this research is either based on what security level should be needed to secure communication between entities, the information sensitivity, or based on the key length. The classification of security levels is shown in Table 1 according to the security functions as, user authenticity, protection for integrity, secrecy and resource availability. This implies different actions in challenge/response authentication.

Table 1: Security level classification.

Level	1	2	3	4
Integrity	No	No	No	Yes
Secrecy	No	No	Low	Yes
Confidentiality	No	Low	Medium	High
Availability	No	Medium	Medium	High

**Security level 1:** When an MS needs services at security level 1, it sends out a resource request to the BS. The BS checks the resources for this request. If the resource for this service is available, the resource approval is replied to the MS to authorize the service. Figure 2 shows the signaling diagram for intra-ASN domain handoff authentication.

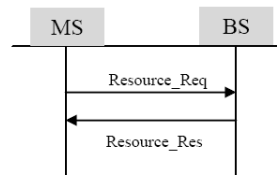


Figure 2: Intra ASN-domain handoff at security level 1.

In the inter-domain handoff authentication, (shown in figure 3), the mobile user must be register in HA in the foreign CSN area. Also, when the LAS receives the request, it sends registration messages to the HA through HAAA.

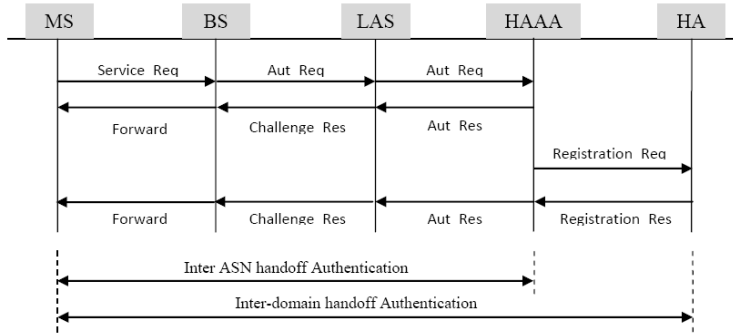


Figure 3: Inter ASN-domain handoff Inter-domain handoff authentication at security level1.

**Security level 2:** Authentication is implemented through a pre-defined list of medium access control (MAC) addresses and no keys are generated for the subsequent communication. In this case, when an MS needs resource in foreign ASN networks, it sends a request to the LAS through BS, which, in turn, requests the MAC address of the MS and relays it to the LAS for verification, (Figure 4). For intra-ASN domain handoff authentication, the LAS has the session SA of the MS, and can verify it.

For inter-ASN and inter-domain authentication (shown in Figure 5), the MS needs to be authenticated at the HAAA because there is no SA between the MS and the LAS. At security level 2, there is no protection available for data integrity and secrecy because no keys and algorithms are distributed to the MS for the communication. But the network resource is slightly protected by identifying the MAC address although the MAC address can be easily forged.

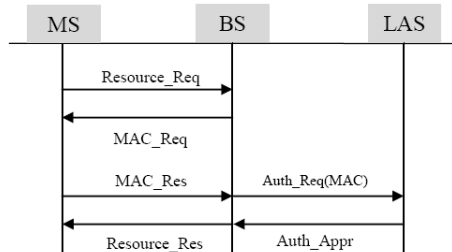


Figure 4: Signaling diagram at security level 2: intra ASN-domain handoff.

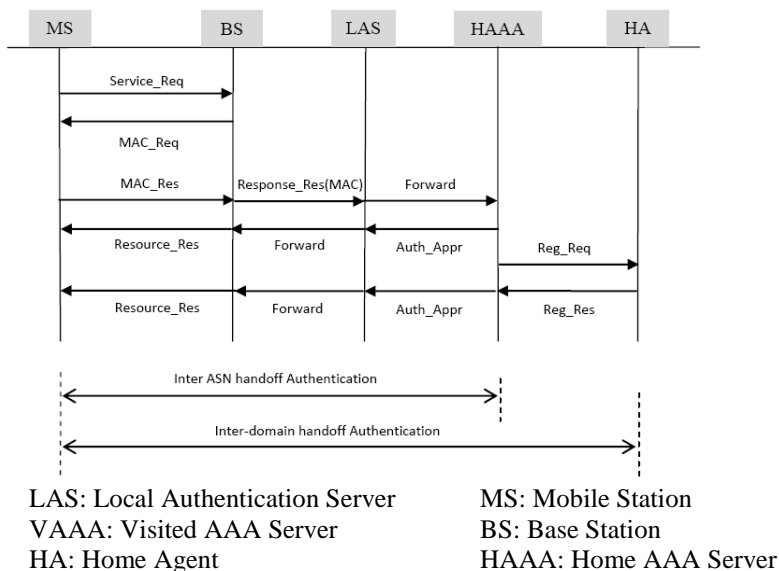


Figure 5: Signaling diagram at security level 2: Inter ASN and inter-domain handoff authentication.

**Security level 3:** Authentication is implemented with credentials encrypted with a shared SA, and no keys are generated for subsequent communications. In this case, the SA between the MS and HAAA is used for inter-ASN domain (Figures 6) and inter-domain (Figures 10) handoff authentications.

Compared to the signaling process at security level 2, the signaling process at security level 3 is almost the same. The difference is that a pair of values (challenge/ response), are used to authenticate the MS instead of the MAC address. The challenge value is a random value generated and sent to the MS from the LAS. The MS encrypts the challenge value with corresponding SA [9].

Almost all cases for WiMAX used RSA to implemented (challenge/response) mechanisms. In the intra ASN-domain handoff authentication, the MS encrypts the challenge value with the SA shared with the

LAS during communication session, and replies the result, a response value to the LAS. The LAS can verify the challenge value by decrypting the response value with the same SA. However, in inter ASN-domain and inter-domain handoff authentication; there is no SA between the MS and the LAS at this moment. The MS must be authenticated by the HAAA. After decrypting and verifying the response value at the HAAA of the MS, the authentication approval is sent back to the LAS for authorizing the resource to the MS. Specially, the registration process is required during the inter-domain handoff authentication. At security level 3, the network resources can be protected by only allowing the access of legitimate users. However, since the data transmission is not protected with encryption after authentication, the integrity and secrecy are not guaranteed. Furthermore, the network resource may be compromised due to the lack of data integrity and secrecy.

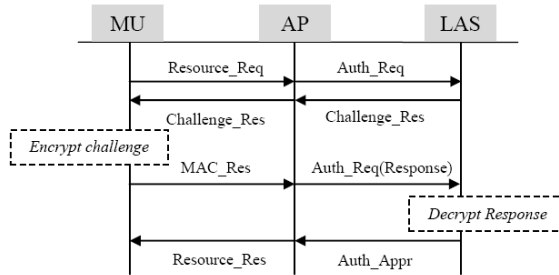


Figure 6: Signaling diagram at security levels 3: intra ASN-domain handoff.

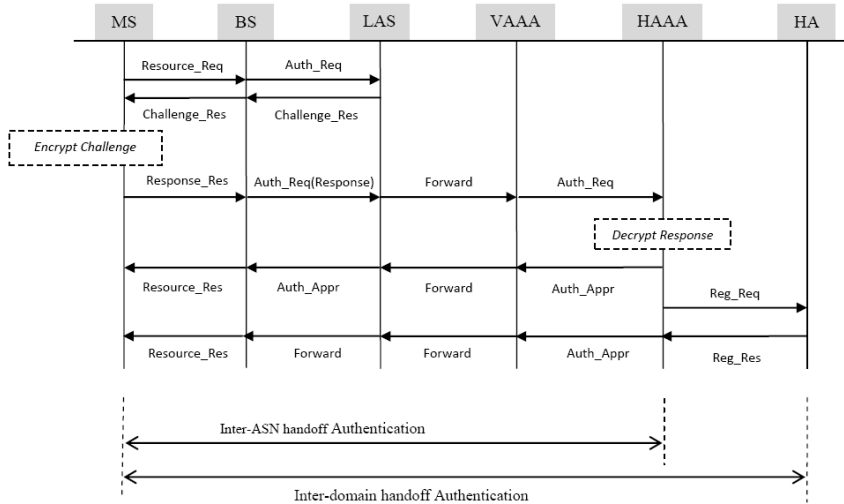


Figure 7: Signaling diagram at security levels 3: Inter ASN-domain handoff authentication.

**Security level 4:** Authentication is implemented with shared SA, and keys are generated for data encryption and message integrity check. The signaling diagram at this security level is shown in Figures 8 and 9 respectively.

This is similar with that at security level 3. The difference between these two security levels is that keys are generated, by the widely used scheme in WiMAX for keys generation which is RSA. After key is generated, it is also encrypted, and transmitted to the communication partners

(MS), after the keys are decrypted by the communication entities, the keys will be used for encryption/decryption and message authentication code to protect the communication. Therefore, the integrity of data can be guaranteed by message integrity check techniques, and the secrecy is protected with data encryption. The network resource is also protected since the identification cannot be compromised due to the protection of data integrity and secrecy.



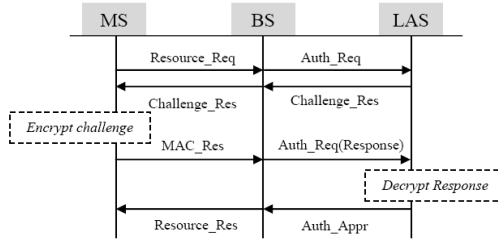


Figure 8: Signaling diagram at security levels 4: intra ASN-domain handoff.

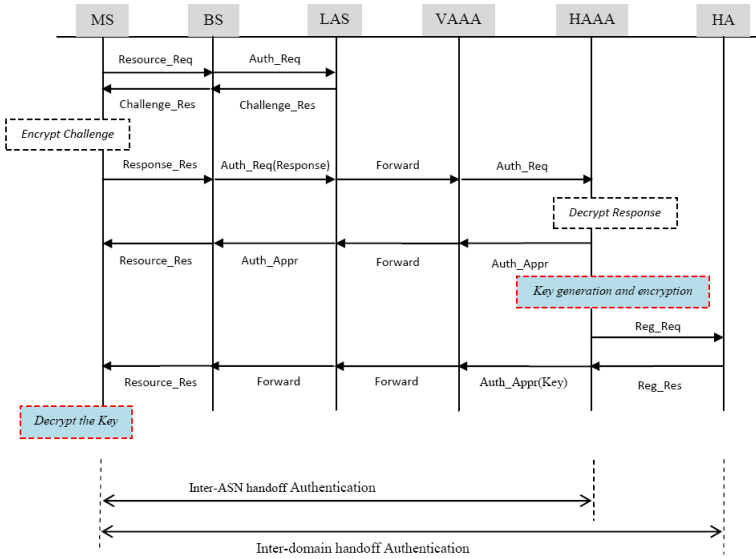


Figure 9: Signaling diagram at security levels 4: Inter ASN-domain handoff authentication.

## 6. Analytical model & Results

In this paper, we focus on the scenario that an MS is roaming into foreign domains (mobile WiMAX). Then, the intra ASN-domain handoff authentication, inter-ASN domain handoff authentication, and inter-domain handoff authentication will be included in our analysis.

### 6.1. Mobility pattern scenario.

The mobility pattern of a Mobile Station (User) in our research is represented by its residence time in one BS, denoted by  $T_r$ . We assume that  $T_r$  is a random variable and the probability density function (PDF) of residence time  $T_r$ , is Gamma distribution

with mean  $m = 1/\mu_r$  minute and variance  $v = 1/\mu_r^2$  [10],

$$f_r(t, \gamma, m) = t^{\gamma-1} \frac{e^{-t\mu_r}}{m^\gamma \Gamma(\gamma)}, \quad (1)$$

for  $t, \gamma$ , and  $m = 1/\mu_r > 0$

Where,  $\mu_r$  is service rate of authentication request.

Then, for easy computations and analysis we need to transfer from time domain to S-domain by applying Laplace transform. The Laplace transform of probability density function (PDF)



$f_r(t, \gamma, 1/\mu_r)$  is  $F_r(s, \gamma, 1/\mu_r)$  and can be written as,

$$F_r(s, \gamma, m) = \left( \frac{\mu_r \gamma}{s + \mu_r + \gamma} \right)^\gamma, \quad (2)$$

$$\text{where } \gamma = \frac{1}{\mu_r^2}$$

Furthermore, when MS moves through the network, then, if the number of BSs passed by an MS is assumed to be uniformly distributed between  $[1, M]$  the probability density function (PDF) of the residence time in the all network domain denoted as of  $f_M(t, \gamma, m)$ , can be expressed with a Laplace transform  $F_M(s, \gamma, m)$ , as follows:

$$F_M(s, \gamma, m) = \frac{1}{M} \left( \frac{\mu_r \gamma}{s + \mu_r \gamma} \right)^\gamma \frac{1 - \left( \frac{\mu_r \gamma}{s + \mu_r \gamma} \right)^M}{1 - \left( \frac{\mu_r \gamma}{s + \mu_r \gamma} \right)^\gamma} \quad (3)$$

Then, when we take in the account the residence time in all network domain, and the mean value of residence time in this network domain we can differentiate the residence time in equation (3) denoted by  $T_M$  as follows.

$$T_M = - \left. \frac{\partial F_M(s)}{\partial s} \right|_{s=0} = \frac{M+1}{2\mu_r} \quad (4)$$

Where  $T_M$  is residence time in all network domain.

## 6.2. Traffic pattern

In this paper, we used call arrival rate and call duration time to indicate traffic patterns. First, we assumed that the call arrival rate of an MS, which includes the incoming calls and outgoing calls, is a Poisson process with average rate  $\lambda_u$ , in this case the PDF of the call inter-arrival time, denoted as  $f_{TR}(\lambda, t)$ , can be determined by,

$$F_{T_A}(t) = \lambda_u e^{-\lambda_u t} \quad (5)$$

Moreover, we assumed that a call duration time, denoted as  $T_D$ , has an exponential distribution with mean value  $1/\eta$ .

Then, the probability density function PDF of exponential distribution (call duration time), denoted as  $f_{TD}(t, \eta)$ , can be written as.

$$f_{T_D}(t) = \eta e^{-\eta t} \quad (6)$$

## 6.3. Performance evaluation analysis

This section discusses the impact of authentication on the performance of the WiMAX communication from different handoff situations.

### 6.3.1. Average authentication cost

In this section, we define authentication cost as the sum of two main components, first one is signaling load which contains all moves from reference point to another and second is the processing load which include all processing for cryptographic techniques during each authentication operation. The average authentication cost,  $C(i)$ , is defined as the sum of the authentication cost over a number of handover authentication requests per unit time at security level  $i$ , which can be written as,

$$C(i) = \sum_{q=1}^3 \lambda_q [C_q^{(s)}(i) + C_q^{(p)}(i)] \quad (7)$$

Where  $q$  is the index of authentication type which represents three types of authentication handoff as discussed in the previous chapter, where  $q = 1$ , is an intra-ASN domain handoff authentication,  $q = 2$  means an inter-ASN domain handoff authentication, and  $q = 3$  is an inter-domain handoff authentication.

We show the cost components by denoting  $C_q^{(s)}(i)$  and  $C_q^{(p)}(i)$  as the signaling load and processing load of



cryptographic techniques, respectively, for the authentication of type  $q$  at security level  $i$ .  $\lambda_q$  is the arrival rate of requests for the authentication type  $q$ , which is related with the mobility and traffic patterns of MSs.

### 6.3.2. Average authentication delay

We define authentication delay as the time from when an MS sends out an authentication request to the instant the MS receives the authentication reply. The average authentication delay,  $T(i)$ , is defined as the sum of an authentication delay over a number of authentication requests in a unit time at security level  $i$ . Then,  $T(i)$  can be written as,

$$T(i) = \sum_{q=1}^3 \lambda_q T_q(i) \quad (8)$$

Where  $T_{q(i)}$  is the authentication delay per operation at security level  $i$  for authentication type  $q$ , and  $\lambda_q$  is the arrival rate of authentication requests with type  $q$ .

## 6.4. Performance analysis per authentication

In this section, we analyze the impact of security on system performance in terms of authentication cost, delay, arrival rates, and handover scanning time.

### 6.4.1. Authentication cost per operation.

The authentication cost,  $C_q$  ( $q = 1,2,3$  and  $i = 1,2,3,4$ ), is composed of  $C_q^{(s)}(i)$  and  $C_q^{(p)}(i)$  as defined in equation (7), which depend on the authentication type  $q$  and security level  $i$ . For convenient analysis, we define a set of cost parameters in Table 2.

Table 2: Authentication cost parameters.

Symbol	Description
$C_s$	Transmission cost on one hop
$C_e$	Encryption cost on one hop
$C_v$	Verification cost at an authentication server
$C_d$	decryption cost on one hop

$C_g$	Key generation cost
$C_{ts}$	Transmission cost for a session key to other communication identities
$C_{rg}$	Registration cost

### 6.4.1.1. Intra ASN-domain handoff authentication

We will derive the cost formula at  $q=1$  for ( $i=1, 2, 3$ , and 4) as:

The transmission costs,  $C_q^{(s)}(i)$ , can be derived from the signaling diagrams in Figures 2 to 9, respectively, by observe how many hops MS does need for authentication request sent out into the receive admission successfully, as follows:

From Figure 3 at security level 1, MS needs to request challenge value from the LAS through a BS first. The distance that the messages traverse is a 2 step in this case. Then we can write the signaling cost at  $q=1$  and  $i=1$  as,

$$C_1^{(s)}(1) = a_{1,1} \cdot C_s = 2 \cdot C_s \quad (11)$$

At security level 2 MS needs resource request from BS. It sends a request to the BS, which need 2 steps which, in turn, requests the MAC address of the MS and relays the MAC address to the LAS for verification. These need 4 steps to be added, as follows,

$$C_1^{(s)}(2) = a_{1,2} \cdot C_s = 6 \cdot C_s \quad (12)$$

In the same way we can obtain the other security levels 3 and 4, and so on

$$C_1^{(s)}(i) = a_{1,3} \cdot C_s = a_{1,4} \cdot C_s = 8 \cdot C_s \quad (13)$$

Similar to the analysis in (13), according to the signaling diagrams in Figures 3, and 5 to 12,  $C_1^{(p)}(i)$  can be written in a general formula as,

$$C_q^{(p)}(i) = \vec{b}_{q,i} \cdot \vec{x}_p, \text{ at } q=1, 2, 3 \text{ and } i=1, 2, 3, 4,$$

Where  $\vec{x}_p$  is a vector to show the cost parameters defined as:



$$\bar{x}_p = [C_e, C_v, C_d, C_g, C_{ts}, C_{rg}] \quad (14)$$

Where all of the cost parameters ( $C_e, C_v, C_d, C_g, C_{ts}, C_{rg}$ ) are defined in table 2, and  $\bar{b}_{q,i}$  are the same dimension vector of  $\bar{x}_p$ . To illustrate the parameters for authentication process we need to determined for all security levels at authentication type  $q=1$  by compact form to easy and convenient analysis,

From Figures (2 to 12) for  $q=1$  at security level  $i=1$ ,

$$\bar{b}_{1,1} = [0,0,0,0,0,0] \quad (15)$$

$$C_1^p(i) = \begin{cases} 0, & i = 1 \\ C_v, & i = 2 \\ C_e + C_v + C_g + (N_h + 2), & i = 3 \\ C_e + C_v + C_g + C_{ts} + (N_h + 2), & i = 4 \end{cases} \quad (20)$$

#### 6.4.1.2. Inter ASN-domain handoff authentication

$$C_2^s(i) = \begin{cases} 9C_s, & i = 1 \\ 11C_s + N_h, & i = 2 \\ 16C_s + N_h, & i = 3 \\ 16C_s + (N_h + 2), & i = 4 \end{cases} \quad (21)$$

$$C_2^p(i) = \begin{cases} 0, & i = 1 \\ C_v, & i = 2 \\ C_e + C_v + C_g + C_{ts} + (N_h), & i = 3 \\ C_e + C_v + C_g + C_{ts} + (N_h + 2), & i = 4 \end{cases} \quad (22)$$

#### 6.4.1.3. Inter-domain handoff authentication

$$C_3^s(i) = \begin{cases} 11C_s + (N_h + 2), & i = 1 \\ 13C_s + (N_h + 2), & i = 2 \\ 13C_s + (N_h + 2), & i = 3 \\ 13C_s + (N_h + 4), & i = 4 \end{cases} \quad (23)$$

$$\bar{b}_{1,2} = [2,1,0,0,0,0] \quad (16)$$

$$\bar{b}_{1,3} = [1,1,1,0,0,0] \quad (17)$$

$$\bar{b}_{1,4} = [1,1,1,0,10,0] \quad (18)$$

Similar to the above mentioned analysis we can collect parameters by compiling the all cost parameters in the close form for  $q=1, 2, 3$  and ( $i=1, 2, 3, 4$ ) as,

$$C_1^s(i) = \begin{cases} 2C_s, & i = 1 \\ 6C_s, & i = 2 \\ 8C_s, & i = 3,4 \end{cases} \quad (19)$$



$$C_3^p(i) = \begin{cases} C_{rg}, & i = 1 \\ 2C_v + C_{rg}, & i = 2 \\ C_e + C_v + C_g + C_{ts} + (N_h + 2), & i = 3 \\ 2C_e + 2C_v + 2C_g + 2C_{ts} + C_{rg} + (N_h + 4), & i = 4 \end{cases} \quad (24)$$

**6.4.2. Delay per authentication.**

To derive the delay for different types of authentications in different security levels, we use the same signaling diagram

shown in Figures 2 to 9. We also define a set of time delay parameters shown in Table 3 for convenient description.

Table 3 Authentication time parameters.

Symbol	Description
$T_{pr}$	Message propagation time on one hop
$T_{tr}$	Message transmission time on one hop
$T_e$	Message encryption time on one hop
$T_a$	Authentication request service and waiting time at the BS
$T_{rq}$	Authentication request service and waiting time at servers
$T_v$	Authentication request verification and waiting time at the HAAA
$T_d$	decryption time on one hop
$T_g$	Key generation time at the HAAA
$T_{ts}$	Transmission time for the session key to the other communication identities such as HA, MS
$T_{rg}$	Registration request service and waiting time at the HA

As mentioned previously at authentication delay,  $T_q(i)$  can be expressed as,

$$T_q(i) = \vec{d}_{q,i} \cdot \vec{x}_i, \text{ For } q=1, 2, 3, \text{ and } i=1, 2, 3, 4.$$

Here,  $\vec{x}_i$  is a vector defined time delay parameters are given below,

$$\vec{x}_i = [T_{pr} + T_r, T_e, T_a, T_{rq}, T_v, T_d, T_g, T_{ts}, T_{rg}] \quad (24)$$

Where all the time components are defined in Table 3, and,  $\vec{d}_{q,i}$  is the same dimension vector of  $\vec{x}_i$  to illustrate the existing delay parameters and its numbers at each operation defined as discussed below:

From the signaling diagram in Figures (2 to 8) we can compute the  $\vec{d}_{q,i}$ , let us compute the complicated case of this vector at  $q=3$  and  $i=4$ .

Since the authentication request process in the case of  $q= 3$  and  $i = 4$  needs to pass the BS four times, the coefficient of  $T_a$ , i.e., authentication request service and waiting time, is 4. Because the authentication messages cross the intermediate authentication servers 2 times, the coefficient of  $T_a$ , i.e., authentication request service and waiting time at a local authentication server, is 2. The authentication message also traverses the HAAA twice when registration is needed. Thus, the coefficient of  $T_v$ , i.e., authentication request service and waiting time at the HAAA, is 2. Since the



authentication in this case also needs one time registration at the HA, the coefficient for  $T_{rg}$ , i.e., registration request service and waiting time at an HAAA, is 1. Because a key is generated at the HAAA for the communication of the MS, the coefficient of  $T_g$ , i.e., key generation time at the HAAA, is 1. The HAAA also needs to transmit a corresponding key to the MSs communication partners, after registration in HA, thus the coefficient of  $T_{ts}$ , i.e., transmission time for the session key to the other communication identities such as HA, is 2. In addition, two pairs of encryption and decryption time are needed between the MS and its HAAA. One pair is for encrypting and decrypting the challenge/response values; the other is for encrypting and decrypting the session key. Thus, the both coefficients of  $T_e$  and  $T_d$  i.e., a pair of encryption and decryption time for a value, is 4.

Then, now we can compute all the delay components for each authentication handoff

#### 6.4.2.1. Intra- ASN domain handoff authentications

$$T_1(i) = \begin{cases} 2(T_{pr} + T_{tr}) + T_a & i = 1 \\ 6(T_{pr} + T_{tr}) + 2T_e + 2T_a + T_v & i = 2 \\ 8(T_{pr} + T_{tr}) + 2T_e + 4T_a + 2T_v + T_d & i = 3,4 \end{cases} \quad (36)$$

#### 6.4.2.2. Inter-ASN domain handoff authentication

$$T_2(i) = \begin{cases} 2(T_{pr} + T_{tr}) + T_a & i = 1 \\ 2(N_h + 1)(T_{pr} + T_{tr}) + 2T_e + 3T_a + 2T_{rq} + T_v & i = 2 \\ 2(N_h + 1)(T_{pr} + T_{tr}) + 2T_e + 4T_a + 2T_{rq} + T_v + T_d & i = 3 \\ 2(N_h + 2)(T_{pr} + T_{tr}) + 2T_e + 4T_a + 2T_{rq} + T_v + 2T_d + T_g + T_{ts} & i = 4 \end{cases} \quad (37)$$

#### 6.4.2.3. Inter-domain handoff authentication

$$T_3(i) = \begin{cases} 11(N_h + 1)(T_{pr} + T_{tr}) + 2T_a + 2T_{rq} + T_{rg} & i = 1 \\ 13(N_h + 2)(T_{pr} + T_{tr}) + 2T_e + 3T_a + 2T_{rq} + 2T_v + T_{rg} & i = 2 \\ 10(N_h + 3)(T_{pr} + T_{tr}) + 2T_e + 4T_a + 3T_{rq} + 2T_v + T_d + T_{rg} & i = 3 \\ 14(N_h + 4)(T_{pr} + T_{tr}) + 2T_e + 4T_a + 3T_{rq} + 2T_v + 2T_d + T_g + T_{ts} + T_{rg} & i = 4 \end{cases} \quad (38)$$

type with each security levels on an arrays form.

$$\vec{d}_{1,1} = [2,0,1,0,0,0,0,0] \quad (25)$$

$$\vec{d}_{1,2} = [6,2,3,0,1,0,0,0] \quad (26)$$

$$\vec{d}_{1,3} = [8,2,2,0,2,1,0,0] \quad (27)$$

$$\vec{d}_{2,1} = [6,0,1,0,0,0,0,0] \quad (28)$$

$$\vec{d}_{2,2} = [11(N_h + 1), 2, 2, 2, 1, 0, 0, 0] \quad (29)$$

$$\vec{d}_{2,3} = [12(N_h + 2), 2, 4, 2, 1, 1, 0, 0] \quad (30)$$

$$\vec{d}_{2,4} = [12(N_h + 2), 2, 4, 2, 1, 2, 1, 1, 0] \quad (31)$$

$$\vec{d}_{3,1} = [11(N_h + 1), 0, 2, 2, 0, 0, 0, 0, 1] \quad (32)$$

$$\vec{d}_{3,2} = [11(N_h + 2), 2, 3, 2, 2, 0, 0, 0, 1] \quad (33)$$

$$\vec{d}_{3,3} = [10(N_h + 3), 2, 4, 3, 2, 1, 0, 0, 1] \quad (34)$$

$$\vec{d}_{3,4} = [14(N_h + 3), 2, 4, 3, 2, 2, 1, 1, 1] \quad (35)$$

Also for more illustration as mentioned at cost analysis we collected the delay vectors in the main equation for each authentication type.



### 6.4.3. Scanning time before handover

This issue is related to the level of security applied when the MS looking for the best neighboring before handover initiation.

In IEEE 802.16e broadband wireless networks, handover delay is mainly caused by target network re-entering process. Decreasing handover delay can improve the successful probability of handovers.

In pre-registration, target BS obtains the service flow and authentication information of this MS through backbone networks before handover. As described previously, although target BS knows the service flow and authentication information about this MS, it still has to send CID updating message to the MS by using REQ-RSP message. Therefore, the average time of pre-registration process is half of the average time for the overall registration process.

In order to analyze and compare the performance of the handover, handover delay is studied in the IEEE 802.16e model. With the cell load ratio is  $Rload$  ( $0 \leq Rload \leq 100\%$ ). Required time parameters of each stage are defined as follows:

- $T_{sync}$  : average time required for downlink synchronization.
- $T_{cont\_rng}$ : average time required for contention based ranging.
- $T_{rng}$  : average time required for fast ranging.
- $T_{Auth}$ : average time required for authorization (authentication time).
- $T_{reg}$ : average time required for registration.

Table 4 (scanning time parameters).

$T_{Scan-1}$	Time scan at security level 1
$T_{Scan-2}$	Time scan at security level 2
$T_{Scan-3}$	Time scan at security level 3
$T_{Scan-4}$	Time scan at security level 4

Each of  $T_{Scan-1}$ ,  $T_{Scan-2}$ ,  $T_{Scan-3}$ ,  $T_{Scan-4}$ , are defined as the average time required for scanning at certain security level, when ‘Scan Type’ equals to 1, 2, 3, and 4 respectively. The number of neighbor BSs that need to be scanned or associated is assumed to be  $N$ .

#### Scan type 1

When ‘Scan Type’ = 1, i.e. MS scans neighbor BSs without association, MS only needs to downlink synchronize with the target BS so as to get the quality information of its physical channel, so  $T_{Scan-1}$  can be calculated is given by equation (39).

$$T_{Scan-1} = N \times T_{Sync} \quad (39)$$

#### Scan type 2.

When ‘Scan Type’ equals to 2, i.e. scan/association without coordination mode, MS not only needs to downlink synchronize with target BS, but also needs to execute a contention-based ranging, so is given by equation (40).

$$T_{Scan-2} = N \times (T_{Sync} + T_{Cont\_rng}) \quad (40)$$

#### Scan type 3.

When ‘Scan Type’ equals to 3, i.e. association with coordination mode, MS not only needs to downlink synchronize with target BS, but also needs to execute a fast ranging process. So  $T_{Scan-3}$  is calculated is given by equation (41).

$$T_{Scan-3} = N \times (T_{Sync} + T_{Rng}) \quad (41)$$

#### Scan type 4.

When ‘Scan Type’ equals to 4, i.e. network assisted association reporting mode, the only difference to association with coordination mode is that target BS does not send RNG-RSP message directly to MS. RNG-RSP message is firstly sent to serving BS through backbone networks. Then serving BS packs all RNG-RSP messages from scanned neighbor BSs into



MS during interleaving intervals of scan duration or normal operation time. Therefore, the average time required for fast ranging is half of that for a contention-based ranging.  $T_{Scn\_4}$  is given by equation (42).

$$T_{Scn\_4} = N \times (T_{Sync} + [1/2 \times T_{Rng}]) \quad (42)$$

### 7. Simulation Results

A Matlab program has been designed to simulate the system described above, depending on the scenarios and assumptions as previously discussed with the simulation parameters shown in table 5

taken into account the use of any RSA encryption scheme. In this case we used 1024 bits RSA modulus  $n$  and 64 bits Encryption exponent  $e$  to ensure security and privacy from breaking RSA algorithm. Moreover, two distinct primes  $p$  and  $q$  are chosen to be 512 bits and randomly generated. This will enable us to generate 1024 bits of RSA modulus  $n$ . Transfers have also been used to facilitate the Laplace transform and transfer of accounts from time domain to S domain to simplify computation process.

Table 5: simulation parameters.

Parameter	$C_s$	$C_e$	$C_v$	$C_d$	$C_g$	$C_{ts}$	$C_{rg}$
Value	10	1	2	1	1024 RSA	110	2
Parameter	$T_{pr}$	$T_{tr}$	$T_e$	$T_a$	$T_{rq}$	$T_v$	$T_{ts}$
Value	40 $\mu$ s	20 ms	1024 RSA	Vari	1024 RSA	1024 RSA	Vari
parameter	$T_g$	$N_h$					
value	2 ms	10hop					
parameter	$\lambda_u$	$\eta$	$\gamma$	$\mu_r$	$\zeta$		
value	0.1 min-1	0.1 min-1	225	1/15 min-1	15s-1		

#### 7.1. Authentication cost analysis.

Referring to equation (7), we note the influence of levels of security on the cost of handover authentication for different times for an MS stays within a one BS.

Figure 10, shows authentication costs at different security levels which decrease with the increase of the residence time of an MS in a BS. This is because the longer an MS stays in the BS, the less the intra-domain handoff authentication requests. If the residence time of an MS approaches infinity, the authentication cost will be stable on this security level more than any other security level, because it does not need authentication process in this case, as discussed previously.

We can see also that the security levels have different effects on the authentication cost at the same residence time in a BS. The higher the security level, the more the authentication cost because higher security levels impose more operations to provide secure services.

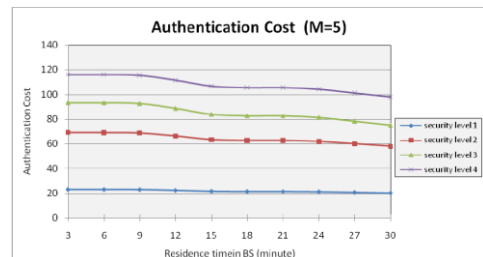


Figure 10 authentication cost Vs residence time in BS (M=3 in ASN)





To clarify this, figure 11 and 12 show the effects of increasing the number of BSs ( $M$ ) in the same ASN on the authentication cost, at the same residence time in the BS and for all security levels.

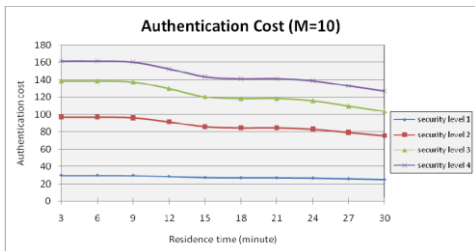


Figure 11 authentication cost Vs residence time in BS ( $M=5$  in ASN)

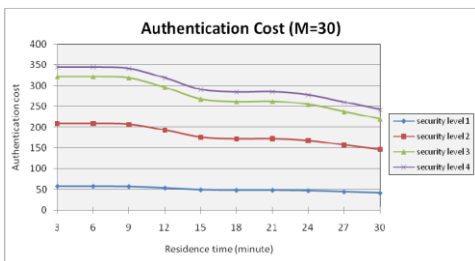


Figure 12 authentication cost Vs residence time in BS ( $M=30$  in ASN)

## 7.2. Authentication delay analysis

Referring to equation (8), we note the impact of security levels on the handover authentication delay for different residence times for a user stays within a one BS.

Figure 13 shows that the authentication delay increases with the increase of the residence time of an MS in a BS and tends to stabilize. Also, we can note that higher security levels cause more authentication delay because of more operations needed to provide secure services.

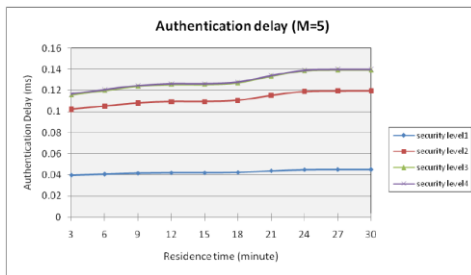


Figure 13 Authentication delay Vs Residence time in BS (minute) at ( $M=5$ ).

We can also note from the curves the considerable continuity between the third security level and fourth security level. This is because of the more similarity in the process between them.

Figure 14 & 15 show the effects of authentication delay at the same proposed residence time in BS for all security levels increasing the number of BSs ( $M$ ) in the ASN region.

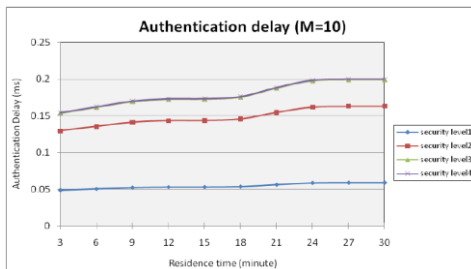


Figure 14 Authentication delay Vs Residence time in BS (minute) at ( $M=10$ ).

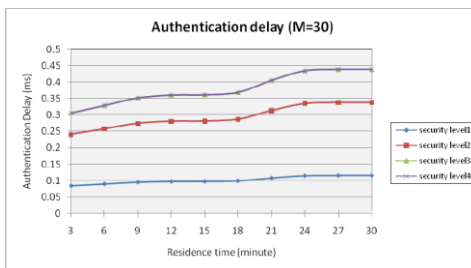


Figure 15 Authentication delay Vs Residence time in BS (minute) at ( $M=30$ ).



We note that the authentication delay increases with the increase of the number of BSs (M). This is because of increasing the number of handover which cause more operation to authenticate the user on each handoff. But it's more stable in the lower security levels.

### 7.3. Effect of cell load at different scanning type authentication efficiency

To provide the MS with best quality of service, the system has to choose the best neighbor BS; eventually the scanning time has the major effect on this process.

Equations (39 to 42) represent scanning time process which is needed to complete handover process successfully, without any impact on system performance.

Figure 16 shows that the scanning time for different scanning types, for different security levels at a given cell load ratio. This Figure also shows the scanning time is directly proportional to the cell load ratio.

Figure 17 shows the performance of scanning time when the number of BSs is increased. When the MS moves from one BS to another, it must choose the best neighbor under a set of conditions for the security and authorization as mentioned earlier.

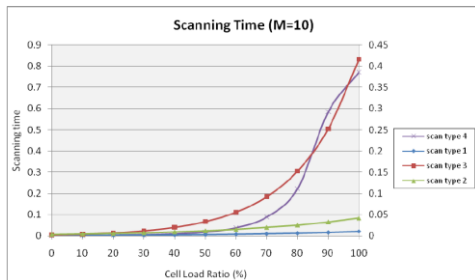


Figure 16 handover scanning time Vs cell load ratio at (M=5).

(Scan type1, 2 and3 secondary axis & scan type 4 primary axis)

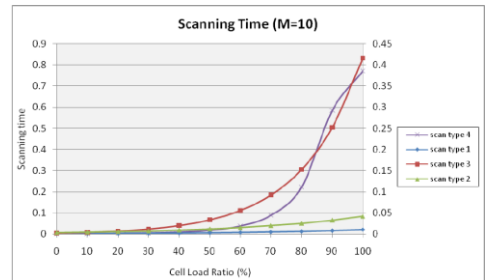


Figure 17 handover scanning time Vs cell load ratio at (M=10). (scan type1,2 and 3 secondary axis & scan type 4 primary axis)

For instance in figure 17, when M=10, the scan time of neighboring stations before the start of handover, at scanning type 4 must not be less than 0.2 ms, which is the maximum allowed authentication delay at security level 4 as shown in figure 17. Based on these results, we find that applying this security mechanism has no effect on the system performance.

### 8. Conclusion

In this paper, an analytic model for the handover authentication, using signaling scheme is presented and investigated, under the assumptions of Poisson arrivals and Gamma mobility pattern. The presented results conclude that the proposed scheme can provide user authenticity at each handover occur under classification of security level and authentication type.

The classifications of security levels to the four levels are provided to simplify the deals with the user situation in the network. So we note that the cost increases with their level of security applied this time and to varying degrees due to the residence time of the MS within the BS domain. Also, cost tends to stabilize with the more time an MS stays at the same domain.



The time it takes for a user to obtain authorization to enter the network (authentication delay) is affected significantly with the number of movements and this is due to the security level applied on time. Furthermore, authentication delay decrease with the more time a user stays at the same domain.

We also conclude in this paper, that the scanning time support the Authentication delay at both handover types and security levels without impact on system performance even at the maximum value of authentication delay.

### References

- [1] Hyung-Joon Kim, "IEEE 802.16/WiMAX Security", Dept. of Electrical and Computer Engineering Stevens Institute of Technology, Hoboken, New Jersey, 2006.
- [2] Tonderai Muchenje\*, Ntima Mabanza, Hippolyte Muyingi, "Security Issues on a Converged WiFi and WiMAX", Telkom Centre of Excellence in Developmental E-Commerce Computer Science Department University of Fort Hare, Alice South Africa, 2008.
- [3] Parviz Yegani, "WiMAX Overview", Cisco Systems IETF-64 Nov. 7-11, 2005 Vancouver, Canada.
- [4] ALCATEL-LUCENT, Alcatel-Lucent 9160 "WiMAX Access Control", at 30/10/2007, 1p7 edition. white paper, "WiMAX Network Architecture, Siemens", (Max Riegel), 2005-12-02.
- [5] Dr: Zeev Roth, "WiMAX Mobility", Alvarion view, WiMAX Forum, Sept 2007.
- [6] Dr. Mustafa Ergen, "The Access Service Network in WiMax", The Role of ASN-GW, WiChorus, Inc., 2008.
- [7] Wei Liang, Wayne Wang, "On performance analysis of challenge/response based authentication in wireless networks", Department of Electrical and Computer Engineering, North Carolina State University, Raleigh, NC 27695-7911, United States, Science Direct, October 2004.
- [8] Syed Ahson and Mohammed Ilyas "WiMAX application hand book" Edited by, CRC Press Taylor & Francis Group, 2008.
- [9] white paper, "Cisco Mobile Wireless Home Agent", Release 4, Cisco Public Information., C78-433929-01, 03/2008.
- [10] Gert de Cooman, "A gentle introduction to imprecise probability models and their behavioural interpretation", SYSTeMS research group, Ghent University, July 14<sup>th</sup> 2003.





## **Web based Image Authentication using watermarking system: an Overview**

Azizah Abdul Manaf<sup>1</sup>, Belal Ahmed Hamida<sup>2,3</sup>, Abdalrahman Salem Alfagi<sup>1,3</sup>, Ahmad W. Naji<sup>2</sup>

<sup>1</sup>Faculty of Computer Science and Information System University Technology Malaysia International Campus Kuala Lumpur alfagi2008@gamil.com

<sup>2</sup>Department of Electrical and Computer Engineering Kulliyyah of Engineering International Islamic University Malaysia 50728 Kuala Lumpur, Malaysia

<sup>3</sup>Engineering Academy Tajoura - Libya

### **ABSTRACT**

With the appearance of digital libraries and the rapid growth of information archive centers on the Internet, The security of information in the web pages has gained more attentions from all researchers due to the importance of digital media integrity in our life. Unlike hardcopies, digital data can be easily modified and distributed. Watermarking is the solution to this issue. By embedding a secure, identifiable mark into the digital data, the ownership, trustiness and content integrity will be ensured. In addition, an image alteration and modification of the watermarked image can be detected. The goal of this paper is to put into perspective the watermarking methods of web page authentication based on principal requirements of watermarking system and its properties as well as the desirable features for an effective performance in order to save the integrity and confidentiality of the web pages from any unwanted or illegal modification. In addition, different web page authentication algorithms discussed concerning to the advantages and disadvantages.

**Keywords :** Digital watermark, Authentication, Web page. Watermark feature, advantages and disadvantages.

### **1. Introduction**

The security demand is getting higher in these days due to easy recreation of digitally generated multimedia data. The rapid growth of the Internet and digital media manifests itself in widespread public forms such as the digital image, the MPEG, and so on, because digital images are easy to copy and transmit. Web sites

are the favorite target for modification and alteration of its contents and this increase the concerns of the owners about the integrity of their sites, such as medical and military sites. Many researchers are aware of the issues of copyright protection, image authentication, and proof of ownership [1].



There are many solutions have been proposed, the traditional method used for authentication is cryptography, where the data is hidden from unauthorized person this preserve confidentiality. The popular method of cryptography is public key encryption, which encrypts data using a private key, and an associated public key used for decryption of secret message. The problems that might be arisen in this method are difficulty of maintenance and distribution of public key [2]. It has great strength in confidentiality, but when the data revealed to unauthorized personnel, there is no protection for content it-self, which is integrity control. Recently, most researchers use a Watermarking system as technique to embed secret information into content for copyright protection and Authentication. A web based image authentication method based in digital watermarking described in this paper. It can provide more controls to image owners and conveniences to clients who want to get authenticity of image by integrating benefits of using Internet to the watermark system. There are several important issues in the watermarking system. First, the embedded watermark should not degrade the quality of the image and should be perceptually invisible to maintain its protective secrecy. Second, the watermark must be robust enough to resist common image processing attacks and not be easily removable; only the owner of the image ought to be able to extract the watermark. Third, the blindness is necessary if it is difficult for us to obtain the original image and watermark [3].

This paper organized as follows: section1, an overview of watermarking system. Section2 is a brief description for watermarking system properties, important requirement for image authentication and watermark application. Section 3 describes Web-Based authentication methods. Section 4 is the related work. Last section is the conclusion.

## 2. Watermarking System

Embedding watermark within a host image is the essence part in watermarking. The information embedded through the modification of pixel, directly using spatial domain or indirectly by frequency domain [4]. The main goal of using watermark in digital communication system is to ensure the existence of integrity and reliability during images transfer between to authorize parties [4].

Thus, the watermarking paradigm is similar to a digital communication system, where its goal is to ensure reliable information shared between the sender and receiver. Watermarking system is composed of three basic parts, embedding part, channel part and recovery part. As an input, the first part requires the watermark ( $w$ ), the cover image ( $c$ ) in which " $w$ " is to be insert and a watermarked work is the output of the embedding system as shown in figure 1.

On the other hand, the decoder is use for watermark extraction and verification. More specifically, the decoder takes the watermarked image as input and extracts the original watermark image opposite to embedding scheme. Furthermore, the watermark can be placed anywhere inside

the web sites, image, text, etc. Normally, the embedding rule designed to preserve image security, fidelity as well as to enhance the robustness of the system. The output of the encoder is the watermarked image [6].

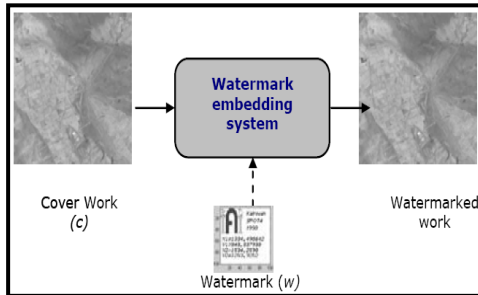


Figure1. Classical watermark system

### 2.1. Properties of Digital Watermark Systems

Watermarking systems has three main properties it could has more but that dependent on the role of watermark that it will play, and also the application. The three properties typically associated with watermark embedding process are Fidelity, Robustness and capacity as show in figure 2

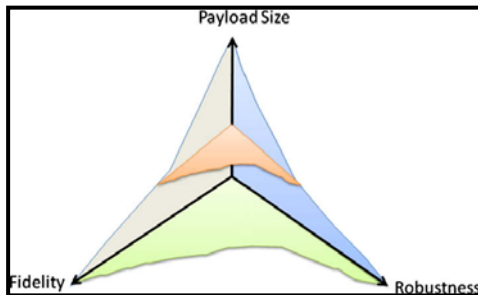


Figure 2. Watermark system properties

**Fidelity:** The main point in fidelity (imperceptible) of the watermarking system is the perceptual difference between the original image and watermarked image, which should be unnoticeable by viewers. However, if viewers noticed a different between the watermarked image and the original then the watermarking system scheme is lossless [7].

**Robustness:** which is the ability to detect the watermark after common signal processing [8]. In other words, embedded watermark should be retrievable before watermarked image is severely degraded to a useless degree [9].

**Capacity:** Capacity is refers to size of the information or number of the bits encoded within unit of time or within a work. For example, the web page data payload refers to either the number of bit per field or frame. The challenges that most researchers faced is to enhance the relationship between the three major properties at same time .This is due to, the conflicting between them [8].

### 2.2. Applications of Digital Watermark

A digital watermark is an invisible signal that is embedded directly in the digital media (images, audio, video, 3D objects, etc.) so that it is inseparable from the digital media. There is a wide range of applications of digital watermarking, including copyright protection, authentication, fingerprinting, copy control and broadcast monitoring, indexing, and medical safety [2]. However, for different kinds of applications, digital watermarking



system has different properties. In addition, the classification of the watermark is mainly based on properties and the characteristics that all most dependent on the type of the application. And to have an effective, watermarking algorithms have to be carefully designed to make a tradeoff between these properties [10].

### 2.3. Authentication Requirements

Each watermarking application has its own special requirements with regard to robustness; security, imperceptible and the amount of data need to be embedded as shown in Figure 3. For example, when digital watermarks are used for purpose of authentication, the invisibility and security should be obvious, while robustness and capacity are just acceptable.

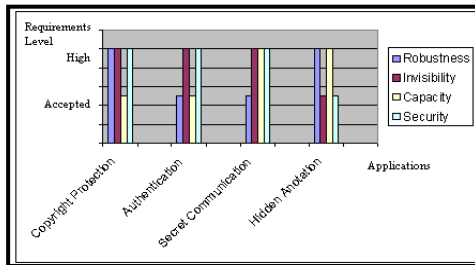


Figure 3. Watermark requirements

With respect to the application of authentication in watermark system, invisible watermarks can classified as robust, semi-fragile and fragile. Robust watermarks can resist image attacks while semi-fragile watermarks can destroyed only when user-specified threshold were exceeded. Fragile watermarks can easily demolished if a slight change occurs on the host image. As a result, unauthorized

modifications on the watermarked images detected easily. That is why fragile watermarking methods were mainly use for the purpose of all multimedia authentications [11].

### 2.4. Watermark in communication system

The basic elements of a watermarking system combined with classical communications system illustrated in Figure 4.

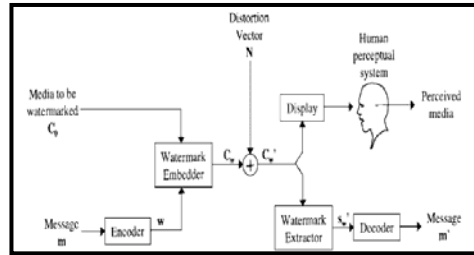


Figure 4. The basic elements of watermark in communication system

### 3. Web-Based Authentication Methods

The methods discussed in this section are Internet based client-server model and watermark embedding scheme. The web-based authentication system consists of two parts: one is a watermark embedding system and the other is authentication system. The first part of embedding system installed in the server as application software that any authorized user could access to the server and generate watermarked image. Once image distributed to other parties, client can access to authentication web page to get verification of image [3]. However, the integrity and reliability of Webpage are





important since the information of media is spread throughout on the internet. For this regard, there are different methods of web page discussed in [12], and presented below.

- (1) **Based on invisible character method:** Invisible character, such as blank (0x20) and tab (0x09), could be embedded at the back of every row of webpage, and has no difference in normal show on the browser. For example, the software denotes the bits “0” and “1” with blank and tab, and then embeds such 8 bytes at the back of every row. The scheme has many disadvantages in security and efficiency, e.g. lengthen the file and easily be detected and attacked.
- (2) **Based on the states of tag letter method:** The letters of a tag are always case-insensitive the scheme hides the message by modifying the written states of the tag letters. File embedded message by this way has no change in show, and does not lengthen the file, and the capacity is considerable. But the upper-case and low-case states of those letters uncover the embedded message [13].
- (3) **Based on attribute pair order method:** Attributes may appear in any order so the order of attributes can be changed, without change the show or length of the file. To define a key attribute and corresponding attribute in the tag, if the order of key attributes before the corresponding attribute, then the order

will denote “1”, the other is “0”. Nevertheless, the capacity is small, and require database to store the attribute pair order.

However, Figure 5 illustrates Internet based client-server model and watermark embedding scheme.

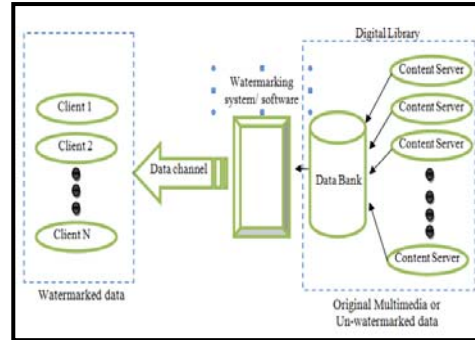


Figure 5 Internet based client-server model.

#### 4. Related work

Many of digital media owners are concerned about protection of the integrity and confidentiality of content. It is very important to prevent unauthorized manipulation and misappropriation of such digitized images. The risks increased when dealing with an open environment like the internet. In many cases such as Medical images, forensic investigations and military images, the confidentiality and integrity are a critical issue due to the special characteristics of those images. In such images, they should keep intact in all circumstances and before any operation, they must check for Integrity and authentication. However, an efficient watermarking algorithm for web sites' authentication



purpose should satisfy the following conditions and carefully designed to make a tradeoff between them [14].

- i. **Imperceptibility:** the watermarked data and the original data should be perceptually indistinguishable.
- ii. **Robustness:** the ability to detect the watermark after common signal processing. In other words, embedded watermark should be retrievable before watermarked image severely degraded to a useless degree.
- iii. **Security:** the embedded information can be detected, decoded, and/or modified only by authorized parties
- iv. **Invisibility:** the watermark should not degrade the quality of the image and should be perceptually invisible.

There are many algorithms have been proposed for using a watermarking system in image authentications. However, some of these algorithms based on fragile watermark while others depend on semi-fragile watermark. A watermark considered fragile if even a single bit corrupted/change in the watermarked image. In addition, fragile watermark is useful for purposes of authentication and integrity attestation. It provides a guarantee that the images did not tampered with.

In contrast, Semi-fragile watermarks are more robust than fragile watermarks and less sensitive to classical user modifications such as JPEG compression. In addition, semi-fragile watermarking seeks to verify that the content of the multimedia has not been modified by illegitimate distortions, while allowing modification by legitimate distortions and to identify any malicious

image tampering while being tolerable to JPEG compression or slight image content alterations.

There are several methods proposed for web page authentication this paper compared most common algorithms based on significant factors. Each algorithm has discussed briefly as following:

a) **M-sequences addition:**

In this method, a watermark embedded in the wavelet domain, where the concept of contrast sensitivity used to find the embedding strength of the watermark. This was an attempt to introduce the concept of adaptive watermarking in which watermark bits inserted according to the characteristics of the pixels in which they are inserted. [15].

**Advantages:**

- This technique is robust to small amount of noise and can accommodate more than one watermark because different segments of m-sequences are uncorrelated.

**Disadvantages:**

- The watermark easily removed or replaced by manipulating the LSB.
- The method does not have good localization properties.

b) **Media Signature scheme:**

In this algorithm, the owner uses his private key to sign on the hash value of the extracted features, then embed the signature to the image, and send watermarked content to the recipients. In the content verification procedure, the recipient can verify the received content's authenticity by using its owner's public key and the associated signature [16].



**Advantages:**

- The watermarking done in such a way that it can indicate the locations of attacks on the content if the authentication procedure fails.
- Capability of convince users visually.

**Disadvantages:**

- The generated signature is unavoidably very large because its size is usually proportional to the image size.
- Content-based signatures usually added to the private or user sections of the images.

**c) Independent component analysis (ICA):**

It is a computational method for separating a multivariate signal into additive subcomponents. In this method, the ICA presumes the watermarked work as a mixture of the original work and the watermarks, and therefore, it can do separation to estimate the watermark. This algorithm aims to find a certain linear transform, which can decompose the objective vectors and make the components of it as independent as possible. The idea is, the image  $I$  and its transpose  $I^T$  can be considered as two independent sources for ICA [17].

**Advantages:**

- The original image not needed for watermark extraction and the public image can be publicly available.
- No a priori watermark information needed.
- The watermark is robust against many attacks.
- The watermark can be any meaningful image.

**Disadvantages:**

- ICA is closely related to the blind source separation (BBS).
- All the independent components must be non- Gaussian.
- The matrix must be of full column rank.

**d) Based on Class Selectors:**

This method based on specification of cascading style sheets (CSS). According to the embedded rule, and the living Class Selectors of some objects in the Operable Block of CSS, the process repeatedly imported to embed information [12].

**Advantages:**

- The algorithm has no difference in normal show on the browser. The secret information can not be discovered. Unless the adversary to look up to the source code of the watermarked-webpage.
- The algorithm has a good imperceptibility and large capacity.
- The algorithm has a good ability to contradict with detection and auto filtration

**Disadvantages:**

- The algorithm has the common shortcoming such as the embedding location separated from the content of the webpage.
- The algorithm has contradicted with detection.

**e) Principal component analysis: (PCA):**

This algorithm presented in 1901. Then it becomes popular technique in real time. However, in this algorithm watermarks generated for web pages through PCA



technique. These watermarks then encoded into the upper and a lower case of the letters in HTML tags of web pages [18]. In addition, PCA extracted information represented by a set of new variables.

**Advantages:**

- It is famous for its strong expressive ability it used for distinguishing between different objects. Thus it could be also useful in telling a counterfeit object from the real one
- The simple PCA method produces approximate solutions to without the need for calculating a variance-covariance matrix and then diagonalizing it and it does not depend on learning parameters.

**Disadvantages:**

- This algorithm embedded a watermark into the tags of HTML.
- PCA algorithm is time-consuming.
- In some web pages any change in HTML tag the site will not work.

**f) Web-based image authentication:**

This method using invisible fragile watermark for authenticate the watermarked image. The process of verification started when transferring watermarked image to the server. Once the image uploaded, server uses its private key to detect watermark and verify whether the transferred image has been tampered with or not [3].

**Table 1. A comparative study of the web page authentication algorithms**

Methods	Factors							
	Deployed	Technique	Fragile/Semi-fragile	Evaluation criteria	Visibility	Mark	Cover	Security
M-Sequences	1996	Multiple watermarks	Semi-fragile	Bit errors/ideal value	Invisible	Bit alteration	LSB	Private Key
Media Signature	2002	DCT	Fragile	Contents-hashing		Signature	Binary bit	
Web-based authenticatio		Server-based authenticator		Check LSB/False pixels		Bit alteration	LSB	Public key
PCA	2006	ULC	PCA	-		HTML		
ICA	2008	Rand.sequenc	Semi-fragile	PSNR		Image	Coefficient	Public image
Class selector base	2010	CSS	-	Matching rules		Bits	HTML	Private Key



As a result, the security of digital images has been a great concern since the expanded use of them over the internet and the effective watermarking system for Web page authentication has several desirable features, they are [19]:

- **On-demand process:** watermarking should apply to multimedia objects only when they retrieved from the digital library or the organization by a remote request. This is to guarantee that the data will be processed only if it is necessary and with the latest technology as well as up-to-date watermarking information.
- **Real-time process:** watermarking should be done (embedded) as part of the real-time data. This is to ensure full compatibility of the watermarking process with the HTTP protocol.
- **Customized process:** the system should allow different clients to retrieve data with different degrees of watermarking. These differences can be defined in terms of the different watermark logos, watermarking technologies, and even object qualities.

## 5. Conclusion

The ease and extent of such manipulations emphasize the need for image authentication techniques in applications where verification of integrity and authenticity of the web page content is essential. This paper has discussed the methods of watermarking systems that were used for web page image authentication. The basic concept of web page authentication briefly explored in which some of the popular algorithms were

discussed. In addition, a comparison between the algorithms techniques in some critical aspects was presented. The advantages and disadvantages of the current known methods have been sorted. Moreover, some of basic watermarking requirements for authentication were presented as well as the properties of the system. In addition, the features of web page authentication process were described.

## ACKNOWLEDGEMENT

We would like to express our appreciation to all those who helped us to understand the importance of knowledge and showed us the best way to gain it.

## 6. References

- [1]. Wei-Hung Lin , Shi-Jinn Horng , Tzong-Wann Kao, Rong-Jian Chen, Yuan-Hsin Chen, Cheng-Ling Lee, Takao Terano. Image copyright protection with forward error correction. *Expert Systems with Applications* 36 (2009) 11888–11894
- [2]. Rafiullah Chamlawi, Asifullah Khan, Imran Usman. Authentication and recovery of images using multiple watermarks. *Computers and Electrical Engineering* (2010)
- [3]. Yusuk Lim, Changsheng Xu, David Dagan Feng. Web based Image Authentication Using Invisible Fragile Watermark. *Australian Computer Society, Inc.* 2002
- [4]. Lin, P.L., C.-K. Hsieh, and P.-W. Huang, A hierarchical digital watermarking method for image tamper detection and recovery. *Pattern Recognition*, 2005. 38(12): p. 2519-2529



- [5]. Shih, F.Y. and Y.-T. Wu, Robust watermarking and compression for medical images based on genetic algorithms. *Information Sciences*, 2005. 175(3): p. 200-216
- [6]. Farah I. R., Ahmed M. B., A Watermarking System Using the Wavelet Technique for Satellite Images. 2006
- [7]. Min-Jen Tsai. A visible watermarking algorithm based on the content and contrast aware (COCO) technique. *J. Vis. Commun. Image R.* 20 (2009) 323–338
- [8]. Wei-Hung Lin a., Yuh-Rau Wang b., Shi-Jinn Horng a., Tzong-Wann Kao d., Yi Pan e. A blind watermarking method using maximum wavelet coefficient quantization. *Expert Systems with Applications*. 2009 Vol.36. pp11509–11516
- [9]. Aburas A. A., Rashidah F. O., intensive Review on Digital Watermarking. *Peocessing of International Conference on science and technology application in industry and education(ICST)*. Penang Malaysia 2008. PP 2531-2536.
- [10]. Huiping guo, Nicolas d. Georganas. jointly verifying ownership of an image using digital watermarking. *springer science, business media, multimedia tools and applications*, 27, 323–349, 2005.
- [11]. Veysel Aslantas a., Saban Ozer b., Serkan Ozturk. A Improving the performance of DCT-based fragile watermarking using intelligent optimization algorithms. *Optics Communications*. 2009.Vol.282. P2806–2817.
- [12]. Guang Sun. An Algorithm of Webpage Information Hiding Based on Class Selectors. *Third International Symposium on Intelligent Information Technology and Security Informatics*. IEEE 2010.
- [13]. Ghosh S., “StegHTML: A Message Hiding Mechanism in HTML Tags”, available:<http://www.cs.virginia.edu/~skg5n/main.pdf>, May, 2007
- [14]. Xunzhan Zhua,\_, Anthony T.S. Hob, Pina Marzilianoa. A new semi-fragile image watermarking with robust tampering restoration using irregular sampling. *Signal Processing: Image Communication* 22 (2007) 515–528.
- [15]. Delaigle J., Vleeschouwer C. De, and Macq B., “Psychovisual Approach to Digital Picture Watermarking,” *Journal of Electronic Imaging*, vol. 7, no. 3, pp. 628-640, July 1998.
- [16]. Qibin Sun, Qi Tian, Shih-Fu Chang. A Robust and Secure Media Signature Scheme for JPEG Images. 0-7803-7713-3/02/. IEEE 2002.
- [17]. Thang Viet Nguyen, Jagdish Chandra Patra. A simple ICA-based digital image watermarking scheme. *Digital Signal Processing* 18 (2008) 762–776.
- [18]. Zhao Q. and Lu H., "PCA-based web page watermarking," *Pattern Recognition*, vol. 40, pp. 1334-1341, 2007
- [19]. Chi C.H., J. Deng Li, X., T.-S. Chua, Automatic proxy-based watermarking for WWW. 2001. 24: p. 144–154.



# ***Chapter VI***

# **Image Processing**



المؤتمر الدولي العربي الليبي الرابع للهندسة الكهربائية والإلكترونية 2010/10/26-23 طرابلس ليبيا





## **Fingerprints Recognition Based on Pseudo Zernike Moments with Multi-Layer Perception as a Classifier**

I.El-Feghi  
EE Dept Al-Fateh University  
Tripoli-Libya  
[idrise@ee.edu.ly](mailto:idrise@ee.edu.ly)

A. Tahar  
Academy of Higher Studies  
Misurata-Libya  
[adel.s.tahar@gmail.com](mailto:adel.s.tahar@gmail.com)

**Abstract**— In this paper, we present a complete fingerprint recognition system using an Artificial Neural Network (ANN). The ANN is trained by back-propagation algorithm on a set of fingerprint images. Pseudo Zernike Moments (PZM) will be used as a features vector for all images. To detect the region of interest on the fingerprint image, we have used shape information which is characterized by elliptical shape PZM of the elliptical shape constitute the input of the ANN. The data set is divided into two sets, training set and test set. The ANN is trained using the training set and tested on the test set which was hidden during training stage. The recognition rate is measured by the number of correctly classified fingerprints. The structure of the ANN is decided experimentally. The proposed algorithm was tested on a database of more than 400 fingerprints with 10 samples of each person fingerprints. Experimental results have shown that the proposed feature extraction method with an ANN classifier gave a faster training phase and yields a 98% recognition rate.

### **I. Introduction**

The importance of fingerprints comes from their uniqueness and portability. It is believed that every person has unique fingerprints which remain invariant over time. Unlike identification cards, fingerprints cannot be lost or stolen. Due to these mentioned properties, automatic fingerprint recognition systems are becoming increasingly important and finding applications in variety of fields. These fields include access control systems, criminal identification and authentication and access to security systems such as

computers or bank teller machines [1][2]. Despite the advances in fingerprint classification, efficient fingerprint verification is stills a challenging problem especially when matching a fingerprint to all registered fingerprint images of large database. A fingerprint is the pattern of ridges and valleys on the surface of finger. The uniqueness of a fingerprint can be determined by the overall pattern of ridges and valleys as well as local ridge anomalies: a ridge bifurcation or a ridge ending, called minutia points[1].



A complete fingerprints recognition system should include three stages. The first stage is detecting the location of the most important features of the fingerprints image, which is difficult and complicated because of the orientation and scaling of the image. The second stage is the extraction of the pertinent features from the localized image and third stage involves classification of the image based on the extracted features vector obtained in the last step. This classification can be performed using artificial Neural Networks (ANN)[3-4]

In order to design a high recognition rate system, the choice of feature vector is very crucial and extraction of pertinent features from two-dimensional images of human fingerprint plays an important role in any fingerprint recognition system.

In this paper, an efficient feature extraction technique is developed. The technique is based on the combination of local and global information of fingerprint images. First, fingerprint localization based on shape information with a new definition for distance measure threshold called fingerprint candidate threshold (FPCT) for distinguishing between non fingerprint image and fingerprint image candidate is introduced. We present the effect of varying the FPCT on the recognition rate of the proposed technique. A new parameter, called the axis correction ratio (ACR), is defined to eliminate irrelevant data from the fingerprint images and to create a subimage for further feature extraction. Once the fingerprint localization process is completed, pseudo-Zernike moment invariant (PZMI)[5] with a new method to

select moment orders are utilized to obtain the feature vector of the fingerprint under examination. In this thesis, PZMI was selected over other types of moments because of its utility in fingerprint recognition approaches. The last step in fingerprint recognition requires classification of the fingerprint image into one of the known classes based on the derived feature vector obtained multilayer perceptron in the previous stage. The multilayer perceptron (MLP) neural network is used as the classifier. The training of the MLP neural network is done, based on the Backpropagation algorithm [6]. It's shown that the proposed feature extraction method with an MLP neural network classifier gives a faster training phase and yields a better recognition rate.

## II. FINGERPRINTS LOCALIZATION

To ensure a robust and accurate feature extraction, the exact location of the fingerprint in an image is needed. The ultimate goal of the fingerprint localization is finding an object in an image as a fingerprint candidate whose shape resembles the shape that contains the most important information of a fingerprint and, therefore, one of the key problems in building automated systems that perform fingerprint recognition task is fingerprint localization. Many algorithms have been proposed for fingerprint localization and detection, which are based on using shape color information, minutiae-based matching and so forth. A critical survey on fingerprint localization and detection can be found [7]. In this paper, we have used a



modified version of the shape information technique for the fingerprint localization presented in that an ellipse can generally approximate the fingerprint of a human. The localization algorithm utilizes the information about the edges of the fingerprint image or the region over which the fingerprint is located. The advantage of the region-based method is its robustness in the presence of noise and changes in illumination. In the region-based method, the connected components are determined by applying a region growing algorithm then, for each connected component with a given minimum size, the best-fit ellipse is computed using the properties of the geometric moments. To find a fingerprint region, an ellipse model with five parameters is used:  $X_0, Y_0$  are the centers of the ellipse,  $\theta$  is the orientation, and  $\alpha$  and  $\beta$  are the minor and the major axes of the ellipse, respectively, to calculate these parameters, first we review the geometric moments. The geometric moments of order  $p + q$  of a digital image are defined as

$$M_{pq} = \sum_x \sum_y f(x, y) x^p y^q, \quad (1)$$

Where  $p, q = 0, 1, 2$ , and  $f(x, y)$  is the gray-scale value of the digital image at  $x$  and  $y$  location. The translation invariant central moments are obtained by placing origin at the center of the image

$$\mu_{pq} = \sum_x \sum_y f(x, y) (x - x_0)^p (y - y_0)^q, \quad (2)$$

$$\theta = \frac{1}{2} \arctan \left( \frac{2\mu_{11}}{\mu_{20} - \mu_{02}} \right), \quad (3)$$

Where  $\mu_{pq}$  denotes the central moment of the connected components as described. The length of the major and the minor axes of the best-fit ellipse can also be computed by evaluating the moment of inertia. With the least and the greatest moments of inertia of an ellipse defined as

$$I_{\text{Min}} = \sum_x \sum_y [(x - x_0) \cos \theta - (y - y_0) \sin \theta]^2, \quad (4)$$

$$I_{\text{Max}} = \sum_x \sum_y [(x - x_0) \sin \theta - (y - y_0) \cos \theta]^2, \quad (5)$$

The length of the major and the minor axes are calculated from as

$$\alpha = \frac{1}{\pi [I_{\text{Max}}^3 / I_{\text{Min}}]^{1/8}}, \quad (6)$$

$$\beta = \frac{1}{\pi [I_{\text{Min}}^3 / I_{\text{Max}}]^{1/8}}. \quad (7)$$

To assess how well the best-fit ellipse approximates the connected components, we use a distance measure between the connected components and the best-fit ellipse as follows:

$$\phi_i = \frac{P_{\text{inside}}}{\mu_{00}}, \quad \phi_o = \frac{P_{\text{outside}}}{\mu_{00}}, \quad (8)$$

Where the  $P_{\text{inside}}$  is the number of background points inside the ellipse,  $P_{\text{outside}}$  is the number of points of the connected components that are outside the ellipse, and  $\mu_{00}$  is the size of the connected component. The connected components are better approximated by their best-fit ellipses when  $\phi_i$  and  $\phi_o$  are as small as



possible. We have named the threshold values for  $\varphi_i$  and  $\varphi_o$  as FPCT. Our experimental study indicates that when FPCT is less than 0.1, the connected component is very similar to ellipse; therefore it is a good candidate as a fingerprint region. If  $\varphi_i$  and  $\varphi_o$  are greater than 0.1, there is no fingerprint region in the input image, therefore, we reject it as a non fingerprint image.

### III. FEATURE EXTRACTION TECHNIQUES

The aim of the feature extractor is to produce a feature vector containing all pertinent information about the fingerprint while having a low dimensionality. In order to design a good fingerprint recognition system, the choice of feature vector is very crucial. To design a system with low to moderate complexity, the feature vectors created from feature extraction stage should contain the most pertinent information about the fingerprint to be recognized. In the statistics-based feature extraction approaches, global information is used to create a set of feature vector elements to perform recognition. A mixture of irrelevant data, which are usually part of a fingerprint image, may result in an incorrect set of feature vector elements. Therefore, data that are irrelevant to fingerprint portion such background should be disregarded in the feature extraction phase. Fingerprint recognition systems should be capable of recognizing fingerprint appearances in a changing environment. Therefore we use PZMI to generate the feature vector elements. Also the feature extractor should create a feature vector with low

dimensionality. The low-dimensional feature vector reduces the computational burden of the recognition system; however, if the choice of the feature elements is not properly made, this in turn may affect the classification performance. Also, as the number of feature elements in the feature extraction step decreases, the neural network classifier becomes small with a simple structure. The proposed feature extractor in this paper yields a feature vector with low dimensionality, and, by disregarding irrelevant data from fingerprint portion of the image, it improves the recognition rate. The proposed feature extraction is done in two steps. In the first step, after fingerprint localization, we create a subimage which contains information needed for the recognition algorithm. In the second step, the feature vector is obtained by calculating the PZMI of the derived subimage.

To create a subimage for feature extraction phase, all pertinent information around the fingerprint region is enclosed in an ellipse while pixel values outside the ellipse are set to zero. Unfortunately, through creation of the subimage with the best-fit ellipse, as described before, many unwanted regions of the fingerprint image may still appear in this subimage. These include part of the background as an example. To overcome this problem, instead of using the best-fit ellipse for creating a subimage, we have defined another ellipse. The proposed ellipse has the same orientation and center as the best-fit ellipse but the lengths of its major and minor axes are calculated from the lengths of the major and minor axes of the best-fit ellipse as follows:

$$A = \rho \cdot \alpha, \quad B = \rho \cdot \beta,$$

Where A and B are the lengths of the major and minor axes of the proposed ellipse, and  $\alpha$  and  $\beta$  are the lengths of the major and minor axes of the best-fit ellipse that have been defined. The coefficient  $\rho$  is called ACR and varies from 0 to 1. Our experimental results with 400 fingerprint images show that the best value for ACR is around 0.90 Fig. 1 shows the effect of ACR ( $\rho$ ). By using the above procedure, data that are irrelevant to fingerprint portion are disregarded. The feature vector is then generated by computing the PZMI of the subimage obtained in the previous stage. It should be noted that the speed of computing the PZMI is considerably increased due to smaller pixel content of the sub images.

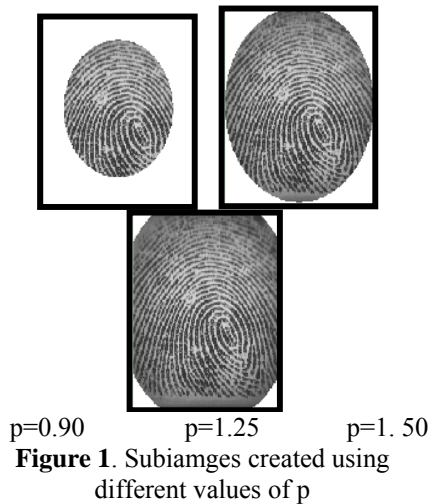


**Figure 1.** Subimages created using different values of  $\rho$

#### IV. PSEUDO ZERNIK MOMENT

Statistics-based approaches for feature extraction are very important in pattern recognition for their computational efficiency and their use of global information in an image for extracting features. The advantages of considering orthogonal moments are that they are shift, rotation, and scale invariants and are very robust in the presence of noise. The invariant properties of moments are utilized as pattern sensitive features in classification and recognition applications [8]. Pseudo-Zernike polynomials are well known and widely used in the analysis of optical systems. Pseudo-Zernike polynomials are orthogonal sets of complex-valued polynomials defined as [5][8].

The PZM is defined as follows:

$$V_{nm}(x, y) = R_{nm}(x, y) \exp\left(jm \tan^{-1}\left(\frac{y}{x}\right)\right), \quad (9)$$

Where  $x^2 + y^2 \leq 1$ ,  $n \geq 0$ ,  $|m| \leq n$ , and the radial polynomials  $\{R_{n,m}\}$  are defined as

$$R_{n,m}(x, y) = \sum_{s=0}^{n-|m|} D_{n,|m|,s} (x^2 + y^2)^{(n-s)/2}, \quad (10)$$

Where

$$D_{n,|m|,s} = (-1)^s \frac{(2n+1-s)!}{s!(n-|m|-s)!(n-|m|-s+1)!}. \quad (11)$$

The PZMI of order  $n$  and repetition  $m$  can be computed using the scale invariant central moments  $CM_{pq}$  and the radial geometric moments  $RM_{pq}$  as follows [5, 7]:

$$\begin{aligned}
 &= \frac{n+1}{\pi} \sum_{\substack{n-|m| \\ (n-m-s) \text{ even}, s=0}}^{n-|m|} D_{n,|m|,s} \\
 &\times \sum_{a=0}^k \sum_{b=0}^m \binom{k}{a} \binom{m}{b} (-j)^b CM_{2k+m-2a-b, 2a+b} \\
 &+ \frac{n+1}{\pi} \sum_{\substack{n-|m| \\ (n-m-s) \text{ odd}, s=0}}^{n-|m|} D_{n,|m|,s} \\
 &\times \sum_{a=0}^d \sum_{b=0}^m \binom{d}{a} \binom{m}{b} (-j)^b RM_{2d+m-2a-b, 2a+b}
 \end{aligned} \quad (12)$$

Where  $k = (n - s - m)/2$ ,  $d = (n - s - m + 1)/2$ , and also  $CM_{pq}$  and  $RM_{pq}$  are as follows:

$$CM_{p,q} = \frac{\mu_{pq}}{M_{00}^{(p+q+2)/2}} \quad (13)$$

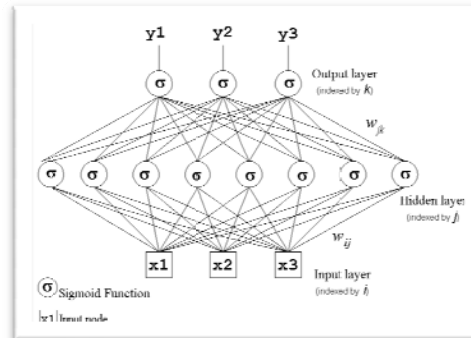
$$RM_{p,q} = \frac{\sum_x \sum_y f(x, y) (\hat{x}^2 + \hat{y}^2)^{1/2} \hat{x}^p \hat{y}^q}{M_{00}^{(p+q+2)/2}} \quad (14)$$

Where  $x = x - x_0$ ,  $y = y - y_0$ , and  $x_0$ ,  $y_0$ ,  $\mu_{pq}$ , and  $M_{pq}$  are defined before.

## VI. MLP CLASSIFIER

Neural network is widely used as a classifier in many fingerprint recognition systems[2][3]. Neural networks have been employed and compared to conventional classifiers for a number of classification problems. The results have shown that the accuracy of the neural network approaches is equivalent to, or slightly better than, other methods. Also, due to the simplicity, generality, and good learning ability of the neural networks. MLP neural networks have been found to be very attractive for many engineering problems because (1) they are universal approximators, (2) they have a very compact topology, and (3) their learning speed is very fast because of their locally tuned neurons. In this paper, an

MLP neural network is used as a classifier in a fingerprint recognition system where the inputs to the neural network are feature vectors derived from the proposed feature extraction technique described in the previous section. The construction of the MLP neural network involves three different layers with feed forward architecture. The input layer of the neural network is a set to the dimension of the PZM. The input units are fully connected to the hidden layer. Connections between the input and hidden layers have unit weights and, as a result, do not have to be trained. The goal of the hidden layer is to cluster the data and reduce its dimensionality. In this structure, the hidden units are referred to as the MLP units. The MLP units are also fully connected to the output layer. The output layer supplies the response of the neural network to the activation pattern applied to the input layer as shown in Fig. 2. The transformation from the input space to the MLP-unit space is nonlinear (nonlinear activation function), whereas the transformation from the MLP-unit space to the output space is linear (linear activation function).



**Finger 2. MLP Structure**



## VII. EXPERIMENTAL RESULTS

A database of 400 fingerprints images was used. This database contains fingerprints of 40 person. For each person there are 10 samples in deferent position. From each image we create a subimage and calculate its PZM. The data set is randomly divided into two different sets. One set is used for training and the second is used for testing. The PZM feature vector constitutes the input to the MLP. The number of input neurons in the MLP is same as the dimension of the PZM and the number of output neurons is 40 since we have 40 classes. The number of hidden neurons is determined experimentally. After training on the training set, the MLP is tested on the test set which has never been seen by the MLP before. If the input vector is classified correctly to it corresponding class, the recognition is considered correct and wrong otherwise. This was repeated several times and the average error which is a measure of the difference between the desired output and the obtained output is recorded. Table 1 shows the obtained results of the recognition, error and number of training cycles.

**Table 1.** Experiment result using 10 hidden neurons

MLP input	Neurons in hidden	system Output	EPOCH	ERROR	recogniti on RATE %
200	10	40	100	0.185809750	79
200	10	40	200	0.180589116	100
200	10	40	500	0.116461593	100
200	10	40	1000	0.086145929	100
200	10	40	5000	0.040339416	100
200	10	40	100.000	0.009695363	100

## VIII. CONCLUSIONS

This paper presented an efficient method for the recognition of human fingerprint in frontal view of fingerprint images. The proposed technique utilizes a modified feature extraction technique which is based on a flexible fingerprint localization algorithm followed by PZM. An MLP neural network was used as a classifier. In this Paper we have introduced several parameters for efficient and robust feature extraction technique These include FPCT, ACR. It has also been shown that the proposed system was able to classify all fingerprints in the database with accuracy of 100%.



### References

- [1] L. Hong, Y. Wang and A. K. Jain, "Fingerprint Image Enhancement: Algorithm and Performance Evaluation ", *IEEE Transactions on PAMI*, vol. 2, no.4, pp: 777-789,1998
- [2] Liu J.,Huang Z., and Chan K., "Direct MinutiaeExtraction from Gray-Level Fingerprint Image by Relationship Examination", in *Int. Conf. on Image Processing*, Vol. 2, pp 427-430, 2000.
- [3] Te-Jen Su; Yan-Yi Du; Ying-Jen Cheng; Yi-Hui Su; "A fingerprint recognition system using cellular neural networks, *on proc. Of 9th International Workshop on Cellular Neural Networks and Their Applications*, pp: 170 – 173, 2005
- [4] Chen Yu; Zhang Jian; Yi Bo; Chen Deyun," A Novel Principal Component Analysis Neural Network Algorithm for Fingerprint Recognition in Online Examination System ,” *On proc. Of APCIP*,vol. 1,pp: 182 – 186,2009
- [5] S. O. Belkasim, M. Shridhar, and M. Ahmadi, "Pattern recognition with moment invariants: a comparative study and new results," *Pattern Recognition*, vol. 24, no. 12, pp. 1117–1138,1991
- [6] Simon Haykin, "Neural networks A comprehensive foundation", Pearson Education, Inc, 2002
- [7] A. Andre . Moenssens," Fingerprint Techniques," In *bylaw enforcement series*, Sep. 1971.
- [8] C. H. Teh and R. T. Chin, "On image analysis by the methods of moments," *IEEE Trans. on Pattern Analysis and Machine Intelligence*, vol. 10, no. 4, pp. 496–513, 1988.





## A New Data Compression Algorithm for Binary Images

**Ahmed Barod**

[amsm\\_barod@yahoo.com](mailto:amsm_barod@yahoo.com)

**The National Authority for  
Scientific Research**

**Ali M.Obaid**

[tamasla@yahoo.com](mailto:tamasla@yahoo.com)

**The Higher Institute of  
Electronics, Baniwalid**

**Ali Ahmed Ali**

[ali\\_ahmed@yahoo.com](mailto:ali_ahmed@yahoo.com)

**The Higher Institute of  
Electronics, Baniwalid**

### Abstract

Data compression is an effective way of reducing data size. The literature enumerates a wide range of well-known compression techniques such as run-length, and Hoffman. The ratio of space saving fluctuates considerably depending on so many factors such as file content, format, and complexity of file structure. However, observing the well-known Win.rar compression program, one could observe an average ratio of 50%. Binary image files are those that contain data of two types; namely black and white pixels. Compression of binary files should in theory attain higher rates that should surpass the barrier of 90%. Testing the Winrar on a random collection of binary images revealed that such higher rates are not always reachable. The objective of this paper is to present a new algorithm for compressing binary images. The algorithm is based on heuristic structural techniques called the method of boxes. Basically the method considers any collection of adjacent pixels of the same level as a box. Thus, recording the coordinates of the box will be an encoding of the entire collection of pixels. Later on, the encoding undergoes further processing. Unless the file is randomly structured to the point that no pattern of organization between the levels can be inferred, a good compression rate can be attained. Compared to the famous Winrar program, the proposed algorithm achieved a much higher ratio.

### Introduction

The final objective of compression techniques is to reduce the redundancies in data representation in order to decrease data storage requirements and hence communication costs [1]. All images we get on the web are in compressed formats. Most modems use compression, and several file systems automatically compress files when stored.

Compression stems from the fact that most real applications are exceptionally large in terms of digital data. A high-quality audio signal requires approximately 1.5 megabits per second for digital representation and storage. A digitized one-hour color movie would require approximately 95 gigabytes of storage. A digitized one-hour color movie of HDTV-quality video will require approximately 560 gigabytes of storage [2].



Though compression may reduce data redundancy considerably, there is still a limit on how small a data file can be compressed. The ultimate size is related to the file's intrinsic redundancy characteristics [3].

The task of compression consists of two components, an **encoding** algorithm that takes a message and generates a compressed representation (hopefully with fewer bits), and a **decoding** algorithm that reconstructs the original message or some approximation of it from the compressed representation. These two components are typically intricately tied together since they both have to understand the shared compressed representation.

### Benefits of Data Compression

The benefits of data compression are related to the fundamental issue of saving in data representation. This saving is reflected in numerous applications. For instance, because of the significant progress in image compression techniques, a single 6 MHz broadcast television channel can carry

HDTV signals to provide better quality audio and video at much higher rates and enhanced resolution without additional bandwidth requirements. Moreover, data compression may enhance the database performance because more compressed records can be packed in a given buffer space in a traditional computer implementation.

Data compression obviously reduces the cost of backup and recovery of data in computer systems by storing the backup of large database files in compressed form[1].

### Classification of Compression Algorithms

Data compression is a method that takes an input data  $D$  and generates a shorter representation of the data,  $c(D)$ , with a fewer number of bits compared to that of  $D$ . The reverse process is called decompression, which takes the compressed data  $c(D)$  and generates or reconstructs the data  $D'$ , as shown in Figure (1). Sometimes the *compression/decompression* is referred to as "CODEC,"

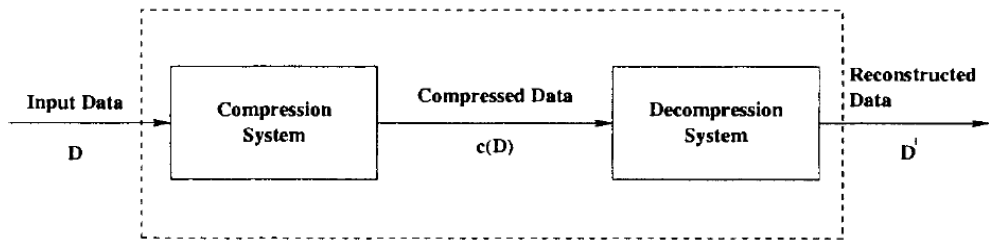


Figure (1), the "codec" system

If the reconstructed data  $D'$  is an exact replica of the original data  $D$ , the compression algorithms are called *lossless*.

On the other hand, the algorithms are *lossy* when  $D'$  is not an exact replica of  $D$ . Usually lossless data compression



techniques are applied on text or scientific data. The lossy compression techniques are usually applicable to data where high fidelity of reconstructed data is not required for perception by the human perceptual system [1].

### Data Compression Model

A model of a typical data compression system can be described using the block diagram shown in Figure (2). A data compression system mainly consists of three major steps: removal *or* reduction in data redundancy, reduction in entropy, and entropy encoding [2].

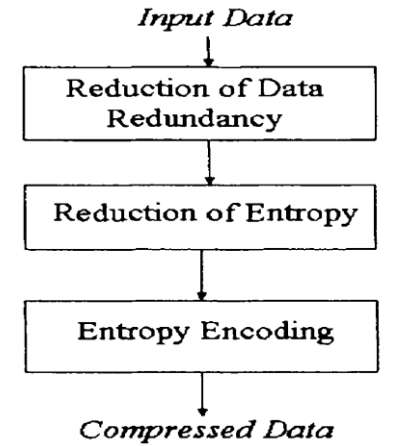


Figure (2), data compression model



### Lossless Image Compression

Huffman coding and run-length coding are example of lossless compression schemes[4]. The basic idea in Huffman coding is to assign short codewords to those input blocks with high probabilities and long codewords to those with low probabilities. Run-length encoding (RLE) is a very simple form of data compression in which *runs* of data are stored as a single data value and count, rather than as the original run.

### Lossy Image Compression

Lossy schemes can push the compression ratios to 10: 1 without visually noticeable degradations. They can reach 100: 1 and greater compression ratios with some noticeable degradations. In general these techniques do not work on the pixel level. In most cases they are mathematical

tools (transformations) that work on the image in frequency domain. Fourier and cosine transformations are good examples of this category [4].

### Outline of the Proposed Algorithm

The compression algorithm consists of several steps that aim to produce the best compression possible. Some of these steps are sequential while others are independent. They could be best described as cooperative. The algorithm could be described by the following steps:

1-Decision on whether to use the image or its invert as a base for the compression should be made. Such a decision is based on a simple heuristic that states: if the number of black pixels is more than half of the total pixels in the image then the image is inverted, Figure (3).

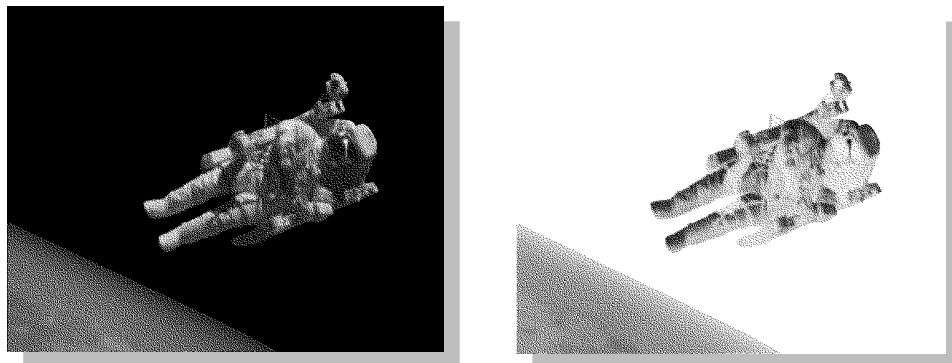


Figure (3), inverting the whole image



2-The entire file is divided into blocks, the size of each is 64 bits (8x8).

3-The content of each block is examined. If the content is only black pixels, then the entire block is represented by a code of two bits (01). However, if it is totally white the code will be (00), Figure (4).

0	0	0	0	0	0	0	0
0	0	0	0	0	0	0	0
0	0	0	0	0	0	0	0
0	0	0	0	0	0	0	0
0	0	0	0	0	0	0	0
0	0	0	0	0	0	0	0
0	0	0	0	0	0	0	0
0	0	0	0	0	0	0	0

Figure (4), white block represented by code "00"

If the pattern is mixed, then black pixels are grouped in the minimum non-overlapping boxes, Figure (5). If the number of non-overlapping boxes is less than five then the coordinates of the two vertices of the descending diagonal of each box are recorded. They represent the code for that box. For instance, the code of the first box in Figure (5) is (0,0,2,2). In binary form this code is (000,000,010,010), i.e. 12 bits long. The representation of the entire block will be achieved by cascading the codes of all boxes in the block. The code of the block of Figure (5) is (000, 000, 010, 010, 001, 100, 010, 111, 100, 001, 100, 001, 101, 010, 111,111). The length of the code will be  $n \times 12$  where n is the number of boxes. It should always be noted that ( $n < 6$ ) to achieve compression.

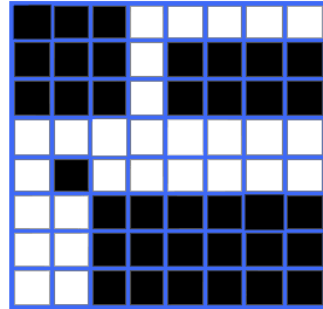


Figure (5), four boxes in the block

4- The code should be reduced through the method of code reduction. The method states that given m similar bits at the right side of the code, it is possible to delete (m-1) of these bits without losing the information about the boxes. The total removed bits should not exceed ten bits. In code of Figure (5), it possible to remove 5 bits, so that the code representing the block is reduced to:

(000000010010,001100010111,100001100001,1010101).

The new code is kept in a buffer as the temporary code representing the block and called *code1*.

5- The same block is subjected to inversion and the number of boxes (after the inversion) is obtained. If the number of boxes obtained in the inverted image is less than the number of boxes obtained in the original image, then we use the inverted version. Therefore, we obtain the block code and apply the method of code reduction. Again the code is kept temporarily and called *code2*. Code2 is



compared with *code1* and the smaller code is kept and called *recent code1*. The other is discarded.

6- Once more, the same block is subjected to the direct representation of the white and black pixels. In this representation the content of the block is transformed into a string of 64 bits where black pixels are ones and white pixels are zeros, Figure (6).

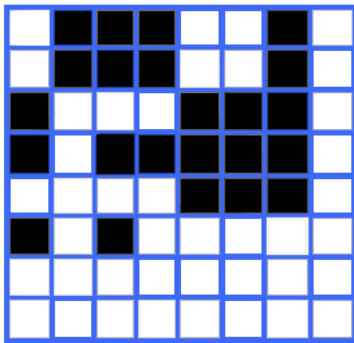


Figure (6), direct representation of pixels

The code is (01110010, 01110010, 10001110, 10111110, 00001110,

10100000, 00000000, 00000000). At the right side of the string, (m-1) similar bits are deleted. The code of Figure (5), thus will be only (01110010, 01110010, 10001110, 10111110, 00001110, 1010). The produced code is kept and called *perusal code1*. Then the image is rotated 90 degrees and again the code, called *perusal code2*, is obtained and reduced in the same manner. Compared to the *perusal code1*, only the shortest code is kept. The image is further rotated 90 degrees and the same process is repeated. The obtained code from each rotation is compared with the old value. Only the shortest code is obtained and kept, called *recent code2*. This code compared to *recent code1*, only the smallest code is kept.

7- For the process of de-compression, all information should be kept in order to undo the compression process. Therefore a header is created for each block. The header contains *control code* and *compression code* followed by so called *sensing flags* and a *number n* that could be added optionally, Figure (7).

Control code	Compression code	Flags code	(optional) n
--------------	------------------	------------	-----------------

Figure (7), block header

The control code indicates whether the block is partitioned to boxes (code 1), or represented by the series direct representation (code 0). Also whether the block (in case of blocks) is not rotated, or rotated 90 degree, 180 degree, or 270-degree clockwise (00,01,10,11,

respectively). The compression code is padded with 0 every fifth bit. This procedure is done to prevent the possible occurrence of any sensing flags pattern.

8-There are three sensing flags: The pattern 0111110 (six ones bordered by zeros) means that the current block is



- attached directly to the previous block (it is possible that itself is the first block).
- b- The pattern 011111110 (seven ones bordered by zeros) means that the current block is separated from the previous block with n white blocks.
  - c- The pattern 0111111110 (eight ones bordered by zeros) means that the current block is separated from the previous block with n blocks. In this case all n blocks are of the same structure as the current block.

9-The file header starts with status bit that has the following interpretations (1- inverted image, 0- non inverted image). It

also contains the height and width of the original image. In both cases (file inverted or not inverted), the same operations are performed.

### Testing the algorithm

A divers set of samples is deliberately used to cover all possible patterns that could be encountered in binary images. These samples were subjected to compression by the proposed algorithm and the very famous compression programs of ZIP, and Win Rar. The results were tabulated in Table (1).

Images	Size (KB)	ZIP	RAR	N. Alg.
White paper	34	99.24%	99.39%	99.74%
Black paper	34	99.14%	99.50%	99.74%
bird	16.8	50.95%	53.50 %	56.61%
space	35.9	79.47%	79.83%	80.33%
Fax mail	59.4	87.39%	88.11%	90.99%

### Conclusion

A method for lossless compression of binary images is proposed. The method is based on dividing the image into standard-size data blocks and then the blocks into a number of non-overlapping boxes, or rectangles. A series of operations is performed on these bocks depending on their structure to obtain a minimum code that is representative of the image pattern in

the block. The proposed algorithm has been tested under a group of different types, sizes and structures of binary images. In most binary images the proposed algorithm achieved a higher rate of compression than both the Zip and Winrar standard compression programs.



## References

- [1] JPEG2000 Standard for Image Compression Concepts, Published by John Wiley & Sons, Inc., Hoboken, New Jersey, 2005.
- [2] Anil K. Jain, *Fundamentals of Digital Image Processing*, Prentice-Hall, Englewood Cliffs, N.J, 1989.
- [3] Moammer M. Enhemed, Mohamed A. Al-sharief, “image data compression using sample selection methods in DCT domain”, BSc project 2006.
- [4] Gregory A. Baxes, *Digital Image Processing*, John Wiley, Canada, 1994.
- [5] Wallace, G., “The JPEG still picture compression standard”, *Communications of the ACM*, 34, pp 30-44, 1991.
- [6] R. C. Gonzalez, and R. E. Woods., *Digital Image Processing*, Addison-Wesley, New York, 1993.
- [7] Jam Parsons, Dan Oja, “Computer Concepts” 5<sup>th</sup> Ed., Course Technology, Thomson Learning.
- [8] Rabbani M., Jones P., *Digital Image Compression Techniques*, Vol. TT7, SPIE, Optical Engineering Press, 1991.





## Object Tracking with Occlusion Handling by Particle Filtering

Ali GANOUN\* and Raphaël CANALS\*\*

\* EE Department, Faculty of Engineering, Alfateh University, LIBYA

\*\* PRISME Institute, University of Orléans, Orleans, FRANCE

[ali.ganoun@garyounis.edu](mailto:ali.ganoun@garyounis.edu), [raphael.canals@univ-orleans.fr](mailto:raphael.canals@univ-orleans.fr)

### Abstract

Robust real time object tracking in grayscale image sequences is a difficult challenge, especially when the object appearance changes because of its deformable properties, movements or luminosity variations. Management of these appearance changes must be done to obtain a good result that needs an update of the object model. We propose an approach to distinguish any occlusion or bad detection in order to control the update step. An approximate mask has also been added to improve the reliability of the model, thus avoiding adding any wrong information from the background. This approach has been successfully applied to track a single object using a particle filter framework.

### 1 Introduction

Object tracking techniques aim at following objects in an image sequence. They should be able to deal with complex interactions and various dynamics in the sequence such as complex occlusions, camera motion, varying lighting conditions and viewing directions. Object tracking is useful in many image-based applications including human-machine interfaces [1], video communication / compression [2] and surveillance systems [3], [4].

In recent years, a great deal of research effort has been expended on the object tracking problem, and as a result different techniques are available in the literature for solving this problem. Among the main techniques, there are contour-based techniques in which tracking is performed by finding the object contour given an

initial contour from the previous frame [5], [6]. A second approach is model-based techniques which exploit the a priori knowledge of the shape of an object in a given scene [7].

Filtering and data association techniques are widely applied in computer vision for various tracking applications, as in the work of Rasmussen and Hager [8] who adapt probabilistic data association filters and joint probabilistic data association filters for tracking complex visual objects. Within the filtering and data association approach, the particle filter technique will be particularly concerns here; it is a Bayesian methodology which applies a recursive filter, based on samples of the object to be tracked [9], [10].



Hybrid techniques have also been developed: they combine various techniques and give considerably better results than those obtained by using only one technique [11], [12].

This paper considers the particle filter technique. While the particle filter is usually used with color sequences, we chose to use the grey-level scale because of its lower data size with a view to real time processing. We also chose a context without any a priori information. Consequently, we cannot use any learning phases: we only have a single model of the object to be tracked extracted from the first image.

Another problem related to object tracking is the occlusion problem. Many techniques exist to handle the occlusion problem with particle filter probabilistic models, such as in the work of Nummiaro et al. [13] who present a system to track people in the presence of occlusion. The proposed tracking method adds the robustness and invariance of color distributions to particle filtering. The probabilistic tracking model proposed in [14] uses a particle filter for a better handling of color clutter in the background, as well as complete occlusion of the tracked object over a few frames.

In this paper we propose an occlusion-handling scheme based on the particle filter framework, which significantly improves the tracking performance in the presence of partial occlusion. Zhou et al [15] have already proposed a similar technique; in their paper, the visual tracker relies on an adaptive appearance model, a velocity

motion model with adaptive noise variance, and an adaptive number of particles, with occlusion handling via robust statistics. The occlusion is declared when the number of outliers in the object of interest compared with the appearance model exceeds a threshold: therefore the appearance model must not be updated. Our approach differs from their approach in the technique of considering the occlusion, as is explained below in more details.

The rest of the paper is structured as follows: in the next section, we present the principle of particle filtering. Our particle filter version is proposed in Section 3. Section 4 demonstrates the results of the proposed approach using several real scene sequences. The paper concludes with some conclusions in section 5.

### **Particle filtering**

Particle filtering (PF) is a sophisticated method for model state estimation; it is a promising technique as it models uncertainty and can, with sufficient samples, deal with many tracking problems such as missing data and occlusions. It is known under different names including the Monte Carlo approach [16], the CONDENSATION algorithm [10] and bootstrap filter [17]. One of the main properties of the particle filter is that it gives an approximate solution to an exact model, rather than the optimal solution to an approximate model as with Kalman filters. It handles non linear models with non-Gaussian noise; as a result, it has been proven to be a powerful technique for tracking non linear systems.



The basic idea of this technique is to evaluate the position of an object by testing its presence on a limited number of points. When this principle is used on object tracking, the result is a local similarity test between the target model and the image, done for every pixel [10], [18].

The major steps of the CONDENSATION algorithm are shown in figure 1. The first step is initialization in which the target is detected and defined; a random number of particles are uniformly distributed inside it in order to represent it correctly. Each particle is represented by its state vector  $X^k$ ,  $k \in \{1, \dots, N\}$  where  $N$  is the number of particles. The initial state vector is given as:

$$X^k = \begin{pmatrix} x & y & v_x & v_y \end{pmatrix}^T \quad (1)$$

where  $x$  and  $v_x$  are the position and speed in  $x$  direction respectively, and  $y$  and  $v_y$  in the  $y$  direction. Initially their respective speeds are null. In the initialization step, a resample procedure identical to the one inserted in the loop is performed.

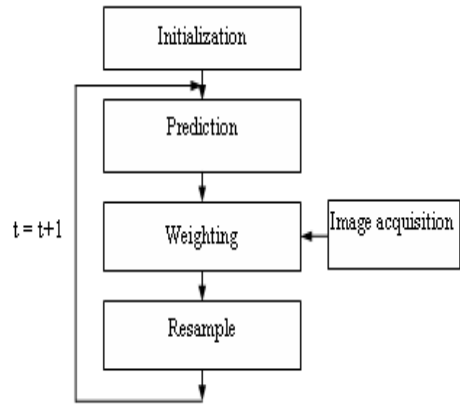


Figure 1: CONDENSATION algorithm.

The resample procedure eliminates particles that have small weights, i.e. low probability, and replicates the particles with larger weights i.e. high probability, in the target. This procedure consists in fact in a particle redistribution which preserves only the most reliable ones.

During the prediction, each particle is modified according to the state model of the region of interest in the video frame. This prediction corresponds to a propagation of particles  $X^k$  at time  $t-1$  and is given by [10], [16]:

$$X_t^k = \begin{pmatrix} 1 & 0 & 1 & 0 \\ 0 & 1 & 0 & 1 \\ 0 & 0 & 1 & 0 \\ 0 & 0 & 0 & 1 \end{pmatrix} \cdot X_{t-1}^k + \eta_t^k \quad (2)$$

$\eta_t^k$  is a noise vector used to simulate the noise in the state vector, and to explore the



expected presence probability during the sequence.

Around each particle considered as a test point, the target model corresponding to its grey-level distribution is compared with the local grey-level distribution. This comparison is carried out by using the Bhattacharyya coefficient defined as [20]:

$$z_t^k = \sum_{l=0}^L \sqrt{p^k(l) \times q^k(l)} \quad (3)$$

where  $z_t^k$  is the similarity criterion,  $L$  is the number of values which can be taken by each pixel (256 for a standard grey-scale image),  $p^k$  is the model histogram and  $q^k$  that of a local area around the  $k^{\text{th}}$  particle. This step is called the weighting or update step.

To obtain better results, it is possible to use the exponential of the criterion distance:

$$w_t^k = \frac{\exp\left(-\left(1 - z_t^k\right)\right)}{\sum_{k=1}^N z_t^k} \quad (4)$$

This criterion is often used in color-based pictures. Applied to grey-scale images, it requires more information to be relevant. To meet this need, a spatial dimension can be used, for example a bi-dimensional weighting window [21].

Many factors, such as the number of particles, the appearance model, and the particle motion model, affect the tracking result. The global result of the tracking is given by the mean state of the particles, i.e.:

$$\bar{X}_t = \sum_{k=1}^N X_t^k w_t^k \quad (5)$$

### 3 Occlusion Handling

The first technique implanted in this work is the one presented in [10]. The tracking result was acceptable with some simple sequences (Figure 2). However, the algorithm failed to track the target in complex sequences in which there were some occlusions or higher appearance changes of the object to be tracked, as shown in Figure 3. In the following subsections we present the modification made to the standard technique in order to improve the tracking algorithm in such cases.

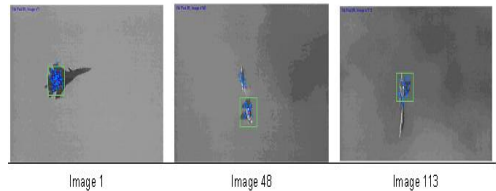


Figure 2: Example of a simple tracking (Avion1 sequence).

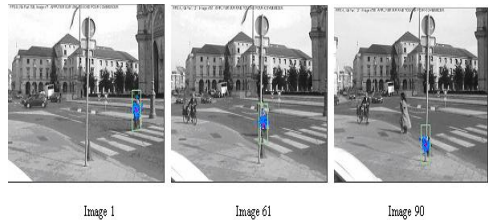




Figure 3: Effect of the systematic model update (Pieton sequence).

### 3.1 Occlusion detector

The problem is the decline in the similarity coefficient and the flatness trend of the output as the tracking develops during the sequence. Indeed, the model is only available when it is extracted from the first image and its appearance becomes more and more obsolete over time. The model therefore needs to be updated only when all the information is available, which is not the case during occlusion, for example. Accordingly, this action must be conditional. In fact, we need to detect this occlusion and to be sure that the target model is valid, that is to say close to the one defined previously.

The principle of our occlusion detector is obtained from the observation of the weighting operation result. In the event of occlusion or bad detection, the bi-dimensional similarity function is leveled as shown in figure 4. This means that the similarity maximum is more difficult to detect and more sensitive to noise: it is more complicated to define where the object is located.

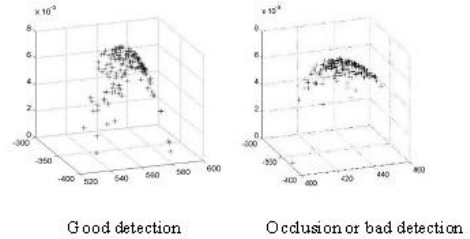


Figure 4: Effect of an occlusion on particles.

We therefore propose to evaluate the flatness of the result by using a dispersion criterion:

$$D_t = \frac{\sum_{k=1}^N w_t^k \times |X_t^k - \bar{X}_t|^2}{Sx^2 + Sy^2} \quad (6)$$

$\bar{X}_t$  is the mean position of the particles,  $Sx$  and  $Sy$  are the model length on the x-axis and y-axis respectively. Thanks to normalization, this criterion is quite constant over many video sequences.

### 3.2 Masking technique

The second recurrent problem is target deformations due to the relative displacement of the target and the camera or simply to natural target deformations. It is therefore not possible to keep the same target size and form throughout the sequence and it is necessary to employ a deformable model in order to manage this problem [22].



The effect of the resample step is to gather the particles around the position where the presence probability is higher. After this step, particles are closer to the object, and they are, in most cases, inside it. So, a very simple way to evaluate the model size and its topology is to use the position of these particles after the resample step: a morphological closing operation is applied in order to define the object (figure 5). The resample depends on the number of efficient particles defined as:

$$N_{\text{eff}} = \frac{1}{\sum_{k=1}^N (w^k)^2} \quad (7)$$

The inefficient particles ( $\bar{N}_{\text{eff}} = N - N_{\text{eff}}$ , ordered by weight) are redistributed around the central target position.

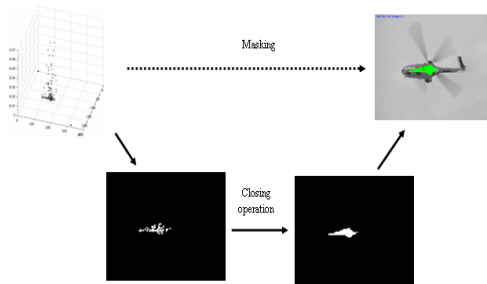


Figure 5: Masking step description.

Particular care must be taken in case of trouble during this step by testing the similarity between the pixels included in the mask and the model previously defined,

to avoid a region belonging to the background being considered as a part of the target.

Because of the closing operation in the masking step, the target topology is limited: the target must not include holes or transparent parts with a grey-level distribution representing the background. To preserve satisfactory operating conditions, an update step is performed only if the grey-level distribution in the mask is close enough to the target model. In this case the grey-level model distribution becomes the distribution of the area included in the mask, otherwise the grey-level model distribution remains unchanged.

### 3.3 Final algorithm

The final tracking algorithm is given in 6. Compared to the standard algorithm presented in Figure 2, we can note that occlusion detection and the masking technique have been added in order to improve the tracking process as will be shown in the following section.

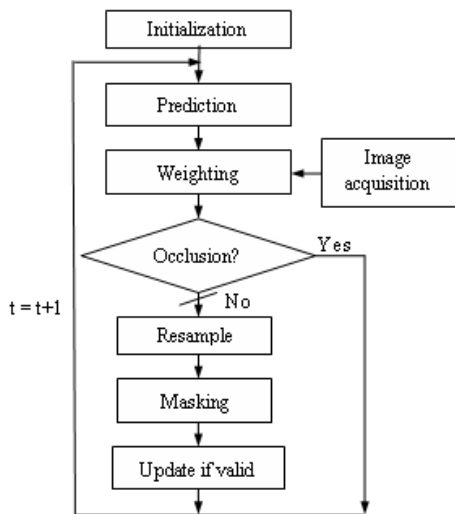


Figure 6: Improvement of the basic algorithm.

## 4 Results

The algorithm was implanted on a 2.8 GHz Pentium. Numerous tests were done on many grey-level image sequences. Only five representative sequences are presented here.

The first sequence is the Avion1 sequence of 128 images (287x177 pixels). The target is sometimes hardly distinguishable from the background and its movements are also unusual (a specific piloting operation). The second sequence is the Pieton one in which we are interested in tracking a woman. This sequence contains 97 images of 720x576 pixels. The appearance of the target does not change a much, but it is partially occluded during

approximately 10 images. Helicop1 is the third sequence of 244 320x240-pixels images in which the appearance of the target changes: the helicopter is often partially hidden by its own blades. The Helicop2 sequence presents the same characteristics as the previous one, except that the target is mainly composed of two very different grey-level values. Moreover its appearance changes a lot throughout the sequence. Finally Avion2 is the last sequence of 157 images (260x260 pixels); the scene is very noisy and the relative target movements in the images are very small.

### 4.1 Particle Number versus Computational Time

One of the main particle filtering configuration parameters is the number of particles influencing the computational time. This number is also a factor of precision concerning target presence probability.

It is important to satisfy both these points: computational time and precision. When the particle number increases, so does the computational time and the target speed averaged on ten samples falls, due to a better localization of the target with greater precision. From figure 7, it can be seen that the curve presenting the speed of the Pieton sequence is different from the others. Indeed, if the particle number is larger, then it will be easier to handle occlusion, and so the target detection and the speed estimation will be less disturbed. The computational time is roughly linear as



the particle number increases since the processing is the same for each particle, depending on the model size (Figure 8).

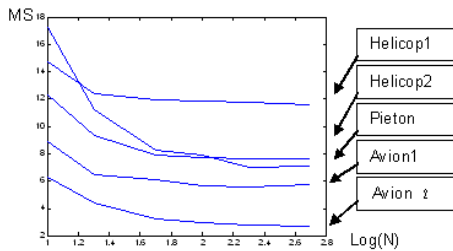


Figure 7: Mean speed of the estimated target (in pixels).

The lack of particles produces a kind of oscillation around the real target position and creates a dispersion of the estimated position. The more particles there are, the longer the computational time and the better the localization of the target. So the number of particles must be chosen carefully. Several tests on many image sequences have demonstrated that this number can be defined as a percentage of the target size on the first image: a value of 10% shows good results.

We chose to use a very simple visualization: a mask with traffic-lights indicating the tracking running state:

- Red corresponds to occlusion detection or bad detection: the target is not found. Particles are not redistributed and the model is not updated. The research area is widened.

- Amber means that the model is slightly occluded or that the extracted target

does not correspond closely to the model. Particles are redistributed, but the model is preserved.

- Green indicates that the target is well located and correctly matches with the model. Particles are redistributed and the model is updated.

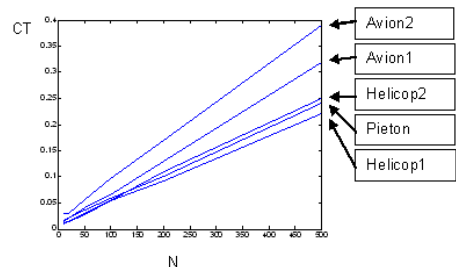


Figure 8: Computational time (in ms per pixel of the model).

#### 4.2 Updating the Model

Figure 3 shows that even though the image plane is not deformable, the model we use must take into account the target changes as well as the grey level distribution variations. Indeed, the grey level distribution defined on the first image will not be valid after few images; the target model must be updated as with the standard PF algorithm. So if the standard PF algorithm is used with a complex sequence such as the Pieton one, the tracker is distracted as shown in Figure 3.

#### 4.3 Occlusion

In the case of occlusion detection, the traffic-lights pass from amber to red. Figure 3 shows a case of occlusion detection without any update step. Because the target





environment is changing, we use the mean of the previous dispersion function values to set the detection threshold. Experiments show that using the ten previous values provide a correct threshold.

The ratio of the dispersion coefficient to its mean is presented in Figure 10. The first falling edge is caused by the incomplete average operation during the initialization step. In this way, total occlusion detection can be easily determined with a simple threshold. To eliminate any ambiguous detection, a trigger must be used. So there is detection when the dispersion function rises above the triple of the mean of the previous values. Detection ends when it falls above that mean.

#### 4.4 Model validity

The model update must be appropriate. Figure 11 demonstrates that the real model shifts slowly. This problem is due to a non-adaptive target model and is damageable when the geometric target appearance changes. This results in a model including more and more information from the background.

Using the masking step allows the algorithm to adapt the target size and topology throughout the image sequence (Figures 12, 13 and 14). Hence the target updated model contains only limited information from the background and the search area can be adapted to the target size.

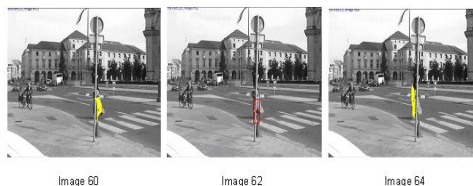


Figure 9: Example of occlusion detection.

This mask limits the update to the pixels which are part of the model. The mask changes geometrically, in accordance with the target size. Results depend on the definition of the target done in the first image. The size of the estimated target is very approximate but is sufficient for camera automation. The transition between amber and green cases is not very efficient. The similarity test result between the model and the pixels included in the mask exhibits considerable fluctuations.

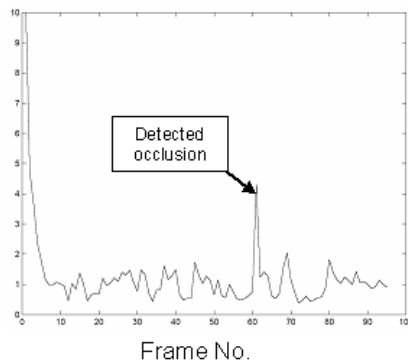


Figure 10: Variation of the dispersion function of the Piéton sequence presented in Figure 9.



Figure 11: Problem with the model update step (Helicop1 sequence).

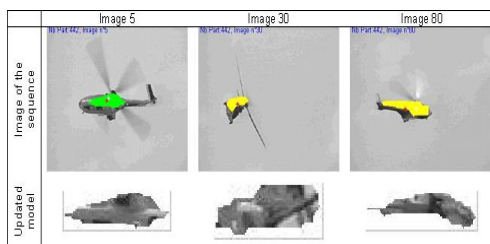


Figure 12: Example of tracking with mask (Helicop1 sequence).

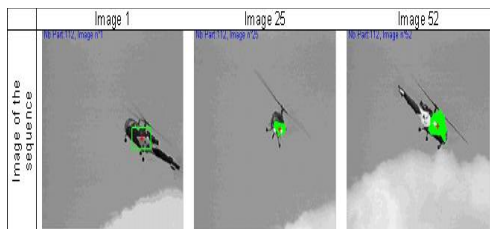


Figure 13: Example of tracking with mask (Helicop2 sequence).

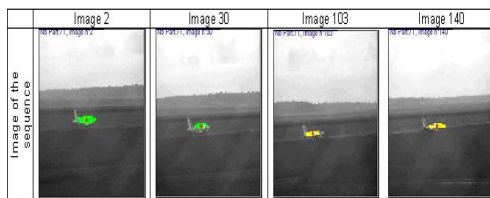


Figure 15: Example of tracking with mask (Avion2 sequence).

#### 4.5 Computational time

The basic CONDENSATION algorithm in Figure 1 corresponds to the red case (occlusion detected) in Figure 6 to which the resample step has been added. This resample step and the prediction step consume only a few percent of the CONDENSATION algorithm time: the main part of this algorithm is the weighting step.

This weighting step consumes around 0.5 ms for each particle and each pixel of the model. The masking step consumption is directly proportional to the model size and takes about 0.3  $\mu$ s per pixel. Continuing with a number of particles equal to 10 percent of the model size, the masking step consumes the same time as the weighting step.

As the time required by occlusion detection is lower than a tenth of a millisecond, the time of this step is insignificant compared to the others. Finally the update step by itself is not time-consuming. Indeed the complete algorithm simply corresponds to the green case (no occlusion) or to the amber one if no update is applied. The time difference between these two cases is negligible.

Table 1 summarizes some statistics about the video sequences and the mean time needed for target tracking with our algorithm for each sequence.



Sequence	Number of particles	Image size	Initial target size	Mean time in milliseconds		
				Red case	Amber case	Green case
Avion1	44	287×177	27×25	38	110	-
Avion2	71	260×260	51×14	31	98	106
Helicop1	176	320×240	58×31	123	220	280
Helicop2	142	320×240	49×23	47	131	150
Pieton	210	720×576	36×96	350	632	-

Table 1: Sequences computation time.

## 5 Conclusions

We have presented an improved particle filter tracking algorithm suitable for object tracking in video sequences. The new approach is very robust as it can overcome occlusion of the tracked object, as well as tracking noise such as varying lighting conditions and viewing directions.

- [1] M. Black and A. Jepson, "A Probabilistic Framework for Matching Temporal Trajectories: Condensation-Based Recognition of Gestures and Expressions," in *European Conference on Computer Vision*, 1998.
- [2] B. Menser and M. Brunig, "Face Detection and Tracking for Video Coding Applications," in *Asilomar Conference on Signals, Systems and Computers*, Pacific Grove, California, USA, 2000, pp. 49-53
- [3] M. Philip, *et al.*, "A Real-time Computer Vision System for Measuring Traffic Parameters," in *IEEE Computer Society Conference*

This algorithm is quite easy to implement and is not time-consuming (apart from the masking step). It could be used for many applications in which the target cannot be totally extracted: the pan / tilt camera control is a perfect example of use. It could also be implemented to track several objects; in this case, if the objects are similar, the dispersion function must be changed to avoid any merging effect.

This technique can be improved by studying in-depth the parameters. For example, the dispersion coefficient is not completely independent of the target. It should be possible to change the number of particles during the image sequence, for example 10% of the model size.

## References

- on Computer Vision and Pattern Recognition \*\*1997*, p. 495.
- [4] M. Greiffenhagen, *et al.*, "Statistical modeling and performance characterization of a real-time dual camera surveillance system," in *Computer Vision and Pattern Recognition*, 2000, pp. 335-342 vol.2.
- [5] M. Kass, *et al.*, "Snakes: Active contour models," *International Journal of Computer Vision*, vol. 1, pp. 321-331, 1988.
- [6] V. Caselles, *et al.*, "Geodesic active contours," in *International Conference on Computer Vision*, Boston, USA 1995, pp. 694-699.
- [7] J. Rehg and T. Kanade, "Model-Based Tracking of Self-Occluding



- Articulated Objects," in *International Conference on Computer Vision*, Boston, USA, 1995, pp. 612-617.
- [8] C. Rasmussen and G. Hager, "Probabilistic Data Association Methods for Tracking Complex Visual Objects," *IEEE Transactions on Pattern Analysis and Machine Intelligence*, vol. 23, pp. 560-576, 2001.
- [9] N. Gordon, *et al.*, "Bayesian State Estimation for Tracking and Guidance Using the Bootstrap Filter," *Journal of Guidance, Control and Dynamics* vol. 18, pp. 1434-1443, \*\*1995.
- [10] M. Isard and A. Blake, "CONDENSATION - Conditional Density Propagation for Visual Tracking," *International Journal of Computer Vision*, vol. 29, pp. 5-28, 1998.
- [11] C. Rao, *et al.*, "View-Invariant Representation and Recognition of Actions," *International Journal of Computer Vision*, vol. 50, pp. 203-226, 2002.
- [12] C. Tomasi and T. Kanade, "Shape and Motion from Image Streams: a Factorization Method," *Proc Natl Acad Sci U S A*, vol. 90, pp. 9795-802, Nov 1 1993.
- [13] K. Nummiaro, *et al.*, "A Color-Based Particle Filter," in *First International Workshop on Generative-Model-Based Vision*, 2002.
- [14] P. Perez, *et al.*, "Color-based Probabilistic Tracking," in *European Conference on Computer Vision*, 2002, pp. 661-675.
- [15] S. Zhou, *et al.*, "Appearance Tracking Using Adaptive Models In a Particle Filter," in *Asian Conference on Computer Vision*, 2004.
- [16] G. Kitagawa, "Monte Carlo Filter and Smoother for Non-Gaussian Nonlinear State Space Models," *Journal of Computational and Graphical Statistics*, vol. 5, pp. 1-25, \*\*1996.
- [17] N. Gordon, *et al.*, "Novel Approach to Nonlinear/Non-Gaussian Bayesian State Estimation," *IEE Proceedings on Radar and Signal Processing*, vol. 140, pp. 107-113, 1993.
- [18] A. Jacquot, *et al.*, "Adaptative Tracking of Non-Rigid Object Based on Color Histograms and Automatic Parameter Selection," in *ORASIS*, 2001.
- [19] A. Ganoun, *et al.*, "Approche de Suivi d'Objet par Courbes de Niveau " in *GRETSI*, Louvain-la-Neuve - Belgique 2005.
- [20] K. Sohail, *et al.*, "Bhattacharyya Coefficient in Correlation of Grey-Scale Objects " *Journal of Multimedia*, vol. 1, pp. 56-61, 2006.
- [21] A. Oppenheim and R. Schaffer, *Discrete-time signal processing*. Englewood Cliffs, N.J.: Prentice Hall, 1989.
- [22] K. Nummiaro, *et al.*, "Object Tracking with an Adaptive Color-Based Particle Filter," in *Symposium for Pattern Recognition of the DAGM*, 2002, pp. 353 - 360.



## Paper NO. 103008

### TEXTURE CLASSIFICATION OF RAW TEXTILE DEFECTS USING SVM

Yassine Ben Salem  
Electric department, ENIM  
System & communication network Unit, ENIM  
Monastir, Tunisia  
[bensalemy73@yahoo.fr](mailto:bensalemy73@yahoo.fr)  
Salem Nasri  
Electric department, ENIM  
System & communication network Unit, ENIM  
Monastir, Tunisia  
[salemnasri@yahoo.fr](mailto:salemnasri@yahoo.fr)

#### Abstract:

In this paper we have compared two methods in texture classification to solve the problem of recognition of defects occurring in a textile manufacture. We have compared local binary patterns method with co-occurrence matrix. The classifier used is the support vector machines (SVM). The system has been tested using TILDA database. The results obtained are interesting and show that LBP is a good method for the problems of recognition and classification defects, it gives a good running time especially for the real time applications.

*Keywords*—Texture classification, woven defects, LBP, GLCM, Support vector machine.

#### Note:

This paper is included in the conference program but not published because the revised copy after introducing the reviewed comments did not arrive in the specified Time



المؤتمر العربي الليبي الدولي الخامس للهندسة الكهربائية والإلكترونية 23-26/10/2010 طرابلس ليبيا



**Paper NO. 103011**

## **Mean Square Error Minimization**

### **Using Interpolative Block Truncation Coding Algorithms**

Elghanai. M. Rhoma, Abdosllam.M. Abobaker, and Elmahdi . A. Elkhazmi

Communication Engineering Department

Higher Institute of Electronics

Bani Waleed, Libya

E-mail: [elganai1962@yahoo.com](mailto:elganai1962@yahoo.com)

*Abstract—*

Block Truncation Coding (BTC) is one of spatial coding techniques of images. This technique has a simple and fast algorithm which achieves constant bit rate of 2 bits per pixel. The compression ratio may be improved by coding only half of the bits in the BTC bit plane of each block; the other half will be interpolated at the receiver. The resulting bit rate will be 1.5 bits per pixel. In this paper, two proposed interpolative algorithms for coding the block truncated image bit plane are presented. Several grey scale test images are used to evaluate the coding efficiency and performance of these algorithms compared with existing algorithms. It is generally shown that the proposed algorithms give better results.

*Keywords-image coding; block truncation coding; interpolative BTC coding; image processing.*

**Note:**

**This paper is included in the conference program but not published because the revised copy after introducing the reviewed comments did not arrive in the specified Time**



المؤتمر العربي الليبي الدولي الخامس للهندسة الكهربائية والإلكترونية 23-26/10/2010 طرابلس ليبيا





## **Payload Encoding Using Variable Length Encoding and YCbCr Color Space in multiple frequency domain steganography**

**Raof Smko, Abdelsalam Almarimi, K. Negrat**

**College of Electronics Technology / Baniwalid - Libya**

[raofsmko@yahoo.com](mailto:raofsmko@yahoo.com), [bekgasem\\_2000@yahoo.com](mailto:bekgasem_2000@yahoo.com), [dr\\_negrat@yahoo.com](mailto:dr_negrat@yahoo.com)

### **Abstract.**

In this paper a multiple frequency domain steganography is proposed; it uses DWT with DCT techniques, which are applied sequentially on the cover image. Embedding the secret message is done in the high frequency coefficients to provide a high imperceptibility; as it is the most important property of any steganography system. For secret message encoding, variable length encoding is used with a special character codes to encode the characters into binary data. This encoding encrypts the secret message and reduces the number of bits used to encode each character, which results in the increment of the capacity.

With this new technique, we got very good results through satisfying and improving the most important properties of steganography such as: Imperceptibility; improved by having the MSE  $\rightarrow 0$  and PSNR  $\rightarrow 128$  db, security; improved by using an encrypted Stego-key and secret message by the encoding, capacity; improved by encoding the secret message characters with variable length codes and embedding the secret message in the YCbCr components instead of the RGB.

Keywords: Steganography, Information Hiding, Frequency Domain, Security.

### **1. Introduction**

The appearance of the Internet is considered to be one of the major events of the last years; information become available on-line, all users who have a computer can easily connect to the Internet and search for the information they want to find [1].

Two techniques are available to achieve this goal: one is cryptography, where the sender uses an encryption key to scramble the message, this scrambled message is transmitted through the insecure public channel, and the reconstruction of the

original, unencrypted message is possible only if the receiver has the appropriate decryption key. The second method is steganography, where the secret message is embedded in another message. Using this technology even the fact that a secret is being transmitted has to be secret [2][3].

Information hiding represents a class of process used to embed data into various forms of media such as image, audio, or text.



There are two types of information hiding the first one is *steganography* and the second is *digital watermarking* [4][5].

*Steganography* serves to hide secret messages in other messages. It's not intended to replace cryptography, but to supplement it. Hiding message with steganography reduces, the chance of a message being detected [6].

A *digital watermark* is a digital signal, or pattern inserted, into a digital image. Since this signal or pattern is present, in the each unaltered copy of the image. The digital watermark may also serve as a digital signature for the copies [6].

## 2. Related Studies

In 1992, Kurak and McHugh [7] suggested a new system in steganography called image downgrading which is a special case of substitution methods and there image acts as secret and cover. Given secret image and cover image same dimensions, sender must change the four least significant bits of cover image with four most significant bits of secret image. in which during embedding process sender split the cover image to 8x8 pixel blocks, each block encode one secret bit. Before communication started the sender and receiver agree previously on the location of two DCT coefficients which will be used in embedding process, comparison done between these two values, if we want to embed secret bit 1, we must check these two values the first one should be grater than second value if not we must swap their positions. Same thing for embedding 0,

The receiver extracts the four significant bits of stego-cover, thereby gaining access to four most significant bits of secret image.

Zhao and Koch [8] are present another scheme of steganography techniques used for binary image (black and white), or in digitalized fax data. In which they divide binary image to rectangular image blocks, and calculate percentage of zero and ones in each block.

Another simple technique presented by Matsui and Tanaka [9], where it is used in fax binary images, because fax images used run length and Huffman for encoding images. They make use from RL technique in which all pixels comes after each other in a sequence manner, where a sequence of white pixels comes then followed by another sequence of black pixels, odd number of those sequences represent 1 and even numbers represent 0.

In the transform domain there are some other techniques can be listed as related works. Zhao and Koch [8] used DCT technique in steganography second point should be grater than first point if not swapping done.

Development done on previous DCT method by Zhao and Koch [10], in which they have used three points instead two points, for comparison. Hiding secret 1,  $p_1 > p_2$  and  $p_1 > p_3$ ; while for embedding 0,  $p_1 < p_2$  and  $p_1 < p_3$ . This will give cover image higher robustness against attacks.

## 3. Research Methodology

Instead of having just a look to previous steganography techniques, comparing, and



analyzing. The proposed stego-system intended to focus on three approaches: firstly; mixes two different frequency domains (DCT and DWT) for making it more imperceptible, robust, and secure. Secondly; variable lengths encoding based data embedding (use a special encoding for encrypting the data before embedding) to make the data recovery not possible by the third party. Thirdly; using YCbCr color space instead of RGB, and embedding the secret message in chrominance (Cb, Cr) parts only and without changing the luminance to increase the imperceptibility, because human eyes is more sensitive for luminosity of the color.

#### 4. Purpose and Contribution

The technique used in this paper allows hiding messages in different bitmap images. Robustness, importability, and capacity were the main characteristics optimized by using this technique. We designed a special software package called (YAD) for implementing the technique, also this software package was designed for implementing this techniques, it also can act as a benchmark for implementing other steganography techniques and make comparison between them. This was one of the main contribution made, hence we can make real comparison depending on the most important characteristics used in any steganography system.

#### 5. System Architecture

The system is made from two major parts; Embedding and Extraction process. The Embedding process hides the secret message inside the cover image and the result will be the stego-image. The other

process is Extraction that extracts the embedded secret message from the stego-image regarding some security issues.

Embedding the secret message goes through several processes, it begins with loading the image (because it uses the colored bitmap image, it loads the image in 3D matrix with values Red, Green, and Blue that comes from decomposing the pixel values) and normalizing its dimensions based on the selected technique (DCT or DWT+DCT).

This step is done to make the image dimensions (width and height) fit the algorithm that transforms the image from spatial domain to frequency domain by taking the largest suitable part from the image and clipping the smallest improper extra pixels.

The next step is to convert the normalized image from RGB space into YCbCr color space. A color vector in RGB is converted by the following equations [11]:

$$Y = 0.299 R + 0.587 G + 0.114 B \quad (1)$$

$$Cb = 0.5 + (B - Y)/2 \quad (2)$$

$$Cr = 0.5 + (G - Y)/2 \quad (3)$$

After normalizing the image dimensions and converting it to YCbCr color space, depending on selected technique; it goes to DCT block, if DCT is chosen, which takes the Discrete Cosine Transform of the normalized image pixel's matrix or to DWT block, if DWT+DCT is chosen, to take the Discrete Wavelet Transform (haar or Daubechies-4, based on the selection) and then to DCT block, by this it uses two



frequency domains to increase the imperceptibility and security level.

Now the image is in transform (or frequency) domain and it will be passed to Embedding block, here before explaining the Embedding block there are two other inputs for the proposed stego system which are the Secret Message (the desired text message to be hidden inside the cover image) and Stego Key (the key for security reason, it is required in the receiving side to extract the message, without this the second party can not recover the hidden secret message).

The Secret Message and Stego Key are comes from the user and they will be passed to "Variable Length Encoding Translation", using adaptive Huffman coding algorithm, for encoding them into the specific encoding translated code. Then they will be passed to the Payload Encoding block, which encodes the payload (payload holds the encapsulation of the whole data; Stego system ID, Length of the secret message, Stego Key, Used Technique, Selected Quarter(s), and the Secret Message itself). The impact and the importance of the Payload will be seen in Extraction Process.

The Embedding block embeds the payload into the frequency transformed image matrix. After that, the recreation of the image will take place by taking the IDCT (Inverse Discrete Cosine Transform), after this if "DWT+DCT" was chosen it will go to IDWT (Inverse Discrete Wavelet Transform – haar or Daubechies-4 based on the selection). Now the image matrix is in spatial domain and the dimensions needs to

be restored to the original (cover Image) dimensions; by passing it to "Restore Image Dimensions" block, this is done to make the Stego image (the image that contains the secret message) exactly looks like the Cover Image.

The technique extracts the secret message without using the Cover-image, it is a blind stego system. Off course the stego-key should be shared between the first and second party to be used in embedding and extraction process.

## 6. Embedding Procedure

This procedure embeds the encoded payload, which is a stream of bytes, into the array of 8x8 DCT coefficients. It works in bit-level, because the payload encoded in bytes before, and there is a variance in embedding the payload bytes.

Embedding is done by inserting each two bits of the payload in one 8x8 block, which selects three points from it which are  $P_1 = X_{7,5}$ ,  $P_2 = X_{7,6}$ , and  $P_3 = X_{7,7}$  as shown in Table (1). The selection of points are done carefully, here it focuses on the imperceptibility which is the most important property of any steganography systems, and therefore it selects the points from the highest frequency elements  $X_{7,5}$ ,  $X_{7,6}$  and  $X_{7,7}$ .

**Table 1, An 8x8 block DCT coefficients, showing  $P_1$ ,  $P_2$ , and  $P_3$**

$X_{0,0}$	$X_{0,1}$	$X_{0,2}$	$X_{0,3}$	$X_{0,4}$	$X_{0,5}$	$X_{0,6}$	$X_{0,7}$
$X_{1,0}$	$X_{1,1}$	$X_{1,2}$	$X_{1,3}$	$X_{1,4}$	$X_{1,5}$	$X_{1,6}$	$X_{1,7}$
$X_{2,0}$	$X_{2,1}$	$X_{2,2}$	$X_{2,3}$	$X_{2,4}$	$X_{2,5}$	$X_{2,6}$	$X_{2,7}$
$X_{3,0}$	$X_{3,1}$	$X_{3,2}$	$X_{3,3}$	$X_{3,4}$	$X_{3,5}$	$X_{3,6}$	$X_{3,7}$
$X_{4,0}$	$X_{4,1}$	$X_{4,2}$	$X_{4,3}$	$X_{4,4}$	$X_{4,5}$	$X_{4,6}$	$X_{4,7}$
$X_{5,0}$	$X_{5,1}$	$X_{5,2}$	$X_{5,3}$	$X_{5,4}$	$X_{5,5}$	$X_{5,6}$	$X_{5,7}$
$X_{6,0}$	$X_{6,1}$	$X_{6,2}$	$X_{6,3}$	$X_{6,4}$	$X_{6,5}$	$X_{6,6}$	$X_{6,7}$
$X_{7,0}$	$X_{7,1}$	$X_{7,2}$	$X_{7,3}$	$X_{7,4}$	$X_{7,5}$	$X_{7,6}$	$X_{7,7}$



After selecting these three points for embedding two bits of the secret message, in any 8x8 block of DCT coefficients, by this the capacity of the cover image can be increased twice, as shown in table (2).

**Table 2, Three point embedding method**

Points expression	Embedded bit values
$P_1 < P_2 < p_3$	00
$P_1 < P_2 > p_3$	01
$P_1 > P_2 < p_3$	10
$P_1 > P_2 > p_3$	11

### 7. Experiment Results

The experiments implemented using special software package, this package have been developed specially for this new technique. The software developed using Microsoft J# 2005 Express Edition, which it produce more flexible for this work in the designing a GUI for the application, and it is fast enough since most of the image processing program needs a long time for execution.

The experiments done on Lena image, the image is colour bitmap 512x512 pixels, and the size of 768 KB.

Figure (1) shows the graph representing the maximum capacity (measured by characters) for the techniques used in the approach. The frequency domain embedding suffers from having a low capacity; for example in DCT we can embed one bit in 64-pixels (8x8), but there is some improvement in our approach which is the use of variable length encoding based encoding, which reduces the number of bits (less than 8 bits) used for

representing a character, and embedding the message in two layers (CbCr).

Because of getting a high imperceptibility in the stego images [11], and found that there is no noticeable distortion at all; that is why the results are:  $MSE \rightarrow 0$  and peak signal to noise ratio  $PSNR \rightarrow 128$  db and the file size remains the same. Another way used for showing the difference between the stego and the original image, which is the Bit difference; or the number of bits changed by the embedding process. Figure (2) shows the chart of comparing the Bit Difference between the original and stego image after embedding the secret message for the different techniques used.

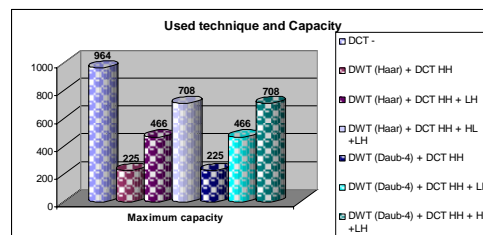


**Figure (1) Capacity in characters for the techniques used.**

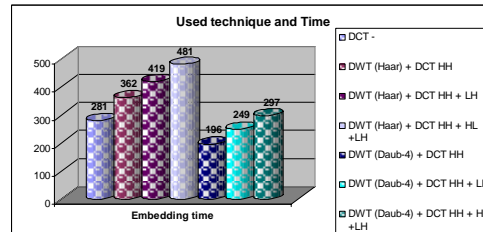


**Figure (2) The bit difference between original and stego image**

The execution of embedding programs usually take a long time, this notation is

very clear to proficient persons whom working in information hiding, because of the big amount processes done in those programs; here some improvements are done in our approach and these results are obtained. Figure (3) shows a graph for the time required in various techniques used for the hardware environment mentioned above in this section.

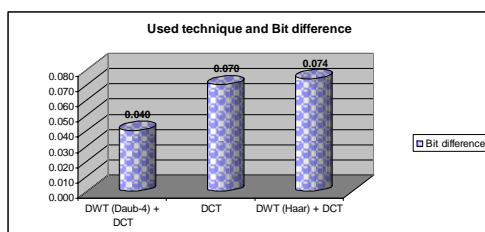


**Figure (4) The time required for various techniques used.**

## 8. Conclusion and Future Works

In this paper a stego system is proposed for image steganography with multiple frequency domains using YCbCr color space, which increased the imperceptibility and robustness as well. Another advanced feature of this work is the use of variable length encoding (Huffman Encoding) dictionary translation code for characters of the secret message to improve the security issue and encrypting the secret message before embedding.

The proposed stego system works on lossless compressed images with Bitmap image files. We can summarize the conclusions as follow:

- There are no noticeable changes between cover and stego images' luminosity histogram, this is in worst case.

- BER  $\rightarrow$  0 for all experimental results; the embedded secret message 100% recovered (extracted) from the stego-image without any errors or changes, which is a challenge in frequency domain data embedding because of looses and rounding processes of values in transformation process.

- The use of fixed difference between the selected points for embedding (DCT and DWT (Daub-4) + DCT is 4, and for DWT (Haar) + DCT is 9), which gives many advantages over the use of maximum threshold; which is widely used in steganography with DCT. Because it needs less time for embedding and it has less distortion in stego-image

- Haar wavelet is simpler to implement and dealing with than the Daubachies-4, but Daubechies-4 is better to use in wavelet transform steganography, because it has less looses of coefficient values in transform and inverse transform processes.

- All techniques of the proposed system are imperceptible enough regarding the two parameters; MSE  $\rightarrow$  0 and PSNR  $\rightarrow$  128 db, and also by having the same image file size (KB) and dimensions (pixels) for the cover and stego images.

- The DWT (Daub-4) + DCT has the minimum bit difference (maximum imperceptibility), then DCT only technique comes with higher bit difference, and then DWT (Haar) + DCT comes with highest bit difference except the (HH) quarter selection which has lower bit difference than DCT only technique.

- The bit difference in both DWT + DCT techniques (Haar and Daub-4) increases



with selecting more quarters (if filled), and (HH) filter band has the minimum bit difference then LH comes and then HL.

- The bit difference increases with the message size; the longer secret message has the higher bit difference.

- The DCT only has the maximum capacity, and then DWT + DCT technique comes with lower capacity.

- In DWT + DCT techniques (Haar and Daub-4), the more quarter selection gives more capacity; three quarters gives the highest capacity, then two quarters come with lower capacity, and then one quarter comes with lowest capacity.

- The capacity is improved by 1.333 comparing with traditional embedding systems, by encoding each character of the secret message with 6-bits. Also the capacity is improved by removing the white space in the secret message done by the dictionary and by embedding the secret message in three layers RGB of the pixel values.

- The use of stego-key made the proposed stego-system be more secure; no secret message can be recovered in stego image if the key is not given correctly.

- The proposed stego-system involves with the high security by using a special dictionary for encoding the secret message characters; it encrypts the secret message before embedding.

- Regarding the capacity, the DCT only technique has the lowest embedding/extraction duration time, then DWT (Daub-4) + DCT comes with a lower embedding/

extraction duration time, and then DWT (Haar) + DCT comes with highest embedding/extraction duration time. And regardless to the capacity, the sequence from lowest to highest embedding/extraction time is; DWT (Daub-4) + DCT, DCT only, and then DWT (Haar) + DCT.

- In DWT + DCT techniques (Haar and Daub-4), the embedding/ extraction duration time increases with the number of selected quarters.

- The embedding/ extraction duration time is increases with the secret message size; the longer message results the higher embedding/ extraction duration time.

- A more robust embedding process can be done by choosing the medium frequency filter bands (HL, LH, HL+LH) in both DWT (Haar) + DCT and DWT (Daub-4) + DCT techniques; embedding in medium frequency filter bands are more robust than the high frequency filter band (HH).

As an ideas for future works, we can apply the same idea on other lossless compressed image files and videos as well.

We can go through using the same proposed system as watermarking system by a small change; selecting the chosen points from medium frequencies in the 8x8 block of the DCT coefficients to increase the robustness, as it is the most important property of any watermark system.

Finally by providing the DWT with more than one stage, like 2 or 3-stage DWT, for increasing the capacity.





## References

- [1] Richard Popa, "*An Analysis of Steganographic Techniques*", The "Politehnica" University of Timisoara, 1998.
- [2] József LENTI, "*STEGANOGRAPHIC METHODS*", H-1521 Budapest, Hungary, June 5, 2000.
- [3] ANDERSON, R. J. – PETITCOLAS, F. A. P., *On The Limits of Steganography*, *IEEE Journal of Selected Areas in Communications*, **16** (4) pp. 474-481, May 1998. Special Issue on Copyright & Privacy Protection. ISSN 0733-8716.
- [4] Khorsheed, Nizar Kamal, "*Image Watermarking Using DCT Domain*", University of Technology, M.sc. Thesis, 2005.
- [5] Uroba Ismail Ibrahim Al-dilaimy, "*Text in Image Steganography*", University of Technology, M.sc. thesis, 2001.
- [6] Hsu, C.T., & Wu, J.L. "*Hidden Digital Watermarks in Images*", *IEEE Transactions on Image Processing*, **8**(1), pp. 58-68. 2003.
- [7] Christian Cachin, "An Information-Theoretic Model for Steganography", in *Proceedings of 2nd Workshop on Information Hiding (D. Aucsmith, editor), Lecture Notes in Computer Science, Springer, 1998.*
- [8] Pei-Chun Chen, May 1999, "On the Study of Watermarking Application in WWW-Modeling, Performance, Analysis, and Applications of Digital Image Watermarking Systems", Master Thesis, National Tsing Hua University.
- [9] Kurak, C., and J. McHughes, "A Cautionary Note On Image Downgrading" in *IEEE Computer Security Application Conference 1992*, proceedings, IEEE Press, 1992.
- [10] Zhao. J. and E. Koch, "Embedding Robust Labels into Image for Copyright Protection." in *Proceedings of the International Conference of Intellectual Property Rights for Information, Knowledge and New Techniques*, Munchen, Wein: Oldenbourg Verlag, 1995.
- [11] Jiri Fridrich, "A New Steganographic Method for Palette-Based Images", Center for Intelligent Systems, SUNY Binghamton, Binghamton, NY 13902-6000. IS&T PICS Conference, pages 285289, 1999.





## Arabic Speech Recognition (ASR)

Abubaker M. F. Abushofa\* and Nadia F. M. Hmad\*\*

\* Dep. of Electrical and Electronic Eng., Faculty of Eng., Alfateh University.

Email: [abushofa@ee.edu.ly](mailto:abushofa@ee.edu.ly)

\*\* Dep. of Electrical & Computer Eng., School of Applied Science and Eng., Academy of Graduate Study.

### Abstract

Automatic speech recognition by computers is a process where speech signals such as Arabic speech are automatically converted into the corresponding sequence of words in text. With recent advances, speech recognizers based upon *hidden Markov models* (HMM) have achieved a high level of performance in controlled environments. Neural Network algorithms such as *Radial Basis Function* (RBF) and *Multi-Layer Perceptron* (MLP) are also used in several applications that are used for complex pattern-classifications.

In this paper, we attempt to develop a recognition system for Arabic speech using Radial Basis Function (RBF) and A Multi-Layer Perceptron (MLP) (as another method that use Back-Propagation algorithm) to recognize isolated Arabic speech to support applications that involve the use of isolated words.

### 1. Introduction

Speech recognition is the process of converting acoustic signals, captured by a microphone or a telephone, to a set of words. The recognized words can be the final results, as for applications such as commands and control, data entry, etc. They can also serve as the input to further linguistic processing in order to achieve speech understanding.

Many aspects of Arabic, speech such as the phonology and the syntax, do not present problems for automatic speech

recognition. Standard, language-independent techniques for acoustic and pronunciation modeling, such as context-dependent phones, can easily be applied to model the acoustic-phonetic properties of Arabic. Some aspects of recognizer training are even easier than in other languages, in particular the task of constructing a pronunciation lexicon since there is a nearly one-to-one letter-to-phone correspondence.

The most difficult problems in developing high-accuracy speech recognition systems for Arabic are the



predominance of non-diacritized text material, the enormous dialectal variety, and the morphological complexity.

Speech recognition system can be characterized into two categories; isolated-word speech recognition and continuous speech recognition.

### 1.1. Isolated Word Recognition

This is the simplest speech recognition mode and the less greedy in terms of CPU requirement. Each word is surrounded by a silence so that word boundaries are well known. The system does not need to find the beginning and the end of each word in a sentence. The word is compared to a list of words model, and the model with the highest score is retained by the system.

### 1.2. Continuous Speech Recognition

Continuous speech recognition is much more natural and user-friendly. It assumes the computer is able to recognize a sequence of words in a sentence. But this mode requires much more CPU and memory, and the recognition accuracy is really inferior compared with the preceding mode. Continuous speech recognition is more difficult than isolated word recognition because of some explanations such as:

- Speaker's pronunciation is less careful.
- Speaking rate is less constant.
- Word boundaries are not necessarily clear.

- There is more variation in stress and intonation (interaction between vocal tract and excitation).

## 2. Speech Recognition Techniques

Speech recognition is tackled in different approaches recently. One of the useful approach or technique is Neural Network algorithms such as Radial Basis Function (RBF) and Multi-Layer Perceptron (MLP). Some approaches use these techniques together to produce high performance systems [1].

An NN is configured for a specific application, such as pattern recognition, data classification, identification, speech, vision and control systems through a learning process [2, 3]. RBF networks have been successfully applied to a large diversity of applications including interpolation [4, 5], chaotic time-series modeling [6], system identification, control engineering [7], electronic device parameter modeling, channel equalization [8-10], speech recognition [9, 11], image restoration [12], shape-from-shading [13], 3-d object modeling [5, 14], motion estimation and moving object segmentation [15], data fusion [16], etc.

## 3. Speech Recognition System

Figure 1 shows a block diagram of a typical speech recognition system. *First*, feature vectors are extracted from a speech waveform, achieved through modeling the human vocal tract using linear predictive coding (LPC), which is then converted to the more robust spectral coefficients.



The *second* stage of the design is to train the system for different utterances of the words in the vocabulary set. These utterances should constitute a good sample set of the various conditions and situations in which the word may be uttered.

This training was implemented using the Radial Basis Function (RBF), and the Back-propagation algorithm with momentum and variable learning rate. The system was tested under different conditions: noisy and clean environments.

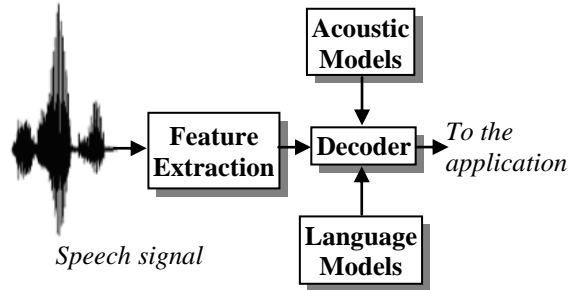


Figure 1: A speech recognition system.

### 3.1. Feature Extraction

Feature vectors are extracted from speech waveforms. A feature vector is usually computed from a window of speech signals (10, 20 ms) in every short time interval (about 10 ms). An utterance is represented as a sequence of these feature vectors.

One technique of feature extraction in speech recognition employs the Linear Predictive Coding (LPC). The basic steps in applying this technique include the following:

#### a) Pre-emphasis

In general, the digitized speech waveform has a high dynamic range and

suffers from additive noise. An example of such a waveform to the Arabic word 'Bahar' (Sea in English) that is shown in Figure 2(a). In order to reduce this range pre-emphasis is applied. By pre-emphasis [17], we imply the application of a high pass filter, which is usually a first-order FIR of the form:

$$H(z) = 1 - az^{-1} \quad \text{Where } 0.9 \leq a \leq 1.0 \quad (1)$$

The pre-emphasizer is implemented as a fixed-coefficient filter or as an adaptive one, where the coefficient  $a$  is adjusted with time according to the autocorrelation values of the speech, ( $a = 0.96$  in our work).

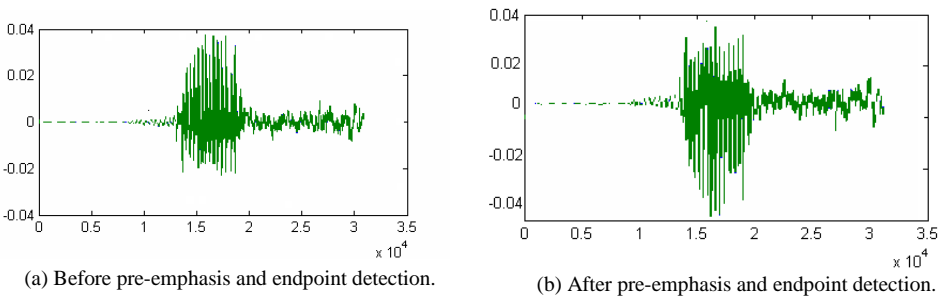


**Figure 2: Speech Waveform of the word 'Bahar'.**

The pre-emphasizer has the effect of spectral flattening which renders the signal less susceptible to finite precision effects (such as overflow and underflow) in any subsequent processing of the signal. The pre-emphasizer is applied and shown in Figure 2(b).

### b) Endpoints detection

The goal of endpoint detection is to isolate the word to be detected from the background noise. It is necessary to trim the word utterance to its tightest limits, in order to avoid errors in the modeling of subsequent utterances of the same word. As we can see from Figure 2(a), a threshold has been applied at both ends of the waveform.

### c) Frame blocking

Since the vocal tract moves mechanically slowly, speech can be assumed to be a random process with slowly varying properties [17]. Hence, the speech is divided into overlapping frames of 20ms every 10ms (pre-emphasized speech signal is blocked into frames of  $N$  samples). The speech signal is assumed to be stationary over each frame and this

property will prove useful in the following steps.

### d) Windowing

To minimize the discontinuity of a signal at the beginning and end of each frame, we window each frame to increase the correlation of the linear predictive coding (LPC) spectral estimates between consecutive frames [17].

The windowing tapers the signal to zero at the beginning and end of each frame. A typical LPC window is the *Hamming window* of the form:

$$w(n) = 0.54 - 0.46\cos\left(\frac{2\pi n}{N-1}\right) \quad (2)$$

Where  $0 \leq n \leq N - 1$

### 3.2. LPC analysis

The LPC coefficients  $a_i$  are the coefficients of the all pass transfer function  $H(z)$  modeling the vocal tract, and the order of the LPC,  $p$ , is also the order of  $H(z)$  defined as:

$$H(z) = \frac{1}{1 - \sum_{i=1}^p a_i z^{-i}} \quad (3)$$

A drawback of LPC estimates is their high sensitivity to quantization noise. Spectral coefficients, which can be derived

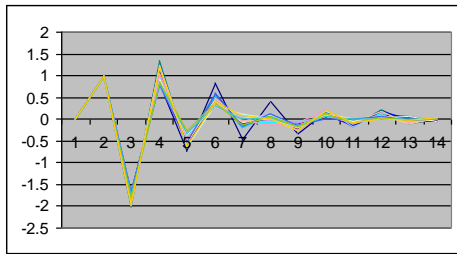


from the LPC coefficients, have lower susceptibility to noise, and were adopted instead.

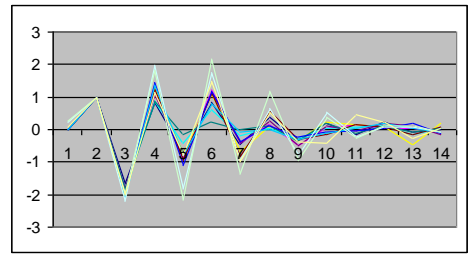
To decrease the sensitivity of high-order and low-order spectral coefficients to noise, the obtained spectral coefficients are multiplied by an appropriate weighting which is a window with the following equation:

$$w_m = \left[ 1 + \frac{q}{2} \sin\left(\frac{\pi m}{q}\right) \right] \quad 1 \leq m \leq q \quad (4)$$

This results in what is known as the weighted spectral coefficients [17].



(a)



(b)

Figure 3: Utterances of the word “fatah”; (a) one speaker 20 times, (b) 12 speakers one at a time.

#### 4. Experimental Results

In this paper, the Radial Basis Function (RBF) and Multi-Layer Perceptron (MLP) transformations are applied to discrete speech recognition. The effectiveness of the

The recorded words are divided into three groups, as shown in Table 1. The first group consists of four general words that are clearly different in sound. The second group consists of four words. These words in turn consist of four pairs of words. Each pair of words sounds similar. Those are chosen to be used to test the strength of the recognition system.

proposed algorithms is quantified through experimental measurements using a set of Arabic words collected from a number of native speakers.

##### 4.1. Details of the recorded set of words

The third and last group contains six words chosen as commands to instruct the operating system to carry out some common tasks such as those used in windows applications.



**Table 1: Words recorded and used to train and test the classifiers.**

No	Word in Arabic	Uttered	Meaning	Group
1.	بحر	Bahar	Sea	1
2.	شمس	Shams	Sun	
3.	أرض	Ard	Earth	
4.	سماء	Sama	Sky	
5.	سَحر	Sahar	Before dawn	2
6.	همس	Hams	Whisper	
7.	عرض	Aard	View	
8.	نداء	Nedaa	Call	
9.	فتح	Fatah	Open	3
10.	إغلاق	Eghlak	Close	
11.	تحديد	Tahdeed	Select	
12.	نسخ	Nasak	Copy	
13.	لصق	Lask	Past	
14.	تحرير	Taheer	Edit	

Each selected group of words was recorded by four male and eight female speakers. Each word was uttered 20 times by each speaker, to produce a total of 280 samples from each word. The speakers' age ranges from 17 to 45 years as shown Table 2.

**Table 2: Users recorded the words.**

Speaker No	Gender	Age	Recording Background
1.	Male	17	Noisy
2.	Female	20	Noisy
3.	Female	20	Noisy
4.	Female	22	Noisy
5.	Female	24	Noisy
6.	Female	24	Quiet
7.	Female	24	Noisy
8.	Male	27	Quiet
9.	Female	26	Quiet
10.	Female	32	Quiet
11.	Female	32	Noisy
12.	Male	33	Noisy
13.	Male	38	Quiet
14.	Female	45	Noisy

From Table 2 it is clear that there is deference between age and gender of speakers, in order to obtain different voice frequencies, and to extend the possibility of using the system by different users.

The previously mentioned 14 words uttered by speakers in two situations. In the first situation, speakers uttered these words in quiet environment (without noise). In the second situation, speakers uttered these words in a noisy environment as indicated in Table 2.

After that, the features of each word were obtained by using Linear Predictive



Coding (LPC) algorithm. The Radial Basis function (RBF) and the Multi-Layer Perceptron (MLP) were used to recognize these words.

A Logistic activation function was applied and mean squared error (MSE) function was obtained, for all words during both the training and testing faces of this process. The mean square error (MSE) function was obtained according to the following equation:

$$E = \frac{1}{2} \sum_i (y_i(\text{desired}) - y_i(\text{actual}))^2 \quad (5)$$

Data samples are divided into two parts. The first part is used for training, and second part is used for testing, as shown in the following section.

#### 4.2. The words in quiet environment (without noise)

All 14 words were uttered by speakers (1, 3, 4, 5 and 6, Table 2) in a quiet

environment (without noise). Each word was uttered 20 times by each speaker which gives a total of 1400 samples. Radial Basis (RBF) and Multi-Layer Perceptron (MLP) were applied to classify these words according to their groups shown in Table 1. The classification results were as follows.

##### a) Radial Basis Function (RBF)

When we used the Radial Basis function (RBF) to recognize the first group of words indicated by the 2<sup>nd</sup> column of Table 3, we obtained a good recognition rate of 93.5%. That was because these words are clearly different in sound from each other.

When we added the words of the second group that are sound similar, the recognition rate dropped to 82% as shown in the 3<sup>rd</sup> column of Table 3.

**Table 3: Recognition rate of words uttered in quiet environment, by RBF.**

<i>Group of words</i>		<i>1<sup>st</sup></i>	<i>2<sup>nd</sup></i>	<i>3<sup>rd</sup></i>	<i>4<sup>th</sup></i>
<b>No. of Data Samples</b>	<b>Total</b>	400	800	600	1400
	<b>Train</b>	200	600	400	400
	<b>Test</b>	200	300	200	1000
<b>Classified</b>		93.5%	82%	90.5%	74.2%
<b>Misclassified</b>		6.95%	4.5%	2.5%	2.6%
<b>Rejected</b>		0.0%	13.5%	7.0%	23.2%
<b>MSE</b>		0.129	0.167	0.128	0.201

Using the third group of words that contains command words we obtained a better recognition rate of 90.5% as indicated in the 4<sup>th</sup> column of Table 3.

Using a mix of words from the three groups in both training and testing faces,

we obtained an overall recognition rate of 74.2%.

##### b) Multi-Layer Perceptron (MLP)

Using Multi-Layer Perceptron (MLP), the recognition rates were lower in all groups as shown in Table 4



The overall recognition rate is 28.14% of misclassification is about 12 times higher compared to 74.2% obtained by the Radial basis function (RBF), particularly the rate in (MLP) than (RBF).

**Table 4: Recognition rate of words uttered in quiet environment, by MLP.**

<i>Group of words</i>		<i>1<sup>st</sup></i>	<i>2<sup>nd</sup></i>	<i>3<sup>rd</sup></i>	<i>4<sup>th</sup></i>
<b>No. of Data Samples</b>	<b>Total</b>	400	800	600	1400
	<b>Train</b>	200	400	300	700
	<b>Test</b>	200	400	300	700
<b>Classified</b>		72%	35%	59.3%	28.14%
<b>Misclassified</b>		16.5%	45%	22.3%	13.57%
<b>Rejected</b>		11.5%	20.0%	18.3%	58.28%
<b>MSE</b>		0.149	0.242	0.186	0.222

#### 4.3. The words in noisy environment

All 14 words were uttered by speakers (8, 9, 10, 11, and 12) in a noisy environment. Each word was uttered 20 times for each speaker, a total of 1400 features were obtained. Radial Basis (RBF) and Multi-Layer Perceptron (MLP) were applied to classify these words.

#### a) Radial Basis Function (RBF)

Comparing the results shown in Table 3 to the results shown in Table 5, we note that the background noise has little effect on the recognition of these words. This is due to the use of LPC algorithm. Figure 4 shows a comparison between the recognition rate of the sample words uttered by 5 speakers in quiet and noisy environment.

**Table 5: Recognition rate of words uttered in noisy environment, by RBF.**

<i>Group of words</i>		<i>1<sup>st</sup></i>	<i>2<sup>nd</sup></i>	<i>3<sup>rd</sup></i>	<i>4<sup>th</sup></i>
<b>No. of Data Samples</b>	<b>Total</b>	400	800	600	1400
	<b>Train</b>	200	600	400	400
	<b>Test</b>	200	300	200	1000
<b>Classified</b>		89%	82.67%	86%	72.2%
<b>Misclassified</b>		3.5%	1.67%	3.0%	1.7%
<b>Rejected</b>		7.5%	15.67%	11.0%	26.1%
<b>MSE</b>		0.126	0.143	0.127	0.154



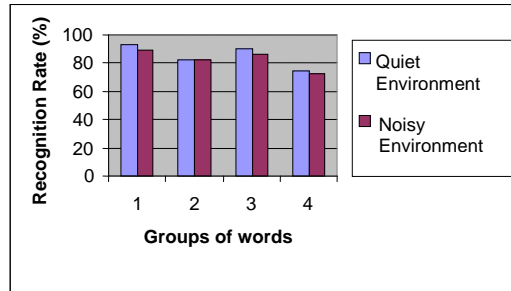


Figure 4: Comparing results to show the effect of noise on the recognition rate.

## b) Multi-Layer Perceptron (MLP)

Table 6: Recognition rate of words uttered in noisy environment, by MLP.

<i>Group of words</i>		<i>1<sup>st</sup></i>	<i>2<sup>nd</sup></i>	<i>3<sup>rd</sup></i>	<i>4<sup>th</sup></i>
<b>No. of Data Samples</b>	<b>Total</b>	400	800	600	1400
	<b>Train</b>	200	400	300	700
	<b>Test</b>	200	400	300	700
<b>Classified</b>		51.5%	27%	51%	14.29%
<b>Misclassified</b>		31%	23.25%	13.67%	8.86%
<b>Rejected</b>		17.5%	49.75%	35.33%	76.86%
<b>MSE</b>		0.172	0.230	0.180	0.227

### 4.4. Mixing words (recorded in quiet and noisy environments)

All 14 words uttered by all speakers (1, 2, 3, ..., 14) in quiet and noisy environments. Each word was uttered 20 times by each speaker. This produced a total of 3920 samples. The features of these samples were used to train and test both RBF and MLP classifiers.

### a) Radial Basis Function (RBF)

We note from Tables 3, 5, 7 and Figure 5 that the recognition results are very close, even though the difference between the numbers of samples is large. This was due to the ability of the LPC algorithm to eliminate the background noise.

**Table 7: Recognition rate of words uttered in quiet and noisy environment, by RBF.**

<i>Group of wards</i>		<i>1<sup>st</sup></i>	<i>2<sup>nd</sup></i>	<i>3<sup>rd</sup></i>	<i>4<sup>th</sup></i>
<b>No. of Data Samples</b>	<b>Total</b>	1120	2140	1680	3920
	<b>Train</b>	560	1070	840	2920
	<b>Test</b>	560	1070	840	1000
<b>Classified</b>		86%	72.6%	82.38%	68.2%
<b>Misclassified</b>		8.04%	6.45%	4.52%	2.9%
<b>Rejected</b>		5.89%	20.93%	13.1%	28.9%
<b>MSE</b>		0.203	0.376	0.264	0.177

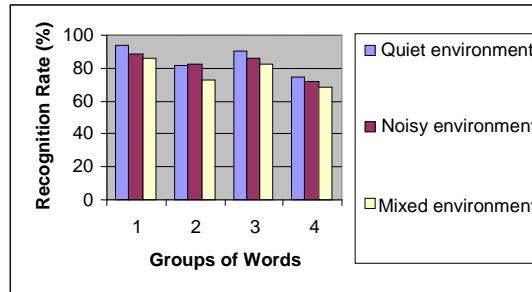


**Figure 5: Comparing results between words uttered in variant environments.**

**b) Multi-Layer Perceptron (MLP)**

The recognition rate obtained by the Multi-Layer perceptron (MLP) classifier

was very much lower than that obtained by the Radial Basis Function (RBF).

**Table 8: The Recognition rate of words uttered in quiet and noisy environment, by MLP.**

<i>Group of words</i>		<i>1<sup>st</sup></i>	<i>2<sup>nd</sup></i>	<i>3<sup>rd</sup></i>	<i>4<sup>th</sup></i>
<b>No. of Data Samples</b>	<b>Total</b>	1220	2140	1680	3800
	<b>Train</b>	620	1140	1000	2800
	<b>Test</b>	500	1000	680	1000
<b>Classified</b>		70.2%	26.3%	39.56%	23.7%
<b>Misclassified</b>		20%	24.7%	28.68%	14.6%
<b>Rejected</b>		9.8%	49%	31.76%	61.7%
<b>MSE</b>		0.178	0.218	0.105	0.227

#### 4.5. Important Results

A very important result is produced when choosing one or two speakers randomly for testing without including any sample in the

training set. The obtained results were very close to those obtained by including some samples from these speakers in the training set, as shown in Figure 6.

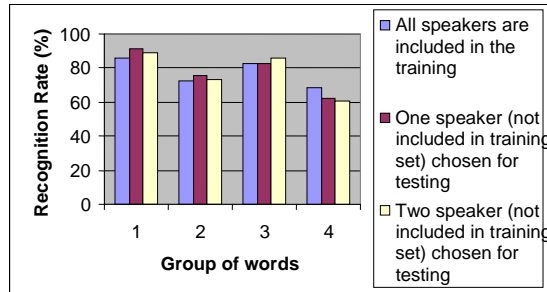


Figure 6: Results obtained by choosing samples from one or two speakers that are not included in the training set.

Table 9 and Table 10 show the results obtained by testing the system by samples from one speaker and two speakers

respectively that were not included in the training set.

Table 9: The results for one speaker that is not included in the training set, by RBF.

<i>Group of words</i>		<i>1<sup>st</sup></i>	<i>2<sup>nd</sup></i>	<i>3<sup>rd</sup></i>	<i>4<sup>th</sup></i>
<b>No. of Data Samples</b>	<b>Total</b>	1120	2140	1680	3800
	<b>Train (13 speakers)</b>	1040	1980	1560	3520
	<b>Test (1 Speaker)</b>	80	160	120	280
<b>Classified</b>		91.2%	75.6%	82.5%	62.5%
<b>Misclassified</b>		2.6%	5.1%	5%	5%
<b>Rejected</b>		6.2%	19.3%	12.5%	32.5%
<b>MSE</b>		0.128	0.173	0.143	0.213



**Table 10: The results for two speakers that are not included in the training set, by RBF.**

<i>Group of words</i>		<i>1<sup>st</sup></i>	<i>2<sup>nd</sup></i>	<i>3<sup>rd</sup></i>	<i>4<sup>th</sup></i>
<b>No. of Data Samples</b>	<b>Total</b>	1120	2140	1680	3800
	<b>Train (12 speakers)</b>	690	1820	1440	3240
	<b>Test (2 Speakers)</b>	160	320	240	560
<b>Classified</b>		89.3%	73.1%	85.8%	60.5%
<b>Misclassified</b>		3.9%	6.6%	3.4%	4.7%
<b>Rejected</b>		6.8%	20.3%	10.8%	34.8%
<b>MSE</b>		0.137	0.173	0.143	0.216

#### 4.6. Further discussions

There were some words that were misclassified with other words. This was due to the following reasons:

- 1- Some words are similar in sound, for example: (Bahar, Sahar), (Ard,

Aard), (Shams, Hams), and (Sama, Nedaa). This similarity can be deduced from Figure 7, which shows a plot of features of words (Bahar, Sahar).

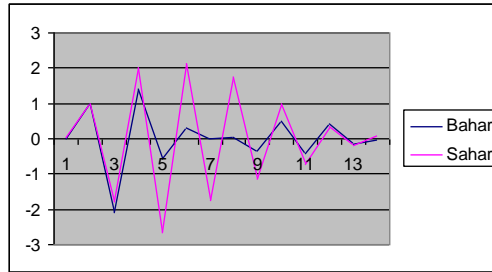


**Figure 7: Similarity between words (Bahar, Sahar).**

- 2- Some words are not similar in sound, but the product of the feature vector by weights vector, during the process of testing gives

same result. For example words (fatah, Eghlak) as shown in Figure 8.

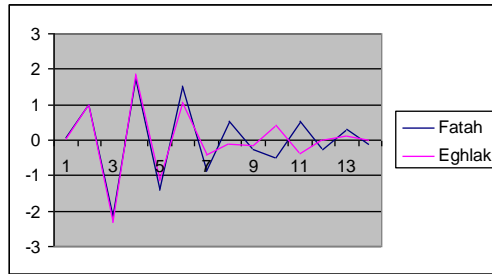


**Figure 8: Similarity between the product of the features vector by weights vector for words for words (Fatah, Eghlak), uttered by one speaker.**

3- In some cases the words are not similar in the sound but the feature vectors of these words produced

by the LPC are very close, for example (sama, Nasak), as shown in Figure 9.

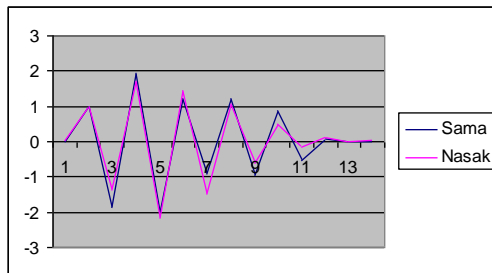


**Figure 9: Similarity between the features vectors produced by LPC for the words (Sama, Nasak) uttered by one speaker.**

## 5. Conclusion

Speech recognition is a challenging issue for most languages, and Arabic language is no exception.

In this paper, we applied a speech recognition to isolated Arabic words. Several samples from these words are recorded by many speakers both with and without background noise.

The features of these words are obtained by the Linear Predictive Coding (LPC)

algorithm. These features are then input to Radial Basis Function (RBF) and Multi Layer Perceptron (MLP) algorithms for recognition. The recognition results obtained from these algorithms are analyzed and compared. Both results were adequate but the results produced by Basis Function (RBF) algorithm were very much better than those produced by Multi Layer Perceptron (MLP) algorithm.

Furthermore, a good result is obtained when the recognition system is tested with



some samples of speech that were not included in the training stage.

### References:

- [1] DongSuk Yuk, "Robust Speech Recognition Using Neural Networks and Hidden Markov Models- Adaptations Using Non-linear Transformations", dissertation, Graduate School, New Brunswick Rutgers, The State University of New Jersey, 1999.
- [2] Eric Keeler, Fundamentals of Speech Synthesis and Speech Recognition, University of Lausanne, Switzerland, JOHN WILEY& SONS,1995.
- [3] Howard Demuth, Mark Beale, Neural Network Toolbox for Use with MATLAB, User's Guide, Version 4. 2002.
- [4] Broomhead, D.S, Lowe, D. "Multivariable functional interpolation and adaptive networks", *Complex Systems*, vol. 2, pp.321-355, 1988.
- [5] Matej, S., Lewitt, R.M., "Practical considerations for 3-D image reconstruction using spherically symmetric volume elements," *IEEE Trans. On Medical Imaging*, vol. 15, no. 1, pp. 68-78, 1996.
- [6] Casdagli, M., "Nonlinear prediction of chaotic time series," *Physica D*, vol. 35, pp. 335-356, 1989.
- [7] Sanner, R. M., Slotine, J.-J. E., "Gaussian networks for direct adaptive control," *IEEE Trans. On Neural Networks*, vol. 3, no. 6, pp. 837-863, 1994.
- [8] Haykin, S., *Neural Networks: A comprehensive Foundation*, Upper Saddle River, NJ: Prentice Hall, 1994.
- [9] Bors, A. G., Gabbouj, G., "Minimal topology for a radial basis function neural network for pattern classification", *Digital Signal Processing: a review journal*, vol. 4, pp. 173-188, 1994.
- [10] Chen, S. Cowan, C. F. N., Grant, P. M. "Orthogonal least squares learning algorithm for radial basis function networks," *IEEE Trans. On Neural Networks*, vol. 2, no. 2, pp. 302-309, 1991.
- [11] Niranjana, M., Fallside, F., "Neural networks and radial basis functions in classifying static speech patterns," *Computer Speech and Language*, vol. 4, pp. 275-289, 1990.
- [12] Cha, I., Kassam, S.A., "RBFN restoration of nonlinearly degraded images," *IEEE Trans. On Image Processing*, vol. 5, no. 6, pp. 964-975, 1996.
- [13] Wei, G.-Q., Hirzinger, G., "Parametric shape-from-shading by radial basis functions," *IEEE Trans. On Pattern Analysis and*



- Machine Intelligence*, vol. 9, no. 4, pp. 353-365, 1997.
- [14] Bors, A. G., Pitas, I., "Object classification in 3-D images using alpha-trimmed mean radial basis function network," *IEEE Trans. On Image Processing*, vol. 8, no. 12, pp. 1744-1756, 1999.
- [15] Bors, A. G., Pitas, I., "Optical flow estimation and moving object segmentation based on median radial basis function network," *IEEE Trans. On Image Processing*, vol. 7, no. 5, pp. 693-702, 1998.
- [16] Chatzis, V., Bors, A. G., Pitas, I., "Multimodal decision-level fusion for person authentication," *IEEE Trans. On Systems, and Cybernetics, Part A: Systems and Humans*, vol. 8, no. 12, pp. 1744-1756, 1999.
- [17] Rabiner, L. and Juang, B. -H., *Fundamentals of Speech Recognition*, PTRPrentice Hall, San Francisco, NJ, 1993.



المؤتمر العربي الليبي الدولي الخامس للهندسة الكهربائية والإلكترونية 23-26/10/2010 طرابلس ليبيا





## Approximating a Long-Tail Covariance Distribution by a Finite Mixture of Exponentials Functions

Rajab Faraj

Computer Engineering Department, Faculty of Engineering, Al-Fatah University

Email: frajab@littnet.net

### Abstract

The goal is to approximating a long-tail covariance distribution by a finite mixture of exponentials over shorter time scales. That is, we approximate a non-exponential function with a sum of exponential terms that we can easily deal with. The quality of the approximation is based on goodness of fit of the approximation by comparing the covariance function of the model with that of the data.

In this paper, we will use classes of heterogeneous ON-OFF sources to match video conferencing data. This is based on matching the total covariance of the heterogeneous sources to the real data. The covariance of the heterogeneous sources is composed of different exponential functions, while in the homogenous case it is just one exponential. The matching is very attractive, because as we will see for a small number of ON-OFF sources it is possible to get good results for the probability of loss and mean queue length. Moreover, the small number of parameters makes the analysis in finding the covariance and the parameters of the sources simple.

We used a well known algorithm (Feldman algorithm) for approximating a long-tail covariance function by a finite mixture of exponentials. However, previous work used the algorithm to fit probability distribution. Our technique is simpler. The matching of the covariance and for the real data to the traffic generated is quite good. The prediction of the queuing performance such as the probability of loss and mean queue length for video conferencing traffic is fair.

Key words: Probability and Stochastic Process, Queuing Theory, ATM.

### 1. THE MATHEMATICAL MODEL

In this section we consider independent classes of ON-OFF sources, let  $N_i$  ( $i= 1, 2, \dots, m$ ) denote the number of sources in class  $i$  to model long-range dependence

traffic such as video [1,3,11]. Within a class the sources are identical and independent. In this model, for the  $i$ th class, packets are generated during talk spurts which are the ON state, and no packets are generated



during the OFF state. The times spent in the ON and OFF states are exponentially distributed with means  $1/\beta_i$  and  $1/\alpha_i$ ,  $i=1, 2, \dots, m$ , respectively. When the source is in the ON state it generates data at rate of  $R_i$ ,  $i=1, 2, \dots, m$ .

The Asynchronous Transfer Mode (ATM) multiplexer consists of a server transmitting cells at a specified line rate and a buffer whose size is determined by the delay constraints on cell transmission. Cells arrive at the multiplexer from a number  $N_i$  ( $i=1, 2, \dots, m$ ) of sources.

Let us consider a 3-class model. The basic idea of the 3-class model is that there are three time frames for transitions: short

$$\left( \sum_{i=1}^m R_i n_i - C \right) \frac{dp_{\dots}(u)}{du} = \sum_{i=1}^m [\alpha_i (N_i - n_i + 1)] p_{\dots n_i - 1}(u) - \{ \alpha_i (N_i - n_i) + \beta_i n_i \} p_{\dots n_i}(u) + \beta_i (n_i + 1) p_{\dots n_i + 1}(u) \quad (1)$$

We express Equation (1) in the following familiar matrix form,

$$D \frac{dp(u)}{du} = p(u)M \quad (2)$$

Where  $D$  is an  $(N_1+1) \times \dots \times (N_m+1)$  diagonal matrix,  $M$  is  $(N_1+1) \times \dots \times (N_m+1)$  infinitesimal generator matrix and  $p(u)$  is a vector equal to  $[p_{00\dots 0}(u) \dots p_{n_1 n_2 \dots n_m}(u)]$ .

In the next section, we introduce the covariance function of Equation (2), which will be used to derive the parameters that characterize the independent  $m$  class ON-OFF sources. That is, the parameters determination is based on second order statistics.

term, medium term and long term, respectively. The transition rates are such that  $\alpha_1 \gg \alpha_2 \dots \gg \alpha_m$  and  $\beta_1 \gg \beta_2 \dots \gg \beta_m$ , where for our model we have  $m=3$ , so that the shorter the time frame, the more rapid the transition.

Let  $[n_1 n_2 \dots n_i \dots n_m; u]$  be the state with  $n_i$  source in class  $i$  ON and the buffer content does not exceed  $u$  and  $p_{n_1 n_2 \dots n_i \dots n_m}(u)$  be its equilibrium probability. Packets are served at a rate of  $C$  packets per time unit. We utilize the fluid flow approximation [2,15], which has shown much promise in the analysis of ATM networks. Similarly to [2] we have the following:

## 2. MODEL PARAMETER DETERMINATION

Our work is based on finding the total covariance of the independent  $m$  classes  $N_1, N_2, \dots, N_m$  heterogeneous ON-OFF source model. Then by matching to the real data [7,8,12], we find out the parameters that characterize the ON-OFF sources by adapting the Feldman algorithm to the fitting of the covariance [4]. We may view this algorithm as analogous to Gram-Schmidt orthogonalization over the time axis. The goal is to approximating a long-tail covariance distribution by a finite mixture of exponentials over shorter time scales. That is, we approximate a non-exponential function with a sum of exponential terms that we can easily deal



with. The quality of the approximation is based on goodness of fit of the approximation by comparing the covariance function of the model with that of the data.

The covariance  $CO$  of the number of packets of a long-tail process as a function of the lag  $k$  and the Hurst parameter  $H$  [3,9,10] behaves asymptotically as:

$$CO(k) \sim k^{2H-2} \quad (3)$$

$$COV(\tau) = \sum_{i=1}^m \alpha_i \beta_i N_i \frac{R_i^2}{(\alpha_i + \beta_i)^2} e^{-(\alpha_i + \beta_i)\tau} \quad (4)$$

Applying the additivity property to Equation 4, we find for the mean  $\mu$ ,

$$\mu = \sum_{i=1}^m \frac{\alpha_i N_i R_i}{(\alpha_i + \beta_i)} \quad (5)$$

And for the variance  $Var$ ,

$$Var = \sum_{i=1}^m \frac{\alpha_i \beta_i N_i R_i^2}{(\alpha_i + \beta_i)^2} \quad (6)$$

Let,

$$COV(\tau) = k_1 e^{-\lambda_1 \tau} + k_2 e^{-\lambda_2 \tau} + \dots + k_m e^{-\lambda_m \tau} = \sum_{i=1}^m k_i e^{-\lambda_i \tau} \quad (9)$$

Equation (9) is a finite mixture of exponentials that approximate the long-tail distribution function given by Equation (3). The idea is to approximate Equation (3) by Equation (9), because performance models with component long-tail distributions tend to be difficult to analyze.

As can be seen from Equation (9) we have  $2m$  unknowns and therefore we need  $2m$

The covariance function given by Equation (3) decays hyperbolically (obeying some power law) as the lag  $k$  increases rather than exponentially, where  $k$  is the lag and  $H$  is the Hurst parameter.

The covariance  $COV(\tau)$  of independent  $m$  class ON-OFF sources described by Equation (2) is simply given by:

$$\lambda_i = \alpha_i + \beta_i, \quad i=1,2,\dots,m \quad (7)$$

$$k_i = \alpha_i \beta_i N_i \frac{R_i^2}{\lambda_i^2}, \quad (8)$$

Substitute Equation (7) and Equation (8) into Equation (4) and assume that frames are generated at rate of  $f$  frames /sec:

Equations to find them. Since the covariance is composed of exponential components  $\lambda_1, \lambda_2, \dots, \lambda_m$ , and  $m$  arguments  $K_1, K_2, \dots, K_m$ , we match at the quantiles:  $0 < c_1 < c_2 < \dots < c_m$ , which represent how many classes that we have. For example, for two classes we have two quantiles  $c_1, c_2$  and for three classes we have three quantiles  $c_1, c_2, c_3$  and so on. In order to



solve  $2m$  Equations to find the  $2m$  unknowns, let  $b$  be a scaling factor such that  $1 < b < (c_i + 1) / c_i$  for all  $i$ ; e.g., we could have  $b=4, c_i=10^{(i-1)} c_1$  for  $2 \leq i \leq m$ .

$\frac{c_2}{c_1} = \frac{c_3}{c_2} = \dots = \frac{c_m}{c_{m-1}}$ . See figure 4 for the three source case.

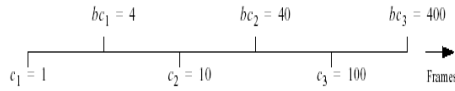


**Figure (4) Illustration of how to choose the quantiles  $c_1, c_2, c_3$  and the Scaling factor  $b$  ( $c_1=1, c_2=10, c_3=100, b=4$ )**

Given the real data and using the technique in [4] we can obtain the exponential components  $\lambda_1, \lambda_2, \dots, \lambda_m$  and the arguments  $K_1, K_2, \dots, K_m$  in reverse order by finding first  $\lambda_m$  and  $K_m$  and then  $\lambda_{m-1}$  and  $K_{m-1}$  so on until we find  $\lambda_1$  and  $K_1$ . From Equation (7)  $\lambda_1 \gg \lambda_2 \gg \dots \gg \lambda_m$ . Therefore, at the quantiles  $c_m$  and  $bc_m$ , only the terms of the covariance that have

$$COV(c_{m-1}) = k_m e^{-\frac{\lambda_m c_{m-1}}{f}} + k_{m-1} e^{-\frac{\lambda_{m-1} c_{m-1}}{f}} \quad (12)$$

$$COV(bc_{m-1}) = k_m e^{-\frac{\lambda_m b c_{m-1}}{f}} + k_{m-1} e^{-\frac{\lambda_{m-1} b c_{m-1}}{f}} \quad (13)$$

where  $\lambda_m$  and  $K_m$  are already known from Equations (10) and (11).

Given  $\lambda_m, K_m, \lambda_{m-1}$  and  $K_{m-1}$  we find the next two unknowns  $\lambda_{m-2}$  and  $K_{m-2}$  at the quantiles  $c_{m-2}$  and  $bc_{m-2}$ ,

$$COV(c_{m-2}) = k_m e^{-\frac{\lambda_m c_{m-2}}{f}} + k_{m-1} e^{-\frac{\lambda_{m-1} c_{m-2}}{f}} + k_{m-2} e^{-\frac{\lambda_{m-2} c_{m-2}}{f}} \quad (14)$$

argument  $\lambda_m$  count and those terms of covariance that have arguments  $\lambda_{m-1}, \lambda_{m-2}, \dots, \lambda_1$  are negligibly small.

Therefore,

$$COV(c_m) = k_m e^{-\frac{\lambda_m c_m}{f}} \quad (10)$$

And

$$COV(bc_m) = k_m e^{-\frac{\lambda_m b c_m}{f}} \quad (11)$$

From Equations (10) and (11), we find the two unknowns  $\lambda_m$  and  $K_m$ .

Now we proceed to find the other two unknowns  $\lambda_{m-1}$  and  $K_{m-1}$  at the quantiles  $c_{m-1}$  and  $bc_{m-1}$ . In this case only the terms of the covariance that have argument  $\lambda_{m-1}$  and  $\lambda_m$  count and the terms of the covariance that have arguments  $\lambda_{m-2}, \lambda_{m-3}, \dots, \lambda_1$  are negligibly small.



$$COV(bc_{m-2}) = k_m e^{-\frac{\lambda_m bc_{m-2}}{f}} + k_{m-1} e^{-\frac{\lambda_{m-1} bc_{m-2}}{f}} + k_{m-2} e^{-\frac{\lambda_{m-2} bc_{m-2}}{f}} \quad (15)$$

And so on until we end up with the last two unknown's  $\lambda_1$  and  $K_1$ .

The final step is to find the parameters that characterize the ON-OFF sources i.e,  $\alpha_1, \beta_1, R_1; \alpha_2, \beta_2, R_2; \dots; \alpha_m, \beta_m, R_m$ . We have a system of  $3m$  (where  $m$  is the number of classes and the factor 3 comes from the fact that each source has 3 parameters to be determined) parameters to be calculated, however we have in hand only  $2m$  known factors ( $\lambda_1, k_1; \lambda_2, k_2; \dots; \lambda_m, k_m$ ). The basic property of our model is given in section 1, where the transitions rates are assumed to be such that  $\alpha_1 \gg \alpha_2 \dots \gg \alpha_m$  and  $\beta_1 \gg \beta_2 \dots \gg \beta_m$ , (already from 7, we have  $\lambda_1 \gg \lambda_2 \gg \dots \gg \lambda_m$ ). We use this assumption in

such a way that we have fewer unknowns to evaluate

$$\alpha_i = 10^{-(i-1)} \alpha_1, \quad i = 2, \dots, m$$

From (8) we find  $R_i$  in terms of  $K_i, \alpha_i$  and  $\beta_i$ ,

$$R_i = \sqrt{\frac{\lambda_i^2 k_i}{\alpha_i \beta_i N_i}} \quad (16)$$

Substitute for  $R_i, \beta_i$  ( $\beta_i = \lambda_i - \alpha_i$ ) in (5) we have, after some manipulation, the following,

$$\sqrt{\frac{\alpha_1 N_1 k_1}{(\lambda_1 - \alpha_1)}} + \sqrt{\frac{\alpha_2 N_2 k_2}{(\lambda_2 - \alpha_2)}} + \dots + \sqrt{\frac{\alpha_i N_i k_i}{(\lambda_i - \alpha_i)}} + \dots + \sqrt{\frac{\alpha_m N_m k_m}{(\lambda_m - \alpha_m)}} = \mu \quad (17)$$

Since  $\alpha_i = 10^{-(i-1)} \alpha_1$ , equation (17) can be written in the following form:

$$\sqrt{\frac{\alpha_1 N_1 k_1}{(\lambda_1 - \alpha_1)}} + \sqrt{\frac{\alpha_1 N_2 k_2}{(10\lambda_2 - \alpha_1)}} + \dots + \sqrt{\frac{\alpha_1 N_i k_i}{(10^{i-1} \lambda_i - \alpha_1)}} + \dots + \sqrt{\frac{\alpha_1 N_m k_m}{(10^{m-1} \lambda_m - \alpha_1)}} = \mu \quad (18)$$

The number of sources  $N_1, N_2, \dots, N_m$  is given in advance. Also, we know the values of  $\lambda_1, \lambda_2, \dots, \lambda_m, K_1, K_2, \dots, K_m$  from matching to the data, and also we know  $\mu$  the estimated mean value of the real data. Therefore, the non-linear Equation (18), which is a function of only one unknown parameter  $\alpha_1$ , can be solved numerically. Knowing the parameters  $\alpha_1, \beta_1, R_1; \alpha_2, \beta_2, R_2; \dots$

;  $\alpha_m, \beta_m, R_m$  can be obtained very easily using Equations (7) and (8).

### 3. NUMERICAL RESULTS

The model can be applied to any number of classes and any number of sources per class. However, as the number of sources increases the solution of Equation (18) becomes more difficult. Because of this, we apply the model to the three classes and one



source per class. Using the video conferencing data available in [7,8,12], we calculate the covariance function for the real data and apply the procedure presented in section 2 to find the parameters for the heterogeneous ON-OFF source model. These three heterogeneous ON-OFF source models are used to generate video traces in Optimization Network (OPNET) program. We generate almost the same number of real data frames of approximately 50,000 frames for video-conferencing sequences. From the real traffic we find the covariance function, and Index of Dispersion for Count (*IDC*) [5] and compare them with that of the generated traffic. Also, as a reference, we calculate covariance, *IDC* based on the Maglaris model with 20 minisources [11].

The values of the parameters depends on the quantiles  $c_i$ 's, the scaling factor  $b$  and the number of frames over which the matching is going to be done. As the number of quantiles, the scaling factor and the number of frames over which the matching is

going to be done increases the accuracy will be increased. However, this is not always possible since increasing the number of quantiles means increasing the number of classes (for the three class model, three quantiles are needed), which makes the solution of Equation (18) more difficult.

Tables 1-2 show, respectively, the estimated parameters  $\alpha_i, \beta_i, R_i$  for two and three class single ON-OFF sources needed to model the video-conferencing data is available in [7]. They also show the estimated exponential components  $\lambda$ 's and the arguments  $k_i$ 's. Given the parameters  $\alpha_i$ 's,  $\beta_i$ 's, and  $R_i$ 's for ON-OFF sources for the Variable Bit Rate (VBR) video traffic traces, a replica of the traffic is generated using OPNET. From the real traffic we find out the covariance function, *IDC* and compare them with that of the generated traffic. We also plot the covariance based on Equation (9).

Table (1) Parameters for the two class single ON-OFF sources matched to the video-conferencing trace over 768 frames with  $C1=1, C2=192$  and  $b=4$

Parameter	$\lambda$	$k$	$\alpha$	$\beta$	$R$
Source1	0.588	5034.2	0.348	0.24	144.4
Source2	0.046	620.78	0.0348	0.011	58.68

Table (2) Parameters for the three class single ON-OFF sources matched to the video-conferencing trace over 768 frames with  $C1=1, C2=16, C3=256$  and  $b=3$

Parameter	$\lambda$	$k$	$\alpha$	$\beta$	$R$
Source1	2.156	401.69	1.79	0.36	53.81
Source2	0.39	4815.4	0.179	0.22	139.3
Source3	0.03	429.1	0.0179	0.016	41.55

As a reference, we compare the statistical measures such as covariance, *IDC*, of the real video conferencing data and the generated video traffic based on heterogeneous ON-OFF source model with

that of the generated traffic based on Maglaris model. To do that we need to find the parameters that characterize the Maglaris model. Using Equations (8), (9),(10) and (11) in the paper of Maglaris



[11] we calculated the parameters of the Maglaris model for the four video traces. These are shown in Table 3 below.

Table (3) Maglaris model parameters for VBR traces, video-conferencing, video. Each video source is characterized by 20 minisources

Parameter	$\alpha$	$\beta$	R
Video conferencing	0.05	0.3	39

#### 4. Covariance and IDC

In this section we consider the matching of the covariance and the *IDC* of the generated traffic to the real data using heterogeneous sources. As a reference, we have generated traffic based on the Maglaris model of 20 minisources [11]. We compare the accuracy of our model with that based on the Maglaris model. Also, we consider the effect of increasing the number of ON-OFF heterogeneous sources to the accuracy of the matching. Given the exponential components  $\lambda_i$ 's and the arguments  $k_i$ 's of the

heterogeneous ON-OFF source model, we see how well the covariance represented by Equation (9) matches the covariance of the real data and that based on the Maglaris model.

The covariances of the real video-conferencing and the generated 3 and 2 class single ON-OFF source are shown in figure 1. We also plot the covariance based on Maglaris model of 20 minisources. In figure 2, we plot the covariance of real video-conferencing and that based on the formula given by Equation (9) of our work and that given by Maglaris of one exponential term, which is given by Equation (5) in [11]. As expected, the accuracy increases as the number of classes increases. Moreover, in comparison with the Maglaris model, the matching based on the 3 class single ON-OFF source is shown to be better. For conferencing data, the match to the traces based on the generated traffic and that using formula (9) is quite good over a large number of lags.

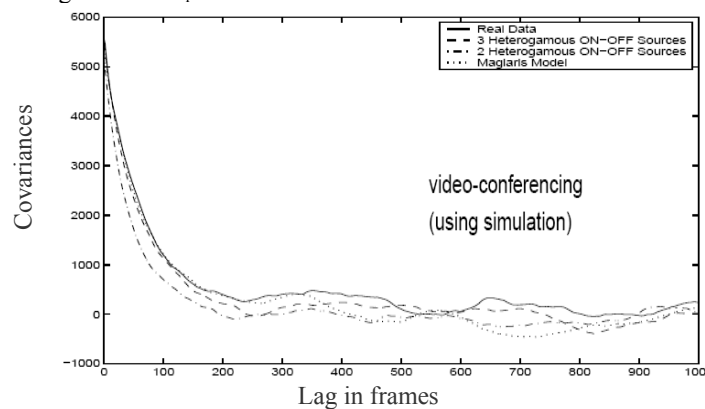


Figure (1) Covariances functions of real video-conferencing data compared with that of Maglaris and generated 3 and 2 class heterogeneous source model, each class has 1 ON-OFF source

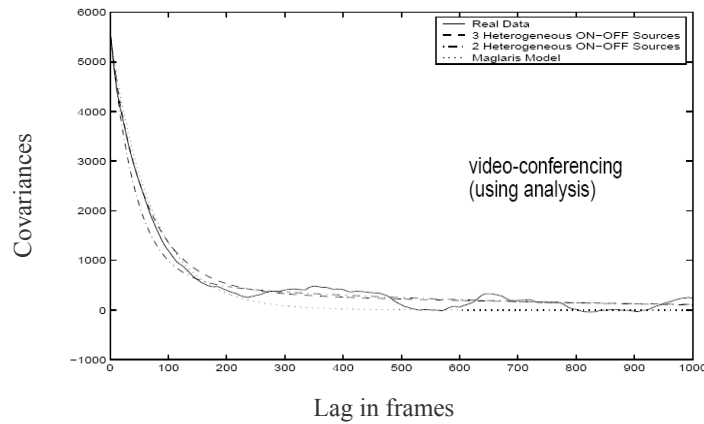


Figure (2) Covariance functions of real video-conferencing data, and using formula (9) for 3 and 2 class heterogeneous source model, each class has 1 ON-OFF source

The other part of matching the heterogeneous sources to the real data is the *IDC*. As shown in figure 3, respectively, the *IDC* of the synthetic video-conferencing traffic matches the *IDC* of the real data. As for the covariance, increasing the number of heterogeneous sources from 2 to 3 will increase the accuracy of the matching. We also show the *IDC* based on the Maglaris model.

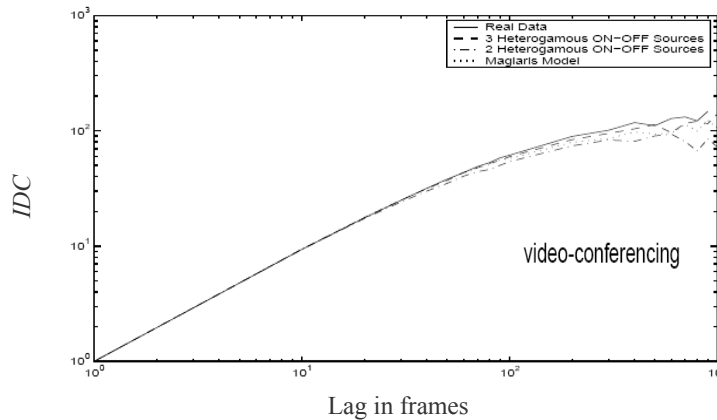


Figure (13) *IDC* of real video-conferencing data compared with that of Maglaris and generated 3 and 2 class heterogeneous source model, each class has 1 ON-OFF source





## 5. CONCLUSION

We have proposed a model for characterizing correlated cell arrival of real bursty video data. Based on a second order statistical analysis, we have used heterogeneous ON-OFF source model to characterize the traffic. The model consists of  $m$  classes of ON-OFF sources. Although the ON-OFF periods are exponentially distributed and the number of sources is small, we have a good matching for the covariance and the  $IDC$ . It is clear from the results we obtained, as the number of classes and the number of ON-OFF sources per class increases, the accuracy of the model will be increased especially for highly correlated traffic. However, increasing the number of classes and number of sources per class will result in analytical and computational complexities.

Using just the 3-heterogeneous ON-OFF source model gives good results for matching the traffic characteristics indices and at the same time the analysis is simple.

## 6. REFERENCES

- [1] Andersen A.T. and Nielsen B, "An application of superpositions of two state Markovian sources to the modelling of self-similar behavior," IEEE INFOCOM97, April 1997, Kobe, Japan.
- [2] Anick D., Mitra D and Sondhi M. M., "Stochastic theory of a data handling system with multiple sources" Bell Syst. Tech. J. 61, 1982.
- [3] Cox D. R., "Long-range dependence: A review", in statistics: An appraisal, Proceedings 50th Anniversary Conference, Iowa State Statistical Library, H. A. David and H. T. David, editors, Iowa State University Press, pp. 55- 74, 1984.
- [4] Feldmann A. and Whitt W., "Fitting mixtures of exponentials to longtail distributions to analyze network performance models," IEEE INFOCOM'97, April 1997, Kobe, Japan.
- [5] Gusella R., "Characterizing the variability of arrivals process with indexes of dispersion," IEEE JSAC, 9(2), pp. 203-211, Apr. 1991.
- [6] Heffes H. and Lucantoni D. M., "A Markov modulated characterization of packetized voice and data traffic and related statistical multiplexer performance", IEEE JSAC, vol. SAC-4, no 6, pp. 856-868, Sep. 1986.
- [7] Heyman D. and Lakshman T. V., "Source models for broadcast video traffic," IEEE/ACM Trans. Networking, vol. 4, no. 1, Feb 1996
- [8] Heyman D. and Lakshman T. V., "What are the implications of long-range dependence for VBR-video traffic Engineering ?," IEEE/ACM Trans. Networking, vol. 4, no. 3, June 1996.
- [9] Hosking J., "Modeling persistence in hydrological time series using fractional differencing", Water Resources Research, 20 (12), 1984.
- [10] Hurst H. E., "Long term storage capacity of reservoirs", Trans. Amer. Soc. Civil Engineers, pp. 770-779, 1951.
- [11] Maglaris B., Anastassiou D., Sen P., Karlsson G., Robbins J., "Performance Models of statistical



- multiplexing in packet video communication," IEEE Trans.
- [12] W. E. Leland, D. V. Wilson, "High time-resolution measurement and analysis of LAN traffic: Implications for LAN interconnection, " in Proc. IEEE INFOCOM'91, Bal Harbour, FL, Apr. 1991, pp. 1360-1366.



## Improved Hand Signature Recognition and Verification using Fuzzy Takagi-Sugeno Model

Idris S. El-Feghi<sup>1</sup> Osama Mohamed Elrajubi<sup>2</sup>  
1- Alfateh University, Email: [idrise@ee.edu.ly](mailto:idrise@ee.edu.ly)  
2- Misurata University, Email: [osrjubi@yahoo.com](mailto:osrjubi@yahoo.com)

### Abstract

In this paper, an automatic handwritten signature verification system for authenticating signatures is presented. The system is based on Takagi-Sugeno (TS) fuzzy model. For improving the performance of the system, a modification on the algorithm of verification phase has been proposed. The fuzzy logic is used in determining the final decision concerned with whether the signature is genuine or not.

The performance of the implemented system is measured by using the False Rejection Rate (FRR), the False Acceptance Rate (FAR), and the Average Error Rate (AER). The efficiency of the system has been tested on local database (880 signatures), and on GPDS300 signature Corpus (9000 signatures).

The performance of the proposed system was compared with traditional systems and the recognition rate for the system on Local database which has increased from 88.33% to 90.21%. On the GPDS300 database, the recognition rate for the system has increased from 74.07% to 77.03%.

### 1. Introduction

“Handwritten signature verification is the process of confirming the identity of a user based on the handwritten signature of the user as a form of behavioral biometrics”[1]. The objective of handwritten signature verification is to extract the common features consistently exist within different signatures written by the same person, and based on these features, to verify whether a signature is genuine [2].

A signature verification system is often categorized in two major classes: on-line signature verification system and off-line

signature verification system. The difference between on-line and off-line signature lies on how data are obtained. In an online system, a signature data can be obtained from an electronic tablet. In this case, dynamic information about writing activity such as speed of writing, pressure applied, pen movement are available. In off-line systems, signatures are written on paper as it has been done traditionally and converted to electronic form with the help of a camera or a scanner and obviously, the dynamic information is not available. In general, the dynamic information represents the main written style of a person. Since the



volume of information available is less, the signature verification using off-line techniques is more difficult [3][4]. On the other hand, the on-line system already has verification rate of 100%. Therefore, nothing of value can be added in this field [5].

## 2. Literature Review

In the second half of 1990s, fuzzy modeling started becoming popular among document processing researchers owing to its ability to classify uncertain and fuzzy data. Xuhua, et al. [6] 1995 attempted fuzzy signature verification by using the Pseudo-Bacterial Genetic Algorithm which was applied for the discovery of fuzzy rules. Ismail & Gad [5] 2000 proposed an offline signature verification system based on fuzzy concepts for the verification of Arabic signatures. For achieving higher recognition rates, Quek and Zhou [7] 2002 developed a system depending on the connection of fuzzy modeling techniques with neural networks. Hanmandlu, et al. [8] 2001 proposed signature verification system by using Takagi-Sugeno (TS) fuzzy model. They took the features as angle ones and fuzzified it by an exponential membership function. Hanmandlu, et al. [9] 2005 proposed signature verification system by modified membership function in Takagi-Sugeno model that includes structural parameters. The structural parameters are devised to take account of possible variations due to handwriting styles and to reflect moods. Freire, et al. [10] 2007 presented a study of

the application of off-line signature using the fuzzy vault construction. A baseline scheme based on quantized maximum and minimum of upper and lower envelopes of the signature image has been proposed.

In this paper, we present system of signature verification by using Takagi-Sugeno fuzzy model. We implemented the system and tested it on two databases.

## 3. The Proposed System

The design of any signature verification system generally requires the solution of five sub-problems: data acquisition, pre-processing, feature extraction, comparison process (training the system, determining the decision) and performance evaluation [2].

The general diagram of signature verification systems is shown in figure (1). The difference between signature verification systems is due to the distinctions of the technique applied in verification stage and the technique used in training stage. In this paper, the fuzzy logic is used in both stages, training and verification stages.

### 3.1 Data Acquisition

In this paper, two databases were used, local database and GPDS300 signature Corpus. Local database was collected, and database "GPDS300 signature Corpus" was obtained from the Internet (webpage <http://www.gpds.ulpgc.es/download/index.htm>) (Universidad de Las Palmas de Gran Canaria, SPAIN) [11][12].

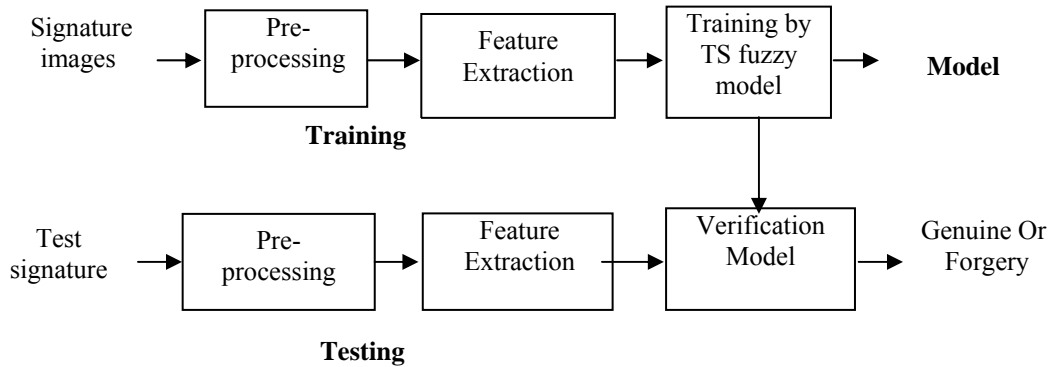


Figure 1: General diagram of signature verification system

### 3.1.1 Local Database

The signatures collected were handwritten on a white sheet of paper, by using any pen. Each signature was handwritten in frame of size 6.5 cm width by 3.25 cm height. The signatures are collected at different times without seeing other signatures signed before, and the signature were scanned at a resolution of 200 dpi. The total number of signatures of Local database was 880 signatures, taken from 40 people.

For each person 10 signatures were used for training the system. The total number of signatures which used in the training phase was  $40 * 10 = 400$  signatures.

For the testing, another 6 original signatures were taken from same people (3 in the same time, and 3 in another time). Six forgery signatures (2 random forgery, 2 simple forgery, and 2 skilled forgery) were taken for each person, and they were forged by another persons. The total number of signatures which used in the testing phase was  $40 * (6 + 6) = 480$  signatures.

### 3.1.2 GPDS300 Signature Corpus

"Off-line signature database. It contains data from 300 individuals. 24 genuine signatures for each individual, plus 30 forgeries of his/her signature. The 24 genuine specimens of each signer were collected in a single day writing sessions. The forgeries were produced from the static image of the genuine signature. Each forger was allowed to practice the signature for as long as s/he wished. Each forger imitated 3 signatures of 5 signers in a single day writing session. The genuine signatures shown to each forger were chosen randomly from the 24 genuine ones. Therefore, for each genuine signature there were 30 skilled forgeries made by 10 forgers from 10 different genuine specimens" [12]. The signatures were in "bmp" format, in black and white and scanned at resolution 300 dpi.

The total number of signatures of GPDS300 signature database which used in this paper was only 9000 signatures (10 signatures for training + 10 genuine signatures for testing



+ 10 forgery signatures for testing for each person from 300 persons).

### 3.2 Pre-processing Stage

The signature images scanned during the data acquisition phase were preprocessed before extraction of the features. The preprocessing stage was implemented both in training and testing phases. The preprocessing stage includes four steps:

*Step 1: Background elimination:* This the process was applied by using iteration threshold Method [13].

*Step 2: Noise reduction:* A noise reduction filter was implemented on the binary image

for eliminating single black pixels and also two black pixels on white background.

*Step 3: Normalization:* In this step, the signatures are scaled to size 80 pixel \* 160 pixel, which considered as standard size.

*Step 4: Skeletonization (thinning):* This step for eliminates the effect of different line thicknesses resulting from the use of different writing pens. We implemented this step by using Mathematics Morphological Method [14].

Figure 2: shows example of signature, after each step of preprocessing, applied in our system.

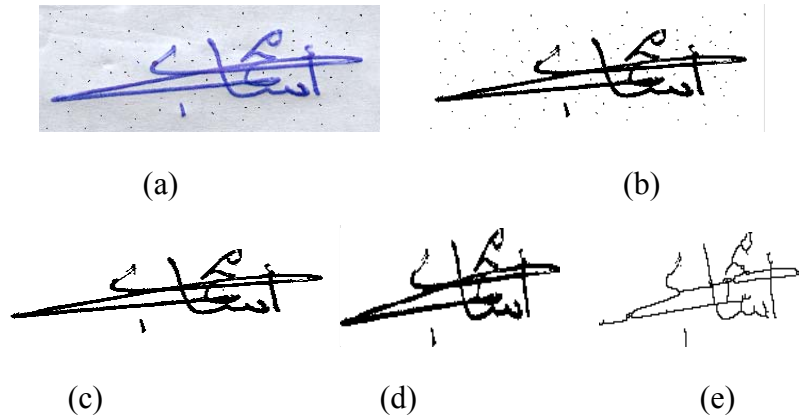


Figure 2: Preprocessing steps: (a) scanning, (b) background elimination, (c) noise removal, (d) Size normalization, (e) thinning applied signatures.

### 3.3 Feature Extraction

In the proposed system, the local features are used as a method for extraction the features of each signature. Local features represent a segment or limited region of the signature image, Although,

they require more computations, they are much more accurate than global features [5][15].



In the system, feature extraction is implemented by using angle features as following:

*Angle Features:* The bottom left corner of each box is taken as the absolute origin (0,0) and angle features are computed with reference to the origin of the box [16].

Step 1: Image is partitioned into 96 parts (8 rows \* 12 columns) by using equal horizontal density approximation method for determining the width of each part, and by determining the same height of each part.

Step 2: Calculate the summation of the angles of all black points in each box taken with respect to the bottom left corner and normalize it by dividing with the number of black points in the box.

### 3.4 Training the System using TS Fuzzy Model

Since the main aim of this system is to establish the authenticity of handwritten signatures by verifying the genuine signatures and rejecting the forged ones.

Each feature (angle features) forms a fuzzy set over large samples. This is because the same feature exhibits variation in different samples gives rise to a fuzzy set.

The system models the uncertainty through a fuzzy model (TS model) as following:

Let  $x_k$  be the  $k^{th}$  feature in a fuzzy set  $A_k$ , so the  $\mu_i$  IF THEN fuzzy rule in TS model has the following form:

$$\text{Rule } k: \text{ IF } x_k \text{ is } A_k \\ \text{THEN } y_k = c_{k0} + c_{k1} x_k \quad (1)$$

Each feature has a rule, so in the system there are many rules as number of features. The fuzzy set  $A_k$  is represented by the following exponential membership function (MF) that includes two structural parameters  $s_k$  and  $t_k$  [16]:

$$\mu_k(x_k) = e^{-\left[ \frac{(1-s_k) + s_k^2 |x_k - \bar{x}_k|}{(1+t_k) + t_k^2 \sigma_k^2} \right]} \quad (2)$$

Where  $\bar{x}_k$  is the mean,  $\sigma_k^2$  is the variance of  $k^{th}$  fuzzy set.

The structural parameters  $s_k, t_k$  are included in the TS model so as to track the intra-class variations in the different samples of signatures obtained from the same individual.

The strength of the rule in Equation (1) is calculated as:

$$w_k = \mu_k(x_k) \quad (3)$$

The total output of TS model can calculate as following:

$$Y = \sum_{k=1}^L w_k y_k \quad (4)$$

Where:  $L$  is the number of rules (The number of parts of signature image).

The performance function is defined as:

$$J = (Y_r - Y)^2 \quad (5)$$

Where:  $Y$  and  $Y_r$  denote the output of the fuzzy model and of the real system respectively. If  $Y_r$  is not available, it can be assumed to be unity [16].

Now to learn the parameters involved in the membership function ( $s_k, t_k$ ) and the consequent parameters  $c_{k0}, c_{k1}$  equation (5) is partially differentiated with respect to each of these parameters, as follow:



$$\begin{aligned} \frac{\partial J}{\partial c_{k1}} &= \frac{\partial J}{\partial Y} \cdot \frac{\partial Y}{\partial y_k} \cdot \frac{\partial y_k}{\partial c_{k1}} \\ &= 2(Y - Y_r) w_k x_k \quad (6) \\ \frac{\partial J}{\partial c_{k0}} &= \frac{\partial J}{\partial Y} \cdot \frac{\partial Y}{\partial y_k} \cdot \frac{\partial y_k}{\partial c_{k0}} \end{aligned}$$

$$= 2[Y - Y_r] w_k = 2\delta w_k \quad (7)$$

$$\begin{aligned} \frac{\partial J}{\partial s_k} &= \frac{\partial J}{\partial Y} \cdot \frac{\partial Y}{\partial w_k} \cdot \frac{\partial w_k}{\partial s_k} \\ &= 2(Y - Y_r) \cdot y_k \cdot \frac{\mu_k \{1 - 2s_k |x_k - \bar{x}_k|\}}{\{(1+t_k) + t_k^2 \sigma_k^2\}} \\ &= 2\delta y_k \mu_k [\{1 - 2s_k |x_k - \bar{x}_k|\} / T] \quad (8) \\ \frac{\partial J}{\partial t_k} &= \frac{\partial J}{\partial Y} \cdot \frac{\partial Y}{\partial w_k} \cdot \frac{\partial w_k}{\partial t_k} \\ &= 2(Y - Y_r) \cdot y_k \mu_k \frac{\{(1-s_k) + s_k^2 |x_k - \bar{x}_k|\} \{1 + 2t_k \sigma_k^2\}}{\{(1+t_k) + t_k^2 \sigma_k^2\}^2} \\ &= 2\delta y_k \mu_k \{(1 - s_k) + s_k^2 |x_k - \bar{x}_k|\} \{1 + 2t_k \sigma_k^2\} / T^2 \quad (9) \end{aligned}$$

Where  $\delta = Y - Y_r$ ,  $T = (1 + t_k) + t_k^2 \sigma_k^2$ , and  $k$  is the rule number.

Updating the parameters

by using the gradient descent learning for  $c_{ki}^{new} = c_{ki}^{old} - \epsilon_1 \frac{\partial J}{\partial c_{ki}}$ ,  $i = 0, 1$  (10)  
updating the parameters the equations is as following:

$$s_k^{new} = s_k^{old} - \epsilon_2 \frac{\partial J}{\partial s_k} \quad (11)$$

$$t_k^{new} = t_k^{old} - \epsilon_3 \frac{\partial J}{\partial t_k} \quad (12)$$





where  $\epsilon_1$ ,  $\epsilon_2$  and  $\epsilon_3$  are the learning coefficients such that  $\epsilon_1$ ,  $\epsilon_2$  and  $\epsilon_3 > 0$ . The equations (10), (11) and (12) must be iterated until the summation of  $\delta$  for all feature values becomes small enough.

After that, by using the last values of parameters (c0, c1, s, t) the membership functions for all the features will be computed. This process is repeated for all training samples of a person.

### 3.5 Verification Phase

After computing the membership functions of all the features for all training samples of a person. First, the extent of variation of the genuine signatures must be known and the maximum and minimum membership functions are determined for each feature over all signatures in the training set. The difference between these two gives the inherent variation in the signatures of a person.

Some tolerance is added to the maximum and other tolerance is deleted from the minimum to increase the range of variation in the different signatures. This tolerance means possible increase in the inherent variation over time.

*Judging the signatures by using the inherent variation.*

If the membership value lies within the range of variation which is given by the difference of minimum and maximum thresholds, it is counted as 'true'.

If the total number of 'true' cases for a particular signature is equal or more than

$$\text{Difference} = \text{Value of feature I} - \text{Average of values feature I for all the training samples} \quad (13)$$

$$\text{Std} = \text{Square root for the variance of the values for feature I} \quad (14)$$

threshold value, this signature is treated as genuine signature. If the total number of 'true' cases for a particular signature is less than threshold value, this signature is treated as forged signature.

The threshold value gives us the least error. This value can be defined by experiment of different values. In our system, threshold value 88 gave us the least error.

### 3.6 A Modification in Verification Phase

As shown in figure 3, the verification phase is concerned with the judgment on the signature. It investigates if the signature is genuine or not, by depending on the features and the parameters which resulted from previous phases of the verification phase.

For improving the performance of the system, modification on the algorithm of verification phase is implemented. It is as follows:

Instead of using counter for defining number of features which its value membership lies within defined range. A fractionary variable is suggested to be used for defining a value which indicates the value membership of each feature in its range taking in to account the membership of the feature value. In other words, the fuzzy logic is proposed to be used in determining the final decision concerned with whether the signature is genuine or not. Algorithm of the proposed modification is as following:



```
If Difference < Std Then
    Count_True = Count_True + 1
Else
    Count_True = Count_True + Std / Difference
End if
If Std = 0 and Difference > 0 Then
    Count_True = Count_True - X
End if
```

Where X is a small value. In this system, it is experimentally set as 0.15 with local database, and 0.27 with GPDS300 database. These values give us the best recognition rate. Figure (3) shows the flowchart for verification phase after the modification.

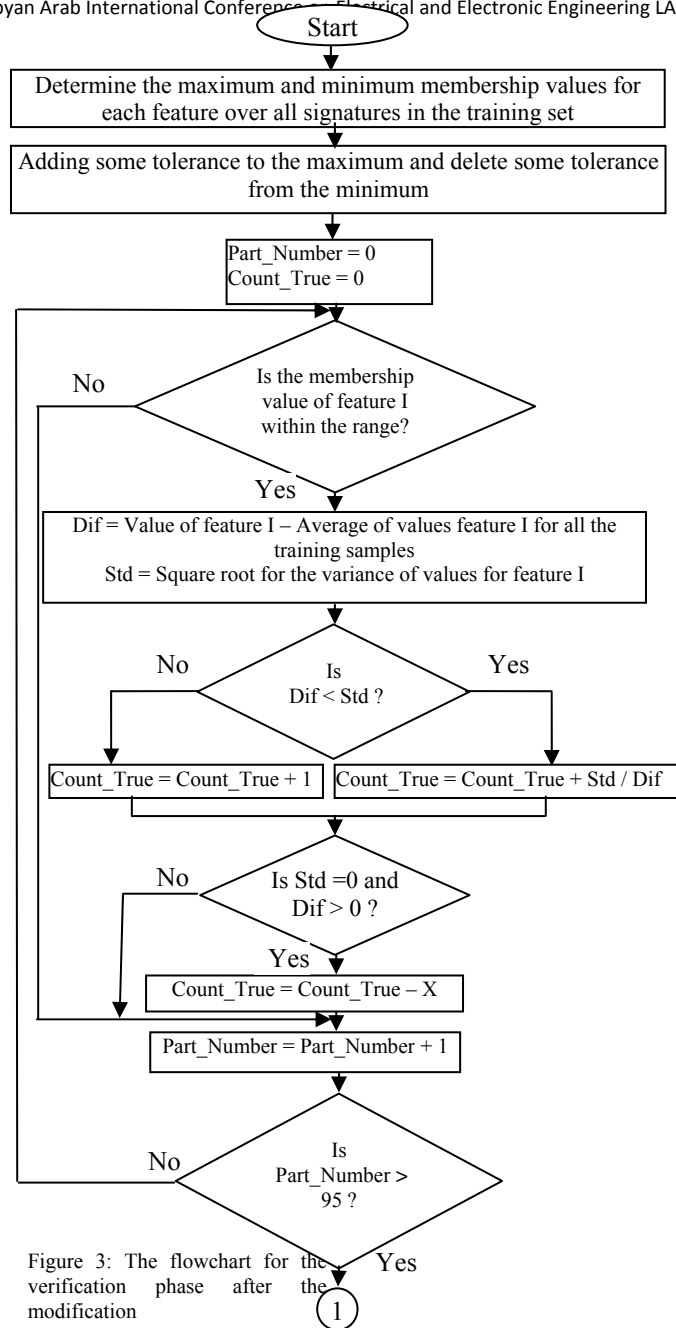


Figure 3: The flowchart for the verification phase after the modification

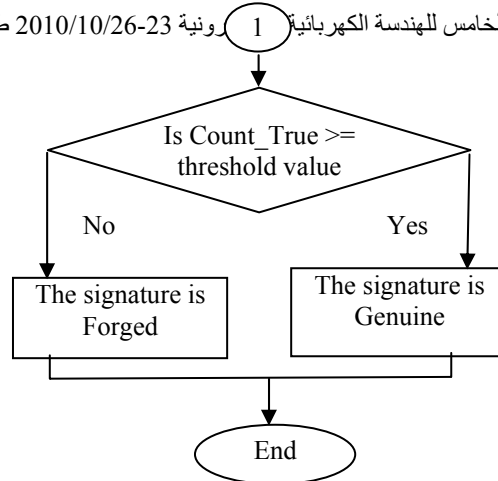


Figure 3: The flowchart for the verification phase after the modification

#### 4. The Results of the System

##### 4.1. Results of the system on the local data set

Table 1 shows the results of the system before the modification in verification phase, and the results of the system after the modification in verification phase, on the local database.

##### 4.2 Results of the system on the data set of "GPDS300 Signature Corpus"

Table 2 shows the results of the system before the modification in verification phase, and the results of the system after the modification in verification phase, on GPDS300 signature Corpus.

Table (1) Results of the system on the local data set.

The System	FRR of Genuine Signatures	FAR of Forged Signatures			Average Error Rate (AER)
		Random Forgery	Simple Forgery	Skilled Forgery	
Before the Modification	11.67	2.5	8.75	23.75	11.67
After the Modification	9.58	1.25	2.5	26.25	9.79



Table (2) Results of the system on data set of "GPDS300 signature Corpus".

The System	FRR of Genuine Signatures	FAR of Forged Signatures	Average Error Rate (AER)
		Skilled Forgery	
Before the Modification	20.06	31.8	25.93
After the Modification	18.43	27.5	22.97

### 5. Conclusions

In this paper, system of signature verification is presented. It is based on Takagi-Sugeno (TS) fuzzy model. Takagi-Sugeno fuzzy model is a hybrid approach that combines a fuzzy rule-based and a mathematical method.

In the absence of common signature databases, it is difficult to compare the system which developed in this research with other systems of signature verification. GPDS signature Corpus used in many researches, but the version GPDS300 which is used in this study is a new version of this signature Corpus. During our survey for a research on signature verification, a research used the version GPDS300 was not found.

By comparing the Average Error Rate (AER) of the system before and after the modification, the Average Error Rate decreased by 2% and 3% of local database and GPDS300 signature Corpus respectively. In other words, the proposed modification on the system improved the recognition rate of the system about 2% on local database and about 3% on GPDS300 signature Corpus. So the proposed modification on the system is important for improving the recognition rate.

False Acceptance Rate of the system after the modification on local database, was 1.25% and 2.5% of Random Forgery and Simple Forgery respectively. They are small rates compared to False Acceptance Rate of Skilled Forgery. False Acceptance Rate of Skilled Forgery is high. It is 26.25% and 27.5% on local database and on GPDS300 signature Corpus respectively, because the possible existence of skilled or traced forgeries may imitate signatures with less variation in shape than genuine signatures.

### 6. References

1. D.Y. Yeung, H. Chang, Y. Xiong, S. George, R. Kashi, T. Matsumoto, and G. Rigoll, "SVC2004: First International Signature Verification Competition," Proc. First International Conference on Biometric Authentication, ICBA, pp. 16-20, 2004.
2. Xiufen Ye, Weiping Hou, Weixing Feng, "Off-line Handwritten Signature Verification With Inflections Feature", Proceedings of the IEEE International Conference on Mechatronics & Automation, pp. 787-792, July 2005.



3. Emre Ozgunduz, Tulin Senturk and M. Elif Karshlgil, "Off-Line Signature Verification and Recognition by Support Vector Machine", Thirteenth European Signal Processing Conference, Sep. 2005.
4. Debasish Jena, Banshidhar Majhi, Saroj Kumar Panigrahy and Sanjay Kumar Jena, "Improved Offline Signature Verification Scheme Using Feature Point Extraction Method", Proc. 7th IEEE Int. Conf. on Cognitive Informatics, pp. 475-480, 2008.
5. M.A. Ismail, Samia Gad, "Off-line Arabic signature recognition and verification", Pattern Recognition, vol. 33, no. 10, pp. 1727-1740, Nov. 2000.
6. Y. Xuhua, T. Furuhasbi, K. Obata, Y. Uchikawa, "Study on signature verification using a new approach to genetic based machine learning", Proceedings of the IEEE International Conference on Systems, Man and Cybernetics, pp. 4383-4386, 1995.
7. C. Quek, R.W. Zhou, "Antiforgery: a novel pseudo-outer product based fuzzy neural network driven signature verification system", Pattern Recognition Letters, vol. 23, pp. 1795-1816, 2002.
8. M. Hanmandlu, K R Murali Mohan, Sourav Chakraborty and Gaurav Garg, "Fuzzy Modeling Based Signature Verification System", Proceedings of the IEEE Sixth International Conference on Document Analysis and Recognition, pp. 110-114, 2001.
9. Madasu Hanmandlu, Mohd. H. M. Yusof and Vamsi K. Madasu, "Off-line signature verification and forgery detection using fuzzy modeling" Pattern Recognition, vol. 38 pp. 341-356, 2005.
10. Manuel R. Freire, Julian Fierrez, Marcos Martinez-Diaz, Javier Ortega-Garcia, "On the Applicability of Off-Line Signatures to the Fuzzy Vault Construction", Ninth International Conference on Document Analysis and Recognition (ICDAR 2007), vol. 2, pp. 1173-1177, Sept. 2007.
11. Francisco Vargas, Miguel A. Ferrer, Carlos M. Travieso, Jesus B.Alonso, "Off-line Handwritten Signature GPDS-960 Corpus", in IAPR 9th International Conference on Document Analysis and Recognition, vol. 2, pp. 764-768, September 2007.
12. Grupo de procesado digital de señales.
13. <http://www.gpds.ulpgc.es/download/index.htm> (Last access, June, 2009)
14. Dr. Idris El-Feghi, "lectures in Image Processing", Department of Computer Science, Academy of Higher Studies, Tripoly-Libya, 2007.
15. Osama M. Elrajubi, "Off-line Signature Verification Based on Fuzzy Logic", Unpublished master's thesis, Academy of Graduate Studies, Tripoli, Libya, 2009.
16. Vamsi K. Madasu and Brian C. Lovell, "An Automatic Offline Signature Verification and Forgery Detection System", IGI Global, pp. 63-94, 2008.



## Oil Palm Fruit Bunch Ripeness Grading System Base on Fruit Colour Using Gabor wavelet Transform and Neural Network

<sup>1</sup>Meftah Salem M Alfatni, <sup>1</sup>Abdul Rashid Mohamed Shariff, <sup>1</sup>Osama M. Ben Saaed ,  
<sup>2</sup>Aouache Mustapha

<sup>1</sup>Spatial and Numerical Modelling Lab, Institute Advanced Technology, Universiti Putra Malaysia, 43400, Serdang, Selangor, Malaysia..

<sup>2</sup>Faculty of Engineering, Universiti Kebangsaan Malaysia, 43600, Bangi, Selangor, Malaysia.

e-mail:Mefth2000@yahoo.com

### Abstract

In recent years, due to the increasing necessity and rise in agricultural production the world over, a fast, easy and accurate classification mechanism of agricultural crops is certainly an important task for high quality products. In this paper the author is going to investigate the quality inspection system of oil palm FFB using an agriculture grading system processing steps as base on the colour as an external feature. The colour variation of oil palm fruit bunch throughout the ripeness stage gives us a good opportunity to get valuable information about the ripeness classes of oil palm FFB. The image processing steps of the system is the Spine of the system by using 2G-R-B colour filter and colour-based segmentation in order to get the region of interest by separate the object from the background. Since extract the object from its background the Gabor filter (GW) algorithm apply to extract the object features in term of vectors of the fruit samples with different classes. This features vectors extracted will be as input to our decision system using the unsupervised learning ANN model for training to be ready to evaluate and classify the different classes of our ripeness grading system. It shows that the accuracy of the oil palm grading system result based on GWF with ANN 78% is significantly higher rate performance compared to the statistical classification system at indoor application 70%.

Keywords: grading system, Gabor filter, neural network, fruit colour

### I Introduction:

Of recent, agricultural product's quality plays a key role in almost all food industry quality assessment. The traditional method of the agricultural product's quality assessment, which is tedious and costly, is

easily influenced by physiological factors, inducing subjective and inconsistent evaluation results (Sun 2006). Machine vision provides innovative solutions in the direction of industrial automation (Malamasa, Petrakisa et al. 2003). The revolution of the computer technologies an

utilized in different methods and techniques by several researchers around the world in order to built new machines for agricultural product's quality such as automatic grading system (Leemans and Destain 2004; Alfatni, Shariff et al. 2008). The use of automatic grading system for inspection increased in recent years. Basically, two inspection stages of the automatic grading system can be identified, viz, external inspection and internal inspection stages (Njoroge, Ninomiya et al. 2002; Malamasa, Petrakisa et al. 2003).

The external grading device is a combination of software as programming language (PL), operating system (OS) with image processing capabilities, while the hardware part comprises of a computer, CCD camera, data acquisition and conveying system (Morimoto, Takeuchi et al. 2000; Abdullah, Guan et al. 2004; Abdullah, Fathinul-Syahir et al. 2005; Marmoa, Amodiob et al. 2005; Riyadi, Rahni et al. 2007; Ghazali, Mustafa et al. 2008).

In this discourse, we set out to underscore the most popular techniques of external automatic grading employed today and their fundamental elements as flexibility, efficiency, speed, cost, reliability as well as robustness. The steps of image processing techniques are also examined, leading to a read masterpiece that summarises the up-to-date techniques for agricultural grading systems design and applications.

## II MATERIALS AND METHODS

This study is confined to the whole bunch of an oil palm fruit. Our grading system includes three categories of fruits ripeness can be listed as under ripe, ripe and over ripe as illustrated in figure 1.



**Figure 1 oil palm fruit bunch ripeness categories.**

The images are collected using the same material which described and discussed by (Alfatni, Shariff et al. 2008), while the system's methodology explanation is deeply discussed in the next sections. Figure 2 below shows the block diagram of the methodology process.



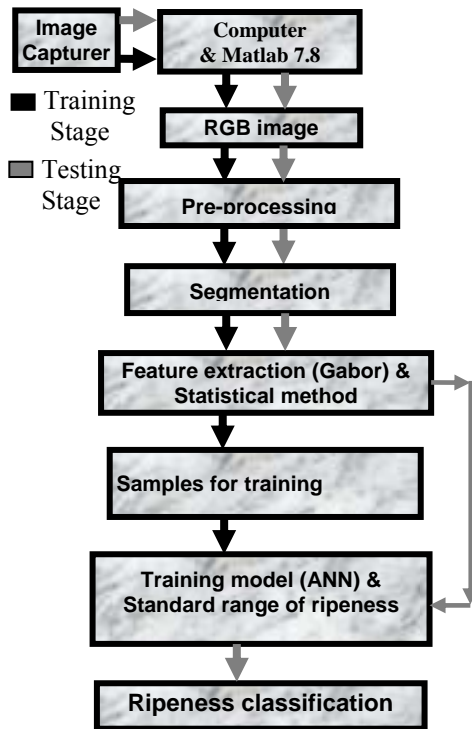


Figure 2 Block diagram of the methodology process.

#### A. Background segmentation

The segmentation technique permits partitioning off images into homogeneous regions, which may have particular common attributes, such as gray levels, mean values, shapes, and textures (FILHO, VITORELLO et al. 1997). Colour Fruit image segmentation subject on colour variation between mature fruits and backgrounds under natural illumination condition using dynamic threshold segmentation method as discussed by (Jian-jun, Han-ping et al. 2009). Woebbecke et

al. (1995a) examined several color indices for weed image segmentation and found excess green (ExG) and modified hue yielded the best near-binary images of weeds. Mayer et al. (1998) applied ExG to Separate plant and soil region for weed species identifications research as well.

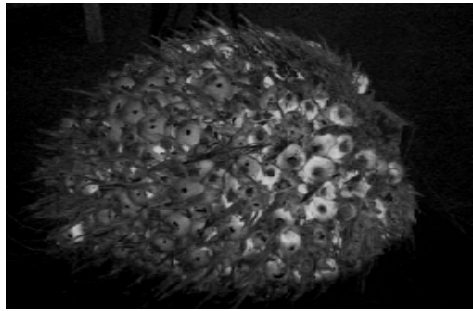
The color index use for background segmentation in this research was called "Modified Excess Red (MExR)". The Modified Excess Red (MExR) was defined as on the expression 1:

$$\text{MExR} = 2 * R - G - B \quad (1)$$

Furthermore, in order to separate the oil palm FFB from its background base on the colour feature, which are dynamic threshold segmentation method based on 2R-G-B chromatic aberration characteristic of fruit image and color-based segmentation using the L\*a\*b\* color space was properly used and investigated. One of results of sample image is given in Fig. 3 a. and b. subsequently.



(a)



(b)



(c)

**Fig. 3 Oil palm image and its dynamic threshold segmentation (a) original image, (b) 2R-G-B gray-level image, (c) color based segmentation**

Figure (3-b) illustrates the dynamic threshold segmentation method to distinguish between the sample image of three different ripeness class of oil palm bunch and its background.

Regarding to the study which carried out by (Jian-jun, Han-ping et al. 2009), the analysis of our result is fundamentally double-apices and very adapt to process requirement of Otsu method. Base on that the Otsu method is applied to segment 2R-G-B gray-level images base on the expression 2.

$$BW = \begin{cases} 255, & f(i,j) \geq T \\ 0, & f(i,j) < T \end{cases} \quad (2)$$

Mean by BW is 255 (white) and indicates to the image object when  $f(i, j)$  is greater than or equal to T. While BW is 0 (black) and indicates to the image background when  $f(i, j)$  is less than to T on the expression 3:

$$f(i,j) = 2R-G-B \quad (3)$$

Where, T is threshold which computed base on Otsu method as on the expression 4:

$$T = \text{Averg} \left[ \max_{0 < t < m-1} \sigma_B^2(t) \right] \quad (4)$$

Where;

$\sigma_B^2(t)$  is group variance between object class and background class.

Figure (3-c) shows the colour-based segmentation using the L\*a\*b\* color space method is robust technique to distinguish between the three different categories for the ripeness class of oil palm bunch and its background.

Comparing to the Modified Excess Red (MExR) was defined earlier. This techniques can be done by calculate sample colors in L\*a\*b\* color space for each region and then classify each pixel using the nearest neighbor rule and display results of nearest neighbor classification, at the end display 'a\*' and 'b\*' values of the labeled colors.



### B. Gabor Wavelet Feature extraction

Since the image background is segmented, the Gabor wavelet filter bank in order to analysis, extract and measure the image feature as shown in the figure 2. The fact that Gabor wavelets have been shown to look a lot like the receptive field profile of simple visual cortex cells, which can achieve joint spatial/spatial frequency analysis motivated the development of Gabor wavelet feature extractor (Porat and Zeevi, 1989; Bovik et al., 1990, 1992; Reed et al., 1993; Mallat, 1996; Naghdy et al., 1996). The two-dimensional Gabor elementary function is defined as on the expression 5:

$$g(x, y) = \frac{1}{2\pi} \exp\left[-\frac{x^2 + y^2}{\sigma^2}\right] \exp[j2\pi(x \cos \phi + y \sin \phi)] \quad (5)$$

Where  $\sigma$  is the variance of Gaussian distribution in both the  $x$  and  $y$  directions,  $\omega_0$  is the frequency of the sinusoid, and  $\theta$  is the orientation of the sinusoid. The Gabor element function actually is a two-dimensional Gaussian envelope modulated by a sinusoid with the frequency  $\omega_0$  and orientation  $\theta$ .

In this research, the Gabor wavelet function used for oil palm bunch feature extraction was same as Naghdy (1996) used and was defined as on the expression 6:

$$h(x, y) = \exp\left[-a^2 j \frac{x^2 + y^2}{y^2}\right] \exp[j\pi a^j (x \cos \phi + y \sin \phi)] \quad (6)$$

Where:

$$\alpha = \frac{1}{\sqrt{2}}, j = 0, 1, 2, \dots \text{and } \theta \in [0, 2\pi]$$

the different choices of frequency  $j$  and orientation  $\theta$  constructed a set of filters.

### C. Decision system

The final step of the oil palm FFB colour grading system is built our decision system. At this stage of our work we evaluate the effect of using Gabor feature extraction techniques with the neural network (ANN) decision system and compared our final result with the previous analysis witch based on statistical analysis

The classification part is carrying out with general two stage namely; Training and testing. Our ANN structure composed of [20 10 1] model. 20 nodes at the first input layer with 10 nodes at the second hidden layer connected with 1 node as the output witch determine the type of our grading system. The mean square error (MSE) generated at 0.001

In addition the normalization of Gabor feature extraction data vector of the known ripeness class of oil palm FFB was used to train the ANN in order to test and validate the system for future unknown sample classification.

The extracted features of the training samples are normalized to be in the target range which are (-1, 0 and 1) for under ripe, ripe and over ripe classes respectively.

### III. RESULTS AND DISCUSSIONS

This paper indicate the comparison between the oil palm grading system using the RGB digital numbers with Oil palm grading system using Gabor wavelet transforms and neural net work and the result of simulation introduced as the following:

#### Oil palm grading system using RGB Digital Numbers

The RGB range of interval values for over ripe, ripe and unripe categories derived from Eq. 7-9 is resented in Table 2 and is used to automatically classify the test images. If the computed RGB DN does not fall within any of the specified range, the FFB is considered as uncategorized. The computer program used the mean color intensity to differentiate between the different colors or ripeness of the fruits by using this formula.

$$\text{Mean of red} = r / \text{number of pixels} \quad (7)$$

$$\text{Mean of green} = g / \text{number of pixels} \quad (8)$$

$$\text{Mean of blue} = b / \text{number of pixels} \quad (9)$$

Where r = red pixel, g = green pixel and b = blue pixel

The computer program calculated the mean color intensity to differentiate between the different colors or ripeness of the fruits. After obtaining the RGB intensity of the samples for each category we compared them with each other in order to calculate the range of RGB intensity of the oil palm fruit bunches for each category as shown in the Table 4. These ranges are placed in the testing program as reference of the ripeness

for testing of bunch. Table 1 the range of RGB intensity of the sample of categories.

category	RGB Intensity range					
	Red		Green		Bleu	
	min	max	min	max	min	max
Ripe	57	91	26	60	34	66
Under ripe	45	65	20	44	25	46
Over ripe	32	60	23	37	26	46

#### Oil palm grading system using Gabor wavelet transforms.

The feature extraction process is implemented by using Gabor wavelet transform, which extracts feature vectors for classification from processed and segmented image of oil palm fruit bunch as region of interest as shown in the figure 4.

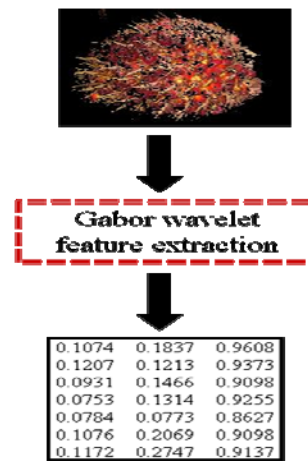
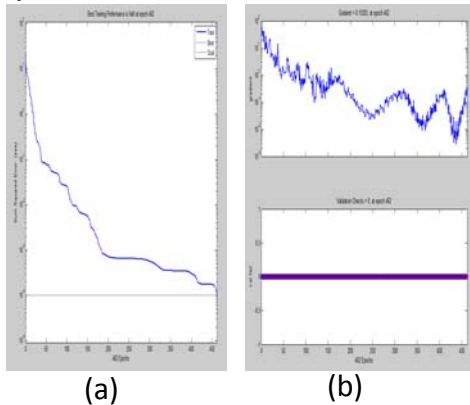


Figure 4. Image feature extraction using Gabor wavelet

The training model result as we see in the figure 5 is ready to be used in the further application in order to test the ripeness of the oil palm fruit. Subsequently, the results of the neural network classification system are evaluated against the human graders to measure accuracy. It shows that the accuracy of the oil palm grading system grading system result based on the training and testing is significantly higher than the result based on the statistical classification system.



**Figure 5 ANN Training result (a) training performance (b) training validation**

Table below show the performance rate of the decision system with both techniques tested indoor with different images from each class

Techniques	Over ripe	ripe	Under ripe	Total %
Gabor	85%	70%	80%	78%
statistical	60%	90%	60%	70%

#### IV Conclusion

In this paper an algorithm based on Gabor wavelets filtering (GWF) and statistical method are presented and implemented for colour texture classification. The oil palm grading system is tested with different method which is statistical classification method based on the digital number average for each ripeness categories in order to get the ripeness range. While the Gabor wavelets and neural network classification method based on training model was properly implemented for the oil palm fruit grading system. Finally, it shows that the accuracy of the oil palm grading system result based on GWF with ANN is significantly higher rate performance compared to the statistical classification system at indoor application.

#### V References:

Abdullah, M. Z., A. S. Fathinul-Syahir, et al. (2005). "Automated inspection system for colour and shape grading of starfruit (*Averrhoa carambola* L.) using machine vision sensor." *Transactions of the Institute of Measurement and Control* **27**(2): 65-87.

Abdullah, M. Z., L. C. Guan, et al. (2004). "The applications of computer vision system and tomographic radar imaging for assessing physical properties of food." *Journal of Food Engineering* **61**: 125-135.

Alfatni, M. S. M., A. R. M. Shariff, et al. (2008). "Oil Palm Fruit Bunch Grading System Using Red, Green and Blue Digital Number." *Journal of Applied Science* **8**(8): 1444-1452.



- FILHO, R. A., Í. VITORELLO, et al. (1997). "Application Of Image Merging, Segmentation and Region Classification Techniques as A New Approach For The Detailed Thematic Mapping Of Soil-Vegetation Assemblages." *Revista Brasileira de Geociências* **27**(2): 207-210.
- Ghazali, K. H., M. M. Mustafa, et al. (2008). "Machine Vision System for Automatic Weeding Strategy using Image Processing Technique." *American-Eurasian J. Agric. & Environ. Sci* **3**(3): 451-458.
- Jian-jun, Y., M. Han-ping, et al. (2009). "Segmentation methods of fruit image based on color difference." *Journal of Communication and Computer* **6**(7):40-45.
- Leemans, V. and M.-F. Destain (2004). "A real-time grading method of apples based on features extracted from defects." *Journal of Food Engineering* **61**: 83-89.
- Malamasa, E. N., E. G. M. Petrakisa, et al. (2003). "A survey on industrial vision systems, applications and tools " *Image and Vision Computing* **21**: 171-188.
- Marmoa, R., S. Amodiob, et al. (2005). "Textural identification of carbonate rocks by image processing and neural network: Methodology proposal and examples." *Computers & Geosciences* **31**: 649-659.
- Morimoto, T., T. Takeuchi, et al. (2000). "Pattern recognition of fruit shape based on the concept of chaos and neural networks." *Computers and Electronics in Agriculture* **26**: 171-186.
- Njoroge, J. B., K. Ninomiya, et al. (2002). Automated Fruit Grading System using Image Processing. S1CE02-0822. Auk 5-7.2MI2, osaks: 1346-1351.
- Riyadi, S., A. A. A. Rahni, et al. (2007). Shape Characteristics Analysis for Papaya Size Classification. The 5th Student Conference on Research and Development –SCORED Malaysia: 1-5.
- Sun, D.-W. (2006). Computer Vision Technology for Food Quality Evaluation. Proceedings of the International Symposium on Novel Technology in Food Processing and Engineering, National Chung Hsing University, Taichung, Taiwan.



### **Imaging of two phase flow in a gravity flow rig using infra-red tomography**

S. Ibrahim, M. F. Rahmat, Mustafa M. Elmajri,  
M. Y. Mohammad Amri, and Siham M. Lebayesh  
Faculty of Electrical Engineering, Universiti Teknologi Malaysia,  
81310 UTM Skudai, Johor.  
Tel: 07-55 35321, Fax: 07 – 55 66272  
[mus\\_utm@yahoo.com](mailto:mus_utm@yahoo.com)

**Abstract-** It is important to obtain data on flow regimes in order to analyze and measure industrial flow. Most of the techniques used to measure two-phase flow averaged the flow's property and as a result, they do not provide data on the nature of the flow regime. Besides they cannot provide accurate measurement if the distribution of flow component is time or spatially varying. The overall aim of this paper is to present an investigation on the use of an optical tomography method based on infra-red sensors for real-time monitoring of solid particles conveyed by a gravity flow rig. Collimating the radiated beam from a light source and passing it via a flow regime ensures that the intensity of radiation detected on the opposite side is linked to the distribution and the absorption coefficients of the different phases in the path of the beam. The information on the flow captured using upstream and downstream infra-red sensors is digitized by the DAS system before it was passed into a computer for analysis such as image reconstructions. This investigation successfully developed and tested an infra-red tomography system to display two-dimensional images of concentration profiles.

Key words: Two phase flow, imaging, infra red, tomography.

#### **2 Introduction**

The field of process tomography is growing rapidly. Tomographic imaging offers a unique opportunity to discover the complexities of structure without the need and non-living things (Syed Salim, 2003).

The application of process tomography is analogous to the application of medical tomographic scanners for investigating the human body, but applied to an industrial

to invade the object (Beck and Williams, 1996). It is an expansion from the early research involving x-ray tomography, which focused on how to obtain 2-D cross-section images of animals, human, process as there is a widespread need for the direct analysis of the internal characteristics of process plants in order to improve the design and operation of equipment. Process tomography can be applied to many types of processes and unit





operations, including pipelines, stirred reactors, fluidized beds, mixers, and separators. Depending on the sensing mechanism used, it is non-invasive, inert, and, non-ionizing. It is therefore applicable in the processing of raw materials: in large scale and intermediate chemical production; and in the food biotechnology areas.

Imaging of flow involved obtaining images of particles and gas bubble (Yang and Liu, 2000) and the measurements can be either done using on-line (real time) or off-line. For on-line measurement, there are many performance aspects that must be considered such as hardware performance, data acquisition (signal interfacing), and algorithm performance. Limited numbers of measurement affect the quality of images obtained. The input channel of the data acquisition system has to be increased with the increase in the number of sensors used.

Process Tomography will improve the operation and design of processes handling multi-component mixtures by enabling boundaries between different components in a process to be imaged in real-time using non-intrusive sensors (Dyakowski, 1996). Information on the flow regime, vector velocity and component concentration distribution in process vessels and pipelines will be determined from the images. The basic idea is to install a number of sensors around the pipe or vessel to be imaged. There are two types of sensor: "hard-field" and "soft-field" sensors. A "hard-field" sensor is equally sensitive to the parameters it measured inside and outside this measurement region (Chan, 2003). For a "soft-field" sensor, sensitivity of the measured parameter depends on the

position in the measurement volume, as well as on the distribution of parameters inside and outside the region. For this reason, image reconstruction is much simpler for "hard-field" sensors such as gamma-ray sensors than for "soft-field" sensors such as capacitance sensors (Isaksen, 1996; Chan, 2003).

This sensor shows data on the nature and distribution of components within the sensing sector. The sensor output signals depend on the position of the component boundaries within their sensing zones. Most tomographic techniques are concerned with abstracting information to form a cross-sectional image. A computer is used to reconstruct a tomographic image of the cross-section being observed by the sensors. This will provide, for instance, identification of the distribution of mixing zones in stirred reactors, interface measurement in complex separation processes, and measurements of two-phase flow boundaries in pipes with applications to multiphase flow measurement. The image data can be analyzed quantitatively for subsequent use to improve process control or to develop models to describe individual processes.

The linear back projection (LBP) algorithm is the most simple and most popular that was initially used in medical tomography. Investigation conducted by Chan (2003) improved flow imaging using 16 alternating fan-beam projections with an image reconstruction rate of 20 fps, but this image reconstruction rate not is sufficient to achieve an accurate measurement of velocity. Instead of using one light source, this project focused on using individual





light source meaning one infra-red LED emitter for one photodiode. This method was then combined with an infra-red tomography system which consist of a hardware fixture, a signal conditioning system, and a data acquisition system by synchronizing the whole process operation.

The process tomography system requires the knowledge of various disciplines such as instrumentation, process, and optics to assist in the design and development of the system. Taking the external influences into account, design of the fixture must be able to avoid the infra-red sensor from being exposed to any kind of ambient light (day light, lamp etc). They also placed around the boundary of the pipe so that light emitted from the emitter will be the only one that is in contact with the solid particle in the pipeline. The choice of infra-red because it is simple to implement, has low power consumption, low circuitry costs, invulnerability to interference from traditional source, signal cannot be jammed (diffused), and high noise immunity.

## 2 System configuration

The aim of a particular measurement is to capitalize on the differences in the characteristics of the process being investigated. In this tomography system, the number of measurements must be increased in which each upstream and downstream sensing arrangement with 64 measurements respectively provide a total of 128 measurements to form two image frames in real time. Hence, measurement is

realized by synchroni-zing the projection system, signal processing by signal conditioning and data acquisition system, and data manipulation taking into account of the frequency response and time response i.e. factors, which influenced the measurement signal.

The infra-red tomography system can be subdivided into three parts: sensor configuration, signal conditioning and data acquisition system and a computer (Figure1). As a whole, a digital timing controller controls the system operation.

The sensor system is at the heart of any tomographic technique. The Siemens SFH4510 infra red emitter and the SFH2510 infra red receiver are selected as they are relatively cheap and has a fast response time. The infra red emitters and receivers are connected to the measurement section via optical fibers.

The sensing array is arranged in a parallel manner to form two upstream and downstream arrays resulting in four parallel projections. Each part (downstream/upstream) consists of a combination of two orthogonal ( $0^\circ$ ,  $90^\circ$ ) and diagonal ( $45^\circ$ ,  $135^\circ$ ) projections. The diagonal projections were arranged in a similar manner to the orthogonal projections with 16 pairs of sensors for each projection as shown in Figure 2. The upstream sensing array and the downstream array is placed 0.1 meter apart. This distance was chosen due to the sampling rate value used in the experiment.

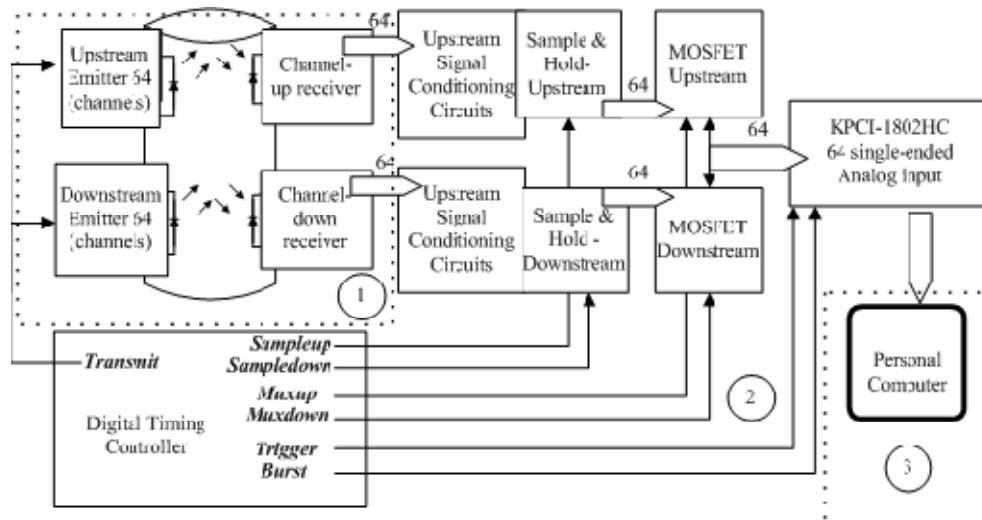


**Figure 1:** A block diagram of the infra-red tomography system.

In the second part both peak voltages received by photodiodes are equal to a level of infrared light intensities and consequently relative to the two different components (solid and air) in the process/pipe traversed by the infra-red beam through an optical fiber. The analog signal is processed by a signal conditioning circuit. Finally, this analog signal is converted into a digital signal by the data acquisition system prior to entering a PC for processing it either off-line or on-line using image reconstruction algorithm. The algorithm is programmed using the Visual C++ software to provide the concentration profile.

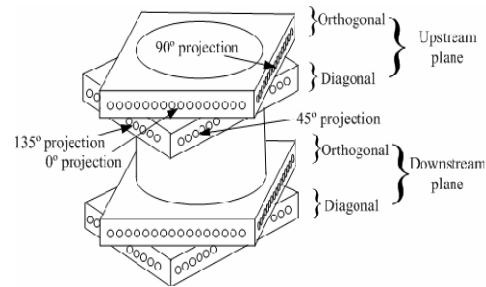


**Figure 2:** The arrangement of fiber optic holes for each projection

### 3 Mathematical modeling

Line integrals and projections are described by making use of the coordinate systems depicted in Figure 3. The line integral represents the integral of several parameters along a line. The object is represented by a two-dimensional function  $f(x, y)$  and each line integral is represented by the projection angle  $\theta$  and a detector

position  $x'$  parameters (Kak and Slaney, 1999).

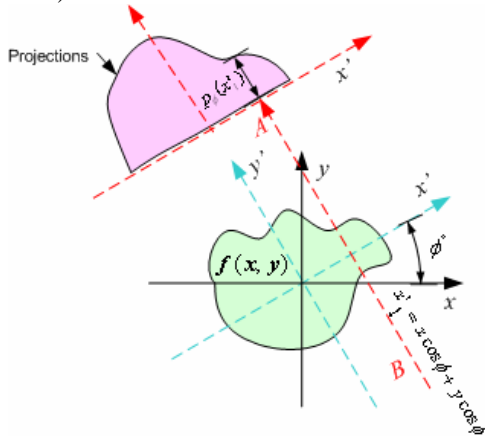


**Figure 3:** An object  $f(x, y)$  and its projection  $p_\phi(x'_1)$ , shown for angle  $\phi^\circ$

The equation of AB in Figure 3 is:

$$x \cos \phi + y \sin \phi = x' \quad [1]$$

Where:

$$\begin{bmatrix} x' \\ y' \end{bmatrix} = \begin{bmatrix} \cos \phi & \sin \phi \\ -\sin \phi & \cos \phi \end{bmatrix} \begin{bmatrix} x \\ y \end{bmatrix} \quad [2]$$

In addition, this resulted in the following line integral

$$p_\phi(x'_1) = \int_{(\phi, x') \text{ line}} f(x, y) ds. \quad [3]$$

$p_\phi(x'_1)$  = projection data for AB line.

$x'_1$  = the coordinate of AB line in  $x'$  plane.

The projection data can be written in discrete form as (Brown et al. 1999):

$$p_\phi(x'_1) = \sum_{y'} (f(x' \cos \phi - y' \sin \phi, x' \sin \phi + y' \cos \phi)) \Delta y' \quad [4]$$

#### 4 Experiments and Results

The measurements made use of an array of 128 infra-red sensors (64 upstream and 64 downstream sensors) by taking output voltage readings based on plastic beads flow which were dropped into a flow rig at various flow rates in range of  $27 \text{ gs}^{-1}$  to  $126 \text{ gs}^{-1}$ . The main sampling frequency chosen is 88.03 Hz, this is because the ability of the data acquisition system DAS which is the time required by the hardware to convert a series of analog signal in a buffer in at least 1 second. The total readings taken are 30 cycles in which each cycle contains 254 buffers and each buffer contains 64 voltage reading samples. Figure 4 shows how one cycle of measurement contains 254 buffers and each buffer contains 64 voltage reading samples.

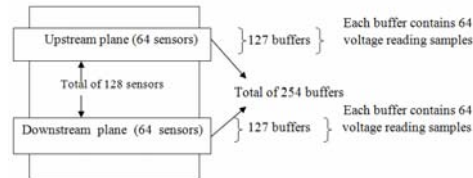


**Figure 4:** One cycle of measurement

The Combined Filtered Linear Back Projection (CFLBP<sub>i+s</sub>) algorithm and Hybrid Linear Back Projection (HLBP) algorithm both at  $32 \times 32$  pixels resolution were selected because they gave a zero or low values of NMSE (Normalized mean square error). The NMSE provides the quantitative information regarding the spreading effect of objects in the



reconstructed image (Chan, 2003). If NMSE provides a high output, this means that the error between the reconstructed images and the flow model image is large, and on the other hand the lower the NMSE percentage value the closer the reconstructed image to the flow model (Md Yunus, 2005).

Figures 5 (a) to (d) show the concentration profiles that represent the upstream and downstream selected samples of reconstructed flow images using the CFLBP<sub>i+s</sub> and HLBP algorithms at a flow rate of  $27\text{gs}^{-1}$  for half flow regime. The circle represents the flow pipe. Ideally the right-hand side of the pipe should have no

flow i.e. it should be 0V. The concentration profiles produced using the CFLBP<sub>i+s</sub> algorithm (Figures 5(a) and (b)) show that the distribution of two phase solid-air flows were forced to converge at the left-hand side of the distribution pipe but the right-hand side of the pipe still has some flow indicating noise. The results obtained using the HLBP algorithm (Figures 5 (c) and (d)) produced a clearer visual image for the same solid-air flow regime compared to the CFLBP<sub>i+s</sub> as most part of the right-hand side of the pipe has no flow or 0V.

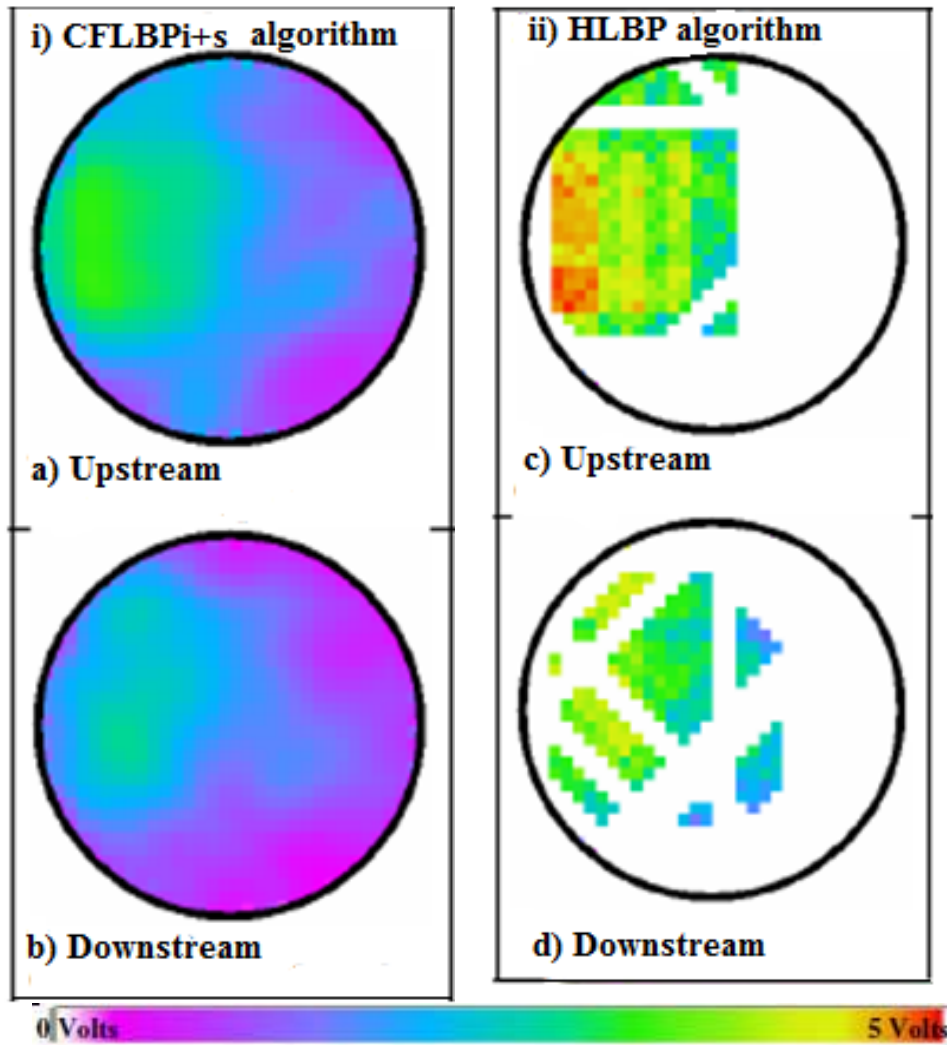


**Figure 5:** Concentration profiles for half flow at a flow rate of  $27 \text{ gs}^{-1}$  (a) Upstream flow using CFLBP<sub>i+s</sub> (b) Downstream flow using CFLBP<sub>i+s</sub>. (c) Upstream flow using HLBP (d) Downstream flow using HLBP.



## 5 Conclusion

A tomography-based flow meter has been constructed and successfully tested. The experiments were aimed at testing on-line the effectiveness of the infra-red imaging system in measuring and visualizing the two-phase solid-gas flow in a flow rig model. The *HLBP* algorithm both at  $32 \times 32$  pixels resolution have been found to be the most suitable image reconstruction algorithms based on the qualitative and quantitative measurements. For further work, more experiments and measurements with use of artificial intelligence such as neural network or fuzzy logic will be carried out in order to achieve image reconstruction or an auto-adjusting sampling rate system.

## REFERENCES

- [1] Abdul Rahim, R., Green R. G., Horbury, N., Dickin, F. J., Naylor, B. D., and Pridmore, T. P. (1993). Further development of a tomographic imaging system using optical fibres for pneumatic conveyors. *Meas. Sci. Technol.* Vol(7): 419-422.
- [2] Beck, M. S. and Williams, R. A. (1996). *Process tomography: a European innovation and its applications.* *Meas. Sci. Technol.* Vol(7): 215-224.
- [3] Brown, B., Smalwod, R., Barber, D., Lawford, P., and Hose, D. (1999). *Medical Physics and Biomedical Engineering.* Bristol: Institute of Physics Publishing.
- [4] Chan, Kok San.(2003). *Real Time Image Reconstruction for Fan Beam Optical Tomography System.* Universiti Teknologi Malaysia: M.Eng. Thesis.
- [5] Dyakowski, T.(1996). *Process Tomography Applied to multi-phase measurement.* *Meas. Sci. Technol.* Vol(7): 343-353.
- [6] Ibrahim, S., Green, R. G., Dutton, K., Abdul Rahim, R., Evans, K. and Goude, A. (1999). *Optical Fibres for Process Tomography: A Design Study.* In: 1st World Congress on Industrial Process Tomography, Buxton, Greater Manchester, April 14-17.
- [7] Isaksen, (1996). 'A review of reconstruction techniques for capacitance tomography', *Meas. Sci. Technol.* Vol(7): 325-337
- [8] Kak, Avinash C. and Slaney Malcom.(1999). *Principle of Computerized Tomography Imaging.* New York.: IE Pres. The Institute of Electrical and Electronics Engineers, Inc
- [9] Md Yunus, M. A. (2005). *Real-Time Imaging of Solid Flow in a Gravity Flow Rig using Infra-Red Tomography.* Masters Thesis, Universiti Teknologi Malaysia, Malaysia.
- [10] Syed Salim, Syed Najib.(2003). *Concentration Profiles and Velocity Measurement Using Ultrasonic Tomography.* Universiti Teknologi Malaysia.: M.Eng. Thesis.
- [11] Yang, W.Q., and Liu, S.(2000). *Role of tomography in gas/solids flow measurement.* *Flow Measurement and Instrumentation.* Vol(11) : 237-244.



## Speaker recognition system using wavelet neural networks.

Eng. K.R.AL SHARI.

Dr. A.H. AMBARAK.

Garyounis University, Electrical and Electronic Engineering department.

Email: [k\\_alshari@yahoo.com](mailto:k_alshari@yahoo.com)

### ABSTRACT

This paper presents an automatic system for speaker recognition based on wavelet neural networks; wavelet analysis is used to extract features from the speech waveform, neural networks are used to match features with known speakers in classification stage to make decision. We study speaker identification system with different features using wavelet analysis and wavelet packet analysis methods. The wavelet analysis has gained a great deal of attention on the field of signal processing; flexibility of this technique is to find time and frequency resolution. Artificial neural networks (ANNs) are being applied to pattern recognition and have successfully been used in automated classification of acoustic signal. In our study we select a feed forward neural network “multilayer perceptron (MLP)” as a classifier due to its ability to compensate discrepancy among the data. The performance of the system is affected by the choice of features using wavelet and the design of neural networks. The recognition rate using wavelet packet analysis is about (85% to 90%), while the recognition rate using wavelet entropy is reached to 93%.

Keywords: speaker recognition system, wavelet analysis, wavelet packet analysis, neural networks, text dependent mode, text independent mode, speaker identification, speaker verification.

### 1. INTRODUCTION

Speaker recognition system is the process of automatically recognizing who is speaking based on basic individual information induced in speech waves.

Speaker recognition is modern technique has been recently used in many fields; such as, banking transactions, shopping, telephone networks, and is mainly used in forensic and criminal fields; speech recognition as one of biometric techniques

rely one or more physical features such as; digital finger print identification, iris scanning, and face recognition.

Speaker recognition is one of biometric techniques that uses to recognize persons who said special sentence ‘*text dependent*’ mode, i.e. “*password*”, or using different sentences in train and test phase. ‘*Text independent*’ mode. [1]

Speaker recognition can be principally divided into speaker verification and



speaker identification. speaker verification is the process of accepting or rejecting the identity claim of a speaker by comparing a set of measurements of the speaker's utterances with a reference set of measurements of the utterance of the person whose identity is being claimed. Speaker identification is the process of determining from which of the registered speakers a given utterance comes. [2]

In speaker recognition we differentiate between low-level and high-level information. High level-information is values like a dialect, an accent, the talking style and the subject manner of context. These features are currently recognized and analyzed by humans. as low level are denoted the information like pitch period, rhythm, tone, spectral magnitude, frequencies, and band widths of an individual's voice.

Speech recognition works with a microphone or with a regular telephone handset, although performance increases with higher quality capture devices. The hardware costs are very low, because today every PC includes a microphone or it can be easily connected one. However voice recognition has got its problems with persons who are husky or mimic another voice. If this happens the user may not be recognized by the system. Additionally, the likelihood of recognition decreases with poor quality microphones and if there's background noise. [3]

The two subtasks above differ considerably in their operational context, as the following comparison makes clear. [4]

Table 1. Comparison between speaker identification and speaker verification.

Identification	Verification
<ul style="list-style-type: none"> <li>◆ Speaker may be reluctant</li> <li>◆ Voices disguise a problem.</li> <li>◆ Must test many patterns.</li> <li>◆ System response can be slow.</li> <li>◆ Vocabulary may be different.</li> <li>◆ Channels may be poor or differing.</li> <li>◆ Signal to noise ratio may be poor.</li> </ul>	<ul style="list-style-type: none"> <li>◆ Speaker is cooperative.</li> <li>◆ Mimicry problem.</li> <li>◆ Need compare to only one pattern.</li> <li>◆ System response must be fast.</li> <li>◆ Vocabulary can be restricted to standard test phrase.</li> <li>◆ Can frequently control channel characteristics.</li> <li>◆ Can usually control signal to noise ratio.</li> </ul>

## 2. WAVELET ANALYSIS

The wavelet analysis has gained a great deal of attention on the field of signal processing. It has many advantages, for example, its ability to find out both frequency and temporal information, and to analyze signals which contain discontinuities and sharp spikes [8].

### 2.1. DISCRETE WAVELET TRANSFORM

The speech signal S has to be analyzed using a discrete wavelet transform (DWT) is processed using wavelet decomposition that decompose a signal S into multi levels n of approximations A and details D, these vectors are obtained by convolving the signal S into two types of filters ( Lo\_D) low pass filter, and (Hi\_D) high pass filter,





followed by down sampling (dyadic decimation) as shown in figure 1 [7].

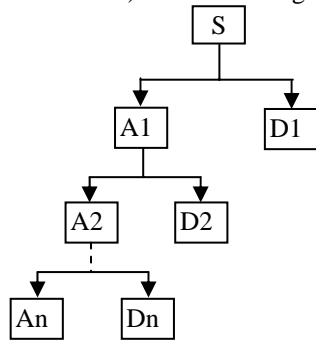


FIGURE 1.a : wavelet decomposition to produce approximation A and details D.

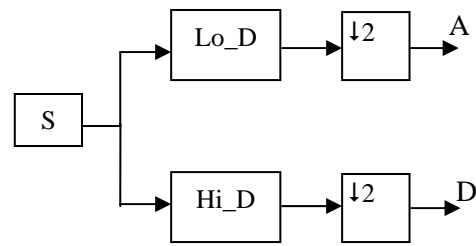


FIGURE 1.b: wavelet decomposition with filters (low, high) and down sampling.

## 2.2. WAVELET PACKET BASES:

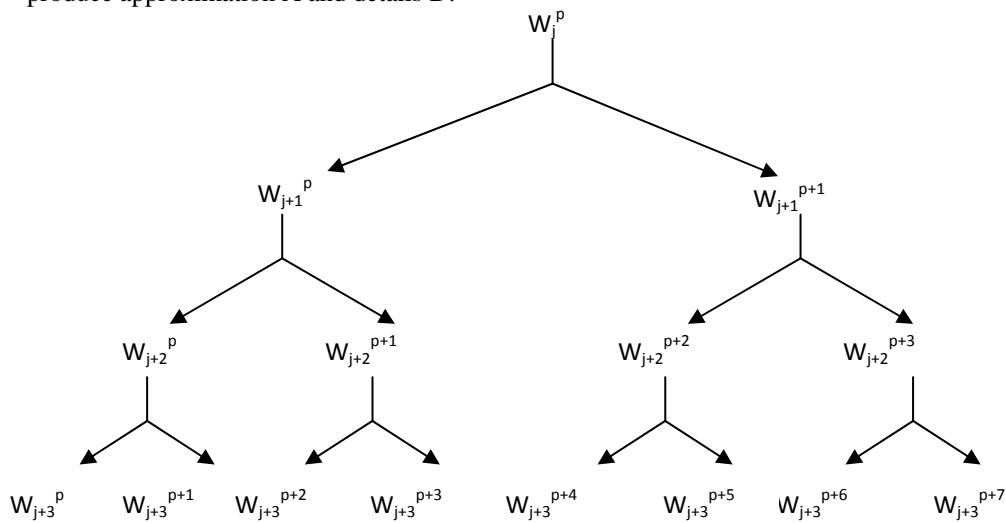


FIGURE 2: binary tree of wavelet packet analysis.

Wavelet packet analysis generalizes the filter bank tree that relates wavelet and conjugate mirror filters. In a decomposition of the signal with the wavelet transform, only the lower frequency band is decomposed, giving a right recursive binary

tree structure, where its right child represents the lower frequency band and its left child represents the higher frequency band. In the corresponding decomposition with the Wavelet packet transforms (WPT), the lower as well as the higher frequency



bands are decomposed giving a balanced binary tree structure. Such a tree is illustrated in figure 2.

For each node in the tree, a wavelet packet space  $W_j^p$  is associated, where  $j$  is the depth, and  $p$  is the number of the nodes to the left of this particular node at the same depth [6].

### 3. EXPERIMENTAL WORK

In the experimental work, a speaker recognition system based on wavelet is used. Figure 3 shows the automatic speaker recognition system used in this study.

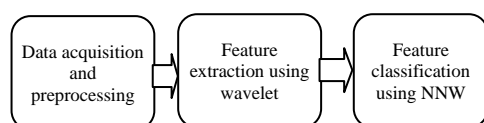


FIGURE 3: the basic structure of automatic speaker recognition system.

We divide the experimental work into two parts; the selection of features is different in two parts.

#### 3.1. PART I

In this part we examine the performance of the system by using wavelet packets in feature extraction stage,

a filter bank is used for noise reduction in preprocessing stage, and the result is affected when changing the wavelet filter and a level of decomposition. The model of the whole system is shown in figure 4

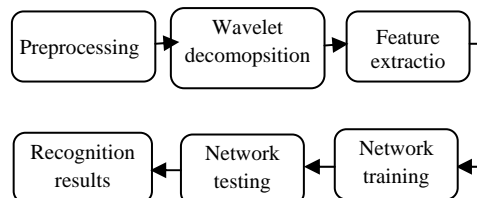


FIGURE 4: the block diagram of the recognition system.

During preprocessing stage the zero mean data was normalized in the range [-1, 1], and a low frequency noise was reduced using moving average filter, all the sounds were decomposed into wavelet coefficients computed from the wavelet coefficients and a feature vector is composed.

A number of feature vectors were introduced to MLP network, finally after training the network, a test set was applied to the trained network to give the result, and recognize a speaker [8].

S																																							
A																D																							
A								D								A								D															
A	A	D		A	D	D		A	A	D		A	D	D		A	A	D		A	D	D		A	D	D		A	A	D		A	D	D					
A	D	A	D	A	D	A	D	A	D	A	D	A	D	A	D	A	D	A	D	A	D	A	D	A	D	A	D	A	D	A	D	A	D	A	D	A	D		
1	2	3	4																																				64

FIGURE 5: wavelet packet decomposition tree. The bin coefficients 2:32 are selected.



### 3.2. PART II

We examine the performance of the system by using wavelet transform in feature extraction stage, a pre emphasize filter in preprocessing stage, and wavelet denoising is used to filter the signal and extract the features, the result is affected when changing the wavelet filter and a level of decomposition.

## 4. FEATURES

### 4.1. Features selected in PART I:

The features were selected in part I using wavelet packet analysis for signal decomposition. The preliminary work starts by choosing level 6 of decomposition. Figure 5 demonstrates the signal  $S$  is analyzed using wavelet to decompose a signal into 64 bins, the bins (2:32) were chosen to extract the main features.

The main features are three parameters; maximum energy, width and position of coefficients.

The maximum energy  $e_m$  is calculated as:

$$E_B(r) = \sum_{n=1}^{32} c^2(n, r), r = 2, 3, \dots, 32 \quad (1)$$

Where  $E_B(r)$  is the bin energy of the wavelet coefficients  $c$  of bin  $r$ .

The average energy  $\bar{E}_B(r)$  at each bin  $r$  was defined as:

$$\bar{E}_B(r) = \frac{E_B(r)}{n_c} \quad (2)$$

A largest average energy is a first parameter selected:

$$E_m = \max(\bar{E}_B(r)) \quad (3)$$

A second parameter of feature vector is “position”  $p$  that represents a number of bin  $r$  in which the maximum energy was located.

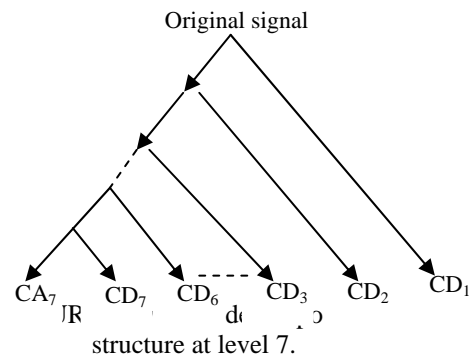
A third parameter is a “width”  $w$  that represents a number of bins  $w$  satisfies the in equality:

$$E_B(r) > Th_2 \quad (4)$$

Where the threshold value was selected as 130 after preliminary test.

### 4.2. Features selected in PART II

Discrete wavelet layer is performed to extract features from processed speaker’s signal; the feature extraction is produced using wavelet decomposition structure tree at level 7, as shown in figure 6.



DWT is applied to the signal using Daubechies-10 ‘db10’ filters. Thus, we obtain two coefficients: approximation coefficients  $CA$  and seven detail coefficients ( $CD_1:CD_7$ ).

An entropy based criterion describes information related properties for



representation the signal, entropy is a common concept in many fields, mainly in signal processing. A method of measuring the entropy appears to be an ideal tool for quantifying the ordering of non stationary signals [9].

The entropy is calculated as defined in equation:

$$E(s) = \frac{\sum |s_i|}{N} \quad (5)$$

Where E: is a wavelet entropy 'real number', s: is a terminal node signal, and  $s_i$  is a waveform of terminal node, and N: is length of coefficients at each node.

## 5. SYSTEM DATABASE

A data base is created by using a sentence: 'besm ellaherrahman erraheem' in Arabic language, as a text dependent pass word in a closed system. A data is divided into two groups.

A first group of data consists of 20 speakers (4 male; and 16 female) were spoken the same sentence 15 times each, so the data size is 300; 200 of them are used for training network as training set, while the remaining 100 is for test set.

The sampling rate of acquired data through a microphone was 11025 Hz; 16 bit accuracy and use PCM in coding. 'Mono channel recording'.

The data was processed in MATLAB environment, and WAVELET tool box.

A second group of data contains the same 20 speakers, uttering the same sentence 25

times each, so the data size is 500; 300 of them for training set and 200 for test set.

## 6. RESULTS

### 6.1. PART I

We start our work with data size is 300, the signal is analyzed using the common type of wavelets; 'Daubechies' at different orders; choose (dB10, dB9, dB5) at different levels of decomposition; choose levels (7,6,5), and the coefficients were selected to give good results.

The following tables show the results at different stages.

Table 2. The recognition rate at different levels of decomposition using 'db10' wavelet filter.

Bins coefficients	1:32 Level 5	1:32 Level 6	1:64 Level 7
Recognition rate	84%	85%	90%

Table 3. The recognition rate at different wavelet filter at level 7 of decomposition at bins (1:64).

Wavelet filter type	dB10	dB9	dB5
Recognition rate	90%	89%	86%

If we increase database to 500 (300 of database in training group, and 200 in testing group); and examine the performance of the system using the



wavelet filter 'db9', at level 7 of decomposition at bins (1:64), we get the rate increases to 92.5%.

### 6.2. PART II

We analyze the signal using different wavelet filters at different levels of decomposition; the following tables show the results.

Table 4. The recognition rate using 'db10' wavelet filter at different levels of decomposition.

Level of decomposition	6	7	8
Recognition rate	91%	93%	94%

Table 5. the recognition rate at different wavelet filters at level 7 of decomposition.

Wavelet filter type	dB5	dB9	dB10
Recognition rate	89%	90%	93%

## 7. DISCUSSION AND CONCLUSION

In this study we aim to recognize the person from his voice, speaker identification mode is performed using text dependent mode and closed set (20 speakers), the wavelet neural network technique is used to analyze the signal, and the signal was processed using wavelet to extract the features and made matching using neural networks.

The wavelet is an effective tool that we use in this study which is the robust and novel

technique is used recently in many fields, especially in DSP applications such as filtering, signal (denoising), thresholding, decomposition and reconstruction with minimum errors.

By using wavelet analysis in signal processing gives the system more flexibility, because it can analyze the signal in terms of scaling and translation that it has immediate relation with time and frequency, that if the level of wavelet decomposition increases the scale will increase too that leads to determine the time when action occurred suddenly and frequency at each level.

The main advantage of wavelet application is identifying pure frequencies when analyzing the signal in terms of approximation and detail coefficients at the last level of decomposition.

Another advent of wavelet analysis is that we can control the number of coefficients that be used in feature extraction by changing the level of decomposition and obtain result about (93 % in our work when increase the features). Although all these advantages we face number of problems that affects to the results:

1. The recording of speech sounds from different speakers is very sensitive to many factors that must be taken into account; i.e. microphone type, distance between speaker and phone, and environment of recording.
2. The choice of the features is the important reason to increase the performance of the system. From our results the reason of a misrecognition of



some speakers or wrong recognition of others is referred to how the features were selected, i.e. in part I of experimental work the position and width features is affected with result, i.e. the resultant of pre filtered signal gives low signal to noise ratio. While the features in part II is more performance than previous one, i.e. wavelet entropy represents the information that is related to the energy and consequently to the amplitude of the signal.

3. The design of the neural network is sensitive to data size, i.e. as the size of data increase will improve the training of network and choosing the network parameters carefully during design; to obtain minimum value of error. (Our work, as data size is 300, the result was 88%, while if the size increase to 500, the result became 90%).

From part I, II; by changing the order of wavelet filter from *db5*, *db9*, *db10* the performance will increase as the order of a filter increases, that it has immediate relation to the order of a filter and the signal regularity.

By increasing the level of decomposition will increase the accuracy of analysis in time and frequency domains that relates to increase the resolution. (The main advantage of wavelet analysis).

#### ACKNOWLEDGMENT

The author wished to thank *GOD* who rounded her with careful to perform this work, and thank the departments of electrical and electronic engineering, and computer department, Garyounis university.

#### REFERENCES

- [1]. Vijay k. madiseti Douglas, B.williams, “*DSP digital signal processing Hnadbook*”, 1999.
- [2]. www.voiceprobem.org, the voice problem web site.
- [3]. Gerik Alexander von Graeventiz, “*About speaker recognition technology*”, Germany.
- [4]. Thomas W.parsons,” *Voice and speech processing*”, hofstra university, 1987.
- [5]. Speak voice print speaker verification, <http://www.t-netix.com>.
- [6]. Todor Ganchev, Mihalios Siafarikas, Nikos Fakatakis "*speaker verification based on wavelet packets*", wire communication laboratory, university of partas, Greece.
- [7]. Michel misiti, Yues misiti, George oppeanheim, Jean micheal poggi; “*wavelet toolbox, for use with matlab*”, 1997 – 2002.
- [8]. Arja Selin, Jari Turunrn, Juha T. Tanttu, “ *wavelets in recognition of bird sounds*”, Dep. Of information technology, tempare university of technology, (22 June 2006).
- [9]. Engin Avci, “*An automatic system for Turkish word recognition using discrete wavelet neural network based on adaptive entropy*”, Dep. Of electronic and computer science, Turkey, (20 Dec. 2006).



## Design of Stable 2-D IIR Digital Filters using Very Strictly Hurwitz Polynomial with Genetics Algorithm

Idris El-Feghi

[idrise@ee.edu.ly](mailto:idrise@ee.edu.ly)

Mohamed Markus

[kobemarkus@hotmail.com](mailto:kobemarkus@hotmail.com)

Myson Alzurgani

[Mzswrgani@yahoo.com](mailto:Mzswrgani@yahoo.com)

EE. Dept. Al-Fateh University, Tripoli-Libya

**Abstract** : Digital filters are becoming increasingly important and finding applications in diverse areas of field. Digital filters are used in different fields such as communication, digital signal processing, medical imaging and seismic data. Designing a stable digital filter from its analog counterpart can be quite hard and stability is not always guaranteed. In this paper, we present a new approach to the design of multidimensional digital filters based on Very Strictly Hurwitz Polynomial (VSHP) and Genetic Algorithm (GA).

### 1. INTRODUCTION

For many years researchers have relied on transformation of 2-variable passive analog network, using double bilinear transformation method to design 2-D recursive filters. This is done to avoid stability problem associated with Infinite Impulse Response (IIR) filters.

Rajan *et al* [1] showed that not all analog filters will yield stable digital filters upon the application of bilinear transformation.

In [2] showed that only a special class of analog filters can be transformed to a stable digital filters using bilinear transformation. This special class of 2-D analog filters should have Very Strictly Hurwitz Polynomial (VSHP) in their denominators. Two-variable VSHP's have been utilized for the design of stable 2-D digital filters by many researchers [21]-[22].

Recently [3] have shown 2-D planar

and beam filters can be designed by transformation of 2-variable passive RLC elements. Here we present a new method for generating, 2-variable VSHP. In this method the properties of positive definite or positive semi-definite matrices and resistive matrix is utilized to generate the desirable 2-variable VSHPs. The presented methodology is an extension of the technique presented in [4] for 2-D VSHP. The application of the generated polynomials is shown through the design of 2-D recursive filters.

### 2. CHARACTERIZATION OF 2-D ANALOG AND RECURSIVE DIGITAL FILTERS

A 2-D analog filter is characterized by its transfer function



$$H_a(s_1, s_2) = \frac{P_2(s_1, s_2)}{P_1(s_1, s_2)} \quad (1)$$

where

$$P_j(s_1, s_2) = \sum_{i_1=0}^{M_1} \sum_{i_2=0}^{M_2} P(i_1, i_2) s_1^{i_1} s_2^{i_2} \quad (2)$$

The denominator of a stable filter must satisfy the following condition

$$P_1(s_1, s_2) = 0 \text{ for } \bigcap_{i=1}^2 s_i \geq 0 \quad (3)$$

An equivalent 2-D digital filter transfer function can be obtained by the application of double bilinear transformation of the variable  $s_1$  and  $s_2$  in eq. (1).

### 3. REQUIRED CONDITIONS FOR A 2- VARIABLE POLYNOMIAL TO BE A VSHP

We will start with a two variable polynomial given by

$$F(s_1, s_2) = s_2 F_1(s_1) + F_2(s_1) \quad (4)$$

Where the degree of one of the variables say(  $s_2$  ) is unity, and  $F_1(s_1)$  and  $F_2(s_1)$  are polynomials in one-variables  $s_1$ . When  $s_2=0$ ,  $F(s_1, s_2)=F_2(s_1)$  shall be VSHP. Similarly, when  $s_2=\alpha$ ,  $F(s_1, s_2)=F_2(s_1)$  which shall also be VSHP

Therefore, in order that  $F(s_1, s_2)$  shall be a VSHP, the polynomials  $F_1(s_1)$  and  $F_2(s_1)$  shall be a 1-variables VSHP.

The polynomial  $F(s_1, s_2)$  will become zero when

$$s_2 = -\frac{F_2(s_1)}{F_1(s_1)} \quad (5)$$

In order that  $F(s_1, s_2)$  is VSHP, its zeroes shall lie strictly in the left-half of  $s_2$ -plane this yield

$$\text{Re}\left(\frac{F_2(s_1)}{F_1(s_1)}\right) \geq 0, \text{ for } \text{Re } s_1 \geq 0 \quad (6)$$

Where  $\text{Re}$  represents the real part

$$F_1(s_1) = (M_A + N_A) \quad (7)$$

And

$$F_2(s_1) = (M_B + N_B) \quad (8)$$

Where

$M_A$  is the Even part  $F_1(s_1)$ ,  $N_A$  is the Odd part of  $F_1(s_1, s_2)$ ,  $M_B$  is the even part of  $F_2(s_1)$  and  $N_B$  is the odd part of  $F_2(s_1, s_2)$

Eq(7) becomes equivalent to

$$M_A M_B - N_A N_B > 0 \text{ for } s_1 = j\omega_1 \text{ and } s_2 = j\omega_2 \quad (9)$$

With this condition, it is readily seen that  $F(s_1, s_2)$  will be a two-variables VSHP.

From the above discussion, we have proved the following theorem.

*Theorem 1* : A two-variables polynomial of type given in eq.(4), where one of the variables is of degree unity, will be a VSHP when the following conditions are satisfied :





- (i)  $F_1(S_1)$  and  $F_2(S_2)$  are one variable VSHP
- (ii) *real part of*  $\frac{F_2(S_1)}{F_1(S_1)}$  is positive in the polynomial  $\text{Re } S_1 > 0$

The degree of the variable  $s_2$  is unity and this may appear restrictive. This is not the case, because a higher degree in  $s_2$  can be obtained by repeating application of VSHP transformations [5].

#### 4. GENERATION OF 2-VARIABLE VSHP

In this method 2-variables VSHP is generated by using the following relationship

$$F_1(s_1, s_2) = \det \left[ \sum_{i=1}^2 A_i \Gamma_i A_i^T s_i + D \Delta D^T + G \right] \quad (10)$$

Where

$A_i$ 's and  $D$  are the upper triangular matrices with unity elements on their diagonal,  $\Gamma_i$ 's and  $\Delta$  are diagonal matrices with non-negative elements; and  $G$  is a skew-symmetric matrix. In view of VSHP transformations, we can attempt to generate 2-variable polynomial in which the degree of each variable is unity. In such a case, these matrices are as follows:

$$A_1 = \begin{bmatrix} 1 & a_1 \\ 0 & 1 \end{bmatrix}, D = \begin{bmatrix} 1 & d \\ 0 & 1 \end{bmatrix}, \Gamma = \begin{bmatrix} \alpha_1^2 & 0 \\ 0 & \alpha_2^2 \end{bmatrix}, \Delta = \begin{bmatrix} \beta_1^2 & 0 \\ 0 & \beta_2^2 \end{bmatrix} \text{ and } G = \begin{bmatrix} 0 & g \\ -g & 0 \end{bmatrix} \quad (11)$$

A SHP polynomial of 2-variables will be obtained by the substitution of the above matrices in eq.(10). This yields

$$F_1(s_1, s_2) = \sum_{i=1}^2 \alpha_i^2 \alpha_{i2}^2 s_i + \sum_{i=1}^2 \sum_{j=1}^2 \alpha_i^2 \alpha_{i2}^2 + \alpha_j^2 \alpha_{j2}^2 + \alpha_{i2}^2 \alpha_{j2}^2 (a_i - a_j)^2 s_i s_j + \sum_{i=1}^2 [\alpha_i^2 \beta_i^2 + \alpha_i^2 \beta_i^2 (a_i - d)^2] s_i + g^2 + \beta_1^2 \beta_2^2 \quad (12)$$

Very Strictly Hurwitz Polynomial is obtained by substituting  $\alpha_i=0$  in Eq.(12) yielding

$$F_1(s_1, s_2) = \sum_{i=1}^2 \sum_{j=1}^2 \alpha_{i2}^2 \alpha_{j2}^2 (a_i - a_j)^2 s_i s_j + \sum_{i=1}^2 [\alpha_i^2 \beta_i^2 + \alpha_i^2 \beta_i^2 (a_i - d)^2] s_i + g^2 + \beta_1^2 \beta_2^2 \quad (13)$$

As can be seen from eq.(13), terms  $s^2$  are not present in VSHP as opposed to SHP. In order that  $F(s_1, s_2)$  is a 2-variable VSHP, it is required that

$$a_1 \neq a_2 \quad (14)$$

Alternatively, one can start with a polynomial

$$Q(s_1, s_2) = a_{11} s_1 s_2 + a_{10} s_1 + a_{01} s_2 + a_{00} \quad (15)$$

The polynomial  $Q(s_1, s_2)$  will be a 2-variable VSHP, when

$$a_{11} > 0, a_{10} > 0, a_{01} > 0 \text{ and } a_{00} > 0 \quad (16)$$

are satisfied. In fact, eq.(15) and eq. (16) will be the same, when

$$\begin{aligned} a_{11} &= \alpha_{12}^2 \alpha_{22}^2 (a_1 - a_2)^2 \\ a_{10} &= [\alpha_{12}^2 \beta_1^2 + \alpha_{12}^2 \beta_2^2 (a_1 - d)^2] \\ a_{01} &= [\alpha_{22}^2 \beta_1^2 + \alpha_{22}^2 \beta_2^2 (a_2 - d)^2] \\ a_{00} &= g^2 + \beta_1^2 \beta_2^2 \end{aligned} \quad (17)$$

By making  $F(s_1, s_2)$  to be  $B(s_1, s_2)$  or  $Q(s_1, s_2)$  it is required to generate  $F_2(s_1, s_2)$  such the condition of theorem 1 is satisfied

**Method 1.** The polynomial  $F_2(s_1, s_2)$  can be generated as enunciated earlier and let it be given by

$$F_2(s_1, s_2) = b_{11} s_1 s_2 + b_{10} s_1 + b_{01} s_2 + b_{00} \quad (18)$$

and this will be a 2-variable VSHP provided that



$$b_{11} > 0, b_{10} > 0, b_{01} > 0 \text{ and } b_{00} > 0 \quad (19)$$

Consider the rational function

$$G_1(s) = \frac{a_{11}s_1s_2 + a_{10}s_1 + a_{01}s_2 + a_{00}}{b_{11}s_1s_2 + b_{10}s_1 + b_{01}s_2 + b_{00}} \quad (20)$$

$$M_A = (a_{11}s_1s_2 + a_{00}) \quad (21)$$

$$N_A = (a_{10}s_1 + a_{01}s_2) \quad (22)$$

$$M_B = (b_{11}s_1s_2 + b_{00}) \quad (23)$$

$$[4(a_{01}b_{01}a_{01}b_{01} + a_{00}b_{00}b_{11}b_{11}) - (a_{10}b_{01} + a_{01}b_{10} - a_{00}b_{11} - a_{11}b_{00})^2] - 64a_{01}b_{01}a_{11}b_{11}a_{00}b_{00}a_{10}b_{10} < 0 \quad (26)$$

It is also observed that eq.(26) is satisfied under a sufficient condition

$$a_{10}b_{01} + a_{01}b_{10} = a_{00}b_{11} + a_{11}b_{00} \quad (27)$$

**Method II :** As an alternative, we can generate a large class of functions which satisfy the condition (26). It is already shown that a two-variable VSHP  $F(s_1, s_2)$  can be generated

Consider

$$G_2(s_1, s_2) = \frac{K_1 F_1(s_1, s_2) + K_2 \frac{\partial F_1(s_1, s_2)}{\partial s_1} + K_3 \frac{\partial F_1(s_1, s_2)}{\partial s_2}}{F_1(s_1, s_2)} \quad (28)$$

Obviously, the real part of  $G_2(s_1, s_2)$  is given by

$$\text{Re}(G_2(j\omega_1, j\omega_2)) = K_1 + \frac{K_2(a_{01}a_{10} + a_{01}a_{10}\omega_1^2) + K_3(a_{01}a_{10} + a_{10}a_{01}\omega_2^2)}{(a_{00} - a_{11}\omega_1\omega_2)^2 + (a_{10}\omega_1 + a_{01}\omega_2)^2} \quad (29)$$

$$N_B = (b_{11}s_1 + b_{00}s_2) \quad (24)$$

This yield

$$M_A M_B - N_A N_B |_{s_1=j\omega_1, s_2=j\omega_2} = a_{11}b_{11}\omega_1^2\omega_2^2 + \omega_1\omega_2(a_{10}b_{01} + a_{01}b_{10} - a_{00}b_{11} - a_{11}b_{00} + a_{10}b_{10}\omega_2 + a_{01}b_{01}\omega_1 - 22 + a_{00}b_{00}) > 0 \quad (25)$$

after some algebraic manipulations, it can be shown that eq.(25) is equivalent to the condition

## 5. DESIGN TECHNIQUES

In the proposed design technique, the derived 2-variables VSHP is assigned to the denominator of analog transfer function as follows:

$$H(s_1, s_2) = \frac{N(s_1, s_2)}{D(s_1, s_2)} \quad (30)$$

The digital equivalent is obtained by using double bilinear transformation [4]. The mean square error between the ideal magnitude response  $|H_1(\omega_1, \omega_2)|$  and the designed magnitude

Response  $|H_d(\omega_1, \omega_2)|$  is used as an objective function for optimization:

$$E_{MSE}(\omega_1, \omega_2, \phi) = |H_1(\omega_1, \omega_2)| - |H_d(\omega_1, \omega_2, \phi)| \quad (31)$$

And



$$E_i^2(\omega_1, \omega_2, \phi) = \sum_{\omega_1, \omega_2} \sum_{I_{PS}} E_{Mag}^2(\omega_1, \omega_2, \phi) \quad (32)$$

Where  $\psi$  is the coefficient vector calculated by minimizing eq(31), and  $I_{PS}$  is the set of all frequencies in the passband and stopband. Minimization of this objective function is carried out using nonlinear Matlab. optimization technique to find the vector  $\psi$ .

### Design Example

A two dimensional digital filter with the following amplitude specifications is designed by using VSHP polynomial:

$$|H_i(\omega_1, \omega_2)| = \begin{cases} 1 & \text{for } 0 \leq \sqrt{\omega_1^2 + \omega_2^2} \leq \frac{\pi}{4} \\ 0 & \text{for } \frac{\pi}{2} \leq \sqrt{\omega_1^2 + \omega_2^2} \leq \pi \end{cases}$$

For this purpose three 2-variable VSHP of the form (30) or (31) are cascaded and the digital form is obtained by using triple bilinear transformation as follows

$$D_1(s_1, s_2) = s_2 F_1(s_1) + F_2(s_1)$$

$$D_2(s_1, s_2) = s_1 F_3(s_2) + F_4(s_2)$$

The designed frequency is

$$H_D(Z_1, Z_2) = \frac{\sum_{i=0}^2 \sum_{j=0}^2 a(i, j) Z_1^{-i} Z_2^{-j}}{D(Z_1, Z_2)}$$

Then minimization of the mean square error of eq(31) was performed using GA.[6-8] First we generate the first generation containing many chromosomes. Each chromosome will

contain 16 genes since we are designing 3x3 IIR filter. The fitness function used here the objective function which is difference between the obtained response and the ideal response. Since stability is guaranteed, we will the genes that minimize the fitness function are the best genes. The algorithm was implemented using MATLAB optimization toolbox. Several values of number of generation of GA and cut-off frequency was used, results are shown in Fig.1,2,and 3.

### CONCLUSIONS

In this paper, we have presented an iterative method to design digital IIR filter using VSHP with genetic algorithm. We have shown that GA is robust

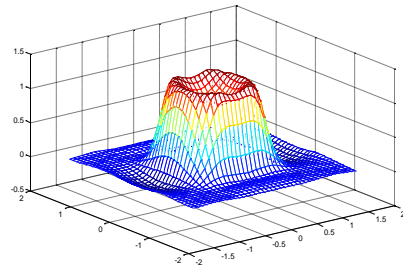


Figure 1 Magnitude response of designed filter with 100 chromosomes in the first generation

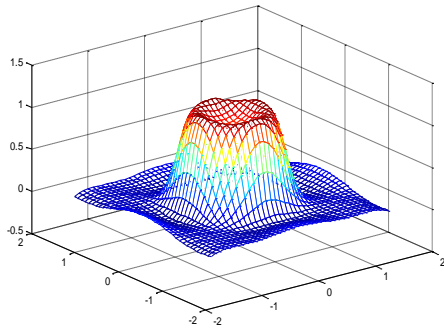


Figure 2 Magnitude response of designed filter with 150 chromosomes in the first generation

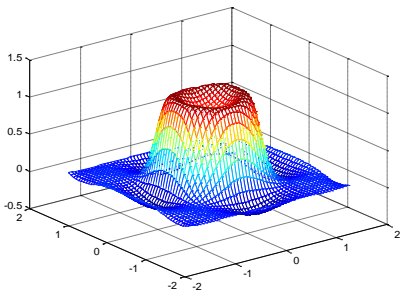


Figure 3 Magnitude response of designed filter with 200 chromosomes in the first generation

## REFERENCES

- [1] [1] P.K. Rajan, H. C , Reddy, M . N . S. swamy and V. Ramachandran, "Generation of two-dimensional digital transfer functions without non-essential singularities of the second kind ", IEEE Trans. On Acoustics, Speech and Signal Processing, V o l . . ASSP-28, pp. 216-223, April 1980.
- [2] V. Ramachandran, 31. Ahmadi, "Design of 2-D Stable Analog and recursive digital filters using properties of even or odd parts of Hurwitz Polynomials ", Journal of Franklin Institute ,Vol. 315, No. 4 , pp. 259-267, April 1983 .
- [3] V. Ramachandran, M. Ahmadi, "Design of Stable 2-D Recursive filters by generation of VSHP using terminated n-port gyrator networks ", Journal of Franklin Institute , Vol. 316, No. 5, pp. 373-380, No. 1983.
- [4] M. Ahmadi, V. Ramachandran, "A new method for generating 2-variable VASHP and its application in the design of 2-dimensional (2-D) recursive digital filter with prescribed magnitude and constant group delay response", Proc . of IEE. P t . G. Vol. 131, NO. 4, pp. 151-155, Aug. 1984.
- [5] Y.A. Abiril. M. Ahmadi, V. Ramachandran, "An alternative approach in generation of two variable VSHP and its application in 2-D recursive digital filter design satisfying a prescribed magnitude with or without constant group delay specification s "Proc . ISCAS'85, Kyoto, Japan, June 85. pp. 10'93-1096.



- [6] Hohn, F.E. "Elementary matrix Algebra" YcXillan Company, 1964.
- [7] R. Fletcher, J. D. Powell, "A Rapid Descent Method for minimization " , Computer Journal, V01.6, 1964, pp. 163-168.
- [8] I. D. Suckley, "Genetic algorithm in the design of FIR 2. R. Cemes, and D. Ait-Boudaoud, "Genetic approach to filters", *IEE Proc. G.*, Vo1.138, pp. 234-238, April 1991.



المؤتمر العربي الليبي الدولي الخامس للهندسة الكهربائية والإلكترونية 2010/10/26-23 طرابلس ليبيا